

VOLUME 12, NUMBERS 1-4, 1999

ISSN 0965-9773

---

**SPECIAL VOLUME — PART A**

---

**THE FOURTH INTERNATIONAL CONFERENCE ON  
NANOSTRUCTURED MATERIALS (NANO '98)  
JUNE 14-19, 1998, STOCKHOLM, SWEDEN**

---

---

# *Nano* **STRUCTURED MATERIALS**

---

**Guest Editors:    *Mamoun Muhammed*  
                         *K.V. Rao***

---

---

---

DISTRIBUTION STATEMENT A:  
Approved for Public Release -  
Distribution Unlimited



**Pergamon**

# Nano STRUCTURED MATERIALS

ISSN 0965-9773

(An Acta Metallurgica, Inc. Journal)

## Principal Editors:

**T. Tsakalakos**  
*Rutgers University, USA*

**B.H. Kear**  
*Rutgers University, USA*

**R.W. Siegel**  
*Rensselaer Polytechnic  
Institute, USA*

## Editorial Staff:

**K. Finnerty**, *Production Editor*

## Editorial Board:

**L.E. Brus**  
*AT&T Bell Laboratories, USA*

**H. Gleiter**  
*Vorstand Des Forschungszentrum  
Karlsruhe  
GMBH, Germany*

**R.E. Smalley**  
*Rice University, USA*

**R.W. Cahn**  
*University of Cambridge, UK*

**G. Thomas**  
*Univ. of California-Berkeley, USA*

**M. Doyama**  
*Nishi-Tokyo University, Japan*

**S. Ranganathan**  
*Indian Institute of Science, India*

**M.J. Yacamán**  
*UNAM, Mexico*

## Associate Editors:

**I.A. Aksay**  
*Princeton University, USA*

**H. Hahn**  
*TH Darmstadt, Germany*

**K. Lu**  
*Chinese Academy of Sciences  
People's Republic of China*

**R.D. Shull**  
*US Department of Commerce,  
USA*

**R.S. Averback**  
*Univ. of Illinois-Champaign, USA*

**S. Iijima**  
*NEC Corporation, Japan*

**M. Magini**  
*ENEA, Italy*

**A. Simopoulos**  
*National Center for Scientific  
Research "Demokritos," Greece*

**A.E. Berkowitz**  
*Univ. of California-San Diego,  
USA*

**A. Inoue**  
*Tohoku University, Japan*

**M.J. Mayo**  
*The Pennsylvania State  
University, USA*

**B.H. Suits**  
*Michigan Technological  
University, USA*

**B. Cantor**  
*University of Oxford, UK*

**A.F. Jankowski,**  
*Lawrence Livermore National  
Laboratory, USA*

**M. Muhammed**  
*Royal Inst. of Technology,  
Sweden*

**A. Thörlén**  
*Chalmers University of  
Technology, Sweden*

**D.M. Cox**  
*Exxon Research & Eng. Co., USA*

**W.L. Johnson**  
*California Inst. of Tech., USA*

**A. Rosén**  
*Chalmers Univ. of Tech., Sweden*

**K. Urban**  
*Forschungszentrum Jülich,  
Germany*

**L.J. de Jongh**  
*Rijksuniversiteit Leiden, The  
Netherlands*

**K. Klabunde**  
*Manhattan, KS*

**I.K. Schuller**  
*Univ. of California-San Diego,  
USA*

**J.R. Weertman**  
*Northwestern University, USA*

**M.S. Dresselhaus**  
*Massachusetts Institute of  
Technology, USA*

**L.C. Klein**  
*Rutgers University, USA*

**R. Schwarz**  
*Los Alamos National Laboratory,  
USA*

**J. Ying**  
*Massachusetts Institute of  
Technology, USA*

**G. Hadjipanayis**  
*University of Delaware, USA*

**C.C. Koch**  
*North Carolina State University,  
USA*

**U. Landman**  
*Georgia Inst. of Tech., USA*

**Editorial Office:** Communications to the Editors and all manuscripts should be sent to Prof. Thomas Tsakalakos, *NanoSTRUCTURED MATERIALS*, College of Engineering, PO Box 909, Brett and Bowser Roads, Piscataway, NJ 08855-0909, USA.

**Publishing, Advertising and Subscription Offices:** Elsevier Science Inc., 655 Avenue of the Americas, New York, NY 10010, USA, E-mail Address: [ESUK.USA@ELSEVIER.COM](mailto:ESUK.USA@ELSEVIER.COM); or Elsevier Science Ltd, The Boulevard, Langford Lane, Kidlington, Oxford, OX51GB, England.

**Published 8 times per year** in the months of February, March, May, June, August, September, October and November. Annual institutional subscription rate (1999): For customers in Europe, The CIS and Japan: NLG 1,704.00. For customers in all other countries: US\$865.00. Special Nano 1998 Conference Optional Volume: For customers in Europe, The CIS and Japan: NLG 1,182.00. For customers in all other countries: US\$600.00. Dutch Guilder prices exclude VAT. Non-VAT registered customers in the European Community will be charged the appropriate VAT in addition to the price listed. Prices include postage and insurance and are subject to change without notice.

**For Advertising Orders & Inquiries:** **North & South America:** Tino DeCarlo, Elsevier Science Inc., 655 Avenue of the Americas, New York, NY 10010-5107, USA. Tel: (212) 633-3815; Fax: (212) 633-3820; E-Mail: [t.decarlo@elsevier.com](mailto:t.decarlo@elsevier.com) **International:** Rachel Gresie-Farthing, Advertising Department, Elsevier Science, The Boulevard, Langford Lane, Kidlington, Oxford, OX5 1GB, United Kingdom. Tel: (+44) (0) 1865 843565; Fax: (+44) (0) 1865 843976; E-Mail: [media@elsevier.co.uk](mailto:media@elsevier.co.uk) **Japan:** Advertising Department, Elsevier Science K.K., Tel: (81) (3) 5561 5033; Fax: (81) (3) 5561 5047.

Any inquiry relating to subscriptions should be sent to:

**The Americas:** Elsevier Science Customer Support Department, P O Box 945, New York, NY 10010, USA [Tel: (+1) 212-633-3730/1-888 4ES-INFO. Fax: (+1) 212-633-3680. E-mail: [usinfo-f@elsevier.com](mailto:usinfo-f@elsevier.com)].

**Japan:** Elsevier Science Customer Support Department, 9-15 Higashi-Azabu 1-chome, Minato-ku, Tokyo 106, Japan [Tel: (+3) 5561-5033. Fax: (+3) 5561-5047. E-mail: [kyl04035@niftyserve.or.jp](mailto:kyl04035@niftyserve.or.jp)].

**Asia Pacific (excluding Japan):** Elsevier Science (Singapore) Pte Ltd, No. 1 Temasek Avenue, 17-01, Millenia Tower, Singapore 039192. [Tel: (+65) 434-3727. Fax: (+65) 337-2230. E-mail: [asiainfo@elsevier.com.sg](mailto:asiainfo@elsevier.com.sg)].

**Rest of the World:** Elsevier Science Customer Service Department, P O Box 211, 10011 AE Amsterdam, The Netherlands, [Tel: (+31) 20-485-3757. Fax: (+31) 20-485-3432. E-mail: [nlinfo-f@elsevier.nl](mailto:nlinfo-f@elsevier.nl)]. For members of the TMS - \$95.00. For members of co-operating societies of ActaMETALLURGICA - \$95.00. For members of sponsoring societies of ActaMETALLURGICA - \$95.00.



# *Nano*STRUCTURED MATERIALS

Companion journal to  
*Acta MATERIALIA* and *Scripta MATERIALIA*

Principal Editors

Thomas Tsakalakos\*

Rutgers University

Bernard H. Kear

Rutgers University

Richard W. Siegel

Rensselaer Polytechnic Institute

## **SPECIAL VOLUME — Part A**

The Fourth International Conference on Nanostructured Materials (NANO '98)  
June 14–19, 1998, Stockholm, Sweden

*Guest Editors:*

*Mamoun Muhammed and K.V. Rao  
Royal Institute of Technology,  
Stockholm, Sweden*

\* Deputy Editor: Professor William E. Mayo



**PERGAMON**

**Copyright © 1999 Acta Metallurgica Inc. All rights reserved**

**Copyright Notice:** It is a condition of publication that manuscripts submitted to this journal *have not been published and will not be simultaneously submitted or published elsewhere*. By submitting a manuscript, the authors agree that the copyright for their article is transferred to the publisher, if and when the article is accepted for publication. However, assignment of copyright is not required from authors who work for organizations which do not permit such assignment. The copyright covers the exclusive rights to reproduce and distribute the article, including reprints, photographic reproductions, microform or any other reproductions of similar nature and translations. No part of this publication may be reproduced, stored in a retrieval system or transmitted in any form or by any means: electrostatic, magnetic tape, mechanical, photocopying, recording or otherwise without permission in writing from the copyright holder.

Please contact Elsevier Science Ltd., who are licensed to administer the copyright of Acta Metallurgica Inc., when seeking use of the copyright material.


**Photocopying.** Single photocopies of single articles may be made for personal use as allowed by national copyright laws. Permission of the publisher and payment of a fee is required for all other photocopying, including multiple or systematic copying, copying for advertising or promotional purposes, resale, and all forms of document delivery. Special rates are available for educational institutions that wish to make photocopies for non-profit educational classroom use.

In the USA, users may clear permissions and make payments through the Copyright Clearance Center, Inc., 222 Rosewood Drive, Danvers, MA 01923, USA; phone: (978) 750-8400, fax: (978) 750-4744, and in the UK through the Copyright Licensing Agency Rapid Clearance Service (CLARCS), 90 Tottenham Court Road, London W1P 0LP, UK; phone: (+44) 171 436 5931; fax: (+44) 171 436 3986. Other countries may have a local reprographic rights agency for payments.

**Permission for other use:** The copyright owner's consent does not extend to copying for general distribution, for promotion, for creating new works, or for resale. All inquiries regarding copyright material from this publication, other than reproduction through the Copyright Clearance Center, should be directed to Elsevier Science Ltd., PO Box 800, Oxford OX5 1DX, U.K. Phone: 44-1865 843830; Fax: 44-1865 853333; E-mail: [permissions@elsevier.co.uk](mailto:permissions@elsevier.co.uk)

Whilst every effort is made by the publishers and editorial board to see that no inaccurate or misleading data, opinion or statement appears in this journal, they wish to make it clear that the data and opinions appearing in the articles and advertisements herein are the sole responsibility of the contributor or advertiser concerned. Accordingly, the publishers, the editorial board and editors, and their respective employees, officers and agents, accept no responsibility whatsoever for the consequences of any such inaccurate or misleading data, opinion or statement.

**Contents Direct** delivers the table of contents of this journal, by e-mail, approximately two to four weeks prior to each issue's publication. To subscribe to this free service, complete and return the form at the back of this issue, or send an e-mail message to [cdsubs@elsevier.com](mailto:cdsubs@elsevier.com).

 The paper used in this publication meets the minimum requirements of American National Standard for Information Sciences-Permanence of Paper for Printed Library Materials, ANSI Z39.48-1984

**Printed in the USA**

---

# *Nano*STRUCTURED MATERIALS

(An Acta Metallurgica, Inc. Journal)

## *AIMS AND SCOPE*

Advances in high performance materials for a variety of applications are now becoming increasingly dependent on our ability to control the size, distribution and morphology of their constituent grains or phases at the nanoscale level (less than 100 nm). Capabilities for synthesizing such nanostructured materials are becoming available, so that it is possible to produce the quantities of materials needed for prototype development and testing.

The primary mission of the journal for *Nano*STRUCTURED MATERIALS is to provide an international and interdisciplinary forum for the effective dissemination of scientific and technical information on synthesis, processing, theory, computational modeling, structure, properties, performance and applications of nanostructured materials. The materials of interest include metals, ceramics, polymers, semiconductors, superconductors, and magnetic, optical and electronic materials, and their composites. Synthesis routes of interest include chemical and physical vapor deposition, mechanical milling, gas phase pyrolysis and condensation, electrodeposition, cryochemical synthesis, laser pyrolysis, gel synthesis, and other methods with applications for structural materials, coatings, thin film devices, membranes, catalysts, sensors, etc.

The following are major areas of concentration of the journal:

- Clusters and cluster assembled materials;
- Ultrafine powders, thin films, coatings, multilayers, and fibrous materials;
- Structure and characterization of nanophases;
- Synthesis and processing of nanostructured materials: physical, chemical, mechanical, and biological methods;
- Properties: mechanical, electrical, optical, rheological, magnetic, etc.;
- Performance and applications: tribology, corrosion, etc.;
- Related fields such as: nanolithography, nanodevices, etc.

*Nano*STRUCTURED MATERIALS will rapidly publish research papers and regular invited review papers on scientific and technical issues in this rapidly evolving field. The journal will strive to maintain an international representation in published papers, and will, from time to time, co-sponsor regional, national and international meetings.

## PREFACE

A remarkable group of almost 500 participants from 40 countries 'self-assembled' in Stockholm for the NANO'98 conference held during June 14-19, 1998. This international conference, with a considerably larger number of participants than in the past three meetings in this series, signified considerable maturity and significant growth in multidisciplinary scientific activity on a global scale.

The well-attended NANO'98 conference offered a "Smorgasbord" (in Swedish Smörgåsbord) of the latest exciting state-of-the-art developments in the field. In total, 572 papers were presented at the conference. There were plenary talks by two Nobel Laureates, 58 invited talks, and an equal number of oral contributory presentations. A unique feature of 'Invited Poster' session consisting of 41 presentations was introduced to highlight some of the novel contributions. This session was particularly appreciated both by the presenters and the participants because of the opportunity for extended informal discussions on specific topics. In addition, three poster-sessions were scheduled covering over 414 presentations, which were displayed till late in the evening. Pouring rain from the skies over Stockholm kept the participants indoors for extended discussions at the poster sessions with good attendance, despite the late hours.

From the contents of the presentations we see clear trends of exploiting the driving force of nanotechnology within the limits of imagination. Chemists are getting closer to post modern alchemy wherein dream materials are being modeled and synthesized almost at a molecular level. Physicists and materials scientists have engineered, atom by atom, features with increasing ease. The art of developing functionalized nanostructured materials exploiting unusual interfacial properties seems to have produced hitherto unknown man-made materials. The consequent natural lead to the world of self-assembled systems appears to bring the field closer to mimicking nature. Exploitations of the size-related properties of nanostructured materials include transparent-to-opaque ceramics, superplasticity, catalysts, and materials with enhanced mechanical properties (e.g. unusually hard material tools etc.), just to name a few. Complex tailored multilayer systems have produced value-added components of promise like the GMR heads, unusual soft and hard magnets, quantum dots, ...

A major effort by the conference Chairs was to ensure the participation of scientists from the "Eastern" countries and to encourage a significant amount of participation from students. It is pleasing to point out that over 90 students have participated in the conference and over 60 prominent scientists representing most of the "Eastern" countries have made important contributions during the conference.

It is a pleasure for us to thank the various individuals who have generously contributed their efforts and time to ensure the success of the conference. The conference chairs would like to thank the International and National Advisory Committees for their suggestions and support for the conference. We extend our special appreciation to the members of the Scientific Programme Committee, who struggled for three days in Stockholm reading through over 730 submitted abstracts in order to assemble the comprehensive programme. The local organizing committee, consisting of a significant number of graduate students and Post doctorals at the Royal Institute of Technology, has worked intensely with all the details of the conference. They also spent very many late nights after the conference to assemble and prepare the camera-ready format of the 400 manuscripts we received. In this, we are especially grateful to Professor Thomas Tsakalakos for his professional help and friendly assistance in finalizing the Proceedings. We specially thank Dr. Andrei Zagorodni for his committed and enthusiastic efforts in the formidable task of handling the manuscripts to finalize the proceedings. The

professional services of Stockholm Convention Bureau, Mrs. Britta Sjöblom in particular, is highly appreciated.

Generous financial support from several organizations has made it possible to hold the conference in Stockholm. We acknowledge and appreciate the support by the following organizations:

Royal Institute of Technology, Sweden  
Swedish Consortium on Clusters and Ultrafine Particles, Sweden  
Brinell Center, Royal Institute of Technology, Sweden  
European Consortium for Nanophase Materials, Switzerland  
Acta Metallurgica Inc., USA  
Alps Electric Company, Japan  
Canon Centre City, Sweden  
Carl Tryggers Stiftelse, Sweden  
Elsevier Science Inc., Switzerland  
Finnair, Finland  
The Office of Naval Research ONR, USA  
European Research Office of the US Army, USARSD-UK  
Swedish Natural Science Research Council, NFR, Sweden  
Swedish Research Council for Engineering Sciences, (TFR), Sweden  
Swedish National Board for Industrial and Technical Development (NUTEK)  
Swedish Royal Academy of Science, Nobel Committee for Physics, Sweden  
Swedish Royal Academy of Science, Nobel Committee for Chemistry, Sweden

We gather from all the feedback we are constantly receiving through numerous letters, e-mails, and personal compliments, the NANO'98 conference held in Stockholm was highly appreciated. NANO'98 was an event to remember marked by outstanding performances from all the attendees, and the strong interactions among the different disciplines. It asserted a high promise and dynamism to this important field of science and technology. The outcome of NANO'98 is documented in the proceedings herewith.

Finally, we want to thank our families, Sunita, Charlotte, Alexandra, Jasmina and Marion who were truly supportive to us before, during, and in the aftermath of NANO'98.

STOCKHOLM, May 1999

Mamoun Muhammed  
K.V. Rao

Professor Mamoun Muhammed  
Materials Chemistry Division  
Royal Institute of Technology  
Brinellvägen 23, II  
SE-100 44 Stockholm - Sweden

Tel+46-8-790 8158 Fax: +46-8-790 9072  
Sec: +468-790 9072  
email: mamoun@matchem.kth.se

---

## **SPECIAL VOLUME**

***The Fourth International Conference on Nanostructured Materials  
(NANO '98)  
June 14–19, 1998, Stockholm, Sweden***

### **Contents – Part A**

Esaki, L.	1	The Evolution of Nanoscale Quantum Effects in Semiconductor Physics
Brinzanik, R., Jensen, P. J., Bennemann, K. H.	9	Simulation of the Magnetic Properties During the Growth of Nanostructured Thin Films
Wakayama, Y., Tanaka, S.	13	Fabrication of Nanoscale Heterojunction of Si/Au and Si/Ag by Surface Droplet Epitaxy
Heim, U., Schwitzgebel, G.	19	Electrochemistry of Nanocrystalline Copper
Yoo, S. H., Sudarshan, T. S., Sethuram, K., Subhash, G., Dowding, R. J.	23	Consolidation and High Strain Rate Mechanical Behavior of Nanocrystalline Tantalum Powders
Shafi, K. V. P. M., Gedanken, A.	29	Sonochemical Approach to the Preparation of Barium Hexaferrite Nanoparticles
Valiev, R. Z., Alexandrov, I. V.	35	Nanostructured Materials from Severe Plastic Deformation
Kitamoto, Y., Abe, M.	41	Nanostructured Oxide Films by Ferrite Plating with Sonochemistry
Magnusson, M. H., Deppert, K., Malm, J.-O., Bovin, J.-O., Samuelson, L.	45	Size-Selected Gold Nanoparticles by Aerosol Technology
Schoeman, B. J., Higberg, K., Sterte, J.	49	Nanoparticles of Microporous Materials

Trudeau, M. L.	55	Nanocrystalline Fe and Fe-Riched Fe-Ni Through Electrodeposition
Reddy, E. P., Rojas, T. C., Sanchez Lopez, J. C., Dominguez, M., Roldan, E., Campora, J., Palma, P., Fernandez, A.	61	Preparation and Characterisation of Cobalt Oxide Nanosized Particles Obtained by an Electrochemical Method
O'Connor, C. J, Seip, C. T., Carpenter, E. E., Li, S., John, V. T.	65	Synthesis and Reactivity of Nanophase Ferrites in Reverse Micellar Solutions
Meyer, F., Dierstein, A., Beck, Ch., Härt, W., Mathur, S., Veith, M. Hempelmann, R.	71	Size-Controlled Synthesis of Nanoscaled Aluminium Using Heterobimetallic Alkoxide Precursors via Water/Oil Microemulsions
Tsuzuki, T., McCormick, P. G.	75	Mechanochemical Synthesis of Metal Sulphide Nanoparticle
Elihn, K., Otten, F., Boman, M., Kruis, E., Fissan, H., Carlsson, J.-O.	79	Nanoparticle Formation by Laser-Assisted Photolysis of Ferrocene
Hornyak G. L., Dillon, A. C., Parilla, P. A., Schenider, J. J., Czap, N., Jones, K. M., Fasoon, F. S., Mason, A., Heben, M. J.	83	Template Synthesis of Carbon Nanotubes
Sivamohan, R., Takahashi, H., Kasuya, A., Tohji, K., Tsunekawa, S., Ito, S., Jeyadevan, B.	89	Liquid Chromatography Used to Size-Separate the Amphiphilic-Molecules Stabilised Nano-Particles of CdS in the 1-10 nm Range
Srdic, V. V., Winterer, M., Miehe, G., Hahn, H.	95	Different Zirconia-Alumina Nanopowders by Modifications of Chemical Vapor Synthesis
Levoska, J., Tyunina, M., Leppävuori, S.	101	Laser Ablation Deposition of Silicon Nanostructures
Schurack, F., Eckert, J. Schultz, L.	107	High Strength Al-Alloys with Nano-Quasicrystalline Phase As Main Component

Oshima, R., Yamamoto, T. A., Mizukoshi, Y., Nagata, Y., Maed, Y.	111	Electron Microscopy of Noble Metal Alloy Nanoparticles Prepared by Sonochemical Methods
Bykov, Yu., Ereemeev, A., Egorov, S., Ivanov, V., Kotov, Yu., Khrustov, V., Sorokin, A.	115	Sintering of Nanostructural Titanium Oxide Using Millimetre-Wave Radiation
Kotov, Y. A., Samatov, O. M.	119	Production of Nanometer-Sized AlN Powders by The Exploding Wire Method
Tamou, Y., Tanaka, S.	123	Formation and Coalescence of Tungsten Nanoparticles Under Electron Beam Irradiation
Schlorke, N., Weiss, B., Eckert, J., Schultz, L.	127	Properties of Mg-Y-Cu Glasses with Nanocrystalline Particles
Tajika, M., Matsubara, H., Rafaniello, W.	131	Microstructural Development in AlN Composite Ceramics
Sotelo, J. A., Niklasson, G. A.	135	Optical Properties of Quasifractal Metal Nanoparticle Aggregates
Tcherdyntsev, V. V., Kaloshkin, S. D., Tomilin, I. A., Shelekhov, E. V., Baldokhin, Yu. V.	139	Formation of Iron-Nickel Nanocrystalline Alloy by Mechanical Alloying
Jiang, J. Z., Yang, X. L., Gao, L., Guo, J. K., Jiang, J. Z.	143	Synthesis and Characterization of Nanocrystalline Zinc Ferrite
Janackovic, Dj., Orlovic, A., Skala, D., Drmanic, S., Kostic-Gvozdenovic, Lj., Jokanovic, V., Uskokovic, D.	147	Synthesis of Nanostructured Mullite from Xerogel and Aerogel Obtained by the Nonhydrolytic Sol-Gel Method
Balamurugan, B., Mehta, B. R., Sharma, S. K.	151	Fabrication and Characterization of $Cd_xZn_{1-x}S$ Nanoparticles
Lazar, K., Beyer, H. K., Onyestyak, Gy., Jönsson, B. J., Varga, L. K., Pronier, S.	155	Iron Nanoparticles in X and Y Zeolites
Jachimowicz, M., Fadeeva, V. I., Matyja, H.	159	High Energy Ball Milling of $Co_{89}B_{11}$ Powders



Zhang, Z., Wahlberg, S., Wang, M., Muhammed, M.	163	Processing of Nanostructured WC-Co Powder from Precursor Obtained by Co-precipitation
Szewczak, E Presz, A., Witek, A., Wyrzykowski, J. W., Matyja, H.	167	Microstructure and Phase Composition of Mechanically Alloyed and Hot Pressed Ti-Al Alloys
Szewczak, E., Wyrzykowski, J. W.	171	Influence of the Mechanical Alloying Parameters On Crystallite Size of Ti-Al Powders
Kakimoto, K. I., Wakai F., Bill, J, Aldinger, F.	175	Fabrication of Polycarbosilane-Derived SiC Bulk Ceramics by Carbothermic Reduction
Lucas, E., Klabunde, K. J.	179	Nanocrystals as Destructive Adsorbents for Mimics of Chemical Warfare Agents
Seip, C. T., O'Connor, C. J.	183	The Fabrication and Organisation of Self-Assembled Metallic Nanoparticles Formed in Reverse Micelles
Liu, W., McCormick, P.G.	187	Formation and Magnetic Properties of Nanosized $\text{Sm}_2\text{Co}_{17}$ Magnetic Particles via Mechanochemical / Thermal Processing
Veith, M., Atherr, A., Lecerf, N., Mathur, S., Valtchev, K., Fritscher, E.	191	Molecular Precursor Approach to Nano-Scaled Ceramics and Metal/Metal Oxide Composites
Begin-Colin, S., Girot, T., Mocellin, A., Le Caër, G.	195	Kinetics of Formation of Nanocrystalline $\text{TiO}_2$ II By High Energy Ball-Milling of Anatase $\text{TiO}_2$
Yu, J. H., Kim, S. Y., Lee, J. S., Ahn, K. H.	199	In-situ Observation of Formation of Nanosized $\text{TiO}_2$ Powders in Chemical Vapor Condensation
Hofmeister, H., Ködderitzsch, P.	203	Nanosized Silicon Particles by Inert Gas Arc Evaporation

---

Hofmeister, H., Drost, W.-G., Berger, A.	207	Oriented Prolate Silver Particles in Glass - Characteristics of Novel Dichroic Polarizers
Yelsukov, E. P., Mikhailik, O. M., Konygin, G. N., Mikhailova, S. S., Povstugar, V. I.	211	Phase Composition Study of Bulk and Surface Layers of Stabilized Iron Powder
Li, S., El-Shall, M. S.	215	Synthesis and Characterization of Photochromic Molybdenum and Tungsten Oxide Nanoparticles
Wu, X. J., Du, L. G., Zhang, H. F., Liu, J. F., Zhou, Y. S., Li, Z. Q., Xiong, L. Y., Bai, Y. L.	221	Synthesis and Tensile Property of Nanocrystalline Metal Copper
Degen, A., Macek, J.	225	Preparation of Submicrometer Nickel Powders by the Reduction from Nonaqueous Media
Werkmeister, K.-St., Rullang, F., Koch, M., Heyer, M., Schwitzgebel, G.	229	Physico-Chemical Characterization of Nanocrystalline (Ni, Fe)
Bender Koch, C., Jiang, J. Z., Mörup, S.	233	Mechanical Milling of Fe <sub>3</sub> O <sub>4</sub> /SiO <sub>2</sub> Oxides: Formation of an Amorphous Fe(II)-Si-O-Containing Phase
Wang, M., Zhang, Yu, Muhammed, M.	237	Synthesis and Characterisation of Nano-Engineered Thermoelectric Skutterudite CoSb <sub>3</sub> via Solution Chemistry Route
Iwama, S., Fukaya, T., Tanaka, K., Ohshita, K., Sakai, Y.	241	Nanocomposite Powders of Fe-C System Produced by the Flowing Gas Plasma Processing
Takacs, L., Mossion, A., Lazar, K., Varga, L. K., Pardavi-Horvath, M., Bakhshai, A.	245	ZnO-Fe Nanocomposites via Ball Milling and Annealing
Tellkamp, V. L., Lavernia, J.	249	Processing and Mechanical Properties of Nanocrystalline 5083 Al Alloy

Glumac, N. G., Skandan, G., Chen, Y. J., Kear, B. H.	253	Particle Size Control During Flat- Flame Synthesis of Nanophase Oxide Powders
Möller, A., Hahn, H.	259	Synthesis and Characterization of Nanocrystalline Ni/ZrO <sub>2</sub> Composite Coatings
Tyunina, M., Levoska, J., Koivusaari, J., Leppävuori, S.	263	Agglomeration and Surface Morphology During Pulsed Laser Deposition of Pb-Zr-Ti-O
Dragieva, I., Stoeva, S., Stoimenov, P., Pavlikianov, E., Klabunde, K.	267	Complex Formation in Solutions For Chemical Synthesis of Nanoscale Particles Prepared by Borohydride Reduction Process
Iqbal, Z., Vijayalakshmi, S., Grebel, H.	271	Microstructure and Optical Properties of Nanostructured Silicon Thin Films and Artificial Dielectrics
Keghelian, P., Melinon, P., Perez, A.	277	Properties of Silicon and Silicon- Carbon Cluster Assembled Films
Westergren, J., Grönbeck, H., Rosén, A., Nordholm, S.	281	Molecular Dynamics Simulation of Metal Cluster Cooling and Heating in Noble Gas Atmosphere
Johansson, C., Åklint, T., Hanson, M., Andersson, M., Tarras-Wahlberg, N., Olsson, E., Wäppling, R., Rosen, A.	287	Deposited Nano-Metre Sized Iron Clusters
Pomogailo, A. D.	291	Polymer-Immobilized Nanoscale and Cluster Metal Particles
Dmitruk, N., Lepeshkina, T., Pavlovska, M., Zabashta, L.	295	Polarizability of Gold Clusters on the GaAs surface
Azzaoui, M. El., Hou, M., Pattyn, H., Verheyden, J., Deweerdt, W., Kooops, G., Zhang, G. L.	299	Lattice Dynamics of Co Nanoparticles in Ag
Negrier, M., Tuaillon, J., Dupuis, V., Tonon, C., Perez, A.	303	Magnetic Co-Sm Mixed-Cluster Assembled Materials

Prevel, B., Palpant, B., Lerme, J., Pellarin, M., Treilleux, M., Saviot, L., Duval, E., Perez, A., Broyer, M.,	307	Comparative Analysis of Optical Properties of Gold and Silver Clusters Embedded in an Alumina Matrix
Xenoulis, A. C., Doukellis, G., Poturiadis, C., Boukos, N., Vlachos, D. S., Tsakalakos, Th.	311	The Size Distribution of Metal Clusters Produced in Plasma-Discharge Hollow-Cathode Source
Saenger, D. U.	315	On the Theory of the Optical Response of an Ensemble of Nanoparticles
Lau, M. L., Gupta, V. V., Lavernia, E. J.	319	Particle Behavior of Nanocrystalline 316-Stainless Steel During High Velocity Oxy-Fuel Thermal Spray
Van Swygenhoven, H., Spaczer, M., Farkas, D., Caro, A.	323	The Role of the Grain Size and the Presence of Low and High Angle Grain Boundaries in the Deformation Mechanism of Nanophase Ni: A Molecular Dynamics Computer Simulation.
Kiss, L. B., Soderlund, J., Niklasson, G. A., Granqvist, C. G.	327	The Real Origin of Lognormal Size Distributions of Nanoparticles in Vapour Growth Processes
Doyama, M., Nozaki, T., Kogure, Y., Yokotsuka, T.	333	Plastic Deformation of Pure Silicon Nanocrystals by Molecular Dynamics
Kebllinski, P., Phillpot, S. R., Wolf, D., Gleiter, H.	339	On the Nature of Grain Boundaries in Nanocrystalline Diamond
Compagnini, G., Pignataro, S., Puglisi, O.	345	Vibrational Analysis of Ion Irradiated Self-Assembled Monolayers
Jokanovic, V., Janackovic, Dj., Spasic, P., Uskokovic, D.	349	Modeling of Nanostructural Design of Ultrafine Mullite Powder Particles Obtained by Ultrasonic Spray Pyrolysis
Smith, G. B., Reuben, A. J.	353	Normal Mode Analysis of Optical Polarisation Response in Nanocomposite Particles

Lin, H.-F., Lin, H.-M., Hsu, S.-L.	357	Molecular Simulation for Gas Adsorption at TiO <sub>2</sub> ( Rutile And Anatase) Surface
Senet, P., Hou, M.	361	Computation of Capacitances of Cu <sub>n</sub> Nanoclusters
Alymov, M. I., Shorshorov, M. Kh.	365	Surface Tension of Ultrafine Particles
Jin Z. H., Lu, K.	369	To What Extent a Crystal Can Be Superheated
Bugaev, A. S., Korshunov, S. M., Kuzmichev, S. D., Sorokoumov, V. E.	373	The Simulation of Charge Transport in the Nanostructure "Camel" and Heterotransistors
Aliev, F. G., Moshchalkov, V. V., Bruynseraede, Y.	377	Anomalous Electron Transport in Magnetic Multilayers Tuned by Electric and Magnetic Fields
Eibeck, P., Spatz, J. P., Möbter, S., Möller, M.	383	Nanostructuring by Ultrathin Di-Block Copolymer/Titanium Composite Films
Josell, D., Carter, W. C., Bonevich, J. E.	387	Stability of Multilayer Structures: Capillary Effects
Suda, Y., Ebihara, K., Baba, K., Abe, H., Grishin, A. M.	391	Crystalline Silicon Nitride Thin Films Grown by Pulsed Yag Laser Deposition
Cottam, M. G., Costa Filho, R. N.	395	Energy Shift and Damping of Dipole-Exchange Spin Waves in Ultrathin Ferromagnetic Films
Crnjak-Orel, Z., Musevic, I.	399	Characterization of Vanadium Oxide and New V/Ce Oxide Films Prepared by Sol Gel Process
Josell, D., van Heerden, D., Schechtman, D., Read, D.	405	Mechanical Properties of Multilayer Materials
Fogel, N. Y., Mikhailov, M. Y., Yuzepovich, O. I., Bomze, Y. V.	409	Superconductivity Reentrance in Strong Magnetic Fields in Mo/Si Multilayers

Hedlund, J., Sterte, J.	413	Synthesis of Thin Molecular Sieve Films
Kikineshi, A., Mishak, A., Palyok, V., Shiplyak, M.	417	Nanolayered Chalcogenide Glass Structures For Optical Recording
Kataby, G., Prozorov, R., Gedanken, A.	421	Characterization of Self-Assembled Alcohols Coating On Amorphous Iron
Zsebök, O., Thordson, J. V., Ilver, L., Andersson, T. G.	425	Surface Morphology and Compositional Variations in Molecular Beam Epitaxy Grown $\text{GaN}_x\text{As}_{1-x}$ Alloys
Hanarp, P., Sutherland, D., Gold, J., Kasemo, B.	429	Nanostructured Model Biomaterial Surfaces Prepared by Colloidal Lithography
Vollath, D., Szabo, D. V., Fuchs, J.	433	Synthesis and Properties of Ceramic - Polymer Composites
Eckert, J., Seidel, M., Xing, L. Q., Börner, I., Weib, B.	439	Nanophase Composites in Easy Glass Forming Systems
Kübler, A., Eckert, J. Schultz, L.	443	Nanoparticles in an Amorphous $\text{Zr}_{55}\text{Al}_{10}\text{Cu}_{30}\text{Ni}_5$ -Matrix. The Formation of Composites by Mechanical Alloying
Simon, U., Jockel, J. Starrost, F. Krasovskii, E. E. Schattke, W.	447	Electronic and Optical Properties of Cetineites: Nanoporous Semiconductors with Zeolite-Like Channel Structure
Naser, J., Ferkel, H.	451	Laser-Induced Synthesis of $\text{Al}_2\text{O}_3/\text{Cu}$ - Nanoparticle Mixtures
Krasnowski, M., Fadeeva, V. I., Matyja, H.	455	Nanocomposites Produced by Mechanical Alloying of the $\text{Al}_{50}\text{Fe}_{25}\text{Ti}_{25}$ Powders Mixture
Sanchez-Lopez, J. C., Reddy, E. P., Rojas, T. C., Sayagues, M. J., Justo, A., Fernandez, A.	459	Preparation and Characterization of CdS and ZnS Nanosized Particles Obtained by The Inert Gas Evaporation Method

---

Khaleel, A., Weifeng, Li., Klabunde, K. J.	463	Nanocrystals as Stoichiometric Reagents with Unique Surface Chemistry. New Adsorbents For Air Purification
Yang, D., Westreich, P., Frindt, R. F.	467	Transition Metal Dichalcogenide / Polymer Nanocomposites
Kim, S. Y., Yu, J. H., Lee, J. S.	471	The Characteristics of Nanosized TiO <sub>2</sub> Powder Synthesized by Chemical Vapor Condensation
Nam, J. G., Lee, J. S.	475	Mechano-Chemical Synthesis of Nanosized Stainless Steel Powder
Knorr, P., Nam, J. G., Lee, J. S.	479	Densification and Microstructural Development of Nanocrystalline $\gamma$ -Ni-Fe Powders During Sintering
Yelsukov, E. P., Lomayeva, S. F., Konygin, G. N., Dorofeev, G. A., Povstugar, V. I., Mikhailova, S. S., Zagainov, A. V., Kadikova, A. H.,	483	Structure, Phase Composition and Magnetic Characteristics of the Nanocrystalline Iron Powders Obtained by Mechanical Milling in Heptane
Keis, K., Vayssieres, L., Lindquist, S.-E., Hagfeldt, A.	487	Nanostructured ZnO Electrodes for Photovoltaic Applications
Sakamoto, K., Tsunawakit, Y.	491	Formation of Nano-Sized Layer Composite by Intercalation to Aluminium Tri-Hydrogen Bis (Orthophosphate) Monohydrate
Chiriac, H., Moga, A. E., Urse, M., Necula, F.	495	Structural and Magnetic Investigation of Mechanically Alloyed Fe <sub>70</sub> Co <sub>3.5</sub> Cu <sub>1</sub> Nb <sub>3</sub> B <sub>9</sub> Si <sub>13.5</sub> Powders
Macek, J., Marinsek, M.	499	Formation of Nickel and Zirconia Nanocomposites by the Coprecipitation Method
Xing, L. Q., Eckert, J., Schultz, L.	503	Deformation Mechanism of Amorphous and Partially Crystallized Alloys

---

Ng, C. B., Schadler, L. S., Siegel, R. W.	507	Synthesis and Mechanical Properties of TiO <sub>2</sub> -Epoxy Nanocomposites
Sasaki, T., Koshizaki, N., Koinuma, M., Matsumoto, Y.	511	Preparation of M/TiO <sub>2</sub> (M=Au, Pt) Nanocomposite Films Using Co-Sputtering Method
Michel, D., Borisov, B. F., Charnaya, E. V., Hoffmann, W.-D., Plotnikov, P. G., Kumzerov, Yu. A.	515	Solidification and Melting of Gallium and Mercury in Porous Glasses as Studied by NMR and Acoustic Techniques
Krüger, J. K., Holtwick, R., le Coutre, A., Baller, J.	519	On the Influence of Nano-Scaling on the Glass Transition of Molecular Liquids
Yamamoto, T. A., Nishimaki, K., Harabe, T., Shiomi, K., Nakagawa, T., Katsura, M.	523	A Magnetic Composites Composed of Iron - Nitride Nanograins Dispersed in a Silver Matrix
Nishimaki, K., Ohmae, S., Yamamoto, T. A., Katsura, M.	527	Formation of Iron-Nitrides by Reaction of Iron Nanoparticles with a Stream of Ammonia
Busmann, H-G, Günther, B. Meyer, U.	531	Polymer Matrix Composites Filled with Nanoporous Metal Powders Preparation and Electrical Properties
Smith, G. B., Dligatch, S.	535	Ellipsometric Studies of Nanocomposite Cermets
Christodoulides, J. A., Shevchenko, N. B., Hadjipanayis, G. C.	539	Preparation of Dy and Mn Nanoparticles
He, L., Allard, Jr, Ma, E.	543	A Method to Produce Two-Phase Nanocomposites in Solid State
Enzo, S., Frattini, R., Canton, P., Mulas, G., Radaelli, P.	547	A Study of Al-Mo Alloys Synthesized by Mechanical Treatment and Annealed In-situ
Merzbacher, C. I., Barker, J. G., Long, J. W., Rolison, D. R.	551	The Morphology of Nanoscale Deposits of Ruthenium Oxide in Silica Aerogels



Würschum, R., Michel, T., Scharwaechter, P., Frank, W., Schaefer, H.-E.	555	Fe Diffusion in Nanocrystalline Alloys and the Influence of Amorphous Intergranular Layers
Lu, K., Zhao, Y. H.	559	Experimental Evidences of Lattice Distortion in Nanocrystalline Materials
Oku, T., Bovin, J.-O., Nakajima, S., Kubota, H., Ohgami, T., Suganuma, K.	563	Nanostructural Characterization of Solid Clusters and Oxide by HREM with Residual Indices
Obratsova, E. D., Bonard, J.-M., Kuznetsov, V. L., Zaikovskii, V. I., Pimenov, S. M., Pozarov, A. S., Terekhov, S. V., Konov, V. I., Obratsov, A. N., Volkov, A. P.	567	Structural Measurements For Single- Wall Carbon Nanotubes by Raman Scattering Technique
Ohnuma, M., Hono, K., Onodera, H., Mitani, S., Ha, J. G., Fujimori, H.	573	Microstructure Change in $\text{Co}_{46}\text{Al}_{19}\text{O}_{35}$ Granular Thin Films by Annealing
Jang, L. Y., Yao, Y. D., Chen, Y. Y.	577	X-Ray Absorption Study in Nanocrystalline Fe, Co, Ni and Cu Metallic Powders
Hupe, O., Bremers, H., Hesse, J., Afanas'ev, A. M., Chuev, M. A.	581	Structural and Magnetic Information About a Nanostructured Ferromagnetic Fe-Cu-Nb-B Alloy by Novel Model Independent Evaluation of Mössbauer Spectra
Girhard, T., Friedrichs, B., Woldt, E., Hesse, J.	585	Nanocrystallisation of FeCuNbB Alloys
Bokhimi, X., Morales, A., Portilla, M., García-Ruiz, A.	589	Hydroxides as Precursors of Nanocrystalline Oxides
Bokhimi, X., Morales, A., Novaro, O., López, T., Gómez, R., Xiao, T. D., Strutt, P. R.	593	Nanocrystalline Tetragonal Zirconia Stabilized with Yttrium and Hydroxyls
Szabo, D. V., Vollath, D.	597	Morphological Characterisation of Nanocrystals with Layered Structures



Pergamon

NanoStructured Materials, Vol. 12, pp. 1–8, 1999

Elsevier Science Ltd

© 1999 Acta Metallurgica Inc.

Printed in the USA. All rights reserved

0965-9773/99/\$—see front matter

PII S0965-9773(99)00055-0

## THE EVOLUTION OF NANOSCALE QUANTUM EFFECTS IN SEMICONDUCTOR PHYSICS

Leo Esaki

Tsukuba, Ibaraki 305-0047

JAPAN

*Abstract -- In the early twentieth century, encounters with physical phenomena which require detailed analyses in nanoscale, such as electron motion, prompted the advent of quantum mechanics, since Newtonian mechanics could not possibly provide an adequate explanation for them. Electron tunneling through nanoscale barriers is the most direct consequence of the law of quantum mechanics, for which the Esaki tunnel diode gave most convincing experimental evidence in 1957. Following the evolutionary path of nanoscience in semiconductor physics, significant milestones are presented, including resonant tunnel diodes, superlattices, quantum wires and dots. ©1999 Acta Metallurgica Inc.*

### INTRODUCTION

The twentieth century will be characterized by the fact that science and technology have made remarkable progress, including the establishment of quantum mechanics, the development of semiconductor devices with the invention of the transistor and the evolution of computers/telecommunications.

In the early century, encounters with physical phenomena such as electron's motion or photon's behavior for which Newtonian mechanics could not possibly provide an adequate explanation, prompted the advent of quantum mechanics. The framework of quantum mechanics was established in the superb work of Werner Heisenberg, Erwin Schrödinger, Paul Dirac and Max Born in the period 1925-26.

During the infancy of the quantum theory, de Broglie (1) introduced a new fundamental hypothesis that matter was endowed with a dualistic nature – particles may also have the characteristics of waves. This hypothesis found expression, in the hands of Schrödinger (2), in the definite form now known as the Schrödinger wave equation, whereby an electron is assumed to be represented by a solution to this equation. The continuous non-zero nature of such solutions, even in classically forbidden regions of negative kinetic energy, implies an ability to penetrate such forbidden regions and a probability of tunneling from one classically allowed region to another. The concept of tunneling itself arises from this quantum-mechanical result, and has no analogy in classical mechanics. The subsequent experimental manifestations of that concept can be regarded as one of the early triumphs of the quantum theory. For instance, in 1928, Fowler and Nordheim (3) explained, on the basis of

electron tunneling, the main features of the phenomenon of electron emission from cold metals by high external electric fields, which had been unexplained since its observation by Lilienfeld in 1922.

In 1932, Wilson (4), Frenkel and Joffe (5), and Nordheim (6) applied quantum mechanical tunneling to the interpretation of metal-semiconductor contact rectifiers such as those made from selenium or cuprous oxide. Apparently, this theory was accepted for a number of years until it was finally discarded after it was realised that it predicted rectification in the wrong direction for ordinary, practical diodes. It is now clear that, in the usual circumstances, the surface barriers met by semiconductors in contact with metals are far too thick to observe any tunneling current.

In 1934, the development of the energy-band theory of solids prompted Zener (7) to propose interband tunneling as an explanation for dielectric breakdown. He calculated the rate of transitions from a filled band to a next-higher unfilled band by the application of an electric field. In effect, he showed that an energy gap could be treated in the manner of a potential barrier. The Zener mechanism in dielectric breakdown, however, has never been proved to be important in reality. If a high electric field is applied to the bulk crystal of a dielectric or semiconductor, avalanche breakdown (electron-hole pair generation) generally precedes tunneling, and thus the field never reaches a critical value for tunneling.

With the invention of the transistor in 1947 came a renewed interest in the tunneling process. Around 1950, the technology of Ge p-n junction diodes was developed, and efforts were made to understand the junction properties. In explaining the reverse-bias characteristic, McAfee, Ryder, Shockley and Sparks (8) applied a modified Zener theory and asserted that low-voltage breakdown in Ge diodes resulted from interband tunneling. Results of later studies, however, indicated that most Ge junctions broke down by avalanche, but by that time the name "Zener diodes" had already been given to the low-breakdown Si diodes. Actually, Zener diodes are almost always avalanche diodes.

### ESAKI TUNNEL DIODE

In these circumstances, in 1956, the investigation of interband tunneling was initiated with heavily-doped Ge p-n junctions, where the junction width was successfully reduced to the range of nanometers.

We first obtained a backward diode which was more conductive in the reverse direction than in the forward direction. In this respect it agreed with the rectification direction predicted by the previously-mentioned old tunneling rectifier theory. The estimated junction width at zero bias was approximately 20 nm. In this junction, the possibility of an avalanche was completely excluded because the breakdown occurs at a voltage much lower than the threshold for electron-hole pair production.

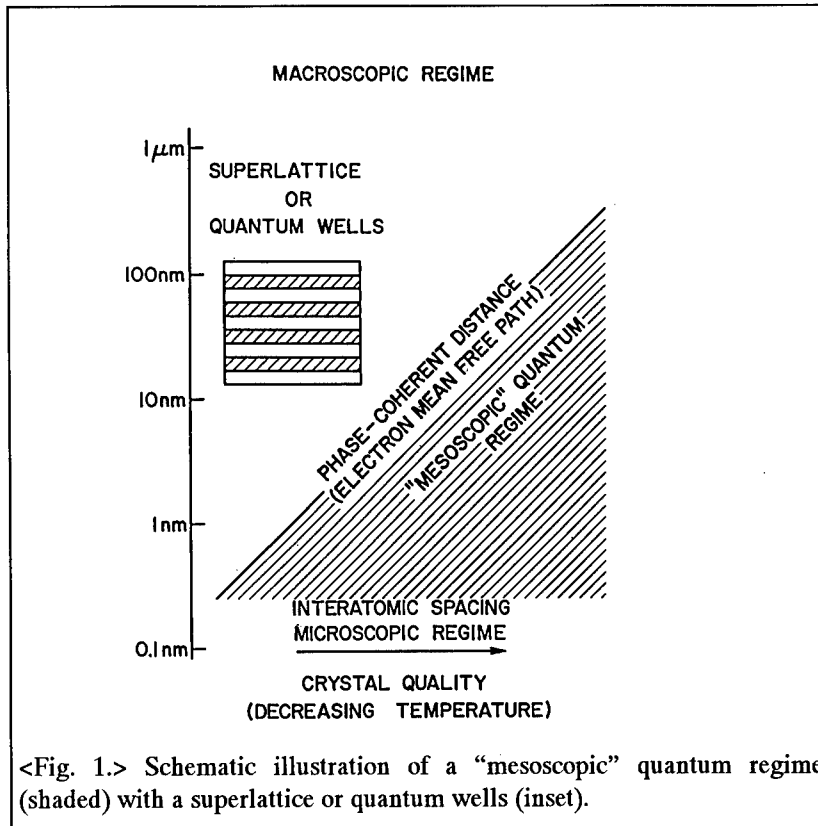
By further narrowing the junction width to less than 10 nm (thereby further decreasing the length of the tunneling path), through a further increase in the doping level, in 1957, the Esaki tunnel diode (9,10) with a negative resistance was obtained. The characteristic of this diode gave convincing evidence for tunneling electrons in solids, a phenomenon which had been clouded by questions for decades. This diode, together with the

backward diode, constituted the first semiconductor quantum electron structure.

## QUANTUM STRUCTURES

In 1969, research on artificially structured materials was initiated when Esaki and Tsu (11,12) proposed an engineered semiconductor superlattice with a one-dimensional periodic potential, where the period in the range of nanometers is substantially longer than the lattice constant of host crystals but shorter than the electron mean free path or the electron phase-coherent length.

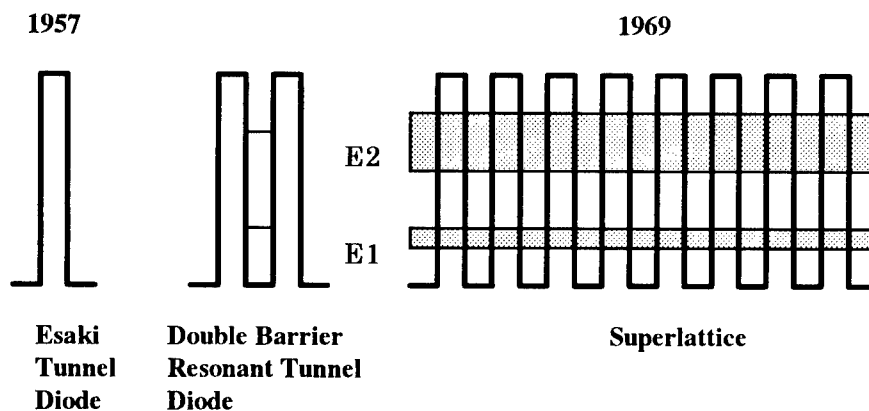
Before arriving at the superlattice concept, we had been examining the feasibility of structural formation of potential barriers and wells that were thin enough to exhibit resonant tunneling (13). A resonant tunnel diode (14,15) appeared to have more spectacular characteristics than the single tunnel barrier Esaki diode. It was thought that advanced technologies using semiconductors might be ready for demonstration of the de Broglie electron waves. Actually, resonant tunneling can be compared to the transmission of an electromagnetic wave through a Fabry-Perot resonator; the equivalent of a Fabry-Perot resonant cavity is formed by the semiconductor potential well sandwiched between two potential barriers.



The idea of the superlattice occurred to us as a natural extension of double-, triple- and multiple-barrier structures: the superlattice consists of a series of potential wells coupled by resonant tunneling. An important parameter for the observation of quantum effects in the structure is the phase-coherence length, which approximates to the electron mean free path. This depends on the bulk quality as well as the interface quality of crystals, and also on the temperatures and the effective mass. As schematically illustrated in Fig. 1, if the characteristic dimensions such as superlattice periods or well widths are reduced below the phase-coherent length, the entire electron system will enter a mesoscopic quantum regime of low dimensionality, on a scale between the macroscopic and microscopic. Our proposal was to explore quantum effects in the mesoscopic regime.

Fig. 2 illustrates schematically the evolutionary path, starting with the Esaki diode of a single potential barrier, then moving to the double-barrier resonant tunnel diode and, finally, reaching the superlattice. The introduction of the one-dimensional superlattice potential perturbs the band structure of the host materials, yielding a series of narrow subbands and forbidden gaps which arise from the subdivision of the Brillouin zone into a series of minizones. Thus, the superlattice was expected to exhibit unprecedented electronic properties. This could be considered to be modern alchemy, for it is intended to transform "common" semiconductors into "super" semiconductors.

At the inception of the superlattice idea, it was recognized that the utilization of long, tailor-made lattice periods provided a unique opportunity to exploit electric field-induced effects. The electron dynamics in the superlattice direction was analyzed for conduction electrons in a narrow subband of a highly perturbed energy-wave vector relationship. The result led to the prediction of a negative differential resistance at a modestly high electric field, which could be a precursor of Bloch oscillations. The superlattice allows us to enter the regime of electric-field-induced quantization: the formation of Stark ladders (16,17), for example, can be proved in a (one-dimensional) superlattice (18), whereas in natural (three-dimensional) crystals the existence and nature of these localized states in a high electric field have been controversial (19,20).



<Fig. 2> From left to right, the Esaki tunnel diode, a resonant tunnel diode and a superlattice.

This was, perhaps, the first proposal which advocated engineering a new semiconductor material by applying the principles of quantum theory and using the most advanced crystal-growth techniques of the day. The proposal was made to the US Army Research Office (ARO), a funding agency, in 1969. It was daringly stated, but with little confidence in a successful outcome at the time: ".....the study of superlattices and observations of quantum mechanical effects on a new physical scale may provide a valuable area of investigation in the field of semiconductors."

Although this proposal was favorably received by ARO, the original version of the paper (11) was rejected for publication by *Physical Review* on a referee's unimaginative assertion that it was "too speculative" and involved "no new physics". The shortened version published in *IBM Journal of Research and Development* (12) was subsequently selected as a Citation Classic by the Institute for Scientific Information (ISI) in July 1987. Our 1969 proposal was also cited as one of the most innovative ideas at the ARO 40th Anniversary Symposium in Durham, North Carolina, in 1991.

At any rate, with the proposal we launched a program to make a "Gedanken-experiment" a reality. In some circles, the proposed material was criticized as being close to impossible to prepare. One of the objections was that a man-made structure with compositional variations in the order of several nanometers could not be thermodynamically stable because of interdiffusional effects. Fortunately, however, it turned out that interdiffusion was negligible at the temperatures involved.

In 1970, Esaki, Chang and Tsu (21) studied a GaAs-GaAs<sub>0.5</sub>P<sub>0.5</sub> superlattice with a period of 20 nm synthesized by CVD (chemical vapor deposition) by Blakeslee and Aliotta (22). Although transport measurements failed to reveal any predicted effect, the specimen probably constituted the first strained-layer superlattice having a relatively large lattice mismatch. Early efforts in our group to obtain epitaxial growth of Ge<sub>1-x</sub>Si<sub>x</sub> and Cd<sub>1-x</sub>Hg<sub>x</sub>Te superlattices were soon abandoned because of rather serious technical problems at that time. Instead, we focused our research effort on compositional GaAs-Ga<sub>1-x</sub>Al<sub>x</sub>As superlattices grown by MBE (molecular beam epitaxy). In 1972, we found a negative resistance in such superlattices (23), which was interpreted in terms of the superlattice effect.

Following the derivation of the voltage dependence of resonant tunnel currents (15), Chang, Esaki and Tsu (24) observed current-voltage characteristics with a negative resistance. Subsequently, Esaki and Chang (25) measured quantum transport properties in a superlattice with a narrow bandwidth, which exhibited an oscillatory behavior. Tsu et al. (26) also performed photocurrent measurements on superlattices subjected to an electric field perpendicular to the plane layers using a semitransparent Schottky contact, which revealed their miniband configurations.

Heteroepitaxy is of great interest for the growth of compositional superlattices. Innovations and improvements in epitaxial techniques such as MBE and MOCVD (metal-organic chemical vapor deposition) have made it possible to prepare high-quality heterostructures with predesigned potential profiles and impurity distributions having dimensional control close to interatomic spacing. This great precision has created our freedom of access to the mesoscopic quantum regime (27,28).

Since a one-dimensional potential can be introduced along the direction of growth, famous examples in the history of one-dimensional mathematical physics, including the above-

mentioned resonant tunneling (13), Kronig-Penney bands (29), Tamm surface states (30), Zener band-to-band tunneling (7), and Stark ladders including Bloch oscillations (16,17,18), all of which had been only textbook exercises, could, for the first time, be practiced in a laboratory. Thus, do-it-yourself quantum mechanics is now possible, since its principles dictate the details of semiconductor structures (31).

Our original proposal (11,12) and pioneering experiments have triggered a wide spectrum of experimental and theoretical investigations on superlattices, quantum wells and quantum wires and dots (32) over the last two decades. A variety of engineered structures now exhibit extraordinary transport and optical properties which do not exist in any known natural crystal. This new degree of freedom offered in semiconductor research through advanced materials engineering has inspired many ingenious experiments, resulting in observations not only of predicted effects but also of phenomena hitherto totally unknown.

The number of papers related to the subject presented at the biennial International Conference on the Physics of Semiconductors has increased tremendously. After 1972, when the first paper (23) was presented, the field went through a short period of incubation before experiencing a phenomenal expansion in the 1980s. It appears that nearly half of all semiconductor physicists in the world are working in this area. Activity at this new frontier of semiconductor physics has in turn given immeasurable stimulus to device physics, provoking innumerable new ideas for applications. Thus, a new class of transport and optoelectronic devices has emerged.

At the opening address of 23rd ICPS, Berlin, 1996, G. Landwehr (33) stated, ".....the impact of two-dimensional systems was highly underestimated by most people at that time except, of course, Leo Esaki who proposed – together with Raphael Tsu – the superlattice concept which has given semiconductor physics an enormous impetus."

### References

1. L. de BROGLIE: 'Waves and Quanta', *Nature*, 1923, **112**, 540
2. E. SCHRÖDINGER: 'Quantisierung als Eigenwertproblem', *Annalen der Physik* (Leipz.), 1926, 4 Folge **79**, 489.
3. R. H. FOWLER and L. NORDHEIM: 'Electron Emission in Intense Electric Fields', *Proceedings of the Royal Society of London*, 1928, **A119**, 173.
4. A. H. WILSON: 'A Note on the Theory of Rectification', *Proceedings of the Royal Society of London*, 1932, **A136**, 487.
5. J. FRENKEL and A. JOFFE: 'On the Electric and Photoelectric Properties of Contacts Between a Metal and a Semiconductor', *Physikalische Zeitschrift der Sowjetunion*, 1932, **1**, 60.
6. L. NORDHEIM: 'Zur Theorie der Detektorwirkung', *Zeitschrift für Physik*, 1932, **75**, 434.
7. C. ZENER: 'A Theory of the Electrical Breakdown of Solid Dielectrics', *Proceedings of the Royal Society of London*, 1934, **145**, 523.
8. K. B. McAFEE, E.J. RYDER, W. SHOCKLEY and M. SPARKS: 'Observations of Zener Current in Germanium p-n Junction', *Physical Review*, 1951, **83**, 650.
9. L. ESAKI: 'New Phenomenon in Narrow Germanium p-n Junctions', *Physical Review*,

- 1958, **109**, 603.
10. L. ESAKI: 'Properties of Heavily-doped Germanium and Narrow p-n Junctions', *Solid State Physics in Electronics and Telecommunications* (Proceedings of International Conference, Brussels, 1958), Vol. 1 *Semiconductors*, Part I, 514, M. Desirant and J. L. Michels ed., Academic Press, New York, 1960.
  11. L. ESAKI and R. TSU: 'Superlattice and Negative Conductivity in Semiconductors', *IBM Research Notes*, 1969, **RC-2418**.
  12. L. ESAKI and R. TSU: 'Superlattice and Negative Differential Conductivity in Semiconductors', *IBM Journal of Research and Development*, 1970, **14**, 61.
  13. D. BOHM: *Quantum Theory*, 283, Prentice Hall, Englewood Cliffs, NJ, 1951.
  14. L. V. IOGENSEN: 'The Possibility of Resonance Transmission of Electrons in Crystals Through a System of Barriers', *Soviet Physics: JETP*, 1964, **18**, 146; *Zh. Eksp. Teor. Fiz.*, 1963, **45**, 207.
  15. R. TSU and L. ESAKI: 'Tunneling in a Finite Superlattice', *Applied Physics Letters*, 1973, **22**, 562.
  16. H. M. JAMES: 'Electronic States in Perturbed Periodic Systems', *Physical Review*, 1949, **76**, 1611.
  17. G. H. WANNIER: *Elements of Solid State Theory*, 190, Cambridge University Press, Cambridge, 1959; 'Wave Functions and Effective Hamiltonian for Bloch Electrons in an Electric Field', *Physical Review*, 1960, **117**, 432.
  18. W. SHOCKLEY: 'Stark Ladders for Finite, One-Dimensional Models of Crystals', *Physical Review Letters*, 1972, **28**, 349.
  19. J. ZAK: 'Stark Ladder in Solids?', *Physical Review Letters*, 1968, **20**, 1477; 'Comment on the existence proofs of the Wannier-Stark Ladder', *Physical Review*, 1991, **B43**, 4519.
  20. A. RABINOVITCH and J. ZAK: 'Electrons in Crystals in a Finite-Range Electric Field', *Physical Review*, 1971, **B4**, 2358.
  21. L. ESAKI, L.L. CHANG and R. TSU: 'A One-Dimensional "Superlattice" in Semiconductors', *Proc. 12th Int. Conf. Low Temp. Phys.*, 551, Kyoto, Japan, 1970.
  22. A. E. BLACKSLIEE and C.F. ALIOTTA: 'Man-made Superlattice Crystals', *IBM Journal of Research and Development*, 1970, **14**, 686.
  23. L. ESAKI, L.L. CHANG, W.E. HOWARD and V.L. RIDEOUT: 'Transport Properties of A GaAs-GaAlAs Superlattice', *Proceedings of 11th International Conference on the Physics of Semiconductors*, 431, Warsaw, Poland, 1972.
  24. L. L. CHANG, L. ESAKI and R. TSU: 'Resonant Tunneling in Semiconductor Double Barriers', *Applied Physics Letters*, 1974, **24**, 593.
  25. L. ESAKI and L.L. CHANG: 'New Transport Phenomenon in a Semiconductor Superlattice', *Physical Review Letters*, 1974, **33**, 495.
  26. R. TSU, L.L. CHANG, G.A. SAI-HALASZ and L. Esaki: 'Effects of Quantum States on the Photocurrent in a "Superlattice"', *Physical Review Letters*, 1975, **34**, 1509.
  27. L. ESAKI: 'A Bird's-Eye View on the Evolution of Semiconductor Superlattices and Quantum Wells', *IEEE Journal of Quantum Electronics*, 1986, **QE-22**, 1611.
  28. L. ESAKI: 'Implications of Semiconductor Superlattice Research', in *Highlights in Condensed Matter Physics and Future Prospects*, 55, L. Esaki ed., Plenum, New York, 1991.



29. R. de L. KRONIG and W.G. PENNEY: 'Quantum Mechanics of Electrons in Crystal Lattices', *Proceedings of the Royal Society of London*, 1931, **A130**, 499.
30. I. TAMM: 'Über eine mögliche Art der Elektronen-bindung', *Physikalische Zeitschrift der Sowjetunion*, 1932, **1**, 733.
31. L. ESAKI: 'Do-it-yourself Quantum Mechanics in Low-dimensional Structures', *Physics Scripta*, 1992, **T42**, 102.
32. S. Tarucha, D. G. Austing, T. Honda, R. J. vander Hage and L. P. Kouwenhoven: 'Shell Filling and Spin Effects in a Few Electron Quantum Dot,' *Physical Review Letters*, 1996, **77**, 3613.
33. G. LANDWEHR: 'Opening Address', *Proceedings of 23rd International Conference on the Physics of Semiconductors* (Berlin, Germany), p.xi, World Scientific Publishing Co., Singapore, 1996.



## SIMULATION OF THE MAGNETIC PROPERTIES DURING THE GROWTH OF NANOSTRUCTURED THIN FILMS

R.Brinzanik<sup>1</sup>, P.J.Jensen<sup>1,2</sup>, and K.H.Bennemann<sup>1</sup>

<sup>1</sup> Institut für Theoretische Physik, Freie Universität Berlin  
Arnimallee 14, D-14 195 Berlin, Germany

<sup>2</sup> Hahn-Meitner-Institut Berlin  
Glienicker Str.100, D-14 109 Berlin, Germany

**Abstract** - - *The interaction of atomic and magnetic structure, as well as the domain formation in nanostructured thin ferromagnetic films is studied. For this purpose we use a simple growth model, resulting in irregularly shaped magnetic islands, and apply rate equations for the temporal development of the magnetic structure. The remanent magnetization is shown as function of coverage, temperature, and lattice anisotropy. A multi-domain structure with small domains is obtained in the case of a rapid growth and for low temperatures.* ©1999 Acta Metallurgica Inc.

The interaction of the atomic and the magnetic structure, which is an important topic of current research, is especially strong for very thin magnetic films [1]. A small change of the preparation conditions may change the structural and the magnetic properties markedly. The recent progress of experimental methods (MFM, SNOM, Kerr- microscope etc.) allows for the investigation of these nanostructured systems in greater detail [2,3], in particular the spatial and temporal magnetic domain formation.

Due to the strong exchange coupling small magnetic clusters or islands are often ferromagnetically ordered. An ensemble of magnetically isolated islands should behave superparamagnetically [4]. However, magnetic anisotropies may hinder the relaxation towards the equilibrium state for temperatures below the so-called blocking temperature, which depends on the strength of the anisotropy, the island size, and the measuring time. The resulting magnetic structure may be not the most favorable single-domain state, but sticks in a metastable multi-domain state with a vanishing remanent magnetization. This feature is observed if the magnetic film is prepared in zero applied magnetic field [2].

In this study we present results for the remanent magnetization and the domain structure in the early states of film growth. We use the Eden model [5] as growth mode. Each atom is added to already existing islands, and stays immovable afterwards. This model corresponds to the case of a fast atomic surface diffusion, and a negligible step diffusion along the island edge. The resulting island shape is rougher than observed, and more compact as compared to a dendritic growth mode.

During the growth of a single layer the magnetic properties are determined. We consider a Heisenberg Hamiltonian with localized spins  $\vec{S}_i$  subject to the exchange coupling  $J$ , the uniaxial lattice anisotropy  $K$ , and an applied magnetic field  $H$ ,

$$\mathcal{H} = -\frac{J}{2} \sum_{\langle i,j \rangle} \vec{S}_i \cdot \vec{S}_j - g\mu_B H \sum_i S_i^z - K \sum_i (S_i^z)^2, \quad (1)$$

( $\mu_B$  Bohr's magneton,  $g$  Landé factor). A  $L \times L$  lattice is assumed with periodic boundary conditions. Due to the anisotropy two different directions of the magnetization ('up' and 'down') are assumed. These are separated by an energy barrier  $\Delta E_l^b > 0$  depending on the individual islands  $l$ , and consisting of competing volume (magnetic field, anisotropy) and surface interactions. The latter is due to the exchange coupling at the interface between neighboring islands which always tends to align the island magnetizations. The decreasing internal magnetic order and effective anisotropy with increasing temperature are taken into account by a mean field estimate. According to measurements [3] the island density is put equal to 0.005 per lattice site.

After adding a certain number of atoms randomly to the islands, the thin film magnetization is allowed to relax for a certain time. During the growth  $\Delta E_l^b$  is permanently calculated for each island. With a Monte Carlo method [6,7] each island is questioned to change its magnetization direction. The respective probability is determined by use of an Arrhenius ansatz

$$f_l = f_o \exp(-\Delta E_l^b / k_B T), \quad (2)$$

with  $T$  the temperature and  $k_B$  the Boltzmann constant.  $f_o \approx 10^9 - 10^{10} \text{ sec}^{-1}$  is the spin precession frequency [4] which determines the time unit. The islands are allowed to rotate only coherently. The remanent magnetization  $M_r$  and other quantities are determined as function of the coverage  $\theta$ , which is a function of time, and is given in ratios of a full monolayer (ML).

First we investigate the effect of temperature and lattice anisotropy on the remanent magnetization. To simulate experiment [3], the magnetic film is fully aligned by an applied magnetic field after each growth step. After removal of the field the film starts to relax to its equilibrium state; the remanent magnetization  $M_r$  is monitored after 5 sec.  $M_r$  decreases, and the onset of magnetization occurs at later states of film growth, if the temperature is increased, cf. Fig.1(a). On the other hand, an increasing anisotropy impedes the relaxation towards equilibrium, resulting in an increasing remanent magnetization, cf. Fig.1(b).

In Fig.2 we show the resulting domain pattern of a full monolayer grown in zero applied field for different growth temperatures and growth velocities. The domains are the smaller the larger the growth velocity and/or the smaller the temperature. If the magnetic islands become too fast too big, the individual islands may have not enough time to overcome the energy barriers to relax into the single-domain state, then a multi-domain state emerges. The consideration of a random growth resulting in irregularly shaped islands seems to be important. Possibly, a spin-glass-like multi-domain state may be stabilized by the exchange coupling between domains. This feature will be investigated by us in greater detail.

In conclusion, we have calculated the remanent magnetization and the domain structure as function of coverage, anisotropy, and temperature during the growth of a single ferromagnetic layer. Since we have used a simplified model, we are able to present only qualitative results here. An improved description is underway.

*Acknowledgement:* Discussion with A.Bauer and H.P.Oepen are gratefully acknowledged. This work was in part supported by the Deutsche Forschungsgemeinschaft.

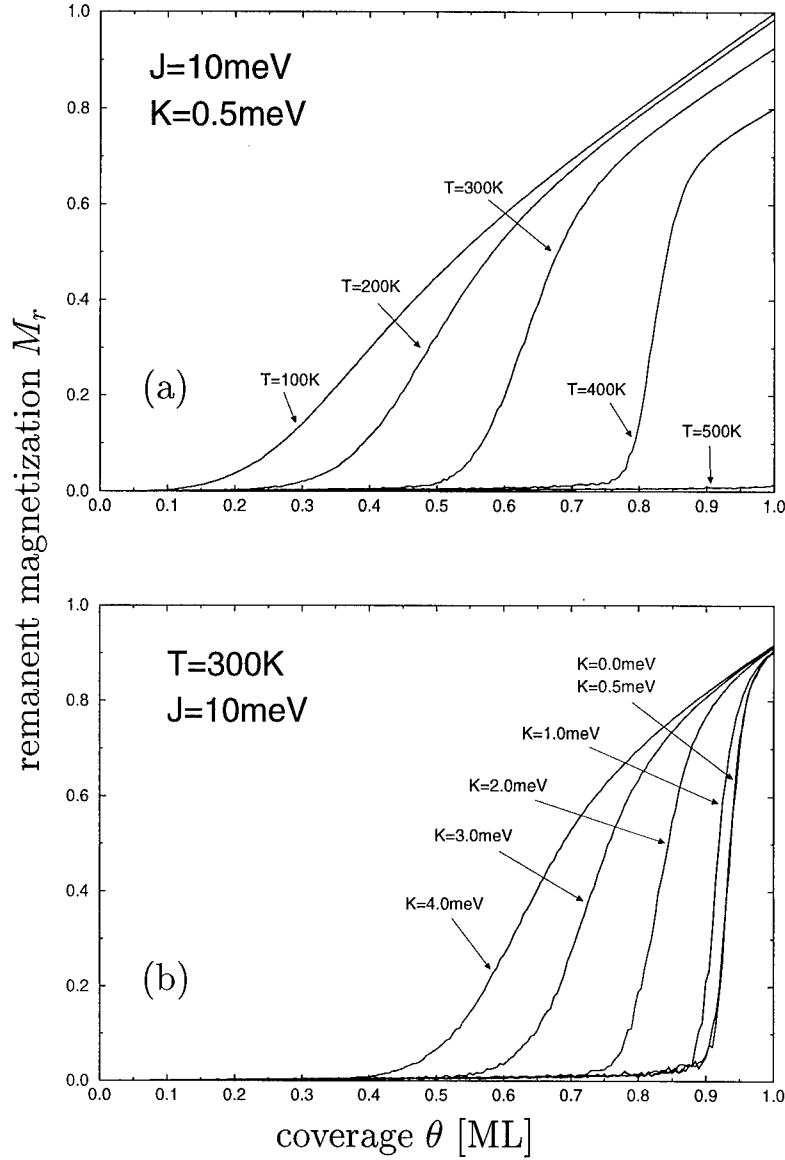


**Fig.1:** Remanent magnetization  $M_r$  as function of the coverage  $\theta$  of a lattice with  $1000 \times 1000$  sites (5,000 islands) after 5 sec relaxation from a fully magnetized state. The different curves refer to different temperatures and constant lattice anisotropy (a), and to different anisotropies and constant temperature (b). We have used  $J = 10\text{ meV}$ .  $M_r$  is determined from 20 to 50 runs.

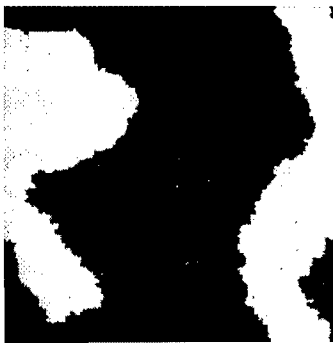
1. For a review see: J.Magn.Magn.Mater. 1991, 100.
2. Allenspach, R. *et al.*, Phys.Rev.Lett., 1990, 65, 3344; Oepen, H.P. *et al.*, Phys.Rev.B, 1997, 55, 2752, and private communication; Bauer, A., unpublished.
3. Fahsold, G., thesis, FU Berlin, 1994.
4. Jacobs, I.S., Bean, C.P., *Magnetism Vol.III*, Academic Press, New York, 1964.
5. Eden, M., Symp. on Information Theory in Biology, Pergamon Press, New York, 1958, p. 359.
6. Nowak, U., preprint (1996).
7. Binder, K., Herrmann, D.W., Monte Carlo Simulation in Statistical Physics, Springer Verlag, Berlin, 1992.



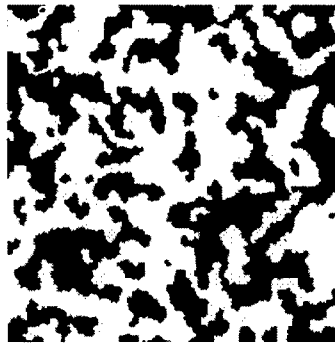
$T = 300 \text{ K}$   
0.01 ML/sec



$T = 300 \text{ K}$   
0.1 ML/sec



$T = 400 \text{ K}$   
0.01 ML/sec



$T = 100 \text{ K}$   
0.01 ML/sec

**Fig.2:** Domain structure of a single magnetic layer ( $\theta = 1 \text{ ML}$ ) of a lattice with  $2000 \times 2000$  sites (20,000 islands) for different growth temperatures and growth velocities as indicated. Gray areas refer to magnetization 'up', and black areas to 'down'. We have used  $J = 10 \text{ meV}$  and  $K = 0.5 \text{ meV}$ .



Pergamon

NanoStructured Materials, Vol. 12, pp. 13–18, 1999

Elsevier Science Ltd

© 1999 Acta Metallurgica Inc.

Printed in the USA. All rights reserved

0965-9773/99/\$—see front matter

PII S0965-9773(99)00057-4

## FABRICATION OF NANOSCALE HETEROJUNCTION OF Si/Au AND Si/Ag BY SURFACE DROPLET EPITAXY

Yutaka Wakayama and Shun-ichiro Tanaka

Tanaka Solid Junction Project, ERATO, Japan Science and Technology Corporation 1-1-1  
Fukuura, Kanazawa-ku, Yokohama 236-0004, Japan

**Abstract**--By using nanoparticles of gold and silver, we succeeded in fabricating nanoscale heterojunctions of Si/Au and Si/Ag on the surface of Si substrates. Formation kinetics are discussed on the basis of a structural and an elemental analysis using a transmission electron microscope (TEM) and energy-dispersive X-ray spectroscopy (EDX). This process is called "surface droplet epitaxy (SDE)". Additionally, the characteristic structure of nanoscale heterojunction, i.e., the epitaxial relation between metal particles and the Si dot with large expansion of the lattice constant of metal particles, is attributed to a size effect of nanoscale materials. ©1999 Acta Metallurgica Inc.

### INTRODUCTION

The main purpose of this study is fabrication of nanometer-scale metal/semiconductor heterojunctions. A self-assembly technique is applied for this purpose, in which alloying and phase separation between metal nanoparticles and the surface layer of the Si substrate took place through thermal annealing and cooling processes.

Recently, quantum-size devices, such as light emitting devices and single-electron devices, have attracted much attention because of their outstanding properties. They are smaller than 10 nm in size and are beyond the processing ability of conventional lithographic techniques. Therefore, the demand for new material design techniques on a nanometer scale has been increasing.

In the growth mechanism such as the Stranski-Krastanov (SK) mode or Volmer-Weber (VW) mode, crystal growth of a 3-dimensional island takes place and enables nanoscale hemispheric dots to be obtained on the substrates. Because these processes do not involve any conventional patterning techniques, they are called 'self-assembly processes' and are mainly applied to compound semiconductors (1-3). For a further improvement of these material design techniques, the fabrication of a heteromaterial junction, for example, between metal and semiconductor, is a crucial issue.

In this paper, we demonstrate a new technique for the fabrication of a metal/Si heterojunction. Our concept is based on assembling nanometer-scale materials instead of the conventional idea of patterning large-scale materials. For this purpose, fine metal particles with nanometer-order diameters were utilized as the starting material.

## EXPERIMENTAL

Single-crystalline Si(111) substrates were chemically cleaned and dipped in HF solution (2 wt.%) for 20sec to remove the oxide layer and to terminate the surface with hydrogen atoms. The substrates were mounted into a vacuum chamber for metal particle deposition.

Nanoparticles of gold and silver were produced by the gas-condensation method. These metals were evaporated by resistance heating in an argon atmosphere. The pressure of the Ar gas was modified from 1 to 10 Torr to control the size of the metal nanoparticles, which were deposited on the Si substrates at room temperature.

The specimens were then introduced into a high-vacuum chamber with a background pressure of less than  $1 \times 10^{-8}$  Torr for heat treatment. Specimen temperatures were elevated to 800°C for gold and 950°C for silver, at the rate of 15°C/min. After remaining at these temperatures for 30min, the specimens were gradually cooled at the rate of -2°C/min to room temperature.

A high-resolution transmission electron microscope (HRTEM, JEOL-2010) and an energy-dispersive X-ray spectroscope (EDX, Oxford-Link ISIS) which is attached to the HRTEM, were used for structural and elemental analyses to investigate the mechanism of the metal/Si bilayer dots formation.

## RESULTS AND DISCUSSION

Figure 1(a) shows a TEM image of the Au nanoparticles of about 10 nm in diameter which were generated at the Ar pressure of 6 Torr. Figure 1(b) shows a cross-sectional TEM image of a postannealed specimen, observed from the [110] direction. This image indicates that a mushroom-shaped bilayer dot was grown on the completely flat surface of the Si substrate.

It was revealed from the EDX analysis that the top hemispheric layer consisted predominantly of Au with a small amount of Si, whereas the lower truncated-cone layer contained only Si (4, 5). Furthermore, the lower Si dot was found to have the same crystal orientation as that of the Si substrate.

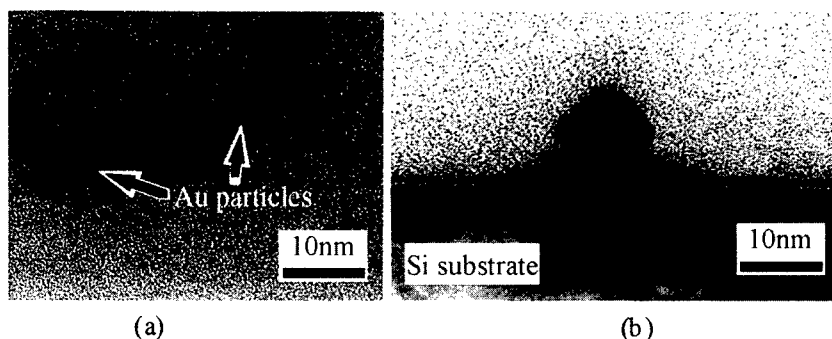


Fig.1 TEM images of (a) Au nanoparticles and (b) postannealed specimen.

In order to clarify the mechanism of the Si/Au bilayer dot formation, we carried out another experiment using the molecular beam epitaxy (MBE) technique.

Gold was deposited on the clean Si substrate from a Knudsen-cell. Then, the temperature of the substrate was kept at 400°C during the deposition. As a result, three-dimensional Au islands with a few hundred nanometer in diameter were grown on the Si substrate, i.e., Stranski-Krastanov mode. One of the specimen, specimen **A**, was briefly exposed to air and reintroduced into the UHV chamber for the thermal annealing at 800°C for 30min. The temperature of another specimen, specimen **B**, was elevated in the UHV immediately after deposition for the same heat-treatment.

Cross-sectional TEM images of these specimens are shown in Figs.2(a) and (b). Different morphologies are obviously observed for both cases. For specimen **A**, a dark contrast under the original Si/Au interface indicates that Au atoms penetrated into the Si substrate. On the other hand, for specimen **B**, the Si/Au interface was moved upward from the original Si surface forming a bilayer structure, marked 1 and 2, similar to the structure shown in Fig.1(b).

The EDX spectra were obtained by varying the distance from the top of the Au island to the Si/Au interface for both specimens. Then, the spot size of the electron beam was converged to 5nm in diameter. In Fig.3, the relative intensity of Si  $L\alpha$  line (1.74 KeV) to the Au  $M\alpha$  line (2.12 KeV) is plotted as a function of the distance. In the case of specimen **A**, the relative intensity of the Si  $L\alpha$  line consistently increased on approaching the interface. This result indicates that solid state interdiffusion of both Si and Au occurred upon thermal annealing, which has been widely observed in the Si-Au binary system (6, 7). In contrast, the ratio of the line intensities of specimen **B** is relatively small,  $Si(L\alpha)/Au(M\alpha) \approx 0.2$ , which value is almost equivalent to that obtained in the above-described Au nanoparticle experiment (4). Additionally, the intensity ratio is constant with respect to the distance. Namely, the small amount Si was dissolved evenly throughout the Au island.

The substantial difference between the two cases lies in the surface condition of the Si substrate. In the former case, the Si surface is considered to be covered by an oxide layer due to the exposure to air. Contrary, the surface is bare during the thermal annealing in the latter case.

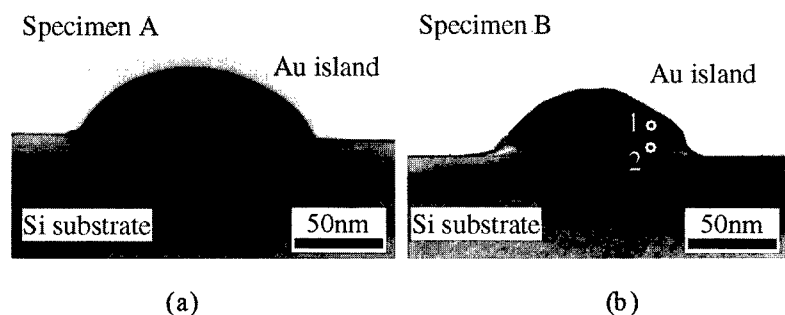


Fig.2 Cross-sectional TEM images of the Au island on the Si(111) surface. (a) Annealed in the UHV after exposure to air. (b) Annealed in the UHV immediately after the deposition. The bilayer structure, marked 1 and 2, was formed on the substrate



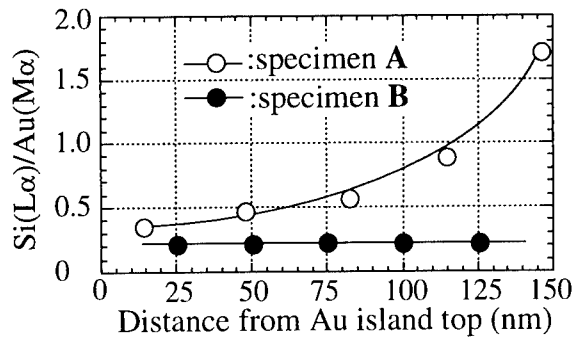


Fig.3 Relative intensity of Si  $L\alpha$  line to Au  $M\alpha$  line of EDX spectra plotted as a function of the distance from the top of the Au island. Open and closed circles correspond to specimens A and B.

On the basis of these experimental results, we deduce the kinetics of the bilayer dot formation as follows. First, the hydrogen atoms terminating the Si surface are removed at above 400°C (8). As a result, the Si atoms can easily diffuse on the clean surface at the annealing temperature (9). Because of the high mobility of the surface-diffusing Si atoms, they are incorporated into the Au nanoparticles preferentially rather than form Si atoms of the rigid substrate. If the oxide layer then covers the Si surface, the surface diffusion of Si atoms is suppressed and solid state interdiffusion occurs across the original Si/Au interface resulting in a gradual distribution of both elements as observed in specimen A. Because the annealing temperature is much higher than the eutectic temperature of the Si-Au binary system, 364°C (10), the alloy is considered to form a liquid phase droplet on the flat Si substrate. Next, the Si atoms are precipitated from the alloy and regrown epitaxially on the substrate during the cooling process. As precipitation proceeds, the size of the alloy becomes small. This is the reason why the Si dot is shaped like a truncated cone. Finally, Si and Au separate at room temperature, leaving a small amount of Si evenly distributed in the Au particle as evidence of the droplet formation. Namely, this process is a kind of liquid phase epitaxy (LPE) in which gold is used as a transport medium for Si growth.

This is similar to the process of vapor-liquid-solid (VLS) growth (11) or 'droplet epitaxy' which was described by Koguchi *et al.* (12). Both of these processes require an additional supply of the gas-phase source for crystal growth. Instead, only thermal annealing is necessary for our process and surface-diffusing Si atoms play an important role in the Si dot formation. Consequently, we call this process "surface droplet epitaxy (SDE)", and it is schematically illustrated in Fig.4.

Based on the above-mentioned discussion, SDE should occur in any eutectic binary system which undergoes an endothermic reaction. Next, we demonstrate a similar experimental result for the Si/Ag system.

Figure 5 shows a cross-sectional TEM image of a heat-treated specimen, viewed from the [110] direction. Ag nanoparticles were produced at the Ar pressure of 4 Torr. For this system, a higher annealing temperature, 950°C, was required for bilayer dot formation. This is considered to be due to the higher eutectic temperature of the Si-Ag binary system, 830°C (10), and lower solubility of Ag than that of Au into Si.

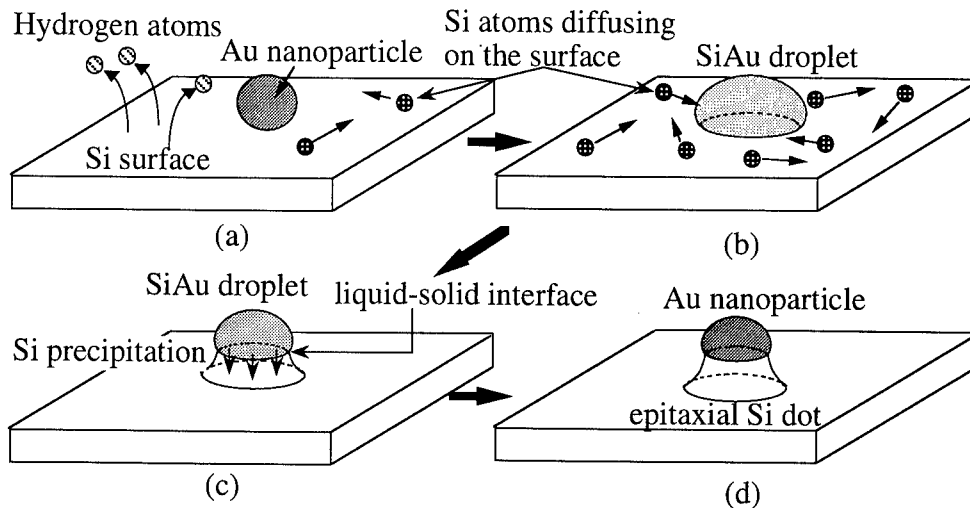


Fig.4 Kinetics of surface droplet epitaxy (SDE). (a) Si atoms diffuse over the clean surface at elevated temperature. (b) Surface-diffusing Si atoms are incorporated into the Au nanoparticles to form SiAu droplets. (c) Si atoms are precipitated from the alloy and grow as an epitaxial Si dot during the cooling process. (d) Si and Au were separated at room temperature on the flat surface.



Fig.5 Cross-sectional TEM image of Si/Ag bilayer dot. Arrows indicate edge dislocations.

In this image, the lattice orientation of the Ag particle as well as that of the Si substrate is consistent with that of the Si substrate. The epitaxial relation between the Si substrates and Ag thin films has been reported earlier (13, 14). For these cases, one edge dislocation is necessary for every four lattice planes of Ag along the interface to accommodate the lattice mismatch in order that the epitaxial relation can be obtained because lattice mismatch between Ag and Si is about 25 %. Six edge dislocations are actually present along the Si/Ag interface as indicated by the arrows in Fig.5. However, eight or nine (111) lattice planes should be present as extra half planes that form the

edge dislocation because thirty-five (111) lattice planes are observed in the Ag particle.

Conversely, the lattice constant of the Ag(111) is found to become larger than that of bulk Ag by about 10 %. This expansion of the lattice plane just compensates for the shortage of two or three dislocations. That is, expansion of the lattice constant in addition to the edge dislocations is responsible for the accommodation of the lattice mismatch. Such considerable expansion of the lattice constant could be observed in the relatively small metal particles of less than about 5 nm in diameter in both Ag-Si and Au-Si binary systems (6). Accordingly, this characteristic structure was considered to be the result of a size effect, i.e., minimization of the total energy of the bilayer dot structure.

### CONCLUSION

Nanoscale heterojunctions of metal/Si were fabricated on a flat Si substrate. The kinetics of these bilayer dot formation was attributed to the liquid phase epitaxy, in which surface diffusion of the Si atoms plays an important role. Consequently, this process was named surface droplet epitaxy (SDE). We consider that the control of size and position of the metal nanoparticle are quite necessary for further development of this technique.

### REFERENCES

1. Oura, K., Naitoh, M., Yamane, J. and Shoji, F. *Surf. Sci.* 1990, 230, L151.
2. Nabetani, Y., Ishikawa, T., Noda, S. and Sasaki, A. *J. Appl. Phys.* 1994, 76, 347.
3. Tersoff, J., Teichert, C. and Lagally, M. G. *Phys. Rev. Lett.* 1996, 76, 1675.
4. Wakayama, Y. and Tanaka, S.-I. *J. Cryst. Growth* 1997, 181, 304.
5. Wakayama, Y., Fujinuma, H. and Tanaka, S.-I. *J. Mater. Res.* in press.
6. Brillson, L. J., Katnani, A. D., Kelly, M. and Margaritondo, G. *J. Vac. Sci. Technol.* 1984, A2, 551.
7. Lu, Z. H., Sham, T. K. and Norton, P. R. *Appl. Phys. Lett.* 1990, 57, 37.
8. Sinniah, K., Sherman, M. G., Lewis, L. B., Weinberg, W. H., Yates Jr., J. T. and Janda, K. C. *J. Chem. Phys.* 1990, 92, 5700.
9. Sakai, A., Ono, H., Ishida, K., Niino, T. and Tatsumi, T. *Jpn. J. Appl. Phys.* 1991, 30, L941.
10. Hansen, M. and Anderko, K. *Constitution of Binary Alloys* (Genium Publishing Corporation, New York, 1991).
11. Wagner, R. S. and Ellis, W. C. *Appl. Phys. Lett.* 1964, 4, 89.
12. Chikyow, T. and Koguchi, N. *Jpn. J. Appl. Phys.* 1990, 29, L2093.
13. LeGoues, F. K., Liehr, M., Renier, M. and Krakow, W. *Philos Mag.* 1988, B57, 179.
14. Shirokoff, J. and Erb, U. *Philos Mag. Lett.* 1988, 58, 255.



Pergamon

NanoStructured Materials, Vol. 12, pp. 19–22, 1999

Elsevier Science Ltd

© 1999 Acta Metallurgica Inc.

Printed in the USA. All rights reserved

0965-9773/99/\$-see front matter

PII S0965-9773(99)00058-6

## ELECTROCHEMISTRY OF NANOCRYSTALLINE COPPER

U. Heim, G. Schwitzgebel

Physical Chemistry, Universität des Saarlandes, P.O. Box 151150, 66041 Saarbrücken,  
Germany

**Abstract** -- Nanocrystalline copper ( $\text{Cu}_{\text{nc}}$ ), prepared by inert gas condensation, pulsed electrodeposition and by ball-milling, was characterized by XRD (mean grain diameter  $D$ ; mean micro strain  $\varepsilon$ ). Under total exclusion of  $\text{O}_2$ , the electrode potentials  $E_{\text{nc}}$  of these materials as well as  $E_{\text{mc}}$  of microcrystalline copper could be measured in acid solutions of  $\text{CuSO}_4$ . The differences  $\Delta E^{\text{ex}} = E_{\text{nc}} - E_{\text{mc}}$  which range up to 16.8 mV for the sample with the lowest diameter,  $D = 8$  nm, are inversely proportional to  $D$  according to a modified Gibbs-Thomson equation, when the deformation energy is taken into account. Thus, it can be concluded that  $\text{Cu}_{\text{nc}}$  forms a metastable equilibrium with Cu ions and that the electrode potentials of  $\text{Cu}_{\text{nc}}$  are quasi reversible, within the time of observation. The intrinsic grain growth of  $\text{Cu}_{\text{nc}}$  (outside the solution) is much slower than the apparent growth in solution. Corrosion on  $\text{Cu}_{\text{nc}}$  could best be detected by electrochemical impedance spectroscopy: Channels and pores in the surface give rise to an unusual diffusion type.

©1999 Acta Metallurgica Inc.

### INTRODUCTION

Electrode materials of nanoscale grains or particles must, on account of their interfacial energy, exhibit a negative shift of their electrode potential ( $E_{\text{nc}}$ ) compared with the microcrystalline electrode of the same material. Successful experiments with  $\text{Pd}_{\text{nc}}$  in a fused salt cell (613 K) have been published, where electrode potentials of the expected polarity and magnitude were found (1). The main problems, grain growth and grain structure relaxation, led to a rather rapid decrease of  $\Delta E^{\text{ex}}$  and caused an overlapping of the time scales of the material changes and of the cell equilibration. In aqueous solutions, where these time scales can be separated, only a small number of metals exhibit their reversible potentials, and if the condition of a not too low recrystallisation temperature must be fulfilled, only silver and copper remain as candidates for systematic electrochemical characterizations of the nanocrystalline state. There are two studies on  $\text{Ag}_{\text{nc}}$ , as a film from the gas phase (2) and as an electrochemical deposit (3). Similar  $\Delta E_{\text{ex}}$  values and time dependences have been found. With the generalized Gibbs-Thomson equation

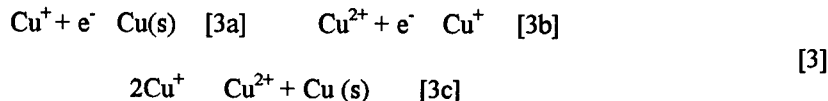
$$(\Delta E^{\text{ex}}) = 2\gamma \cdot V_{\text{M}} \cdot \gamma \cdot F^{-1} D^{-1} n_{\text{e}}^{-1} \quad [1]$$

(g: geometrical factor (4);  $V_M$ : molar volume;  $\gamma$ : specific interfacial free energy, F: Faraday constant, D: grain diameter,  $n_e$ : number of exchanged electrons)

The time dependence has been interpreted (3) as a law of grain growth (eq.[2]), but on

$$(\Delta E^{\text{ex}})^{-2} = k_1 + k_2 t \quad [2]$$

account of the rapid growth D could not be determined. The difficulties one encounters in the electrochemistry of copper lie hid in its two step electrode kinetics, which is usually expressed by the electrode reactions or an equilibrium (eqs.[3]). On account of the high



constant  $K = 2 \cdot 10^6$  of the eq.[3c] the  $\text{Cu}^+$  concentration is by a factor of more than  $10^{-2}$  lower than that of  $\text{Cu}^{2+}$ . But the exchange current of reaction [3a] is several orders of magnitudes higher than that of reaction [3b]. Therefore, rather high overpotentials appear when  $\text{Cu}^+$  is oxidized by traces of dissolved oxygen because the  $\text{Cu}^+$  concentration can only be reestablished by a change of eq.[3c] from the right to left side. More than at other metals the electrochemical activity of Cu is located at a rather small fraction of the surface, probably at regions with high concentrations of kink sites. The amount of these active sites strongly depends on the history of the surface, on its pretreatment and on adsorption of impurities.

## EXPERIMENTAL

The cell vessels were designed for five electrodes, which were dipped into or taken out of the solution by mere tilting of the cell. The inert gas flow could be stopped by two valves and short-circuited, so that the cell was completely closed. Electrolyte solutions, 0.1 m  $\text{CuSO}_4$  in 0.5 m or 0.05 m  $\text{H}_2\text{SO}_4$ , were made with chemicals of analytical purity grade and bidistilled water. For corrosion suppression (see below) Cu-powder of the same purity was added in some cases to the cell solution. Electrodes of commercial Cu (99,99 %) were pretreated by mechanical or anodical polishing.  $\text{Cu}_{\text{nc}}$  samples were obtained by inert-gas condensation, pulsed electrodeposition and by ball-milling. After rinsing the cell for at least 8 hours with inert gas the sample electrodes were dipped into the solution of the cell. Corrosion processes stopped completely, when the cell was closed (see above) and the remaining  $\text{O}_2$  had reacted with copper. The electrical potentials of the Cu electrodes were measured versus  $\text{Hg}/\text{Hg}_2\text{SO}_4$  electrodes in the cell solution but separated by a diaphragm. For recording the EMF, the electrometers (Keithly) were connected with computers. Electrode kinetics, corrosion and impedance spectra (EG & G) were studied in the three-electrode circuit with a further Cu electrode. XRD (Siemens D500) patterns were generated with  $\text{Cu}_{K\alpha}$  radiation. The [111] and [222] reflections were recorded with high resolution for detailed peak analysis. In order to determine D and crystallite strain  $\epsilon$  the method of Warren and Averbach (5) was used.

Spherical grain size and a log-normal distribution (Fig.1) were supposed, and the area-weighted diameter  $D$  as well as the average micro strain  $\varepsilon$  were used for the evaluation of the results (see DISCUSSION).

## RESULTS

The example of Fig.1 yields a qualitative measure for the growth rates. A consequence of the grain growth is seen in Fig.2, where the time dependence of the electrode potentials of  $\text{Cu}_{\text{nc}}$  and  $\text{Cu}_{\text{mc}}$  are compared. On account of its lower exchange current,  $\text{Cu}_{\text{mc}}$  is much more sensible for  $\text{O}_2$  traces. in the streaming  $\text{N}_2$ . The aging of all  $\text{Cu}_{\text{nc}}$  electrodes led to more or less fast potential increases. Laws between  $\Delta E^{-2}$  (eg. [1]) and  $\Delta E^{-1/2}$ , linearly dependent on time, were found and then used for extrapolations to  $t = 0$ .

Very interesting informations could be taken from impedance spectra in the lower frequency range. Diffusion of the Warburg type was found at  $\text{Cu}_{\text{nc}}$  surfaces during corrosion, which means that  $\text{O}_2$  or  $\text{Cu}^+$  diffusion was rate determining. After eliminating corrosion, an unusual Nyquist plot was observed (Fig.3), independently for stirred or standing solutions. Diffusion with a slope of  $25^\circ$  has been observed for grain boundary diffusion in alloys (6). Here, this means diffusion within channels and pores remaining from the preceding corrosion. The formation of such surface features could be confirmed by SEM analysis.

## DISCUSSION

The surface of  $\text{Cu}_{\text{nc}}$  is in a global metastable state, because it does not fulfill the Gibbs-Wulff criterium, a big fraction of the crystallite faces are not in equilibrium: they have the tendency to grow with energy release until they disappear. Nevertheless, it can be assumed that non-equilibrium faces are in a local equilibrium with the surroundings phase, so that they show their own local chemical potential  $\mu_i^*$ . But the phenomenological quantity  $E_{\text{nc}}$  gives an average of different local values of  $\mu_i^*$ . Within the framework of the electrochemical

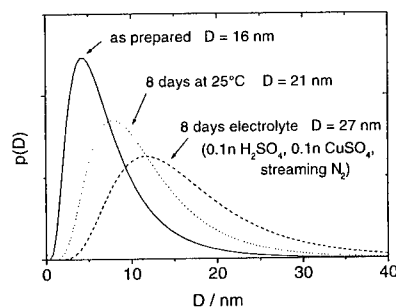


Fig.1 Size distribution of  $\text{Cu}_{\text{nc}}$  (i.g. cond.) after different times

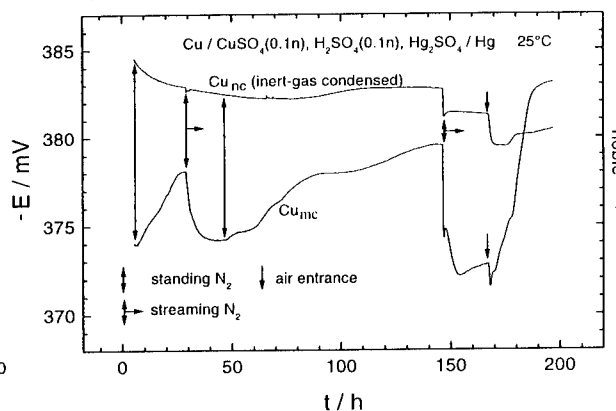


Fig.2 Electrode potentials of  $\text{Cu}_{\text{nc}}$  and  $\text{Cu}_{\text{mc}}$   
Influence of corrosion by  $\text{O}_2$  traces

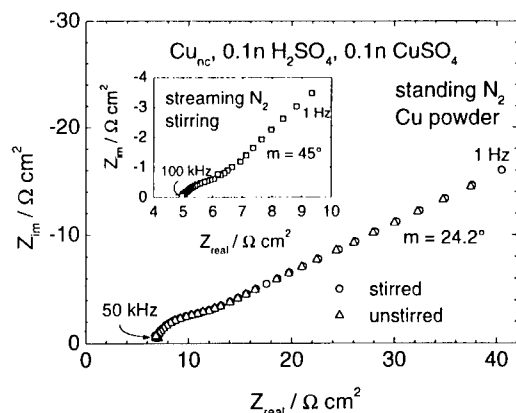


Fig.3 Corrosion in the Nyquist plot

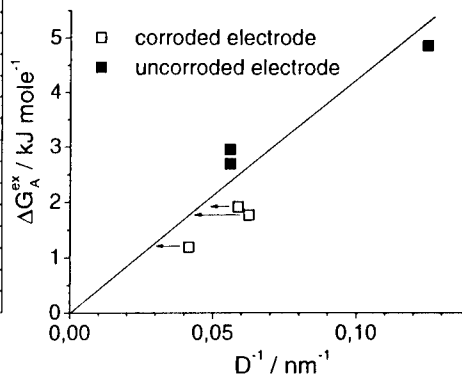


Fig.4 Gibbs-Thomson plot

charge transfer theory in its simplest form, we suppose the anodic process to start from a kink (or ad-atom) site of an increased energy level. The transition state in the double layer is supposed not to depend on the face type. In a straight-forward derivation an enhanced exchange current  $I_0^*$  is found. As a consequence, the  $\text{Cu}^+$  activity in contact with  $\text{Cu}_{\text{nc}} = \text{Cu}^*$  will be higher than with normal  $\text{Cu}_{\text{mc}}$ . In eqs.[3a] and [3b] the activities  $a^*(\text{Cu}^+)$  and  $a^*(\text{Cu})$  must be used (8). As a result the electrode potential is shifted to lower values.

A similar discussion can be led for the excess energy of crystals which are not in mechanical equilibrium, so that  $\Delta E^{\text{ex}}$  contains also contributions from strain energy. Therefore, the excess free energy,  $\Delta G^{\text{ex}} = -n_0 F \Delta E^{\text{ex}}$ , is composed of the contributions from the interfaces,  $\Delta G_A^{\text{ex}}$ , and from strain,  $\Delta G_S^{\text{ex}}$ . When  $\Delta G_S^{\text{ex}}$  is calculated (7) and subtracted from  $\Delta G^{\text{ex}}$  the remaining  $\Delta G_A^{\text{ex}}$  can be plotted according to eq.[1]. Fig.4 shows the expected proportionality to  $D^{-1}$ , when one confines to uncorroded electrode samples.

### References

1. Gärtner, F., Bormann R., Birringer, R. and Tschöpe, A., *Scripta Mater.*, 1996, **35**, 805
2. Henning, D. and Weil, K.G., *Ber. Bunsenges. Phys. Chem.*, 1978, **82**, 265
3. Villain, S., Knauth, P. and Schwitzgebel, G., *J. Phys. Chem.*, 1997, **B 101**, 7452
4. Chen, L.E. and Spaepen, F. *J. Appl. Phys.*, 1991, **69**, 689.
5. Natter, H. and Hempelmann R., *Ber. Bunsenges. Phys. Chem.*, 1996, **100**, 55
6. Lang, J. and Schwitzgebel, G., *Ber. Bunsenges. Phys. Chem.*, 1984, **88**, 711
7. Lewis, D. and Pearce, C.E., *Electrochim. Acta*, 1971, **16**, 747
8. Schwitzgebel, G., Gräf, Ch.P. and Heim, U., *in preparation*

### ACKNOWLEDGEMENT

The support of the "Deutsche Forschungsgemeinschaft" in the frame of the "Sonderforschungsbereich 277 Grenzflächenbestimmte Materialien" is gratefully acknowledged.



Pergamon

NanoStructured Materials, Vol. 12, pp. 23–28, 1999

Elsevier Science Ltd

© 1999 Acta Metallurgica Inc.

Printed in the USA. All rights reserved

0965-9773/99/\$—see front matter

PII S0965-9773(99)00059-8

## CONSOLIDATION AND HIGH STRAIN RATE MECHANICAL BEHAVIOR OF NANOCRYSTALLINE TANTALUM POWDER

Sang H. Yoo, T.S. Sudarshan, Krupa Sethuram

Materials Modification Inc, 2929-P1 Eskridge Rd, Fairfax, VA, 22031

Ghatu Subhash

Assistant Professor, Michigan Technological University, Houghton, MI, 49931

R.J. Dowding

Army Research Laboratory, AMSRL-WM-MD, Aberdeen Proving Ground, MD, 21005

**Abstract** -- High ductility and strength exhibited in nanograined materials can potentially be exploited in explosively formed penetrator liner applications. Both coarse and nanocrystalline tantalum powder were consolidated by Plasma Pressure Compaction ( $P^2C$ ) to study the effect of grain size on dynamic compression properties. The powders were consolidated rapidly with 1 minute of isothermal holding time to retain initial microstructure. The  $P^2C$  consolidated specimens were cut by electric discharge machining (EDM), polished for SEM characterization, and tested in dynamic compression using a Kolsky apparatus. The effect of grain size on yield stress and strain was investigated at various strain rates for a coarse grained and a nanograined specimen. Especially, the high strain rate response of nanocrystalline tantalum is discussed in this paper. ©1999 Acta Metallurgica Inc.

### INTRODUCTION

The high density and ductility of tantalum make it an attractive material for ballistic applications such as explosively formed penetrators (EFPs). The dynamic formability of an EFP depends on the physical and mechanical properties of the material, especially the initial crystallographic texture and the evolved deformation texture. To fabricate a tantalum EFP that meets dynamic formability requirements, processing-microstructure-property relationships must be established.

High strain rate deformation is the most critical performance feature for an EFP. Deformation studies at low strain rates have indicated that ductile behavior is observed in polycrystalline metals with fine grain structure including tantalum [1]. Therefore, it is important to understand the effect of grain size refinement on the flow and failure behavior for polycrystalline tantalum at high strain rates. In this study, the deformation behavior of two tantalum materials will be initially investigated especially with respect to their grain size at high loading rates.



## EXPERIMENTAL PROCEDURE

Tantalum powder (-325 mesh) was obtained from Trinitech (Twinsburg, OH) and tantalum nanopowder (<100 nm) was procured from the Army Research Laboratory (Aberdeen, MD). Initial particle size was analyzed by the BET technique (Coulter, SA 3100). The powders were consolidated by Plasma Pressure Compaction, and density was measured using Archimedes' principle. Dynamic and quasistatic compression tests were performed on the consolidated samples at Michigan Technological University (Houghton, MI).

### *Plasma Pressure Compaction*

Plasma Pressure Compaction (P<sup>2</sup>C) is a rapid consolidation technique that was developed by Materials Modification Inc, Fairfax, VA. In the P<sup>2</sup>C process, powders are simply poured into a graphite die without any additive and binder and compressed by graphite punches. At the beginning of the process, pulsed DC voltage is applied through the powder compacts to generate an interparticle plasma that activates the surface of the particles by removing the oxide and contaminant layers. Subsequently, DC voltage is applied to achieve rapid densification by resistance sintering under uniaxial pressure.

For tantalum consolidation, uniaxial pressure of 50 MPa was applied initially to the powder compact through graphite punches to establish a current path. DC pulses of 60 millisecond duration were applied at maximum amplitude of 1300 ampere, and the voltage varied between 0 to 5 V for total of 3 minutes to generate interparticle plasma which leads to surface activation. After the pulsed DC voltage application, constant DC voltage was applied to raise the sintering temperature rapidly at a rate of 500 °C/min. and held at 1750 °C and 2000 °C for less than 1 minute. The temperature was measured at the graphite die surface using an optical pyrometer.

### *Dynamic Compression Testing*

In 1949, Kolsky developed a technique for the measurement of the properties of materials undergoing homogeneous deformation at fairly high strain rates [2]. The procedure has become known as the "Kolsky bar" or "split Hopkinson pressure bar (SHPB)". Since then, this technique has become the most widely used testing procedure for dynamic property measurement at strain rates between  $10^2$  to  $10^4$  s<sup>-1</sup>.

In this study, cylindrical test specimens of diameter 2.5 mm and length 4.5 mm were cut from the consolidated samples using EDM. Room temperature, high strain rate experiments were performed using the SHPB apparatus to study compression behavior of tantalum at dynamic loading conditions.

## RESULTS AND DISCUSSION

### *Plasma Pressure Compaction of Tantalum Powders*

The particle size of tantalum powder was analyzed by using BET. The surface area of the particles was calculated by measuring the amount of gas adsorbed on the surface. The measured surface area can be used to estimate average particle size by assuming that particles

are spherical. Table 1 shows surface area and average particle size of the tantalum powders consolidated by P<sup>2</sup>C.

Table 1 BET analysis of the tantalum powders.

Powders	Gas	Surface Area	Average Particle Size
Coarse Tantalum	Nitrogen	0.024 m <sup>2</sup> /g	15µm
Nano Tantalum	Nitrogen	5.772 m <sup>2</sup> /g	63 nm

The tantalum powders with particle size 15µm and 63 nm were consolidated at 2000 °C and 1750 °C, respectively at the same pressure and isothermal holding time by Plasma Pressure Compaction (P<sup>2</sup>C). The consolidation conditions and resulting densities are shown in Table 2. The results show that tantalum powders can be consolidated to high density in a short cycle time in the P<sup>2</sup>C process.

Table 2. Effect of sintering parameters on density of consolidated samples.

Powder Type	Temperature °C	Holding Time min	Pressure MPa	Density %
Ta (15µm)	2000	< 1	50	95
Ta (63 nm)	1750	< 1	50	95

Plasma Pressure Compaction is a novel consolidation technique capable of rapid densification by surface activation, particle welding, and plastic deformation mechanisms. The P<sup>2</sup>C consolidation of both coarse and nanocrystalline tantalum powders showed that the densification is enhanced as the particle size is reduced from 15µm to 63 nm. Nanocrystalline tantalum powder was consolidated to 95 % of the theoretical density at 250 °C below the sintering temperature required to achieve the same density with coarse tantalum powder. In both cases, the total cycle time required to consolidate tantalum powder was less than 10 minutes which is considerably shorter than conventional resistance sintering techniques.

The nanocrystalline particles have very high surface area which promotes densification. However, the greater intrinsic driving force associated with nanocrystalline particle size is not always available for sintering. Nanocrystalline particles have high cohesive force due to Van der Waals' attraction resulting in formation of agglomerates. Agglomerated particles resist compressive force by forming large interagglomerate voids which may not be broken up during the formation of the green body. In addition, nanocrystalline powders are so reactive that appreciable oxidation and adsorption of various gases occur upon exposure to the atmosphere. Surface oxides act as a diffusion barrier between particles and volatile contaminants cause outgassing during consolidation.

Despite such difficulties, P<sup>2</sup>C was able to rapidly consolidate nanocrystalline tantalum powder to high density. The successful densification of the nanopowder can be attributed to activating sintering mechanisms in the P<sup>2</sup>C process. In the initial stage of P<sup>2</sup>C, a pulsed DC voltage is applied directly through the powder compact. Electrical discharge takes at the interparticle gaps in the form of arc, plasma, and sparks which promote removal of oxides and other contaminants from the particle surfaces by generating significant heat and pressure [3]. Subsequently, external pressure and direct application of DC voltage accelerate the densification by inducing localized heating and plastic deformation at the interparticle contact areas.

Nevertheless, the SEM and EDAX results indicate that oxide phases are present in the nanocrystalline tantalum (Figure 1). Dense nanocrystalline tantalum without oxide phases may be produced by optimizing P<sup>2</sup>C consolidation parameters such as the pulsed DC voltage application (current, voltage, on-time, off-time, and baseline), constant DC voltage application (current density, voltage, and alternating polarity) heating rate, temperature, pressure, and isothermal holding time.

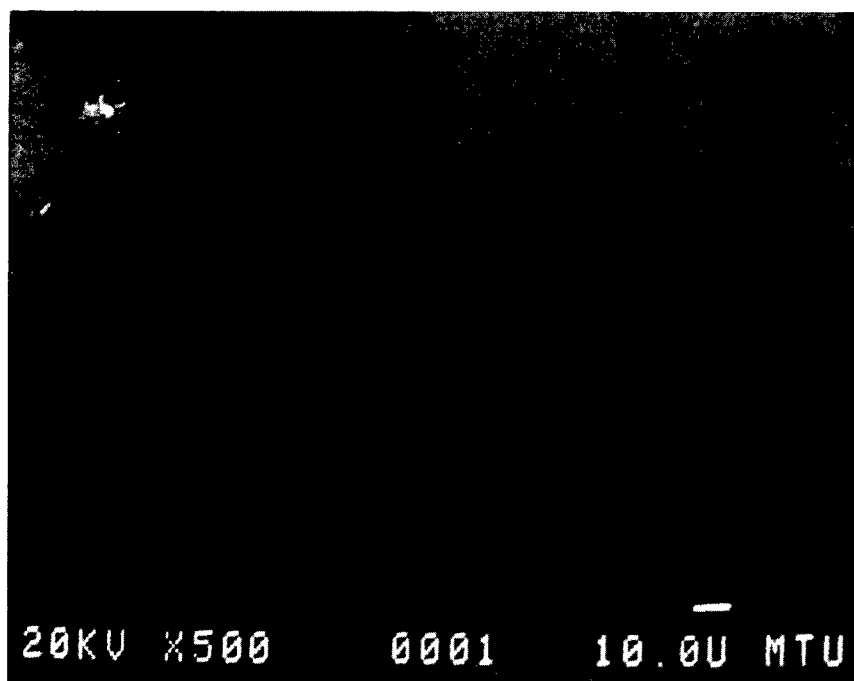


Figure 1 SEM picture of nanocrystalline tantalum consolidated by P<sup>2</sup>C. Dark areas indicate oxide phases

#### *Dynamic Compression of Consolidated Tantalum Specimens*

At high strain rates, both coarse tantalum and nano-tantalum exhibited ductile deformation behavior without significant brittleness/fracture. Stress-strain curves for the tantalum specimens are shown in Figures 2 and 3. Flow stress was essentially independent of strain rate, especially in the coarse tantalum specimen. This is in contrast to previous results wherein the flow stress of tantalum with grain size of  $\sim 3 \mu\text{m}$  and its alloys has been observed to increase with increasing strain rate ( $3000 - 10^3 \text{ s}^{-1}$ ) due to the high Peierl's stress in bcc metals [4]. Dynamic deformation testing should be conducted at a wider range of strain rate to confirm this result.

Tantalum normally exhibits significant strain hardening which is a function of the strain rate and pre-straining (cold work). Strain hardening is also found to be strongly dependent on texture and strain rate. However, strain hardening behavior was not observed in the P<sup>2</sup>C consolidated tantalum specimens at high strain rates. Moreover, nano-tantalum tends

to soften at high strain rates whereas coarse tantalum maintains its flow stress. It has been shown that prestraining reduces the hardening rate and limits the tensile failure strain [5]. Thus, plastic deformation occurring during the P<sup>2</sup>C process may have contributed to the dynamic compression behavior.

The compressive true stress-true strain response of tantalum consolidated from 15 $\mu$ m powder was found to be dependent on the applied strain rate (Figure 2). The strain increased with increasing strain rate while flow stress remained relatively constant. True strain between 0.11-0.18 was observed at a flow stress of 900-1000 MPa when compressed at strain rates between 1000-2500/s. The results correspond well with previous studies on dynamic compression properties of tantalum [5]. However, the lack of strain hardening observed in this P<sup>2</sup>C consolidated tantalum may be an advantage for high deformation rate applications.

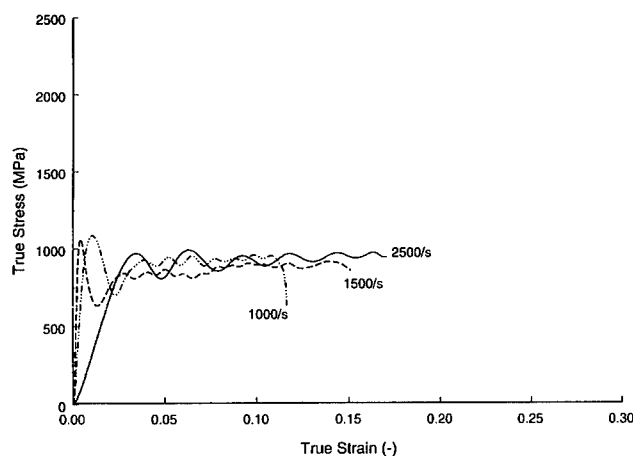


Figure 2 True stress-true strain curve of tantalum consolidated from coarse powder.

Ductility and flow stress increased dramatically as initial particle size is reduced below 100 nm. As shown in Figure 3, true strain and flow stress increased to 0.7 and 2400 MPa upon impact at strain rates of 9000/s and 12000/s. To the authors' knowledge, such a large strain at high flow stress has not been observed in randomly-oriented polycrystalline tantalum. The increase in flow strength of tantalum can be explained as follows. (1) grain boundary strengthening due to decrease in grain size as predicted by the Hall-Petch relation, and (2) presence of oxide phase detected in the nano-tantalum specimens.

Tantalum's properties, such as yield behavior, are highly sensitive to impurity and oxygen contents [4]. Typically, presence of oxide phase in the tantalum may increase the flow strength, but with a dramatic reduction in ductility because oxides are usually hard and brittle fracture initiating phases. In contrast, a significant increase in ductility has been observed in the rapidly consolidated nanocrystalline tantalum specimen despite a large amount of oxide phases. It is speculated that ductility of nano-tantalum is strongly influenced by its ultrafine grain size rather than the oxide phases present in the specimen. Even greater ductility may be achieved if the P<sup>2</sup>C consolidation parameters are optimized to remove most

of the oxygen in the initial particles. Further study must be conducted to understand the deformation mechanisms of the P<sup>2</sup>C consolidated nanocrystalline specimen.

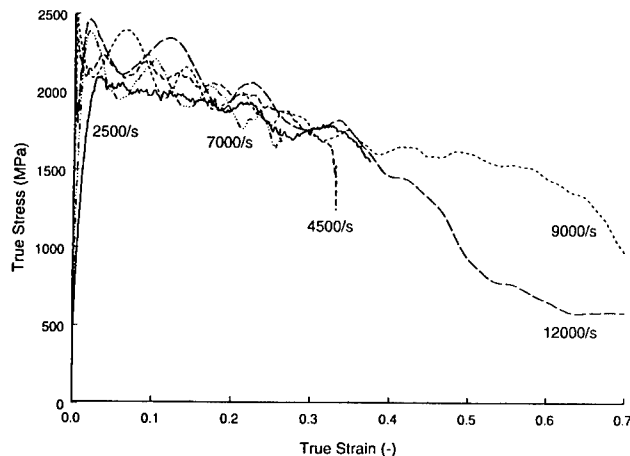


Figure 3 True stress-true strain curve for tantalum consolidated from nanocrystalline powder.

### SUMMARY

- Nanocrystalline tantalum powders were consolidated rapidly to high density by P<sup>2</sup>C at a temperature 250 °C lower than coarse tantalum powder due to large intrinsic driving force associated with fine particles.
- Increased flow stress was not observed with increasing strain rate as is common in BCC metals with a high Peierl's stress.
- P<sup>2</sup>C consolidated tantalum is suitable for high strain deformation applications because it does not exhibit strain hardening behavior.
- Flow stress and ductility were increased dramatically in the nanocrystalline tantalum with an early onset of softening despite the significant amount of oxide phase.
- Further investigation is required to understand the deformation mechanisms at high strain rates.

### REFERENCES

- [1] J. Karch, R. Birringer, and H. Gleiter, *Nature*, **330**, p556, 1987.
- [2] H. Kolsky, *Proceedings of the Research Society of London*, **B62**, p676, 1949.
- [3] S. H. Yoo, Master Thesis, "The Field Effects in PAS," Department of Chemical Engineering and Materials Science, University of California, Davis, June 1996.
- [4] G. Ravichandran, *Materials and Manufacturing Processes* **9**, 6, p1031, 1994.
- [5] G.T. Gray and A.D. Rollet, in *High Strain Behavior of Refractory Metals and Alloys*, edited by R. Asfahani, E. Chen, and A. Crowson, The Minerals, Metals & Materials Society, p303, 1992.



## SONOCHEMICAL APPROACH TO THE PREPARATION OF BARIUM HEXAFERRITE NANOPARTICLES

K. V. P. M. Shafi, A. Gedanken\*

Department of Chemistry, Bar-Ilan University, Ramat-Gan 52900, Israel

*Abstract -- A new method, via. the sonochemical decomposition of the solutions of organic precursors, for the synthesis of nanostructured crystalline single phase  $\text{BaFe}_{12}\text{O}_{19}$  particles is proposed. Nanosized amorphous precursor powders for  $\text{BaFe}_{12}\text{O}_{19}$ , were prepared by the sonochemical decomposition of the solutions of  $\text{Fe}(\text{CO})_5$  and  $\text{Ba}[\text{OOCCH}(\text{C}_2\text{H}_5)\text{C}_4\text{H}_9]_2$  in decane, under air at 273 K. The amorphous nature of these particles was confirmed by various techniques, such as SEM, TEM, SAED, and XRD, and the magnetic measurements indicated the superparamagnetic nature. The XRD of the heated sample of this confirmed the formation of single phase  $\text{BaFe}_{12}\text{O}_{19}$ , and the TEM micrograph revealed near uniform platelets with sizes less than 50 nm. The observed magnetization measured upto a field of 1.5 kG of the nanocrystalline  $\text{BaFe}_{12}\text{O}_{19}$  sample ( $48 \text{ emu g}^{-1}$ ) was significantly lower than that for the reported multidomain bulk particles ( $72 \text{ emu g}^{-1}$ ), reflecting the ultrafine nature of the sample. ©1999 Acta Metallurgica Inc.*

### INTRODUCTION

Hexagonal magnetic hard ferrite such as Barium hexaferrite,  $\text{BaFe}_{12}\text{O}_{19}$  is of great scientific and technological importance. Owing to their large crystalline anisotropy, high intrinsic coercivity, they are being used in the production of permanent magnets and in fabrication of certain microwave devices. Fine particles of  $\text{BaFe}_{12}\text{O}_{19}$  are currently used in high density perpendicular magnetic recording media. A wide range of low temperature chemical methods has been used to prepare ultrafine  $\text{BaFe}_{12}\text{O}_{19}$  particles, including the citrate precursor (1), pyrosol (2), combustion (3), chemical coprecipitation (4), sol-gel (5), and the microemulsion (6) methods. Barring the citrate precursor method, in all above methods, formation of single-phase  $\text{BaFe}_{12}\text{O}_{19}$  takes place at  $900^\circ \text{C}$  or above, and the particles obtained are of relatively larger sizes,  $> 50 \text{ nm}$ . Control over the size of the particles and uniformity, purity and good crystallinity is the major difficulty, in these synthetic methods.

Acoustic cavitation (the formation, growth, and subsequent implosive collapse of a bubble in an ultrasonically irradiated liquid) generates a transient localized hot spot with an effective temperature of  $5000 \text{ K}$  and a sub-microsecond collapse time (7). The rapid cavitation cooling rate ( $> 10^9 \text{ K s}^{-1}$ ) is much higher than that obtained by the conventional melt-spinning ( $10^5$  to  $10^6 \text{ K s}^{-1}$ ) technique (8) used to prepare amorphous materials.

Nanosized amorphous powders of Ni,  $\gamma$ -Fe<sub>2</sub>O<sub>3</sub>, NiFe<sub>2</sub>O<sub>4</sub>, Fe-Ni, and Co-Ni were prepared by this sonochemical method (9-13).

We have adopted this methodology, sonochemical decomposition technique to get the amorphous BaFe<sub>12</sub>O<sub>19</sub> precursor in colloidal solution, where the particles are in the nanometer size regime and are homogeneously distributed. The precursor is extracted from the solution as powder by precipitation or by evaporation and then calcined at low temperature (700° C) to get the final BaFe<sub>12</sub>O<sub>19</sub> crystalline nanoparticles.

### EXPERIMENTAL

A Decane solution of Fe(CO)<sub>5</sub> (Aldrich) and Barium ethylhexanoate, Ba[OOCCH(C<sub>2</sub>H<sub>5</sub>)C<sub>4</sub>H<sub>9</sub>]<sub>2</sub>, (Strem) in stoichiometric ratio, was decomposed by high intensity ultrasonication at 273 K, under air atmosphere, with a high intensity ultrasonic probe (Sonics and Materials, Model VC-600, 1.25-cm Ti horn, 20 kHz, 100 W cm<sup>-2</sup>). After four hours of irradiation, a reddish brown colored homogeneous colloidal solution was obtained. The precursor was extracted as powder from the solution by evaporation and or precipitation, which was then centrifuged and washed with pentane. Centrifuging and washing were repeated at least five times, and the product was then dried under vacuum. The precursor was then calcined at low temperature (700° C) to get the final BaFe<sub>12</sub>O<sub>19</sub> crystalline nanoparticles.

Powder X-ray diffractograms were recorded on a Rigaku X-ray diffractometer (Cu K $\alpha$  radiation,  $\lambda$  = 0.15418 nm). Scanning electron microscopy and energy dispersive X-ray analysis (EDX) were carried out on a JEOL-JSM-840 electron microscope. Transmission electron micrographs were obtained with a JEOL-JEM100SX electron microscope. Magnetization loops were measured at room temperature, using an Oxford Instrument Vibrating Sample Magnetometer. Elemental analyses were carried out on EA 1110 CHNS-O analyzer.

### RESULTS AND DISCUSSIONS

The compositions were determined by elemental and energy-dispersive X-ray analyses. The IR spectra of the precursor samples showed peaks characteristic of adsorbed ethylhexanoate ions on the surface. These adsorbed surfactants probably play an important role in stabilizing the amorphous structure of the samples. A scanning micrograph of powder shows coral-like features typical for non-crystalline materials. A drop of a suspension of amorphous BaFe<sub>12</sub>O<sub>19</sub> precursor in hexane was placed on a carbon coated Formvar copper grid (dia. 3 mm) and allowed to evaporate. Transmission electron micrograph (Fig. 1) reveals an array of rings of diameter about 600 nm that is much less than the ring reported by Ohara et al. and other 3D rings reported elsewhere (14). The annular width of the rings is about 25 nm. The selected area electron diffraction (SAED) pattern of the annular region shows the material is indeed amorphous with no evidence of ordered structure. The magnified image of the annular region reveals the aggregates of nanoparticles with overall diameters < 10 nm. The exact size of our particles is difficult to determine as these are aggregated. A closer look at the TEM picture, shows that the particles

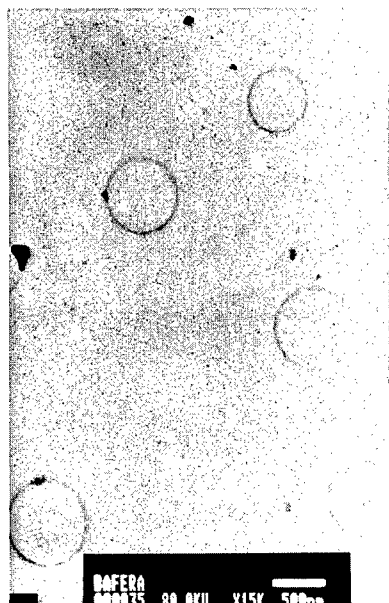


Fig. 1. TEM micrograph of amorphous BaFe<sub>12</sub>O<sub>19</sub> particle, showing Nanoring superstructures.

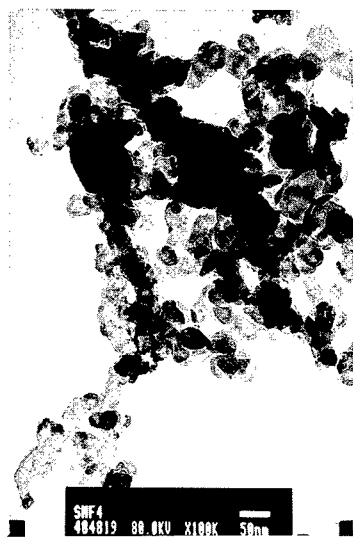


Fig. 2. TEM micrograph of crystalline BaFe<sub>12</sub>O<sub>19</sub> particles



inside and outside the rings are in uniform concentration that is very different from what Ohara et al. has observed. TEM micrograph of the heated specimen (Fig. 2), clearly shows near uniform particles with sizes less than 50 nm. The X-ray diffraction pattern for amorphous precursor, as well as the heated samples are depicted in Fig. 3. The amorphous solid does not show any peaks characteristic of crystalline materials. After heat treatment under air at 700° C for 5 h, the XRD pattern indicates a pure hexaferrite phase, with all major peaks matching the standard pattern of bulk crystalline  $\text{BaFe}_{12}\text{O}_{19}$ .

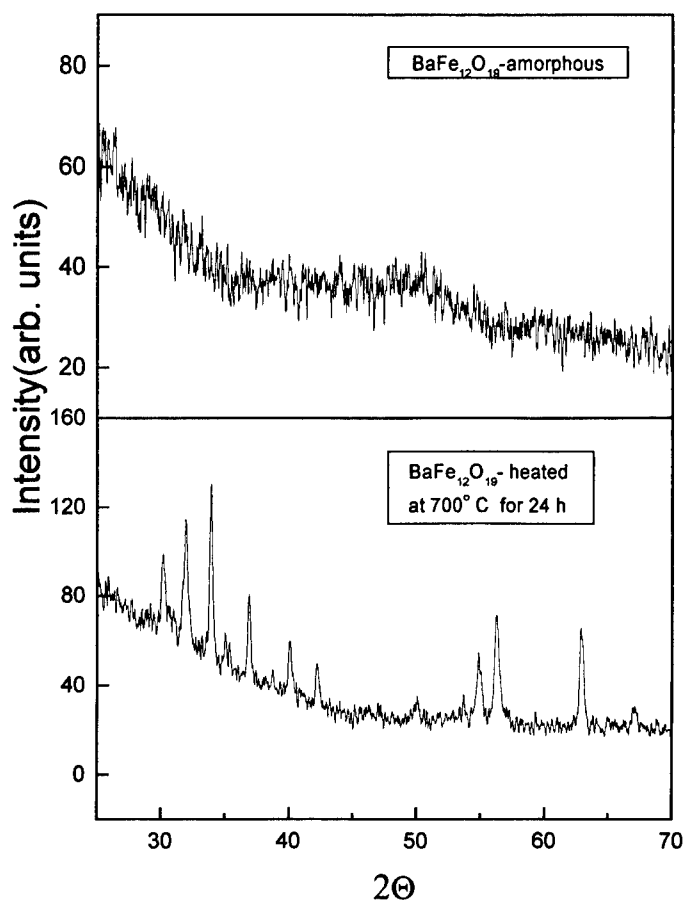


Fig. 3. XRD patterns for amorphous and crystalline  $\text{BaFe}_{12}\text{O}_{19}$  particle.

Room temperature magnetization curves of the as-prepared amorphous sample measured by VSM, does not reach saturation even at a magnetic field of 15 kGauss, and no hysteresis is found, indicating the particles are superparamagnetic. The magnetization (M) vs Field (H) curve is not found to be pure Langevin type owing to the distribution of particle sizes and the randomly oriented anisotropy axes. The Fig. 4 shows the magnetization curve of the

annealed sample  $\text{BaFe}_{12}\text{O}_{19}$ , heated for 15h at  $700^\circ\text{C}$ . The curve does not saturate even at 15 kOe, because of the high anisotropy field, of the order of 16 kOe, typical for a barium hexaferrite M-type structure.

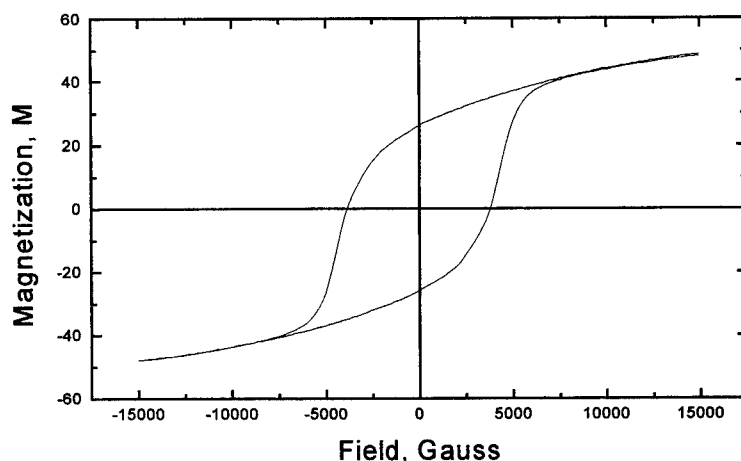


Fig. 4. Room temperature magnetization curve for crystalline  $\text{BaFe}_{12}\text{O}_{19}$ .

In the spinel type structure, the anisotropy field can be expected to be lower and hence the magnetization curves approach saturation at relatively lower fields. The observed values of magnetization of the annealed sample  $48\text{ emu g}^{-1}$ , at high enough field of 15 kG, is significantly lower than that for the reported (15) saturation magnetization for single crystals of  $\text{BaFe}_{12}\text{O}_{19}$  particles, i.e.  $72\text{ emu g}^{-1}$ , and this reflects the ultrafine nature of our sample. Various theories, including surface effects, spin canting and sample inhomogeneity have been proposed to account for the relatively low magnetization in fine particles. Specifically, the difference in the magnetization value between bulk and our nano-sized materials can be attributed to the small particle size effect. It is known that the magnetic properties like saturation magnetization and magnetic hyperfine field value, of nanoparticles are much smaller than those of the corresponding bulk materials (11,16). The energy of a magnetic particle in an external field is proportional to its size or volume via the number of magnetic molecules in a single magnetic domain. When this energy becomes comparable to  $kT$ , thermal fluctuations will significantly reduce the total magnetic moment at a given field. Another aspect for the reduced magnetization is the large surface to volume ratio for small particles. The magnetic molecules on the surface lack the complete co-ordination and also the spins are disordered. Another factor is the magnetic reverse domain formation. Haneda et al.(17) have reported the reverse domain formation, even for stress free formed barium hexaferrite particle of the order of 100-200 nm in size. The small impurities of antiferromagnetic metal oxides and carbides can also decrease the total magnetization. The observed magnetic properties of the barium ferrite particles at room temperature are : saturation magnetization,  $M_s = 48\text{ emu/g}$ , remnance magnetization,  $M_r = 25\text{ emu/g}$ , intrinsic

coercive field,  $H_c = 3980$  Oe and squareness ratio = 0.52. For  $BaFe_{12}O_{19}$  single crystal, a theoretical value of  $H_c$  of 6700 Oe has been estimated (18). The low value of coercive field in our system can be explained due to the low crystalline anisotropy which arises from crystal imperfection and the high degree of aggregation.

### CONCLUSION

A new method, via. the Sonochemical decomposition of the solutions of volatile organic precursors, for the synthesis of nanostructured crystalline single domain  $BaFe_{12}O_{19}$  particles is proposed.

### REFERENCES

1. Sankaranaryanan, V.K.; Khan, D.C. , *J. Mag. Magn. Mater.*, 1996, 153, 337.
2. Cabanas, M.V.; Gonzalez-Calvet, Labeau, M.; Molard, P.; Pernet, M. and Valett-Regi, M., *J. Solid State Chem.*, 1992, 101, 265.
3. Castro, S.; Gayoso, M.; Rivas, J.; Geneche, J. M. and Mira, J., *J. Mag. Magn. Mater.*, 1996, 152, 61.
4. Popov, O.; Rachev, P.;Mikhov, M.; Calderon, F.; Sanchez, J.L.; and Laccbue,F., *J. Mag. Magn. Mater.*, 1991, 99, 119.
5. Lucchini, E.; Meriani, S.; Delben, F. and Paoletti, S., *J. Mater. Sci.*, 1984, 19, 121.
6. Pillai, V.; Kumar, P.; Multani, P.S.; and Shah, D.O., *Colloids and Surfaces A: Physicochemical and Engineering Aspects*, 1993, 80, 69.
7. Flint, E. B. and Suslick, K. S., *Science*, 1991, 253, 1397.
8. Greer, A . L., *Science*, 1995, 267, 1947.
9. Koltypin, Yu.; Kataby, G.; Cao, X.; Prozorov, R. and Gedanken, A., *J. Non-Cryst. Solids*, 1996, 201, 159.
10. Cao,X.; Prozorov, R.; Koltypin, Yu.; Kataby, G.; Felner, I., and Gedanken, A., *J. Mater. Res* , 1997, 12, 402.
11. Shafi, K.V.P. M.; Koltypin, Yu.; Gedanken, A.; Prozorov, R.; Balogh, J.; Lendvai, J., and Felner, I., *J. Phys . Chem B*, 1997, 101, 6409.
12. Shafi, K.V.P. M.; Gedanken, A.; Goldfarb, R.B., and Felner, I., *J. Appl. Physic*, 1997, 81, 6901.
13. Shafi, K.V.P. M.; Gedanken, A.; Goldfarb, R.B., and Felner, I., *J. Mater. Chem*, 1998, 8, 769.
14. Ohara, P.C.; Heath, J.R., and Gelbart, W.G., *Ang. Chem. Int. Ed. Engl.* 1997, 36, 1078.
15. Shirk, B.T., and Buessem, *J. Appl. Phys.* 1969, 40, 1294.
16. Pannaparayil, T.; Marande, R.; Komerneni, S., and Sankar,S.G., *J. Appl. Phys.*, 1988, 64, 5641.
17. Haneda, K., and Morrish, H., *IEEE Trans. Magn.* 1989, 25, 2597.
18. Haneda, K., and Kojima H., *J. Appl. Phys.* 1973, 44, 3760.



Pergamon

NanoStructured Materials, Vol. 12, pp. 35–40, 1999

Elsevier Science Ltd

© 1999 Acta Metallurgica Inc.

Printed in the USA. All rights reserved

0965-9773/99/\$—see front matter

PII S0965-9773(99)00061-6

## NANOSTRUCTURED MATERIALS FROM SEVERE PLASTIC DEFORMATION

**R.Z. Valiev and I.V. Alexandrov**

Institute of Physics of Advanced Materials, Ufa State Aviation Technical University,  
450000, K.Marksa, 12, Ufa, Russia

***Abstract** - Recent results of the development of the severe plastic deformation methods to fabricate bulk nanostructured materials as well as results of their thorough structural characterization and investigations of their unusual deformation behavior and novel mechanical properties are presented. The structural model of nanomaterials processed by severe plastic deformation methods is developed on the basis of the obtained results.*

©1999 Acta Metallurgica Inc.

### INTRODUCTION

The technique resulting in fabrication of nano- and submicrocrystalline metals and alloys which was called severe plastic deformation (SPD) (1,2) assumes intense straining under high applied pressure at low temperatures (usually less than  $0.4 T_m$ ). Significant refinement of microstructure by large straining, for example, drawing or rolling, was revealed long time ago (3,4). However, as a rule, these methods lead to processing of a cell structure with low angle boundaries. As for SPD, it can form nanostructures with high angle grain boundaries (1,2).

Recent investigations showed that properties of nanostructured materials (NSMs) processed by SPD differ from properties of the corresponding coarse-grained materials (1,2). In particular, it was established that even fundamental parameters usually non-sensitive to structure such as Curie and Debye temperatures, elastic moduli, saturation magnetization, etc., can be changed in these materials. A significant increase in engineering properties, such as superstrength, superplasticity, elevated damping, attractive electric and magnetic properties and others, have also arosed great interest among the researchers. The character of unusual properties is caused by a specific internal structure that determines the necessity in thorough structural investigations of NSMs.

The present paper considers in brief recent results of studies of a structural characterization and development of a structural model as well as investigation and analysis of deformation behavior of NSMs processed by SPD.

### PROCESSING OF BULK NANOSTRUCTURED MATERIALS

Processing of nanostructured materials can be realized via special SPD methods, namely, torsion straining under high pressure and equal-channel angular (ECA) pressing and others.

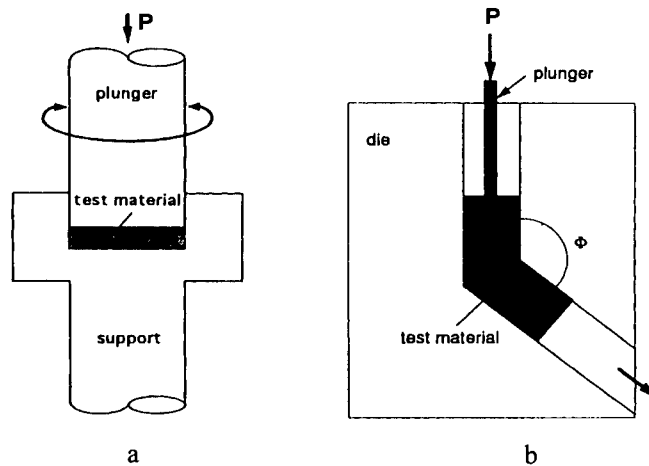


Figure 1. Principles of SPD methods: torsion straining under high pressure (a), ECA pressing (b).

During torsion straining the disc type billets, up to 20 mm in diameter and 1 mm in thick, were imposed to torsion under hydrostatic pressure of several GPa (Figure 1a).

During ECA pressing the billets, about 20 mm in diameter and up to 100 mm in length, were pressed several times through two crossing at an angle of 90° channels with equal cross sections (Figure 1b). Each pass through the channels results in additional strain approximately equal to 1. During ECA pressing from 8 to 12 passes were used.

It should be noted that formation of homogeneous nanostructures in bulk samples requires optimization of temperature-strain rate conditions of SPD, friction conditions between the material imposed to deformation and the tooling, and the magnitude and the character of deformation. As a rule, this task is specific for each material.

Recent investigations showed that SPD can be used not only for structure refinement but also as a method of powder consolidation (5). It was also shown that torsion straining under high pressure of several GPa can provide at room temperature a density of about 100% in bulk nanostructured samples.

## STRUCTURAL CHARACTERIZATION

TEM studies testify that SPD can provide formation of nanostructures in various metals including alloys and intermetallics. The resulting grain size depends on an applied method of SPD, processing regimes and material phase composition. In pure metals the severe torsion straining usually leads to formation of an equiaxed grain structure with a mean grain size of 50-150 nm, while ECA pressing provides a grain size of 200-300 nm. However, during SPD a decrease in the grain size can be obtained via varying parameters such as applied pressure, temperature and strain rate. Typical structures processed in Cu by severe torsion straining and ECA pressing are shown in Figure 2. It is seen that SPD results in formation of sufficiently homogeneous equiaxed structures. The observed diffraction patterns testify that the given structures are of a grain type having mainly high angle grain boundaries (6,7).

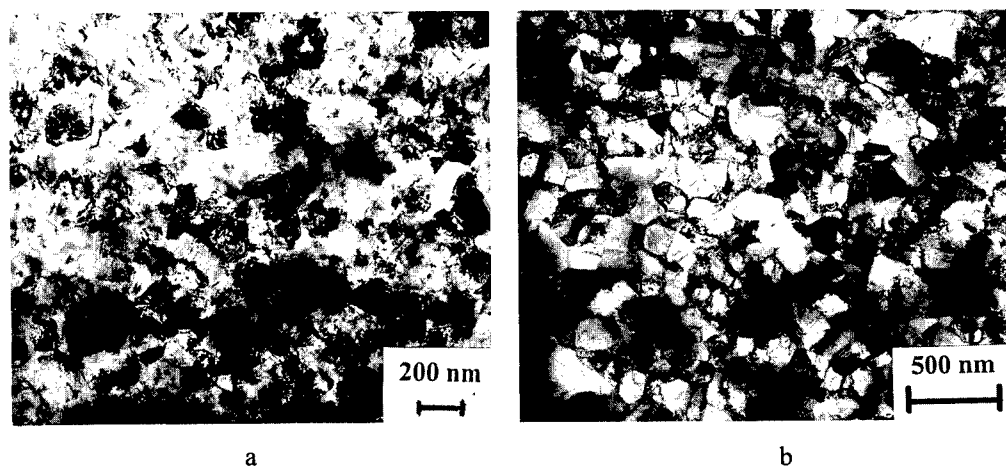


Figure 2. Typical nanostructures of Cu subjected to severe torsion straining (a) and ECA pressing (b).

A number of structural investigations of NSMs have been carried out in recent years. Their goal was not only to measure size and shape of grains but also to analyze specific defect structures including grain boundaries (GBs). These investigations confirmed the existence of non-equilibrium (non-relaxed) grain boundaries in such materials. The non-equilibrium GBs are connected with presence of grain boundary defects of high density. HREM studies of GBs in several metals and alloys subjected to SPD revealed a number of specific features (8,9). First of all, the crystallographic width of GBs is less than 1 nm, similar to the one usually observed in annealed materials. However, elastically distorted zones being several nanometers in width are observed in NSMs. Dilatation of a crystal lattice achieves 1.5% in such areas (8). Moreover, extrinsic steps and facets were revealed at GBs, which are responsible for long range elastic stresses causing distortions of a crystal lattice (9). The non-equilibrium GBs with defect structure exhibit often in TEM the spread diffusion contrast observed on GBs in different NSMs (1,10).

The results of X-ray analysis (11, 12) showed that X-ray patterns of the NSMs processed by SPD have a number of features distinguished from coarse-grained materials. Firstly, the relative maximum intensities of their X-ray peaks significantly differ from the corresponding tabular values. It is especially prominent in the samples processed by consolidation of ultra disperse powders (Figure 3). The mean grain size of these samples being equal to 15–20 nm is the minimal among the considered cases. The investigations showed the X-ray peak broadening is connected not only with the refinement of structure but also on the growth of crystal lattice microdistortions. Simultaneously the intense processes of texture formation occur during SPD.

It was established (11,12) that the grain size determined by TEM is usually much larger than the size of grains-crystallites determined by the X-ray structural analysis. The differences in grain sizes revealed by different methods are attributed to strong distortions of a crystal lattice and are typical for nanostructures forming by SPD.

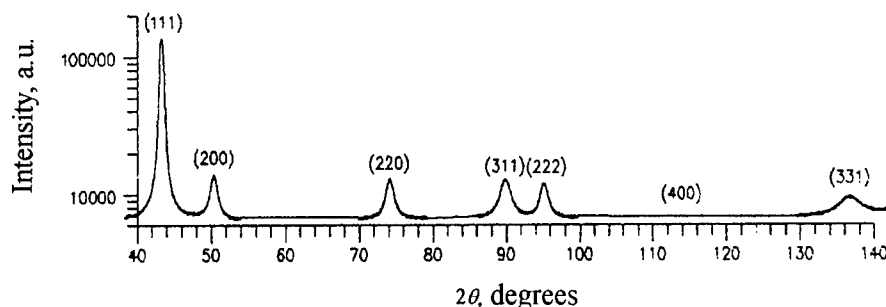


Figure 3. The X-ray pattern of Cu consolidated by severe torsion straining out of powder imposed to ball milling for 100 h.

One more typical feature of X-ray patterns of NSMs processed by SPD consists in a fraction of Lorentz function in the form of a profile of X-ray peaks achieving 90-100% (13). An increase in its fraction is also connected with a defect structure and microdistortions of a crystal lattice. The results of computer modeling of NSMs X-ray patterns confirm this fact too (14).

The results of X-ray structural analysis also showed that a value of Debye-Waller parameter in Cu subjected to SPD was higher than in starting Cu by 50% (13). In the nanostructured Cu the calculated values of atomic displacements happened to be equal to  $0.0126 \pm 0.0003$  nm that being 5.0% of the shortest distance between atoms. The Debye temperature was  $233 \pm 6$  K that was lower than a tabular value by 23%. Evidently, this is caused by distortions of a crystal lattice from defect GBs.

The results given above develop a structural model of nanomaterials processed by SPD (15). The present approach is based on concepts of the non-equilibrium grain boundaries containing extrinsic grain boundary dislocations of high density and the disclinations (16,17). Dislocations and disclinations initiate long range elastic stresses near grain boundaries and triple junctions and are responsible for excess energy of grain boundaries and dilatation of a crystal lattice. In the case of the grain size decreased to  $10 \div 20$  nm a crystal lattice of the whole grain happened to be elastically distorted (Figure 4). Such an unusual atomic structure of GBs and near boundary areas can be responsible for changes in physical and mechanical properties of nanostructured materials.

## DEFORMATION BEHAVIOR AND MECHANICAL PROPERTIES

The compression testing of nanostructured Cu showed that a view of true «stress-strain» curves depends on both the strain rate and the temperature of testing (Figure 5) (18). This and other recent investigations (19,20) allow us to conclude that deformation behavior of NSMs significantly differs from behavior of the corresponding coarse-grained materials. In particular, it confirms by the absence of strain hardening, the combination of high strength and significant ductility, non-stability in respect to low temperature annealing inherent in NSMs.

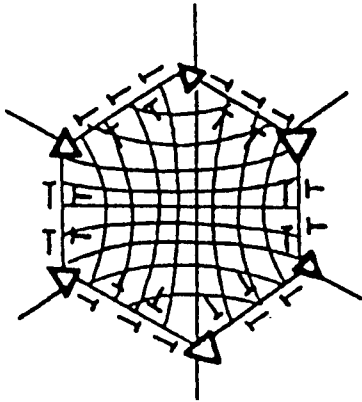


Figure 4. Structural model of a nanostructured material processed by SPD.

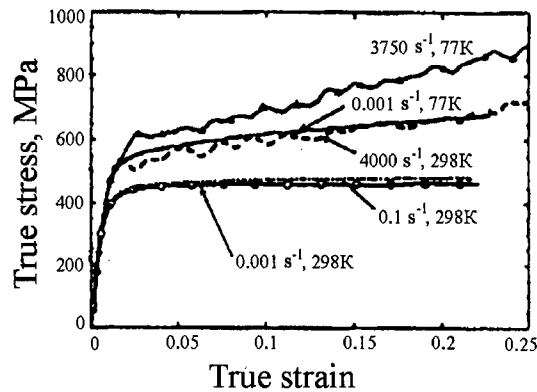


Figure 5. True stress-strain dependence for SPD Cu at different temperatures and strain rates.

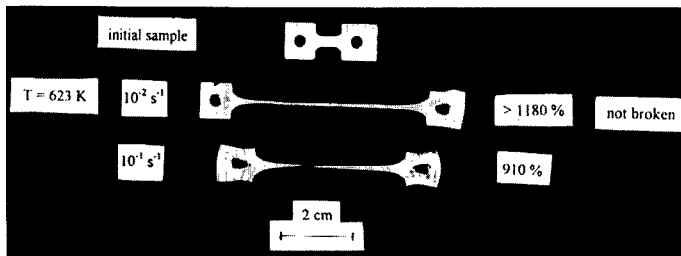


Figure 6. The appearance of high strain rate superplasticity in the Al-Mg-Li-Zr (1420) alloy, processed by ECA pressing.

The given behavior is conditioned not only by the presence of ultra fine grains but the specific defect structure of processed NSMs as well. (20). One more very interesting example is observation of superplasticity of NSMs at high strain rates and relatively low temperatures (Figure 6) (21). This phenomenon is very attractive in terms of forming complex shape articles.

### CONCLUDING REMARKS

Recent results demonstrate that bulk nanostructured metals and alloys can be successfully fabricated by SPD techniques. The processed materials are characterized either by the presence of ultrafine grains and also by the specific defect structure attributed to high density of extrinsic grain boundary dislocations resulting in crystal lattice distortions and



dilatation. These notions can be used as a basis for understanding the unusual deformation behavior and advanced properties of NSMs.

### REFERENCES

1. Valiev, R.Z., Korznikov, A.V., Mulyukov, R.R., *Mat. Sci. Enginer.*, 1993, A168, 141.
2. *Ultrafine-grained materials prepared by severe plastic deformation*, ed. by R.Z. Valiev, *Annales de Chimie. Science des Materiaux*, 1996, 21, 369.
3. Langford, G., Cohen, M., *Trans. ASM*, 1969, 82, 623.
4. Pavlov, V.A., *Phys. Metal. Metallurg.*, 1989, 67, 924.
5. Valiev, R.Z., In *Synthesis and processing of nanocrystalline powder*, ed. by D.L. Bourell, The Minerals, Metals and Materials Society, 1996, 153.
6. Valiev, R.Z., Krasilnikov, N.A., Tsenev, N.K., *Mater. Sci. Enginer.*, 1991, A137, 35.
7. Mishin, O.V., Gertsman, V. Yu., Valiev, R.Z., Gottstein, G., *Scr. Mater.*, 1996, 35, 873.
8. Valiev, R.Z., Musalimov, R.Sh., *Phys. Metals Metallogr.*, 1994, 78, 114.
9. Horita, Z., Smith, D.J., Furukawa, M., Nemoto, M., Valiev, R.Z., Langdon, T.G.; *J. Mater. Res.*, 1996, 11, 1880.
10. Musalimov, R.Sh., Valiev, R.Z., *Scr. Metall. Mater.*, 1982, 12, 1685.
11. Alexandrov, I.V., Zhang, K., Lu, K., Valiev, R.Z., *Nanostr. Mater.*, 1997, 9, 347.
12. Zhang, K., Alexandrov, I.V., Valiev, R.Z., Lu, K., *J. Appl. Phys.*, 1996, 21, 407.
13. Zhang, K., Alexandrov, I.V., Kilmametov, A.R., Valiev, R.Z., Lu, K., *J. Phys. D: Appl. Phys.*, 1997, 30, 3008.
14. Alexandrov, I.V., Valiev, R.Z., *Phil. Mag.*, 1996, B 73, 861.
15. Valiev, R.Z., *Nanostr. Mater.*, 1995, 6, 73.
16. Nazarov, A.A., Romanov, A.E., Valiev, R.Z., *Acta Metall. Mater.*, 1993, 41, 1033.
17. Gertsman, V.Yu., Birringer, R., Valiev, R.Z., Gleiter, H., *Scr. Mater.*, 1994, 30, 229.
18. Gray III, G.T., Lowe, T.C., Cady, C.M., Valiev, R.Z., Aleksandrov, I.V., *Nanostr. Mater.*, 1997, 9, 477.
19. Valiev, R.Z., Kozlov, E.V., Ivanov, Yu.F., Lian, J., Nazarov, A.A., Baudelet, B., *Acta Metall. Mater.*, 1994, 42, 2467.
20. Valiev, R.Z., *Mater. Sci. Forum*, 1997, 243-245, 207.
21. Valiev, R.Z., Salimonenko, D.A., Tsenev, N.K., Berbon, P.B., Langdon, T.G., *Scr. Mater.*, 1997, 37, 1945.



Pergamon

NanoStructured Materials, Vol. 12, pp. 41–44, 1999

Elsevier Science Ltd

© 1999 Acta Metallurgica Inc.

Printed in the USA. All rights reserved

0965-9773/99/\$—see front matter

PII S0965-9773(99)00062-8

## NANOSTRUCTURED OXIDE FILMS BY FERRITE PLATING WITH SONOCHEMISTRY

Yoshitaka Kitamoto and Masanori Abe

Department of Physical Electronics, Tokyo Institute of Technology

O-okayama, Meguro-ku, Tokyo, 152-8552, JAPAN

**Abstract** — Applying power ultrasound waves (19.5 kHz, 600 W) to 300 ml of  $\text{FeCl}_2$  aqueous solution (pH=7.0) at 70 °C, we successfully encapsulated polyacrylate spheres of 250 nm in average diameter with magnetite ferrite coatings. This broke the previous lower limit (300 nm) of the size of the particles to be encapsulated; without application of the ultrasound waves, the ferrite coating became discontinuous or insular. From TEM observations of the cross sections, the polymer spheres were covered with uniform columnar crystallites of 30–40 nm at the bottom and 60–70 nm at the top in diameter. The ultrasound waves produce on the polymer surfaces OH groups, which work as ferrite nucleation sites; this improved the quality of the ferrite coatings. The ferrite-encapsulated particles will greatly improve the performance of the enzyme immunoassay as a cancer test reagent.

©1999 Acta Metallurgica Inc.

### INTRODUCTION

Sonochemistry, the use of power ultrasound to stimulate chemical processes in liquids, is currently the focus in a wide range of chemical materials science and technology, since it causes novel chemical and physical reactions that do not occur unless sonically stimulated (1). The power ultrasound generates in the liquids localized "hot spots" of extremely high temperatures (~3,000K) and high pressures (~1,000atm) due to collapse of cavitation bubbles; the hot spots activate not only chemical reactions but also dynamics of ions. This paper reports that combining sonochemistry with ferrite plating, a chemical ferrite film synthesis (2), broke the limitation inherent in the ferrite plating. Since the hot spots are localized, the average temperature of the solution is kept at below 100°C. It allows us to use non-heat-resistant substrates, as well as in cases without applying the ultrasound. We performed ferrite plating, with and without the ultrasonic stimulation, on polyacrylate microspheres of 250 nm in average diameter in order to fabricate magnetically-separable carrier particles in clinical enzyme immunoassay (3, 4).

### EXPERIMENTAL

As show in Fig. 1, ultrasound waves (19.5 kHz, 600 W) were applied through a horn (30 mmφ) to an aqueous reaction solution (300 ml) of  $\text{FeCl}_2$  kept at 70°C, in which polyacrylate spheres, 250 nm in average diameter, were dispersed. A  $\text{NaNO}_2$  solution, an oxidizing agent, was supplied to the solution keeping the oxidation-reduction potential (ORP) at -500 mV, and a  $\text{NH}_4\text{OH}$  solution to

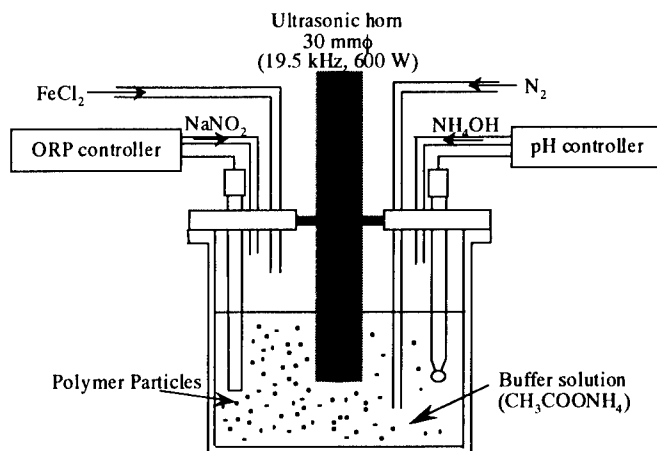


Fig. 1 Apparatus of ultrasound enhanced ferrite plating for polymer microspheres.

keep the pH value at 7.0. For comparison, we also performed the ferrite plating without the sonication, agitating the aqueous solution with a spinning stirrer that was replaced for the ultrasound horn. The surfaces of the ferrite coatings were observed by a field emission type SEM. The cross sections of the plated particles were observed by TEM on ultramicrotome-slices (60 nm in thickness) of an acrylate resin in which the particles were embedded. The crystallographic and magnetic properties of the synthesized coatings were investigated at room temperature, using a  $\text{CuK}\alpha$  X-ray diffractometer, a  $\text{Co}^{57}$ -Mössbauer spectrometer and a vibrating sample magnetometer.

## RESULTS AND DISCUSSION

As Fig. 2(a) shows, the spheres plated with the sonication for 90 minutes were entirely encapsulated with continuous ferrite coatings. On the other hand, when plated without the sonication, the ferrite coatings covered the surfaces only in part as shown in Fig. 2(b). SEM photographs in Fig. 3 show the surfaces of the spheres at the initial stage of the film synthesis with the sonication for (a) 1 min and (b) 2 min. They show that the number of grains of 30–40 nm in size increases with increasing the reaction time. Figure 4 shows the dark field image of the cross sections of the spheres plated with the sonication observed by TEM. Uniform ferrite grains like columns are observed on the polyacrylate spheres. The columnar diameter near the sphere surface is 30–40 nm; this value corresponds with the grain size seen in Fig. 3. The diameter increases with the coating thickness, reaching 60–70 nm at the coating surface. Taking the thickness of the magnetite coating (100 nm) and the diameter of the microspheres (250 nm) into account, the grain size should increase to 60–70 nm at the top from 30–40 nm at the bottom. In the electron diffraction, the selected area of which corresponds to a single sphere with the ferrite coating, while the diffraction pattern of the coating synthesized without the sonication was a ring one, that of the coating with the sonication was a spot one. These electron diffraction patterns suggest that crystallographic texture of each grain seen in Fig. 4 is well oriented like a single crystal.

These morphological and crystallographic improvements in the ferrite coatings synthesized

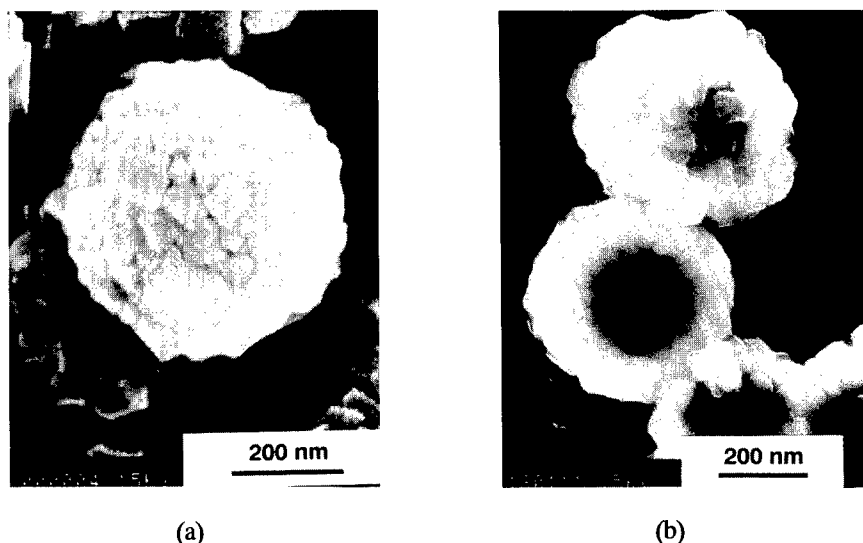


Fig. 2 SEM observations of polyacrylate microspheres, which were plated (a) with sonication for 90 min and (b) without sonication for 90 min.

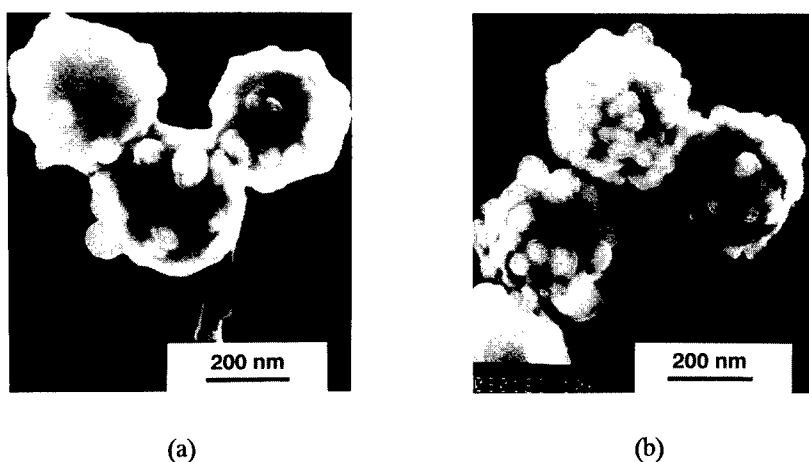


Fig. 3 SEM observations of spheres, which were plated with sonication for (a) 1 min and (b) 2 min.

with the sonication are derived not only from the activation of the ion migration by the ultrasound stimulation. The hot spots generated in the sonicated aqueous solution produce such radicals as  $\text{OH}^\bullet$  and  $\text{H}^\bullet$  (1), which bring about OH groups on the surfaces of the polyacrylate spheres; the OH groups work as the nucleation sites for the ferrite plating (2). Therefore, the ferrite coatings synthesized with the sonication were composed of uniform and fine grains, and became continuous (Figs. 2(a) and 4), while those synthesized without the sonication were incompletely covering the surface (Fig. 2(b)).

The ferrite coatings that were synthesized with and without the sonication from the  $\text{FeCl}_2$  aqueous solution were single-phase magnetite as examined by the X-ray diffractometry. Their Mössbauer spectra were computer-fitted, as a typical example is shown in Fig. 5. Paramagnetic

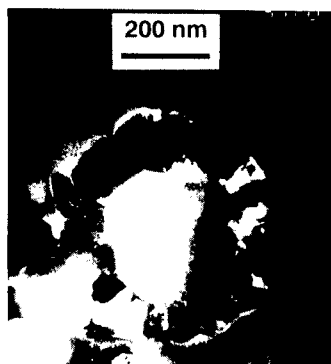


Fig. 4 Cross section of spheres, which were plated with sonication observed by TEM.

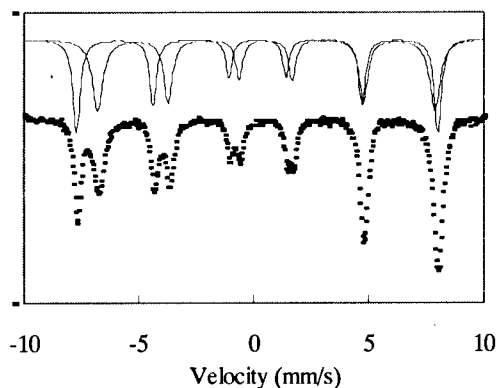


Fig. 5 Mössbauer spectrum for ferrite coatings synthesized with sonication for 90 min.

impurity phase is not exhibited in the spectrum. The magnetization  $M_s$  was 92 emu/g that corresponds to the value of bulk magnetite. The entirely encapsulated particles fabricated with the sonication should show better performance in magnetic separation, since they have larger area covered with ferrite coatings resulting in the larger magnetization.

### CONCLUSION

The power ultrasound waves enabled us to encapsulate the polyacrylate spheres of 250 nm in diameter. This is because the sonication increased the number of the OH groups (the nucleation sites of the ferrite coatings) on the polymer surface. TEM observations of the cross sections revealed that crystallographic texture of each grain is well oriented.  $M_s$  was 92 emu/g that is almost equal to the bulk value. Therefore, the encapsulated particles synthesized with the sonication will improve the performance as magnetically-separable carrier for antibody in an enzyme immunoassay for cancer test.

### ACKNOWLEDGEMENT

This study has been financially supported by Grant-in-Aid for Scientific Research (C) from the Ministry of Education, Science, Sports and Culture; and by the "Research for the Future" Program, from the Japan Society for the Promotion of Science.

### REFERENCES

1. T.J. Mason, Chem. Industry, **18**, January, 47, 1993.
2. M. Abe, T. Itoh and Y. Tamaura, Thin Solid Films, **216**, 155, 1992.
3. S. Nagahata, M. Sasaki, K. Yoshita, et al., Proc. 6th Int. conf. Ferrites (ICF 6), 279, 1992.
4. I. Nishizono, S. Iida, N. Suzuki, H. Kawada, et al., Clin. Chem., **37**, 1639, 1991.



## SIZE-SELECTED GOLD NANOPARTICLES BY AEROSOL TECHNOLOGY

Martin H. Magnusson, Knut Deppert, Jan-Olle Malm<sup>1</sup>,  
Jan-Olov Bovin<sup>1</sup>, and Lars Samuelson

Solid State Physics, Lund University, Box 118, 221 00 Lund, Sweden

<sup>1</sup>Inorganic Chemistry 2, Lund University, Box 124, 221 00 Lund, Sweden

**Abstract** -- We have produced size-selected gold particles with sizes below 30 nm by means of aerosol technology. The method allows for particles of many different materials to be produced with high purity and narrow size distribution, and it allows easy transport and deposition of the particles onto any substrate. The particle quality has been investigated by transmission electron microscopy, revealing a high degree of crystallinity, especially after sintering at high temperatures. ©1999 Acta Metallurgica Inc.

### INTRODUCTION

The use of very small particles as building blocks in electronic circuits and nanostructured materials demands that these particles be produced with high efficiency and purity. For many applications, e.g., where Coulomb blockade or quantum size effects are studied, it is important that the particles have a narrow size distribution. A common means for producing particles with a narrow size distribution is colloid chemistry, which can give good results. A problem with colloids is that the particles must be coated with a surfactant if they are not to coalesce, which will inevitably introduce some contaminants. Also, wet chemical methods are, in general, less clean than gas-phase methods, and usually involve production in batches. In our approach, through aerosol technology, the particles are produced in a continuous flow, and in a very clean environment. The method is naturally suited for large scale production. We present a characterization of the method itself, and of the gold particles produced.

### EXPERIMENTAL

A schematic of the aerosol fabrication apparatus is shown in fig. 1; it is similar to the one previously used to produce nanoparticles of Ag (1). It works as follows: A ceramic boat containing high purity gold (99.9999%) is placed inside a tube furnace, which is heated to 1650 °C, creating a gold vapor. Through the furnace passes a flow of nitrogen carrier gas, at 1.68 l/min (purity >99.998%). As the gold vapor leaves the heated zone, it condenses into particles, which then start to coagulate, resulting in a wide size distribution (2). The aerosol thus created is passed through a charging device, which uses UV light to create free electrons

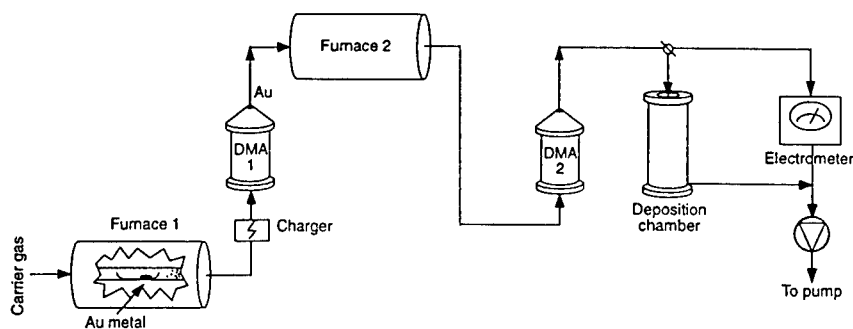


Figure 1: Schematic of the aerosol fabrication machine.

and positively charged particles. The free electrons can then charge the neutral particles, and the net effect is an aerosol consisting of uncharged and both positively and negatively charged particles. Due to the Coulomb blockade effect in such small objects, multiply charged particles are rare. The charged aerosol is then sent through a differential mobility analyzer (DMA), which classifies the particles according to their aerodynamic diameter (3); this diameter is the same as the geometric diameter only if the particle is spherical. By balancing the force from an electric field with the drag from a gas flow used to flush unwanted particles, it is possible to extract particles of a certain size, the distribution of which can be made as narrow as 5% of the mean diameter. We know from earlier studies (4) that the theory for the DMA gives a slight overestimate of the particle diameter; the TEM study in the present work was not aimed at size statistics, but all the particles investigated have a diameter that is somewhat smaller than the one set on the DMA. The particle concentration is measured with an electrometer.

After the DMA, the aerosol consists of particles of the same size, and all are (singly) charged, either positively or negatively, depending on the polarity of the electric field in the device. Due to their coagulation history, the particles are not very compact, but have a fractal-like structure. In order to make them spherical, the particles are sintered in a second tube furnace. To monitor the change in the particle diameter, a second DMA is used. By setting the first DMA to a fixed diameter, and by scanning the second DMA, we can obtain the size distribution of the particles after the sintering furnace, for different sintering temperatures.

To study the crystallinity of the particles, high resolution transmission electron microscopy (TEM) was used. The particles were collected on standard grids for TEM; since the particles are still charged, they can easily be collected on any substrate by means of an electric field. The TEM studies were made on both sintered and unsintered particles. The sintering process, needed to make the particles spherical, is best understood by combining the size distribution obtained by the DMA with the structural and morphological information from the TEM.

## RESULTS

Both the DMA and the TEM measurements confirm that particles are produced in the desired size range. The particles have a spread in their size distribution of approximately 20%.

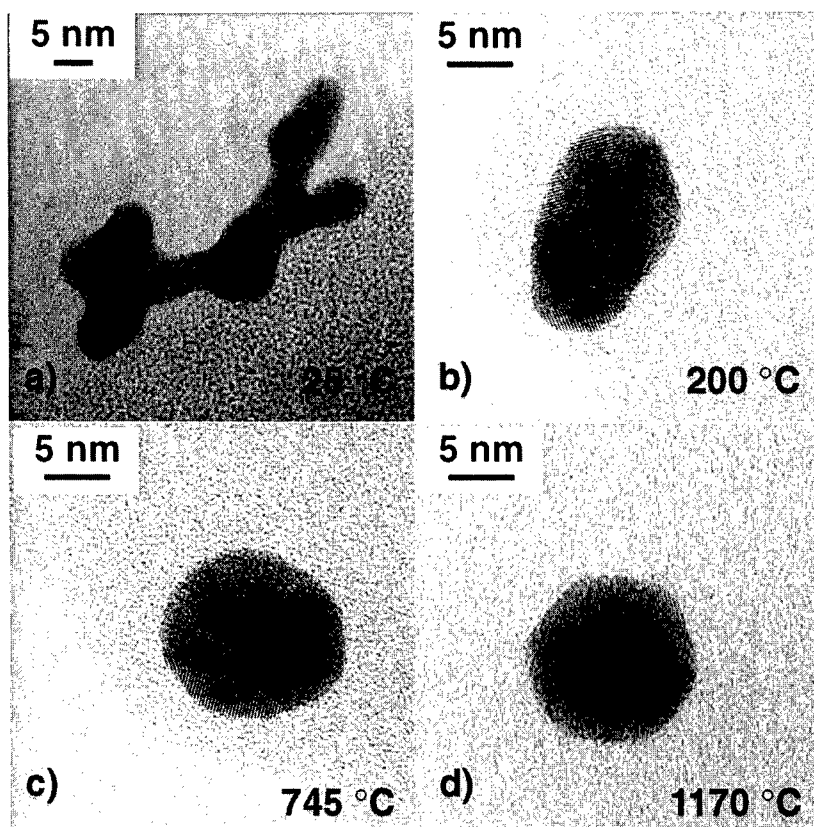


*Figure 2: TEM images of gold particles sintered at different temperatures. Note how the compacting of the particles is accompanied by an increase in crystallinity. Also note the faceting of particle d) sintered at 1170 °C.*

The amount of particles produced is sufficient for electronics applications; when deposited onto a substrate, the surface coverage is around  $3 \cdot 10^8 \text{ cm}^{-2} \text{ min}^{-1}$ .

The particles leaving the evaporation furnace are agglomerates, consisting of a number of smaller particles, cf. fig. 2 a). The size scan performed with the DMA shows that the particle diameter after the sintering furnace decreases by approximately 10% as the sintering temperature is raised from 25 °C to 200 °C, and after this the diameter remains constant. From the change in particle diameter, it thus seems as if the sintering process is more or less complete above 200 °C. The TEM study shows, however, that this is not the case. Although the particles sintered at 200 °C are compact, they are polycrystalline and may contain voids. With increasing temperature, the particles become more compact and more crystalline. Figure 2 shows four examples of gold particles sintered at different temperatures: a): unsintered (25 °C), b-d): sintered at 200 °C, 745 °C, and 1170 °C, respectively. The particles sintered at 745 °C, fig. 2 c), are spherical but polycrystalline, and they resemble particles of similar size grown in



colloid solution. The last temperature is above the melting point of gold, so the crystallinity should be fairly high, which can be seen in fig. 2 d). The forming of facets may not be surprising, since the particle has had time to crystallize when leaving the sintering furnace.

### CONCLUSIONS

We have produced size-selected particles of gold. The particles are very irregular in their shape if they are not sintered. After sintering, the particles become compact, spherical, and even highly crystalline, depending on the sintering temperature. We believe that well-defined particles of this kind will become important in future electronics applications.

### ACKNOWLEDGEMENTS

The work was performed within the Nanometer Structure Consortium and was financed by NFR, TFR, NUTEK, SSF, and the ESPRIT Charge program, project No. 22953.

### REFERENCES

1. K. Deppert, I. Maximov, L. Samuelson, H.-C. Hansson, and A. Wiedensohler, *Appl. Phys. Lett.*, **64**, 3293 (1994).
2. H. G. Scheibel and J. Porstendörfer, *J. Aerosol Sci.*, **14**, 113 (1983).
3. E. O. Knutson and K. T. Whitby, *J. Aerosol Sci.*, **6**, 443 (1975).
4. D. Hummes, S. Neumann, F. Schmidt, M. Drötboom, H. Fissan, K. Deppert, T. Junno, J.-O. Malm, and L. Samuelson, *J. Aerosol Sci.*, **27**, S163 (1996).



Pergamon

NanoStructured Materials, Vol. 12, pp. 49–54, 1999

Elsevier Science Ltd

© 1999 Acta Metallurgica Inc.

Printed in the USA. All rights reserved

0965-9773/99/\$—see front matter

PII S0965-9773(99)00064-1

## NANOPARTICLES OF MICROPOROUS MATERIALS

B. J. Schoeman<sup>†</sup>, K. Higberg and J. Sterte

Division of Chemical Technology, Luleå University of Technology, S-971 87 Luleå, Sweden,

<sup>†</sup>Central & New Businesses R&D, The Dow Chemical Company, Midland, MI 48674, USA.

**Abstract** — *The hydrolysis and condensation of tetraethoxy silane in the presence of structure directing agents, such as the tetraalkylammonium cations, results in the formation of microporous siliceous particles with average sizes in the range 2 to 5 nm, the size being a function of the hydrolysis conditions and the composition of the mixture. Increased dilution favors larger particles while increased pH results in smaller particles. The option of isomorphous substitution of silicon for either alumina or titania is also shown to result in nano-sized particles where the substituted metals exist in the tetrahedral coordination.*

©1999 Acta Metallurgica Inc.

## INTRODUCTION

Microporous materials, in particular zeolites or molecular sieves, play a significant role within the field of catalysis. Another application for zeolites is as ion-exchangers in detergent formulations and several other novel application areas may be envisaged. Over the past decades, a wealth of literature has appeared in which the procedures for the synthesis of these materials is presented. The general zeolite synthesis route is via the hydrothermal treatment (at typically 100°C and autogeneous pressure) of an aqueous alkaline metallosilicate- or silicate gel. The microporous crystals obtained by hydrothermal treatment are generally in the micron size range although it is possible to decrease the average crystallite size by for example, reducing the temperature of crystallization (1) or the addition of trace amounts of growth inhibiting agents (2). However, in certain catalytic applications smaller crystal sizes are required due to, for example, diffusional limitations. There are now several reports in the literature describing methods to prepare smaller crystals in the colloid size range, wherein crystal sizes are typically 30 to 200nm (3).

A material that has attracted attention is the molecular sieve Silicalite-1 (4). The ideal unit cell composition is  $(\text{TPAOH})_4(\text{SiO}_2)_{96}$  where TPAOH is tetrapropylammonium hydroxide and serves as the structure directing agent (SDA). The quaternary ammonium cation may be introduced to the synthesis mixture as the salt, typically the bromide, or as the hydroxide. If the latter is employed as an aqueous solution together with a silane as the silica source, a water clear synthesis solution is obtained following the hydrolysis of the silane. The hydrolyzed solution may then be heat treated at 100°C to ultimately yield a colloidal

suspension of silicalite-1 crystals (5). Manipulation of the synthesis parameters allows for the synthesis of crystallites in the size range 50 to several hundred nanometers.

It was very recently recognized that the TPA (tetrapropylammonium)-stabilized silicate precursor solutions following hydrolysis but *prior to hydrothermal treatment* at elevated temperatures contain sub-colloidal particles with sizes smaller than 5nm (6). The present study highlights the parameters influencing the preparation of the nanosized particles.

## EXPERIMENTAL

### *Materials*

The silica source was always tetraethoxy silane - TEOS (Merck, GC grade >98%) and the alumina source was alumina isopropoxide (Sigma). The tetraalkylammonium ions were derived from the respective hydroxides viz. Tetramethylammonium - TMA (TMAOH  $5\text{H}_2\text{O}$ , Sigma), Tetraethylammonium - TEA (Sigma, 40% in water), Tetrapropylammonium - TPA (Sigma, 1M in water, 6ppm Na, < 5 ppm K) and Tetrabutylammonium - TBA (Sigma, 40% in water, 21 ppm Na, 10 ppm K). The sodium source was NaOH (Labassco, Sweden).

### *Precursor Preparation*

A typical precursor preparation entails the hydrolysis of tetraethoxy silane (TEOS) in the presence of a dilute aqueous solution of a tetraalkylammonium (TAA) hydroxide where the alkyl group may be as described above. All reactions were performed at room temperature (ca. 23°C) for at least 24 hours unless specified otherwise. Typical molar compositions of the precursor solutions are;  $x \text{ TAAOH} + 25 \text{ SiO}_2 + y \text{ H}_2\text{O} + 100 \text{ EtOH}$  (EtOH = ethanol, the hydrolysis product) where  $3 \leq x \leq 9$  and  $480 \leq y \leq 1500$ .

### *Characterization*

Particle size analyses were performed using a Brookhaven Instruments BI200SM equipped with a 2W Lexel Ar-ion laser operating at 514.5nm in the angular range 30 - 155°. The Non-Negative Least Squares (NNLS) data analysis method was used to determine the diffusion coefficients from which the average particle size was calculated. All samples were filtered through 0.2  $\mu\text{m}$  nominal pore size Gelman Sciences filter membranes prior to analysis. Diffuse Reflectance FT-i.r. (DRIFT) spectra were recorded with a Perkin Elmer FT-i.r. 1760X spectrometer (200 scans, resolution 2  $\text{cm}^{-1}$ ) using the KBr wafer technique. FT-Raman spectra were recorded using a Perkin Elmer PE1700X NIR FT-Raman spectrometer equipped with a Nd:YAG laser (300 scans, resolution 4  $\text{cm}^{-1}$ ).  $^{27}\text{Al}$  MAS NMR spectra were recorded with a Chemagnetics CMX-370 spectrometer (8.36T) with a single 90° pulse over 2.4  $\mu\text{s}$ . A standard double bearing 7.5mm rotor system ( $\text{ZrO}_2$ ) was used. Spinning speeds were either 3000, 5000 or 7000 Hz. Chemical shifts were referenced to a 1.125M  $\text{Al}_2(\text{SO}_4)_3$  solution. Thermogravimetric analyses (TGA) were performed using a Perkin Elmer TGA 7 Analyzer with  $\text{N}_2$  and a heating rate of 10°/min. Specific surface area measurements were performed on calcined samples using a Micromeritics ASAP 2010 instrument and specific

surface areas were calculated using the BET equation. Samples were degassed at 100°C prior to analysis. The calcining conditions were varied considerably in an attempt to determine the optimum conditions. As an example, the powders were calcined in air at various temperatures in the range 250 to 400°C for exactly 4 minutes.

## RESULTS AND DISCUSSION

Two samples with the same batch composition: 9 TBAOH 25 SiO<sub>2</sub> 480 H<sub>2</sub>O 100 EtOH, hydrolyzed at 25°C and at 8°C for 30 days produces two sols that when hydrothermally treated at 100°C, yield significantly different results - 60 and 90nm respectively as measured with light scattering. Quite clearly, the hydrolysis conditions are a major factor influencing the crystallization product and hence it is clear that the characteristics of the precursor sol prior to hydrothermal treatment are strongly affected.

All solutions prepared as described above are "water-clear" solutions that may best be described as aquasols containing discrete particles with diameters in the lower colloid size range, < 5nm. Due to the small particle size, they do not scatter light visible to the naked eye, but the presence of particles is easily detected with light scattering techniques as is shown in Figure 1. As described above, hydrothermal treatment of the TPA-silicate precursor sols yield colloidal silicalite-1 crystals in the size range 50 to several hundred nanometers. Due to their relatively large size, these materials exhibit the X-ray diffraction (XRD) patterns typical for this crystalline phase (4). Powder samples of the precursor sols prior to hydrothermal treatment do not however possess so-called XRD crystallinity (as opposed to FT-i.r. (infra red) crystallinity or short range order). If at this stage of the discussion it is assumed that the particles are spherical with an average size of 3nm, and that the particles are silicalite-1 with unit cell dimensions of 20.1 x 19.9 x 13.4 Å, it may be calculated that each particle is made up of only 2 to 3 unit cells. It appears that the 'degree of crystallinity' in particles of such small size relative to the unit cell dimensions is insufficient to exhibit Bragg

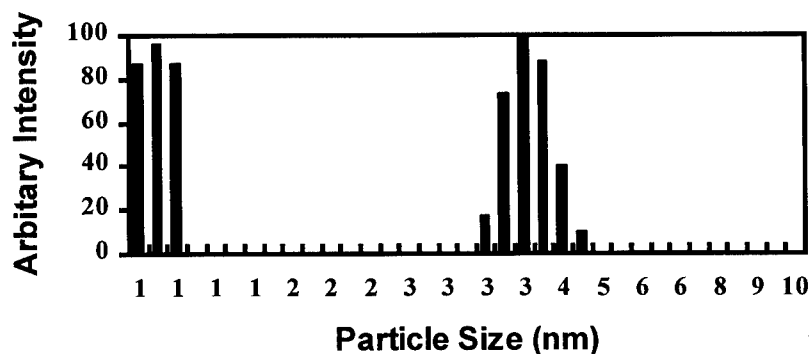


FIGURE 1

The Particle Size Distribution in a Precursor Sol Denoted T1 (see Table 1) as obtained from the Brookhaven Instruments BI200SM

reflections (although work on this issue is in progress). Electron diffraction patterns have not been observed either.

Under controlled conditions, partial removal of the organic base renders the outer pore region accessible to probe molecules such as  $N_2$ . Although the specific surface area of degassed samples calculated according to the BET equation vary, values in the range 50 to 300  $m^2/g$  have been recorded. The isotherms are of Type III - indicating plate-like particles and a highly hydroxylated surface. The most probable reason for the poor reproducibility of the calculated BET surface areas is the inherent instability of the microporous particles towards elevated temperatures (*vide infra*).

FT-i.r. analysis of freeze dried powders of the de-ionized sols with the molar composition 9TAAOH 25SiO<sub>2</sub> 480H<sub>2</sub>O 100EtOH (where TAA is as defined above) yield spectra (not shown here) that are essentially identical. Of significance is the presence of the absorbance band at  $\sim 550\text{ cm}^{-1}$ , ascribed to the stretching of tetrahedral double rings (7). This secondary building unit is present in the parent crystals synthesized using these compositions and the presence of this absorbance band strongly suggests that the particles are structured similarly to the parent crystal. The thermal instability of the powders is clearly seen in the i.r. spectra of de-ionized powders calcined at temperatures between 250 and 400°C for 4 minutes. The absorbance band at  $\sim 550\text{ cm}^{-1}$  progressively diminishes in intensity with increasing temperature and exposure to 400°C for only 4 minutes results in the disappearance of this band indicating structural collapse.

FT-Raman spectra of the de-ionized precursor powders clearly indicate the presence of the organic SDA's in spite of the fact that the greater part of these species has been removed by de-ionization. The presence of the SDA in these samples suggests that these molecules are entrapped in the structure thus providing further support for the notion that these particles are indeed microporous. Recent  $^{29}\text{Si}$  MAS NMR studies on these materials unequivocally confirm this notion (8).

TGA data recorded with de-ionized powders (molar compositions 9TBAOH 25SiO<sub>2</sub> zH<sub>2</sub>O 100EtOH, z=480 and 1500) indicate weight losses in the temperature intervals 25 to 167°C (due to water loss) and 167 to 476°C (due to SDA decomposition). The weight loss in the latter range is between 6.4 and 11.5 wt%. If it is assumed that the unit cell composition is 2 TBAOH 96 SiO<sub>2</sub> (9), the theoretical weight loss due to the SDA is 8.3 wt% which indicates that the observed weight loss is due to structurally trapped SDA.

Table 1 shows the average particle size measured with DLS for four sols made up with TPAOH and TBAOH as the SDA's. In general it may be stated that the average particle size increases with dilution. Cryo-TEM micrographs confirm these results. The probable reason for this result is firstly that the higher pH in concentrated sols requires more silica to remain in solution as solubilized species, i.e. corresponding to the equilibrium silica concentration and, secondly, there are more particles in solution in concentrated sols and hence the material available is distributed over a greater number of centers and hence the smaller particle size. The results of angular light scattering studies performed between 30° and 155° to determine whether the particle populations are mono- or bi-modal are shown in Figure 2. Quite clearly, the average particle size is essentially constant over the entire angular range indicating the absence of large scattering centers. The mono-modal nature of these systems is confirmed by cryo-TEM micrographs. Table 2 shows the average particle size as a function

TABLE 1  
The Influence of Sol Dilution on the Average Particle Size

Sample	Composition	Viscosity (cP)	Size (nm)
S1	9TPAOH 25SiO <sub>2</sub> 480H <sub>2</sub> O 100EtOH	5.7	2.1
S2	9TPAOH 25SiO <sub>2</sub> 1500H <sub>2</sub> O 100EtOH	2.3	2.8
T1	9TBAOH 25SiO <sub>2</sub> 480H <sub>2</sub> O 100EtOH	6.7	2.6
T2	9TBAOH 25SiO <sub>2</sub> 1500H <sub>2</sub> O 100EtOH	2.3	3.4

of alkalinity. Since there are few data points no extensive conclusions may be drawn however it is clear that the pH plays a significant role in the size of the particles. Recognizing the fact that the nanoparticles are the product of a base-catalyzed hydrolysis allows for the tailoring of the particles properties, e.g. choosing the appropriate hydrolysis conditions and silane(s) choice provides a route to size tailoring or the presence of alumina, titania or other metal alkoxides during hydrolysis/condensation allows for compositional tailoring. If the above results are considered as a whole, it may be stated that the nanoparticles do possess an ordered microporous structure. and hence, the possibility of preparing novel catalytically active materials is possible. Further modifications may be made to the properties of the resulting hydrolysis product by the introduction of trace amounts of alumina and/or titania (preferably during the hydrolysis of the silane) as mentioned. Trace amounts of the latter present in the microporous structure have been shown to yield material active in phenol hydroxylation and 1-hexene epoxidation using H<sub>2</sub>O<sub>2</sub> as an oxidant [10]. The introduction of alumina results in the incorporation of the alumina in the tetrahedral coordination

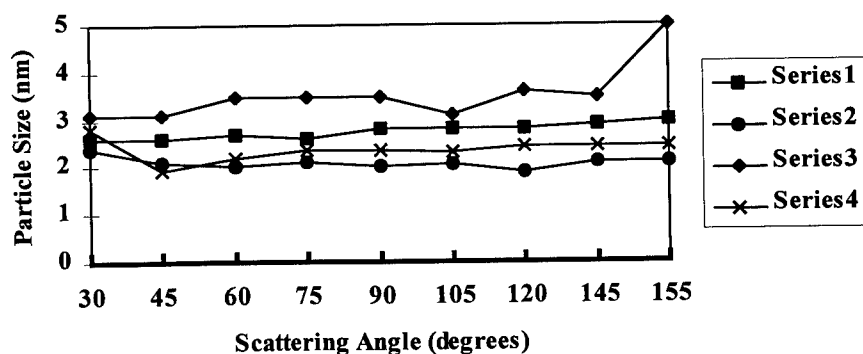


FIGURE 2

The Average Particle Size as a Function of Scattering Angle in Solutions with Molar Compositions 9TPAOH 25SiO<sub>2</sub> xH<sub>2</sub>O 100EtOH (x = 1500, Series 1 and x = 480, Series 2) and 9TBAOH 25SiO<sub>2</sub> yH<sub>2</sub>O 100EtOH (y = 1500, Series 3 and y = 480, Series 4).

TABLE 2  
The Influence of Alkalinity on the Average Particle Size

Sample	Composition	Viscosity (cP)	Size (nm)
T1	9TBAOH 25SiO <sub>2</sub> 480H <sub>2</sub> O 100EtOH	6.7	2.6
T3	8TBAOH 25SiO <sub>2</sub> 480H <sub>2</sub> O 100EtOH	5.2	3.2
T4	7TBAOH 25SiO <sub>2</sub> 480H <sub>2</sub> O 100EtOH	5.1	2.7
T5	5TBAOH 25SiO <sub>2</sub> 480H <sub>2</sub> O 100EtOH	4.6	2.3
T6	3TBAOH 25SiO <sub>2</sub> 480H <sub>2</sub> O 100EtOH	4.6	2.1

as found by <sup>27</sup>Al MAS NMR. There are no traces of octahedrally coordinated Al (indicative of extra-framework Al) hence suggesting that all alumina is framework alumina.

## CONCLUSIONS

The hydrolysis and condensation of monomeric silica in the presence of SDA's results in the formation of nano-sized particles that display microporosity and structural properties similar to the parent crystalline phase - TPA silicalite-1. These observations allow for the preparation of a novel class of materials with interesting properties for catalysis (as will be reported elsewhere).

## ACKNOWLEDGMENTS

The authors thank the Swedish Council for Engineering Sciences (TFR) for financial support.

## REFERENCES

- Verduijn, J. P., PCT Int. Appl. 92/13799, 1992; PCT Int. Appl. 92/14680, 1992.
- Albers, E. W., Edwards, G. C. and Vaughan, D. E. W., US Patent 3 755 538, 1973.
- Schoeman, B. J., Sterte, J. and Otterstedt, J.-E., *Zeolites*, 1994, **14**, 110.
- Grose, R. W. and Flanigen, E. M., US Patent 4 061 724, 1977.
- Persson, A. E., Schoeman, B. J., Sterte, J. and Otterstedt, J.-E., *Zeolites*, **14**, 1994, 557.
- Schoeman, B. J., in *Progress in Zeolites and Microporous Materials*, Eds. H. Chon, S.-K. Ihm and Y. S. Uh, Elsevier, Amsterdam, 1996, p. 647.
- Jacobs, P. A., Derouane, E. and Weitkamp, J., *J. Chem. Soc., Chem Commun.*, 1981, 591.
- Martens, J. A., Kirschhock, C., Schoeman, B. J., Ravishankar, R., et al. 'Nano-Sized Powders of Silicalite-Type Zeolites', Manuscript in preparation.
- de Vos Burchart, E., van Koningsveld, H. and van de Graaf, B., *Microporous Materials*, 1997, **8**, 215.
- Ravishankar, R., Schoeman, B., et. al., Presented at the 12th International Zeolite Conference, Baltimore, July 1998.



Pergamon

NanoStructured Materials, Vol. 12, pp. 55–60, 1999

Elsevier Science Ltd

© 1999 Acta Metallurgica Inc.

Printed in the USA. All rights reserved

0965-9773/99/\$—see front matter

PII S0965-9773(99)00065-3

## NANOCRYSTALLINE Fe AND Fe-RICHED Fe-Ni THROUGH ELECTRODEPOSITION

Michel L. Trudeau

Emerging Technologies, Hydro-Quebec, 1800 Boul. Lionel-Boulet, Varennes, Quebec,  
Canada, J3X 1S1, trudeaum@ireq.ca

**ABSTRACT** - There is a constant need for new softer magnetic materials, especially with high saturation moments. A number of studies have shown that by decreasing the average crystal size of a material below 20 nm, it is possible to reduce its magnetic losses. This was clearly demonstrated in nanostructured magnetic alloys based on the thermal crystallization of amorphous ribbons. However, this demonstration has been very difficult for other nanostructured materials, mainly because most of them are based on powder processing. This study presents the synthesis and properties of nanostructured magnetic materials produced by pulsed electrodeposition. Surprisingly, compared to other synthesis techniques, electrodeposition has received little attention for producing large quantities of fully dense nanostructured materials. In this work we describe some of the electrodeposition parameters leading to the production of nanostructured Fe and Fe-riched Fe-Ni alloys. Some magnetic properties obtained using a vibrating sample magnetometer are also presented.

©1999 Acta Metallurgica Inc.

### INTRODUCTION

The field of nanostructured materials has grown considerably in the last fifteen years. More and more researchers realize that the control of materials structure on the nanometer scale is the key to unique properties. At the same time, high throughput synthesis processes have been developed. It is interesting to look briefly back at one area that was, 10 years ago, clearly at the far front of the present nanostructure revolution. In 1988, Yoshizawa et al. [1] presented a study on nanocomposite magnetic materials produced by the thermal annealing of amorphous ribbons. They showed at that time that, through a judicious choice of the materials composition, it was possible during thermal annealing to favor an increase in the nucleation rate and a reduction of the grain growth. The final end products were nanocomposite ribbons composed of  $\alpha$ -Fe(Si) crystals, having an average size of the order of 15 nm, that are surrounded by an amorphous phase. From the time of their discovery, the large interest for these materials was related to their very low coercivity that is combined with their large saturation magnetization associated with the presence of  $\alpha$ -Fe crystals. These nanostructured alloys were seen as the perfect materials for low loss magnetic applications. Following this



work, Herzer published a series of articles [2,3] based on the random anisotropy model (RAM) [4] that explained the relation between the grains size and the coercive fields. This model indicates that below a critical value,  $L_0$  (the ferromagnetic exchange length), the magnetization will not follow the randomly oriented easy axis of the individual grain but is forced to align by the exchange interaction. The local anisotropy average out over with the increasing number of grains. In these circumstances the value of the coercive field,  $H_C$ , should then decrease with the crystallite size as  $D^6$ .

Up to now, most of the experiments that were successful to obtain this  $D^6$  dependence have been for thermally annealed amorphous ribbons. Up to now, it has not been possible to reproduce non-ambiguously such a behavior for nanostructured materials synthesized through the densification of nanostructured powders. Two main explanations exist for that. The first one is that soft magnets need to be fully densified and relax to have good properties. The other difficulties is that most powders that have been produced up to now always end up with a small contamination layer at the surface of the crystals, most often an oxide, that is detrimental to the magnetic softness.

In view of all these reasons, we are presently investigating the synthesis and properties of magnetic materials, with high saturation fields, through pulse electrodeposition. In the present paper we describe some of the parameters as well as some properties for pure iron and iron rich Fe-Ni electrodeposited alloys.

## EXPERIMENTAL DETAILS

The magnetic materials were produced by pulse electrodeposition. In pulse electrodeposition a D.C. current is applied for a short period time,  $t_{on}$ , that is followed by a period of time when no current is applied,  $t_{off}$ . Typical values for  $t_{on}$  and  $t_{off}$  are between 1 and 40 ms and between 40 and 300 ms respectively. Through the use of a high current density as well as some grain growth inhibitors, such as saccharine, it is possible to increase the nucleation rate and reduce grain growth. Detailed on Fe-Ni pulse electrodeposition have been reviewed recently by Grimmet et al. [5,6]. They found that alloys with composition from pure Ni to about 92 at.% Fe, with grain size around 10 nm, could be obtained using a Ni sulfamate and Fe chloride solution.

The structure of the materials prepared was investigated using x-ray diffraction using Mo or Cu  $K_\alpha$  radiation and with a high resolution S-4700 SEM from Hitachi. The volume-weighted average column length and internal strain of the crystals were obtained from x-ray spectra, after correction for  $K_\alpha^2$  and instrumental broadening, based on the equation described in Klug and Alexander [7], considering that the broadening due to strain could be approximated by a Gaussian distribution, while that due to the crystallite size is better described by a Lorentzian. The error in size determination is quite important using this technique, of at least 20-30%. A semi-quantitative assessment of the Fe and Ni concentration was done using energy dispersive x-ray. The surface chemistry was studied using a PHI-5500 XPS from Perkin-Elmer, using Al  $K_\alpha$  radiation. The peak position were referenced to C-(C,H) contaminants at 284.8 eV. Magnetic measurements was done using a vibrating sample

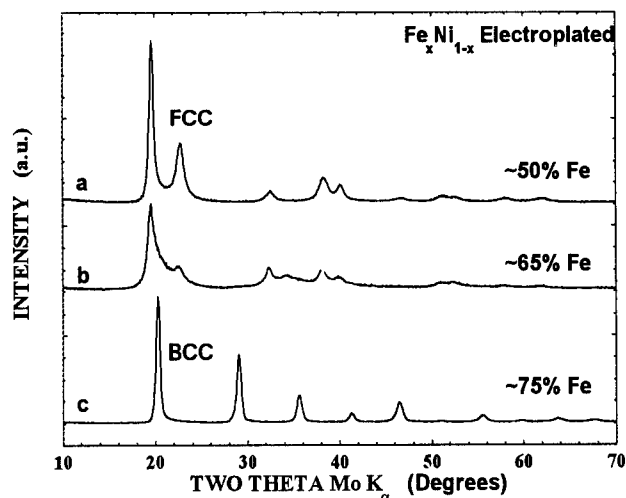


Figure 1 X-ray spectrum for three different Fe-Ni alloys prepared using pulse electrodeposition

magnetometer. Finally, the recrystallization temperature of the nanocrystalline materials was obtained using a DSC-7 from Perkin-Elmer.

As mentioned, the bath composition for the FeNi electrodeposition was based on the work of Grimmer et al. [5,6] and was composed mainly of:

0.75 M Nickel Sulfamate  
 0.25 M Ferrous Chloride  
 0.5 M Boric Acid  
 0.5 g/l sodium lauryl sulfate  
 1 g/l ascorbic acid

Saccharine was added between 1 to 10 g/l as a grain refining agent. The pH of the solution was varied between 2 and 3, while the temperature was controlled between 22 and 65 °C. For their parts,  $t_{on}$  was set between 1 and 40 ms while  $t_{off}$  was varied 100 to 360 ms. The peak current density was varied from 0.2 to 1.2 A/cm<sup>2</sup>. Ni and Fe-Ni anodes were used. Most of the deposits were obtained without solution stirring.

For iron electrodeposition, the composition of the solution was based on a sulfate-chloride bath [8] and was composed mainly of:

250 g/l Ferrous sulfate  
 42 g/l Ferrous chloride  
 10 g/l ammonium chloride

Again, in some cases 1 to 10 g/l of saccharine was added to the solution in order to reduce the grain size. In some circumstances other additives were used: between 0 and 1 g/l

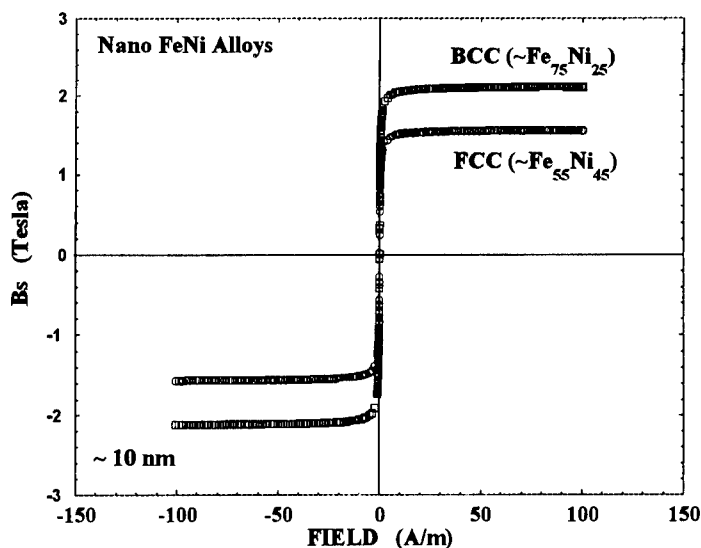


Figure 2 Hysteresis loops for two nanostructured Fe-Ni alloys prepared by pulse electrodeposition

Na lauryl sulfate, from 0 to 30 g/l Boric acid and from 0 to 15 g/l sodium carbonate. The temperature of the solution was varied from 25 to 65 °C and the pH from 3.5 to 6.0. Peak current density was of the order of 1 A/cm<sup>2</sup>.

In most cases, depositions were made on titanium cathode in order to facilitate their removal from the substrate which allows to perform experiments on self supported samples. One should also mention that the more additives are added to the solutions the larger is the contamination problem of the samples. For this reason, most of the experiments were done with the lowest amount of additive as possible. Finally, for both systems some samples were also prepared in normal D.C. mode without pulses. Under these condition the current density used was between 3 and 10 A/dm<sup>2</sup>.

## RESULTS AND DISCUSSION

Figure 1 presents the x-ray spectrum for three different electrodeposited Fe-Ni alloys. The crystallite size for the different samples was found to be around 10 nm. The iron atomic concentration for the fcc alloy was found to be around 55 %, while for the bcc is was around 75 %. At concentration of about 65 at.% (sample b) a mixed fcc/bcc phase was obtained. With most of the other parameters equals, plating at room temperature seems to lead more to the formation of bcc (high iron) alloys, while electrodeposition at temperature around 50 °C lead to the formation of the fcc phase. As expected, high peak current density seems to be necessary to the formation of a nanostructured materials.

Figure 2 presents the hysteresis curves for nanostructured (10 nm) fcc and a bcc samples. As can be expected the value of  $B_s$  increases with the Fe content when going from the

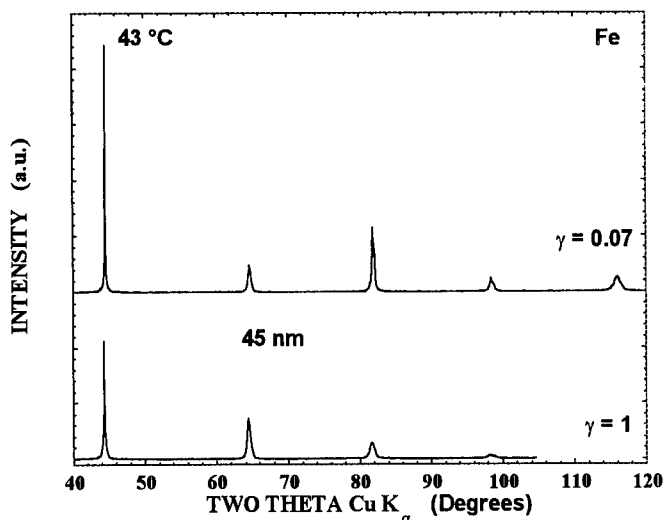


Figure 3 X-ray spectrum for two different Fe samples prepared by electrodeposition with ( $\gamma=0.7$ ) and without pulses ( $\gamma=1$ ).

fcc to the bcc phase. Also, as seen on this figure the value of the coercive field is quite low, and this especially for the fcc alloy. Without any annealing treatment,  $H_c$  was found to be about 4 Oe for the bcc alloy and 0.5 for the fcc.

For pure iron, reduction of the crystallite size below 20 nm was found to be more difficult. Figure 3 a and b present the x-ray spectrum for samples obtained with and without current pulses. Interestingly, the average crystallite size for the iron obtained without pulses at pH 3.5, 43 °C and for a current density of 6.4 A/dm<sup>2</sup> was found to be about 45 nm, quite comparable to the value obtained for a sample prepared with  $t_{on}$  and  $t_{off}$  of 3 and 40 ms respectively and with a peak current density of 47 A/dm<sup>2</sup>. Impurities analysis revealed the following contaminants concentration in most materials produced without additives in the solutions: O<sub>2</sub> at 0.09 wt%, N<sub>2</sub> at 0.03 wt%, C at 0.05 wt%, S at 0.02 wt% and H<sub>2</sub> at 0.08 wt%. This indicates that electrodeposition can lead to *very pure* nanostructured materials, with less contaminants than in most materials produced through the different powder synthesis techniques. With a higher peak current densities or with the addition of saccharine, smaller crystallites were obtained (below 10 nm) but this was normally associated with a higher contaminants concentration or burning of the samples. It was also found that the higher the bath temperature (at least at pH 3.5) the lower was the average size (between 25 and 60 °C). Details on the influence of the different electrodeposition parameters will be published elsewhere.

Compare to the Fe-Ni alloys, the Fe deposits were found to be much more brittle. The surface of samples that were produced without pulses was found to be covered by cavities, due most probably to hydrogen evolution. On the other hand for the pulsed-prepared samples no surface cavities were apparent. Similar results were recently reported by El-Sherik et al. [9] for Ni electrodeposition. Hysteresis measurements gave values for the saturation magnetization of

about 2.2 Tesla, as expected for iron, and coercive fields of about 4 Oe for non-annealed samples.

Without saccharine in the solution, no preferential texture was observed for the iron deposits produce by pulsed deposition. On the other hand, as seen in figure 3, without pulses some textures along the 110 direction is apparent (for  $\gamma = 1$ ). However, with the presence of saccharine in the bath, the samples were found to be highly texture along the 211 direction.

The thermal stability of the different materials was investigated. In general the stability was found to decrease with the increased amount of Fe in the alloys. For the fcc materials, the recrystallization temperature was found to be around 420-450 °C, while it was more around 390-400 °C for the bcc samples.

The surface of some of the samples were examined by XPS. In most case, the surface was covered by a thin oxide layer. However, metallic iron was observed at the surface indicative of the small thickness of this oxide layer.

## CONCLUSION

Nanostructured Fe-rich soft magnetic materials could present some major technological advantages because of their predicted low coercivity and high saturation magnetization. However, in order to obtain such materials it is necessary to produce fully dense and relax alloys, with an average crystallite size well below 20 nm and most probably even below 10 nm. Pulse electrodeposition is probably the only technique that can synthesize such materials, at least economically. All, other synthesis techniques, based on powder processing, will not be able to give fully densified materials without grain growth or without the presence of large amount of impurities (such as oxygen or hydrogen).

The results presented in this work show clearly the great potential of this technique. It has been demonstrated here that fully dense iron-based nanostructured materials, with high  $B_s$  values and low coercivity, can be easily synthesized using pulse-electrodeposition. Moreover, electrodeposition is not limited to the production of plates, since electroforming can be used easily to produce, in a single step process, complex shapes for particular applications.

## REFERENCES

- [1] Y. Yoshisawa, S. Oguma and K. Yamauchi, J. Appl. Phys. **64**, 6044, (1988)
- [2] G. Herzer, Mater. Sci. & Eng. **A133**, 1 (1991).
- [3] G. Herzer, Script. T49, 307, (1993)
- [4] R. Alben, J.J. Becker and M.C. Chi, J. Appl. Phys. **49**, 1653, (1978).
- [5] D.L. Grimmett, M. Schwartz and K. Nobe, J. Electrochem. Soc. **137**, 3414, (1990).
- [6] D.L. Grimmett, M. Schwartz and K. Nobe, J. Electrochem. Soc. **140**, 973, (1993).
- [7] H.P. Klug and L.E. Alexander, *X-ray Diffraction Procedures for Polycrystalline and Amorphous Materials*, 2nd ed., Wiley, New York, (1974)
- [8] *Modern Electroplating*, ed. By F.A. Lowenheim, Wiley & Sons, 2<sup>nd</sup> ed. (1967).
- [9] A.M. El-Sherik, U. Erb and J. Page, Surf. And Coatings Tech. **88**, 70, (1996).



Pergamon

NanoStructured Materials, Vol. 12, pp. 61–64, 1999

Elsevier Science Ltd

© 1999 Acta Metallurgica Inc.

Printed in the USA. All rights reserved

0965-9773/99/\$—see front matter

PII S0965-9773(99)00066-5

## PREPARATION AND CHARACTERIZATION OF COBALT OXIDE NANOSIZED PARTICLES OBTAINED BY AN ELECTROCHEMICAL METHOD

E.P. Reddy<sup>1</sup>, T.C. Rojas<sup>1</sup>, J.C. Sánchez-López<sup>1</sup>, M. Domínguez<sup>3</sup>, E. Roldán<sup>3</sup>, J. Cámpora<sup>2</sup>, P. Palma<sup>2</sup>, A. Fernández<sup>1</sup>

<sup>1</sup> Instituto de Ciencia de Materiales de Sevilla and Dpto. Química Inorgánica.

<sup>2</sup> Instituto de Investigaciones Químicas and Dpto. Química Inorgánica.

Centro de Investigaciones Científicas Isla de la Cartuja.

Avda. Américo Vespucio s/n, 41092-Sevilla, Spain.

<sup>3</sup> Dpto. de Química-Física, Universidad de Sevilla, C/Prof. García González s/n, 41012-Sevilla.

**Abstract**—An electrochemical process has been described by which metal foils are anodically dissolved and the metal salts formed as intermediates are cathodically reduced with formation of metal clusters stabilized by tetraalkylammonium salts. The electrolysis process has been investigated by cyclic voltammetry showing the formation of reduced cobalt adatoms followed by cluster formation. In the present paper we have studied such process for the preparation of nanosized Co clusters and their ulterior oxidation to cobalt oxide nanosized particles stable in air. The TEM analysis shows the formation of homogeneous particles (2–4 nm in diameter) embedded in a surfactant protective matrix. Electron diffraction shows broad but clear peaks corresponding to the formation of very small CoO crystallites. X-Ray Absorption (XAS), Electron Energy Loss (EELS) and X-Ray Photoelectron (XPS) spectroscopies have been used to characterize the materials showing the stabilization of small cobalt oxide clusters. ©1999 Acta Metallurgica Inc.

### I. INTRODUCTION

The study of magnetic properties of fine particles was traditionally urged by both a technological and theoretical interest connected with the possibility to develop a better understanding of magnetic phenomena related to size effects. Innovative nanostructured systems with excellent soft and hard magnetic properties (1,2) have been developed, which at present play an important role in modern technology and research. In particular, the preparation and characterization of nanometric particles of antiferromagnetic materials is interesting due to the presence of a superparamagnetic behavior, resulting from an imperfect compensation of the magnetic sublattices at the particle surface (3).

Recently, an electrochemical process has been described (4,5) by which metal foils are anodically dissolved and the metal salts formed as intermediates are cathodically reduced with formation of metal clusters stabilized by tetraalkylammonium salts. In the present paper we have studied such process for the preparation of nanosized Co clusters and their ulterior oxidation to cobalt oxide nanosized particles, stable in air. The characterization of the resulting

powder by X-Ray Absorption (XAS), Electron Energy Loss (EELS) and X-Ray Photoelectron (XPS) spectroscopies completes the present study.

## II. EXPERIMENTAL

For the synthesis process we employed cobalt and platinum sheets (25x25 mm) as anode and cathode respectively, the two being 5 mm apart. Tetra-n-octylammonium bromide (0.1 M) in tetrahydrofuran (THF) has been used simultaneously as supporting electrolyte and stabilizer for the clusters. Electrolysis was carried out under  $N_2$  atmosphere applying a constant current (30 mA) with a dc power supply (Thandar TS3023S). The transparent electrolyte solution become dark brown during electrolysis and a black precipitate formed. This precipitate was separated and dried under nitrogen flux and finally exposed to air.

TEM examination of the samples was carried out in a Philips CM200 microscope working at 200 kV. The samples were dispersed in ethanol by sonication and dropped on a copper grid coated with a carbon film. XPS spectra were recorded in a VG-Escalab 210 spectrometer working in the constant analyzer energy mode with a pass energy of 50 eV and using Mg  $K\alpha$  radiation as excitation-source. The binding energy (BE) reference was taken at the C1s peak at 284.6 eV. XAS spectra were recorded at the DCI storage ring in LURE (France) running at 1.85 GeV with an average current of 250 mA. Spectra were recorded at the Co K-edge at ca. 7720 eV. Finally, EELS spectra were acquired in the Philips CM200 microscope fitted with a Gatan model 766-2K parallel detection electron spectrometer.

Linear sweep cyclic voltammetric measurements were performed with a CAEM PGA1210 potentiostat/generator provided with iR drop compensation. All measurements were carried out in a conventional three-electrode electrochemical cell at 25°C. The working electrode was a polycrystalline platinum disk. A platinum wire of large area and a NaCl saturated Ag/AgCl were used as auxiliary and reference electrodes, respectively. Connection of the reference electrode was made through a salt bridge filled with the same solution that was used in the electrochemical cell.

## III. RESULTS AND DISCUSSION

Firstly the electrolysis process has been investigated by cyclic voltammetry. In Figure 1a it is shown a cyclic voltammogram obtained at a scan rate of 50 mV/s. Two reduction waves can be distinguished. The first wave is diffusion controlled ( $\log i_p$  vs.  $\log v$  slope: 0.5) in all the conditions. When the switching potential is fixed to -400 mV, an anodic wave appears (Figure 1b), indicating that this first diffusion controlled process is reversible. At more negative potentials a second non-diffusion-controlled sharp wave appears (Figure 1a) whose characteristics are in agreement with a nucleation process (6). This fact is confirmed by the loop observed in the reverse scan (Figure 1a). The nucleation process is a kinetic process which depends on the potential scan rate. At high enough scan rate (Figure 1c) the nucleation process is in an early stage and the loop is not observed. Although a detailed and quantitative interpretation will be made in the future, the cyclic voltammetric experiments are in agreement with the general picture (7) in which the first step is the formation of reduced cobalt adatoms in the vicinity of ammonium ions near the electrode surface. In a second stage, the Co adatoms form clusters which are protected by the ammonium ions.

The bright field TEM image in Figure 2a shows homogeneously distributed nanosized particles (2-4 nm in diameter) embedded in a surfactant protective matrix. Also the dark field

image in Figure 2b highlights the formation of very small and homogeneous crystallites. Electron diffraction (Figure 2c) shows broad but clear rings corresponding to small CoO crystalline nanoparticles. These results suggest a mechanism for the formation of cobalt oxide nanoparticles that involves the oxidation of metallic Co clusters by residual oxygen. The small size of the oxide nanoparticles is also stabilized by the surfactant. In fact, its removal by adequate solvents produces the formation of large CoO crystals due to the high surface energy of the very small nanometric particles.

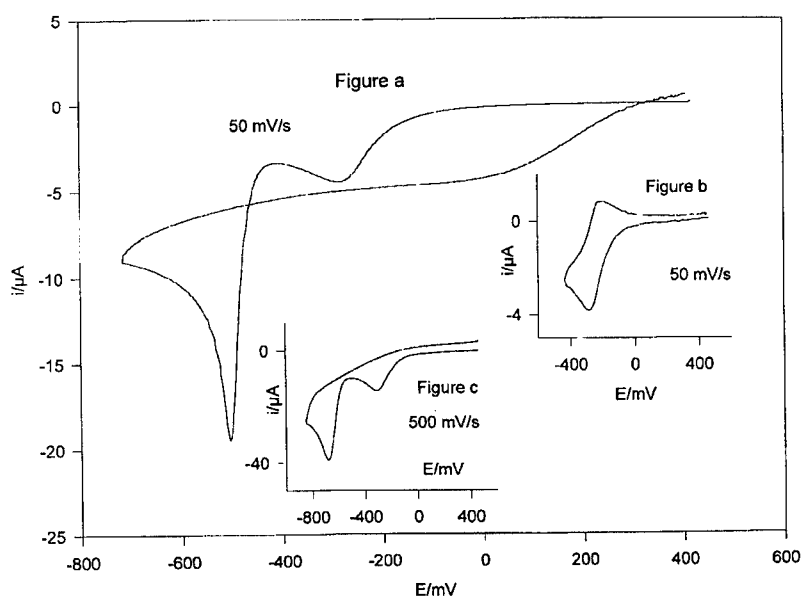


Figure 1. Linear sweep cyclic voltammograms of a 1mM  $\text{Co}^{2+}$  solution in 0.1 M tetra-n-octylammonium bromide/THF. All potentials are referred to the Ag/AgCl/NaCl saturated aqueous electrode.

Further characterization of the samples has been carried out by XPS. The Co2p photoelectron spectrum shows the main  $2p_{3/2}$  peak at 780.8 eV which corresponds to the presence of oxidized cobalt. In addition, the intensity of the shake up resonance transitions obtained for this sample has been correlated with the presence of  $\text{Co}^{2+}$  and/or  $\text{Co}^{3+}$  species (8). The Co K-edge recorded by XAS, as well as the O K-edge and Co  $L_{2,3}$ -edges recorded by EELS demonstrated clearly the presence of oxidized cobalt particles stabilized by the tetraalkylammonium salt. The use of shorter chain surfactants like tetra-n-butylammonium acetate produced a poor stabilization of the clusters. Formation of big agglomerates on the platinum electrode has been observed in that case.

#### IV. CONCLUSIONS

It has been shown that the electrochemical reduction of cobalt cations in the presence of tetraalkylammonium salts produces stabilized metal clusters that cannot be reversibly oxidized during a cyclic voltammetry experiment. An ulterior oxygen exposure produces cobalt oxide nanosized particles stabilized by the ammonium salt.



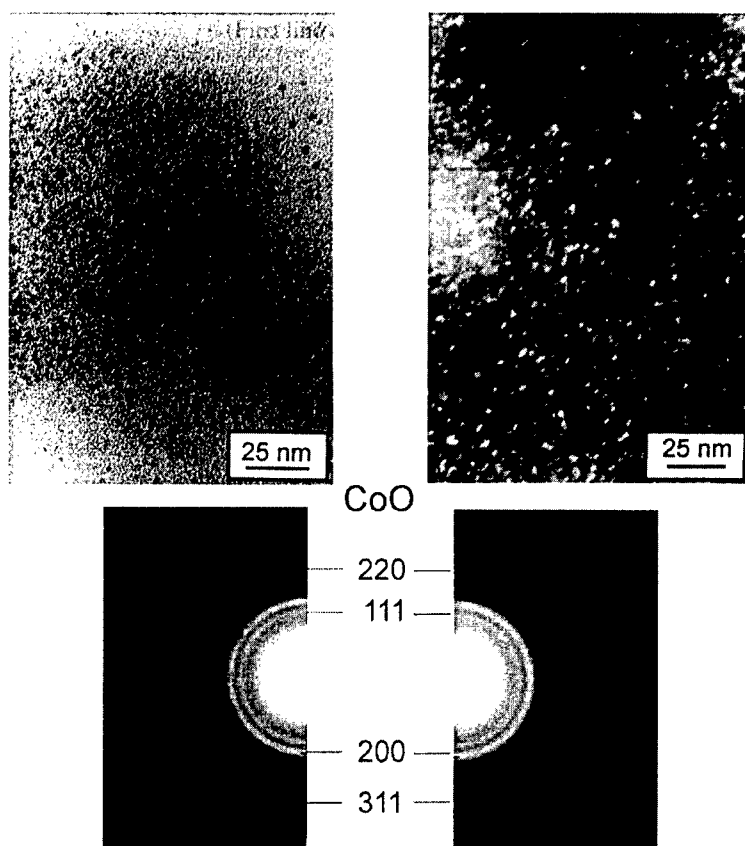


Figure 2. Bright field (a), dark field (b) and electron diffraction pattern (c) for the nanosized cobalt oxide particles.

#### ACKNOWLEDGEMENTS

Authors thank the DGES (Project NR.: PB96-0863-C02-02) for financial support.

#### REFERENCES

1. Yoshizawa, Y., Oguma, S., Yamauchi, K., *Journal Applied Physics*, 1988, 64, 6044.
2. Kneller, E.F., Hawig, R., *IEEE Trans. Magn MAG-27*, 1991, 3588.
3. Dormann, J.L., Fiorani, D., eds., *"Magnetic Properties of Fine Particles"*, North-Holland, Amsterdam 1992.
4. Reetz, M.T., Helbig, W., *Journal American Chemical Society*, 1994, 116, 7401.
5. Reetz, M.T., Helbig, W., Quaiser, S.A., *Chemistry of Materials*, 1995, 7, 2227.
6. Maestre, M., Sánchez, M., Rodríguez-Amaro, R., Muñoz, E., Ruíz, J.J., Camacho, L., *Journal Electroanalytical Chemistry*, 1994, 31, 373.
7. Becker, S.A., Schäfer, R., Festag J.R., Wendorff, J.H., Hensel, F., Pebler, J., Quaiser, S.A., Helbig, W., Reetz, M.T., *Surface Reviews and Letters*, 1996, 3, 1121.
8. Briggs, D., Gibson, U.A., *Chemical Physics Letters*, 1974, 25, 493.



Pergamon

NanoStructured Materials, Vol. 12, pp. 65–70, 1999

Elsevier Science Ltd

© 1999 Acta Metallurgica Inc.

Printed in the USA. All rights reserved

0965-9773/99/\$—see front matter

PII S0965-9773(99)00067-7

## SYNTHESIS AND REACTIVITY OF NANOPHASE FERRITES IN REVERSE MICELLAR SOLUTIONS

Charles J. O'Connor, Candace T. Seip, Everett E. Carpenter,  
Sichu Li, and Vijay T. John  
Advanced Materials Research Institute, University of New Orleans,  
New Orleans, LA 70148, USA.

**Abstract**—Self assembly preparative techniques in confined media that lead to magnetic materials with nanometer dimensions are described. Synthesis of nanoparticles using the restricted environments offered by surfactant systems such as water-in-oil microemulsions (reverse micelles) provide excellent control over particle size, inter-particle spacing, and particle shape. These environments have been used in the synthesis of  $\gamma\text{-Fe}_2\text{O}_3$ ,  $\text{Fe}_3\text{O}_4$ ,  $\text{MnFe}_2\text{O}_4$ , and  $\text{CoFe}_2\text{O}_4$  with particle sizes ranging from 10–20 nm. The controlled environment of the reverse micelle also allows sequential synthesis which can produce a core-shell type structure, for example  $\text{Fe}_3\text{O}_4$  nanoparticles with MnO coatings. Lyotropic liquid crystal media also offer template effects for the synthesis of magnetic nanostructures. The nanoscale ordering of magnetic particles when synthesized in lyotropic liquid crystal gels is characterized. The structures, theory and modeling concepts, and novel physical properties of these materials are discussed with emphasis given to the differences between course and fine grained magnetic materials. ©1999 Acta Metallurgica Inc.

### INTRODUCTION

An interesting approach that is used in synthesis of nanophase materials is to employ the spatially and geometrically restricted, self-assembling media of reverse micelles and microstructured gel phases. Reverse micelles, for example, are water-in-oil microemulsions where microdroplets of water are stabilized in non-aqueous solution by a surfactant. Our earlier studies on ferrite synthesis in these systems have shown particle growth restricted to the nanometer range with a narrow size distribution. These preparations employed reverse micelles formed with a twin-tailed anionic surfactant *bis*-(2-ethylhexyl) sodium sulfosuccinate (AOT). Ferrite nanoparticles exhibit classical superparamagnetic behavior and the colloidal dimensions allow the particles to be suspended in solution, thereby creating a ferro-fluid. We have also found a novel method of folding polymer chains around the particles thus forming polymer microspheres that encapsulate the nanophase materials (1). We have extended this reaction scheme to include sequential reaction conditions to prepare a core/shell nano-structured material.

An interesting application of nanophase particles is in the formation of intelligent gels that can respond to external stimuli (2). The composition of such gels is a polymer network swollen in a solvent. To the external stimuli such as temperature, pH, electric field, light, and magnetic field, the viscosity or the volume of the gel can change (3). Such sensitive responses to the stimuli present potential novel applications in sensors, controlled delivery systems, separators, and artificial muscles (4).

In this report, the preparation and characterization of nanometer sized magnetic particles, composite core-shell particles, and particle-gel assemblies are presented.

## EXPERIMENTAL

### *Materials*

All chemicals used during the course of this work were of analytical grade. These were used as received from a commercial source (Aldrich Chemical). The surfactant AOT had a variable moisture content when purchased and was therefore dried at 70°C for several hours to remove this moisture to a  $w_o$  ( $[H_2O]/[AOT]$ ) below 0.4.

### *Synthesis*

**Ferrite Particles.** By using dioctyl sulfosuccinate (AOT) and isooctane, reverse micelles can be made with a water pool of a specific size controlled by the water/surfactant ratio. This combination of oil phase, surfactant, and aqueous solutions allows a very narrow distribution of sizes from 5 nm up to 30 nm micelles. At the extreme size limits of 5 nm and 30 nm, the size distribution increases due to problems in micelle stability and crystallization. This system has been used extensively as the reaction environment for the growth of nanophase ferrites.

The synthesis of the ferrite  $Fe_3O_4$  is prepared using an injection technique. Two separate micelle solutions are prepared with the desired size using 0.65M AOT in isooctane solution and aqueous solutions of 0.92M  $FeSO_4$  as a metal containing solution, and aqueous  $NH_4OH$ . For example if 10 nm particles are to be made, 10 ml of  $FeSO_4(aq)$  are mixed with 90 ml of AOT. Any suspended impurities of the micelles are removed by centrifuging at 3500 rpm for 15 minutes. The clear micelle solutions are mixed together with constant stirring (low speed) using a magnetic stir plate. As the solutions are mixed, the solution turns green, and then a few minutes later will turn reddish in color. Over the course of 2 hours the ferrite crystallizes inside the aqueous cores. Mixed ferrites can be formed in the same fashion as that of  $Fe_3O_4$ . The metal containing micelle solution is prepared using 1:2 molar ratio of 1M  $FeSO_4$  and 1M  $MSO_4$ , where  $M = Mn$  or  $Co$ .

The ferrite is removed from the reaction mixture by a magnetic separation technique. The reaction solution is transferred to a separatory funnel placed in a magnetic field. The mixture is washed several times with large excesses of a 50:50 methanol/water solution. The ferrite particles are retained in the separatory funnel by the magnetic field as the surfactant and other by-products are washed away.

This same technique can be used to synthesize  $\gamma-Fe_2O_3$ . The only change to the synthesis from that of  $Fe_3O_4$  is a third micelle solution of 30% hydrogen peroxide. After the

$\text{Fe}^{2+}$  micelle solution has been mixed with the  $\text{NH}_4\text{OH}$  solution, the third solution of  $\text{H}_2\text{O}_2$  is added. This helps to facilitate the complete oxidation of  $\text{Fe}^{2+}$  to  $\text{Fe}^{3+}$ . The ferrites are collected in the same fashion as described above.

This technique also offers an opportunity for sequential synthesis in fabrication of core-shell structures. A ferrite is synthesized in the above manner as the core and placed in a solution of larger micelles. For example, if the core particle is 10 nm then the particle is placed in a 15 nm micelle solution, depending on the desired thickness of the shell. To form the MnO coating, the ferrite core particle is placed in a 1.0M  $\text{KMnO}_4$  (aq) solution. The second micelle is formed using hydrazine as a reducing agent. The micelle solutions are mixed and allowed to stir for 2 hours. The core-shell product is separated from the coating particles using the magnetic separation technique described above.

**Ferrite Chlorophenol Gel.** A portion of the dry reversed micelle is dissolved in  $\text{CCl}_4$  to prepare a 0.3 M AOT solution in  $\text{CCl}_4$ . An equal volume of 0.3 M p-chlorophenol in  $\text{CCl}_4$  is then added and the solution thoroughly mixed. A transparent reddish-brown gel formed immediately. Other gels with different concentrations of the AOT and p-chlorophenol, or with different volume ratio of AOT:p-chlorophenol, are prepared with the same procedure.

#### *Magnetic Experiments*

Magnetic experiments were carried out using a Quantum Design MPMS-5S SQUID magnetometer. Calibration and measurement techniques are described elsewhere (5). The DC susceptibility experiments were performed from 2K through 300K at a field of 1000gauss. Two different procedures were used for the dc magnetic susceptibility experiments: (1) zero field cooling, where the sample was slowly cooled in zero field to a temperature of 1.7 K, at which point the measuring field of 1.0 kG was switched on and the magnetization was then measured as a function of temperature; (2) field cooling, where the field of 1.0 kG was turned on at a temperature well above the superparamagnetic blocking temperature before the sample was cooled to 1.7 K. Standard magnetization versus applied magnetic field hysteresis loops were recorded at temperatures both below and above the blocking temperature by completing one cycle of 5T to -5T at temperatures of 2K and 300K.

#### *Electron Microscopy*

A Zeiss EM 10C Transmission Electronic Microscope (TEM) was used for the observation of the ferrite particles in gel. A thin layer of the gel was deposited on a TEM grid coated carbon membrane. It was then heated to 200°C at a rate of 5°C/min, and subsequently to 260°C at a rate of 2°C/min. Heating removed the organic solvent and surfactant, and left the particles on the TEM grid.

## **RESULTS AND DISCUSSION**

Nanoparticles of  $\text{Fe}_3\text{O}_4$ , MnO, and  $\text{Fe}_3\text{O}_4/\text{MnO}$  composites with approximately 10nm dimensions were prepared and isolated as powders. DC magnetic susceptibility experiments were performed on these particles. Figure 1 illustrates the DC magnetic susceptibility of the

nano-particles under field cooled and zero field cooled conditions. The materials displayed superparamagnetic behavior with a blocking temperature of about 40K.

An extension of the simple reverse micelle synthetic approach employs the sequential crystallization of a  $\text{Fe}_3\text{O}_4$  core material surrounded by an antiferromagnetic (MnO) shell material. A schematic diagram of a core shell particle is illustrated in Figure 2. The rationale behind the preparation of these core-shell structures is that these composite systems could

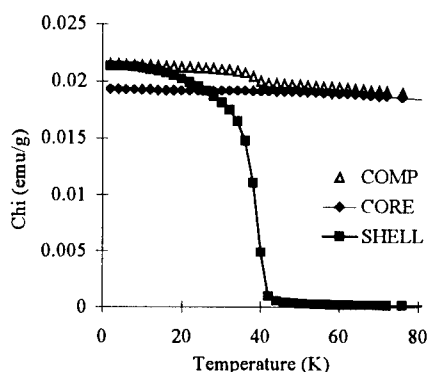


Figure 1. Magnetic susceptibility of  $\text{Fe}_3\text{O}_4$ , MnO, and  $\text{Fe}_3\text{O}_4/\text{MnO}$  particles as described in text.

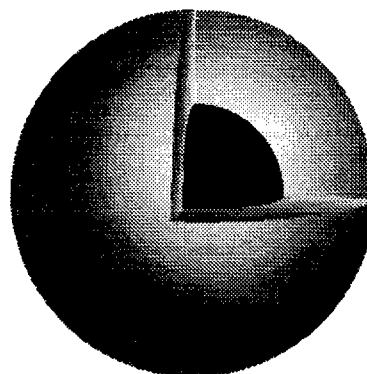


Figure 2: Schematic of a core shell

result in spin bias exchange at the boundary of the superparamagnetic particles and, as a consequence of single domain characteristics, lead to enhanced coercivity and apparent ferromagnetic behavior (6).

The same DC susceptibility and magnetization verses field experiments were performed on the  $\text{Fe}_3\text{O}_4/\text{MnO}$  core-shell composite material. Because the lattice match between the ferrite and MnO is similar, a thin manganese oxide layer can coat the ferrite center. The core-shell composite material also displayed superparamagnetic behavior with a blocking temperature of 40K (see Figure 1). Below the blocking temperature ( $T=2\text{K}$ ), the particles displayed a magnetic moment of 0.379 emu/g, and a  $H_c=300\text{G}$ . Above the blocking temperature at 300K, the particles were superparamagnetic with a moment of 2.980 emu/g. For comparison purposes a particle was made using the same procedure of the composite only without the  $\text{Fe}_3\text{O}_4$  present (*i.e.*, a MnO nanoparticle). The field cooled behavior of MnO resembles the recently reported behavior in nanophase  $\text{KMnF}_3$  (7). There is a reproducible 10% increase in the susceptibility of the composite material over that of the  $\text{Fe}_3\text{O}_4$  core alone. This presumably comes from the added presence of the uncompensated spins in the shell material. However, the coercivity drops by 25%. TEM micrographs verify the presence of MnO in the core-shell composite. X-ray powder diffraction experiments on the composite displayed an increase in an amorphous material, but showed no presence of MnO, probably due to poor crystallinity in the coating.

Temperature dependent dc magnetic susceptibility data for the samples were obtained by two different methods, field cooled (FC) and zero field cooled (ZFC). At high temperature, FC and ZFC magnetization data exhibit the same trend and are coincident. However, they diverge significantly at low temperature. The ZFC curve data show a dramatic decrease in magnetization, while the FC data reach a plateau. The ZFC data also show a

sharp maximum in the magnetization when plotted as a function of temperature. This maximum is a characteristic of spin glass materials (8). It occurs at about 40K for each of the ferrite-containing particles studied here. This blocking temperature is further verified with TRM and IRM experiments.

The field dependent hysteresis loops were measured at temperatures both below and above the blocking temperature. Figure 3 shows the hysteresis curves at 2K (a) and 100 K (b). The magnetization versus field data at 100 K illustrate the data to be perfectly superimposable within experimental error as the field is cycled between  $\pm 50$  kG, with zero coercivity. This lack of coercive hysteresis is characteristic of superparamagnetic particles or single-domain

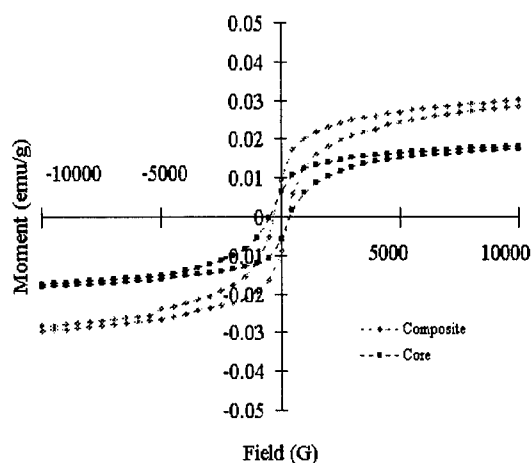


Figure 3. Magnetic hysteresis of  $\text{Fe}_3\text{O}_4$  particles as described in text.

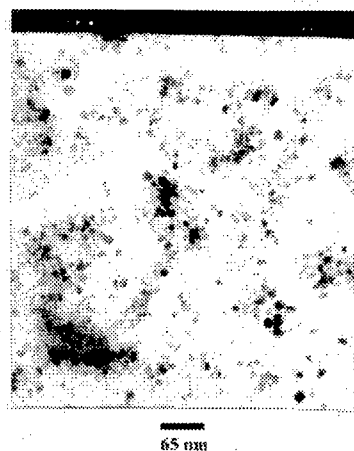


Figure 4. TEM image of the particles in the gel media.

particles of very small dimensions. As the temperature is significantly lowered, the sample starts to display some hysteresis. The presence of hysteresis at temperatures below the blocking temperature, together with the absence of hysteresis at temperatures above the blocking temperature, confirms the superparamagnetic behavior of these materials.

#### *Ferrite Chlorophenol Organogel*

The ferrite chlorophenol organogel was prepared as described in the experimental section. It was found that the magnetic behavior of the ferrite gel matches that of ferrites in reversed micelles. This reveals that the ferrite particles do not aggregate in the gel media. The result is consistent with the TEM observation. For the studies of the ferrite chlorophenol gel formation, two series of gel samples were prepared: 1) 0.3 M AOT/ $\text{CCl}_4$  mixed with 0.3 M chlorophenol/ $\text{CCl}_4$  with different volume ratios; 2) various concentrations of AOT/ $\text{CCl}_4$  (0.2 to 0.6 M) mixed with the same concentration of chlorophenol/ $\text{CCl}_4$  and volume ratio.

The ferrite particles incorporated into the gel are coated with surfactant AOT. Figure 4 is the TEM image of the particles in the gel media. They are scattered and distributed throughout the gel. The size of the particles ranges from 10 to 15 nm. They are spherical in

shape. The size and the shape of the particles are controlled by the template effect provided by the reverse micelles during the synthesis of the particles. The concentration of the ferrite nanoparticles in the gel depends on the concentration of AOT, the hardness of the gel, and the size of the particles. From the NMR characterizations, we can assume that most of the AOT and chlorophenol molecules are located close to the particles. Since the AOT and chlorophenol molecules are the two components assembling into the gel network, we propose that more gel strands extend around the surface of the ferrite particles. In other words, the ferrite particles are surrounded by gel strands.

### CONCLUSION

Nanosized materials can be prepared in reverse micelles with a narrow size distribution. The reverse micelle synthetic technique allows a sequential preparation procedure that will lead to a core shell structure in the resulting particle. The core shell synthetic procedure is most successful when there is a close match in lattice parameters of the two components as with the ferrite/MnO system.

Nanosize ferrite particles can be incorporated into a chlorophenol organogel to yield a magnetic organogel. The particles can be suspended in the gel media, and serve as an agent of magnetic properties. The magnetic properties of the gel are dependent on that of the incorporated ferrite particles. The introduction of the ferrite particles causes more gel strands to form around the particles. This system can be considered as a precursor example for a magnetic sensitive gel. It gives us a hint that a magnetic sensitive gel might be generated by adjusting the components in the system and applying proper stimuli.

**Acknowledgements:** We gratefully acknowledge the support of this work by the Advanced Materials Research Institute through DOD/DARPA Grant No. MDA972-97-1-0003.

### REFERENCES

1. Kommareddi, N.S., Tata, M., John, V.T., McPherson, G.L., Herman, M.F., Lee, Y.S., O'Connor, C.J., Akkara, J.A., and Kaplan, D.L., *Chem. Mater.*, **1996**, 8, 801.
2. Dagani, R. *C&E News*, **1997**, June 9, 26.
3. Tanaka, T.; *Science*, **1982**, 218, 467; Tanaka, T. *Phys. Rev. Lett.* **1978**, 40, 820; Dusek, K. *Advanced in Polymer Science*, **1993**, Vol. 109, Responsive Gels, Volume transition I; Dusek, K. *Advanced in Polymer Science*, **1993**, Vol. 109.
4. Suzuki, A.; *Advances in Polymer Science*, 1993, Vol. 110, 201; Osada, Y.; Okuzaki, H.; Hori, H. *Nature*, **1992**, Vol. 355, 16.
5. O'Connor, C.J. *Prog. Inorg. Chem.*, **1982**, 29, 203.
6. Shi, J., Gider, S., Babcock, K., Awschalom, D.D., *Science*, **1996**, 271, 937.
7. O'Connor, C.J., Carpenter, E., and Sangregorio, C., unpublished results.
8. Haushalter, R.C., O'Connor, C.J., Haushalter, J.P., Umarji, A.M., and Shenoy, G.K., *Angewandte Chemie*, **1984**, 97, 147; *Angew. Chem. Int. Ed. Engl.*, **1984**, 23, 169; O'Connor, C. J. in "Research Frontiers in Magnetochemistry", O'Connor, C.J., Editor, (World Scientific Publishing, Inc., Singapore, London, New Jersey), **1993** 109.



Pergamon

NanoStructured Materials, Vol. 12, pp. 71-74, 1999

Elsevier Science Ltd

© 1999 Acta Metallurgica Inc.

Printed in the USA. All rights reserved

0965-9773/99/\$-see front matter

PII S0965-9773(99)00068-9

## SIZE-CONTROLLED SYNTHESIS OF NANOSCALED ALUMINIUM SPINELS USING HETEROBIMETALLIC ALKOXIDE PRECURSORS VIA WATER/OIL MICROEMULSIONS

F. Meyer,<sup>1</sup> A. Dierstein,<sup>1</sup> Ch. Beck,<sup>1</sup> W. Härtl<sup>1</sup> and R. Hempelmann<sup>1</sup>  
S. Mathur<sup>2</sup> and M. Veith<sup>2</sup>

(1) Physical Chemistry (2) Inorganic Chemistry

University of Saarland, D-66123 Saarbrücken, Germany

**Abstract** -- Nanosized spinels of type  $MAl_2O_4$  ( $M = Mg, Co, Ni, Cu$ ) were prepared by a sol-gel type hydrolysis of alkoxides in the inverse micelles of w/o microemulsions. Heterobimetallic alkoxides  $M[Al(OPr^i)_4]_2$  containing both metallic elements in the desired stoichiometric ratio were employed as single-source precursors. The structure and thus metal stoichiometry in the molecules was established by single crystal X-ray diffraction analysis. By varying the hydrophilic chain length of the detergent, the diameter of the water droplets can be tuned in the nanometer range, as determined by dynamic light scattering. The size of the resulting spinel nano-particles as evaluated from XRD peak profile analysis, correlates to the droplet size. The results of the ceramic syntheses using the different types of alkoxide precursors were compared which reveal the advantage of a single source approach.

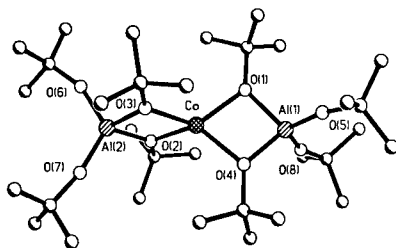
©1999 Acta Metallurgica Inc.

### INTRODUCTION

We are investigating molecular routes to advanced ceramic materials via the gas phase using the CVD technique and via the liquid phase in microemulsion mediated sol-gel processes (1-3). Using alkoxide precursors, we have synthesised and characterised nano-sized  $Al/Al_2O_3$  composites and  $ABO_3$  type perovskite ceramics (1-2,4). Usually for the synthesis of ternary oxides mixtures of binary alkoxides are used as precursors. The main drawback of this route is the differential hydrolysis behaviour (kinetics) of individual components which often leads to the formation of mixed phases and non-ideal stoichiometries in the final ceramic. This limitation can be overcome by employing well-characterised heterometal molecules ('single-source') with metallic elements present in the ratio corresponding to the targeted ceramic. We have reported on the potential of microemulsion technique for size-controlled synthesis of various nanocrystalline ferroelectrics (3,4). We report here the use of hetero-bimetallic alkoxides  $[M\{Al(OPr^i)_4\}_2]$  ( $M(II) = Mg, Ni, Co, Cu$ ) in a microemulsion assisted sol-gel process to obtain high-purity nano-scaled  $MAl_2O_4$  ceramics which show significant potential for diverse applications (e.g., catalysts, pigments, infrared windows) (5,6).



### Synthesis and Characterisation of the Precursor



The precursor compounds, e.g.  $[\text{Co}\{\text{Al}(\text{OR})_4\}_2]$  ( $\text{R} = \text{Pr}^i, \text{Bu}^i$ ), were prepared following the procedure of Mehrotra and coworkers (7). In order to determine the definitive composition, the structures of the tert-butoxide derivatives were examined using single crystal X-ray diffraction analysis (Figure 1). The molecule consists of a spirocyclic core made up of two planar 'AlO<sub>2</sub>Co' four-membered rings, joined at cobalt center. With two terminal ligands present on each of the aluminium atoms, all the metallic elements are present in a quasi-tetrahedral environment of oxygen atoms.

Microemulsions are thermodynamically stable, translucent systems consisting of oil, water, surfactant and/or a cosurfactant formed spontaneously. Our microemulsion mediated synthesis of nano-oxides is based on the principle of confining the hydrolysis reactions of alkoxide molecules in tiny water droplets of this water/oil (w/o) emulsion. The size of these nano-reactors can be tuned either by varying the concentrations of the components or by the hydrophilic chain length of the surfactant. This micelle-mediated hydrolysis offers control on particle size in the nanometer range as the initial micelle size corresponds to the resulting crystallite size (4,8). The microemulsions contain cyclohexane or n-heptane as oil phase, nonionic surfactant (Tergitols: TNP-7, TNP-10 or TNP-35; nonylphenol poly(n) ethylenglycolether with n = 7, 10 or 15) and 1-octanol as co-surfactant. The oil was mixed with 1-octanol and surfactant and stirred for several minutes. To these components, the stoichiometric amount of water was added with a microsyringe followed by vigorous stirring until a translucent microemulsion was formed. This w/o microemulsion was added dropwise to the stirred solution of the respective alkoxide(s) in dry isopropanol under nitrogen and stirred for 2 hours. The solvents were evaporated from the sol and the micelles were cracked with acetone. The product was dried and extracted (Soxhlet) in cyclohexane for 24 hours. The initially amorphous powder was calcined in a preheated tube furnace at 1000°C (15-30 minutes) to obtain nano-crystalline  $\text{MAl}_2\text{O}_4$  spinels devoid of any organic impurities. Finally, an XRD analysis was performed using a Siemens D-500 diffractometer with  $\text{Cu-K}_\alpha$  radiation. The particle size distribution was determined from the evaluation of the peak profile by a modified Warren-Averbach method (9).

### Comparison of Product Synthesised Using Different Precursor Systems

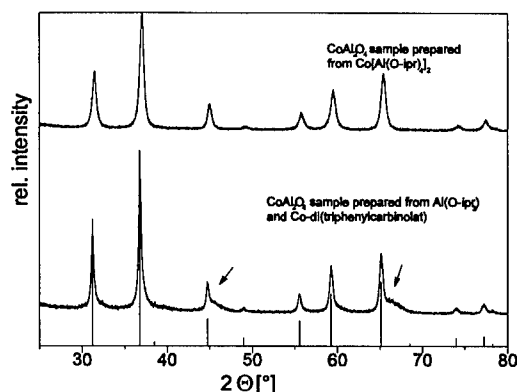


**Figure 2:** XRDs of nano-Co-Al spinel (calcined at 1000°C) obtained using the single-source precursor and the mixture of individual precursors. Arrows indicate impurities and improperly resolved peaks in the case of the multi-component system. The vertical lines originate from the JCPDS data base.

In order to establish the advantages of single-source precursors, the syntheses performed using mixed-metal compounds, e.g.  $[M\{Al(OBu^i)_4\}_2]$ , were compared with a multi-component process, where stoichiometric mixtures of individual alkoxides ( $[Al(OPr^i)_3]_4$  and  $M(OR)_2$ ) were employed. Although syntheses and characterizations were performed for a variety of aluminates such as  $MgAl_2O_4$  or  $CuAl_2O_4$ , (10), for the sake of brevity only the  $CoAl_2O_4$  system is discussed. It is clearly deducible from Figure 2, that the nano-particles obtained from the single source precursor method possess a high degree of purity and exhibit better crystallinity than the samples prepared by using two separate precursors. Moreover, the product obtained in the case of heterometal precursor is morphologically pure and only this product allows a Warren-Averbach analysis where a perfect peak shape is essential. This study nicely demonstrates the potential of single-source precursor strategy in obtaining high-purity ceramics as different hydrolysis kinetics can be avoided using hetero-metal molecules (11,12).

### Controlling the Particle Size by Varying the Chain Length of the Surfactants

Among the many parameters influencing the particle size distribution, such as the primary droplet size, the calcination temperature and time, and the ratios of the microemulsion compounds, the chemical nature of the precursors is particularly important. All these process variables have been optimised in the present study to yield high purity nano-oxides. It is known (4) that an increase in the hydrophilic chain length decreases the micellar diameter as less emulgator molecules are needed to stabilize the microdroplets. It is thus expected that TNP-35 affords the smallest droplets and the smallest ceramic particles. Table 1 exhibits that only the hydrophilic chain length of the surfactant has been changed with all other parameters constant. Table 2 and Figure 3 show that the surfactant with the longest hydrophilic chain, TNP-35, really yields the smallest nanocrystallites although due to the calcination step a correlation between initial droplet size and final crystallite size is qualitative and the maximum of the distribution is

not shifting to that extent as the average crystallite size does.

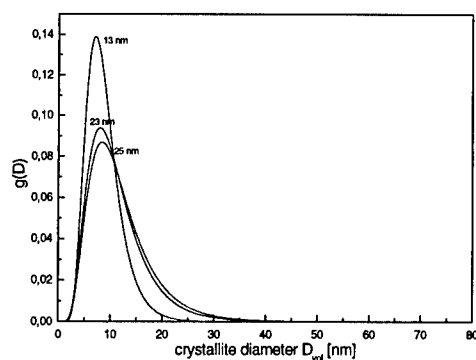


TABLE 1:  
Molar Ratios of the Components

n-heptane	TNP-(n)	1-octanol	water
10.2	0.1	0.8	1

TABLE 2:  
Resulting Crystallite Sizes

TNP	-35	-10	-7
$D_v$ [nm]	13	23	25

**Figure 3:** Particle size distributions of calcined (15 minutes at 1000°C)  $\text{CoAl}_2\text{O}_4$  samples derived from the single-source precursor and by using different tergitols in the same molar concentrations to adjust the micelle size

### ACKNOWLEDGEMENT

The authors gratefully acknowledge the financial support of the Deutsche Forschungsgemeinschaft in the framework of Sonderforschungsbereich 277 „Grenzflächenbestimmte Materialien,,.

R.H. and M. V. also thank the Fonds der Chemischen Industrie for generous support.

### REFERENCES

1. Veith, M., Faber, S., Hempelman R., Janssen, S., Prewo, J. and Eckerlebe, H., *J. Mater. Sci.*, 1996, 31, 2009.
2. Veith, M. and Kneip, S., *J. Mater. Sci. Lett.*, 1994, 13, 335.
3. Herrig H. and Hempelmann R., *Materials Letter* 27, 287 (1996).
4. Beck Ch., Härtl W. and Hempelmann R., *J. Mat. Res.*, in print
5. Lopez M., Fernandez M. et al., *J. Mat. Sci. Lett.* 12, 1619 (1993)
6. Debsikdar J.C., *J. Mat. Sci.*, 20, 4454, (1985)
7. Singh, J. V. and Mehrotra, R. C., *Can. J. Chem.*, 1984, 62, 1003.
8. Härtl W., Beck Ch., Roth M., Meyer F. and Hempelmann R., *Ber. Bunsenges. Phys. Chem.*, 101, 1714 (1997)
9. Natter H. and Hempelmann R., *J. Phys. Chem.*, 100, 19525 (1996)
10. Meyer F., Hempelmann R., Mathur S. and Veith M., *To be published*
11. Chandler, C. D., Roger, C. and Hampden-Smith, M., *J. Chem. Rev.*, 1993, 93, 1205
12. Veith, M., Mathur, S. and Mathur, C., *Polyhedron*, 1998, 17, 1005



Pergamon

NanoStructured Materials, Vol. 12, pp. 75–78, 1999

Elsevier Science Ltd

© 1999 Acta Metallurgica Inc.

Printed in the USA. All rights reserved

0965-9773/99/\$—see front matter

PII S0965-9773(99)00069-0

## MECHANOCHEMICAL SYNTHESIS OF METAL SULPHIDE NANOPARTICLES

Takuya Tsuzuki and Paul G. McCormick

Special Research Centre for Advanced Mineral and Materials Processing  
The University of Western Australia, Nedlands, Perth, WA 6907, Australia

**Abstract** — The synthesis of ZnS, CdS and  $Ce_2S_3$  nanoparticles by mechanochemical reaction has been reviewed. During mechanical milling, solid-state displacement reactions between the respective metal chloride and alkali sulphide or alkaline earth sulphide were induced in a steady-state manner, leading to the formation of metal sulphide nanoparticles. A simple washing process to remove the chloride by-product yielded separated particles of ZnS, CdS and  $Ce_2S_3$  of ~8 nm, ~4 nm and ~20 nm, respectively. The resulting particles and crystallite sizes were dependent on the milling conditions, starting materials and the presence of a diluent. Structural change with decreasing particle size was observed for CdS and  $Ce_2S_3$ . ©1999 Acta Metallurgica Inc.

### INTRODUCTION

Metal sulphides have been recognised as advanced materials for many applications including opto-electric materials, phosphors, pigments and magnetic materials. Nanoparticles have significant potential for these applications due to their small size, high-surface area and low sintering temperatures. In particular, semiconductor quantum dots have attracted considerable attention in many fields of science (1). In recent years, a number of studies have been carried out to develop methods for synthesising sulphide nanoparticles (1-4). Recently, Ding et al. (5-9) have reported the synthesis of nano-sized particles of a number of transition metals and ceramics including Fe, Cu, Ni, Co,  $Al_2O_3$  and  $ZrO_2$  by mechanochemical processing. This paper reviews the synthesis of ZnS, CdS and  $Ce_2S_3$  nanoparticles by mechanochemical reactions between the respective metal chloride and alkali sulphide or alkaline earth sulphide (10,11).

### MECHANOCHEMICAL PROCESSING

Mechanochemical processing is a novel method involving the mechanical activation of solid-state displacement chemical reactions, either during ball milling or during subsequent heat treatment (12). This process is characterised by the repeated welding and fracture of reacting particles during ball-powder collisions, which continually regenerate reacting interfaces. As a consequence, reactions which would normally require high temperatures to occur, due to

separation of the reacting phases by the product phases, can occur at low temperatures in a ball mill. For example, mechanical milling of a mixture of  $\text{FeCl}_3$  and Na powders causes the reaction  $\text{FeCl}_3 + 3\text{Na} \rightarrow \text{Fe} + 3\text{NaCl}$  to occur (5). Careful control of milling conditions to avoid combustion enables the reactions to occur in a steady-state manner. On completion of the reaction, the as-milled powders usually consist of a nanocomposite mixture of the product phases. A simple washing process to remove the by-product phase yields particles of the desired phase.

### SYNTHESIS OF SULPHIDES

Sulphide nanoparticles were synthesised via the reactions [1-8] listed in Table 1. The starting materials were anhydrous  $\text{ZnCl}_2$ ,  $\text{CdCl}_2$ ,  $\text{CeCl}_3$  and commercial grade (CG) CaS. Mechanically alloyed (MA) CaS and  $\text{Na}_2\text{S}$ , which comprise considerably smaller particles (~ 20 nm) than CG-CaS (>100 nm), were also used as a starting reactant.  $\text{CaCl}_2$  and NaCl were used as a diluent. The reactants were sealed in a hardened steel vial with steel balls under a high-purity Ar-gas atmosphere. Milling was performed with a Spex 8000 mixer/mill. The powders were milled for the time required to complete the reaction.

All the reactions in Table 1 occurred during milling in a steady state manner. The resulting particles and crystallite sizes were dependent on the milling conditions, starting materials and the presence of a diluent. It was only possible to form separated single crystal nanoparticles in samples milled with a diluent. The powders synthesised via the reactions [1] and [6] consisted of large aggregates of crystallites, whilst the reactions [2] and [7] resulted in separated single crystal nanoparticles. It is clear that the volume ratio of the minor to major product phases must be sufficiently small for separated nanoparticles of the minor phase to form.

The particle size of the sulphide products is related to the particle size of the starting reactant. The reaction using MA-CaS (reaction [3]) resulted in smaller ZnS particle size (crystallite size) than using CG-CaS (reaction [2]). The same tendency was observed for  $\text{Ce}_2\text{S}_3$  (reactions [7] and [8]). In a nano-composite of the reactants formed during milling, the effective reaction volume is determined by the crystallite size of the reactants. ZnS particle size is determined by the effective reaction volume from which ZnS particles are nucleated. Therefore, small particles of ZnS are obtained from small particles of the reactant.

Comparing the reactions [3] and [4], it is evident that addition of a diluent has little effect on the sulphide particle size. This supports the view that the effective reaction volume is mainly associated with the size of starting reactants, providing the same milling conditions are applied.

Grinding-ball size is another factor which influences the particle size. For CdS, the particle size decreased with decreasing milling-ball size (reaction [5]). CdS is a II-VI semiconductor with a direct band-gap of 2.4 eV. Since the CdS particles were smaller than the exciton Bohr diameter of 8 nm, a quantum size effect was observed as a blue-shift of the band-gap energy (11,13). Figure 1 shows a TEM image of the CdS quantum dots.

While all the ZnS particles had a cubic structure (zinc-blende), a structural transition with decreasing particle size was observed for CdS and  $\text{Ce}_2\text{S}_3$ . The structure of CdS changed from a mixture of wurtzite (hexagonal) and zinc-blende (cubic) to zinc-blende, as the mean

TABLE 1

XRD Crystallite Size,  $d_{\text{crystal}}$ , of the Obtained Sulphide Powders  
as a Function of Grinding-Ball Size,  $D_{\text{ball}}$ , and Starting Powders.

$R_V$  is the volume ratio of the chloride to the sulphide in the product phase.

Product	Reaction equation	$R_V$	$D_{\text{ball}}$ (mm)	$d_{\text{crystal}}$ (nm)
ZnS	$\text{ZnCl}_2 + \text{CG-CaS} \rightarrow \text{ZnS} + \text{CaCl}_2$ [1]	3:1	12.7	12
	$\text{ZnCl}_2 + \text{CG-CaS} + 3.6\text{CaCl}_2 \rightarrow \text{ZnS} + 4.6\text{CaCl}_2$ [2]	10:1	12.7	16
	$\text{ZnCl}_2 + \text{MA-CaS} + 3.6\text{CaCl}_2 \rightarrow \text{ZnS} + 4.6\text{CaCl}_2$ [3]	10:1	12.7	8.0
	$\text{ZnCl}_2 + \text{MA-CaS} + 8.2\text{CaCl}_2 \rightarrow \text{ZnS} + 9.2\text{CaCl}_2$ [4]	20:1	12.7	8.6
CdS	$\text{CdCl}_2 + \text{MA-Na}_2\text{S} + 16\text{NaCl} \rightarrow \text{CdS} + 18\text{NaCl}$ [5]	16:1	12.7	8.2
		16:1	9.5	6.5
		16:1	6.4	5.9
		16:1	4.8	4.3
$\text{Ce}_2\text{S}_3$	$\text{CeCl}_3 + \text{CG-CaS} \rightarrow \text{Ce}_2\text{S}_3 + \text{CaCl}_2$ [6]	2:1	12.7	32
	$\text{CeCl}_3 + \text{CG-CaS} + 11\text{CaCl}_2 \rightarrow \text{Ce}_2\text{S}_3 + 12\text{CaCl}_2$ [7]	10:1	12.7	29
	$\text{CeCl}_3 + \text{MA-CaS} + 11\text{CaCl}_2 \rightarrow \text{Ce}_2\text{S}_3 + 12\text{CaCl}_2$ [8]	10:1	12.7	20

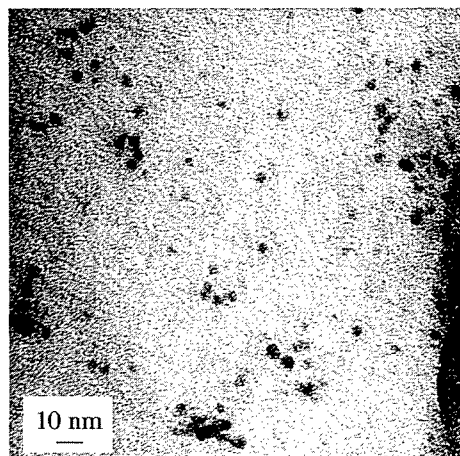


Figure 1. TEM micrograph of the CdS quantum dots synthesised by mechano-chemical processing.

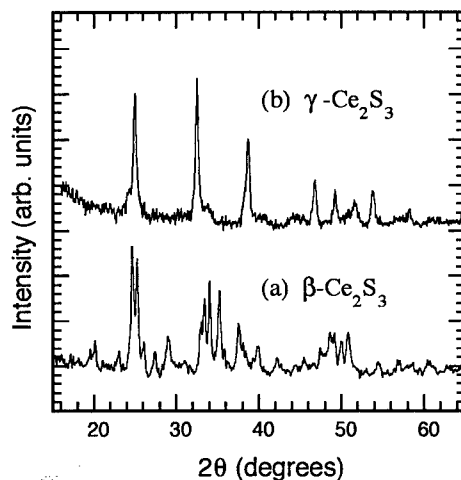


Figure 2. X-ray diffraction patterns of milled and washed  $\text{Ce}_2\text{S}_3$  powders via the reactions (a)  $\text{CeCl}_3 + \text{CG-CaS} \rightarrow \text{Ce}_2\text{S}_3 + \text{CaCl}_2$ , and (b)  $\text{CeCl}_3 + \text{MA-CaS} + 11\text{CaCl}_2 \rightarrow \text{Ce}_2\text{S}_3 + 12\text{CaCl}_2$ .

particle size decreased (11). In  $\text{Ce}_2\text{S}_3$ , the particles with mean diameter of  $>30$  nm had the tetragonal  $\beta$ - $\text{Ce}_2\text{S}_3$  structure, whereas particles smaller than 20 nm had the cubic  $\gamma$ - $\text{Ce}_2\text{S}_3$  structure (Figure 2). It is interesting to note that these cubic structures in CdS and  $\text{Ce}_2\text{S}_3$  are thermodynamically metastable at room temperature. Size dependence of the structure in nanoparticles has also been reported for  $\text{Al}_2\text{O}_3$  (8,14) and  $\text{ZrO}_2$  (9,15), and has been explained as an surface-energy effect (14,15).

## CONCLUSIONS

Mechanochemical processing enables the direct synthesis of sulphide nanoparticles without the need for high temperatures. The average particle size can be controlled by changing milling conditions and starting materials. This novel synthesis method is applicable for the synthesis of a wide range of sulphide and other chalcogenide nanoparticles. Moreover, it has significant potential for large scale production due to high efficiency and low cost process.

## REFERENCES

1. Brus, S.E., *Journal of Physical Chemistry*, 1986, 90, 2555.
2. Henglein, A., Fojtik, A. and Weller, H., *Berichte der Bunsengesellschaft für Physikalische Chemie*, 1987, 91, 441.
3. Ekimov, A., *Journal of Luminescence*, 1997, 70, 1.
4. Takada, T., Mackenzie, J.D., Yamate, M., Kang, K., Payghambarian, N., Reeves, R.J., Knobbe, E.T. and Powell, R.C., *Journal of Materials Science*, 1996, 31, 423.
5. Ding, J., Miao, W.F., McCormick, P.G. and Street, R., *Applied Physics Letters*, 1995, 67, 3804.
6. Ding, J., Tsuzuki, T., McCormick, P.G. and Street, R., *Journal of Alloys and Compounds*, 1996, 234, L1.
7. Ding, J., Tsuzuki, T., McCormick, P.G. and Street, R., *Journal of Physics D: Applied Physics*, 1996, 29, 2365.
8. Ding, J., Tsuzuki, T. and McCormick, P.G., *Journal of American Ceramic Society*, 1996, 79, 2956.
9. Ding, J., Tsuzuki, T. and McCormick P.G., *Nanostructured Materials*, 1997, 8, 75.
10. Tsuzuki, T., Ding, J. and McCormick P.G., *Physica B*, 1997, 239, 378.
11. Tsuzuki, T. and McCormick, P.G., *Applied Physics A*, 1997, 65, 607.
12. McCormick, P.G., Ding, J., Yang, H. and Tsuzuki, T., *Materials Research 96*, The Institute of Metals and Materials Australia, 1996, vol.1, p.85.
13. Nakashima, P.N.H., Tsuzuki, T. and Johnson, A.W.S., *Journal of Applied Physics*, submitted for publication.
14. McHale, J.M., Aurox, A., Perrotta, A.J. and Navrotsky, A., *Science*, 1997, 277, 788.
15. Winterer, M., Nitsche, R., Redfern, S.A.T., Schmahl, W.W. and Hahn, H., *Nanostructured Materials*, 1995, 5, 679.



Pergamon

NanoStructured Materials, Vol. 12, pp. 79–82, 1999

Elsevier Science Ltd

© 1999 Acta Metallurgica Inc.

Printed in the USA. All rights reserved

0965-9773/99/\$—see front matter

PII S0965-9773(99)00070-7

## NANOPARTICLE FORMATION BY LASER-ASSISTED PHOTOLYSIS OF FERROCENE.

**K. Elihn, F. Otten\*, M. Boman, F. E. Kruis\*, H. Fissan\*, J.-O. Carlsson.**  
Inorganic Chemistry, The Ångström Laboratory, Box 538, Uppsala University,  
751 21 Uppsala, Sweden.

\* Process and Aerosol Measurement Technology, Gerhard-Mercator University, Duisburg  
47057 Duisburg, Germany.

**Abstract-** *Laser-assisted formation of iron-containing nanoparticles has been performed by photolytic dissociation of ferrocene vapour by a pulsed ArF excimer laser at 193 nm. The process was carried out at atmospheric pressure, either in an inert atmosphere of argon or in a reactive gas mixture of argon and oxygen. Differential mobility analysers, DMA's, were used for the determination of the particle sizes. By changing laser parameters such as beam size, pulse energy and repetition rate, particle sizes ranging from 3 to 100 nm, were generated. Morphology and size of the nanoparticles were studied via transmission electron microscopy, TEM, and structural information was obtained from electron diffraction. Chemical composition was determined through X-ray photoelectron spectroscopy, XPS, and energy dispersive X-ray spectroscopy, EDX. ©1999 Acta Metallurgica Inc.*

### INTRODUCTION

Many approaches exist for the synthesis of nanoparticles (1-3). The disadvantage with many of them is their high process temperature, which gives an increased number of agglomerated particles. To reduce the number of agglomerates, a lower reactor temperature is required and/or a lower primary particle concentration. On the other hand, by maintaining a low particle concentration, only a limited amount of nanoparticles can be produced.

Two techniques, one for generating nanoparticles and one for determination of particle size, have been combined in this paper. Nanoparticles were synthesised through the laser-assisted photolytic dissociation of ferrocene,  $\text{Fe}(\text{C}_5\text{H}_5)_2$ . The multiphoton dissociation and ionisation of ferrocene in the uv/vis range have been studied elsewhere (4,5) and dissociation mechanisms have been proposed (6). In these experiments the distribution of particle sizes was measured by using a differential mobility analyser, DMA, allowing real-time particle size measurements.

### EXPERIMENTAL

A pulsed ArF excimer laser (Lambda Physik EMG 103; pulse width 16 ns) operating at a wavelength of 193 nm was used for the photolysis of the ferrocene vapour. The particle reactor



consisted of a stainless steel tube, with quartz windows at opposing ends of the reactor. The laser beam was passed through both windows of the reactor in order to prevent laser ablation of the reactor walls. Through the use of a variable aperture, the size of the unfocused beam ranged between 4 and 80 mm<sup>2</sup>. The pulse energy was varied between 0.74 and 5.2 mJ and laser repetition rate between 2 and 100 Hz. The photolytic dissociation is a non-thermal process performed at room temperature in this investigation.

The ferrocene was sublimed at room temperature, and transported to the particle reactor by a carrier gas (100 sccm of argon). Argon gas at a flow rate of 1400 sccm was used to purge the entrance window to prevent condensation of ferrocene onto the window. The rapid argon flow maintains the particle concentration low and the residence time of the particles in the reactor short, reducing the probability of agglomeration. When adding oxygen as a reactant gas, the argon purge flow was decreased so that the total flow of 1500 sccm was maintained through the reactor. All experiments were performed at atmospheric pressure.

A differential mobility particle sizer, DMPS (7), which measured the size of charged particles according to their electrical mobility, was employed to determine the size distribution of the particles in the reactor. The DMPS includes a radioactive <sup>242</sup>Am charger, a nano-DMA (8) for particles up to 30 nm or a Hauke-DMA (9) for particles up to 100 nm in diameter, an ultrafine condensation particle counter, UCPC, and a controlling computer which corrects for the losses of particles in the equipment. The flow of argon sheath gas through the DMA was 15 000 sccm.

Morphology, structure and chemical composition of the nanoparticles were analysed by transmission electron microscopy, TEM, electron diffraction, X-ray photoelectron spectroscopy, XPS, and energy dispersive X-ray spectroscopy, EDX.

## RESULTS AND DISCUSSION

The size of the particles was found to follow a log-normal distribution. The particle sizes,  $D_p$ , at the maximum particle concentration of the corrected size distributions given by the DMPS, are plotted as a function of the beam size, pulse energy and repetition rate of the laser.

As the size of the unfocused beam was changed, large variations in particle diameter were obtained, see Fig. 1a. While varying the beam size, the repetition rate was set to 2 Hz. The largest beam size of 80 mm<sup>2</sup> gave a  $D_p$  of 22.3 nm. When decreasing the beam size to 25 mm<sup>2</sup> a lowered  $D_p$  of 15.0 nm was obtained. A further decrease to 15 mm<sup>2</sup> and 4 mm<sup>2</sup> gave corrected particle diameters of 8.0 and 4.2 nm, respectively.

In Fig. 1b, the  $D_p$  as a function of the pulse energies of the laser is shown. In these experiments a beam size of 4 mm<sup>2</sup> was used, and the repetition rate was set to 20 Hz. The pulse energies used were 5.2, 3.7, 2.2 and 0.74 mJ, which gave corrected particle diameters of 9.1, 8.4, 6.1 and 3.6 nm respectively.

Fig. 1c shows the relation between  $D_p$  and the repetition rate. While the repetition rate was varied, the beam size was set to 4 mm<sup>2</sup>. The largest repetition rate of 100 Hz gave particles with a  $D_p$  of 18.0 nm. Then the repetition rate was decreased to 80, 50, 20, 10 and 5 Hz, which gave corrected particle diameters of 17.0, 15.0, 10.4, 7.5 and 5.8 nm, respectively. The smallest repetition rate of 2 Hz gave the smallest  $D_p$  of 3.1 nm.

All the changes of the laser parameters also affected the laser power.

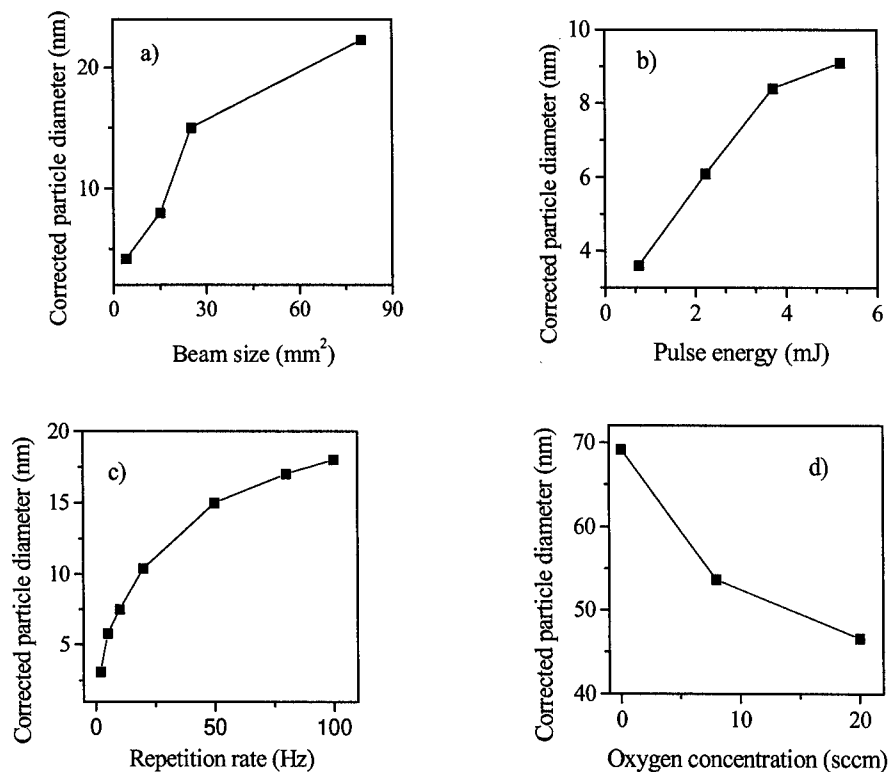


Figure 1. Corrected particle diameters plotted against a) beam size ( $2\text{ Hz}$ ), b) pulse energy ( $4\text{ mm}^2$ ,  $20\text{ Hz}$ ), c) repetition rate ( $4\text{ mm}^2$ ) and d) oxygen concentration ( $80\text{ mm}^2$ ,  $44\text{ mJ}$ ,  $20\text{ Hz}$ )

The increasing trends in figures 1 a-c, was not linear but declined over the examined ranges. The corrected particle diameters as a function of increasing beam size, pulse energy and repetition rate in these figures, approximately follows a cube root dependence.

To minimise the carbon content in the particles and eliminate the carbon residue, a few percent of oxygen was added to promote the oxidation of ferrocene. While changing the concentration of oxygen in the reactor, the laser parameters were set to a beam size of  $80\text{ mm}^2$ , a pulse energy of  $44\text{ mJ}$ , and a repetition rate of  $20\text{ Hz}$ . The  $D_p$  decreased with increasing oxygen concentration, see Fig. 1d. When no oxygen was added, a  $D_p$  of  $69.2\text{ nm}$  was obtained. An addition of 8 and  $20\text{ sccm}$  of oxygen to the reactor gave corrected particle diameters of  $53.7$  and  $46.6\text{ nm}$ , respectively. The reduced  $D_p$  is a result of the minimisation of the carbon content of the particles.

The deposited particles (10) were analysed by X-ray photoelectron spectroscopy, XPS. These measurements showed that iron and carbon were present in the experiments performed in both argon and the argon/oxygen gas mixture. As no fully covered substrate surface was obtained, the composition of the particles could not be determined. The carbon could have originated from the particles as well as from the uncovered substrate surface. Energy dispersive

X-ray spectroscopy, EDX, of specific particles confirmed iron. Since this EDX equipment only detects elements heavier than fluorine, carbon could not be detected.

The particle size and morphology of the particles were analysed by transmission electron microscopy, TEM. The particles generated in an argon atmosphere had irregular shapes with high concentration of agglomerates. They had a dark iron-rich core and a brighter surface layer of oxide, carbide or possibly carbon residue from the organometallic precursor. Electron diffraction revealed that the particles are amorphous.

In the oxygen/argon gas mixture, the particles turned out to be spherical with less agglomerates. Electron diffraction patterns of the particles corresponds best to  $\text{Fe}_2\text{O}_3$  and Fe.

### SUMMARY

Formation of nanoparticles has been performed by photolytic dissociation of ferrocene. In the experiments made in an argon atmosphere, an increasing beam size, repetition rate and pulse energy of the laser, resulted in an increased particle diameter. An addition of a few percent of oxygen gave a decrease in particle diameter.

### ACKNOWLEDGEMENTS

We are most grateful to Jun Lu for running the TEM and Torvald Andersson for helping with the XPS. We also gratefully acknowledge the Swedish Research Council for the Engineering Sciences and the Ångström Consortium for the financing.

### REFERENCES

1. Kruis, F.E., Fissan, H. and Peled, A., *J. Aerosol Sci.*, **29/5-6**, 511, 1998.
2. Jonsson, B.J., Turkki, T., Strom, V., El-Shall, M.S. and Rao, K.V., *J. Appl. Phys.*, **79**, 5063, 1996.
3. El-Shall, M.S., Li, S., Gravier, D. and Pernisz, U., *Nanotechnology: Molecularly Designed Materials*, ed. Chow, G. and Gonsalves, K.E., ACS Symposium Series 622, 79, 1996.
4. Opitz, J. and Härter, P., *Int. J. Mass Spectrom. Ion Process.*, **121**, 183, 1992.
5. Niles, S., Prinslow, D.A., Wight, C.A., Armentrout, P.B., *J. Chem. Phys.*, **97/5**, 3115, 1992.
6. Ray, U., Hou, H.Q., Zhang, Z., Schwarz, W., Vernon, M., *J. Chem. Phys.*, **90/8**, 4248, 1989.
7. Fissan, H., Helsper, C. and Thielen, H.J., *J. Aerosol Sci.*, **14**, 354, 1983.
8. Chen, D.R., Pui, D.Y.H., Hummes, D., Fissan, H., Quant, F.R. and Sem, G.J., *J. Aerosol Sci.*, **29/5-6**, 497, 1998.
9. Winklmayr, W., Reischl, G.P., Lindner, A.O. and Berner, A., *J. Aerosol Sci.*, **22**, 289, 1991.
10. Otten, F., Elihn, K., Kruis, F.E., Boman, M., Carlsson, J.-O., Fissan, H., *to be published*.



## TEMPLATE SYNTHESIS OF CARBON NANOTUBES

G.L. Hornyak<sup>1</sup>, A.C. Dillon<sup>1</sup>, P.A. Parilla<sup>1</sup>, J.J. Schneider<sup>2</sup>,  
N. Czap<sup>2</sup>, K.M. Jones<sup>1</sup>, F.S. Fasoon<sup>1</sup>, A. Mason<sup>1</sup>, and M.J. Heben<sup>1</sup>

<sup>1</sup> National Renewable Energy Laboratory 1617 Cole Blvd., Golden, Colorado 80401 USA

<sup>2</sup> Institut für Anorganische Chemie, Universität Essen, 45117 Essen, Germany

**Abstract** -- The template synthesis and characterization of carbon nanotubes (CNTs) formed in porous alumina membranes (PAM) by the thermal chemical vapor decomposition (CVD) of propylene (Pr) gas are described. We found that the graphitic character of CNTs improved as CVD temperature was increased from 500 to 800 °C. Samples showed progressive increases in metallic appearance and layered tube wall structure and decreases in electrical resistance. No further enhancement of graphitization was observed among samples formed at 800, 900 and 1000 °C. X-ray diffraction (XRD) indicated that long-range order was absent in all CNTs tested. Localized crystalline domains of graphitic carbon, however, were detected by Raman spectroscopy and seen in light and dark field transmission electron microscopy (TEM) images. CNTs formed in the presence of catalytic Fe and Co particles at 600 and 700 °C with a Pr/N<sub>2</sub> flow rate of 94 sccm (standard cubic centimeters per minute) showed slightly lower electrical resistance than CNTs formed in control experiments. The catalytic effects of Fe and Co were observed for samples made at 800 °C with a 50 sccm Pr/N<sub>2</sub> flow rate as “nanotubes within nanotubes” were formed. No major differences were found between catalyst-containing and control samples formed at temperatures greater than or equal to 800 °C at 94 sccm.

©1999 Acta Metallurgica Inc.

### INTRODUCTION

Single-wall CNTs formed by an arc-discharge process were shown here at NREL to stabilize adsorbed hydrogen at moderate temperatures (1) and to demonstrate selectivity of CO<sub>2</sub> over CH<sub>4</sub> in gas separation experiments (2). Study of transport and adsorption properties of CNTs would be greatly facilitated, however, if nanotubes could be aligned within a well-defined matrix. PAMs, formed by the anodic electrolysis of aluminum, consist of hexagonally packed parallel pore channels and offer a possible means of achieving an ordered array of CNTs. Control over anodization parameters can produce pore diameters ranging from 2 to 500 nm, porosities from 20 to 70% and pore densities from 10<sup>7</sup> to 10<sup>12</sup> cm<sup>-2</sup> (3). The resulting PAMs are optically transparent in the visible range of the spectrum, resistant to most chemicals except for strong acids and bases and stable to temperatures in excess of 1000 °C (3). Template synthesis of nanotubes by CVD has been investigated during the past five years by a handful of research groups (4-6). We are now interested in the fabrication and characterization of ordered arrays of CNTs for applications that include their use as a medium for hydrogen storage, as lithium battery electrode materials and as natural gas purifiers. The degree of graphitization of template synthesized CNTs as a function of CVD conditions and catalysts is of great interest.

## EXPERIMENTAL

PAM templates were formed by anodizing high purity aluminum plates in a 10 wt.% sulfuric acid solution at 20 V for 4 h at 0 °C (3). PAMs were removed from the aluminum plate surface by a voltage reduction procedure with subsequent acid detachment (3). The resulting membranes were approximately 30  $\mu\text{m}$  thick and 30% porous with an average pore diameter of 32 nm. Selected membranes that were heat-treated at 900 °C for 5 h between quartz plates to enhance flattening yielded a pore diameter of *ca.* 50 nm. Robust PAMs, with thickness greater than 200  $\mu\text{m}$ , were fabricated in 20 wt.%  $\text{H}_2\text{SO}_4$  at 20 V for 12 h at -5 °C.

Chemical vapor deposition was accomplished in a 3-zone furnace by: 1) purging in  $\text{N}_2$  for 1 h at 500 °C, 2) heating in forming gas for 2 h at temperatures ranging from 500 to 800 °C and 3) heating in 2.5 vol.% Pr in  $\text{N}_2$  for 2 h at temperatures ranging from 500 to 1000 °C. The flow rate of the gas was fixed at either 94 (high) or 50 (low) sccm. Samples for TEM, XRD, SEM (scanning electron microscopy), EPMA (electron probe microanalysis) and Raman spectroscopy were prepared by removing the host alumina by ultrasonication in concentrated HF. The resulting suspension was centrifuged, decanted, rinsed and suspended in ethanol.

The degree of graphitization was evaluated by light and dark field TEM imaging, measurement of the transverse electrical resistance of the membrane (along the length of the CNTs) with 0.31  $\text{cm}^2$  contacts, Raman spectroscopy, XRD and sample appearance. Cobalt catalysts were formed *in situ* by aqueous incipient wetness impregnation (AIWI) of PAM pore channels with 0.3M  $\text{CoSO}_4$  or  $\text{Co}(\text{NO}_3)_2$  (6).  $\text{Fe}_2\text{O}_3$  nanoparticles were formed by the low temperature decomposition of *bis*( $\eta$ -toluene) $\text{Fe}(\text{0})$  at -78 °C (7). These catalyst precursors were converted into metals by reduction in forming gas at temperatures of 600 to 800 °C.

## RESULTS and DISCUSSION

Figure 1 shows an SEM image of a nanotube array formed in a robust PAM with thickness of *ca.* 200  $\mu\text{m}$ . The alumina matrix was dissolved in concentrated HF *without* ultrasonication. The array remained intact after HF treatment due to the presence of the carbonaceous surface layers. The CNTs were formed at 600 °C without catalysts for a 3 h Pr deposition time at 94 sccm. As expected, the tubes are 200  $\mu\text{m}$  in length and have a diameter of *ca.* 30 nm. The aspect ratio of the CNTs in this array is nearly 7000.

In Figure 2a, a TEM image of CNTs formed at 800 °C without the aid of catalysts is shown. These tubes were liberated from the alumina template by dissolution in HF *with* ultrasonication. Numerous single and bundled CNTs are evident. Nanotubes formed at 500 and 600 °C did not survive ultrasonication during HF treatment. In these cases, TEM images revealed agglomerations of unstructured carbon. CNTs formed at 800 °C or greater survived ultrasonication but were found by EPMA to contain as much as 50 wt.% alumina.

Qualitative evaluation of the degree of graphitization of non-catalytic samples is given in Table 1. Sample surface appearance proceeded from “shiny black” to “silvery reflective” as CVD temperature was increased from 500 to 800 °C. Above 800 °C, the appearance became a duller gray-metallic as thicker surface layers were formed at higher deposition rates. Layering in nanotube walls was first observed in TEM images of 700 °C samples (600 °C specimen CNT structures did not survive HF with ultrasonication). The degree of layering improved in samples formed at higher temperatures (Figure 2b), but graphitization was still confined to a length scale



**Figure 1.** Robust array of carbon nanotubes (aspect ratio *ca.* 7000) formed at 600 °C.

less than a few nm. No major differences in terms of CNT wall layered structure were detected among samples made at 800, 900 and 1000 °C. Transverse electrical resistance of samples decreased dramatically as CVD temperature was increased from 500 to 800 °C, but no significant differences in electrical resistance were detected among samples formed at 800 °C or higher.

Raman spectra for samples formed at various temperatures (Figure 2c) revealed a broad feature at *ca.* 1360  $\text{cm}^{-1}$ , associated with disorder within a graphite lattice, and a broad feature at *ca.* 1600  $\text{cm}^{-1}$ , attributed to one of the fundamental Raman modes of crystalline graphite (8). The fact that the two peaks have nearly identical magnitude indicates the presence of nanocrystalline graphite with domain size less than 10 nm (8). Compared to the 600 and 700 °C sample spectra, the 800 and 1000 °C spectra showed an attendant decrease in signal intensity in both peaks. Dark field TEM image data also confirmed the presence of crystalline domains in samples formed at 700 °C (Figure 2d) or greater.

**TABLE 1**

CVD Temperature	Surface Appearance	Structure of CNT Wall	Electrical Resistance	Raman Analysis	XRD Analysis
500 °C	Shiny Black	Amorphous	$>10^6 \Omega$	Insuff. Sample	Insuff. Sample
600 °C	Glassy Black	Amorphous	$>10^3 \Omega$	+ Nanographite	Insuff. Sample
700 °C	Shiny Slate	Incipient Layers	$<100 \Omega$	+ Nanographite	Insuff. Sample
800 °C	Reflective Silver Mirror	Well-Defined Layers	$<2 \Omega$	+ Nanographite	No Long-Range Order
900 °C	Dull Metallic Gray	Well-Defined Layers	$<1 \Omega$	No Sample	No Long-Range Order
1000 °C	Dull Metallic	Well-Defined	$<1 \Omega$	+ Nanographite	No Sample

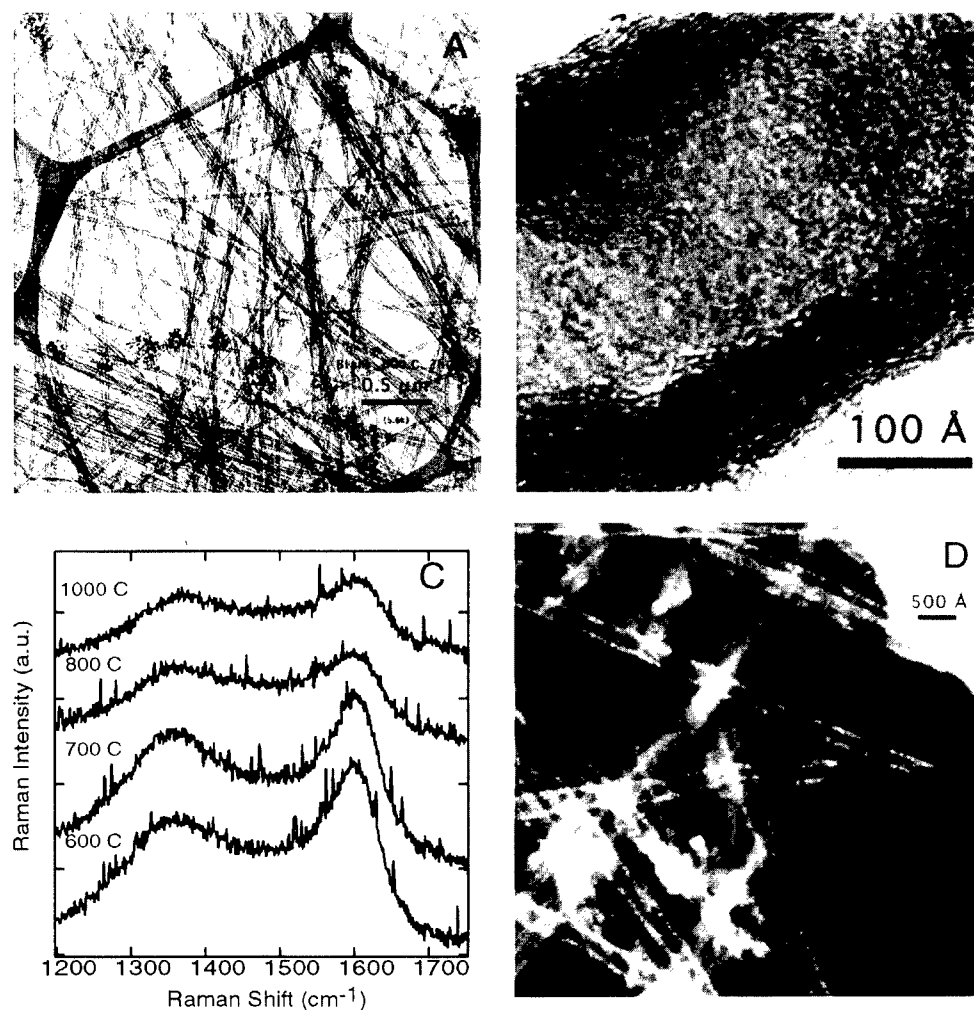


**Figure 2.** (A) TEM image of carbon nanotubes formed at 800 °C CVD conditions and liberated from the PAM by immersion in concentrated HF with ultrasonication. These CNTs have aspect ratio exceeding 1000 and vividly demonstrate the result of the template synthesis process. (B) TEM image of a tube wall of a CNT formed by CVD at 900 °C with the aid of Fe catalysts. The wall thickness is ca. 8 nm. Although layering is evident, long-range order is absent. (C) Raman spectra of CNTs obtained with laser excitation at 488 nm. The features apparent at 1360 cm<sup>-1</sup> and 1600 cm<sup>-1</sup> indicate the presence of nanocrystalline graphite. Peak intensity was diminished in the 800 and 1000 °C sample spectra. The presence of more turbostratic graphite and alumina may have interfered with the signal. (D) TEM dark field image of tube walls of CNTs formed at 700 °C. The bright centers along the pore channel walls correspond to crystalline domains. These domains were not well pronounced in CNTs formed at temperatures lower than 700 °C. The image indicates that the domain size is small.

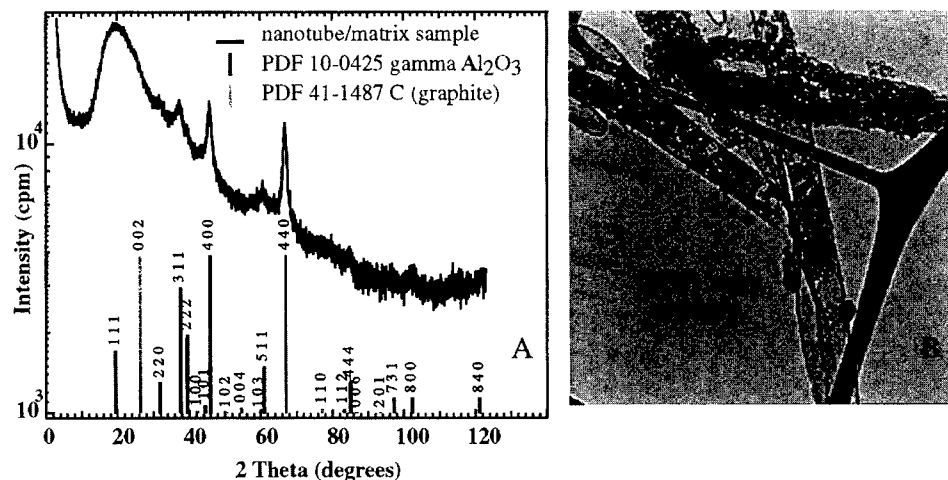


**Figure 3.** (A) XRD spectrum of a sample formed at 800 °C shows several  $\gamma$ -alumina peaks (black numbers) but no signal from the primary [002] peak for graphite (gray numbers). This suggests that long-range order is absent in CNTs prepared by our method and that the population of graphitic crystallites is small. (B) “Nanotubes within nanotubes” are shown. These small CNTs were formed with the aid of catalytic Fe nanoparticles. The smaller nanotubes have an outer diameter of *ca.* 10 nm and wall thickness less than 2 nm. Cobalt doped PAMs also generated smaller nanotubes within the major CNT formed in the PAM channel.

XRD data showed that long-range order was absent in all samples tested. The XRD spectrum shown in Figure 3a corresponds to a sample formed at 800 °C CVD that underwent immersion in concentrated HF with ultrasonication. The features at [311], [400] and [440] of the XRD spectrum displayed in Figure 3a do not correspond to graphite but rather to  $\gamma$ -alumina. Amorphous hydrated alumina, found initially in PAMs, is converted to the  $\gamma$ -alumina phase during exposure to temperatures greater than 500 °C.

Under low flow rate CVD conditions (50 sccm, 800 °C), Co and Fe catalyst particles induced the growth of smaller nanotubes (Figure 3b) within the major CNT tube defined by the template PAM pore channel wall. The smaller nanotubes were highly curled and were found in the majority of pore channels. No such catalytic effects were observed for samples formed at the higher flow rate (94 sccm). A slight decrease in the electrical resistance of catalyst-influenced samples with respect to controls was detected for the 600, 700 and 800 °C CVD sets, but no significant differences were found between catalytic and control samples formed at higher temperatures. EPMA results indicated the presence of *ca.* 1 wt.% sulfur as well as alumina in HF-treated CNT samples. The CNTs, whether in the PAM or not, exuded a strong sulfur odor when ground with mortar and pestle. The presence of sulfur is not surprising since the PAMs are formed in a sulfuric acid electrolyte and 10 to 15 wt.% sulfate is incorporated (3).

## CONCLUSIONS

Ordered arrays of carbon nanotubes with aspect ratios from 1000 to 7000 have been successfully synthesized in porous alumina templates by CVD reactions. The degree of



graphitization, however, of samples formed from 800 to 1000 °C was not as high as expected. Although TEM images showed that the relative degree of order in the layers improved and that electrical resistance decreased in samples formed at increasing CVD temperatures, no further improvement was observed in samples formed at temperatures greater than 800 °C. Tomita *et al* (5) concluded, in reference to samples made by a similar procedure, that the average domain size was less than 10 nm and that their CNTs were not well graphitized. Accordingly, XRD, Raman and TEM results jointly agreed that long-range order was lacking in the high temperature CVD samples. Perturbations induced by the non-uniform nature of the pore channel walls of PAMs may preclude the formation of layered graphite with long-range order. Localized order was evident, however, in TEM light and dark field images and was demonstrated in Raman spectra of samples formed at 600 °C or greater.

The shape and relative intensity of the Raman peaks indicated that nanographite domains were less than 10 nm in size. In fact, the Raman spectra are very similar to those of glassy carbon prepared by the thermal decomposition of phenolic resins (9). The surprising decrease in intensity of the peak at 1360 cm<sup>-1</sup> with increasing temperature is consistent with the formation of larger nanocrystals, but an expected sharpening of the peak at *ca.* 1600 cm<sup>-1</sup> was never observed. The presence of *ca.* 50 wt.% alumina and turbostratic surface graphite in the samples formed at higher CVD temperatures may have interfered with Raman signal acquisition. Post-CVD heat treatments have been suggested as a means of enhancing graphitization (5,6).

Fe and Co nanoparticle catalysts induced the growth of “nanotubes within nanotubes” under low flow rate conditions at 800 °C in what was essentially a one-step process. No internal nanotubes were formed, however, at 94 sccm. The rate of carbon deposition at higher CVD gas flows and temperatures may have overwhelmed the competing process of metal-mediated nanotube formation. In addition, the generation of reduced sulfur compounds at higher temperatures may have poisoned catalysts (10). Future work will focus on the catalytic effects of Co, Fe and Ni nanoparticles at temperatures ranging from 600 to 800 °C, the use of non-sulfur bearing PAMs and the study of CNT growth mechanisms using other CVD gases.

### ACKNOWLEDGMENTS

This work was supported by the Office of Energy Research (Advanced Energy Projects Division) of the US Department of Energy under Contract No. DE-AC36-83CH10093.

### REFERENCES

1. Dillon,A.C.;Jones,K.;Bekkedahl,T.;Kiang,C.;Bethune,D.;Heben,M.*Nature***1997**,386,377.
2. Dillon,A.C.;Heben,M.J.**1997**,Unpub. Results.
3. Hornyak,G.L. *Ph.D. Dissertation*, **1997**,Colorado State University.
4. Yang,D.;Baughman,R.;Hornyak,G.L.;Martin,C.R.*Allied Signal* **1993**,Unpub. Results.
5. Kyotani,T.;Tsai,L.;Tomita,A.*Chem.Mater.* **1996**,8,2109.
6. Che,G.;Lakshmi,B.B.;Martin,C.R.;Fisher,E.R.*Chem.Mater.* **1998**,10,260.
7. Schneider,J.;Czap,N.;Hornyak,G.L.;Heben,M.J.,*Nano '98 Bk.of Abs.* **1998**, P1-10,210.
8. Tunistra,F.;Kocing,J.L.;*J.Phys.Chem.***1970**,53,1126.
9. Tallant,D.R.;Parmeter,J.E.;Simpson,R.L.*Diamond&Rel.Mater.***1995**,4,191.
10. Motojima,S.;Hasegawa,I.;Kagiya,S.;Momiyama,M.*Appl.Phys.Lett.* **1993**,62,2322.



## LIQUID CHROMATOGRAPHY USED TO SIZE-SEPARATE THE AMPHIPHILIC-MOLECULES STABILIZED NANO-PARTICLES OF CDS IN THE 1-10NM RANGE.

R.Sivamohan\*, H.Takahashi<sup>1</sup>, A.Kasuya, K.Tojji<sup>1</sup>, S.Tsunekawa, S.Ito and B. Jeyadevan

Institute for Materials Research, Tohoku University, Sendai, 980-8577, Japan.

<sup>1</sup>Dept. of Geosciences and Technology, Tohoku University, Aoba, Sendai, 980-77, Japan

*Abstract--The making of nano-particles in the 1-10nm range in micro-emulsions, the surface coating of these by the amphiphilic-molecules in the same microemulsion and the subsequent treatment of the oil-phase based particles in the liquid chromatography (HPLC) is the focus of this work. A HPLC column with Silica (5µm diameter, 120Å pore size) with C<sub>18</sub> (ODS) bonded phase was used. Toluene is used as the mobile phase. The CdS nanoparticles in the mobile phase were continuously monitored by ultra-violet spectroscopy. The CdS products were collected at different time intervals. For a relatively coarse feed, in 5.7nm range, a rich product with a sharp size distribution can be obtained. High resolution transmission electron micrograph shows that the product is well crystallized. The eluted products from the HPLC were treated separately in a Size Exclusion Chromatography. Elution times for size-exclusion-chromatography show that the different HPLC products come out in different time intervals suggesting the possibility of nanoparticle size separation by this method. ©1999 Acta Metallurgica Inc.*

### INTRODUCTION

It is commonly expected that nano-particles in the range of 1-10nm exhibit unusual chemical, electronic, magnetic and optical properties due to their sizes which are extremely close to the molecular dimensions [1-3]. The separation of these nano-particles into close-size fractions is expected to enhance further the above mentioned unusual properties. Pileni [4] notes that manipulating the nearly monodispersed nanometer size crystallites with an arbitrary diameter presents a number of difficulties. Nevertheless, various research groups have attempted to obtain nearly mono dispersed particles by testing various techniques such as reverse and normal micelles, zeolites, size-selective precipitation, size-exclusion-chromatography (SEC), and HPLC. Fisher et al [5] employed SEC to fractionate extremely small CdS particles. The particles they studied were not coated with a protective layer of surfactant molecules, and therefore, in their study they concentrated on the growth nature of the particles. They found that as the particles grow the beginning of absorption is shifted to longer wavelengths. In another study, Fisher et al [6] investigated the small CdS particles by

HPLC. In this work also the authors concentrated on the growth nature of the particles only. It is well known that in the case of unstabilized very small nanoparticles, the thermal growth causes a gradual increase in size that is ascribed to Ostwald ripening.

Since the period of 1986-1989 when these two works were carried out, there have been no major work on the application of chromatography to size-fractionate the nano particles since then. We, recently, saw an abstract by Wilcoxon and Craft [7] which claims that the nanoparticles can be separated from the surfactants and other by products of the reaction by using a variety of HPLC columns and that the HPLC columns are able to separate the nanoparticles based upon a combination of size exclusion and chemical affinity mechanisms.

## EXPERIMENTAL

All the chemicals used are of analytical grade. The water used was from the Yamato Millipore WQ 500 Autopure system. CdS particles were treated with two surfactants, Sodium oleate and Lauric acid. A concentration of  $1.31 \times 10^{-1}$  M sodium oleate, (MW 304.4, CMC  $2.1 \times 10^{-3}$  M) was dissolved in 50ml of water (2g oleate in 50ml of water). 150ml of toluene added to this water and stirred intensively until a stable emulsion was formed. The emulsification was performed using a homogenizer (AM-9, Nihonseiki Co.). The emulsion produced is opaque and white. Normally dispersed particles having a diameter of less than about 1/4 of the wavelength of visible light (i.e., 120nm), cause Rayleigh scattering of the light and therefore appear transparent to the eye. To this emulsion, 10ml of  $\text{Na}_2\text{S} \cdot 9\text{H}_2\text{O}$  (0.78g/50ml) was added and stirred. Afterwards, 10ml of  $\text{CdSO}_4$  (1.96g/50ml) was added, as 1ml aliquots while being stirred. The ratio of the cadmium and sulfur ions  $[\text{Cd}^{2+}]/[\text{S}^{2-}]$  is 3. The formation of CdS was observed during stirring by the greenish yellow color of the CdS. The emulsion also broke down into two phases, a water phase and an oil phase, during stirring. The oil phase containing the CdS was recovered by centrifuging and evaporation in a rotary evaporator. The evaporated CdS product was redispersed in toluene again.

With Lauric acid,  $(\text{CH}_3(\text{CH}_2)_{10}\text{COOH})$ , MW 200.32, CMC (sodium salt)  $2.6 \times 10^{-2}$  M, a concentration of  $4.0 \times 10^{-1}$  M was used. First, the Lauric acid was neutralized with NaOH in order to produce the sodium salt of the Lauric acid which is sodium decanoate. 50ml of water was used. 150ml of toluene was used. CdS nanoparticle preparation with the lauric acid was performed by the same way as that described above for the oleate.

In the beginning of this experimental work, the synthesis of CdS particles was examined by resonance Raman scattering and electron diffraction. A peak was obtained at the frequency of  $302 \text{ cm}^{-1}$  which is characteristic for CdS precipitated from the mixture  $\text{CdSO}_4$  and  $\text{Na}_2\text{S}$ . Electron diffraction pattern showed the CdS structure to be predominantly cubic. EDX showed the presence of Cd and S atoms.

### *Chromatographic measurements*

The size separation was done with HPLC using a monomeric octadecyl silica column (Waters' Puresil C18, 20mmx250cm). This is a reversed phase preparative column using a

bonded phase. Silica (5  $\mu\text{m}$ , 120  $\text{\AA}$  pore size) with  $\text{C}_{18}$  (ODS) bonded phase as the stationary phase. The toluene only was used as the mobile phase. The products of reaction produced in microemulsions were always filtered through a 100nm PTFE filter under vacuum (TOYO Roshi Kaisha Ltd., Japan) before being introduced into the chromatographic system. The absorbance measurements were done at 330nm.

In the case of Size Exclusion Chromatography (SEC) tests, STYRAGEL HR2 column (7.8x300mm) from Waters Co was used. This column is normally used for the analysis of low-molecular weight polymers. The column is packed with 5  $\mu\text{m}$  particles. The particles are fully porous, highly cross-linked styrene-divinylbenzene copolymer. The mobile phase used here was also toluene 100%.

## RESULTS and DISCUSSION

The total volume in a HPLC column,  $V_T$ , is made up of three parts (8).

$$V_T = V_{ss} + V_s + V_m$$

$V_{ss}$  = Volume occupied by the solid support

$V_s$  = Volume occupied by the stationary phase (ODS coating on the solid particles)

$V_m$  = Volume occupied by the mobile phase

In the case of porous solid particles,  $V_m$  includes both the interparticle volume (space between the particles) and the internal volume of the particles. The total porosity is the fraction of ( $V_m / V_T$ ). This figure can be as high as 0.80 meaning a tightly packed bed of porous particles is still about 80% empty. If the particles are nonporous this figure drops to about 0.40. We can see here that the internal volume of the porous particles in a HPLC column can be about 40%. The basis of our attempt to employ the HPLC as a Size Exclusive chromatography rests on this fact that there is about 40% internal volume of the particles which we can make use to achieve nanoparticle size-fractionation.

When size-fractionating the surfactant coated nanoparticles by HPLC, the size of the pores in the silica particles becomes an important factor. The pore size may be too unsuitable to admit the relatively large nanoparticles but still can admit the smaller ones. In this way we can expect the larger nanoparticles elute first before the smaller ones. We tried to exploit this mechanism in the HPLC to size fractionate the nanoparticles.

Fig. 1 shows the results obtained by eluting the Lauric surfactant coated CdS nanoparticles in the HPLC column. Three products were collected, designated as CdSL2-1, CdSL2-2 and CdSL2-3. The TEM micrographs showed that the products which elute first were larger in size than the products which elute last. The optical spectra of these products (fig. 2) also confirmed that there is a relationship between the increasing shift in the optical spectrum and the time of elution. HRTEM micrographs were taken for the product CdSL2-2. These micrographs confirmed via their well-aligned lattice pattern that the CdS nanoparticles were well crystallized and have a cubic structure. A statistical analysis of the particle sizes of the individual particles identified in these micrographs was done. Imaging at  $3 \times 10^6$  magnification allows to make the correct measurements of 30-35 individual nanoparticles. The particles are 85% between 5 and 5.6nm in diameter.

The HPLC products obtained above, CdSL2-1, CdSL2-2 and CdSL2-3, were separately treated by Size Exclusion Chromatography in the STYRAGEL HR2 column. The

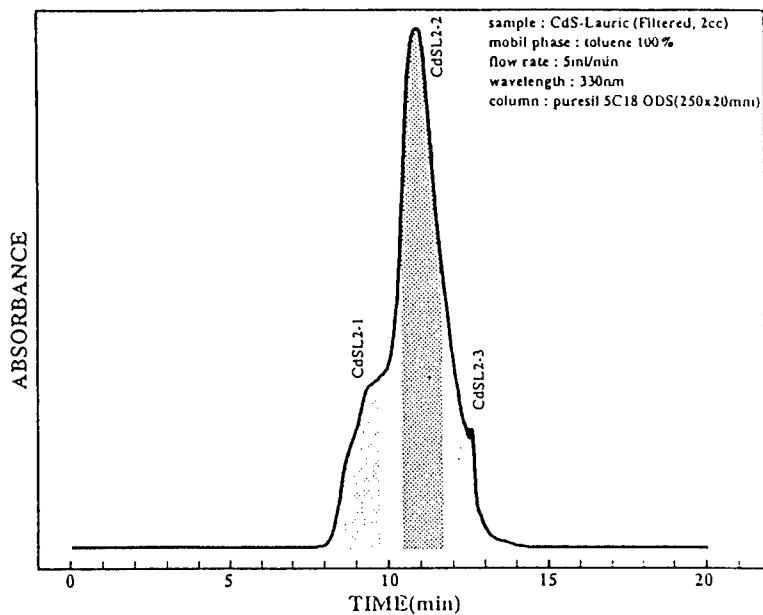


Fig. 1 HPLC chromatogram for Lauric coated CdS

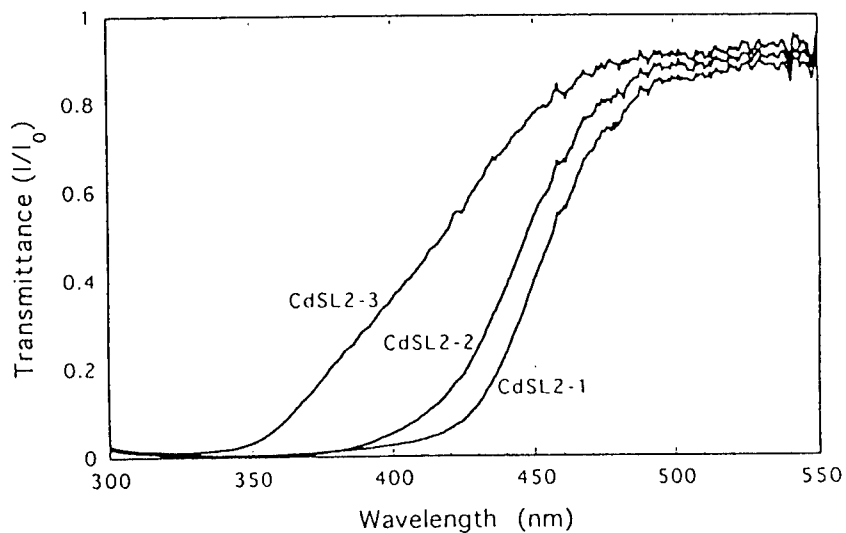


Fig. 2 Optical spectra of the chromatographic products of Lauric coated CdS

results are shown in fig. 3. It can be seen that the products of different sizes elute from the column at different time intervals. Nevertheless, in Size Exclusion Chromatography the higher molecular weight components are expected to elute first. Fisher et al [5], who used a SEC column to fractionate nanoparticles, also have found that the larger particles eluted first. Our results do not show such a relationship between decreasing particle size and increasing elution time, although products of different sizes elute at different times. The reason for this anomalous behavior might be that the particular column, Styragel HR2, we used is unsuitable

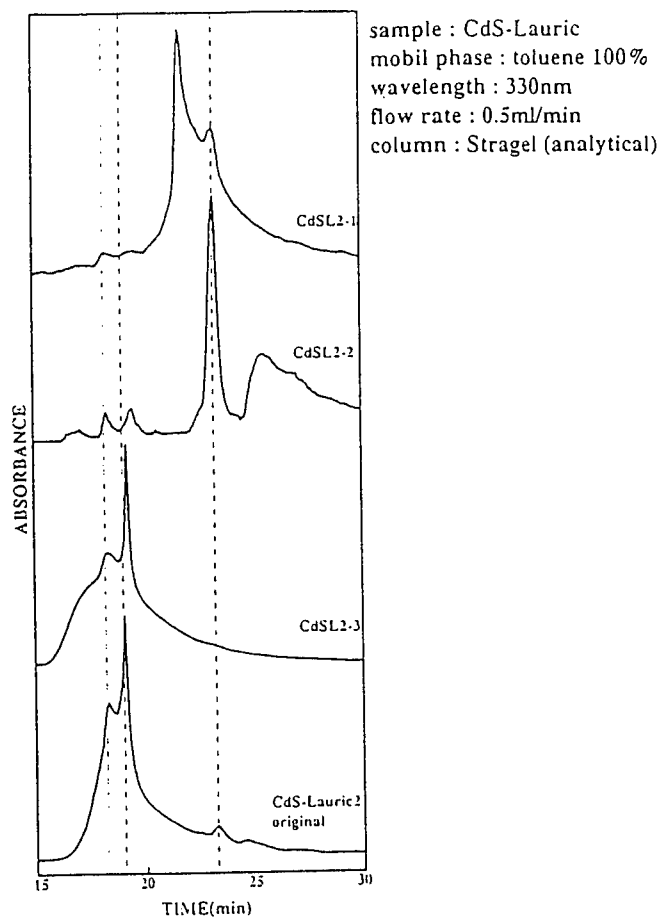


Fig. 3 SEC chromatogram for the HPLC separated CdS-Lauric products

for the particular sizes of the nanoparticles we tested. We, now, have a different SEC column known as Styragel HMW 6E which is designed for the analysis of ultrahigh-molecular-weight polymers. The stationary phase particles are 20  $\mu\text{m}$  in size. We have plans to investigate these two particular SEC columns' performances in size fractionating the nano-particles.

Similar experiments were performed with oleate-coated CdS particles. The mobile phase was 100%-toluene. The result shows 5 products. Our experience with HPLC has shown, that in general, the larger nanoparticles only elute out first from the column. At this stage, the question was whether we could suppress these larger particles inside the column and take out the smaller fractions. We tried it by changing the mobile phase to slightly polar one, toluene:ethanol = 90%:10%. The intention was to employ the *solvophobic* mechanism of the liquid chromatography [8]. Lyophobic nanoparticles aggregate by van der Waals forces. The adsorption of amphiphilic species on the nanoparticles gives rise to a steric barrier to aggregation. The efficiency of the steric stabilization is strongly dependent on the interaction of the alkyl groups with the solvent. Gradual addition of a nonsolvent (in our case ethanol) produces a size dependent aggregation of nanoparticles with the ODS coated stationary phase of the HPLC column. The results show that we have succeeded in suppressing the larger nano particles and taking out only the smallest fraction. The work is being continued on taking out the larger fractions as well.

This work was supported by CREST research program at Japan Science and Technology Institute.

## REFERENCES

1. Takahashi, T, Goto T. et al., *Materials Sci. Eng.*, 1996, A217/218, 42.
2. Edelstein, A.S. and Cammarata, R.C. "Nanomaterials", Institute of Physics Publishing, Bristol and Philadelphia, 1996, 596 pp.
3. Sasaki, T. "Molecular Nanosheets of Quasi-TiO<sub>2</sub>: Preparation and Self Assembling" Proceedings, 11th Toyota conference, "Nanostructured Materials", November 5-8, 1997.
4. Pileni, M.P., *Langmuir*, 1997, 13, 3266
5. Fisher, C.H., Weller, H. et al., *Ber. Bunsenges. Phys. Chem.*, 1986, 90, 46.
6. Fisher, C.H., Weller, H., Katsikas, L and Henglein, A., *Langmuir*, 1989, 5, 429.
7. Wilcoxon J.P. and Craft S.A., *Nanostructured Materials*, 1997, 2 (1-8), 85.
8. Miller J.M., "Chromatography - Concepts and Contrasts", John Wiley & Sons, Inc., 1988 296 pp.



## DIFFERENT ZIRCONIA-ALUMINA NANOPOWDERS BY MODIFICATIONS OF CHEMICAL VAPOR SYNTHESIS

V.V. Srdic§, M. Winterer, G. Miehe\* and H. Hahn

Thin Films Division, \*Structural Analysis Division, Materials Science Department,  
Darmstadt University of Technology, Germany

§On leave from: Faculty of Technology, Inorganic Technology and Materials Science  
Department, University of Novi Sad, Yugoslavia

**Abstract** -- Ultra-fine, nanocrystalline zirconia/alumina ( $n\text{-ZrO}_2/\text{Al}_2\text{O}_3$ ) powders are synthesized by chemical vapor synthesis (CVS) using a variable, modular gas flow reactor. Results for three different  $n\text{-ZrO}_2/\text{Al}_2\text{O}_3$  powders are presented: single phase particles formed by doping zirconia with alumina, coated particles, and composite powder consisting of mixed particles of  $n\text{-Al}_2\text{O}_3$  and  $n\text{-ZrO}_2$ . ©1999 Acta Metallurgica Inc.

### INTRODUCTION

Recently, a novel gas phase process, chemical vapor synthesis (CVS), has been developed for the synthesis of  $n\text{-ZrO}_2$  powders (1, 2). In this process volatile metalorganic precursors are decomposed in a hot wall reactor at reduced pressures forming non-agglomerated nanocrystalline particles. The inherent advantages of the CVS process are: (a) the formation of nanoparticles from molecular or atomic species in a completely homogeneous state (vapor), (b) a well defined reaction zone in which temperature, pressure and mass flows are controllable and reproducible. In this paper, the opportunities of this “bottom-up” strategy are demonstrated by the microstructural variations of nanoparticles obtained by modifications of the reactor geometry. The  $\text{ZrO}_2/3 \text{ mol\% Al}_2\text{O}_3$  system was chosen as an example to demonstrate the unique opportunities of CVS.

### EXPERIMENTAL

The different assemblies of the modular CVS reactor used in the present work are shown schematically in Figure 1. Generally, the reactor consists of precursor delivery units, different types of reaction zones, a powder collection zone and a pumping unit consisting of a roots pump and a backing pump.

The precursors are delivered to the reaction zones by bubbling controlled helium gas flows through bubblers with liquid zirconium-t-butoxide (ZTB) and aluminium-s-butoxide (ASB) held constant at 80°C and 175°C, respectively. The powder consisting of zirconia doped with 3 mol% of alumina, labeled ZA-3d, is synthesized using a hot wall reactor (fig. 1a) consisting of an alumina tube with an inner diameter of 19 mm heated by a resistance furnace



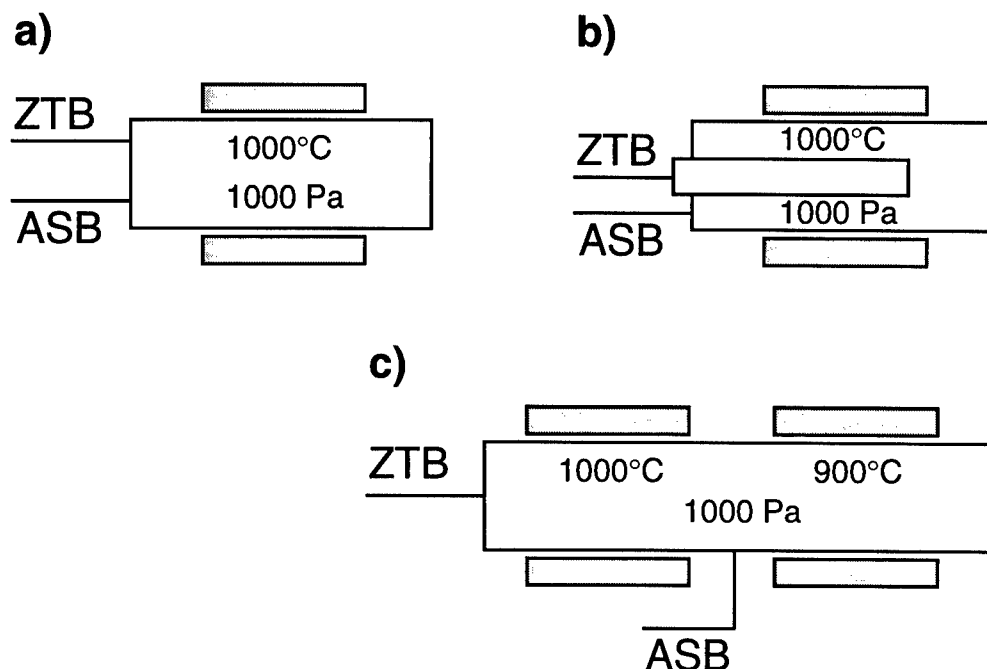


Figure 1. The different types of modular CVS reactor used for synthesis of doped, mixed and coated  $n\text{-ZrO}_2/\text{Al}_2\text{O}_3$  powders.

to 1000°C. Precursor vapors (ASB and ZTB) and helium flows are mixed before reacting with an additional flow of oxygen assuring complete oxidation of the product. The *coated* powder with a core/shell structure, termed ZA-3c, is synthesized by two reaction zones in a serial arrangement (fig. 1b). In the first reactor precursor molecules of one component are reacted forming small oxides nanoparticles, which are used as seeds for heterogeneous nucleation of the second component in the second reactor. The *mixed* powder of alumina and zirconia, denoted as ZA-3m, is synthesized with two parallel CVS lines (fig. 1c). The system consists of a thin wall alumina tube with inner diameter of 10 mm positioned coaxially inside an alumina tube with an inner diameter of 19 mm heated by a resistance furnace. A mixed ASB/He/O<sub>2</sub> flow is submitted to one line and a ZTB/He/O<sub>2</sub> gas flow to the second.

The nanoparticles are separated from the gas stream by thermophoresis produced in the cylindrical collector by the temperature gradient between a heated quartz lamp and the water cooled collector wall. The alumina content in the powders can be controlled reproducibly by the ratio of the helium flow rates through the bubblers containing ASB and ZTB. Additionally, the as-synthesized  $n\text{-ZrO}_2/\text{Al}_2\text{O}_3$  powders are annealed in air at 700°C for 3 h.

The as-synthesized and annealed powders are characterized by X-ray diffraction using a Siemens D5000 instrument with Ni-filtered Cu-K $\alpha$  radiation, nitrogen adsorption measured by a Quantachrom Autosorb-3B instrument and transmission electron microscopy (TEM) performed with a Philips CM20 Ultra Twin microscope operated at 200 kV. The alumina content is determined by energy dispersive X-ray analysis (EDX) with appropriate standards using a high-resolution scanning electron microscope (HRSEM Philips XS 30) operated at 10 kV.

## RESULTS AND DISCUSSION

The as-synthesized  $n\text{-ZrO}_2/\text{Al}_2\text{O}_3$  powders are non or weakly agglomerated, with very small average crystallite sizes determined from the XRD (X-ray diffraction) line broadening between 4 to 6 nm and large surface areas ranging from 190 to 250  $\text{m}^2/\text{g}$  (Table 1). The XRD pattern of the pure  $n\text{-ZrO}_2$  (ZA-0) and all three as-synthesized samples (ZA-3d, ZA-3c and ZA-3m) are quite similar (Figure 2a). According to the detailed line shape analysis of the diffractograms the volume fraction of the tetragonal phase is higher in all as-synthesized  $n\text{-ZrO}_2/\text{Al}_2\text{O}_3$  powders compared to pure  $n\text{-ZrO}_2$  (Table 1). During annealing in air at 700°C for 3 h the fraction of the tetragonal phase decreases by almost one order of magnitude for the pure  $n\text{-ZrO}_2$  sample, whereas for the other samples only by a factor of two (Figure 2b and Table 1). The average particle sizes calculated from BET (Brunauer-Emmett-Teller nitrogen adsorption isotherm) and crystallite sizes calculated from XRD line broadening (Table 1) increase. The largest increase is found in the mixed powder sample (ZA-3m), the smallest in the coated sample (ZA-3c) where the increase is larger for the monoclinic phase fraction.

The stabilization of the tetragonal phase in pure CVS  $n\text{-ZrO}_2$  may be due to size or surface enthalpy effects (2). However, in case of the  $n\text{-ZrO}_2/\text{Al}_2\text{O}_3$  samples clearly a partial stabilization by alumina is observed. In the annealed samples the tetragonal fraction is larger than in the pure  $n\text{-ZrO}_2$  sample by a factor of about five. An increase in the fraction of the tetragonal phase in alumina doped zirconia powders (ZA-3d, as-synthesized and annealed) can be explained by the formation of a solid solution of zirconia and alumina, already mentioned in the literature for wet-chemical (3, 4) and gas phase (5, 6) synthesized powders.

The as-synthesized coated powder (ZA-3c) has a considerably lower specific surface area and a larger average particle size calculated from BET (Table 1) consistent with a larger particle size observed in TEM, but the XRD domain (crystallite) size is slightly smaller than in case of pure zirconia. The TEM micrographs shown in Figure 3 reveal that the particles of the pure  $n\text{-ZrO}_2$  are terminated by very sharp edges displaying high degrees of crystallinity (2).

TABLE 1  
Characteristics of As-synthesized and Annealed Powders.

Sample notation	$S_v$ [ $\text{m}^2/\text{g}$ ]	$d_{\text{BET}}$ [nm]	$d_{\text{TEM}}$ [nm]	$C_{\text{tXRD}}$ [nm]	$C_{\text{mXRD}}$ [nm]	$f_t$ [vol %]
<i>as-synthesized powders</i>						
ZA-0	224	4.6	5.7	4.6	6.1	77
ZA-3d	245	4.2	-	3.7	4.9	83
ZA-3c	193	5.3	6.5	4.2	4.5	83
ZA-3m	231	4.4	-	4.7	5.0	86
<i>annealed powders</i>						
ZA-0	46	22.7	-	17.6	16.9	8
ZA-3d	55	18.9	-	12.3	13.1	38
ZA-3c	68	15.1	-	9.1	17.4	32
ZA-3m	47	22.0	-	18.6	22.4	48

$S_v$  - specific surface area;  $d$  - particle size determined by the method indicated;

$C_t$  - tetragonal,  $C_m$  - monoclinic crystallite size calculate from XRD line broadening;

$f_t$  - volume fraction of tetragonal phase.

However, particles of coated ZA-3c sample have smooth edges and in some case observable core/shell structure. The details of the growth process in the two stage reactor are not known. Therefore, it is assumed that the thin coating on the  $\text{ZrO}_2$  particles which are formed in the first stage grows from a mixture of ASB entering into the second stage and a rest of unreacted zirconia molecular species. Thus, a core/shell structure is obtained with a pure  $\text{ZrO}_2$  core and a shell consisting of a solid solution with a high concentration of alumina. Due to the high alumina content the shell is amorphous as observed in doped  $\text{n-ZrO}_2/\text{Al}_2\text{O}_3$  CVS-samples with more than 30 mol %  $\text{Al}_2\text{O}_3$  (5). Similarly, Vollath et al. (7) observed amorphous coatings on  $\text{ZrO}_2$  particles prepared by microwave plasma processing. This complex structure of the nanoparticles explains the rounded edges due to an amorphous isotropic surface, the observed particle size with decreased domain size of the crystalline  $\text{ZrO}_2$  part and inhibited growth during annealing as also observed in the amorphous CVS powders of zirconia doped with more than 30 mol %  $\text{Al}_2\text{O}_3$  (5). Corresponding to the small domain size of the pure  $\text{ZrO}_2$  the tetragonal phase is stabilized in the majority of the particles.

It is expected that in the co-axial hot wall reactor  $\text{n-ZrO}_2$  and  $\text{n-Al}_2\text{O}_3$  particles will be separately formed and mixed as individual particles in the gas flow. The as-synthesized ZA-3m powder has an increased fraction of tetragonal zirconia compared to pure  $\text{n-ZrO}_2$ . The annealed powder has the largest tetragonal fraction of all four annealed samples. On the base of the present limited data the reasons for those facts cannot be determined. Two reasons seem to be plausible - the residence time is proportional to the cross section of the reaction tube and consequently is shorter for the parallel CVS lines. Unreacted precursor or monomer species may therefore still exist at the position where the separated particle flows are mixed and alumina doped zirconia could be formed.

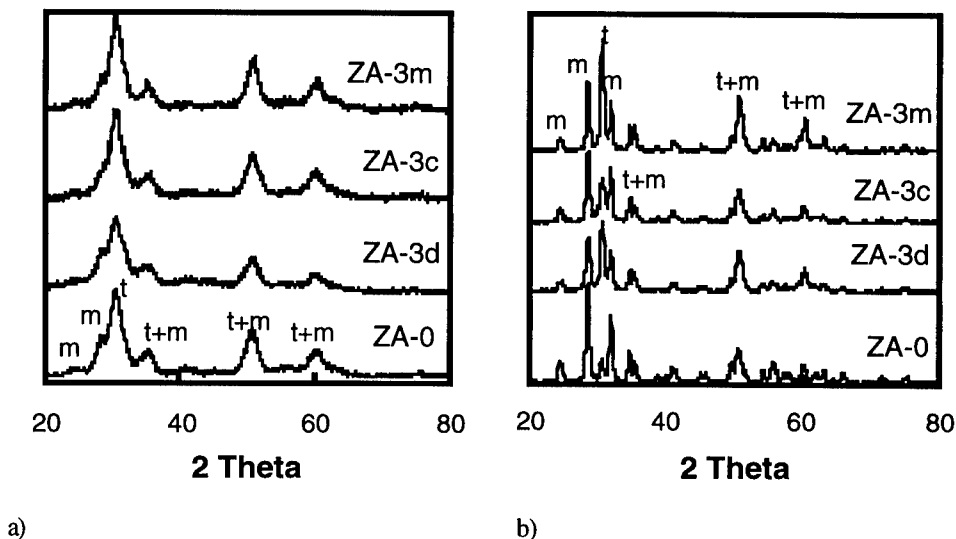


Figure 2. XRD patterns of: a) as-synthesized and b) annealed pure  $\text{n-ZrO}_2$  and doped, coated and mixed  $\text{n-ZrO}_2$  with 3 mol %  $\text{Al}_2\text{O}_3$  powders.

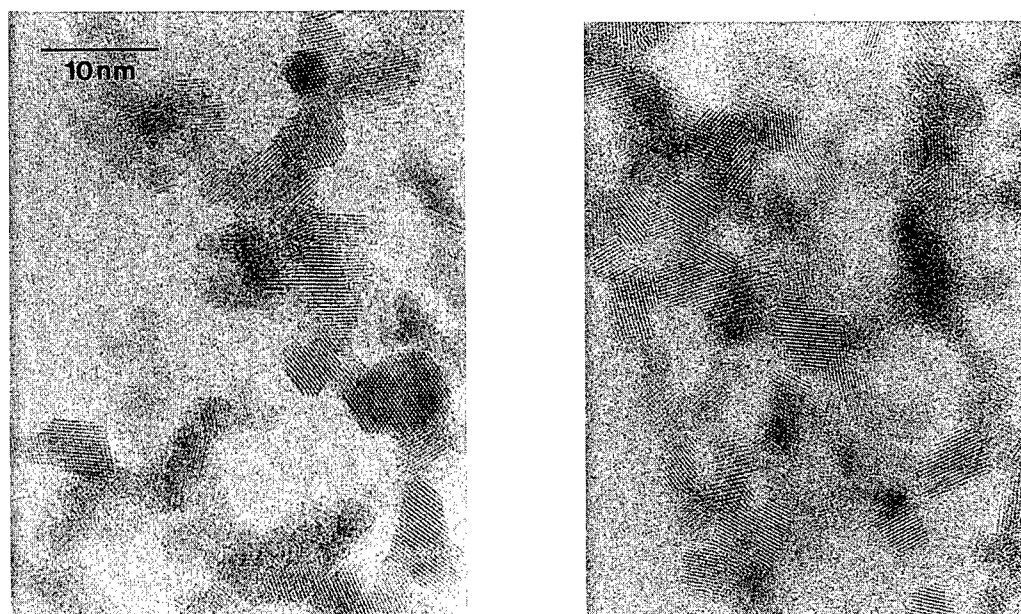


Figure 3. TEM micrographs of CVS as-synthesized pure n-ZrO<sub>2</sub> (left) and coated n-ZrO<sub>2</sub> / 3 mol % Al<sub>2</sub>O<sub>3</sub> powders (right).

Thus, it is believed that the ZA-3m powder consists of a mixture of zirconia doped with alumina, pure zirconia and pure alumina particles. The relative increase of the grain growth (about a factor of 1.5 compared to the doped sample) could be a consequence of the inhomogeneity of the sample.

### CONCLUSIONS

Ultra-fine, crystalline and non or weakly agglomerated doped, coated and mixed n-ZrO<sub>2</sub> / Al<sub>2</sub>O<sub>3</sub> powders with 3 mol% Al<sub>2</sub>O<sub>3</sub> were produced by modifications of the chemical vapor synthesis process. Three different structures of the nanoparticles were obtained: (a) doped, single phase particles of a solid solution of alumina in zirconia; (b) coated particles exhibiting a thin amorphous alumina rich shell on a pure zirconia core; (c) mixed powders of a mixture of zirconia doped with alumina, pure zirconia and pure alumina particles.

### ACKNOWLEDGEMENTS

Vladimir V. Srdic is grateful for a research fellowship by the Alexander von Humboldt Foundation.

### REFERENCES

1. Chang, W., Skandan, G., Danforth S.C., Kear B.H. and Hahn, H., *Nanostructured Materials*, 1994, 4, 507.
2. Srdic, V.V., Winterer, M. and Hahn, H., accepted by *Journal of the American Ceramic Society*, 1998.
3. Yamaguchi, O., Shirai, M. and Yoshinaka M., *Journal of the American Ceramic Society*, 1988, 71, C-510.
4. Balmer, M.L., Lange, F.F. and Levi C.G., *Journal of the American Ceramic Society*, 1994, 77, 2069.
5. Srdic, V.V., Winterer, M. and Hahn, H., *Journal of the American Ceramic Society*, 1998, submitted.
6. Ferkel, H., Naser, J. and Riehemann, W., *Nanostructured Materials*, 1997, 8, 457.
7. Vollath, D. and Szabo, D.V., *Nanostructured Materials*, 1994, 4, 927.



Pergamon

NanoStructured Materials, Vol. 12, pp. 101–106, 1999

Elsevier Science Ltd

© 1999 Acta Metallurgica Inc.

Printed in the USA. All rights reserved

0965-9773/99/\$—see front matter

PII S0965-9773(99)00074-4

## LASER ABLATION DEPOSITION OF SILICON NANOSTRUCTURES

J. Levoska, M. Tyunina\*, and S. Leppävuori

Microelectronics and Material Physics Laboratories and EMPART Research Group of  
Infotech Oulu, University of Oulu, PL 444, FIN-90571 Oulu, Finland;

\*permanent address: Institute of Solid State Physics, University of Latvia, Riga, Latvia

**Abstract** – Pulsed laser deposition with an off-axis geometry in a low-pressure argon ambient was used to produce films of nanosized silicon clusters or crystallites. Size selection was achieved by the distance of the deposit from the target. The local film structure and the crystallite size of the films were studied as a function of the distance from the target using micro-Raman spectroscopy. The nanocrystal size on the off-axis placed substrate varied in the range 1...5 nm, increasing with increasing distance from the target; this made it possible to achieve size selection of the nanocrystals. The surface morphology of the deposits was studied using scanning electron microscopy. Room temperature photoluminescence of the samples with 514.5 nm excitation was rather weak. Silicon 2p core photoelectron spectra showed the existence of a silicon dioxide layer on the surface of the nanoparticles.

©1999 Acta Metallurgica Inc.

### INTRODUCTION

A serious limitation of silicon technology in optoelectronics is that bulk crystalline silicon does not emit light due to its indirect band gap. Since the discovery of efficient visible light emission from porous silicon (1), considerable attention has been paid to the study of photoluminescent silicon nanostructures of different types: nanocrystals, clusters, chain-like structures, etched bulk surfaces, superlattices, etc. (2), where quantum size effects modify the band gap and make luminescence possible. Although the importance of quantum confinement for luminescence in silicon nanostructures is under discussion (3), luminescence seems to be connected to small sized structures, where the ratio of surface or interface atoms to bulk Si atoms is large. The small dimensions can be achieved by various ways: either (a) reduction of the silicon crystal size, e.g. by anodic etching to form a porous surface layer (1), or by laser treatment of the surface (4), or (b) growing nanostructures, e.g. by laser crystallization of amorphous silicon (5), incorporate silicon nanoparticles inside silicon dioxide (6), deposition of superlattices (7), or deposition of nanocrystalline films by various methods.

In laser-assisted methods, silicon clusters have usually been produced by condensation of laser ablated material in a supersonic high-pressure inert gas jet (8). The size selection has been achieved by quadrupole mass filters, or by mechanical velocity filters (9). Normal pulsed laser ablation in a constant inert gas ambient has also been used for production of silicon nanoparticles or films (10–13), and the size distribution has been found to depend on the pressure

and nature of the ambient gas (12, 13) and on the laser fluence (13). In this study, normal pulsed laser deposition with an off-axis geometry in a low-pressure argon ambient was used to produce films of nanosized silicon clusters or crystallites. The effect of argon gas pressure and the distance from the target on the crystallite size was studied.

The nanocrystal size on the off-axis placed substrate was found to depend on the distance, which made it possible to use it as a size selection method.

### EXPERIMENTAL

The films were deposited in both off-axis and on-axis geometries using an XeCl excimer laser, n-type silicon wafer target and MgO (100) and Si (100) single crystal substrates at room temperature. The deposition arrangement is shown in Fig. 1. The laser radiation was focused to a square spot on the target with an angle of incidence of  $45^\circ$ . The laser fluence was  $4\text{--}5\text{ J/cm}^2$ . The deposit was collected onto the substrates both at a distance of 30 mm opposite to the rotating target (on-axis geometry) and perpendicular to the target (off-axis geometry) with the nearest edge 10 mm from the target. The ambient Ar gas pressure was varied from  $10^{-5}$  to 2 mbar. The duration of deposition was controlled by the number of laser pulses in the range from 3000 to 60000.

The surface morphology of the films was studied using scanning electron microscopy (SEM). The local film structure and luminescence properties of the off-axis deposited films were studied as a function of the distance from the target using a Jobin-Yvon T 64000 micro-Raman spectrometer in triple subtractive configuration and  $\text{Ar}^+$  laser excitation at 514.5 nm. Photoemission studies were carried out using synchrotron radiation on the beamline BL41 at MAX-lab, Lund, Sweden.

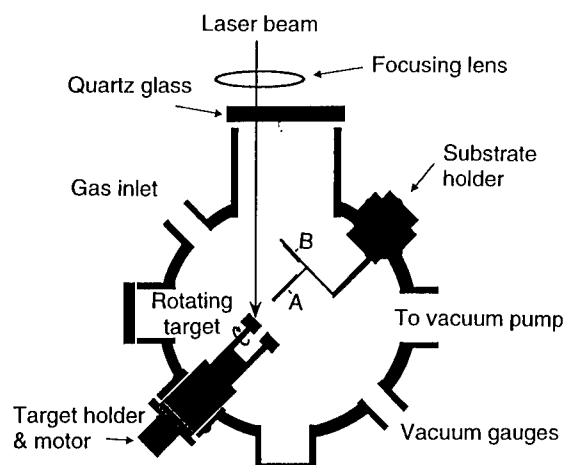


Fig. 1. Laser ablation deposition arrangement (schematic). A: off-axis substrate, B: on-axis substrate.

## RESULTS AND DISCUSSION

### *Microstructure*

SEM studies revealed that the microscopic morphology of thin films (3000 laser pulses, thickness  $<100$  nm) was rather featureless, consisting of regions with dimensions in the range of tens of nanometers (Fig. 2a). With increasing number of laser pulses, surface roughening and formation of "soft" agglomerates occurred (Fig 2b), and a columnar structure started to develop (Fig. 2c). In the pulsed laser deposition of amorphous oxides in a gas ambient, similar surface roughening with an increasing number of laser pulses has been observed (14). At long distances, an almost regular macroscopic pattern was developing (Fig. 2d). The size range of nanoparticles observed in Raman measurements (c.f. below) was outside the resolution limits of the SEM measurements.

### *Raman spectroscopy and size of nanocrystallites*

At low Ar pressures ( $<0.2$  mbar) the films were amorphous, and their Raman spectrum consisted of a broad band centered near  $480\text{ cm}^{-1}$  (Fig. 3) In the pressure range 0.4-2 mbar nanocrystalline films were obtained. In the Raman spectra, the line of crystalline silicon at  $521\text{ cm}^{-1}$  was moved to lower wavenumbers, due to relaxation of the selection rule  $q \approx 0$  in small crystals. In Fig. 3, Raman spectra from an off-axis deposited film are shown, measured at dif-

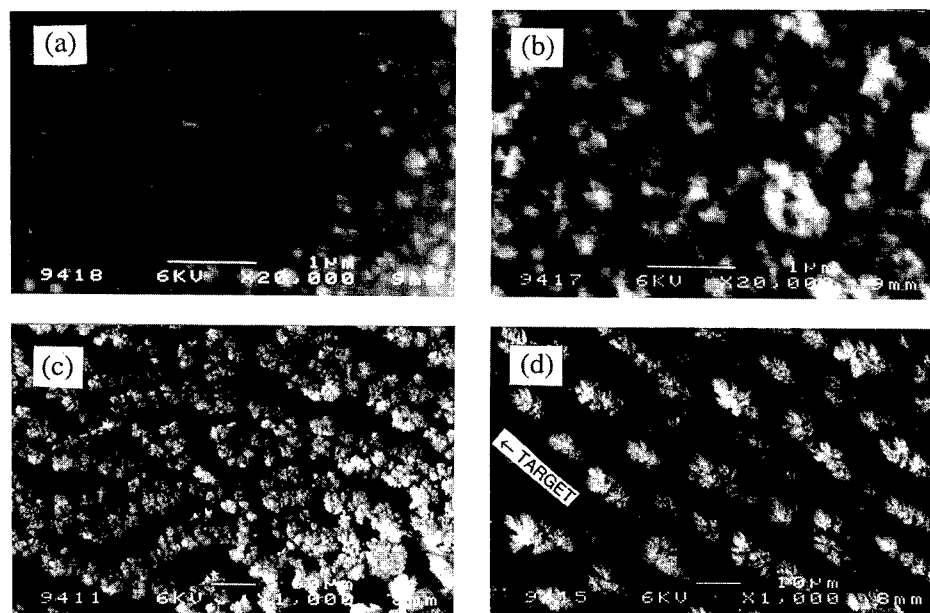


Fig. 2. SEM images of deposits produced in 2 mbar argon in off-axis geometry. Deposit at 0.5 mm from the edge nearest to the target with (a) 3000, (b) 30000, and (c) 60000 pulses (note different scale); (d) as in (c) but at a distance of 5 mm.



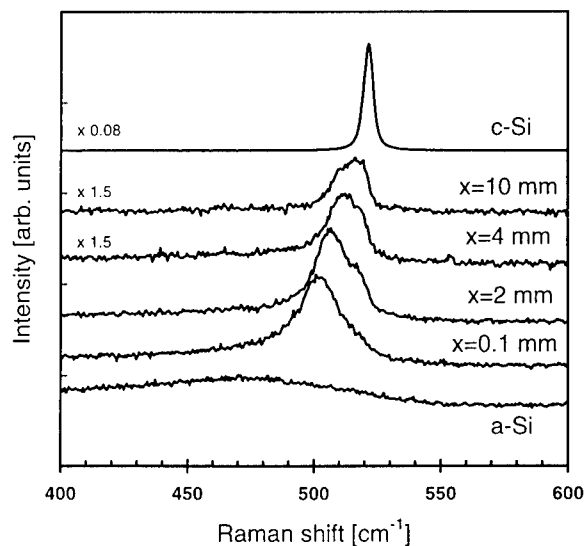


Fig. 3. Raman spectra of a deposits produced in 2 mbar argon in off-axis geometry, measured at various distances from the edge nearest to the target. For comparison, spectra from a Si crystal, and from an amorphous film obtained in on-axis geometry in vacuum, is shown.

ferent distances from the edge nearest to the target. The corresponding positions of the Raman peak are shown in Fig. 4a. Using a relationship between Raman shift and crystal size (15), it was found that the nanocrystal size varied in the range 1-5 nm, increasing with increasing distance from the target (Fig 4b). Increasing gas pressure moved the size distribution towards the target.

The explanation for the observed size distribution as a function of distance from the target is not evident. Cluster condensation in the plasma plume requires certain thermodynamic

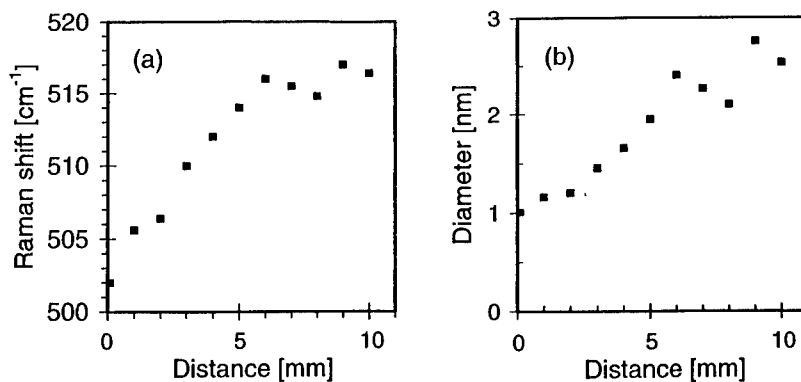


Fig. 4. (a) The position of the Raman peak measured from the deposit at various distances from the edge nearest to the target. (b) The size of nanocrystals, calculated from (a).

conditions, such as density, pressure and temperature. These conditions can be achieved during the plume expansion in a gas at a certain distance from the target. From classical thermodynamics it is known that the size of the nucleus of a new phase (clusters) is a function of the above mentioned parameters. So, the size distribution could be initially determined by the spatial distribution of condensation conditions, leading to a spatial (and temporal) distribution. After a set of clusters of different sizes has been formed, the clusters still move away from the target. Due to collisions, small clusters will be retarded and scattered in a gas more effectively than large ones, so that the off-axis positioned substrate receives more small clusters near the target.

However, the processes of condensation and desorption on the substrate (and film) surface might also contribute to the final distribution. If the energy distribution of species along the target-to-substrate direction is considered, the highest energy will be at the edge nearest to the target. Hence, the desorption rate there will be the highest and the condensation rate the lowest. If the clusters or nanocrystals grow both in the plume and on the surface, or only on the surface, then it is reasonable to expect larger clusters when the energy of impinging species is lower, i.e. at the greater distance from the target.

#### *Other characterization*

The measured room temperature photoluminescence of the samples (Fig 5), excited by 514.5 nm radiation was rather weak, probably because of the low excitation energy, which is even lower than the calculated band gap (16) for the smallest crystallites. A weak size dependence was observed in the photoluminescence spectra: a broad photoluminescence band which peaked between 600 and 700 nm, became more high-energy weighted with decreasing nanocluster size. This could indicate the broadening of the band gap.

Photoelectron spectroscopy was used to detect the oxidation state of the surface of silicon nanocrystals. In the Si 2p core photoelectron spectra, the main contribution was from Si atoms in  $\text{Si}^{4+}$  state, showing that the surface of the nanocrystals was covered with an  $\text{SiO}_2$  layer. In valence band photoemission studies, the charging of the surface of the samples inhibited the deduction of anything about the band-edge changes, especially in the samples with the smallest crystal sizes where the effect would be most prominent.

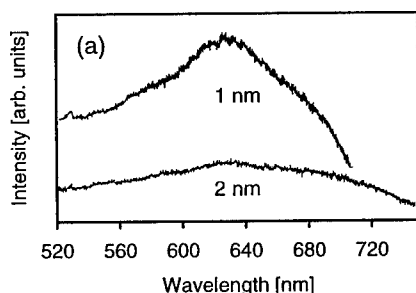


Fig. 5. Photoluminescence spectra of nanoparticles with an average crystal size of 1 nm and 2 nm. Excitation wavelength 514.5 nm.

## CONCLUSIONS

Pulsed laser deposition with an off-axis geometry in low-pressure argon ambient was used to produce films of nanosized silicon clusters or crystallites. Nanocrystals were obtained in the size range of 1-5 nm, measured by Raman spectroscopy. The nanocrystal size on the off-axis placed substrate was found to increase with increasing distance from the target, which made it possible to use it as a size selection method.

## REFERENCES

1. Canham, L.T., *Appl. Phys. Lett.*, 1990, 57, 1046.
2. See e.g. Kanemitsu, Y., *Physics Reports*, 1995, 263, 1.
3. See e.g. John, G.C. and Singh, V.A., *Physics Reports*, 1995, 263, 93; Gole, J.L., Dudel, F.P., Grantier, D., and Dixon, D.A., *Phys. Rev. B.*, 1997, 56, 2137.
4. Savin, D. P., Roizin, Y. O., Demchenko, D.A., Mugénski, E., and Sokólska, I., *Appl. Phys. Lett.*, 1996, 69, 3048.
5. Huang, X., Li, Z., Wu, W., Chen, X., Li, W., Hong, L., Li, Q., and Chen, K., *Mater. Res. Soc. Symp. Proc.* 1996, 397, 375.
6. Ito, T., Ohta, T., and Hiraki, A., *Jpn. J. Appl. Phys. Part 2*, 1992, 31, L1.
7. Lu, Z.H., Lockwood, D.J., and Baribeau, J.-M., *Nature*, 1995, 378, 258.
8. See e.g. Jarrod, M. F. *Science*, 1991, 252, 1085.
9. Werva, E. and Kolenbrander, K.D., *Mater. Res. Soc. Symp. Proc.* 1996, 397, 381.
10. Okada, R. and Iijima, S., *Appl. Phys. Lett.*, 1991, 58, 1662.
11. Fujishiro, H. and Furukawa, S., *J. Phys.: Condens. Matter*, 1991, 3, 7539.
12. Yoshida, T., Takeyama, S. Yamada, Y., and Mutoh, K., *Appl. Phys. Lett.*, 1996, 68, 1772.
13. Marine, W., Movtchan, I., Simakine, A., Patrone, L., Dreyfus, R., Sentis, M., Autric, M., and Merk, N., *Mater. Res. Soc. Symp. Proc.* 1996, 397, 365.
14. Tyunina, M., Levoska, J., Koivusaari, K.J., and Leppävuori, S., submitted to *Nanostructured Materials*.
15. Zi, J., Büscher, H., Falter, C., Ludwig, W., Zhang, K., and Xie, X., *Appl. Phys. Lett.*, 1996, 69, 200.
16. Hill, N.A. and Whaley, K.B., *Phys. Rev. Lett.*, 1995, 75, 1130; Ögüt, S., Chelikowsky, J.R., and Louie, S.G., *Phys. Rev. Lett.*, 1997, 79, 1770.



## HIGH STRENGTH AL-ALLOYS WITH NANO-QUASICRYSTALLINE PHASE AS MAIN COMPONENT

F. Schurack, J. Eckert and L. Schultz

IFW Dresden, Institut für Metallische Werkstoffe, D-01171 Dresden, Germany

**Abstract** -- The formation of quasicrystals by ball milling as well as by rapid quenching in the systems AlMnCe and AlMnFe was investigated. Melt spinning resulted in a nanoscale mixed structure of up to 60 vol.% quasicrystalline particles embedded in a fcc Al-matrix revealing a strong influence of the alloy composition on the solidification behaviour. Milling leads to the formation of an amorphous phase, however, there was no significant effect for Ce addition on phase formation. While the use of process-control agent or different milling atmospheres mainly affects the powder morphology, the milling intensity and, hence, the temperature during milling was found to be the most important parameter concerning phase evolution. The nature of observed metastable phase transitions was clarified by DSC measurements combined with x-ray diffraction. ©1999 Acta Metallurgica Inc.

### INTRODUCTION

Amorphous Al-based alloys with high specific strength were first prepared by Inoue *et al.* (1) by rapid quenching from the melt. Further strength increase was obtained by embedding nanocrystalline particles in an amorphous matrix (2). In particular, better performance was achieved by the creation of a mixed structure of nanosized amorphous or quasicrystalline particles in a fcc Al-matrix. The application of quasicrystalline particles has been reported to result in the best combination of strength and ductility (3). Although there are first informations about mechanical properties of such alloys obtained from thin ribbons and extruded gas atomized powders (4,5) more intensive investigations on bulk material are required.

The present paper focuses on the preparation of such materials by solid state reaction via ball milling of powders with special emphasis on the formation of quasicrystals depending on stoichiometry variations and different processing conditions.

### EXPERIMENTAL

Milling experiments starting from prealloyed ingots as well as from pure element powder mixtures were performed using a RETSCH PM4000 planetary ball mill. The milling was carried out in argon atmosphere ( $O_2$ ,  $H_2O < 1$  ppm), under hydrogen ( $p_{H_2} \sim 5$  bar), in air (1 bar) as well as in liquid nitrogen. The vials and the balls were made of hardened steel. The powders were milled at a ball-to-powder mass ratio of 14:1 at different intensities (100 - 300 rpm). The amount of contamination with Fe by wear debris from the milling tools was less than

0.05 at.%. Melt spinning experiments were performed in argon atmosphere resulting in ribbons with cross sections from  $0.02 \text{ mm} \times 2 \text{ mm}$  to  $0.04 \text{ mm} \times 10 \text{ mm}$ . The microstructure was characterized by x-ray diffraction (XRD) using a Philips PW1050 diffractometer with Co-K $\alpha$  radiation. Transmission electron microscopical (TEM) observations and microanalysis were performed with a JEOL 2000FX analytical microscope at 200 kV acceleration voltage and an energy dispersive x-ray spectrometer. The thermal stability of the microstructure was analyzed by differential scanning calorimetry (Perkin Elmer DSC7) at 40K/min heating rate. Microhardness measurements were done with a Vickers microhardness tester with 0.098 N to 0.98 N static load. Ten indentations were used to determine average hardness values.

## RESULTS AND DISCUSSION

Powders of  $\text{Al}_{86}\text{Mn}_{14}$ ,  $\text{Al}_{86}\text{Mn}_{12}\text{Ce}_2$ ,  $\text{Al}_{92}\text{Mn}_6\text{Ce}_2$  and  $\text{Al}_{91}\text{Mn}_7\text{Fe}_2$  were milled in argon atmosphere from prealloyed ingots consisting of a mixture of intermetallic phases and aluminum. Figure 1 shows the phase evolution after different milling times. The sample with binary quasicrystal stoichiometry reveals an amorphous phase coexisting with fcc Al after milling. The substitution of Mn by 2 at.% Ce caused an amorphous phase in which the aluminum was fully contained. Moreover, at this state of milling the development of a new phase different from the starting intermetallic phases can be seen for the  $\text{Al}_{86}\text{Mn}_{12}\text{Ce}_2$  sample. The nature of this phase is not yet clear because the small peaks in the XRD pattern complicate an unambiguous phase determination. However, just by comparing the  $d$ -values there is evidence that a quasicrystalline phase was formed. Unfortunately, annealing of the powder did not result in remarkable grain growth of this phase but lead to a phase transition at about 280°C

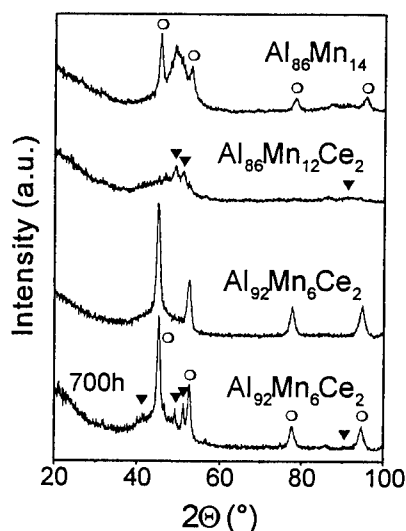


Fig.1: XRD-pattern of powder samples for different compositions milled at 300 rpm for 400 h or 700 h respectively (○-fcc-Al, ▼-icosahedral phase).

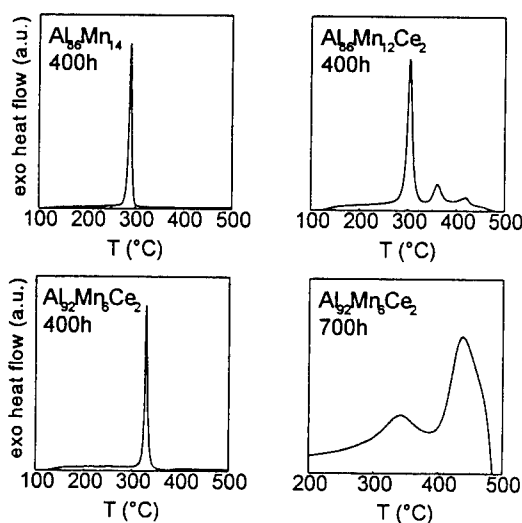


Fig.2: DSC-plots of milled powder samples corresponding to the XRD-patterns in Figure1. Measurements were performed at 40K/min heating rate.

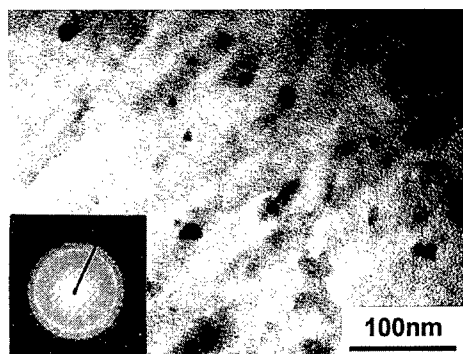


Fig.3: TEM bright field image from an  $\text{Al}_{92}\text{Mn}_6\text{Ce}_2$  powder sample after milling for 700 h

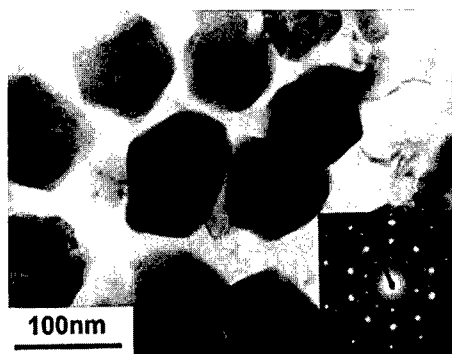


Fig.4: TEM bright field image of a  $\text{Al}_{92}\text{Mn}_6\text{Ce}_2$  melt spun ribbon and selected area diffraction image taken from one of the particles.

as shown in the corresponding DSC plot (Figure 2).

Isothermal DSC experiments proved that this transition is not due to grain growth of nanocrystalline phases but a true phase transition. The XRD analysis of the powder after transition revealed precipitation of  $\text{Al}_6\text{Mn}$ . Further heating of the sample results in additional formation of  $\text{Al}_4\text{Ce}$  at about  $330^\circ\text{C}$  and subsequent grain growth of these compounds. There is also an amorphization of the starting intermetallics for the  $\text{Al}_{92}\text{Mn}_6\text{Ce}_2$  sample again exhibiting the characteristic transition into the  $\text{Al}_6\text{Mn}$  phase at about  $300^\circ\text{C}$ . Surprisingly in contrast to  $\text{Al}_{86}\text{Mn}_{12}\text{Ce}_2$  there is no crystallization of  $\text{Al}_4\text{Ce}$ . This can be explained by the larger amount of Ce dissolved in Al. Extended milling up to 700 h brings up the crystallization of a phase which may be identified to have icosahedral structure. This was confirmed by the occurrence of an additional exothermic peak in the DSC plot at  $400^\circ\text{C}$ . The similarity of this peak with the crystallization peak found for the quasicrystal phase transition in melt spun ribbons of same composition is a further indication for the quasicrystalline nature of this phase. On the other hand, it must be taken into account that by comparing the XRD standard patterns these peaks could also origin from  $\text{Al}_6\text{Mn}$ . Definite information on the phase composition of the powder can be expected from TEM investigations. However the extremely small grain size of the particles of even less than 10 nm (Figure 3) prevents a more detailed analysis.

Similar results were observed for  $\text{Al}_{91}\text{Mn}_7\text{Fe}_2$  (not shown here in detail). However, there seems to be a weaker influence of Fe additions on phase formation than for Ce additions since the phase evolution during milling is rather similar to the one in the binary Al-Mn alloy.

For comparison, melt spinning experiments were performed, resulting in the formation of quasicrystals embedded in a fcc Al-matrix. The grain size of the quasicrystals is about 50-100 nm (Figure 4). The analysis of different samples with different composition revealed a much more significant influence of Ce addition on the phase formation than for the solid state reaction during the milling. Furthermore, the phase evolution in  $\text{Al}_{91}\text{Mn}_7\text{Fe}_2$  is more similar to the one in  $\text{Al}_{86}\text{Mn}_{14}$ . The missing of some peaks of icosahedral structure suggests that there are structural differences between the different samples. Besides a slightly higher transition temperature this assumption is also confirmed by the finding of different compositions of icosahedral phase. While the quasicrystals in  $\text{Al}_{91}\text{Mn}_7\text{Fe}_2$  form along the classical composition

of about 81 at.% Al, 14 at.% Mn and 5 at.% Fe, the composition of the icosahedral phase in  $\text{Al}_{92}\text{Mn}_6\text{Ce}_2$  was found to be  $\text{Al}_{87.8}\text{Mn}_{7.9}\text{Ce}_{4.3}$ .

Crushing and milling the ribbons resulted in complete amorphization of the quasicrystalline phase. Extended milling at high intensity caused crystallization of most likely the same phase as found after extended milling of ingots, which is supported by the appearance of rather the same kind of phase transition.

Microhardness measurements on the ribbons reveal hardness values of about 283 HV to 383 HV depending on the composition and morphology of the sample suggesting possible tensile strengths in the range of more than 850 MPa. Similar investigations for powders are in progress.

### SUMMARY

Quasicrystal formation in AlMnCe/Fe alloys was investigated in dependence on compositional changes as well as on the processing technique. In the case of rapid quenching Ce addition strongly influences the volume fraction of quasicrystals as well as their grain morphology. Milling of prealloyed compounds and pure element mixtures results first in amorphization followed by subsequent crystallization. Changes in the Ce content of the powders do not have a comparable significant influence on phase formation during milling. Further investigations are needed to clarify the nature of phases created by milling. Also the variation of the atmosphere of milling did not lead to changes in the phase formation characteristics. However, there is a grain refining effect according to the expectations when milling in liquid nitrogen, hydrogen or in air. More important is the energy input upon milling in order to induce metastable phase formation.

### ACKNOWLEDGEMENTS

We thank C. Badura for performing the melt spinning experiments and H. Saage for invaluable assistance with the TEM work. The work was financially supported by the German Science Foundation (DFG Schwerpunktprogramm "Quasikristalle"; Grant EC 111/8-1).

### REFERENCES

1. Inoue, A., Othara, K. and Masumoto, T., *Japanese Journal of Applied Physics*, 1988, 27, 479.
2. Inoue, A., Masumoto, N. and Masumoto, T., *Materials Transactions of the Japanese Institute of Metals*, 1990, 31, 493.
3. Inoue, A., Watanabe, W., Kimura, H.M., Takahashi, F., Nagata, A. and Masumoto, T., *Materials Transactions of the Japanese Institute of Metals*, 1992, 33, 723.
4. Inoue, A., Kimura, H.M., Kita, K., *New Horizons in Quasicrystals. Edited by Goldman, Sordélet, Thiel, Dubois; Singapore: World Scientific*, 1997, 256.
5. Büchler, E.H., Watanabe, E. and Kazama, N.S., *International Journal of Non-Equilibrium Processing*, 1997, 10, 35.



## ELECTRON MICROSCOPY OF NOBLE METAL ALLOY NANOPARTICLES PREPARED BY SONOCHEMICAL METHODS

R.Oshima, T.A.Yamamoto<sup>+</sup>, Y.Mizukoshi<sup>++</sup>, Y.Nagata and Y.Maeda<sup>++</sup>

Research Institute for Advanced Science and Technology, Osaka Prefecture University,  
Sakai, Osaka 599-8570 Japan

<sup>+</sup> Faculty of Engineering, Osaka University, Suita, Osaka 565-0781, Japan

<sup>++</sup> Faculty of Engineering, Osaka Prefecture University, Sakai, Osaka 599-8531, Japan

**Abstract**—Argon-saturated aqueous solutions of  $\text{NaAuCl}_4$  and  $\text{PdCl}_2$  or  $\text{K}_2\text{PtCl}_4$  were reduced simultaneously by ultrasound irradiation to prepare noble metal alloy nanoparticles. Droplets recovered from colloidal dispersions were placed on carbon-supported copper grids, and dried in a vacuum. They were examined by TEM, HRTEM, and nano-area energy dispersion X-ray spectroscopy (EDX). The Au-Pd nanoparticles exhibited monodisperse distribution (8 nm), and consisted of a gold core and a palladium shell. Au-Pt alloy nanoparticles could not be produced from  $\text{NaAuCl}_4$  and  $\text{K}_2\text{PtCl}_4$  aqueous solutions either by simultaneous or successive reduction. ©1999 Acta Metallurgica Inc.

### INTRODUCTION

There have been numerous reports on physical and chemical techniques for the preparation of nanoparticles. The evaporation of metal elements in an inert gas atmosphere is a conventional physical method of preparation. On the other hand, a sonochemical method may provide an advanced technique. Recently, the authors have reported that Au, Pd, and Pt nanoparticles have been successfully produced by the reduction of aqueous solutions with metal ions using ultrasound irradiation (1,2). In the present study, a sonochemical method has been developed to prepare binary noble metal alloy nanoparticles by the simultaneous reduction of a mixture of aqueous solutions with various concentrations of Au, Pd, or Pt metal ions. The nanoparticle characterization was carried out by transmission electron microscopy.

### EXPERIMENTAL

Aqueous solutions of  $\text{NaAuCl}_4$ ,  $\text{PdCl}_2$  and  $\text{K}_2\text{PtCl}_4$  were prepared, and mixed with designated concentrations. Some surface active agents of sodium dodecyl sulfate or water soluble polymer were also added to the solutions. Sample solutions of 60 ml were charged in cylindrical glass vessels, and were irradiated for various periods from 600 s to 3.6 ks with 200 kHz ultrasonic waves at  $6\text{W}/\text{cm}^2$  input power. The system was water cooled during irradiation.



The apparatus is shown in Fig. 1. Droplets of colloidal dispersions were placed on copper grids covered with thin carbon films, and were dried in a vacuum. They were examined by conventional transmission electron microscopy (TEM), high resolution electron microscopy (HRTEM), and nano-area energy dispersion X-ray spectroscopy (EDX) with Hitachi HF-2000 and JEM-2010F electron microscopes furnished with a field emission gun.

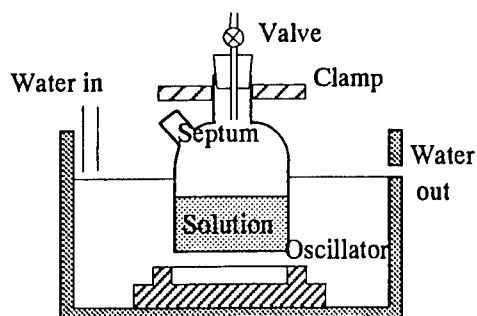


Figure 1  
Illustration of apparatus

## RESULTS AND DISCUSSION

Figure 2 is a set of TEM micrographs showing the monometal nanoparticles of Au, Pd, and Pt made from ultrasonic irradiation of  $\text{NaAuCl}_4$ ,  $\text{PdCl}_2$  and  $\text{K}_2\text{PtCl}_4$  aqueous solutions. Particle sizes were measured on the micrographs, and distributed from 2 to 20 nm. The Pt particles were smaller than those of Au and Pd. Figure 3 shows a TEM micrograph of Au-Pd alloy particles prepared from a mixture of aqueous solutions with an equimolar concentration of Au and Pd ions using the sonochemical method. The particle size distribution exhibits monodispersive characteristics with a mean size of 7.9 nm. Since the X-ray diffractometry showed a mixture of Au and Pd and no indication of Au-Pd solid solutions, HRTEM observations were carried out to examine the fine structure of the particles. HRTEM micrographs of the particles with a nominal concentration ratio of Au to Pd of 1:1 and 1:4 are presented in Fig. 5(a) and (b), respectively. A moiré pattern is observed in the middle of a particle, and the periphery contrast of the particle is different from that of the middle. This feature is more distinguished in (b). Accordingly, we suppose that the particle consists of a double layer, that is, a core-shell structure, which was confirmed by further nano-area EDX experiments. The particle was measured by converging electron beams on the whole particle.

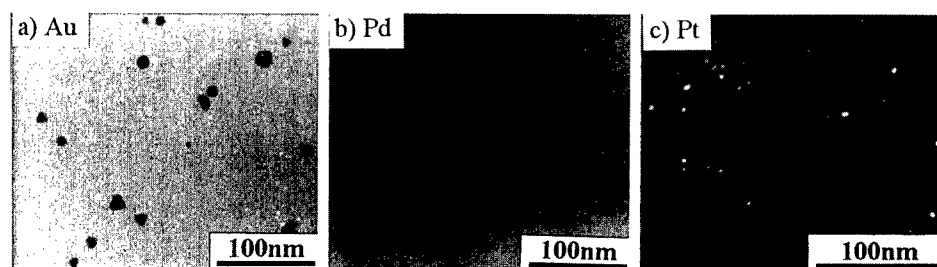


Figure 2

TEM micrographs of Au, Pd and Pt nanoparticles prepared by ultrasound irradiation.  
a) and b) bright field images, and c) dark field image.

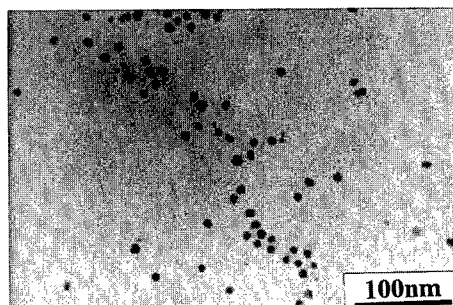


Figure 3

TEM image of Au-Pd alloy nanoparticles.

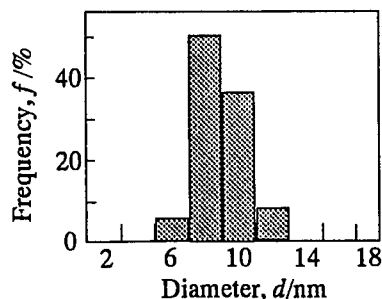


Figure 4

Size distribution of Au-Pd nanoparticles.

the middle, and its periphery. The smallest probe beam size used was 0.7 nm in diameter. The results are summarized in Table 1.

The present study contrasts with the results of Yasuda et al. who carried out in-situ successive evaporation experiments on Au-Cu binary alloys in an electron microscope (3). They reported that alloying easily takes place in particles smaller than 6 nm in diameter at low temperatures. In the spectrophotometry during ultrasound irradiation, we observed that Au was reduced first, and then Pd was successively reduced, which is compatible with the fine structures of Au-Pd particles observed by HRTEM. We also found that particle sizes were influenced by surfactants. The present results indicate that the surface of reduced Au aggregations of several nanometers are stabilized in an early stage by surfactant covering, and then Pd atoms are deposited on pre-existing Au particles.

When  $\text{NaAuCl}_4$  and  $\text{K}_2\text{PtCl}_4$  aqueous solutions were mixed, Au and Pt ions reacted, and Au particles instantly precipitated. Accordingly, the successive reduction of Au and Pt was performed to make alloy particles. After Au was completely reduced by ultrasound irradiation, a  $\text{K}_2\text{PtCl}_4$  aqueous solution was added to the colloidal dispersive, and again irradiated with ultrasound waves. In this case, however, only a mixture of Au and Pt nanoparticles was obtained. This may be due to the difference in atomic interactions of Au with Pd and Pt, which is suggested by the phase diagrams of Au-Pd and Au-Pt binary alloy systems (4). In the Au-Pd system, a continuous solid solution is formed, but phase separation occurs in the Au-Pt system.

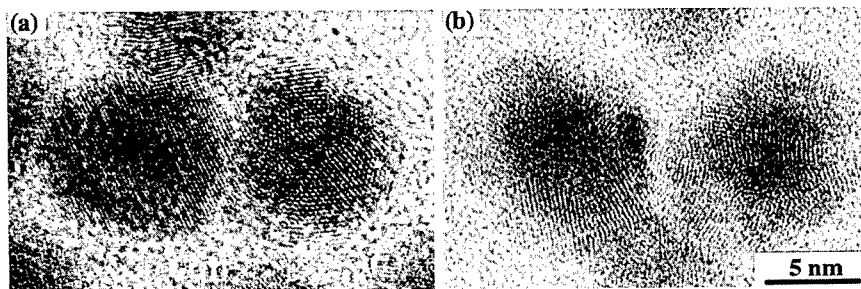


Figure 5

HRTEM micrographs of AuPd(a) and AuPd<sub>4</sub>(b) nanoparticles.

TABLE I  
Nano-area EDX measurements for AuPd and AuPd<sub>4</sub> nanoparticles.

(1) AuPd			
	whole particle	middle of particle	periphery of particle
Pd content(at%)	50.4	24.0	96.4
Au content(at%)	49.6	76.0	3.6

(2) AuPd <sub>4</sub>			
	whole particle	middle of particle	periphery of particle
Pd content(at%)	75.1	44.2	99.3
Au content(at%)	24.9	55.8	0.7

### SUMMARY

Au-Pd and Au-Pt alloy nanoparticles were made from a mixture of aqueous solutions with Au, Pd, and Pt ions by simultaneous reduction using a sonochemical method. The characterization of the nanoparticles was performed by electron microscopy. The results are summarized as follows.

- (1) Au-Pd alloy nanoparticles approximately 8 nm were obtained. They exhibited a core-shell structure of Au with a Pd shell.
- (2) Binary alloy nanoparticles of Au-Pt were difficult to prepare.
- (3) The difference in nanoparticle formation behavior between Au-Pd and Au-Pt results from different chemical interactions of Au with Pd and Pt.

### ACKNOWLEDGMENTS

The present work was supported in part by a Grant-in-Aid for Cooperative Research from the Ministry of Education, Scientific and Culture, Japan. We wish to express our thanks to Mr. N. Fujita of the Technology Research Institute of Osaka Prefecture for the use of the Hitachi HF-2000 electron microscope. We also to the JEOL company for kindly permitting us to use a JEM-2010F electron microscope.

### REFERENCES

- (1) Nagata, Y., Mizukoshi, Y., Okitsu, K. and Maeda, Y., *Radiation Research*, 1996, **146**, 333.
- (2) Okitsu, K., Mizukoshi, Y., Bando, H., Yamamoto, T., Nagata, Y. and Maeda, Y., *Ultrasonics Sonochemistry*, 1996, **3**, 249.
- (3) Yasuda, H. and Mori, H., *Zeitschrift fur Physik*, 1994, **31**, 131.
- (4) Hansen, M., *Constitution of Binary Alloys*, Genium Publishing Corporation, 1991, p.224 and p.227.



## SINTERING OF NANOSTRUCTURAL TITANIUM OXIDE USING MILLIMETER-WAVE RADIATION

Yu. Bykov<sup>1</sup>, A. Ereemeev<sup>1</sup>, S. Egorov<sup>1</sup>, V. Ivanov<sup>2</sup>, Yu. Kotov<sup>2</sup>, V. Khrustov<sup>2</sup>, and A. Sorokin<sup>1</sup>

<sup>1</sup> - Institute of Applied Physics, Russian Academy of Sciences, 46 Ulyanov str., 603600, Nizhny Novgorod, Russia

<sup>2</sup> - Institute of Electrophysics, Ural Division of the Russian Academy of Sciences, 34 Komsomolskaya str., 620049, Ekaterinburg, Russia

**Abstract** – A comparative study of sintering of different nanocrystalline  $\text{TiO}_2$  powder materials has been made. Two types of powders (produced by gas condensation and wire explosion methods) and two techniques of compacting were used for the fabrication of the green samples. Microwave and conventional sintering have been compared too. Grains grow dramatically with increasing of the density of samples. No significant dependence of the grain size on the methods of fabrication of powders, technique of compacting or method of processing has been found. Despite the larger amount of the anatase, the microhardness of microwave sintered samples is about 10% higher than that of the conventionally sintered samples. ©1999 Acta Metallurgica Inc.

### INTRODUCTION

Many methods for fabrication of nanocrystalline powders and compacts have been developed to date. The problem of nanostructural ceramics fabrication greatly depends on the development of an adequate method for densification of nanopowder compact while retaining the grain size on the nanometric scale. Microwave ceramics sintering is regarded as a promising method to solve the problem (1).

The present study is focused on microwave sintering of the samples fabricated from  $\text{TiO}_2$  powder synthesized by two methods - wire electrical explosion and gas condensation, and compacted using two techniques - cold isostatic pressing (CIP) and magnetic dynamic compacting (MDC) (2). Comparison of microwave and fast conventional sintering was also under investigation. The volumetric microwave heating necessitates the use of a thermal insulation to make the temperature distribution more uniform within heated samples. Comparison of kinetics of sintering in different thermal insulations has been made as well.

### EXPERIMENTAL

Two types of  $\text{TiO}_2$  powders were used in the experiment. A powder produced by *Nanophase*

TABLE 1

Specific surface (S), grain shape (Shape), grain size (d), mass of grains over 100 nm (M), maximum grain size ( $d_{\max}$ ), rutile to anatase ratio (Ru/An) and density ( $\rho$ ) for as-produced powders.

	S, m <sup>2</sup> /g	Shape	d, nm	M, mass %	$d_{\max}$ , $\mu$ m	Ru/An	$\rho$ , g/cm <sup>3</sup>
NT	51	Sphere	30	5.8	10	10/90	0.28
IEP	70	Sphere	21	2.1	10	22/78	0.14

*Technologies Corp., USA* (NT-powder) was made by gas condensation method, and other powder produced by the *Institute of Electrophysics, Russia*, (IEP-powder) was made by a wire explosion method. Comparative data of the powders are listed in the Table 1.

Two techniques were used to fabricate green samples. Samples made by CIP technique with a pressure of 600 MPa had a near spherical shape of 7 mm in diameter with density  $\rho_0 \approx 2.65$  g/cm<sup>3</sup>. Samples produced by MDC technique had a shape of thin disks with a diameter of 15 mm, thickness 2 mm and density  $\rho_0 \approx 3.2$  g/cm<sup>3</sup>.

For microwave sintering, samples were placed into a fused quartz cup filled with different solid and powder thermal insulating materials. A sample surrounded by thermal insulation was placed into the multimode untuned cavity. The temperature of the sample was measured with a thermocouple put in close contact with the bottom part of the sample. Samples were heated with the millimeter-wave radiation at the frequency of 84 GHz.

After microwave processing, the shrinkage, density and microhardness of samples were measured. Microhardness was measured with a load of 200 g. Phase composition and grain size were obtained by X-ray diffraction from the surface of the samples.

## RESULTS AND DISCUSSION

First experiments showed that a simple one-step heating process, namely heating with a constant heating rate up to the temperature of sintering, was not suitable for sintering of the nanocrystalline compacts. The green samples contain large enough amount of absorbed water and gases, degassing of the samples is active up to 500°C, and fast heating rate at the initial stage of the process leads to swelling of the samples. A four-step heating regime was chosen for the further experiments: heating with the rate of 5°C/min up to 540°C, holding of the constant temperature during 15 min, heating with a specified heating rate (50°C/min or 100°C/min) up to the specified maximum temperature and holding at the maximum temperature from 0 to 15 min. Fast conventional heating was performed in the same regimes as microwave heating.

Fig. 1 represents the experimental data on the densification of the samples made of NT-powder versus temperature. Samples compacted by CIP technique were heated with microwaves in two thermal insulations: 60 mm size quartz cup filled with a coarse grained Al<sub>2</sub>O<sub>3</sub> powder (curve 2) and 30 mm size quartz cup filled with a coarse grained ZrO<sub>2</sub> powder (curve 1). The samples were heated with the rate of 100°C/min. The difference in the kinetics curves following from the Fig.1 implies that the temperature distributions within the samples heated in these thermal insulations differed from each other at the equal surface temperature

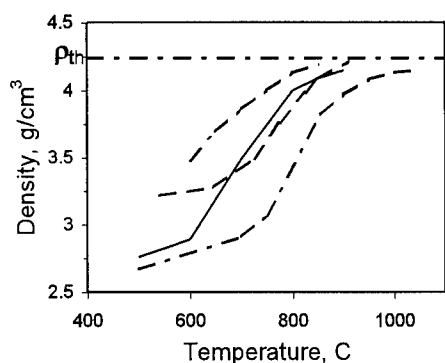


**Fig. 1. Density vs temperature for microwave (1, 2, 4) and conventionally (3) heated samples compacted by CIP (1, 2) and MDC (3, 4) techniques,  $\rho_{th}$  – theoretical density.**

of samples. It means that comparison of the results obtained at the different conditions of sintering must be based not on the temperature of samples but on their density.

Fig. 1 shows also the experimental data of the microwave (curve 4) and fast conventional sintering (curve 3) of the samples made by MDC technique. Porous alumina based material produced by *Ferro Corp. USA* was used as a thermal insulation for microwave heating. Heating rate of 50°C/min was realized in these experiments. The shift of the kinetics curves 3 and 4 arises supposedly from the same cause as described above – from the different temperature distributions pertinent to microwave and fast conventional sintering. Data given in Fig. 1 show that maximum achieved densities of

samples are the same for both techniques of compacting (CIP and MDC) and reach 0.98 – 0.99 of the theoretical value.

Fig. 2 represents the dependencies of grain sizes, quantity of anatase and microhardness versus density of all the investigated samples. It is worth to note that despite the different techniques of powder fabrication, the samples made of NT and IEP powders show the similar values of the measured parameters (Fig. 2).

For all the materials and conditions of processing the average grain size increases slowly up to about 100 nm at density 3.9 g/cm<sup>3</sup> and then increases fast above 300 nm (the limit of the method) at density 4.15 – 4.2 g/cm<sup>3</sup>. Up to densities 3.9 g/cm<sup>3</sup> grain size of microwave sintered samples is lower than that of conventionally sintered samples. At higher densities no significant dependencies on the methods of fabrication of powders, technique of compacting or method of processing are seen.

The maximum value of microhardness in our experiments (Fig. 2) was close to the microhardness of the monocrystalline rutile (3). Microwave sintered samples have larger amount of a rather “soft” anatase phase than conventionally sintered samples. Despite this fact the microhardness of microwave sintered samples is about 10% higher than of the conventionally sintered samples at same density values (Fig. 2). It means that microwave heating provides stronger bonds between adjacent grains than conventional heating. The mechanism of the influence of the microwave radiation on the bonds between grains must be subject for further investigation.

## CONCLUSIONS

The experimental results show that grains grow dramatically with increasing of the density of samples. At high densities no significant dependence of the grain size on the methods of fabrication of powders, technique of compacting or method of sintering was found.

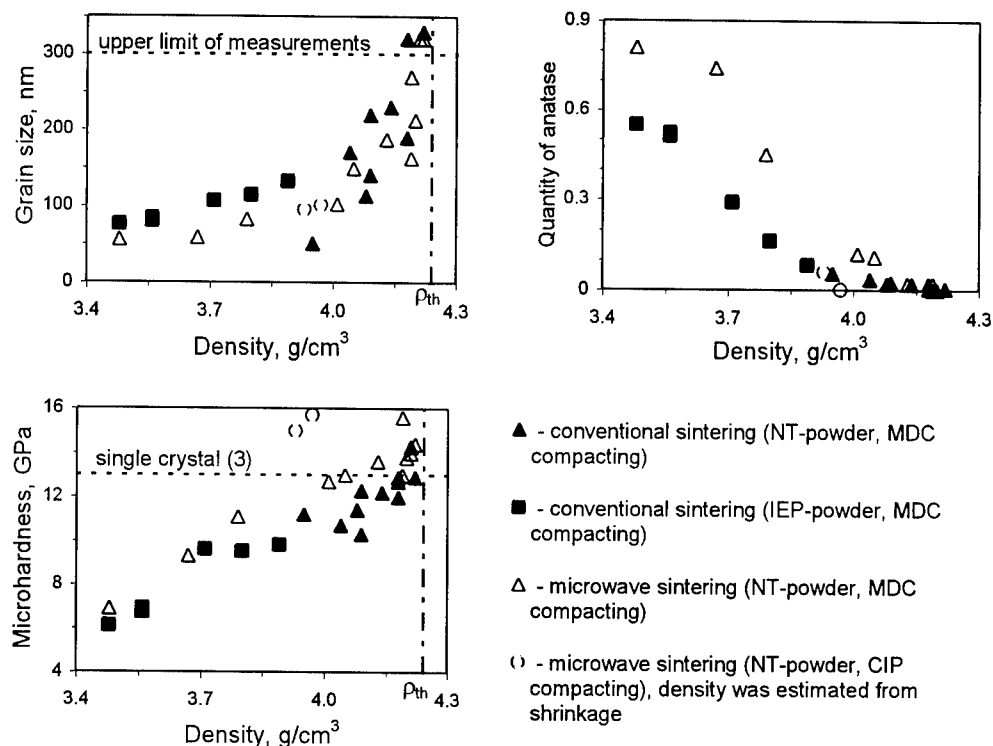


**Fig. 2. Grain size, quantity of anatase and microhardness vs density for MDC and CIP compacted samples made from NT and IEP powders by microwave and conventional sintering.**

Microwave radiation enhances the strength of bonds between grains. The mechanism of the enhancement is a problem for further investigations.

#### ACKNOWLEDGEMENTS

The present work was supported by the Commission of the European Communities under the RTD programme "Cooperation with Third Countries and International Organizations", contract # IC15-CT97-0713 (DG 12 – SNRD) and Russian Basic Research Foundation (grant # 97-02-17252).

#### REFERENCES

1. Eastman, J.A. et al., *Mat. Res. Soc. Symp. Proc.*, 1991, **189**, 273.
2. Ivanov, V. et al., *NanoStructured Materials*, 1995, **6**, 287.
3. Mayo, M.J. et al., *Journal of Materials Research*, 1990, **5**, 1073.



## PRODUCTION OF NANOMETER-SIZED AlN POWDERS BY THE EXPLODING WIRE METHOD

Y. A. Kotov and O.M. Samatov

Institute of Electrophysics, Ural Division of the Russian Academy of Sciences

34 Komsomolskaya St., 620049 Ekaterinburg, Russia

**Abstract** — We have performed experiments to explore the possibility of making pure nanometer-sized AlN powders by electrical explosion of aluminum wire in an atmosphere of nitrogen-containing gases. It is shown that raising the density of the energy injected into the metal, applying increased pressures, and a high working-gas flow rate help assure the production of AlN powders with a specific surface up to  $53 \text{ m}^2/\text{g}$ ,  $d_{\text{BET}} = 35 \text{ nm}$ . Particle shape ranges from nearly spherical to rigorous-cut particles. The yield of such powder accounts for 50 % of the total mass of powder. The powder thus produced contains no more than 1 wt.% of impurities, including oxygen. ©1999 Acta Metallurgica Inc.

### INTRODUCTION

Much interest is currently being shown in the production of AlN nanopowders. This is because, AlN ceramics combines high thermal conductivity, thermal stability and electrical resistivity with a low thermal expansion coefficient and a low level of losses at high frequencies (1–3). On the other hand, no method has as yet been developed for the production of such powders at an acceptable commercial cost. Electrical explosion of wire (EEW) is one of the promising methods for the production of low-cost nanopowders.

The typical particle size of metal powders produced by this method reduces substantially with increasing superheat of the metal,  $K = W/W_s$  (where  $W$  is the energy injected into the exploding wire and  $W_s$  the wire sublimation energy) (4, 5), diminishes inconsiderably with decreasing wire diameter  $D$  (5, 8), and increases as the surrounding-gas pressure  $P$  is raised (6). The  $K$  dependence of the specific surface of Al powder made by explosion in argon under normal conditions is given in Fig. 1.

Taking into account the dissociation of the required amount of  $\text{N}_2$ , 5.6 kJ is absorbed per gram of Al participating in the reaction to form AlN. Owing to that, the temperature of the expanding Al vapor should lower at a faster rate and the condensation will terminate at a higher vapor concentration. The particles thus produced should be bigger in size than Al particles obtained in argon under the same conditions.

Data reported on the production of AlN powders by the EEW method are scanty in the literature. Thus, by exploding Al foil in an atmosphere of  $\text{N}_2$ , the authors of Ref. (7) have obtained powder with an AlN content,  $C_{\text{AlN}}$ , of up to 17.5 wt. %; no further data are quoted. The author of Ref. (8) has made a more detailed study of  $S_s$  and  $C_{\text{AlN}}$  as a function of  $\text{N}_2$



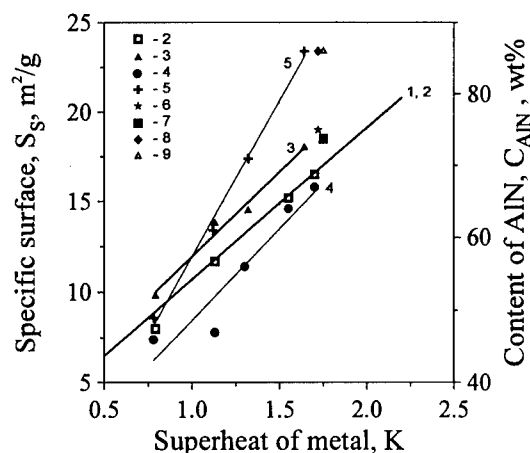


Fig. 1. Dependence of the specific surface of powder on the superheat of an aluminum wire exploding in: 1- argon, at  $P = 10^5$  Pa,  $D = 0.45$  mm (5); 2- nitrogen,  $P = 10^5$  Pa,  $D = 0.45$  mm; 3- nitrogen,  $P = 3 \times 10^5$  Pa,  $D = 0.45$  mm.; 4 and 5- AlN content of powders from curves 2 and 3, respectively; 6 and 7-  $S_s$  for wire diameters of 0.31 and 0.4 mm, nitrogen  $P = 3 \cdot 10^5$  Pa, respectively; 8 and 9- AlN content of powders produced under conditions 6 and 7, respectively.

pressure and metal superheat. However, he analyzed only the powder precipitated in the electric filter (EF). But the fraction of the powder obtained in the electric filter is not known. The purpose of the present work was to explore the impact of explosion conditions on the specific surface of powder and on the AlN content of it.

## EXPERIMENTAL

Explosions of Al wire were effected in an airtight 50-l chamber preliminarily evacuated and then filled with nitrogen at the pressure chosen. In performing explosions, we used a 3- $\mu$ f capacitor bank, which was discharged into the wire in a circuit with an inductance of 1.1  $\mu$ H. The superheat of the metal was varied by changing the bank charging voltage,  $U_0$ , as well as the length and diameter of the exploding wire. The energy injected into the wire was determined from current traces. Most of the experiments were carried out with 0.45 mm dia. wire. After 20 explosions, the chamber was opened, and the powder was collected from the walls and analyzed. Specific surface was measured by the BET method with the use of a mixture of argon with helium. Particle shape was investigated with the aid of electron microscopes: JEM-200 and JSM-T220. The AlN content was determined with the aid of an X-ray diffractometer and also by DTA analysis, from the melting peak of aluminum.

## RESULTS AND DISCUSSION

Our findings show (Fig. 1) that for  $P=10^5$  Pa the specific surface vs  $K$  has virtually the same values as it has for Al. The surprising thing, however, is that the  $K$  dependence of  $S_s$  at  $P = 3 \cdot 10^5$  Pa lies higher than it does at  $P = 10^5$  Pa. However, raising the pressure further (up to  $5 \times 10^5$  Pa) at the same  $K = 1.7$  yielded no increase in  $S_s$  and  $C_{AIN}$ . The fraction of AlN in the powder at  $P=3 \cdot 10^5$  Pa was found to be much higher (up to 86 wt %) then in the case of  $P = 10^5$  Pa (up to 68 wt. %). It may then be assumed that an

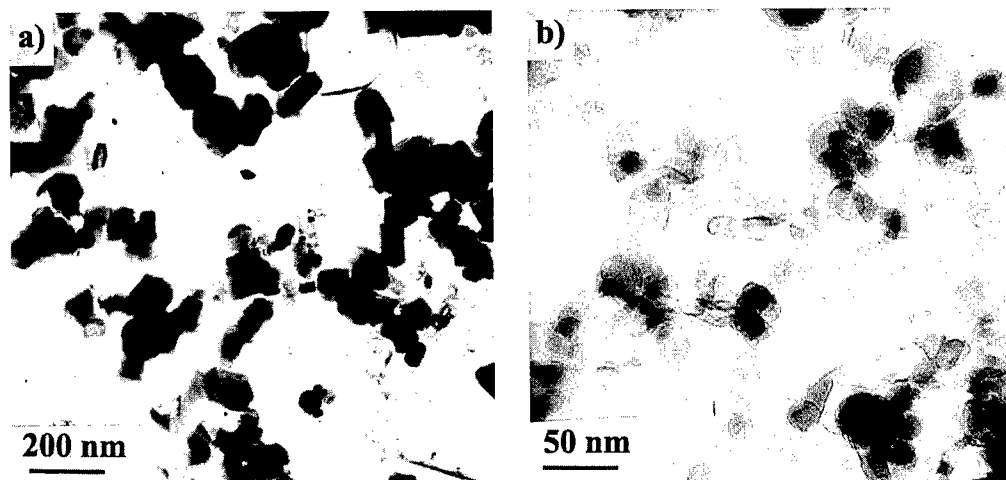


Fig. 2. Photographs of AlN powders, made with the aid of a transmission electron microscope: a, explosion in nitrogen; b, explosion in a mixture of  $N_2$  and  $NH_3$ .

increase in  $N_2$  pressure in some region can give a reduction in the size of particles produced, owing to an increase in the concentration of nitrogen atoms and, correspondingly, in the part of AlN condensing from the vapor phase. With about the same  $K$  values and at  $P = 3 \cdot 10^5$  Pa, the values of  $S_s$  and  $C_{AIN}$  attained when exploding 0.31 and 0.4 mm dia. wire turned out to be close to those obtained by explosion of 0.45 mm dia. wire (Fig. 1).

As can be seen from Fig. 1,  $C_{AIN}$  and  $S_s$  depend most heavily on  $K$ . But, with the conditions chosen, an attempt to further raise the superheat leads to an arc discharge developing along the wire, and injecting energy into the metal becomes inefficient. The superheat can be elevated by lowering the inductance of the circuit, with  $P = 3 \cdot 10^5$  Pa of  $N_2$ , and increasing  $U_0$ ; but we have not made these experiments so far.

Assuming coarser particles to contain less AlN, we decided to separate the powder produced. To this end, two cyclones in tandem and EF were incorporated in the setup. With the nitrogen blowthrough rate of 26 l/min,  $P = 1.2 \cdot 10^5$  Pa,  $K = 1.75$ , and  $D = 0.45$  mm, the EF-produced powder had  $S_s = 23$  m<sup>2</sup>/g and  $C_{AIN} = 82$  wt. %, values that are much higher than those obtained without separation (Fig. 1).

To facilitate the reaction of Al with N, we decided to use the more chemically active ammonia ( $NH_3$ ), which has a considerably lower dissociation energy and gives a positive energy balance under electrical explosion conditions.

As found in preliminary experiments,  $S_s$  and  $C_{AIN}$  increase when the volume concentration of  $NH_3$  is increased to  $\sim 20\%$  in the mixture with  $N_2$ . For this  $NH_3$  concentration, with the pressure of the mixture  $P = 10^5$  Pa,  $K = 1.45$ , and  $D = 0.45$  mm, the experiments performed have shown that the powders produced in EF possess a specific surface of 53 m<sup>2</sup>/g ( $d_{BET}$  35 nm) and the yield for this powder amounts to 50% of the total mass of powder, or to about 100 g/h. An analysis of this powder with an STOE Stadi-P X-ray diffractometer, which has a sensitivity of detection of 1%, has shown that the powder contains no other impurities but AlN. This permits us to assert that the powder contains

over 99 wt. % of AlN. To further improve the quality of the powder, it is necessary to use more sensitive analysis methods.

A comparison of the photos of AlN powders produced by explosion in nitrogen and in a mixture of nitrogen with NH<sub>3</sub> (Fig. 2) shows that in the first case the particles produced have sharp clear-cut facets, whereas the particles produced by explosion in a mixture of N<sub>2</sub> and NH<sub>3</sub> are more roundish in shape. This corroborates our assumption that in N<sub>2</sub> particles are formed mainly owing to the diffusion of nitrogen from the surface, while in the second case they arise from the vapor phase, by condensation, which is a more nonequilibrium process.

## CONCLUSION

Our experiments have shown that by electrical explosion of aluminum wire in nitrogen at  $P = 3 \cdot 10^5$  Pa, by superheating the metal beyond 1.7, and using powder separation, it is apparently possible to produce AlN powders with a specific surface of  $\sim 30$  m<sup>2</sup>/g and with an AlN content of over 95 wt. %.

Using a mixture of N<sub>2</sub> and NH<sub>3</sub> (up to 20 vol. %) permits powders with  $S_s > 50$  m<sup>2</sup>/g and an AlN content of over 99 wt. % to be produced under less arduous explosion conditions.

## ACKNOWLEDGMENTS

We wish to express our sincere appreciation to our colleagues who have made analyses of the powders and acknowledge the support by the INCO COPERNICUS Foundation under contract No. IC15-CT97-0713.

## REFERENCES

1. Slack, G.A. Phys. Chem. Solids, 1973, 34, 321.
2. Slack, G.A., Tanzilli, R.A., Pohl, R.O. and Vandersande, J.W., Phys. Chem. Solids, 1987, 48, 7, 642.
3. Kurokawa, V., Utsumi, K. and Takamizawa, H. American Ceramic Society, 1988, 71, 588.
4. Kotov, Yu. A. and Yavorovsky, N.A.. Fizika i khimiya obrabotki materialov, 1978, No. 4, 24 (in Russian)
5. Kotov, Yu.A., Azarkevich, E.I., Beketov, I.V., Demina, T.M., Muzarkaev, A.M. and Samatov, O.M. Key Engineering Materials (Proceeding of Euro Ceramics V) 1977, 132-136, 173.
6. Glazunov, G.P. et al. Voprosy atomnoi nauki i tekhniki. Seriya atomnoye materialovedeniye, 1978, 1, 21. (in Russian)
7. Joncich, M.J., Vaughn, J.W. and Knutsen, B.F.. Canad. J. of Chem., 1966, 44, 137.
8. Lerner, M.I. Doctoral thesis, Polytechnic Institute, Tomsk, 1988. (in Russian)



Pergamon

NanoStructured Materials, Vol. 12, pp. 123–126, 1999

Elsevier Science Ltd

© 1999 Acta Metallurgica Inc.

Printed in the USA. All rights reserved

0965-9773/99/\$—see front matter

PII S0965-9773(99)00079-3

## FORMATION AND COALESCENCE OF TUNGSTEN NANOPARTICLES UNDER ELECTRON BEAM IRRADIATION

Yoshitaka Tamou and Shun-ichiro Tanaka

Tanaka Solid Junction Project, Japan Science and Technology Corporation  
1-1-1 Fukuura, Kanazawa-ku, Yokohama 236-0004 Japan

**Abstract** -- Powder particles of tungsten oxide ( $WO_3$ ) were irradiated by an electron beam with an energy of 200 keV in a transmission electron microscope (TEM) at room temperature. A number of nanocrystals were induced inside the single crystal particle as a result of irradiation damage. Electron energy loss spectroscopy (EELS) analysis revealed a decrease in the oxygen content in the particle which suggested decomposition of the tungsten oxide. In the vicinity of the irradiated area, a number of spherical ultrafine particles of 2–6 nm in diameter were observed. It is revealed that these ultrafine particles are oxide free tungsten. These nanoparticles migrated under the subsequent electron beam irradiation. A few nanoparticles which came into contact were observed to coalesce each other to form a single crystal. The mobility of the atoms was enhanced by the electron beam irradiation under ultrahigh vacuum in a TEM.

©1999 Acta Metallurgica Inc.

### INTRODUCTION

Transmission electron microscope (TEM) has been used to observe the atomistic structure and behavior of ultrafine particles. The effect of electron beam irradiation on ultrafine particles has also been studied with respect to the dynamic behavior and instability of various materials. Xu and Tanaka(1) have reported the formation and bonding of Al nanoparticles obtained from the irradiation of the metastable oxide phase. In this paper, tungsten oxide ( $WO_3$ ) powder particles are irradiated by an electron beam in a TEM. Phase transformation of the oxide is studied and observations of the deposition of W nanoparticles are described. The nanoscopic evolution of these nanoparticles under subsequent irradiation is investigated.

### EXPERIMENTAL

$WO_3$  powder particles were used for the electron beam irradiation experiment. The particle size of the powder was under  $5 \times 10^{-5}$  m and the purity was 99.99%. The powder was put on an amorphous carbon film supported by a microgrid on a copper mesh. The specimen was inserted into the pole piece of the TEM. The TEM employed for this study was Hitachi HF-2000 equipped with a field emission gun. The accelerating voltage was 200 kV. Electron beam irradiation was conducted at room temperature with a back pressure of  $1.2\text{--}2.0 \times 10^{-6}$  Pa in the column. The intensity of the electron beam was  $1.5 \times 10^6$  –  $6 \times 10^8$  A/m<sup>2</sup> ( $9 \times 10^{20}$  –  $4 \times 10^{23}$  e/cm<sup>2</sup>s). During the

irradiation, high resolution images and diffraction patterns were intermittently photographed on the films. The products were also analyzed by energy dispersive X-ray spectroscopy (EDS) and electron energy loss spectroscopy (EELS).

## RESULTS AND DISCUSSION

### *Electron Beam Irradiation*

A single crystal  $\text{WO}_3$  powder particle was irradiated with a probe current of  $1.6 \times 10^6 \text{ A/m}^2$  at room temperature. Fig. 1 shows the transmission electron micrographs of the particle before and after electron beam irradiation, respectively. A number of subgrains were induced inside the particle as a result of irradiation damage. The evolution of the microstructure was clearly observed from the diffraction patterns. The spotted pattern of the single crystal  $\text{WO}_3$  in Fig. 1(a) was transformed to a diffuse ring-like pattern in Fig. 1(b) which indicates the amorphization by the electron beam irradiation. The ring-like pattern in Fig. 1(b) consists of a number of small spots with traces of the original single crystal. Nanocrystals were formed in the particle by the irradiation. The EELS analysis in Fig. 2 shows the decrease in oxygen content in the particle after irradiation which indicates decomposition of the oxide phase. The volume decrease of the particle is significant of displacement of atoms by the irradiation. No deposit, however, was observed around the irradiated area.

When a  $\text{WO}_3$  particle was irradiated with a probe current of  $6 \times 10^8 \text{ A/m}^2$  for a few seconds, a number of spherical ultrafine particles were deposited in the vicinity of the irradiated area as shown in Fig. 3. These nanoparticles have a sharp size distribution ranging from 2 to 6 nm with

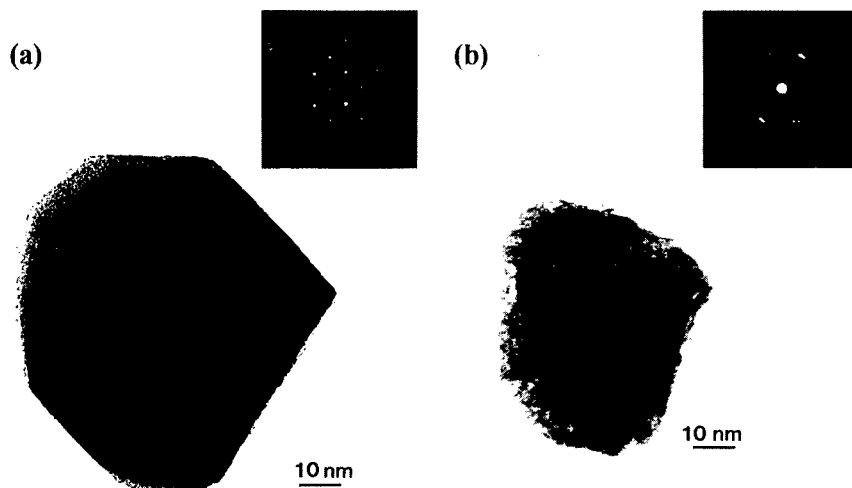


Fig. 1 TEM bright field images and selected area diffraction patterns of  $\text{WO}_3$  particle.  
(a) as is, (b) irradiated at  $1.6 \times 10^6 \text{ A/m}^2$  for 1800 s.

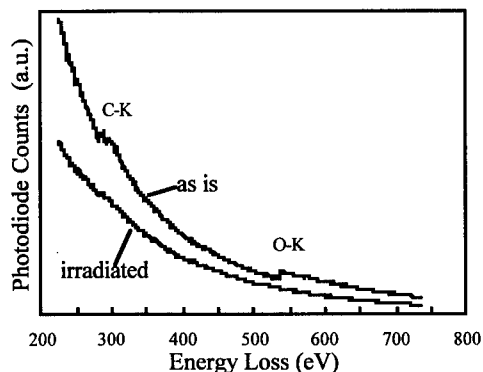


Fig.2 EELS spectra of  $\text{WO}_3$  particle irradiated by electron beam.

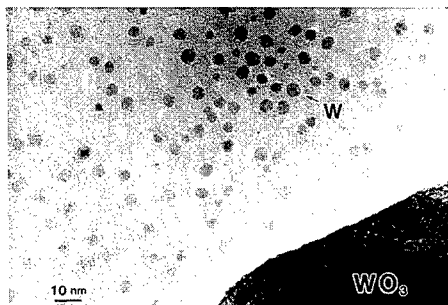


Fig.3 W nanoparticles deposited by electron beam irradiation of a  $\text{WO}_3$  particle. (Probe current:  $6 \times 10^8 \text{ A/m}^2$ )

an average diameter of 4.3 nm. EDS and EELS analyses revealed these nanoparticles as oxide-free tungsten.  $\text{WO}_3$  is thermodynamically stable under the experimental conditions used in this study. Kinetic considerations such as the knock-on effect and/or the charge effect should be considered to account for the decomposition of  $\text{WO}_3$ . Local energy density of the electron beam was sufficient to break the W-O bonding in the irradiated area. A certain amount of tungsten flux, however, was necessary for deposition of W nanoparticles.

#### *Electron Beam Irradiation Induced Coalescence*

Next, these W nanoparticles were irradiated by the electron beam with the current density of  $1.5 \times 10^6 \text{ A/m}^2$ . These nanoparticles migrated under the subsequent electron beam irradiation. A few nanoparticles which came into contact were observed to coalesce each other to form a single crystal particle. Fig.4 shows the coalescence sequence of four nanoparticles. After 120 s irradiation, the two nanoparticles indicated by arrows A came into contact to form a neck. The coalescence progressed through neck growth. At 240 s, particle A became a single crystal which is confirmed by the parallel fringes inside the particle. Neck growth was also observed between the particles indicated by arrows B. The particles A and B almost came into contact at this stage. At 360 s, a neck was formed between particles A and B. By 480 s, the four nanoparticles had become a single particle. From the parallel fringes inside the particle at 600 s, it is confirmed that the coalescence of four nanoparticles formed a single crystal particle. The mobility of nanoparticles was enhanced by electron beam irradiation under ultrahigh vacuum in a TEM.

### SUMMARY

Ultrafine  $\text{WO}_3$  particles were irradiated by an electron beam with an energy of 200 keV. W nanoparticles were deposited in the vicinity of the irradiated area along with the decomposition of the oxide phase. Under the subsequent irradiation, these nanoparticles which came into contact coalesced each other to form a single particle. Under ultrahigh vacuum in a TEM, the mobility of the atoms was enhanced by the electron beam irradiation. This may imply the feasibility of electron beam technology as a nanofabrication process of assembling nanostructured materials.

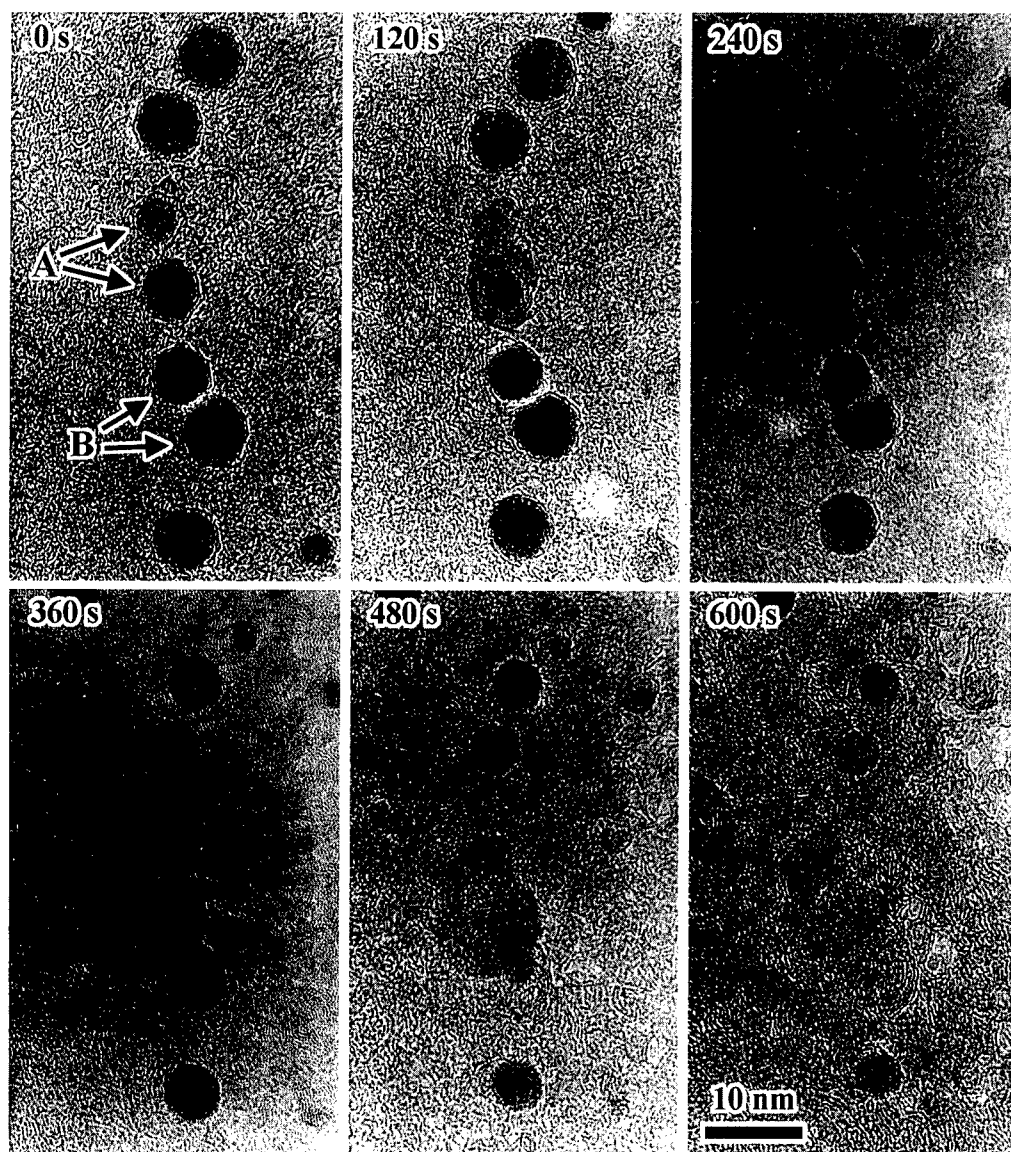


Fig.4 Coalescence of four W nanoparticles induced by the electron beam irradiation. The two particles indicated by arrows A came into contact at 120 s and coalesced each other subsequently. Between the particles indicated by arrows B, a neck growth was observed at 240 s. Particles A and B formed a neck at 360 s and became a single particle at 480 s. The parallel fringes were observed inside the particle at 600 s. (Probe current:  $1.5 \times 10^6$  A/m<sup>2</sup>)

#### REFERENCE

1. Xu, B.S. and Tanaka, S., *NanoStructured Materials*, 1995, 6, 727.



Pergamon

NanoStructured Materials, Vol. 12, pp. 127-130, 1999  
Elsevier Science Ltd

© 1999 Acta Metallurgica Inc.  
Printed in the USA. All rights reserved  
0965-9773/99/\$-see front matter

PII S0965-9773(99)00080-X

## PROPERTIES OF Mg-Y-Cu GLASSES WITH NANOCRYSTALLINE PARTICLES

N. Schlorke, B. Weiss, J. Eckert and L. Schultz

IFW Dresden, Institut für Metallische Werkstoffe, Postfach 270016, D-01171  
Dresden, Germany

**Abstract** -- Nanocrystals embedded in an amorphous Mg-Y-Cu phase can lead to an increase in fracture stress compared to the homogeneous amorphous alloy. Therefore, mechanical alloying of elemental Mg, Y and Cu powders with Si-, Ce-,  $Y_2O_3$ - and MgO-additives was used to prepare amorphous/nanocrystalline phase mixtures. Despite the existence of nanocrystalline particles in the amorphous matrix, all samples exhibit a temperature difference  $\Delta T_x (= T_x - T_g)$  between the crystallization temperature  $T_x$  and the glass transition temperature  $T_g$  of about 50 - 60 K and a decrease of viscosity above  $T_g$ . The additives enhance the thermal stability of the amorphous Mg-Y-Cu phase. Bulk amorphous/nanocrystalline samples can be prepared via consolidation and subsequent hot working in the viscous state above  $T_g$ . Finally, first results on the mechanical properties of the samples are presented. ©1999 Acta Metallurgica Inc.

### INTRODUCTION

Bulk amorphous Mg-Ln-TM (Ln = lanthanide metal, TM = transition metal) alloys with high strength, good ductility and low density (1) exhibiting a wide supercooled liquid region before crystallization and a decrease in viscosity above the glass transition temperature (2,3) are potential materials for high specific strength structural applications. Nanocrystals embedded in an amorphous matrix can lead to a further increase in fracture stress compared to the homogeneous amorphous alloys (4) due to a suppression of shear band propagation by these nanocrystalline particles uniformly dispersed in the amorphous matrix (5,6). For solidification from the melt, e.g. rapid quenching or slow cooling, these additives can act as heterogeneous nucleation sites and, thus, are expected to deteriorate the thermal stability (7). Furthermore, the diameter of bulk samples prepared by slow cooling is limited by the critical cooling rate of the alloy. However, mechanical alloying (MA) of powder mixtures blended with dispersoids and subsequent consolidation of the powder in the viscous state can reveal bulk samples without limitations of size or geometry, as it was done to form bulk  $Mg_{55}Y_{15}Cu_{30}$  samples (3). Hence, this study investigates the thermal stability and Vickers microhardness of amorphous/nanocrystalline samples prepared by MA and blending with oxide- and metallic dispersoids.



## EXPERIMENTAL

For MA elemental Mg, Y and Cu powders were mixed with Ce or Si (purity 99.9%, particle size  $\leq 150 \mu\text{m}$ ) to obtain  $(\text{Mg}_{0.55}\text{Y}_{0.15}\text{Cu}_{0.30})_{100-x}(\text{Si,Ce})_x$  powders or second phase MgO or  $\text{Y}_2\text{O}_3$  particles were added to elemental Mg, Y and Cu powder with the expected  $\text{Mg}_{55}\text{Y}_{15}\text{Cu}_{30}$  stoichiometry. The milling experiments were performed in a Retsch PM 4000 planetary ball mill (rotation speed of 180 rpm) using hardened steel tools and a ball-to-powder weight ratio of 15:1. All sample handling was done under argon atmosphere. The structure of the samples was investigated by X-ray diffraction (Philips PW 1050 diffractometer,  $\text{CoK}\alpha$  radiation). Thermal analysis was done in a Perkin-Elmer DSC 7 differential scanning calorimeter under a flow of purified argon. Viscosity measurements were performed in a Perkin-Elmer TMA 7 analyzer with a quartz penetration probe and a static force of 2.6 N under argon atmosphere with a heating rate of 10K/min [for details, see Ref. (8)]. For Vickers microhardness testing, the samples were resin bonded, mechanically grinded and polished and a load of 0.2 N was applied during a time period of 10 seconds in a Neophot hardness tester.

## RESULTS AND DISCUSSION

Figure 1 shows the X-ray diffraction patterns for the MA  $\text{Mg}_{55}\text{Y}_{15}\text{Cu}_{30}$  powders with different additives in comparison to powder without additives. For all samples a broad diffuse maximum characteristic for an amorphous phase and different additional crystalline diffraction peaks due to the different additives are obvious. The powder without additives shows crystalline diffraction peaks of unreacted Mg, Y and Cu as well as  $\text{Y}_2\text{O}_3$  formed by partial oxidation of Y. For the  $\text{Y}_2\text{O}_3$  and MgO composites the average grain size was roughly estimated to be about 10 - 20 nm using the well-known Scherrer formula.

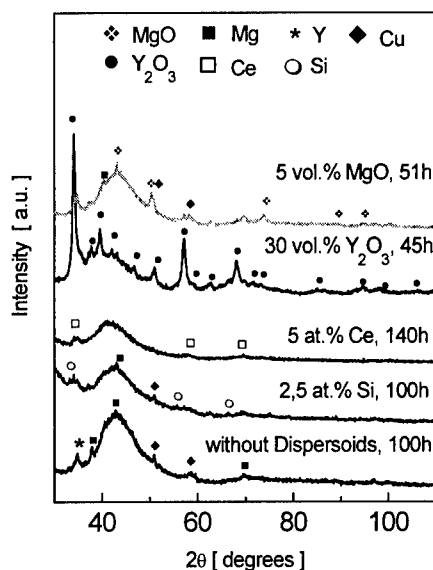


Fig.1: X-ray diffraction patterns of the powders with different additives.

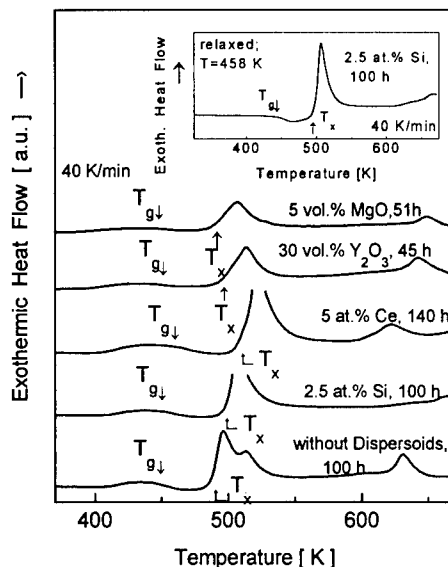


Fig.2: DSC scans for the powders with different additives and DSC scan for 2.5 at.% Si added and heated to 458 K (inset).

TABLE 1

Thermal Stability Data  $T_x$ ,  $T_g$  and  $\Delta T_x$  and Vickers Microhardness  $H_m$  of Mechanically Alloyed (MA)  $\text{Mg}_{55}\text{Y}_{15}\text{Cu}_{30}$  Powder with or without Additives.

Additives	$T_g$ [K]	$T_x$ [K]	$\Delta T_x$ [K]	$H_m$
without	441	489	48	355
2.5 at.% Si	444	498	54	318
5.0 at.% Ce	451	511	60	332
30 vol.% $\text{Y}_2\text{O}_3$	443	495	53	494
5 vol.% MgO	439	490	51	/

All samples exhibit a low-temperature exothermic signal that is due to the relaxation of the amorphous phase [Fig. 2] (7). The inset in Fig. 2 shows the DSC scan after relaxation above the glass transition temperature  $T_g$  for the sample with 2.5 at.% Si as a typical example. Table 1 summarizes the values for the thermal properties for all samples after this relaxation step. For the samples the endothermic signal characteristic for the glass transition starts at about 440 K and the crystallization starts at about 490 K. The X-ray diffraction analysis and DSC investigations prove that MA of  $\text{Mg}_{55}\text{Y}_{15}\text{Cu}_{30}$  powder blended with 2.5 at.% Si, 5 at.% Ce, 5 vol.% MgO and 30 vol.%  $\text{Y}_2\text{O}_3$  additives leads to glassy material.  $T_g$  and  $T_x$  are nearly identical for samples with and without oxide additives. Thus, an extended supercooled liquid region  $\Delta T_x$  can be maintained in the presence of MgO and  $\text{Y}_2\text{O}_3$  particles. This indicates, that these oxide dispersoids do not dissolve in the amorphous matrix and do not act as heterogeneous nucleation sites for crystallization. In contrast, the addition of 5 at.% Ce and 2.5 at.% Si leads to an increase of  $T_x$  whereas  $T_g$  is nearly identical to the powder without additives. The addition of 5 at.% Ce reveals the strongest increase of  $T_x$  by about 22 K to 511 K, thus leading to the largest supercooled liquid region  $\Delta T_x (= T_x - T_g)$  of 60 K. Therefore, we assume that the Ce and Si additives partially dissolve in the amorphous matrix either during milling or during heating in the DSC causing a distinct increase of thermal stability.

The samples with additives exhibit a decrease in viscosity  $\eta$  above  $T_g$ . At higher temperatures  $\eta$  increases again due to crystallization of the amorphous phase. This is shown in Fig. 3 for the  $\text{Mg}_{55}\text{Y}_{15}\text{Cu}_{30}$ -5 vol.% MgO composite as a typical example in comparison with the dispersoid-free powder. The viscosity  $\eta$  is determined by using the Stefan equation (9,10)

$$\eta = \frac{2 F h^3}{3 \pi a^4 (dh / dt)} \quad (1)$$

( $F$ : applied load,  $a$ : radius of the plates,  $h$ : sample height). The decrease of viscosity proves the good deformability of the powders with nanocrystalline dispersoids at temperatures above  $T_g$

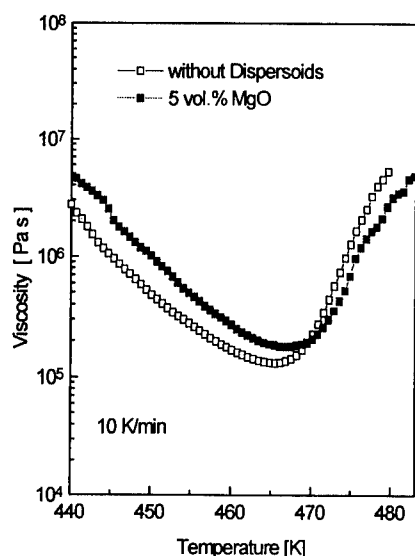


Fig. 3: Viscosity of the powder without additives and with 5 vol.% MgO as a function of temperature.

and, therefore, promises the formation of dense bulk composites with different size and shape as it was already shown for powder without additives (7).

The microhardness  $H_m$  of the powders varies from 355 for the sample without additives and 494 for the  $Mg_{55}Y_{15}Cu_{30}-Y_2O_3$  composite (Table 1). Hence, an addition of 30 vol.% of second phase  $Y_2O_3$  particles effectively enhance the mechanical strength. The suppression of shear band propagation due to nanocrystalline precipitates in the amorphous matrix is probably the reason for this increase in strength, similar as it was found for nanocrystalline metallic precipitates in an amorphous Zr-based matrix (4,5). For 2.5 at.% Si and 5 at.% Ce in  $(Mg_{0.55}Y_{0.15}Cu_{0.30})_{100-x}(Si,Ce)_x$  no enhancement in microhardness is found. This observation is in agreement with the above assumption that the metallic particles are not stable during milling but are dissolved in the amorphous matrix.

### ACKNOWLEDGEMENTS

The authors want to thank S. Schinnerling, H. Schulze, W. Gude, O. de Haas and U. Kühn for excellent cooperation and technical assistance, and A. Kübler and L.Q. Xing for stimulating discussions. N. Schlorke gratefully acknowledges financial support from the German Science Foundation (Graduiertenkolleg "Struktur- und Korrelationseffekte in Festkörpern").

### REFERENCES

1. Kim, S.G., Inoue, A. and Masumoto, T., *Mater. Trans. JIM*, 1990, 31, 929.
2. Kato, A., Inoue, A., Horikiri, H. and Masumoto, T., *Mater. Trans. JIM*, 1994, 351, 25.
3. Eckert, J., Schlorke, N., R.T. Miranda, C.A. and Schultz, L., *Synthesis /Processing of Lightweight Materials II*, ed. by Ward-Close, C.M., Froes, F.H., Chellman, D.J. and Cho, S.S., The Minerals, Metals and Materials Society, Warrendale, 1997, 383.
4. Inoue, A. and Masumoto, T., *Mater. Sci. Eng.*, 1993, A173, 1.
5. Dougherty, G. M., Shiflet, G. J. and Poon, S. J., *Acta Metall. Mater.*, 1994, 42, 2275.
6. Xing, L.Q., Ochinn, P., Harmelin, M., Faudot, F. and Bigot, J., *J. Non-Cryst. Solids.*, 1996, 205-207, 597.
7. Kui, H. W., Greer, A. L. and Turnbull, D., *Appl. Phys. Lett.*, 1984, 45, 615.
8. Kübler, A., Eckert, J., Gebert, A. and Schultz, L., *Appl. Phys. Lett.* (submitted).
9. Stefan, M. J., *Akademie der Wissenschaften und der Literatur (Mainz) Mathematisch-Naturwissenschaftliche Klasse*, 1874, 69, 713.
10. Diennes, G. J. and Klemm, H. F., *Appl. Phys.*, 1946, 17, 458.



Pergamon

NanoStructured Materials, Vol. 12, pp. 131-134, 1999

Elsevier Science Ltd

© 1999 Acta Metallurgica Inc.

Printed in the USA. All rights reserved

0965-9773/99/\$-see front matter

PII S0965-9773(99)00081-1

## MICROSTRUCTURAL DEVELOPMENT IN AlN COMPOSITE CERAMICS

Masahiko Tajika, Hideaki Matsubara and William Rafaniello\*

Synergy Ceramics Laboratory Fine Ceramics Research Association

2-4-1, Mutsuno, Atsuta-ku, Nagoya, 456-8587 JAPAN

\*The Dow Chemical Company, Midland, MI 48674 USA

**Abstract**--AlN-BN composite ceramics were fabricated by sintering a mixture of fine AlN and BN powders containing  $Y_2O_3$  as the sintering aid at 1850°C in nitrogen atmosphere. BN contents up to 15 vol% were studied. The heat treatment of sintered AlN-BN composite was performed at 1800°C in nitrogen atmosphere. BN particles in the composite showed large anisotropic grain growth during sintering, and the shape of grown BN particles appeared to be plate-like. Moreover, the heat treatment gave very interesting microstructures of the composite, in which many more interfaces between AlN grains were observed and most of the secondary phase was located at triple points of AlN grains. The resultant microstructural change is thought to be due to the change in the ratio of interfacial energy (between grain and liquid) and grain boundary energy (between grains). ©1999 Acta Metallurgica Inc.

## INTRODUCTION

Since aluminum nitride (AlN) has high thermal conductivity and good electrical properties, it is often considered as one of the candidate materials for heat management of semiconductor devices with high power (1,2,3). Recently AlN-BN composite ceramics have been developed with excellent properties such as good machinability and high heat shock resistance, and they are expected to find application in various fields (4,5,6). The purpose of this study was to understand microstructural development in the AlN-BN composite ceramic system. In particular, this study focused on microstructural change during heat treatment of sintered AlN-BN composites and microstructure/properties relationships.

## EXPERIMENT

Mixtures of fine AlN and BN powders containing  $Y_2O_3$  powder as a sintering aid were first pressed uniaxially at 24.5 MPa to form a disk and then isostatically pressed at 294 MPa. The compacts were set in a BN crucible and were sintered at 1850°C for 1-20 h in nitrogen atmosphere to be nearly full density. BN contents examined were 5, 10 and 15 vol%. The  $Y_2O_3$  additions were kept constant at 5 wt.% on an AlN powder basis. Heat treatment of the AlN-BN

composite samples was performed at 1800°C for 50 h in nitrogen atmosphere. Microstructures were observed using a scanning electron microscope. Thermal diffusivity and mechanical properties were evaluated using laser flash and IF (indentation fracture) methods, respectively.

## RESULTS AND DISCUSSION

### *Microstructures of AlN-BN Composites*

Figure 1 shows the microstructures of sintered AlN bodies with and without 10 vol% BN powder before and after heat treatment. Isotropic AlN grain growth was observed with the rounded particles surrounded by the liquid phase. BN grew anisotropically in a plate-like configuration. The BN particles were located along AlN grain boundaries both before and after the heat treatment, with some smaller BN particles being contained within AlN grains. BN did not seem to influence AlN grain growth, but the liquid phase did appear to accelerate the anisotropic grain growth of BN. The yttrium aluminate grain boundary phase in AlN-BN composites existed at triple points of the AlN grains after heat treatment, which was similar to monolithic AlN. Figure 2 shows the microstructures of heat treated composites containing 5, and 15 vol% of BN were similar to those of 10 vol% samples. It is considered that  $\gamma_{sl}/\gamma_{ss}$  value change at the heat treatment temperature was responsible for the microstructural change (7,8).

### *Properties of the Composites*

Figure 3 shows thermal diffusivity of AlN and AlN-BN composite before and after heat treatment. From these results it was found that the heat treatment resulted in a remarkable improvement of thermal diffusivity of both AlN and AlN-BN composite. The improvement was considered to be due to microstructural change resulted from the difference of  $\gamma_{sl}/\gamma_{ss}$  value in heat treatment. In AlN-BN composites, the heat treatment was also shown to be fairly effective for improving thermal diffusivity. BN additions made the thermal diffusivity of the composites lower. Hardness of the composites also decreased with the amount of BN addition as shown in fig.4. Fracture toughness showed the largest value at 15 vol% of BN addition among the samples.

## CONCLUSIONS

AlN-BN composites were prepared with sintering of AlN-BN powder mixtures at 1850°C and heat treated at 1800°C in nitrogen atmosphere.

- (1) AlN showed isotropic grain growth, having rounded particles surrounded by the grain boundary phase, while the BN grains were anisotropic, having a plate-like shape.
- (2) BN particles were observed predominantly at AlN grain boundaries although a few BN particles were observed within AlN grains.
- (3) Heat treatment of these samples resulted in dramatic microstructural changes and an improvement in the composites' thermal diffusivity.

### ACKNOWLEDGMENT

This research was sponsored by NEDO, under the Synergy Ceramics Project of the International Science and Technology Frontier (ISTF) Program promoted by AIST, MITI, Japan. The authors are members of the Joint Research Consortium of Synergy Ceramics.

### REFERENCES

1. Sheppard L.M., *Am. Ceram. Soc. Bull.*, **69**(11)1801(1990)
2. Kuramoto N., Taniguchi H., Numata Y. and Aso I., *Yogyo-Kyokai-Shi*, **93**(9)41(1985)
3. Kurokawa Y., Utsumi K. and Takamizawa H., *J. Am. Ceram. Soc.*, **71**(7)588(1988)
4. Mazdiyasi K.S., Ruh R., and Hermes E. E., *Am. Ceram. Soc. Bull.*, **64**(8)1149(1985)
5. Funahashi T. and Isomer K., *Seramikkusu*, **26**(8)749(1991)
6. Gam J., Ha J., Cheong D. and Han K., Materials Processing and Design: Grain-Boundary-Controlled Properties of Fine Ceramics II, *Ceramic Transactions*, **44**, Ed. by Niihara K., Ishizaki K. and Isotani M., Am.Ceram.Soc., Westerville, OH, USA, p.387,
7. Kim W.J., Kim D.K. and Kim C.H., *J. Am. Ceram. Soc.*, **79**(4)1066(1996)
8. Tajika M., Matsubara H. and Rafaniello W., submitted to *J. Am. Ceram. Soc.*

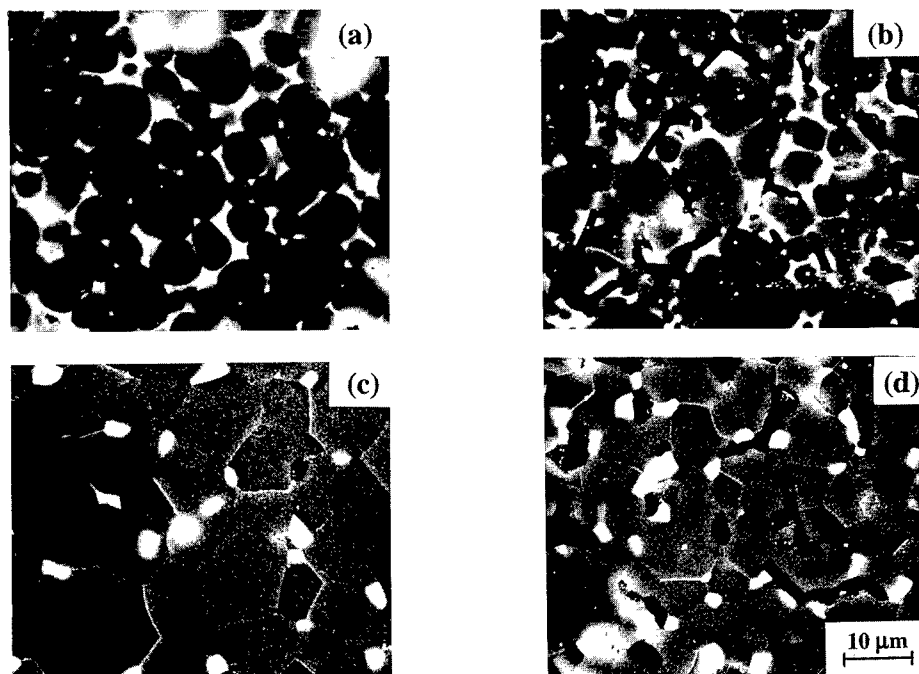


Fig. 1. Microstructures of AlN bodies with 0 vol% ((a) and (c)) and 10 vol% BN powder ((b) and (d)) before and after heat treatment (HT). (before HT: (a) and (b), after HT: (c) and (d)) Sintering conditions were 1850°C for 5h.

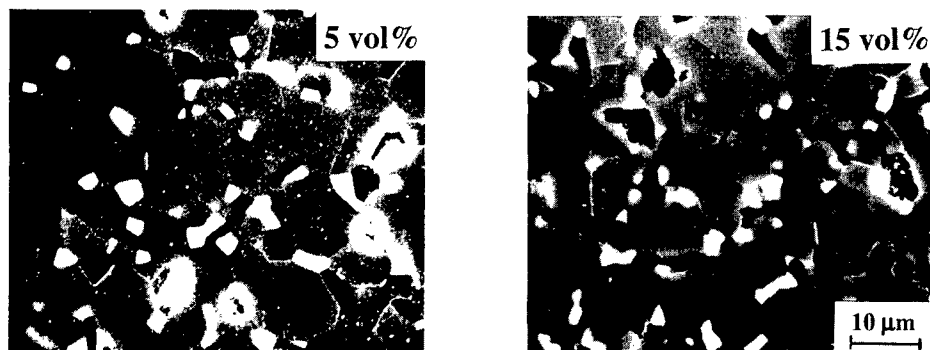


Fig. 2. Microstructures of heat treated composites with 5 and 15 vol% of BN.

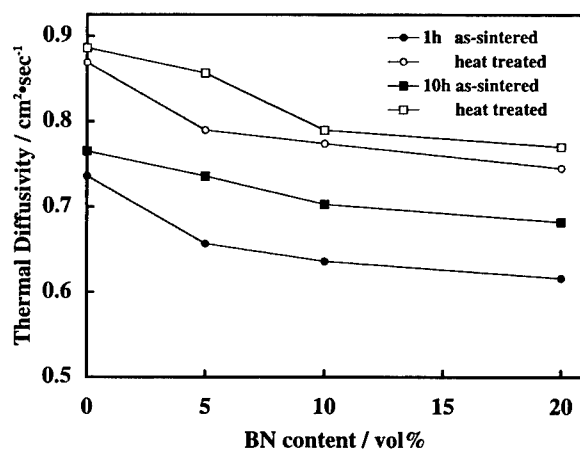


Fig. 3. Thermal diffusivity of AlN-BN composites before and after heat treatment.

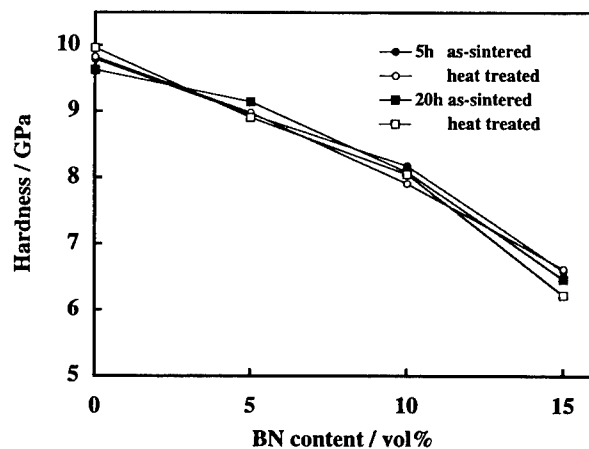


Fig. 4. Hardness of AlN-BN composites before and after heat treatment.



Pergamon

NanoStructured Materials, Vol. 12, pp. 135–138, 1999

Elsevier Science Ltd

© 1999 Acta Metallurgica Inc.

Printed in the USA. All rights reserved

0965-9773/99/\$—see front matter

PII S0965-9773(99)00082-3

## OPTICAL PROPERTIES OF QUASIFRACTAL METAL NANOPARTICLE AGGREGATES

J.A. Sotelo\* and G.A. Niklasson#

\*Dpto. de Física y Matemáticas, Universidad Peruana Cayetano Heredia,

Apto. 5045, Lima, Peru

#Department of Materials Science, The Ångström Laboratory, Uppsala University,

P.O. Box 534, S-75121 Uppsala, Sweden

**Abstract**—We calculate the optical extinction efficiency of two-dimensional small quasifractal aggregates consisting of metal nanoparticles. Computations were carried out in the octupolar approximation for aggregates of 25 particles. Calculations for gold particles much smaller than the wavelength of light showed two major peaks in the extinction in the visible wavelength range. These are due to the localized plasma resonance of the conduction electrons in a single particle and in the whole aggregate, respectively. Going to larger aggregate sizes, or including higher multipoles shifts the low frequency peak towards still lower frequencies. For particles with a radius of 30 Å the octupolar solution is well approximated by including interactions up to the third nearest neighbor particles only. On the other hand a simple iterative method earlier proposed by us does not give good results at low frequencies.

©1999 Acta Metallurgica Inc.

### INTRODUCTION

The optical properties of fractal aggregates consisting of small particles have recently been studied in considerable detail. Aggregates of dielectric particles have been treated by the mean field theory (1,2), within the anomalous diffraction approximation (3) and by the coupled dipole method (4). Theoretical work on aggregates of metallic particles has been reviewed by Shalaev (5). The coupled dipole method has been applied also to this case (6); other approaches encompass computations of the surface mode spectrum (7) and modeling the aggregate as a LCR-network (8). Computations of optical properties of touching metallic particles are especially demanding, since a large number of multipoles may be needed for high accuracy. For small nanoparticles in the Rayleigh limit more than 10 multipoles may be necessary, because of the highly nonuniform fields at the contact points (9). We have previously suggested an iterative procedure based on the construction rule of a deterministic fractal structure (10). The optical properties were computed by the rigorous theory of Gérardy and Ausloos (GA) (11) for electromagnetic scattering by an aggregate composed of touching spherical particles, but each iterative step requires computations only for a small cluster of 5 to 10 particles. In this paper we test the iterative approach against full calculations for medium sized clusters. We use the formulation of Gérardy and Ausloos (11,12) to compute the extinction cross section of a fractal aggregate composed of touching metallic spheres. Most of our computations were carried out for the 25 particle quasifractal cluster depicted in fig. 1. Some computations have also been carried out for the three-dimensional analogue having 49 particles, as well as a 125 particle cluster being the next stage of the construction in fig. 1.



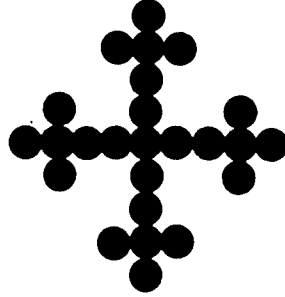


Fig. 1. A quasifractal aggregate consisting of 25 touching particles.

### THEORY

The GA theory gives an exact solution to Maxwell's equations for an arbitrary configuration of spheres. We consider a system of  $N$  homogeneous metallic spheres of radius  $R$  and dielectric function  $\epsilon(\omega)$ , embedded in a matrix of dielectric constant  $\epsilon_m$  and submitted to a plane polarized electromagnetic field. The incident and scattered fields are expanded in spherical vector wave functions. The response of this system is obtained by solving a system of linear independent equations for the coefficients of the expansion,  $c_\mu$  and  $d_\mu$ , of the scattered wave, namely (11)

$$\Gamma_n^{-1} c_v - \sum_{\mu} (c_\mu J_{\mu v} + d_\mu C_{\mu v}) = a_v \quad [1]$$

$$\Delta_n^{-1} d_v - \sum_{\mu} (c_\mu C_{\mu v} + d_\mu J_{\mu v}) = b_v, \quad [2]$$

where one equation for each  $v$  is implied. Here  $\mu$  denotes the triplet of indices  $(q, p, i)$  and  $v$  denotes  $(n, m, j)$ . The indices  $q$  and  $n$  denote the polar order,  $p = -q, \dots, q$ ,  $m = -n, \dots, n$ , and the indices  $i, j$  number the particles in the cluster. Moreover,  $a_v$  and  $b_v$  are the coefficients of the expansion of the incident wave in terms of vector wave functions defined in a coordinate frame centered on particle  $j$  (11). The multipolar electric and magnetic susceptibilities of a sphere are denoted by  $\Delta_n$  and  $\Gamma_n$ , respectively. The coefficients  $J_{\mu v}$  and  $C_{\mu v}$  describe the transformation of the spherical vector wave functions from a frame centered on particle  $i$  to a frame centered on particle  $j$ . Analytical expressions for these coefficients have been given by Gérardy and Ausloos (11). It should be noted that terms with  $i=j$  are omitted from the sums in eqs. [1] and [2].

Limiting  $n$  and  $q$  in eqs. [1] and [2] to integers less than or equal to  $L$ , we obtain a system of  $2NL(L+2)$  equations whose solution is the  $2^L$ -polar approximation to the electromagnetic response of the cluster. The extinction efficiency,  $Q_{ext}$ , i.e. the extinction cross-section in units of the total geometrical cross-section can then be obtained from (11)

$$Q_{ext} = -(\pi N K^2 R^2)^{-1} \sum_v \text{Re} (a_v c_v + b_v d_v), \quad [3]$$

where  $K=2\pi/\lambda$  and  $\lambda$  denotes the wavelength in the matrix. In our computations for a 25-particle aggregate composed of gold spheres, we have included terms up to  $L=3$ . In the case of 125 particles, it was only possible to use the dipole approximation. The dielectric function of the metal was described by a Drude expression, with plasma and relaxation frequencies appropriate for gold, as described previously (10). In some cases we also used data for bulk gold (13). The Drude relaxation frequency,  $\gamma$ , was corrected for surface scattering of the conduction electrons by the expression  $\gamma = \gamma_b + (v_F/R)$ . Here  $b$  stands for the bulk value and  $v_F$  denotes the Fermi velocity. The particle radius was put between 30 Å and 300 Å.

## RESULTS AND DISCUSSION

Below we present some results for the extinction of quasifractal Drude gold aggregates. We concentrate in this paper on small metal particles of radius 30 Å, for which the extinction is mainly due to absorption. In figure 2a, the results of our previous iterative procedure is compared with calculations for a 25-particle aggregate. The iterative procedure involved two steps: first a computation for an aggregate of 5 particles and secondly, a computation for 5 "effective" particles with properties obtained from the first step (10). It is seen that both approaches give similar results at high frequencies and around the single particle localized plasmon absorption peak at  $\omega/\omega_p \approx 1/\sqrt{3}$ . However, the low frequency absorption is grossly underestimated by the iterative calculation and the position of the low frequency peak is not reproduced. The reason for this is probably that the iterative method does not fully include the multipolar interactions in the aggregate. Additional computations show that the low frequency absorption tail increases, and the associated peak shifts towards lower frequencies, as the aggregate size increases, or as more long-range interactions in the aggregate are taken into account. The low frequency peak structure is obviously strongly influenced by

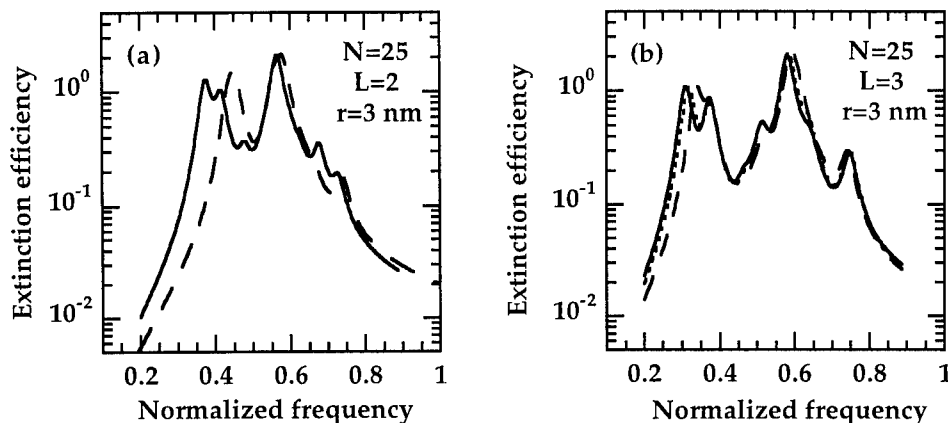


Fig. 2. Extinction efficiency as a function of frequency, normalized to the plasma frequency, for aggregates of Drude gold nanoparticles of radius 3 nm. The number of particles,  $N$ , and the order of multipolar approximation,  $L$ , are given in the figure. In (a) results of full calculations are given by the line and of the iterative method described in the text by dashes. In (b) full calculations (line) are compared to  $q$ 'th nearest neighbor approximations with  $q=1$  (dashes) and  $q=3$  (dots).

interactions over the whole aggregate. Additional minor peaks due to the fractal structure and the quadrupole and octupole terms can also be observed.

An interesting possibility to simplify calculations of optical extinction for fractal aggregates is illustrated in fig. 2b. Full calculations in the octupolar approximation are compared to the case where only the multipolar interactions between a particle and its  $q$ 'th nearest neighbors are taken into account. It is seen that the full octupolar calculation is reproduced very well by choosing  $q=3$ . This result suggests that the interactions in a fractal cluster are important only over a limited range. The situation becomes worse as the particle size increases, though; for particles with radius 300 Å, even  $q=5$  is not an entirely satisfactory approximation. This may be due to the increased strength of the quadrupolar and octupolar terms in these larger particles.

It is interesting to note that the use of the experimental dielectric function of gold (13) gives extinction spectra where the peak structure is less distinct. This is especially so in the high frequency region where the interband transitions in gold give the main contribution to the absorption. Only the two main peaks discussed above can be discerned.

## CONCLUSIONS

We have explored methods of calculating the optical response of fractal aggregates consisting of metal particles. A problem with computations for touching metallic nanoparticles is the high multipolar orders needed to obtain a good description of the low frequency region of the spectrum. Limiting the interactions between the particles to the third nearest neighbors appears to be a good approximation, at least in some cases.

## ACKNOWLEDGMENTS

This work was financially supported by a grant from the Swedish Natural Science Research Council. One of us (J.A.S.) would like to thank the Swedish Institute for a scholarship.

## REFERENCES

1. Berry, M.V. and Percival, I.C., *Optica Acta*, 1986, 33, 577.
2. Botet, R., Rannou, P. and Cabane, M., *Appl. Opt.*, 1997, 36, 8791.
3. Khlebtsov, N.G., *J. Mod. Opt.*, 1993, 40, 2221.
4. Mulholland, G.W., Bohren, C.F. and Fuller, K.A., *Langmuir*, 1994, 10, 2533.
5. Shalaev, V.M., *Phys. Rep.*, 1996, 272, 62.
6. Markel, V.A., Shalaev, V.M., Stechel, E.B., Kim, W. and Armstrong, R.L., *Phys. Rev. B*, 1996, 53, 2425.
7. Claro, F. and Fuchs, R., *Phys. Rev. B*, 1991, 44, 4109.
8. Zabel, I.I.H. and Stroud, D., *Phys. Rev. B*, 1992, 46, 8132.
9. Mackowski, D.W., *J. Opt. Soc. Am. A*, 1994, 11, 2851.
10. Sotelo, J.A. and Niklasson, G.A., *Z. Phys. D*, 1991, 20, 321.
11. Gérardy, J.M. and Ausloos, M., *Phys. Rev. B*, 1982, 25, 4204.
12. Quinten, M. and Kreibig, U., *Appl. Opt.*, 1993, 32, 6173.
13. Johnson, P.B. and Christy, R.W., *Phys. Rev. B*, 1972, 6, 4370.



Pergamon

NanoStructured Materials, Vol. 12, pp. 139–142, 1999

Elsevier Science Ltd

© 1999 Acta Metallurgica Inc.

Printed in the USA. All rights reserved

0965-9773/99/\$—see front matter

PII S0965-9773(99)00083-5

## FORMATION OF IRON-NICKEL NANOCRYSTALLINE ALLOY BY MECHANICAL ALLOYING

V.V. Tcherdyntsev<sup>1</sup>, S.D. Kaloshkin<sup>1</sup>, I.A. Tomilin<sup>1</sup>, E.V. Shelekhov<sup>1</sup>, Yu.V. Baldokhin<sup>2</sup>

<sup>1</sup>Department of Physical Chemistry, Moscow Steel and Alloys Institute, Leninsky prosp., 4, Moscow, 117936, Russia, vvch@phch.misa.ac.ru

<sup>2</sup>Institute of Chemical Physics Academy of Science, Kosygina str., 4, Moscow 117334, Russia

**Abstract** —  $Fe_{1-x}Ni_x$  alloys were prepared by mechanical alloying of elemental powders in high-energy planetary ball mill in a wide concentration range of components ( $10 \leq x \leq 90$ ). The structure was studied by X-ray diffractometry. It is shown that concentration ranges of single-phase solid solution of MA samples are markedly wider than that of thermodynamically stable alloys. Character of X-ray peaks indicates that there is a high density of crystalline lattice defects including stacking faults. Block sizes, calculated without considering stacking faults presence, was found to be 8 - 15 nm, and calculated with considering of stacking faults 30 - 80 nm. The results were discussed on the basis of thermodynamic model of MA. ©1999 Acta Metallurgica Inc.

### INTRODUCTION

Possibility of production of nonequilibrium phases and very defective structures induce especial interest to the processes which occur during MA. It is possible to prepare amorphous phases, supersaturated solid solutions, and other nonequilibrium structures by MA. Unusual distribution of structure defects comparing to those in the alloys prepared by traditional methods is typical for the MA alloys.

Iron-nickel alloys are of great interest due to their magnetic and mechanical properties. There are some studies, where structure and properties of MA iron-nickel alloys were investigated. Unfortunately, investigation of MA Fe-Ni alloys in a wide concentration range was reported only in few studies [1 - 3]. Concentration ranges of b.c.c. and f.c.c. phases existing in MA Fe-Ni alloys depend on milling intensity: an increase of intensity leads to extending of the concentration range of existing of f.c.c phase and to narrowing of that of b.c.c phase [1, 3]. This phenomena may be associated with an increase of the temperature in the mill [1] or with a dependence of the density of structure defects on milling intensity [3].

The aim of the present work is to study structure of MA Fe-Ni alloys in a wide concentration range. A study of magnetic hyperfine interaction in this system, which is also of interest, will be published separately [4].

### EXPERIMENTAL PROCEDURE

Pure carbonyl Fe (powder, purity 99.95 %) and electrolytic Ni (powder, purity 99.5 %) were used as starting materials. The following compositions were studied:  $\text{Fe}_{1-x}\text{Ni}_x$ , where  $x = 10, 20, 22, 24, 26, 28, 30, 32, 34, 36, 38, 40, 50, 60, 65, 70, 75, 80, 85$ , and 90 at. %. MA was carried out in a AGO-2U planetary ball mill in air atmosphere. About 15 g of material and 150 g of steel balls 8 mm in diameter were loaded into steel hermetic vials ( $160 \text{ cm}^3$ ). All the samples were milled for 1 hour. A specific power of the process was estimated to be about 10-20 W/g depending on the method of determination. Annealing of samples was carried out for 0.5 hours at 350 and 650°C in argon atmosphere.

A DRON-3 diffractometer with  $\text{Co K}\alpha$  and  $\text{Cu K}\alpha$  radiations was used to study the phase composition and crystalline structure of the samples. Structure parameters were computer-determined. An original method [5] was used to determine stacking faults concentration.

### RESULTS

Fig. 1 shows concentration ranges of phase existence in as-milled and annealed samples according to X-ray data and according to the equilibrium phase diagram [6]. One can see that in MA alloy concentration ranges of existence of single-phase solid solutions are markedly extended. In contrast to the stable diagram,  $\text{FeNi}_3$  compound was not observed in MA alloys. Annealing of MA alloys at 350 °C does not lead to any change of

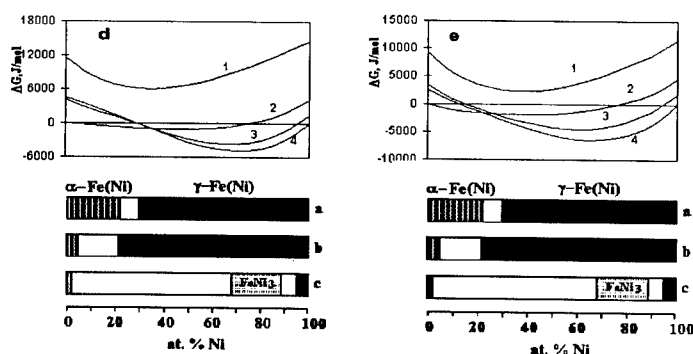


Fig. 1. Concentration ranges of phase existing in as-milled (a), annealed at 650°C (b), and thermodynamically stable [6] (c) alloys; Diagrams of Gibbs energy for Fe-Ni system at 300 K (d) and 600 K (e). 1 - liquid alloys; 2 - b.c.c. structure; 3 - h.c.p. structure; 4 - f.c.c. structure.

crystalline structure, but annealing at 650°C leads to the b.c.c.+f.c.c.  $\rightarrow$  f.c.c. phase transformation in alloys with  $x = 22 - 28$  at. % and to the b.c.c.  $\rightarrow$  b.c.c.+f.c.c. transformation in alloys with  $x = 10$  and 20 at. % (see. Fig. 1b). This transformation, which is far from equilibrium (Fig. 1c), becomes possible, because equilibrium state in Fe-Ni system may be reached only by very slow cooling.

The X-ray diffraction patterns of MA samples are characterised by significant peak broadening. Crystallite sizes and microstrains, which are calculated from the experimental data, were found to be within the ranges 8 - 15 nm and 0.5 - 0.8 % respectively. Fig. 2 shows lattice parameters of f.c.c. alloys vs. alloy composition. Lattice parameters of these phases for equilibrium alloy [7] are also presented on Fig. 2. It is easily seen that equilibrium alloys lattice parameters are smaller than those of MA alloys. The same effect was found in our previous work for Fe-Mn alloys [9].

It is known that ball milling of materials can lead to the formation of structures with high concentration of stacking faults. Concentration of stacking faults in all MA alloys with the f.c.c. structure was determined from the X-ray diffraction data. Fig. 3a shows a dependence of stacking fault probability  $\alpha$  on the MA alloy composition. True crystallite sizes proved to be almost an order of magnitude larger than corresponding apparent values, which were determined ignoring the presence stacking faults in crystalline lattice. The typical values of true crystallite sizes fall in the range 20 - 80 nm. Stacking fault concentration decreases with increasing Ni content.

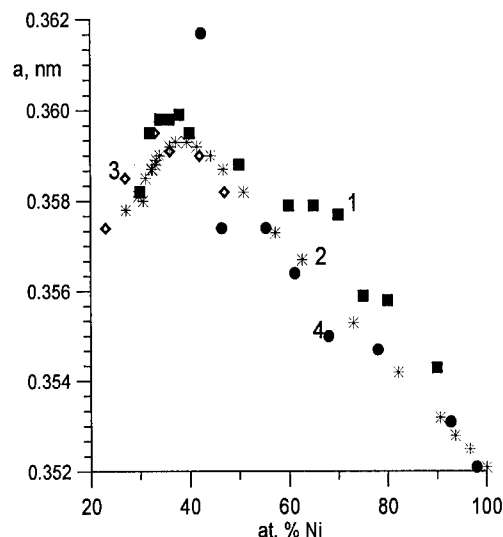


Fig. 2. Lattice parameter of f.c.c. phase: 1- this study; 2- for thermodynamically equilibrium alloys [7]; 3- For mechanically alloyed alloys [3]. 4- For electrodeposited alloys [8].

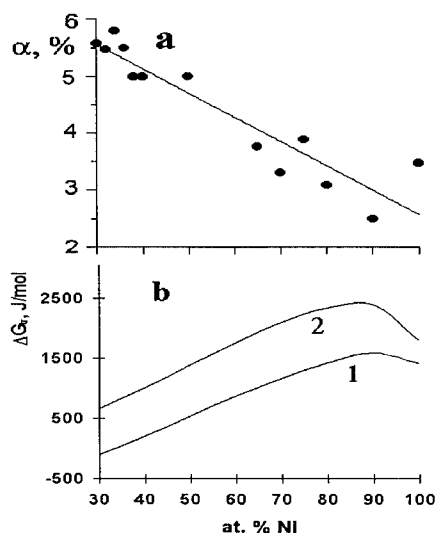


Fig. 3. Dependence of stacking faults concentration  $\alpha$  (a) and difference between Gibbs energy of h.c.p. and f.c.c. phases (b) on alloy content. 1- for 300K, 2- for 600 K.

## DISCUSSION

This above-mentioned results may be discussed on the base of thermodynamical model of MA [10]. Figure 1 shows Gibbs energy diagram for Fe-Ni system at 300K (d) and 600K (e), calculated on the base of data [11]. It is known, that MA process tend to form single-phase alloys, because decreasing of Gibbs energy by wide double-phase region formation is impossible due to the processes of compulsory levelling of the chemical composition during MA. It is rearkable that experimental ranges of phase existing in our case are in the better agreement with Gibbs energy diagram for 600, than for 300 K. The same result was observed for Fe-Mn system [9], which is associate with effect of temperature increasing in the vial during MA. On the base of Gibbs enerdy diagramms, a question about a reason of dependence of ranges of phase existence on milling intensity in Fe-Ni alloys [1, 3] may be explane. Really, it is easy to see from Fig. 1 that the concentration range of existing of f.c.c phase expands, and that of b.c.c. phase narrows down with increasing temperature, i.e. above-mentioned phenomena depend on the temperature in the vial, as it was proposed in [3].

As was proposed in [12], stacking faults concentration depend on difference between free energy of h.c.p. and f.c.c. phase. This difference for 300K (a) and 600K (b), which was calculated on the base of Fig. 1, is shown on Fig. 3b. Indeed, stacking faults concentration increase with decreasing of the difference between Gibbs energy ob these two phases.

On the base of discussion, we can conclude that thermodynamyc model is very useful for explanation of the structure of MA alloys.

This study was supported by RFBR grant no. 97-03-33630a

## REFERENCES

1. Kurt, C. and Schultz, L., *J. Appl. Phys.*, 1993, 73, 1975.
2. Kurt, C. and Schultz, L., *J. Appl. Phys.*, 1993, 73, 6588.
3. Hong, L.B. and Fultz, B., *J. Appl. Phys.*, 1996, 79, 3946.
4. Baldokhin, Yu.V., Tcherdyntsev, V.V., Kaloshkin, S.D., Kochetov, G.A., and Pustov, Yu.A., *J. Magn Magn Mater.*, to be published.
5. Shelekhov, E.V., Kaloshkin, S.D., and Tcherdyntsev V.V., *Izv. Vyssh. Ucebn. Zaved: Chern. Metall.*, to be published.
6. Massalski, T.B. (Ed), *Binary Alloys Phase Diagrams*, Am.Soc. Met., 1987, V. 1.
7. Vol, A.E.: *Stroenie i svoistva dvoynykh splavov*, Moscow, Nauka, 1962, V. 2.
8. Jatrykh, E., Budzinski, M., and Jurawitz, J.K., *Hyperfine Inter.*, 1992, 73, 225.
9. Tcherdyntsev, V.V., Kaloshkin, S.D., Tomilin, I.A., Shelekhov, E.V., and Baldokhin, Yu.V., *Z. Metallkde*, to be published.
10. Kaloshkin, S.D., Tomilin, I.A., and Tcherdyntsev, V.V., this issue.
11. Mogutnov, B.M., Tomilin, I.A., and Shvartsman, L.A., *Termodinamika Splavov Zheleza*, Moscow, Metallurgia, 1984.
12. Foley, J.H., Cahn, R.W., and Raynor, G.V., *Acta Met.*, 1963, 11, 355.



Pergamon

NanoStructured Materials, Vol. 12, pp. 143–146, 1999

Elsevier Science Ltd

© 1999 Acta Metallurgica Inc.

Printed in the USA. All rights reserved

0965-9773/99/\$—see front matter

PII S0965-9773(99)00084-7

## SYNTHESIS AND CHARACTERIZATION OF NANOCRYSTALLINE ZINC FERRITE

J. S. Jiang\*, X. L. Yang \*, L. Gao<sup>+</sup>, J. K. Guo<sup>+</sup>, and J. Z. Jiang<sup>#</sup>

\* Department of Chemistry and Physics, East China Normal University,  
Shanghai 200062, P. R. China

<sup>+</sup> The State Key Lab on High Performance Ceramics and Superfine Microstructure, Shanghai  
Institute of Ceramics, Chinese Academy of Sciences, Shanghai 200050, P. R. China

<sup>#</sup> Department of Physics, Building 307, Technical University of Denmark,  
DK-2800 Lyngby, Denmark

**Abstract** -- Nanocrystalline zinc ferrite powders with a partially inverted spinel structure were synthesized by high-energy ball milling in a closed container at ambient temperature from a mixture of  $\alpha$ -Fe<sub>2</sub>O<sub>3</sub> and ZnO crystalline powders in equimolar ratio. From low-temperature and in-field Mössbauer measurements it is revealed that ZnFe<sub>2</sub>O<sub>4</sub> particles prepared are in superparamagnetic state at ambient temperature. A doublet with an average quadrupole splitting of 0.8 mm/s is observed for the as-milled sample at 295 K, which is much larger than that for bulk ZnFe<sub>2</sub>O<sub>4</sub> prepared by traditional ceramic method and that for ultrafine ZnFe<sub>2</sub>O<sub>4</sub> particles prepared by the co-precipitation method. This indicates larger structural defects in the nanometer-sized ZnFe<sub>2</sub>O<sub>4</sub> particles prepared by high-energy ball milling.

©1999 Acta Metallurgica Inc.

### INTRODUCTION

High-energy ball milling ( mechanical alloying or mechanical grinding ) has been widely used for the synthesis of materials, which are far from equilibrium, such as nanocrystalline, amorphous, and supersaturated alloys and ceramics(1~4). Lefelshtel et al.(5)and Kosmac and Courtney(6) have reported on the attempted synthesis of ZnFe<sub>2</sub>O<sub>4</sub> and NiFe<sub>2</sub>O<sub>4</sub> by milling of  $\alpha$ -Fe<sub>2</sub>O<sub>3</sub> with ZnO and NiO powders, respectively. The formation of single spinel phases was not achieved.

By virtue of magnetic properties, zinc ferrite, ZnFe<sub>2</sub>O<sub>4</sub>, and its solid solutions with other ferrites are widely used in the electronic industry. ZnFe<sub>2</sub>O<sub>4</sub> has a normal spinel structure with zinc ions exclusively occupied in the tetrahedral sites. Several techniques, e.g., co-precipitation(7), sol-gel(8), and twin roller quenching(9), have been applied to synthesized ZnFe<sub>2</sub>O<sub>4</sub> with a partially inverted spinel structure. In this work, we applied the high-energy ball milling technique and successfully synthesized nanocrystalline zinc ferrite in a closed container from a powder mixture of  $\alpha$ -Fe<sub>2</sub>O<sub>3</sub> and ZnO at ambient temperature. The phase evolution and



the microstructure of the zinc ferrite prepared are studied by x-ray diffraction, transmission electron microscopy, and Mössbauer spectroscopy.

## EXPERIMENTAL

The starting materials for the high-energy ball milling were crystalline powders of  $\alpha$ - $\text{Fe}_2\text{O}_3$  (99.5% purity) and ZnO (99.5% purity) mixed together in equimolar ratio. High-energy ball milling was carried out in a planetary ball mill. The milling was performed in a closed container with a hardened-steel vial of 100 cm<sup>3</sup> volume and 60 hardened-steel balls of a diameter of 8 mm at ambient temperature in air without any additives(10). The ball-to-powder mass charge ratio of 20:1 was chosen. After selected milling times, the mill was stopped and a small amount of powder was removed from the vial for examination. The phase evolution and structure of samples after different milling times were characterized by x-ray diffraction (XRD) (RAX-10) using  $\text{CuK}\alpha$  radiation ( $\lambda = 0.154$  nm) and Mössbauer spectroscopy using a source of  $^{57}\text{Co}$  in a Pd matrix. The morphology and microstructure of the as-milled samples were studied using transmission electron microscopy (TEM) (JEM-200cx). The microstructure of the as-milled sample was further investigated by low-temperature and in-field Mössbauer spectroscopy using a closed-circle helium cryostat and an electromagnet. Hyperfine interaction parameters were derived from the Mössbauer spectra using a least-squares method. The spectrometer was calibrated using a standard 25  $\mu\text{m}$   $\alpha$ -Fe foil. The contamination in the milled samples, originating from the abrasion of the vial and balls was measured by energy dispersive spectroscopy (EDS) using scanning electron microscopy (SEM) (KYKY-2000).

## RESULTS AND DISCUSSION

Figure 1 shows XRD patterns of samples with an equimolar mixture of  $\alpha$ - $\text{Fe}_2\text{O}_3$  and ZnO milled after different times. For the powder mixture (milling time 0h) sharp diffraction peaks

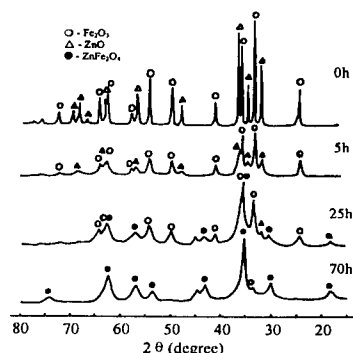


Figure 1. XRD patterns of  $\alpha$ - $\text{Fe}_2\text{O}_3$  - ZnO samples after different milling times (0h, 5h, 25h and 70h).

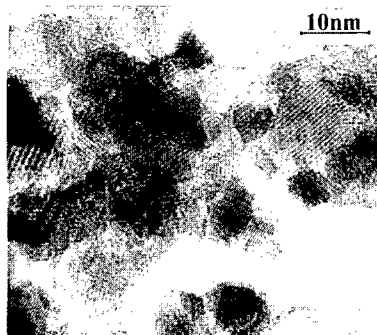


Figure 2. TEM micrograph of the sample milled for 70h.

from well-crystallized  $\alpha\text{-Fe}_2\text{O}_3$  and ZnO are present on the XRD pattern. The pattern of the sample after 5h milling shows peak broadening of the constituents as a consequence of crystallite size reduction and/or strain induced by milling. After increasing the milling time to 25h, four new peaks located at about  $2\theta = 18.2^\circ$ ,  $29.9^\circ$ ,  $42.8^\circ$  and  $44.5^\circ$  can be resolved. Among them, three peaks ( $2\theta = 18.2^\circ$ ,  $29.9^\circ$  and  $42.8^\circ$ ) are attributed to the  $\text{ZnFe}_2\text{O}_4$  spinel phase, one peak ( $2\theta = 44.5^\circ$ ) may be assigned to the stainless steel contamination of the abrasion of vials and balls during milling process(10). After 70h of milling, the spinel phase is dominant while two tiny peaks at  $2\theta = 44.5^\circ$  (from contamination) and at  $2\theta = 33.3^\circ$  (from trace of un-reacted  $\alpha\text{-Fe}_2\text{O}_3$ ) can still be observed. Upon increasing the milling time to 90h, the XRD pattern shows no visible difference from the pattern of the sample milled 70h (XRD pattern not presented). Using Scherrer's equation, the crystallite size of  $\text{ZnFe}_2\text{O}_4$  in the sample milled 70h was estimated to be about 14 nm, which is further confirmed by TEM measurements, as shown in Fig.2. It is found that  $\text{ZnFe}_2\text{O}_4$  powders are crystalline and have an average crystallite size of about 8–10 nm and a nearly spherical shape.

Figure 3 shows the Mössbauer spectra for samples after different milling times at ambient temperature. For milling times of 0 and 5h, the Mössbauer spectra were identical to those of  $\alpha\text{-Fe}_2\text{O}_3$ . A tiny doublet was detected after a milling time of 5h. A significant change was observed after 25h with the appearance of the doublet and the line broadening of sextet. The doublet could be attributed to the  $\text{ZnFe}_2\text{O}_4$  ferrite and/or small superparamagnetic  $\alpha\text{-Fe}_2\text{O}_3$ . In order to clarify the nature of the doublet, we performed a Mössbauer measurement of the pure  $\alpha\text{-Fe}_2\text{O}_3$  powder milled for 120h in the same condition used. No doublet was found in the Mössbauer spectrum. Thus, the doublet in Fig.3 is due to the  $\text{ZnFe}_2\text{O}_4$  ferrite. This infers that a milling time of 25h some of  $\alpha\text{-Fe}_2\text{O}_3$  have already reacted with ZnO to form  $\text{ZnFe}_2\text{O}_4$ . After a milling time of 70h, the spectrum is dominated by a superparamagnetic relaxation component with a broadened doublet. The average quadrupole splitting of the doublet is about 0.80 mm/s, which is larger than for bulk  $\text{ZnFe}_2\text{O}_4$  (0.33 mm/s)(11) and that for ultrafine  $\text{ZnFe}_2\text{O}_4$  particles

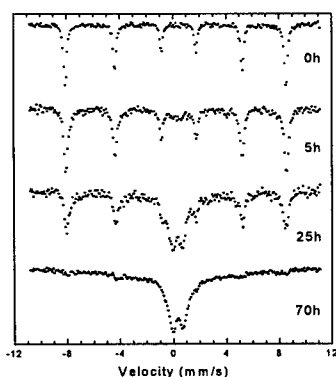


Figure 3. Mössbauer spectra recorded for the  $\alpha\text{-Fe}_2\text{O}_3$ -ZnO samples after different milling times (0h, 5h, 25h and 70h) at room temperature.

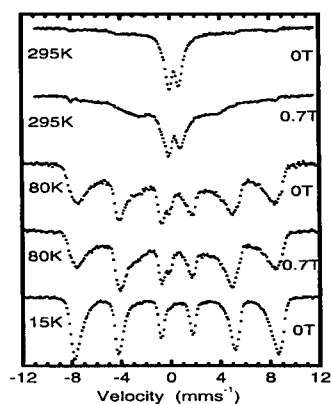


Figure 4. Mössbauer spectra recorded for the sample milled for 90h at various temperatures with and without magnetic field.

( $\sim 0.57$  mm/s) prepared by the co-precipitation method(7). The large quadrupole splitting value of the as-milled  $\text{ZnFe}_2\text{O}_4$  may be mainly resulted from a high concentration of structural defects created during high-energy ball milling. In addition, an EDS analysis of the sample milled for 90h shows that sample contains approximately 4.9 at.% Cr atoms, originating from the abrasion of the vial and balls. The influence of the contamination on the quadrupole splitting of the doublet can not be ruled out at present. Figure 4 shows the Mössbauer spectra of the sample milled for 90h at different temperatures with and without applied magnetic field. At 295K, the spectrum in an applied magnetic field of 0.7T perpendicular to the direction of propagation of the  $\gamma$ -rays differs from the spectrum recorded at 295K in zero field. The magnetic relaxation component is enhanced at the expense of the doublet. This indicates the formation of small superparamagnetic  $\text{ZnFe}_2\text{O}_4$  particles, although the magnetic transition temperature is approximately 10K for the bulk normal spinel  $\text{ZnFe}_2\text{O}_4$ (12). Magnetic splitting and a polarization effect are clearly revealed in the spectra recorded at 80K. It was suggested that magnetic transition temperature could be enhanced by partial inversion in the  $\text{ZnFe}_2\text{O}_4$  phase. The spectrum recorded at 15K shows a broadened sextet and a tiny single line with a negative isomer shift. The latter is attributed to the stainless steel contamination and the former to the partially inverted  $\text{ZnFe}_2\text{O}_4$  particles prepared by high-energy ball milling.

In conclusion, nanocrystalline zinc ferrite powders with a partially inverted spinel structure were synthesized by high-energy ball milling at ambient temperature from a powder mixture of  $\alpha\text{-Fe}_2\text{O}_3$  and ZnO. At room temperature, the nanocrystalline zinc ferrite shows a superparamagnetic state with a large quadrupole splitting, indicating a higher defect concentration induced by high-energy ball milling than that in the samples prepared by the co-precipitation method.

## REFERENCES

1. C. C. Kock, *Ann. Rev. Mat. Sci.*, **19**, 121(1989); *Nanostruct. Mater.*, **2**, 109(1993).
2. J. Z. Jiang, C. Gente, and P. Bormann, *Mater. Sci. Eng. A* **242**, 268(1998).
3. E. Gaffet, M. Abdellaoui and N. Malhouroux-Gaffet, *Mater. Trans., JIM*, **36**, 198(1996).
4. J. Z. Jiang, R. Lin, S. Mørup, K. Nielsen, F. W. Poulsen, F. J. Berry, and R. Clausen, *Phys. Rev. B* **55**, 11(1997); *ibid* **55**, 14830(1997).
5. N. Lefelshtel, S. Nativ, I. J. Lin, and Y. Zimmels, *Powder Technol.* **20**, 211(1978).
6. T. Kosmac and T. H. Courtney, *J. Mater. Res.* **7**, 1519(1992).
7. T. Sato, K. Haneda, M. Seki and T. Iijima, *Appl. Phys. A*, **50**, 13(1990).
8. H. H. Hamdeh, J. C. Ho, S. A. Oliver, R. J. Willey, G. Oliveri, and G. Bussa, *J. Appl. Phys.* **81**, 1851 (1997).
9. K. Tanaka, Y. Nakahara, K. Hirao, and N. Soga, *J. Magn. Magn. Mater.* **131**, 120 (1994).
10. J. Z. Jiang, Y. X. Zhou, S. Mørup and C. Bender Kock, *Nanostruct. Mater.*, **7**, 401(1996).
11. T. Mizoguchi and M. Tanaka, *J. Phys. Soc. Japan* **18**, 1301(1963).
12. W. Schiessl, W. Potzel, H. Karzel, M. Steiner, G. M. Kalvius, A. Martin, M. K. Krause, I. Halevy, G. Will, M. Hillberg, and R. Wäppling, *Phys. Rev. B* **53**, 9143(1996).



## SYNTHESIS OF NANOSTRUCTURED MULLITE FROM XEROGEL AND AEROGEL OBTAINED BY THE NON-HYDROLYTIC SOL-GEL METHOD

Dj.Janackovic<sup>1</sup>, A.Orlovic<sup>1</sup>, D.Skala<sup>1</sup>, S.Drmanic<sup>1</sup>, Lj.Kostic-Gvozdenovic<sup>1</sup>,  
V.Jokanovic<sup>2</sup>, D.Uskokovic<sup>3</sup>

<sup>1</sup> Faculty of Technology and Metallurgy, Karnegijeva 4, 11000 Belgrade, Yugoslavia

<sup>2</sup> Institute for Nuclear and Other Mineral Raw Materials, Belgrade

<sup>3</sup> Institute of Technical Science of Serbian Academy of Sciences and Arts, Belgrade

*Abstract -- Synthesis and nanostructure evolution of mullite ( $3\text{Al}_2\text{O}_3 \cdot 2\text{SiO}_2$ ) from xero- and aerogels, obtained by the non-hydrolytic sol-gel process are described. Mullite crystallization and gel nanostructure evolution after heat treatment were studied by differential-thermal, x-ray diffraction, infrared and thermomicroscopic analysis as well as by scanning electron microscopy. Crystallization of mullite from both gels starts at  $900^\circ\text{C}$  and further increase in temperature increases the size of crystallites formed from 32 to 100 nm and 12 to 20 nm in the case of xero- and aerogels, respectively. Accelerated sintering of aerogels in the temperature range 900 to  $1000^\circ\text{C}$  is a consequence of the viscous flow of the amorphous  $\text{SiO}_2$  phase.*

©1999 Acta Metallurgica Inc.

### INTRODUCTION

Due to its good mechanical, thermal and electrical properties, mullite ceramics has been widely used in various technical fields and has been the object of considerable research (1,2). As the properties of the final product depend significantly on the characteristics of the powder used, special attention has been devoted to its synthesis. Various processes such as hydrothermal synthesis, coprecipitation, sol-gel, spray pyrolysis, etc, have been used to prepare nanometer mullite powders of high homogeneity, purity and sinterability (1-3). Non-hydrolytic sol-gel process is based on the reactions of metal halogenides with alkoxides, ethers and alcohols followed by oxygen bridges formation between metal cations which facilitate an easy production of gels. Synthesis of mullite by this process proceeds via either mullite with tetragonal symmetry or  $\gamma\text{-Al}_2\text{O}_3$  depending on the type of precursor used (4,5). Structure, phase composition and sinterability during thermal evolution of mullite aerogels, synthesized from boehmite and colloidal  $\text{SiO}_2$  sols by hydrolytic sol-gel process, show that the synthesis is based on the reaction of  $\gamma\text{-Al}_2\text{O}_3$  with amorphous  $\text{SiO}_2$ , and that the accelerated sintering, occurring at temperatures between 1100 and  $1200^\circ\text{C}$ , is a consequence of the viscous flow of amorphous  $\text{SiO}_2$  (6,7). In this paper, differences in crystallization, nanostructure evolution and sinterability of mullite from xero and aerogels obtained by non-hydrolytic sol-gel technique have been determined.

## EXPERIMENTAL

Synthesis of mullite precursor gel was performed by dissolving 38.4 g  $\text{AlCl}_3$  (Fluka, puriss.) in a mixture of 33  $\text{cm}^3$  diethyl ether and 67  $\text{cm}^3$   $\text{CCl}_4$  (Merck). Then, 21.5  $\text{cm}^3$  TEOS (Merck selectpur.) was added. Gelation took place in an autoclave at  $110^\circ\text{C} \pm 2^\circ\text{C}$ . The obtained gel appeared brown in color. Xerogels were obtained by drying the gel in a drying oven at  $130^\circ\text{C}$  in a stream of  $\text{N}_2$  for 8 hours. Aerogels were obtained by gel drying by supercritical  $\text{CO}_2$  at  $40^\circ\text{C}$  and 200 bars for 8 hours in Autoclave Engineers SCE Screening System. Xero- and aerogels were heated at temperatures from 900 to  $1400^\circ\text{C}$  for 2 hours. X-ray diffraction analysis of samples was made by a SIEMENS D500 with  $\text{CuK}\alpha$  radiation in the  $2\theta$  angle range  $10,000$  to  $70,000^\circ$  with a step of 0.02. Infrared spectroscopy (IR) analysis of samples was made using a MB BOMEN HARTMANN instrument in the wavenumber range from 400 to  $4000\text{ cm}^{-1}$ . The samples were prepared by the KBr method at a ratio (sample:KBr)=1:75. DT analysis was made using an Aminco apparatus at a heating rate of  $10^\circ\text{C}/\text{min}$  in air. Relative linear shrinkage was determined using an E. LEITZ thermomicroscope at temperatures up to  $1450^\circ\text{C}$  and a heating rate of  $10^\circ\text{C}/\text{min}$ . SEM micrographs of xero- and aerogels, heated at  $1400^\circ\text{C}$ , were collected by a SEM Philips, XL 30 instrument.

## RESULTS AND DISCUSSION

DTA diagrams of xero- and aerogels revealed endothermal peaks in the temperature range 100 to  $300^\circ\text{C}$  corresponding to the removal of the condensation products of the residual functional (alkoxide and chloride) groups as well as of the residual solvent. Exo peaks at 975 and  $980^\circ\text{C}$  for xero- and aerogels, respectively, corresponds to the tetragonal mullite (mullite with tetragonal symmetry and composition with higher  $\text{Al}_2\text{O}_3$  content then stoichiometric) crystallization or  $\text{Al}_2\text{Si}$ -spinel phase (1).

Figure 1 illustrates the x-ray analysis data on xero- and aerogels heated at 900, 1000, 1100 and  $1400^\circ\text{C}$  for 2 hours. Diffraction peaks observed for both gels correspond to mullite according to the ASTM 15-0776 card. Higher crystallinity of xerogels compared to that of aerogels is evident. Also, intensity of the diffraction peaks increases with increasing heating temperature in the case of xerogels, while it remains unchanged in the case of aerogels. The dimensions of mullite crystallites formed from xero- and aerogels heated at different temperatures, determined by the half-height width of reflexion at  $2\theta=49.90^\circ$  according to the Scherrer formula, are reported in Table 1. The size of crystallites from xerogels is three to five times greater than that from aerogels, i.e., mullite crystallite growth in the case of aerogels is considerably decelerated.

Figure 2 shows relative linear shrinkage of xero- and aerogel samples heated to  $1450^\circ\text{C}$  at a heating rate of  $10^\circ\text{C}/\text{min}$ . Increased shrinkage of aerogel samples in the temperature range from 950 to  $1000^\circ\text{C}$  coincides obviously with the temperature of appearance of the exothermal peak on the given DT curve, i.e., crystallization of mullite.

IR spectra of aerogels are given in Figure 3. For the sample heated at  $900^\circ\text{C}$  a spectrum characteristic of mullite is easily recognized: bands at 465 and  $1108\text{ cm}^{-1}$  characteristic of  $\text{SiO}_2$ , bands at 745, 895 and  $1170\text{ cm}^{-1}$  corresponding to tetrahedral and

those at 565 and 830  $\text{cm}^{-1}$  corresponding to octahedral coordination of aluminum. Increase in temperature to 1400°C leads to a better arrangement of the mullite structure, but the bands of amorphous  $\text{SiO}_2$  are evidently far more intense than the ones of stoichiometric (3:2) mullite, indicating the presence of amorphous  $\text{SiO}_2$  phase.

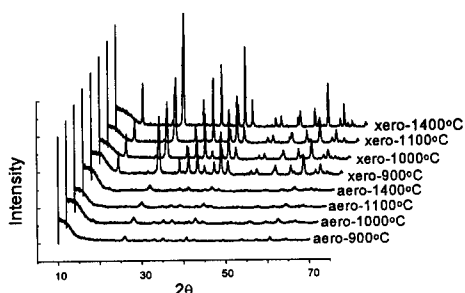


Fig.1. X-ray analysis of xero and aero gels heated at 900, 1000, 1100 and 1400°C.

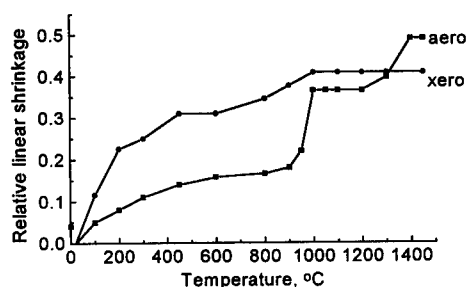


Fig.2. Relative linear shrinkage of xero and aero gels during heating.

TABLE 1

Crystallite size (in nm) of xero- and aerogels heated at 900, 1000, 1100 and 1400°C for 2 h.

Sample/Temperature	900°C	1000°C	1100°C	1400°C
Xerogel	32,0	38,0	51,0	101,0
Aerogel	12,0	14,6	-	20,8

Figure 4 shows the IR spectra of xerogels heated at 900 and 1400°C. At 900°C bands correspond to tetragonal mullite appear: bands at 1130 and 440  $\text{cm}^{-1}$  are attributed to Si-O-Si bonds, bands at 1180, 903 and 724  $\text{cm}^{-1}$  correspond to the tetrahedral coordination of Al, while those at 820 and 570  $\text{cm}^{-1}$  refer to the octahedral coordination of aluminum characteristic of a well-arranged mullite structure. In the temperature range 900 to 1400°C there is, practically, no change in the spectra except an increased intensity of the band at 1170  $\text{cm}^{-1}$  compared to that at 1130  $\text{cm}^{-1}$ , i.e., a better arrangement of the orthorhombic mullite structure (1).

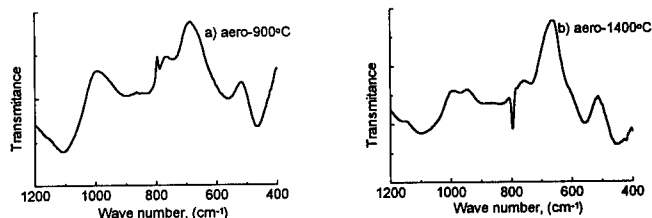


Fig.3. IR spectra of aerogel heated at 900 (a) and 1400°C (b).

Figures 5 and 6 illustrate the microstructures of xero- and aerogels heated at 1400°C. As can be seen the xerogels have particles 100 to 500 nm in size and pores of about 300 nm. In the case of aerogels, particles and pores cannot be seen but the structure similar to an amorphous one. Differences observed in the structures, IR spectra and shrinkage during heating of xero- and aerogels are the result of phase separations (a mullite and an  $\text{SiO}_2$ -rich phase) at temperatures from 950 to 1000°C. The

presence of amorphous  $\text{SiO}_2$  phase in the case of aerogels causes their accelerated sintering, due to the viscous flow of  $\text{SiO}_2$  phase, contrary to xerogels where the phase separations are far less pronounced. Phase separations with aerogels are probably a consequence of aluminum compounds extraction during supercritical drying which results from an incomplete reaction of precursor during gelation.

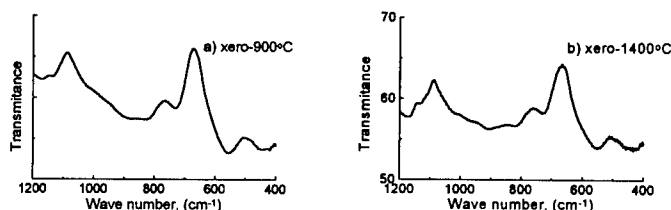


Fig.4. IR spectra of xerogel heated at 900 (a) and 1400°C (b).

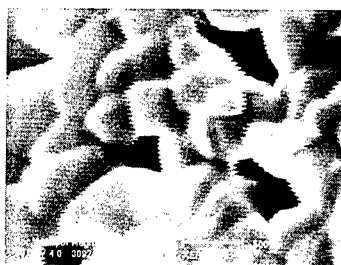


Fig.5. SEM micrograph of xerogel heated at 1400°C.

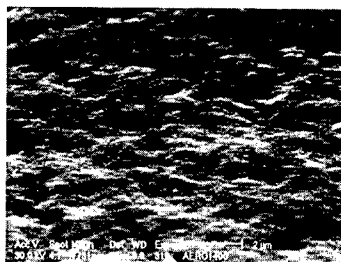


Fig.6. SEM micrograph of aerogel heated at 1400°C.

## CONCLUSION

Mullite precursor xero- and aerogels were synthesized by non-hydrolytic sol-gel procedure and subsequently dried in a stream of  $\text{N}_2$  and supercritical  $\text{CO}_2$ , respectively. Crystallization of mullite from both gels starts at 900°C. Increase in heating temperature changes the size of crystallite formed from 32 to 100 nm in the case of xerogels and from 12 to 20 nm in the case of aerogels. The difference in relative linear shrinkage and microstructure of gels during heating indicate different mechanisms of sintering resulting from phase separations. Accelerated sintering of aerogels in the temperature range 900 to 1000°C is a consequence of the viscous flow of the amorphous  $\text{SiO}_2$  phase.

## REFERENCES

1. Schneider, H., Okada, K., Pask, J.A., Mullite and Mullite Ceramics, John Wiley & Sons, 1994.
2. Janackovic, Dj., Jokanovic, V., Kostic-Gvozdenovic, Lj., Zivkovic, Lj., Uskokovic, D., J.Mater.Res., 1996, 11, 1706.
3. Janackovic, Dj., Jokanovic, V., Kostic-Gvozdenovic, Lj., Uskokovic, D., NanoStruct.Mater., 1998, 10, (accepted for publication).
4. Acosta, S., Corriu, R., Leclercq, D., Mutin, P.H., Vioux, A., J.Sol-Gel Sci.Tehmol., 1994, 2, 5.
5. Acosta, S., Corriu, R., Leclercq, D., Mutin, P.H., Vioux, A., MRS.Symp.Proc, 1994, 346, 345.
6. Cluzel, F., Larnac, G., Phalippou, J., J.Mater.Sci., 1991, 26, 5979.
7. Rahaman, M.N., De Jonghe, L.C., Shinde, S.L., Tewari, P.H., J.Am.Ceram.Soc., 1988, 71, C-338.



Pergamon

NanoStructured Materials, Vol. 12, pp. 151–154, 1999

Elsevier Science Ltd

© 1999 Acta Metallurgica Inc.

Printed in the USA. All rights reserved

0965-9773/99/\$—see front matter

PII S0965-9773(99)00086-0

## FABRICATION AND CHARACTERIZATION OF $\text{Cd}_x\text{Zn}_{(1-x)}\text{S}$ NANO PARTICLES

B. Balamurugan, B.R. Mehta and S.K. Sharma\*

Thin Film Laboratory, Indian Institute of Technology Delhi,

New Delhi-110 016, India. <brmehta@physics.iitd.ernet.in>

\* Electron Microscopy Division, National Physical Laboratory, Delhi-110 052, India.

*Abstract: In the present studies,  $\text{Cd}_x\text{Zn}_{(1-x)}\text{S}$  nanoparticles have been prepared by chemical capping method. Optical absorption, X-ray diffraction and transmission electron microscopy studies have been carried out. Size of the nano particles have been calculated from the XRD and optical absorption data. These studies indicate towards a kinetically controlled growth of nano particles. The growth of the  $\text{Cd}_x\text{Zn}_{(1-x)}\text{S}$  nano particles is also affected by the action of the capping agent. ©1999 Acta Metallurgica Inc.*

## INTRODUCTION

The driving force for the increased interest in semiconductor nano particle research is both new physics as well as novel technological applications. Growth of nano particles of a variety of semiconductor materials of well controlled dimensions and composition is the important first-step towards the realization of these objectives.

The central objective of the present study is to use the chemical capping method to grow semiconductor nano particles comprising of the solid solutions of CdS and ZnS. To understand the growth behavior of  $\text{Cd}_x\text{Zn}_{(1-x)}\text{S}$  nanoparticles, the optical and structural properties of these nano particles have been studied as a function of the composition (X).

## PREPARATION OF NANO PARTICLES

In the present study, chemical capping method has been used for growing nano particles with thiophenol as the capping agent. The following master solutions with 0.1 molarity were used for preparing  $\text{Cd}_x\text{Zn}_{(1-x)}\text{S}$  nanoparticles.

Solution (a): 2.67 g cadmium acetate, 80 ml methanol and 20ml acetonitrile.

Solution (b): 2.19 g zinc acetate, 80 ml methanol and 20ml acetonitrile.

Solution (c): 0.8g sodium sulfide, 50 ml methanol and 50ml water.

Solution (d): 1.1 ml thiophenol, 100 ml acetonitrile.

Solutions (a) and (b) were mixed together and stirred for 30 minutes. Solution (d) was slowly added to the above mixture followed by stirring for 30 minutes. Solution (c) was slowly added to the above mixture while keeping the stirring on. This resulted in a whitish



yellow coloured solution indicating the formation of  $\text{Cd}_x\text{Zn}_{(1-x)}\text{S}$  nanoparticles. Since thiophenol capped  $\text{Cd}_x\text{Zn}_{(1-x)}\text{S}$  particles are non-dispersable in methanol-water mixture, nanoparticles settle down in the solution. Finally, the nanoparticles are decanted, collected and vacuum dried. The  $\text{Cd}_x\text{Zn}_{(1-x)}\text{S}$  nanoparticles samples S1, S2, S3 and S4 having  $X=0.00, 0.50, 0.75$  and  $1.00$  were prepared by mixing appropriate amounts of master solutions in such a way that Sulphur / Thiophenol (S/Sph) ratio = 1 in all the samples. Thiophenol plays an important role in controlling the size of nano particles(1). The use of acetonitrile increases the dispersion of nanoparticles in polar medium like Di-Methyl Formaldehyde (DMF).

## RESULTS AND DISCUSSION

The absorption spectra of  $\text{Cd}_x\text{Zn}_{(1-x)}\text{S}$  nano samples obtained using Hitachi 330 spectrophotometer are shown in Fig. 1. The chemically capped nanoparticles were dispersed in DMF and kept in a quartz cell for optical absorption measurements. Weak exciton features appear in the absorbance spectra at higher wavelengths (2) for nano particles in samples S3 and S4. The dependence of absorption edge as a function of Cd concentraton is shown in Fig. 2. For comparison, the dependence for the bulk  $\text{Cd}_x\text{Zn}_{(1-x)}\text{S}$  (3) is also shown in Fig. 2. The deviation in bandgap from the corresponding bulk value,  $\Delta E$ , was used for estimating the particle size from the effective mass approximation relationship (4). The values of  $m_e$ ,  $m_h$  and  $\epsilon$  for samples S1 and S4 used for these calculations were obtained from the literature (4). The values of  $\Delta E$  along with the calculated particle size of various  $\text{Cd}_x\text{Zn}_{(1-x)}\text{S}$

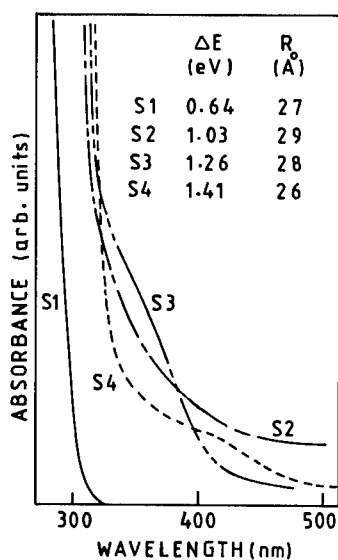


Fig. 1. Absorption spectra of  $\text{Cd}_x\text{Zn}_{(1-x)}\text{S}$  nano particle samples

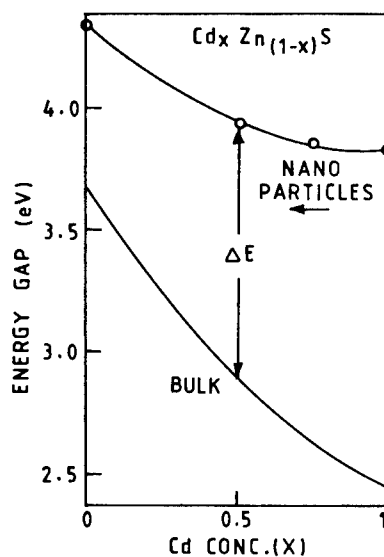


Fig. 2. Energy gap vs. Cd conc. for nano particles and bulk  $\text{Cd}_x\text{Zn}_{(1-x)}\text{S}$

samples are given in the inset in Fig. 2. It may be mentioned here that the absorption edge of  $\text{Cd}_x\text{Zn}_{(1-x)}\text{S}$  samples with  $x=0.5$  and  $0.75$  are closer to the absorption edge of CdS than what is expected from the bulk value of the absorption edge at the same value of  $x$ . This observation will be discussed later.

Rigaku X-ray diffractometer was used for obtaining X-ray diffractograms for samples S1, S2, S4 as shown in Fig. 3. Broad X-ray diffraction (XRD) peaks are attributed to the absence of long range order at nano dimensions in these samples. One peak in the X-ray diffractogram of the sample S4 could not be identified. A comparison of the observed  $d$  values from the XRD data for the samples S1, S2 and S4 with the standard values for the bulk  $\text{Cd}_x\text{Zn}_{(1-x)}\text{S}$  is shown in the Table 1. Using the full width at half maximum (FWHM) of these peaks, the particle size was estimated by using Scherrer's equation (5) and the values are given in Table 1. It may be mentioned here that presence of strain and structural disorder in nano particles can alter the  $d$  values and FWHM and the broad peaks observed in the nano particles samples may be also due to the overlapp of more than one XRD peaks (6). The large width of the XRD peaks will apparently yield lower values of particle size. It may also be noted that calculations of particle size using effective mass approximation require values of  $m_e^*$ ,  $m_h^*$  and  $\epsilon$ . In the present case, the bulk values for CdS and ZnS have been used (4). Thus, the values of particle size obtained from XRD and optical studies can be quite different.

Heat of formation for ZnS (-64.6 Kcal/ gm-mole) is higher as compared to CdS (-54 Kcal/ gm-mole) (7). From this consideration, ZnS should be easier to form than CdS. During the growth of the nano particles, CdS formation should be less and thus the concentration ( $x$ ) in the nano particle should be lower than the starting solution. If the growth was solely

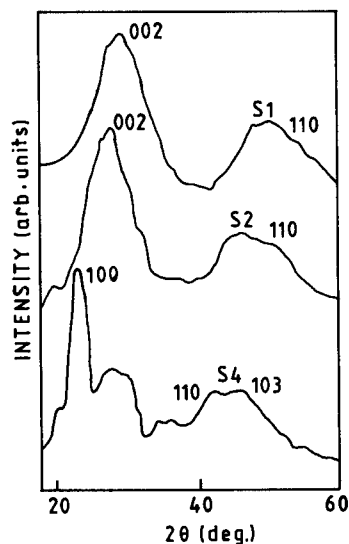


Fig. 3. X-ray diffractograms for samples S1, S2 and S4.

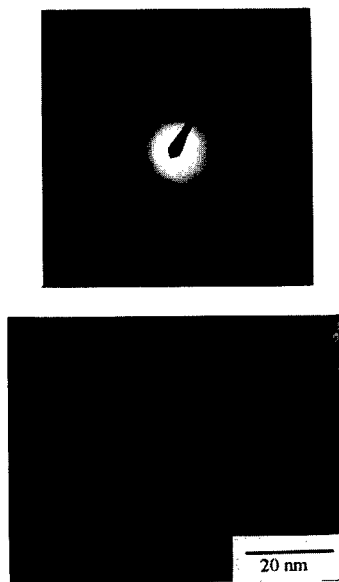


Fig. 4. TEM micrograph and diffraction pattern for sample S2

TABLE I  
XRD and Electron Diffraction data

Name	(X)	2 $\theta$ degree	d (A) XRD	d(A) TEM	d (A) Bulk (8)	(hkl)	FWHM (A)	Size (A)
S1	0	28.85 47.80	3.092 1.852	3.0 1.9	3.128 1.911	(002) (110)	7.9	11
S2	0.5	26.90 45.40	3.312 1.996	3.3 1.9	--	--	7.2	12
S4	1.0	24.50 42.85 46.50	3.594 2.109 1.992	--	3.580 2.068 1.898	(100) (110) (103)	2.8	31

guided by thermodynamical considerations, the absorption edge of nano particles with  $X=0.5$  and  $0.75$  should have been closer to ZnS. The observation that the absorption edge of sample S2 and S3 are closer to the absorption edge of CdS indicates that reaction kinetic considerations dominate during the nano particle growth. Presence of capping agent may also alter the composition of  $\text{Cd}_x\text{Zn}_{(1-x)}\text{S}$  nano particles in comparison to the starting solution.

The Phillips TEM model was used to obtain electron diffraction pattern and the  $\text{Cd}_x\text{Zn}_{(1-x)}\text{S}$  nano particle samples. A typical TEM micrograph and the electron diffraction pattern for  $\text{Cd}_x\text{Zn}_{(1-x)}\text{S}$  sample S2 are shown in Fig. 4. Size of  $\text{Cd}_x\text{Zn}_{(1-x)}\text{S}$  nano particles is in 10A to 40A range. Similar d values are obtained from electron and X-ray diffraction for samples S1, S2 and S4 (Table 1) and the comparison with the bulk values (8) indicates that the  $\text{Cd}_x\text{Zn}_{(1-x)}\text{S}$  nano particles have hexagonal crystal structure. The d values obtained for sample S2 are in-between the values for sample S1 and S4 indicating the formation of  $\text{Cd}_x\text{Zn}_{(1-x)}\text{S}$  solid solution in the nano particles.

In conclusions,  $\text{Cd}_x\text{Zn}_{(1-x)}\text{S}$  nano particles have been prepared by chemical capping method for the first time. Optical absorption and diffraction studies confirm the formation of  $\text{Cd}_x\text{Zn}_{(1-x)}\text{S}$  solid solution. Concentration (X) and the size of the nano particles determine the shift in the absorption edge. Kinetics of the reaction and the difference in the capping effectiveness of thiophenol with respect to Cd and Zn seem to affect the size and composition of  $\text{Cd}_x\text{Zn}_{(1-x)}\text{S}$  nano particles.

#### REFERENCES

1. N. Herron, Y. Wang and H. Eckert, *J. Am. Chem. Soc.*, 1990, 112, 1322.
2. W.M. Kane, J.P. Spratt, L.W. Hershinger and I. H. Khan, *J. Electrochemical Soc.*, 1966, 113, 136.
3. C.B. Murray, D.J. Norris and M.G. Bawendi, *J. Am. Chem. Soc.* 1993, 115, 8706.
4. P.E. Lippen and M. Lannoo, *Physical Review B*, 1989, 39, 10935.
5. Y. Wang and N. Herron, *Physical Review B*, 1990, 42, 7253.
6. J. Cizeron and M.P. Pileni, *Nanostructured Materials*, 1997, 8, 419.
7. H.E. Barner and R.V. Scheurman, *Handbook of Thermo Chemical Data*, John Wiley & Sons, Inc. 1978, p.235.
8. ASTM Cards, 6-0314, 5-0492



## IRON NANOPARTICLES IN X AND Y ZEOLITES

K. Lázár<sup>1</sup>, H.K. Beyer<sup>2</sup>, G. Onyestyák<sup>2</sup>, B.J. Jönsson<sup>3</sup>, L.K. Varga<sup>4</sup>, S. Pronier<sup>5</sup>

<sup>1</sup> Institute of Isotope and Surface Chemistry, Budapest, P.O.B. 77, H-1525, Hungary

<sup>2</sup> Institute of Chemistry, Budapest, P.O.B. 17, H-1525, Hungary

<sup>3</sup> Dept. Condensed Matter Physics, Royal Inst. Technology, S-10044 Stockholm, Sweden

<sup>4</sup> Institute of Solid State Physics, Budapest, P.O.B. 49, H-1525, Hungary

<sup>5</sup> LACCO, URA CNRS 350, Université de Poitiers, F-86022 Cedex, Poitiers, France

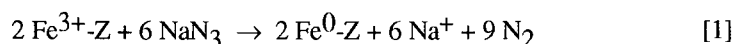
**Abstract** Strong reduction of extra-framework iron ions was attempted by sodium azide to form metallic iron particles with dimensions of a few nanometers. Na-X and Na-Y zeolites were partially ion exchanged to 5 wt % Fe content. The iron-zeolites were mixed with sodium azide, evacuated at 550 K and heated to 800 K in nitrogen to form sodium vapour by decomposing  $\text{NaN}_3$ . The sodium exerts strong reduction, a part of iron can be reduced to zerovalent state to form particles in the nanometer size range, as in situ Mössbauer spectroscopy, AC susceptibility, X-ray diffraction and transmission electron microscopy studies revealed. Simultaneous partial recrystallization of the zeolite is also observed.

©1999 Acta Metallurgica Inc.

## INTRODUCTION

Zeolites may provide an appropriate hosting media for stabilising high dispersion metallic phase in nanometer size region. For preparation, as a possible way, strong reduction of extra-framework ions can be suggested. The method was attempted for iron, eg. by using sodium vapour: at 1066 K (1), and at lower temperature (673 K) with prolonged periods (5 - 48 h) (2); a part of iron ions was reduced to metallic state in both cases.

To attain the same reducing effect the "local generation" of sodium vapour can also be suggested by decomposing sodium azide in a mixture:



where -Z refers to the X or Y zeolite matrix. It is supposed that the reduction may proceed in the cages, at a temperature exceeding slightly that necessary to decompose  $\text{NaN}_3$ , and the metallic particles formed are retained in the cages. In fact, upon the decomposition of sodium azide  $\text{Na}_4^{3+}$ ,  $\text{Na}_6^{5+}$  and  $\text{Na}_x^0$  clusters are formed (3); they have the capability for reduction.

In the present work we report on the results of the attempted reduction of iron in Fe-X and Fe-Y by Eq. [1]. Methods of X-ray diffraction (XRD), AC susceptibility, in situ Mössbauer spectroscopy and transmission electron microscopy (TEM) are used for characterisation of the products.

## EXPERIMENTAL

Sodium ions in X and Y zeolites (with  $\text{SiO}_2/\text{Al}_2\text{O}_3$  moduli 2.75 and 5.11, respectively) were ion exchanged partially for iron (5 wt % Fe content). After drying the adsorbed water was removed by an overnight heating at 620 K. Then the iron-zeolites were mixed mechanically with  $\text{NaN}_3$  (10 % excess to stoichiometry) in a dry box under argon atmosphere. Finally the mixtures were placed to an in situ Mössbauer cell, then they were evacuated ( $10^{-1}$  Pa) at 550 K, and the azide was decomposed by heating at 800 K in nitrogen. For characterisation of products methods of in situ Mössbauer spectroscopy and ex situ XRD, in phase AC susceptibility, and TEM combined with electron diffraction were used.

## RESULTS

### X-ray diffraction (XRD)

X-ray diffractograms reveal partial recrystallization for X zeolite, with appearance of non-porous aluminium silicate phase(s), with typical reflections at  $2\Theta = 21.1$  and  $34.8$  degree. In the Y zeolite the original crystallinity was essentially preserved. Reflections of metallic iron crystals were not observed (the size limit to detect reflections is ca. 10 nm).

### AC susceptibility

The dependence of the in-phase AC susceptibility on temperature for the Fe-X +  $\text{NaN}_3$  sample is shown in Fig. 1. A characteristic break appears at 120 K at different frequencies: the exponential dependence changes to a linear one. The exponential increase is characteristic of metallic iron, the break indicates the presence of nanoparticles (4). In case of oxidized iron nanoparticles a similar behaviour was found (with a break at 100 K) in Ref. (5).

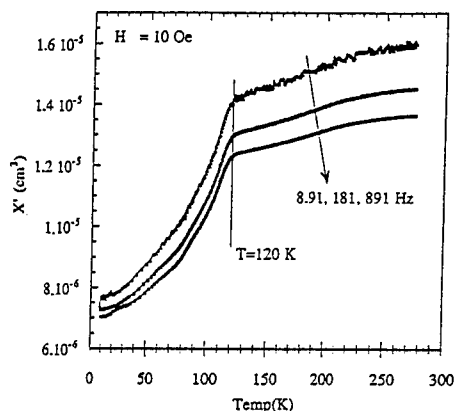


Fig. 1. Temperature dependence of the in-phase AC susceptibility of the Fe-X +  $\text{NaN}_3$  sample at various frequencies

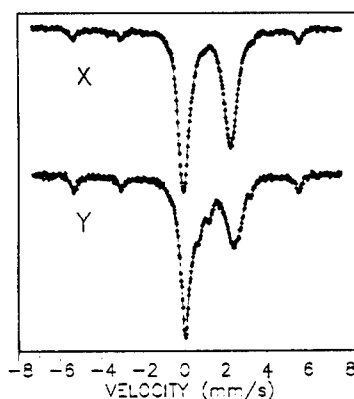


Fig. 2. 77 K in situ Mössbauer spectra of Fe-X +  $\text{NaN}_3$  (top) and Fe-Y +  $\text{NaN}_3$  (bottom) samples

### Mössbauer spectroscopy

77 K in situ Mössbauer spectra are presented in Fig. 2. Two types of zerovalent iron are identified (with and without magnetic splitting), and  $\text{Fe}^{2+}$  ions were found in various coordination states (Table 1).  $\text{Fe}^{3+}$  component (indicative for oxides) was not detected.

### Transmission Electron Microscopy (TEM)

TEM measurements were performed on the X zeolite sample. Iron containing particles were observed dominantly in a narrow, 4 - 7 nm size range. Electron diffractograms obtained on larger particles revealed the presence of FeO (12 nm) and  $\text{Fe}_3\text{O}_4$  (36 nm).

## DISCUSSION

The analysis of data clearly attests for formation of metallic iron nanoparticles. Their existence is directly manifested in the Mössbauer spectra (recorded in situ). The metallic component formed exists primarily in two characteristic sizes; particles in 4-6 nm range, and clusters smaller than 1 nm. (Prior to the other, ex situ measurements, probably secondary oxidation of particles had taken place due to exposure to air.) AC susceptibility curves and TEM and electron diffraction images indicate presence of iron-containing particles.

The first size range can be directly obtained from TEM images, and can be estimated from the lack of the reflections of metallic iron (or oxides) in the X-ray diffractograms (< 10 nm), combined with the appearance of the magnetic sextet in Mössbauer spectra (> 4 nm (6)). As for

TABLE 1  
Spectral Components in the 77 K In Situ Mössbauer Spectra  
(IS: isomer shift, related to  $\alpha$ -iron, mm/s; QS: quadrupole splitting, mm/s; MHF: magnetic hyperfine field, Tesla; RI: relative intensity, %)

Fe-X + $\text{NaN}_3$					Fe-Y + $\text{NaN}_3$			
	IS	QS	MHF	RI	IS	QS	MHF	RI
$\text{Fe}^0$	0.10		33.8	10	0.10		33.7	12
$\text{Fe}^0$	0.02			9	0.03			18
$\text{Fe}^{2+}$					0.96	0.52		12
$\text{Fe}^{2+}$	1.01	2.44		24	1.08	2.33		35
$\text{Fe}^{2+}$	1.13	1.75		28				
$\text{Fe}^{2+}$	1.20	2.54		28				
$\text{Fe}^{2+}$					1.48	2.28		22

the existence of iron clusters we may rely primarily on the Mössbauer spectra (singlet component at IS 0.0 mm/s). These clusters do not appear in TEM (the estimated lower limit for detection of particles is ca. 2 nm), the most appropriate assumption is that they are stabilised inside the zeolite cages (pore diameter 1 nm).

It should be noted that considerable recrystallization of the zeolite lattice has also taken place simultaneously in the X zeolite (as X-ray diffractograms attested for formation of non-porous aluminosilicate phase(s)). In contrast, the structure of Y zeolite was practically preserved. In correspondence, different  $\text{Fe}^{2+}$  species are identified for the two samples in the Mössbauer spectra; some are characteristic for the non-porous aluminosilicates in the transformed Fe-X sample, the others are occupying various extra-framework positions in the Fe-Y sample. Thus, the greater proportion of reduction in Fe-Y can also be interpreted by the different extent of lattice transformation. The recrystallization of X lattice is more pronounced by two reasons: first, the amount of sodium is ca. 1.5 half times as large as that in the Y zeolite, and second, the X lattice originally is less stable due to the smaller  $\text{SiO}_2/\text{Al}_2\text{O}_3$  modulus. Thus, the  $\text{Fe}^{2+}$  ions are less accessible in the X structure since they are incorporated partially to the aluminosilicate before they could be reduced. In Y zeolite the porous structure is preserved in a larger extent, the extra framework iron ions are longer accessible for reduction.

## CONCLUSION

In summary, it may be concluded, that iron nanoparticles can successfully be prepared in zeolite cages by sodium generated upon heating the Fe-Z +  $\text{NaN}_3$  mixtures. Two size ranges are dominating: particles in 4 - 6 nanometer range and clusters smaller than 1 nm. The reduction process is accompanied with partial recrystallization of the zeolite lattice (dominantly in the X zeolite). This process results in a limitation to the accessibility of iron ions and thus, to the extent of reduction.

## ACKNOWLEDGEMENTS

The financial supports provided by the Commission of the European Communities in the COST D5 project (CIPE CT 92 6107) and obtained from the Hungarian National Research Fund (OTKA T021131) are thankfully acknowledged.

## REFERENCES

1. Lee, J.B., *J. Catal.*, **68**, 27, (1981).
2. Schmidt, F., Gunsser, W., Adolph, J., *A.C.S. Symp. Series*, **40**, 293, (1977).
3. Brock, M., Edwards, C., Förster, H., Schröder, M., *Stud. Surf. Sci. Catal.*, **84**, 1515, (1994).
4. Dormann, J.L., Bessais, L., Fiorani, D., *J. Phys. C: Solid State Phys.*, **21**, 2015, (1988).
5. Turkki, T., Jönsson, B.J., Ström, V., Medelius, H., El-Shall, M.S., Rao, K.V., *J. Korean Magnetism Society*, **2**, 745, (1995).
6. Clausen, B.S., Topsøe, H., Mørup, S., *Appl. Catal.*, **48**, 327, (1989).



Pergamon

NanoStructured Materials, Vol. 12, pp. 159–162, 1999

Elsevier Science Ltd

© 1999 Acta Metallurgica Inc.

Printed in the USA. All rights reserved

0965-9773/99/\$-see front matter

PII S0965-9773(99)00088-4

## HIGH ENERGY BALL MILLING OF $\text{Co}_{89}\text{B}_{11}$ POWDERS

M. Jachimowicz, V.I. Fadeeva<sup>1</sup>, H. Matyja

Department of Materials Science and Engineering, Warsaw University of Technology,  
Narbutta 85, 02-524 Warsaw, Poland

<sup>1</sup> Department of Chemistry, Moscow State University, Leninski Gory, 119899 GSP,  
Moscow-234, Russia

**Abstract** - - Mechanical alloying was performed on elemental cobalt and boron powders with atomic ratio  $\text{Co}_{89}\text{B}_{11}$ . X-ray diffraction analysis (XRD) and differential scanning calorimetry were used to characterize the structure of the milled samples before and after the heating. The high-energy ball milling was found to influence the resulting phases. The starting powder consisted of the two modifications of cobalt: hcp (hexagonal close packed) and fcc (face centered cubic). Depending on the milling time, single hcp, single fcc, amorphous phases or their mixture were formed. After milling for 20 h, one can observe that the fcc phase transforms into hcp. Further milling caused the amorphization of the alloy. The fcc phase formed from the amorphous matrix only after 80 h of milling and then transformed partially into the hexagonal phase after further milling. The average crystallite size in the final sample obtained after 150 h of ball milling was about 6 nm. ©1999 Acta Metallurgica Inc.

### INTRODUCTION

Mechanical alloying (MA) is an effective method for the preparation of amorphous and nanocrystalline metal powders (1,2). Ball-milling generates numerous structure defects and may lead to the refinement of the grain size which can results in the formation of a nanostructure or in amorphization.

MA method has been successfully applied for the preparation of powders of metal-metalloid alloys (3,4). Co-based alloys are particularly interesting because of the phase transformations that proceed in pure cobalt. The fcc to hcp and hcp to fcc transformations in cobalt has been the subject of a number of investigations (5-7). Corrias et al. (8,9) applied mechanical alloying to different Co-B compositions.

In this paper we report the results of the high energy ball-milling of the  $\text{Co}_{89}\text{B}_{11}$  powder mixture. X-ray diffraction and differential scanning calorimetry monitored the structure of the starting material and of the milled samples at different stages of milling.



## EXPERIMENTAL DETAILS

Crystalline Co (99,5%) and B (99,7%) powders were used as the starting materials. Mechanical alloying of the  $\text{Co}_{89}\text{B}_{11}$  composition was performed. The elemental powder mixture sufficient to create the 5:1 ball to powder mass ratio, was sealed in a glove-bag under an argon atmosphere.

The ball milling processes were conducted in a vibratory mill. After processing, small quantities of powder were removed from the vial in a glove-bag filled with argon. The structure of the milled powders were examined by an X-ray (XRD) diffraction analysis using  $\text{CoK}\alpha$  radiation ( $\lambda = 0.179021$  nm).

Calorimetric measurements were carried out in a Perkin Elmer DSC-7 unit. The heating rate was  $20^\circ\text{C}/\text{min}$ , the temperature was varied from room temperature to  $720^\circ\text{C}$  and the protective atmosphere (flowing) was composed of argon.

## RESULTS AND DISCUSSION

Fig.1 shows the X-ray diffraction patterns determined at selected time intervals. The starting mixture consists of two allotropic modifications of cobalt i.e. the face centered cubic (fcc) and hexagonal close-packed (hcp) phases, which usually coexist at room temperature. No peaks representative of B were detected which can be attributed to the low scattering factor of B.

Milling for 20 h is sufficient to make the fcc peak components disappear from the pattern and only the single hcp Co phase is observed. Further milling resulted in broadening diffraction lines and increasing background. After 60 h of milling, only a diffuse halo is detectable. This may be attributed to the amorphization of the Co-B powders. Prolonged milling up to 150 h results in re-crystallization of the amorphous phase. Fcc Co is the first crystalline phase formed from the amorphous matrix only after 80 h of milling. After 150 h of milling the hcp phase predominates in the alloy structure. The phase transformations in  $\text{Co}_{89}\text{B}_{11}$  alloy induced by ball-milling can be described as follows:  $\text{hcp} + \text{fcc} \rightarrow \text{hcp} \rightarrow \text{hcp} + \text{amorphous} \rightarrow \text{amorphous} \rightarrow \text{fcc} + \text{amorphous} \rightarrow \text{hcp} + \text{fcc}$ .

DSC then examined the structural changes occurring in the Co-B powders during MA. The sequence of DSC curves taken after various milling times is shown in Fig. 2. For the sample after 60 h of milling there is one exothermic peak at  $520^\circ\text{C}$  on the registered curve. For milling times shorter than 60 h one diffuse exothermic effect is visible within the temperature range from  $380^\circ\text{C}$  to  $520^\circ\text{C}$ . For milling times longer than 60 h (80 h and 110 h) a broad effect in the temperature range  $450$ - $550^\circ\text{C}$  is observed.

Table 1 gives the structures of ball milled Co-B powders after different milling times, the calculated values of the Co lattice parameters and the average grain sizes.

The increase of the cobalt lattice parameter originates during ball-milling. In particular significant changes are observed in the parameter  $a$  of the hcp phase. This may be attributed to the dissolution of boron in the cobalt crystalline lattice and to the formation of a supersaturated Co(B) solid solution.

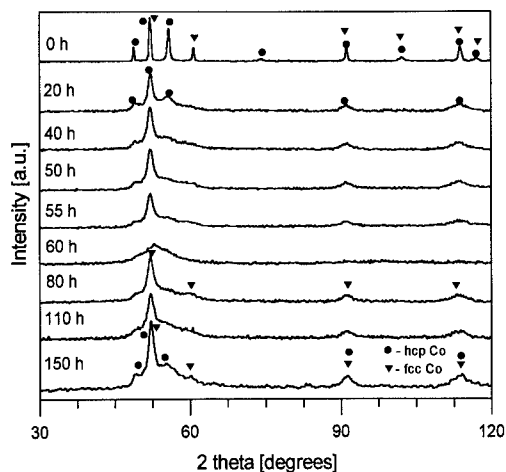


Figure 1. X-ray diffraction patterns of  $\text{Co}_{89}\text{B}_{11}$  alloy after various milling times.

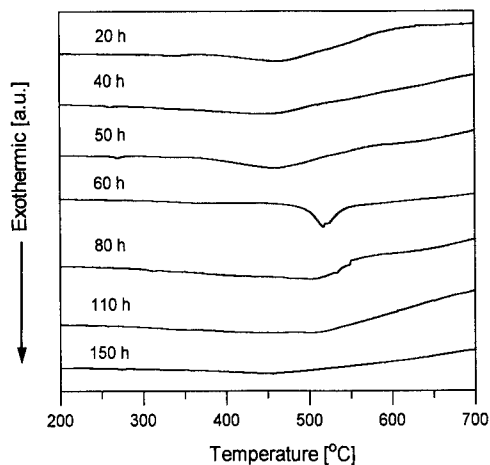


Figure 2. DSC traces of  $\text{Co}_{89}\text{B}_{11}$  powders after various milling times.

TABLE I

Structure, lattice parameters, and grain sizes of  $\text{Co}_{89}\text{B}_{11}$  alloy as a function of milling time

time [h]	structure	$a$ [nm]	$c$ [nm]	$d$ [nm]
0	hcp fcc	0.2507 0.3543	0.4070	97
20	hcp	0.2511	0.4076	11
40	hcp	0.2510	0.4091	5
50	hcp	0.2511	0.4078	5
55	hcp	0.2510	0.4082	4
60	Amorphous	-	-	-
60 <sub>heat-treated 720 °C</sub>	(hcp+fcc)Co+ Co <sub>2</sub> B+Co <sub>3</sub> B	0.2503 0.3543	0.4083	23
80	fcc+Am	0.3552	-	6
110	fcc+Am	0.3547	-	6
150	hcp fcc	0.2504 3.5449	0.4077	6
150 <sub>heat-treated 950 °C 1h</sub>	fcc Co+Co <sub>2</sub> B+ Co <sub>3</sub> B	0.3545	-	25

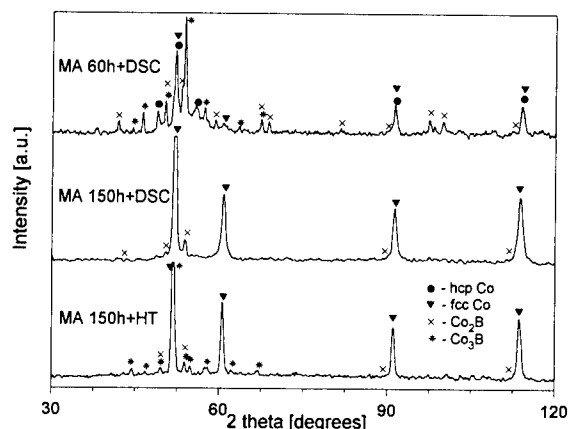


Figure 3. X-ray patterns of the ball-milled  $\text{Co}_{89}\text{B}_{11}$  samples after continuous heating up to  $720^\circ\text{C}$  (DSC) and isothermal annealing at  $950^\circ\text{C}$  for 2 h (HT).

In order to identify by X-ray diffraction the phase changes with temperature, continuous heating up to  $720^\circ\text{C}$  during DSC runs and isothermal annealing at  $950^\circ\text{C}$  for 2 h were performed. The X-ray patterns for the samples heat-treated at  $720^\circ\text{C}$  and isothermally annealed are shown in Fig.3. The X-ray spectra recorded after continuously heating the sample milled for 150 h reveal peaks correspond to the fcc Co and t- $\text{Co}_2\text{B}$  phases. After isothermal annealing the t- $\text{Co}_2\text{B}$  partially transforms into  $\text{Co}_3\text{B}$  which is a stable phase at this alloy composition. The diffraction pattern obtained for the heat-treated sample after 60 h of milling consists of diffraction lines of the fcc Co, hcp Co, t- $\text{Co}_2\text{B}$  and  $\text{Co}_3\text{B}$  phases.

#### ACKNOWLEDGEMENTS

The authors acknowledge to the financial support provided by KBN (Grant No. 7T08D 024 12).

#### REFERENCES

1. Lee, P.Y., Koch, C.C., *J. Non-Cryst. Solids*, 1987, **94**, 88.
2. Koch, C.C., Cho, Y.S., *Nanostructured Mater.*, 1992, **1**, 207.
3. Okamura, H., Ishihara, K.N., Shingu, P.H., Park, H.S., *J. Mater. Sci.*, 1992, **27**, 153.
4. Surinach, S., Baro, M.D., Segura, J., Clavaguera-Mora, N., *Mater. Sci. Forum*, 1992, **88-90**, 275.
5. Cardellini, F., Mazzone, G., *Philo. Mag.*, 1993, **67A**, 1289.
6. Baricco, M., Cowlam, N., Schiffrini, L., Macri, P.P., Enzo, S., *Philo. Mag.*, 1993, **68B**, 957.
7. Huang, J.Y., Wu, Y.K., Ye, H.Q., Lu, K., *Nanostructured Mater.*, 1995, **6**, 723.
8. Corrias, A., Ennas, G., Lichieri, G., Marongiu, G., *Mater. Sci. Eng.*, 1991, **A145**, 123.
9. Corrias, A., Ennas, G., Marongiu, G., Musinu, A., Paschina, G., *J. Non-Cryst. Solids*, 1992, **150**, 487.



Pergamon

NanoStructured Materials, Vol. 12, pp. 163-166, 1999

Elsevier Science Ltd

© 1999 Acta Metallurgica Inc.

Printed in the USA. All rights reserved

0965-9773/99/\$-see front matter

PII S0965-9773(99)00089-6

## PROCESSING OF NANOSTRUCTURED WC-Co POWDER FROM PRECURSOR OBTAINED BY CO-PRECIPITATION

Zongyin Zhang, Sverker Wahlberg, Mingsheng Wang and Mamoun Muhammed,  
Department of Materials Science and Engineering, Materials Chemistry Division,  
Royal Institute of Technology, SE-100 44 Stockholm

**Abstract** – The paper reports the processing of a homogenous cobalt tungstate salt synthesised by co-precipitation starting from ammonium paratungstate and cobalt hydroxide. Different processing parameters such as temperatures and times of reduction and carburization and the composition of the carburization gas were studied. Powders of W and Co were obtained after the reduction of the precursor at 600 °C, 650 °C and 700 °C. The specific surface area of W-Co powders increased with decreasing reduction temperature. The carburization was carried out at 700 °C for 3 hours in different CO/CO<sub>2</sub> - mixtures. The extent of the reaction was found to depend on the CO/CO<sub>2</sub> - ratio. A nanophase WC-Co powder agglomerated at the micrometer scale was obtained after carburization in a 90%CO/10%CO<sub>2</sub> gas-mixture. ©1999 Acta Metallurgica Inc.

### INTRODUCTION

WC-Co cemented carbides are today an integral component of many industrial operations including mining, grinding and metal cutting. Their widespread use results from the composite properties of high hardness and toughness. The mechanical properties are strongly dependent on the microstructural scale, e.g. the hardness increases with decreasing carbide grain size. Conventional grades are made from powders with grain sizes typically within 1-10 µm. Several efforts to reduce the size down below 100 nm have been made during the last decade (1). Nanostructured powders have been prepared and evaluations of sintered materials shows improved properties as compared to the conventional grades. A critical step in the preparation of nano grade powders is to obtain an ideal mixture of the different components, i.e. uniformity of the composition on the nano scale. A feasible technique is to start from a homogenous precursor containing ions of W and Co mixed on the atomic scale. The precursor is converted to a uniform nanostructured WC-Co powder by reduction and carburization. One successful example is the spray conversion process developed at Rutgers University and Nanodyne (2,3). Precursor salts, prepared by spray drying of homogenous cobalt tungstate solutions, are processed to nanostructured WC-Co powders by gas-phase reduction/carburization in a fluidised bed. Homogenous precursors can also be obtained by co-precipitation techniques. One example is solid salts containing the Keggin anion [H<sub>2</sub>Co<sub>2</sub>W<sub>11</sub>O<sub>40</sub>]<sup>8-</sup> prepared from solutions of sodium tungstate (Na<sub>2</sub>WO<sub>4</sub>) or

ammonium metatungstate (  $(\text{NH}_4)_6[\text{H}_2\text{W}_{12}\text{O}_{40}]$  ) and cobalt acetate (4). The method is restricted to certain compositions close to the stoichiometry of the anion ( $\text{W}/\text{Co} \sim 5.5$ ). A second alternative is the precipitation of non-stoichiometric salts from suspensions ammonium paratungstate ( $(\text{NH}_4)_{10}[\text{H}_2\text{W}_{12}\text{O}_{42}]$  ) and cobalt hydroxide (5,6). The composition of these salts can be varied in a wider range by changing the relative amounts of the different starting materials. In this paper, we report the processing of such salt with the stoichiometry  $\text{W}/\text{Co} = 4.8$  corresponding to WC-Co materials containing 6 % Co. The aim has been to investigate the effect of several different processing parameters, such as temperature, time and atmosphere and to characterize the nanostructured W-Co and WC-Co powders obtained.

### EXPERIMENTAL PROCEDURE

A precursor salt containing 66 % W and 4.42 % Co, prepared by co-precipitation starting from ammonium paratungstate and cobalt hydroxide (5,6), was reduced at 600, 650 and 700 °C in  $\text{H}_2$ . The reduction times were 3 or 6 hrs. Powders reduced at 700 °C were directly carburized at 700 °C during 3 hrs in different mixtures of CO and  $\text{CO}_2$  (70%CO/30% $\text{CO}_2$ , 80%CO/20% $\text{CO}_2$ , and 90%CO/10% $\text{CO}_2$ ). The samples were heated (5°C/min) up to the reduction temperatures in  $\text{H}_2$  and left to cool in  $\text{N}_2$  after reduction or carburization. The total gas flow was about 400 ml/min. The powders were characterized using electron microscopy (SEM, TEM), X-ray diffraction (XRD) and multi – point BET.

### RESULTS AND DISCUSSION

The precursor was completely reduced at 700 °C and 650 °C after less than 3 hours and at 600 °C after less than 6 hours, as shown in Fig.1. The powder reduced at 600 °C for hours contained a mixture of W and  $\text{WO}_2$  phases. The specific surface area of the reduced powders was increasing with decreasing reduction temperature (8.7  $\text{m}^2/\text{g}$  at 700°C, 15  $\text{m}^2/\text{g}$  at 650°C and 18  $\text{m}^2/\text{g}$  at 600°C). The average particle size of the reduced powders, as calculated

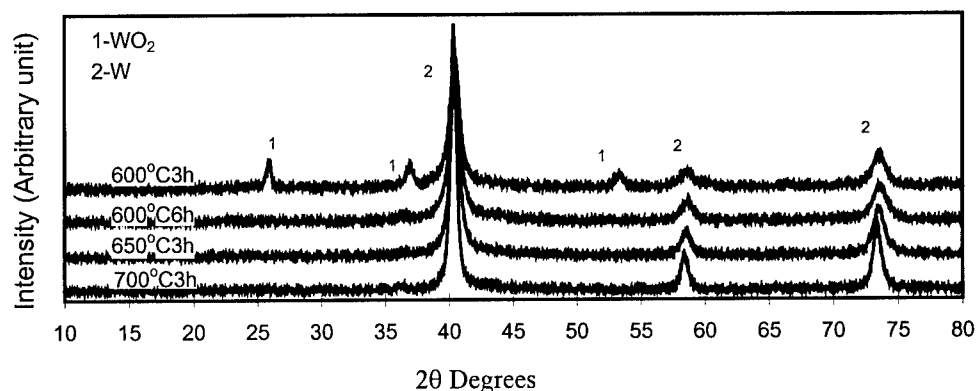


Fig.1, X-ray diffraction pattern of the powders reduced at different temperatures and times

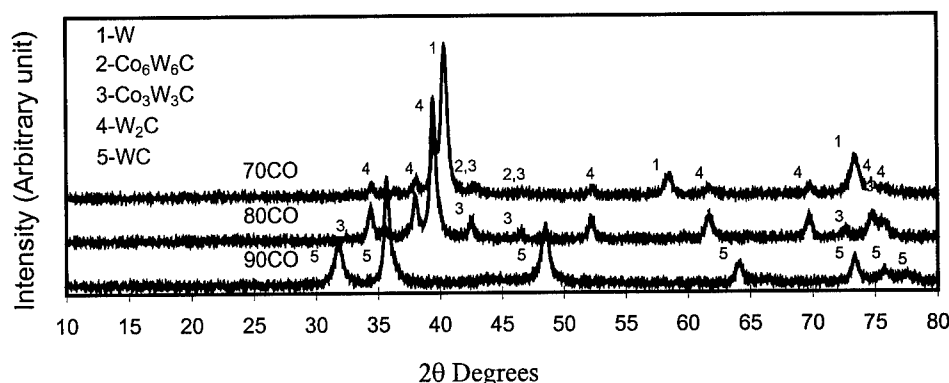


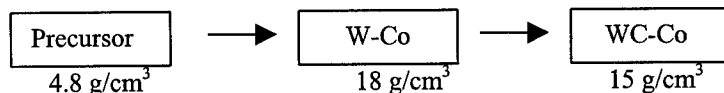
Fig.2, X-ray diffraction pattern of the powders carburized at 700 °C for 3 hours

from the BET- data, was 38 nm at 700 °C, 22 nm at 650 °C and 18 nm at 600 °C.

Powders reduced at 700 °C, were carburised in different CO/CO<sub>2</sub> mixtures at 700 °C for 3 hours. The phase constituents were found to vary with the CO/CO<sub>2</sub> ratio in the gas. A mixture of W, W<sub>2</sub>C, W<sub>6</sub>Co<sub>6</sub>C and/or W<sub>3</sub>Co<sub>3</sub>C was obtained using a gas mixture of 70 %CO and 30 % CO<sub>2</sub>. An increase in the concentration of CO up to 80% resulted in the formation W<sub>2</sub>C and W<sub>3</sub>Co<sub>3</sub>C. Full conversion to WC was obtained using 90%CO/10%CO<sub>2</sub> - atmosphere. The content of total carbon was determined to be 12 %, about twice the stoichiometric amount in WC. The increase in amount of bounded carbon with increasing CO/CO<sub>2</sub> ratios suggests a reaction path starting with metallic W-Co particles ending with a WC-Co mixture:



The particle size of the final WC-Co powder was measured by several methods. Calculations using the broadening of the XRD peaks resulted in 20-30 nm. The specific surface area (8.1 m<sup>2</sup>/g) corresponds to spherical particles with a size of about 50 nm. TEM micrographs showed a similar result. SEM and TEM micrographs also showed that the nano-grains formed agglomerates with size and shape similar to the original flake-like precursor salt particles (Fig. 3). The nanostructured WC-Co powder is formed from the precursor via a series of decomposition reduction and carburization reactions. The process involves a five-fold decrease in volume illustrated by the density change indicated below:



The micron-sized precursor particles are broken into smaller fragments. The fragments shrink further through reduction and carburisation reactions and finally nano-sized WC-Co particles in micrometer scale agglomerates are formed (Fig. 3)

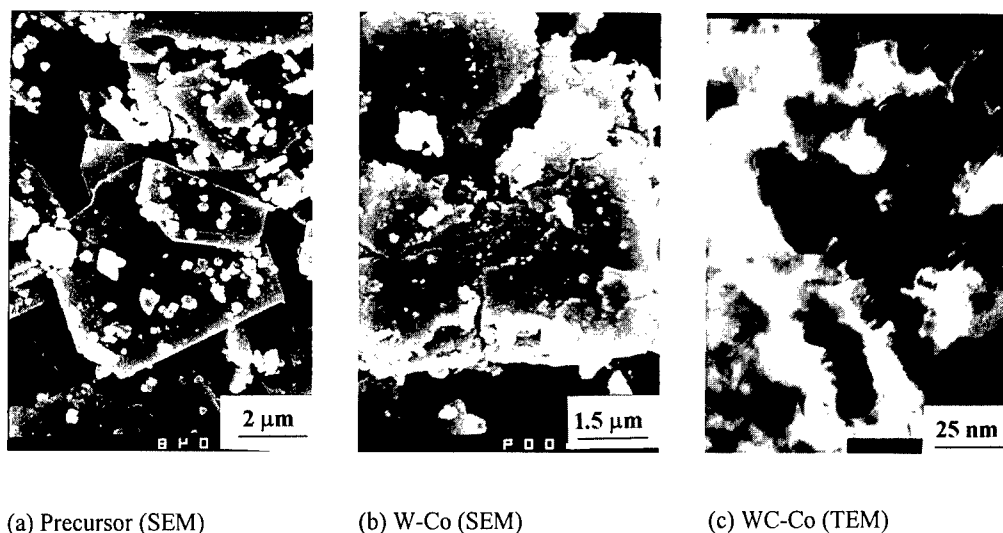


Fig.3, Micrographs of precursor, W-Co and WC-Co powders

### CONCLUSIONS

The specific surface area of the reduced powders increased with decreasing reduction temperature. The reduction temperature has a large influence on the particle size of the reduced powder. The rate of carburization in carbon monoxide - carbon dioxide atmospheres was found to be strongly depending on the ratio carbon monoxide / carbon dioxide. Nanostructured WC-Co powder in micron sized agglomerates was obtained after carburisation at 700 °C. The particle size decreased at least  $10^2$  times during processing from precursor to WC-Co powder.

### REFERENCES

1. Yao, Z., Stiglich, J.J. and Sudarshan, T.S., Metal Powder Report, March, 26 (1998)
2. Kear, B.H. and McCandlish, L.E., Nanostructured Mater. Vol.3, 19 (1993)
3. Seegopaul, P. and McCandlish, L.E., Metal Powder Report, April, 16 (1996)
4. Wahlberg, S., Grenthe, I. and Muhammed M., Nanostructured Mater., Vol.9, 105 (1997)
5. Muhammed, M., Wahlberg, S. and Grenthe, I., U.S. Pat. No. 5,594,929 (1997)
6. Wahlberg, S., Grenthe I. and Muhammed, M., manuscript in preparation.



Pergamon

NanoStructured Materials, Vol. 12, pp. 167-170, 1999

Elsevier Science Ltd

© 1999 Acta Metallurgica Inc.

Printed in the USA. All rights reserved

0965-9773/99/\$-see front matter

PII S0965-9773(99)00090-2

## MICROSTRUCTURE AND PHASE COMPOSITION OF MECHANICALLY ALLOYED AND HOT PRESSED Ti-Al ALLOYS

E. Szewczak<sup>a</sup>, A. Presz<sup>b</sup>, A. Witek<sup>b</sup>, J.W. Wyrzykowski<sup>a</sup>, H. Matyja<sup>a</sup>

<sup>a</sup>Department of Materials Science and Engineering, Warsaw University of Technology  
Narbutta 85, 02-524 Warsaw, Poland

<sup>b</sup>High Pressure Research Center „UNIPRESS”, Polish Academy of Science, Sokołowska  
29/37, 01-142 Warsaw, Poland

**Abstract** - Elemental mixtures of  $Ti_xAl_{100-x}$  ( $x=75, 50, 35$  at.%) were mechanically alloyed in a vibratory ball mill and then hot pressed. This permitted us to obtain fully dense bulk samples of Ti-Al intermetallics with a grain size of the order of  $10^2$  nm. The microhardness of the samples was about 500-900 HV 0,2 according to the composition and no brittle cracking was observed during the microhardness measurements. Scanning electron microscopy linked with energy dispersive spectroscopy was used for the structural and compositional analysis. ©1999 Acta Metallurgica Inc.

### INTRODUCTION

Mechanical alloying (MA) is a technique offering an opportunity not only for microstructural refinement but also for producing material of highly homogeneous structure and composition. Unfortunately the MA powders are difficult to compact and require high pressures and temperatures. The unique microstructure produced by MA can be destroyed during prolonged heating, which can lead to coarsening of the microstructure and can destroy chemical homogeneity. The aim of this work was to present the results of hot pressing of mechanically alloyed Ti-Al alloys and to show how their microstructure and phase composition are affected by this method.

### EXPERIMENTAL PROCEDURE

Elemental blends of Al of 99.8% purity and Ti of 99.5% purity, with the compositions  $Ti_xAl_{100-x}$  ( $x=75, 50, 35$  at.%) were mechanically alloyed for 120 hours in a vibratory ball mill, with stainless steel vial and balls. No process control agents were used. The powders were loaded into vials under an argon atmosphere. After MA, the powders were consolidated by hot pressing under a pressure of 4 GPa at a temperature of 900°C.

The powders after MA and the consolidated compacts were characterised by X-ray diffraction (XRD) using  $CuK\alpha$  radiation. Scanning electron microscopy (SEM) linked with energy dispersive spectroscopy (EDS) were used for the structural and compositional



analysis of compacts. Microhardness tests were performed using a ZWICK tester with a load of 200 G (HV0.2) applied for 15 s.

## RESULTS AND DISCUSSION

XRD patterns of all the Ti-Al powders after 120 h of milling (Fig. 1) indicate that the supersaturated h.c.p. Ti(Al) solid solution has formed. In the  $\text{Ti}_{75}\text{Al}_{25}$  (Fig. 1a) and  $\text{Ti}_{35}\text{Al}_{65}$  (Fig. 1c) alloys a contribution of an amorphous phase is in addition observed. In the  $\text{Ti}_{35}\text{Al}_{65}$  alloy the presence of the f.c.c. Al(Ti) phase is also probable (1). During consolidation, phase transitions have taken place. XRD patterns of the samples subjected to hot pressing are shown in Fig. 1d-f.

The SEM image of the  $\text{Ti}_{75}\text{Al}_{25}$  alloy (Fig. 2a) shows two kinds of regions: dark and light. Both of them have the same composition as analyzed by EDS and both seem to be composed of fine grains of about 250 nm. The XRD pattern of this sample (Fig. 1d) indicates that the alloy is composed at least of two phases. One was identified as  $\text{Ti}_3\text{Al}$  with the lattice parameter  $a=5.81 \pm 0.02 \text{ \AA}$  and  $c=4.71 \pm 0.02 \text{ \AA}$ . The peaks marked as "1", "2" and "3" can be interpreted in two ways. If we assume that all these peaks represent the same phase and index them as the hexagonal phase, we obtain the lattice parameters:  $a=4.84 (\pm 0.06) \text{ \AA}$ ,  $c=2.75 (\pm 0.06) \text{ \AA}$ , which are close to the parameters of high-pressure  $\omega$ -Ti form  $a=4.625 \text{ \AA}$ ,  $c=2.813 \text{ \AA}$ , related in (2) as remaining after the release of pressure. Taking into account the EDS and SEM results, phase represented by "1", "2" and "3" peaks should be composed of about 75% Ti and 25% Al, and thus it may be the  $\omega$ -Ti(Al) solid solution.

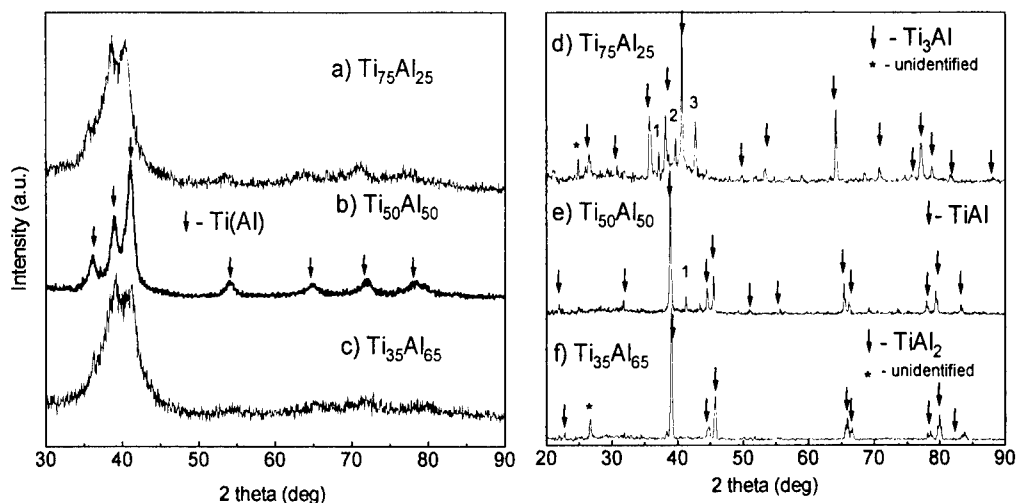


Fig. 1 XRD patterns of (a-c)- powders after 120 h of MA and (d-f)- samples after hot pressing.

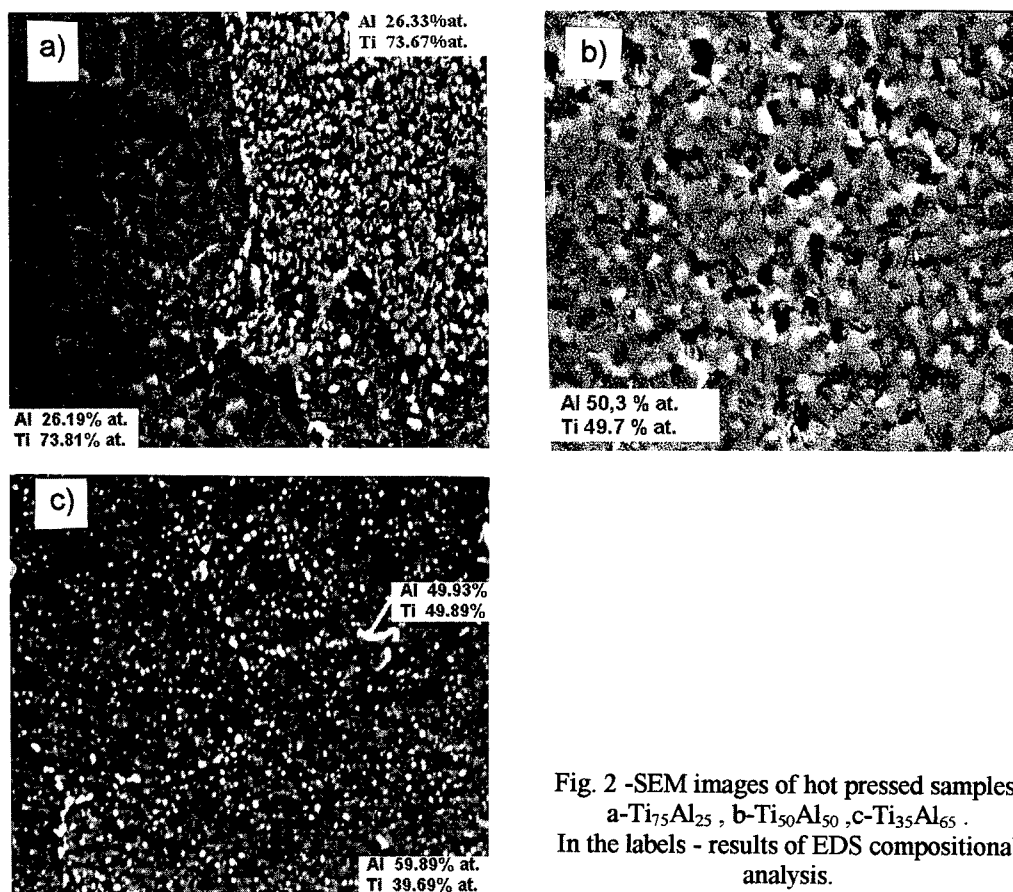


Fig. 2 -SEM images of hot pressed samples:  
a-Ti<sub>75</sub>Al<sub>25</sub>, b-Ti<sub>50</sub>Al<sub>50</sub>, c-Ti<sub>35</sub>Al<sub>65</sub>.  
In the labels - results of EDS compositional analysis.

Assuming that "1", "2" and "3" peaks do not represent the same phase, peaks "1" and "3" could be interpreted as coming from the TiN phase. Peak "2" agrees with the 100% intensity Al<sub>2</sub>Ti<sub>4</sub>C<sub>2</sub> peak. This interpretation is not, however, in good agreement with the EDS results, since this method should detect carbon.

In the case of the Ti<sub>50</sub>Al<sub>50</sub> alloy (Fig. 1e), the main phase obtained after hot pressing is AlTi. The low intensity peak marked as "1" is the 100% intensity peak of the Ti<sub>3</sub>Al phase. The crystallite size evaluated from the X-ray peak broadening (Tab.1) is not in conformity with the SEM image (Fig.2b) unless we would realize that the light and dark regions of about 600 nm in the SEM image may be composed of a few coherently diffracting domains whose size has been determined from the X-ray diffraction pattern.

Hot pressed Ti<sub>35</sub>Al<sub>65</sub> alloy is mainly composed of the TiAl<sub>2</sub> phase with HfGa<sub>2</sub> structure (3) and the lattice parameters  $a=3.99(\pm 0.03)$  and  $c=24.29(\pm 0.03)$  Å. Some depleted-of-Al precipitations, probably of AlTi phase, whose peaks partly overlap the peaks of the TiAl<sub>2</sub> phase are visible in the SEM image of the sample (Fig. 2c). Precipitations seems to be distributed in a specific way - most likely at the boundaries of the pressed powder particles, which indicates

TABLE 1

Densities and Microhardness Values and Crystallite Size Evaluated from XRD Peaks Broadenings (4) of Samples After Hot Pressing (For Comparison, Table Also Gives Values Obtained for Samples After Explosive Compaction (5)).

Technique	Hot pressing			Explosive compaction	
Composition	Ti <sub>75</sub> Al <sub>25</sub>	Ti <sub>50</sub> Al <sub>50</sub>	Ti <sub>35</sub> Al <sub>65</sub>	Ti <sub>75</sub> Al <sub>25</sub>	Ti <sub>50</sub> Al <sub>50</sub>
Density [g/cm <sup>3</sup> ]	4.24 (±0.02)	3.81 (±0.03)	3.59 (±0.02)	3.8 (±0.1)	3.3 (±0.12)
Microhardness [kg/mm <sup>2</sup> ] (standard deviation)	856 (112)	524 (13)	640 (23)	592 (72)	568 (48)
Crystallite size (nm)	223	177	-	-	-

that the surface of the powder has been depleted of Al. It is difficult to evaluate the crystallite size because the peaks overlap. In the SEM image (Fig.2c) the average grain size is about 200 nm. EDS analysis indicates the presence of 0.18% - 0.42% of Fe in the alloy. The Ti<sub>35</sub>Al<sub>65</sub> powder, rich in Al, is more liable to coating the vial and balls than other compositions, and this could be the reason of the increased Fe content.

All the samples were fully dense and showed high hardness (Tab.1). No cracks were observed around the impressions of the indenter after the microhardness test which evidenced an increased ductility.

## CONCLUSIONS

Mechanical alloying combined with hot pressing permits producing fully dense bulk samples of Ti<sub>3</sub>Al, TiAl and TiAl<sub>2</sub> intermetallics. The samples have a fine grained microstructure and no brittle cracking was observed during the microhardness tests, which indicates to an increased ductility.

## ACKNOWLEDGMENTS

This work was supported by the grant No. 7T08A02412 of the Science Research Committee.

## REFERENCES

1. A.V. Leonov, E. Szewczak, O.E. Gladilina, H.Matyja, V. I. Fadeeva, Mater. Sci. Forum, 235-238, 67, (1997).
2. W.B. Pearson, "Handbook of lattice spacings and structures of metals", Pergamon Press (1967), p. 1280.
3. Mabuchi, T. Asai, Y. Nakayama, Scr. Metall. Mater., 23, 685, (1989).
4. G.K. Williamson, W.H. Hall, Acta Metall., 3, 473, (1953).
5. E.Szewczak, J.Paszula, A.Leonov, H.Matyja, Mater. Sci. Eng., A226-228, 115, (1997)



Pergamon

NanoStructured Materials, Vol. 12, pp. 171-174, 1999

Elsevier Science Ltd

© 1999 Acta Metallurgica Inc.

Printed in the USA. All rights reserved

0965-9773/99/\$-see front matter

PII S0965-9773(99)00091-4

## INFLUENCE OF THE MECHANICAL ALLOYING PARAMETERS ON CRYSTALLITE SIZE OF Ti-Al POWDERS

E. Szewczak, J.W. Wyrzykowski

Department of Materials Science and Engineering, Warsaw University of Technology  
Narbutta 85, 02-524 Warsaw, Poland

**Abstract** - Nanocrystalline  $Ti_xAl_{100-x}$  ( $x=75, 50, 40, 35$  at.%) alloys were prepared by mechanical alloying. The influence of milling parameters (the milling equipment, milling time and energy) on the crystallite size of the alloys obtained as well as on the thermal stability of the crystallite size was examined. The powders were characterized by X-ray diffraction, scanning differential calorimetry and transmission electron microscopy. Attention was also paid to the influence of the phase transitions during heating of milled powders upon the crystallite size of the product. ©1999 Acta Metallurgica Inc.

### INTRODUCTION

It is well known that mechanical alloying (MA) is a new process for producing nanocrystalline alloys. Thanks to the very fine and stable dispersoids, and the high density of lattice defects produced during MA, the grain growth during hot consolidation is expected to be limited. The ultimate grain size of MA and hot consolidation products depends on the intrinsic properties of the material (e.g. the kinetics of recovery and recrystallization) and on processing conditions including milling parameters, such as time and energy or the kind of mill. Milling parameters affect not only grain size of the as-milled alloy, but also the thermal stability of this grain size. MA usually allows us to produce metastable phases, which, when heated, undergo phase transitions. The kind of the transition depends on the alloy composition and is another factor affecting the grain size of the product.

In this work, the influence of milling parameters and the composition of Ti-Al alloys on the crystallite size of mechanically alloyed and then heat treated alloys was examined.

### EXPERIMENTAL PROCEDURE

Elemental blends of Al of 99.8% purity and Ti of 99.5% purity, with the compositions  $Ti_xAl_{100-x}$  ( $x=75, 50, 40, 35$  at.%) were mechanically alloyed in three kinds of mills: vibratory with a ball-to-powder weight ratio of 8:1, a high energy planetary mill with a ball-to-powder weight ratio of 20:1 and Fritsch planetary mill with a ball-to-powder weight ratio of 10:1. No process control agents were added. Powders were loaded into vials under an argon

atmosphere. The powders were characterised by X-ray diffraction (XRD) using  $\text{CuK}\alpha$  and  $\text{CoK}\alpha$  radiations. The grain size was evaluated from XRD peak broadenings (1). The typical error in this evaluation did not exceed 10%. Transmission electron microscopy (TEM) observations were made in a PHILIPS EM 300. Heat treatment was performed in a Perkin-Elmer DSC analyser at a heating rate of  $20^\circ\text{C}/\text{min}$ .

## RESULTS AND DISCUSSION

Milling of all the powders in a vibratory mill for 100 h resulted in the formation of h.c.p. Ti(Al) solid solutions (Fig.1a-d). In the  $\text{Ti}_{35}\text{Al}_{65}$  alloy a certain contribution of amorphous phase was observed (Fig.1d).

The metastable products of MA of all the compositions underwent phase transitions during heating. Except  $\text{Ti}_{75}\text{Al}_{25}$  alloy, where the hexagonal  $\text{Ti}_3\text{Al}$  compound has been obtained (Fig.1e), in the other compositions exothermic transitions of hexagonal to cubic and then to tetragonal phase occurred (Fig.1f-h). It has been shown (3,4), that the mechanism of the h.c.p.  $\rightarrow$  f.c.c. transition can be explained in terms of the stacking fault formation phenomenon. The density of stacking faults, which in the h.c.p. lattice represent the layers of the f.c.c. phase, increases with increasing Al content (3). Stacking faults can be the nuclei for f.c.c. phase so that the greater the density of stacking faults before heating, the smaller the grains of alloys obtained after heating. The results given in Tab.1 are consistent with this hypothesis. Evaluation of the grain size of powders just after milling, by the Hall method (1) is not possible because the stacking faults cause non-linear Williamson-Hall plots (2) (Fig.2). Thus, the grain sizes of  $\text{Ti}_{75}\text{Al}_{25}$  and  $\text{Ti}_{50}\text{Al}_{50}$  were characterized by TEM and appeared to be about 40 nm in the former and 30 nm in the latter alloy. Although the difference is not

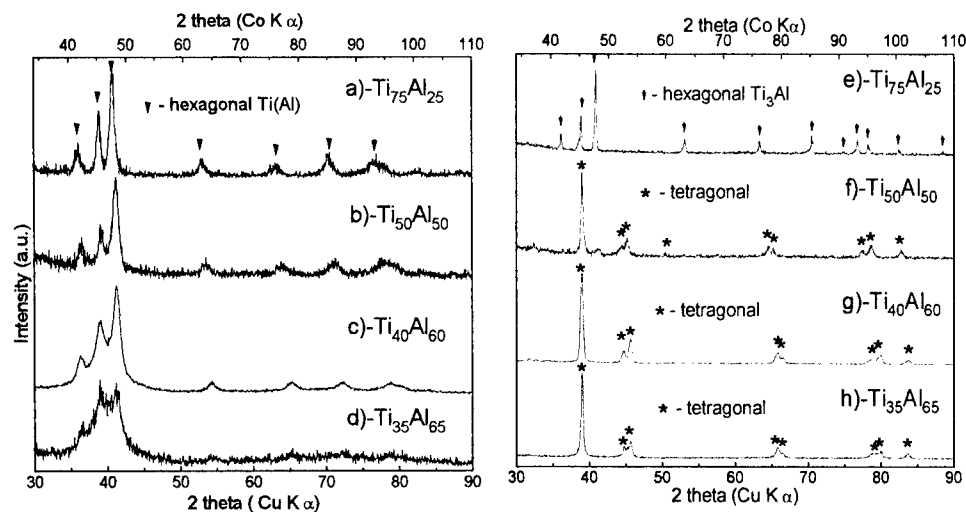


Fig. 1. XRD patterns of Al-Ti powders: a-d - directly after 100 h of milling in a vibratory mill; e-h - after milling and heating in a calorimeter (a,b,e,f -  $\text{CoK}\alpha$ ; c,d,g,h -  $\text{CuK}\alpha$  radiation).

TABLE 1

Crystallite Sizes of Alloys of Various Compositions After 100 h of Milling and Heating in a Calorimeter up to 720°C.

Composition	Ti <sub>75</sub> Al <sub>25</sub>	Ti <sub>50</sub> Al <sub>50</sub>	Ti <sub>40</sub> Al <sub>60</sub>	Ti <sub>35</sub> Al <sub>65</sub>
Crystallite size (nm)	180	61	50	36

TABLE 2

Effect of Milling Time and Kind of Mill on Crystallite Size of Alloys of Various Compositions After Milling and Heating in Calorimeter up to 720°C.

Composition	Ti <sub>75</sub> Al <sub>25</sub>	Ti <sub>35</sub> Al <sub>65</sub>	Ti <sub>50</sub> Al <sub>50</sub>				
Kind of mill	vibratory	vibratory		vibratory	planetary	high energy planetary	
Milling time (h)	Cryst. size(nm)	Cryst. size(nm)	Milling time (h)	Cryst. size (nm)	Cryst. size (nm)	Milling time (h)	Cryst. size (nm)
70	295	65	100	61	76	7	88
100	180	36	150	46	23	8	63
120	80	-	200	45	26		

significant, after heat treatment it becomes much greater, which can be related to the absence of the h.c.p. → f.c.c. transition in Ti<sub>75</sub>Al<sub>25</sub> alloy.

Until the milling time, which is characteristic of each alloy composition, was reached, the material coated the vial and balls and no free particles of powder were observed. With the Ti<sub>75</sub>Al<sub>25</sub> and Ti<sub>35</sub>Al<sub>65</sub> compositions the first powder in a vibratory mill appeared after about 70 hours, while with the Ti<sub>50</sub>Al<sub>50</sub> composition only after 100 hours of milling.

Fig.2 shows Williamson-Hall plots for Ti<sub>50</sub>Al<sub>50</sub> alloys after milling in two kinds of mills and for various times of milling. The slope of the plot is directly proportional to the strain and y-intercept is inversely proportional to the crystallite size, so that these plots can be used for visual indication of character of defect changes. One can see that the plots have changed after different times of milling (strains increase and grain size decreases with increasing milling time). After heat treatment the plots become almost linear (considerable decrease of the stacking fault density) and their slopes are of the order of 10<sup>-4</sup>.

The influence of milling time on the crystallite size is rather evident (Tab. 2). The differences between the grain size of powders milled in a vibratory and Fritsch mill are not significant. In both cases (002) peak breadths after 200 h of milling become incommensurable large compared with the other peak breadths (Fig.2). This is probably the influence of some contribution of the amorphous phase.

A alloy, which after heating has crystallite size below 100 nm can be obtained as early as after 7 hours in a high energy planetary mill, but only studies of its mechanical properties, thermal stability of its grain size and the homogeneity of the alloy could answer whether it is advantageous to use such high energies. It has been shown in (5), that the most homogeneous and stable nanocrystalline alloys can be produced by milling methods that require less energy but longer milling times. On the other hand, if the milling time is too long, the probability of introducing impurities (including Fe from the vial and balls) increases.

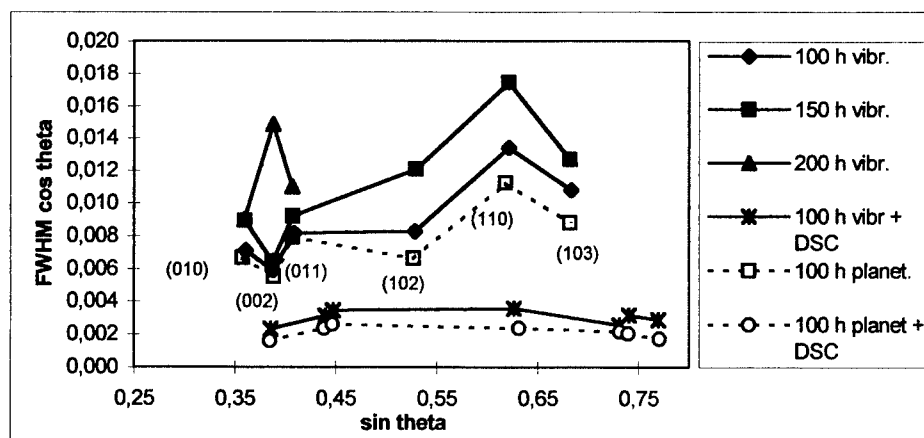


Fig.2. Williamson-Hall plots for  $\text{Ti}_{50}\text{Al}_{50}$  samples after milling in vibratory and planetary mills and after heating in a calorimeter

### CONCLUSIONS

Crystalite size of Ti-Al alloys after milling and subsequent heating strongly depends on the alloy composition, which can be related not only to the differences in deformation and strengthening mechanisms, but also to the type of phase transitions during heating.

Crystalite size of the alloys milled planetary and vibratory and then heat treated, decreases with increasing milling time but after certain time reaches an almost constant value.

Effect of the kind of mill is not pronounced, except with a high energy planetary mill in which the time required for the alloy to achieve the desired crystallite size is about ten times as short as that needed in the other mills used.

### ACKNOWLEDGMENTS

This work was supported by the 7T08A02412 grant of Science Research Committee.

### REFERENCES

1. G.K. Williamson, W.H. Hall, *Acta Metallurgica* **1**, 22 (1953)
2. F.W. Gayle, F.S. Biancaniello, *NanoStructured Materials*, **6**, 429, (1995)
3. A.V. Leonov, E. Szewczak, O.E. Gladilina, H. Matyja, V. I. Fadeeva, *Mater. Sci. Forum* **235-238**, 67, (1997)
4. T. Fujii, K. Ameyama, *Mater. Sci. Forum* **235-238**, 451, (1997)
5. J.-H. Ahn, H. Chung, *Materials and Manufacturing Processes*, **9**, No.4, 637, (1994)



Pergamon

NanoStructured Materials, Vol. 12, pp. 175–178, 1999

Elsevier Science Ltd

© 1999 Acta Metallurgica Inc.

Printed in the USA. All rights reserved

0965-9773/99/\$—see front matter

PII S0965-9773(99)00092-6

## FABRICATION OF POLYCARBOSILANE-DERIVED SiC BULK CERAMICS BY CARBOTHERMIC REDUCTION

— Effect of Green Density on Crystallinity of Pyrolyzed Compacts —

Ken-ichi Kakimoto<sup>1</sup>, Fumihiro Wakai<sup>1</sup>, Joachim Bill<sup>2</sup> and Fritz Aldinger<sup>2</sup>

<sup>1</sup>Ceramics Superplasticity Project, ICORP, Japan Science and Technology Corporation

JFCC 2F, 2-4-1, Atsuta-ku, Nagoya 456-8587, Japan

<sup>2</sup>Max-Planck-Institut für Metallforschung, Pulvermetallurgisches Laboratorium

Heisenbergstraße 5, 70569 Stuttgart, Germany

**Abstract** — We have recently demonstrated that the fabrication of SiC bulk ceramics with various atomic ratio of Si:C:O is achieved by pyrolysis and subsequent heat treatment of shaped polycarbosilane (PCS) compacts after controlling oxygen content. The procedure is a novel processing route of the combination of polymer precursor techniques, powder technological process and high-temperature material chemistry. This paper deals with the investigation of the effect of the green density and specimen size on the crystallization and densification behavior during the pyrolysis conversion from polymer into ceramic grade. It is reported that the pyrolyzed PCS compact with a higher green density shows a finer microstructure and a smaller pore size. ©1999 Acta Metallurgica Inc.

### INTRODUCTION

Polycarbosilane (PCS) has been widely used as a precursor polymer for preparing nano-structured SiC ceramics in several forms of powders, binders, coatings, whiskers, fibers and composite's matrix sources. Most of the fabrication procedures follow the pioneering work done by Yajima and his co-workers on continuous long fibers: the melt-spinning of PCS to form green filaments, the chemical cross-linking by oxygen to make them infusible and their pyrolysis conversion into ceramic fibers at elevated temperatures (1). The microstructure of such materials varies depending on their thermal history. The general trends with increasing temperature are: amorphous solid, small  $\beta$ -SiC crystals (<2 nm) with amorphous carbon and SiC<sub>x</sub>O<sub>y</sub> intergranular phase, then large  $\beta$ -SiC grains with graphite and small amounts of amorphous SiC<sub>x</sub>O<sub>y</sub> (2). The decrease in the molar fraction of amorphous SiC<sub>x</sub>O<sub>y</sub> with increasing temperature results from the phase transition into  $\beta$ -SiC with a release of CO and SiO gases. This decomposition occurs according to the carbothermic reduction mechanism which has been commercially applied for the production of fine  $\beta$ -SiC powder from SiO<sub>2</sub> and C powder mixture. Therefore, an appropriate conversion of some amount of the SiC<sub>x</sub>O<sub>y</sub> phase into  $\beta$ -SiC crystals can be expected to produce distinctive PCS-derived ceramics with various compositions and



microstructures. In the preceding paper, we have first demonstrated that the fabrication of SiC bulk ceramics with various atomic ratio of Si:C:O is achieved by pyrolysis and subsequent heat treatment of shaped PCS compacts (3). Oxidation of the starting PCS powder was found to support densification of the compact during pyrolysis.

The present study focuses on the effect of green density and specimen size on crystallization and densification during the pyrolysis conversion from polymer into ceramic grade by using one source of oxidized PCS powder.

### EXPERIMENTAL

Fine PCS powder (Nippon Carbon Co., Ltd., Japan) was used as a raw material. PCS consists of two part constituent  $\text{MeSiHCH}_2$  and  $\text{Me}_2\text{SiCH}_2$ . Prior to the production of compacts, PCS powder was carefully heat-treated below  $180^\circ\text{C}$  in air to form Si-O-Si cross linkages within the molecular structure. This treatment rendered infusibility of PCS so that the shape of the compacts was retained during the pyrolysis step. In this study, total cross-linking period of 100 min was applied to prepare the powder (PCS-6) whose composition became  $\text{SiC}_{1.36}\text{O}_{0.26}$  after pyrolysis (3). PCS-6 was ground, then cold-isostatically pressed with rubber molds at a final pressure of 625 MPa to form three kinds of cylindrical green compacts, PCS-6A, -6B and -6C. They are characterized by different size and/or green density, as indicated in Table 1. PCS-6B showed a slightly higher density than PCS-6A owing to size effects. To obtain a much higher density than PCS-6B, PCS-6C was prepared by an initial isostatic pressing the powder at 200 MPa, followed by repressing without a mold at 625 MPa.

The compacts were pyrolyzed in a quartz tube under Ar flow at  $1300^\circ\text{C}$  with a heating rate of  $2^\circ\text{C}/\text{min}$  and a holding time of 60 min. The pyrolyzed compacts were characterized by X-ray diffraction (XRD) analysis and mercury porosimetry.

### RESULTS AND DISCUSSION

During pyrolysis up to  $1200^\circ\text{C}$ , PCS is converted completely into an inorganic amorphous solid by demethanation and dehydrogenation. At higher temperatures  $\beta$ -SiC forms with the evolution of CO and SiO gases (4). Figure 1 shows that  $\beta$ -SiC diffraction peaks broaden and the intensities decreases with increasing green density of powder compacts, indicating the decrease of the crystallinity. A line broadening analysis of the (111) peak revealed

TABLE 1  
Characterization of Cylindrical Green Compacts

Sample	Diameter (mm)	Height (mm)	Density ( $\text{g}/\text{cm}^3$ ) <sup>†</sup>
PCS-6A	10	10	0.94
PCS-6B	5	5	0.98
PCS-6C	5	5	1.10

<sup>†</sup> defined as mass per unit volume.

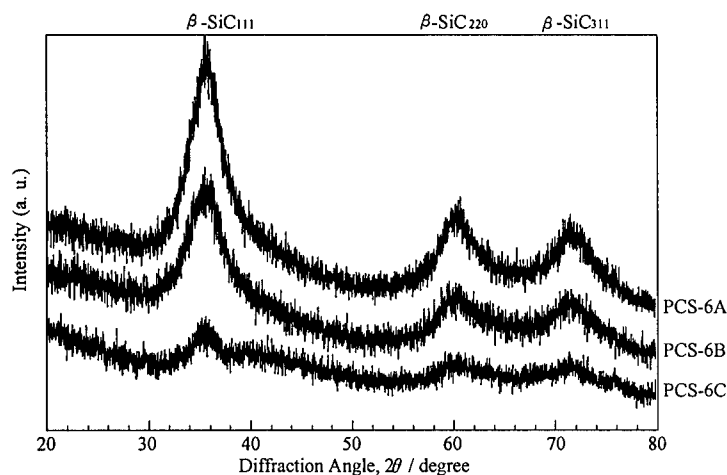


Figure 1. XRD patterns of pyrolyzed PCS-6A, -6B and -6C.

grain sizes of 3.3, 2.7 and 1.8 nm for PCS-6A, -6B and -6C, respectively.

The crystallization of an amorphous solid involves two stages: nucleation and the subsequent growth of the crystalline phase. Thermodynamically, the compact density can be regarded as a temperature-equivalent parameter in influencing the free-energy barriers for nucleating the crystallization (5). As compact green density increases, the enhanced concentration of nuclei available promotes the crystallization. For this reason, higher green compact density often leads to intense grain growth at lower temperatures. However, it is interesting to note that the present work demonstrated the opposite trend. While the above theory may be true in situations where the materials are conventional amorphous solids, it might not hold in the case of polymer-derived materials. The reason is that the releasing behavior of pyrolytic gases seems to correlate substantially with the crystallization behavior, as the following speculation: the pyrolytic gas diffuses out less smoothly from the compact with a high green density, and thereby suppresses the successive gas evolution with a rise in internal gas pressure, so that  $\beta$ -SiC formation is delayed. This proposed mechanism would best accommodate that PCS-6C kept the finest crystallinity of the specimens examined. Comparison of the XRD results among the three kinds of compacts indicates as well that the crystallinity of pyrolyzed compacts was affected mainly by the green density rather than the specimen size, since PCS-6C demonstrated a finer microstructure than PCS-6B despite both green compacts had the same specimen size. It is therefore believed that an increase in green compact density is helpful to keep its fine microstructure at higher temperatures.

Figure 2 confirms that the most frequent pore diameter of the pyrolyzed compact is reduced also by increasing density of the green compact, while all compacts show similar pore distributions in size beyond  $10\ \mu\text{m}$  due to the edge effect of packing. PCS-6C, with the highest green compact density, demonstrates the smallest mean pore size of the pyrolyzed compacts examined. Such small pore-size distribution seems likely to have already formed in the state of the green compact, since a higher packing density should lead to a smaller mean pore size in the

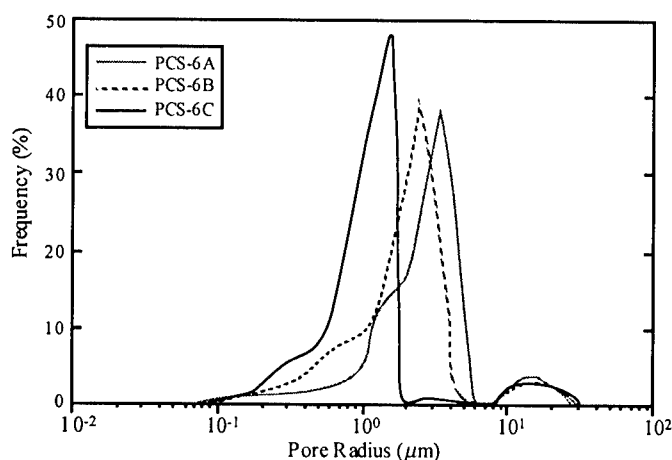


Figure 2. Pore-size distributions of pyrolyzed PCS-6A, -6B and -6C.

green compact. Therefore, it is possible to consider that the highest packing density provided the smallest mean pore size as well as the finest microstructure for PCS-6C after pyrolysis.

### CONCLUSION

Fabrication of polymer-derived bulk ceramics starts by using thermodynamically non-equilibrium precursor powder which is pyrolyzed into amorphous solid with a gas release during the ceramic conversion. The crystallization of the amorphous solid is obviously different from other conventional amorphous ceramics in that the crystallization is less excited with increasing green compact density. Therefore, higher densities are essential to obtain pyrolyzed compacts with finer microstructures and smaller pore sizes.

### REFERENCES

1. Yajima, S., Okamura, K., Hayashi, J. and Omori, M., *J. Am. Ceram. Soc.*, 1976, 59, 324.
2. Monthieux, M. and Delverdier, O., *J. Eur. Ceram. Soc.*, 1996, 16, 721.
3. Kakimoto, K., Wakai, F., Bill, J. and Aldinger, F., in *Proceedings of the 6th International Symposium on Ceramic Materials and Components for Engines*, eds. K. Niihara *et al.*, Japan Fine Ceramics Association, 1997, Arita, p. 866.
4. Hasegawa, Y. and Okamura, K., *J. Mater. Sci.*, 1983, 18, 3633.
5. Kingery, W. D., Bowen, H. K. and Uhlmann, D. R., *Introduction to Ceramics*, 2nd ed., Wiley, New York, 1976, p. 320.



Pergamon

NanoStructured Materials, Vol. 12, pp. 179–182, 1999

Elsevier Science Ltd

© 1999 Acta Metallurgica Inc.

Printed in the USA. All rights reserved

0965-9773/99/\$-see front matter

PII S0965-9773(99)00093-8

## NANOCRYSTALS AS DESTRUCTIVE ADSORBANTS FOR MIMCS OF CHEMICAL WARFARE AGENTS

E.M. Lucas, K.I. Klabunde

Department of Chemistry, Kansas State University  
Manhattan, KS 66506, USA

**Abstract** – Hexafluoropropylene (HFP), is destructively adsorbed with specially prepared nanoscale magnesium oxide powders producing  $\text{MgF}_2$ , CO,  $\text{CO}_2$  and graphite. The reaction occurs best at 450°C with a 2:1 surface oxide-to-HFP ratio. The reaction is monitored using pulsed U-tube reactors which shows the elution of large amounts of CO and  $\text{CO}_2$ , which steadily decreases as the surface oxides are depleted. The elution of small amounts of  $\text{C}_2\text{F}_4$  is also seen close to the breakthrough point of the reaction. The solid product is partially enclosed in graphite and has a 2:1 ratio of MgO to  $\text{MgF}_2$ , confirmed by elemental analysis. Powder XRD shows only the presence of  $\text{MgF}_2$  in the solid, indicating the MgO has lost all crystallinity during the reaction. FT-IR of the solid during and after reaction indicates the presence of  $\text{CF}_2$  and hexafluoropropylene epoxide as intermediates.

©1999 Acta Metallurgica Inc.

### INTRODUCTION

High surface area metal oxide particles have been shown to destructively adsorb chlorinated hydrocarbons.(1,2,3) These reactions produce non-toxic  $\text{CaCl}_2$  and various carbon oxides which make these high surface area metal oxides prime candidates for study in the disposal of simple halocarbons. High surface area MgO has also been used to destructively adsorb various organophosphorous mimics of "warfare agents."(4) In this same capacity, hexafluoropropylene ( $\text{C}_3\text{F}_6$ ) is a prime candidate for this type of study.

The metal oxide chosen is magnesium oxide. The Lewis base sites on the nanoparticle MgO react well with perfluorovinyl groups, which in this case is further enhanced by the electron withdrawing effects of the trifluoromethyl group. The magnesium oxide is produced by an aerogel method in which the  $\text{Mg}(\text{OH})_2$  gel undergoes hypercritical drying and is then calcined to 500°C. The resulting nanoparticles have surface areas of approximately 300–400  $\text{m}^2/\text{g}$  and average crystallite sizes of 4 nm.

## EXPERIMENTAL SECTION

### *Gas Chromatograph Pulse Reactor*

These experiments allowed separation and quantification of gaseous products as they came off the surface of the MgO. A pyrex U-tube containing MgO (0.125g) was attached to a gas chromatography instrument (Gow Mac series 580) such that when the gaseous HFP was injected, it would flow over the powder and then into the column (Alltech Porapak Q 80/100) kept at 75°C for product separation. Injection quantities were 0.5 ml at 20 psi (approx.  $2.78 \times 10^{-5}$  mol/inj) with the injector at 120°C. The reactor tube was heated to the desired temperature using a furnace, the reactants and products were moved by Helium carrier gas (20 ml/min). Products were detected by a thermal conductivity detector set at 110 mv and 180°C. Retention times for the varying elutants were CO: 1:20 min., CO<sub>2</sub>: 1:35 min., C<sub>2</sub>F<sub>4</sub>: 4:12 min., C<sub>3</sub>F<sub>6</sub>: 6:18 min.

### *Reagents*

Aerogel prepared MgO preparation has been described previously (5). Amounts used for pulse reactor experiments (0.09g - 0.12g) were adjusted so that the number of surface moles MgO were kept constant ( $6.95 \times 10^{-4}$  moles) which allowed for 25 injections of HFP forming a 1:1 surface oxide to HFP mole ratio. The number of surface moles was determined using a previously described procedure. (6)

### *Infrared Spectroscopy*

Studies were performed using special cell which allowed monitoring of reaction without moving of sample in beam, this way the same point was always being studied. Mg(OH)<sub>2</sub> is pressed on a tungsten grid connected to a temperature controller then calcined to 500°C. The grid is then heated to the desired temperature (studies done from 25°C - 450°C) and exposed to 5 Torr of gaseous HFP, after which the cell is evacuated to  $10^{-5}$  Torr. The instrument is a Mattson R/S-1 FT-IR spectrometer with an MCT liquid nitrogen cooled detector.

## RESULTS

### *G.C. Pulse Reactions*

Reactions were carried out from room temperature to 500°C. Optimal results were obtained at 450°C where the breakthrough number, the number of injections before HFP began appearing in the products, was 12. At this point the surface is considered almost depleted of reactive sites. This relates to approximately two surface MgO's per mole HFP injected. Figure 1 shows a graph of the cumulative number of moles HFP destroyed per surface mole of MgO. The black line indicates the ideal if all moles were destroyed in a 1:1 ratio, from this it is readily obvious where each reaction temperature deviates from the ideal. For the full 25 injections 83% of the HFP is destroyed at 450°C. The reaction at 500°C does slightly

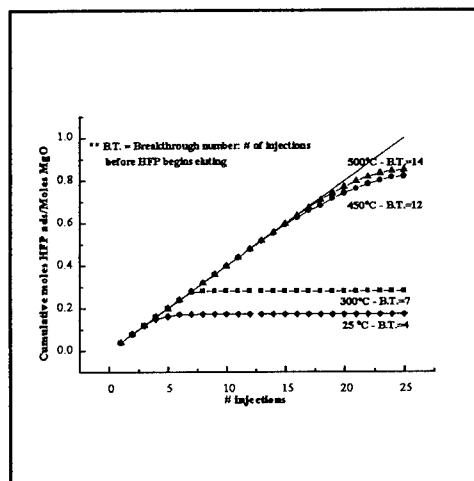


**Figure 1:** Cumulative moles of HFP destroyed per surface mole of MgO.

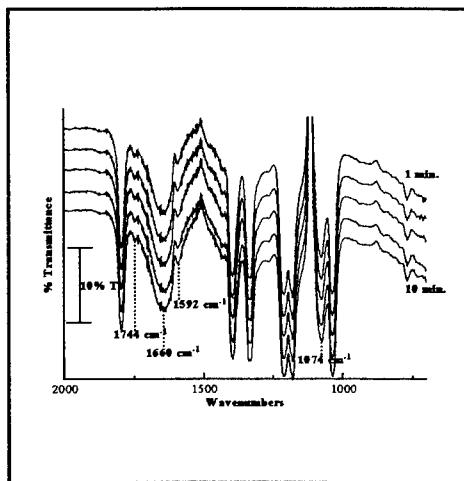


**Figure 2:** Hexafluoropropylene adsorbed on MgO @ 450°C. HFP 5 Torr 1-10 min.

outperform the 450°C reaction, breakthrough number = 14, 85% destruction, but not efficiency is gained at this temperature.

At 450°C large amounts of CO and CO<sub>2</sub> began to elute off immediately, approximately 1.5 moles CO and 2.0 moles CO<sub>2</sub> per mole of HFP injected. This amount stayed constant until past the breakthrough point when the amounts began to steadily decrease. At the breakthrough point, small amounts of C<sub>2</sub>F<sub>4</sub> begin to elute off (1 mole for every 7.5 moles of HFP injected) at all temperatures. The powdered solid after reaction was carbon black at high temperatures, MgO started out white, indicating the breakdown of organics on the surface. Powder XRD showed only the presence of MgF<sub>2</sub> at high temperatures, low temperature reactions showed mainly MgO. Elemental analysis (Galbraith Inc.) gave Mg - 35.62%, Fluorine - 17.12%, Carbon - 5.55%. This shows two MgO's for every MgF<sub>2</sub> present.

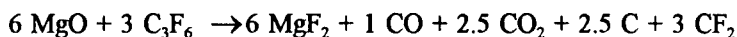
#### FT-IR Studies

Studies were performed at 25°C, 150°C, 400°C and 450°C. Major peaks appearing, outside of hexafluoropropylene peaks, while the cell is held at 5 Torr HFP are at 1744 cm<sup>-1</sup>, 1660 cm<sup>-1</sup>, 1592 cm<sup>-1</sup> and 1074 cm<sup>-1</sup>. The HFP peaks essentially disappear upon evacuation of cell showing the compound to be only physisorbed. The peak at 1744 cm<sup>-1</sup> is barely perceptible at room temperature, but steadily increases in intensity as the temperature is increased. This peak is possibly due to an  $\alpha,\alpha'$  dihalogen substituted aldehyde. This is reinforced by small peaks near 2800. When the cell is evacuated at lower temperatures this peak is much more visible, at higher temperatures this peak disappears during evacuation. The peak at 1660 cm<sup>-1</sup> is most likely due to a C=C bond, again this one gains intensity as temperature is increased and does not disappear during evacuation. The peak at 1590 does not appear till 450°C, but does stay on during evacuation of cell. This peak relates well to the presence of a hexafluoropropyl epoxide. (7) The peak at 1074 cm<sup>-1</sup> does not appear till 450°C as well, and also stays strong during evacuation. This peak is indicative of a CF<sub>2</sub> stretch either related to the epoxide recently

formed or to  $\text{CF}_2$  bound to the acidic  $\text{Mg}^{2+}$  sites. The presence of  $\text{C}_2\text{F}_4$  in the products as the sites begin to fall short lends credence to the idea that  $\text{CF}_2$  is being forced off the surface, and forming tetrafluoroethylene ( $\Delta H_{\text{rxn}} = -596 \text{ kJ/mol}$ ), by incoming HFP's.

### DISCUSSION

Elemental analysis as well as quantification of elutants at  $450^\circ\text{C}$  gives a chemical reaction of:



This relates to a 2 surface oxide to 1 hexafluoropropylene ratio. The calculated  $\Delta H_{\text{rxn}} = -1168 \text{ kJ/mol}$ , which means there must be a very high activation energy. The fact that the HFP is only physisorbed shows that, until the surface sites are depleted, all the HFP is destroyed and converted into non-toxic compounds. The IR indicates that the hexafluoropropylene adsorbs to the surface through one of two arrangements. At low temperature the reaction favors rearrangement of the fluorines to produce a fluoroaldehyde, which readily desorbs during evacuation. While being held at the surface, the fluorines bind with the  $\text{Mg}^{2+}$  and replace the  $\text{O}^{2-}$  forming  $\text{MgF}_2$  and CO or  $\text{CO}_2$ . The carbon bound to the oxygen likely stays bound to the surface as  $\text{CF}_2$  which is later seen eluting off as  $\text{C}_2\text{F}_4$ . At high temperatures the reaction also uses breaking of the double bond to form an epoxide.

The high efficiency of destruction of the hexafluoropropylene, shows that this procedure could be quite effective for destruction of fluorocarbons as well as the "warfare agent" the HFP is mimicking. While only the surface of the particles reacted with the adsorbent, the small particle size and high surface area gave an overall bulk MgO-to-HFP mole ratio of 9:1.

### ACKNOWLEDGEMENTS

The authors wish to thank the U.S. Army Research Office for their support.

### REFERENCES

- (1) Koper, O.; Li, X.L.; Klabunde, K.J. *Chem. Mater.* 1993, **5**, 500.
- (2) Koper, O.B.; Wovchko, E.A.; Glass, J.A.; Yates, J.T. Jr.; Klabunde, K.J. *Langmuir* 1995, **11**, 2054.
- (3) Koper, O.; Lagadic, I.; Klabunde, K.J. *Chem. Mater.* 1997, **9**, 838.
- (4) Li, Y.X.; Schlup, J.R.; Klabunde, K.J. *Langmuir* 1991, **7**, 1394.
- (5) Utamapanya, S.; Klabunde, K.J.; Schlup, J.R. *Chem. Mater.* 1991, **3**, 175.
- (6) Li, X.Y.; Klabunde, K.J. *Langmuir* 1991, **7**, 1388.
- (7) U.S. Pat. 3,358,003 (Dec. 12, 1967), Eleuterio, H.S.; Meschke, R.W. (to E. I. du Pont de Nemours & Co., Inc.)



Pergamon

NanoStructured Materials, Vol. 12, pp. 183–186, 1999

Elsevier Science Ltd

© 1999 Acta Metallurgica Inc.

Printed in the USA. All rights reserved

0965-9773/99/\$—see front matter

PII S0965-9773(99)00094-X

## THE FABRICATION AND ORGANIZATION OF SELF-ASSEMBLED METALLIC NANOPARTICLES FORMED IN REVERSE MICELLES

Candace T. Seip and Charles J. O'Connor

Advanced Materials Research Institute, University of New Orleans, New Orleans, LA 70148.

**Abstract**—Metallic iron nanoparticles are synthesized in reverse micelles of cetyltrimethyl-ammonium bromide (CTAB) using hydrazine as a reducing agent. Once the iron nanoparticles have formed inside the micelle, an aqueous solution of  $\text{HAuCl}_4$  is added to the iron/CTAB mixture. Addition of the aqueous gold solution increases the size of the reverse micelle and the  $\text{Au(III)}$  is reduced to  $\text{Au(0)}$  via excess hydrazine. Because gold and iron grow with complementary crystal structures, the metallic gold forms a coating on the outer surface of the iron particles. The gold shells on the iron particles provide functionality and thin films of the gold coated particles have been made by self-assembly reactions between the gold surface of the particle and thiol functionalized substrates. ©1999 Acta Metallurgica Inc.

### INTRODUCTION

The demand for smaller materials for use in high density storage media is one of the fundamental motivations for the fabrication of nanoscale magnetic materials. The development of a high density magnetic memory device may be more readily achieved by patterning magnetic nanoparticles into organized assemblies on the surface of a substrate. This paper will discuss the attempts of patterning magnetic nanoscale particles onto substrates by taking advantage of the chemical adhesion between a substrate and a non-magnetic coating surrounding the magnetic nanoparticles.

An increasingly popular method of yielding nanoparticles takes advantage of molecular self-assembly (1). By controlling the amount of surfactant and water, fabrication of particles in water-in-oil microemulsions (reverse micelles) affords great control over the size and shape of the particles (2). Our procedure takes advantage of two self-organizing processes. First, we employ the reverse micelle method to synthesize metallic nanoparticles in the water pools of the reverse micelle. We subsequently take advantage of the constricted environment of the reverse micelle and use it to form a layer of gold on the core magnet. In a second self-organizing process, since gold and sulfur form spontaneous bonds, the gold coating will direct the ferromagnetic nanoparticles into an ordered array on the surface of a thiol functionalized substrate such as silicon or glass to produce a thin film. Multilayers of gold coated iron nanoparticles can be formed by additional self-assembly reactions, Figure 1.



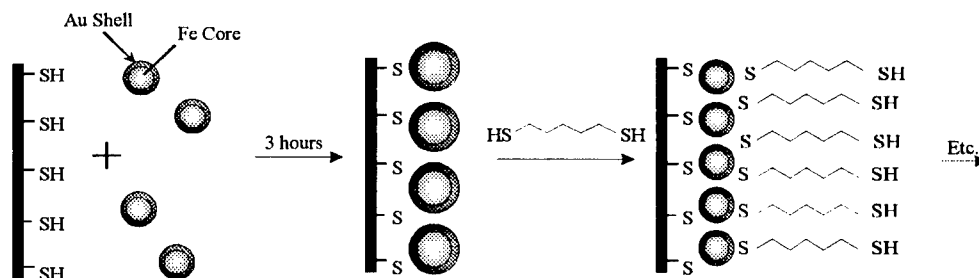


**Figure 1.** Formation of mono and multilayers of Au coated Fe nanoparticles on a thiolated substrate based on chemical self-assembly.

## EXPERIMENTAL

### *Synthesis*

Metallic iron nanoparticles are synthesized in reverse micelles of cetyltrimethylammonium bromide (CTAB) (3). Iron(II) is incorporated into the water pools of a reverse micellar solution formed by using CTAB as the surfactant, butanol as a cosurfactant, and octane as the oil phase. Hydrazine is injected into the solution reducing Fe(II) to Fe(0). The metallic iron particles grow to fill the centers of the micelle and minimal aggregation of iron centers occurs since the organic portions of the micelle keep particles separate. After complete reaction, chloroauric acid is added to the iron/CTAB mixture. Addition of the chloroauric acid solution increases the size of the reverse micelle and the Au(III) is reduced to Au(0) via excess hydrazine. Since gold and iron grow with complementary crystal structures, the metallic gold forms a coating on the outer surface of the iron particles. The gold shells on the iron particles provide the functionality required to form organized arrays. Thin films of the gold coated particles are made by self-assembly reactions between the gold surface of the particle and (3-Mercaptopropyl)trimethoxysilane functionalized substrates.

### *Instrumentation*

Magnetic experiments were carried out using a Quantum Design MPMS-5S SQUID magnetometer. Calibration and measurement techniques are described elsewhere (4). DC susceptibility experiments were performed from 2K through 300K with a measuring field of 1kG. Standard magnetization versus magnetic field hysteresis loops were recorded at temperatures both below and above the blocking temperature by cycling between 50kG and -50kG.

TEM images were performed on a Zeiss 100 microscope. A Phillips-Norelco X-Ray diffractometer with a graphite monochromator and PMT detector was used to obtain XRD plots.

## RESULTS AND DISCUSSION

Samples of gold coated iron nanoparticles were separated on a magnet and washed with solutions of chloroform and methanol. Since CTAB is soluble in this solvent system, it and any other non-magnetic by-products are washed away from the gold coated iron particles. An X-Ray diffraction pattern was obtained on a powder sample of gold coated iron and is presented in Figure 2. From the position of the peaks, it is clear that only gold and iron exist in the sample and the 2.5nm thick gold coating effectively prevents any oxidation of the metallic iron core.

TEM images, shown in Figure 3, illustrate the dramatic differences between samples prepared in two different ways. The image presented in Figure 3A was obtained by placing a drop of a methanol suspension of 15nm gold coated iron particles onto a formvar coated TEM grid and allowing the solvent to evaporate. Aggregation of the particles due to the attraction of the magnetic cores is prevalent as expected. Figure 3B shows the patterning of 15 nm gold coated iron particles onto a thiol functionalized SiO TEM grid. No agglomeration is noticed in this sample and areas are organized into small arrays.

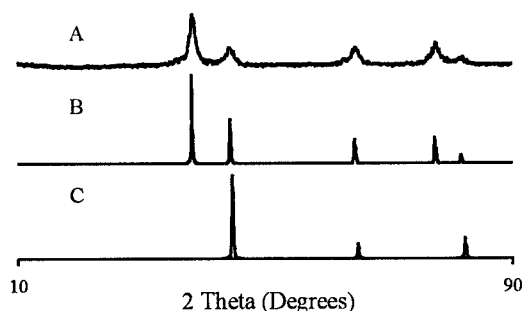


**Figure 2.** XRD pattern of (A) gold coated iron nanoparticles; (B) Au metal; (C) Fe metal.

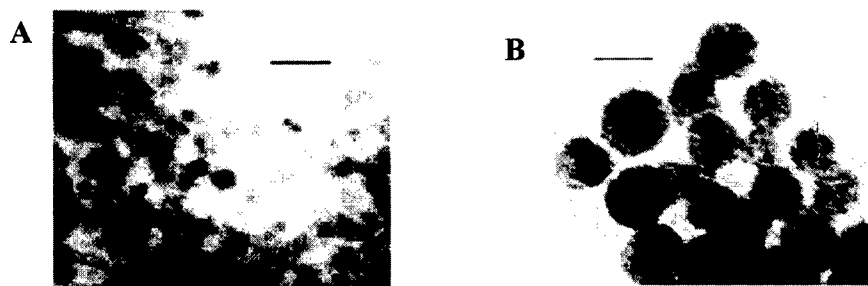


**Figure 3.** TEM images of (A) 15 nm Au/Fe nanoparticles (bar = 50nm); (B) 4x4 array of self-assembled 15 nm Au/Fe nanoparticles on a thiolated SiO TEM grid (bar = 15nm).

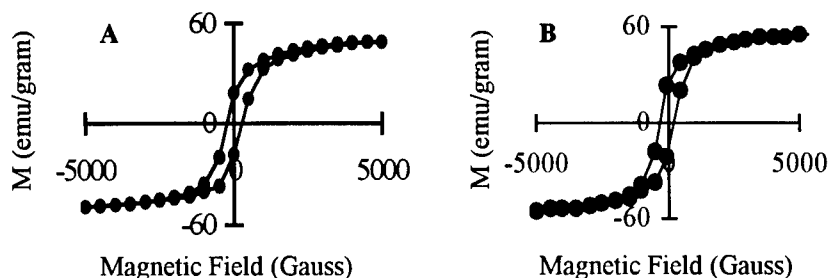


**Figure 4.** Magnetization as a function of field for (A) 15 nm iron and (B) 15 nm gold coated iron nanoparticles measured at a temperature of 2K.

Magnetic measurements performed on powdered samples of gold coated iron nanoparticles illustrate that the gold has a minimal effect on the magnetic properties when compared to that of pure iron. Blocking temperatures are 8 K and coercivity is 275 G in both cases. As shown in Figure 4, the only difference in the properties for the iron and gold coated iron lies in the remanent magnetization. The smaller moment of 18emu/gram for the gold coated iron is due to the additional non-magnetic mass of gold as compared with 22emu/gram for pure 15 nm iron. From the Scherrer equation, the magnetic grain size is estimated as 12nm. This is in excellent agreement with a total particle size of approximately 15nm as the gold coating is expected to be about 2.5nm thick.

## CONCLUSION

TEM images of self-assembled gold coated nanoparticles onto thiolated TEM grids show dramatic differences when compared to images of non self-assembled particles. The magnetic results demonstrate that the gold coating on the iron particles has a negligible effect on the magnetic properties and should not dramatically change the properties of the assembled particles. Work involving gold coated cobalt and cobalt platinum alloy particles is currently being investigated.

## ACKNOWLEDGMENT

We gratefully acknowledge the support of this work by the Advanced Materials Research Institute through DOD/DARPA Grant No. MDA972-97-1-0003.

## REFERENCES

1. Pillai, V., and Shah, D.V., *J. Magn. And Mag. Mater.*, **1996**, 163, 243.
2. Pileni, M.P., *J. Phys. Chem.*, **1993**, 97, 6961.
3. Boutonnet, M., Kizling, J., Stenius, P., and Maire, G., *Colloids and Surf.*, **1982**, 5, 209.
4. O'Connor, C.J., *Prog. Inorg. Chem.*, **1982**, 29, 20.



## FORMATION AND MAGNETIC PROPERTIES OF NANOSIZED $\text{Sm}_2\text{Co}_{17}$ MAGNETIC PARTICLES VIA MECHANOCHEMICAL/THERMAL PROCESSING

W. Liu and P.G. McCormick

Special Research Centre for Advanced Mineral and Materials Processing

The University of Western Australia, Nedlands, WA 6907, Australia

**Abstract**—Nano-sized  $\text{Sm}_2\text{Co}_{17}$  magnetic particles have been prepared by mechanical milling and subsequent heat treatment of a mixture of  $\text{Sm}_2\text{O}_3$ ,  $\text{CoO}$  and  $\text{Ca}$  with a suitable amount of  $\text{CaO}$  as diluent. The mechanical milling produced a nanostructured composite consisting of a nanocrystalline  $\text{CaO}$  supersaturated with  $\text{Ca}$ ,  $\text{CoO}$  and  $\text{Sm}_2\text{O}_3$ ,  $\text{Co}$  nanoparticles and a small amount of  $\text{CoO}$ . Heat treatment of as-milled powders at temperatures above  $300^\circ\text{C}$  resulted in the formation of ultrafine  $\text{Sm}_2\text{Co}_{17}$  particles of 10–250 nm in size embedded in a  $\text{CaO}$  matrix. The particle size of  $\text{Sm}_2\text{Co}_{17}$  grew larger and its distribution became wider with increasing heat treatment temperature. A high coercivity of 14.2 kOe was measured on the ultrafine  $\text{Sm}_2\text{Co}_{17}$  particles embedded in the  $\text{CaO}$  matrix in the sample heat treated at  $800^\circ\text{C}$ .

©1999 Acta Metallurgica Inc.

### 1. INTRODUCTION

Numerous methods have been employed to prepare metallic nanoparticles. Techniques frequently used include chemical reduction, gas evaporation and condensation and sputtering deposition. Recent studies have shown that mechanochemical processing holds significant potential for the synthesis of a wide range of nano-sized metallic and ceramic powders in an efficient and economical manner (1, 2). The process involves mechanical milling a mixture of precursor powders to form a nanostructured composite. The starting powders react either during milling or subsequent heat treatment so that separated nanocrystals of desired phase embedded in a salt or oxide matrix can be obtained. The salt or oxide is then removed by an appropriate washing technique. In our previous paper (3), we demonstrated that the mechanochemical processing could also be used for synthesizing  $\text{Sm}_2\text{Co}_{17}$  nanoparticles from their respective oxides. The purpose of the present work is to provide further structure and property measurements in an effort to clarify the mechanism responsible for the formation of the ultrafine  $\text{Sm}_2\text{Co}_{17}$  particles by this novel method.

### 2. EXPERIMENTAL PROCEDURES

The reaction used in this work was:  $\text{Sm}_2\text{O}_3 + 17\text{CoO} + 20\text{Ca} = \text{Sm}_2\text{Co}_{17} + 20\text{CaO}$ . Details of the sample preparation were given in (3). The structure was studied using a Siemens D5000 X-ray diffractometer (XRD) with monochromatic  $\text{CuK}\alpha$  radiation and a Philips EM430 transmission electron microscope (TEM). Measurements of magnetic hysteresis were carried out

at room temperature using cold-pressed cylinders in an Aerosonics VSM3001 vibrating sample magnetometer under a maximum applied field of 50 kOe.

### 3. RESULTS AND DISCUSSION

#### 3.1 Structure of the as-milled sample

In our previous work (3), it was found that the as-milled powder consisted of a nanocrystalline CaO and a small amount of CoO on examination with XRD (Figure 1). TEM observations showed that the CaO had a grain size of ~10nm and a poor crystallinity. Further calculations revealed that the lattice constant of the cubic CaO phase in the as-milled sample increased slightly compared with that of the starting CaO. This indicated the formation of a supersaturated solid solution during milling since all the reactants have very limited solubility in CaO at room temperature.

Magnetic measurements of the as-milled sample revealed the presence of a soft magnetic phase with a coercivity of about 400 Oe. However, due to the large volume fraction of the diluent CaO and the extremely fine as-milled structure, XRD and TEM measurements could not establish the nature and arrangement of this soft magnetic phase in the as-milled sample. In order to obtain more information about this soft phase, the as-milled powder was washed and the recovered solid was studied. Three components, i.e. Co, CoO and  $\text{Sm}_2\text{O}_3$ , were present in the washed powder as evidenced by the XRD diffraction pattern given in Figure 1. The broad diffraction peaks suggested a fine grain structure associated with these phases. TEM studies showed that the washed powder consisted of nano-sized crystals of 5-20 nm in size (Fig. 2). The selected area diffraction pattern indicated that the fcc Co was the dominant phase although weak, diffused diffraction rings associated with CoO and  $\text{Sm}_2\text{O}_3$  were also discernible. Therefore, it can be concluded that the soft magnetic phase in the as-milled sample is nano-sized fcc Co particles reduced from CoO by Ca during milling.

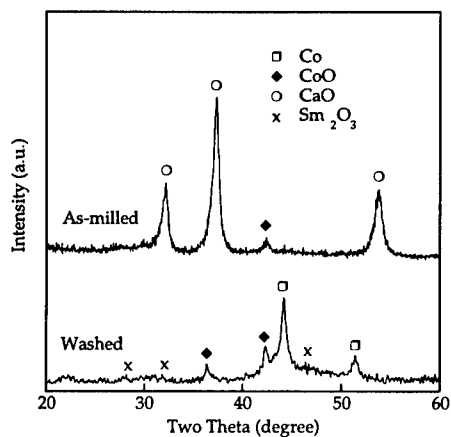


Fig.1 X-ray diffraction patterns for as-milled sample before and after washing.

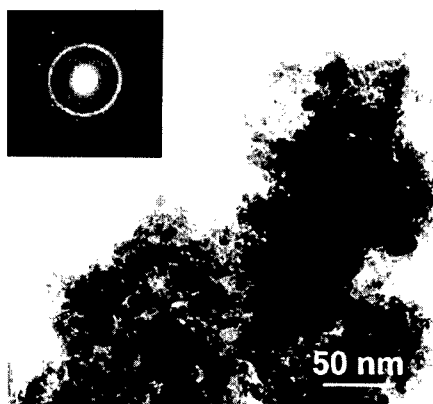


Figure 2. TEM bright field image and corresponding diffraction pattern for as-milled sample after washing.

### 3.2 Formation of ultrafine $\text{Sm}_2\text{Co}_{17}$ alloy particles during heat treatment

The phase transitions during heat treatment of the as-milled sample were identified by means of XRD measurements. As shown in Figure 3. No significant changes were observed on the XRD pattern of the sample heat treated at 250°C. Heat treatment at 300°C resulted in the disappearance of the CoO peak and the emergence of peaks associated with the  $\text{Sm}_2\text{Co}_{17}$  phase. The relative intensities of the  $\text{Sm}_2\text{Co}_{17}$  peaks increased with increasing temperature up to 800°C. At higher temperatures, the precipitation of Co was observed due to Sm vaporization.

The variation of the magnetic properties with heat treatment temperature is shown in Figure 4. The values of the as-milled sample were also plotted for comparison. The initial increase in the maximum magnetisation of the samples heat treated at 200°C and 250°C was attributed to the reduction of the residual CoO to Co. Heat treatment at temperatures between 300–800 °C resulted in a substantial increase in the coercivity while the maximum magnetisation decreased slowly to a minimum at about 800°C. These changes in the magnetic properties were associated with the formation of  $\text{Sm}_2\text{Co}_{17}$  phase as evidenced by the XRD results. The hysteresis loops of the sample heat-treated at temperatures below 800°C exhibited two-phase behaviour while the sample heat treated at 800°C appeared to contain only single hard phase. Analysis of magnetic susceptibility indicated that the amount of the magnetically hard phase increased at the expense of the soft phase up to 800°C. At higher temperatures, the coercivity dropped slightly from the peak value of 14.2 kOe at 800°C to 12.5 kOe at 900°C due to the precipitation of Co. These coercivity values are considerably higher than the reported values for binary  $\text{Sm}_2\text{Co}_{17}$  bulk alloys or micron-sized powders prepared by conventional mechanical grinding (4).

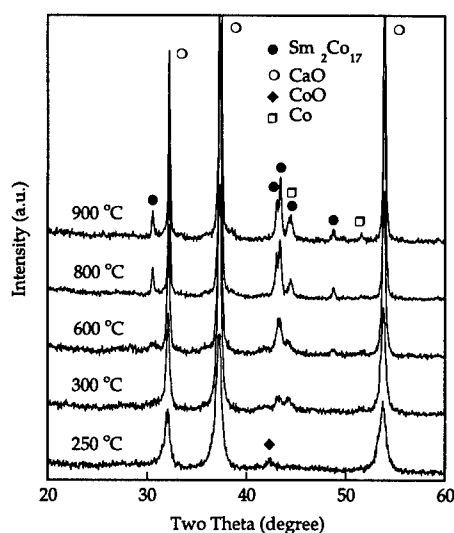


Figure 3. X-ray diffraction patterns for samples heat treated at different temperatures.

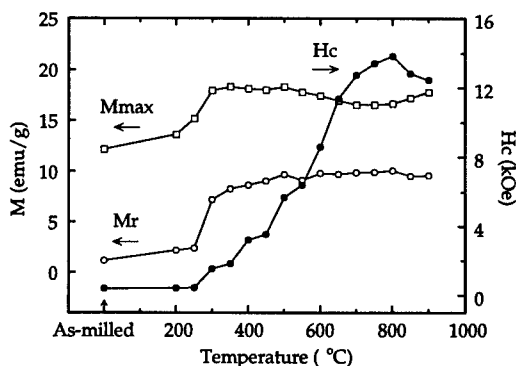


Figure 4. Effect of heat treatment temperature on the magnetic properties

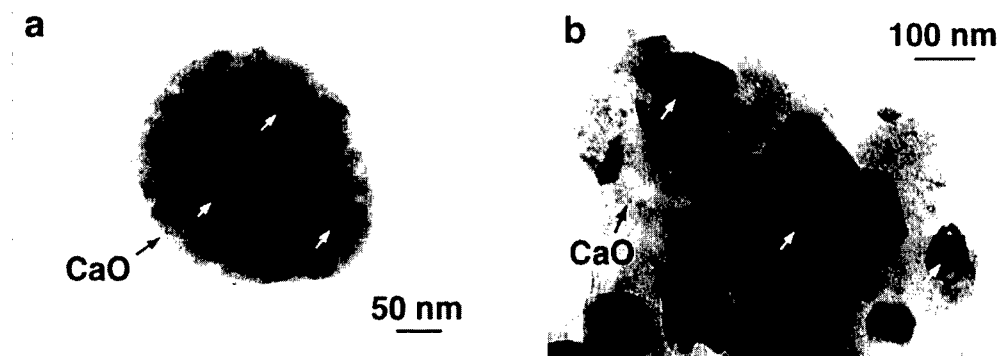


Figure 5. Typical TEM bright field images for samples heat treated at 600°C (a) and 800°C (b); arrows indicate the  $\text{Sm}_2\text{Co}_{17}$  particles.

TEM studies on the heat-treated samples revealed a two-phase structure of  $\text{Sm}_2\text{Co}_{17}$  particles embedded in a CaO matrix. The  $\text{Sm}_2\text{Co}_{17}$  particles became larger with increasing heat treatment temperature. As an example, Figure 5 shows typical TEM bright field micrographs of the samples heat treated at 600°C and 800°C, respectively. It may be seen that the  $\text{Sm}_2\text{Co}_{17}$  particles (indicated by the arrows on the micrographs) in the sample heated treated at 600°C had smaller and more uniform particle size than their high temperature counterpart. By sampling different areas of the bright-field TEM micrographs, the size range of the ultrafine  $\text{Sm}_2\text{Co}_{17}$  particles was determined to be 7-90 nm and 10-250 nm for the sample heat treated at 600° and 800°C, respectively.

#### 4. CONCLUSION

In summary, the ultrafine  $\text{Sm}_2\text{Co}_{17}$  alloy particles of 10--250 nm in size can be prepared by mechanical milling and subsequent heat treatment of a mixture of  $\text{Sm}_2\text{O}_3$ , CoO, CaO and Ca. In addition to mixing the reactants and forming a nanocrystalline CaO supersaturated with Ca, CoO and  $\text{Sm}_2\text{O}_3$ , the mechanical milling induces a partial reduction of CoO to Co nanoparticles by Ca. Heat treatment at temperatures above 300°C results in the formation of nano-sized  $\text{Sm}_2\text{Co}_{17}$  particles dispersed in a CaO matrix. The amount of the  $\text{Sm}_2\text{Co}_{17}$  phase increases at the expense of the Co metal with increasing heat treatment temperature. The  $\text{Sm}_2\text{Co}_{17}$  particles formed at higher temperatures have a larger average particle size and a wider size distribution compared with their low temperature counterparts. The ultrafine  $\text{Sm}_2\text{Co}_{17}$  particles embedded in the CaO matrix reached a high coercivity value of 14.2 kOe in the sample heat-treated at 800°C.

#### REFERENCES

1. Ding, J., Miao, W.F., McCormick, P.G. and Street, R., Appl. Phys. Lett., 1995, 67, 3804.
2. Ding, J., Tsuzuki, T., McCormick, P.G. and Street, R., J. Am. Cera. Soc., 1996, 79, 2956.
3. Liu, W. and McCormick, P.G., submitted for publication, 1998.
4. Kumar, K., J. Appl. Phys., 1988, 63, R13.



Pergamon

NanoStructured Materials, Vol. 12, pp. 191–194, 1999

Elsevier Science Ltd

© 1999 Acta Metallurgica Inc.

Printed in the USA. All rights reserved

0965-9773/99/\$—see front matter

PII S0965-9773(99)00096-3

## MOLECULAR PRECURSOR APPROACH TO NANO-SCALED CERAMICS AND METAL/METAL OXIDE COMPOSITES

M. Veith\*, A. Altherr, N. Lecerf, S. Mathur, K. Valtchev and E. Fritscher

Institute of Inorganic Chemistry, University of Saarland, D-66041 Saarbruecken, Germany

**Abstract--** Heterometal alkoxides are used as single-source precursors to obtain nano-scaled thin layers and powders of a variety of oxide ceramics and composites. The hydride alkoxide  $[Mg\{H_2Al(OBu^i)_2\}_2]$  has been used for low-temperature deposits of crystalline  $MgAl_2O_4$  spinel. The mixed-metal alkoxide  $[BaZr(OPr^i)_3(OH)(Pr^iOH)_3]_2$ , based on 1:1 stoichiometry of the metals, has been used for clean and selective synthesis (sol-gel) of nano-crystalline  $BaZrO_3$  ceramic. Using heterometal alkoxide  $[Ni_2Sn_2(OBu^i)_8]$  in a CVD process gave a binary intermetallic compound ( $Ni_3Sn_4$ ) in an oxide matrix ( $SnO_2$ ). The composite system  $Ni/Al_2O_3$  obtained on reducing  $NiO$  with  $[H_2Al(OBu^i)]_2$  shows remarkably high catalytic activity in hydrogenation of C-C double bonds. Thin layers of a composite containing nano-sized  $Ni/Al_2O_3$  have been deposited using  $[Ni\{Al(OPr^i)_4\}_2]$  in a CVD process.

©1999 Acta Metallurgica Inc.

### INTRODUCTION

Molecular routes to ceramics (oxides, nitrides) and composites (metal (alloy) / metal oxide) provide good control over purity, composition, homogeneity and microstructure of the resulting materials (1). The molecular precursor approach based on the preformation of ceramic materials in gas or solution phases necessitates well-defined starting molecules with metal ratios compatible with the targeted ceramic materials (2). We are developing single-source precursor routes to different ceramic materials *via* Chemical Vapour Deposition (CVD) and Sol-Gel processes. To this end, we have shown that the tailored precursors with a predefined reaction (decomposition) chemistry can enforce a molecular level homogeneity in the obtained materials (3-5). We report here our investigations on the preparation and characterisation of useful ceramics and composites using heterometal alkoxides.

### OXIDE CERAMICS

*n-MgAl<sub>2</sub>O<sub>4</sub> from CVD of a Single-source Precursor  $[Mg\{H_2Al(OBu^i)_2\}_2]$*

Magnesium aluminium spinel is a promising electronic material finding applications for its infrared transmission characteristics, thermal shock resistance and chemical durability.



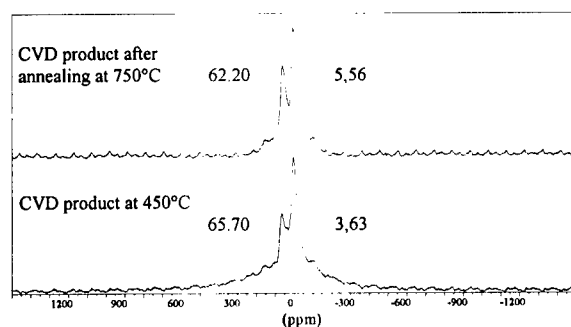


**Figure 1:** The  $^{27}\text{Al}$  CP MAS NMR spectra of the CVD product obtained at 450 °C and after the heat treatment at 750 °C.

The  $\text{MgAl}_2\text{O}_4$  spinel obtained from classical MOCVD process (6) suffers from the intrinsic problems of high carbon contents and high sintering temperatures necessary to obtain crystalline materials. To reduce the organic contents by adopting an appropriate ligand combination and to enhance the volatility, we have synthesised a new Mg-Al hydrido heterometal alkoxide  $[\text{Mg}\{\text{H}_2\text{Al}(\text{O}^i\text{Bu})_2\}_2]$  containing the elements Mg, Al and O in the ratio desired for  $\text{MgAl}_2\text{O}_4$ . Indeed, this molecule is an extraordinary precursor for the crystalline (XRD analysis) deposits of  $\text{MgAl}_2\text{O}_4$  at very low temperature (450 °C) and with low carbon contents (< 0.4 %). The glow discharge mass spectrometry and EDX analysis confirms the composition to be  $\text{MgAl}_2\text{O}_4$ . The  $^{27}\text{Al}$  CP MAS NMR spectrum shows distinct signals for tetra- and hexa-coordinated aluminum centers. This indicates that the ceramic obtained from CVD process has an inverse structure with Al(III) occupying both tetrahedral and octahedral holes which is in contrast to the natural Mg-Al spinel.

*(b) BaZrO<sub>3</sub> from single-source precursor  $[\text{BaZr}(\text{OPr}^i)_5(\text{OH})(\text{Pr}^i\text{OH})_3]_2$*

The dielectric ceramics such as  $\text{BaTiO}_3$  and  $\text{BaZrO}_3$  are finding extensive electronic applications due to their high dielectric constant and ferroelectricity (1). We have recently reported (7) on a Ba-Zr mixed-metal alkoxide  $[\text{BaZr}(\text{OPr}^i)_5(\text{OH})(\text{Pr}^i\text{OH})_3]$  with Ba:Zr stoichiometry of 1:1 which has proved to be an excellent single-source precursor for clean and selective synthesis of  $\text{BaZrO}_3$  (Figure 2). The solution synthesis of  $\text{BaMO}_3$  (M = Ti, Zr) oxides is usually performed using a mixture of two alkoxide precursors in desired molar ratios for *in-situ* generation of an assumed 'single-source' heterometal precursor. However, the undefined nature of species existing in such heterometal solutions and the various thermodynamically stable heterometal combinations that can result from the two precursor components often leads to inhomogeneity (phase separation, non-stoichiometric products) in the final material. In view of the above, the use of the title derivative for obtaining high-purity  $\text{BaZrO}_3$  ceramic demonstrates the potential of well-defined precursors in materials syntheses. Hydrolysis was performed by adding 2 moles of  $\text{H}_2\text{O}$  (in isopropanol) to THF solution of an authentic sample of precursor. The gel resulting from partial removal of volatiles was dried and the powder obtained was calcined at 400 °C in vacuum. Controlled pyrolysis (600 °C/ 12 h) showed the formation of single-phase  $\text{BaZrO}_3$ . The XRD analysis (Figure 2) of a sample calcined at 800 °C (2 h) shows nano-crystalline (30-40 nm)  $\text{BaZrO}_3$  without any noticeable impurity.

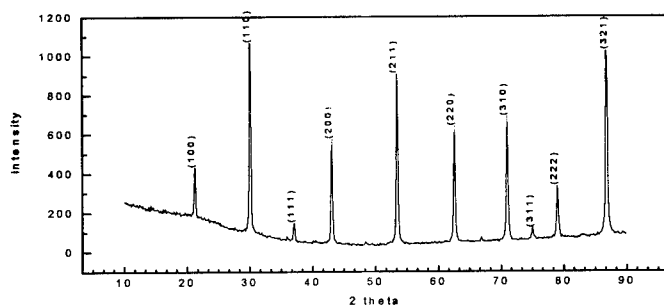


**Figure 2.** The XRD trace of the BaZrO<sub>3</sub> ceramic calcined at 800 °C (6 h) [JCPDS card number: 6-399]

### METAL / METAL OXIDE COMPOSITES

#### *Ni<sub>3</sub>Sn<sub>4</sub> intermetallic in an SnO<sub>2</sub> matrix via CVD of [Ni<sub>2</sub>Sn<sub>2</sub>(OBU<sup>I</sup>)<sub>8</sub>]*

We have previously shown that the decomposition of the heterometal alkoxide BaSn<sub>2</sub>(OBU<sup>I</sup>)<sub>6</sub> in a CVD process produces a regular dispersion of metallic particles (β - Sn) in an oxide matrix (BaSnO<sub>3</sub>) (3). Curiously, the related stannate compound [Ni<sub>2</sub>Sn<sub>2</sub>(OBU<sup>I</sup>)<sub>8</sub>] (8) follows a different decomposition path and for the first time, the formation of a binary alloy in a ceramic matrix is observed, in an MOCVD process. The XRD analysis indicated the composition to be Ni<sub>3</sub>Sn<sub>4</sub> / SnO<sub>2</sub>. The elemental composition and the oxidation states of the Sn and Ni atoms were confirmed by X-ray photoelectron spectroscopy which showed the presence of SnO<sub>2</sub> and elemental Sn and Ni. The Mössbauer spectra (Figure 3) of the obtained composite when compared with the standard samples, support the XRD and XPS analysis and confirm the presence of Ni<sub>3</sub>Sn<sub>4</sub> alloy in an SnO<sub>2</sub> matrix. Such composites with an intermetallic present in an oxide matrix can be of considerable importance due to their electrical and magnetic properties and efforts in this direction are currently underway.

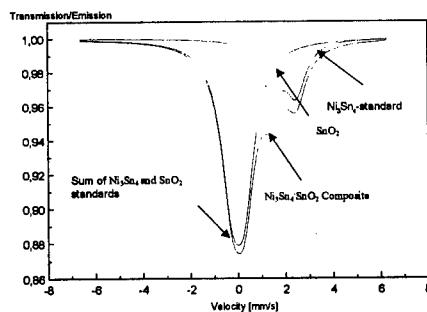


**Figure 3.** A comparison of the Mössbauer spectra of standard SnO<sub>2</sub> oxide and Ni<sub>3</sub>Sn<sub>4</sub> alloy with the composite obtained in the CVD of [Ni<sub>2</sub>Sn<sub>2</sub>(OBU<sup>I</sup>)<sub>8</sub>]

### *Nanostructured Ni/Al<sub>2</sub>O<sub>3</sub> Composite for Catalytic Applications*

Alumina-supported transition metals are widely used as catalysts in various technical processes. The chemical vapour deposition of the hydride alkoxide [<sup>i</sup>BuOAlH<sub>2</sub>]<sub>2</sub> over NiO powder reduces nickel oxide to produce a Ni/Al<sub>2</sub>O<sub>3</sub> composite system. The mass spectrometric analysis revealed isobutene and hydrogen as the predominant gas components (eq. 1).



X-ray diffraction of the composite powders showed Ni as the only crystalline phase, the aluminum oxide component being amorphous. The particle size, determined by XRD analysis was in the range 50-100 nm. Interestingly, this composite showed extremely high catalytic activity in hydrogenation of organic C-C double bond (e.g., styrene, maleic acid), moreover the catalytic activity is retained even after many reaction cycles. Also, the catalyst is selective towards the unsaturated C-C double bonds and leaves the other reactive sites unaffected. A comparative study with other catalysts (e.g., Raney nickel) is in progress. The observed catalytic activity of the Ni/Al<sub>2</sub>O<sub>3</sub> composite prompted us to deposit thin layers of this material for application purposes. Using [Ni{Al(O<sup>i</sup>Pr)<sub>4</sub>}<sub>2</sub>] (9) in a CVD process, we have deposited composite containing nano-scaled Ni/Al<sub>2</sub>O<sub>3</sub>. Mass spectrometry revealed isopropanol, acetone, propene and hydrogen as the volatile thermolysis products. The EDX analysis was in agreement with the Ni:Al ratio (1:2) similar to that of the precursor. Although, XRD patterns confirms the presence of Ni(0), further efforts are mandatory for a quantitative determination of the Ni(0) content.

### ACKNOWLEDGEMENT

Authors are thankful to the Deutsche Forschungsgemeinschaft for the financial support of the research project SFB 277 at the University of Saarland, Saarbruecken, Germany.

### REFERENCES

1. Chandler, C. D., Roger, C. and Hampden-Smith, M. J. *Chem. Rev.*, 1993, 93, 1205.
2. Veith, M., Mathur, S. and Mathur, C. *Polyhedron*, 1998, 17, 1005.
3. Veith, M. and Kneip, S. *J. Mater. Sci. Lett.*, 1994, 13, 335.
4. Veith, M., Faber, S., Hempelman, R., Janssen, S., Prewo and J., Eckerlebe, H., *J. Mater. Sci.*, 1996, 31, 2009.
5. Veith, M., Kneip, S., Jungmann, A. and Hüfner S., *Z. Anorg. allg. Chem.*, 1997, 623, 1507.
6. Rocheleau, R. E., Zhang, Z., Gilje, J. W., and Meese-Marktscheffel, J. A. *Chem. Mater.*, 1994, 6, 1615.
7. Veith, M., Mathur, S., Huch, V. and Decker T., *Eur. J. Inorg. Chem.*, 1998 (in press).
8. Veith, M., Hans, J., Stahl, L., May, L., Huch, V., and Sebald, A., *Z. Naturforsch.* 1991, 46b, 403.
9. Singh, J. V. and Mehrotra, R. C. *Can. J. Chem.*, 1984, 62, 1003.



Pergamon

NanoStructured Materials, Vol. 12, pp. 195-198, 1999

Elsevier Science Ltd

© 1999 Acta Metallurgica Inc.

Printed in the USA. All rights reserved

0965-9773/99/\$-see front matter

PII S0965-9773(99)00097-5

## KINETICS OF FORMATION OF NANOCRYSTALLINE $\text{TiO}_2$ II BY HIGH ENERGY BALL-MILLING OF ANATASE $\text{TiO}_2$

S. Begin-Colin, T. Girot, A. Mocellin, G. Le Caër

Laboratoire de Science et Génie des Matériaux Métalliques, UMR CNRS 7584,  
Ecole des Mines, 54042 Nancy Cedex, FRANCE.

**Abstract** -- Ball-milling is a way of inducing phase transformations, chemical reactions and changes in the reactivity of solids. The high pressure and high temperature phase of  $\text{TiO}_2$  :  $\text{TiO}_2$  II is formed transiently during room-temperature grinding of anatase  $\text{TiO}_2$ . Rutile is the only phase present after prolonged ball milling. The influences of physical and of chemical processing conditions on the kinetics of phase transformations are considered.

©1999 Acta Metallurgica Inc.

### INTRODUCTION

Besides synthesis of crystalline materials with nanometer sized grains, high energy ball-milling is a way of inducing phase transformations in solids. Polymorphic transformations may take place during dry milling in various oxides (1-3). Various polymorphs may further appear transiently even for short milling times. Many oxides formed in such conditions are metastable at ambient temperature and pressure and exist at equilibrium only at high temperature or/and at high pressure. Mechanical alloying and grinding of materials are thus complex processes which depend on many factors, for instance, on the type of mills, on physical and chemical parameters such as milling dynamical conditions, temperature, nature of the atmosphere, chemical composition of the powder mixtures, chemical nature of grinding tools...

We have investigated the influence of some milling parameters on the polymorphic transformations induced by grinding anatase  $\text{TiO}_2$ . Anatase  $\text{TiO}_2$  is transformed by high energy ball-milling into rutile via the  $\alpha$ - $\text{PbO}_2$  type high pressure modification of  $\text{TiO}_2$  :  $\text{TiO}_2$  II whatever the materials constituting the milling tools. We have investigated the effect of two parameters on the kinetics of transformation of anatase  $\text{TiO}_2$  into  $\text{TiO}_2$  II and of  $\text{TiO}_2$  II into rutile : the nature of grinding media and the powder to ball weight ratio.

### EXPERIMENTAL DETAILS

Continuous grinding was performed in a planetary ball mill (Fritsch Pulverisette 7) in air. The powder to ball weight ratios were  $R=1/40$ ,  $1/30$  and  $1/20$ . The grinding tools are made either of steel (Fe-13%Cr) or of alumina, the volume of the vial is approximately  $45 \text{ cm}^3$  and seven balls of diameter  $\varnothing \approx 15 \text{ mm}$  are used.

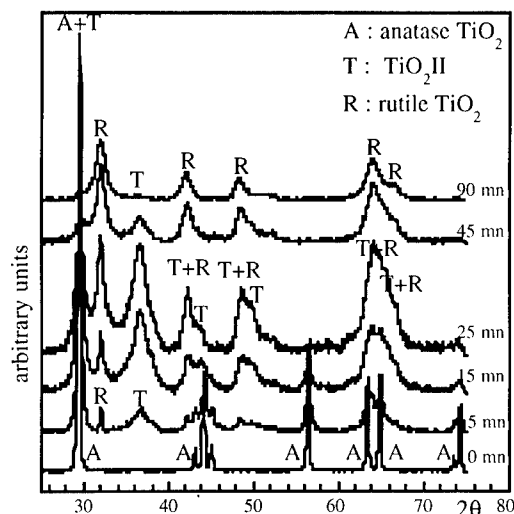


Figure 1 : XRD patterns of anatase  $\text{TiO}_2$  as a function of time ( steel grinding tools,  $R = 1/40$ )

The resulting powders were all characterized by X-ray diffraction (XRD) using  $\text{Co K}\alpha$  radiation. The different phases were quantified using the Klug Alexander method (4).

## RESULTS AND DISCUSSION

Figure 1 displays the XRD patterns of anatase ground in steel grinding media. The general evolution of volume fractions of these phases as a function of milling time is given in figures 2 and 3. Similar curves are obtained no matter what milling conditions are used. The shapes of curves confirm direct observation of X-Ray diffraction results where  $\text{TiO}_2\text{II}$  was observed as an intermediate phase in the anatase-rutile transformation. To analyze the results, two phase transformations are considered as taking place sequentially :



For both grinding media and both phase transformations, the higher the powder to ball weight ratio  $R$ , the slower is the kinetics (figure 2). From a general point of view, the influence of  $R$  on the kinetic reaction rate of both phase transitions can be observed by multiplying the time data with  $R=1/20$  by 2.6 and  $R=1/30$  by 1.3 resulting in all curves superimposing themselves. In figure 3, we can compare the effect of the nature of grinding tools on the kinetic of both phase transitions. For the formation of  $\text{TiO}_2\text{II}$ , the kinetics are of the same order for both grinding media at the beginning of the transformation but the yield in  $\text{TiO}_2\text{II}$  is greater with steel tools than with alumina tools. The influence of grinding tools is clearly observed for the second transformation where with steel tools, the kinetics of rutile formation is slower than with alumina tools. These observations are confirmed by data given in table 1.

The irreversible anatase-rutile transformation in  $\text{TiO}_2$  is reported to occur by a nucleation-growth process (5-7). Therefore some authors have demonstrated that impurities, which often induce oxygen vacancies and/or  $\text{Ti}^{3+}$  formation, modifies the kinetic of the transformation (8-10).

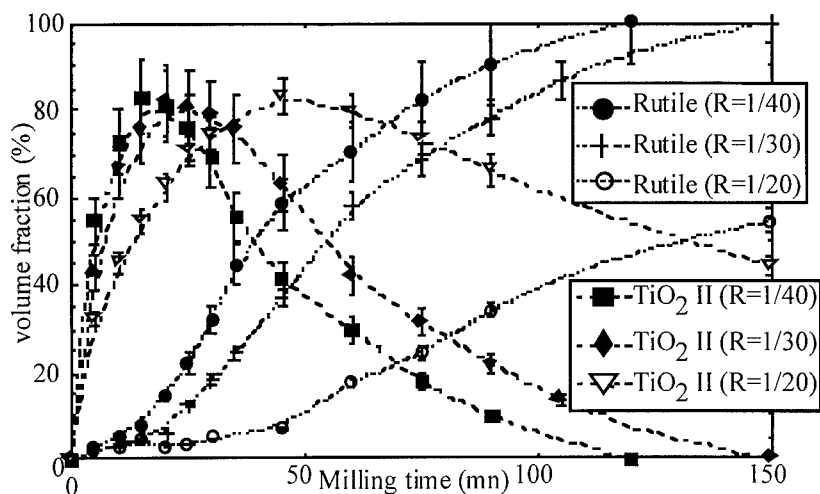


Figure 2 : Evolution of the volume fraction of  $\text{TiO}_2\text{II}$  and rutile as a function of milling time and of  $R$  in steel grinding media

The presence of such defects in ground powders is not to be excluded and must also play a role in the kinetics. The contamination by grinding tools has to be taken into account. However models based on the Hertz impact theory show that the maximal contact pressure, on a volume of powder trapped between two balls, is higher and that the trapped volume is smaller with alumina than with steel grinding tools. Thus the contact pressure by unity of volume of trapped powder is higher with alumina than with grinding steel tools. This might explain that the kinetics is faster with alumina than with steel grinding (11,12).

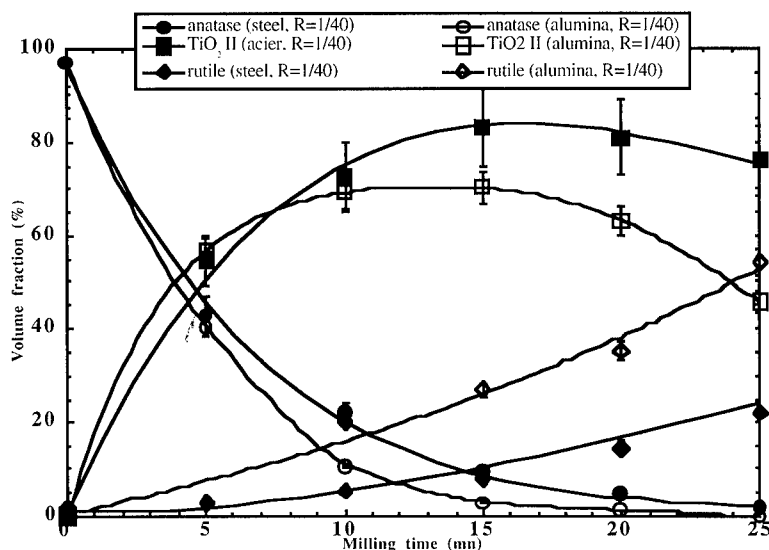


Figure 3 : Comparison of the evolution of volume fraction as a function of the nature of grinding media with  $R = 1/40$

TABLE I  
Volume Fraction of Different Phases as a function of Grinding Parameters and when the  
Maximal Fraction in TiO<sub>2</sub>II is reached

	R	time (mn)	maximal volume fraction (%) in TiO <sub>2</sub> II	volume fraction (%) in anatase	volume fraction (%) in rutile
Steel	1/40	15	83.1	9.2	7.7
	1/30	20	82.4	11.8	5.8
	1/20	45	83.1	9.7	7.2
Al <sub>2</sub> O <sub>3</sub>	1/40	15	70.3	2.9	26.8
	1/30	20	74.1	4.0	21.9

### CONCLUSIONS

The influence of the nature of grinding media and of the powder to ball weight ratio (R) on the transformation of anatase in TiO<sub>2</sub>II and of TiO<sub>2</sub>II in rutile by grinding has been studied. As expected, the ratio R acts only on the reaction rate. To understand the effect of milling on the kinetics of phase transformation and to apply models developed on this process, other parameters have to be varied such as the diameter of balls, the rotation speed of the vials...The chemical environment during these phase transformations, for example : oxygen vacancies formation, contamination..., also needs to be investigated. Such a kinetic study will help us also to approach the mechanisms of these phase transformations induced by grinding.

### ACKNOWLEDGMENTS

The authors would like to thank Pr. T. Ring for helpful discussions.

### REFERENCES

- (1) S. Begin-Colin , G. Le Caër , A. Mocellin, M. Zandona, *Phil. Mag. Let.*, 1994, 69, 1.
- (2) S. Begin-Colin , G. Le Caër , M. Zandona, E. Bouzy & B. Malaman, *J. of Alloys and Comp.*, 1995, 227, 157.
- (3) D. Michel, D., F. Faudot, E. Gaffet, L. Mazerolles, *Rev. Métallurgie*, 1993, 9, 219.
- (4) H. P. Klug & L. E. Alexander, X-ray diffraction procedures for polycrystalline and amorphous material, John Wiley, New York, 2nd Edition, 1974, p.534.
- (5) C.N.R. Rao & K. J. Rao, "Phase transitions in Solids", MacGraw-Hill, New York, 1978.
- (6) S.R. Yoganarasimhan & C.N.R. Rao, *Trans. Farad. Soc.*, 1962, 58, 1579.
- (7) A.W. Czanderna, C. N. R. Rao & J.M. Honing, *Trans. Farad. Soc.*, 1958, 54, 1069.
- (8) R.D. Shannon & J.A. Pask, *J. Am. Ceram. Soc.*, 1972, 48, 391.
- (9) E.F. Heald & C.W. Weiss, *Am. Mineral.*, 1972, 57, 10.
- (10) K.J.D. Mackensie, *Trans. J. Br. Ceram. Soc.*, 1975, 74, 7.
- (11) M. Abdellaoui, E. Gaffet, *Acta Metall. Mater.*, 1995, 43, 1087
- (12) D. R. Maurice, T. H. Courtney, *Metall. Trans.*, 1990, 21A, 289



Pergamon

NanoStructured Materials, Vol. 12, pp. 199-202, 1999

Elsevier Science Ltd

© 1999 Acta Metallurgica Inc.

Printed in the USA. All rights reserved

0965-9773/99/\$-see front matter

PII S0965-9773(99)00098-7

## IN-SITU OBSERVATION OF FORMATION OF NANOSIZED TiO<sub>2</sub> POWDER IN CHEMICAL VAPOR CONDENSATION

J.H. Yu, S.Y. Kim, J.S. Lee, and K.H. Ahn\*

Department of Metallurgy and Materials Science

\*Department of Mechanical Engineering

Hanyang University, Ansan, 425-791 KOREA

**Abstract --** *The present study has attempted to in-situ observe the formation of nanosized TiO<sub>2</sub> powder during chemical vapor condensation process. For this purpose, the powders were sampled at various positions in the furnace using a quartz collecting rod of which surface acts as the powder condensation site. It was discussed in terms of size effect on the phase stability that the fine anatase particle transformed to the coarse rutile phase by growing in the high temperature region. Also the parabolic particle growth with the distance of reaction tube was explicated by computed residence time with solving temperature and gas velocity distribution numerically for different oxygen flow rate conditions. ©1999 Acta Metallurgica Inc.*

### INTRODUCTION

Chemical vapor condensation (CVC) process has been reported to be appropriate for synthesizing the high purity and non-agglomerated ultrafine particles with superior functional properties (1). Also it has a great potential for industrial applications compared to other vapor synthesis methods. However, the formation process of nanosized powder in the CVC process is not fully understood because of some limitations in determining the thermodynamic and kinetic parameters, i.e. temperature and gas velocity distribution, supersaturation ratio and residence time (2,3). The present study attempted to examine closely the particle growth of nanosized titania during the CVC process by defining the residence time accurately. For this purpose, the residence time was numerically computed by solving the equations of convective heat and mass transfer for the steady state flow condition. The particle growth which is in-situ observed in the course of the reaction is discussed in comparison with the result of computer simulation and also in terms of phase stability of nanosized titania particles.

#### *Theory of Numerical Modeling*

The growth process in the CVC reactor is analyzed numerically by first determining the temperature and gas velocity distribution in the reaction tube using the Semi-Implicit Method for Pressure-Linked Equation (SIMPLE) algorithm developed by Patanker (4). The program solves for the steady state flow field assuming conservation of mass, conservation of momentum and conservation of energy. The governing equations are as follow:



$$\nabla \cdot \rho \vec{u} = 0 \quad [1]$$

$$\vec{u} \cdot \nabla \rho \vec{u} = -\nabla p + \nabla \cdot \nabla \mu \vec{u} \quad [2]$$

$$\vec{u} \cdot \nabla \rho C_p T = \nabla \cdot k \nabla T \quad [3]$$

where  $\rho$  is gas density,  $\vec{u}$  is gas velocity,  $p$  is pressure,  $\mu$  is viscosity of gas,  $C_p$  is specific heat,  $T$  is absolute temperature, and  $k$  is thermal conductivity. The numerical analysis was performed by FORTRAN compiler. A total 102 grid lines in the flow direction and 17 grid lines in the radial direction were used for the solution of the heat and the fluid flow equation. In this simulation, the flow is two dimensional and incompressible in cylindrical coordinates. Based on the numerical simulation results, the gas residence time in the reaction tube is found and the particle growth by monodispersed particle coagulation is estimated by the following equation (5),

$$D_p(t) = D_{p0} (1 + N_0 \cdot K \cdot t)^{1/3} \quad [4]$$

where  $D_p$  and  $D_{p0}$  are particle and monomer size of titania, respectively.  $N_0$  is monomer initial concentration,  $K$  is coagulation coefficient, and  $t$  is residence time. The simulation of particle growth was performed for the reaction tube of 60 cm in length under the conditions of 1000°C and various oxygen flow rates.

## EXPERIMENTAL

Precursor of titanium-tetra-isopropoxide (TTIP, Sigma-Aldrich Co., 99.999%) was fed into the hot wall reactor tube with a rate of 0.376 ml/min by helium carrier gas of 1slm. The flow rate of oxygen reactant gas was varied in the range of 1 slm to 2 slm. The temperature and total pressure in the reactor of the CVC system were 1000°C and 10 mbar, respectively. In the course of the reaction the titania particles from the gas phase were deposited on the surface of quartz rod which is located horizontally at the center of the reactor tube. The crystallite size of titania powders collected at various positions as depicted in Figure 1 was estimated using Scherrer formula by X-ray diffractometry and discussed in comparison with that of theoretical calculations on the basis of equation [4].

## RESULTS, DISCUSSION AND CONCLUSION

Figure 1 represents the schematics for the collecting positions of titania particles on the quartz rod and the temperature distribution in the hot wall reactor. The temperatures at each position marked as A, B, C, and D were 978°C at 20 cm, 1002°C at 35 cm, 998°C at 50 cm, and 202°C at 70 cm, respectively. On the basis of these conditions, the gas velocity distribution was calculated by computer simulation using the SIMPLE algorithm which simultaneously

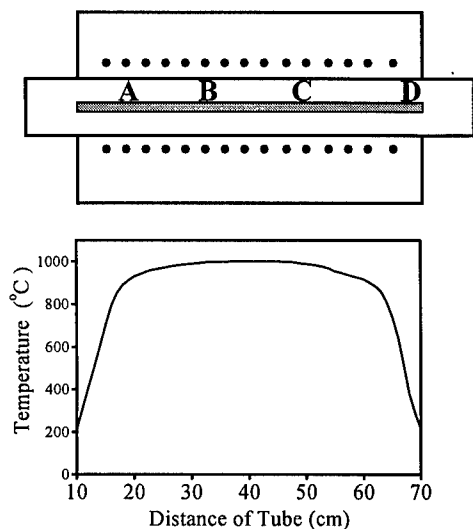


Figure 1. A schematics for the particle collecting system and the temperature distribution in the reactor.

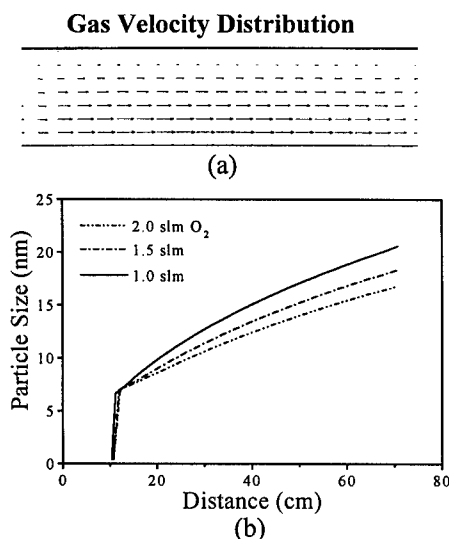


Figure 2. Computational simulations of gas velocity distribution and particle growth in the reactor according to equation [4].

simulates the temperature distribution in the cylindrical reactor. This calculation was conducted for the constant oxygen flow rate of 2 slm. It is seen in the Figure 2(a) that the gas velocity is much faster at the center zone than the side in the reactor. This is mainly due to a large difference of temperature at both zones. On the basis of the gas velocity data, the residence time corresponding to each oxygen flow rate was calculated and then applied for predicting particle growth in the reactor using equation [4]. Figure 2(b) represents the result of particle size change versus oxygen flow rate. As depicted here, titania monomers underwent explosive formation of the particles at the position of about 10 cm. This may be attributed to the higher concentration of very fine titania monomers in the initial stage. It is noted that the particle size abruptly increases up to about 7 nm and thereafter grows with increasing distance. At the position of 70 cm, the residence time and particle size for oxygen flow rates of 1.0, 1.5 and 2.0 slm were calculated to 8.4 ms (20nm), 6.6 ms (18 nm) and 5.6 ms (17 nm), respectively. This result indicates that the residence time and particle size decrease with increasing oxygen flow rate. It seems that a higher stream velocity due to larger total gas flow is responsible for the above result.

The theoretical results in Figure 2 were checked experimentally. First, Figure 3 shows the X-ray diffraction patterns for titania powders collected at each position of Figure 1. The powders of the positions of A, B and C have almost same rutile phase while the D powder consists of anatase phase and a small amount of rutile. Based on the X-ray patterns, the crystallite size was calculated using Scherrer formula and plotted versus oxygen flow rate in Figure 4. It is seen that the crystallite size in the region of A-C having above 40 nm slightly decreases with increasing distance and, however, at D position it steeply falls below 20 nm. This result intuitively seems contradictory to that of computational simulations of Figure 2. The

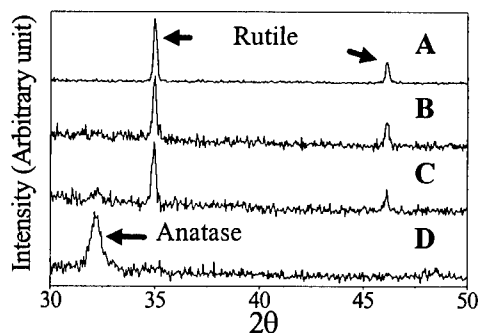


Figure 3. XRD diffraction patterns of collected titania powders at each positions.

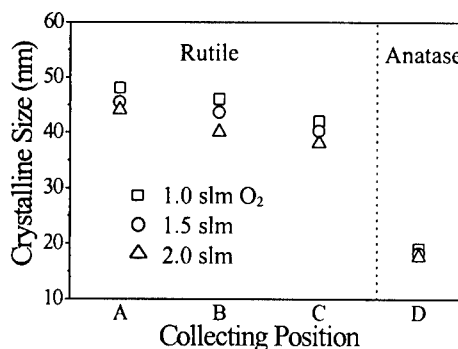


Figure 4. Variation of particle size sampled at each positions in the reaction tube.

reason for this discrepancy can be due to the cluster sintering simultaneously occurring during deposition.

Actually, the higher temperature positions of A, B and C are exposed to the conditions of rapid sintering and particle growth. Considering the results of Figures 3 and 4, at lower temperature position the stronger anatase peak and the smaller crystallite size are observed. According to recent report (6), phase transformation of titania from anatase to rutile can occur only when the anatase cluster reaches a critical size of 10-15 nm independent of temperature. Interestingly, this critical size of 10-15 nm seems to be consistent with the crystallite size of the anatase of D position. Conclusively, the larger rutile particles at higher temperature positions is thought to result from the sintering effect of transformed rutile particles.

#### ACKNOWLEDGMENT

The author gratefully acknowledge the financial support of the Korean Ministry of Science and Technology.

#### REFERENCES

1. Siegel, R.W., *NanoStructured Materials*, 1994, 4, 121.
2. Panda, S. and Pratsinis, S.E., *NanoStructured Materials*, 1995, 5, 755.
3. Clark, T.J., Banash, M.A., Cruse, R.W., Mininni, R.M., and S.J. Rohman, *NanoStructured Materials*, 1994, 4, 723.
4. Patankar, S.V., *Numerical Heat Transfer and Fluid Flow*, McGraw-Hill, New York, 1980.
5. Hinds, W.C., *Aerosol Technology*, John Wiley & Sons, New York, 1982.
6. Gribb, A.A. and Banfield, J.F., *American Mineralogist*, 1997, 82, in press.



Pergamon

NanoStructured Materials, Vol. 12, pp. 203–206, 1999

Elsevier Science Ltd

© 1999 Acta Metallurgica Inc.

Printed in the USA. All rights reserved

0965-9773/99/\$—see front matter

PII S0965-9773(99)00099-9

## NANOSIZED SILICON PARTICLES BY INERT GAS ARC EVAPORATION

H. Hofmeister and P. Ködderitzsch

Max Planck Institute of Microstructure Physics, Weinberg 2, D-06120 Halle, Germany

**Abstract** -- We have explored the possibilities of inert gas arc evaporation for fabrication of nanosized Si particles and studied agglomeration, size, shape, crystallinity, surface roughness and internal structure of these particles by conventional and high resolution electron microscopy. The rarely used technique yielded single crystalline, spherical Si particles 3 - 16 nm in size completely free of planar lattice defects. The particles, covered by thin amorphous oxide shells, are agglomerated into chains and tangles. The lattice of diamond cubic type exhibits contractions which decrease as with decreasing particle size the oxide shell thickness is reduced. This effect is ascribed to compressive stress at the Si/oxide interface.  
©1999 Acta Metallurgica Inc.

### INTRODUCTION

Silicon based materials having structural characteristics on the nanometer scale exhibit interesting optoelectronic properties that result from size-induced quantum confinement effects as well as the presence of Si–O bonds at the surface [1-3]. While erosive surface techniques are widely used to process bulk silicon [4,5], there is a growing interest in the fabrication of particulate silicon showing comparable properties. Such materials are designed to achieve, by embedding in a passivating matrix, stability against influences of the ambient. Various methods of synthesis are reported ranging from co-sputtering of Si and silica, ion implantation of Si into silica, laser ablation and gas phase evaporation of silicon, to plasma-assisted decomposition of silane [6-12]. We have explored the possibilities of inert gas arc evaporation of silicon for producing nanosized Si particles of high crystallinity and perfection.

### EXPERIMENTAL

Aggregation and condensation in inert gas atmosphere of the highly supersaturated vapour originating from arc discharges ignited at solid Si electrodes were utilized to deposit thin layers of Si particles. Arc evaporation of silicon of 5N purity was achieved by indirectly preheated Si electrodes powered with short pulses of 60 - 100 A in an Ar gas atmosphere of about 2 mbar pressure. Carbon coated microgrids placed at an appropriate distance above the arc evaporator served to collect particles from the gas stream. For structural characterisation by transmission electron microscopy (TEM) a conventional JEM 100C (100 kV) and a high resolution electron microscope (HREM) JEM 4000EX (400 kV) were used. HREM images were recorded at optimum imaging conditions (near Scherzer focus). The spacings of lattice plane fringes were determined by means of digital image processing and evaluation.

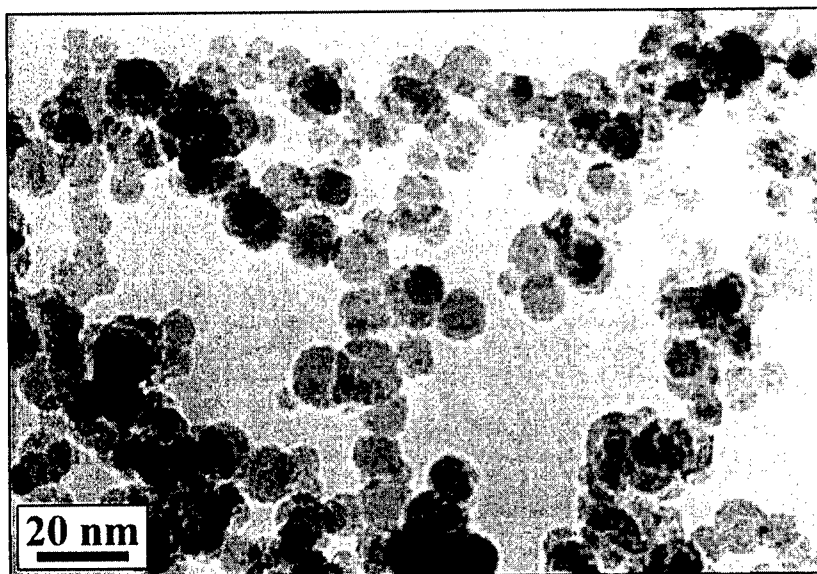


Fig. 1: Chains of agglomerated Si particles bridging a hole in the supporting carbon film

### RESULTS AND DISCUSSION

Investigation of the Si particulates by high resolution electron microscopy revealed structural characteristics related to the peculiarities of the particle synthesis. Under the conditions mentioned above, inert gas arc evaporation yields spherical particles of about 3 to 16 nm diameter. The particle size distribution of a typical layer of which Fig. 1 shows a selection is given in Fig. 2 (crystalline core data only). The apparently bimodal distribution points to in-

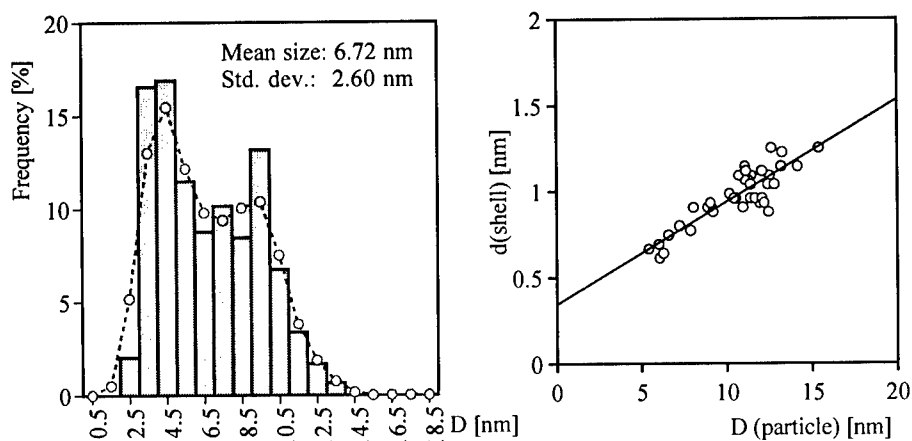


Fig. 2: Particle size distribution as determined from crystalline core dimensions (left plot); and oxide shell thickness in dependence on the size of crystalline particle cores (right)

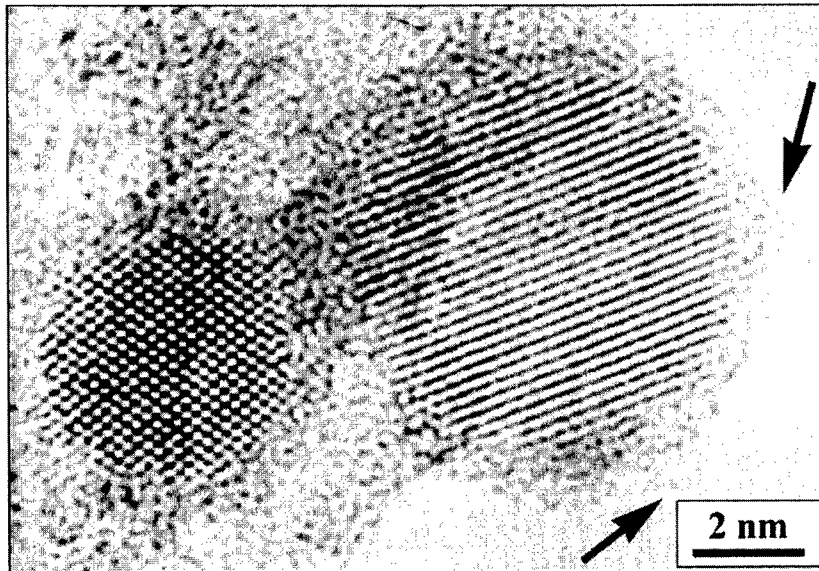


Fig. 3: HREM image of single crystalline Si particles covered by amorphous oxide forming rough surfaces (see arrows)

teraction processes in the very beginning of particle formation. As may be recognised from Fig. 3 the particles are completely covered by amorphous oxide shells. The thickness of these shells linearly decrease from about 1.5 to 0.5 nm with decreasing particle size as shown in Fig. 2. The particles loosely adhering to each other are considerably agglomerated into chain-like and tangle-like structures. There is no indication of particle coalescence or sintering, which

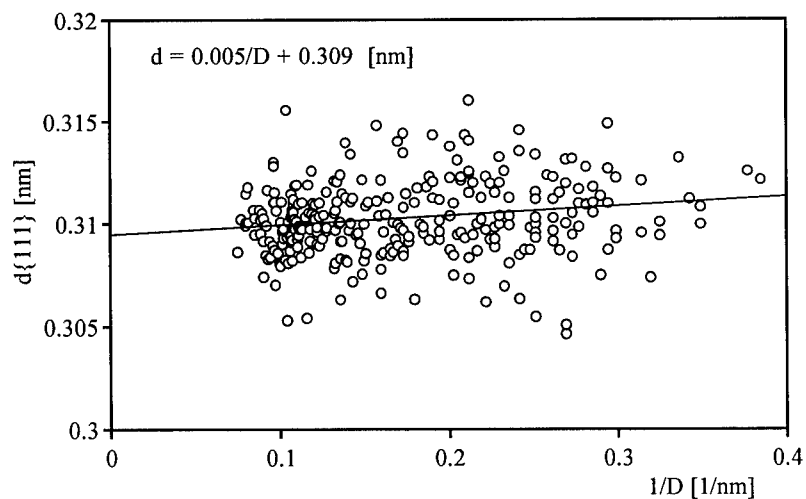


Fig. 4: Spacing of {111} lattice plane fringes in dependence on the reciprocal particle size

points to the fact that oxidation is already starting before deposition of the particles. They are single crystalline and completely free of planar lattice defects. According to lattice structure analysis by means of the reciprocal space representation (diffractogram) of digitized HREM images the lattice of diamond cubic type exhibits distinctly reduced spacing as compared to the bulk value. This lattice compression diminishes for decreasing particle size as demonstrated by Fig. 4.

With the formation of oxide at the particle surface compressive stress to accommodate the volume expansion arises that may attain values of several GPa [13], hence enabling lattice contraction of the observed extent. The stress at the Si/oxide interface ought to diminish with decreasing particle size according to the oxide thickness decrease. From the size dependence of the lattice contraction (see linear regression in the lattice spacing vs. reciprocal particle size plot of Fig. 4) an interface stress of  $-1.17 \text{ N/m}$  indicating a strong interaction is determined. This behaviour may be influenced by an oxygen content varying with oxide shell thickness.

### CONCLUSION

In conclusion, it may be stated that inert gas arc evaporation is well suited for producing nanosized Si particles of high crystallinity and perfection. Coverage of these particles by amorphous oxide shells causes lattice contractions which diminish with decreasing oxide shell thickness for decreasing particle sizes. Since the electron density of states in nanosized Si particles may severely be influenced by such lattice compressions our findings shed new light on the optoelectronic properties of oxide passivated Si nanoparticles.

### REFERENCES

- [1] Tamura, H., Rückschloss, M., Virschem, T. and Veprek, S., *Thin Solid Films*, 1995, 255, 92.
- [2] Li, S., Silvers, S. and El-Shall, M.S., *J. Phys. Chem.* 1997, 101, 1794.
- [3] Li, S., Silvers, S. and El-Shall, M.S., *Materials Research Symposium Proceedings Series*, 1997, 452, 141.
- [4] Gösele, U. and Lehmann, V., *Materials Chemistry and Physics*, 1995, 40, 253.
- [5] Ludwig, M.H., Augustin, A., Hummel, R.E. and Gross, T., *J. Appl. Phys.*, 1996, 80, 5318.
- [6] Zacharias, M., Dimova-Malinovska, D. and Stutzmann, M., *Phil. Mag. B*, 1996, 73, 799.
- [7] Shimizu-Iwayama, T., Nakao, S. and Saitoh, K., *Nucl. Instr. Meth. Phys. Res. B*, 1996, 120, 97.
- [8] Movtchan, I.A., Dreyfus, R.W., Marine, W., Sentis, M., Autric, M., Le Lay, G. and Merk, N., *Thin Solid Films*, 1995, 255, 286.
- [9] Dihn, L.N., *Phys. Rev. B*, 1996, 54, 5029.
- [10] Hofmeister, H., Dutta, J. and Hofmann, H., *Phys. Rev. B*, 1996, 54, 2856.
- [11] Hofmeister, H., Ködderitzsch, P. and Gösele, U., *Ber. Bunsenges. Phys. Chem.*, 1997, 101, 1647.
- [12] Hofmeister, H., Ködderitzsch, P. and Dutta, J., *J. Non-Crystalline Solids*, 1998, 232 - 234, 182.
- [13] Liu, H.I., Biegelsen, D.K., Johnson, N.M., Ponce F.A. and Pease, R.F.W., *J. Vac. Sci. Technol. B*, 1993, 11, 2532.



## ORIENTED PROLATE SILVER PARTICLES IN GLASS - CHARACTERISTICS OF NOVEL DICHROIC POLARIZERS

H. Hofmeister\*, W.-G. Drost<sup>o</sup> and A. Berger<sup>o</sup>

\*Max-Planck-Institut für Mikrostrukturphysik, Weinberg 2, D-06120 Halle, Germany

<sup>o</sup>Farbige Optoelektronische Bauelemente GmbH, Weinbergweg 23, D-06120 Halle, Germany

**Abstract** -- Nanosized spherical silver particles in glass, introduced by an ion exchange plus annealing procedure, have been deformed at elevated temperatures to uniformly arranged prolate spheroidal particles by homogeneous glass stretching at constant stress. Thereupon, the optical absorption band splits into two bands according to the long and short axes of the deformed particles. Since colour and polarizing effect of these particles may widely be controlled by variation of their aspect ratio this technique enables the fabrication of novel dichroic polarizers with spectral characteristics throughout the whole visible range. Local thermally induced shape relaxation of deformed particles makes colour structuring possible on the micrometer scale. Characterisation of these materials by optical absorption spectroscopy and transmission electron microscopy demonstrates the influence of deformation and shape relaxation on their spectral and polarizing properties. ©1999 Acta Metallurgica Inc.

### INTRODUCTION

Spherical Ag particles of various sizes and number density in soda-lime glass are readily obtained by Na/Ag ion exchange and subsequent reduction treatment [1-3]. Stretching at elevated temperatures of such coloured glasses results in elongated particles uniformly oriented along the direction of deformation. Consequently, the optical absorption of the spherical particles splits into two bands according to the long and short axes of the now spheroid-shaped particles. The position of these absorption bands may be tuned by varying the initial size of the spherical particles and the degree of glass deformation that determines the aspect ratio of the prolate particles [4,5]. Basing on this procedure, novel dichroic polarizers of high mechanical, chemical and thermal durability can be fabricated which have a wide range of dichroic colours accessible. Thermally induced shape relaxation of deformed Ag particles to a well-defined extent within sharply bounded areas [6,7] can be utilized for microstructuring with strip or pixel dimensions less than 10  $\mu\text{m}$ .

### EXPERIMENTAL

Spherical Ag particles of 4 - 40 nm size were formed in commercial soda-lime glass by ion exchange in a  $\text{NaNO}_3/\text{AgNO}_3$  melt mixture and subsequent annealing at 560 °C. Stretching of the coloured glasses was done at 650 °C by pulling at constant stress of 50 - 150 N/mm<sup>2</sup> so to obtain elongated particles (mean aspect ratio 2.4 - 5.5). Microstructuring is achieved by patterned laser light illumination or electron beam lithography which allows continuous proc-



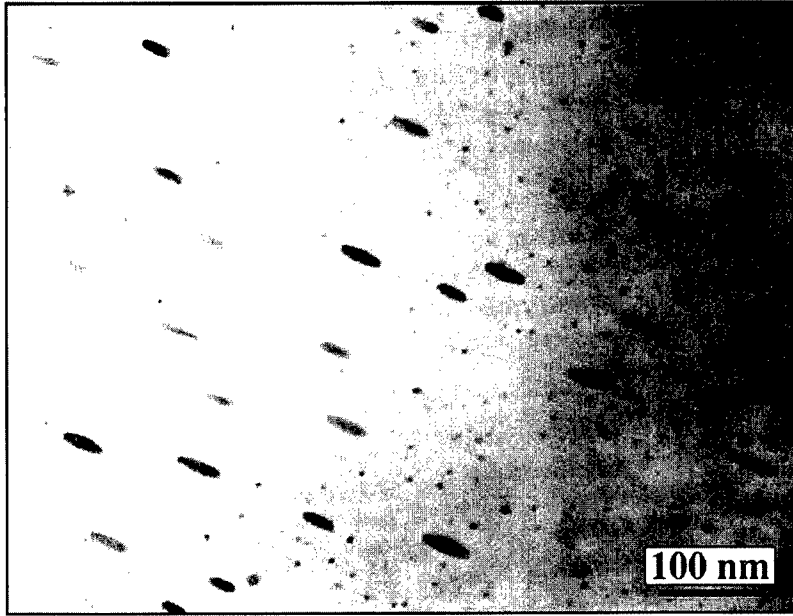


Fig. 1: Prolate Ag particles (mean aspect ratio 2.46) deformed by glass stretching at  $50 \text{ N/mm}^2$  pressing of glass sheets up to 30 cm width by means of a cascaded air lock system.

## RESULTS AND DISCUSSION

The Fig. 1 demonstrates uniform arrangement of deformed particles for a glass stretching factor of about 4 leading to a mean aspect of 2.46. Because of the surface curvature restrictions only particles larger than a critical value  $D^*$  are affected by the deformation process. The correspond-

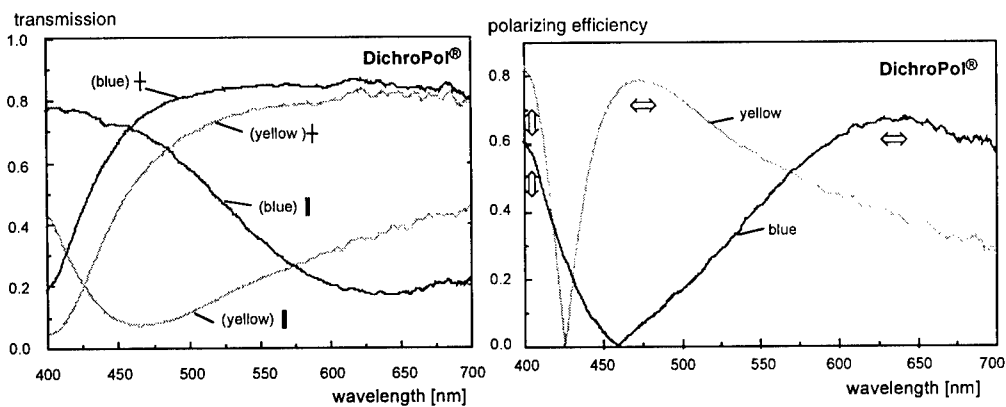


Fig. 2: Transmission of parallel (||) and perpendicular (⊥) linearly polarized light, (left plot), and polarization, parallel (||) and perpendicular (⊥) to stretching direction, (right), of two types of dichroic glass polarizers (blue, and yellow)

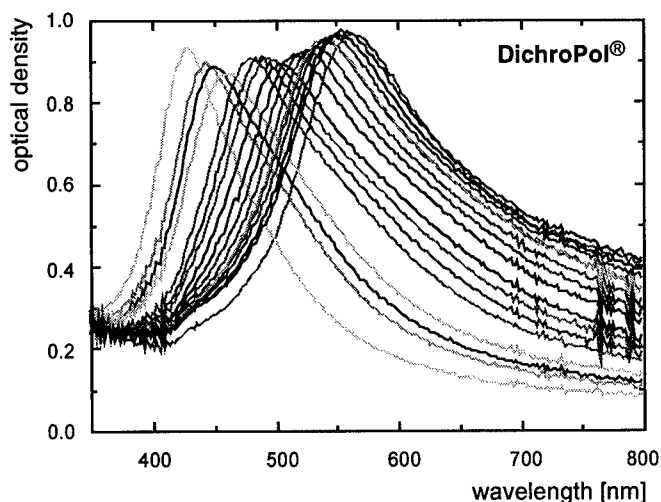


Fig. 3: Optical density spectra of a stripe patterned 17 steps colour wedge fabricated by local thermally induced shape relaxation with linear increase of irradiation dose

ing spectra for this dichroic glass polarizers (yellow type), representing its colour (transmission) and polarizing effect, are shown in Fig. 2 together with those for another, heavier stretched glass (blue type). The glass stretching factor of the latter one is about 6 leading to a mean aspect ratio of the deformed particles of 3.38.

Fig. 3 shows a set of spectra from a striped colour wedge demonstrating the possibilities of microstructuring by means of local thermally induced shape relaxation. The stripes (160  $\mu\text{m}$

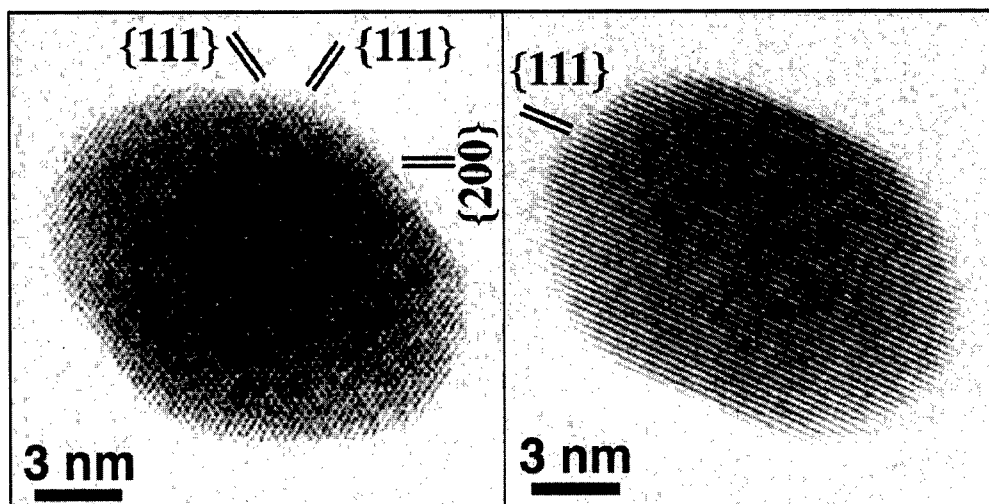


Fig. 4: Spindle and rod-like shape deviations from the spheroid-shape depending on the orientation of the particle crystal lattice with respect to the stretching direction

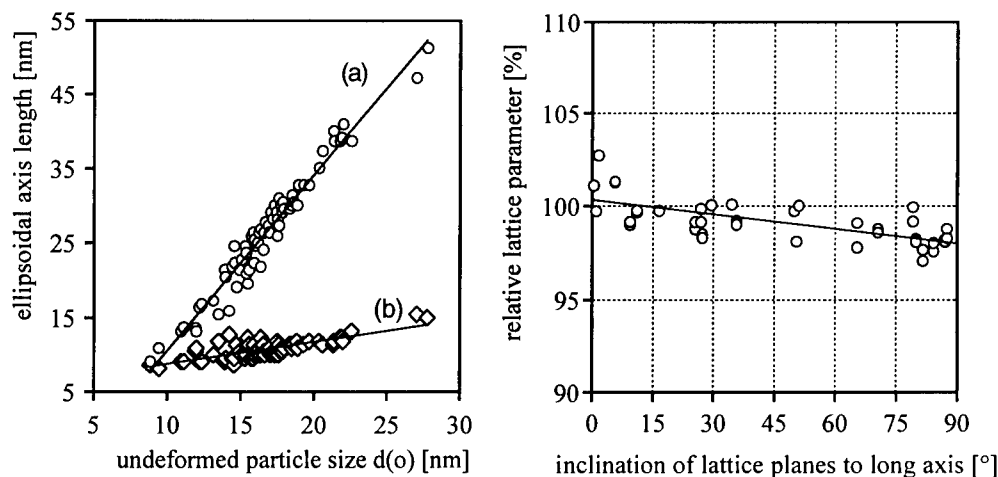


Fig. 5: Spheroid axes length as a function of the undeformed particle size  $d(o)$ , (left plot); and  $\{111\}$  lattice fringe spacing in dependence on their inclination to the long axis, (right)

width; 40  $\mu\text{m}$  spacing; 70 mm length), each one represented by its spectrum, were fabricated with stepwise linear increase of the irradiation dose during patterning.

The uniformity of particle deformation in such materials is still limited for two reasons: (i) a random orientation of their crystal lattice with respect to the stretching direction, and (ii) the distribution of undeformed particle sizes. The first one produces, deviating from the spheroid, rod-like and spindle shapes, in particular, for stretching parallel and perpendicular to  $\{111\}$  lattice planes, respectively, as shown in Fig. 4. The second one leads to a distribution of spheroid axes lengths as may be recognized from Fig 5(a). Both contribute to a certain distribution of the aspect ratio the width of which is decisive for the applicability for filtering and polarizing purposes. Lattice inhomogeneities with respect to the stretching direction have been detected by high resolution electron microscopy. Evaluation of the spacings of lattice plane fringes as a function of their inclination to the long axis as shown in Fig. 5(b) reveals a lattice contraction opposed to the stretching direction. Such compressive strains frozen-in within the glass matrix need to be removed carefully since they could influence the reliability of spectral characteristics of dichroic glass polarizers.

## REFERENCES

- [1] Berg, K.-J., Berger, A. and Hofmeister, H., *Z. Phys. D*, 1991, 20, 309.
- [2] Berger, A., Berg, K.-J. and Hofmeister, H., *Z. Phys. D*, 1991, 20, 313.
- [3] Berger, A., *J. Non-Crystalline Solids*, 1992, 151, 88.
- [4] Berger, A. and Hofmeister, H., *Nanostructured Materials*, 1993, 3, 53.
- [5] Berger, A., *J. Non-Crystalline Solids*, 1993, 163, 185.
- [6] Drost, W.-G., Ph.D. thesis, University of Halle, 1991, p. 46.
- [7] Wahl, M., Gleske, G., Drost, W.-G. and Cornelius, H.-J., Proc. 12. Electronic Displays '97 Conf., Chemnitz 1997, p. 104.



Pergamon

NanoStructured Materials, Vol. 12, pp. 211–214, 1999

Elsevier Science Ltd

© 1999 Acta Metallurgica Inc.

Printed in the USA. All rights reserved

0965-9773/99/\$-see front matter

PII S0965-9773(99)00101-4

## PHASE COMPOSITION STUDY OF BULK AND SURFACE LAYERS OF STABILIZED IRON POWDER

E.P.Yelsukov, \*O.M.Mikhailik, G.N.Konygin, S.S.Mikhailova, V.I.Povstugar

Physical -Technical Institute UrB RAS, 132 Kirov str, 426001 Izhevsk, Russia,

\*SRC Sonar NAS of Ukraine, Kiev, Ukraine

**Abstract**—Mössbauer spectroscopy and X-ray diffraction were used to study iron powders in process of their preparation by high temperature reduction of  $\alpha$ -FeOOH in hydrogen. It was found that the following conversions occur both in the bulk and on the surface of the particles obtained in process of reduction of  $\alpha$ -FeOOH up to  $\alpha$ -Fe:  $\alpha$ -FeOOH  $\rightarrow$   $\text{Fe}_3\text{O}_4$   $\rightarrow$   $\alpha$ -Fe. After the complete reduction a slight quantity of the  $\gamma$ -FeOOH phase is present in the surface layer of iron particles in contrast to the bulk. ©1999 Acta Metallurgica Inc.

Finely dispersed ferromagnetic materials are applied as magnetic liquid bases, fillers for metal-polymer composites, and microcarriers of biologically active substances. The characteristics of finely dispersed iron powders (FDIP) as well as physico-chemical processes during the interaction of the powders between themselves and with the environment are grossly determined by the surface layer structure. Hence, the investigation of the phase composition both in bulk and on particle surfaces is of great interest. Transmission Mössbauer spectroscopy is an effective technique to study atomic and chemical structure of substances including FDIP (1,2). In this work we have studied the structural and chemical conversions during preparation of FDIP by high temperature reduction of  $\alpha$ -FeOOH by means of transmission Mössbauer spectroscopy, X-ray diffraction and electron microscopy.

### EXPERIMENTAL

Mössbauer spectra were recorded on a conventional spectrometer operated in the constant acceleration mode and equipped with the  $^{57}\text{Co}$ -source in the Cr-matrix.  $\gamma$ -radiation was registered by resonance scintillation detector. The effective thickness of the investigated powders was 14–20  $\mu\text{m}$ . Each channel of the counting scale registered  $2 \cdot 10^5$  pulses. X-ray diffraction structure was obtained according to Bregg-Brentano scheme on DRON-UM1 using  $\text{CoK}\alpha$  radiation through the Fe-filter. All measurements were taken at room temperature.

High temperature reduction of  $\alpha$ -FeOOH was conducted in  $\text{H}_2$ -flow at 360–380°C. To study the phase content of FDIP surface layers by means of Mössbauer spectroscopy a two-stage technique was used to synthesize  $^{56}\text{Fe}$  particles with the  $^{57}\text{Fe}$  surface layer. On the first stage  $^{56}\text{FeOOH}$  was subjected to a high-temperature reduction in  $\text{H}_2$ -flow to form powdered  $^{56}\text{Fe}$  followed by a surface deposition of  $^{57}\text{FeOOH}$ . The resulting sample was subjected to

re-reduction. Oleic acid was taken as a stabilizing coating. According to the electron microscopic study the average size of the resultant particles was  $\sim 90$  nm and their shape was close to spherical.

## RESULTS AND DISCUSSION

Mössbauer spectrum of the original  $\alpha$ -FeOOH comprises two components (Fig1-1). The observed strong component at  $H=363$  kOe is well-correlated with the value  $H=360$  kOe for this compound (3). The value of the hyperfine field of a weak component with  $H=475$  kOe is close to that of  $\text{Fe}_3\text{O}_4$  (3). This evidences that a slight quantity of magnetite  $\text{Fe}_3\text{O}_4$  (6 wt.%) is present in the sample along with  $\alpha$ -FeOOH.

### *Bulk Study*

After an hour reduction two intensive components with  $H_1=490$  kOe and  $H_2=458$  kOe corresponding to the hyperfine field values for  $\text{Fe}_3\text{O}_4$  appear in Mössbauer spectrum and a weak component with  $H_3=331$  kOe from  $\alpha$ -Fe (3). After three hours reduction the intensity of the  $H_3$  component drastically increases (Fig.1-3) and embraces the whole spectrum, representing after five hours of reduction only  $H_3$ -component (Fig.1-4). It follows from the spectra obtained that weight fractions of  $\alpha$ -Fe in the samples subjected to reduction for 1,3 and 5 hours are 2%,

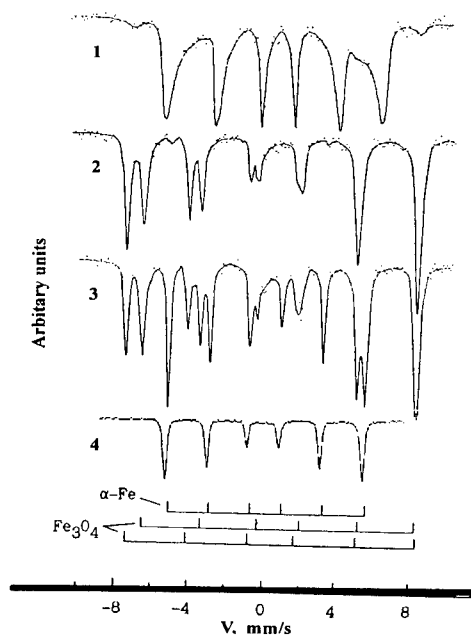


Fig.1. Mössbauer spectra of FDIP, prepared by reduction of  $\alpha$ -FeOOH in  $\text{H}_2$  flow, taken at different time: 1 - original  $\alpha$ -FeOOH, 2 - 1 hour, 3 - 3 hours, 4 - 5 hours.

30% and 100%, respectively. The comparison of the obtained Mössbauer spectra with those of standard samples FeO and Fe<sub>2</sub>O<sub>3</sub> does not indicate the formation of these phases in process of reduction. Hereby it is evident from the data obtained that the following conversions occur in process of reduction of  $\alpha$ -FeOOH up to  $\alpha$ -Fe:  $\alpha$ -FeOOH  $\rightarrow$  Fe<sub>3</sub>O<sub>4</sub>  $\rightarrow$   $\alpha$ -Fe.

### Surface Study

Low-intensity lines from  $\alpha$ -Fe, which result from the incomplete removal of <sup>57</sup>Fe from <sup>56</sup>Fe, are observed in Mössbauer spectrum of <sup>56</sup>Fe (Fig. 2a-1). A high-quality spectrum was recorded for <sup>56</sup>Fe powder with assumed <sup>57</sup>FeOOH layer. The two components (Fig. 2b-2) are practically observed on the P(H) plot at H=470 kOe and H=0. Since no lines are practically attributable to hydroxide in Mössbauer spectrum and the P(H) plot at H=360 kOe, the obtained data evidence that when <sup>57</sup>Fe-compound is being deposited on  $\alpha$ -<sup>56</sup>Fe particles, no  $\alpha$ -<sup>57</sup>FeOOH

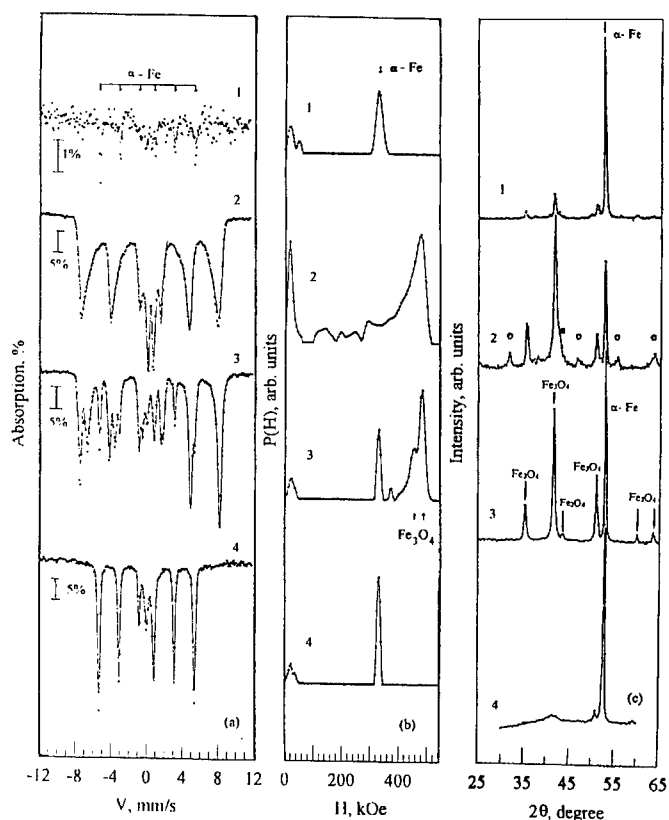


Fig. 2. Mössbauer spectra (a), P(H) (b) and X-ray diffraction patterns (c): 1-initial <sup>56</sup>Fe powder, 2-<sup>56</sup>Fe with assumed <sup>57</sup>FeOOH surface layer, 3-after partial reduction, 4-after complete reduction.

layer forms on its surface. At the same time lines attributed to  $\alpha$ -Fe (~20 mass%) and  $\text{Fe}_3\text{O}_4$  (~80 mass%) as well as to the phase labelled by circles are present on the X-ray diffraction pattern of this sample (Fig. 2c-2). The line position of this phase as well as the resultant paramagnetic doublet parameters in Mössbauer spectrum (Fig 2c-1) allow them to be assigned to  $\gamma$ -FeOOH (3-5).

Judging by the main lines in X-ray diffraction pattern and the line at  $H=470$  kOe in  $P(H)$ , which is inherent to  $^{57}\text{Fe}_3\text{O}_4$ , it is this magnetic phase, instead of  $\alpha$ - $^{57}\text{FeOOH}$ , that is present on the surface layer of  $\alpha$ - $^{56}\text{Fe}$  powder. The Mössbauer spectrum features of this phase does not, however, coincide with the spectra of the crystalline  $\text{Fe}_3\text{O}_4$  (3). It may be conjectured that during the deposition a disordered or highly distorted  $\text{Fe}_3\text{O}_4$  phase is formed on the surface, which gives not two lines at  $H_1=490$  and  $H_2=460$  kOe (3) but a wide distribution of hyperfine magnetic fields. Besides, some  $\gamma$ -FeOOH is also found in the surface layer. Based on the average particle sizes ~90 nm and assuming their spherical shape and the amount of the surface deposited layer about 20 wt% of the original  $\alpha$ - $^{56}\text{Fe}$ , the thickness of the surface layer, from which Mössbauer spectrum was registered, was approximately estimated to be 4-5 nm. After partial reduction in  $\text{H}_2$ -flow two phases, namely,  $\text{Fe}_3\text{O}_4$  (~45 mass%) and  $\alpha$ -Fe (~55 mass%) are observed on the surface of the obtained particles according to the Mössbauer spectrum,  $P(H)$ -plot (Figure 2a,b,c-3) and X-ray pattern. The form and the parameters of Mössbauer spectrum are in good correlation with the reported data (3). The experimental data (Fig. 2a,b,c-4) show that after complete reduction the particles are essentially  $^{56}\text{Fe}$  with the  $^{57}\text{Fe}$  surface layer. In contrast to bulk (Fig.1-4) a small quantity of the  $\gamma$ -FeOOH phase is present in the surface layer as evidenced by a paramagnetic doublet in Mössbauer spectrum (Fig 2a-4).

Mössbauer spectroscopy and X-ray diffraction were thus used to investigate changes in phase content both of the bulk and the surface layers of FDIP in process of their preparation by high-temperature reduction in  $\text{H}_2$  flow. It has been demonstrated that using a special sample preparation technique one can study the surface layers several nm thick by means of transmission Mössbauer spectroscopy, and not just conversion electrons Mössbauer spectroscopy [6-8].

## REFERENCES

1. Mikhailik, O.M., Shklovskaya, N.I., Suzdalev, I.P., Imshenik V.K. and Chuiko, A.A., *Zhurnal Prikladnoi Khimii*, 1988 61, 2414. (in Russian)
2. Van der Kraan, A.M., *Phys. Stat. Sol. (a)*, 1973, 18, 215.
3. *Chemical Applications of Mössbauer Spectroscopy*, ed. by Goldanskii, V.I. and Herber, R.H., Academic Press, New-York and London, 1968.
4. *Powder diffraction File, Alphabetical Index, Inorganic phases*, International Center for Diffraction Data, Pennsylvania, 1985.
5. Kulgavchuk, D.S., *Nukleonika*, XIV, 777, 1969.
6. Przybylski, M., and Gradmann, U., *Phys. Rev. Lett.*, 1987, 59, 1152.
7. Fujii, T., Takano, M., Katano, R., Bando, Y. and Isozumi, Y., *J. Appl. Phys.*, 1990, 68, 1735
8. Korecki J. and Gradmann, U., *Phys. Rev. Lett.*, 1985, 55, 2491.



Pergamon

NanoStructured Materials, Vol. 12, pp. 215–219, 1999  
Elsevier Science Ltd

© 1999 Acta Metallurgica Inc.

Printed in the USA. All rights reserved  
0965-9773/99/\$—see front matter

PII S0965-9773(99)00102-6

## SYNTHESIS AND CHARACTERIZATION OF PHOTOCHROMIC MOLYBDENUM AND TUNGSTEN OXIDE NANOPARTICLES

Shoutian Li and M. Samy El-Shall\*

Department of Chemistry  
Virginia Commonwealth University  
Richmond, VA 23284-2006

**Abstract:** *Weblike aggregates of coalesced MoO<sub>3</sub> and WO<sub>3</sub> nanoparticles have been prepared by a laser vaporization-controlled condensation technique. The nanoparticles show a very strong photochromic effect: the color change is one order of magnitude faster than that observed for the corresponding bulk material. The photochromic effect is also observed upon exposure of the MoO<sub>3</sub> nanoparticles to normal room light. ©1999 Acta Metallurgica Inc.*

### INTRODUCTION

Molybdenum and tungsten trioxides are photochromic materials that change color upon going from one oxidation state to another by absorption of light (1). The photochromic materials have potential practical applications in areas such as displays, imaging devices, “smart windows”, and solar energy conversion (2,3,4). In the last two decades, intense interest has been focused on the bulk photochromic materials, while nanoscale particles have not been given much attention. In this paper, we study the photochromic properties of MoO<sub>3</sub> nanoparticles and find that the color change for the nanoparticles is one order of magnitude faster than that observed for bulk MoO<sub>3</sub>. We also present a brief characterization of the tungsten oxide nanoparticles.

### EXPERIMENTAL

The molybdenum and tungsten oxide nanoparticles were prepared by a laser vaporization-controlled condensation (LVCC) technique that has been described in several publications (5). The method is based on coupling laser vaporization of metals with controlled condensation from the vapor phase, which eliminates the need for high temperatures and for chemical precursors and leads to good control over particle size and aggregation. Detailed description of the method and the reaction chamber can be found elsewhere (5). Here, we only offer a brief description of the experimental parameters. The Mo or the W metal atomic vapor was generated by pulsed laser vaporization using the second harmonic (532 nm) of a Nd:YAG laser (30–50 mJ/pulse). The Mo and W targets, with a stated purity of 99.95%, were obtained from Aldrich. The reaction chamber was filled with O<sub>2</sub> at a pressure of 800 torr, which acted as



a carrier as well as a reactive gas. The bottom plate was kept at room temperature while the top plate, where the nanoparticles were deposited, was kept between  $-80^{\circ}\text{C}$  and  $-90^{\circ}\text{C}$ .

Reflection UV-vis absorption spectra were obtained from a Shimadzu UV-265 spectrometer with  $\text{BaSO}_4$  as a reference. For the photochromic effect studies, the nanoparticles pressed on the smooth surface of the  $\text{BaSO}_4$  substrate were exposed to an excimer laser beam (308 nm, 72 mJ/pulse) for a desired time and then the samples were transferred to the UV-265 spectrometer to record the absorption spectra.

### RESULTS AND DISCUSSION

The Mo and W oxide nanoparticles prepared by the LVCC method and deposited on glass substrates, exhibit highly organized weblike structures characterized by long-range order through the sample as revealed by the SEM micrographs shown in Figure 1 for Mo oxide. It is clear that the primary spherical Mo oxide particles are aggregated into long chainlike strands. Each of the strands is composed of numerous individual particles of fairly uniform size. The chainlike strands are linked together into closed loops which form a web network. The long-range order of this three-dimensional weblike structure is also observed for other particles prepared by the same technique (6).

The  $\text{MoO}_3$  nanoparticles appear a white-pale-green color. The bulk  $\text{MoO}_3$  obtained from Aldrich is gray. It is interesting that blue Mo oxide nanoparticles are obtained when the  $\text{O}_2$

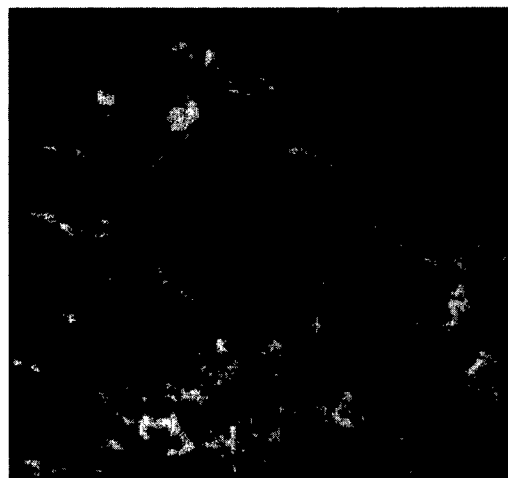


Figure 1. SEM micrograph of  $\text{MoO}_3$  nanoparticles.

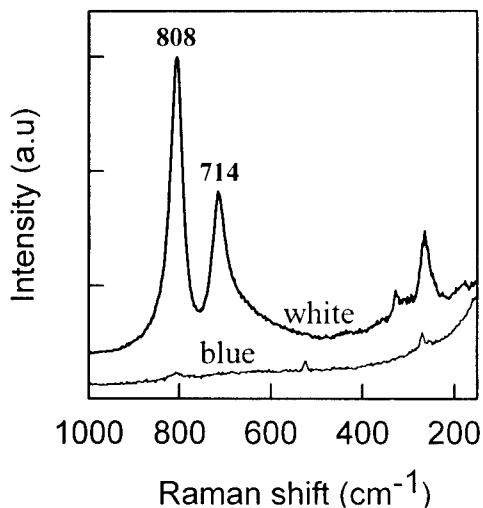


Figure 2. Raman spectra of  $\text{WO}_3$  nanoparticles before (white) and after (blue) the 532 nm laser irradiation.

content in the reaction chamber (using He as carrier gas) is in the range of 1% to 90%. The white nanoparticles made in a pure  $\text{O}_2$  environment are molybdenum trioxide particles, while the blue particles contain the  $\text{Mo(V)}$  oxide composition.

The X-ray diffraction pattern of  $\text{WO}_3$  nanoparticles indicates a monoclinic crystalline structure similar to the bulk material. The color of bulk  $\text{WO}_3$  is yellow while the  $\text{WO}_3$  nanoparticles prepared by the LVCC method exhibit a white color. This white color changes to blue upon irradiation of the nanoparticles with the second harmonic of the Nd:YAG laser (532 nm) in air. We measured the IR and the Raman spectra of the particles before and after the irradiation and the Raman spectra are shown in Figures 2. The spectra measured after irradiation clearly show all the features associated with the reduction of  $\text{WO}_3$  to  $\text{W}_2\text{O}_5$ . These features include the decrease in the IR absorption at  $800\text{ cm}^{-1}$  and the disappearance of the Raman bands at  $802\text{ cm}^{-1}$  and  $716\text{ cm}^{-1}$ , which are the characteristic IR and Raman features of  $\text{WO}_3$ .

The  $\text{MoO}_3$  nanoparticles show a strong photochromic effect. The dependence of the UV-vis absorption spectra of the white molybdenum trioxide sample (prepared in 800 torr  $\text{O}_2$  in the reaction chamber) on the irradiation time of an excimer laser (308nm, 72mJ/pulse) is shown in Figure 3. The change in absorbance is seen across the visible range; the largest change occurs from 600 nm to 860 nm. For example, the change of absorbance at 750 nm is 0.7409 after the irradiation of the nanoparticle sample for 36 min. For comparison, a series of UV-vis spectra of bulk  $\text{MoO}_3$  (Aldrich) was also measured at different irradiation times under the same conditions as the nanoparticle sample and the results are shown in Figure 4. The change of absorbance at 750 nm is only 0.0506 for the bulk  $\text{MoO}_3$  after irradiation with the excimer laser for 36 min. Thus, the color change in the nanoparticle sample is 15 times stronger than that of the bulk sample under similar irradiation conditions. The dependencies of the change in absorbance on the irradiation time for the nanoparticle and bulk samples are shown in Figure 5.

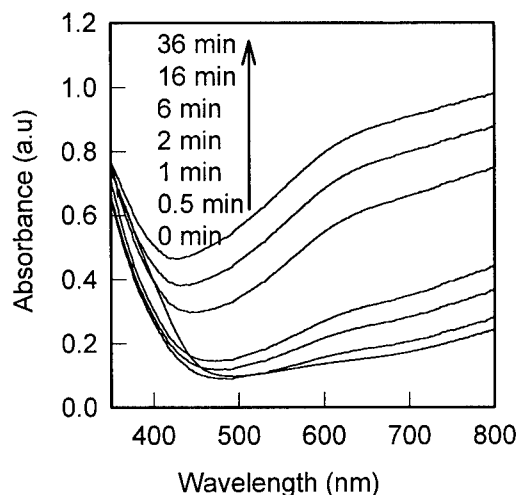


Figure 3. UV-vis spectra of white  $\text{MoO}_3$  nanoparticles as a function of the irradiation time.

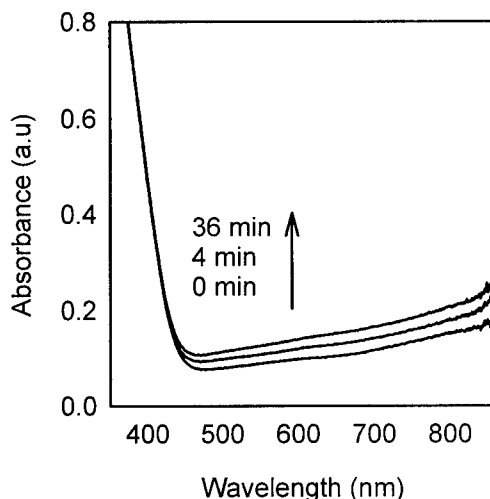


Figure 4. UV-vis spectra of bulk  $\text{MoO}_3$  as a function of the irradiation time.

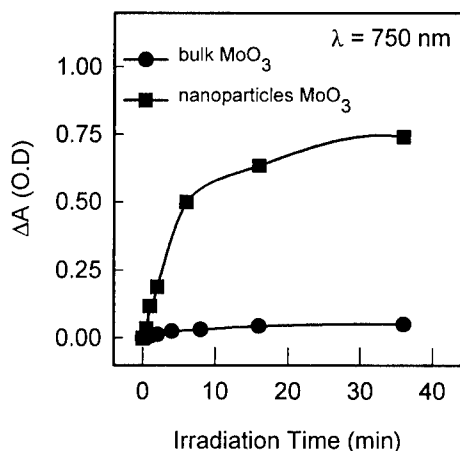


Figure 5. The change of absorbance for  $\text{MoO}_3$  nanoparticles (square-line) and bulk  $\text{MoO}_3$  (circle-line) as a function of the irradiation time with 308 nm laser.

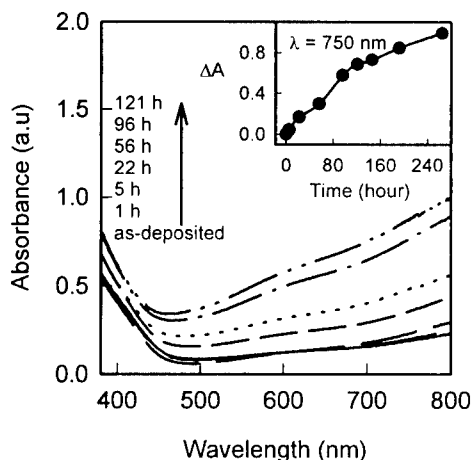


Figure 6. UV-vis absorption of  $\text{MoO}_3$  nanoparticles as a function of exposure time in air. Insert shows the absorbance change at 750 nm as a function of time.

The white molybdenum trioxide particles are not stable: they slowly change their color to blue after the sample is stored at ambient conditions. We measured the absorption spectra at different times after removing the  $\text{MoO}_3$  nanoparticles from the reaction chamber and the results are shown in Figure 6. The insert in Figure 6 shows the absorbance change at  $\lambda=750$  nm at different times. The spectrum of the as-deposited particles was measured one hour after removing the particles from the reaction chamber and the times given in Figure 6 were measured relative to the time of measuring the absorption spectrum of the as-deposited particles. After 10 days, the absorbance at 750 nm increased to 0.99. This color change upon exposure to room light is similar to the laser-induced photochromic effect except that the time scale is different (see Figure 2). This indicates that for  $\text{MoO}_3$  nanoparticles, the photochromic effect can take place even at the ambient conditions. This behavior is different from the white  $\text{WO}_3$  nanoparticles, which are stable under ambient conditions.

The photochromic effect of  $\text{MoO}_3$  nanoparticles is comparable to the electrochromic effect of  $\text{MoO}_3$  thin films studied by other groups (7,8).

## CONCLUSIONS

Molybdenum and tungsten oxide nanoparticles have been prepared by the LVCC method. The nanoparticles show a very strong photochromic effect: the color change is one order of magnitude faster than for bulk  $\text{MoO}_3$ . The  $\text{MoO}_3$  nanoparticles exhibit the photochromic effect upon exposure to normal room light.

### ACKNOWLEDGMENT

The authors gratefully acknowledge financial support from the NASA Microgravity Materials Science Program (Grant NAG8-1276).

### REFERENCES

1. Durr, H; Bouas-Laurent, H. *Photochromism – Molecules and Systems*, PP.5, Elsevier: Amsterdam, Oxford, New York and Tokyo, 1990.
2. Mortimer, R. *J. Chem. Soc. Rev.* 26, 147, 1997.
3. Yao, J. N.; Hashimoto, K.; Fujishima, A. *Nature*, 355, 624, 1992.
4. Bechinger, C.; Ferrere, S.; Zaban, A.; Sprague, J.; and Gregg, B. A. *Nature*, 383, 608, 1996.
5. Li, S.; Silvers, S. J.; El-Shall, M. S. *J. Phys. Chem.* 101, 1794, 1997.
6. El-Shall, M. S.; Li, S.; Turkki, T.; Graiver, D.; Pernisz, U. C.; Baraton, M. E. *J. Phys. Chem.* 99, 17805, 1995.
7. (a) Yao, J. N.; Loo, B. H.; Hashimoto, K.; Fujishima, A. *J. Electroanal. Chem.* 290, 263, 1990. (b) Yao, J. N.; Loo, B. H.; Fujishima, A. *Ber. Bunsengers. Phys. Chem.* 94, 13, 1990.
8. Yao, J. N.; Loo, B. H.; Hashimoto, K.; Fujishima, A. *Ber. Bunsengers. Phys. Chem.* 95, 557, 1991.



Pergamon

NanoStructured Materials, Vol. 12, pp. 221–224, 1999

Elsevier Science Ltd

© 1999 Acta Metallurgica Inc.

Printed in the USA. All rights reserved

0965-9773/99/\$—see front matter

PII S0965-9773(99)00103-8

## SYNTHESIS AND TENSILE PROPERTY OF NANOCRYSTALLINE METAL COPPER

X.J. Wu<sup>1,2</sup>, L.G. Du<sup>1</sup>, H.F. Zhang<sup>1</sup>, J.F. Liu<sup>1</sup>, Y.S. Zhou<sup>1</sup>, Z.Q. Li<sup>1</sup>, L.Y. Xiong<sup>3</sup> and Y.L. Bai<sup>2</sup>

1, Department of Materials Science and Engineering, Zhejiang University,  
Hangzhou 310027, China

2, Laboratory of Non-linear Mechanics of Continuous Media, Institute of Mechanics,  
Academia Sinica, Beijing 100080, China

3, Institute of Metals Research, Academia Sinica, Shenyang 110015, China

**Abstract**—A large disk-shaped specimen of nanocrystalline metal copper, with a diameter of 80 mm and thickness 5 mm, was synthesized by an inert gas condensation and in-situ warm compacting technique. The grain size and density of the specimen are 36 nm and 94.3 % of standard density, respectively. The positron lifetime and intensity were measured for monitoring the defects in the specimen. The results indicated that the size and amount of the vacancies and microvoids in the large specimen are close to that found in the small specimens of other nanostructured materials prepared by the same technique. The tensile stress-strain curve has been precisely measured by using the load cell and foil strain gauge. The results showed that the elastic modulus, yield stress, fracture strength, elongation and microhardness are 0.65, 1.42, 1.82, 0.20 and 6 times of that for coarse-grained polycrystalline metal copper, respectively. ©1999 Acta Metallurgica Inc.

### INTRODUCTION

Many studies revealed that the microhardness of nanostructured (nano)-metals, -alloys, -intermetallic compounds and -ceramics enhances by factors from 2 to 7 than their coarse-grained counterparts (1-4). This novel mechanical property is important both for fundamental research and applications of nano-materials. But the hardness is insufficient for evaluating the mechanical property of materials. Elastic modulus, strength and ductility, which can be conducted from tensile tests, are generally used to characterize the basic mechanical property. Up to now, only a few results concerning tensile tests for nano-materials have been reported (5-9), owing to the difficulty for fabricating relatively large specimens with grain size less than 100 nm. On the other hand, mechanical properties are sensitive to imperfection and purity of materials, hence synthesis of fully dense nano-materials without contamination is very important.

The present paper describes the fabrication of a large specimen of nano-metal Cu by means of an inert gas condensation and in situ warm compacting technique, provides the experimental results on defects and tensile properties of the specimen, and indicates the influence of air contamination of nanoparticles in the specimen on the tensile property.

## EXPERIMENTAL PROCEDURE

The nano-Cu specimen used in this investigation was synthesized by an inert gas condensation and in-situ warm compacting technique. The nano-particles of metal copper were fabricated from high purity precursor metal copper evaporated by ARC heating into 400 Pa of Ar gas in an evaporating chamber. After an evaporation /gas condensation run, the vacuum of evaporating chamber was returned to a vacuum of  $9 \times 10^{-6}$  Pa. Subsequently the collected nano-particles were consolidated at 200°C in an in-situ compacting unit under a pressure of 1.0 GPa. The dimension of a disc-shaped specimen produced is 80 mm in diameter and 5 mm thickness, as shown in Figure 1, which might be the largest specimen of nano-metals synthesized by inert gas condensation and in-situ compacting technique. The density of the specimen was measured by using Archimedes principle. The average grain size was determined by a Fourier analysis x-ray diffraction (XRD). The positron life times and intensities, which are sensitive to defects in nano-materials, were monitored by using a fast-fast coincidence ORTEC system.

The tensile tests were performed on a tensile device attached in a S-570 type scanning electron microscope (SEM) for the samples with the gauge length of 6 mm, width 2 mm and thickness 1.5 mm, which were cut from the large disc of nano-Cu. The stress and strain of every sample were precisely measured by means of a load cell and a constantan foil strain gauge attached on the center of the gauge section. For investigating the influence of contamination on tensile property, another disc of nano-Cu was prepared by exposing the nano-particles in air for 1 hour before compacting in vacuum.

## RESULTS AND DISCUSSION

The average grain size and density of the specimen prepared are 36 nm and 94.3 % of standard density, respectively. The results of positron life times and intensities for nano-Cu were listed in Table 1. The relevant results found in nano-Fe (10,11), -NiP (12) -TiO<sub>2</sub> (13) were also listed in Table 1 for comparison. The positron life times  $\tau_1$  and  $\tau_2$  for nano-Cu are in the range of that measured in nano-Fe, -TiO<sub>2</sub> and -NiP. The lifetime  $\tau_1$  ( $175 \pm 5$  ps) for nano-Cu is nearly the same as that for nano-Fe ( $180 \pm 15$  ps) and hence should be taken as the indication of the presence of free volumes with the size comparable to that of a monovacancy in the interfaces. The lifetime  $\tau_2$  ( $345 \pm 7$  ps) for nano-Cu is quite similar to that for nano-Fe ( $360 \pm 30$  ps), -NiP ( $350 \pm 20$  ps) and -TiO<sub>2</sub> ( $385 \pm 16$  ps) and should be corresponding to the presence of free volumes, with the size comparable to a cluster of 10-15 vacancies, at the intersection of two or three crystallite interfaces. The lifetimes  $\tau_3$  ( $3498 \pm 763$  ps) for nano-Cu is longer than that found in nano-Fe, -NiP and -TiO<sub>2</sub>. It should be attributed to the formation of larger microvoids in nano-Cu. The size of microvoids in the present specimen is larger than that found in nano-Fe, -NiP and -TiO<sub>2</sub>, but the amount of them is quite small (only  $0.6 \pm 0.3\%$ ) and less than that found in nano-Fe and -TiO<sub>2</sub>. The main defects in the present specimen are monovacancies and vacancy-clusters with the equivalent amount ( $I_1/I_2 = 1.08$ ). In general, the vacancy and microvoid-like defects formed in the present large specimen are similar to that found in the small specimens of nano-Fe and -TiO<sub>2</sub>, synthesized by the same technique.

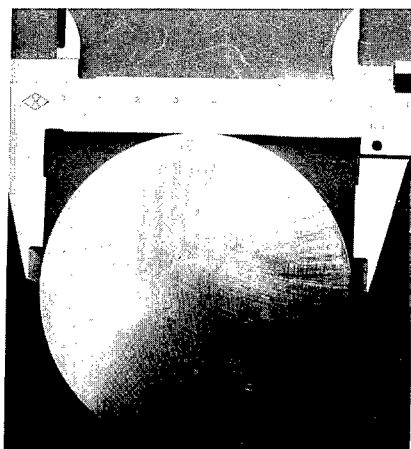


Figure 1, Photograph of a large specimen of nanocrystalline metal copper with diameter of 80 mm and thickness 5 mm.

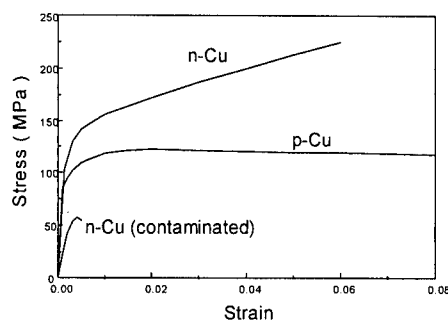


Figure 2, Stress-strain curves for nanocrystalline metal copper with clean and air contaminated interfaces, as well as for coarse-grained polycrystalline metal copper, respectively.

The stress-strain curves for the samples of nano-Cu with clean and air-contaminated interfaces, as well as of polycrystalline metal copper are shown in Figure 2. The elastic modulus, yield stress, fracture strength and elongation are 84 GPa, 118 MPa, 237 MPa, and 0.06, respectively, which are 0.65, 1.42, 1.82, and 0.15 times of that of coarse-grained polycopper. The morphology of fracture surfaces of nano-Cu observed by SEM is mainly intergranular, but with small amount of ductile fracture characteristics. The microhardness of the present sample is 6 times higher than that of poly-Cu. It could be seen from Figure 2 that

Table 1 Positron lifetimes and intensities for nano-Cu and other nano-materials

	$\tau_1$	$\tau_2$	$\tau_3$	$\tau_4$	$I_1$	$I_2$	$I_3+I_4$	$I_1/I_2$	References
	(ps)	(ps)	(ps)	(ps)	(%)	(%)	(%)		
nano-Cu	175.4 $\pm 5$	345 $\pm 7$	3498 $\pm 763$		51.7 $\pm 3$	47.7 $\pm 3$	0.6 $\pm 0.3$	1.08	
nano-Fe	180 $\pm 15$	360 $\pm 30$	1200 $\pm 200$	4000 $\pm 500$			10-30	0.5-1.0	10, 11
nano-NiP	152.3 $\pm 1.3$	350 $\pm 20$	1470 $\pm 96$		94.4 $\pm 1.3$	4.5 $\pm 1.2$	1.1 $\pm 0.1$	21.0	12
nano-TiO <sub>2</sub>	226 $\pm 15$	385 $\pm 16$	1939 $\pm 66$		37.9 $\pm 8.2$	55.9 $\pm 8.0$	6.2 $\pm 0.2$	0.67	13

the tensile property of the air-contaminated sample is very poor. Its tensile strength is only one fourth of that of nano-Cu with clean interfaces, and its elongation is less than 0.005.

### CONCLUSIONS

A large disc-shaped specimen of nanocrystalline metal copper with the diameter of 80 mm and thickness 5 mm has been successfully synthesized by an inert gas condensation and in-situ warm compacting technique. Its grain size and density are 36 nm and 94.3 % of standard density, respectively. The measurement of positron lifetime and intensity indicates that the size and amount of monovacancies, vacancy-clusters and microvoids in the large specimen of nano-Cu are close to that found in the small specimens of other nanostructured materials synthesized by the same technique. The tensile property of nano-Cu shows reduced elastic modulus and ductility, and enhanced yield stress and fracture strength, comparing with that of the coarse-grained polycrystalline metal copper. But the microhardness of nano-Cu enhances extremely, which is not in proportion to the enhancement of the tensile strength. The degradation of tensile property is observed for the nano-Cu with air-contaminated interfaces.

### ACKNOWLEDGEMENTS

This work was supported by the National Natural Science Foundation of China under Grant 59431021 and by the Laboratory for Nonlinear Mechanics of Continuous Media, Institute of Mechanics, Academia Sinica.

### REFERENCES

1. Gleiter, H., Prog. Mater. Sci., 1989, 33, 223.
2. Suryanarayana, S., Mukhopadhyay, D., Pataikov, S.V. and Froes, F.H., J. Mater. Res., 1992, 7, 2114.
3. Siegel, R.W., Mater. Sci. Forum, 1997, 235-238, 851.
4. Qin, X.Y., Wu X.J. and Zhang, L.D., Nanocrystalline Materials, 1995, 5, 101.
5. Nieman, G.W., Weertman J.R. and Siegel, R.W., Scripta Metall. Mater., 1990, 24, 145.
6. Guenther, B., Baalman A. and Weiss, H., Mater. Res. Soc. Symp. Proc., 1990, 195, 611.
7. Nieman, G.W., Weertman J.R. and Siegel, R.W., J. Mater. Res., 1991, 6, 1012.
8. Valiev, R.Z., Mater. Sci. Eng., 1997, A234-236, 59.
9. Rittner, M.N., Weertman, J.R., Eastman, J.A., Yoder, K.B. and Stone, D.S., Mater. Sci. Eng., 1997, A237, 185.
10. Schaefer, H.E., and Wurschum, R., Phys. Lett., 1987, 119A, 370.
11. Schaefer, H.E., Wurschum, R., Birringer, R. and Gleiter, H., Phys. Rev., 1988, B38, 9545.
12. Shi, M.L., Xiong, L.Y., Deng, W., Lu, K. and Patu, S., J. Appl. Phys., 1991, 69, 4451.
13. Xiong, L.Y., Deng, W., Zhu, J., Dupasquier, A., Wu, X.J. and Ji, X.L., Mater. Sci. Forum, 1995, 175-178, 577.





Pergamon

NanoStructured Materials, Vol. 12, pp. 225–228, 1999

Elsevier Science Ltd

© 1999 Acta Metallurgica Inc.

Printed in the USA. All rights reserved

0965-9773/99/\$—see front matter

PII S0965-9773(99)00104-X

## PREPARATION OF SUBMICROMETER NICKEL POWDERS BY THE REDUCTION FROM NONAQUEOUS MEDIA

Andrej Degen and Jadran Maček

University of Ljubljana, Faculty of Chemistry and Chemical Technology  
1000 Ljubljana, Aškerčeva 5, Slovenia

**ABSTRACT**— Nickel powders in the submicrometer size range were prepared by a chemical reduction-precipitation method from nonaqueous solutions of nickel salts. Hydrazine was used as the reducing agent and paraffin oil, ethylene glycol, di- and tri-ethanolamine as the reaction media in order to carry out the reactions at higher temperatures, and, for the latter two media, to provide the appropriate basic environment for the reduction. The characteristics of the resulting end products, especially the particle size and size distribution, as well as the micromorphological characteristics, the yield of the reaction and the purity of the nickel powders, depend on the reaction conditions. The mean particle size of the nickel powders can be lowered also by changing the homogenous nucleation into a heterogeneous one by adding traces of palladium. Nickel powders with mean particle sizes ranging from 0.1 to several  $\mu\text{m}$  and with up to 99.8% purity were obtained in this way.

©1999 Acta Metallurgica Inc.

### INTRODUCTION

Fine nickel powders have been studied extensively of late due to their numerous applications in technology. They can be prepared by a variety of physical and chemical processes. The process should be chosen in accordance with the desired nickel powder properties and the economical aspects of the process should also be taken into account.

One of the possible preparation methods is the reduction of nickel cations from solutions of nickel salts by a powerful reducing agent. The rate and yield of the reaction are both enhanced at higher reaction temperatures. The reaction temperature of an aqueous medium is limited by the relatively low boiling point of water unless the experiment is carried out at higher pressure in an autoclave. High-pressure work can be avoided if the reaction takes place in appropriate nonaqueous media with a higher boiling point. In addition to extending the temperature range, the use of nonaqueous solvents also enables the modification of other significant reaction parameters, such as the basicity of the medium, viscosity, etc.

### EXPERIMENTAL

In these experiments paraffin oil (PO), ethileneglycol (EG), diethanolamine (DEA) and triethanolamine (TEA) solvents were used. The first one is a nonpolar solvent, the second one

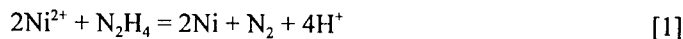
is a polar one, as are the final two, although they also have pronounced basic properties, TEA more than DEA.

Nickel powders were prepared from analytical grade  $\text{Ni}(\text{CH}_3\text{COO})_2 \cdot 4\text{H}_2\text{O}$  that was dissolved in the PO, EG, DEA and TEA solvents. A combination of two solvents was also tested. Reactions were carried out in 500 ml glass beakers equipped with stirrers. Nickel precursor was dissolved in the reaction medium ( $\text{Ni}^{2+}$  - concentration 5g/l) and heated to 180 - 220°C. Hydrazine was added either in the form of a 24% aqueous solution of hydrazine hydrate ( $\text{N}_2\text{H}_4 \cdot \text{H}_2\text{O}$ ) or as an anhydrous solution of hydrazine in the same solvent that was used as the reaction medium (1). In some experiments a small amount of  $\text{PdCl}_2 \cdot 2\text{H}_2\text{O}$  was also added into the starting solution of nickel salt.

After the addition of the reducing agent to the heated nickel precursor solution, dark gray nickel powders precipitated from the reaction mixture after several minutes. They were filtered off, washed with acetone and dried in a vacuum dessicator. Their characteristics were determined by a chemical analysis for the nickel content (volumetric titration with EDTA) (2), a scanning electron microscope (JEOL T400).

## DISCUSSION

The reduction of nickel ions by hydrazine is often described in the literature as a reaction of  $\text{Ni}^{2+}$  ions with hydrazine molecules in neutral and basic environments, or hydrazinium ions,  $\text{N}_2\text{H}_5^+$ , in moderately acidic media (1):



The reaction does not proceed according to this reaction scheme, but first a complex ion is formed between the nickel cation, hydrazine and anion. In cases where nickel chloride hexahydrate was used as the precursor salt the already well-known complex  $\text{Ni}(\text{N}_2\text{H}_4)_2\text{Cl}_2$  was formed, isolated and confirmed by chemical analysis (1). If lower concentrations of nickel salt (5g/l) are used, this complex remains dissolved, but at higher concentrations (10 - 20 g/l), a precipitate forms. The use of hydrazine as a reducing agent is advantageous since during the reaction it decomposes into gaseous nitrogen and hydrogen cations that do not contaminate the end product.

The results of the experiments are shown in Table 1. They were obtained with a 5 g/l starting concentration of nickel acetate and with a 1:2 molar ratio of hydrazine to nickel at a reaction temperature of 185°C. The results reveal that the purity of the obtained product as well as the particle size are strongly affected by the solvent characteristics. In mixtures of PO and DEA, the purity of nickel powders is not appropriate, e.g. in the range from 87 - 95%. However, in pure DEA (Figure 1.) and TEA and all mixtures of both solvents, products with a nickel content over 99% can be obtained. The particles are spherical in shape and their diameters, as determined by SEM micrographs, range from 1.55 to 0.35  $\mu\text{m}$ . The more basic medium facilitates the reduction of nickel ions by hydrazine, enhances the nucleation rate and the precipitation of the same amount of nickel from the solution from the larger number of nuclei results in smaller particle sizes according to the mass balance of the reaction. The yields of the reactions are for the same reason also better in more basic media, approaching 100% in

TABLE 1

Solvent [vol. %]	Reaction yield [%]	Ni content [w. %]	$d_{AV}$ [ $\mu\text{m}$ ]
PO (100%)	*	*	*
PO + DEA (12%)	33.88	95.09	1.55
PO + DEA (29%)	27.20	93.41	1.42
PO + DEA (47%)	24.69	84.21	1.37
PO + DEA (64%)	29.27	87.69	1.20
DEA (100%)	87.09	99.45	0.70
DEA + TEA (25%)	88.26	99.77	0.69
DEA + TEA (50%)	89.44	99.50	0.65
DEA + TEA (75%)	90.02	99.47	0.58
TEA (100%)	~100	99.07	0.35

\*nickel acetate is not soluble in pure paraffin oil

pure TEA. The purity of the nickel powders depends on the reaction conditions. The deviation of nickel content from 100% is due to the incomplete reduction and washing of the product. In spite of very thorough washing with acetone, traces of the reaction medium remain in the crevices and capillaries in the nickel powder particles and cannot be removed. The properties of the reaction medium and the intended further utilization of the powders show whether this minor residual amount of solvent can be detrimental for the intended use of the product. If the powders undergo further thermal treatment, these residues will leave nickel powder at temperatures above the boiling point of the solvent.

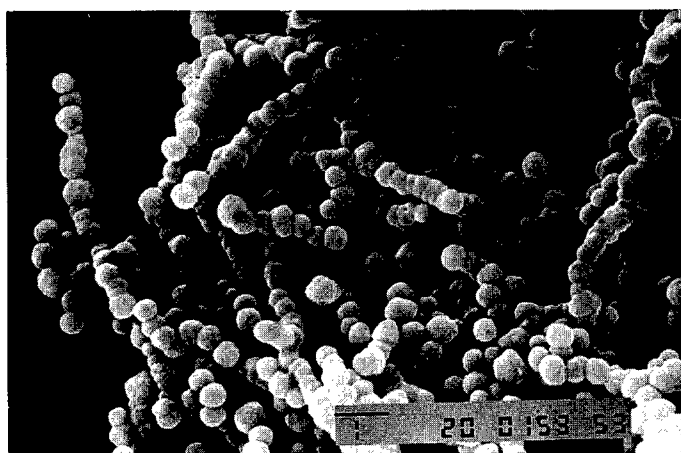


FIGURE 1.: Nickel powder prepared in DEA at 185°C

Another way to strongly affect the particle size of the product is to add small amounts of a metal that under the reaction conditions reduces much more easily (3), e.g. before the reduction of the nickel ions starts (Table 2). The reaction mechanism for the reduction - precipitation of nickel thus changes from a primary homogenous to secondary heterogeneous

TABLE 2

Precursor	Ni(OH) <sub>2</sub>		Ni(CH <sub>3</sub> COO) <sub>2</sub> ·4H <sub>2</sub> O	
Ni <sup>2+</sup> : Pd <sup>2+</sup>	Ni content [%]	d <sub>AV</sub> [μm]	Ni[%] content	d <sub>AV</sub> [μm]
2000	96.01	0.57	99.67	1.75
200	95.94	0.35	99.26	0.56
20	88.32	0.10	87.39	0.27

nucleation. The addition of PdCl<sub>2</sub>·2H<sub>2</sub>O in the ratio of 2000, 200 and 20 moles of nickel per mole of palladium to an EG solvent markedly changes the particle size. Palladium also affects the quality of the obtained nickel powders. Since EG is polar but not a basic reagent, the products obtained by reduction with hydrazine are always inferior with respect to Ni content compared to products obtained with DEA and TEA. This can also partially be attributed to the incomplete removal of the solvent when washing since with diminishing particle size their specific surface area increases and more of the solvent adheres to it.

## CONCLUSION

The reduction of nickel salts from their solutions through the use of nonaqueous solvents appreciably broadens the choice of experimental conditions. This can be achieved by selecting a reaction medium with the desired and required properties with respect to polarity, basicity, viscosity, boiling point and other properties. Furthermore, reaction conditions can also be tuned to a particular need by combining various solvents. A broad range of products with different characteristics can be obtained, but the best results with regard to the purity and lower average sizes of nickel powders can be obtained with TEA and MEA. The introduction of palladium salt into the reaction medium can further lower the size of the powders by changing the mechanism of nucleation and precipitation from a primary homogenous one to a secondary heterogeneous one and can also have some catalytic effect on the reaction as well.

## ACKNOWLEDGMENTS

This research was financed by the Ministry of Science and Technology of the Republic Slovenia.

## REFERENCES

1. Schmidt, E.W., *Hydrazine and its Derivates*, 1<sup>st</sup> Ed., John Wiley & Sons, New York, 1984
2. Flaschka, H.A., *EDTA Titrations*, 2<sup>nd</sup> Ed, Pergamon Press Ltd., London, 1964, p. 83.
3. Ducamp-Sanguesa, C., Herrera-Urbina, R., Figlarz, M., *Solid State Ionics* **63-65** (1993) p. 25-30.



Pergamon

NanoStructured Materials, Vol. 12, pp. 229–232, 1999

Elsevier Science Ltd

© 1999 Acta Metallurgica Inc.

Printed in the USA. All rights reserved

0965-9773/99/\$—see front matter

PII S0965-9773(99)00105-1

## PHYSICO-CHEMICAL CHARACTERIZATION OF NANOCRYSTALLINE (Fe, Ni) ALLOYS

K.-St. Werkmeister, F. Rullang, M. Koch, M. Heyer, G. Schwitzgebel

Universität des Saarlandes, FR 11.3 Physikalische Chemie

Postfach 151150, D-66041 Saarbrücken, Germany

*Abstract -- Nanocrystalline (Fe, Ni) alloys were prepared using pulsed electrodeposition (PE) and mechanical alloying (MA). When compared with thermally alloyed metals the phase separation into fcc and bcc is more pronounced, but incomplete mixing cannot be avoided especially in the MA samples. The specific interfacial enthalpies determined by solution calorimetry (SC) are systematically higher than those from differential scanning calorimetry (DSC). Electromotive force (EMF) measurements with solid electrolyte cells showed that the metastability of fcc alloys (e.g. invar) causes large shifts in the electrode potential. Corrosion processes of nanocrystalline (Fe, Ni) were observed and studied by atomic force microscopy (AFM), by DSC and especially by electrochemical impedance spectroscopy (EIS).*

©1999 Acta Metallurgica Inc.

### Introduction

Actually, nanocrystalline (nc) materials with magnetic properties are of scientific and practical interest because of special effects occurring, when the grain size is smaller than the extension of the magnetic domains (1). A prerequisite for these studies are structural and physico-chemical characterizations. XRD (x-ray diffraction) is a usual method for getting basic structural information concerning the phase composition and the mean grain size ( $D_V$ : volume averaged) e.g. by the Warren-Averbach method (2). This method furnishes also the mean micro strain as an energetic parameter. A further energetic parameter, the specific interfacial enthalpy  $\gamma_H$ , which is connected to  $D_V$  and the molar excess enthalpy  $\Delta H^{ex}$ , by the generalized Gibbs-Thompson equation:

$$\gamma_H = D_V \cdot \Delta H^{ex} / (2 \cdot g \cdot V_M) \quad (g: \text{geometrical factor (3)}, V_M: \text{molar volume}) \quad [1]$$

is in principle accessible by SC and DSC. In some two-component systems like (Fe, Ni) at least two more effects must be observed: incomplete mixing leads to variations in grain composition, and metastable phases may appear (e.g. the invar effect (4, 5)). The latter effect produces also considerable problems in EMF measurements, which often have been used in order to determine free energy data of equilibrium systems. The aim of the present work is to show how some of these difficulties can be dealt with and how some discrepancies can be interpreted.

## Experimental

nc Ni and nc (Fe, Ni) samples were prepared by pulsed electrodeposition (PE) (6) and mechanical alloying (MA) (7). PE samples were deposited on rotating disc electrodes (RDE) (540 rpm) in an acid sulfate bath, from which by composition variation alloys of different metal contents, grain size and texture were prepared. MA samples were produced by ball milling weighed amounts of Fe and Ni for 4 h in a SPEX 8000 mill. SC experiments were performed in a calorimeter (ZIROX Actron5) using  $\text{FeCl}_3$  as solvent. Electrochemical impedance measurements were used for corrosion studies (EG&G M6310). XRD patterns were generated by  $\text{CuK}\alpha$  (Siemens D500). The composition of the alloys was determined by using EDX on a SEM (CamScam S4). A Nanoscope III (DI) was used for AFM contact mode images.

## Results and Discussion

PE samples with molar fractions of iron  $x \leq 0.50 \pm 0.05$  showed only diffraction lines of the fcc phase ( $D_V \geq 10$  nm), whereas for  $x > 0.50$  the alloy always appears in two phases (bcc+fcc). For  $x = 0.90 \pm 0.05$  only lines of bcc (Fe, Ni) alloys were found. These alloys were highly textured (strong (110) reflections) and the peak analysis leads to grain sizes  $\geq 30$  nm.

For  $x \leq 0.4$  (fig. 1), mechanical alloying of Fe and Ni leads to nc (Fe, Ni) alloys, the lattice constants of which come close to values of microcrystalline (mc) samples (4). Not all fcc reflections can be evaluated (interference of fcc (111) and (222) with bcc (110) and (220) reflections). A deviation in the lattice constant for  $x = 0.33$  can probably be explained by the formation of the  $\text{FeNi}_3$  sublattice that does not appear in the mc sample. For  $x \geq 0.5$  increasing amounts of bcc phase could be seen in diffractogram. The further decrease of the fcc lattice constant with increasing Fe content (similar to the mc samples) is likely an effect of the presence of at least two different fcc alloy types, an Fe-rich (by alloying Ni into Fe) and a Ni-rich (by alloying Fe into Ni). For  $x \geq 0.8$  the fcc phase disappeared.  $D_V$  lies between 32 nm (pure Fe) and 38 nm (pure Ni).

### *Solution Calorimetry and Differential Scanning Calorimetry*

A summary of SC and DSC results is shown in fig. 2. MA (Fe, Ni) samples of several grain sizes have been obtained by annealing nc alloys to the given temperatures. The values from both methods lie on straight lines according to equation [1]. DSC results for  $D_V < 13$  nm from (8) have not been finally explained by the authors. The enhanced  $\Delta H^{\text{ex}}$  for the unannealed MA Ni77Fe23 sample is caused by relaxation of grain boundaries (9) (for nc Ni between 370 and 500 K). Grain growth corresponds to the maximal DSC peak at about 570 K.  $\gamma_H$  have been calculated with eq. [1]:  $2.7 \text{ J m}^{-2}$  (Ni, SC, 298 K);  $5.1 \text{ J m}^{-2}$  (Fe23Ni77, SC, 298 K) and  $1.0 \text{ J m}^{-2}$  (Ni, DSC, 570 K, see above). PE and MA samples give the same results. The reason for the difference between DSC and SC results is not known up to now. Formally the difference could be explained by assuming a lower molar heat capacity for the nanostate than for the microstate. This assumption would be contradictory to other authors (10). A fundamental discussion concerning heat capacities can only be given when all contributions to the heat effects,

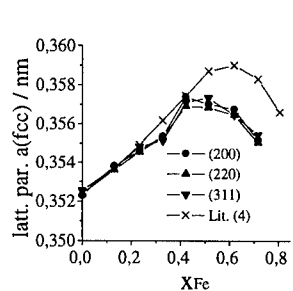


Fig.1 Lattice parameter  $a(\text{fcc})$  of nc MA (Fe, Ni) alloys

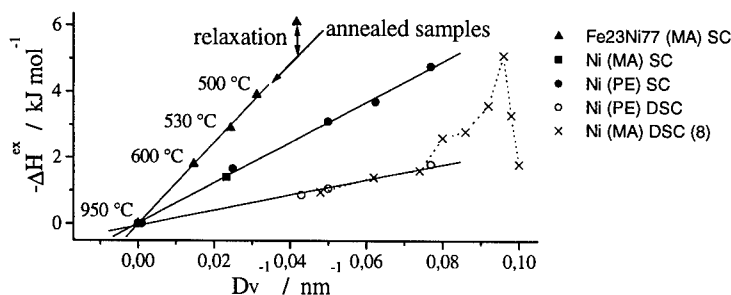


Fig.2 Gibbs-Thompson plot (eq.[1])

especially the oxidation (visible in AFM pictures), are analysed in detail.

#### EMF measurements

EMF measurements between 650 and 900 K were performed in a cell of the type: mc (Fe, Ni),  $\text{FeF}_2$ , NaF |  $\beta\text{-Na}_2\text{Al}_{22}\text{O}_{34}$  | NaF,  $\text{FeF}_2$ , Fe (symbolic notation), using  $\beta$ -alumina as solid electrolyte. They remain in the fcc phase although a bcc phase should separate according to the phase diagram (e.g. invar) (11). Negative EMFs were obtained (i.e. Fe in the alloy seems to be less noble than pure Fe), which demonstrates the thermodynamical metastability of the system. The meaning in terms of partial free enthalpies is explained in fig. 4, but the significance of the excess integral free enthalpy  $\Delta G^{\text{meta}}$  is to be further investigated.

#### AFM investigations

AFM images show a regular layer structure (fig. 3) which leads certainly to systematic errors in grain size determination with XRD. In a typical line scan of this sample plateau heights of about 20 nm and widths of about 150 nm can be seen ( $D_v = 32$  nm by Warren-Averbach). Rapid oxidation of the particles manifests itself in flattening of the sharp edges and in the formation of pustules.

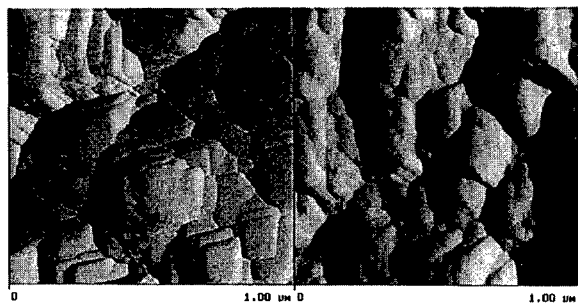


Fig.3 AFM deflection mode image of PE Fe90Ni10 (left: as prepared, right: 21 d after preparation)

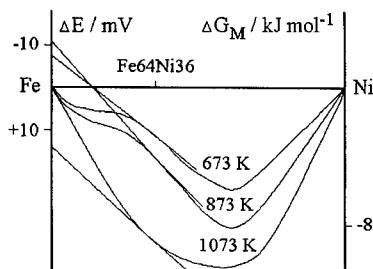


Fig.4 Hypothetical  $\Delta G_M/\Delta E$ -x plot of fcc (Fe, Ni)

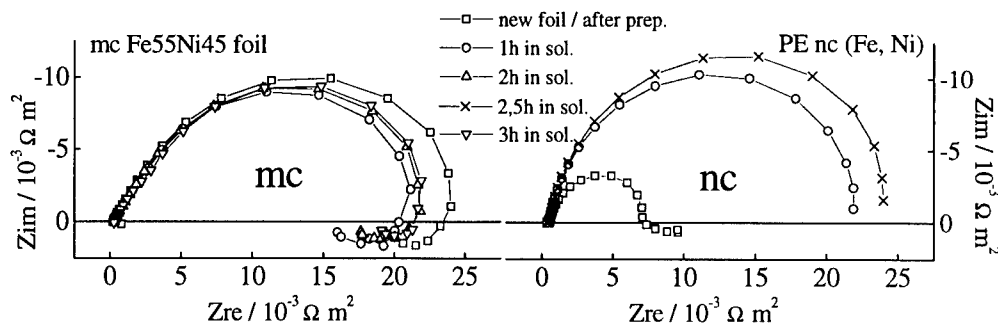


Fig.5 Impedance spectra of (Fe, Ni)-alloys at open circuit potential  
(frequency range:  $10^5\text{Hz}..10^2\text{Hz}$ ; ac-signal: 5mV)

### Electrochemical Impedance Spectroscopy

Impedance spectra of nc PE (Fe, Ni) alloys have been compared to those of a polished mc Fe55Ni45 foil (fig. 5), both on a RDE. A considerably smaller impedance  $|Z|$  for nc than for mc samples was found immediately after preparation, but it comes close to that one of mc samples (see also (12)) within 2 h. Without going into a detailed analysis by using equivalent circuits, this comparison shows the rapid corrosion of nc alloys, which can also be seen in the AFM pictures.

### Acknowledgements

This work was financially supported by the Deutsche Forschungsgemeinschaft in the frame of the SFB 277 "Grenzflächenbestimmte Materialien". Special thanks to Dr. habil. J. Weißmüller for helpful discussion.

### References

1. Schäfer, A. and Hubert, A., *J. Appl. Phys.*, 1991, **69**, 5325
2. Warren, B.E., *X-Ray Diffraction*, Dover, New York, 1990
3. Chen, L.C. and Spaepen, F., *J. Appl. Phys.*, 1991, **69**, 686
4. Swartzendruber, L.J., *Journal of Phase Equilibria*, 1991, **12**, 288
5. Katsuki, A., *Physics and Applications of Invar Alloys*, Maruzen, Tokyo, 1978
6. Natter, H. and Hempelmann, R., *J. Phys. Chem.*, 1996, **100**, 19525
7. Hays, V., Marchand, R., Saindrenan, G. and Gaffet, E., *Nanostruct. Mater.*, 1996, **7**, 411
8. Eckert, J., Holzer, J.C., Krill, C.E. and Johnson, W.L., *J. Mater. Res.*, 1992, **7**, 1751
9. Rupp, J. and Birringer, R., *Phys. Rev.*, 1987, **B36**, 7888
10. Yao, Y.D., Chen, Y.Y., Hsu, C.M., Lin, H.M., Tung, C.Y., Tai, M.F., Wang, D.H., Wu, K.T. and Suo, C.T., *Nanostruct. Mater.*, 1995, **6**, 933
11. Tanji, Y., Nakagawa, Y., Saito, Y., Nishimura, K. and Nakatsuka, K., *Phys. Stat. Sol. (a)*, 1979, **56**, 513
12. Berthier, F. and Priester, L., *The Iron-Nickel Alloys*, Lavoisier, Londres, 1996, p. 241





Pergamon

NanoStructured Materials, Vol. 12, pp. 233-236, 1999

Elsevier Science Ltd

© 1999 Acta Metallurgica Inc.

Printed in the USA. All rights reserved

0965-9773/99/\$-see front matter

PII S0965-9773(99)00106-3

## MECHANICAL MILLING OF $\text{Fe}_3\text{O}_4/\text{SiO}_2$ : FORMATION OF AN AMORPHOUS $\text{Fe(II)-Si-O}$ -CONTAINING PHASE

C. Bender Koch

Chemistry Department, The Royal Veterinary and Agricultural University, Thorvaldsensvej 40,  
DK-1871 Frederiksberg C, Denmark

J.Z. Jiang and S. Mørup

Department of Physics, Building 307, Technical University of Denmark, DK-2800 Lyngby,  
Denmark.

**Abstract --** The product of ball milling of magnetite and amorphous silica (40 mole%  $\text{Fe}_3\text{O}_4$  in  $\text{SiO}_2$ ) for an extended period of time (800 h) in a closed vial, has been investigated by Mössbauer spectroscopy, X-ray diffraction and infrared spectroscopy. It is found that the milling induces extensive reduction of  $\text{Fe(III)}$ . The material constitutes a mixture of ultrafine Fe-rich spinel particles (magnetite/maghemite) and an amorphous  $\text{Fe(II)}$ -containing silicate with a magnetic transition temperature of approximately 25 K. The amorphous phase has a rather high Fe content and is distinctly different from the initial amorphous silica.

©1999 Acta Metallurgica Inc.

### INTRODUCTION

Recently Christodoulides and Hadjipanayis (1) reported that large coercivities were found in nanostructured  $\text{Fe/SiO}_2$  granular materials prepared by sputtering. It was proposed that the material is a composite with a metallic core surrounded by a Fe-Si-O shell. The exchange between the metal and the oxide was suggested to be of major importance for the magnetic behaviour of the whole material. Their analysis of Mössbauer spectra obtained at 17 and 300 K suggested that in addition to metallic alloys an  $\text{Fe(II)}$  high-spin component is present in the samples. At low temperature this  $\text{Fe(II)}$  component exhibited magnetic order and was interpreted as a ferrous silicate of composition  $\text{Fe}_2\text{SiO}_4$ . The proposition can partially be supported by the fact that both  $\alpha$ - and  $\gamma$ - $\text{Fe}_2\text{SiO}_4$  do order magnetically within that temperature interval ( $T_N$  66 and 15 K, respectively (2)). However, the quadrupole splitting they reported for the  $\text{Fe(II)}$  in the  $\text{Fe}_2\text{SiO}_4$ -phase ( $2.00 \text{ mm}^{-1}$  at 300 K) is significantly smaller than those reported for  $\alpha$ - and  $\gamma$ - $\text{Fe}_2\text{SiO}_4$  ( $> 2.6 \text{ mm}^{-1}$  (3)). The assignment may thus only in part explain the properties on the material.

It is commonly anticipated that materials produced by sputtering and ball milling may exhibit related properties. González et al.(4) also concluded that a core/shell textural relation was important for the magnetic properties of the  $\text{Ni/SiO}_2$  system prepared by ball-milling, but their study did not indicate formation of a metal cation/silica oxide phase.

In order to get more insight into the structure of this type of material we have extended our recent study of ball-milling of  $\text{Fe}_2\text{O}_3$  in  $\text{SiO}_2$  (5) with the aim to produce and characterize the properties of materials in Fe(II,III)-Si oxide systems.

## EXPERIMENTAL

A mixture of 40 mole%  $\text{Fe}_3\text{O}_4$  in  $\text{SiO}_2$  was ball milled for 800 h in a closed container. Both oxides were of analytical grade and the iron oxide had rather large crystal sizes (several  $\mu\text{m}$ ) and a well-defined crystal structure (magnetite), whereas the silica (Grace) was in the form of approximately 200  $\mu\text{m}$  particles with an amorphous structure. A planetary ball mill (Fritsch Pulverisette 5) with hardened stainless steel vial and balls was used. The product was investigated by X-ray powder diffraction using a Siemens D5000 diffractometer and  $\text{Co K}\alpha$  radiation, infrared spectroscopy using a Perkin Elmer 2000 FT-IR and the KBr pressed pellet technique, and by Mössbauer spectroscopy using a conventional constant acceleration spectrometer. Isomer shifts are given relative to the centroid of the spectrum of  $\alpha\text{-Fe}$  measured at room temperature. Abrasion of the mill inevitably causes contamination of the sample. Based on measurement of the Cr content in the sample we estimate a contamination level less than 2 wt. %.

## RESULTS AND DISCUSSION

The XRD pattern of the sample milled for 800 h (Fig.1) is interpreted as a mixture of two components: a cubic spinel phase exhibiting line broadening, superimposed on a very broad diffraction maximum with a peak at approximately  $40^\circ 2\theta$  (0.26 nm). Prior to the milling the XRD pattern of the silica exhibits a maximum at approximately  $29^\circ 2\theta$  (0.35 nm). No trace of such a peak due to amorphous silica can be detected indicating that a new amorphous Fe-Si-O phase has formed. The cubic spinel-type phase has cell parameters intermediate between maghemite and magnetite, however, due to the width of the lines the precision is not very high. No lines due to  $\alpha\text{-FeSiO}_4$  can be detected in the diffractogram.

The infrared spectra (not shown) exhibit a marked shift in the position of the Si-O maxima from approximately  $1100\text{ cm}^{-1}$  for the amorphous silica to  $930\text{ cm}^{-1}$  for the sample after ball milling. This shift indicates formation of extensive Si-O-Fe bonding supporting the interpretation of the XRD pattern.

The Mössbauer spectrum of the milled sample obtained at 295 K (Fig.2) consists of a magnetically split component with broad lines and an average magnetic hyperfine field of approximately 40 T. A simple fit using one sextet and two doublets yields  $\Delta E_Q$  and  $\delta$  of 2.0 and 1.1, and 1.0 and 0.5  $\text{mms}^{-1}$  for the nonmagnetic Fe(II) and Fe(III), respectively. The relative abundance of the components is approximately 70 % Fe(II), 20 % Fe(III), and 10 % in the magnetic component. This shows a change from a Fe(II)/Fe(III) ratio of 0.5 in the magnetite to  $> 2.0$  in the resulting material. This finding is in line with the previously demonstrated strong reducing power of ball milling in closed containers (5,6).

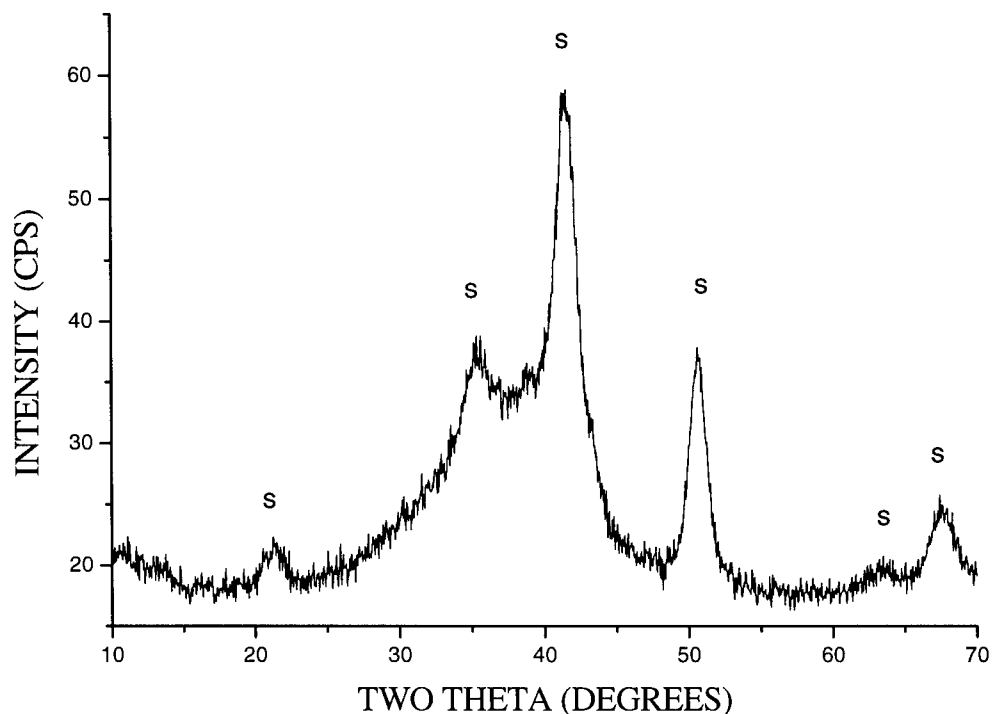


Fig.1. XRD pattern of the 40 mole%  $\text{Fe}_3\text{O}_4$  in  $\text{SiO}_2$  sample milled for 800 h in a closed container. The peaks of the cubic spinel are marked with s.

The parameters of the Fe(II) component are similar to those reported for the Fe/ $\text{SiO}_2$  granular material (1). The values are typical for octahedrally coordinated iron and compares well with those reported in previous investigations of iron in silica for relative high iron contents (7).

Lowering of the temperature to 80 K induces magnetic splitting of the Fe(III) component with strong asymmetric broadening of the lines. This may be caused by several effects: the produced particles are small and may be close to their superparamagnetic blocking temperature where relaxation phenomena are prominent. Part of the spinel phase may exhibit non-resolved sextets due to A/B components and finally substitutions and defects in the structure may cause variation in the local environment. The hyperfine parameters (maximum magnetic hyperfine field of  $49.6 \pm 1$  T and a negligible quadrupole shift indicate that a maghemite-like spinel dominates. Application of an outer magnetic field demonstrates that part of the sextet exhibit polarization indicating a ferro- or ferrimagnetic ordering. The increase in the relative sextet area between 80 and 40 K is very small and the paramagnetic Fe(II) component has effectively the same relative area at the two temperatures.

The lines of the paramagnetic Fe(II) component are markedly different in width. This asymmetry is characteristic of materials like glasses exhibiting a number of slightly different cation positions. The absence of paramagnetic component of Fe(III) in the spectra below 40 K

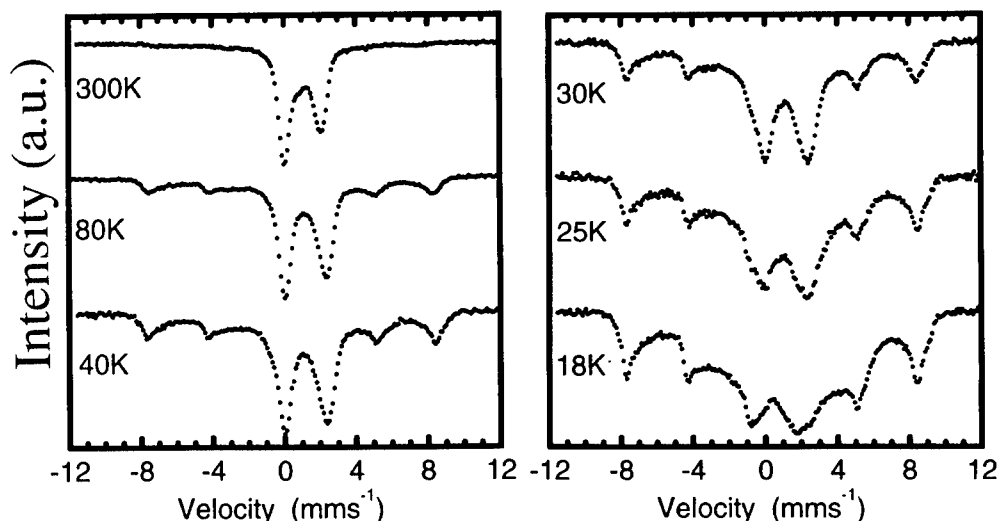


Fig. 2. Mössbauer spectra of the 40 mole%  $\text{Fe}_3\text{O}_4$  in  $\text{SiO}_2$  sample milled for 800 h in a closed container measured at the indicated temperatures.

indicates that the Fe(III)-rich part of the sample orders independently of the Fe(II)-containing part. Lowering of the temperature to 30 K induces a very broad non-resolved component in the central part of the spectrum. This broad component increases in intensity on further lowering of the temperature but no distinctly resolved lines due to the magnetically ordered Fe(II) component is resolved. This indicates topological and/or magnetic disorder in the glass. From the temperature dependence of the spectra we estimate a magnetic transition temperature of approximately 25 K. This temperature is comparable to the magnetic ordering temperature inferred for the Fe/ $\text{SiO}_2$  granular particles (1).

These results lead us to conclude that the resulting material is a two-phase system of Fe-rich spinel(s) and a heterogeneous Fe(II)-containing glass.

## REFERENCES

1. Christodoulides, J.A. and Hadjipanayis, G.C., *Materials Science Forum*, 1997, 235-238, 651.
2. Suito, K., Tsutsui, Y., Nasu, S., Onodera, A. and Fujita, F.E., *Mat. Res. Soc. Symp. Proc.*, 1984, 22, 295.
3. Choe, I., Ingalls, R., Brown, J.M. and Sato-Sorensen, Y., *Phys. Chem. Minerals*, 1992, 19, 236.
4. González, E.M., Montero, M.I., Cebollada, F., De Julián, Vincent, J.L. and González, J.M., *Europhysics Letters*, 1998, 42, 91.
5. Jiang, J.Z., Zhou, Y.X., Mørup, S. and Bender Koch, C., *NanoStructured Materials*, 1996, 7, 401.
6. Linderroth, S., Jiang, J.Z., and Mørup, S., *Materials Science Forum*, 1997, 235 - 238, 205.
7. Clausen, B.S., Topsøe, H. and Mørup, S., *Applied Catalysis*, 1989, 48, 327.



## SYNTHESIS AND CHARACTERIZATION OF NANO-ENGINEERED THERMOELECTRIC SKUTTERUDITE VIA SOLUTION CHEMISTRY ROUTE

M. Wang, Yu Zhang and M. Muhammed

Materials Chemistry Division, Royal Institute of Technology, 100 44 Stockholm, SWEDEN

**Abstract**--The thermoelectric materials  $\text{CoSb}_3$  with Skutterudite structure, have been prepared via a chemical solution route. A precursor consisting of a well-defined mixture of Co oxalate and Sb oxide in a ratio of 1:3 mole was prepared. The precursor was calcined and reduced under hydrogen atmosphere whereby the  $\text{CoSb}_3$  with Skutterudite structure has been thus obtained. The materials obtained at the various processing steps were characterised by SEM, XRD, TGA and BET techniques. ©1999 Acta Metallurgica Inc.

### INTRODUCTION

The investigation of new thermoelectric materials has been recently an attractive area for both scientific research and applications of thermoelectric devices of high efficiency of energy conversion (1-8). The performance of these novel materials can be enhanced dramatically through engineering and processing the materials on a nanometer scale. Such nano-engineered thermoelectrics materials (NETEM) with tailored intergranular defects are expected to play a very important role in the development of "clean" energy conversion systems. Among a number of promising materials, most interesting is a large family of Skutterudites (8).

For the synthesis of NETEM, the process development can be based on one of three types of chemical techniques: 1) electrolysis (e.g., electrodeposition), pyrolysis (e.g., laser pyrolysis), or 3) hydrolysis (e.g., solution chemical processing). All of these techniques have their respective advantages and disadvantages.

Solution chemistry routes, including precipitation and sol-gel processes, have been widely adopted to synthesize the various powder materials with desired particle size down to nano-scale. Based on the hydrolysis of all reactants in aqueous solutions, a solution chemical route, such as precipitation, are usually advantageous in high productivity/reproducibility, low costing, and particularly feasible for the synthesis of multi-components compounds with high purity and homogeneity of the desired structure. By choosing the proper operating conditions, e.g., concentrations of all the reactants, especially pH, in a reaction media, the chemical and morphological properties of a powder product can be controlled on nanometer scale. In this respect, the use of thermodynamic modelling of solution systems is essential for engineering of the synthesis process (9,10).

In this paper, a novel chemical route is presented for the synthesis of NETEM of Skutterudite  $\text{CoSb}_3$ . The processing methods and characterization results of the precursors, intermediates and Skutterudite products are respectively discussed.

## EXPERIMENTAL

### *Precursor synthesis*

In order to choose and optimize a coprecipitation process for the precursor synthesis, the solution chemistry of  $\text{Co}^{2+}\text{-Sb}^{3+}\text{-NH}_4^+\text{-H}^+\text{-C}_2\text{O}_4^{2-}\text{-Cl}^-$  system in aqueous solution were investigated by using thermodynamic modelling of the equilibria of chemical reactions involved. The general principle and procedure of the modelling have been reported earlier (9,10) and the details of this particular system will be presented elsewhere.

Based on the modelling results, the optimal experimental conditions for coprecipitation of  $\text{Sb}_2\text{O}_3$  and  $\text{CoC}_2\text{O}_4$  were selected. The starting solutions were 1 M  $\text{SbCl}_3$  in 3 M  $\text{HCl}$ , 1 M  $\text{CoCl}_2$ , 0.2 M  $\text{H}_2\text{C}_2\text{O}_4$ , and 1 M  $\text{NH}_3$ , prepared by dissolving the respective chemicals into the deionized water. The synthesis was carried out by mixing the solutions of  $\text{CoCl}_2$ ,  $\text{SbCl}_3$  and  $\text{H}_2\text{C}_2\text{O}_4$  to precipitate the desired precursor. The pH of the reaction mixture was adjusted between 3-10 by adding the  $\text{NH}_3$  solution. The obtained precipitates were filtrated, washed and dried at  $80^\circ\text{C}$  overnight.

### *Thermal processing*

The samples of the powder precursor were processed in a tube furnace under the controlled conditions using the following scheme: 1) Heating the samples, while flowing nitrogen, to the calcination temperature ( $350^\circ\text{C}$ ) and remaining there for 2 hours; 2) Heating the samples, while flowing hydrogen, to the reduction temperature ( $450\text{-}600^\circ\text{C}$ ) and remaining there for 3 hours; and 3) Furnace-cooling (3-4 hours) under the hydrogen atmosphere.

### *Characterisations*

The samples obtained at different processing stages were characterised. The chemical analysis of the samples was made by AAS (Atomic Absorption Spectroscopy, SpectrAA-200, Varian) while the thermal analysis by TGA (Thermogravimetric Analyzer, TGA7, Perkin Elmer). The crystal structure was analysed by XRD (X-ray diffraction with Co K radiation,  $\lambda=1.7902 \text{ \AA}$ ). The powder morphology was examined by SEM (Scanning Electron Microscopy, JSM-25SII, JEOL). The surface area was measured by a BET analyzer (Gemini 2370, Micromeritics) and the density was measured by a Pycnometer (Accupyc 1330, Micromeritics).

## RESULTS AND DISCUSSIONS

### *Coprecipitation*

The results of thermodynamic modelling indicate that, between  $\text{pH}=3\text{-}10$ , a complete coprecipitation of  $\text{Sb}_2\text{O}_3$  and  $\text{CoC}_2\text{O}_4$  should be expected while maintaining a molar ratio of  $\text{Sb}:\text{Co}:\text{C}_2\text{O}_4 = 3:1:1$ . The modelling results were experimentally confirmed. Chemical analysis of the residual solution indicated that more than 99% of Sb and Co were precipitated. The coprecipitated samples were very fine powders in pink colour. As shown by SEM photograph in Fig. 1a, there are two types of the particles: needle-like of  $\sim 100 \text{ nm}$  in diameter and rock-like of  $\sim 1 \text{ }\mu\text{m}$ . The needle- and rock-like particles are found to be  $\text{Sb}_2\text{O}_3$  and  $\text{CoC}_2\text{O}_4 \cdot 2\text{H}_2\text{O}$ , respectively. XRD analysis of the coprecipitated power has shown only one crystalline form that is identified to be  $\text{Sb}_2\text{O}_3$ , while Co compound appears to be X-ray amorphous (Fig. 2). The TGA study has indicated that Co compound should be in a form of  $\text{CoC}_2\text{O}_4 \cdot 2\text{H}_2\text{O}$  (Fig. 3).

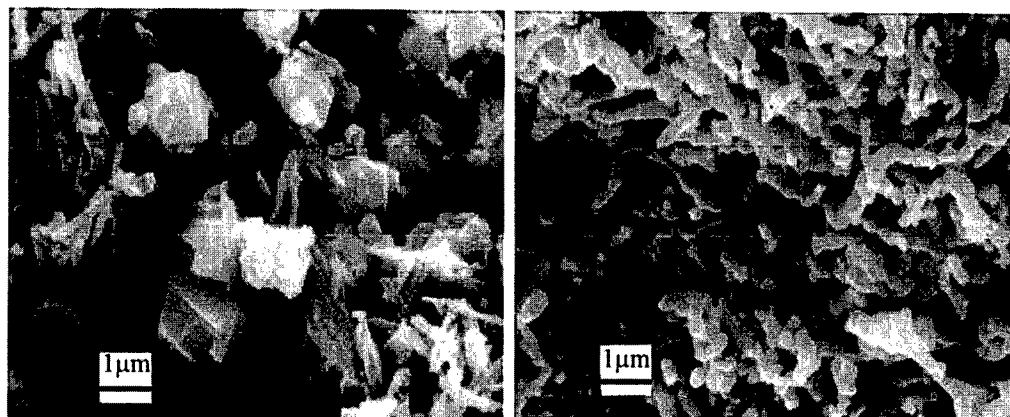


Fig. 1. SEM of the powders: (a) coprecipitated (b) reduced at 500 °C with  $H_2$

### Thermal Decomposition

In Fig. 3, TGA curve of the coprecipitated sample is presented in comparison with those of pure  $Sb_2O_3$  and  $CoC_2O_4 \cdot 2H_2O$ . Pure  $Sb_2O_3$  sublimates at temperatures above 500°C. Pure  $CoC_2O_4 \cdot 2H_2O$  starts losing its crystalline water at 150°C and then decomposing to  $Co_3O_4$  at 340°C. The coprecipitated sample has a similar pattern to that of pure  $CoC_2O_4 \cdot 2H_2O$  up to 500°C though its decomposition to  $Co_3O_4$  starts at 320°C. Above 500°C, the pattern, which shows the weight increasing, differs completely from either of pure  $Sb_2O_3$  and  $CoC_2O_4 \cdot 2H_2O$ . The increased weight is due to the oxidation of  $Sb_2O_3$  into  $Sb_2O_4$ , instead of losing weight by sublimation in pure form of  $Sb_2O_3$ . It is likely that the co-existing  $Co_3O_4$  may act as a catalyst for the oxidation of  $Sb_2O_3$ . As shown in Fig. 2, formation of  $Sb_2O_4$  is identified by XRD analysis of the sample calcined at 550°C for 2 hours, and this compound is found stable upon heating up to 900°C.

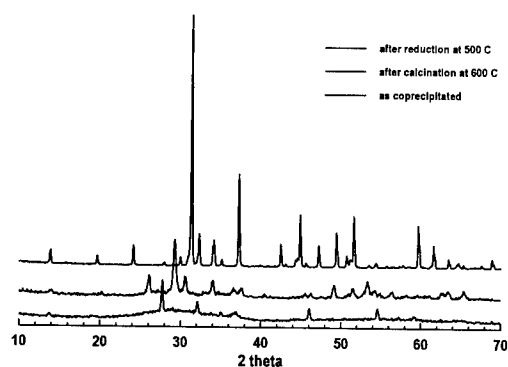


Fig.2. XRD patterns of the powders produced after different processing steps

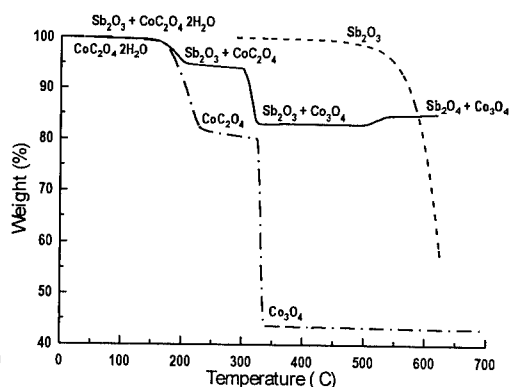


Fig. 3. TGA patterns of the coprecipitated and pure compounds

### Reduction

Fig. 1b shows SEM photograph of the sample reduced at 500°C. As seen, the almost uniform sphere nanoparticles are linked into a net-like morphology. Fig. 2 shows the XRD pattern of the reduced powder. Skutterudite phase of  $\text{CoSb}_3$  is estimated to be at least 95% of the materials. The surface area of the sample is 3.5  $\text{m}^2/\text{g}$  and the density is 8.5  $\text{g}/\text{cm}^3$ .

### CONCLUSIONS

The feasibilities of the currently developed route can be summarised as follows,

- Very intimate mixing of hydrolysed components, Co and Sb in the present case, is designed and synthesized on atomic scale in the solution, resulting in well coprecipitated powder precursor.
- Further heating treatments, calcination and reduction, of the coprecipitated precursor are simple and straightforward, requiring relatively low temperature (500°C lower than using a laser pyrolysis route), short time and easy operation than using any other existing routes.
- The calcined oxide powder is stable to maintain the constant ratio of Co to Sb during the heating treatments, which overcomes the problem with continuous loss of Sb due to the sublimation of  $\text{Sb}_2\text{O}_3$  upon heating when using a mechanical mixture of single oxides.
- The reduction of the calcined oxides in  $\text{H}_2$  can directly produce the Skutterudite  $\text{CoSb}_3$ , in reasonably high phase, without further treatment such as annealing, which are usually needed when using electrolysis or pyrolysis techniques.

### REFERENCES

1. Rowe, D.M. (Editor), CRC Handbook of Thermoelectrics, CRC press 1994.
2. Tritt, M.T. Science 272 (1996), 5, 1276-1277.
3. Sales, B.C., Mandrus, D., Williams, R.K., Science 272(1996), 5, 1277-1328.
4. Mahan, G.D., Sales, B.C., and Sharp, J.W., Phys. Today, (1997), p.42.
5. Borshchevsky, A., Fleurial, J.P., Allevato, E., and Caillat, T., American Institute of Physics, 1995, p.3-6.
6. Fleurial, J.P., Caillat, T., and Borshchevsky, A., American Institute of Physics, 1995, p.40-43.
7. Caillat, T., Borshchevsky, A., and Fleurial, J.P., American Institute of Physics, 1995, p.58-61.
8. Sales, B.C., MRS Bulletin, 23 (1998), 1, 15-21
9. Zhang Yu; Fang Z.; Muhammed M.; Rao K.V.; Skumryev V.; Medelius, H. and Costa, J.L., The synthesis of superconducting bismuth compounds via oxalate coprecipitation, Physica C 157(1), 108 (1989).
10. Wang L.; Zhang Yu; Muhammed M.; Zakharchenko I.V.; Rao K.V. and Medelius H., Synthesis of nanophase oxalate precursors of  $\text{YBaCuO}$  superconductor by coprecipitation in microemulsions, J. Mater. Chem., 5 (1995), 309.





Pergamon

NanoStructured Materials, Vol. 12, pp. 241–244, 1999

Elsevier Science Ltd

© 1999 Acta Metallurgica Inc.

Printed in the USA. All rights reserved

0965-9773/99/\$-see front matter

PII S0965-9773(99)00108-7

## NANOCOMPOSITE POWDERS OF Fe-C SYSTEM PRODUCED BY THE FLOWING GAS PLASMA PROCESSING

S.Iwama<sup>1</sup>, T.Fukaya<sup>1,\*</sup>, K.Tanaka<sup>1</sup>, K.Ohshita<sup>2</sup> and Y.Sakai<sup>2</sup>

<sup>1</sup>Department of Applied Electronics, Daido Institute of Technology

2-21 Daido-cho, Minami-ku, Nagoya 457-8531, Japan

<sup>2</sup>Department of Chemistry, Daido Institute of Technology

40 Hakusui-cho, Minamiku, Nagoya 457-8532, Japan

\*Present Address: TOYOTA MACS INC.,

2 Toyota-cho, Toyota 471-0826, Japan

*Abstract --Nanometer-sized  $\alpha$ -Fe particles formed by the gas evaporation method were transferred into the microwave plasma region with a carrier gas of Ar including a small amount of CH<sub>4</sub>. Particles collected after the plasma region were found to show a composite phase of Fe-C system that consisted of  $\alpha$ -Fe and  $\gamma$ -Fe (Austenite) and Fe<sub>3</sub>C. Moessbauer spectroscopy was used to estimate the relative yield of these three phases. An increase of  $\gamma$ -Fe is followed by the decrease of  $\alpha$ -Fe with increasing CH<sub>4</sub> content. Formation of Fe<sub>3</sub>C was recognized at 0.5vol% of CH<sub>4</sub> in Ar gas and became more remarkable when the CH<sub>4</sub> content was increased. HRTEM observation revealed the individual particles to be a concentric shell structure composed of the Fe-C system. ©1999 Acta Metallurgica Inc.*

### INTRODUCTION

Recently many kinds of nanocomposite materials such as carbon nanocapsule[1] and zeolite including metal clusters in it[2] have attracted a great number of investigators exploring its capabilities in both the fundamental and application fields. In order to realize scientific interests, technological improvements are required in every stage of investigation. Surface decoration of nanoparticles[3] is also a potential technique which must be developed in the near future.

One of the present authors already reported the microwave plasma processing for preparing  $\gamma$ -Fe nanoparticles[4]. That was characterized as a unique annealing method accompanied by a phase transition from  $\alpha$  to  $\gamma$ -Fe nanoparticles. As discussed in the previous paper, a realization of a non-equilibrium thermal state between nanoparticles and the plasma gas was a key-technology for a higher abundance of  $\gamma$ -Fe. The present study has been done to fill the necessary experiments on the formation not only of  $\gamma$ -Fe but also of Fe-C system nanoparticles. The flowing gas plasma processing has been found to be a useful method for the surface decoration of nanoparticles.

## EXPERIMENTAL

The experimental apparatus was composed mainly of the evaporation chamber and the microwave plasma processing unit as illustrated (a) and (b) in Fig.1. Iron was evaporated from the tungsten boat in a mixed flowing gas of Ar and CH<sub>4</sub> by the resistive heating, the evaporation temperature being kept constant at 1900K. The thus prepared  $\alpha$ -Fe nanoparticles were transferred into the plasma region together with the carrier gas by evacuating it using a mechanical booster pumping system. The plasma was generated by two microwave power units with 2.45GHz using H<sub>01</sub> mode in the cavity resonator, the typical incident microwave power being 500W each. The flow rate of CH<sub>4</sub> was adjusted from 0 to 45ml/min, while that of Ar was kept constant at 3l/min. Under these conditions of gas flow rate, the pressure in the evaporation chamber was 4Torr and the gas velocity in the plasma region was 30m/s. Plasma processed particles were collected on a room temperature substrate after the plasma region. The X-ray diffraction measurement(XRD), the high resolution transmission electron microscopy (HRTEM) and the Moessbauer spectroscopy were carried out to examine the structure and the composition of the particles.

## RESULTS AND DISCUSSION

In the XRD pattern of the plasma processed powder, two phases of  $\alpha$ -Fe and  $\gamma$ -Fe can be easily identified because of the simplicity of the patterns; the former is of body centered cubic(bcc) and the latter of face centered cubic(fcc). The lattice expansion of  $\gamma$ -Fe was detected from XRD 111 peak shift as shown in Fig.2, where the expansion increases linearly with the increase of partial pressure of CH<sub>4</sub> in the Ar gas. According to the empirical relation[5], the carbon content in the present  $\gamma$ -Fe nanoparticles was estimated to be from 0.9 to 1.5wt%, which is consistent with the solid solution of carbon in the Austenite phase in the Fe-C diagram[6]. However, the solid solution of carbon in the bcc lattice, which is known as the Martensite, cannot be recognized clearly.

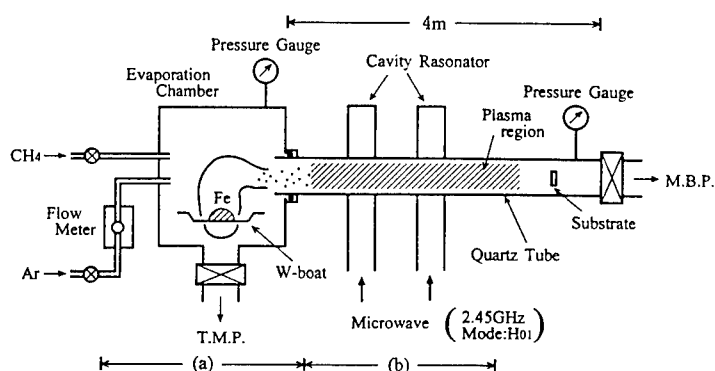


Fig.1 Illustration of the experimental apparatus. The quartz tube (24mm in inner diameter) penetrates two cavity resonators, the distance of them being 90cm.

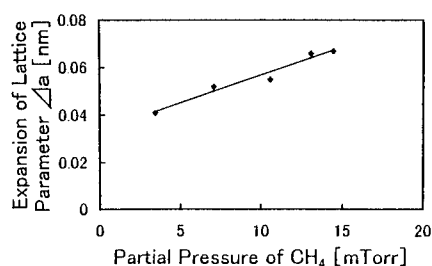


Fig.2 Lattice expansion of  $\gamma$ -Fe vs. partial pressure of  $\text{CH}_4$ . In this case, Ar pressure was adjusted to keep  $\text{CH}_4$  content at the constant of 1000ppm.

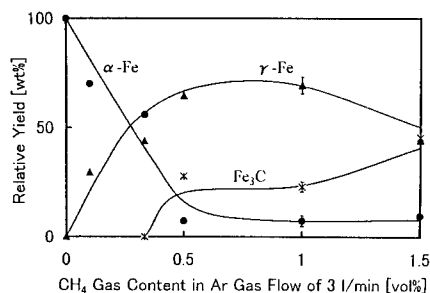


Fig.4 Diagram for the relative yield of Fe-C system vs.  $\text{CH}_4$  content in the constant Ar flow rate.

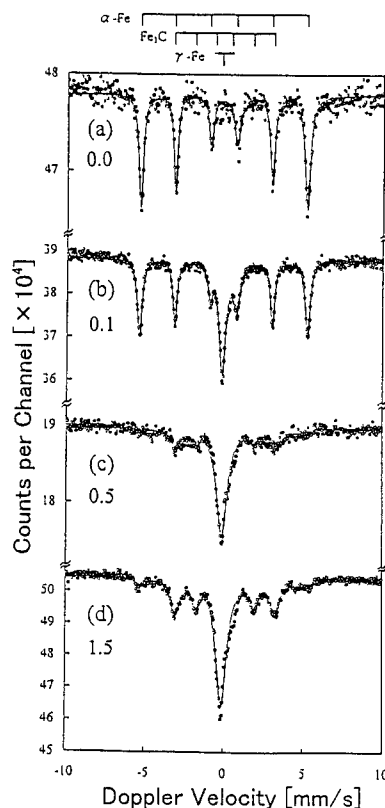


Fig.3 Moessbauer spectra of nanoparticles of Fe-C system. The numerals in the graph indicate the  $\text{CH}_4$  content in vol%.

When the  $\text{CH}_4$  content was increased, additional lines appear near the  $\alpha$ -Fe and  $\gamma$ -Fe XRD peaks, and some of them were assigned to  $\text{Fe}_3\text{C}$ . In order to determine the relative amount of these phases, the Moessbauer spectra were measured at room temperature by using an Austin Science S-600 Moessbauer spectrometer against  $370\text{-MBq}^{57}\text{Co/Rh}$ . The Doppler velocity was calibrated with an  $\alpha$ -Fe foil. Figure 3 shows the spectra of four specimens formed in the different  $\text{CH}_4$  content : (a) 0.0, (b) 0.1, (c) 0.5 and (d) 1.5vol% in Ar gas. Three phases of  $\alpha$ -Fe,  $\gamma$ -Fe and  $\text{Fe}_3\text{C}$  can be distinguished from each other by the different magnetic properties of them, *i.e.* ferromagnetic for  $\alpha$ -Fe and  $\text{Fe}_3\text{C}$ , and paramagnetic for  $\gamma$ -Fe.

The spectra were fitted by a personal computer as a linear combination of thirteen Lorentzians with the least-squares method. Figure 4 shows the obtained diagram for the relative yield of three phases against the  $\text{CH}_4$  content in the Ar gas flow rate of 3l/min. The  $\gamma$ -Fe increases accompanying the decrease of  $\alpha$ -Fe with the increase of  $\text{CH}_4$  content to about 0.5vol%. The relative yield keeps nearly constant for the  $\text{CH}_4$  content between 0.5 to 1.0vol%,

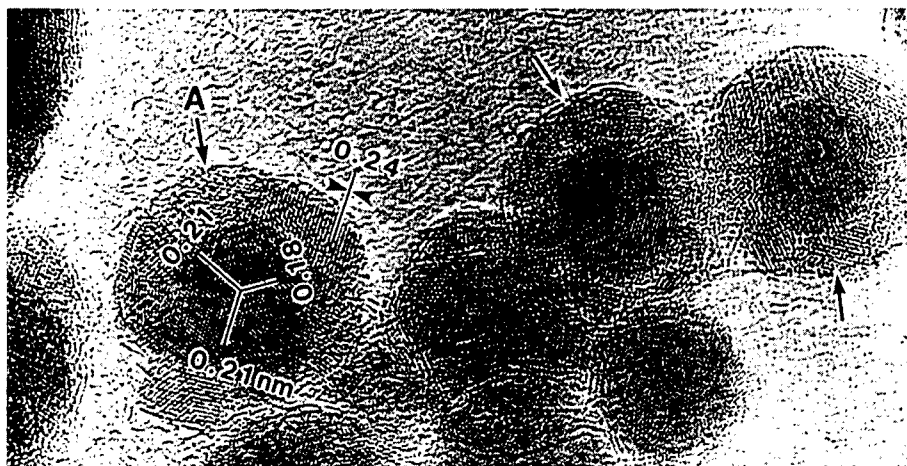


Fig.5 An electron microscopic image of Fe-C nanoparticles showing a concentric shell structure.

each amount being 70, 25 and 5wt% for  $\gamma$ -Fe,  $\text{Fe}_3\text{C}$  and  $\alpha$ -Fe, respectively. The  $\gamma$ -Fe was found to decrease accompanying the increase of  $\text{Fe}_3\text{C}$  with increasing of  $\text{CH}_4$  content over 1.0vol%. The relative yield of  $\alpha$ -Fe, however, still remains constant.

A HRTEM image of nanoparticles prepared in the  $\text{CH}_4$  content of 0.5vol% was shown in Fig.5. Many particles indicated by arrows in the micrograph show a concentric shell structure, the thickness being nearly 3nm. The core of particle (A) can be assigned to  $\gamma$ -Fe with [011] zone axis and the shell with spacing of 0.24nm is probably due to  $\text{Fe}_3\text{C}(210)$ , which is a more progressive phase than the  $\gamma$ -Fe in carbonization. The shell structure reflects the fact that the carbon supply in the plasma region occurs through the surface of the nanoparticle. Furthermore, the increase of  $\text{Fe}_3\text{C}$  accompanying the decrease of  $\gamma$ -Fe shown in the higher  $\text{CH}_4$  content region in Fig.4 may be interpreted by the growth of the shell in the individual nanoparticles.

#### ACKNOWLEDGEMENTS

The authors would like to thank Prof.K.Mihama for his stimulating discussions during the course of this study. A part of this work was supported by a Grant-in Aid for Scientific Research from the Ministry of Education, Science, Sports and Culture.

#### REFERENCES

1. Saito,Y. Ma,J. Nakashima,J. and Masuda,M., *Z.Phys.*,1997, **D40**, 170
2. Nozue,Y. Kodaira,T. Ohwashi,S. Goto,T. and Terasaki,O., *Phys.Rev.*, 1993, **B48**, 12253.
3. Sato,T. Hasko,D.G. and Ahmed,H., *J.Vac.Sci.Technol.*, 1997, **B15**, 45.
4. Hayakawa,K. and Iwama,S., *J.Cryst.Growth*, 1990, **92**, 88.
5. Roberts,C.S., *Trans.A.I.M.E.*, 1953, **197**, 203.
6. Bentz,M.G. and Eliot,J.F., *Trans.A.I.M.E.*, 1961, **221**, 323.



## ZnO-Fe NANOCOMPOSITES VIA BALL MILLING AND ANNEALING

L. Takacs<sup>1</sup>, A. Mossion<sup>2,3</sup>, K. Lázár<sup>3</sup>, L. K. Varga<sup>4</sup>, M. Pardavi-Horvath<sup>5</sup> and  
A. Bakhshai<sup>6</sup>

<sup>1</sup> University of Maryland, Baltimore County, Dept. of Physics, Baltimore, MD 21250, USA

<sup>2</sup> University of Poitiers, Department of Chemistry, 36022 Poitiers, France

<sup>3</sup> Institute of Isotope and Surface Chemistry, H-1525, Budapest, P.O.B. 77, Hungary

<sup>4</sup> Research Institute for Solid State Physics, H-1525, Budapest, P.O.B. 49, Hungary

<sup>5</sup> The George Washington University, Institute for Magnetism Research,  
Washington, D.C. 20052, USA

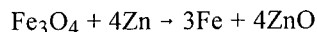
<sup>6</sup> Goucher College, Department of Physics, Towson, MD 21204, USA

**Abstract**—Metallic iron can be formed by reacting  $\text{Fe}_3\text{O}_4$  with Zn in a ball mill. A mixed Fe-Zn oxide forms first, followed by decomposition into Fe and ZnO upon further milling. A large amount of Zn remain dissolved in the bcc phase and a fraction of the Fe retains an oxidized state. Decomposition can also be achieved by annealing the intermediate oxide. This process is investigated by thermomagnetic measurements, XRD, and Mössbauer spectroscopy. It is shown that the intermediate phase decomposes at relatively low (300–400°C) annealing temperatures. The separation of Fe and Zn between the metal and oxide phases of the end product is more complete than found in samples prepared by milling alone.

©1999 Acta Metallurgica Inc.

### INTRODUCTION

The reduction of a metal oxide with a more reactive metal can be induced by ball milling [1]. For example, an iron-alumina nanocomposite was produced by reducing  $\text{Fe}_3\text{O}_4$  with Al metal [2]. In order to avoid a self-sustaining reaction without diluting the reactants with an inert additive, a less reactive metal, Zn, was chosen as the reducing agent [3]:



This reaction proceeds through an intermediate mixed oxide phase which coexists with the reactants and the products over a significant portion of the process. This intermediate phase decomposes into a bcc alloy and an oxide upon continued milling. However, the separation of the two metals is not complete: The bcc phase is a supersaturated  $\text{FeZn}$  solid solution, its Zn content decreases from over 25 at.% when the phase is first detected to about 7 at.% after 9 hours of milling. Mössbauer spectroscopy indicates that nearly 20% of the Fe content remains oxidized at the end of the milling process. As no separate oxide phase is detected by X-ray diffraction, this Fe fraction is probably dissolved in the ZnO phase [3]. The presence of a small amorphous fraction is also possible. The particle size is about 20–30 nm as estimated from the XRD line widths and TEM investigations [4].

The present investigation reports on a two-step treatment, whereby milling is used to reach an intermediate state and the final product is obtained via annealing. The objective is to compare the decomposition of the intermediate oxide by annealing and continued ball milling. Similar combination of mechanochemical processing and annealing was found beneficial to prepare  $\text{ZnFe}_2\text{O}_4$  from  $\text{ZnO}$  and  $\text{Fe}_2\text{O}_3$  [5].

### EXPERIMENTAL

Ball milling was carried out in SPEX 8000 Mixer Mills with round bottom stainless steel vials and steel balls. The  $\text{Fe}_3\text{O}_4$  and Zn powders were filled into the vial in an argon-flushed glove box. The composition of the starting powder mixture corresponded to the stoichiometry with 10% additional Zn. Samples for XRD and thermomagnetic measurements were ampuled under vacuum and annealed in a tube furnace.

Thermomagnetic curves were measured in a Perkin-Elmer thermogravimetric analyzer fitted with a small external permanent magnet to generate a weak dc magnetic field ( $\sim 40$  Oe) at the sample. The samples were in flowing Ar during these measurements.

The phase composition of the samples was analyzed using a Philips X-ray diffractometer with vertical goniometer and  $\text{Cu K}\alpha$  radiation.

Mössbauer spectroscopy was performed using a conventional constant acceleration spectrometer and a 20-mCi  $^{57}\text{Co}$  in Rh matrix source. The samples were placed in a furnace where *in situ* heat treatments were performed in flowing nitrogen gas.

### RESULTS AND DISCUSSION

The characteristic temperature of the decomposition of the intermediate phase has been determined by thermomagnetic measurements. Fig. 1 shows the results for a sample milled for 150 min. The initial magnetization is not zero, indicating the presence of  $\text{Fe}_3\text{O}_4$ , Fe or both. This is anticipated as the two steps of the chemical process overlap. The magnetization increases between  $200^\circ\text{C}$  and  $350^\circ\text{C}$ . We associate this change with the crystallization of Fe. The presence of Fe is confirmed by the sharp decrease observed at its Curie temperature.

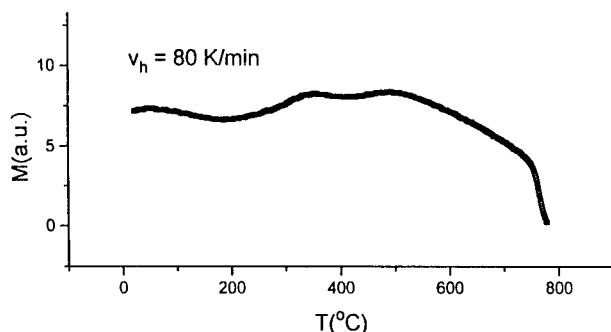


Figure 1. Thermomagnetic curve of a sample ball milled for 150 min.

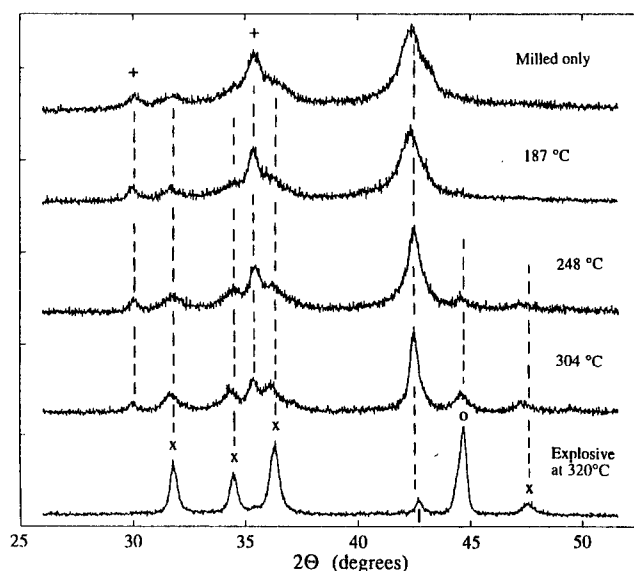


Figure 2. X-ray diffraction patterns of samples ball milled for one hour followed by annealing for one hour at the indicated temperatures. The diffraction peaks originate from  $\text{Fe}_3\text{O}_4$  (+),  $\text{ZnO}$  (x), bcc Fe (o) and a cubic oxide phase ( $\emptyset$ ).

X-ray diffraction results are presented in Fig. 2 for samples milled for one hour and then annealed for one hour at various temperatures. The diffraction pattern of the "as milled" sample indicates the presence of residual magnetite and some  $\text{ZnO}$ . The broad peak at about  $42.5^\circ$  corresponds to the intermediate mixed oxide; the presence of some bcc  $\text{FeZn}$  alloy is possible. Annealing at  $187^\circ\text{C}$  has very little effect on the XRD pattern. After annealing at  $248^\circ\text{C}$ , the (1 1 0) peak of bcc Fe appears, very close to its position for pure iron. The intensity of this peak is larger for the higher annealing temperature of  $304^\circ\text{C}$ . This behavior is distinctly different from what was observed when the bcc phase was produced by milling for longer times [3]. In that case, the bcc phase is a highly supersaturated  $\text{FeZn}$  solid solution. As the milling time increases, the (1 1 0) peak of the bcc phase gradually separates from the broad peak of the intermediate phase and shifts toward the line position of pure iron. However, when the intermediate oxide decomposes during annealing, the bcc phase crystallizes with very little zinc content. This result is confirmed by the Mössbauer measurements. The intensity of the bcc peak increases as the temperature or the time of the annealing is increased, but the line position remains unchanged. The decreasing line widths with increasing annealing temperature indicate grain growth. When a sample milled for one hour was inserted into the pre-heated tube furnace at  $320^\circ\text{C}$ , a thermal runaway reaction was initiated and the sample crystallized into the final phases of  $\text{ZnO}$  and Fe. Only a small residue of the intermediate phase remained.

Mössbauer spectroscopy was performed on samples ball milled for 90 and 150 minutes and then annealed in nitrogen atmosphere for one hour *in situ* at increasing temperatures. Spectra were obtained at 77 K and room temperature and decomposed to contributions from magnetite, metallic iron, and ferric and ferrous components. The relative intensity of the various components is shown in Fig. 3 for the room temperature spectra.

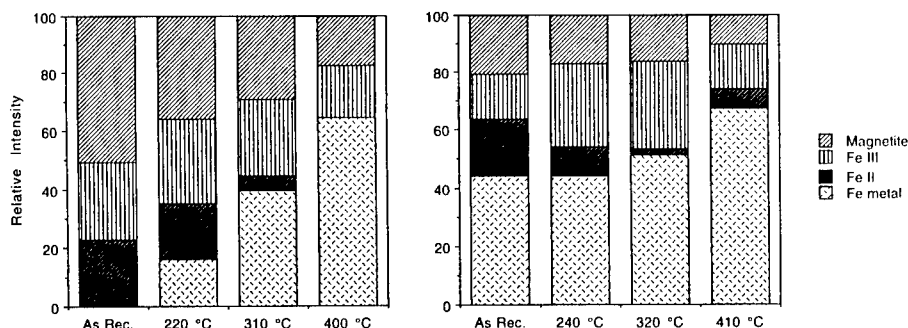


Figure 3. Relative intensity of the components of the room temperature Mössbauer spectra for samples milled for 90 min (left graph) and 150 min (right graph.)

The comparison of the 90- and 150-minute milled samples reveals that (i) no detectable amount of metallic iron was produced by ball milling alone for processing times shorter than 150 min, (ii) mechanical activation promotes the formation of metallic iron also at shorter milling times, as shown by the formation of iron already at 220°C after 90 min of milling, and (iii) the final extent of conversion to the metallic state (after annealing at about 400°C) was about 2/3 of the total iron content, regardless of the different milling times.

The 77 K and the room temperature Mössbauer spectra were compared in order to determine if a significant superparamagnetic fraction was present. Superparamagnetism of both iron and magnetite was observed in the as-milled samples and after the lowest temperature annealing, but not after annealings at 310°C and 400°C.

In conclusion, there are differences between the decomposition of the intermediate phase as induced by milling and annealing. In particular, the intermixing of Fe and Zn between the metal and oxide phases is enhanced when the process is completed by milling alone.

#### ACKNOWLEDGEMENTS

This work was partly supported by the National Science Foundation under Grant. No. DMR-9712141. One of us (L.K.V.) is thankful for the hospitality of Prof. K.V. Rao of the Condensed Matter Physics Department at the Royal Institute of Technology in Stockholm. A.M. acknowledges funding from the exchange program between the French and Hungarian Ministries of Education.

#### REFERENCES

- [1] M. Pardavi-Horvath and L. Takacs, *Scripta Met. Mater.* 33, 1731 (1995).
- [2] M. Pardavi-Horvath and L. Takacs, *IEEE Trans. Magn.* 28, 3186 (1992).
- [3] L. Takacs, R.C. Reno, and M. Pardavi-Horvath, *Hyperfine Interactions* 112, 247 (1998).
- [4] M. Pardavi-Horvath, L. Takacs, and F. Cser, *IEEE Trans. Magn.* 31, 3775 (1995).
- [5] V. Šepelák et al., *Mater. Sci. Forum* 235-238, 139 (1997).





Pergamon

NanoStructured Materials, Vol. 12, pp. 249–252, 1999

Elsevier Science Ltd

© 1999 Acta Metallurgica Inc.

Printed in the USA. All rights reserved

0965-9773/99/\$-see front matter

PII S0965-9773(99)00110-5

## PROCESSING AND MECHANICAL PROPERTIES OF NANOCRYSTALLINE 5083 Al ALLOY

V.L. Tellkamp and E.J. Lavernia

Materials Science and Engineering, University of California, Irvine  
916 Engineering Tower, Irvine, Ca. 92697-2710, USA

**Abstract** – A commercial aluminum alloy, 5083, was processed using a cryomilling synthesis approach to produce nanocrystalline powders. The powders were subsequently degassed, HIPped, and extruded to produce a thermally stable bulk nanocrystalline material. The grain size at each processing step was measured utilizing both X-ray diffraction and transmission electron microscopy. The mechanical properties of the n-5083 extruded material were determined utilizing ASTM E8-93, Standard Test Methods for Tension Testing of Metallic Materials. The nanocrystalline 5083 was found to have a 30% increase in yield strength and ultimate strength over the strongest commercially available form of 5083 with no corresponding decrease in elongation. Grain boundary sliding is proposed as a possible mechanism for the observed enhanced ductility.

©1999 Acta Metallurgica Inc.

### INTRODUCTION

Interest in the field of nanocrystalline materials has grown tremendously in recent years. The potential for improved mechanical properties, by reducing the grain size to the nanocrystalline regime, of both metals and ceramics has been demonstrated by several researchers [1–4]. Most of this potential has been demonstrated on thin films or very small samples using either hardness data or compression data to project mechanical behavior. Very few data have been presented on tensile samples due to the difficulty in manufacturing a large quantity of material with a nanocrystalline (<100nm) grain size. The objective of this study was to develop a processing technique to produce large enough samples so that a standardized tensile test could be employed to generate tensile data and thereby accurately determine the tensile characteristics of a nanocrystalline material.

Several researchers have examined the thermal stability of nanocrystalline powders generated by mechanical alloying or mechanical milling [5,6]. The materials which were found to have the highest thermal stability were either pure Al or alloys which contained significant quantities of Al. In this research project, a commercial aluminum alloy, 5083, was selected to promote thermal stability of the nanocrystalline grains while simultaneously providing a well-characterized material to compare mechanical properties.

## EXPERIMENTAL

Spray atomized 5083 Al (4.4Mg, 0.7Mn, 0.15Cr, balance Al) powder with a particle size less than 150 microns was mechanically milled under liquid nitrogen in a process known as cryomilling. Details of this processing method can be found in reference [6]. The resultant powders were degassed at 300°C under a vacuum of  $10^{-6}$  torr. Consolidation was completed with an ABB Autoclave MIH-3.1 Hot Isostatic Press (HIP), operating at 523 K and 200MPa. The HIPped samples were then extruded at 523 K with an extrusion ratio of 9 to 1. The grain size after each step in the processing sequence was measured by both X-ray diffraction and transmission electron microscopy (TEM). X-ray diffraction was conducted on a Siemens D5000 diffractometer with MoK $\alpha$  radiation. Grain size was measured utilizing the full-width, half-maximum peak broadening technique, corrected for K $\alpha_2$  and instrumental broadening [7]. TEM micrographs were prepared on a JEOL 4000 operating at 200kV. Hardness was measured on a Wilson Hardness Tester with a Rockwell B scale. Density measurements were made with the Archimedes principle under ASTM B328. Tensile specimens were machined according to ASTM E8 Small-Size Specimens Proportional to Standard instructions. Tensile data was collected on an Instron Model 5584 with a 30kN load cell.

## RESULTS AND DISCUSSION

Table 1 lists the grain size as a function of processing condition. There was very limited grain growth measured with either thermal or thermo-mechanical processing. An excellent correlation was found between the X-ray grain size and the TEM grain size. Table 2 contains the hardness and density data for the nanocrystalline 5083 and commercial 5083 in

**TABLE 1**  
**Grain Size after Each Processing Step**

	X-ray Grain Size (nm)	TEM Grain Size(nm)
<b>Cryomilled powder</b>	<b>24</b>	<b>30 <math>\pm</math> 13</b>
<b>HIPped compact</b>	<b>28</b>	<b>35 <math>\pm</math> 10</b>
<b>Extrusion</b>	<b>34</b>	<b>29 <math>\pm</math> 14</b>

**TABLE 2**  
**Hardness and Density of Nanocrystalline 5083 Aluminum**

	n-5083Al	5083-0 <sup>9</sup>
<b>Hardness</b>	<b>63 Rockwell B</b>	<b>37.5 Rockwell B</b>
<b>Density</b>	<b>99.6%</b>	<b>100%</b>

the untreated condition. It is evident from these data that the nanocrystalline material is significantly (~70%) harder than the commercial material and that full density has been achieved through the processing sequence.

Figure 1 illustrates the stress-strain curve of the nanocrystalline 5083 and commercial 5083 in the untreated condition. Table 3 compares the yield strength, ultimate strength, and elongation of the nanocrystalline 5083 to the same values for both the untreated 5083-0 and the strongest form of 5083 (5083-H343) available.

The most significant item of interest from this data is the significant (~30%) increase in both yield strength and ultimate strength of the nanocrystalline 5083 over the 5083-H343 material with no decrease in elongation. This observation of increased strength with no corresponding decrease in elongation stands in stark contrast to the behavior of conventional materials. A possible mechanism for this behavior may be grain boundary sliding due to the nanocrystalline grain size. Creep studies are currently underway to verify this hypothesis.

Also of interest, is the shape of the stress-strain curve for the nanocrystalline 5083. Commercial 5083 Al is a work hardenable alloy and the increasing slope of the stress-strain curve after yielding is evidence of such. The nanocrystalline 5083 is characterized by a much flatter slope indicating that little work hardening is occurring in the nanocrystalline grains. There appear to be discontinuities in the plastic deformation regime of the nanocrystalline 5083. The shape of these discontinuities combined with the flattened slope suggests that simultaneous work hardening and recovery processes may be present during deformation. The room temperature tensile test is at  $0.34 T_{mp}$  for this alloy; therefore, recovery processes are possible. Current work is underway to clarify this behavior including the possible influence of microstructural texture as a result of the extrusion process.

**FIGURE 1**

Stress vs. Strain

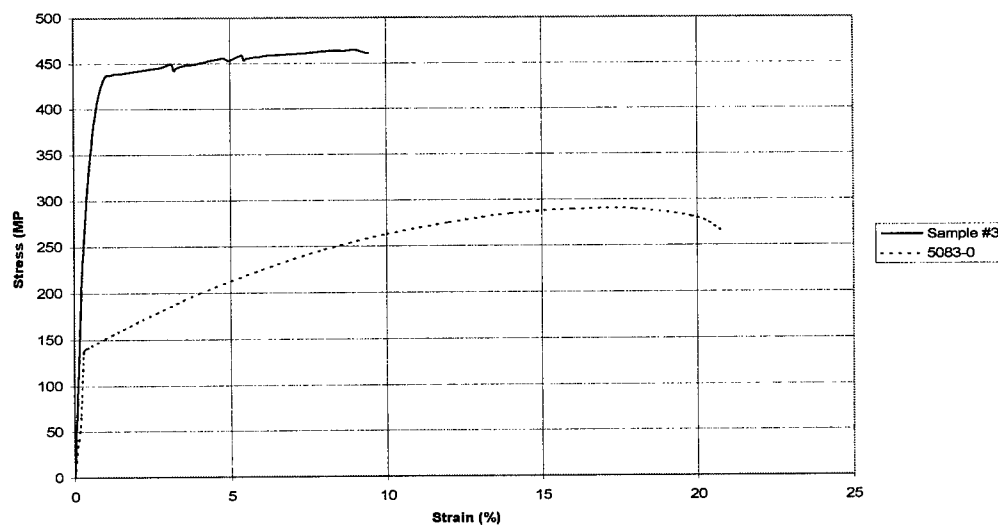


**TABLE 3**  
**Mechanical Properties of n-5083 Compared to Commercial 5083**

	n-5083	5083-0 <sup>8</sup>	5083-H343 <sup>8</sup>
Yield Strength	334 MPa	124 MPa	269 MPa
Ultimate Strength	462 MPa	276 MPa	345 MPa
Elongation	8.4%	16%	8%

### CONCLUSIONS

A bulk nanocrystalline extrusion of 5083 Al with a thermally stable grain size of approximately 25 - 35nm was produced and the mechanical behavior was characterized following ASTM E8 - 93. This material was found to have a significant increase (~30%) in yield strength and ultimate strength over the strongest form of commercial 5083 available with no corresponding decrease in elongation. Grain boundary sliding is thought to be the possible mechanism for this phenomenon.

### ACKNOWLEDGEMENTS

The authors wish to thank the Office of Naval Research, specifically Dr. Lawrence Kabacoff, under contract No. ONR N00014-94-1-0017 and ASSERT grant No. N00014-98-1-0569 for the financial support of this project.

### REFERENCES

1. Nieman, G.W., Weertman, J.R., *J. Mater. Res.*, **6**, 1012, 1991.
2. Higashi, K., et al., *Materials Science and Engineering*, **A181/A182**, 1068, 1994.
3. Gray III, G.T., et al., *NanoStructured Materials*, **9**, 477, 1997.
4. Rawers, J., et al., *NanoStructured Materials*, **9**, 197, 1997.
5. Luton, M.J., et al., *Mat. Res. Soc. Proc.*, **132**, 79, 1989.
6. Perez, R.J., Huang, B., Laverania, E.J., *NanoStructured Materials*, **7**, 565, 1996.
7. Cullity, B.D., *Elements of X-ray Diffraction*, Addison-Wesley, Massachusetts, 1978, p. 101.
8. Davis, J.R., *ASM Specialty Handbook - Aluminum and Aluminum Alloys*, ASM International, Materials Park, Ohio, 1994, p. 675.
9. Brandes, E.A., *Smithell's Metals Reference Book*, 7<sup>th</sup> Edition, Butterworth-Heinemann, London, 1992.



Pergamon

NanoStructured Materials, Vol. 12, pp. 253-258, 1999

Elsevier Science Ltd

© 1999 Acta Metallurgica Inc.

Printed in the USA. All rights reserved

0965-9773/99/\$-see front matter

PII S0965-9773(99)00111-7

## PARTICLE SIZE CONTROL DURING FLAT FLAME SYNTHESIS OF NANOPHASE OXIDE POWDERS

N. G. Glumac, G. Skandan<sup>1</sup>, Y. J. Chen, and B. H. Kear

College of Engineering, Rutgers University, Piscataway, NJ 08855-0909

<sup>1</sup>Nanopowder Enterprises Inc., Piscataway, NJ 08854

**Abstract** – *Combustion Flame - Chemical Vapor Condensation (CF-CVC) is currently under investigation as a candidate for large-scale production of non-agglomerated oxide nanopowders. This process involves controlled pyrolysis of precursors and condensation in the gas phase to form nanoparticles. In this study, the influence of reactor parameters including pressure, substrate standoff distance, and precursor concentration on silica particle size are measured. The results indicate that particle size is strongly dependent on standoff distance and precursor concentration, but less dependent on pressure. Furthermore, the particle size is observed to decrease with increasing precursor concentration, which is different from results of previous flame studies where the substrate was absent. Samples taken from near the substrate show a markedly different particle size than those taken from the walls of the chamber, which suggests that some particle trajectories escape the rapid quench zone near the substrate. ©1999 Acta Metallurgica Inc.*

### INTRODUCTION

Combustion Flame - Chemical Vapor Condensation offers the potential for the production of non-agglomerated oxide nanopowders in a scalable reactor. Previous studies have demonstrated the ability to produce loosely agglomerated alumina and titania powders in the 10-50 nm size range (1), as well as the scalability of the process (2). While some preliminary work has been done on flame and particle characteristics (3), much remains unknown about the CF-CVC process. For example, there is little information on the dependence of particle characteristics on process parameters. In this paper, we present the first results of such parametric studies, and suggest possible explanations for the observed dependencies.

### EXPERIMENTAL

The basic experimental setup for CF-CVC is described in detail elsewhere (3) and is shown in Figure 1. In brief, a flat flame burner is supplied with a mixture of hydrogen and oxygen. A nitrogen carrier gas is bubbled through hexamethyldisilazane (HMDS), and the precursor vapor is mixed with fuel and oxidizer before entering the burner. Parallel to and below the burner is a water-cooled substrate maintained at slightly above room

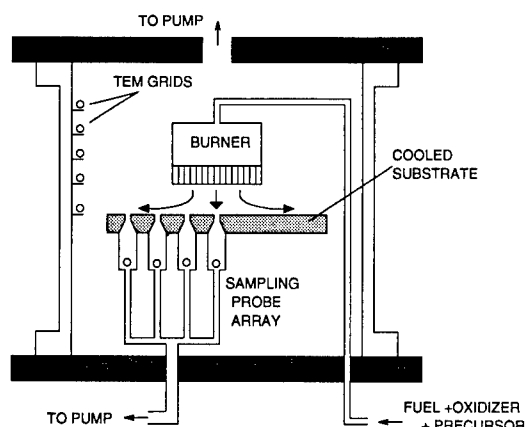


Figure 1: The experimental setup for the CF-CVC process. The relative locations of the sampling positions are shown.

temperature. The spacing between the burner and substrate, denoted the gap distance, can be varied from 1 to 5 cm. The chamber pressure is maintained at 10 to 50 Torr by closed-loop pressure control via a throttle valve in the pump line.

For these experiments, powder samples are taken at various locations in the reactor. At the walls, a vertical steel rod supports a series of 3 mm copper TEM grids which are held at different vertical positions. An aluminum shield covers the grids during startup to avoid any influence of the startup transient. Once the shield is removed, the reactor is allowed to run approximately one minute, and then the samples are removed and analyzed under the TEM. At the substrate, an array of 1 mm holes is drilled at various radial locations. Beneath each hole is a quartz sampling probe which samples gas and particles from the substrate surface. A separate vacuum line maintains the pressure in the probes at roughly 2 Torr, insuring that there is a rapid expansion and quench after gas and particulates enter the probe orifice. Powders deposit on a TEM grid in the back of each probe.

## RESULTS

Powder collected through the centerline substrate probe is shown in Figure 2. The deposited particles display a small mean diameter (10-30 nm), and agglomerates consist of only two or three particles. However, deposits collected near the chamber wall, Figure 3, are much larger (50-80 nm) and more agglomerated. To investigate this difference in particle properties, samples were taken from a series of radial locations under a large substrate. The sampling locations were directly below the burner center ( $r = 0$ ) to  $r = 10.2$  cm ( $4.1 \times$  burner radius). After one minute of run time, a visible deposit encompassed all of the sampling ports except the most distant ( $r = 10.2$  cm) location. Mean diameters of the powder particles from each location are shown in Figure 4. From each of the locations within the visible deposit region, the particles were small ( $< 35$  nm)

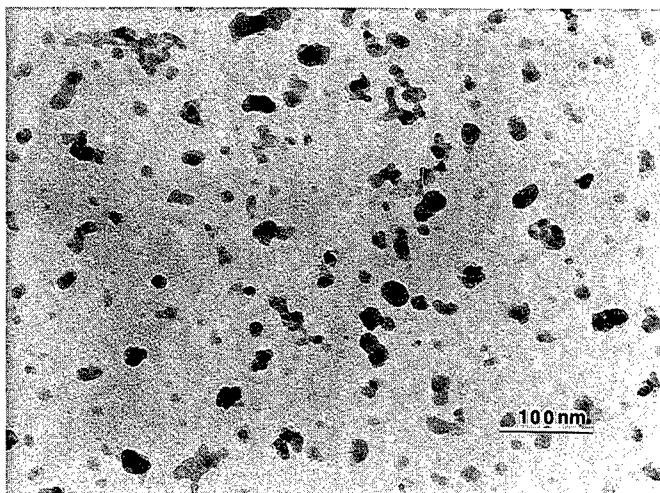


Figure 2: A TEM photograph of silica particles collected on a TEM grid placed beneath the substrate at the burner centerline.

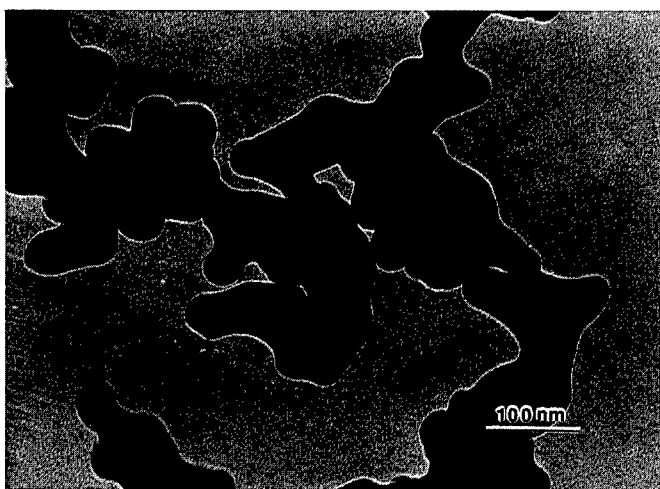


Figure 3: A TEM photograph of silica particles collected on a TEM grid placed near the wall of the chamber at the same vertical position as the substrate.

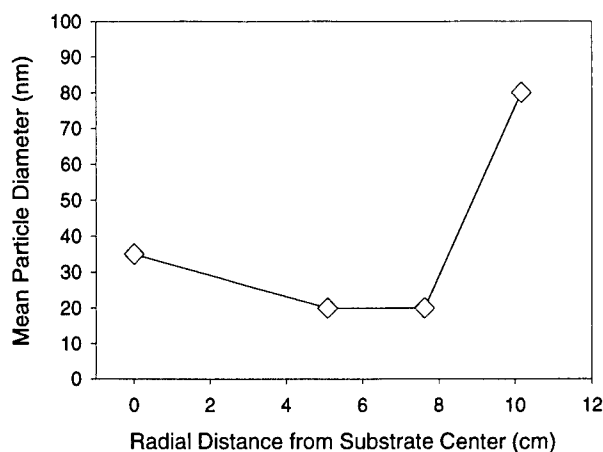


Figure 4: Mean primary particle diameter for samples taken beneath the substrate at different radial locations. The burner radius is 2.5 cm.

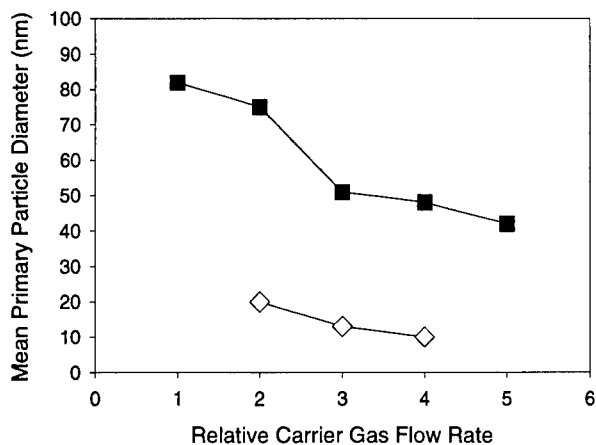


Figure 5: Mean primary particle diameter for samples taken beneath the substrate (diamonds) and at the chamber wall (squares) for varying precursor concentrations. For reference, the carrier gas flow rate of 2 corresponds to an HMDS precursor mass flow rate of .005 g/s.



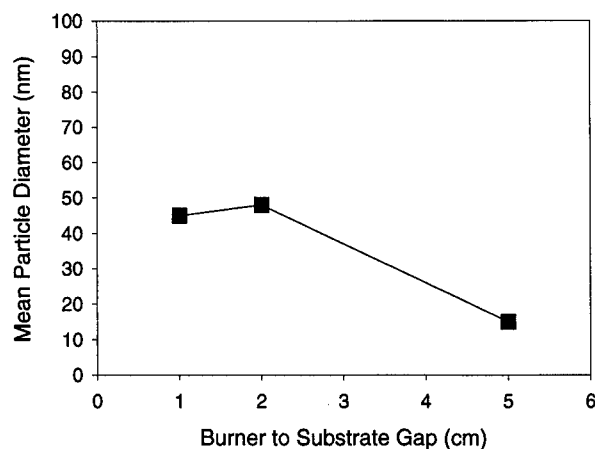


Figure 6: Mean primary particle diameter for samples taken at the chamber wall for varying standoff distance.

and non-agglomerated, while the most distant sampling port, approximately 1 cm beyond the visible deposit, had a much sparser deposit on the grid and showed significantly larger and more agglomerated particles.

The effect of precursor concentration on particle size was investigated by running several cases with different precursor flow rates. For these runs, the  $H_2/O_2$  equivalence ratio was 0.8 (fuel-lean), the chamber pressure was 20 Torr, and the standoff distance was 2 cm. Mean particle diameters for samples collected beneath the substrate and at the wall are shown in Figure 5. In both cases, an inverse dependence of particle size on precursor concentration is observed.

The influence of standoff distance on particle size is shown in Figure 6 for samples collected at the wall. Despite the increased residence time, particle size appears to decrease with increasing standoff distance beyond 2 cm.

## DISCUSSION

The abrupt change in mean particle size, as observed in Figure 5, suggests that the deposit consists of particles which follow two classes of trajectories: 1) those in which deposited particles impact the substrate immediately after condensation, and 2) those in which the substrate is bypassed. In the former case, residence times are expected to be very short ( $<10$  ms) based on trajectory calculations which include thermophoretic and drag forces. Thus, the particle size and degree of agglomeration are expected to be small compared to, for example, atmospheric pressure powder synthesis in flames.

However, in case 2), the particles do not experience the rapid quench induced by the substrate, and thus would be expected to have time/temperature histories characterized by significantly longer periods of time in the hot regions, leading to increased particle size and degree of agglomeration. In addition, there may be a significant contribution to the large, agglomerated powder observed at the chamber walls from particles which travel through the quench zone but do not stick to the substrate and from those which stick but are later entrained back into the flow. These particles might then flow back into hot zones adjacent to the burner and grow via surface addition of monomers or by agglomeration.

The effect of precursor concentration on particle size is opposite to that observed in similar  $\text{H}_2/\text{O}_2/\text{SiH}_4$  flames (4,5) in which there was no substrate. Since the substrate induces a substantially different time/temperature history in the flow, arguments previously used to explain the variation of mean diameter with precursor concentration may not apply directly here. It is notable, however, that while the  $\text{H}_2/\text{O}_2$  equivalence ratio was held constant for these runs, the total equivalence ratio (including the precursor) increased, making the flames at higher precursor concentrations more oxygen deficient.

The effects of standoff distance on mean particle size is likewise not fully explained. The data seem to indicate a shift in the fraction of trajectories which impact or are influenced by the substrate as the gap distance is increased. Trajectory calculations to test this hypothesis are underway.

### CONCLUSION

The particle size distribution in CF-CVC follows a bimodal distribution which appears to indicate two classes of particle trajectories. Particle size is shown to be strongly influenced by precursor concentration; however, equivalence ratio effects may contribute significantly to these results. Further studies are aimed at modifying the reactor geometry to eliminate trajectories in which a rapid quench is avoided.

### ACKNOWLEDGMENTS

This work was supported by grants from the National Science Foundation (CTS-97-03357) and the Office of Naval Research under contract number N00014-97-1-0240.

### REFERENCES

1. Chen, Y.J., Glumac, N.G., Skandan, G., and Kear, B.H., *Materials Letters*, 1998, 34, 148.
2. Skandan, G., Chen, Y.J., Glumac, N.G., and Kear, B.H., submitted for publication to *Powder Technology*.
3. Glumac, N.G., Chen, Y.J., Skandan, G., *Journal of Materials Research*, (in press).
4. Lindackers, D. and Roth, P., *Berichte der Bunsen-Gesellschaft fur Physikalische Chemie*, 1997, 101, 1718.
5. Lindackers, D., Strecker, M.G.D., and Roth, P., *Nanostructured Materials*, 1994, 4, 545.



Pergamon

NanoStructured Materials, Vol. 12, pp. 259–262, 1999

Elsevier Science Ltd

© 1999 Acta Metallurgica Inc.

Printed in the USA. All rights reserved

0965-9773/99/\$—see front matter

PII S0965-9773(99)00112-9

## SYNTHESIS AND CHARACTERIZATION OF NANOCRYSTALLINE Ni/ZrO<sub>2</sub> COMPOSITE COATINGS

A. Möller, H. Hahn

Thin Films Division, Materials Science Department, Darmstadt University of Technology,  
Petersenstr. 23, 64287 Darmstadt, Germany, e-mail:dh58@hrzpub.tu-darmstadt.de

**Abstract** – Nanocrystalline Ni/ZrO<sub>2</sub>-composite coatings were produced by codeposition of ZrO<sub>2</sub> particles during electroplating of Ni. In this process nanocrystalline ceramic powders with grain sizes below 10 nm were suspended in the plating solution and the ceramic particles codeposit with the metal to produce nanocrystalline metal matrix composite coatings. The influence of the plating parameters on the content and dispersion of the codeposited ceramic particles was investigated. Additionally, the microstructure of the coating was examined and the experimental results were correlated to the mechanical properties of the coatings. It was shown that the ceramic particles cause an increase in hardness, which depends on the amount of codeposited ZrO<sub>2</sub>. ©1999 Acta Metallurgica Inc.

### INTRODUCTION

Several properties of n-metals are improved compared to their microcrystalline counterparts. For example in n-nickel produced by electrodeposition the Vickers hardness increases from 140 to 650, when the grain size is reduced to the 10 nm range [1]. Additionally, nanocrystalline metals show lower wear rates, better resistance against localized corrosion and different magnetic properties [2]. Unfortunately these beneficial properties of n-materials are lost at elevated temperatures because grain growth starts in metallic samples at rather low temperatures, depending on the purity of the grain boundaries. In the case of n-nickel at the smallest grain sizes investigated, a reduction in grain size does not increase the hardness further and the so called inverse Hall Petch behavior is observed [1]. To overcome these limitations, the synthesis of a metal matrix ceramic composite seems promising, if the particles prevent or suppress grain boundary migration resulting in enhanced thermal stability. The ceramic particles in the metal matrix should also act as obstacles to dislocation movement and grain boundary sliding thus increasing the hardness over the limit of the pure n-metal. Both effects depend on the number of ceramic particles and their dispersion. A metal matrix nano/nano-composite is, therefore, favorable (Niihara concept).

Nanocrystalline metals and alloys have been mainly produced by inert gas condensation, ball milling and electrodeposition. For the synthesis of metal matrix composites electrodeposition can be used if the ceramic particles are dispersed in the electrolyte and can be deposited during electroplating simultaneously process. Compared to other production methods,

electrocodeposition shows several advantages: it represents a low temperature process without vacuum, realizes high deposition rates in the range of 100  $\mu\text{m}/\text{hour}$  and enables the synthesis of a wide range of metal matrix ceramic composites through the combination of electrolytes with different ceramic particles. Also, a possible industrial scale production can be realized quickly because existing electroplating plants can still be used.

Nanocrystalline Zirconia and Nickel were selected for this study to compare the results with other systems, e.g.,  $\text{Ni}/\text{Al}_2\text{O}_3$  [3].

## EXPERIMENTAL

Nanocrystalline  $\text{ZrO}_2$  powders are produced by inert gas condensation. These powders consist of a mixture of the tetragonal and monoclinic phases and have grain sizes in the range of 4-10 nm and specific surface areas of 190  $\text{m}^2/\text{g}$  [4].

10 - 50 g/l of ceramic particles were suspended by stirring at pH 2.5 in a Watts type electrolyte containing 300 g/l  $\text{NiSO}_4$ , 45 g/l  $\text{NiCl}_2$ , 45 g/l boric acid and 1 g/l Saccharin. DC-plating was carried out at 333 K on polished Ti-substrates with nominal current densities of 0.01 - 0.1  $\text{A}/\text{cm}^2$ .

The deposits were stripped mechanically off the substrate, cut into smaller pieces, embedded in resin and polished using standard metallographic techniques to obtain cross sectional samples. The Vickers hardness was obtained by a LECO M-400-G2 hardness tester. The content of ceramic in the metal matrix was determined by electron probe microanalysis (CAMEBAX SX 50) at 15 kV using wavelength dispersive techniques in combination with standards. High Resolution Scanning Electron Microscopy (HRSEM) was used to determine the size of the ceramic particles in the metal matrix. The grain size and microstrain of the metal were evaluated by peak broadening analysis of X-ray diffraction patterns (SIEMENS D5000) following the technique developed by Williamson and Hall [5].

## RESULTS

The results of X-ray peak broadening analyses for the Ni-metal performed on  $\text{Ni}/\text{ZrO}_2$  samples with three different average  $\text{ZrO}_2$  contents are summarized in Table 1. It is shown that the grain sizes,  $D$ , obtained from the analysis of two different reflex groups (h00 and nnn) are in the nanocrystalline range and not very much effected by the amount of deposited ceramic particles. Also, the microstrain shows no dependence on the  $\text{ZrO}_2$  content. It can be concluded from these results that the size of the metallic grains is not affected by the codeposition of ceramic particles.

TABLE 1  
XRD peak broadening analyses for DC-plated  $\text{Ni}/\text{ZrO}_2$  samples

$\text{ZrO}_2$ [wt%]	$D_{h00}$ [nm]	$D_{nnn}$ [nm]	$\epsilon_{\text{micro}}(h00)$	$\epsilon_{\text{micro}}(nnn)$
0.02	$46 \pm 5$	$34 \pm 5$	$0.0041 \pm 0.0005$	$0.0038 \pm 0.0005$
0.7	$48 \pm 5$	$32 \pm 5$	$0.0040 \pm 0.0005$	$0.0037 \pm 0.0005$
0.9	$38 \pm 5$	$34 \pm 5$	$0.0048 \pm 0.0005$	$0.0039 \pm 0.0005$

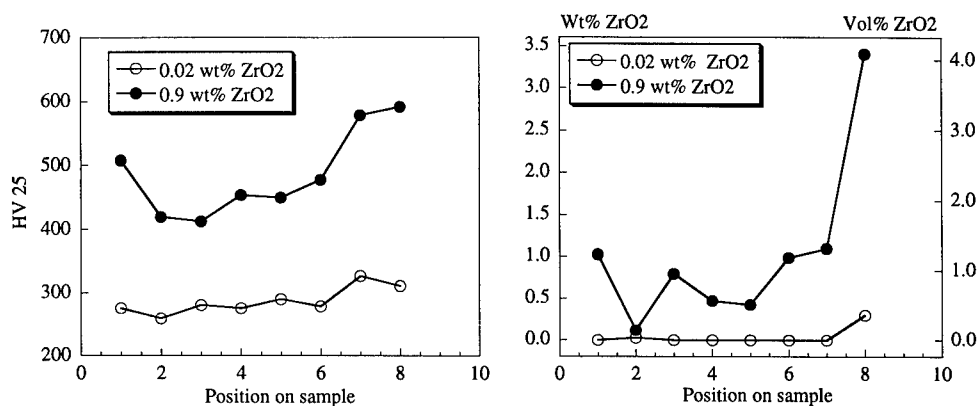


Figure 1a (left): Vickers hardness as a function of the position on the sample for two different ZrO<sub>2</sub> contents, 1b (right) ZrO<sub>2</sub> content as a function of the position on the sample

Figure 1a (left side) shows the results of a Vickers hardness test of electroplated Ni/ZrO<sub>2</sub> samples with two different average ZrO<sub>2</sub> contents. It is evident that the material with the higher ZrO<sub>2</sub> content is harder than the material with the lower amount of ceramic particles inside. The hardness of the harder sample varies greatly as a function of the position on the sample. This behaviour can be related to the ZrO<sub>2</sub> content as shown in figure 1b (right side). Clearly a correlation of hardness with ZrO<sub>2</sub> content is observed: the higher the ceramic content, the higher the hardness.

Two HRSEM-pictures of a composite material containing 0.9 wt% ZrO<sub>2</sub> are shown in figure 2. The two dark areas in figure 2 have been identified as ceramic particles by energy dispersive X-ray analysis (EDX). It is evident that the ceramic particles are agglomerates or aggregates of the smaller ZrO<sub>2</sub>-nanograins. The ceramic particles detected are in the size range between 70 and 500 nm.

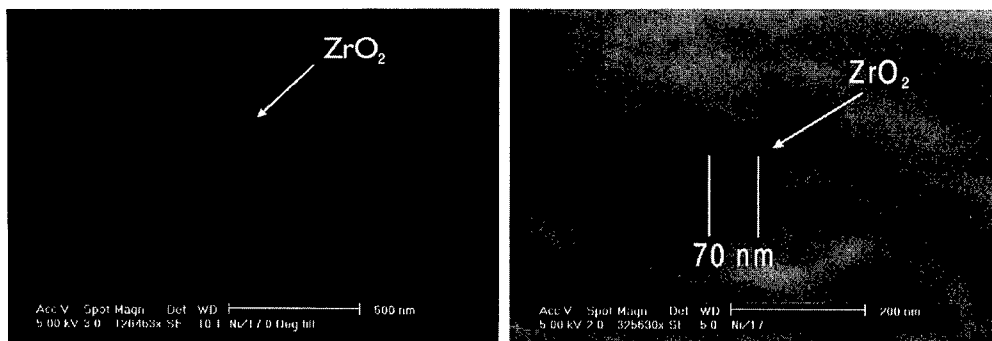


Figure 2: HRSEM pictures of ZrO<sub>2</sub> grains in Ni-matrix

Thus, the distribution of nano-ceramic particles is not yet optimized. Most likely the agglomeration of nanoparticles in the aqueous electrolyte is the reason for deposition of the large particles. Preliminary results have shown that without using surfactants nanoparticles with sizes in the range of less than 10 nm aggregate to form particles in the range found in the electrodeposited samples. Therefore, it seems necessary to use appropriate surfactants to suppress or prevent agglomeration in order to incorporate smaller particles.

The performed experiments are in good agreement with results obtained for other composites produced by electrocodeposition, e.g., Ni/Al<sub>2</sub>O<sub>3</sub> [3]. In these systems the incorporation of nanoparticles also causes an increase in hardness, although the coatings have been annealed resulting in grain growth and stress relaxation of the metal. Unfortunately, a detailed study relating the observed increase in hardness to microstructural parameters, like metal and ceramic grain size distributions, volume fraction of codeposited particles, metal-ceramic-interface properties, stresses etc., is still missing for these materials.

### SUMMARY

Nanocrystalline Ni/ZrO<sub>2</sub> composite coatings were produced by codeposition of ceramic particles during electroplating of Ni in a Watts type electrolyte bath. The amount of codeposited ceramic varied between 0 and 3.7 wt.%. An increase in hardness is observed for the composite material with higher average ceramic content. The variations in the hardness of the high ceramic content samples were correlated with the local amount of ceramic particles in the matrix as shown by electron probe microanalysis. X-ray diffraction peak broadening analysis showed that the size of the metal grains and the microstrain in the metal were not affected by the codeposition process of ceramic particles. It is concluded that the increase in hardness is caused by the ceramic particles in the composite coating.

### REFERENCES

- [1] A.M. El-Sherik et al, *Scripta Metall.* **27** (1992) p. 1185
- [2] M.J. Aus et al, *Mat. Res. Soc. Symp. Proc.* **318** (1994) p. 35
- [3] H. Ferkel, B. Mueller, W. Riehemann, *Mater. Sci. Eng., A* **234-236** (1997) p. 474
- [4] R. Nitsche, M. Rodewald, G. Skandan, H. Fuess and H. Hahn, *Nanostruct. Mater.* , **7** (1996) p. 535
- [5] G.K. Williamson and W.H. Hall, *Acta Metall.* **1** (1953) p. 22



## AGGLOMERATION AND SURFACE MORPHOLOGY DURING PULSED LASER DEPOSITION OF Pb-Zr-Ti-O

M. Tyunina\*, J. Levoska, K.J. Koivusaari, and S. Leppävuori

Microelectronics and Material Physics Laboratories and EMPART Research Group of Infotech Oulu, University of Oulu, PL 444, FIN-90571 Oulu, Finland;

\*permanent address: Institute of Solid State Physics, University of Latvia, Riga, Latvia

**Abstract** – The agglomeration and clustering processes occurring during pulsed laser deposition were studied by analyzing the nanometer scale surface morphology of an amorphous lead zirconate titanate deposit using scanning electron microscopy and atomic force microscopy. The surface roughening of the deposit depended on the pressure and nature of the ambient gas, as well as on the duration of deposition. The development of surface features is discussed in terms of agglomeration in the plume and the adsorption of species and surface diffusion. The power law dependence of surface roughness on the number of laser shots, observed in oxygen and in argon, is explained by the assumption of cluster generation in the plume. ©1999 Acta Metallurgica Inc.

### INTRODUCTION

Experimental and theoretical studies of surface evolution during film deposition have progressed rapidly over recent years. The major research has been focused on molecular beam epitaxy of metals and semiconductors. Much less attention has been paid to pulsed laser deposition (PLD), which has been successfully applied to the deposition of various thin film materials (1), including ferroelectrics (2). To our knowledge, there are no studies reported on the atomic processes on the surface during PLD of ferroelectric films.

Atomic processes on the surface during PLD can possess certain peculiarities compared to other deposition techniques. The high energy of the species arriving onto the substrate surface causes high surface mobility. The energy of species depends on the deposition conditions, e.g. laser fluence, pressure of ambient gas, target-to-substrate distance, etc.. Chemical reactions and processes of agglomeration, resulting in the formation of polyatomic species and clusters, can take place in the plume during its expansion into a gas (3). These agglomeration processes can affect the composition and microstructure of the films. Direct studies of the agglomeration in the plume are rather complicated. Studies of the surface roughening can give additional information about the agglomeration processes.

Here we present results of scanning electron microscopy (SEM) and atomic force microscopy (AFM) studies of the surface morphology of the deposit produced by laser ablation of ferroelectric lead zirconate titanate, Pb-Zr-Ti-O (PZT). The surface roughness was analyzed with respect to various deposition parameters, including the laser fluence, the pressure and nature of the ambient gas, and the duration of deposition.

## EXPERIMENTAL

Laser ablation of PZT was performed using an XeCl excimer laser. The laser radiation was focused to a square spot on the surface of the ceramic PZT target with an angle of incidence of  $45^\circ$ . The laser fluence was varied in the range of 0.3 to  $3.0 \text{ J/cm}^2$ . The deposit was collected onto Si (100) substrates at a distance of 20 mm opposite to the rotating target. The deposition was performed at room temperature in vacuum, in oxygen and in argon. The ambient gas pressure was varied from the base  $10^{-5}$  mbar to 1 mbar. The duration of deposition was controlled by the number of laser shots in the range from 1 to 60000. The surface morphology was studied using SEM and AFM. Energy dispersive x-ray spectroscopy (EDX) was used for the measurement of the thickness and composition of the deposit.

## RESULTS AND DISCUSSION

PZT deposition both in vacuum and in a gas (oxygen or argon) at pressures below 0.4 mbar resulted in rather smooth surfaces. Only droplet type particles, typical for PLD, could be detected by SEM. An increase in gas pressure to 0.4 -1.0 mbar resulted in deposits consisting of small agglomerates with lateral dimensions less than 100 nm (Fig.1). Besides a morphological change, the increase in ambient gas pressure led to considerable changes in the deposition rate and composition of the deposit, reported previously in detail (4).

The formation of agglomerates, responsible for the surface morphology at high oxygen pressure, could be connected with the agglomeration processes in the plume. Chemical reactions of lead oxidation could take place during expansion of the plume into oxygen (5). They could stimulate further agglomeration in the plume (3). However, the morphological changes were similar both in a reactive oxygen ambient and in an inert argon ambient. This could be explained by the agglomeration processes taking place on the substrate surface rather than in the plume. Such agglomeration could be determined by a considerable decrease in the surface diffusion of adsorbed species due to a decrease of the energy of the species in a gas as a result of collisions with gas molecules.

AFM measurements of the roughness of PZT deposited in vacuum and in ambients of oxygen or argon were performed as a function of the duration of deposition. To compare the characteristics from different batches of samples, contact mode AFM scans (1 mm x 1 mm) of particle free areas of the deposit were used. The deposits obtained in vacuum had a smooth surface irrespective of the thickness. The average height of the surface features, determined as

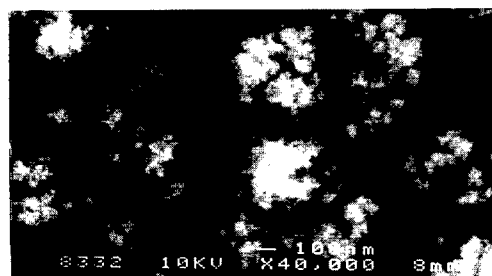


Fig. 1. A SEM image of a PZT deposit produced in 0.8 mbar oxygen.



characteristics from different batches of samples, contact mode AFM scans (1 mm x 1 mm) of particle free areas of the deposit were used. The deposits obtained in vacuum had a smooth surface irrespective of the thickness. The average height of the surface features, determined as the maximum of the height distribution, was about 1 nm (Fig. 2a) in the deposit produced by 10-60000 laser shots, which corresponded to a thickness of 0.1-300 nm (4). The PZT ablation in a gas resulted in deposits with a noticeably rough surface. The average height of the features increased with the number of laser shots to 15-20 nm after 20 000 shots (Fig. 2b).

Although SEM studies did not reveal difference in the surface of deposits produced in oxygen and in argon, AFM measurements showed different evolution of the surface roughness with respect to the nature of gas. It can be seen from Fig. 3 that, with an increase in the number of laser shots, the roughness of the deposit in vacuum remained constant, while the roughness of the deposit in a gas increased. The roughening was more evident in oxygen than in argon. Detailed analysis of the experimental data in Fig. 3 revealed a power law dependence  $h \sim N^n$ , of the average height  $h$ , on the number of laser shots,  $N$ , for the deposition in a gas. The exponent  $n$  was 0.4 and 0.6 for the deposition in oxygen and in argon, respectively.

The evolution of surface morphology is usually considered as an interplay between deposition of atoms onto the surface and surface diffusion of adatoms. The migration of adatoms is determined by the interaction of adatoms with the substrate surface, e.g. with steps. The modeling of deposition with non-thermal diffusion due to step-edge barriers has shown the possibility of mound formation (6). The average mound size can vary by a power law ( $\sim \text{time}^n$ ), where the exponents  $n$  are in the range 0.2-0.3. The surface roughening during PZT deposition in a gas was consistent with the model conclusions. However, the dependence of  $n$  on the nature of the gas was unclear.

Similar deposition rates and compositions of deposit were found for the PZT ablation both in oxygen and in argon (4), revealing similar deposition kinetics. But an expected similar surface evolution was not observed. It has been shown (7) that a short-range attraction of adatoms towards clusters on the substrate surface can lead to mound formation, even without step-edge barriers. The deposition of the clusters from the plume, at the initial stage, could result in surface roughening at the later stage, even if the fraction of clusters in the plume is small.

The observed surface coarsening agreed with considerations of cluster deposition. The probability of oxidation and cluster formation in argon was less than that in oxygen. This resulted in a lower density of the deposited clusters and a smoother surface at the initial stage. The lower density of clusters and, respectively, of adatom-cluster barriers, which inhibit surface mobility, determined a lower surface mobility in argon. This lower surface mobility could

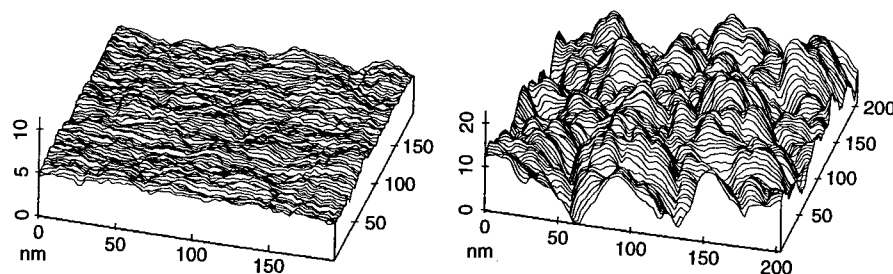


Fig. 2. Three dimensional AFM images of PZT deposit produced in vacuum by 15000 laser shots (a), and produced in 0.2 mbar oxygen by 5000 laser shots (b).

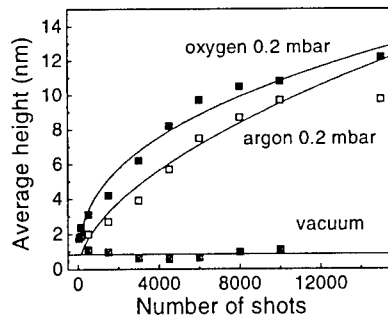


Fig. 3. The average height of surface features as a function of the number of laser shots for a PZT deposit in 0.2 mbar oxygen (solid squares), 0.2 mbar argon (open squares) and in vacuum (crossed squares). Laser fluence  $2 \text{ J/cm}^2$ . Fit to the power law: continuous lines.

could result in relatively faster surface roughening and a larger value of  $n$  at the later stage. In oxygen, effective deposition of clusters could result in a larger height of the surface features at the initial stage and, a slower roughening with  $n=0.4$  at the later stage due to higher density of adatom-cluster barriers.

In contrast to the surface roughening in a gas, the surface evolution in vacuum could not be explained by non-thermal mobility. The high energies of ablated species in vacuum determined the relatively low rate of adsorption and high surface mobility. These tendencies resulted in the formation of a smooth surface (8).

## CONCLUSIONS

Surface roughening of the deposit during laser ablation of PZT was studied by SEM and AFM as a function of gas pressure and duration of deposition. The smooth surface of deposits in vacuum can be explained by a relatively low adsorption rate of species and their high surface mobility. A power law dependence of surface roughness on the number of laser shots was found in a gas. This was explained by non-thermal mobility of species on the surface with adatom cluster barriers. The different density of clusters formed in oxygen compared to that in argon resulted in different roughening kinetics in these two cases.

## REFERENCES

1. e.g. *Mater. Res. Soc. Symp. Proc.* 397 (1996).
2. e.g. *Mater. Res. Soc. Symp. Proc.* 433 (1996).
3. Amoroso, S., Berardi, V., Dente, A., Spinelli, N., Armenante, M., Velotta, R., Fuso, F., Allegrini, M., and Arimondo, E., *J. Appl. Phys.*, 1995, 78, 494.
4. Tyunina, M., Levoska, J., and Leppävuori, S., *J. Appl. Phys.*, 1998, 83, 5489.
5. Chertihin, G.V. and Andrews, L., *J. Chem. Phys.*, 1996, 105, 2561.
6. S'milauer, P.S. and Vvedensky, D.D., *Phys. Rev. B*, 1995, 52, 14263.
7. Amar, J.G. and Family, F., *Phys. Rev. Lett.*, 1996, 77, 4584.
8. Bales, G.S. and Chrzan, D.C., *Phys. Rev. B*, 1994, 50, 6057.



Pergamon

NanoStructured Materials, Vol. 12, pp. 267–270, 1999

Elsevier Science Ltd

© 1999 Acta Metallurgica Inc.

Printed in the USA. All rights reserved

0965-9773/99/\$—see front matter

PII S0965-9773(99)00114-2

## COMPLEX FORMATION IN SOLUTIONS FOR CHEMICAL SYNTHESIS OF NANOSCALED PARTICLES PREPARED BY BOROHYDRIDE REDUCTION PROCESS

I. Dragieva, S. Stoeva<sup>1</sup>, P. Stoimenov<sup>1</sup>, E. Pavlikianov<sup>2</sup> and K. Klabunde<sup>3</sup>

Bulgarian Academy of Sciences, CLEPS, 1113 Sofia, Bulgaria

<sup>1</sup> State University of Sofia, Depart. Chemistry, 1126 Sofia, Bulgaria

<sup>2</sup> Technical University, 7004 Russe, Bulgaria

<sup>3</sup> Kansas State Univ., Depart. Chemistry, KS 66506, USA

**Abstract** – Complex forming agents are often used in chemical synthesis of nanoscale particles by means of a borohydride reduction process. Their influence on the rate of nucleation and a growth of particles without oxide/hydroxides shell are estimated earlier. In this paper experimental data are presented about the synthesis of Fe-Nd-B-H particles from chloride water solutions by reduction with sodium borohydride, as well as synthesis of Fe-Nd-Si-B-H particles, containing silicon, by using hexafluorosilicate of iron(II). According to the estimated influence of the aqua-complex structures on the synthesis of amorphous or nanocrystalline particles, synthesis of initial complex salts – precursors *trans*- and *cis*-[bis(ethylenediamine)dichloro cobalt(III)] chloride is carried out. The influence of the metal complex used in water solutions by a reduction with sodium borohydride on the composition, the structure and specific surface area of prepared nanoscale particles is investigated.

©1999 Acta Metallurgica Inc.

### INTRODUCTION

The present paper deals with the influence of complex used on synthesis of three types of nanoscaled systems: Fe-Nd-B-H, Fe-Nd-Si-B-H and Co-N-B-H obtained as particles using a borohydride reduction process. The Fe-Nd-B alloy is the strongest permanent magnet material known, but little is known about the properties of Fe-Nd-B small particles (1, 2). Special attention was paid to the synthesis of nanoparticles containing metallic silicon (1). The studies cited in the literature are mostly on the preparation of silicon (and silica) nanoparticles by vapor deposition techniques, in micro-emulsions, by sol-gel and emulsion-gel processes, by multiple low energy oxygen ion implantation etc. Many authors have paid special attention to the influence of the particle size and quantum size effects on the luminescence properties of nanoscaled silicon (3, 4). No reports are available about the synthesis of nanoscaled silicon by chemical reduction processes or about the incorporation of silicon in metal nanoparticles (1). For the synthesis of nanoparticles containing metallic silicon it was need to use as salts hexafluorosilicate of Fe(II). The same salts was used earlier by us in the electrodeposition of iron layers containing nitrogen and silicon (5, 6). According to the estimated influence of the aqua-complex structures on the synthesis of amorphous or nanocrystalline particles (7) synthesis of initial complex salts - precursors *trans*- and *cis*-[bis(ethylenediamine)dichlorocobalt(III)] chloride is carried out. This compound exists in these both isomeric forms in respect to the chlorine atoms (and to the nitrogen-cobalt bond too) (8). The aim of this work is not only to show the formation of metal-metal bond in nanoparticles obtained by a borohydride reduction containing Nd and Si, but also to present the possibility for synthesis of metal nanoparticles, containing more metalloid atoms like nitrogen, boron and hydrogen as neighbors to the cobalt odd atoms using such kind of complexes as precursors.

## EXPERIMENTAL

The above systems were synthesized by means of a reduction of aqueous solutions of salts:  $\text{FeCl}_2 \cdot 6\text{H}_2\text{O}$  (or  $\text{Fe}[\text{SiF}_6] \cdot 6\text{H}_2\text{O}$  in the second case) and  $\text{NdCl}_3 \cdot 6\text{H}_2\text{O}$  with  $\text{NaBH}_4$  using 'Tea' apparatus working in earlier recommended and well known conditions without oxidation of Fe(II) or Nd(III). After filtering and drying in vacuum furnace particles were analyzed for a content of Nd using ICP-type APL 3620, for a content of Si (by atom absorption. spectrophotometer), for a content of boron (by chemical analysis) and for hydrogen - by LECO RH-3. Specific surface area by BET for some samples were estimated too. *Trans* form of  $[\text{Co}(\text{C}_2\text{H}_4(\text{NH}_2)_2)_2\text{Cl}_2]\text{Cl}$  was synthesized using  $\text{CoCl}_2 \cdot 6\text{H}_2\text{O}$  and fuming ethylenediamine (9). On the base of those prepared solid Co(III) complex we can determine the concentration of  $\text{NaBH}_4$  according to our knowledge about the mechanism of borohydride reduction process (10). The presence of *chelate* rings of ethylenediamine in these complexes adds additional stability of the salt solution and the rate of reduction with  $\text{NaBH}_4$  is strongly decreased. After a reduction of aqueous complex solution with  $\text{NaBH}_4$ , the obtained nanoparticles are filtered, washed and dried in vacuum. In some cases the colloidal solution was evaporated in vacuum furnace at room temperatures. TEM and Selective Area Electron Diffraction studies were performed with JEM-200 CX, JEOL, Japan.

## RESULTS AND DISCUSSION

Analytical data for the content of elements of particles with compositions Fe-Nd-B-H and Fe-Nd-Si-B-H obtained by borohydride reduction are shown in Table 1. The pH value of

TABLE 1  
Analytical Determined Content of Elements in Fe-Nd-B-H and Fe-Nd-Si-B-H  
Nanoparticles Obtained by Borohydride Reduction

Composition of the initial salt solution	Nd at %	B at %	H at %	Fe at %	Si at %	SSA m <sup>2</sup> /g
$\text{Fe}_{60}\text{Nd}_{40}$	5.22	18.47	35.39	40.92		
$\text{Fe}_{62}\text{Nd}_{38}$	5.12	17.27	37.11	40.50		
$\text{Fe}_{64}\text{Nd}_{36}$	5.74	19.46	29.44	45.37		
$\text{Fe}_{66}\text{Nd}_{34}$	4.98	17.43	32.73	44.86		
$\text{Fe}_{68}\text{Nd}_{32}$	5.58	19.71	27.53	47.17		
$\text{Fe}_{70}\text{Nd}_{30}$	4.23	14.51	34.30	46.96		
$\text{Fe}_{72}\text{Nd}_{28}$	4.06	13.88	34.39	47.67		
$\text{Fe}_{74}\text{Nd}_{26}$	4.58	16.05	33.40	45.98		
$\text{Fe}_{76}\text{Nd}_{24}$	4.16	16.80	27.82	51.22		
$\text{Fe}_{78}\text{Nd}_{22}$	4.31	19.60	24.68	51.41		
$\text{Fe}_{92.6}\text{Nd}_{7.4}$	1.39	6.91	10.53	79.03	2.13	11
$\text{Fe}_{92.4}\text{Nd}_{7.6}$	2.17	5.94	21.39	66.64	3.85	26
$\text{Fe}_{92.0}\text{Nd}_{8.0}$	2.18	3.99	24.87	64.51	4.45	24
$\text{Fe}_{90.4}\text{Nd}_{9.6}$	2.03	7.70	15.30	68.79	6.18	15
$\text{Fe}_{90.3}\text{Nd}_{9.7}$	1.86	5.59	12.37	79.30	0.89	14
$\text{Fe}_{88.2}\text{Nd}_{11.8}$	2.89	6.91	21.67	67.71	0.83	20

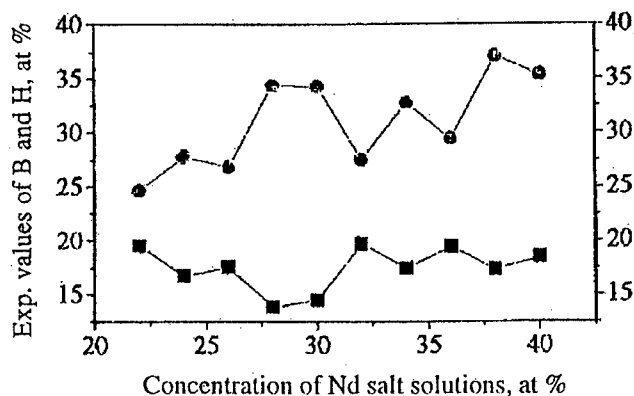


Figure 1. Influence of the initial salt solution concentration on the content of boron (■) and hydrogen (●) in nanoparticles of the Fe-Nd-B-H system

the initial salt solution for the system Fe-Nd-B-H is near to 5 for all solutions irrespectively of the change in Nd(III) solution concentration. The pH value of the initial salt solution for the second system Fe-Nd-Si-B-H is near to 1. The concentration of  $\text{NaBH}_4$  is a constant value for both systems and is in accordance with the mechanism of a reduction and the concentration of salt solutions used. For the first system (Fe-Nd-B-H) the influence of the higher concentration of Nd(III) solution is well observed as a results of lower iron content in nanoparticles obtained. The dependence between boron and hydrogen content is well known (10), but this fact is very well observed in Fig. 1. In the whole range of concentrations used of Nd(III) the increasing in the boron content follows the decreasing in the hydrogen content in nanoparticles for the same experimental sample.

The incorporated metallic silicon in nanoparticles by means of a borohydride reduction of initial salt solution containing hexafluorosilicate of Fe(II) decreased the content of boron and hydrogen in nanoparticles with composition Fe-Nd-Si-B-H (see Table 1). The content of hydrogen in these nanoparticles is strongly dependent on their specific surface area. The higher specific surface area of nanoparticles, the higher is the content of hydrogen in this kind of particles.

The reduction of *trans*-[bis(ethylenediamine)dichlorocobalt(III)] chloride solution with  $\text{NaBH}_4$  solution was carried out using 'Tea' apparatus. Consideration and determination of the size and structure of separate nanosized particles (Fig. 2a, Fig. 2b) and particles extracted from colloidal solution (Fig. 2c, Fig. 2d) was possibly by means of an original preparative technique for electron microscopy studies using a magnification of 280 000X.

The separate magnetic nanoparticles shown in Fig. 2a and Fig. 2b are crystalline but they are obviously different in composition. Particles shown in Fig. 2d are of a special interest for us as a shape and structure observed. We suppose that the preparation by means of borohydride reduction of magnetic and crystalline Co-N-B-H nanoparticles is realized in this experiment using *trans*-complex of Co(III)-[Co( $\text{C}_2\text{H}_4(\text{NH}_2)_2$ ) $_2\text{Cl}_2$ ]Cl as precursor for the initial salt solution.

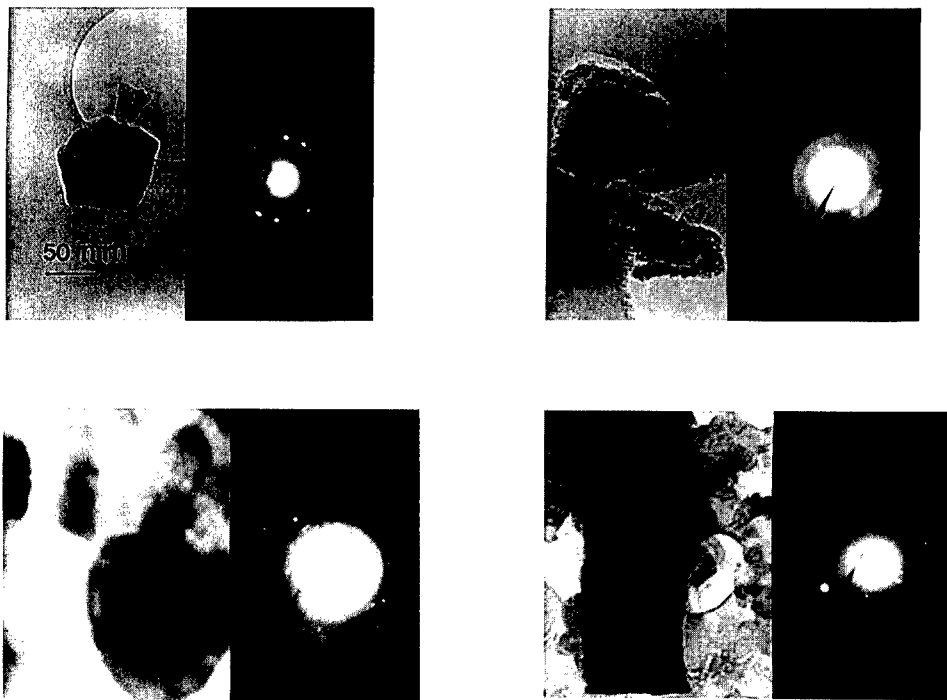


Figure 2. TEM and SAED of types of: 2a, 2b - filtered separate Co-N-B-H nanoparticles; 2c, 2d - extracted from a colloidal solution Co-N-B-H nanoparticles, magnification 280 000x

### REFERENCES

1. Dragieva, I., *AIP Conf. Proc. 231, Boron-Rich Solids*, AIP, New York, 1991, p.516.
2. Zhang, D., Glavee, G., Klabunde, J. K., Hadjipanayis, G. and Sorensen, C., *High Temp. Mat. Sci.*, 1996, **36**, 93.
3. Zhang, D., Kolbas, R., Milewski, P., Lichtenwalner, D., Kingon, A. and Zavada, J. *Appl. Phys. Lett.* 1994, **65**, 2684.
4. Seraphin, A., Werwa, E. and Kolenbrander, K., *J. Mat. Res.*, 1997, **12**, 3386.
5. Stoyanov, V., Dragieva, I. and Pavlikianova, A., *Adv. Surf. Eng., vol. II*, Royal Soc. Chem., UK, 1997, p. 290.
6. Nikolov, S., Pavlikianova, A., Pavlikianov, E. and Dragieva, I., *Proc. AMTECH '95*, TechnUniv. Russe, Bulgaria, 1995, p. 164.
7. Krastev, V., Stoycheva, M., Lefterova, E., Dragieva, I. and Stoyanov, Z., *J. Alloys and Compounds*, **240**, 1/2 (1996) 186.
8. Basolo, F. and Pearson, R., *Mechanism of Inorganic. A Study of Metal Complexes in Solution*, John Wiley and Sons, New York, 1967, p. 241.
9. Rindermann, W. and Van Eldik, R. *Inorg. Chim. Acta* 1982, **64**, L203.
10. Dragieva, I., Mehandjiev, D., Lefterova, E., Stoycheva, M. and Stoyanov, Z., *J. Magn. Magn. Mat.*, 1995, **140-144**, 455.



Pergamon

NanoStructured Materials, Vol. 12, pp. 271–276, 1999

Elsevier Science Ltd

© 1999 Acta Metallurgica Inc.

Printed in the USA. All rights reserved

0965-9773/99/\$—see front matter

PII S0965-9773(99)00115-4

## MICROSTRUCTURE AND OPTICAL PROPERTIES OF NANOSTRUCTURED SILICON THIN FILMS AND ARTIFICIAL DIELECTRICS

Zafar Iqbal\*, S. Vijayalakshmi<sup>#</sup> and Haim Grebel<sup>#</sup>

\*Research and Technology, AlliedSignal Inc, Morristown, New Jersey 07962, USA

<sup>#</sup>Optical Waveguide Laboratory, New Jersey Institute of Technology, Newark, New Jersey  
07102, USA

*Abstract—Thin films on various substrates and artificial dielectrics in fused silica composed of silicon nanoclusters and nanocrystals, have been grown by excimer laser ablation and Si ion implantation, respectively. The nanoscale structure of the laser ablated films have been shown by conventional and surface-enhanced micro-Raman scattering and transmission electron microscopy to be composed of silicon droplets surrounded by silicon nanoclusters. The droplets are composed of micro- and nano-crystalline silicon embedded in silicon nanoclusters. The as-prepared ion implanted samples are composed of silicon nanoclusters only, but on annealing, silicon nanocrystals and larger nanoclusters are precipitated. The as-prepared and annealed ion implanted samples, show size-dependent visible photoluminescence, while the laser ablated films show weak visible photoluminescence on annealing and large optical non-linear responses – the latter probably due to inter-cluster coupling within the droplets. ©1999 Acta Metallurgica Inc.*

### INTRODUCTION

Quantum confinement in nanophase silicon below about 10 nm in size opens up new physics as well as potential technological applications. Confinement in an indirect band gap material like silicon can enhance luminescence (1), which is forbidden in the bulk material, to levels that can be high enough to trigger lasing. Moreover, the appearance of enhanced third order, non-linear optical coefficients in nanoclustered semiconductors (2,3) suggests the use of these materials in all-optical switching devices. We have been recently studying the growth of silicon clusters and nanocrystals on silica, silica superlattices and quartz to form artificial dielectrics and thin films. In this paper, we will describe two growth methods that we have employed, and discuss the nanoscale structure, photoluminescence and non-linear optical properties of the materials obtained.

## EXPERIMENTAL

### *Growth Methods*

The samples containing the silicon clusters were prepared by two methods. In the first method, laser ablation was employed using a KrF excimer laser beam ( $\lambda=248$  nm, average power = 3 W, pulse duration = 8 ns, repetition rate = 50 Hz). The laser beam was focused to a 100  $\mu\text{m}$  spot on a silicon wafer target (<100> oriented and n-type carrier density of  $10^{16} \text{ cm}^{-3}$ ), which had been previously cleaned by HF and methanol. Films were deposited on quartz, fused silica, silicon wafer, single crystal KBr and metal substrates. The substrates were carefully cleaned with methanol and acetone before the deposition runs. The substrates were positioned 3 cm from the silicon target and the ambient pressure in the chamber was maintained near  $10^{-6}$  Torr. Deposition was carried out typically for 10 minutes at room temperature. In the second method carried out by C.W. White and his collaborators at Oak Ridge National Laboratory, silicon ions (400 keV) were implanted into silica matrices (Corning 7940) to various doses of the order of  $10^{17}/\text{cm}^2$ . At this energy, the projected range of excess Si is ca. 600 nm and the profile has a half-width of ca. 300 nm. The samples were studied in the as-prepared state and also after annealing for 1 hour in flowing argon and 4% hydrogen in order to induce precipitation to nanoclusters and nanocrystals within the silica matrix.

### *Characterization and Measurement Techniques*

Micro-Raman and photoluminescence measurements were carried out at a spatial resolution of 1 or 2  $\mu\text{m}$  using an Instruments SA microspectrometer with a cooled charge coupled device (CCD) detector and an argon ion laser emitting at 514.5 nm. In order to avoid thermal effects, the total laser power at the sample was maintained in the 0.2 to 0.5 mW range. Conventional Raman data were obtained on the as-prepared and the annealed samples, while surface-enhanced spectra were obtained on samples on which a 10 nm film of silver had been deposited by magnetron sputtering. Transmission electron microscopy (TEM) was carried out using a Hitachi 800 200 kV microscope.

Atomic force microscopy (AFM) was carried out using a Digital Instruments Nanoscope III system with a piezoelectric tube scanner of effective range from 0.5 to 15  $\mu\text{m}$ . The nonlinear index of refraction and the third order susceptibility were measured using the Z-scan technique (4) with a Q-switched Nd:YAG laser (pulse duration = 8 ns) at  $\lambda=532$  and 355 nm at a repetition rate of 10 Hz. The lifetime of the nonlinearity was determined using a pump-probe technique.

## RESULTS AND DISCUSSION

Optical microscopy of the laser ablated samples using a laser scanning microscope (Karl Zeiss LSM) showed that due to the directional nature of plume, the films obtained had three distinct thickness regions: I - faint yellow and 100 nm thick, II - yellow and 200 nm thick and III - brown and 400 nm thick. The films consisted of round droplets ranging from about 3 to 10  $\mu\text{m}$  in diameter, which are separated by smooth regions. Conventional micro-Raman data at a



spatial resolution of  $1\ \mu\text{m}$  in the  $200\text{--}800\ \text{cm}^{-1}$  frequency range are displayed in Fig.1 for the droplet region of a laser ablated sample on aluminum. In addition, spectra for unannealed and annealed ion implanted sample, and the spectra of electrochemically etched porous silicon and

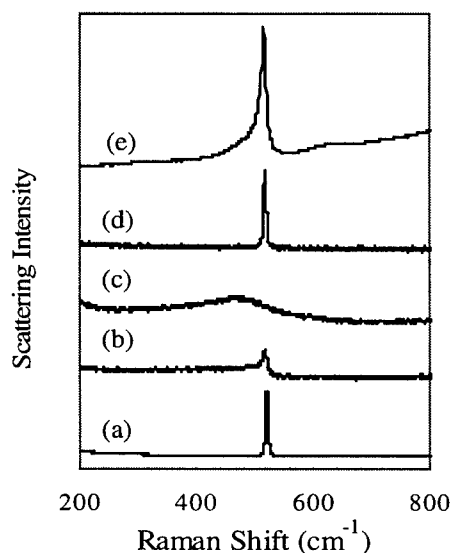


Figure 1: Conventional Raman scattering with peak positions in parentheses from (a) single crystal Si ( $520\ \text{cm}^{-1}$ ) (b) an annealed ion implanted sample ( $517.8\ \text{cm}^{-1}$ ), (c) an as-prepared ion implanted sample ( $467\ \text{cm}^{-1}$ ), (d) an as-prepared laser ablated sample within a droplet ( $517.8\ \text{cm}^{-1}$ ), and (e) a sample of porous Si ( $516\ \text{cm}^{-1}$ ).

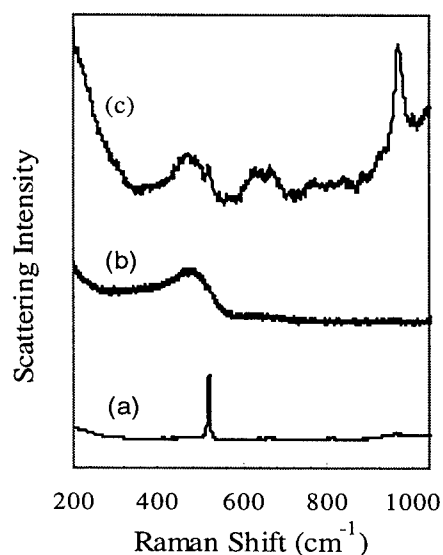


Figure 2: Surface Enhanced Raman Spectra from a laser ablated film (a) within a droplet and (c) between droplets. Spectrum (b) shows conventional Raman scattering from the region between droplets.

single crystal silicon in the same spectral range, are also shown. Fig.2 shows surface enhanced micro-Raman spectra in the  $200\text{--}1000\ \text{cm}^{-1}$  range for a similar laser ablated sample in the droplet and smooth regions, and the normal spectrum for the smooth region of a laser-ablated sample.

The data clearly show the one-phonon line of cubic silicon in the droplet region of the laser ablated sample, in the annealed ion implanted sample and in porous silicon, but the peak frequencies are typically shifted down from the value of  $520\ \text{cm}^{-1}$  for single crystal silicon. Frequency downshifts are a likely consequence of quantum localization in nanocrystals, as discussed by Iqbal and Veprek (5) and Campbell and Fauchet (6). As reported in refs. (5) and (6), the frequency shifts and associated line broadening correlate with x-ray diffraction determined crystallite sizes and hence can be used to determine the diameter of cubic silicon nanocrystals. In the droplet region of the laser ablated samples, micro-Raman imaging reveals particles with phonon frequencies ranging from  $517$  to  $520\ \text{cm}^{-1}$  with no indication of lines

near  $1000\text{ cm}^{-1}$  due to Si-O stretching modes. The latter is consistent with x-ray photoelectron spectra and the absence of photoluminescence in as-prepared laser ablated samples (see below). A crystallite size of 8 nm is estimated for the particles in a droplet with a phonon frequency of  $517\text{ cm}^{-1}$  and for the annealed ion implanted sample. The average crystallite size decreases to 6 nm for the sample of porous silicon. In the droplet regions of the laser ablated samples, however, the phonon line is relatively narrow and symmetric, suggesting that the downshift observed in some particles may be associated either with strain in the crystallites or the formation of a non-cubic silicon structure. Further studies regarding this are currently in progress.

In the ion implanted sample a broad band peaking at  $467\text{ cm}^{-1}$  transforms on annealing to a narrower peak at  $493\text{ cm}^{-1}$  and a phonon line at  $517.8\text{ cm}^{-1}$  (Fig.1). A broad feature with a deconvoluted peak position of  $480\text{ cm}^{-1}$  can also be seen in the spectrum of porous silicon, but this feature is not observed in spectra from the droplets in the laser ablated sample. Surface-enhancement (Fig.2a), however, reveals a broad peak at  $480\text{ cm}^{-1}$  in the droplet region. Normal Raman scattering from the smooth region between the droplets shows a broad band with two features: a shoulder at  $420\text{ cm}^{-1}$  and a peak at  $480\text{ cm}^{-1}$ . The surface-enhanced spectrum of the smooth region (Fig.2c) shows a narrower band at  $480\text{ cm}^{-1}$  and in some regions a crystalline peak at  $519.6\text{ cm}^{-1}$  from embedded nanograins. A surprising feature in the surface enhanced spectrum is the appearance of a relatively strong line at  $967\text{ cm}^{-1}$ , which can be assigned either to the second harmonic of the line at  $480\text{ cm}^{-1}$  or to an amorphous SiC surface film formed via carbon contamination. The broad features between 600 and  $700\text{ cm}^{-1}$  and between 750 and  $900\text{ cm}^{-1}$  may also be associated with this amorphous phase.

The broad line varying in peak frequency from  $467$  to  $495\text{ cm}^{-1}$  as a function of growth conditions and annealing, can be assigned to the phonon density-of-states spectrum of a continuous random silicon network. A second feature at  $420\text{ cm}^{-1}$  observed in the smooth region between droplets of the laser ablated sample can be attributed to Si-O bonds in this silicon network. However, the relatively symmetric shape of the above line suggests that the earlier (7) and more recent explanation (8) of this line in terms of a well-defined Si-Si shearing mode of a network of 1.5-3.0 nm-sized silicon clusters (9), may be a more appropriate interpretation. The present results indicate that such nanoclusters in the ion implanted sample increase in size to form nanocrystals on annealing. It is expected that the critical size where this transformation to nanocrystals occurs is near 3.5 nm, as first pointed out by Veprek et al (10).

Transmission electron microscopy allows a direct look at the regions within and around the droplets of a laser ablated sample prepared on a KBr substrate, which was dissolved in water and the ablated film floated on to a microscope grid. The TEM image of a droplet and its corresponding diffraction pattern are shown in Fig.3. The image reveals particles ranging from somewhat below 6 nm to above 200 nm, consistent with the micro-Raman data showing nanocrystallite domains in a typical droplet with a diameter of 8 nm. The smooth region outside the droplet is amorphous with no indication of any contrast due to short range order. Similar smooth regions with no indication of crystallinity are also evident within the droplets. This is supported by the observation of a broad line due to nanoclusters in the surface enhanced Raman data (Fig.2a). Atomic force microscopy indicates a cluster-like structure within the smooth regions between the droplets, based on height measurements for a sample prepared on quartz. The average heights range from 7 nm in the light yellow region to 50 nm in the brown region (11). TEM images taken from annealed ion implanted samples show

nanocrystallites with sizes in the 5 to 6 nm range (12) which are lower than those obtained from the Raman data on similar samples. The reasons for this are unclear at present.

Photoluminescence (PL) excited in the green shows an emission peak at 660 nm with a long wavelength tail for the as-prepared implanted sample, which is a factor of ten weaker than the visible PL emission in our sample of porous silicon (Fig.4). The PL emission from the ion implanted sample shifts to 780 nm on annealing, in agreement with the observed increase in size of the nanocrystals and clusters in the sample indicated by the micro-Raman data. The as-prepared laser ablated samples on the other hand do not display PL, but weak emissions at 580

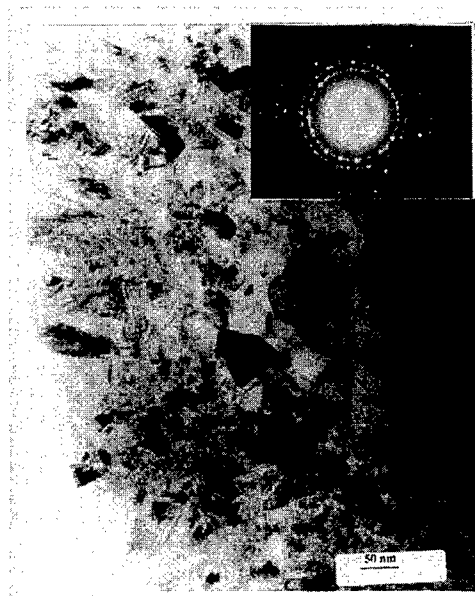


Figure 3: Transmission Electron Microscope image and corresponding electron diffraction pattern (inset) of a region within a droplet of a laser ablated film.

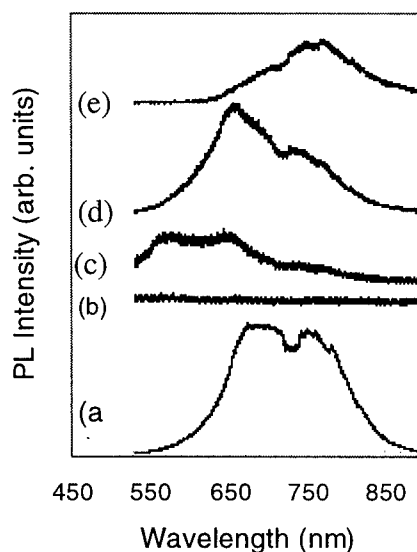


Figure 4: Photoluminescence spectra from (a) porous Si, (b) laser ablated unannealed film, (c) laser ablated annealed sample, (d) ion implanted unannealed sample, and (e) ion implanted annealed sample

and 660 nm are observed on annealing. This result shows quite clearly that PL in nanosized silicon requires, in addition to quantum confinement, a sizable oxide matrix such as formed here by ion-implantation.

The non-linear optical properties of the laser ablated and implanted samples were studied at 355 and 532 nm by use of Z-scan and pump probe techniques (2,3). Non-linear susceptibility  $\text{Re}[\chi^{(3)}]$  values as high as  $2.28 \times 10^{-5}$  esu were measured at 355 nm for the laser ablated film which is three orders of magnitude higher than that reported for porous silicon at 665 nm (13). The values at 532 nm are negative and are as high as  $-(1.33 \pm 0.33) \times 10^{-3}$  esu. At intensities above saturation, the non-linear susceptibility for the implanted samples is positive and comparable to that for the laser ablated films. The laser ablated films, however, showed a

much larger effect below saturation compared with the ion-implanted samples, which showed no non-linearity under these conditions. This may indicate an additional effect due to the presence of aggregated silicon nanostructures in the laser ablated films. Lifetime constants obtained are about 3-5 ns limited by the 8 ns laser pulse-width and are comparable for samples grown by both techniques. For the ion-implanted sample, the non-linear absorption coefficient,  $[\alpha_2(I)]$  increases with increasing intensity reaching saturation at high intensity values. For the laser ablated sample  $\alpha_2(I)$  changes from a positive to a negative value with the zero crossing occurring at an intensity of  $0.03 \text{ MW/cm}^2$ . The negative sign for the nonlinear susceptibility is probably due to the fact that the non-linear virtual state is below resonance for the laser ablated films.

In summary, we have investigated the nanoscale morphology, photoluminescence and non-linear optical properties of laser ablated and ion implanted silicon films. The laser ablated films consist of nanocrystals in the size range from about 6 to 200 nm located in the droplets. Nanoclusters below 3 nm in size are dispersed between the droplets and also within the droplets. The ion implanted samples consist only of nanoclusters in the as-prepared samples, but on annealing both nanoclusters and nanocrystals of similar size as in the laser ablated films are precipitated within the silica matrix. Visible photoluminescence is seen in the ion implanted samples, but only very weakly in annealed laser ablated films. Large optical non-linearities are seen in the laser ablated films probably due to strong inter-cluster and nanocrystal coupling within the droplets.

## REFERENCES

1. Alivisatos, A.P., *Science*, 1996, 271, 933.
2. Vijayalakshmi, S., George, M.A. and Grebel, H., *Appl. Phys. Lett.*, 1997, 70, 708.
3. Vijayalakshmi, S., Shen, F. and Grebel, H., *Appl. Phys. Lett.* 1997, 71, 3332.
4. Sheik-Bahae, M., Said, A.A., Hagan, D.J. and Van Stryland, E.W., *IEEE J. Quantum Electron.*, 1990, 26, 760.
5. Iqbal, Z. and Veprek, S., *J. Phys. C: Solid State Phys.*, 1982, 15, 377.
6. Campbell, I.H. and Fauchet, P.M., *Solid State Commun.*, 1986, 58, 739.
7. Iqbal, Z., Veprek, S., Webb, A.P. and Capezzuto, P., *Solid State Commun.*, 1981, 37, 993.
8. Wu, X.L., Yuan, X.Y., Tong, S., Liu, X.N., Bao, X.M., Jiang, S.S., Zhang, X.K. and Feng, D., *Solid State Commun.*, 1997, 104, 355.
9. Phillips, J.C., Bean, J.C., Wilson, B.A. and Ourmazd, A., *Nature*, 1987, 325, 121.
10. Veprek, S., Iqbal, Z. and Sarott, F.-A., *Philos. Mag.*, 1982, B45, 137.
11. For more details see: Vijayalakshmi, S., Iqbal, Z., George, M.A., Federici, J. and Grebel, H., *Thin Solid Films*, 1998, 336, 1.
12. White, C.W., Budai, J.D., Withrow, S.P., Zhu, J.G., Pennycook, S.J., Zühr, R.A., Hembree, D.M., Henderson, D.O., Magruder, R.H., Yacaman, M.J., Mondragon, G. and Prawer, S., *Nuclear. Instruments and Methods in Physics Research: Section B*, 1997, 127/128, 545.
13. Henari, F.Z., Morgenstern, K., Blau, W.J., Karavanskii, V.A. and Dneprovskii, S., *Appl. Phys. Lett.*, 1995, 67, 323.



Pergamon

NanoStructured Materials, Vol. 12, pp. 277–280, 1999

Elsevier Science Ltd

© 1999 Acta Metallurgica Inc.

Printed in the USA. All rights reserved

0965-9773/99/\$-see front matter

PII S0965-9773(99)00116-6

## PROPERTIES OF SILICON AND SILICON-CARBON CLUSTER ASSEMBLED FILMS

P.Keghelian, P.Melinon, A.Perez

Département de physique des matériaux, Université Lyon I  
43 Bd du 11 Nov, 69622 Villeurbanne cedex, France.

**Abstract--** *Si- and SiC cluster-assembled films have been produced in a laser vaporization source and analyzed in terms of electronic structure and vibrational density of states. In small silicon clusters (nanometer size range), we put on evidence five-fold rings into the films. In the case of SiC clusters, we observe the lack of the chemical order.*

©1999 Acta Metallurgica Inc.

### INTRODUCTION

Since the two past decades, the physics of assembled materials obtained from cluster deposition has opened a large field of potential applications. Such materials could be obtained if the free cluster characteristics are not destroyed during their deposition onto a substrate ("soft landing"). Thus, the films properties are governed by the properties of the nanograins themselves (*i.e.* supported clusters) and the interaction between the adjacent grains. This powerful method is promising in the case of binary-compounds since the stoichiometry of each component is fully adjustable. Moreover, homogeneous films can be obtained from immiscible components. Since we deposit very small clusters, the range order in the film is limited to the supported cluster one (nanometer scale). The random stacking of the grains avoids the formation of a long range order. Let us emphasize that the classical methods used to synthesize amorphous films (a-Si or a-SiC) are based from the atom per atom growth or directly by the amorphization of a crystal. In our case, the films are prepared by random stacking of preformed free clusters. This difference could explain the original properties and the new class of « amorphous materials » synthesized by low energy cluster beam deposition.

### EXPERIMENTAL

Covalent clusters are produced in a laser vaporization source (1). Briefly, clusters are formed by laser ablation of a Si rod or polycrystalline SiC rod associated with a high pressure (4 to 6 bars) helium burst injected in the nucleation chamber of the source. Some cluster ions arising directly from the source are deviated in a reflectron time of flight (TOF) mass spectrometer to characterize the abundance mass distributions. The mean free cluster sizes were about Si<sub>50</sub> and (SiC)<sub>12</sub> respectively. The free cluster properties are investigated by abundance and photoinduced dissociation mass spectroscopy. They are deposited in UHV conditions onto different substrates. Films of about 100 nm thickness are produced and analyzed by several techniques including Raman (RS) and X-Ray photoemission (XPS) spectroscopies. Morphologies are deduced from diffraction and microscopy techniques. Because of the strong

reactivity towards oxygen, XPS is performed in situ while RS is performed ex situ after film coating (2). Let us emphasize that the stoichiometry of the film is entirely governed by the initial rod one. In our case, we have obtained an equimolar Si-C amorphous alloy. We focus on electronic (e-DOS) and phonon densities of states (p-DOS). The e-DOS is deduced from the XPS spectrum near the Fermi level after several corrections such as atomic-like cross sections and inelastic scattering. The p-DOS is given by the first order Raman spectroscopy since the lack of medium and long range order induces the breakdown of the selection rules. The Raman spectrum differs from the p-DOS by the modulation of the Raman tensor efficiency which depends on the frequency and the type of atoms or bonds.

## RESULTS

As mentioned above, the film properties are governed by the free cluster property itself. We have deposited Si clusters in the range 20-100 atoms where we expect a nearly  $sp^3$  configuration with a lot of pentagonal rings (3,4). The small SiC cluster shapes (20-100 atoms) are rather poor resolved. In order to obtain some information, we have studied in the free phase the dissociation channels after photoinduced dissociation (5). No clear magic size is detected but rather the main effects of a lower binding energy of silicon as compared to carbon atoms. This one reveals cautiously a trend to phase separation within the cluster. At the opposite, rich carbon compounds with respect on silicon reveal the formation of hetero-fullerenes (6) such as  $Si_2C_{58}$ . Si- and SiC-films have been observed in transmission electron microscopy and atomic field microscopy in tapping mode. In the case of silicon, one observes small supported grains having a size lower than 2 nm diameter. The film appears amorphous-like since the resolution of the microscope does not allow the observation of particles down to 0.5 nm diameter. For SiC-film, we observe small supported grains having 7 nm diameter greater than the expected free cluster size. Nevertheless, the inner structure of the supported grains does not reveal a short or medium range order. Therefore, we believe that the observed particles are formed by the coalescence of the free clusters on the substrate without merging.

### *Electronic DOS*

The valence band (VB) obtained for Si- film is given in the figure 1(a) (left side). For comparison, we give the e-DOS of diamond (c) and clathrate (b). The clathrate-crystal (7) is constituted by the periodic arrangement of Si-fullerenes ( $Si_{28}$ ) having at least 87 % of five-membered rings while the diamond is formed by even-membered rings. The s-like, p-like and  $sp$ -like characters have been assigned through the theoretical VB spectra obtained by first principles calculations for both diamond and clathrate phases. We observe clearly the merging between the s-like and  $sp$ -like bands in the Si-cluster assembled films (a). In both crystals (b,c), the p-like bands are unchanged while the s-like and  $sp$ -like bands are not at the same position. Therefore, the presence of a large number of odd-membered rings in our films induces the filling of the valley between s-like and  $sp$ -like bands which are not merged in both crystals. For SiC, we observe (fig.1 right side) the lack of the ionic sub band gap without merging effect between s-like and  $sp$ -like bands. The positions and the characters of each band have been deduced from the theoretical valence band spectrum using a tight binding model. Such behavior is rather attributed to a large mixing of C-C, Si-Si and Si-C bonds with several coordinations rather than the presence of five-membered rings like in silicon. We believe that

the odd-membered rings destroy the chemical order between C and Si atoms and destabilize the network. Such result agrees with the theoretical model of Finocchi et al.(8).

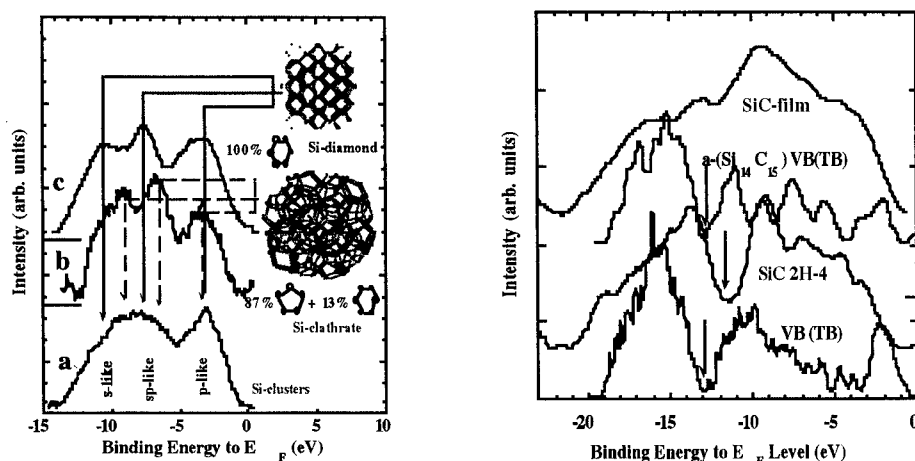


Figure 1: (left) Valence band spectra of Si-film (a) compared to those of diamond (c) and clathrate (b). The arrows show the expected bands (full line: diamond, dashed line: clathrate). (Right) Valence band spectra of SiC-film compared to the SiC crystal (SiC 2H-4). The theoretical Valence bands in Tight Binding scheme for crystal (labeled VB(TB)) and small cluster  $Si_{14}C_{15}$  (labeled a-  $Si_{14}C_{15}$  VB(TB)) are shown. The arrows show the ionic subband gap.

#### Dynamic properties: Raman spectroscopy

The first order Raman spectrum of Si-film is shown in figure (2) (left side). This spectrum is close to a-Si produced by ion implantation. By analogy with the crystalline phases (diamond and clathrate), we attribute three contributions in this spectrum (arrows) corresponding to the well-known TA, LA-LO and TO branches. Because of the selection rules, we are not able to obtain the whole p-DOS in both crystals. For comparison, we have studied by neutron inelastic scattering, the complete p-DOS of both diamond and clathrate phases since in such method the selection rules are broken. The positions of the three bands depend on the ring parity and can be used to probe our sample. It seems that the Si-film is intermediate between both crystals p-DOS which agrees with the e-DOS measurements. Let us remember that the quantitative disorder (distribution of angles and distances around the  $sp^3$  tetrahedral) induces a broadening of the bands without changes drastically their positions. This is the same effect than observed in the e-DOS where the s-like and p-like merging is attributed to a filling of the valley by new states rather than a broadening effect. The typical Raman spectrum of the SiC cluster film is shown in figure 2 (right side). The Raman spectrum is close to those observed in other amorphous structures (9) and can be modeled by three components rich clusters in silicon ( $100-500\text{ cm}^{-1}$ ), in carbon ( $1100-1600\text{ cm}^{-1}$ ) and stoichiometric SiC compounds ( $600-1100\text{ cm}^{-1}$ ) respectively. For comparison, we present the Raman spectra of pure carbon (1) and silicon (9) clusters having a mean cluster size in the free phase close to our SiC free clusters. These clusters have been prepared in the same source with silicon and carbon rods. To guide the eye, we give the Raman peaks observed in our SiC crystal sample.

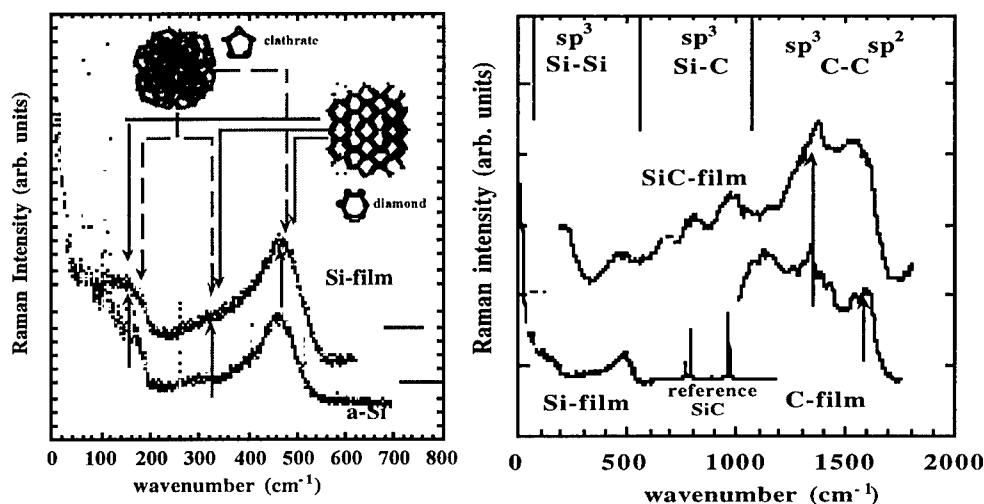


Figure 2: (Left) Raman spectra of Si-film compared to a-Si obtained by ion implantation. The upper arrows show the positions of the main bands in diamond (full) and clathrate (dashed). (Right) Raman spectra of SiC-film (upper) compared to pure C- and Si-films. The Raman peaks in SiC crystal are also shown.

## CONCLUSION

We have prepared Si- and SiC-assembled films by deposition of free clusters in nanometer size range. Both films appear amorphous-like with a large number of five-fold rings in Si-films. In the case of SiC-films we observe a complex structure with a partial lack of the chemical order.

## REFERENCES

- (1) Mélinon P., Paillard V., Dupuis V., Perez A., Jensen P., Hoareau A., Broyer M., Vialle J.L., Pellarin M., Baguenard B., Lerme J., Int. J. Mod. Phys. B, 1995, 9, 339.
- (2) Mélinon P., Kéghélian P., Prével B., Dupuis V., Perez A., Champagnon B., Guyot Y., Rousset J.L., Delichère P., J.Chem.Phys., 1998, 108, 4607.
- (3) Röthlisberger U., Andreoni W., Parinello M., Phys. Rev. Lett., 1994, 72, 665.
- (4) Ho K.M., Shvartsburg A.A., Bicaï Pan Lu Z.Y., Wang C.Z., Wacker J.G., Fye J.L., Jarrold M.F., Nature (London), 1998, 392, 582.
- (5) Pellarin M., Ray C., Mélinon P., Lermé J., Vialle J.L., Kéghélian P., Perez A., Broyer M., Chem. Phys. Lett., 1997, 277, 96.
- (6) Ray C., Pellarin M., Lermé J., Vialle J.L., Broyer M., Blase X., Mélinon P., Kéghélian P., Perez A., Phys. Rev. Lett., 1998, 80, 5365.
- (7) Rény E., Ménétrier M., Cros C., Pouchard M., Sénégas J., C.R. Acad. Sci. Paris, 1998, 1, Série II, 129 and references therein.
- (8) Finocchi F., Galli G., Parinello M., Bertoni C.M., Phys. Rev. Lett., 1992, 68, 3044.
- (9) Chehaidar A., Carles R., Zwick A., Meunier C., Cros B., Durand J., J. of Non-Crystalline Solids, 1994, 169, 37.





Pergamon

NanoStructured Materials, Vol. 12, pp. 281–286, 1999

Elsevier Science Ltd

© 1999 Acta Metallurgica Inc.

Printed in the USA. All rights reserved

0965-9773/99/\$—see front matter

PII S0965-9773(99)00117-8

## MOLECULAR DYNAMICS SIMULATION OF METAL CLUSTER COOLING AND HEATING IN NOBLE GAS ATMOSPHERE

Jan Westergren, Henrik Grönbeck, Arne Rosén and Sture Nordholm

Department of Experimental Physics and Department of Physical Chemistry

Chalmers University of Technology and Göteborg University, SE-412 96 Göteborg, Sweden

**ABSTRACT** -- Metal cluster properties such as ionization potential and reactivity strongly depend on the temperature of the cluster. Using molecular dynamics simulation we have investigated how much energy is transferred from noble gas atoms to unsupported  $\text{Pd}_{13}$  clusters in collisions. Furthermore we propose a two-term density of states for  $\text{Pd}_{13}$  which leads to excellent prediction of the caloric equation of state obtained in simulations. Knowing the heat capacity of the cluster, the energy transfer can be converted into change of cluster temperature per collision at constant gas temperature and the cooling and heating of the cluster can be predicted. The predictions were in good agreement with cooling and heating simulations. Approximately 2000 collisions are required to cool  $\text{Pd}_{13}$  from 1500 K to 100 K in a helium gas at 100 K. ©1999 Acta Metallurgica Inc.

### INTRODUCTION

In cluster experiments it has been observed that many properties depend on the internal cluster temperature. For instance, the ionization potential (1,2) and reactivity (3) show a strong dependence on the temperature. Unfortunately, there is not yet any method developed for a direct measurement of the temperature. However, experimental methods involving heat baths have been presented recently. Chandezon *et al.* (4) have studied the evaporation of sodium clusters at various temperatures utilizing a helium heat bath. Schmidt *et al.* (5) have used a heat bath to thermalize sodium clusters at various temperatures and they have then been able to plot the caloric equation of state, i.e. the energy as a function of the temperature, for sodium clusters.

It is often assumed that the clusters reach thermal equilibrium with the surrounding gas. With molecular dynamics (MD) simulations we have studied the cooling and heating processes of  $\text{Pd}_{13}$  in various noble gas atmospheres. In earlier work we have obtained the heat capacity for  $\text{Pd}_{13}$  at various temperatures (6) and energy transfer data in collisions between  $\text{Pd}_{13}$  and gas atoms for the temperature ranges of 100 K to 900 K for the gas and 100 K to 1700 K for the cluster (7,8). We found some general trends in the dependence of the energy transfer on e.g. interaction potentials between  $\text{Pd}_{13}$  and the gas atom. With approximations of constant cluster heat capacity, collision cross-section and efficiency in energy transfer, a rough estimation of the cooling/heating time can be made.

### SIMULATION DETAILS

We have studied the average energy transfer,  $\bar{\epsilon}$ , to a  $\text{Pd}_{13}$  cluster in collisions with a helium atom for various gas and cluster temperatures. The averages are based on 30,000 collisions. The speed of the gas atoms colliding with the cluster should be distributed according to a speed-weighted Maxwell-Boltzmann distribution (9):

$$f_v(v) = \frac{\mu^2}{2(k_b T_g)^2} v^3 \exp\left(-\frac{\mu v^2}{2k_b T_g}\right) \quad [1]$$

where  $\mu$  is the mass of the gas atoms,  $k_b$  is Boltzmann's constant and  $T_g$  is the temperature of the gas. The impact parameter,  $b$ , is also randomly generated for each collision. The interaction between the gas atom and the cluster never vanishes but it becomes insignificant for large  $b$ . We say that a collision has occurred when a gas atom has passed the cluster with an impact parameter less than  $b_{max}$ , where  $b_{max}$  should be chosen so that no significant energy transfer occurs for  $b > b_{max}$ . The distribution of  $b$  should be  $f_b(b) = 2b/b_{max}^2$ ,  $0 \leq b \leq b_{max}$ .

It is important to note that the average energy transfer depends on the choice of  $b_{max}$ . However, the quantity  $\bar{\epsilon} \cdot b_{max}^2$  is independent of  $b_{max}$ , provided that trajectories with  $b > b_{max}$  would give insignificant energy transfer. In the results, the energy transfer is given as a normalized quantity:

$$\bar{\epsilon}_{norm} = \bar{\epsilon} \cdot \left(\frac{b_{max}}{b_0}\right)^2 \quad [2]$$

where  $b_0$  is an arbitrary distance which we have set to 6.5 Å. Moreover, the number of collisions a cluster experiences per second,  $z$ , increases with  $b_{max}$  and the energy transfer *per second* is  $b_{max}$ -independent (9):

$$\bar{\epsilon}(\text{per second}) = z \cdot \bar{\epsilon} = \left(p_g \sqrt{\frac{8\pi}{mk_b T_g}} \cdot b_{max}^2\right) \cdot \bar{\epsilon} \quad [3]$$

where  $p_g$  is the gas pressure.

For the analysis we have related the energy transfer in the simulated collisions to the optimal energy transfer. As a model for the optimal transfer, the *ergodic collision theory* (ECT) has been employed (10). In the ECT, the colliding species are considered to be in microcanonical equilibrium after the collision. Under the approximation that we can use a thermal analysis on a microcanonical system, the microcanonical equilibrium may be stated as

$$E_{\text{Pd}_{13}}(T_c) + \frac{3}{2} k_b T_g = E_{\text{Pd}_{13}}(T'_c) + \frac{3}{2} k_b T'_c \quad [4]$$

where  $T'_c$  is the common temperature of the species after the collision. Substituting  $\Delta E_{\text{Pd}_{13}} \approx C_{\text{Pd}_{13}} \cdot \Delta T_c$  into Eq. 4, the optimal energy transfer may be expressed as (8)

$$\langle \Delta E \rangle_{ECT} \equiv E_{Pd_{13}}(T_c) - E_{Pd_{13}}(T_g) \approx \frac{1}{\frac{1}{C_{Pd_{13}}(T_c)} + \frac{2}{3k_b}} (T_c - T_g) \quad [5]$$

where  $C$  is the heat capacity. Note that in the ECT, the energy transfer is *from* the cluster. As a measure of the energy transfer efficiency in the simulated collisions we use an efficiency factor (8):

$$\beta_E = \frac{-\bar{\epsilon}_{norm}}{\langle \Delta E \rangle_{ECT}} \cdot \frac{b_0^2}{(\min b_{max})^2} \quad [6]$$

where  $\min b_{max}$  is the minimal possible choice of  $b_{max}$ , which however provides for estimations.  $\min b_{max}$  is what the simulations propose to be a 'realistic' collision cross-section.

We have used a Many-Body Alloy potential for the interaction between the metal atoms and the Lennard-Jones potential for the interaction between one metal atom and the gas atoms. (See (7,8) for a more detailed description of the simulations.)

## ENERGY TRANSFER RESULTS

In Fig. 1a,b the average energy transfer and the energy transfer efficiency, respectively, versus the temperature of  $Pd_{13}$ , are plotted for various helium temperatures. Except for low gas temperatures, there is a clear jump in the efficiency at about  $T_c = 950$  K, which is within the temperature interval where the cluster melts. However, the efficiency is fairly independent of cluster temperature as long as the cluster does not change phase. Moreover, we note that the efficiency increases with decreasing gas temperature.

## HEAT CAPACITY

Besides  $\bar{\epsilon}$  or  $\beta_E$  data for various  $T_g$  and  $T_c$ , the prediction of the cooling and heating of a cluster in a noble gas atmosphere requires the heat capacity of the cluster in the temperature interval of the cooling/heating. In molecular dynamics simulations with a Nosé-Hoover thermostat, the caloric equation of state for  $Pd_{13}$  was obtained (6). (See Fig. 2a.) The rings show the total energy versus temperature.

The heat capacity is closely related to the classical density of states of the cluster which we model as a two-term function:

$$\rho(E) = X \left( (E - E_0)^{n_1} + k_2 (E - E_0)^{n_2} \right) \quad [7]$$

where  $X$ ,  $n_1$ ,  $n_2$ ,  $E_0$  and  $k_2$  are parameters. The two terms may be interpreted as two separated energy minima in the phase space, the first corresponding to a solid cluster structure and the second to a molten cluster structure. For a canonical system the total energy may be obtained from the Boltzmann distribution as

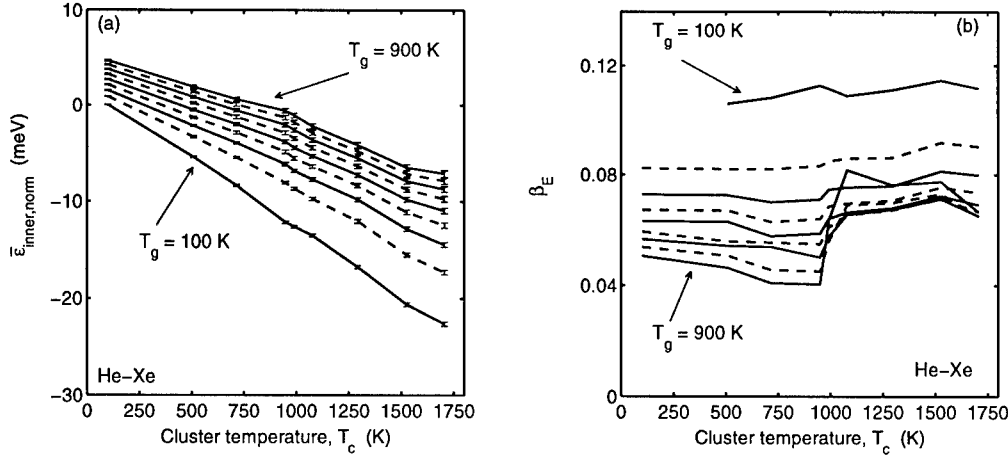


FIG 1a. The average energy transfer in collisions between  $\text{Pd}_{13}$  and helium atoms. The gas temperature is from the top 900 K, 800 K, ..., 100 K.

FIG 1b. The energy transfer efficiency of the collisions in Fig. 1a calculated with Eq. 6. The gas temperature is from the bottom on the left 900 K, 800 K, ..., 100 K.

$$\langle E \rangle = \frac{\int_{E_0}^{\infty} E \cdot \rho(E) e^{-E/k_b T} dE}{\int_{E_0}^{\infty} \rho(E) e^{-E/k_b T} dE} = E_0 + k_b T \frac{n_1 + 1 + k_2 (k_b T)^{n_2 - n_1} \frac{\Gamma(n_2 + 2)}{\Gamma(n_1 + 1)}}{1 + k_2 (k_b T)^{n_2 - n_1} \frac{\Gamma(n_2 + 1)}{\Gamma(n_1 + 1)}} \quad [8]$$

The best fit of the expression in Eq. 8 to simulation data (rings in Fig. 2a) is obtained for  $n_1 = 45.3$ ,  $n_2 = 61.0$ ,  $E_0 = -34.8$  eV and  $k_2 = 1.35 \cdot 10^{-10}$ .  $X$  is not determinable. With these parameters the solid curve in Fig. 2a results. The agreement is excellent. Knowing the caloric equation of state, the heat capacities may be calculated since  $C = d\langle E \rangle / dT$ . In Fig. 2b the heat capacity is illustrated. The solid line is the numerical derivative of simulation data and the dashed one is derived from Eq. 8.

### COOLING AND HEATING

The cooling and heating of a cluster in a gas atmosphere at constant temperature  $T_g$  we predict with a difference equation:

$$T_c(m+1) = T_c(m) - \frac{\beta_E}{1 + \frac{2C_{\text{Pd}_{13}}(T_c(m))}{3k_b}} (T_c(m) - T_g) \cdot \frac{(\min b_{\max})^2}{b_{\max}^2} \quad [9]$$

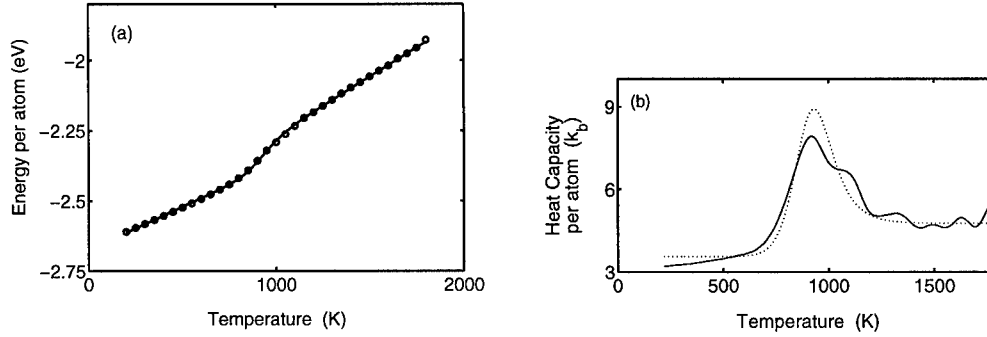


FIG 2a. The total energy of  $\text{Pd}_{13}$  versus the temperature. The rings are from simulations and the dotted line is given by Eq. 8.

FIG 2b. The heat capacity of  $\text{Pd}_{13}$  versus the temperature. The solid line is the numerical derivative of the simulations data in Fig 2a. The dotted line is derived from Eq. 8.

where  $T_c(m)$  is the cluster temperature after  $m$  collisions. In Fig. 3a the cooling of  $\text{Pd}_{13}$  from 1500 K in a helium gas at 100 K is predicted as the solid line. The prediction is based on interpolations of  $\beta_E$  in Fig. 1b and the heat capacity data in Fig. 2b. In order to test this prediction, we simulated the cooling of the cluster with MD simulations. The dots in Fig. 3a are temperature averages based on three cooling simulations. The agreement is good. In Fig. 3b heating of  $\text{Pd}_{13}$  in helium at 500 K and 900 K respectively is predicted (solid lines). The dots for the heating to 900 K are based on three simulations but the agreement with the predicted heating is not as good as for cooling. The larger fluctuations of the warm cluster is partly due to that we have used the kinetic energy of an individual cluster to calculate the temperature. The kinetic energy of an individual cluster in a canonical ensemble at  $T_c$  is distributed and the variance increases with the temperature which therefore implies higher 'temperature' fluctuations at 900 K than when cooling the cluster to 100 K. Calculations in analogy with Eq. 8, using the fact that the density of states for the internal kinetic energy of a cluster with  $N$  atoms is given by  $\rho(E_{kin}) \propto E_{kin}^{-(3N-5)/2}$  (11), the standard deviation of the kinetic energy may be obtained as

$$\sigma = T_c \sqrt{2/(3N-3)}. \quad [10]$$

For  $\text{Pd}_{13}$  at  $T_c = 100$  K,  $\sigma = 25$  K and at  $T_c = 900$  K,  $\sigma = 210$  K. The dots representing the heating to 500 K are based on ten simulations and show much smaller fluctuations.

If the heat capacity,  $\beta_E$  and  $\min b_{max}$  may be considered constant within a cluster temperature interval, the time required to cool or heat the cluster is given by

$$t_{cooling} = \frac{1 + \frac{2C_{cluster}}{3k_b}}{\beta_E p_g \sqrt{\frac{8\pi}{mk_b T_g}} \cdot (\min b_{max})^2} \cdot \ln \frac{\Delta T_{initial}}{\Delta T_{equilibrium}} \quad [11]$$

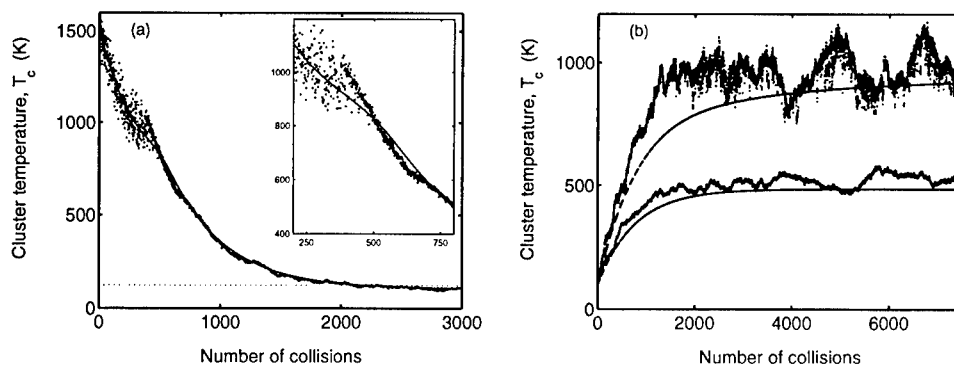


FIG 3a. The temperature under cooling of Pd<sub>13</sub> in a helium atmosphere at 100 K. The solid line is predicted using Eq. 9, the dots are from simulations.

FIG 3b. The temperature under heating of Pd<sub>13</sub> in a helium atmosphere at 500 K (lower curve) and 900 K, respectively. The solid lines are predicted using Eq. 9, the dots are from simulations.

where  $\Delta T_{initial}$  is the initial temperature difference between the gas and the metal cluster. In Eq. 11 the cluster temperature never reaches the gas temperature. Hence, we have to set a temperature difference  $\Delta T_{equilibrium}$  at which we regard the clusters being in thermal equilibrium with the gas. A first estimation could be to use the standard deviation of the kinetic energy, i.e.  $\Delta T_{equilibrium} = 25$  K for Pd<sub>13</sub> when  $T_g = 100$  K. However, a specific cluster property may be very temperature sensitive and smaller  $\Delta T_{equilibrium}$  may be used when the temperature dependence is better known. For instance, the evaporation spectrum of sodium clusters shows clear differences when the temperature is raised from 42°C to 62°C (Ref. 4).

## REFERENCES

1. Homer, M., Persson, J.L., Honea, E.C. and Whetten, R.L., Z. Phys. D, **22**, 441, 1991
2. Kappes, M., Schär, M., Röthlischer, U., Yeretzian, C. and Schumacher, E., Phys. Rev. Lett., **143**, 251, 1988
3. Holmgren, L., Andersson, M. and Rosén, A., J. Chem. Phys., **109**, 3232, 1998
4. Chandezon, F., Hansen, P., Ristori, C., Pedersen, J., Westergaard, J. and Bjørnholm, S., Chem. Phys. Lett., **277**, 450, 1997
5. Schmidt, M., Kusche, R., Kronmüller, W., von Issendorff, B. and Haberland, H., Phys. Rev. Lett., **79**, 99, 1997
6. Grönbeck, H., Tománek, D., Kim, S.G. and Rosén, A., Chem. Phys. Lett., **264**, 40, 1997
7. Westergren, J., Grönbeck, H., Kim, S.G. and Tománek, D., J. Chem. Phys., **107**, 3071, 1997
8. Westergren, J., Grönbeck, H., Rosén, A. and Nordholm, S., J. Chem. Phys., **109**, 9848, 1998
9. Derived from Atkins, P. W., *Physical Chemistry*, Oxford Univ. Press, 1987, pp 649,653
10. Nordholm, S., Freasier, B. and Jolly, D., Chem. Phys., **25**, 433, 1977
11. See e.g. Westergren, J. *Thesis at Chalmers University of Technology*, Göteborg, 1998



## DEPOSITED NANO-METRE SIZED IRON CLUSTERS

C. Johansson<sup>a</sup>, T. Åklint<sup>a</sup>, M. Hanson<sup>a</sup>, M. Andersson<sup>a</sup>, N. Tarras-Wahlberg<sup>a</sup>,  
E. Olsson<sup>b</sup>, B. Kalska<sup>b</sup>, R. Wäppling<sup>b</sup> and A. Rosén<sup>a</sup>

<sup>a</sup> Department of Experimental Physics, Chalmers University of Technology and  
Göteborg University, S-412 96 Göteborg, Sweden.

<sup>b</sup> The Ångström Laboratory, Uppsala University, S-751 21 Uppsala, Sweden.

**Abstract** — We have produced films of iron clusters in a laser vaporization source. The iron clusters were deposited on glass microslides and graphite substrates. The films were analyzed with transmission electron microscopy (TEM), Mössbauer spectroscopy, magnetic measurements and atomic force microscopy (AFM). The TEM results show that the sizes of the deposited iron clusters are in the range from 2 nm to about 10 nm. From Mössbauer measurements we found that the particles undergo fast superparamagnetic relaxation at room temperature and become thermally blocked at lower temperatures. From hysteresis loops we obtained that the saturation magnetization of the films was in the range of bulk  $\alpha$ -iron and the coercivity and remanence increase with decreasing temperature, typical for a system of mono-domain particles with a size distribution. The results from the AFM yield a cluster size in the same range as determined by TEM. ©1999 Acta Metallurgica Inc.

## INTRODUCTION

Mono-domain magnetic particles are of great interest due to the capability of using them in memory devices with a high packing density (1) and as model systems for studying fundamental magnetic properties (2). It is known that particles smaller than a critical size of about 20 nm become single magnetic domains (3). When decreasing the particle size or raising the temperature the particles may become superparamagnetic (4), i.e. the orientation of the magnetization fluctuates fast compared to the measuring time which is used to study the particles. When using mono-domain particles in memory devices, the particle sizes must be between the critical mono-domain size and the size for fast superparamagnetic relaxation. Thus, it is important to study the fundamental magnetic properties of small magnetic particles. Small magnetic particles can be manufactured with different methods, e.g. by chemical precipitation techniques. An interesting new method is to deposit clusters on different kinds of substrates (5,6). The questions that arise when manufacturing mono-domain particles are how the particle sizes and the magnetic properties of the particles are correlated to the manufacturing parameters in the process, in this case the cluster production parameters. In order to gain further understanding of this kind of questions we have started a new project using a recently developed laser vaporization cluster source. In this paper we will present some preliminary results of clusters containing ordinary iron and <sup>57</sup>Fe deposited on glass microslides and highly oriented pyrolytic graphite substrates (HOPG).

## EXPERIMENTAL

The clusters were produced in a new manufactured laser vaporization cluster source (6). The experimental setup for the cluster production is shown in fig. 1. A pulsed laser beam is focused on the target surface and generates a hot plasma.

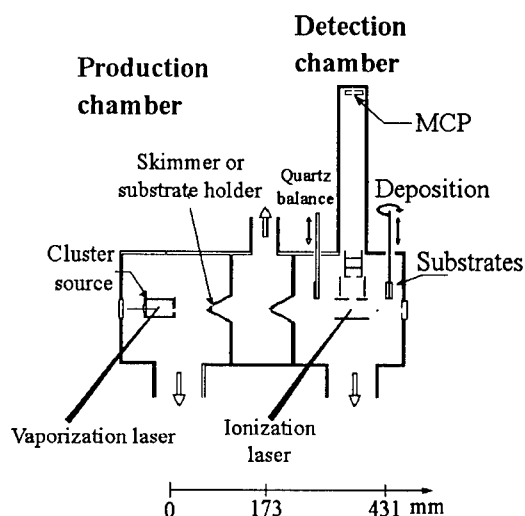


Fig. 1 The experimental setup for the production of the clusters.

The vaporized atoms are transported in a continuous flow of 30 mbar He gas at 30 mbar and condense into clusters. The cluster beam expands through a flat nozzle into the production chamber with a background pressure of  $10^{-2}$  mbar. The substrates can be placed either just after the cluster source or at the end of the detection chamber. The detection chamber is equipped with a time of flight mass spectrometer to monitor the size distribution and a quartz balance. In these studies we have placed the substrates just after the cluster source. Deposition during 5-20 minutes gave cluster films with a mean thickness from about 50 nm to 200 nm.

In order to characterize the cluster films we used transmission electron microscopy (TEM), Mössbauer spectroscopy, magnetic measurements and atomic force microscopy (AFM). The TEM samples were obtained by depositing ordinary iron and  $^{57}\text{Fe}$  on Cu-grids covered with graphite. The Mössbauer samples contained deposited  $^{57}\text{Fe}$  on HOPG substrates with a film thickness of about 200 nm. Mössbauer spectra were recorded in the temperature range from 295 K down to 4 K in zero field. The samples for the magnetic measurements contained ordinary iron and  $^{57}\text{Fe}$  on both glass microslides and HOPG substrates. The thickness of the cluster films in this case was in the range from 50-150 nm. Measurements were carried out in the field range  $\pm 2$  T and at temperatures from 295 K down to 10 K. The films prepared for the magnetic measurements were also used for the characterization of cluster sizes with the AFM in the tapping mode.



## RESULTS AND DISCUSSION

The analysis of the TEM images yielded that the particles are ellipsoidal in shape and have sizes in the range from 2 nm to 10 nm. In fig. 2 Mössbauer spectra of deposited  $^{57}\text{Fe}$  at 295 K and 4 K can be seen. The spectra revealed the presence of the characteristic sextet of  $\alpha$ -iron constituting about 1/3 of the signal and a closely related satellite at 10% intensity plus a "non-magnetic" component. The temperature dependence of the spectra show the typical behavior of magnetic mono-domain particles that, to a major (the "non-magnetic") part, are superparamagnetic at 295 K and becomes thermally blocked at lower temperatures. The hyperfine field vs. temperature dependence indicates a distribution in grain sizes and from the spectra it is possible to conclude that the film contains about 50 % iron oxides or oxide hydroxides. Comparing with literature data a preliminary assignment to predominance of  $\beta$ -FeOOH is made.

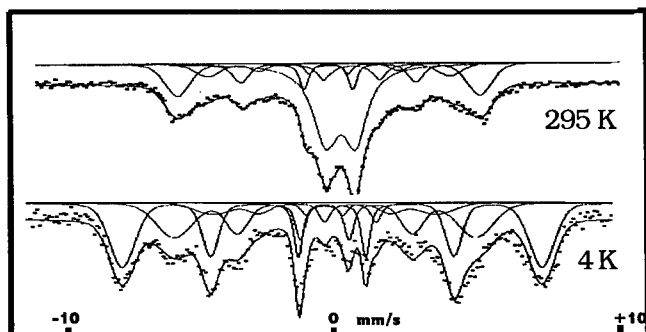


Fig. 2 Mössbauer spectra of deposited  $^{57}\text{Fe}$  on HOPG substrate at 295 K and 4 K.

In fig. 3a a hysteresis loop can be seen at 30 K for  $^{57}\text{Fe}$  iron deposited on HOPG substrate and in fig. 3b the temperature dependence of the coercivity,  $B_C$ , and remanence,  $M_r$  is shown. The saturation magnetization is almost the same as for  $\alpha$ -Fe. The increase of  $B_C$  and  $M_r$  when decreasing the temperature is a typical behaviour of mono-domain particles that become thermally blocked at low temperatures. In our earlier measurements of deposited ordinary iron on microslides (6) we found that  $B_C$  and  $M_r$  varied in a wider temperature range, probably due to a wider distribution of cluster sizes. Thus the distribution of cluster sizes depends on the used substrate.

The pictures from the AFM measurements show that the deposited films contain clusters with sizes of about 7 nm, i.e. the same as the TEM results. From the AFM pictures it is also possible to see that the surface of the films is rough due to individual clusters and agglomerates of clusters. The mean size of the agglomerates is about 50 nm. We will continue these promising preliminary studies by varying the substrate temperature, deposition rate and the cluster material e.g. Ni and Co.

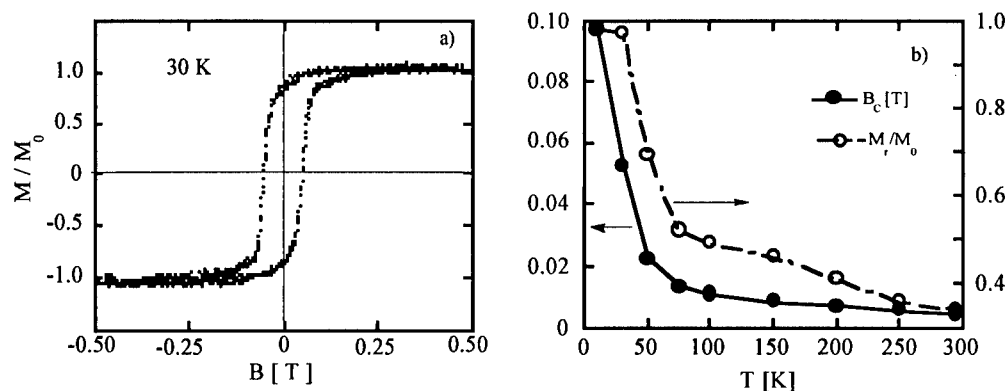


Fig. 3 a) Hysteresis loop at 30 K for  $^{57}\text{Fe}$  iron deposited on HOPG substrates.  $M_0$  is the magnetization at 0.5 T. b) The temperature dependence of  $B_c$  and  $M_r$ . The lines in fig. 3b are just guides for the eye.

#### Acknowledgements

We gratefully acknowledge financial support from Knut and Alice Wallenberg's foundation, as well as funding by the Swedish Natural Science Research Council, NFR, and the National Swedish Board for Technical Development, NUTEK, through the Interdisciplinary Materials Research Consortia.

#### References

1. A. E. Berkowitz, J. R. Mitchell, M. J. Carey, A. P. Young, S. Zhang, F. E. Spada, F. T. Parker, A. Hutten, and G. Thomas, Phys. Rev. Lett. **68** 3749 1992.
2. C. Johansson, M. Hanson, M. S. Pedersen, and S. Mørup, J. Magn. Magn. Mat. **173** 5 1997.
3. B. D. Cullity, Introduction to Magnetic Materials, Addison-Wesley Publishing Company 1972.
4. C. P. Bean and J. D. Livingston, J. Appl. Phys. **30** 120S 1959.
5. J. P. Perez, V. Dupuis, J. Tuaillon, A. Perez, V. Paillard, P. Melinon, M. Treilleux, L. Thomas, B. Barbara, B. Bouchet-Fabre, J. Magn. Magn. Mat. **145** 74 1995.
6. T. Åklint, C. Johansson, M. Hanson, E. Olsson, F. Gustavsson, R. Wäppling and A. Rosén. Journal of Applied Organometallic Chemistry **12** 1 1998.



Pergamon

NanoStructured Materials, Vol. 12, pp. 291–294, 1999

Elsevier Science Ltd

© 1999 Acta Metallurgica Inc.

Printed in the USA. All rights reserved

0965-9773/99/\$—see front matter

PII S0965-9773(99)00119-1

## POLYMER-IMMOBILIZED NANOSCALE AND CLUSTER METAL PARTICLES

A.D.Pomogailo

Institute of Chemical Physics in Chernogolovka, Russian Academy of Sciences,  
142432 Chernogolovka, Moscow Region, Russian Federation

**Abstract** *The essential data on the immobilization of nanoscale and cluster metal particles in polymeric matrices are considered and systematized for both macroligands and the matrices formed in situ. Special attention is paid to the controlled chemical passivation (stabilization) of extremely active particles of colloidal size using high - molecular - weight compounds. The routes of formation of polymer - immobilized nanoparticles directly in the polymer medium are analysed. This allows the preparation of compositions characterized not only by the most regular distribution of these particles over the bulk of polymer but also by a strong chemical interaction between the components. Studies in the field of polymer-analogous transformations, which offer a promising approach to the binding of mono- and heterometallic clusters as a new direction in the physicochemistry of nanoparticles, are discussed. The basic fields of the application of the products obtained and the prospects of the development of this direction are outlined. ©1999 Acta Metallurgica Inc.*

### INTRODUCTION

The possibility of combining the physicochemical properties of metals and polymers in a single material and of regulating these properties through concentrational changes has long been under discussion. The progress in this direction is stimulated by the ever-growing interest in this problem shown in many fields of chemistry, physics, and materials science. Two major stages may be differentiated in the development of this direction. At the beginning, major attention has been given to the synthesis of ultrasmall metal particles of nanometre size, their improvement, and bringing into practical usage. The second stage of studies in this field focused on the development of effective methods for the stabilization of metal nanoparticles with the help of polymers.

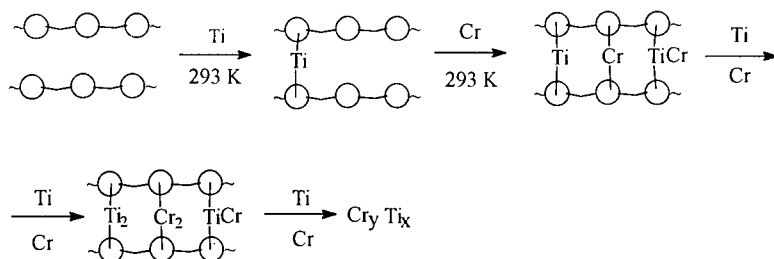
These studies were largely advanced by the development of metal-polymer composite materials possessing specific physicochemical and mechanical properties. The spectrum of practical uses of these materials has been expanded by the discovery of their specific catalytic properties (1), which display close similarity to those of polymer-immobilized catalysts (2,3), by their application in chemisorptional and photographic processes, *etc.* The nanoparticles of certain metals are endowed with biological activity. At present the data on the structure and properties of polymer-immobilized nanoparticles stand in need of the systematisation.

## DISCUSSION

The adhesion between polymers and metals is determined by a number of factors, among which the most essential are the nature of the molecular forces, surface defects, internal strain, and electrical charges. They are best described within the framework of the theory of 'molecular solder' based on the concept of structural-mechanical factors of the stability of dispersion systems and spatial networks of the coagulation structure type (4). There are two basically different modes of the matrix isolation of nanoparticles. The first one is the most usual and consists in mere addition of a suspended or solubilised polymeric stabiliser to a prepared dispersion of particles. There are other versions of this technique including mixing of metal powders with latexes. Latex is mixed with the metal phase particles having a size smaller than that of latex particles (100 and 700 nm, respectively) and, after the stabilisation of the resultant mixture, the dispersive medium is removed. Then the coagulates are heated and moulded to produce samples of metal polymers. The second approach is based on the preparation of dispersions in the presence of a stabiliser or in the production of a stabiliser from its precursor in the presence of a prepared dispersion of nanoparticles. A widespread version of this method is the formation of nanoparticles in a polymeric medium. This makes it possible to prepare compositions in which the mixing occurs prior to the resin solidification. The materials produced are remarkable not only for the most uniform distribution of metal particles over the polymer bulk but also for strong chemical interaction of the metal with the polymer.

### *Typical formation processes of nanometric particles in polymers*

*Technique of the atomic metal evaporation.* The most attractive, from the technological viewpoint, are the methods of cryochemical deposition (most frequently, vacuum deposition at pressures of  $10^{-1}$ - $10^{-4}$  Pa) of atomic (gaseous) metal on thin ( $\sim 1000$  nm) polymeric supports. The latter are usually high-molecular weight paraffins, polyesters, oligo- and polyolefins, polydienes, vinyl- and phenyl-siloxane polymers. The metal atoms are first deposited at temperatures of 77K and above (5). Then, the stabilisation of small clusters stable at low temperatures is carried out. The cryochemical method allows the preparation of both homo- and heterometallic polymer-immobilised cluster particles. Thus the consecutive or simultaneous deposition of vapour of different metals, e.g., Mo and Ti or Ti and Cr, especially at high concentrations, yields to the non-solvated bimetallic clusters which are close in size to the colloidal particles or to small clusters (the cluster  $\text{Mo}_x\text{Ti}_y$  includes 13 atoms):



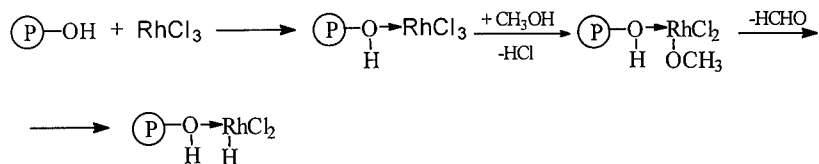
*Preparation of polymer-immobilized nanoparticles by polymerization in plasma .*

Polymerisation in plasma is initiated by ions, excited molecules, and protons with sufficiently high energy. The role of polymer-forming substances is played by relatively simple compounds ( $\text{CH}_4$ ,  $\text{CF}_4$ , benzene, chlorobenzene). This technique is well-suited for the preparation of microencapsulated nanoparticles (the so-called metal-doped polymeric films). Thin composite films are formed under the conditions of simultaneous polymerisation of corresponding compounds and vacuum evaporation of metals. Various modifications of this method (3 and refs there) have been reported that differ basically in the mode of preparation and introduction of nanoparticles. Metallopolymers with the formal composition  $(\text{C}_3\text{F}_4\text{O}_{0.6}\text{Mo}_{0.3})_n$  and  $(\text{C}_3\text{F}_3.9\text{O}_{0.3}\text{Cu}_{0.3})_m$  have been prepared and characterised (6). The polymerisation in a glow discharge makes it possible to produce thin polymeric films of controlled size on the surface of nanoparticles prepared *in situ*.

*Preparation of metal sols in polymers by the thermal decompositions of precursor compounds.* Heating of volatile metal compounds (primarily, carbonyls,  $\pi$ -allylic complexes, formates, acetates, and organometallic compounds) in organic media or in gas phase to leads to their degradation with the liberation of metals or their oxides in the form of dispersed phase. If these reactions are carried out in the presence of polymers, it is the simplest and the apparently the most widespread method for the introduction of large (sometimes up to 90 mass %) quantities of colloidal particles. Thus, the stable homogeneous polymer-immobilised dispersions of colloidal particles of Fe, Co, Cr, Mo, W, Re, Mn, Ni, Pd, Pt, Ru, Rh, Os, and Ir can be produced using the thermal decompositions of their precursor compounds (7,8).

*Reductive methods in the synthesis of polymer-immobilised nanoparticles.* The reductive methods appear to be most common techniques for the preparation of polymer-immobilised nanoparticles. They may be divided into two types different in principle. The first type, or the 'impregnation' method consists in the chemical reduction of metals from solutions or suspensions of their salts or radiation-chemical reduction in the presence of macroligands. The second type resides on the reduction of mononuclear metal complexes chemically bound with polymers. The first method is more widely applied because it meets better the needs of catalysis. In particular, metal blacks, ultradispersed powders, *etc.* are prepared thereby. For example, Raney nickel is stabilised by incorporating it into the silicone rubber (9).

The mechanism underlying the reduction of metal ions chemically bound with polymers is rather complex (3 and refs. there). For example, when a solution of  $\text{RhCl}_3$  is boiled in the presence of PVA, several chemical transformations take place:



These reactions lead to a homogeneous colloid resulting from the disproportionation of rhodium hydrides and subsequent growth of particles. The 13-nuclear clusters formed have the structure of a face centred lattice. The clusters are 4 nm in diameter. They interact with the protective polymer owing to electrostatic attraction or to physical adsorption, and possibly to the formation of coordination bonds.

There are other methods for the preparation of polymer immobilized nanoparticles. Among of them one can indicate electrochemical methods, the ways including simultaneous formation of the polymer matrix and nanoparticles, polymer-analogous transformations in the immobilisation of metal clusters.

### CONCLUSION

Among theoretical problems of the formation of clusters and nanoparticles, the most topical seem to be the questions of structural-morphological and spatial organisation of these systems at the local, molecular, and supramolecular levels, including thermodynamic peculiarities of their formation. The most important problem seems to be the stabilisation of nanoparticles by monolayers of polymers and Langmuir-Blodgett films.

One may expect further progress in the development of novel methods for the preparation of polymer-immobilised nanoparticles. A promising direct synthesis of these products appears to be the dissolution of zerovalent metals in solutions of polymers that function as macroligands with subsequent recrystallisation of particles. The polymer-immobilized nanoparticles are already used to solve specific technological problems associated with the surface modification: its metallisation, the imparting of antistatic and magnetic properties to it, design of new materials for photo- and cinematography, *etc.* Many of these principles are employed in the rapidly developing field known as nanotechnology (10, 11) and are likely to form the basis of a new branch of science which may be defined as chemistry of highly organised compounds, including supramolecular chemistry.

### REFERENCES

1. *Metal clusters in catalysis*. (Eds. B.C.Gates, L.Guczi, H.Knosinger). Elsevier, Amsterdam, 1986; *Clusters and Colloids*. (Ed. G.Schmid). VCH.Weinheim, 1994.
2. Pomogailo, A.D., *Kataliz Immobilizovannymi Kompleksami* (Catalysis by Immobilized Complexes), Nauka, Moscow, 1991
3. Pomogailo, A.D., *Russ.Chem.Rev.*, 1997, **66**, 679
4. Rebinder, P.A., *Izbranyye Trudy. Poverkhnostnye Yavleniya v Dispersnykh Sredakh* (Selected Works. Surface Phenomena in Dispersion Media), Nauka, Moscow, 1978
5. Moscovits, M., Ozin, G.A., *Cryochemistry*, Wiley-Interscience, New York, 1979
6. Yasuda, H., *Plasma Polymerisation*, Academic Press, Orlando, 1985
7. Smith, T.W., Wychick, D., *J. Phys. Chem.* 1980, **84**, 1621
8. US P.4 252 671 - US P.4 252 678 (1981)
9. Tai, A., Imachi, Y., Harada, T., Izumi, Y., *Chem.Lett.*, 1981, **11**, 1651.
10. *Nanotechnology. Molecularly Designed Materials*. Eds. G.-M.Chow, K.E.Gonsalves.Am.Chem.Soc.Washington.1996.
11. Wollenberger, H., (ed.), *Abstracts Meeting International Conference on Electronic Materials (ICEM-96). Symposium V. Nanophase and Nanocomposite Materials* December 2-5,1996, Boston,Massachusetts. Proceedings published as Volume 457 of the Materials Research Society Symposium Proceeding Series.Washington.1996



## POLARIZABILITY OF GOLD CLUSTERS ON THE GaAs SURFACE

N.Dmitruk<sup>(1)</sup>, T.Lepeshkina<sup>(1)</sup>, M.Pavlovskaya<sup>(2)</sup>, L.Zabashta<sup>(3)</sup>

<sup>(1)</sup> Institute of Semiconductor Physics of NASU, Kyiv, Ukraine, 45 prosp.Nauki,  
252650 Kyiv, Ukraine; e-mail: nicola@dep39.semicond.kiev.ua

<sup>(2)</sup> Taras Shevchenko National University, Kyiv, Ukraine,

<sup>(3)</sup> Sumy State University, Sumy, Ukraine.

**Abstract.** Here we used the chemical method of deposition of nanoparticles from water solution of metal salts on a less electropositivity substrates. The size-dependent polarizability of Au nanoparticles on the GaAs substrate was investigated by reflective ellipsometry methods: MAI and VASE. ©1999 Acta Metallurgica Inc.

### INTRODUCTION

Ultrafine particles having diameters larger than 1nm and less than 1µm and called nanoparticles are of interest for physicists along of their extraordinary physical properties that are size-dependent. Besides, metallic micro- and nano-particles affect both electronic and structure properties of semiconductor surface. Ensembles of such particles are known as island (discontinuous) films possess specific electrodynamical (optical) properties described by their polarizability. We study this property of Au nanoparticles on the GaAs substrate by the ellipsometric methods: multi-angle-of-incidence (MAI) and variable - angle spectroscopic ellipsometry (VASE).

### SAMPLE PREPARATION AND EXPERIMENTAL PROCEDURE

In this paper gold islands were deposited from an aqueous solution of AuCl<sub>3</sub> with the Au<sup>3+</sup> ions concentration C of (1–16)×10<sup>-5</sup> gram-ion/l at pH=1÷2 [1]. An illumination with the hν>1.5 eV light promoted the process of electrochemical deposition because after adsorption from solution the Au<sup>3+</sup> ions have been neutralized by the capture of valence or free electrons according to the reaction



i.e. continuous process of generation of broken atomic bonds and dissolution of substrate material near a gold islet takes place. After removal of gold coating by its dissolution in water solution of ammonium persulphate we obtained the weak wavy surface of GaAs with the root-mean-square roughness δ about 10 nm.

The morphologies of the discontinuous metal film and of the microrelief GaAs surface were examined with an electron microscope using a carbon replica with or without

shadowing. The electrodynamical properties of small metallic particles are investigated by MAI ellipsometry with the LEF-3M laser ellipsometer with a fixed compensator and He-Ne laser ( $\lambda=632.8$  nm) as a light source and by spectroscopic ellipsometer with non-compensated Beattie method at three incident angles in vicinity of the main angle of incidence in the range of wavelength  $\lambda=0.27 - 1.15$   $\mu\text{m}$  (VASE). The optical parameters  $n_{ef}$  and  $k_{ef}$  of surface layer have been calculated on the experimental incidence angle dependencies of polarization angles  $\Psi(\varphi)$ ,  $\Delta(\varphi)$  by solving the inverse ellipsometric problem. Last was solved with the help of a package of applied programs ELLA created using Tikhonov's regularization method [2].

So, varying the exposure time of the GaAs substrate and the  $\text{Au}^{3+}$  ion concentration  $C=(1\div 16)\times 10^{-5}$  g-ion/l, one can control coating morphology, Au nanoparticles size and their concentration in the ranges:  $d=3-50$  nm and  $N=5\times 10^{10}-10^{12}$   $\text{cm}^{-2}$ , respectively.

## RESULTS AND DISCUSSION

The maximal changes of the parameters  $\delta\Delta=\Delta-\bar{\Delta}$  and  $\delta\psi=\psi-\bar{\psi}$  ( $\bar{\Delta}$  and  $\bar{\psi}$  correspond to an oxidized undoped real surface) for the angle of light incidence  $\varphi=75^\circ$  and the gold concentrations in solutions ( $C=8-16\times 10^{-5}$  g-ion/l) reach as much as  $|\delta\psi|=55^\circ$  and  $|\delta\Delta|=19^\circ$ . The dependencies  $\delta\Delta(\varphi)$  and  $\delta\psi(\varphi)$  are nonmonotonous and change the sign at  $\varphi=75^\circ$ .

A preliminary analysis of experimental data within the scope of semiconductor-dielectric film models and semiconductor-homogeneous metal film models has shown that the surface structure can not be described within the scope of the simple models mentioned. The disagreement is obviously explained by optical inhomogeneity of the surface coatings formed. Data on the morphology and structure of metal coatings show that metal coatings have a clearly seen island structure; the surface density, radius, and height of the islands change greatly with changing doping conditions. A GaAs surface doped to the utmost coating appears to be inhomogeneous with a strongly developed relief in the metal coating.

Experimental data  $\psi(\lambda)$ ,  $\Delta(\lambda)$  for three samples Au/GaAs at one fixed incidence angle are shown on Fig. 1. As a rule we can see of rather smooth both decrease of  $\psi$  and increase of  $\Delta$ ; some small non-monotonous peculiarities of spectra perhaps are possibly conditioned by the experimental errors. If the free electrons behaviour dominates in the infrared, in the visible and ultraviolet the interband absorption dominates. Of course, these peculiarities are revealed more definitely in the spectra of refractive index  $n$  and absorption index  $k$ . The last values were obtained from  $\Delta(\lambda)$ ,  $\psi(\lambda)$  spectra by means of solution of inverse ellipsometric problem using minimum three incidence angles in the vicinity of main angle of incidence.

The optical parameters of GaAs substrate ( $n_s$ ,  $k_s$ ) are considered as known and three parameters of surface absorptive films ( $n_f$ ,  $k_f$ ,  $d_f$  – effective thickness) are being determined by solution of inverse ellipsometric problem. Certainly the condition  $d_f(\lambda)=const$  was used at these calculations. The results obtained are shown in Fig. 2. The spectroscopic behaviour of both  $n_f(\lambda)$  and  $k_f(\lambda)$  depend on Au nanoparticles (clusters) dimensions  $d$  which correlate with  $d_f$  value. Two following results are important for building optical model of discontinuous gold films on GaAs substrate: 1) according electron micrographs with



shadowing the gold islets have the round form (at small value of coating  $C \cdot t \cong 1 \times 10^{-5}$  (g-ion/l) min) and may be considered as sphere; 2) the calculation of absolute limits [3] imposed on admissible values of the effective dielectric function  $\varepsilon'_{ef}$ ,  $\varepsilon''_{ef}$  for surface layer consisting of gold, GaAs, its native oxides and air, revealed that the experimental data correspond better to 3D isotropy model. In this case we may use the modified Bruggeman's symmetrical theory [3] to calculation of the specific polarizability:

$$\alpha' = \alpha / (4/3\pi d^3) = 3 \{ (\varepsilon_i - \varepsilon_m) / (\varepsilon_i + 2\varepsilon_m) \}, \quad (1)$$

where  $d$  is the diameter of islet,  $\varepsilon_i$  and  $\varepsilon_m$  is the dielectric function of islet material and matrix, respectively; the corresponding formula is

$$\sum_i f_i \frac{\varepsilon_i - \varepsilon_{ef}}{\varepsilon_i + 2\varepsilon_{ef}} = 0, \quad (2)$$

where  $f_i$  is the volume fraction of the  $i$ -phase,  $\varepsilon_i$  is its dielectric function and  $\varepsilon_{ef}$  is the effective dielectric function of 3D composite. Then we can calculate the complex specific polarizability of gold clusters by formula:

$$\alpha' = 3 \frac{1 - f_1}{f_1} \frac{\varepsilon_{ef} - \varepsilon_2}{2\varepsilon_{ef} + \varepsilon_2}, \quad (3)$$

where  $f_1$  is the volume fraction of gold in effective surface layer, which can be calculated from electron micrographs,  $\varepsilon_{ef}$  is the effective dielectric function obtained from the inverse ellipsometric problem solution,  $\varepsilon_2$  is the dielectric function of the surroundings which below will be chosen  $\varepsilon_2 \approx 1$ . In Fig.3 the value  $\alpha'$  for three samples Au/GaAs obtained are presented together with the theoretical value  $\alpha'$  for gold spheres. It is seen that  $Re\alpha'$  for gold islets is much less than ones for pure gold spheres and the spectral dependencies  $\alpha'(\lambda)$  are different too. They are size-dependent.

## CONCLUSIONS

The technology of preparation of gold clusters on GaAs substrate is elaborated. Using MAI and VASE ellipsometric measurements we calculated the effective dielectric parameters  $n_{ef}$ ,  $k_{ef}$  and the effective thickness of gold film. Then the complex specific polarizability of gold clusters was obtained. The physical reasons of the size dependence of polarizability will be analyzed in the future.

**Acknowledgment.** This work was partly supported by the Ukrainian Fund of Fundamental Investigations under the grant 2.4/729.

## REFERENCES

1. Dmitruk N.L., Kolbasov G.Ya. et al., *Thin Sol. Films*, 1981, **75**, 341.
2. Dmitruk N.L., Zabashta L.A., Zabashta O.I. and Storizhko V.E., *Surface investigations*, 1997, **12**, 1411.
3. Aspnes D.E., *Thin Sol. Films*, 1982, **89**, 249.

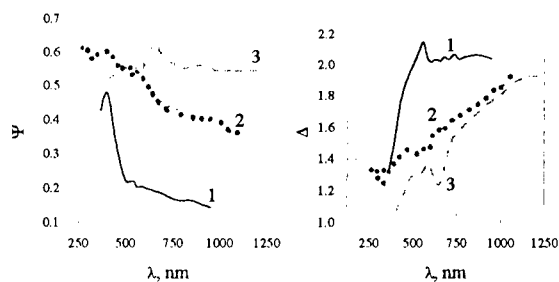


Fig.1. Experimental spectra  $\psi$  and  $\Delta$  for three samples Au/GaAs, corresponding such C values: 1 -  $1 \times 10^{-5}$ , 2 -  $4 \times 10^{-5}$ , 3 -  $8 \times 10^{-5}$  g-ion/l.

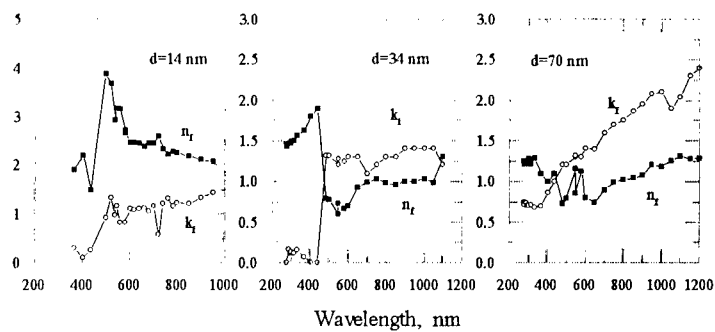


Fig.2. Spectra  $n_f$  and  $k_f$  for three samples Au/GaAs with the effective thickness  $d_f=14$  - (a), 34 - (b) and 70 nm - (c).

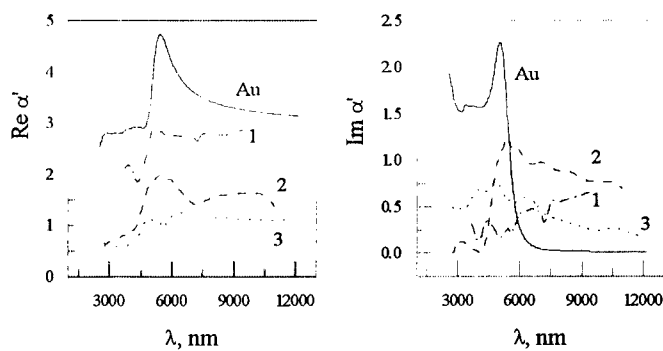


Fig.3. Calculated spectra  $Re\alpha'$  and  $Im\alpha'$  for three samples Au/GaAs (1-3) and for gold spheres (Au).



## LATTICE DYNAMICS OF Co NANOPARTICLES IN Ag

M. El Azzaoui(a), M. Hou(a), H. Pattyn(b), J. Verheyden(b), W. Deweerdt(b),  
G. Koops(b) and G.L. Zhang (b,c)

(a) Physique des Solides Irradiés, CP 234, Université Libre de Bruxelles, Bd. du Triomphe,  
B-1050 Bruxelles, Belgium

(b) Institute for Nuclear and Radiation Physics, Physics Department, K.U.Leuven  
Celestijnenlaan 200D, B-3001 Leuven, Belgium

(c) Shanghai Institute of Nuclear Research, Chinese Academy of Sciences, Shanghai  
201800, P.R. China

**Abstract:** A comparison is made between the lattice dynamics of cobalt embedded in silver, studied by Mössbauer spectroscopy and by classical molecular dynamics (MD). The MD is achieved in the NPT ensemble by means of the Rahman Parrinello technique which accounts for the temporal fluctuations of all the components of the stress tensor. Atomic interactions are described within an empirical embedded atom model.

The mean square thermal vibration amplitude of substitutional Co is calculated and found to compare well with experimental value extracted from Mössbauer spectroscopy. Mössbauer spectroscopy shows the Debye temperature to be cluster size dependent and a comparison with MD suggests the possibility of quantitative cluster size estimates.

©1999 Acta Metallurgica Inc.

### 1. INTRODUCTION

Mössbauer spectroscopy is a very suitable technique to measure dynamic properties of nanoprecipitates because only the local environment of the probe atom is reflected in the corresponding spectral component and, moreover, different environments give rise to different spectral components. The intensity of a spectral component is proportional to the recoilless fraction of the corresponding site in the sample. The Debye model relates this recoilless fraction to the Debye temperature  $\theta_D$ . By plotting the normalised intensity (*i.e.* the area of a component divided by the non resonant background) of a component as a function of measuring temperature and fitting this behaviour according to the Debye model,  $\theta_D$  can be determined.

The classical molecular dynamics method is used to calculate the temperature dependence of the mean square thermal vibration amplitude (msqa) of substitutional cobalt as well as averaged inside cobalt nanoprecipitates. The results are discussed in relation with the Mössbauer spectroscopy data.

## 2. THE MOLECULAR DYNAMICS METHOD

The MD calculations are performed at constant pressure and constant temperature. This is achieved with a time-dependent metric tensor which allows the volume and the shape of the MD cell to vary with time without any isotropy requirement [1]. For our MD simulations we have used the embedded atom model (EAM) [2] based on a method suggested by Johnson [3]. This method allows to fully determine the embedding function in the case of an alloy on the basis of the knowledge of the atomic volume, the cohesive energy, the vacancy formation energy and the elastic constants of its bulk elemental components. Such a potential however still requires assessment on the basis of experimental data and the present work contributes to this assessment. More detail and the model parameters for the Co-Ag system are given elsewhere [4].

## 3. SUBSTITUTIONAL $^{57}\text{Co}$ AND Co NANOPARTICLES IN Ag

The msqa of substitutional Co in Ag is evaluated by MD as a function of temperature and the results are given in Figure 1.

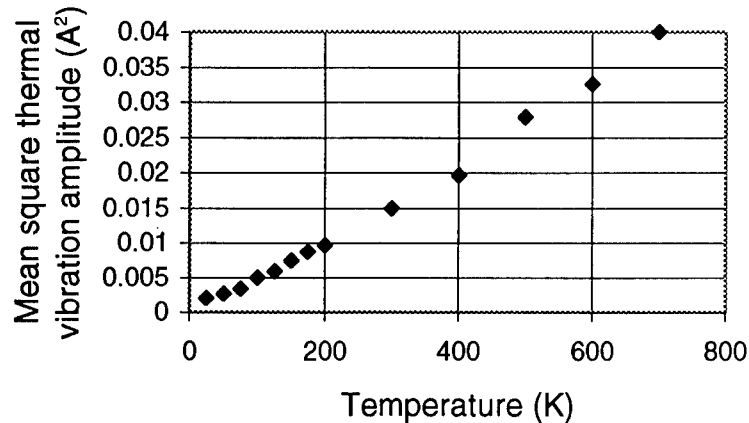


Figure 1: msqa versus temperature for a substitutional Co in Ag as obtained by MD.

Consistently with the Debye model, the dependence is quadratic in the low temperature limit and linear in the high temperature limit. A temperature  $\theta_D = 218$  K is derived from a fit of the data in fig. 1 to the Debye model. On the other hand, the Mössbauer spectrum of a polycrystalline Ag foil, implanted at room temperature (RT) with  $5 \cdot 10^{13} \text{ at.cm}^{-2}$   $^{57}\text{Co}$  consists of a single line which corresponds to substitutional Co. We recorded a Mössbauer spectrum at 100, 200 and 293 K. From the behaviour of the intensity of the single line with temperature we could determine  $\theta_D$ . We found a value of 211(18) K. It is also in excellent agreement with the MD results mentioned above.

Cobalt clusters are modelled as truncated fcc octahedra and we here report results for a cluster of 405 atoms embedded in a silver matrix. In contrast with the bulk phase, the

fcc structure of this nanocluster is found stable and its dynamic properties can be studied. The  $msq$  is dependent on the distance from the centre of the cluster and a detailed analysis is reported in [4]. A mean Debye temperature can be estimated similarly to the case of the substitutional Co and a value around 230 K is found. The question now arises to compare with Mössbauer data.

Cobalt clusters are produced by ion implantation of Co into a polycrystalline Ag foil.

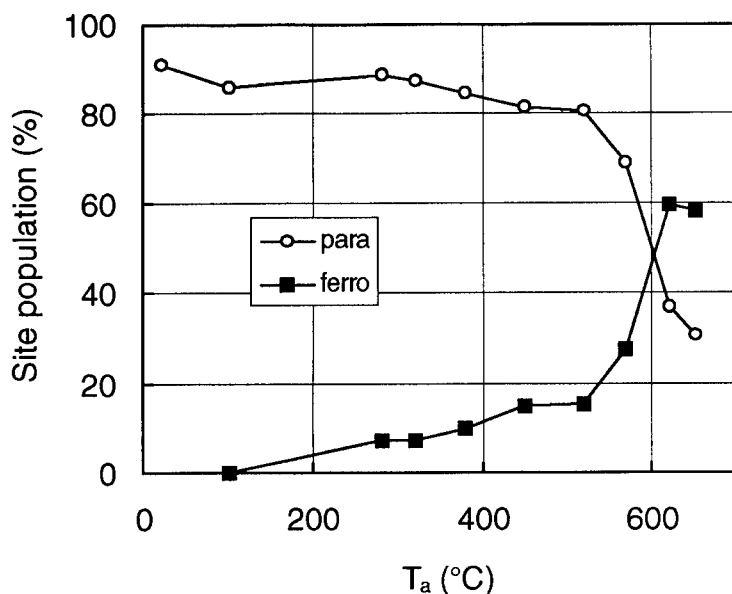


Figure 2 : Intensity of the main spectral components vs. annealing temperature  $T_a$

The intensities of different components of the Mössbauer spectra are plotted as a function of annealing temperature in figure 2. We divided the spectral intensity of each component by the recoilless fraction obtained by the method described in [4]. One thus obtains the real site occupations.

$\theta_D$  of the ferromagnetic (FM) and superparamagnetic (SPM) components have been determined from measurements at 20 °C and 200 °C after annealing at  $T_a = 520, 570, 620$  and 650 °C. We assumed  $\theta_D$  to be the same for the data obtained below  $T_a = 520$  °C. In figure 2 we see how the SPM Co particles turn into FM particles. The intensity increase of the FM component indicates that either the FM particles increase in size or increase in number.

From the intensity ratio of a component at the two measuring temperatures, its corresponding  $\theta_D$  can be determined. The transferred fraction ( $\alpha$ ) gives information about the size distribution. From the uncorrected ( $\alpha=0$ ) intensity ratio at  $T_a=650$  °C, we determine

the  $\theta_D$  value for the FM fraction, 410 K. From there on, we could determine  $\alpha$  and  $\theta_D$  for the SPM fraction. The results are summarised in table 1.

$T_a$ (°C)	$\alpha$	$\theta_D$ (SPM) (K)	$\theta_D$ (SPM + FM) (K)
520	0,0110	247	269
570	0,0078	279	312
620	0,0096	274	351
650	0	320	375

*Table 1 : Calculated values for  $\alpha$  and  $\theta_D$  (SPM) a function of annealing temperature.  $\theta_D$  (SPM + FM) is the mean Debye temperature for all Co particles.*

From the  $\theta_D$  values of the SPM fraction in table 1, we can conclude that  $\theta_D$  for the smallest Co particles is close to the value for substitutional Co in Ag (211(18) K) and that it increases with increasing  $T_a$  (increasing particle size) to a value that corresponds to the bulk value for Co. It is also close to the value obtained by MD for the 405 atoms cluster. This suggests that a comparison between computed and experimental Debye temperatures may be used to estimate cluster sizes quantitatively. Further investigations are undertaken in this direction.

**Acknowledgement:** This work is supported by the Belgian OSTC under contract IUAP P4/10.

#### REFERENCES

- [1] M. Parrinello and A. Rahman; J. Appl. Phys. **52**,12(1981)7182
- [2] S. Daw and M.I. Baskes; Phys. Lett. **50**(1983)1285
- [3] R.A. Johnson; Phys. Rev. **B39**,17(1989)12554
- [4] M. El Azzaoui, M. Hou, H. Pattyn, J. Verheyden, W. Deweerdt, G. Koops and G.L. Zhang, in preparation.



Pergamon

NanoStructured Materials, Vol. 12, pp. 303–306, 1999

Elsevier Science Ltd

© 1999 Acta Metallurgica Inc.

Printed in the USA. All rights reserved

0965-9773/99/\$-see front matter

PII S0965-9773(99)00122-1

## MAGNETIC PROPERTIES OF Co-Sm MIXED-CLUSTER ASSEMBLED MATERIALS

M. Négrier, J. Tuillon, V. Dupuis, C. Tonon, A. Perez

Département de Physique des Matériaux-UMR CNRS 5586

Université Claude Bernard Lyon 1, 69622 Villeurbanne, France.

**Abstract --** Nanosize Co-Sm mixed clusters were prepared in the gas phase from a SmCo<sub>5</sub>-solid target mounted in a laser vaporization source. Both, nanostructured pure Co-Sm films, and films of isolated Co-Sm clusters embedded in a silver matrix were prepared. Composition and structure of the deposits were characterized by Rutherford Backscattering, transmission electron microscopy and X-ray photoelectron spectrometry. SQUID-magnetometry measurements down to 2.3 K were performed to study the magnetic behavior of the samples. ©1999 Acta Metallurgica Inc.

### INTRODUCTION

Preparation and study of original magnetic nanostructures are a subject of growing interest on account of the great potential applications in the fields of high-density data storage, sensors, and spin electronic devices. On the fundamental point of view, interesting properties are expected as the dimensions of the magnetic objects become comparable to characteristic nanoscopic length scales such as the magnetic monodomain size. In this context, various magnetic systems of specific geometry and dimension are produced : (i) two-dimensional (2D) structures such as multilayers (1), (ii) one-dimensional (1D) objects such as nanowires (2), and (iii) zero-dimensional (0D) forms such as patterned submicrometer-sized dots (3) or atomic clusters (4). In this last case, the nanostructured systems produced by the Low Energy Cluster Beam Deposition technique (LECBD) offers some unique opportunities (5). This technique consists in depositing, on a substrate, neutral clusters beam produced in the gas phase using a gas condensation sources (6). In the low energy regime, nanosize clusters are not fragmented upon impact on the substrate leading to a film growth by a nearly random stacking process of the incident free clusters. Previous results about these magnetic nanostructures prepared by LECBD (Fe, Co or Ni films) (7, 8), and Co-clusters embedded in Ag-matrix clearly emphasize the competition between the intrinsic cluster properties and the cluster interactions to influence the magnetic behavior. In this context, our objective is to produce such nanosize magnetic clusters with a strong magnetic anisotropy in order to influence their superparamagnetic behavior and to increase their blocking temperature. This could be achieved in the gas phase by preparing clusters with specific compositions, unattainable by conventional preparation techniques. To modify the magnetic anisotropy we have chosen transition metal-rare earth mixed clusters and specially SmCo<sub>5</sub> clusters reported in this paper.

In the case of a deposit of clusters on a substrate, supported clusters interact by direct contact and the magnetic behavior of such systems is well described in the framework of the

random anisotropy model previously developed by E. Chudnowski (9) for amorphous magnetic materials, but with a local order extended to the grain size. In the case of nanosize clusters embedded in a matrix, the role and possible control of the interactions between clusters are clearly shown. As an example, a giant magnetoresistance (GMR) effect was observed as a function of the clusters concentration for Co-clusters embedded in a silver matrix (10). But in that case, the magnetocrystalline anisotropy of the nanosize pure Co-particles is low enough and their blocking temperatures are in the range of 20-30 K. Thus, the idea to use rather mixed clusters which associate an element with a high magnetic moment at room temperature (as for transition metals), and one with a high anisotropy (as for rare earths) to obtain nanoparticles with a large local anisotropy has been tested.

## RESULTS AND DISCUSSION

Nanosize Co-Sm mixed clusters were prepared in the gas phase from a  $\text{SmCo}_5$ -solid target mounted in a laser vaporization source, described elsewhere (4). The distributions of free clusters were characterized in a time of flight mass spectrometer prior to depositions at room temperature using the Low Energy Cluster Beam Deposition technique (LECBD). Co-Sm clusters were directly deposited on various substrates or embedded in a silver matrix. Both nanostructured films were prepared with thicknesses up to several hundreds nanometers.

The composition of the samples were studied using the Rutherford Back Scattering spectrometry technique (RBS) measurements which confirms the conservation in the films of the  $\text{SmCo}_5$  target stoichiometry. The size distribution of these supported mixed clusters, obtained from TEM observations, (figure 1) is centered around 3 nm with a rather narrow size dispersion. The XPS spectra, (figure 2), show the characteristic peaks of the pure Co phase and the ones of the  $\text{Sm}_2\text{O}_3$  phase. Because the only oxidized element is samarium, a possible structure for these mixed-clusters could be a core of pure Co surrounded by a skin of Sm-oxide. The segregation of Sm-atoms at the surface of these mixed clusters could be explained by the difference between the radius of Co and Sm-atoms (Co : 0.074 nm, Sm : 0.104 nm) and between the surface energy of Co and Sm (Co : 2550 mJ/m<sup>2</sup>, Sm : < 1100 mJ/m<sup>2</sup>) (11). The interpretations of X-ray absorption and diffraction spectra recently obtained using the synchrotron radiation facilities at LURE (Orsay, France) are in progress to determine the crystalline structure of the  $\text{SmCo}_5$ -clusters and the atomic local.

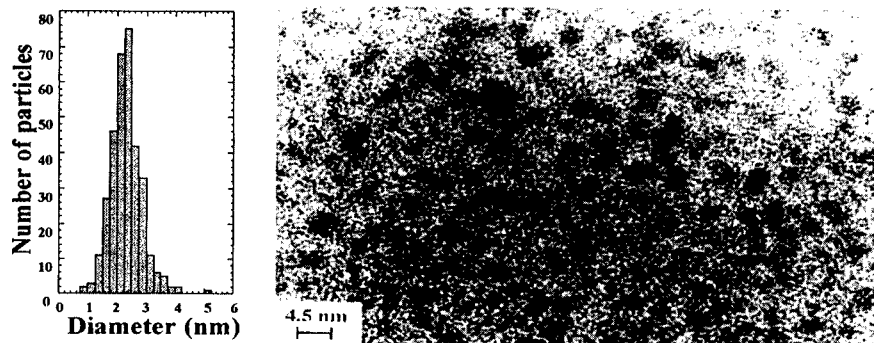


Figure 1: Distribution size of  $\text{SmCo}_5$ -clusters obtained using TEM image of  $\text{SmCo}_5$ -cluster film. The film was prepared at room temperature on an amorphous carbon coated grid.



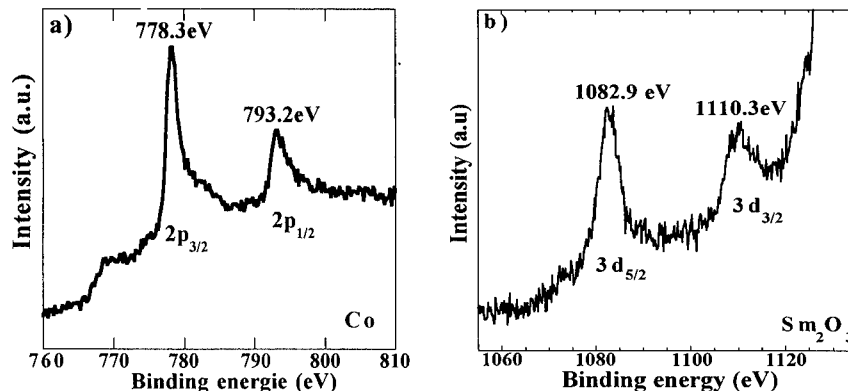


Figure 2: X-ray photoelectron spectrum of a  $\text{SmCo}_5$ -cluster film 50 nm thick deposited at 300 K after Ar-ion cleaning of the surface. The binding energies correspond to pure-Co (a) and  $\text{Sm}_2\text{O}_3$  oxide of Sm (b).

To study the magnetic properties we used a commercial superconducting quantum interference device (SQUID) magnetometer at the Laboratoire de Physique du Solide, Nancy, France. Two types of measurements were performed : classical hysteresis loops and zero field cooled-field cooled diagrams (ZFC-FC). To analyze the effect of Sm, we compare the properties of the  $\text{SmCo}_5$  clusters embedded in Ag-matrix films ( $\text{SmCo}_5/\text{Ag}$ ) with those of previous (Co/Ag) ones. Hysteresis loops presented in figure 3 are at 5 K for samples containing 10% (volumic) of clusters (Co or  $\text{SmCo}_5$ ) in the Ag-matrix. We observe that the hysteresis loop of  $\text{SmCo}_5$  completely loses the square shape to tend to the characteristic

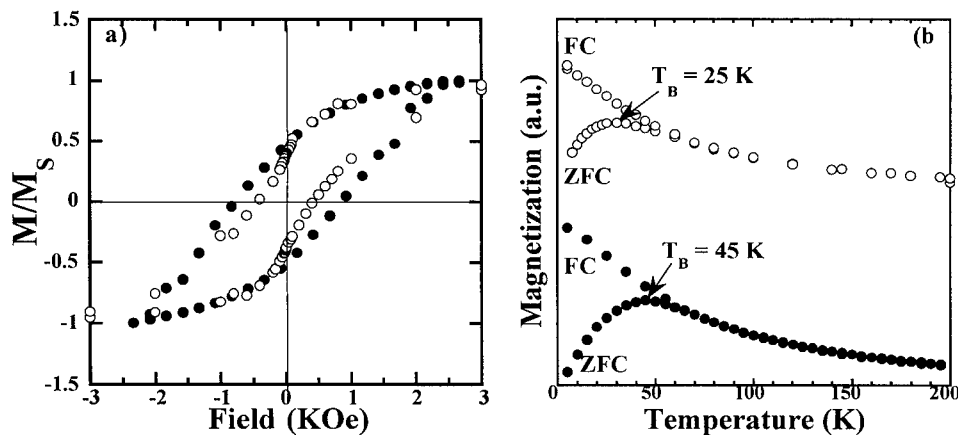


Figure 3: Hysteresis loops and ZFC-FC diagrams at 50 Oe for Co-clusters embedded in Ag-matrix (open circles) and  $\text{SmCo}_5$ -clusters embedded in Ag-matrix (empty circles) with a volumic concentration equal to 10 %.

shape of a system with anisotropy (12). The coercive field has been found to be equal to 0.8 KOe for the  $\text{SmCo}_5/\text{Ag}$  sample to compare to 0.4 KOe for the Co/Ag one. The ZFC-FC

diagrams for these samples are shown in figure 3b. Notice the same characteristic superparamagnetic-behavior of the magnetization versus temperature ( $M\alpha 1/T$ ) above the blocking temperature for both samples. However, the main result is the increase of this blocking temperature: 45 K for the  $\text{SmCo}_5/\text{Ag}$  sample compared to 25 K for the  $\text{Co}/\text{Ag}$  one.

## CONCLUSION

Finally, these preliminary results seem to confirm an increase of the magnetic anisotropy in the mixed  $\text{SmCo}_5$  clusters films compared to the pure Co-cluster films. Unfortunately, the heterogeneous structure of  $\text{SmCo}_5$ -clusters does not allow to reach the expected high magnetocrystalline anisotropy as in the bulk well-crystallized  $\text{SmCo}_5$  phase. Further experiments to improve the crystallinity and homogeneous distribution of Sm in the clusters are in progress.

## ACKNOWLEDGEMENTS

The authors are indebted to Dr M. Pellarin (Laboratoire de Spectrometrie Ionique et Moléculaire, Université Lyon I, France, and to Dr Catherine Dufour (Laboratoire de Physique des Solides, Université Nancy, France) for their supports in the  $\text{SmCo}_5$ -clusters preparation and characterization in the gas phase, and SQUID-magnetometry measurements, respectively.

## REFERENCES

- (1) Bruno P., Chappert C., Phys. Rev. B, 1992, 46, 261.
- (2) Meier J., Doudin B., Ansermet J.-Ph., J. Appl. Phys. 1996, 79 (8), 6010.
- (3) Hehn M., Padovani S., Ounadjela K., Bucher J.P., Phys. Rev. B, 1997, 54, 3428.
- (4) Perez A., Mélinon P., Dupuis V., Jensen P., Prével B., Tuaillon J., Bardotti L., Martet C., Treilleux M., Broyer B., Pellarin M., Vialle J.L., Palpant B., J. Phys-D : Applied Physics, 1997, 30, 1.
- (5) Rousset J. L., Cadrot A.M., Cadette Santos Aires F.J., Renouprez A., Melinon P., Perez A., Pellarin M., Vialle J.L., Broyer M., J. Chem. Phys., 1995, 102, 8574.
- (6) Milani P., de Heer W., Rev. Sci. Instr. 1990, 61, 1835.
- (7) Perez J.P., Dupuis V., Tuaillon J., Perez A., Paillard V., Mélinon P., Treilleux M., Thomas L., Barbara B., Bouchet-Fabre B., JMMM, 1995, 145, 74.
- (8) Tuaillon J., Dupuis V., Mélinon P., Prével B., Treilleux M., Perez A., Pellarin M., Vialle J.L., Broyer M., Phil. Mag. A 1997, 76, 493.
- (9) Chudnovski E.M., J. Appl. Phys., 1988, 64, 5770.
- (10) Tuaillon J., Dupuis V., Prevel B., Perez A., Mélinon P., Parent F., Steren L.B., Morel R., Barthelemy A., Fert A., Phys. Rev. B, 1997, 55, 3683.
- (11) De Boer F.R., Boom R. Mattens W.C.M., Miedena A.R., Cohesion in metals, De Boer F.R., Petifor D.G. Editors, Elsevier, Amsterdam 1989.
- (12) Wernsdorfer W., Hasselbach K., Benoit A., Mailly D., Barbara B., Tuaillon J., Perez J.P., Dupuis V., Guiraud G., Perez A., J. Appl. Phys, 1995, 78, 7192.



Pergamon

NanoStructured Materials, Vol. 12, pp. 307-310, 1999

Elsevier Science Ltd

© 1999 Acta Metallurgica Inc.

Printed in the USA. All rights reserved

0965-9773/99/\$-see front matter

PII S0965-9773(99)00123-3

## COMPARATIVE ANALYSIS OF OPTICAL PROPERTIES OF GOLD AND SILVER CLUSTERS EMBEDDED IN AN ALUMINA MATRIX

B. Prével<sup>+</sup>, B. Palpant<sup>\*</sup>, J. Lermé<sup>\*</sup>, M. Pellarin<sup>\*</sup>, M. Treilleux<sup>+</sup>, L. Saviot<sup>\*\*</sup>,  
E. Duval<sup>\*\*</sup>, A. Perez<sup>+</sup> and M. Broyer<sup>\*</sup>

<sup>+</sup> Département de Physique des Matériaux,

<sup>\*</sup> Laboratoire de Spectrométrie Ionique et Moléculaire,

<sup>\*\*</sup> Laboratoire de Physico-Chimie des Matériaux Luminescents  
Université Claude Bernard Lyon-1, 43, bd du 11 novembre 1918,  
69622 Villeurbanne Cedex, France.

**Abstract** -- The optical properties of nanocomposite thin films of gold and silver clusters embedded in an alumina matrix have been investigated. The samples have been characterized by several techniques in order to determine their composition, morphology and cluster size distribution. Ellipsometry and photoabsorption measurements have been performed. The differences in the optical properties of the various samples reflect finite size effects. Time Dependent Local-Density-Approximation (TDLDA) calculations, taking into account the d-electrons and matrix screening effects, are consistent with observed size evolutions of the Mie frequency. Low frequency Raman scattering spectra exhibit a strong size-dependent band related to quadrupolar vibration modes of the clusters.

©1999 Acta Metallurgica Inc.

### INTRODUCTION

In noble metal clusters the polarization of the d-electrons play a central part in the dynamical response of the valence electron cloud excited by light (1). In particular the screening of the Coulomb interaction between valence electrons by the core-electrons results in a large red-shift of the dipolar surface plasmon frequency, as compared to the value predicted within the free electron gas model. In the case of matrix-embedded small-radius metal spheres ( $R \ll \lambda$ ) the dipolar collective excitation is predicted in the Mie-theory to occur roughly at  $\omega_s = \omega_p / \{2\epsilon_m + \text{Re}[\epsilon_d(\omega_s)]\}^{1/2}$ , where  $\omega_p$  is the volume plasma frequency,  $\epsilon_m$  is the dielectric constant of the embedding matrix and  $\epsilon_d$  is the complex dielectric function corresponding to the core-electrons ( $\text{Re}[\epsilon_d] \approx 5$  and 10 in the vicinity of  $\omega_s$  for silver and gold, respectively). The influence of the d-electrons is reflected also in the size evolution of the Mie frequency  $\omega_s$ . In contrast with alkali clusters, which exhibit a noticeable red-shift trend with decreasing cluster size due to the spillout phenomenon, the size behaviour is reversed in the case of free  $\text{Ag}_N^+$  and  $\text{Au}_N^+$  clusters (2,3), namely a slight blue-shift trend is observed. This feature can be explained by assuming that, owing to the localized character of the nd-wavefunctions, the screening is less effective over a layer close to the cluster surface (4). The skin region of reduced polarizability, the influence of

which increases with decreasing size, induces a blue-shift trend competing with the spillout effect. In this communication we report on experimental and theoretical investigations on the size-evolution of the optical properties of alumina-embedded noble metal clusters (5), as well as recent low-frequency Raman scattering spectra providing information about the vibrational modes of the particles (6).

### SAMPLE PRODUCTION AND CHARACTERIZATION

Gold and silver clusters are produced by laser vaporization and samples are elaborated by the Low-Energy Cluster Beam Deposition Technique (7). The alumina matrix is evaporated from a crucible heated by an electron gun. The neutral clusters and the matrix are deposited on different substrates -depending on the characterization technique- at room temperature in a chamber under vacuum of  $10^{-7}$  Torr. Clusters and matrix deposition rates are measured by two quartz balances. This allows to choose the thickness as well as the volumic metal fraction ( $q \approx 4\%$ ) in the samples.

Thickness and ellipsometric measurements reveal an important porosity of the alumina matrix ( $\approx 45\%$ ). Rutherford Back-Scattering allows to determine the composition and atomic concentration in the thin films. Transmission Electron Microscopy (TEM) is performed on the different samples. The particles are roughly spherical and randomly distributed in the matrix. Size distributions are deduced from the micrographs over a population of 700 up to 3000 particles per sample. The mean diameter ranges from 2.0 to 3.7 nm for gold particules and from 3.0 to 7.1 nm for silver particules, depending on the sample. X-ray diffraction and scattering experiments performed in LURE (Orsay, France) reveal a fcc structure and confirm the mean size of the clusters (5).

### OPTICAL PROPERTIES

Transmittance measurements, performed on the films deposited on suprasil substrates, over the wavelength domain 200-1000 nm, with a Varian Cary spectrophotometer, lead to the determination of the absorption versus energy. Results are displayed in Fig. 1 for various size distributions. For each curve, one observes a more or less pronounced absorption band, centered around 2.4 eV for gold samples, and around 2.9 eV for silver samples. For gold this band is superimposed on an increasing signal due to the interband transitions, whereas interband transitions occur at higher energies in the case of silver. The absorption band is due to the surface plasmon resonance corresponding to the collective oscillation of the conduction electrons with respect to the ionic background. For gold the band is broadened and damped as the cluster size decreases. Moreover a slight but noticeable blue-shift evolution is observed with decreasing size. In the case of silver clusters the location of the Mie-band is quasi size-independent, as well as (approximately) the band width.

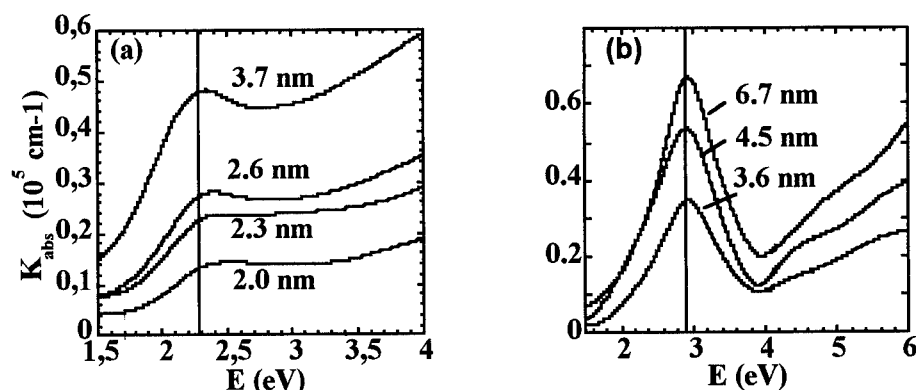


**Figure 1 :** Absorption coefficient for different gold (a) and silver (b) samples. The vertical line indicates the bulk limit value given by the Maxwell-Garnett theory.

TDLDA calculations, taking into account the d-electrons and embedding porous-matrix screening effects, have been carried out within a multi-layered dielectric model (8,9). The complex functions  $\epsilon_d(\omega)$  characterizing the dielectric properties of the ionic-core background is extracted from the experimental complex index of both bulk metals. With regard to the location of the Mie-band as a function of the particle size, the analysis of the results emphasizes the crucial part played by the  $\omega$ -dependence of  $\epsilon_d(\omega)$  in the arbitration of the competing blue- and red-shift trends induced by, respectively, the skin region of reduced polarizability (thickness parameter  $d$ ) and the spillout effect (9). The parameter  $d$ , which is expected to be similar for silver and gold, is fitted in order to reproduce the experimental data on free  $\text{Ag}_N^+$  clusters (2). The local porosity at the metal-alumina matrix interface is mimicked by assuming a "vacuum rind" of thickness  $d_m$  around the clusters. The results obtained for free ( $d_m=\infty$ ), fully-embedded ( $d_m=0$ ) and porous alumina matrix-embedded ( $d_m=2$  a.u.)  $\text{Ag}_N$  clusters are displayed in Fig.2, as well as the results for  $\text{Au}_N$  clusters ( $d_m=2$  a.u.).

### LOW-FREQUENCY RAMAN SCATTERING

Low-frequency Raman scattering experiments have been performed on the  $\text{Ag}_N:\text{Al}_2\text{O}_3$  composite samples. When the excitation wavelength is close to the maximum of the Mie band ( $\approx 400$  nm) the Raman spectra exhibit a relatively strong band located around  $10\text{ cm}^{-1}$ , the maximum of which depends on the mean cluster radius in a consistent way ( $\omega_{\text{vib}} \sim \alpha/R$ , see Fig. 3). The Raman band corresponds to the quadrupolar vibration mode of the clusters (6). Moreover the maximum of the Raman band shifts towards lower frequencies when the excitation laser wavelength is increased up to 676 nm. This feature is not completely elucidated so far, but is suspected to reflect the cluster shape-dependence of both the Mie frequency and the vibration mode.

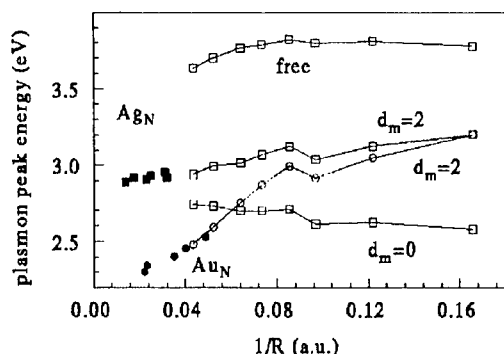


**Figure 2 :** Maximum of the Mie resonance band for  $Ag_N$  (squares) and  $Au_N$  clusters (circles). Theory: empty symbols. Experiment: black symbols.

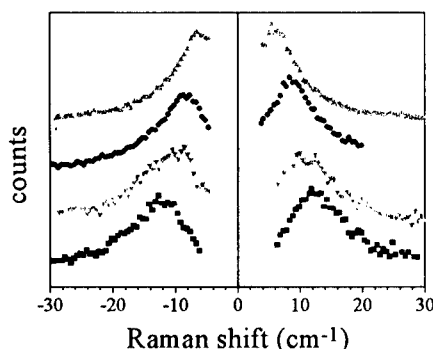


**Figure 3 :** Raman scattering spectra recorded for  $Ag_N$ :alumina samples. The mean diameter of the size distributions are 3.1 (lower curve); 3.8; 5.5 and 7.1 nm (upper curve).

#### REFERENCES

1. Kreibig, U. and Vollmer, M., *Optical Properties of Metal Clusters*, Springer, 1995.
2. Tiggesbäumker, J., Köller, L., Meiwe-Broer, K.H. and Liebsch, A., *Phys. Rev. A*, 1993, **48**, R1749.
3. Lindinger, M., Dasgupta, K., Dietrich, G., Krückeberg, S., Kuznetsov, S., Lützenkirchen, K., Schweikhard, L., Walther, C. and Ziegler, J., *Z. Phys. D*, 1997, **40**, 347.
4. Liebsch, A., *Phys. Rev. B*, 1993, **48**, 11317.
5. Palpant, B., Prével, B., Lermé, J., Cottancin, E., Pellarin, M., Treilleux, M., Perez, A., Vialle, J.L. and Broyer, M., *Phys. Rev. B*, 1998, **57**, 1963.
6. Mariotto, G., Montagna, M., Vilianni, G., Duval, E., Lefrant, S., Rzepka, E. and Mai, C., *Europhys. Lett.*, 1988, **6**, 239.
7. Melinon, P., Paillard, V., Dupuis, V., Perez, A., Jensen, P., Hoareau, A., Perez, J.P., Tuaille, J., Broyer, M., Vialle, J.L., Pellarin, M., Baguenard, B. and Lermé, J., *J. of Modern Phys. B*, 1995, **9**, 339.
8. Serra, L.I. and Rubio, A., *Z. Phys. D*, 1997, **40**, 262.
9. Lermé, J., Palpant, B., Prével, B., Pellarin, M., Treilleux, M., Vialle, J.L., Perez, A. and Broyer, M., *Phys. Rev. Lett.*, 1998 (in press).



Pergamon

NanoStructured Materials, Vol. 12, pp. 311–314, 1999

Elsevier Science Ltd

© 1999 Acta Metallurgica Inc.

Printed in the USA. All rights reserved

0965-9773/99/\$—see front matter

PII S0965-9773(99)00124-5

## THE SIZE DISTRIBUTION OF METAL CLUSTERS PRODUCED IN PLASMA-DISCHARGE HOLLOW-CATHODE SOURCE

A.C. Xenoulis\*, G. Doukellis\*, C. Potiriadis\*, N. Boukos\*, D.S. Vlachos\*  
and Th. Tsakalakos\*\*

\*NCSR Demokritos, 15310 Agia Paraskevi, Athens, Greece

\*\*Rutgers University, Piscataway, New Jersey 08855-0909, USA

**Abstract** – The mean size of Cu clusters produced in a hollow-cathode, dc plasma-discharge source, increases significantly with decreasing flow rate and less pronouncedly with increasing Ar/He abundance ratio and increasing discharge current. The effect of pressure is mixed. Between 0.4 and 0.6 mbar the size is not affected. Above 0.6 mbar, the size increases significantly with increasing pressure. With the help of the above parameters, the mean cluster size can be shifted at will between 20 and 250 Å. Implications concerning the mechanisms associated with clustering in plasma are discussed. ©1999 Acta Metallurgica Inc.

### INTRODUCTION

The full utilization of a plasma generating cluster source (such as the magnetron, the pulsed-arc and the hollow-cathode source) is prevented by the insufficient understanding of clustering in plasma. On the other hand, the influence of various source parameters (including temperature, pressure, velocity and type of the gas and dimensions of the condensation cell) on clustering of neutral particles produced in an oven-heated or supersonic-expansion source has been well studied over the years (1). In the present study the size effect of some of the above classical parameters is investigated, utilizing a plasma generating, hollow-cathode source (2), where (in addition to neutral) positive and negative metal particles coexist during the time of cluster formation (3). An other important difference between an oven-heated and a plasma-discharge source is that in the second the initial concentration of metal particles is not an independent variable, since pressure, velocity and type of the inert gas affect not only the clustering but also the sputtering rate. The purpose of the study is to observe whether and/or to what extent these, well known, parameters are also relevant to clustering in plasma. The only previous commensurate data of which we are aware have to do with geometry and temperature effects studied in a magnetron source (4).

### EXPERIMENTAL

A detailed description and performance of the hollow-cathode source used has been already presented (2). Briefly, metal atoms are sputtered from the inner walls of a hollow cathode under a dc plasma discharge. The discharge is operated under a forced Ar flow at about 1 mbar pressure, leading to the aggregation of atoms to clusters. The clusters are swept by the gas stream through a nozzle, fly inertly through a skimmer and are deposited on carbon—

coated TEM grids located about 50 cm away from the cathode. The deposited clusters are transferred in the air and examined with a Philips CM20 TEM operating at 200 kV.

## RESULTS AND DISCUSSION

In order to observe the effect of flow rate, two different pumps were used. Figure 1 shows that with the smaller pump the mean cluster size and the width of the size distribution ( $110 \pm 22$  Å) are about four times larger compared to those obtained with the larger pump ( $32 \pm 4$  Å). The parameters affected by pumping speed are interaction times and sputtering rates. The sputtering caused by the larger pump ( $9.2 \times 10^{16}$  atoms  $\text{sec}^{-1}$ ) was about three times smaller than that caused by the smaller ( $29.0 \times 10^{16}$  atoms  $\text{sec}^{-1}$ ). Therefore, sputtering rates and interaction times are both partly responsible for the mean size seen in Figure 1.

Figure 2 demonstrates the effect of inert gas pressure on cluster size and sputtering rates. For pressure between 0.4 and 0.6 mbar the cluster size remains the same within the experimental error. Considering that at 0.6 mbar the sputtering rate is by far the highest, these data suggest that for equal number of initial Cu atoms the cluster size would significantly decrease between 0.4 and 0.6 mbar, in contradistinction to the expected trend (1). It is usually assumed that a high gas pressure facilitates coagulation due to better cooling. In the present case, however, certain plasma parameters will also be affected. For instance, the changing pressure will change the electron temperature, thus affecting coagulation and cluster size, as it has been demonstrated by Monte Carlo calculations (5).

The present size distributions were found to follow the lognormal distribution (6), a feature also seen in magnetron clustering (7). Results associated with the three specimens of Figure 2 are shown in Figure 3. Lognormal behavior has been identified exclusively in clustering of neutral particles (6). The reappearance of the same distribution in plasma clustering where charged particles are involved, constitutes an experimental evidence in favor of the theoretical contention that lognormal size distribution is a universal feature of clustering, irrespectively of the particular mechanisms involved (8).

The next source parameter investigated was the discharge current. In general, an increase in discharge current caused an increase in cluster size. For instance, the mean cluster

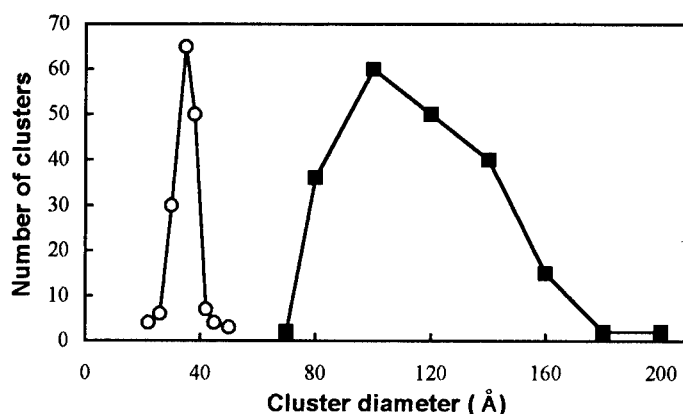


Figure 1. Effect of pumping speed on cluster size distribution (circles: 50 m³/h; squares: 15 m³/h)



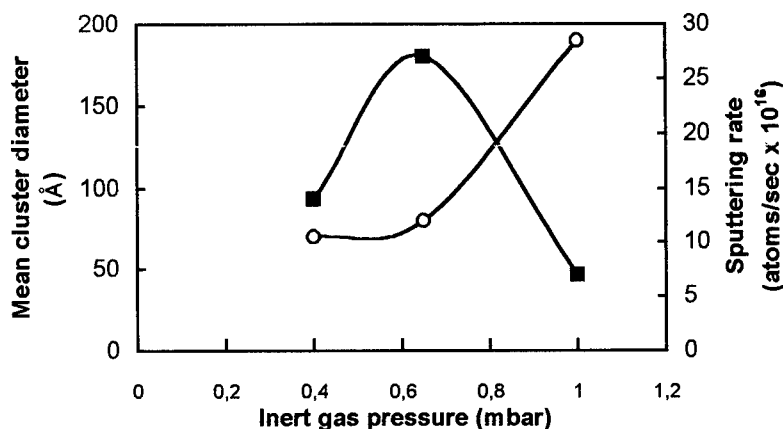


Figure 2. Effect of gas pressure on cluster mean size (circles) and sputtering rate (squares).

diameter increases from 40 Å at 200 mA, to about 60 and 75 Å at 300 and 400 mA, respectively. However, the results are not easily reproducible when big current steps are used. All these seem manifestations of conditioning instabilities known, for instance, to be associated with big voltage changes in particle accelerators.

The last parameter tested was the composition of the inert gas. It was found, for instance, that a mean cluster diameter of 87 Å obtained with a mixture of one part Ar and two parts He, increased to 118 Å when that mixture was replaced by pure Ar. Qualitatively, this is a typical effect of the gas type on size (1).

### CONCLUSIONS

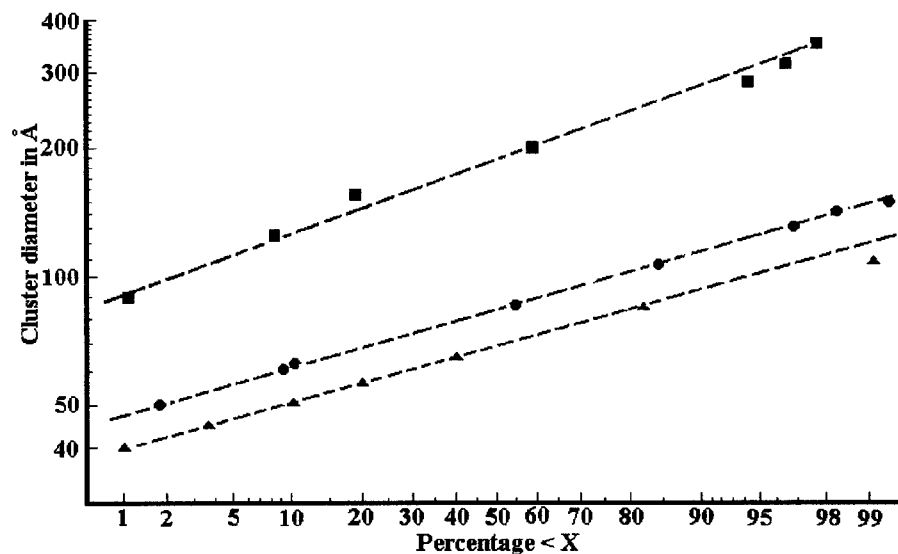


Figure 3. Log normal probability plot of size distribution of the specimens shown in fig. 2. (triangles: 0.4 mbar, circles: 0.65 mbar and squares: 1.0 mbar)

In a plasma-discharge source negatively and positively ionized metal particles coexist during the time of coagulation (3), suggesting that electrostatic interactions should be, at least partially, responsible for clustering in plasma. Nevertheless, the effects of the classical coagulation parameters investigated here (with the exception of pressure) were found, at least qualitatively, in agreement with previous results associated predominantly with clustering of neutral particles (1). Two, more or less mutually exclusive, interpretations seem appropriate. Either the presence of the plasma modifies the interactions between ionized particles to such a large extent that finally they cluster the same way with neutrals; or the examined coagulation parameters are associated with universal size effects, which do not depend on the particular clustering mechanisms involved. We have already intimated that this is the case with the lognormal size distribution, which seems to constitute such a universal property. The effect of flow rate on cluster size must be also universal, because the flow rate determines the interaction time (the later being inversely proportional to the former), which in turn determines the cluster size (the later being proportional to the interaction time). However, the effect of pressure on cluster size presently identified at low pressure, seems to be different in a plasma-discharge source than in an oven-heated source. It should be finally noted that due to the interplay between sputtering and clustering in a plasma-discharge source, a direct quantitative comparison of that source with an oven-heated source demands high quality data, associated with very clearly determined source conditions, which do not seem to be presently available in the literature. In any event, a theory attempting to describe clustering in a plasma source should comply with the size effects presently identified. It should be noted that in a very recent Monte Carlo simulation of clustering in plasma, a lognormal size distribution as well as an effect of pressure on clustering characteristic to the plasma discharge, due to induced plasma electron temperature differences, have been explicitly identified (5).

#### ACKNOWLEDGMENT

This research was supported in part by the Greek Ministry of Development under contract #PENED-1881 and by the International Atomic Energy Agency under contract #9386

#### REFERENCES

1. Haberland, H., in *Clusters of Atoms and Molecules*, I. ed. Haberland, H., Springer Verlag, Berlin, 1995.
2. Xenoulis, A. C., Trouposkiadis, P., Potiriadis, C., Papastaikoudis, C., Katsanos, A. A. and Clouvas, A., *Nanostructured Materials*, 1996, 7, 473
3. Xenoulis, A. C., Doukellis, G., Tsouris, P., Karydas, A., Potiriadis, C., Katsanos, A. A. and Tsakalakos, Th., *Vacuum*, 1998, 50, in press
4. Goto, M., Murakami, J., Tai, Y., Yoshimura, K., Igarasahi, K. and Tanemura, S., *Z. Phys.*, 1997, D40, 115.
5. Vlachos, D., Xenoulis, A. C., and Tsakalakos, T., this volume.
6. Granqvist, C. and Buhrmann, R., *J. Appl. Phys.*, 1976, 47, 2200.
7. Haberland, H., Mall, M., Moseler, M., Qiang, Y., Reiners, T. and Thurner, Y., *J. Vac. Sci. Tech.*, 1994, A12, 2995
8. Soderlund J, Kiss L. B., Niklasson, G. A. and Granqvist, C. G., *Phys. Rev. Lett.*, 1998, 80, 2386



Pergamon

NanoStructured Materials, Vol. 12, pp. 315-318, 1999

Elsevier Science Ltd

© 1999 Acta Metallurgica Inc.

Printed in the USA. All rights reserved

0965-9773/99/\$-see front matter

PII S0965-9773(99)00125-7

## ON THE THEORY OF THE OPTICAL RESPONSE OF AN ENSEMBLE OF NANOPARTICLES

Dirk Uwe Saenger

Institut für Neue Materialien, Im Stadtwald 43, 66123 Saarbrücken, Germany

**Abstract** -- Using a modified mode-coupling approach, incorporating exchange and correlation contributions due to the electron-electron interaction, the optical absorption of an ensemble of nanoparticles in the presence of microscopic disorder is calculated. It is shown, that microscopic disorder generates a significant broadening and redshift of all resonances in the regime where fluctuations of the transitions induced by disorder exceed the electron-electron correlation energy. At lower impurity concentrations, the electron-electron interaction can effectively narrow the resonance lines close to the band gap of the nanoparticles. In the latter regime the absorption spectrum looks like the absorption spectrum of a high-quality bulk semiconductor with the difference, that the level spacing between resonances is enlarged due to quantum-size effects. This spectral feature is measured in a system consisting of GaAs nanoparticles in a crystalline AlAs matrix as grown by molecular beam epitaxy, while in the former regime also the lowest resonances are strongly broadened as usually measured by other methods. ©1999 Acta Metallurgica Inc.

### INTRODUCTION

In a number of physical systems, the traditional approach to electron dynamics, of expanding electron wavefunctions in delocalized plane waves is entirely inadequate. Conspicuous examples are materials, where the electrons are strongly localized due to the strong on-site repulsion, due to strong disorder or due to both interactions, such as the strongly disordered high-Tc-superconductors, amorphous or nanostructured materials. In particular, when applied to systems containing semiconducting or metallic nanoparticles embedded in a non-crystalline (fluid, glassy or polymeric) or a crystalline matrix, the wave functions are strongly localized over the volume of the particles. Especially, systems produced by wet-chemical or colloidal methods [1,2], respectively, metal-organic vapour phase epitaxy (MOVPE) [3,4] or molecular beam epitaxy (MBE) [5] represent excellent systems to study basic properties of physical systems with strongly localized electrons.

In this paper, we are particularly concerned with the optical response of semiconducting nanoparticles embedded in non-crystalline or crystalline matrices. Following a model proposed in a recent publication [6], we investigate a system, where the particles have the same size, shape and impurity concentration, but the different realization of microscopic disorder, which is strongly enhanced at the surface of the particles, makes these particles distinguishable at the microscopic level. An ensemble average over the different realizations of microscopic disorder yields a broadening and redshift of the spectra. The macroscopic optical response of the whole system is considered in the dynamic Maxwell-Garnett approximation, which is exact for cubic lattices [6,7], and corresponds to the random-phase diagrams usually considered in mode-coupling theory (non-linear feedback mechanism). In this paper, we incorporate additional quantum-mechanical modifications, such as exchange and correlation contributions due to the electron-electron interactions, yielding a line narrowing (delocalization) and an additional redshift of the spectra.

As a result, it is shown, that the absorption spectra show a large redshift and a strong broadening for a high surface disorder. In that case, the absorption spectrum looks like the absorption spectrum of a low-quality bulk semiconductor with the difference, that quantum size effects close to the band gap can still be detected due to the larger level spacing. These spectra are measured in systems produced by colloidal methods or by MOVPE [1-4]. Lowering the impurity concentration at the surface, a strong line narrowing and, consequently, a delocalization of the exciton, due to the electron-electron correlation energy for the lowest resonances is possible. In that regime, the absorption spectrum looks like the absorption spectrum of a high-quality bulk semiconductor with the difference that the level spacing between resonances is enlarged due to quantum size effects. Such a spectrum is measured in a system of GaAs nanoparticles embedded in a crystalline AlAs matrix as grown by MBE [5].

The paper is organized as follows. In the next section the model studied will be explained. Furthermore, some results are presented and, at the end of the paper, we draw some conclusions.

## FORMALISM AND RESULTS

In our model [6], we consider a monodisperse ensemble of spherical nanoparticles embedded in a matrix with a electric and magnetic permeability of  $\epsilon_0$  and  $\mu_0$ , respectively. Following Mahan [7], the macroscopic response of the system is described in the framework of a dynamic Maxwell-Garnett approximation, which is exact, if the particles form a cubic lattice. As an input of such a theory, we have to compute the ensemble averaged permeabilities per particle, usually called the average particle [6].

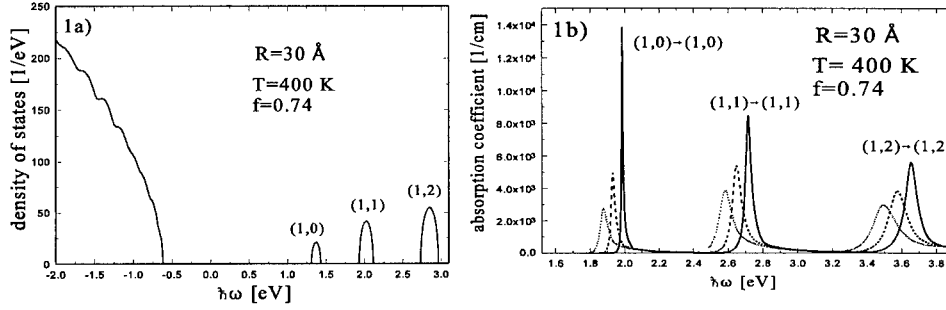


**Fig 1: a)** The density of states per unit energy for particles with a radius of  $R=30\text{ \AA}$  is shown, choosing for the surface disorder parameter  $a$  the value 1. For the lowest conductance band states the radial and angular quantum numbers are indicated. **In b)** the absorption coefficient, varying the surface disorder parameter  $a$ , is drawn. The solid line corresponds to  $a=1$ , the dashed line to  $a=2$ , and the dotted line to  $a=3$ . The hole and electron states which are dominantly involved in the transitions are indicated.

If the particles are not magnetic, we can concentrate the calculations on the computation of the electric permeability, which is defined in the isotropic long wavelengths limit by

$$\epsilon_{\alpha\beta}(\omega) = \epsilon_{\infty} \delta_{\alpha\beta} + \frac{4\pi}{\omega} i e^2 \hbar \int_V \frac{d\mathbf{r}_1}{V} \int_V d\mathbf{r}_2 \int_{-\infty}^{\infty} d\hbar\omega_1 \quad (1)$$

$$\times \bar{m}_{\alpha\beta}(\mathbf{r}_1, \mathbf{r}_2, \omega_1) / \hbar\omega_1 (\hbar\omega - \hbar\omega_1 + i\delta^+)$$

where  $\epsilon_{\infty}$  describes the electric permeability of the bound core electrons. As an input, we have to compute the spectral function  $m_{\alpha\beta}(\mathbf{r}_1, \mathbf{r}_2, \omega)$  of the irreducible current-density correlation function. We consider the vertex corrections due to the electron-electron interaction and the interaction with potential fluctuations in the framework of a shielded potential approximation and the self-consistent Born approximation, respectively (for a detailed discussion of the used approximations see Ref. 6). Explicit calculations are performed for the interband absorption close to the bandgap of GaAs nanoparticles of a radius of  $30\text{ \AA}$  as a model system. In Fig. 1 a, we show the one-particle density of states per unit energy and in Fig 1 b the absorption coefficient, varying the surface disorder parameter  $a$ . For the volume fraction  $f$ , which is occupied by semiconducting nanoparticles, we choose 0.74 (face-centered cubic lattice) and we performed calculations for a temperatures of 400 K. Note that in our model, the absorption spectra are nearly temperature independent for temperatures much smaller than the bandgap of the embedded semiconductor, which is in agreement with measurements in Ref. 5. The potential fluctuations are simulated by short range scatterers  $V_i = U \sum_j \delta(\mathbf{r}-\mathbf{r}_i)$ , where  $U$  represents the strength of the impurity potential. The inhomogeneous impurity concentration in the case of spherical nanoparticles is assumed to be of the form  $n_i(\mathbf{r}) = n_i \{1 + a \exp[-(\mathbf{r}-\mathbf{R})^2/2b^2]\}$ , where  $a$  and  $b$  fix the height and the width of the enhanced impurity concentration

close to the surface. For the free parameter  $n_i U^2$  we choose the value  $30 \text{ eV}^2 \text{Å}^2$  and the width  $b$  of the disordered layer is  $10 \text{ Å}$ . As seen in Fig. 1a), the heavy-hole states are strongly modified by level-mixing effects due to the electron-impurity interaction. They are strongly broadened and are shifted to higher energies due to quantum-mechanical level repulsion effects, resulting in a reduction of the band gap and, therefore, in a redshift of the absorption spectrum. Additionally, the density of states of the heavy hole states looks like the density of states of the bulk material, only in the lowest conductance band states is it possible to detect discretization effects. Furthermore, the linewidth of the one-particle spectral function increases with increasing angular momentum as indicated in Fig. 1a. With the input of these one-particle states, we are able to compute the two-particle states and, finally, the absorption coefficient of the system. The result for the absorption coefficient, varying the surface disorder parameter  $a$ , are drawn in Fig. 1b. As seen, the absorption shifts red and is strongly broadened with increasing surface disorder. The redshift is mainly produced by quantum-mechanical level-repulsion effects between heavy-hole states, as pointed out above. The broadening is produced by the individual realization of microscopic disorder in the particles. Only in the case, when the electron-electron correlation energy is larger than the induced fluctuations, i.e. at lower impurity concentrations at the surface of the particles, a strong-line narrowing effect for the lowest resonance, i.e. an artificial Frenkel exciton, can be observed. Such a spectrum is observed in a system produced by MBE [5].

## CONCLUSION

In conclusion, we have shown, that microscopic disorder has a considerable influence on the absorption spectra of semiconducting nanoparticles. Explicit calculations were performed for small GaAs nanoparticles at the band gap of the embedded semiconductor. A strong broadening and redshift of the absorption spectra occurs with increasing surface disorder. Only in the case, where the electron-electron correlation energy is larger than the induced fluctuations, a strong line narrowing effect for the lowest excitonic resonance (artificial Frenkel exciton) takes place.

## REFERENCES

1. C. R. Cagan et al., Phys. Rev. Lett. **76**, 1517 (1996)
2. C. B. Murray, C. R. Kagan, and M. G. Bawendi, Science **270**, 1335 (1995)
3. R. Nötzel, J. Temmyo, and T. Tamamura, Nature **369**, 131 (1994)
4. M. Grundmann et al., Phys. Rev. Lett. **74**, 4043 (1995)
5. R. Nötzel and K. Ploog, Adv. Materials **5**, 22 (1993)
6. D. U. Saenger, Phys. Rev. B **54**, 14604 (1996)
7. G. D. Mahan, Phys. Rev. B **38**, 9500 (1988)



Pergamon

NanoStructured Materials, Vol. 12, pp. 319-322, 1999

Elsevier Science Ltd

© 1999 Acta Metallurgica Inc.

Printed in the USA. All rights reserved

0965-9773/99/\$-see front matter

PII S0965-9773(99)00126-9

## PARTICLE BEHAVIOR OF NANOCRYSTALLINE 316-STAINLESS STEEL DURING HIGH VELOCITY OXY-FUEL THERMAL SPRAY

M.L. Lau, V.V. Gupta and E.J. Lavernia

Department of Chemical and Biochemical Engineering and Materials Science  
University of California, Irvine, Irvine, CA 92697-2575

**Abstract**--The present paper investigates the particle behavior of nanocrystalline 316-stainless steel powders during high velocity oxy-fuel (HVOF) spray. The feedstock powders were synthesized by mechanical milling to produce flake-shaped agglomerates with an average grain size of less than 50 nm. The powders were then introduced into the HVOF spray to produce a nanocrystalline coating. A mathematical model is developed to study the variation of different agglomerate sizes resulting from the mechanical milling process on the particle behavior during thermal spraying. A generalized Newtonian equation describing the momentum transfer was used, which incorporates a geometric ratio to account for the size and morphological variations of the micron-sized agglomerates with nano-grained structure. Particle velocity from the numerical calculations indicated that the velocity profile depends strongly on the thickness of the particles, which is a function of milling time and milling media.

©1999 Acta Metallurgica Inc.

### INTRODUCTION

Thermal spray is a coating process which has evolved to produce various metallic, non-metallic, and ceramic coatings (1). In recent year, thermal spraying using nanocrystalline feedstock powders has yielded coatings with higher hardness, strength, and corrosion resistance than those of the conventional counterparts (2-5). For instance, high velocity oxy-fuel spray of WC/12Co and WC/15Co nanocomposite coatings shows a 28% increase in hardness while the toughness of the nanocomposite remains constant when compared to that of the conventional coatings (6). More recently, inert gas atomized 316-stainless steel powders were mechanically milled in methanol and liquid nitrogen separately to produce nanocrystalline powders and the powders were thermally sprayed by HVOF (7). The resultant coatings exhibited significant increase in microhardness. For example, an 48% increase in microhardness was observed in the thermal sprayed coating when methanol milled stainless steel powders was used as the feedstock (7). The objective of the present paper is to investigate the particle behavior during the thermal spraying process. In particular, a mathematical model was used to predict the momentum behavior of the micron-sized agglomerates with nanocrystalline grain structure during the HVOF spraying process. The generalized Newtonian momentum equation is changed to account for the variation of the flake-shaped agglomerates produced by mechanical milling.

### EXPERIMENTAL PROCEDURE

Pre-alloyed 316-stainless steel powders (17 wt.% Cr, 12 wt.% Ni, 2.5 wt.% Mo, 1 wt.% Si, 0.1 wt.% C and balance Fe, Sulzer Metco (US) Inc.) with a nominal particle size of  $45 \pm 11 \mu\text{m}$  were chosen for the study. The powders were mechanical milled in either methanol or liquid nitrogen environment for 10 hrs. Subsequently the nanocrystalline powders was thermally sprayed using a Sulzer Metco DJ 2600 HVOF spray system on the 1020-stainless steel substrates. Hydrogen gas was used as fuel with a hypersonic gas velocity of approximately 2000 m/s and a pressure of 0.28 MPa was generated. The details associated with the HVOF experiment can be found elsewhere (7).

The generalized equation describing the velocity profile of the impinging particles can be expressed by the Newtonian equation (8-10). Although the momentum transport between the hypersonic flame gas and the particles involves the drag force, force due to pressure gradients and added mass, Basset history term, and external potential forces, the drag force is dominant in the case of the HVOF thermal spraying (1).

$$V_p \rho_p \frac{dv_p}{dt} = A_p C_{drag} \rho_g |v_g - v_p| (v_g - v_p) \quad [1]$$

$V_p$  is the volume of the particles ( $\text{m}^3$ );  $\rho_p$  and  $\rho_g$  are densities of the particle and flame gas respectively ( $\text{kg}/\text{m}^3$ );  $v_p$ ,  $v_g$  are particle velocity and flame gas velocity (m/s);  $t$  is the time (s);  $A_p$  is particle area ( $\text{m}^2$ ); and  $C_{drag}$  is the drag coefficient (unitless).

Although the drag coefficient of non-spherical particles is difficult to predict due to the influence of particle orientation, the flow patterns are similar to those described for spheres (11). The drag coefficient for spherical particles, which is a function of the Reynolds number, is defined as  $C_{drag} = (1 + 0.189 \text{Re}^{0.632})$  [2] at low Reynolds number range ( $21 < \text{Re} < 200$ ) (1).

The Reynolds number is expressed as  $\text{Re} = \frac{\rho_g d_p v_p}{\eta_g}$  [3], where  $d_p$  is the characteristic particle dimension (m) and  $\eta_g$  is the dynamic viscosity of the gas ( $\text{N}\cdot\text{s}/\text{m}^2$ ).

### RESULTS AND DISCUSSION

Mechanical milling of the as-received stainless steel powders produced flake-shaped agglomerates with the size between  $27\text{--}253 \mu\text{m}$  for the methanol milled powders and  $28\text{--}85 \mu\text{m}$  for the cryomilled powders. The BET surface areas of the as-received and methanol milled and cryomilled powders, determined by a particle surface area analyzer (Coulter SA3100), are shown in TABLE 1. The process of mechanical milling increases the specific surface areas and hence the chemical reactivity of the powders.

The velocity profile of the stainless steel agglomerates and thickness is shown in Figure 1. The area is expressed as the shape of two faces of an ellipse to account for the geometry of the irregular flakes,  $A_d = 2\pi r^2 n$  [4]. In equation [4],  $r$  is the radius of the particle (m) and  $n$  is the aspect ratio (unitless). Furthermore, the volume,  $V_d$  is then expressed



as  $V_d = A_d c$  [5], in which  $c$  is the thickness of the particle (m) measured by scanning electron microscopy.

TABLE I  
Surface Areas of the As-received 316-stainless Steel, Methanol Milled and Cryomilled powders

	Surface area (m <sup>2</sup> /g)
As-received 316-stainless steel powders	0.043
Cryomilled (10 hrs.) powders	0.698
Methanol milled (10 hrs.) powders	9.539

The calculated velocity profile shown in Figure 1 yields the variations in the particle behavior of methanol milled and cryomilled agglomerates. The particle size used in the present mathematical model corresponds to the cumulative weight fraction ( $d_{10}$ ,  $d_{50}$ , and  $d_{90}$ ) of the particle size distribution, determined by a Microtrac Standard Range Particle Analyzer, of the nanocrystalline powders feedstock produced by the mechanical milling process. The particle size distribution for the methanol milled powders indicates a wide size distribution, from 27 to 253  $\mu\text{m}$ . The effect of the wide particle size distribution can be observed in the velocity profiles of the methanol milled powders. The particle velocity increases steeply initially, with respect to the axial distance from the powder injection to the exit of the gun barrel (approximately 70 mm). Then the particle velocity decreases due to the rapid mixing between the fuel gas and the surrounding atmosphere. As the particle thickness increases, the momentum transport decreases due to the increasing drag. According the Figure 1, the methanol milled steel agglomerates with the particle size of 27  $\mu\text{m}$  attains a maximum velocity at approximately 1850 m/s and slowly decelerates to 1275 m/s before reaching the substrate. The velocity profile of methanol milled agglomerates behaves differently than that of cryomilled agglomerates. The surface areas between the methanol and cryomilled agglomerates contributed to the observed differences in the velocity profile. For instance, although the particle size corresponding to the 10 cumulative weight percent between methanol milled ( $d_{10}=27 \mu\text{m}$ ) and cryomilled ( $d_{10}=28 \mu\text{m}$ ) particles differs negligibly, the thickness of the corresponding cryomilled particles is approximately 75% larger than that of the methanol particles. In effect, the momentum transport of the methanol milled agglomerates is more efficient than that of the cryomilled agglomerates. Ongoing studies are continued to determine the energy transport of the methanol milled and cryomilled agglomerates.

## CONCLUSIONS

One-dimensional Newtonian equation is employed to predict the momentum transport between the nanocrystalline 316-stainless steel agglomerates and the flame gas during high velocity oxygen-fuel thermal spraying. A geometric ratio is used to account for the size and morphological variations of the micron-sized agglomerates with nano-grained structure. The calculated particle velocity indicated that the velocity profile depends strongly on the thickness of the particles, which is a function of milling time and milling media. The momentum transport of methanol milled particles is more efficient than that of cryomilled particles due to the difference in particle morphology.

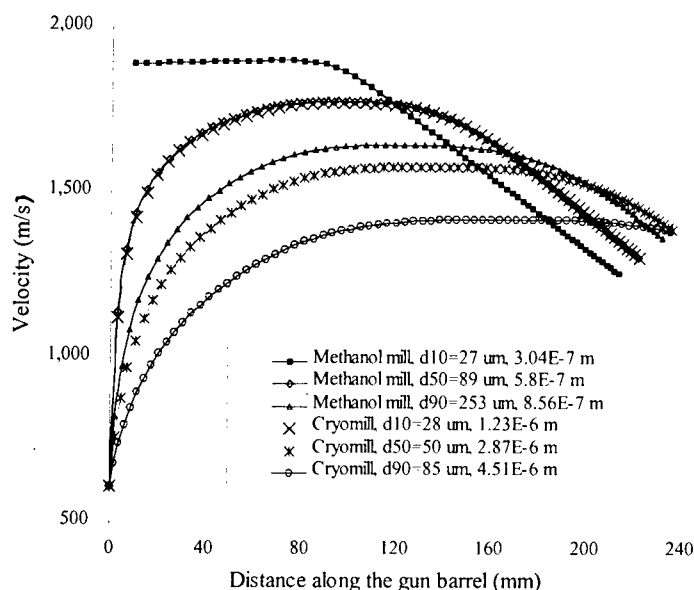


Figure 1. Velocity profile of methanol milled and cryomilled 316-stainless steel agglomerates and thickness along the gun barrel during HVOF spraying.

#### ACKNOWLEDGMENTS

The authors would like to acknowledge the financial support by the Office of Naval Research under grant No.N00014-94-1-0017 and No.N00014-98-1-0569 for the present research. The authors also thank Coulter Corp. (M. Reyes, Miami, Florida) for the donation of the SA3100 surface particle analyzer.

#### REFERENCES

1. Pawlowski, L., *The Science and Engineering of Thermal Spray Coatings*, John Wiley & Sons, England, 1995.
2. Stewart, D.A., Dent, A.H., Harris, S.J., Horlock, A.J., McCartney, D.G. and Shipway, P.H., *Journal of Thermal Spray Tech.*, 1998, in press.
3. Lau, M.L., Jiang, H.G. and Lavernia, E.J., *J. Thermal Spray Tech.*, 1998, in press.
4. Kear, B.H., Skandan, G. and Sadangi, R., High pressure synthesis of nanophase WC/Co/diamond Powders: implications for thermal spraying, presented in Thermal Spray Processing of Nanoscale Materials, 1997, Davos, Switzerland.
5. Tellkamp, V., Lau, M., Fabel, A. and Lavernia, E.J., *NanoStructured Matls.*, 1996, 9, 489.
6. Jia, K. and Fisher, T.E., *J. Thermal Spray Tech.*, 1997, in press.
7. Lau, M.L., Jiang, H.G. and Lavernia, E.J., *Thermal Spraying: Meeting the Challenges of the 21st Century*, Coddet, C., ed. 1998, Nice, France, 379.
8. Liang, X., Lavernia, E.J., Wolfenstine, J. and Sickinger, A., *J. Thermal Spray Tech.*, 1995, 4, 252.
9. Pfender, E. and Lee, Y.C., *Plasma Chem. and Plasma Proc.*, 1985, 5, 211.
10. Tawfik, H.H. and Zimmerman, F., *J. Thermal Spray Tech.*, 1997, 6, 345.
11. Clift, R., Grace, J.R. and Weber, M.E., *Bubbles, Drops, and Particles*, Academic Press, Inc., New York, 1978, p.142.



## THE ROLE OF GRAIN SIZE AND THE PRESENCE OF LOW AND HIGH ANGLE GRAIN BOUNDARIES IN THE DEFORMATION MECHANISM OF NANOPHASE Ni: A MOLECULAR DYNAMICS COMPUTER SIMULATION

H. Van Swygenhoven<sup>1</sup>, M. Spaczer<sup>1</sup>, D. Farkas<sup>2</sup>, and A. Caro<sup>3</sup>

<sup>1</sup> Paul Scherrer Institute, CH-5232 Villigen PSI, Switzerland, helena.vs@psi.ch

<sup>2</sup> MSE, Virginia Polytechnic Institut, Blacksburg, VA 24061, USA, diana@vt.edu

<sup>3</sup> Centro Atómico Bariloche, 8400 Bariloche, Argentina, caro@cab.cnea.edu.ar

**Abstract** - The mechanisms of plastic deformation of computer simulated nanophase Ni are studied for samples with mainly high angle (HA) grain boundaries and with mean grain sizes ranging from 3 to 12 nm, and for samples with mainly low angle (LA) grain boundaries with mean grain size of 5.2 nm. The influence of the grain size and grain boundary type on the deformation mechanism is discussed on the atomic level. ©1999 Acta Metallurgica Inc.

### INTRODUCTION

Nano-crystalline phases have become one focus of attention to material scientists because the Hall-Petch relation, when extrapolated to nanometer range grain sizes, predicts extremely hard materials. However, experimental evidence suggests that in the nanometer range the Hall-Petch relation apparently fails to describe the observations; a new regime appears, possibly controlled by grain boundary plasticity, whose quantitative description is still controversial [1-5].

In nanophase solids a large fraction of atoms (up to 50%) are boundary atoms, thus inter-crystalline, as opposed to intra-crystalline, deformation mechanisms are expected to become relevant. At the same time, dislocation sources inside grains can hardly exist because of size and image force limitations; only dislocation emitted from a boundary can eventually travel across the grain. From these arguments it is then likely to expect a change in regime, from dislocation-dominated Hall-Petch to a boundary dominated new one. The purpose of this paper is to present some results pointing in that direction, which are part of an exhaustive computer simulation study of these systems covering grain sizes between 3 and 12 nm, random and textured orientations, at various temperatures (300-500 K) and loads [6-11].

### SIMULATION METHOD

High load plastic behavior is studied on several computer generated nanophase Ni samples, five with mainly high angle grain boundaries and mean grain size 3.4, 5.2, 8.0, 10.0 and 12.0 nm, and two with mainly low angle grain boundaries and a mean grain size of 5.2 nm. For details of simulation procedure and sample properties we refer to other contribution of the same authors in this conference and to [6-11]. The relaxed samples are loaded under uniaxial

stress of 1.5 GPa and strain-time curves are recorded. The deformation mechanism on an atomic level is studied by visual inspection of slices, by using local crystalline order (see the other contribution to this conference), and by images obtained in the 3D CAVE™ virtual reality environment at Virginia Tech. ([www.cave.vt.edu](http://www.cave.vt.edu)).

## RESULTS AND DISCUSSION

Visual inspection of sample slices reveal some characteristic features : Prior to deformation, grain interior is free of extended defects both in the high and low angle samples. We particularly focus our attention to atoms with hcp environment because they reflect the possible presence of  $a_0/6[112]$  partial edge dislocations in the fcc structure. In fact a grain traveled across by such a dislocation shows a pair of neighboring  $\{111\}$  planes with atoms having local hcp environment. In small grains, dislocations can not be created by sources inside the grains, but at the interfaces. There we observe small clusters of atoms with hcp environment; their number is larger in the LA samples than in the random case. We also observe that at the largest grain size studied (12 nm) the boundaries are less disordered, with faceted shapes.

Fig. 1a shows the high load plastic deformation of the HA samples with different mean grain sizes. The strain rate is plotted as function of grain size in Fig. 1b. For grain sizes between 12 and 8 nm, the strain rate is rather independent of the grain size, but for smaller grain sizes the strain rate increases. This indicates a change in the deformation mechanism as the grain size becomes smaller.

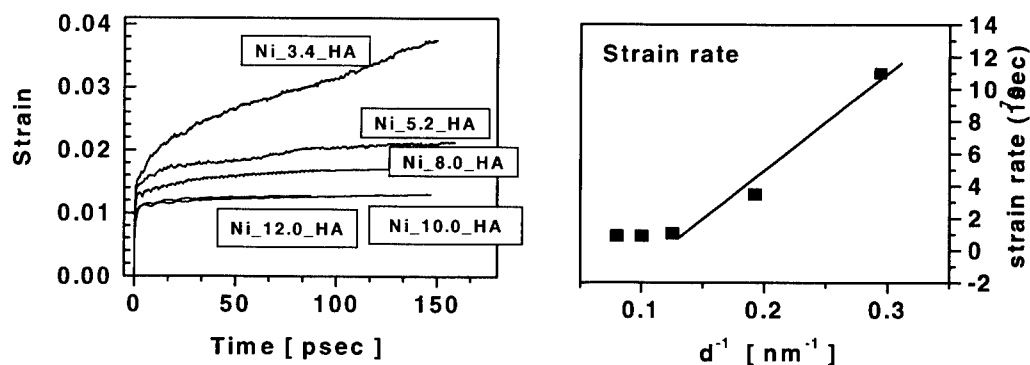


Fig. 1. High load plastic deformation at various average grain sizes

In previous work we discussed the deformation mechanism for grain sizes below 8 nm in terms of a model based on GB viscosity controlled by a self-diffusion mechanism at the disordered interface, activated by thermal energy and stress [8-11]. We calculated the activation energy and found a value comparable for the migration energy for self-diffusion. The reported  $1/d$  dependence of strain rate, which is represented by the straight line in Fig. 1b is a consequence of a geometric argument: grain boundaries act as slip channels and their number

per unit volume follows the surface to volume ratio of the sphere,  $1/d$ . This argument certainly has its limitations when going to larger grain sizes, because the boundaries do not form channels in the limit  $D/d \rightarrow 0$ , where  $D$  is the grain boundary width. What Fig. 1 shows is a transition between an inter grain channeled slip behavior for  $d \leq 8\text{nm}$  and an intermediate mechanism controlled by a decreasing contribution from GB sliding and an increasing contribution of intra grain dislocation slip. There are several experimental indications for such a transition [1-5].

In spite of our efforts, we have been yet unable to detect significant dislocation activity even in the 12 nm HA samples; however in textured (LA) samples, where the larger degree of coherence in the interfaces helps transferring the shear component of the applied stress into the grain interior, clear motion of partial edge dislocations is observed already at an average grain size of 5.2 nm. We performed visual observations of this deformation mechanism at the 3D visualization in the CAVE<sup>TM</sup> at Virginia Tech. Time as well as 3D navigation appeared to be a powerful technique to locate and identify dislocations, measure their Burgers vectors, characterize the nature of the stacking fault and follow the process by which partials are created at the boundary, travel across the grain and annihilate at the facing boundary.

Making slices of several deformed HA samples we find an increasing number of small hcp planes in the grain boundary of the deformed sample. Fig. 2 shows a slice of a HA sample with 5.2 nm average grain size before (a) and after (b) deformation : small hcp clusters grow during deformation into plane, staying in the grain boundary. At larger grain sizes, we observed relatively less hcp planes at the same deformation time, the deformation level however being much less. This indicates a transition to another deformation mechanism, which probably will be a mechanism based on dislocations as is well known for coarse grain polycrystalline material.

Fig. 3 shows three pictures taken in the CAVE<sup>TM</sup> at three different moments of deformation. For clarity we removed the fcc atoms, colored the GB atoms blue and the hcp atoms red. On the first picture we look inside the grain and observe in the upper right corner a small hcp cluster. On the second picture the creation of the stacking fault well inside the grain can be observed. A movie of this process can be seen in [www.cmsms.vt.edu](http://www.cmsms.vt.edu).

## CONCLUSIONS

We have shown that in samples with mainly high angle grain boundaries the strain rate increases with decreasing mean grain size (8 nm - 3 nm). At these grain sizes the deformation is fully accommodated by the grain boundaries producing slide of grains against each other. Above a critical value in the range of 10 nm, the strain rate becomes independent of the grain size indicating a transition into a new regime. We have also shown that there is a considerable influence of the grain boundary structure on the deformation process of similar size nano samples. In samples with mainly low angle grain boundaries the deformation has also contributions from intra grain slip due to partial dislocations which create stacking faults inside the grains.

## REFERENCES

1. P.G. Sanders, J.A. Eastman, J.R. Weertman, *Acta Mater.*, 1997, 45(10) 4019
2. K. Lu, H.Y. Zhang, Y. Zhong, H.J. Fecht, *J. Mater. Res.*, 1997, 12(4), 923
3. R.W. Siegel, G.E. Fougere, *Nanostruct. Mater.*, 1995, 6, 205
4. V.Y. Gertsman, M. Hoffman, H. Gleiter, R. Birringer, *Acta Met. Mater.*, 1994, 42, 3539
5. R.Z. Valiev, et al. *Materials Science Forum*, 1997, 235-238, 497
6. H. Van Swygenhoven and A. Caro, *Nanostruct. Mater.*, 1997, 9(1-8) 669
7. H. Van Swygenhoven and A. Caro, *Mater. Res. Symp.*, 1997, 492
8. H. Van Swygenhoven and A. Caro, *Appl. Phys. Lett.*, 1997, 71, 12
9. H. Van Swygenhoven, M. Spaczer, A. Caro, *Proc. MRS Fall Meeting*, 1997
10. H. Van Swygenhoven, M. Spaczer, A. Caro, *Proc. TMS Fall Meeting*, 1998
11. H. Van Swygenhoven, M. Spaczer, A. Caro, submitted for publication

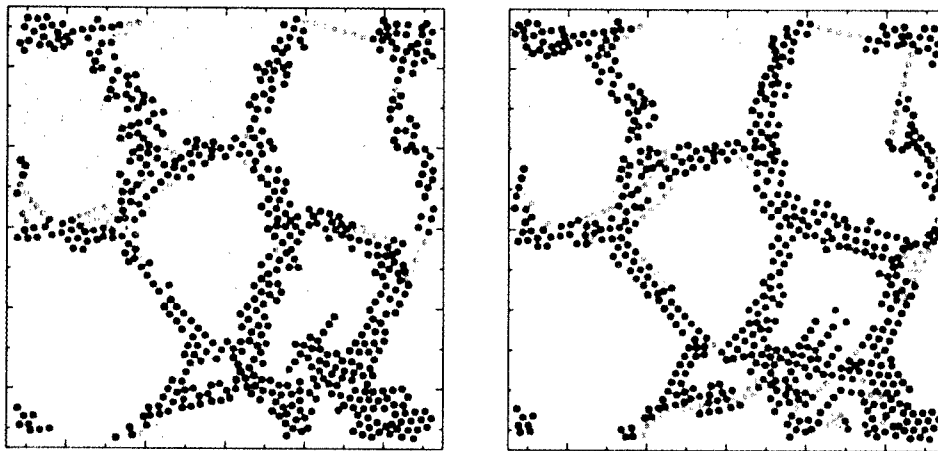


Fig. 2. Typical configuration in Ni with HA grain boundaries before and after deformation  
(Orange circles are hcp atoms, green (blue) circles are other 12 coordinated (non-12 coordinated) atoms, open circles are fcc atoms)

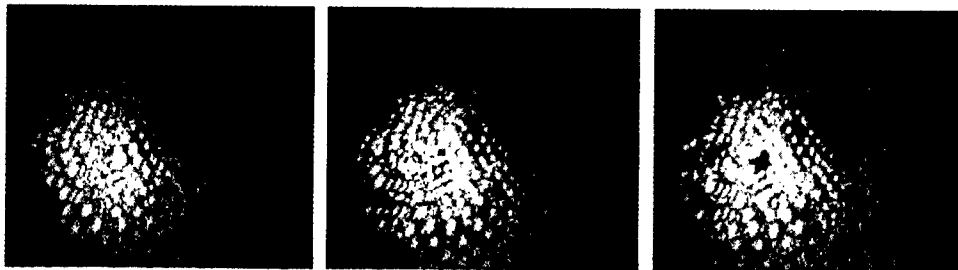


Fig. 3. The motion of a stacking fault toward the grain interior in textured (LA) Ni.  
( Red/blue spheres are hcp/GB atoms, while empty space indicates the removed fcc atoms )



Pergamon

NanoStructured Materials, Vol. 12, pp. 327–332, 1999

Elsevier Science Ltd

© 1999 Acta Metallurgica Inc.

Printed in the USA. All rights reserved

0965-9773/99/\$—see front matter

PII S0965-9773(99)00128-2

## THE REAL ORIGIN OF LOGNORMAL SIZE DISTRIBUTIONS OF NANOPARTICLES IN VAPOR GROWTH PROCESSES

L. B. Kiss, J. Söderlund, G. A. Niklasson, and C. G. Granqvist

Department of Materials Science, The Ångström Laboratory, Uppsala University  
P. O. Box 534, SE-751 21, Uppsala, Sweden

**Abstract** *In modern nanoparticle production methods, such as inert-gas evaporation, a strong effort is made to avoid coagulation of particles. Therefore, the classical coagulation models are not suitable for predicting the particle size distribution. This paper presents a new model that explains lognormal particle size distributions from first principles in a physically realistic way, without coagulation. The model is completely different from the previously applied growth models; it is based on a random residence time approach, where the time available for the particles to grow is random and determines the size distribution. The model is generally relevant in fields such as nanoparticle physics, aerosol science, environmental science and fractal growth, whenever particle growth occurs during transport through a growth zone due to diffusion and drift. Predictions made from the model agree with published experimental data obtained with the inert-gas evaporation technique.*

©1999 Acta Metallurgica Inc.

### INTRODUCTION

The particle size distribution of a finely divided system is often found to be lognormal (1). This is an important aspect of nanoparticle science (1–10), soil science (11), environmental science (12, 13), biology (14) and medical science (15). A random physical quantity has a lognormal distribution if its logarithm is normally distributed. The earliest models of the lognormal distribution were based on Kolmogorov's simple idea (see in (1)) of stone cracking where the relative change of the fragment volumes were taken to be stationary random variables. The same idea, in a time-reversed fashion, was used later by Granqvist and Buhrman (1) in a growth model attempting to explain the origin of lognormal distributions of gas-evaporated nanoparticles (16–19). Lognormality in this case is obtained by realizing that the stationary relative volume change corresponds to a simple random process: a random walk with drift on an exponential scale. Since the random walk, with or without drift, yields a normal distribution on the exponential scale, the distribution is lognormal on a linear scale.

These models are mathematically correct but their physical applicability is limited by the need of stationarity of the relative growth fractions during an elementary growth process.

More recent theories on lognormal distributions are based on related but more sophisticated models of coagulation due to Smoluchowsky (5). The Smoluchowsky model deals with a *closed system* where an initially large population of small particles coagulate. Coagulation and mass conservation controls the process. Over time, the mean particle size increases and the system gradually runs out from small particles. There are a large number of possible different solutions of the Smoluchowsky model and the lognormal distribution is only one of many possibilities. Within the frame of this model, it seems to be very hard to find the reason of the generality of lognormal distributions in fine particle systems.

Friedlander and Wang (6) introduced a model for the "self-preserving" lognormal size distribution. They assumed an initial lognormal size distribution and sought a solution consistent with the Smoluchowsky model, such that the distribution remains lognormal throughout the coagulation process even if the mean particle size and the width of the distribution change. Note that it was not explained how the distribution initially became lognormal.

In today's theories (see (7, 8) and references therein), the situation is similar. In both analytical and numerical models, the lognormal distribution is *postulated* and the system is forced to stay in the lognormal state, or at least the initial distribution of the particles is taken to be lognormal. It is therefore worthwhile to ask the following question: is there any way to predict the lognormal distribution *from first principles*, in a physically realistic way?

This question becomes even more important considering that in powerful modern nanoparticle fabrication methods (16–19), such as the inert gas evaporation and chemical vapor deposition techniques, the relevant physical system is *not a closed, relaxing system*, it is the opposite; *an open, stationarily driven system*. In this case, models based on the theory of Smoluchowsky are irrelevant. Still, the distribution of particle sizes is often experimentally found to be lognormal (3–10).

### THE RANDOM GROWTH DURATION MODEL

The model is based on the following key assumptions:

- i* There is an active zone where the particle growth takes place. Outside this zone the growth is negligible;
- ii* Small nucleus particles enter into the active zone and travel through it. The particles are collected either at the end of the zone, or further away at a fixed location;
- iii* Particle transport occurs through diffusion and drift;
- iv* The time dependence of particle size in the active zone is a power function of time with an arbitrary power exponent (including the case of linear time dependence).

Note that assumption *iv* is trivial if the particle growth is due to atomic vapor absorption.



which provides a growth linear in time. Another practical case is fractal growth, where the time dependence is a power function of time with exponent usually different from 1.

The model, based on assumptions *i-iv*, was used in extensive numerical simulations (2), where the residence time distribution was determined as a function of the relative influence of diffusion transport versus drift transport. Given the drift velocity  $\delta$ , a critical drift velocity  $\delta_0$  is defined such that the mean residence times due to diffusion and to drift are equal. It is easily shown that  $\delta_0 \propto D/L$ , where  $D$  is the diffusion coefficient and  $L$  is the size of the active zone. The situation when  $\delta/\delta_0 \gg 1$  is referred to as the strong drift case. In this case, the particle transport is to a major extent due to drift. This is often true in real experimental situations, for example due to convection. The simulations showed that the residence time distribution is exactly lognormal in the strong drift case (2). Problems similar to this are treated in the field of random processes where they are known as "residence time problems" or "first passage time problems" (22). No analytic solution exists for this particular problem in the practical case of strong drift, not even in one dimension (23).

In Figure 1, a particle size distribution obtained at medium drift is shown. The number of particles in this simulation was  $10^5$  and the size of the growth zone was 200. In Figure 2, the same data are shown in a log-probability plot. The straight line in this plot indicates that the distribution is lognormal with striking accuracy. It should be emphasized that the lognormal size distribution is obtained from first principles on a physically sound basis. The model can be expected to be useful in a wide range of particle systems where conditions *i-iv* apply.

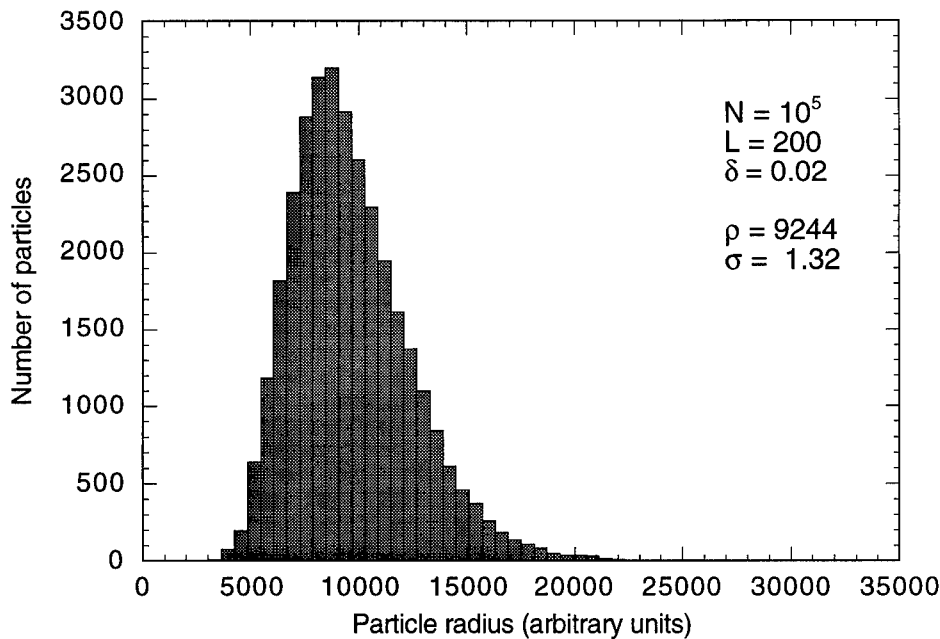


Figure 1. Histogram of simulated particle sizes obtained at medium drift,  $\delta = 12\delta_0$ .

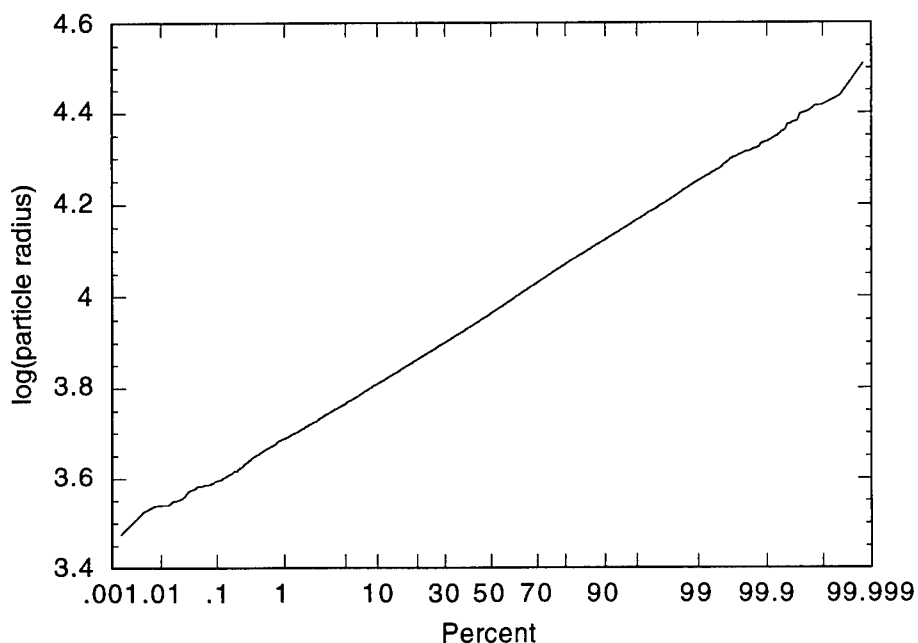


Figure 2. Log-probability plot of the data shown in Fig. 1.

## EXPERIMENTAL VERIFICATION AND TECHNICAL APPLICATIONS

The roles of drift and diffusion in relation to the size  $L$  of the growth zone were investigated. In Fig. 3, the normalized geometric mean particle size  $\rho/L^2$  is plotted versus the normalized drift velocity  $\delta/\delta_0$ .  $\rho$  is the geometric mean (median) particle size. The data points suggest a scaling law between  $\rho/L^2$  and  $\delta/\delta_0$ . Also in Fig. 3, another scaling law is obtained, which interrelates the geometric standard deviation  $\sigma$  and the normalized drift velocity  $\delta/\delta_0$ . Since the quantity  $\sigma$  determines the relative width of the lognormal distribution, the results provide key information for technical applications, since the practical use of nanoparticles requires both a small median size and a narrow size distribution. Published experimental results obtained with the inert-gas evaporation technique are in excellent agreement with the strong drift region of the quantity  $\rho/L^2$  in Fig. 3 (2).

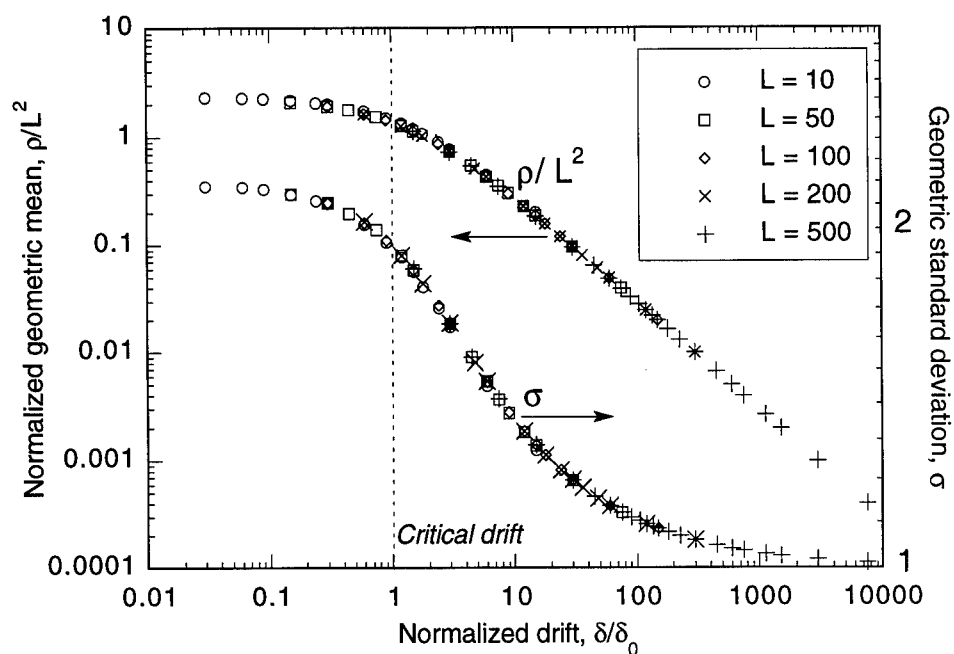


Figure 3. Scaling plots of key parameters for nanotechnology: the mean particle size and the size distribution width. Both quantities decrease with increasing drift.

### CONCLUSION

A new model provides insight into the physical origin of lognormal particle size distributions found in open, stationary systems common in modern nanotechnology. The model is based on a residence time approach, where the size distribution is determined by the distribution of random growth times, instead of the commonly used coagulation models. To our knowledge, this is the first model able to explain from first principles the size distribution of nanoparticles made with the gas evaporation technique and similar methods. Predictions made from the model are in good agreement with experimental data, and can also be used to optimize the production of nanoparticles for technical applications.

### REFERENCES

1. Granqvist C G and Buhrman R A 1976 *J. Appl. Phys.* **47** 2200
2. Söderlund J, Kiss L B, Niklasson G A, Granqvist C-G 1998 *Phys. Rev. Lett.* **80** 2386
3. Kaatz F H, Chow G M, Edelstein A S 1993 *J. Materials Res.* **8** 995

4. Yun Xiong, Pratsinis S E 1991 *J. Aerosol Sci.* 22 637
5. Smoluchowsky M V 1917 *Z. Phys. Chem.* 92 129
6. Friedlander S K and Wang C S 1966 *J. Colloid Interface Sci.* 22 126
7. Lee K W, Lee Y J, Han D S 1997 *J. Colloid and Interface Sci.* 188 486
8. Otto, E, Stratmann F, Fissan H, Vemury S, Pratsinis S E 1994 *Particle & Particle Syst. Charact.* 11 359
9. Wang C R, Huang, R B, Liu Z Y, Zheng L S 1994 *Chem. Phys. Lett.* 227 103
10. Heintzenberg, J 1994 *Aerosol Sci. Technol.* 21 46
11. Wagner L E, Ding D 1994 *Trans. ASAE* 37 815
12. Kim Y, Sievering H, Boatman J, Wellman D, Pszenny A 1995 *J. Geophys. Res.* 100 23027
13. Yue G K, Thomason L W, Poole L R, Wang P-H, Baumgardner D, Dye J E 1995 *Geophys. Res. Lett.* 22 2933
14. Koziol J A 1996 *J. Theor. Biol.* 180 81
15. Marinov M I 1984 *Spectroscopy Lett.* 17 1
16. Siegel R W, 1991 *Annu. Rev. Matter. Sci.* 21 559
17. Hayashi Ch, Uyeda R, Tasaki, A, editors 1997 *Ultra-Fine Particles: Exploratory Science and Technology*, Noyes, Westwood
18. Gleiter H 1992 *Nanostruct. Mater.* 1 1
19. Oda M 1996, in Ref. (12) 133
20. Kottler F 1950 *Franklin Inst.* 250 339
21. Irani R R 1959 *J. Phys. Chem.* 63 1603
22. Doering Ch R, Kiss L B, Shlesinger M F, editors, 1997 *Unsolved Problems of Noise* World Scientific, Singapore, London
23. Doering Ch R 1997, in Ref. (22)



## PLASTIC DEFORMATION OF PURE SILICON NANOCRYSTALS BY MOLECULAR DYNAMICS

Masao DOYAMA<sup>1)</sup>, Tadatosh NOZAKI<sup>1)</sup>, Yoshiaki KOGURE<sup>1)</sup>,  
and Tatsuo YOKOTSUKA<sup>2)</sup>,

1) Teikyo University of Science & Technology, Uenohara, Yamanashi 409-0193 Japan,  
e-mail: doyama@ntu.ac.jp

2) Matsushita Research Institute Tokyo, Inc. 3-10-1 Higashimita, Tamaku, Kawasaki-City,  
Kanagawa 214 Japan

**Abstract** -- This paper is the results of high speed deformations of pure silicon nano crystals using the molecular dynamics. The paper suggests that plastic deformation may be possible for the silicon with a high speed deformation even at room temperature. The potential used was three body Stillinger-Weber potential.

The size of a crystal is  $6(X) \times 16(Y) \times 2(Z)$  [nm].  $x$ ,  $y$  and  $z$  axes are taken in  $[\bar{1}10]$ ,  $[\bar{1}\bar{1}2]$  and  $[111]$  direction, respectively.  $[110]$  direction is the cutting direction.  $(111)$  is the cutting plane and a slip plane. A sharp vertical solid edge was advanced in the  $x$  direction with a speed of 10 m/s. The simulation was extended up to 400,000 steps.

In front of the cutting edge, atoms are pushed up. The chip becomes amorphous. The creation of dislocations was not clearly observed, instead the amorphous region extended on the surface of cutting.

Another nano size single crystal was compressed using molecular dynamic method. The surfaces are  $(111)$ ,  $(\bar{1}10)$  and  $(\bar{1}\bar{1}2)$ . The compressed direction was  $[\bar{1}\bar{1}\bar{1}]$ . It was found that silicon crystals are possible to be compressed with a high speed deformation.

©1999 Acta Metallurgica Inc.

### Introduction

Micromachining is becoming a quite important process of electronic industries. Device production process of silicon is also important and the scale is becoming finer and finer. Silicon is brittle at room temperature and cannot be deformed plastically. In these processes, micromachining is one of the important processes in the field of electronic devices. Cutting, compression and shearing of single crystals have been simulated using molecular dynamics. In this paper silicon single crystals were cut by idealized tools. Compression and are also performed by simulation.

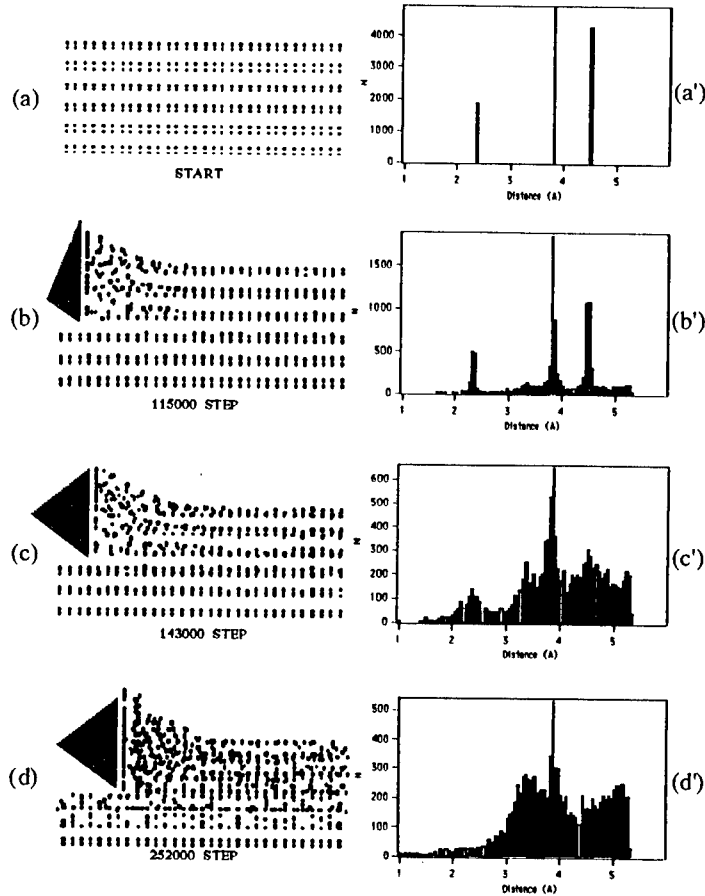


Fig. 1. Projection of atomic positions on  $(\bar{1}\bar{1}2)$  planes in three layer mode and radial distribution functions near the cutting tool for corresponding steps.

### The potential and model

The potential used here was proposed by Stillinger and Weber[1-3]. The specimen used was a rectangular three dimensional single crystal having 1116 atoms with surfaces  $(\bar{1}\bar{1}0)$ ,  $(\bar{1}\bar{1}0)$ ,  $(1\bar{1}\bar{2})$ ,  $(\bar{1}\bar{1}2)$ ,  $(111)$ , and  $(\bar{1}\bar{1}\bar{1})$ . The simulation of cutting a thin layer off the  $(111)$  surface of silicon has been carried out. The size of a crystal is  $6.0 [x] \times 1.6 [y] \times 2.0 [z]$  [nm].  $x$ ,  $y$ , and  $z$  axes are taken in  $[\bar{1}\bar{1}0]$ ,  $[\bar{1}\bar{1}2]$ , and  $[111]$  directions, respectively.  $[\bar{1}\bar{1}0]$  direction is the cutting direction.  $(111)$  is a slip plane. A sharp solid edge shown in Fig. 1 was advanced in the  $x$  direction with a speed of 10 m/s. All surfaces were free. The time step

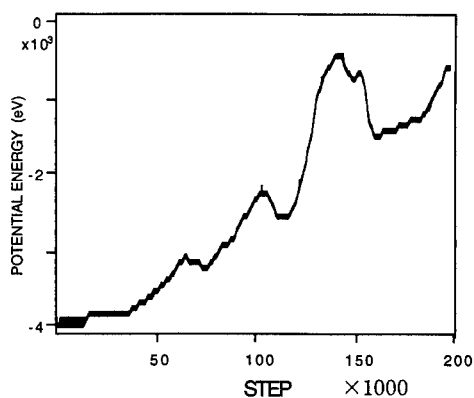


Fig. 2. Crystal energy of the specimen during cutting.

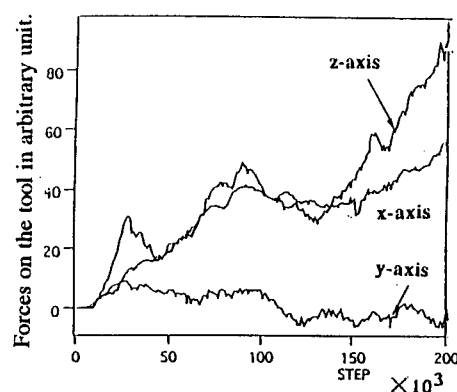


Fig. 3. Force on the tool during cutting.

interval was taken to be  $1 \times 10^{-16}$  sec. The simulation was performed up to 400,000 steps. The thickness of the cut was set to 2, 4 and 6 atomic layers of silicon from the top of the crystal. The kinetic energy was reduced to zero (quench) every 100 steps. The specimen for compression is the same as that for cutting. The crystal was uniformly compressed in the  $[\bar{1}\bar{1}1]$  direction.

### Results and discussions

The position of atoms projected onto the (112) plane, are shown in Fig. 1. Figures 1 (a), (b), (c) and (d) are at the start of cutting, 115,000, 143,000 and 252,000 steps, respectively. Atoms in front of the cutting edge were severely displaced and near the cutting

edge, atoms were pushed up. The deformed region next to the tool became amorphous. In Fig. 1 the radial distribution function in this region is also shown. Figures 1(c) and (d) show the region is amorphous. The slip plane is parallel to the cutting direction. The creation of dislocations was not clearly observed, but the amorphous region was extended. Moreover the cut surface also became amorphous as the cutting proceeded. The crystal energy against time step is plotted in Fig. 2. The forces on the tool are plotted in Fig. 3. The energy of the specimen increased as the cutting proceeds up to 60,000 steps. At 60,000 steps, the chip was plastically deformed and became amorphous. The crystal also became amorphous. Figure 4 shows the projection of atomic positions on  $(\bar{1}\bar{1}2)$  during compression. Figure 5 is the crystal energy of the specimen during compression and Fig. 6 is the stress on the tool during compression.

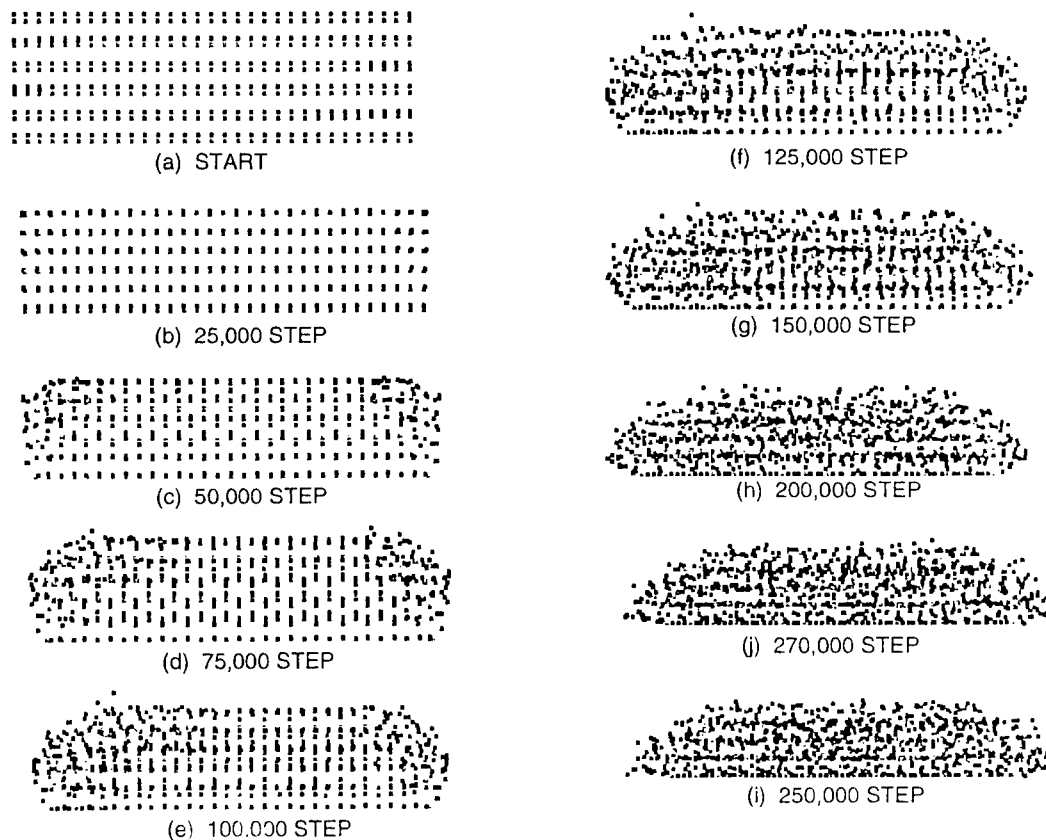


Fig. 4. Projection of atomic positions on  $(\bar{1}\bar{1}2)$  during compression.



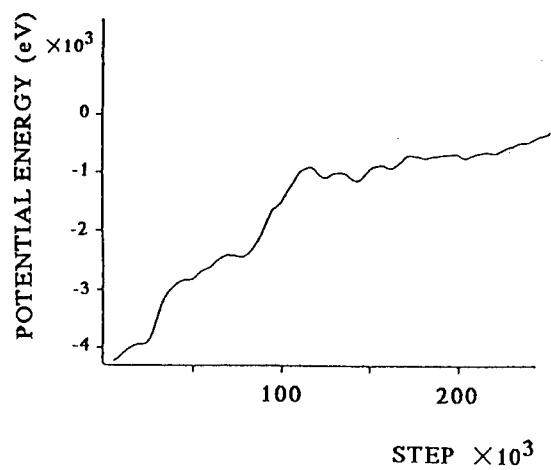


Fig. 5. Crystal energy of the specimen during compression.

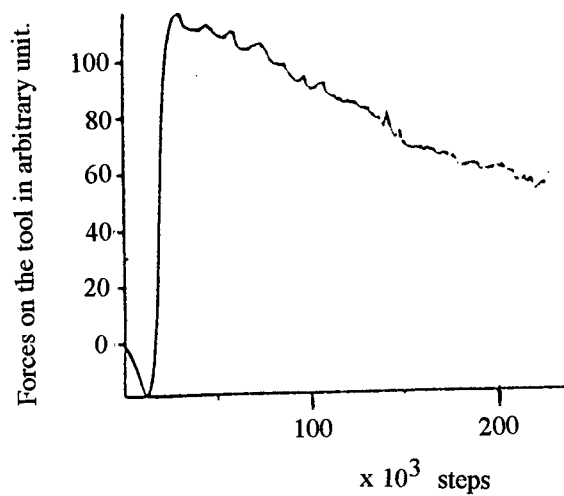


Fig. 6. Force on the tool during compression in [111].

## Conclusion

The results presented in Figs. 1-3 were for a cutting speed of 10m/s but results have also been carried out for various speeds between 10 and 50 m/s. In all cases the results are qualitatively the same with amorphisation occurring in all cases, first in the area near the tool and then spreading across the entire crystal as time progresses. Similar results also obtained for copper show a qualitatively different behavior. In this case the specimen surface did not become. This was determined by examination of the radial distribution function in case of copper similarly to the way it was obtained for silicon in Fig. 1. In copper the atoms moved and shuffled much more than in silicon where dislocations were never observed, the specimen always becoming amorphous. Silicon single crystals were also found to be harder than those of metals.

The compression simulations of silicon also showed that under the conditions of high speed compression, silicon could be plastically compressed. From this pilot study with small crystals we conclude that further investigation with larger crystal sizes could yield important information concerning the strength of materials and the way in which they respond under various deformations.

## Reference

1. Stillinger, F. H. and Weber, T. A., *Phys. Rev.* 1985, B31, 5262.
2. Stillinger, F. H. and Weber, T. A., *J. Phys. Chem.* 1983, 87, 2833.
3. Stillinger, F. H. and Weber, T. A., *J. Chem. Phys.* 1984, 80, 4434.



## ON THE NATURE OF GRAIN BOUNDARIES IN NANOCRYSTALLINE DIAMOND

P. Keblinski<sup>a,b</sup>, S. R. Phillpot<sup>a</sup>, D. Wolf<sup>a</sup> and H. Gleiter<sup>b</sup>

<sup>a</sup> Materials Science Division, Argonne National Laboratory, Argonne, IL 60439, USA.

<sup>b</sup> Forschungszentrum Karlsruhe, 76021 Karlsruhe, Germany.

**Abstract:** *The atomic structures of a few representative large-unit-cell grain boundaries thought to largely determine the behavior of nanocrystalline diamond are determined via Monte-Carlo simulation. In these highly disordered grain boundaries up to 80% of the C atoms exhibit local  $sp^2$  bonding. However, because the three-coordinated C atoms are poorly connected to each other, graphite-like electrical conduction through the grain boundaries is unlikely without "bridging" impurities. Surprisingly, based on their fracture energies, the high-energy, large-unit-cell boundaries are more stable against brittle decohesion into free surfaces than low-energy ones and perhaps even the perfect crystal. ©1999 Acta Metallurgica Inc.*

### INTRODUCTION

The low-pressure synthesis of rather pure nanocrystalline diamond films from fullerene precursors [1] suggests that for a small enough grain size the diamond structure may be energetically preferred over graphite [2]. Due to the small grain size of typically about 15 nm in these films [3], a non-negligible fraction of the carbon atoms is situated in the grain boundaries (GBs). The surprisingly high wear resistance [4] of these films even after the substrate is removed and their high corrosion resistance [5] suggest that the grains are strongly bonded together. Also, grain-boundary carbon is thought to be responsible for the absorption and scattering of light in these films, their electrical conductivity and electron-emission properties [5]. In spite of all these indications of a possibly critical role of GB carbon in the remarkable properties of nanocrystalline diamond films, to date the atomic structures of the GBs are essentially not known.

By contrast with silicon, carbon can form both  $sp^3$ - and  $sp^2$ -hybridized electronic states, as evidenced by the existence of two energetically rather similar bulk phases, diamond and graphite. In highly disordered environments one can expect that the tetrahedral bonds of diamond-like carbon atoms can only be stretched and distorted to a certain degree before changing hybridization from  $sp^3$  to  $sp^2$ . Like dangling bonds in silicon GBs, three-coordinated C atoms can be expected to be electro-optically active; however, by contrast with silicon, the p electrons in  $sp^2$ -bonded, graphite-like local environments can, at least in principle, be expected to be rather mobile - provided the three-coordinated C sites are spatially connected to each other. The graphite-like electrical conductivity of amorphous carbon, with up to 80% of the atoms being three-coordinated [6], provides evidence for such behavior. It therefore appears that diamond GBs have a potential for becoming electrically conductive.

The main goal of this study is to elucidate the effects of  $sp^3$  vs.  $sp^2$  bonding, with particular emphasis on the role of nearest-neighbor coordination, in the atomic structure, energy and stability of a few representative GBs thought to largely determine the behavior of nanocrystalline diamond. Throughout we use Tersoff's semi-empirical carbon potential [7] rather than a more sophisticated, electronic-structure based approach (such as the tight-binding or Car-Parrinello methods). This choice is motivated by the fact that our simulations of large-unit-cell GBs involve typically several thousand atoms and very long simulation times. Our simulations reveal that typically up to 80% of the C atoms in these highly disordered grain boundaries exhibit local  $sp^2$ -type bonding. However, because the three-coordinated C atoms are poorly connected to each-other, any type of graphite-like electrical conduction through the GBs is not likely, unless "bridging" impurities provide the missing connections. Surprisingly, based on their fracture energies, the *high-energy*, large-unit-cell boundaries are more stable against brittle decohesion into free surfaces than the low-energy ones and apparently even the perfect crystal, a finding that may partially explain the high mechanical strength and good corrosion and wear resistance of nanocrystalline diamond films. (For a more comprehensive account of our results, see Ref. 8.)

## MODEL GRAIN BOUNDARIES AND SIMULATION RESULTS

Recent molecular dynamics simulations of bicrystalline GBs in Si [9] demonstrated the importance of high-temperature equilibration. Therefore, by contrast with earlier zero-temperature simulations of diamond GBs [10-13], here we determine *high-temperature equilibrated* GB atomic structures and energies using Monte-Carlo simulations. Furthermore, a recent molecular dynamics study of fully dense nanocrystalline Si with a uniform grain size that was grown from the melt into which small, randomly oriented crystalline seeds were inserted [14], exposed remarkable similarities between the highly constrained GBs in such a model nanocrystalline microstructure and *high-energy, large-unit-cell bicrystalline* GBs [9]. This study suggests that a nanocrystalline microstructure with random grain misorientations and a small grain size may be viewed as a filter for singling out only the large-unit cell or incommensurate, mostly high-energy boundaries in the GB phase space comprised of the five macroscopic GB degrees of freedom [14]. Without actually simulating nanocrystalline diamond directly, these insights enable us to choose a few bicrystalline GBs for this study as representative for the GBs likely present in nanocrystalline diamond.

In practice, the incommensurate or large-unit-cell GBs in a nanocrystalline microstructure with random grain orientations are distributed randomly over all possible GB planes. From a geometric and energetic point of view, the (100) plane in the diamond lattice is representative of virtually all GB planes other than (111) and (110) because fully 50% of the bonds of atoms at the GB involve partners on the opposite side of the interface; the remaining bonds are between atoms on the same side of the GB (see Fig. 1). This planar bond geometry, combined with the relatively small interplanar spacing of the (100) planes, results in significant structural disorder, and hence a high energy, for *high-angle* (i.e., large-unit-cell) twist boundaries. By contrast, the (111) and (110) planes are geometrically and energetically unique in that only 25% of the nearest-neighbor bonds involve atoms across the interface (see Fig. 1). Because relatively little structural disorder is therefore generated even for large twist angles, these planes are low-energy GB planes. All other GB planes are either vicinal to these "special" planes or generic high-energy planes.

For purely statistical reasons, in a more or less random microstructure more of the large-unit-cell GBs will be situated on high-energy planes than on one of the special or vicinal planes.

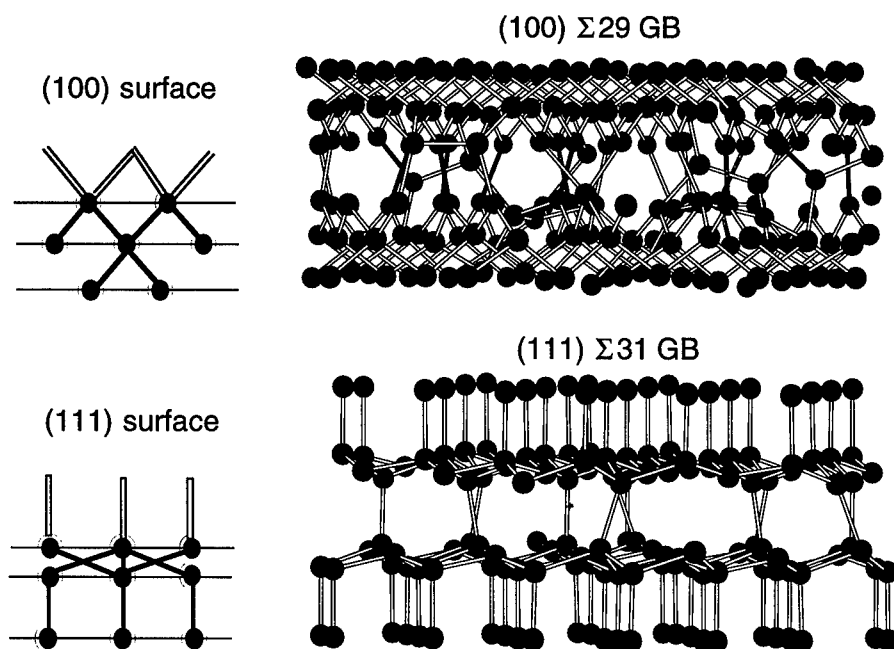


FIG. 1. Left: Geometry of the bulk-terminated (111) and (100) free surfaces in diamond (schematic). Right: Projected structures of the high-temperature relaxed (100)  $\Sigma 29$  and (111)  $\Sigma 31$  twist boundaries in diamond. All the nearest-neighbor bonds between GB atoms are shown.

As a representative *high-energy* GB we choose the (100)  $\phi=43.60^\circ$  ( $\Sigma 29$ ) twist boundary, with a planar unit-cell area that is  $\Sigma=29$  times larger than that of the primitive planar unit cell of diamond (100) planes; as a representative *low-energy* GB we consider the (111)  $\phi=42.10^\circ$  ( $\Sigma 31$ ) twist GB, with a planar unit-cell area  $\Sigma=31$  times larger than that of perfect-crystal (111) planes. Both boundaries are readily generated by a twist rotation of two free (100) or (111) surfaces about the GB-plane normal by the respective angle  $\phi$ . We deliberately omit symmetric tilt GBs because they are geometrically so special due to their extremely small planar GB unit cells, with the effect that their broken-bond behavior is of little interest.

During a typical high-temperature Monte-Carlo equilibration, the GB structure is kept at a temperature of about 80% of the melting point for an extensive time period, after which the system is slowly cooled down to zero temperature and characterized. (See Ref. 8 for further details.) The projected structures of our two model GBs obtained after high-temperature annealing are shown in Fig. 1. The (111) boundary is clearly more ordered than the (100) boundary, as also evidenced by its lower energy of  $E_{GB}=4290$  erg/cm<sup>2</sup> compared to 6150 erg/cm<sup>2</sup> for the (100) GB. The average nearest-neighbor coordination,  $\langle C \rangle$ , of 3.50 and 3.16 for the atoms in the two center planes of the (111) and (100) GB, respectively, is indicative of a significant fraction of GB atoms being only three-fold coordinated. Analysis of  $\langle C \rangle$  reveals that, indeed, in the (111) GB 50% of all GB atoms are three-coordinated compared to 80% in the (100) GB, with practically all other atoms being four-coordinated.

These differences are strikingly apparent in the related bond-angle distribution functions in Fig. 2. The presence of equal fractions of three- and four-coordinated C atoms and the high degree

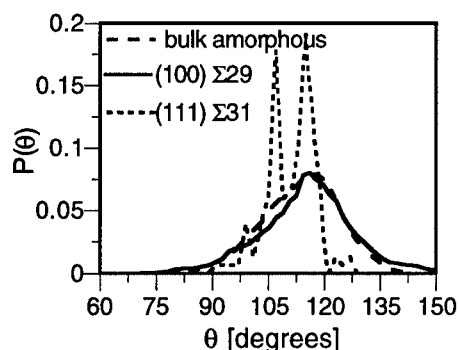


Fig. 2 Bond-angle distributions,  $P(\theta)$  (in arbitrary units), for the atoms in the two center planes of the high-temperature relaxed (100)  $\Sigma 29$  and (111)  $\Sigma 31$  twist GBs in diamond by comparison with  $P(\theta)$  for amorphous carbon.

of structural ordering in the (111) GB gives rise to two rather sharp peaks, one at  $\sim 107^\circ$  near the  $sp^3$  bond angle of  $109.47^\circ$  and the other at  $\sim 116^\circ$  near the  $sp^2$  bond angle of  $120^\circ$ . By contrast, the similarity of the bond-angle distribution function of the (100) GB with that of bulk amorphous carbon, with a broad peak centered at  $\sim 116^\circ$  near the  $sp^2$  bond angle (see Fig. 2), indicates the presence of mostly three-coordinated C atoms and significant structural disordering at the GB.

It is interesting to note that the effect of high-temperature annealing is much less pronounced in these two diamond GBs than in the same boundaries in Si. [8] For example, the energy of the (100) GB decreases by only about 3% in diamond compared to over 20% in Si. Moreover, by

contrast with Si, in diamond the coordination of the GB atoms remains practically unchanged. Nevertheless, the plane-by-plane energy profile across the diamond GBs changes noticeably during the high-temperature treatment (for the profiles of the (100) GB, see Ref. 8) as do the related bond-angle distribution functions. These observations indicate that, although the GB atoms reshuffle noticeably during the heat treatment while redistributing the excess energy over a slightly wider region and lowering the peak energy, the  $sp^2$ -bonded C atoms already present in the zero-temperature relaxed input structure experience virtually no driving force for recovering  $sp^3$  bonding. By contrast, in silicon a huge driving force exists for the initially three-coordinated atoms in the zero-temperature relaxed GB to recover, as much as possible, their full four-fold coordination during the heat treatment, even at the price of severe GB disordering. [8,9]

The atomic structures in Fig. 1 show that the GB width,  $d$ , is only two atomic planes; i.e., typically less than one lattice parameter. For example, for the (100) GB in Fig. 1,  $d \approx 2d(100) = 0.5a_0 \sim 1.8 \text{ \AA}$  (where  $a_0 = 3.56 \text{ \AA}$  is the lattice parameter). Assuming that in the nanocrystalline microstructure, on average, 75% of the GB atoms are three-fold coordinated, we can then estimate the total volume fraction of three-coordinated atoms,  $\langle C_3^{\text{tot}} \rangle$ , as a function of the grain size. From recent Raman-scattering experiments on nanocrystalline diamond films grown from fullerene precursors it was estimated that for a grain size of  $D \sim 15 \text{ nm}$ ,  $\langle C_3^{\text{tot}} \rangle \sim 1\text{--}2\%$  [4]. For simplicity, we assume spherically shaped grains with a uniform grain diameter,  $D$ , giving the relation  $\langle C_3^{\text{tot}} \rangle = 2.25 d/D$ . Consistent with the experiments, for  $D = 15 \text{ nm}$  and  $d \sim 2 \text{ \AA}$  this expression yields a value of  $\langle C_3^{\text{tot}} \rangle \sim 3\%$ .

The GB stability against brittle decohesion into two free surfaces is characterized by the work of adhesion,  $W_{\text{ad}} = 2\gamma - E^{\text{GB}}$ , where  $\gamma$  is the related free-surface energy. Although diamond surfaces are well-known to reconstruct [15], so as to obtain at least an upper bound for  $W_{\text{ad}}$  for our two model GBs, we have determined the zero-temperature relaxed energies,  $\gamma = 6170 \text{ erg/cm}^2$  and  $2550 \text{ erg/cm}^2$  of the *unreconstructed* (100) and (111) surfaces [8]. Surprisingly, according to the values of  $W_{\text{ad}}$  of 6190 and 816  $\text{erg/cm}^2$  thus obtained for the (100) and (111) GB, in spite of its lower GB energy the latter is considerably less stable. Moreover, the value of  $W_{\text{ad}}$  for the high-energy GBs is even higher than the perfect-crystal cleavage energy,  $2\gamma(111) = 5100 \text{ erg/cm}^2$ . These results suggest that nanocrystalline diamond (likely containing a large fraction of *high-*

energy, large-unit-cell GBs) may be mechanically stronger than coarser-grained diamond (likely with a significant fraction of low-energy, small-unit-cell "special" GBs) or even perfect-crystal diamond; i.e., the dominating brittle-fracture mode in nanocrystalline diamond may be intra- rather than intergranular.

This intriguing behavior is mostly due to the different numbers of bonds per unit area across the GB and degrees of  $sp^2$  hybridization on high- and low-energy GB planes (see Fig. 1). As already mentioned, in the unrelaxed (111) GB only one of the four bonds of every GB carbon atom is bonded across the interface; by contrast, in the (100) GB, *two* of the four bonds involve atoms across the GB plane (Fig. 1). Moreover, due to the change in hybridization during relaxation, in the (111) GB about 50% of these GB bonds are lost, by comparison with typically only 35-40% in the (100) GB. As a consequence of these two effects, the (100) GB exhibits a significantly higher bond density across the GB, therefore with a much higher work of adhesion. By contrast, the relatively few GB bonds left in the (111) GB have the effect that the GB energy is only slightly lower than that of two free surfaces ( $E_{GB}/2\gamma=0.84$ ), with a consequently rather low work of adhesion.

Finally, we investigate the degree of connectivity amongst the three-coordinated carbon atoms in our two model GBs. Clearly, like in the unreconstructed free (111) surface (see Fig. 1) individual three-coordinated GB atoms are totally disconnected from each other in the (111) GB because all three of their bonds involve four-coordinated atoms in the same grain (Fig. 1). A plan-view of the distribution of the three-coordinated C atoms within the planar unit cell of the

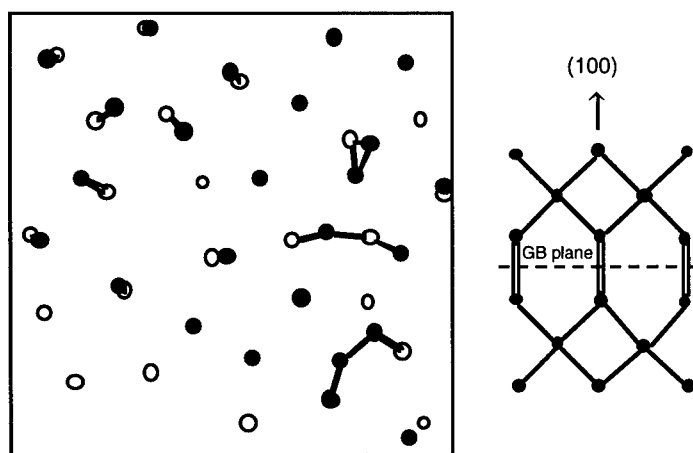


FIG. 3. Bonding in the (100)  $\Sigma 29$  boundary. Left: Plan-view of the distribution of only the three-coordinated C atoms within the GB planar unit cell. Full and open circles symbolize atoms on opposite sides of the GB. Lines connecting some of the atoms indicate an  $sp^2$ -like bond between them. Right: Edge-on view of the same GB illustrates the graphite-like p bonds between atoms on opposite sides of the GB (schematic). In practice, due to the structural disordering across the GB, not all these  $sp^2$  bonds actually exist, likely giving rise to some dangling bonds.

(100) GB is shown in the left half of Fig. 3. Interestingly, in spite of 80% of the GB carbon atoms being three-fold coordinated, other than for the  $sp^2$  bonded atom pairs connected across the GB (see the edge-on view in the right half of Fig. 3) these atoms are almost completely disconnected from one-another. The reasons for this extremely small degree of connectivity are, again, mostly geometrical: Given that within their own (100) planes, the three-coordinated GB atoms are not bonded amongst themselves (Fig. 1), typically two of the three bonds of each of these GB atoms involve *four*-coordinated atoms within the same grain while only one bond is capable of

connecting with another three-coordinated atom, however across the GB (right half of Fig. 3). Hence, in spite of an apparently graphite-like coordination, the connectivity within the GB is far from graphitic.

## CONCLUSIONS

In conclusion, it appears that the relatively high stability of the high-energy, large-unit-cell GBs predominantly present in nanocrystalline microstructures with random grain misorientations is mostly due to geometric factors associated with the bonding across the high-energy GB planes. As a consequence of the ability of diamond to change hybridization in a structurally disordered environment, already relatively small bond distortions are capable of locally inducing  $sp^2$ -type bonding. This competition between structural disordering and local hybridization change, completely absent in silicon, translates into relatively more ordered GB structures in diamond than in Si and results in typically 70-80% of the GB carbon atoms being only three-fold coordinated. For mostly geometric reasons, these potentially active sites are poorly connected to each other; the GBs in pure nanocrystalline diamond are therefore probably insulators. Intriguingly, however, in spite of this relatively low degree of connectivity, one could easily envision dramatic changes in the electrical behavior of diamond GBs induced, for example, by small amounts of hydrogen or certain other impurities.

**ACKNOWLEDGMENTS.** We have greatly benefited from discussions with O. Auciello, F. Cleri, D. Gruen and A. Krauss. PK gratefully acknowledges support from the Alexander von Humboldt Foundation. SRP and DW are supported by the US Department of Energy, BES-Materials Science under Contract No. W-31-109-Eng-38.

## REFERENCES

\*Electronic address: keblinski@anl.gov

1. D. Gruen, *et al. J. Appl. Phys.* **75**, 1758 (1994).
2. J. A. Nuth, *Nature* **329**, 589 (1987).
3. R. Csencsits, *et al., Solid State Phen.* **51-52**, 261 (1996).
4. A. Erdemir, D. M. Gruen, and A. R. Krauss, *Diamond and Rel. Mats.* **5**, 923 (1996).
5. D. M. Gruen, A. R. Krauss and O. Auciello *private communication*.
6. F. Li, and J. S. Lannin, *Phys. Rev. Lett.* **65**, 1905 (1990).
7. J. Tersoff, *Phys. Rev. Lett.* **61**, 2879 (1988).
8. P. Keblinski, *et al., J. Mater. Res.* **13** (1998).
9. P. Keblinski, *et al., Phys. Rev. Lett.* **77**, 2965 (1996); *J. Am. Cer. Soc.* **80**, 717 (1997).
10. M. Kohyama, *et al., Interface Sci.*, **4**, 157 (1996).
11. J. Narayan, J. and A. S. Nandedkar, *Phil. Mag. B* **63**, 1181 (1991).
12. J. R. Morris, C. L. Fu and K. M. Ho, 1996, *Phys. Rev. B* **54**, 132.
13. Z. Q. Wang, S. A. Dregia and D. Stroud, *Phys. Rev. B* **49** 8206 (1994).
14. P. Keblinski, *et al., Acta Mater.* **45**, 987 (1997).
15. B. B. PATE, *Surf. Sci.* **165**, 83 (1986).





## VIBRATIONAL ANALYSIS OF ION IRRADIATED SELF-ASSEMBLED MONOLAYERS

G. Compagnini, S. Pignataro, O. Puglisi

Dipartimento di Scienze Chimiche, V.le A. Doria 6 -95125 Catania (Italy)

**Abstract** -- We present some results on the modification of the vibrational features of alkanethiol self assembled monolayers upon ion irradiation ( $H^+$  100 keV ions) through Surface Enhanced Spectroscopies. These monolayers are chemisorbed onto rough silver surfaces as checked by AFM. Low fluences ( $10^{12}$ - $10^{14}$  ions/cm<sup>2</sup>) ion irradiation will be used to induce simple chemical reactions in alkanethiol molecules seen through the loss of  $CH_3$  stretching features and formation of  $C=C$  double bonds. ©1999 Acta Metallurgica Inc.

### INTRODUCTION

Self-assembly of alkanethiol monolayers on gold or silver substrates is a fast and easy method for preparing organic films with well defined physical and chemical properties(1,2). Most of the applications which involve the use of Self Assembled Monolayers (SAM) are due to the surface properties of these layers and then to the nature of the last functional group(3). Many of the technological applications of these films involve, in one manner or another, the exposure of the organic surface to particle bombardment or photon irradiation(4,5). In this case both physical and chemical processes can be induced in and on the organic film for such conditions. Then it is extremely important to understand as much as possible the sensitivity of the surface to these treatments. Moreover the use of alkanethiol SAM to study fundamental particle-solid interactions is particular interesting because these monolayers are well ordered onto the surface and almost homogeneously distributed.

The study of these systems has been recently improved by the use of surface enhanced vibrational spectroscopies. These techniques are sensitive to the adsorption of various organic and inorganic species onto suitable substrates, in such a way to increase the cross sections of several orders of magnitude. In particular Surface Enhanced Raman Spectroscopy (SERS)(6) and Surface Enhanced Infrared Spectroscopy (SEIRS)(7) give the possibility to explore the vibrational features of these films just because they can be chemisorbed onto silver or gold substrates. In this paper we present a vibrational study of the modifications of alkanethiol SAMs onto silver surfaces when the ultrathin film is exposed to keV light ion beams.

### EXPERIMENTAL SECTION

Surface Enhanced active surfaces were prepared by plasma oxidation and reduction cycles as reported elsewhere(8). In this way we obtain a rough surface whose morphological features

have been checked through the use of Atomic Force Microscopy. Dodecanethiole [ $\text{CH}_3(\text{CH}_2)_{11}\text{SH}$ ] (Aldrich) has been self assembled onto SERS active samples to ensure the formation of one monolayer onto the silver surface as already reported in literature(9).

Ion irradiation has been performed through an electrostatic accelerator with a  $\text{H}^+$  300 keV ion beam swept at fluences ranging from  $10^{12}$  to  $1 \times 10^{14}$  ions/ $\text{cm}^2$ . Montecarlo TRIM code calculations show an almost inelastic energy loss deposition with a stopping power cross section of about  $5.3 \times 10^{-15}$  eV/(at./ $\text{cm}^2$ ).

All Raman spectra were performed through the use of an Ar ion laser working at 514.5 nm and a Jobin Yvon U1000 double monochromator equipped with an Hamamatsu photomultiplier. Infrared spectra have been obtained using a diffuse reflectance integration sphere coupled with a Perkin Elmer FT infrared spectrometer in the 400-4400  $\text{cm}^{-1}$  range.

Contact angle measurements have been performed using a Kernco contact angle meter.

## RESULTS AND DISCUSSION

Fig.1 reports Surface Enhanced Raman Spectra of as deposited and ion irradiated dodecanethiole (DDM) SAMs on rough silver surfaces together with a Normal Raman (NR) spectrum of bulk (liquid) DDM. A number of considerations can be done about ordering and chemisorption of these molecules onto rough silver surfaces.

The signal at about 2580  $\text{cm}^{-1}$ , always found in liquid DDM and assigned to an SH stretching mode, is lost in the SERS spectrum when the alkanethiol is adsorbed. This testifies both the chemisorption of the molecules and the absence of further molecules on top of the first layer. Moreover, there is a clear indication in the C-S stretching region (600-900  $\text{cm}^{-1}$ ) that only one of the two conformations allowed for this organic structure (trans and gauche, T and G in the figure) is observed in the adsorbate while they are both found in the bulk NR spectrum. This is consistent with the data available in literature where it was shown that only the trans conformation survives to the self assembling(9).

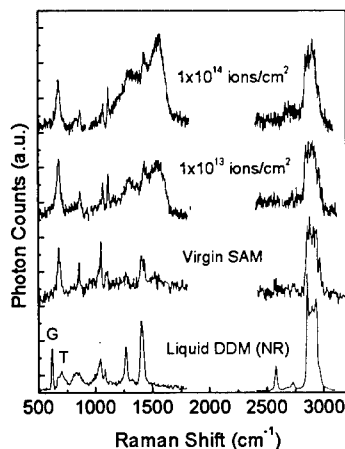


Fig1: SERS of DDM self-assembled monolayers irradiated at different ion fluences together with a Normal (NR) spectrum.

Then, these molecules are ordered with their sulphur tails bonded to the surface atoms and the  $\text{CH}_3$  heads to define a new surface. Ion irradiation produces a dramatic change in the SERS spectra of SAM even at very low fluences. This change has been observed by the appearance of a prominent broad structure located between  $1100$  and  $1600\text{ cm}^{-1}$ . This is generally attributed to the presence of  $\text{C}=\text{C}$  double bonds. In this contest we observe that the cross section for Raman scattering due to  $\text{C}=\text{C}$  stretching vibrations is very high compared to the one for a single bond. Then even few  $\text{C}=\text{C}$  bonds leads to a detectable signal(10). The formation of  $\text{C}=\text{C}$  bonds upon ion irradiation is one of the most efficient processes observed in carbon based materials either polymers and hydrocarbons or diamond and diamond-like materials, in which a prevalence of tetrahedrally co-ordinated carbons are present.

In order to understand more about the ion beam induced modifications, we performed a series of infrared spectra in the diffuse reflectance configuration whose results are reported in Fig.2, confined to the CH stretching region ( $2800\text{--}3100\text{ cm}^{-1}$ ). It is well known that infrared spectroscopy onto rough silver surfaces leads to a great enhancement in the vibrational cross section too. This allows us to detect quantities as small as those found in a SAM. Infrared spectra reported in Fig.2 can be deconvoluted using five vibrational structures assigned as follows:

- a)  $\text{CH}_3$  and  $\text{CH}_2$  antisymmetric stretching at  $2960$  and  $2922\text{ cm}^{-1}$  respectively;
- b)  $\text{CH}_3$  and  $\text{CH}_2$  symmetric stretching at  $2875$  and  $2850\text{ cm}^{-1}$  respectively;
- c) Fermi resonance coupled symmetric  $\text{CH}_3$  stretching at  $2936\text{ cm}^{-1}$ .

A look at the variation of these signals by increasing ion fluence shows a decrease of both symmetric and antisymmetric  $\text{CH}_3$  signals, compared with the  $\text{CH}_2$  ones. The latter signals come from the whole DDM backbone and can be used as a reference. To quantify this observation we performed a least square fit of each spectrum using five lorentian curves. The results have been referred to the  $\text{CH}_2/\text{CH}_3$  ratio value in the virgin DDM molecule ( $\text{CH}_2/\text{CH}_3=11$ ). In this way we obtained a consistent trend in the symmetric and antisymmetric  $\text{CH}_2/\text{CH}_3$  values as function of ion fluence as reported in fig.3. In the same figure we also reported the water liquid contact angle data.

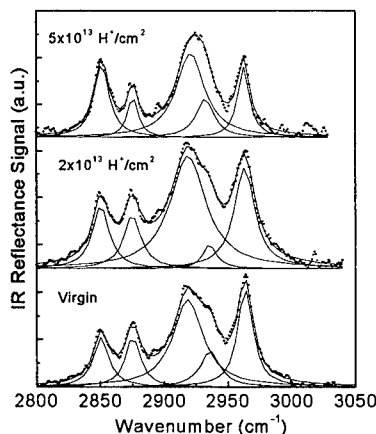


Fig.2: Surface Enhanced Infrared Spectra of alkanethiol self-assembled monolayers irradiated at different ion fluences.

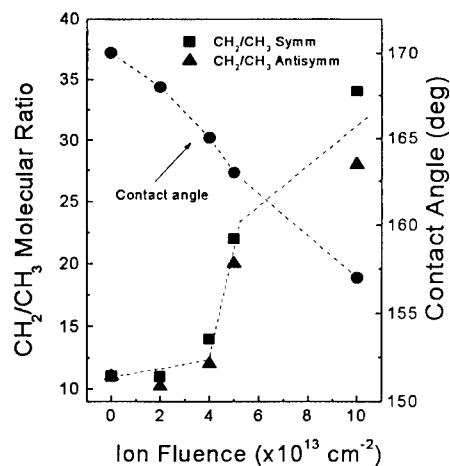


Fig.3:  $\text{CH}_2/\text{CH}_3$  integrated ratios as function of ion fluences.  
Here are also the obtained water contact angle values reported.

It is generally agreed that the wetting response of these organic films arise from 0.5 nm surface region. Once again, wetting data indicate that ion irradiation changes the ambient interface from a layer of  $\text{CH}_3$  groups to a more polar one. In summary, the obtained data show that the irradiated SAM has lost a significant amount of the original aliphatic hydrocarbon character at the head to become a rather carbonaceous material, while it remains almost unchanged close to the silver interface. Several chemical mechanisms can be invoked for such a transformation. One of them is the cross-link of each two DDM molecule through a double bond located at the head of the molecules with consequent evolution of hydrogen. Further experiments are in progress to evaluate the consistence of such an hypothesis.

#### ACKNOWLEDGEMENTS

CNR and MURST are acknowledged for their partial financial support.

#### REFERENCES

1. A.Ulman, *An introduction to ultrathin organic films from Langmuir-Blodgett to Self-Assembly*, Academic Press, Boston, 1991
2. G.K.Jennings and P.E.Laibinis, *J.Am.Chem.Soc.* 1997, 119, 5208
3. Q.Ye, J.Fang, L.Sun, *J.Phys.Chem.* 1997, 101, 8221
4. G.Gillen, S.Wight, J.Bennett, M.J.Tarlov, *Appl.Phys.Lett.* 1994, 65, 534
5. Tiberio, H.G.Craighead, M.Larcel, T.Lau, C.W.Sheen, D.L.Allara, *Appl.Phys.Lett.* 1993, 62, 476
6. A.Otto, I.Mrozek, H.Grabborn and W.Akermann, *J.Phys.:Cond.Matter* 1992, 4, 1143
7. W.Knoll, M.R.Philpott, W.G.Golden, *J.Chem.Phys.* 1982, 77, 219
8. G.Compagnini, B.Pignataro, B.Pelligra, *Chem.Phys.Lett.* 1997, 272, 453
9. M.A.Bryant and J.E.Pemberton, *J.Am.Chem.Soc.* 1991, 113, 3629
10. N.Wada, P.J.Gaczi and S.A.Solin, *J.Non-Cryst.Sol.* 1980, 35/36, 543



## MODELING OF NANOSTRUCTURAL DESIGN OF ULTRAFINE MULLITE POWDER PARTICLES OBTAINED BY ULTRASONIC SPRAY PYROLYSIS

<sup>1</sup>V.Jokanovic, <sup>2</sup>Dj.Janackovic, <sup>3</sup>P.Spasic, <sup>4</sup>D.Uskokovic,

<sup>1</sup>Institute for Technology of Nuclear and Other Mineral Raw Materials, Franchet

D'Eperey 86, 11000 Belgrade, Yugoslavia

<sup>2</sup>Faculty for Technology and Metallurgy, Belgrade

<sup>3</sup>Military Medical Academy, Belgrade

<sup>4</sup>Institute for Technical Sciences, Serbian Academy of Sciences and Arts, Belgrade

*Abstract* In this paper, a model of substructure design of mullite powder particles obtained by spray pyrolysis in the field of ultrasound excitation is described. Based on this model, the size of subparticles (nanoparticles) constituting the substructure of so obtained powder is described and compared to experimentally determined values. High agreement between theoretical and experimental values confirmed the value of the theoretical model and its wide applicability in estimation of particle substructure for mullite powder obtained under the conditions of the periodical physical field activity.

©1999 Acta Metallurgica Inc.

### INTRODUCTION

The process of spray pyrolysis performed under influence of the ultrasound force field is a typical process of the material synthesis in periodical physical field. The general model of synthesis, defined and described in our previous works (1-10), indicated the possibility to determine average size of the powder particles and their size distribution spectrum. Apart from that, by further development of the model (which treats the aerosol drop as macroelement of the system exposed to influence of the periodical physical field, transferred onto drop in the moment of its separation from the liquid meniscus), it becomes possible to derive further substructuring of the system on the level of its basic constituting elements- subdrops. After solidification of the aerosol drops, substructure of nanostructural dimensions is obtained.

In this paper, the coding mechanism determining substructure of the powder particles obtained by the ultrasonic spray pyrolysis is presented via the mechanism of harmonisation of the force physical field of the ultrasonic generator and induced oscillating field of the aerosol drop itself.

### EXPERIMENTAL

For the mullite ( $M_3$ ) synthesis, starting 0.025 M aqueous solution was prepared

in the following way: TEOS previously dissolved in ethanol was added in aqueous solution of  $\text{Al}(\text{NO}_3)_3 \cdot 9\text{H}_2\text{O}$  ( $t=353\text{ K}$ ,  $\text{pH}=1$ ) with  $\text{HNO}_3$  addition (as a catalyst for TEOS hydrolysis), in the ratio TEOS:ethanol:water=1:2:17. In this way, the TEOS was completely hydrolyzed forming silicic acid.

The solution atomization was carried out with an ultrasonic GAPUSOL-RBI-9001 atomizer at a resonant frequency of 2.5 MHz and a capacity of 400 cm<sup>3</sup>/h, generating aerosol droplets of a mean diameter of 2  $\mu\text{m}$ . Aerosol droplets were then inserted into an air stream at a flow rate of 30-40 dm<sup>3</sup>/h, in a one meter long furnace, at 900°C. The residence time of droplets/particles inside the furnace was 95 s assuming that the air flow rate and droplet velocities are equal. The heating rate of droplets/particles was 18°C/s. Transmission electron microscopy (TEM) was done by a JEOL-JEM-100cx instrument, with sample preparation by sealing with epoxy resin and by mechanical sample thinning.

## RESULTS AND DISCUSSION

### *Theoretical model*

After separation of the aerosol drop from the surface of the liquid meniscus, the drop continues to be the carrier of excitation transferred onto it in the moment of its separation, behaving as induced mechanical oscillator whose characteristic frequency is determined by the drop geometry and frequency of excitation by degenerated frequency of the ultrasound oscillator, as already explained.

Under influence of the excitation field, centrally symmetric standing wave is formed whose propagation through the aerosol drop causes formation of a great number of nanooscillators-nanodrops, which in the end of the solidification process cause formation of the system subparticles and complete define its substructure.

In order to determine diameter of these substructure nanoelements one should start from the wave equation that defines propagation of disturbance through the given medium, as follows:

$$\frac{\partial^2 \varphi}{\partial t^2} = c^2 \frac{1}{r^2} \frac{\partial}{\partial r} \left( r^2 \frac{\partial \varphi}{\partial r} \right), \quad [1]$$

where  $\varphi$  is rate potential,  $c$  is rate of the wave propagation through the drop,  $r$  is drop radius and  $t$  is time.

Solution of the given equation is of the following form:

$$\varphi = \frac{f_1(ct - r)}{r} + \frac{f_2(ct + r)}{r}, \quad [2]$$

where  $f_1$  and  $f_2$  are random functions. From monochromatic spherical wave (the condition evidently satisfied in our case, since each drop corresponds to one excitation frequency), it is possible to obtain the final solution of equation [2], as follows:

$$\varphi = Ae^{-2\pi f t} \frac{\sin kr}{r}, \quad [3]$$

where  $f$  is drop excitation frequency,  $A$  is wave amplitude and  $k=w/c$  is wave number ( $w$  is circular frequency).

On condition that  $d\varphi/dr = 0$  and  $r=R$ , the following equation is obtained:

$$\operatorname{tg} kR = kR \quad [4]$$

Graphic solution of equation [4] has the following form:

$$\omega = \frac{Nc}{R}, \text{ and } f = \frac{N'c}{R}, \quad [5]$$

where  $N$  and  $N'$  are the number constants, taking the following values:  $N=4.49; 7.6; 10.8; 14.0; 17.2; 24.0; \dots$ ; and  $N'=0.715; 1.21; 1.72; 2.23; 2.74; 3.82; \dots$

Based on obtained values of the subdrop frequency, the radii of subparticles / nanoparticles were determined according to the following equation:

$$d_p = d \left( \frac{cM_M}{\rho M_s} \right), \quad [6]$$

where  $d_p$  is particle diameter,  $c$  is concentration of the spraying solution,  $\rho$  is mullite density and  $M_s$  is the solution molecular weight.

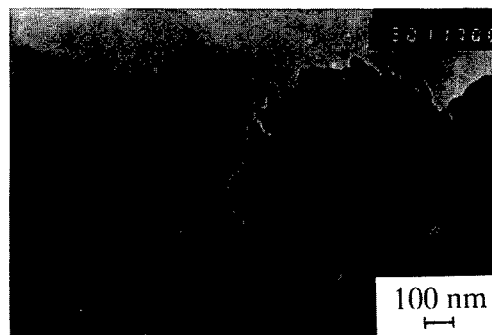
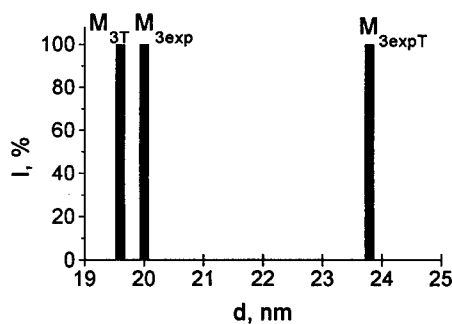


Fig.1. Theoretically estimated and experimentally determined subparticle size.

Fig.2 TEM micrograph of mullite powder.

Analysis of the nanostructural design of selected mullite powder particles was carried out with particles close in size to the average particle size. Theoretically determined values of frequency and size of the aerosol subdrops, determined according to equations [5] for average size of aerosol drops (1-5), and size of respective

subparticles - nanoparticles constituting substructure of the given powder, determined according to equation [6] are shown in Fig.1.

On assumption that size of spherical subdrops (subparticles) is uniform, theoretically determined value ( $M_{3T}$ ) was found to be 79.3 nm (subdrop size) and 19.6 nm (subparticle size) for  $M_3$  powder. If replacing theoretically by experimentally obtained average size and calculated anticipated subparticle size from them, the value of 23.79 nm ( $M_{3expT}$ ) is obtained for mullite powder. Analysis of experimentally determined size of powder subparticles ( $M_{3exp}$ ) (by analysing the image obtained by the transmission electron microscopy) showed that their average values of mullite powder were in the range of about 20 nm (Fig.2). Following to subsequent crystallisation and sintering of obtained mullite powders, the nanocrystals whose diameter remained unchanged ( $\approx 20$  nm) were connected into cylinders, about 100 nm long, formed by linking of particles along certain direction (powder particle diameter) .

### CONCLUSION

In this paper, results of the general theoretical model enabling one to determine size of particles - subparticles obtained by harmonisation of given periodical field and internal physical field induced in the system exposed to such excitation, are presented.

Verification of this model was performed with mullite powder, obtained by spraying in ultrasonic field. Results obtained by verification of agreement between theoretically estimated and experimentally determined size of particles and subparticles and their population balances confirmed that these values could be theoretically predicted. This fact is of particular importance because it indicates the possibility of the structural coding even at the finest, nanolevel, with high degree of certainty.

### REFERENCES

1. Jokanović, V., Janačković, Dj., Spasić, A.M., Uskoković, D., Mater.Trans., JIM, 1996, 37, 627.
2. Jokanović, V., Janačković, Dj., Uskoković, D., Key Engin. Mater.,132-136, (1997), 213.
3. Janačković, Dj., Jokanović, V., Kostić-Gvozdenović, Lj., Živković, Lj., Uskoković, D., J.Mater.Res., 1996, 11, 1706.
4. Janačković, Dj., Jokanović, V., Kostić-Gvozdenović, Lj., Uskoković, D., Mater.Sci. Forum., 1996, 214, 215.
5. Janačković, Dj., Jokanović, V., Kostić-Gvozdenović, Lj., Zec, S., Uskoković, D., J.Mater.Sci., 1997, 32, 163.
6. Janačković, Dj., Jokanović, V., Kostić-Gvozdenović, Lj., Uskoković, D., Nanostruct.Mater., 1998, 10, (accepted for publication).
7. Nedeljković, J., Šaponjić, Z., Rakočević, Z., Jokanović, V., Uskoković, D., Nanostruct.Mater., 1997, 9, 125.
8. Šaponjić, Z.V., Rakočević, Z., Dimitrijević, N.M., Nedeljković, J.M., Jokanović, V., Uskoković, D.P., Nanostruct.Mater., 1998, 10, (accepted for publication).
9. Jokanović, V., Janačković, Dj., Čurčić, R., Živanović, P., Uskoković, D., Mater.Sci.Forum, 1998, 282-283, 65.
10. Jokanović, V., Janačković, Dj., Uskoković, D., 1998, (to be published).





Pergamon

NanoStructured Materials, Vol. 12, pp. 353–356, 1999

Elsevier Science Ltd

© 1999 Acta Metallurgica Inc.

Printed in the USA. All rights reserved

0965-9773/99/\$—see front matter

PII S0965-9773(99)00133-6

## NORMAL MODE ANALYSIS OF OPTICAL POLARISATION RESPONSE IN NANOCOMPOSITE PARTICLES

G.B. Smith and A.J. Reuben

Department of Applied Physics, University of Technology, Sydney  
PO Box 123 , Broadway, NSW 2007 Australia

**Abstract** - A new technique for establishing the spectral density and resonance positions of normal optical modes in fine particle systems is outlined and applied to finite chains of closely spaced aluminium cylinders. The method uses multiple conformal frames and a new type of structure factor. Finite chain results are compared to those of the pair and infinite chain on a per particle basis. One key result is the dominance and strong red shift of the fundamental mode as chain length increases beyond a few cylinders. Another is that this fundamental mode is largely isolated in the long UV, visible and NIR wavelength range. Surprisingly long chains (typically > 100 cylinders) are needed to give results resembling the infinite chain, unless gaps are large.

©1999 Acta Metallurgica Inc.

### INTRODUCTION

Fine particle arrays where the particle size is much less than wavelength can be analysed by quasi-static effective medium theory. A new approach to optical properties [1] covering any size finite array as well as the infinite array is applied to chains of metal cylinders. In the classical Maxwell-Garnett (MG) and Bruggemann models for random arrays only dipoles contribute, while in existing infinite lattice treatments many multipoles contribute and convergence requires assumptions based on the fact the array is really finite. Our method inherently converges at all cluster sizes.

Normal mode equations separate explicitly the contribution of microstructure and materials properties. Then one can more confidently determine whether the metal particles themselves have anomalous optical response. A key unresolved aspect of nanomaterials science is when do small metal structures give non-metallic response. Some evidence exists at readily observable sizes [2,3]. A generalised integral representation of the normal modes can empirically fit optical data [4]. This assumes either an admix of geometry's or many touching particles. It is useful in verifying trends predicted by our models. Results for multipolar response in pairs of spheres and cylinders are well established [5] but higher number clusters are not well understood, though there has been some work [6]. The resonant absorption positions, one for each mode, relate to the eigenfunctions of our special new type of structure factor [1].

A general feature is that some ordered clusters, especially near linear or chain like ones, mimic the spectral response, over a broad band, of random systems. In the classical random array theories this mode is determined by depolarisation factor and hence particle shape. The possibility that it is the array and not the particle shape that is most important has already been

highlighted for solar energy materials [7]. From a data fitting perspective similar equations are used but the fitting parameters have different meanings. An approximate view supported by our fundamental mode location, is that the chain actually behaves like a single long ellipsoid. Its spectral weight however is down because there are non-vanishing short Ultra-Violet modes.

### MODES BY AN EFFICIENT NEW TECHNIQUE

Two or more co-ordinate frames, most or all of which are two particle frames, are superimposed to generate the whole structure [1]. For some problems we use an infinite frame[8]. These methods lead much more rapidly to the natural modes of the system than using separate frames on every particle. Boundary conditions apply on particle surfaces. The key to the approach is the establishment of the link between the local variables. This step leads to a geometric structure factor  $\underline{S}$  linking the sub-clusters.  $\underline{S}$  is a new type of structure factor, since the traditional one refers to individual frames on each particle. It separates out in the boundary equations needed to solve for the potential expansion coefficients in terms of the applied potential, and is off-diagonal. We take fields parallel to the chain axis. Replace  $\epsilon$  by  $-1/\epsilon$  for transverse fields. The resultant matrix equation is diagonalized to find the normal mode decomposition of the particle polarizability [1] (scaled to particle area here, volume in three dimensions). For a system in air whose particles have dielectric constant  $\epsilon$ , it is given by the following equation with spectral weights  $g_n$  and effective depolarisation factors  $L_n$ , determined purely from geometry

$$\langle \chi \rangle = \sum_n \frac{g_n}{\frac{1}{\epsilon - 1} + L_n} \quad (1).$$

Each mode clearly has an absorption resonance whose position is determined by the vanishing of the real part of the denominator. Results for other structures are covered elsewhere [1]. The focus on chains of particles here helps us to examine two important issues :

- (i) how the resonance structure evolves as the number of particles in a chain increases, including the rate of approach to "infinite chain" behaviour,
- (ii) How the resonance structure evolves with inter-particle spacing.

A very important result follows from a study of long but finite length chains.

#### *Cylinder chain results*

We now show how chains of aluminium cylinders beyond a certain length can give results that are easily confused with standard effective medium theory. The fundamental mode with  $n = 1$  dominates response in the long UV, visible, NIR spectral ranges in Al/insulator or even Al/air composites when the aluminium forms cylinder chains. Figures 1(a) and 1(b) demonstrate how this effect evolves via plots of  $Im \langle \chi \rangle$  for a pair, a chain of 50 cylinders and an infinite chain in air with a gap between neighbouring cylinders of just 2.5% of centre-to-centre separation. One distinct mode is observed plus clusters of modes at higher energy. This is seen even in the pair of fig.1, but there the fundamental is weaker than the higher modes up to  $n = 4$ . As the number of cylinders in the chain increases the  $n = 1$  mode rapidly rises in

intensity and also is strongly red shifted. However the higher order modes change slightly in intensity and thus become weak relative to the fundamental. Once the chain has more than 10 cylinders the fundamental dominates absorption. A chain may thus have one very strong

TABLE 1

*The fundamental mode characteristics of a closely spaced chain of cylinders with adjacent centres separated by 2.05 radii, for fields parallel to the chain axis.*

cylinders in chain	$L_1$	$g_1$
1	0.50	1.00
2	0.18	0.13
50	0.073	0.7239
infinite	0.054	0.7843

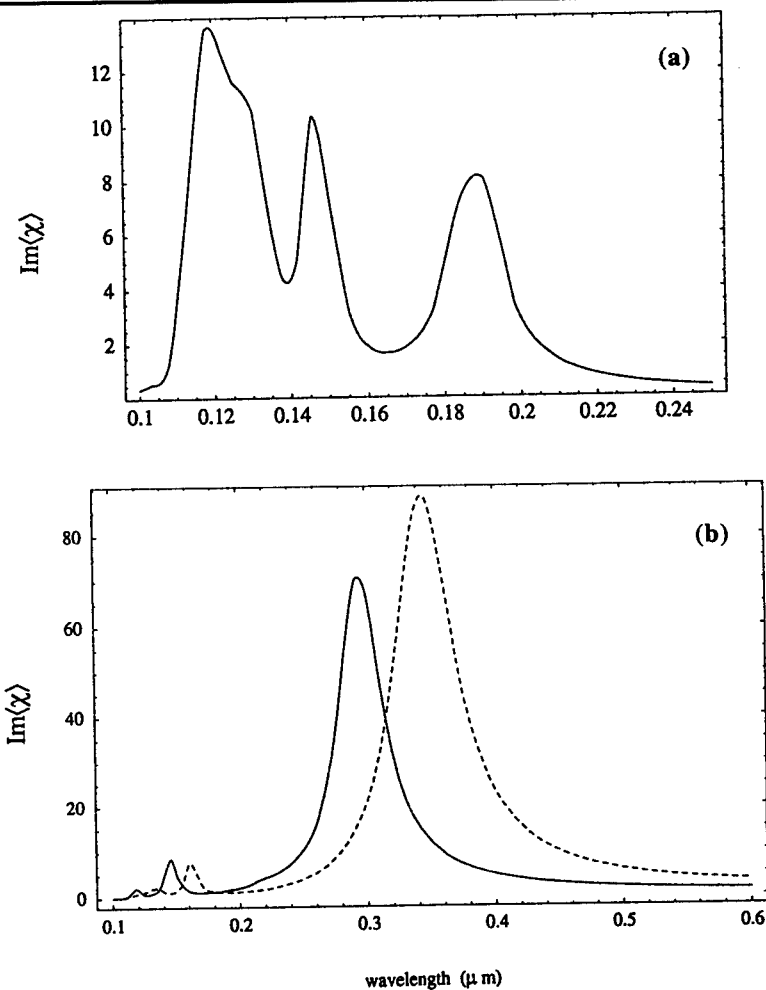


Figure 1. Absorption spectrum per cylinder of Al cylinder arrays in air for (a) cylinder pair (b) chain of 50 cylinders (solid) and infinite chain (dashed)

intrinsic absorption mode. The underlying numerical results appear in Table 1. As separation increases or decreases, similar results follow even if extremely close to touching, though then longer computer times are needed. At large gaps the effects are slower to develop and weaker. Comparing the chain of 50 to the infinite chain we see quite distinct resonance locations but similar strengths. By 50 cylinders the  $g_1$  value is close to its limit but the resonance position is still well away from the infinite chain value and moves slowly with further increase in length. This result highlights a long range order effect. The infinite chain retains the higher energy modes similar to the pair with change confined mainly to the fundamental mode. Using MG theory we would take whatever "L" parameter gave best fit and most likely assume an incorrect shape since there the relevant "effective" L parameter is actually  $L(1 - f)$  with  $f$  the fill factor determined by cylinder area and number per unit area, and  $L = 0.5$ , the depolarisation factor of the isolated cylinder. Note that the spectral density from modes with  $n > 1$  still sums to 0.216 for the infinite chain. In practice we may have interest in a film containing many chains of slightly different length. The results of Heilmann et al [6] are interesting in this regard, with the most dense films having effective depolarisation factors distributed with maximum weight around  $L = 0.05$ . As fill factors increase we expect average chains to get longer and a distribution of lengths could be envisaged.

## CONCLUSIONS

The normal polarisation modes of chains of small aluminium cylinders have been exactly analysed for spectral response at UV, optical and infra red frequencies in finite length and infinite chains. The fundamental mode dominates the long UV, visible and IR response. Very long chains are required at small separations before the spectral response gets quite close to that of the infinite chain. We also note that for metal in an insulator (replace  $\epsilon$  by  $\epsilon/\epsilon_h$  with  $\epsilon_h$  the oxide dielectric constant) the effects presented here become even more striking in that the fundamental peak is in the visible with strong absorption out to thermal IR wavelengths possible. With silver in place of aluminium visible and IR absorption is even stronger.

## REFERENCES

1. Reuben, A.J. and Smith, G.B. in press Phys. Rev. E. (publication due June/July 1998)
2. Joerger, R., Forcht, K., Gombert, A., Graf, W., Heinzl, A., Kohl M., and Weimar, U. Fresenius J. Anal. Chem., 1995, 353, 713.
3. Smith, G.B. and Dligatch, S., this Proceedings
4. Heilmann, A., Werner, J., Schwarzenberg, D., Henkel, S., Grosse, P., and Theiss, W., Thin Solid Films, 1995, 270, 103.
5. Vagov, A.V., Radchik, A. and Smith, G.B., Phys. Rev. Lett., 1994, 73, 1035.
6. Claro F. and Fuchs, R., Phys. Rev. B., 1986, 33, 7956.
7. Smith, G.B., Radchik, A.V., Reuben, A.J., Moses, P., Skryabin I. and Dligatch, S., in press Solar Energy Materials and Solar Cells
8. Kempe, J. Radchik A.V. and Smith, G.B., Proc. Roy. Soc. Lond. Ser. A, 1996, 452, 1845.



## MOLECULAR SIMULATION FOR GAS ADSORPTION AT TiO<sub>2</sub> (RUTILE AND ANATASE) SURFACE

Hsin-Fu Lin<sup>1</sup>, Hong-Ming Lin<sup>1</sup>, Shaw-Ling Hsu<sup>2</sup>

<sup>1</sup>Dept. of Materials Engineering, Tatung Institute of Technology, Taipei 104, Taiwan, R.O.C.

<sup>2</sup>Polymer Science and Engineering, University of Massachusetts, Amherst, MA, U. S. A.

**Abstract** -- In this study, the simulation for gas adsorption on TiO<sub>2</sub> was performed using the "SORPTION" module in the software of molecular simulation. The properties of gas adsorption at the surface of TiO<sub>2</sub> are predicted by Monte-Carlo method. The open force field theory is used to calculate the interaction energies between CO gas and rutile or anatase TiO<sub>2</sub> surface. Existence of different energy peaks in energy analysis suggests that adsorption of CO gas occurs at various atomic sites of rutile or anatase TiO<sub>2</sub> surface.

©1999 Acta Metallurgica Inc.

### INTRODUCTION

Several studies on synthesis, characteristics, properties of nanocrystalline (NC) TiO<sub>2</sub> particles have been published [1-3], and titanium dioxide has been used in a great variety of applications, as well. Especially, titanium dioxide is an intriguing support material in heterogeneous catalysis, and it has been used as a semiconductor surface in sensor applications. It is the purpose of this study to build up the database for nanocrystalline gas sensors of multi-functions and good selectivity. To evaluate adsorption properties of NC rutile or anatase TiO<sub>2</sub> particle, molecular simulation is employed to calculate the binding energies of CO gas on TiO<sub>2</sub> surface at different temperatures and pressures in this study.

### THEORETICAL SIMULATION

#### *Simulation Techniques*

In this study, simulation is performed using "SORPTION" module in molecular simulation software of Cerius 2\_1.6 (Molecular Simulation Inc.). The properties of gas adsorption at surface of TiO<sub>2</sub> are predicted by Monte-Carlo method[4], and the interaction energies between gas molecules and TiO<sub>2</sub> surface are calculated by the theory of open force field [5]. Equilibrium is achieved when the temperature and the chemical potential of the gas inside the framework are equal to the temperature and the chemical potential of the free gas outside the framework. The initial configuration contains no adsorbate molecules; each subsequent configuration is generated by one of four steps: (i) create a molecule, (ii) destroy a molecule, (iii) translate, (iv) rotate, for which the acceptance criteria are different. Each generated configuration is accepted or rejected using a Metropolis algorithm [6] based on the configuration energy change.

### Energy Calculation

Energy calculation in this simulation is confined to inter-molecular or non-bond energies. Since both the framework and the adsorbates are held internally rigid during the simulation, no valence energy terms are required in the energy calculation. Thus, only van der Waals and Coulomb energy of the adsorbate/framework system are calculated. Adsorbate/framework electrostatics is evaluated using the Ewald summation method[7], which accelerates the long-range Coulomb calculation. Since the non-periodicity of the adsorbates precludes the use of the Ewald summation method, adsorbate/adsorbate electrostatics is evaluated directly.

### Variables for Simulation

Small periodic framework models of  $\text{TiO}_2$  crystal are built up first by arranging  $6 \times 6 \times 6$  superlattice of rutile unit cell and  $6 \times 6 \times 3$  of anatase due to the working space limitation of software. These two models are then made nearly spherical in shape by 15% facetting along  $\{110\}$  planes. To calculate Coulomb energy, partial net charges[8] are placed on each atom of the frameworks. Since the framework structure must be of neutral charge, average charge is set to be zero, and partial effective charges are consequently obtained. In addition, charge equilibration [9] is applied to calculate partial charges on models of gas adsorbate [10]. The simulation of adsorption properties of CO gas on NC rutile and anatase  $\text{TiO}_2$  surface is performed at different temperatures of 473, 573, 673, 773, 873 K and pressures of 0.1, 0.5, 1.0 kPa in this study.

## RESULTS AND DISCUSSION

The mean loading curves show the average number of adsorbate molecules that are packed within the pores after equilibrium is achieved, which is equivalent to adsorption isotherms, as shown in Figure 1(a) and (b). For adsorption of CO gas on rutile or anatase  $\text{TiO}_2$  surface, the adsorption capacity increases with increasing pressures but decreases with increasing temperatures.

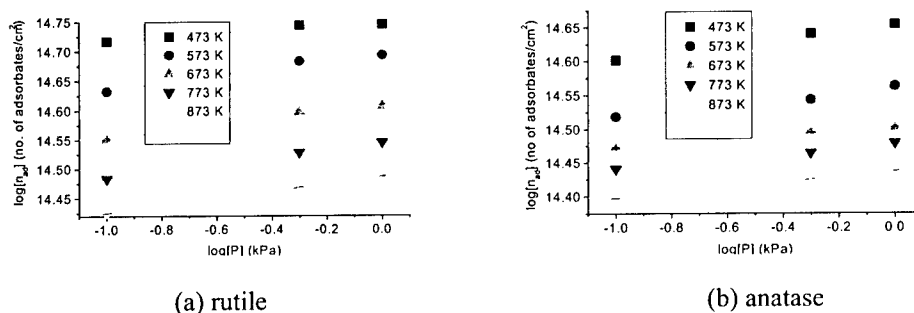
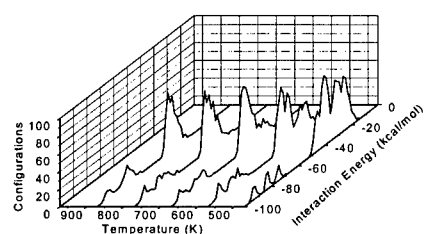
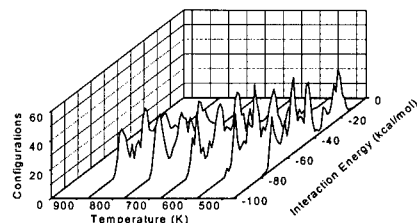
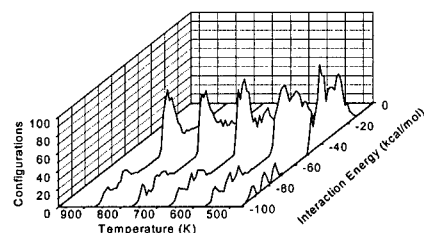
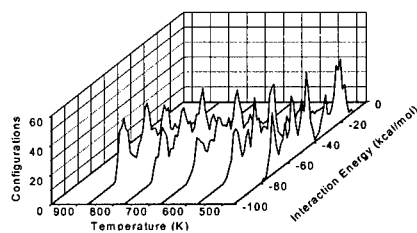
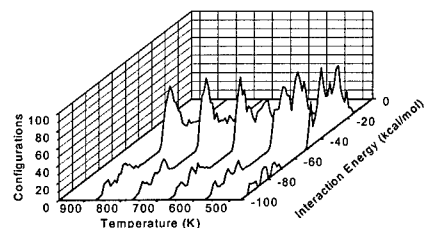
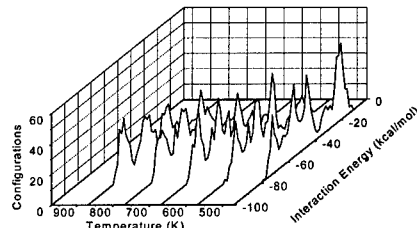


Figure 1: Adsorption isotherms for CO interaction with (a) rutile and (b) anatase.

(1)  $P = 0.1$  kPa(1)  $P = 0.1$  kPa(2)  $P = 0.5$  kPa(2)  $P = 0.5$  kPa(3)  $P = 1.0$  kPa(3)  $P = 1.0$  kPaFigure 2 (a): Energy distribution for different CO gas pressures on rutile  $\text{TiO}_2$  surface.Figure 2 (b): Energy distribution for different CO gas pressures on anatase  $\text{TiO}_2$  surface.

Energy analysis shows energy distribution in form of number of accepted configurations versus the interaction energy over the selected range. The energy distribution of adsorbates CO on either rutile or anatase  $\text{TiO}_2$  particle can be apparently divided into two portions[11], as shown in Figures 2(a) and 2(b). The energy distribution suggests that there is a stronger chemisorption between CO gas and anatase  $\text{TiO}_2$  than that of rutile  $\text{TiO}_2$ . There is large number of configurations for anatase structure appearing in higher interaction energy range. That indicates the anatase structure of  $\text{TiO}_2$  has a greater catalytic activity or selectivity for CO gas than that of rutile structure of  $\text{TiO}_2$ .

The results also show the energy peaks are shifted from lower interaction energy to higher interaction energy while the temperature is increased, because it needs more interaction energy for gas molecules to react with  $\text{TiO}_2$  surface. Meanwhile, it can be observed that energy peaks diminish gradually with increasing temperature. This could be attributed to thermal desorption or fluctuation at higher temperatures due to escape of adsorbed gas molecules after obtaining energy larger than binding energy. In addition, each energy peak also can be considered as one preferred binding position. In other word, existence of different energy peaks in the energy distribution infers that adsorption of CO gas molecules might occur at various binding sites.

### CONCLUSIONS

The simulation results can be used semi-quantitatively to compare the adsorption properties of CO gas on the rutile and anatase  $\text{TiO}_2$  surfaces. From the adsorption isotherms, it is found that the amount of CO gas adsorption increases as the pressure is increased, while it decreases as the temperature is raised. The energy distribution suggests that CO gas is reacted with anatase structure by a strong chemical bond than that of rutile structure. The results indicate the anatase structure of  $\text{TiO}_2$  has a greater catalytic activity or selectivity for CO gas than that of rutile structure of  $\text{TiO}_2$ .

### ACKNOWLEDGMENTS

We would like to thank the National Science Council, Republic of China for financial support through Contract Number NSC 86-2216-E-036-013.

### REFERENCES

1. R. W. Siegel, S. Ramasamy, H. Hahn, Li Zongquan and Lu Ting, *J. Mater. Res.*, **3**(6), 1367(1988).
2. H. Hahn, J. Logas and R. S. Averback, *J. Mater. Res.*, **5**(3), 609(1990).
3. U. Balachandran, N. G. Eror, *J. Mater. Sci.*, **23**, 2676(1988).
4. K. Binder, "Monte Carlo Methods in Statistical Physics", Springer-Verlag, New York (1986).
5. A. K. Rappé, C. J. Casewit, K. S. Colwell, W. A. Goddard III and W. M. Skiff, *J. Am. Chem. Soc.*, **114**, 10024(1992).
6. N. Metropolis, A. W. Rosenbluth, M. N. Rosenbluth and A.H. Teller, *J. Chem. Phys.*, **21**(6), 1087(1953).
7. N. Karasawa and W. A. Goddard III, *J. Phys. Chem.*, **93**, 7320(1989).
8. B. Silvi, N. Fourati, R. Nada and C. R. A. Catlow, *J. Phys. Chem. Solids*, **52**(8), 1005(1991).
9. A. K. Rappé and W. A. Goddard III, *J. Phys. Chem.*, **95**, 3358(1991).
10. L. Pauling, "The Nature of the Chemical Bond", 3<sup>rd</sup> edition, Cornell University Press (1960).
11. A. Mandelis, "Physics, Chemistry and Technology of Solid State Gas Sensor Devices", John Wiley & Sons, Inc. (1993)



COMPUTATION OF CAPACITANCES OF  $Cu_n$  NANOCCLUSERSP. Senet<sup>(1)</sup> and M. Hou<sup>(2)</sup>(1) Laboratoire de Physique du Solide, FUNDP, Rue de Bruxelles 61,  
B-5000 Namur, Belgium(2) Physique des Solides Irradiés CP 234, ULB, Bd du Triomphe,  
B-1050 Bruxelles, Belgium

**Abstract** The capacitance  $C$  of isolated clusters  $Cu_n$  ( $n=13$  to  $535$ ) is computed by using an atomistic model based on DFT concepts and realistic cluster geometries. The equilibrium OK atomic configurations are evaluated independently by means of heating and cooling cycles modelled classically by MD using a tight binding cohesion model. The dependence of  $C$  over the cluster size calculated numerically is compared to available experimental data and to the simple classical and jellium  $1/R$  behavior. Variation of  $C$  with the cluster topology is studied by computing the chemical hardness  $\eta=e^2/4\pi\epsilon_0 C$  of isomers of  $Cu_{44}$ .

©1999 Acta Metallurgica Inc.

## 1. INTRODUCTION

The differential capacitance  $C$  of a cluster is one of the most important quantities for the description of electron transfer phenomena at the nanoscale (1). In chemistry, the energy  $e^2/4\pi\epsilon_0 C$  is called the chemical hardness  $\eta$  of the system and is defined as the second derivative of the total energy  $E$  of the cluster relative to its electron number  $N$  at the ground-state geometry (2). The derivative is approximated by the difference between the chemical potential  $\mu=dE/dN$  evaluated to the left and to the right of an integer value of  $N$

$$\eta=e^2/4\pi\epsilon_0 C = I - A \quad [1]$$

where  $I$  and  $A$  are the ionisation potential and the electronic affinity of the cluster (2).

$\eta$  depends on the cluster size, i.e. on the number of atoms  $n$ . *Ab initio* calculations of  $\eta$  for various clusters ( $Na_n$ ,  $Al_n$ ) represented by spherical or ellipsoidal jellium models, where the metal ions are smeared out in a positive background, show that  $\eta$  is nearly proportional to  $n^{-1/3}$ , i.e. to  $1/R$  where  $R$  is the cluster radius (3). For spherical clusters, the size dependence of  $C=e^2/4\pi\epsilon_0 \eta$  is well represented by

$$C = R+d = r_s n^{1/3} + d \quad [2]$$

where  $R+d$  is the radial location of the image plane, which is shifted towards vacuum because of the spill-out of the electronic density at the surface ( $d$  is of the order of  $1\text{\AA}$ ) (3). One has

introduced in Eq. [2] the Seitz radius  $r_s$  i.e. the radius of a sphere containing exactly one electron, assuming one valence electron/atom.

Comparison of  $e^2/4\pi\epsilon_0 C$  deduced from Eq. [2] with experiment is qualitatively satisfactory though deviations are observed (3). Indeed, the real geometry of metal nanoclusters can largely depart from the simple spherical or ellipsoidal geometries and  $\eta$  is thus expected to depend also on the detail of the cluster topology. This could affect the size dependence predicted by Eq. [2]. On the other hand, a given  $n$  or radius does not correspond to a unique structure since small and medium size metal clusters have many isomers. It is known in chemistry that isomers of small molecules have in general different hardnesses and that the most stable isomer is the hardest (4). In the present work, one will estimate the variation of  $\eta$  with the cluster size and topology by computing the hardness of  $\text{Cu}_n$  clusters for  $n=13$  to 535 and of isomers of  $\text{Cu}_{44}$  by using realistic geometries and a simple density-functional atomistic model.

The paper is organised as follows.  $\text{Cu}_n$  cluster geometries and the simulation method are described next. Sec. 3 contains a brief description of the atomistic model. Numerical results are presented and discussed in Sec. 4.

## 2. STRUCTURE OF $\text{Cu}_n$ CLUSTERS

Cluster morphologies are obtained by means of classical molecular dynamics (MD). The initial arbitrary configurations are obtained by cutting spheres of various radii in the bulk fcc Cu structure.

The interatomic forces used in the MD simulations are derived numerically from an expression of the cohesion energy based on the second moment approximation of the tight binding model (5) in its short range version suggested in (6). The binding energy is parametrized on elastic and energetic bulk Cu properties (6).

Stable clusters are obtained by heating and slow cooling cycles down to 0 K.

When  $n=13$ , 55 and 147, a perfect stacking of one, two and three icosahedra is found respectively. Because of the Ih symmetry these clusters are the most spherical ones. For  $n<200$  and different from the above mentioned values, all stable clusters have low symmetry, thus giving rise to an infinite variety of possible isomers. For  $535>n>200$ , the clusters are found to remain fcc with a cuboid morphology. A more detailed study of structural and morphological properties of small clusters will be given elsewhere (7).

## 3. ATOMISTIC MODEL

$\eta$  of a cluster is calculated as the variation of the electronic chemical potential  $\mu$  of the cluster due to its charging with one electron, evaluated at a frozen geometry by using the electronegativity equalisation method (EEM) (8). This method has been modified in order to introduce a realistic description of the polarizabilities and cohesion energies of the Cu clusters (7). Basically, each Cu atom is described by its hardness  $\eta_a$  and its dipole polarizability  $\alpha_a$  which are  $\eta_a = I_a - A_a = 6.5$  eV (2) and  $\alpha_a = 9 \text{ \AA}^3$  (9). Physically speaking, each atom is thus described here as a spherical capacitive and polarizable object.

The variation of the electronic density of the cluster resulting of an additional charge is represented by point induced charges and dipole moments at the atomic sites. The charged atoms interact through Coulomb forces and through a nearest-neighbour charge-charge coupling constant  $A = -0.45$  eV which is related to the cohesion energy (7). The equilibrium configuration of these charges and dipoles upon charging is calculated self-consistently by minimising the total energy relative to the charges and to the dipoles as in EEM (8). This yields to a linear set of equations which is solved numerically by standard methods.

#### 4. RESULTS AND DISCUSSION

Numerical calculations of  $C$  based on the structures obtained by MD are summarized in Fig. 1. Except for  $n=201$ , the variation of  $C$  with  $n$  is in excellent agreement with Eq. [2]. A linear fit to our data yields  $r_s = 1.445$  Å and  $d = 0.575$  Å. The former value is close to the value of bulk Cu (1.413 Å). It is interesting to note that the deviation observed at  $n=201$  corresponds precisely to a change in the cluster morphologies being icosahedral or of low symmetry below 200 and fcc above. This could explain the relative electronic softness of  $\text{Cu}_{201}$ .

For  $n=13, 16$  and  $28$  the experimental and theoretical values (in brackets) of  $\eta$  can be compared. They are 3.37 (3.68) eV, 3.32 (3.54) eV and 3.05 (2.87) eV, respectively (7).

Calculations of  $\eta$  for ten isomers of  $\text{Cu}_{44}$  are presented in Fig. 2. The variations of  $\eta$  are found of the same order of magnitude as the variations of the cohesive energy. However there is no linear correlation between the two quantities though the isomers having the two lowest energies also have the larger hardnesses.

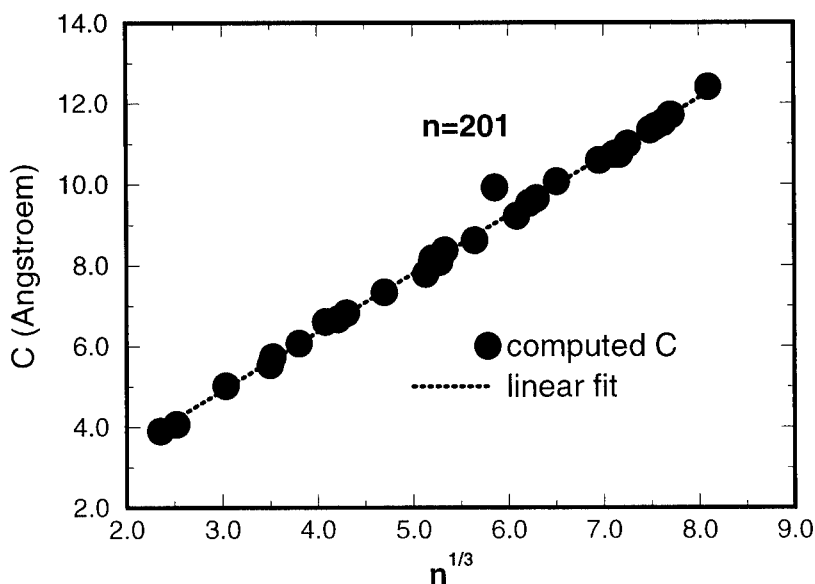


Fig. 1 Computed capacitances  $C$  for  $\text{Cu}_n$  clusters

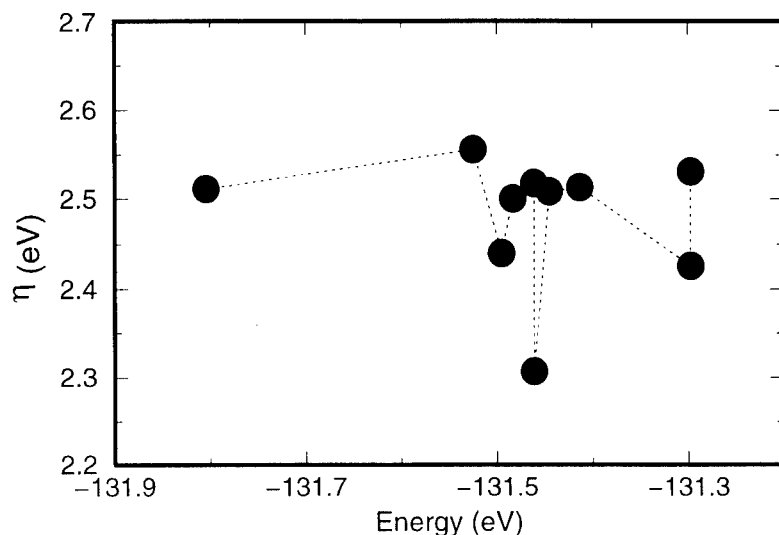


Fig. 2 Hardnesses of isomers of  $\text{Cu}_{44}$

It should be noted that both electronic (HOMO-LUMO gap) and structural (Jahn-Teller distortions) effects due to the closing of electronic shells (3) are not described by the present approach. The small deviation between the present theory and experiment (0.3 eV) for  $\eta$  gives an estimation of the order of magnitude of such effects. On the other hand, JT distortions - which exist only for high symmetric clusters - are found to be small (0.03 Å) for  $\text{Cu}_n$  clusters (10). Moreover, one observes that atomistic calculations of  $C$  agree very well with Eq. [2] predicted by quantum jellium model. In conclusion, the present discrete model gives a satisfactory description of  $C$  of nanoclusters and could be improved by including quantum electronic shell effects (7).

This work is funded by the PAI/IUAP P4/10 project on reduced dimensionality systems. P. S. is grateful to the National Fund of Research Belgium (FNRS) for his support.

1. Jian Wang, Hong Guo, Jose-Luis Mozos, C. C. Wan, Gianni Taraschi, and Qingrong Zheng, *Phys. Rev. Lett.* **80**, 4277 (1998).
2. R. G. Parr and R. G. Pearson, *J. Am. Chem. Soc.* **105**, 7512 (1983).
3. J. A. Alonso and L. C. Balás in *Chemical hardness, Struct. Bonding* **80**, edited by K. D. Sen, Springer Verlag, Berlin, 1993, p. 229.
4. For a review see, P. K. Chattaraj, *Proc. Indian natn. Sci. Acad.* **62**, 513 (1996).
5. F. Ducastelle, *J. de Physique* **31**, 1055 (1970).
6. G. J. Ackland and V. Vitek, *Phys. Rev.* **B41**, 10324 (1990).
7. P. Senet and M. Hou, in preparation.
8. B. G. Baekelandt, W. J. Mortier and R. A. Schoonheydt in *Chemical hardness, Struct. Bonding* **80**, edited by K. D. Sen, Springer Verlag, Berlin, 1993, p. 187.
9. *Handbook of Chemistry and Physics*, 79<sup>th</sup> edition, CRC Press, 1998.
10. U. Lammers and G. Bortsel, *Phys. Rev.* **B49**, 17360 (1994).



Pergamon

NanoStructured Materials, Vol. 12, pp. 365–368, 1999

Elsevier Science Ltd

© 1999 Acta Metallurgica Inc.

Printed in the USA. All rights reserved

0965-9773/99/\$-see front matter

PII S0965-9773(99)00136-1

## SURFACE TENSION OF ULTRAFINE PARTICLES

M.I. Alymov and M.Kh. Shorshorov

Baikov Institute of Metallurgy and Materials Science, Russian Academy of Science,  
Leninsky prospect 49, Moscow, 117334, Russia

**Abstract** — *Thermodynamic properties of ultrafine particles were investigated based on the thermodynamics of small systems. The size factor dependence of melting temperature and surface tension were established for ultrafine particles. Substantial influence of size factor on surface tension of ultrafine particles with radius less than 10 nm was shown.*

©1999 Acta Metallurgica Inc.

### INTRODUCTION

The consideration of an ensemble of small systems is the main idea of the thermodynamics of small systems developed by T. Hill (1). The difference between the thermodynamics of small (disperse) systems and macroscopic thermodynamics is in the consideration of the additional degree of freedom connected with the size of small system. An ultrafine particle is implied by a small system. Then thermodynamic potential  $F$  is the function of temperature, pressure, and size of a system (2).

### RESULTS AND DISCUSSION

Let us consider the melting of an ultrafine particle with volume  $V$  consisting of  $n$  atoms ( $n = V/\Omega$ , where  $\Omega$  is an atom volume). The thermodynamic potential of the particle in solid state  $F_{\text{sol}}$  is

$$F_{\text{sol}} = n \mu_0 + \sigma_{\text{s-l}} S \quad [1]$$

where  $\mu_0$  is the chemical potential of the atom,  $\sigma_{\text{s-g}}$  is the coefficient of surface tension (specific free surface energy) on a crystal-gas boundary, and  $S$  is the surface area of the particle. In order to take into account the shape of the particle, let us write the second item in the form

$$\sigma_{\text{s-g}} S = a_{\text{s-g}} n^{2/3} \quad [2]$$

where

$$a_{\text{s-g}} = \alpha \sigma_{\text{s-g}} \Omega^{2/3} \quad [3]$$

An atom volume  $\Omega$  (we presume that the atom volumes in solid and liquid phases are approximately the same) and the coefficient of particle shape  $\alpha$  are determined by formulas

$$\alpha = S V^{-2/3} \quad [4]$$

and

$$\Omega = (4/3) \pi r_a^3 \quad [5]$$

where  $r_a$  is the radius of atom.

Taking into account relation [2], we can express the thermodynamic potential of the solid particle as

$$F_{sol} = n \mu_0 + a_{s-g} n^{2/3} \quad [6]$$

The thermodynamic potential of the particle in liquid state can be expressed as follows  
(3)

$$F_{liq} = n \mu_0 + n \Delta h_s (1 - T_m/T_s) + a_{l-g} n^{2/3} \quad [7]$$

$$\Delta h_s = \Delta H_s / N_a \quad [8]$$

where  $\Delta H_s$  is the melting enthalpy of a mole of the material,  $N_a$  is Avogadro number,  $T_s$  is the melting temperature of massive material (macroscopic system), and  $T_m$  is the melting temperature of the ultrafine particle. Thermodynamic potentials of particles in solid and liquid state are equal in the point of melting (4), so, taking into account that

$$\sigma_{s-g} = \sigma_{s-l} + \sigma_{l-g} \quad [9]$$

we can get from equations [6] and [7]

$$\sigma_{s-l} = \alpha^{-1} \Omega^{-2/3} N_a^{-1} \Delta H_s n^{1/3} (1 - T_m/T_s) \quad [10]$$

$$T_m/T_s = 1 - \sigma_{s-l} \alpha \Omega^{2/3} N_a / (\Delta H_s n^{1/3}) \quad [11]$$

If particles size dependence of ultrafine particles melting temperature is known, then equation [10] permits us to determine particles size dependence of  $\sigma_{s-l}$ . Relationships for a spherical particle are as follows:

$$\alpha = 4\pi(4\pi/3)^{-2/3} \quad [12]$$

$$n = (4\pi/3)R^3/\Omega \quad [13]$$

$$T_m/T_s = 1 - 3\sigma_{s-l} \Omega N_a / (\Delta H_s R) \quad [14]$$

Relationships for a disk-shaped particle with ratio between its diameter  $2R$  and height  $h$  equal to  $\eta = 2R/h$  are as follows

$$\alpha = (2\pi)^{1/3} (1 + 2/\eta)^{2/3} \quad [15]$$

$$n = 2\pi R^3/(\eta \Omega) \quad [16]$$

$$T_m/T_s = 1 - (2 + \eta) \sigma_{s-l} \Omega N_a / (\Delta H_s R) \quad [17]$$

Using [11], [14], and [17], we can calculate the melting temperature of ultrafine particles with the account of  $\sigma_{s-l}$ . One should stress that the equation for the disk-shaped particle with  $\eta = 1$  [17] coincides with this for spherical particles [14].

Taking into account the results of (5), we receive

$$T_m/T_s = (1 + \alpha / n^{1/3})(\Delta H_s - \Delta H_f) / \Delta S_s \quad [18]$$

where  $\Delta H_f = 2/3 \alpha \sigma_{s-g} \Omega^{2/3} N_a n^{-1/3}$ , and  $\Delta S_s$  is a melting enthalpy. Using the equation  $\Delta H_s = \Delta S_s T_s$ , we receive

$$T_m/T_s = (1 + \alpha / n^{1/3})(1 - \Delta H_f / \Delta H_s) \quad [19]$$

The equation [19] has the following form for spherical particles in view of [12] and [13]:

$$T_m/T_s = (1 + 3 \Omega^{1/3}/R)(1 - 2 \sigma_{s-g} \Omega N_a / (\Delta H_s R)) \quad [20]$$

In view of [15] and [16] equation [19] takes the following form for a disk-shaped particle:

$$T_m/T_s = (1 + (2 + \eta)\Omega^{1/3}/R)(1 - 2 (2 + \eta) \sigma_{s-g} \Omega N_a / (3\Delta H_s R)) \quad [21]$$

Received equations [19-21] also permit us to calculate the melting temperature of ultrafine particles in view of  $\sigma_{s-g}$ . One should stress that the equation for the disk-shaped particle with  $\eta = 1$  [21] coincides with this for spherical particles [20].

Let us calculate  $\sigma_{s-l}$  and  $\sigma_{s-g}$  by received equations using the experimental data for Sn (6) and Au (7). As equations for disk-shaped particles with  $\eta = 1$  coincides with equations for spherical particles, we shall use equations for spherical particles, because they are more general.

The values of  $\sigma_{s-l}$  and  $\sigma_{s-g}$  for big particles must be equal to their values for massive material. Then, using the experimental data for  $T_m$  (8), a melting temperature of small particles with big radius (6, 7), and  $\sigma_{s-l}$  for material in massive state (9), we receive  $\eta$ . Calculations by equation [17] showed that  $\eta$  is equal to 3.5 and 3.0 for Sn and Au, respectively.

Particle radius  $R$  dependencies of  $T_m/T_s$  for Sn (by the data from (6)) and Au (by the data from (7)) and values  $\sigma_{s-l}$  and  $\sigma_{s-g}$  and calculated by equations [17] and [21], respectively, are presented in Fig. 1 (a, b). The value of  $\sigma_{l-g}$  is determined by equation [9]. The results of calculation show that  $\sigma_{s-g}$  almost not depend of particles size,  $\sigma_{s-l}$  increases, and  $\sigma_{l-g}$  decreases as particle size decreases for particles with radius less than 10 nm.

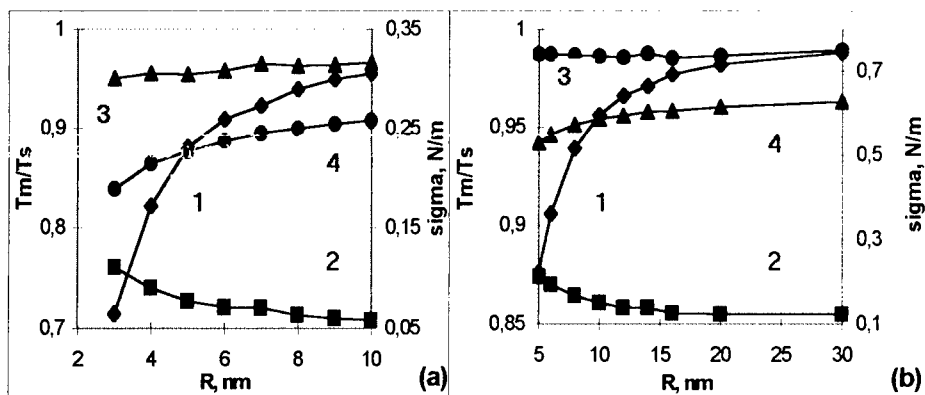


Fig. 1. Melting temperature  $T_m/T_s$ (1) and surface tension  $\sigma_{s-l}$ (2),  $\sigma_{s-g}$ (3) and  $\sigma_{l-g}$ (4) as a function of the radius ( $R$ ) for Sn (a) and Au (b).

## CONCLUSIONS

The estimation of size and shape dependence of the melting temperature and the surface tension for ultrafine particles is done. It is shown that the surface tension in ultrafine particles with radius less than 10 nm depends of their shape and form. The results of surface tension calculation show that surface tension  $\sigma_{s-l}$  grows and  $\sigma_{l-g}$  falls as particle size decreases, and  $\sigma_{s-g}$  almost does not depend of particle size.

## REFERENCES

1. Hill, T.L., *Thermodynamics of Small Systems*, Benjamin inc., New York, 1964, p. 370.
2. Fyodorov V.B., Shorshorov M.Kh. and Khakimova D.K., *Carbon and its Interaction with Metals*, Metallurgy, Moscow, 1978, p. 240 (in Russian).
3. Fyodorov V.B., Shorshorov M.Kh., Kalashnikov E.G. and Shorshorov M.Kh., *Fizika i Khimiya Obrabotky Materialov*, 1976, 3, 74 (in Russian).
4. Frenkel Ya.I., *Introduction in Theory of Metals*, OGIZ, Moscow, 1948, p.240 (in Russian).
5. Shorshorov M.Kh., Fyodorov V.B., Gusev O.V. and others, *Fizika i Khimiya Obrabotky Materialov*, 1975, 6, 57 (in Russian).
6. Wronski C.R.W., *Brit. J. Appl. Phys.*, 1967, 12, 1731.
7. Sambles J.R., *Proc. Roy. Soc.*, 1971, 2, 339.
8. Smithells C.I., *Metals Reference Book*, Butterworth and Co. Ltd., London, 1976, p.447.
9. Hollomon D.N. and Tarnball D., *Progress in Physics of Metals*, Metallurgizdat, Moscow, 1956, p.304 (in Russian).





Pergamon

NanoStructured Materials, Vol. 12, pp. 369–372, 1999  
Elsevier Science Ltd

© 1999 Acta Metallurgica Inc.

Printed in the USA. All rights reserved  
0965-9773/99/\$-see front matter

PII S0965-9773(99)00137-3

## TO WHAT EXTENT A CRYSTAL CAN BE SUPERHEATED

Z.H. Jin and K. Lu

State Key Lab for RSA, Institute of Metal Research, Chinese Academy of Sciences,  
Shenyang 110015, P. R. China

**Abstract** – Effects of size and surface/interface on melting of clusters and thin films are studied with molecular dynamics (MD) via many-body type interatomic potentials. Providing coherent/semicoherent grain boundary conditions, the melting points of confined clusters and thin films at given sizes can be significantly elevated. The relationship between the degree of superheating and size can be well predicted using the homogeneous nucleation theory for melting. In strengthening the constraint conditions, such as by limiting the nucleation size to be small enough, the melting point can be significantly elevated to and even beyond the upper-limit predicted using other thermodynamic or mechanical models. ©1999 Acta Metallurgica Inc.

### INTRODUCTION

The origin of melting of substances still remains to be a much debating subject [1, 2]. The situation becomes even more pressing due to many pieces of experimental evidences on metastable superheating of confined particles observed during the last decade [3–6]. Many factors, such as size, shape, presence or absence of free surfaces, the degree of the interfacial coherency and the kinetic effects, may play crucial roles. However, a general agreement about the underlying superheating and melting mechanism is still needed.

Recently, Lu and Li [7] performed a careful analysis of a homogeneous nucleation theory for melting and their conclusions may be two folds. (i) For an ideal bulk crystal without any free surfaces (or other extrinsic defects), a kinetic limit for an intrinsic superheating can be defined which appears to be the lowest in comparing with the entropy, volume and rigidity catastrophes [8, 9]. (ii) A criterion can be drawn on the relationship between the degree of superheating and the size of the nucleate. For small particles imbedded in high-melting-point matrices, such a criterion is extremely useful in predicting the degree of superheating, in viewing that the constrained crystallite melts homogeneously as a single nucleate. MD simulations for superheating and melting of surface-free bulk single crystal [10] have further supported these conclusions.

For further clarifying the applicability of the homogeneous nucleation theory, we have performed MD simulations for confined particles and thin films, and some new results have been briefly summarized in this paper.

### MODEL CONSTRUCTIONS

We have used the Sutton-Chen (SC) type many-body potentials [11] in our simulations. Two systems have been simulated. First, for Pb clusters coated with Al, the potential parameters have been adjusted in obtaining a reasonable description of the Al-Pb interaction [12]. Second, by adjusting one parameter for Al, we can define a series of 'model' metals with any desirable melting temperatures but the same lattice parameter at zero temperature. So we can build up confined particles or thin films without significant lattice-mismatch effects. For convenience of numerical evaluations, we have simulated confined thin films, which consist of atoms of a model material of which the melting point is a quarter of that for the host material (Al).

## RESULTS

### *Melting of Coated Pb Clusters*

Two Pb clusters with 201 ( $\text{Pb}^{201}$ ) and 249 ( $\text{Pb}^{249}$ ) atoms were selected and each has been embedded into the core of a truncated-octahedral  $\text{Al}^{4033}$  cluster. For  $\text{Pb}^{201}$ , which is also truncated-octahedron, is in a parallel cube-cube relationship with the Al coating. For  $\text{Pb}^{249}$ , which is 'spherical', no parallel orientational relationship exists with the Al coating. The two clusters represent respectively the two typical grain boundary (GB) structures of the melt-spun and ball-milled Pb granular in Al as observed experimentally [13]. They show quite different melting properties. For  $\text{Pb}^{201}$ , semicoherent interfaces can be formed and the Pb core can be superheated up to 750 K against  $610 \pm 10$  K of the thermal equilibrium melting point ( $T_0$ ) for the SC Pb metal, followed by a simultaneous melting of both the core and the coating. While for  $\text{Pb}^{249}$ , no effective semicoherent interface can be formed, and the core permelts at about 500 K without the broken of the outer-shell Al crystalline structure. These results are in accordance with the experimental observations and can provide further evidences that superheating of confined particles occurs because of the existence of epitaxy GBs. It is also observed that the formation of a semicoherent Al-Pb GB is accompanied by a generation of dislocations through the Al coatings, and melting is initiated within the interior of  $\text{Pb}^{201}$ , rather than at the interfaces.

### *Melting of Confined Thin Films*

To avoid lattice-mismatch effects, we have performed MD simulations for melting of model thin-film crystals (10 (111) layers for film A and 4 (111) layers for film B) fully confined by Al matrix. The results demonstrate that both samples melt at much higher temperatures than any free surfaces for a bulk crystal. The confined film A melts at about 306 K, while B melts at about 430 K, against  $T_0 = 245 \pm 10$  K of the model crystal. It is promising in finding out that melting is initiated homogeneously from the interior of the confined thin films, rather than heterogeneously at the interfaces. The crystallinity of the outer two layers of the confined film tends to survive up to a rather high temperature as illustrated in FIG. 1.

## DISCUSSION

Based on the classic homogeneous nucleation theory, the relationship between the degree of superheating  $\Delta T$  and the critical size (radius  $r_c$ ) of a spherical embryo can be written as

$$\Delta T/T_0 = (2\gamma_{LS}/r_c + \Delta E)/L_0 \quad (1)$$

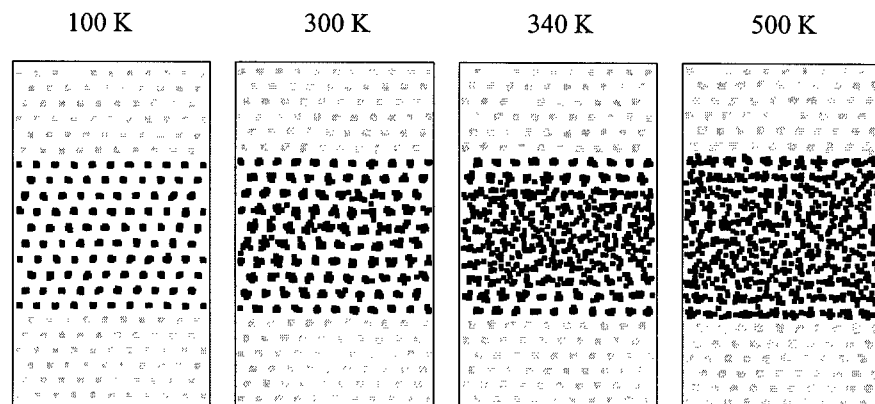


FIG. 1. Positions of the atoms projected onto the  $x$ - $z$  plane for a MD simulated confined thin film at different temperatures before and after melting.

where  $L_0$  is the latent heat at  $T_0$ ,  $\chi_{LS}$  is the solid-liquid interface free energy, and  $\Delta E$  reflects the strain effects caused by volume change on melting [14]. The relationship can be generalized to the case either for confined particles or thin films in replacing  $\chi_{LS}$  by  $\chi_{LM} - \chi_{SM}$ , i.e., the liquid and solid particle (or film)-matrix interfacial energy difference on melting. Superheating will occur when the value of  $\chi_{LM} - \chi_{SM}$  is positive.

For our simulated systems, it is found that the  $\chi_{LM} - \chi_{SM}$  value is very close to the  $\chi_{LS}$  value of the corresponding pure substance, in providing a strong evidence that the homogeneously nucleation theory is quite applicable in predicting the superheating behaviors. Such as for Pb clusters, with  $\chi_{LS}$  and  $r_c$  being  $3.3 \times 10^{-2} \text{ J/m}^2$  and  $12.5 \text{ \AA}$  respectively,  $\Delta T$  is calculated to be 130-150 K ( $\Delta E/L_0 \sim 3.2\%$  for Pb), in rather good agreement with the MD results. On the other hand, for confined thin films, the  $\chi_{LM} - \chi_{SM}$  value can be calculated via a energy minimization procedure, which appears to be about  $3 \times 10^{-2} \text{ J/m}^2$ , very close to a quarter of  $11 \times 10^{-2} \text{ J/m}^2$  for Al as given in the literature [15]. As an example, FIG. 2 shows such a comparison of the  $\Delta T/T_0$  vs. size relationship between theory and MD data for the confined thin-films. It is worth noting that, as in the case of the confined film B, the possible superheating degree ( $\Delta T \sim 0.75 T_0$ , see also FIG. 2.) can exceed the upper limit as predicted from entropy or rigidity models ( $\Delta T \leq 0.38 T_0$  for Al), and the underlying mechanism still deserves to be further clarified.

## CONCLUSION

In summary, some new results on superheating and melting mechanisms has been described. By simulating melting behaviors of confined particles and thin films, it is found that the existence of coherent or semicoherent GBs is essential for possible superheating. Melting can take place homogeneously at the interior of confined particles or thin films, rather than heterogeneously at the interfaces, and the degree of superheating is controlled by both size and strength of the constraint.

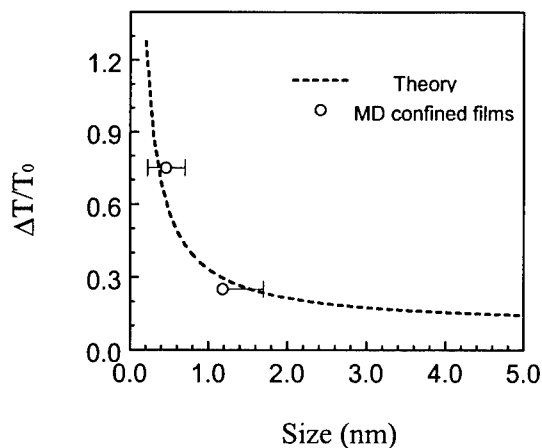


FIG. 2. Degree of superheating of two MD simulated confined thin films against the curve predicted using homogeneous nucleation theory. Error bars indicate the uncertainties in evaluating the effective nucleation size on melting.

#### ACKNOWLEDGEMENTS

This work is financially supported by the National Science Foundation of China (under grants of 59625101&59841004) and the 'Pan Deng' project on computational material science.

#### REFERENCES

1. R. W. Cahn, *Nature (London)*, 1986, **668**, 32.
2. D. Wolf, P. R. Okamoto, S. Yip, J. F. Lutsko and M. Kluge, *J. Mater. Res.*, 1990, **5**, 286.
3. J. Däges, H. Gleiter and J.H. Perepezko, *Phys. Lett.*, 1986, A **119**, 79.
4. C.J. Rossouw and S.E. Donnelly, *Phys. Rev. Lett.*, 1985, **55**, 2960.
5. D.L. Zhang and B. Cantor, *Acta Metall. Mater.*, 1991, **39**, 1591.
6. L. Gråbæk, J. Bohr, H. H. Anderson, A. Johnson, E. Johnson, A. Sarholt-Kristensen and I. K. Robinson, *Phys. Rev.*, 1992, B **45**, 2628.
7. K. Lu and Y. Li, *Phys. Rev. Lett.*, 1998, in press.
8. H.J. Fecht and W.L. Johnson, *Nature (London)*, 1988, **334**, 50.
9. J.L. Tallon, *Nature (London)*, 1989, **342**, 658.
10. Z.H. Jin and K. Lu, *Philos. Mag. Lett.*, 1998, in press.
11. A.P. Sutton and J. Chen, *Philos. Mag. Lett.*, 1990, **61**, 139.
12. Z.H. Jin, H.W. Sheng, and K. Lu, to be published.
13. H.W. Sheng, G. Ren, L.M. Peng, Z.Q. Hu and K. Lu, *Philos. Mag. Lett.*, 1996, **73**, 179.
14. G.L. Allen, W.W. Gile, and W.A. Jesser, *Acta Metall.*, 1980, **28**, 1695.
15. F.D. Di Tolla, F. Ercolessi, and E. Tosatti, *Phys. Rev. Lett.*, 1995, **74**, 3201.



Pergamon

NanoStructured Materials, Vol. 12, pp. 373-376, 1999

Elsevier Science Ltd

© 1999 Acta Metallurgica Inc.

Printed in the USA. All rights reserved

0965-9773/99/\$-see front matter

PII S0965-9773(99)00138-5

## THE SIMULATION OF CHARGE TRANSPORT IN THE NANOSTRUCTURE "CAMEL" AND HETEROTRANSISTORS

A.S.Bugaev, S.M.Korshunov, S.D.Kuzmichev, V.E.Sorokoumov

Moscow Institute of Physics and Technology, Dolgoprudny,  
Moscow Region, Russia, 141700.

**Abstract** – *Heterojunction bipolar GaAs transistor with AlGaAs emitter and Si-"Camel"-transistor were simulated using manyparticles method for hot electrons and stochastic dynamics method for equilibrium holes and electrons. Some transient processes were investigated at times of the order  $10^{-11}$  s. Dynamics of transient processes is affected by electron space charge and unequipotentiality of base region. ©1999 Acta Metallurgica Inc.*

### I. INTRODUCTION

The progress in modern semiconductor microelectronics stimulates the development of electron device models which take into account many physical processes taking place in such devices. The study of charge transport in semiconductor nanostructures is of fundamental importance both from the point of view of basic physics and its application to electron devices. The applied aspect of the problem is even more important, since modern electronics depends heavily on sophisticated knowledge of many aspects of charge transport in semiconductors.

The main characteristics of camel- and heterotransistors are conditioned by peculiarities of transport of nonequilibrium ("hot") electrons in active region of the device. In this area hot electrons are injected from the emitter through the potential barrier at the boundary between the emitter and the base.

### II. RESULTS

The structure and geometry of HBT-transistor are shown in fig.1. This structure consists of  $Al_{0.3}Ga_{0.7}As$  emitter  $n^+$ -region, narrow  $GaAs$  base  $p^{++}$ -region and  $GaAs$  collector  $n^+$ -region. Heterojunction position coincide with the boundary between the base and the emitter. Due to the small width of  $p^{++}$ -base (300 nm) almost collisionless (ballistic) transition of electrons through active region of device is achieved.

The structure of camel-transistor is shown in fig.9. This structure consists of emitter  $n^+$ -region, narrow base  $n^{++}$ -region and collector  $n^+$ -region. The maxima of potential barriers coincide with the position of thin  $p^{++}$ -layers. The

small width of  $p^{++}$  - layers ( 30 nm ) and base layer provide almost collision-less (ballistic) transit of electrons through active region of the device. Classical kinetic equations for one particle distribution functions of electrons are used for describing nonequilibrium processes in electron-hole plasma under the influence of self-consistent electric field. Coupled collisions are not taken into account. Characteristic times of nonstationary processes in the investigation are chosen to be much less than the times determining generation-recombination processes. The generation-recombination members are omitted in kinetic equation. The scattering of electrons on phonons and impurities are assumed to be three-dimensional and are simulated by Monte-Carlo method. Charge carrier equilibrium equations are solved by the method of stochastic dynamics of macroparticles. (1,2)

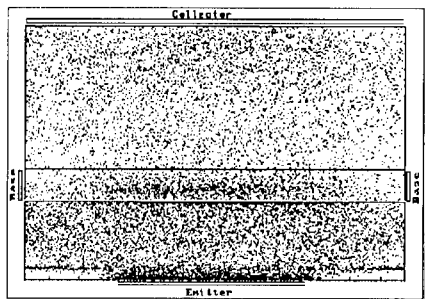


fig. 1

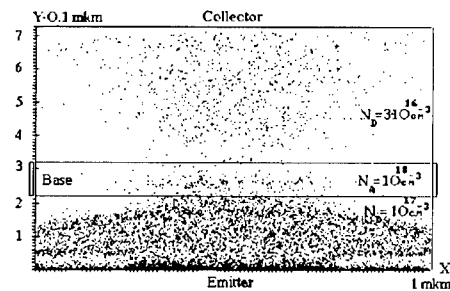


fig. 2

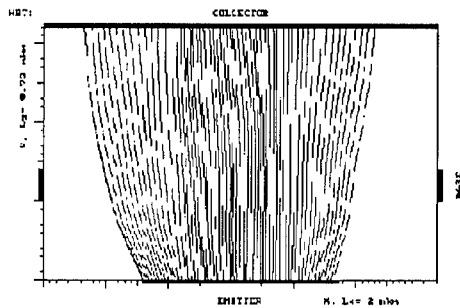


fig. 3

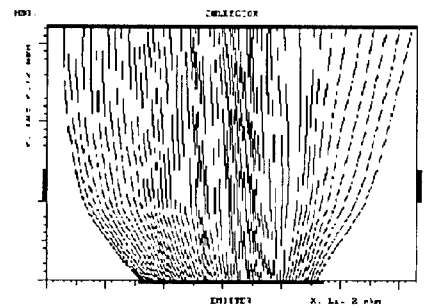


fig. 4

Boundary conditions for equations are determined by the injection and reflection properties of different parts of the boundary and by the electrodes potential and zero normal derivative of potential at the other parts of boundary where the electrodes are absent. Initial conditions are chosen from the condition of quasineutrality in the emitter, base and collector areas.

The scientific and applied software package was created for the numerical simulation of nanostructure semiconductor devices by ensemble Monte-Carlo particles method. The investigations of the dynamic operation and optimization of the parameters of nanostructure camel and heterotransistors were carried out.

The results of the simulation of the HBT-transistor with different emitter-base voltages and the same emitter collector voltages are shown in the figures

1-6. On the fig. 1-2 are represented two-dimensional distributions of electrons in the structure for open and closed regimes respectively. On the fig. 3-4 are represented two-dimensional distributions of electron flow in the structure for the same regimes. One can see differences in current character with positive (fig. 1) and negative (fig. 2) base voltages. The two-dimensional plots of the bottom of the conduction band for the  $\Gamma$  valley electrons are shown in fig. 5-6. The main characteristics of this transistor are conditioned by peculiarities of transport of nonequilibrium ("hot") electrons in the active region of device. In this region hot electrons are injected from the emitter region through the potential barrier on the boundary between emitter and base regions.

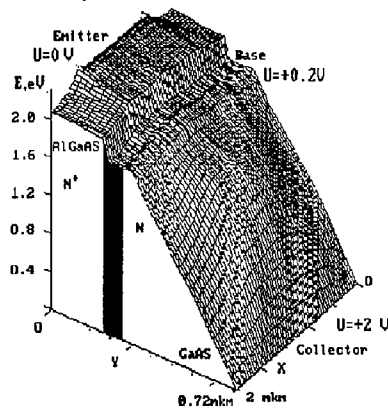


fig. 5

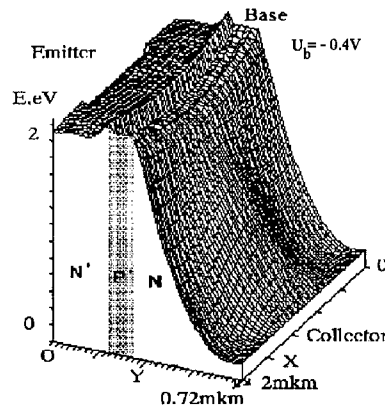


fig. 6

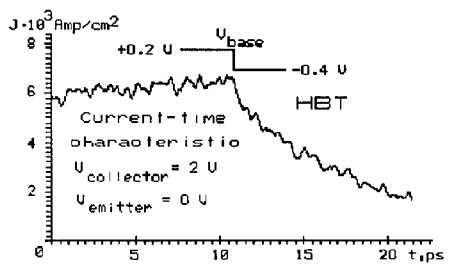


fig. 7

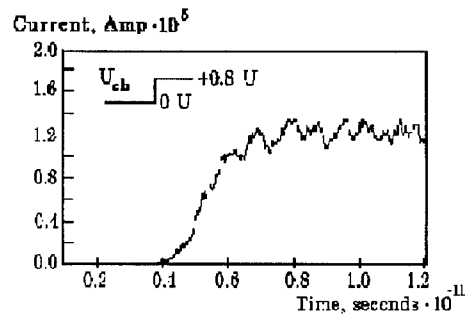


fig. 8

One can see distinct difference in heterojunction potential shape with positive and negative base potential. The base potential is not constant along  $x$  axis due to the minor mobility of the holes and the influence of the emitter contact. The volume charge area of electrons injected in the collector region, which defines the current character in this part of the structure, appears in the large current mode. The volume charge area near the emitter contact has great influence on the current character too. The electrons near the emitter are moving aside to the base contacts and gathering in the center near the heterojunction, and moving to the edges near the collector contact (fig. 1, 2). One can see from this pictures

that the transistor control is implemented by changing the electron flow width near the base area center and essentially depends upon the potential distribution along the  $x$  axis of the base and emitter regions.

The time dependence of the collector current density during step-case change of base potential is shown in fig. 7. The potential difference between emitter and collector remains constant (2 V).

Some results of the simulation of the "Camel"-transistor are shown in the figures 8-10. The two-dimensional plot of the electrical potential in camel-structure is shown in fig. 10.

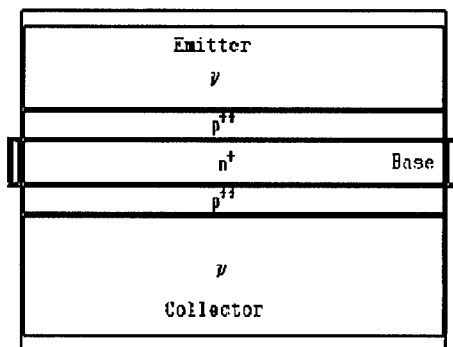


fig. 9

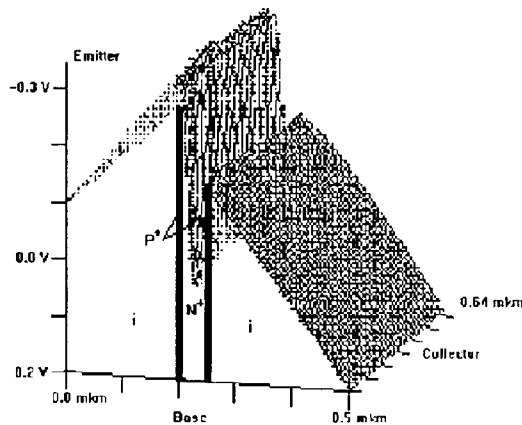


fig. 10

The time dependence of the collector current density during step-case change of base potential is shown in fig. 8. The potential difference between base and collector remains constant. One can see that the switching time is about 10 picoseconds.

### III. CONCLUSION

The results of the computer simulation of HBT-transistor show the importance of the behavior of the holes in base region (due to their minor mobility) and the electron volume charge in emitter region in the switching process. The minor mobility of the holes does not allow abrupt changes of the potential in the center of base region, while the negative charge of the "virtual cathode" electrons helps the current to grow during opening the transistor and to drop during closing. One can see that the switching times for both types of transistors ("Camel" and HBT) are about 10 picoseconds, that corresponds to the working frequencies about 300 GHz.

### IV. REFERENCES

1. Adachi S., *J. Appl. Phys.*, 1985, Vol.58,3, pp R1-R29.
2. Jacobony C., Reggiani L., 1983, *Review of Modern Physics*, Vol.55, No.3, p.645.





## ANOMALOUS ELECTRON TRANSPORT IN MAGNETIC MULTILAYERS TUNED BY ELECTRIC AND MAGNETIC FIELDS

F.G. Aliev, V.V. Moshchalkov and Y. Bruynseraede

Laboratorium voor Vaste-Stoffysica en Magnetisme, Katholieke Universiteit Leuven,  
Celestijnenlaan 200D, B3001 Leuven, Belgium

**Abstract** -- We report on anomalous quantum electron transport in low dimensional systems, which may be tuned by varying electric and magnetic fields. In magnetic trilayers Co/M/Co (M- nonmagnetic metallic spacer), which have been used to reveal ground state of disordered two-dimensional metal, at low temperatures a crossover from the logarithmic to the anomalous non-Fermi liquid behavior ( $\Delta\rho \sim \beta \sqrt{T}$ ) is observed. This crossover is probably due to scattering of electrons by symmetrical two-level systems. We also demonstrate that magnetic multilayers, with enhanced spin dependent scattering effects, may be used to study quantum magnetic phase (QPT) transition phenomena. We observed that through phase transition from antiferromagnet to the ferromagnet induced by magnetic field the spin-dependent contribution to the resistivity varies as  $\Delta\rho_s \sim T^\alpha$  with  $\alpha=f(H)$ . In the vicinity of QPT, the spin dependent contribution to the resistivity varies linearly with temperature.

©1999 Acta Metallurgica Inc.

### Introduction

Recently quantum electron transport phenomena in metallic low-dimensional systems have attracted much attention due to both fundamental and applied aspects. For the quasi 2D electron systems most of the research on quantum electron transport have been carried out on thin films (1). The ground state properties of metallic magnetic multilayers (MML) have not been investigated so far.

In the present work we report on the anomalous electron transport properties in two different types of metallic magnetic multilayers. First, magnetic trilayers in which the low temperature electron transport ( $T < 10\text{K}$ ) is dominated by electron-electron interactions induced by interface disorder (1). A detailed study of the temperature dependences of the resistivity at different applied electric (E) and magnetic (H) fields clearly shows that in the limit  $E \rightarrow 0$  and  $T \rightarrow 0$  the resistivity  $\rho(T)$  varies as  $\Delta\rho \sim \beta \sqrt{T}$  with  $\beta$  independent of the magnetic field up to 13 Tesla. This cut-off of electron-electron interactions could be ascribed to the two-channel Kondo scattering (2,3) of the electrons on symmetrical two-level systems (TLS). The second type of multilayers is characterized by an important spin dependent electron scattering compared to the disorder scattering effect. This allows to study spin dependent electron transport near the quantum phase transition (QPT) when going from antiferromagnetic (AF) state into ferromagnetic (FM) state tuned by the magnetic field. The

used system are the antiferromagnetically coupled multilayers  $[\text{Fe}(12\text{\AA})/\text{Cr}(12\text{\AA})]_{10}$  which demonstrate giant magnetoresistive effects (GMR) due to transition from AF to FM alignment of the Fe layers in magnetic field (see Ref.4 for a recent experimental review). By using isothermal magnetoresistance (MR) measurements, we reconstructed the magnetic phase diagram for different orientations of the field with respect to the film plane and determined the characteristic fields corresponding to the appearance of a nonzero Neel vector at low temperatures. The temperature dependence of the resistivity measured at different magnetic fields makes it possible to determine the contribution to the resistivity  $\rho_s$  due to AF coupling nearby and far away from QPT point. We observed that  $\rho_s$  is almost linear as a function of temperature near the QPT.

A detailed description of sample preparation and structural characterization have been reported elsewhere (5).

### Ground state electron transport in zero-biased magnetic trilayers

Figure 1 shows the temperature dependence of the resistivity of a  $\text{Co}(45\text{\AA})/(\text{Cr}(6\text{\AA})/\text{Ag}(9\text{\AA}))/\text{Co}(45\text{\AA})$  trilayer at different applied electric fields. Above about 100mK the electrical resistivity varies as  $\rho \approx A \log T + C$  which is due to two-dimensional electron-electron interactions in presence of disorder (1,6). Below  $T \sim 100\text{mK}$  the electric resistivity deviates from the  $\log T$  behavior and is strongly dependent on electric field.

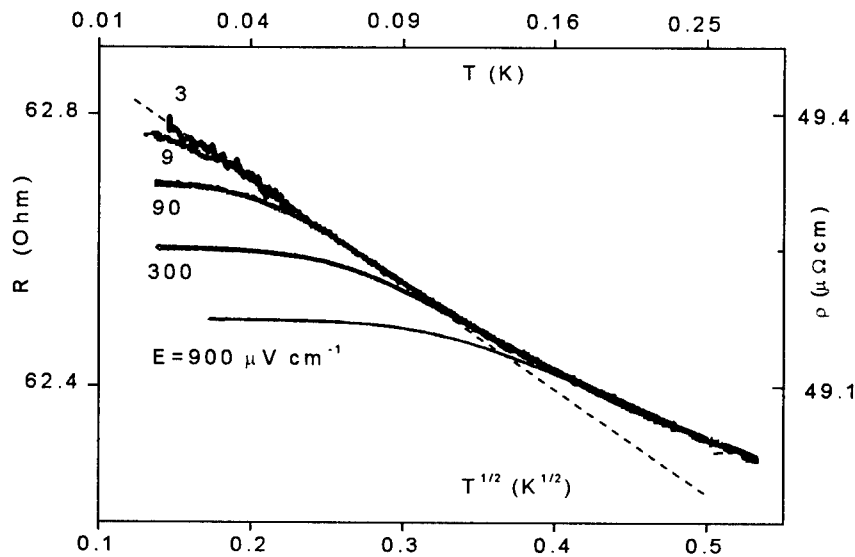


Figure 1. Temperature dependence of resistivity of  $\text{Co}(45\text{\AA})/(\text{Cr}(6\text{\AA})/\text{Ag}(9\text{\AA}))/\text{Co}(45\text{\AA})$  trilayers at different electric field values plotted as  $\Delta\rho \sim T^{1/2}$ .

In the limit  $E \rightarrow 0$   $\Delta\rho$  is proportional to  $T^{1/2}$  down to 20mK. A similar temperature dependence of  $\rho$  was also observed in other Co/M/Co trilayers (M=Cr; Ag; Ag/Cr). Figure 2 demonstrates how characteristic temperature, below which the anomalous dependence shows up, varies with the normalized logarithmic slope ( $-A/C$ ).

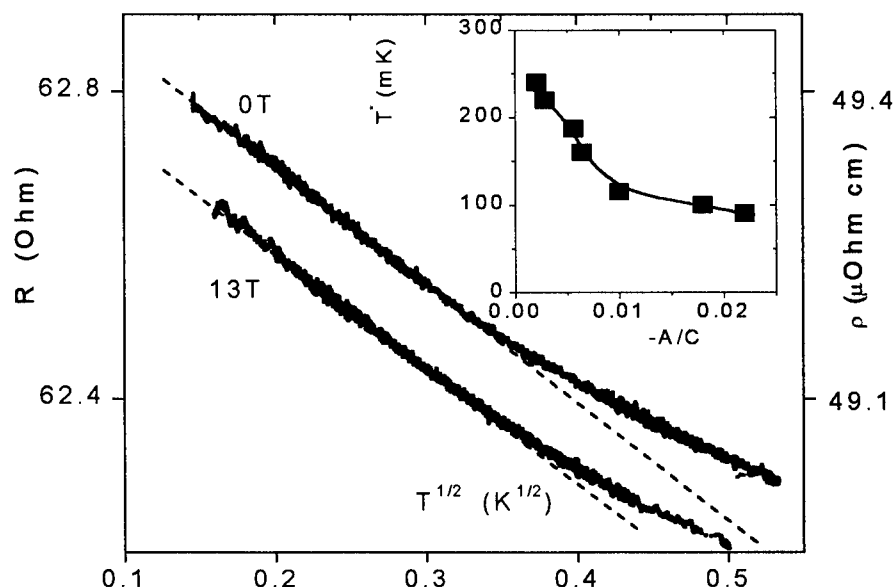


Figure 2. Temperature dependence of resistivity of Co(45Å)/(Cr(6Å)/Ag(9Å)/Co(45Å) in 0T and 13T. The insert shows dependence of the temperature where deviation from the  $\log T$  dependence appears ( $T^*$ ) on the normalized logarithmic slope ( $-A/C$ ) which reflects strength of electron-electron interactions (see Ref. 6).

The mechanism, which could be responsible for the unconventional saturation of the resistance in Co/M/Co trilayers, is the scattering of electrons by symmetrical TLS which cuts-off electron-electron interactions and results in  $\Delta\rho \sim \beta \sqrt{T}$ . This explanation is supported by the observation that the slope  $\Delta\rho \sim \beta \sqrt{T}$  is not influenced by magnetic field up to 13 Tesla (see Figure 2).

### Quantum magnetic phase transition in magnetic multilayers

Let us now move to the situation where spin dependent scattering dominates over the Coulomb interactions and orbital scattering effects. In this case conditions for the quantum electron transport may occur near zero temperature for a phase transition from the FM into the AF state. A common way to tune quantum magnetic transition is to use non-

thermal control parameter such as composition or pressure (7). Specific for antiferromagnetically coupled MML is that QPT may be precisely and easily tuned by applying magnetic fields below a few Tesla (Figure 3).

Insert in the Figure 3 shows typical isothermal magnetoresistance curve measured in parallel to the plane field. The largest part of MR is linear  $\Delta\rho(H)=\rho(0)-\rho(H)\sim H$ . The perpendicular MR may be fitted by parabolic field dependence  $\Delta\rho(H)\sim H^2$ . The characteristic saturation field  $H_s$  is defined as a magnetic field which corresponds to the disappearance of the Neel vector  $N=\mathbf{M}_1-\mathbf{M}_2$  where  $\mathbf{M}_{1,2}$  are magnetization vectors of the coupled Fe layers, i.e. as a field where deviation from the linear (quadratic) decrease of MR starts (Fig. 3).

Figure 3 shows in-plane  $T_{AF}-H_s$  phase diagram indicating on transition from FM to the AF state as deduced from  $\rho$  vs  $H$  measurements shown in the insert of Figure 3. By linear extrapolation we find  $T_{AF}\approx 0K$  when  $H=H_s^0\approx 7.5kG$  for the parallel and  $H=H_s^0\approx 27kG$  for the perpendicular configurations.

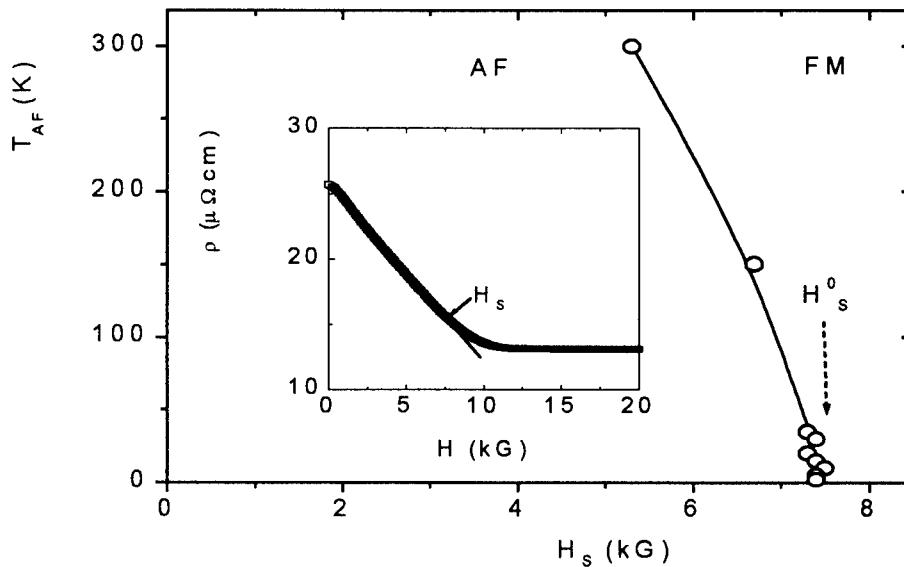


Figure 3. Magnetic phase diagram of  $[Fe(12\text{\AA})/Cr(12\text{\AA})]_{10}$  multilayer in parallel magnetic field. The arrow shows critical field  $H_s^0$  which corresponds to  $T_{AF}=0K$ . The insert shows MR in parallel magnetic field at  $T=1.9K$ .

Temperature variation of spin dependent part of the magnetoresistance was studied so far only as the difference between the electroresistivity of collinear AF (at  $H=0$ ) and FM ( $H>H_s^0$ ) states (8). In order to determine variation with temperature of the spin-dependent part in electrical resistivity  $\rho_s=\rho(T, H)-\rho(T, 2H_s^0)$  with temperature for each applied field  $\rho(T, H)$  is measured for different fixed magnetic fields varied from  $H\approx 2H_s^0$  through  $H\approx H_s^0$  to  $H=0$  and oriented perpendicular or parallel to the film plane. Qualitatively the experimental

data (Figure 4) is similar for both field orientations when scaled by corresponding values of  $H_s^0$ . A central and nontrivial aspect of the obtained data is the linear variation of  $\rho_s$  at low temperatures in the vicinity of  $H \approx H_s^0$  i.e. when the magnetic phase transition with  $T_{AF} \approx 0K$  is tuned. In general, we have found that for a different magnetic fields ( $0 < H \sim H_s^0$ ) the observed spin dependent contribution may be fitted by a power law  $\Delta\rho_s \sim T^\alpha$  in a wide temperature interval below 120K. For  $H > H_s^0$  the temperature interval, where power law may be obtained, is reduced.

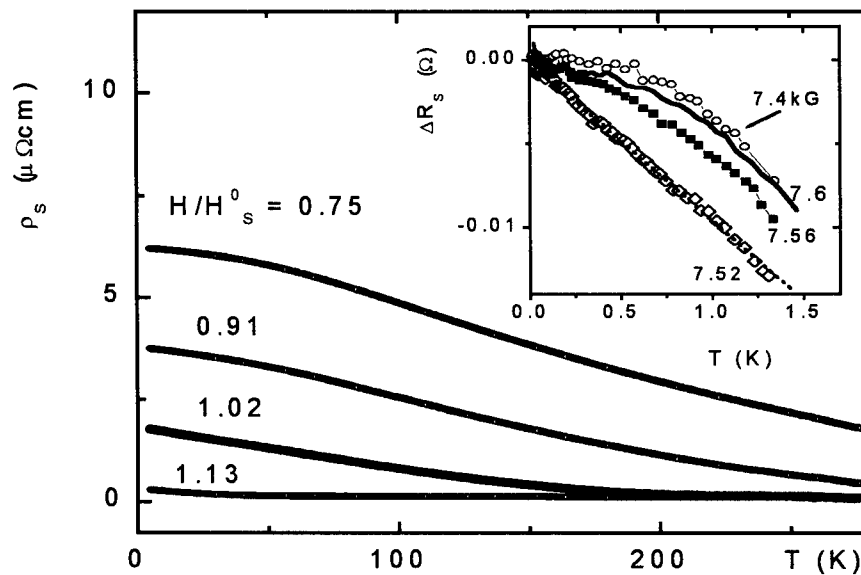


Figure 4. Temperature dependences of spin dependent contribution into resistivity  $\rho_s(T)$  in  $[\text{Fe}(12\text{\AA})/\text{Cr}(12\text{\AA})]_{10}$  multilayer in different magnetic fields (in units  $H/H_s^0$ ). The insert shows ground state temperature variation of resistance  $\Delta R_s(T)$  for the parallel magnetic fields close to the point where fine tuning of the quantum magnetic phase transition is provided by applying magnetic field.

Spin dependent scattering, studied near  $H \sim H_s^0$  at the interval of ultralow temperatures, confirms specific character of the QPT point. (see insert in the Figure 4). For all magnetic fields, except those corresponding to  $H = H_s^0$ , spin dependent contribution into resistivity saturates as  $T \rightarrow 0K$ . That doesn't occur for the narrow field interval around QPT:  $\rho_s(H=H_s^0)$  is almost linear as a function of temperature between 20mK and 1.2K.

The obtained experimental results can not be explained in framework of conventional spin-fluctuation theories (9,10) which predict  $\Delta\rho_s \sim T^\alpha$  near zero temperature magnetic phase transition with  $4/3 < \alpha < 5/3$  determined by the type (ferro/antiferro) of paramagnons and degree of disorder. Spin fluctuations in heavy electron system near their

AF instability may result in a certain temperature range where  $\rho_s(T)$  varies almost linearly with  $T$ . However the dependence  $\Delta\rho_s \sim T^{3/2}$  predicted for very low temperatures (11) is in a contradiction with the present experiment.

### Summary

Asymptotic behavior of the electrical resistivity in the metallic trilayers  $\Delta\rho \sim \beta \sqrt{T}$  was observed at very low temperatures. This behavior could arise from the cut-off of the two-dimensional electron-electron interactions by the interaction of electrons with symmetrical two-level systems which determines non Fermi-liquid nature of the ground state of the disordered two-dimensional metal. In the case when spin dependent scattering determines the ground state properties, we have demonstrated a novel possibility to tune and study electron transport near quantum phase transition from ferromagnet to antiferromagnet. For the interval of magnetic fields, where formation of Neel vector at zero temperature may be expected, we observe a linear vs. temperature variation of spin dependent resistivity which still has to be accounted by the theory.

### Acknowledgments

We would like to acknowledge R. Schad, G. Verbanck and K. Temst for sample preparation and characterization. F.G.A. thanks C. Van Haesendonck for useful discussions. The work has been supported by the Belgian Inter University Attraction Poles (IUAP) and Flemish Concerted Action (GOA) Programs as well as by the Fund for Scientific Research-Flanders.

### References

1. Lee P. and Ramakrishnan T.V., *Rev. Mod. Phys.* 1985, 57, 287.
2. Muramansu A. and Guinea F., *Phys. Rev. Lett.*, 1986, 86, 2337.
3. Affleck I. and Ludwig A.A.W., *Phys. Rev.*, 1993, B48, 7297.
4. Fert A., Grunberg P., Barthelemy A., Petroff F., and Zinn W., *J. Magn. & Magn. Mat.*, 1995, 140-144, 1.
5. Schad R., Potter C.D., Beilen P., Verbanck G., Moshchalkov V.V., and Bruynseraede Y., *Appl. Phys. Lett.*, 1994, 64, 3500.
6. Aliev F.G., Kunnen E., Temst K., Mae K., Verbanck G., Barnas J., Moshchalkov V.V., and Bruynseraede Y., *Phys. Rev. Lett.*, 1997, 78, 134.
7. von Löhneysen H., *J. Phys.* 1996, F48, 9689, and references therein.
8. Mattson J.E., Brubakker M.E., Sowers C.H., Conover M., Qiu Z., and Baser S.D., *Phys. Rev.*, 1991, B44, 9378.
9. Millis A.J., *Phys. Rev.*, 1993, B48, 7183.
10. Continentino M., *Z. Phys.* 1996, B101, 197.
11. Moriya T. and Takimoto T., *J. Phys. Soc. Jap.*, 1996, 64, 960.



Pergamon

NanoStructured Materials, Vol. 12, pp. 383–386, 1999

Elsevier Science Ltd

© 1999 Acta Metallurgica Inc.

Printed in the USA. All rights reserved

0965-9773/99/\$—see front matter

PII S0965-9773(99)00140-3

## NANOSTRUCTURING BY ULTRATHIN DIBLOCK COPOLYMER/TITANIUM COMPOSITE FILMS

Peter Eibeck, Joachim P. Spatz, Stefan Mößmer and Martin Möller\*

Universität Ulm, Organische Chemie III-Makromolekulare Chemie, D-89081 Ulm

e-mail: martin.moeller@chemie.uni-ulm.de

Thomas Herzog and Paul Ziemann

Universität Ulm, Abteilung Festkörperphysik, D-89081 Ulm

**Abstract:** *The usability of ultrathin diblock copolymer films providing a heterogeneous chemical surface in a new nanolithographic technique is described. This technique allows the parallel preparation of periodic point pattern in an inorganic substrate. Diblock copolymers of polystyrene (PS) and poly-2-vinylpyridine (P2VP) are adsorbed from a nonselective solvent like chloroform on an ionic, high surface energy substrate (mica). Under these conditions formation of a regular, chemically heterogeneous nm-sized surface structure is observed consisting of isolated PS clusters which dewet the substrate covered by a 1nm thick film of adsorbed P2VP. Vapour deposition of titanium on the heterogeneous surface occurs preferentially on the less polar polystyrene islands. This way Ti films with regular thickness variations are formed corresponding to the pattern of the laterally segregated PS-b-P2VP film. The films are employed as lithographic masks allowing the transfer of the initial polymer pattern into the inorganic substrate with high aspect ratios. ©1999 Acta Metallurgica Inc.*

### INTRODUCTION

Modern lithographic methods based on X-ray, electron or ion beam techniques allow the preparation of structures being smaller than 100nm(1). However, due to the serial nature of these methods, they are not suitable when structuring of a macroscopic area is required. Therefore there is a need for complementary approaches which allow the parallel preparation of nanometer range patterns(2-5). Based on molecular concepts from organic(6) and macromolecular chemistry(7-10) efforts are made to imitate the "bottom up" approach of nature. Here we report an intermediate approach, using a self-assembled diblock copolymer mask in

combination with a conventional ion etching technique for the preparation of mesoscopic periodic "point" pattern into an inorganic substrate. The microdomain pattern of a thin diblock copolymer film can be used to etch a 3D surface pattern into an underlying substrate(11,12). Usability and versatility of such an etching process depend strongly on the aspect ratios which can be reached, i.e., the maximum length to deepness ratio of the etched pits. So far, the diblock copolymer approach has allowed etching of structures with an aspect ratio of 1-2(11,12).

### EXPERIMENTAL AND DISCUSSION

We have studied the formation of ultrathin films of a polystyrene-block-poly(2-vinylpyridine) diblock copolymer on mica, i.e. a highly polar ionic substrate(13,14). Applied in a  $\text{CHCl}_3$  solution the 2-vinylpyridine block is strongly adsorbed and forms a wetting layer of only about 1nm thickness. Due to the unfavourable interaction and elastic contributions to the free energy, the polystyrene blocks do not cover the layer of adsorbed poly(2-vinylpyridine) but dewet to yield rather defined and regularly arranged clusters as schematically shown in figure 1. In contrast to thicker diblock copolymer films, both blocks form part of the surface, thus resulting in a chemically heterogeneous surface structure of less polar polystyrene domains surrounded by the poly(2-vinylpyridine) adsorbate layer(13,14). This phenomenon can be observed on various substrates (e.g., GaAs or Si wafers) but best results, i.e., ordering and cluster uniformity, were obtained on an ionic substrate like mica. As it will be shown below, the deposition of a thin metal layer like Ti on top of such a chemically heterogeneous film leads to a preferential growth of the metal on top of the PS-block.

PS-b-P2VP diblock copolymers were prepared and characterized as described before(5). Adsorption of the diblock copolymer film onto the substrate(13,14) was achieved by dipping a freshly cleaved piece of mica into a dilute diblock copolymer solution in chloroform. Then the substrate was pulled out at a constant velocity of 10mm/min. The resulting films did not change their structure when they were annealed above the glass temperature at 150°C for 3 days. The resulting dry films were studied by scanning force microscopy (SFM) using a Nanoscope III from Digital Instruments and applying the contact mode with  $\text{Si}_3\text{N}_4$  tips from Nanosensors with a force constant of 0.06 N/m.

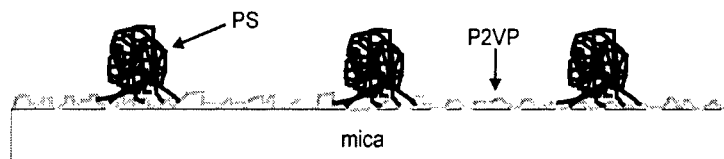


Figure 1: schematic representation of an ultrathin lateral phase separated PS-b-P2VP diblock copolymer film on mica



TABLE 1  
Average Thickness of Vapor Deposited Ti Films as Determined by a Quartz Microbalance  
and the Corresponding Cluster Height as Determined from SFM

Ti layer thickness [nm]	cluster height [nm]
0	6.6
4.5	10.7
11	7.6
19.6	6.2
40	4.5

The height of the clusters, their lateral diameter and periodicity is controlled by the molecular weight of the polymer blocks. So far, cluster periodicities between 70 and 400nm, cluster diameters from 30 to 160nm and cluster heights from 3 to 12nm have been observed. In a second step, the laterally segregated films were coated with a thin layer of Ti deposited by electron beam evaporation. Table 1 shows the inhomogeneous deposition of Ti on a PS<sub>340</sub>-b-P2VP<sub>190</sub> (subscripts depict the degree of polymerisation) diblock copolymer film. The average total Ti layer thickness varied between 0 and 40nm. The thickness values were determined independently by a quartz microbalance. The cluster periodicity (120nm) was not affected by the evaporation process and, similarly, the diameter (50nm) practically remained constant. However, the PS cluster height increased significantly stronger than what was expected from the average metal layer thickness. For example, when a Ti-layer of 4.5nm average thickness was deposited on the polymer film, the cluster height increased from 6.6nm for the pure polymer film to 10.7nm. Only for very thick Ti films, the height of the Ti covered PS blocks leveled off. Obviously, the initial growth of the Ti occurred preferentially on top of the polystyrene. Favourable polystyrene/metal interactions have been reported before. For example, a symmetrical polystyrene-block-polymethylmethacrylate diblock copolymer has been found to preferably contact to a gold layer via the PS block(10).

The selective deposition of Ti on top of the self-organized polymer structure can be exploited for nanolithography. For this purpose, the Ti coated sample was exposed to a 1.1 keV Ar<sup>+</sup> beam (20μA/cm<sup>2</sup>) for 5, 10 and 15min respectively in order to sputter erode the Ti layer and taking advantage of its thickness variation. Fig. 2 shows micrographs of the 4.5nm Ti-coated sample before and after 5min of etching. In the latter state the height of the islands has increased to 13nm. Further ion etching did not lead to higher structures indicating that already after 5min the polymer/Ti mask has been removed.

In conclusion it has been demonstrated that thin PS-b-P2VP diblock copolymer films form a pattern of strong wettability contrast for Ti coatings with the special advantage that large variations in PS cluster size and periodicity can be achieved simply by variation of the block lengths. The favourable PS/Ti interaction can be exploited to form sputtering masks for nanolithography, which use the diblock copolymer pattern as a template. In the present case, the initial polymer structure of 6.6nm high PS islands allowed the preparation of 13nm high structures with the same lateral dimensions in the substrate.

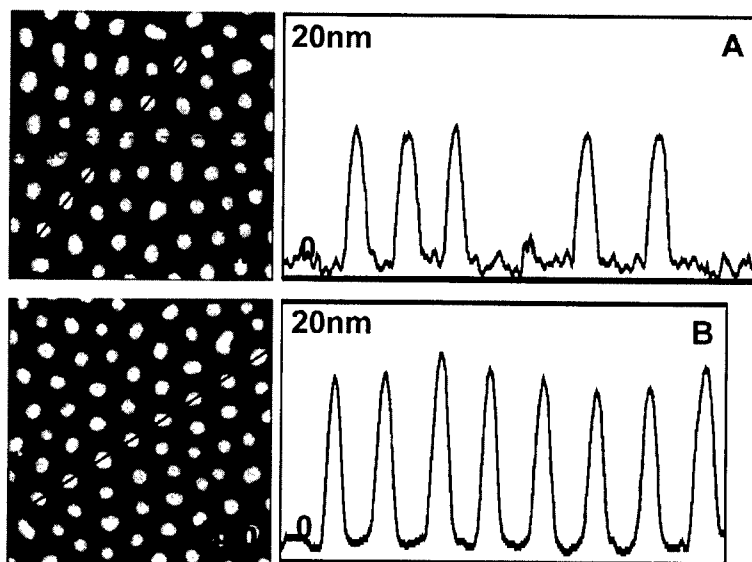


Figure 2: AFM micrographs and cross sections of ultrathin lateral phase separated PS<sub>340</sub>-b-P2VP<sub>190</sub> diblock copolymer films, scanned area 1  $\mu\text{m}^2$ . (A) covered with a Ti-film (mean thickness 4.5nm) (B) the same sample after 5min of Ar-ion etching.

## REFERENCES

1. I. Brodie, J.J. Muray, *The Physics of Micro/Nano-Fabrication*. Plenum Press, New York, 1992
2. P.G. Collins, A. Zettl, H. Bando, A. Thess, R.E. Smalley, *Science* 1997, 278, 100
3. D.H. Pearson, R.J. Tonucci, *Adv. Mater.* 1996, 8, 1031
4. C.A. Mirkin, R.L. Letsinger, R.C. Mucic, J.J. Storhoff, *Nature* 1996, 382, 607
5. J.P. Spatz, S. Mößmer, M. Möller, *Chem. Eur. J.* 1996, 2, 1552
6. J.-M. Lehn, *Supramolecular Chemistry*, VCH Verlagsgesellschaft, Weinheim, ed. 1, 1995
7. E. Kim, Y. Xia, X.-M. Zhao, G.M. Whitesides, *Adv. Mater.* 1997, 9, 651
8. L. Zhang, A. Eisenberg, *Science* 1995, 268, 1728
9. J.P. Spatz, S. Mößmer, M. Möller, M. *Angew. Chemie Int. Ed. Engl.* 1996, 35, 1510
10. D.M. Anderson, E.L. Thomas, *Macromolecules* 1988, 21, 3221
11. P. Mansky, C.K. Harrison, P.M. Chaikin, R.A. Register, N. Yao, *Appl. Phys. Lett.* 1996, 68, 2586
12. M. Park, C.K. Harrison, P.M. Chaikin, R.A. Register, D.H. Adamson, *Science* 1997, 276, 1401
13. J.P. Spatz, S. Sheiko, M. Möller, *Adv. Mater.* 1996, 8, 513
14. J.P. Spatz, M. Möller, M. Noeske, R.J. Behm, M. Pietralla, *Macromolecules* 1997, 30, 3874



Pergamon

NanoStructured Materials, Vol. 12, pp. 387-390, 1999  
Published by Elsevier Science Ltd  
Printed in the USA. All rights reserved  
0965-9773/99/\$-see front matter

PII S0965-9773(99)00141-5

## STABILITY OF MULTILAYER STRUCTURES: CAPILLARY EFFECTS

D. Josell, W.C. Carter, and J.E. Bonevich

National Institute of Standards and Technology, Gaithersburg, MD 20899

*The long term stability of multilayer materials composed of nonreactive, immiscible materials is related to the equilibrium shapes of the individual grains within the layers. These shapes are determined by the free energies and locations of the interfaces within the multilayer. We link the results of zero creep experiments with measured grain boundary groove angles to understand experimental observations of multilayer stability. ©1999 Acta Metallurgica Inc.*

### INTRODUCTION

Equilibrium interfaces in a multilayer have the same shape as the surface of an appropriate bubble raft, i.e. the surface formed by joining truncated spheres (1), when the layers are composed of grains that are either square or hexagonal in the plane of the layers. As required, these surfaces have constant curvature and exhibit constant groove angles along grain boundaries (GBs). Using this geometry, it is possible to determine the depth of the pits formed where GBs meet (triple junctions in the hexagonal grain model and quadrajunctions in the square grain model). Models that assume an axisymmetric geometry around triple junctions, neglecting GB grooves, see Srolovitz and Safran (2), predict infinitely deep GB groove depths at the triple junctions.

In fact, though some multilayer materials do develop holes at GB triple junctions (pinch-off), others do not. Pinch-off at GBs occurs during both zero creep experiments to determine free energies of interfaces (3,4,5) and pulsed heating experiments to determine the thermal resistance of interfaces (6,7). In this paper we apply the capillary models of Ref. 1 to understand this behavior.

### STABILITY OF MULTILAYERS

Three instabilities associated with capillary forces can degrade multilayer structures (8). The first is the absence of a free energy minimizing microstructure compatible with the grain dimensions and interfacial free energies. The second is externally applied forces that are inappropriate for balancing the capillary forces within the multilayer. The third arises when the equilibrium value of the applied forces decreases as the system expands. This paper

concentrates on the absence of an equilibrium geometry because it is the most likely source of rapid pinch-off at triple junctions. Though the latter instabilities both play a role in multilayer breakdown, they typically require that the specimen undergo substantial strains, making them relevant only in the longer term.

Of creep tested multilayers with layers thicker than 1  $\mu\text{m}$ , Ni/Ag, Fe/Ag, and Co/Ag develop shallow groove angles where the Ag GBs intersect the interfaces between layers. They also exhibit few pinch-off sites, all associated with the non-Ag GBs (8). In contrast, Co/Cu, and Fe/Cu multilayers with similar layer thickness develop deep grooves that rapidly lead to pinch-off at most GBs (8). Images of creep tested multilayers viewed in cross section have been published (4,5,8), some multilayers exhibiting GB grooves without pinch-off, others exhibiting dramatic degradation of the layer quality. Examples are shown in Fig. 1.

Because different multilayer materials deform at different rates at a given temperature, a criterion for comparison of stabilities is necessary. Creep experiments provide such a criterion because a non-zero steady-state strain-rate is indicative of plasticity in both layers. A simple criterion is that a film is resistant to pinch-off if it maintains its layered structure in spite of relatively substantial plastic strains during the creep test. Significant degradation after insignificant creep strain is a sign of poor resistance to pinch-off. Strain histories recorded during creep tests of multilayers are published elsewhere (4,5). In a typical successful creep test, on a Ni/Ag multilayer with 43 layers, 1 cm wide and less than 25  $\mu\text{m}$  thick, positive (negative) strain-rates of  $10^{-8}$  to  $10^{-7} \text{ s}^{-1}$  were recorded at applied loads of 30 g (20 g) during a creep test conducted at 700  $^{\circ}\text{C}$  (4).

For grains that are square in-plane, with grain centers staggered so that they are between the quadrajunctions in the adjacent layers, zero thickness at the quadrajunctions (pinch-off) does not occur if the ratio of the grain width  $w$  and average thickness  $t$  satisfy

$$\frac{t}{w} \geq \int_0^1 \int_0^1 \sqrt{4A^2 - (\xi+B)^2 - (\eta+B)^2} d\eta d\xi - \sqrt{4A^2 - 2B^2} \quad [1]$$

where  $A = \gamma_i/(\gamma_1 - \gamma_2)$  and  $B = \gamma_2/(\gamma_1 - \gamma_2)$ , with  $\gamma_1 > \gamma_2$  (1). Smaller interface free energy  $\gamma_i$  (small

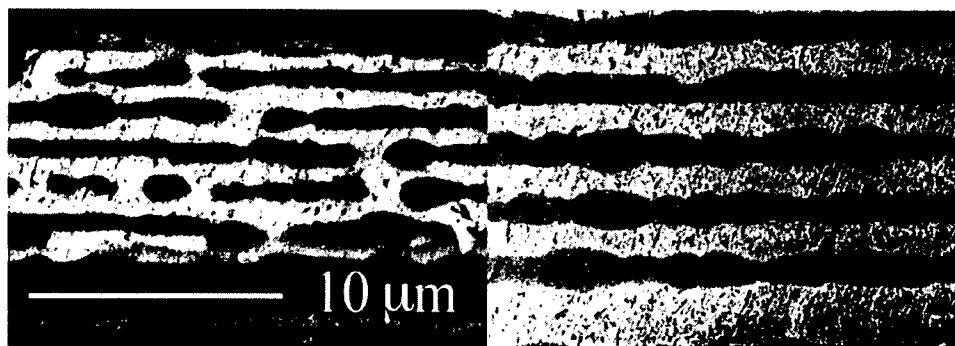


Fig. 1 Comparison of Ni/Ag multilayers (Ni layers dark) with different layer thickness after creep tests at 700  $^{\circ}\text{C}$  for 100 hours (left) and 725  $^{\circ}\text{C}$  for 115 hours (right) – same magnification.

TABLE I

Groove Angles and Associated Maximum Grain Dimensions For Continuous Layers

Multilayer	$2\theta_1$ (°)	$2\theta_2$ (°)	Maximum aspect ratio $w/t$
Ni/Ag (4)	$118 \pm 10$	$168 \pm 11$	2.1
Co/Cu	$114 \pm 12$	$132 \pm 14$	1.39

Subscript 1 (2) groove angles are associated with grain boundaries in layers of the first (second) listed element, etc. Uncertainties in dihedral groove angles represent the standard deviation of measured values.

values of  $A$ ) or closer GB free energies  $\gamma_1$  and  $\gamma_2$  result in smaller maximum values of the aspect ratio  $w/t$  without pinch-off. The ratio of GB free energy  $\gamma_{m(=1,2)}$  and interface free energy  $\gamma_i$  is obtained from the dihedral groove angle  $2\theta_m$  using the relationship  $\gamma_m/2\gamma_i = \cos\theta_m$ . Average values of groove angles formed where GBs intersect the interfaces between layers, determined from creep tested films by TEM and SEM, are summarized in Table I. Using these values in Eq. [1] it is possible to determine whether a multilayer structure of known grain dimensions can, absent coarsening of the grains, evolve to a stable geometry (1). It is evident from Eq. [1] that significant coarsening in the plane of the layer (increasing in-plane dimension  $w$ ) destabilizes the structure. However, because coarsening frequently stagnates in thin films (9), a structure that is initially stable against pinch-off may remain so through long anneals.

Table I shows grain aspect ratios at which pinch-off is predicted to occur in Ni/Ag and Co/Cu as determined by substitution of measured groove angles (Table I) in Eq. [1]. The groove angles were obtained by TEM of Cu and Co GB grooves in a creep tested specimen (see Fig. 2). As a result of the relatively small and similar values of the Cu and Co GB groove angles, the



Fig. 2 Creep tested Co/Cu multilayer after approximately 60 hours at 830 °C.

Co/Cu multilayer is predicted to be less tolerant of grain growth in the plane of the layers (smaller maximum value of  $w/t$ ). In contrast, the larger Ag GB groove angles in the Ni/Ag multilayers are predicted to permit larger in-plane grain dimensions to exist without pinch-off. These results are consistent with experiments (4,8).

Grain aspect ratios  $w/t$  and micrographs (e.g., Fig. 1) have been published for creep tested Ni/Ag multilayers (4). Grains with smaller aspect ratios  $w/t$  were found in the films with thicker layers,  $w/t \approx 2.7$  and 2.1 for 0.7  $\mu\text{m}$  and 1.4  $\mu\text{m}$  thick layers, respectively. Consistent with the relative values of their aspect ratios, no pinch-off is visible in a film with  $w/t \approx 2.1$  (thicker layers) while moderate pinch-off is visible in films with  $w/t \approx 2.7$  (thinner layers). Though both aspect ratios are as large or larger than the pinch-off value of  $w/t = 2.1$  predicted by the square grain model, actual grains are better modeled as six-sided, and the value of  $w/t$  predicted for pinch-off in an hexagonal grain model will be larger. This is because the in-plane distance from grain centers to quadrjunctions of square grains is large compared to the in-plane distance to triple junctions of equivalent in-plane area hexagonal grains.

To model the actual geometry of a multilayer requires knowledge of the free energy, orientation and location of every interface it contains. The square grain capillary model (1) used above assumes nonvarying grain dimensions and groove angles. Neither of these is true of real multilayers. As a result, there can be some pinch-off sites in otherwise stable multilayers as well as intact junctions within generally unstable multilayers (see Fig. 1). Nonetheless, the susceptibility of Co/Cu multilayers to pinch-off versus the stability of Ni/Ag multilayers is qualitatively consistent with the more restrictive aspect ratio  $w/t$  permitted by the square grain model for continuous layering in Co/Cu multilayers (Table I). Furthermore, it is possible that the observed breakdown during failed creep experiments of Ni/Ag multilayers with layers less than 0.1  $\mu\text{m}$  thick (4) can be explained as pinch-off caused by the noted increase of aspect ratio  $w/t$  with decreasing layer thickness.

## REFERENCES

1. D. Josell, S.R. Coriell and G. McFadden, *Acta Metall. Mater.* **43**, 1987 (1995).
2. D.J. Srolovitz and S.A. Safran, *J. Appl. Phys.* **60**, 247 (1986).
3. D. Josell and F. Spaepen, *Acta Metall. Mater.* **41**, 3007 (1993).
4. D. Josell and F. Spaepen, *Acta Metall. Mater.* **41**, 3017 (1993).
5. D. Josell and Z.L. Wang, *Mat. Res. Soc. Symp. Proc. Vol. 356*, 357 (1995).
6. D. Josell, A. Cezairliyan, D. van Heerden and B.T. Murray, *Int. J. Thermophysics* **18**, 865 (1997).
7. D. Josell, A. Cezairliyan, D. van Heerden and B.T. Murray, *Nanostruc. Materials* **9**, 727 (1997).
8. D. Josell and W.C. Carter, in Creep and Stress Relaxation in Miniature Structures and Components, Ed. H.D. Merchant, 271 (Minerals, Metals and Materials Society, Warrendale, PA, 1996).
9. H.J. Frost, C.V. Thompson and D.T. Walton, *Acta Metall.* **38**, 1455 (1990).



Pergamon

NanoStructured Materials, Vol. 12, pp. 391-394, 1999

Elsevier Science Ltd

© 1999 Acta Metallurgica Inc.

Printed in the USA. All rights reserved

0965-9773/99/\$-see front matter

PII S0965-9773(99)00142-7

## CRYSTALLINE SILICON NITRIDE THIN FILMS GROWN BY PULSED YAG LASER DEPOSITION

**Y. Suda**

Department of Electrical Engineering, Sasebo National College of Technology,  
1-1 Okishin-machi, Sasebo, Nagasaki 857-1193, Japan

**K. Ebihara**

Department of Electrical and Computer Engineering, Kumamoto University,  
2-39-1 Kurokami, Kumamoto 860-8555, Japan

**K. Baba**

Technology Center of Nagasaki, 2-1303-8 Ikeda, Omura, Nagasaki 856-0026, Japan

**H. Abe**

Ceramic Research Center of Nagasaki, 605-2 Hasami-cho, Nagasaki 859-3726, Japan

**A. M. Grishin**

Department of Condensed Matter Physics, Royal Institute of Technology,  
S-100 44 Stockholm, Sweden

**Abstract** -- Silicon nitride (SiN) and silicon (Si) thin films have been prepared on Si (100) substrates using pulsed Nd:YAG laser ( $\lambda=532$  nm) deposition. The laser beam is incident on the  $\text{Si}_3\text{N}_4$  and Si targets. The films are grown using the energy density  $3.8 \text{ J/cm}^2$  at a laser repetition rate of 10 Hz. The nitrogen gas pressure in the chamber is 10.0 Pa. The experiments have been done at different substrate temperatures. The films have been characterized by field-emission secondary electron microscopy (FE-SEM), Fourier transform infrared spectroscopy (FT-IR) and glancing angle X-ray diffraction (GXR). FE-SEM shows that the SiN film consists of many particles whose sizes are about 200 - 800 nm. GXR indicates that crystalline  $\text{Si}_3\text{N}_4$  and Si thin films are obtained using  $\text{Si}_3\text{N}_4$  and Si targets, respectively. ©1999 Acta Metallurgica Inc.

### Introduction

Silicon nitride ( $\text{Si}_3\text{N}_4$ ) is a compound that has applications in structural ceramics, high-temperature electronics, and tribology.  $\text{Si}_3\text{N}_4$  can be used in extremely harsh environments because of its thermal, chemical, and mechanical stability. SiN films have been widely used in microelectronics for surface passivation and encapsulation in LSIs, as well as for gate insulator layers in thin-film transistors (TFTs) (1). Recently SiN films have been also used for membrane type bolometers (2,3). SiN films have been synthesized by a variety of techniques, including plasma-enhanced chemical vapor deposition (PE-CVD) (1), ion-beam assisted deposition (IBAD) (4) and pulsed laser deposition (PLD) (5). These films have been found to be mainly amorphous. In this paper, we describe a pulsed Nd:YAG laser deposition (PLD) process for the preparation of crystalline SiN and Si thin films and the characteristics of these films.

### Experimental

A schematic illustration of the PLD apparatus used for this study is shown in Fig. 1 (6). As a light source we used a 532 nm pulsed YAG laser (Lumonics YM600) with a pulse width 6.5 ns. The laser beam was focused on the  $\text{Si}_3\text{N}_4$  target (purity, 99.9%) and the Si target (purity, 99.999%), which were placed in the stainless deposition chamber at  $45^\circ$ . The laser energy density  $E_d$  was fixed at  $3.8 \text{ J/cm}^2$ . The targets were rotated at about 20 rpm to avoid pitting of the target during the deposition. Single crystal Si (100) substrates of approx.  $4 \text{ cm}^2$  area were ultrasonically cleaned in consecutive baths of ethanol and rinsing of high purity deionized water prior to loading in the deposition chamber. Prior to each deposition, the Si (100) substrates were sputter cleaned to remove any residual contamination. The Si (100) substrates were located at a distance of 60 mm from the facing target and were heated up to  $T_s = 700^\circ\text{C}$  by an IR lamp. The gas pressure was varied from base pressure (below  $4.0 \times 10^{-4} \text{ Pa}$ ) to 10.0 Pa (100% nitrogen). After 18000 to 36000 laser shots at a 10 Hz repetition rate, the deposition process was completed. The film thickness of 180 - 360 nm has been measured by an  $\alpha$ -step meter (KLA-tencor AS500). The deposition rate was about 6 nm/min. Table 1 shows the deposition conditions for the preparation of SiN thin films.

The surface morphology and structure of the SiN films were examined by field-emission secondary electron microscopy (FE-SEM; JEOL JSM-6300F) and Fourier transform infrared spectroscopy (FT-IR; JEOL JIR-5500), respectively. The crystalline structure and crystallographic orientation of the films were identified by glancing angle X-ray diffraction (GXRD; JEOL JDX3530) using  $\text{CuK}\alpha$  radiation. The angle of incidence was kept at  $1.0^\circ$ .

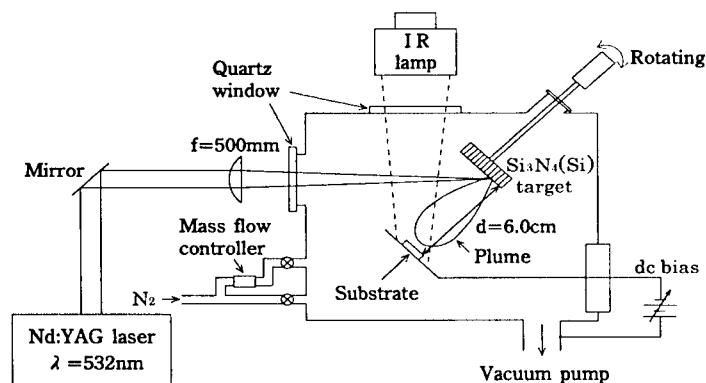


Fig.1 Schematic diagram of the pulsed Nd: YAG laser deposition system.

### Results and discussion

The surface morphology of SiN films on the Si (100) substrate was examined by FE-SEM seen in Fig. 2. The surface of this film, prepared at  $P_{\text{N}_2}=10.0 \text{ Pa}$ ,  $E_d=3.8 \text{ J/cm}^2$ ,  $d=6.0 \text{ cm}$  and  $T_s=700^\circ\text{C}$ , consists of many rugged particles with sizes about 200 - 800 nm. Fig. 3 shows the FT-IR absorption spectrum of SiN thin film grown at  $P_{\text{N}_2}=10.0 \text{ Pa}$  and  $T_s=700^\circ\text{C}$ . As can be seen in Fig. 3, absorption peaks appear at around  $800 - 1200 \text{ cm}^{-1}$  and  $450 - 600 \text{ cm}^{-1}$  due to the  $\text{Si}_3\text{N}_4$  crystalline structure (7).



Table 1  
Deposition Conditions for  $\text{Si}_3\text{N}_4$  Thin Films

Laser	Pulsed Nd:YAG laser Wavelength $\lambda = 532$ nm Pulsed width $\tau = 6.5$ ns Energy density $E_d = 3.8$ J/cm <sup>2</sup> Repetition rate 10 Hz
Target	$\text{Si}_3\text{N}_4$ (purity 99.9%) Si (purity 99.999%)
Target-substrate distance	$d = 6.0$ cm
Rotating speed of the target	$\sim 20$ rpm
Substrate	Si (100)
Ultimate pressure	$< 4.0 \times 10^{-4}$ Pa
Gas pressure	$\sim 10.0$ Pa (100% Nitrogen)
Substrate temperature	$T_s = \text{room temp.} - 700^\circ\text{C}$
Deposition time	30 - 60 min

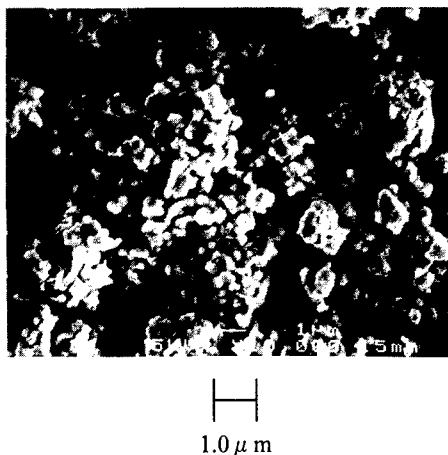


Fig. 2 FE-SEM micrograph of the SiN film deposited at  $P_{\text{N}_2} = 10.0$  Pa using a  $\text{Si}_3\text{N}_4$  target ( $E_d = 3.8$  J/cm<sup>2</sup>,  $d = 6.0$  cm,  $T_s = 700^\circ\text{C}$ ).

Detailed glancing angle X-ray diffraction measurements were carried out to study the crystalline properties of the laser deposited SiN films. Fig. 4 shows the XRD pattern of a reference target pellet of  $\text{Si}_3\text{N}_4$ . XRD patterns of as-deposited films grown at  $P_{\text{N}_2} = 10.0$  Pa and  $T_s = 700^\circ\text{C}$  using  $\text{Si}_3\text{N}_4$  and Si targets are shown in Fig. 5 and Fig. 6, respectively. When the  $\text{Si}_3\text{N}_4$  target is used (Fig. 5), the X-ray reflections correspond to single phase polycrystalline  $\text{Si}_3\text{N}_4$ . For the sample deposited by the ablation of the Si target in a  $\text{N}_2$  atmosphere (Fig. 6), there are only the distinct peaks of Si: (111), (220), (311), (400) and (331). The ratio of intensities of these peaks almost coincides with the diffraction pattern of an ideal Si powder, which indicates that this Si film has a nearly random polycrystalline structure. For samples deposited at room temperature using  $\text{Si}_3\text{N}_4$  and Si targets, crystalline peaks of  $\text{Si}_3\text{N}_4$  and Si also appear, respectively. Nevertheless, the crystalline quality of the Si film is better at a substrate temperature of  $700^\circ\text{C}$ .

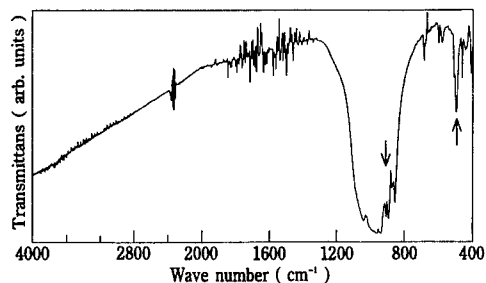


Fig.3 FT-IR absorption spectrum of the SiN film deposited at  $T_s = 700^\circ\text{C}$  by using  $\text{Si}_3\text{N}_4$  target ( $P_{\text{N}_2} = 10.0$  Pa).

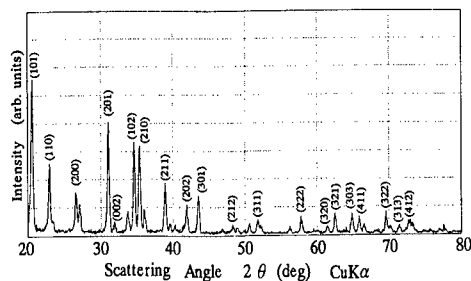


Fig.4  $\theta - 2\theta$  X-ray diffraction pattern in  $\text{CuK}\alpha$  radiation obtained from a  $\text{Si}_3\text{N}_4$  target.

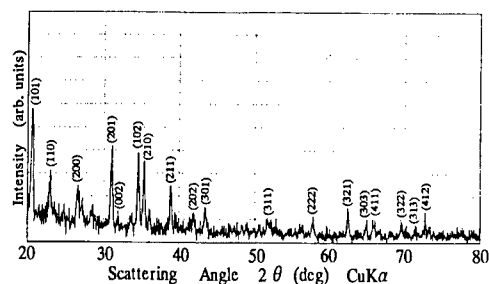


Fig.5 Glancing angle ( $\theta_{\text{sample}} = 1^\circ$ ) X-ray diffraction pattern of as-deposited SiN film prepared at  $T_s = 700^\circ\text{C}$  using a  $\text{Si}_3\text{N}_4$  target ( $P_{\text{N}_2} = 10.0$  Pa).

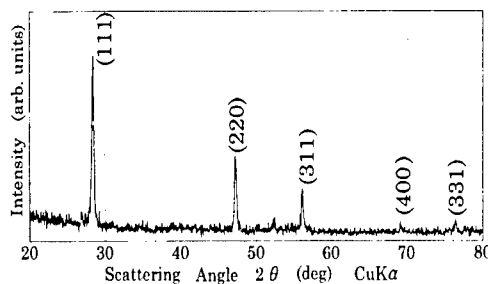


Fig.6 Glancing angle ( $\theta_{\text{sample}} = 1^\circ$ ) X-ray diffraction pattern of as-deposited Si film prepared at  $T_s = 700^\circ\text{C}$  using a Si target ( $P_{\text{N}_2} = 10.0$  Pa).

### Conclusions

In this study, pulsed Nd:YAG laser deposition has been used to prepare appropriate crystalline SiN and Si thin films. The following results were obtained:

- (1) Crystalline  $\text{Si}_3\text{N}_4$  thin films are obtained at substrate temperatures from room temp. -  $700^\circ\text{C}$  and a laser energy density of  $3.8 \text{ J/cm}^2$  using a  $\text{Si}_3\text{N}_4$  target. The film surface morphology needs to be improved.
- (2) High quality crystalline Si thin films are grown at substrate temperatures from room temp. -  $700^\circ\text{C}$  using a Si target.

### Acknowledgments

The authors wish to thank Dr. T. Ikegami and Dr. Y. Yamagata at Kumamoto University for their helpful discussions, R. Terajima and M. Emura at Sasebo National College of Technology for their experimental help and R. Hatada at Technology Center of Nagasaki for her technical assistance with the data. This work was supported in part by the grant-in-aid of Kyushu Industrial Technology Center.

### References

1. Yeh, W.C., Ishibashi, R., Morishita, S. and Matsumura, M., *Jpn. J. Appl. Phys.*, 1996, 35, 1509
2. Bang, C.A., Rice, J.P., Flik, M.I., Rudman, D.A., Schmidt, M.A., *J. of MEMS*, 1993, 2, 160
3. Johnson, B.R., Foote, M.C., Marsh, H.A., Hunt, B.D., *Proc. SPIE*, 1995, 2267
4. Natishan, P.M., McCafferty, Donovan, E.P., Brown, D.W. and Huber, G.K., *Surface and Coating Technology*, 1992, 51, 30
5. Sankur, H., *Mater. Res. Soc. Symp. Proc.*, 1984, 29, 373
6. Suda, Y., Nakazono, T., Ebihara, K. and Baba, K., *Thin Solid Films*, 1996, 281-282, 324
7. Traft, E.A., *J. Electrochem. Soc.*, 1971, 118, 1341



Pergamon

NanoStructured Materials, Vol. 12, pp. 395–398, 1999

Elsevier Science Ltd

© 1999 Acta Metallurgica Inc.

Printed in the USA. All rights reserved

0965-9773/99/\$—see front matter

PII S0965-9773(99)00143-9

## ENERGY SHIFT AND DAMPING OF DIPOLE-EXCHANGE SPIN WAVES IN ULTRATHIN FERROMAGNETIC FILMS

M.G. Cottam<sup>a</sup> and R.N. Costa Filho<sup>b</sup>

<sup>a</sup> Dept. of Physics and Astronomy, University of Western Ontario,  
London, Ontario N6A 3K7, Canada

<sup>b</sup> Dept. de Física, Universidade Federal do Ceara, 60455-760 Fortaleza-Ce, Brazil

**Abstract** — A finite-temperature perturbation formalism is developed to study the processes of spin-wave interactions in ultrathin ferromagnetic films, including the effects of both the long-range magnetic dipole-dipole interactions and the short-range exchange interactions. By contrast with previous macroscopic methods for evaluating spin-wave interactions, the dipolar terms are treated here within a Hamiltonian method, together with exchange and anisotropy terms, to obtain a theory applicable to ultrathin films at temperatures below the Curie temperature. The contributions to the energy shift and the damping (or reciprocal lifetime) of the dipole-exchange spin waves due to three-magnon and four magnon processes are calculated. Numerical examples are presented.

©1999 Acta Metallurgica Inc.

### INTRODUCTION

A theory is developed for the *nonlinear* dynamics of discrete spin waves (SW) in ferromagnetic films, including the effects of the short-range exchange coupling and the longer-range magnetic dipole-dipole coupling between spins. We employ a microscopic approach with a Hamiltonian representation of the dipole-dipole terms, whereas previous works on dipole-exchange SW interactions in films (1) used a macroscopic or continuous-medium theory, appropriate for small wave vectors, where the dipolar terms are introduced using Maxwell's equations. This enables us to obtain results applicable for ultrathin films and/or for all wave vectors and to probe the limitations of the macroscopic theories.

In a *linear* SW approximation for ferromagnetic films, it is known from microscopic theories (2) that the excitation spectrum may consist of several discrete branches describing the surface modes and the quantized (or standing) bulk modes. By taking higher-order effects into account we obtain a description of the interactions between these SW modes. At low temperatures  $T \ll T_C$  the dominant processes involve three- and four-magnon scattering, by analogy with infinite ferromagnets (1). However, in the present case the interaction terms may involve SW modes from either the same or different discrete branches.

The theory involves generalizing a previous calculation for nonlinear SW processes in semi-infinite Heisenberg ferromagnets (3) to include the dipole-dipole interactions and effects of finite film thickness. The dipolar terms are evaluated microscopically in a similar manner to recent work for ferromagnetic and antiferromagnetic films in the linear SW regime (4,5). Applications of the theory to thin films of the ferromagnetic semiconductor EuO are given.

### THEORY AND APPLICATIONS

The ferromagnetic film consists of  $N$  atomic layers (in the  $xz$  plane) with an external magnetic field of magnitude  $H_0$  applied parallel to the surface (along the  $z$ -axis, taken as the direction of magnetization). The Hamiltonian is

$$H = -g\mu_B H_0 \sum_i S_i^z - \frac{1}{2} \sum_{ij} J_{ij} \mathbf{S}_i \cdot \mathbf{S}_j + \frac{1}{2} (g\mu_B)^2 \sum_{ij} D_{ij}^{\alpha\beta} S_i^\alpha S_j^\beta \quad [1]$$

where we assume for simplicity that the spins  $\mathbf{S}_i$  lie on a simple cubic lattice with spacing  $a$ . Here  $J_{ij}$  is the exchange coupling between sites labeled  $i$  and  $j$ , taken to have the value  $J$  between nearest neighbors. The last term in equation [1] represents the long-range dipole-dipole coupling, where  $\alpha$  and  $\beta$  denote components  $x$ ,  $y$ , or  $z$ , while

$$D_{ij}^{\alpha\beta} = \left\{ |\mathbf{r}_{ij}|^2 \delta_{\alpha\beta} - 3r_{ij}^\alpha r_{ij}^\beta \right\} / |\mathbf{r}_{ij}|^5 \quad (\mathbf{r}_{ij} = \mathbf{r}_j - \mathbf{r}_i) \quad [2]$$

The next step is to set up a diagrammatic perturbation method, following a general approach used for semi-infinite Heisenberg ferromagnets (3), generalized here to include the dipolar terms and the film geometry. The Hamiltonian is written in terms of boson operators using the Holstein-Primakoff transformation and expanded as  $H = H^{(2)} + H^{(3)} + H^{(4)} + \dots$  (apart from a constant), where  $H^{(m)}$  denotes the term involving a product of  $m$  boson operators. The bilinear term  $H^{(2)}$  describes the non-interacting (linear) SW modes in the film. Following the method in (3) each operator can be transformed to a representation using a 2D wave vector  $\mathbf{q} = (q_x, q_z)$  parallel to the film surfaces and a layer index  $n$  ( $= 1, 2, \dots, N$ ). The corresponding transforms of the long-range dipolar interactions defined in equation [2] involve slowly converging sums, which are evaluated as in (4). Next, following (3), a linear transformation can be found to new boson operators so that  $H^{(2)}$  takes a diagonalized form. Its eigenvalues yield the energies  $E_\nu(\mathbf{q})$  of the discrete SW branches, where  $\nu$  ( $= 1, 2, \dots, N$ ) labels the branches.

We are interested in the *nonlinear* aspects of the SW dynamics, which are described in leading order for  $T \ll T_C$  by  $H^{(3)}$  and  $H^{(4)}$ . The term  $H^{(3)}$  depends only on the dipolar interactions, while  $H^{(4)}$  has dipolar and exchange parts. They describe three-magnon and four-magnon processes, respectively, in the film geometry. We have calculated the SW energy shift  $\Delta E_\nu(\mathbf{q})$  and damping  $\Gamma_\nu(\mathbf{q})$  for SW branch  $\nu$  at in-plane wave vector  $\mathbf{q}$  using a diagrammatic perturbation method. The method, which is a generalization of (3) for Heisenberg ferromagnets, basically involves defining unperturbed Green functions with respect to the diagonalized  $H^{(2)}$ . The perturbation terms  $H^{(3)}$  and  $H^{(4)}$  are then transformed to the new boson operators and used to define interaction vertices within a Feynman diagram formalism.

The above theory has been applied to EuO ( $T_C \sim 69$  K), for which the dipolar terms have a significant effect on the long-wavelength SW properties and also thin-film samples have been employed in SW experiments using Brillouin light scattering (6). For the magnetic parameters we take  $4\pi M = 2.4$  T ( $M$  = magnetization),  $H_{Ex} = 38$  T for the bulk exchange field, and  $H_0 = 0.3$  T. From these data (and the relation  $g\mu_B H_{Ex} = 6SJ$  for a sc structure with spin  $S$ ) we deduce an *effective*  $J$  to use in the present theory. Note that the  $J$  value is effective because EuO has a fcc structure. The effect of the crystal structure will be examined in a later work.

TABLE 1  
Linear SW frequencies for the lowest branches in EuO films

$N$	Branch	SW Frequency (GHz)		
		$q_x a/\pi = 0$	$q_x a/\pi = 0.05$	$q_x a/\pi = 0.1$
10	1	28.1	45.2	56.8
10	2	51.1	58.8	75.2
20	1	28.2	38.2	53.0
20	2	34.4	48.9	61.4

In Table 1 we show examples of the linear SW dispersion relations for 10- and 20-layer films and for small  $q_x$ . We take the case of  $q_z = 0$  (the Voigt geometry), for which a surface Damon-Eshbach (DE) mode is predicted in the magnetostatic continuum limit (1). The DE mode frequency would start at  $\sim 28$  GHz and tend to  $\sim 42$  GHz with increasing  $q_x$ . For  $N = 10$  its analogs in the microscopic theory is branch 1. For  $N = 20$  its analog is a hybridization of branches 1 and 2, which come close in frequency (but do not cross) when  $q_x a/\pi \sim 0.004$ . This is an example of "mode repulsion", which is well known in the literature (6). The increase in SW frequency at larger  $q_x$  is an effect due to exchange.

Next we show the damping and energy shift of SW branches 1 and 2 for  $N = 10$  and branch 1 for  $N = 20$  in a low temperature limit. In these cases the dominant mechanism comes from the three-magnon term  $H^{(3)}$  in second order. For example, for the damping of a SW of wave vector  $\mathbf{q}$  and branch  $\nu$ , our results arise due splitting and confluence processes whereby  $E_\nu(\mathbf{q}) = E_\lambda(\mathbf{k}) \pm E_\mu(\mathbf{q}-\mathbf{k})$ , with conservation of energy and in-plane wave vector. The labels  $\lambda$  and  $\mu$  may be different from  $\nu$ . The damping (see Fig. 1) is slightly larger for branch 2, which is mainly because there are SW branches above and below it, giving more ways to satisfy the conservation conditions. In the case of the SW energy shifts (Fig. 2) the inter-branch terms are more important. This is a consequence that  $\Delta E_\nu(\mathbf{q})$  and  $\Gamma_\nu(\mathbf{q})$  come from real and imaginary

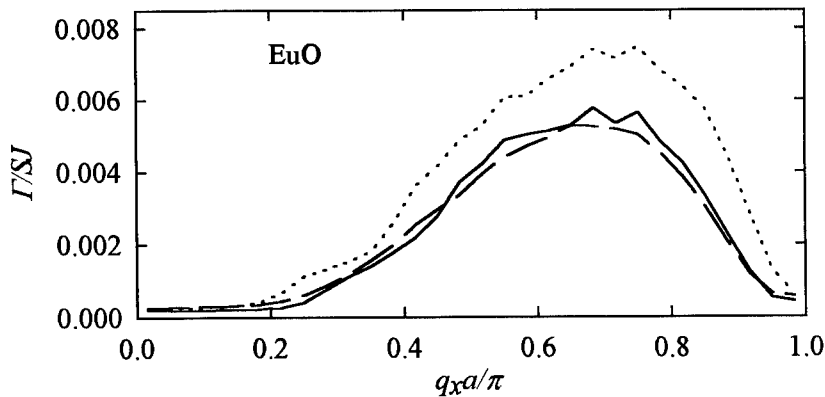


Figure 1. The relative SW damping  $\Gamma/SJ$  (solid line -  $N=10$ , branch 1; dotted line -  $N=10$ , branch 2; dashed line -  $N=20$ , branch 1).

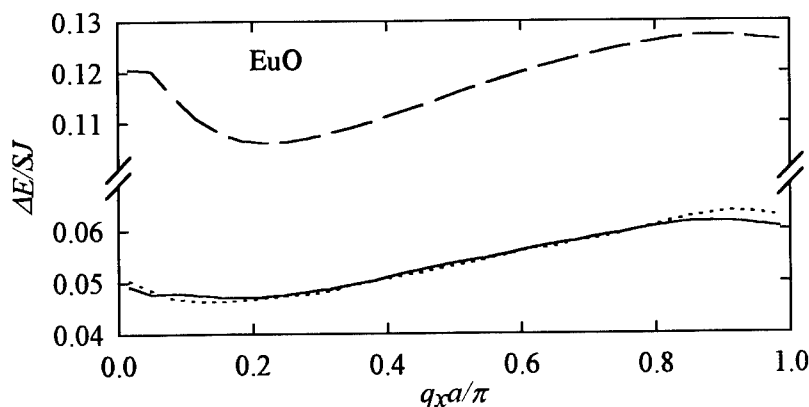


Figure 2. The relative SW energy shift  $\Delta E/SJ$  (solid line -  $N=10$ , branch 1; dotted line -  $N=10$ , branch 2; dashed line -  $N=20$ , branch 1).

parts, respectively, of self-energy terms in the diagram formalism, by analogy with (3). The energy shift has a weaker dependence on  $q_x$  and it is larger for the thicker film.

### CONCLUSIONS

We have developed a microscopic theory for interactions between the dipole-exchange SW modes in ultrathin ferromagnetic films. Applications have been made to evaluate the energy shift and damping of SW modes in EuO. Inelastic light scattering would be an appropriate experimental technique to probe these effects (6). Other applications of the nonlinear theory could be to examine SW instabilities in ultrathin films under conditions of parallel or perpendicular "pumping" by a microwave field.

### ACKNOWLEDGMENTS

This research was supported by the government agencies NSERC (of Canada) and CAPES and FUNCAP (of Brazil).

### REFERENCES

1. See, e.g., Wigen, P.E. (editor), *Nonlinear Phenomena and Chaos in Magnetic Materials*, World Scientific, Singapore, 1994.
2. Wolfram, T., and De Wames, R.E., *Progr. Surf. Sci.*, 1972, **2**, 233.
3. Kontos, D., and Cottam, M.G., *J. Phys. C*, 1986, **19**, 1189 and 1203.
4. Erickson, R.P., and Mills, D.L., *Phys. Rev. B*, 1991, **43**, 10715.
5. Nörtemann, F.C., Stamps, R.L., and Camley, R.E., *Phys Rev B*, 1993, **47**, 11910.
6. See, e.g., Grünberg, P., in *Light Scattering in Solids V*, Springer, Berlin 1989, p. 303.



## CHARACTERIZATION OF VANADIUM OXIDE AND NEW V/Ce OXIDE FILMS PREPARED BY SOL-GEL PROCESS

Z. Crnjak Orel<sup>1</sup> and I. Muševič<sup>2,3</sup>

<sup>1</sup>National Institute of Chemistry, Hajdrihova 19, SI-1001 Ljubljana, Slovenia

<sup>2</sup>Faculty of Mathematics and Physics, University of Ljubljana, Slovenia

<sup>3</sup>“J. Stefan” Institute, Ljubljana, Slovenia

**Abstract** — The preparation of vanadium oxide and new mixed V/Ce oxide thin films as intercalation compound for lithium ions (at 55 and 38 at. % of V) started from aqueous inorganic precursors. Thin films were prepared via the sol-gel process by dip-coating only once. Glass slides covered with  $\text{SnO}_2\text{:F}$  were used as substrates. The influence of added cerium precursors on the electrochemical optical and structural properties of thin films was studied by cycling voltammetry (CV), in-situ ultraviolet and visible (UV-VIS) spectroscopy, atomic force microscopy (AFM) and IR spectroscopy. The addition of  $\text{CeO}_2$  improved the poor stability of vanadium oxide films and enhanced their ion-charge capacity up to 30  $\text{mC/cm}^2$ . In all films the process of intercalation of lithium ions was followed by in-situ UV-VIS spectroscopy and ex-situ FT-IR spectroscopy performed at near-grazing incidence angle. The intercalation of  $\text{Li}^+$  ions was confirmed through shifting of the absorbance edge in UV-VIS spectra and by the observed shifts of V-O<sub>v</sub> vibrations in the IR spectra. The surface of the films was also characterized by AFM imaging before and after cycling in 1M  $\text{LiClO}_4$  in propylene carbonate electrolyte. ©1999 Acta Metallurgica Inc.

## INTRODUCTION

Previous studies have caused big interest in using the sol-gel process for the preparation of oxide compounds (1). The inorganic sol-gel process is one well known synthetic route for the preparation of various oxide materials ( $\text{SiO}_2$ ,  $\text{V}_2\text{O}_5$ ,  $\text{SnO}_2$ ) (1). The sol-gel synthesis is based on the hydrolysis of an inorganic precursors in aqueous solution followed by the condensation, gelation, aging, drying and densification. A great variety of materials have been synthesized in this way as powders or thin film layers with potential application in optical electronics, as catalysts protective films, etc. Final materials can be applied to any desired shape. By dip-coating, coil-coating, spraying or screen printing technique the almost all of materials can be coated.

Recently we prepared  $\text{CeO}_2/\text{SnO}_2$  (2,3,4) films via the inorganic sol-gel route as counter electrode in electrochromic devices for smart windows. A counter electrode must be transparent under a charge insertion for practical uses.  $\text{CeO}_2$  containing films are known to be able to remain transparent irrespective of  $\text{Li}^+$  ions content (5). Our best sample prepared

by one dip showed a very good capacity ( $10 \text{ mC/cm}^2$ ) for intercalation/deintercalation of  $\text{Li}^+$  ion in 0.1 M LiOH, but in 1 M  $\text{LiClO}_4$  in propylene carbonate (PC) electrolyte the capacity was only  $4.5 \text{ mC/cm}^2$ . The stability and transmittance of the films were very good and did not change even after 2400 cycles. Because of the enhanced electrochemical stability we decided to prepare mixed vanadium oxide/ $\text{CeO}_2$  and  $\text{V}_x\text{O}_y$  thin films. We extended the study to vanadium oxides because  $\text{V}_2\text{O}_5$  is very well known as intercalation host for small ions (6); in addition their long-term durability in "safe" range (1.8 to 3.9 V vs. Li) in 1M  $\text{LiClO}_4$  in PC electrolyte has been reported by Cogan et al. (7) and Talledo et al. (8). Their films were prepared by DC magnetron sputtering.

The aim of the present work is the preparation of a stable, transparent counter electrode via the inorganic sol-gel process by dip-coating technique. All V-oxide films and V/Ce-oxide films were deposited via one single deposition step.

## EXPERIMENTAL

The preparation of an aqueous dispersion of hydrated oxide (sol) of  $\text{V}_2\text{O}_5$ ,  $\text{CeO}_2$  and mixed vanadium oxide/ $\text{CeO}_2$  started from a solution of the corresponding metal oxide or metal salts,  $\text{V}_2\text{O}_5$  and  $\text{Ce}(\text{NH}_4)_2(\text{NO}_3)_6$ , respectively. Crystalline  $\text{V}_2\text{O}_5$  was dissolved (9) in 6 % nitric acid to obtain 0.044M aqueous solution. By the evaporation of water the desired concentration of  $\text{V}_2\text{O}_5$  was obtained, which was directly used for the preparation of pure vanadium oxide thin films. Mixed V/Ce-oxide film at different atomic percent (at. %) of V in V/Ce-oxide (55, 38 at.%) was prepared by adding, an adequate concentration of  $\text{CeO}_2$  sol prepared as previously described (2,3) into the  $\text{V}_2\text{O}_5$  sol. All films were deposited by the dip-coating methods with a pulling speed of 10 cm/min on  $\text{SnO}_2\cdot\text{F}$  glass plates ( $2 \times 3 \times 0.1 \text{ cm}^3$ ) with only one dipping (a sheet resistance/square -  $R_{\square} \approx 12 \Omega$ ).

The EG&PAR-Mod 273 potentiostat galvanostat with electrochemical analysis software was used for cyclic voltammetric and chronocoulometric experiments. Platinum and  $\text{Ag}/\text{AgCl}/1\text{M LiCl}$  in methanol served as counter and reference electrode, respectively. The working electrode area was  $1 \text{ cm}^2$  in electrolyte solution (30 ml 1M  $\text{LiClO}_4$  in propylene carbonate (PC)). The scanning rate was  $20 \text{ mV/s}^{-1}$ . Cycling and chronocoulometric measurements were performed at potentials of +2.0 V and -1.5 V. UV-VIS spectroelectrochemical measurements were performed on a HP845 UV-VIS systems diode array spectrophotometer with an EG&G PAR 273 computer controlled potentiostat-galvanostat.

Microstructure evolution was also characterized by atomic force microscopy (AFM). A Nanoscope III AFM was used in the constant force mode and with a scanning rate of 2 Hz (2 lines  $\text{s}^{-1}$ ). Park Scientific Ultralever probes with typical probe radius of the order of 10 nm were used in the experiments.

The FT-IR spectra were recorded with a Perkin-Elmer 2000 spectrometer at a near grazing incidence angle (NGIA at  $80^\circ$ ). Wire grid polarizers were used.



## RESULTS AND DISCUSSION

Cyclic voltammetry is very useful technique for determining the cycling durability and reversibility of the charge exchange. The voltage was varied between  $-1.5\text{ V}$  and  $+2.0\text{ V}$  vs.  $\text{Ag}/\text{AgCl}$  for all films. Tolledo et al. (6), Cogan et al. (7) reported long term durability of their  $\text{V}_2\text{O}_5$  films for the range  $2.6\text{ V}$  and  $3.9\text{ V}$  vs.  $\text{Li}$  electrodes. When they used a wider range ( $1.8\text{--}3.9\text{ V}$ ) the voltamogram was significantly different (disordered materials).

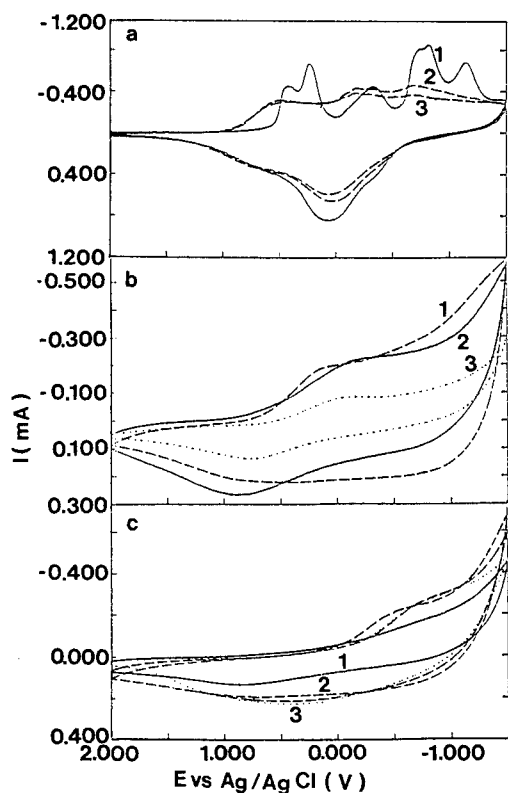


Figure 1. Cyclic voltammograms of dip-coated films ( $400^\circ\text{C}$  for  $5\text{ min.}$ ) at potential scan rate of  $20\text{ mVs}^{-1}$  in  $\text{LiClO}_4$  in PC: a) vanadium oxide: 1 - first cycle, 2 - fourth cycle, 3 -  $8^{\text{th}}$  cycle; b) V/Ce oxide at 55 at. % of V: 1 - first cycle, 2 -  $40^{\text{th}}$  cycle, 3 -  $700^{\text{th}}$  cycle; c) V/Ce oxide at 38 at. % of V: 1 - first cycle, 2 -  $100^{\text{th}}$  and  $180^{\text{th}}$  cycle, 3 -  $720^{\text{th}}$  cycle.

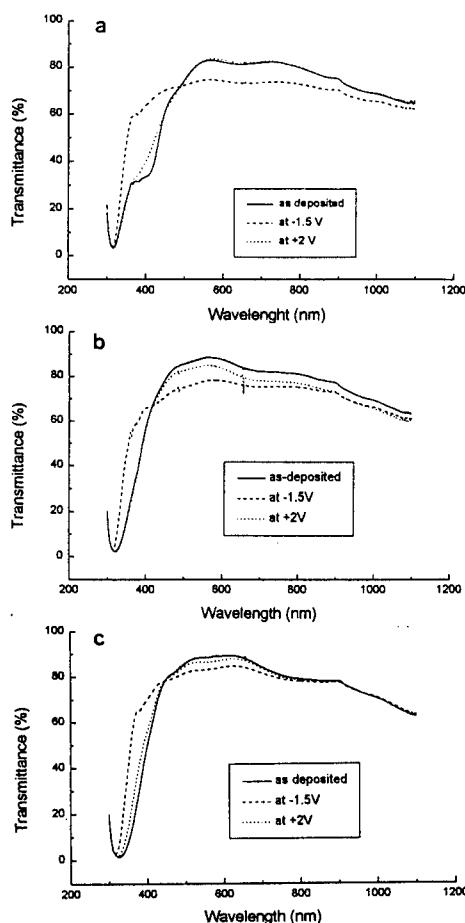


Figure 2. Transmittance (UV-VIS-NIR) spectra of a) V-oxide, b) V/Ce oxide at 55 at. % of V, c) V/Ce oxide at 38 at. % of V.

Fig. 1a shows data for pure vanadium oxide film heated at 400°C for 5 min. The first voltammogram is very similar to the voltammogram of crystalline film, but the second one and all the following ones changed and are similar to the voltammograms of disordered films (6). Also the amount of inserted and extracted charge changed for each following cycle. To improve the cycling durability of V-oxide films in a wide voltage range, mixed oxide films at 55 and 38 at. % of V in V/Ce-oxide were prepared (10). All films were tested for their cycling durability in the same wide voltage range (-1.5 V to +2 V vs. Ag/AgCl). Fig. 1b,c show first cyclic voltammogram of V/Ce-oxide film at 55 and 38 at. % of V. The first voltammograms for both films are very similar to the film of pure CeO<sub>2</sub> (2,4) and they show only featureless current insertion/extraction. It is clearly seen in Fig. 1 that for film of V/Ce oxide (55 at. % of V) after 40 cycles the voltammogram starts to diminish. Voltammograms for films of V/Ce oxide (38 at. % of V) starts to diminish slowly after about 100 cycles and after 700 cycles, the voltammogram is still higher than the first one. The amount of inserted/extracted charge change during the cycling but after 700 cycles it was about 20 mC/cm<sup>2</sup> and 28 mC/cm<sup>2</sup> for Ce/V oxide at 55 at. % of V and 38 at. % of V, respectively. For all films UV-VIS transmission spectra were measured in-situ in as-deposited state at -1.5 V and +2 V (Fig. 2a,b,c). The optical transmittance in the 300< $\lambda$ <1000 nm wavelength range for films of V-oxide and V/Ce-oxide, did not change significantly after cycling. The transmittance after the intercalation of Li<sup>+</sup> ion in the range from 500-800 nm was for pure vanadium oxide and V/Ce oxide at 55 at. % of V, 10 % lower and for only 5 % lower for V/Ce oxide at 38 at. % of V. Fundamental absorption edge shifts after the intercalation of Li<sup>+</sup> ions and curve does not reproduce the as deposited curve which implies that some of Li<sup>+</sup> ions remains in the film (11). This is similar to results reported by Talledo et al. (8).

The same films were also characterized by AFM, before and after cycling (Fig. 3). Typically, we observe amorphous grains of the size of 50-100 nm on the surface of V-oxide and V/Ce-oxide (at 55 at. % of V) films before and after cycling. The results clearly indicate that the surface roughness of both films decreases after cycling. The RMS (root mean square) surface roughness of these films decreases from 11 nm to 6 nm in V-oxide films and from 40 nm to 30 nm in V/Ce oxide (at 55 at. % of V) films. On the contrary, pristine V/Ce-oxide (at 38 at. % of V) films are extremely flat, with a typical RMS surface roughness of only 2 nm and no observable grain structure. However, after cycling, these films show an increased RMS surface roughness of 8 nm and a grain structure with a typical grain size of 100 nm. Surface topography (AFM data) of the film in terms of RMS surface roughness is consistent with cycling properties of the film. The change of RMS surface roughness can be correlated with corresponding available surfaces of the film which is connected with the content of Li<sup>+</sup> ions. The surface changes could be associated with similar electrochemical behavior of V and V/Ce-oxide at 55 at. % of V (slight increase of cyclogram) and completely different cycling properties for Ce/V oxide at 38 at. % of V. The obtained amorphous properties of the films were also proved by X-ray spectroscopy (10). All single dip-coated films (400°C for 5 min.) were characterized by X-ray diffraction (XRD) method. The results indicated that films were amorphous due to the absence of any diffraction line except for the presence of the SnO<sub>2</sub> line from the substrate. The infrared (IR) spectra of all films on SnO:F covered glass substrate were obtained by near-grazing-incidence angle (NGIA - 80°) detected in p-polarization. For pure V-oxide film we obtained similar results as for V<sub>2</sub>O<sub>5</sub> prepared by d.c. magnetron sputtering on ITO coated plate.

Due to the intercalation of  $\text{Li}^+$  ions the absorption maxima at  $1030$  and  $970\text{ cm}^{-1}$  (V-O stretching) were observed (10) at lower wavenumbers (lattice softening). Also the quantity of intercalated lithium increased the shift to lower wavenumbers. In mixed V/Ce oxide films at 55 and 38 at. % of V oxide only one band was observed at  $955$  and  $919\text{ cm}^{-1}$ , respectively. The band in IR spectra of V/Ce oxide film at 55 at. % of V after intercalation of  $\text{Li}^+$  ions at  $-1.5\text{ V}$  (Fig. 4b) is shifted to  $928\text{ cm}^{-1}$ . Fig. 4c shows the spectra of deintercalated  $\text{Li}^+$  ions at  $+2\text{ V}$ . The initial state was not achieved, therefore some of the  $\text{Li}^+$  ions must still be in the films.

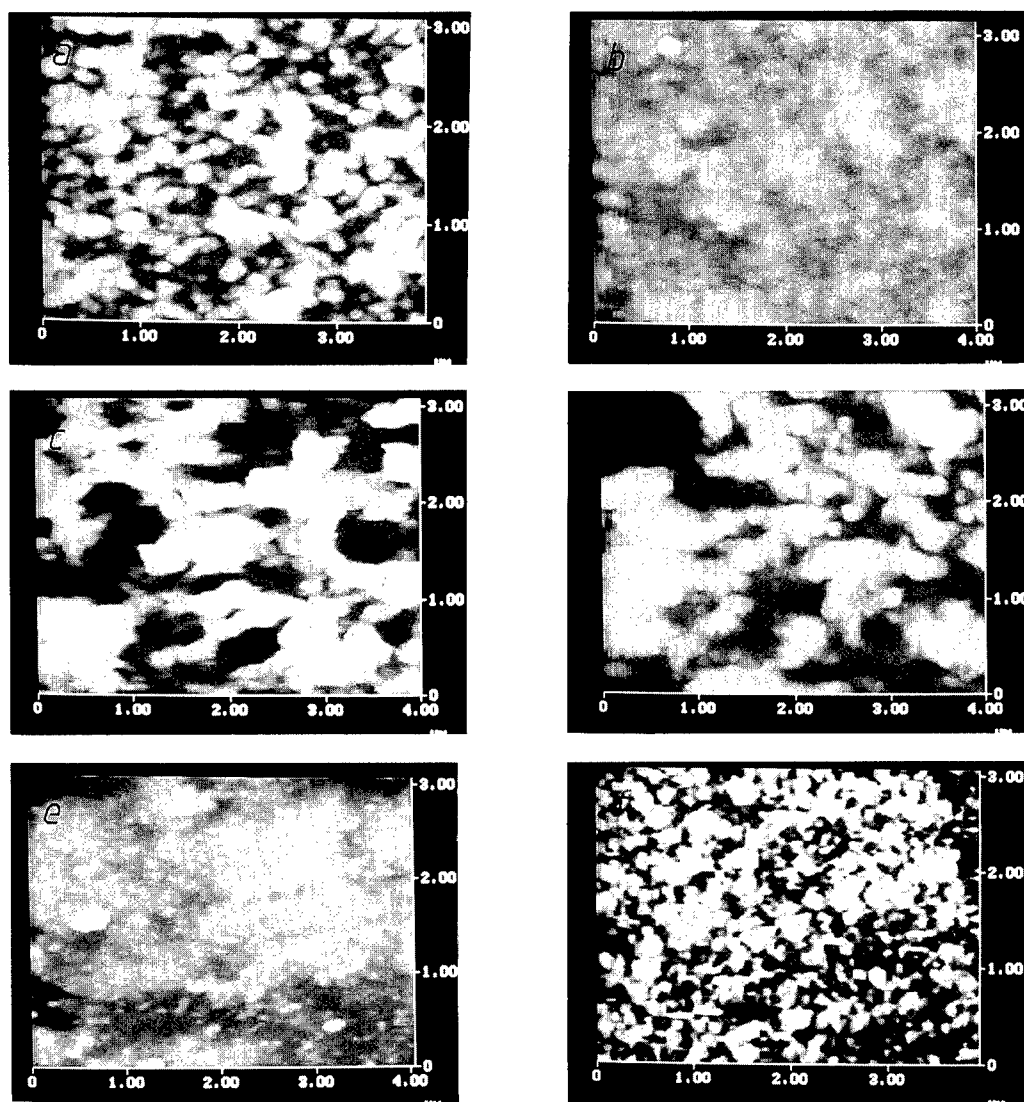


Figure 3. AFM micrographs of dip-coated films heated at  $400^{\circ}\text{C}$ . a) V-oxide, b) V-oxide after cycling, c) V/Ce oxide at 55 at. % of V, d) V/Ce oxide at 55 at. % of V after cycling, e) V/Ce oxide at 38 at. % of V, f) V/Ce oxide at 38 at. % of V after cycling.

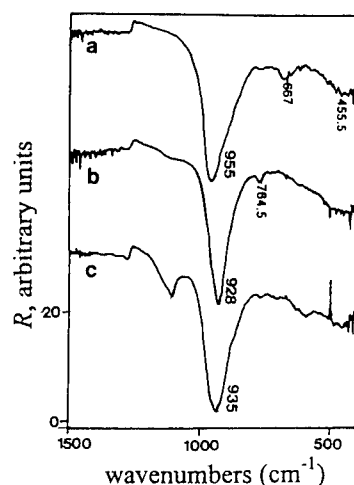


Figure 4. NGIA reflectivity spectra of V/Ce oxide film at 55 at. % of V: a) as deposited, b) at -1.5 V for 120 s, c) at +2 V for 120 s.

## CONCLUSION

V-oxide and V/Ce-oxide thin films were prepared from aqueous precursors by a single dipping at 400°C for 5 min. Electrochemical stability of pure V-oxide in wide range (-1.5 to +2 V vs. Ag/AgCl) was improved after the addition of CeO<sub>2</sub>. The quantity of intercalated Li<sup>+</sup> ion is related to the film surface roughness. Films at 55 and 38 at. % could be successfully used as counter electrode for smart window due to their long cycling stability.

## ACKNOWLEDGMENT

This work was supported by the Ministry of Science and Technology of Slovenia.

## REFERENCES

- (1) Gacoin, T., Malier, L. and Boilot, J.-P., *Chemical. Materials*, 1997, 9, 1502.
- (2) Crnjak Orel, Z., Orel, B., *Journal of Material Science*, 1995, 30, 2284.
- (3) Crnjak Orel, Z., Muševič, I. and Orel, B., in: *Nanoparticles in Solids and Solutions*, J.H.Fendler and I. Dékány (Eds.), Kluwer Academic Publishers, 1996, p. 519.
- (4) Crnjak Orel, Z., Orel, B., *Solar Energy Materials and Solar Cells*, 1996, 40, 205.
- (5) Veszeli, M., Kullman, L., Azens, A., Granqvist, C., *J.Appl.Phys.*, 1997, 81, 2024.
- (6) Talledo, A. and Granqvist, C.G., *J. Phys. D: Applied Physics*, 1997, 27, 2445.
- (7) Cogan, S.F., Nguyen, N.M., Perrotti, S.J. and Rauh, R.D., *J.Appl.Phys.*, 1989, 66, 1333.
- (8) Talledo, A. and Granqvist, C.G., *J.Appl.Phys.*, 1995, 77, 4655.
- (9) Sullivan, R.J., Srinivasan, T.T., Newnham, R.E., *Commun. Am.Cer.Soc.*, 1990, 73, 3715.
- (10) Crnjak Orel, Z., *Solid State Ionics*, 1999, 115, 105.
- (11) Wruch, D., Ramamurthi, and Rubin, M., *Thin Solid Films*, 1989, 181, 79.



## MECHANICAL PROPERTIES OF MULTILAYER MATERIALS

D. Josell<sup>1</sup>, D. van Heerden<sup>2</sup>, D. Shechtman<sup>3</sup> and D. Read<sup>4</sup>

<sup>1</sup>National Institute of Standards and Technology, Gaithersburg, MD 20899

<sup>2</sup>The Johns Hopkins University, Baltimore, MD

<sup>3</sup>Technion, Haifa, Israel

<sup>4</sup>National Institute of Standards and Technology, Boulder, MD

*We conducted tensile tests of free standing Al/Ti multilayer thin films in order to determine the dependence of yield stress on layer thickness. The multilayers studied were composed of fcc and hcp Ti layers. The Al layers were approximately twice the thickness of the Ti layers. Because a controversy exists concerning the crystalline structure of Ti in Al/Ti multilayers, we also present microstructural results. ©1999 Acta Metallurgica Inc.*

### INTRODUCTION

Because of practical difficulties associated with handling thin films, mechanical properties of multilayer thin film materials are frequently inferred from the results of nanoindentation studies. However, because of the complicated stress state under a nanoindenter tip, it is unclear whether yield stresses thus obtained are accurate. We therefore present the results of tensile tests on Al/Ti multilayer thin films. The multilayer films studied were composed of Al and Ti, with the Al layers intentionally twice the thickness of the Ti layers to lower the density of the structure. The thickness of each pair of Ti and Al layers, the composition modulation wavelength (CMW), was varied between 13 and 90 nm. X-ray diffraction studies of the as-deposited films indicated a strong (00.1) texturing of the hcp Ti layers and (111) texturing of the fcc Al layers. Artifacts induced during preparation for study by transmission electron microscopy (TEM) are discussed.

### TENSILE TESTS AND MICROSTRUCTURAL STUDIES

Stress-strain curves were obtained for specimens with different values of CMW (1). We observed a distinct transition from elastic to plastic behavior with all films. Plastic strain as a function of stress was obtained by subtracting the elastic strain (extrapolated from the linear region of the stress-strain curve) from the measured (total) strain. Figure 1 shows the dependence of the plastic strain on applied stress for films with four different CMWs. The dependence of the yield stress (defined in Fig. 1) on CMW is evident. Though the authors are

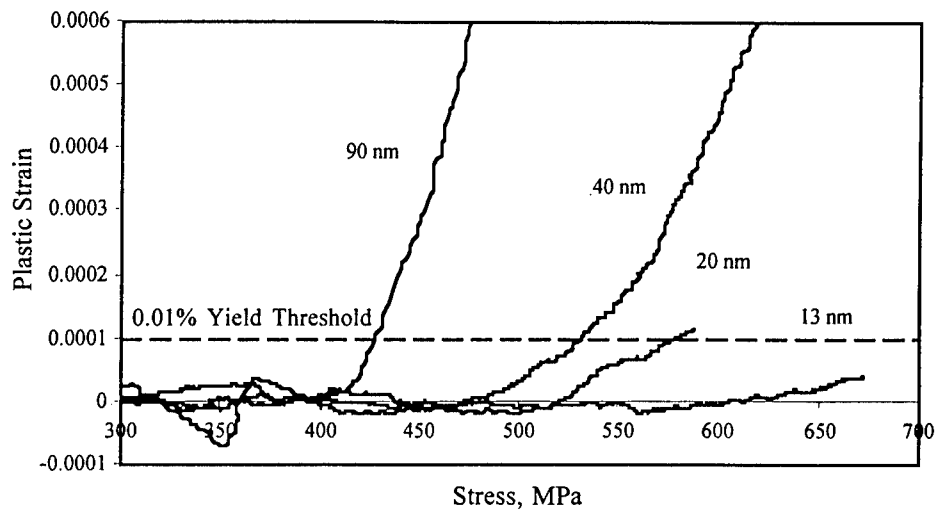


Fig. 1 Plastic strain versus applied stress for Al/Ti multilayers with indicated CMWs (Ref (1)).

unaware of published tensile properties of Al/Ti multilayers, results published by Lehoczky (2,3) for Al/Cu multilayers show a 0.2% yield stress independent of CMW for CMW less than 140 nm. Based on nanoindentation results, a Hall-Petch dependence of yield stress on CMW, i.e. proportional to  $\text{CMW}^{-1/2}$ , was deduced for Al/Ti multilayers (with equal Ti and Al layer thickness) (4). As shown in Fig. 2, our results fall between these two behaviors.

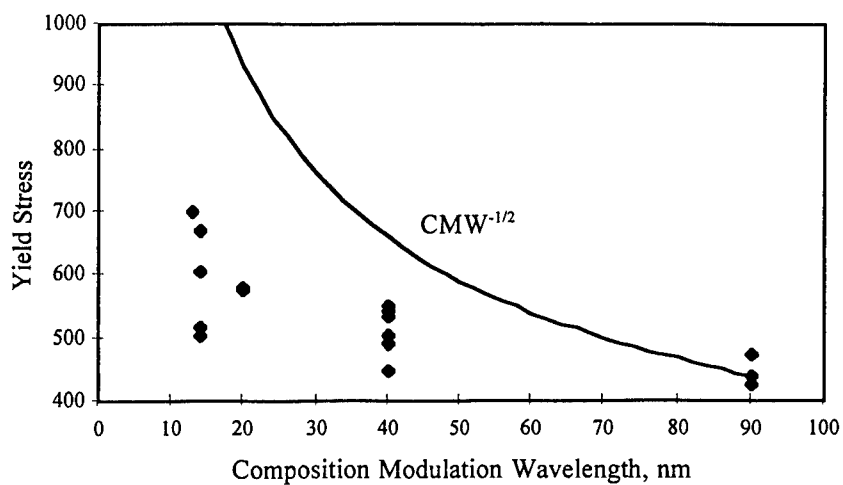


Fig. 2 Yield stress as a function of CMW for Al/Ti multilayers (Ref. (1)).



Fig. 3 High resolution TEM image of a section of Ti/Al multilayer. The interface between the fcc Ti and fcc Al is evident from the change of contrast, lattice spacing and the twinned orientations.

Figure 3 shows a cross section view of a Ti/Al multilayer after it has been prepared for TEM. The abc...abc stacking of the layers indicates that both the Ti and the Al layers have fcc structures with (111) texturing in the growth direction. TEM diffraction patterns taken along different zone axes including the four-fold (100) confirm that both the Ti and Al are fcc (5). However, x-ray diffraction scans of as-deposited Ti/Al multilayer films taken in the symmetric reflection and transmission geometries indicate that the films deposit with hcp Ti and fcc Al (5,6). Figure 4 shows the digitized intensity of a TEM (111) diffraction spot versus x-ray diffraction data taken in the symmetric reflection geometry, both plotted versus the magnitude of the scattering vector in the growth direction. The x-ray diffraction scan shows (111) textured fcc Al and (00.1) textured hcp Ti plus satellites (5.2 nm CMW). The unambiguous observations of hcp Ti by x-ray diffraction and fcc Ti by TEM indicate that a transformation has occurred during specimen preparation for the cross-section TEM (5,6). In light of the observed transformation, reports by Ahuja and Fraser (4) and Banerjee, Ahuja and Fraser (7) claiming to have fabricated fcc Ti (and hcp Al as well) based solely on TEM observation, are questionable. Determination of the as-deposited structure, e.g. by x-ray diffraction, is necessary.

### SUMMARY

We have presented the results of tensile tests on Al/Ti multilayer thin films. Though our results show a dependence of the yield stress on the layer thickness, it is weaker than the

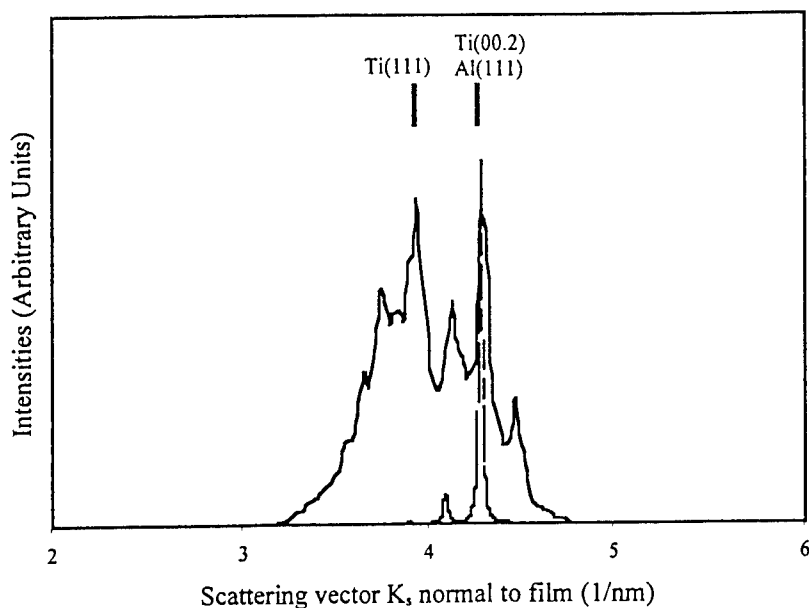


Fig. 4 X-ray diffraction data (dashed) and digitized TEM diffraction data (solid) showing the appearance of a new phase in the specimen prepared for TEM (rms count noise < 1% full scale).

Hall-Petch behavior frequently assumed. Microstructural studies show the films deposit with fcc Al and hcp Ti. The existence of fcc Ti in TEM micrographs is seen to be an artifact of specimen preparation, likely also true of fcc Ti observed in other multilayers by TEM (4,7).

#### ACKNOWLEDGEMENTS

D. Josell and D. Shechtman acknowledge the support of the United States – Israel Binational Science Foundation.

#### REFERENCES

1. D. Josell, D. van Heerden, D. Read and D. Shechtman, "Tensile Testing Low Density Multilayers: Aluminum/Titanium", J. Mater. Res., in press.
2. S.L. Lehoczký, J. Appl. Phys. **49**, 5479 (1978).
3. S.L. Lehoczký, Phys. Rev. Lett. **41**, 1814 (1978).
4. R. Ahuja and J.L. Fraser, J. Electron. Mater. **23**, 1027 (1994).
5. D. van Heerden, D. Josell and D. Shechtman, Acta Mater. **44**, 297 (1996).
6. D. Shechtman, D. van Heerden and D. Josell, Mater. Lett. **20**, 329 (1994).
7. R. Banarjee, R. Ahuja, and H.L. Fraser, Phys. Rev. Lett. **76**, 3778 (1996).





Pergamon

NanoStructured Materials, Vol. 12, pp. 409–412, 1999

Elsevier Science Ltd

© 1999 Acta Metallurgica Inc.

Printed in the USA. All rights reserved

0965-9773/99/\$-see front matter

PII S0965-9773(99)00146-4

## SUPERCONDUCTIVITY REENTRANCE IN STRONG MAGNETIC FIELDS IN MO/SI MULTILAYERS.

N.Ya.Fogel, M.Yu.Mikhailov, O.I.Yuzepovich, Yu.V.Bomze.

B.Verkin Institute for Low Temperature Physics and Engineering,

47 Lenin Avenue, 310164 Kharkov, Ukraine. E-mail: fogel@ilt.kharkov.ua

**Abstract** - Novel reentrance phenomenon is discovered on Mo/Si multilayers which occurs in parallel to the layers and slightly inclined magnetic fields. This effect may be explained in terms of the intrinsic pinning and vortex lattice (VL) commensurability with underlying layered structure. The locations of the zero resistance regions correspond to the stable VL configurations or to the transitions between two commensurate lattices. It is suggested that resistive method may be used as a new tool of the VL structure study in layered superconductors. ©1999 Acta Metallurgica Inc.

### INTRODUCTION

Vortex lattice (VL) structure in layered superconductors differs essentially from the simple triangular one observed in homogeneous type II superconductors, unless the magnetic field  $H$  is parallel to the  $c$  axis. Different type arrangements of VL are predicted theoretically for the cases when magnetic field is parallel or inclined to the layer planes. Different theoretical approaches including anisotropic 3D London and Ginzburg-Landau (GL) models, as well as the Lawrence-Doniach (LD) model were used (1-8). According to the results of Ref.1 obtained within the London approximation, the unit cell of the VL should be strongly distorted with respect to the equilateral triangle, and VL parameters should depend intrinsically on the anisotropy parameter  $\gamma=(M/m)^{1/2}$  and the angle between  $H$  and anisotropy axis. Here  $M$  is the effective mass along  $c$ ,  $m$  is the in-plane mass. The commensurability effect has been outside the scope of this work. The latter was considered in the paper (2) of Ivlev, Kopnin and Pokrovsky (IKP). It was shown that in the case of  $H_{\parallel}$ , when the intrinsic pinning energy  $E_p$  exceeds the elastic energy of a VL shear deformation  $E_{el}$ , the vortices cannot cross the layers, period  $Z_0$  along  $c$  is fixed and it is determined by the initial conditions under which VL was formed. This means that VL should be always commensurate with the layered structure period  $s$  at any  $H$  values (the distance between vortices in the direction normal to the layers  $Z_0=Ns$ ,  $N$  is an integer). In the opposite limit case VL parameters are determined by the applied magnetic field. It was shown that the free energy of the rhombic lattice in the commensurate state as a function of  $H$  displays two minima corresponding to the different orientations of the unit cell vectors with respect to the layer planes. In the instability region there is a lot of metastable states corresponding to the different displacements of the vortex rows relative to each other in the neighboring interlayers (2,3). They can be

dynamically accessible at the  $\mathbf{H}$  variation (4). In the framework of LD approach for relatively high parallel magnetic fields a sequence of the first-order phase transitions between VLs with different  $N$  is predicted (4). For the tilted fields many versions of the vortex arrangement are suggested (5-7). The most exotic among possible VL configurations in the tilted magnetic fields is so-named combined lattice consisting of two vortex "species" oriented in different directions (5,6). Obviously, due to the nonstandard VL structure and intrinsic pinning many unusual effects can arise in layered superconductors. In the tilted fields the direction of magnetization vector  $\mathbf{M}$  in many cases does not coincide with the external field direction (1,7). In parallel magnetic fields the critical current should be an oscillating function of magnetic field (8).

### EXPERIMENTAL DATA AND DISCUSSION.

The experiments have been carried out on two Mo/Si multilayered samples: sample A with Mo layer thickness  $d_{Mo}=22\text{\AA}$  and Si layer thickness  $d_{Si}=34\text{\AA}$ ; sample B with the same  $d_{Mo}$  value and  $d_{Si}$  value of  $44\text{\AA}$ . The number of bilayers in the both samples is 50. The sample preparation and characterization are described in Ref.9. The sample wavelength and individual layer thicknesses are determined from small angle X-ray diffractometry. At all orientations of  $\mathbf{H}$  with respect to the layers the transport current  $\mathbf{I}$  directed along the layers was always perpendicular to  $\mathbf{H}$ . The precision of  $\mathbf{H}$  alignment with the layer planes was about  $0.2^\circ$ .

In Fig. 1a the resistance as a function of  $H$  at different temperatures for the angle  $\theta=0$  is shown for sample A ( $\theta=0$  for  $\mathbf{H}$  parallel to the layers). Beginning from some reduced temperature ( $t=0.96$ ) on  $R$  vs  $H$  curve a step appears which develops at lower temperatures into a minimum. At further  $T$  diminishing instead of  $R$  minimum the zero resistance region appears which manifests reentrance of superconductivity. After ZRR at still larger fields resistance appears again. As we keep going down in temperature, the ZRR becomes wider. For understanding the reentrance phenomenon scale it should be mentioned that normal resistance of sample A is  $42.4\text{ Ohm}$ . Resistance as a function of  $H_{||}$  for another sample is shown in Fig. 1b.

Reentrance behavior is very sensitive to the deviation of  $\mathbf{H}$  orientation from parallel to the layer planes (Fig.2). The  $R$  minima are observed until some critical angle  $\theta_{cr}$ .

Reentrance phenomenon is also sensitive to the magnetic history. When one begins measurements with the first switching on of  $\mathbf{H}$  sweep at sufficiently low temperature,

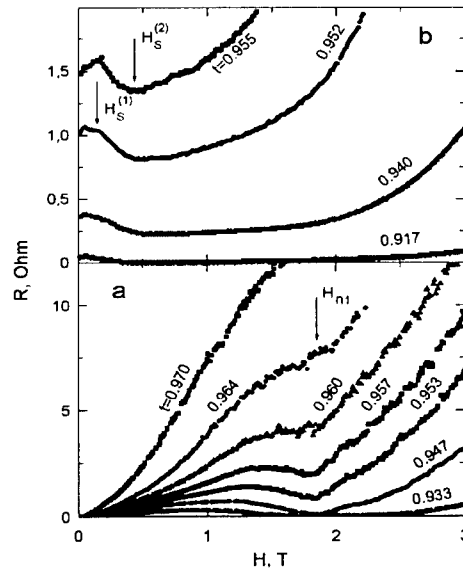
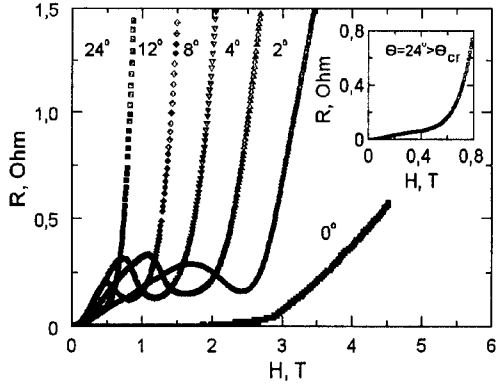


Fig. 1. Resistance as a function of parallel magnetic field at different reduced temperatures  $t=T/T_c$  for sample A (a) and sample B (b). The arrows show values of  $H_s$  and  $H_n$  (see the text).



**Fig.2.** Resistance as a function of magnetic field for different its orientations with respect to the layer planes for sample A.

another realization of  $R$  vs  $H$  curves may be obtained on the same sample (Fig.3). In this case two ranges of ZRR are observed, i.e. reentrance of superconductivity arises twice during one magnetic field sweep.

The natural assumption explaining appearance of reentrance is connected with nonmonotonic dependence of the critical current  $I_c$  on magnetic field. The measurements of  $I_c$  vs  $H$  dependences confirm this supposition as Fig.4 shows. Positions of the minima on  $R$  vs  $H$  curve coincide with locations of the maxima on  $I_c$  vs  $H$  curve, and vice versa. For the interpretation of the data obtained let us, first of all, determine physical meaning of the temperature  $T_0$  where the signs of developing ZRR states appear. It follows from the experimental data that beginning from this temperature transverse coherence length  $\xi_L(T)$  becomes equal to or less than  $s/2$ , i.e. below  $T_0$  the confinement of the vortex cores between superconducting layers starts to develop. In this situation intrinsic pinning should become more pronounced, and transition to the limit  $E_p > E_{el}$  may be expected. Thus,  $T_0$  manifests by itself the transition to the regime of strong layering (2).

Among a large variety of possible VL configurations proposed theoretically there are arrangements corresponding to the commensurate lattices. When  $E_p \gg E_{el}$  the lattice should be commensurate with SL wavelength at all magnetic field values (2). According to IKP the stable states of the commensurate lattices correspond to the conditions:

$$p = \pi / \sqrt{3}, p = \pi \sqrt{3}. \quad [1]$$

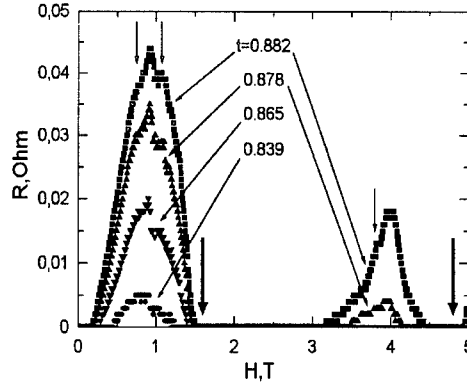


**Fig.3.** Resistance as a function of  $H_{||}$  at the different temperatures for sample A for a case when at  $t=0.882$  the sample was in a virgin state. Thick arrows show values of  $H_s$ , thin vertical ones mark additional features of  $R$  vs  $H$  curves described in the text.

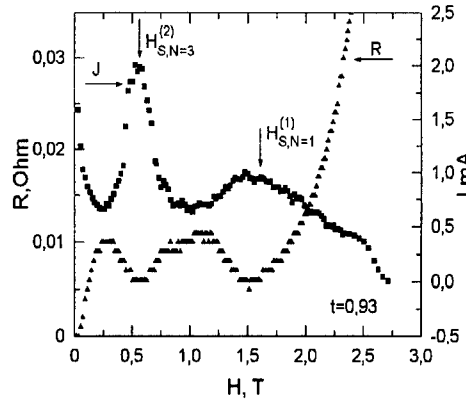


**Fig.4.**  $I_c$  and  $R$  as a function of magnetic field for sample A ( $\theta = 0^\circ$ ).

Here  $p$  is a reduced magnetic field:

$$p = 2\pi N^2 s^2 \gamma H / \Phi_0. \quad [2]$$

Using formulae [1], [2] one can define  $H_s$  values corresponding to the stable states (i.e. to the free energy minima) for different commensurability orders. The anisotropy parameter  $\gamma$  is equal to 11.8 and 23.5 for samples A and B respectively. It appears that two calculated values of  $H_s$  for  $N=1$  get in the both ZRR ranges for sample A (these values are shown by thick arrows in Fig.3). The same situation is observed for sample B (Fig.1b).

Beside the stable VL configurations rather different VL states may exist which are dynamically accessible at the magnetic field variation (2,3). Under the conditions of strong pinning shear instability of the commensurate lattice leads to the breaking of symmetry: neighboring vortex chains locked between superconducting layers may be shifted one relative to another (3). A lot of these "shifted" lattices correspond to the metastable states, i.e. to the local minima of free energy. One may believe that metastable states of VL may be probed in dynamic experiments, i.e. by resistive or critical current measurements. We suggest that a number of additional features observed on  $R$  vs  $H$  curves along with the main minima (in particular, like steps; see thin arrows in Fig.3), may be an evidence of these metastable states.

The predictions about VL structure in layered superconductors obtained in the paper of Bulaevskii and Clem (4) (BC) in the framework of LD model are rather different from those obtained on the base of 3D anisotropic London or GL approach. The series of the phase transitions between different commensurate phases should occur at definite magnetic field values  $H_n$ . For this effect the value of the characteristic field  $H_0 = \Phi_0 / \gamma \kappa^2$  where Josephson cores of the vortices begin to overlap is essential. For sample A the transition between commensurate phases corresponding to  $Z_0=s$  and  $Z_0=2s$  should occur in the field  $H_1 \sim H_0/3 = 1.84\text{T}$ , while the next transition in the field  $H_2 \sim H_0/8 = 0.69\text{T}$ . The position of the minima in Fig.1a is just consistent with the field  $H_1$  estimated above. However, at the field close to  $H_2 = 0.69\text{T}$  there is only a peculiarity on the derivative  $dR/dH$ .

It is rather puzzling that in spite of the differences in the approach and predictions of GL and LD models, one can find on the same sample the patterns corresponding to the both scenarios in the same range of magnetic fields. Further experiments are needed for understand the correlation between VL initial state and the preferable scenario.

1. Campbell, J., Doria, M.M. and Kogan, V.G., *Phys.Rev.B*, **38**, 2439, 1988.
2. Ivlev, B.I., Kopnin, N.B. and Pokrovsky, V.L., *J.Low Temp.Phys*, **80**, 187, 1990.
3. Levitov, L.S. *Phys.Rev.Lett.*, **66**, 224, 1991.
4. Bulaevskii, L. and Clem, J.R., *Phys.Rev.B*, **44**, 10234, 1991.
5. Bulaevskii, L.N., Ledvij, M. and Kogan, V.G., *Phys.Rev.B*, **46**, 366, 1992.
6. Daemen, L.L., Campbell, L.J., Simonov, A.Yu. and Kogan, V.G., *Phys.Rev.Lett.*, **70**, 2948, 1993.
7. Grishin, A.M., Martinovich, A.Yu., Yampol'skii, S.V., *Zh.Eksp.Teor.Fiz.*, **30**, 1930, 1990.
8. Ami, S. and Maki, K., *Progr.Theor.Phys.*, **53**, 1, 1975.
9. Fogel, N.Ya., Buchstab, E.I., Pokhila, A.S., Erenburg, A.I. and Langer, V., *Phys.Rev.B*, **53**, 71, 1996.



Pergamon

NanoStructured Materials, Vol. 12, pp. 413–416, 1999

Elsevier Science Ltd

© 1999 Acta Metallurgica Inc.

Printed in the USA. All rights reserved

0965-9773/99/\$—see front matter

PII S0965-9773(99)00147-6

## SYNTHESIS OF THIN MOLECULAR SIEVE FILMS

J. Hedlund and J. Sterte

Division of Chemical Technology

Luleå University of Technology, 971 87 Luleå, Sweden

**Abstract** *A method to synthesize thin films of various molecular sieves on a number of substrates employing pre-seeding has been developed. The substrate is modified to enable adsorption of seed crystals. Substrates with an originally negative surface charge are charge reversed by adsorption of cationic polymer molecules. Nobel metal substrates are first silanized to obtain a negative surface charge. Nano seed crystals are adsorbed on the modified substrates from a sol and induced to grow in a synthesis solution to form a dense film with controlled thickness. The versatility of the method may be of great value in the development of novel applications. Films have been tested in membrane and sensor applications with successful results. ©1999 Acta Metallurgica Inc.*

### INTRODUCTION

Zeolites are crystalline porous aluminosilicates belonging to the group of molecular sieves. About 100 zeolite structure types are known today [1]. The pores in zeolites are between ca 0.3 and 1 nm in size. The zeolite framework is a three dimensional tetrahedral network of oxygen ions with one  $\text{Si}^{4+}$  or  $\text{Al}^{3+}$  ion situated inside each oxygen tetrahedron. The amount of  $\text{Al}^{3+}$ -ions determines the framework charge which is balanced by non-framework cations. These cations are exchangeable and give the zeolite its ion-exchange capacity. Zeolites often have catalytic properties which can be modified by exchange of non framework cations or by incorporation of other cations than aluminum in the framework in the synthesis. Zeolite based membranes and sensors with well defined pores of molecular dimensions have the potential to exhibit novel characteristics. This paper summarizes selected work in the development of the seed film method for the synthesis of thin molecular sieve films. However, the method may be applicable to the synthesis of thin films of all types of materials and not restricted to molecular sieve films.

### EXPERIMENTAL

Details concerning the experimental procedures can be found elsewhere [2–6]. Colloidal seed crystals are synthesized and purified by centrifugation and redispersion to obtain a seed sol [7] with a solids content of 2.5% and a pH of 10. The substrate is rinsed in several steps prior to modification. Nobel metal substrates are silanized during 3h in a methanolic  $\gamma$ -

mercaptopropyl trimethoxysilane solution after rinsing. The silanized noble metal surface is hydrolyzed for 15h in a 0.1M HCl solution. Substrates such as silicon, quartz, alumina and silanized noble metal, are contacted with a dilute aqueous solution containing cationic polymer molecules (Berocell 6100, Eka Chemicals AB, Sweden) to obtain a positive surface charge, see Figure 1 (A). The modified substrates are immersed in a seed sol in order to adsorb seed crystals on the surfaces, see Figure 1 (B). The sequence polymer adsorption - seed adsorption can be repeated to increase the amount of adsorbed seed crystals. The seeded substrates are treated in a molecular sieve precursor solution at elevated temperature to induce growth of the seed crystals into dense films, see Figure 1 (C).

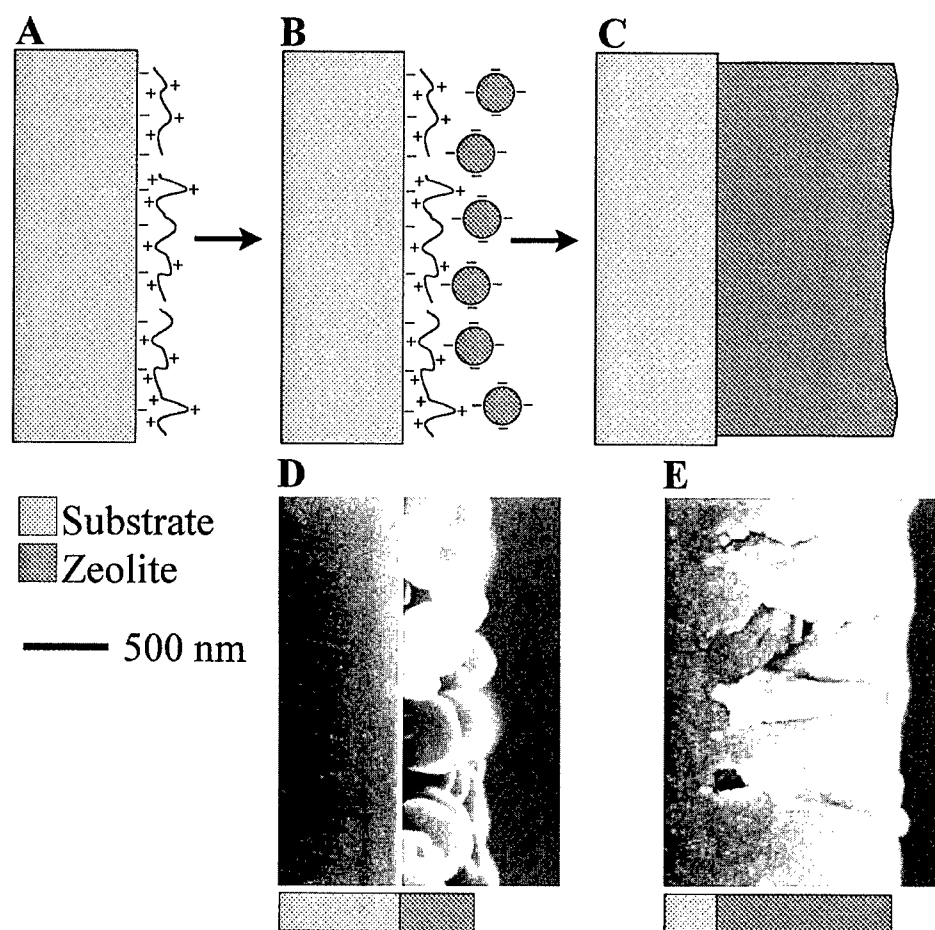


Figure 1. A schematic drawing of a modified substrate is shown in (A), a seeded substrate in (B) and the film formed after hydrothermal treatment in (C). Corresponding SEM photographs showing a side view of a monolayer of 350 nm silicalite-1 seeds on a silicon wafer is shown in (D) and a 1000 nm thick silicalite-1 film formed after hydrothermal treatment of the seeded substrate is shown in (E).

## RESULTS AND DISCUSSION

### *TPA-Silicalite-1 films on silicon wafers*

The seed film method was originally developed for the synthesis of thin TPA-silicalite-1 films on polished silicon wafers [2]. It was shown that the films consisted solely of silicalite-1 and that the film thickness increased linearly with synthesis time and the size of the seed crystals determined the starting point for the linear increase in film thickness. The films were shown to be continuous and the results were reproducible. Continuous films with thickness ranging from 100 to 650 nm were synthesized from wafers seeded with 51 nm silicalite-1 seeds, and films with thickness ranging from 300 to 800 nm were synthesized on wafers seeded with 149 nm seeds. TPA-silicalite-1 films have to be calcined to remove the organic template molecule and expose the pore system to render the zeolite useful. This may introduce cracks in the zeolite film which can be detected by SEM or by permeation experiments.

In a more recent work [3], the influence of seed size, amount of seeds and the film thickness on the preferred orientation in thin TPA-silicalite-1 films on silicon wafers was investigated with XRD and SEM, see Figure 1 (D) and (E). In thin films, most of the crystalline material is oriented with the b-axis perpendicular to the substrate surface. In thick films, most of the crystalline material is oriented with the a-axis perpendicular to the substrate surface. The change in preferred orientation with film thickness is faster when small seeds are used. The amount of adsorbed seeds has a larger influence on the preferred orientation when large seeds are used. A mechanism explaining these trends has been proposed. According to this model, the shape and orientation of the seed crystals and the growth rate of the crystal faces determine the orientation of the final film. The choice of size and coverage of seeds can thus be used to control the preferred orientation of the crystals in a film of given thickness within certain limitations.

The silicalite-1 films were studied by spectroscopic ellipsometry [8]. The film thickness as determined by ellipsometry was in accordance with SEM observations and calculated film thickness from Kr-adsorption data. The void fraction (0.32-0.33) in the zeolite film and sorption isotherms at room temperature for vapors of water, toluene, 1-propanol and hexane in nitrogen gas were determined. The adsorbate volumes at saturation and void fractions for the films were in accordance with other results determined on powders.

### *ZSM-5 films*

To circumvent the problems associated with calcination of as-synthesized films, *vide supra*, the seed film method was used to synthesize thin ZSM-5 films on quartz substrates in the absence of organic template molecules [4]. These films may be of great value for the development of zeolite based membranes since calcination is not necessary to open up the pore structure after synthesis. Films with a thickness of 500 nm were obtained by hydrothermal treatment of seeded substrates in a synthesis gel free from organic template molecules, i.e. TPA<sup>+</sup>. ZSM-5 films synthesized in the absence of organic template molecules on alumina membranes showed excellent permeation characteristics. High flux rates and large permselectivities calculated from single gas experiments were obtained.

### *Noble metal substrates*

Continuous films of silicalite-1 with thickness ranging from 100-400 nm were grown on gold substrates [5]. A 250 nm silicalite-1 film was grown on the gold electrode of a quartz crystal microbalance and sorption isotherms at room temperature for n-pentane, n-hexane and cyclohexane were calculated from recorded QCM-data [9].

### *Other zeolite types*

In addition to the MFI-type zeolites (silicalite-1 and ZSM-5), films of zeolite NA have been prepared using this approach [6]. Work is currently in progress aiming at the preparation of films of a number of other zeolites, such as zeolites Y and Beta.

## ACKNOWLEDGMENTS

The authors acknowledge the Swedish Research Council for Engineering Sciences (TFR) for financial support of this work.

## REFERENCES

1. Meier, W.M., and Olson, D.H., *Zeolites*, 1996, 17, 1.
2. Hedlund, J., Schoeman, B.J., and Sterte, J., *Progress in Zeolites and Microporous Materials* 1997, 105, 2203, Elsevier Science, Amsterdam.
3. Hedlund, J., Mintova, S., and Sterte, J. subm. to *Microporous and Mesoporous Materials*.
4. Mintova, S., Hedlund, J., Valtchev, V., Schoeman, B., and Sterte, J., *J Mater Chem*, 1997, 7, 2341.
5. Mintova, S., Valtchev, V., Engström, V., Schoeman, B., and Sterte, J., *Microporous Materials*, 1997, 11, 149.
6. Hedlund, J., Schoeman, B., and Sterte, J., *Chem Commun*, 1997, 1193
7. Schoeman, B.J., *Synthesis and Properties of Colloidal Zeolite*, 1994, Chalmers University of Technology, Göteborg.
8. Bjorklund, R., Hedlund, J., Sterte, J., and Arwin, H., *J Phys Chem B*, 1998, 102, 2245.
9. Mintova, S., Schoeman, B., Valtchev, V., Sterte, J., Mo, S., and Bein, T., *Advanced Materials*, 1997, 9, 585.





## NANOLAYERED CHALCOGENIDE GLASS STRUCTURES FOR OPTICAL RECORDING

A. Kikineshi, A. Mishak, V. Palyok, M. Shpiyak

Department of Solid State Electronics, Uzhgorod State University,  
Pidhirna str.46, Uzhgorod, 29400, Ukraine

*Abstract-Nanostructure processing offers new methods for tailoring light-sensitive chalcogenide glass layers and photophysical processes to promote optical recording in these materials. Cyclic vacuum thermal evaporation of initial glasses allows layered structures to be obtained with 8-20 nm compositional modulation period, ~1 nm roughness of interfaces and total thicknesses up to 1  $\mu\text{m}$ . It is shown that besides common features of thermal stability, optical properties in amorphous layers additional effects appear in nanostructures, connected with possible interdiffusion, stress and thermodynamical parameters change. These depend on the modulation period, type of combined materials and laser treatment or annealing conditions, influencing the resulting characteristics of the recording process.*

©1999 Acta Metallurgica Inc.

### INTRODUCTION

The well-known reversible effects of optical parameters change (optical transmission  $\Delta\tau$ , reflection  $\Delta R$ , refractivity  $\Delta n$ ) in  $\text{As}_2\text{S}_3$ ,  $\text{AsSe}$ -type chalcogenide amorphous semiconductor layers under the influence of bandgap illumination and thermal annealing are attractive both for the fundamental investigations of the disordered solids and for applications in holography, digital optical recording (1-3). It means that photodarkening or photobleaching, accompanied by phase modulation of the sensitive layer, as well as information readout and erasing, may be realized in a real time-scale. Besides optical recording the mentioned processes serve as important methods for investigations of structural transformations. The mechanisms of these effects are based on the short- or medium-range order (0.4-2.0 nm large clusters) transformations and depend on the glass composition, chemical bonding, technology conditions.

Irreversible transformations towards the more stable amorphous structure also occur in as-deposited films, and a photo-thermoinduced crystallization is possible in the proper compositions (2,3). Optical parameters and their changes depend on the given glass, amorphous layer composition and structure. The last were for a long time the main factors of tailoring recording parameters. But the artificial size restrictions in ultra-thin layers, nanoclusters formation also essentially influence thermodynamical, mechanical, electrical and optical properties of metals and semiconductors, even of amorphous ones (4,5). So it was to be expected that nanostructure processing influence the induced structural transformations. This paper deals with experiments on optical recording in amorphous nanolayered structures and with the analysis of possible structural changes, differences between homogeneous and modulated layers.

## EXPERIMENTAL

The nanolayered structures were prepared by conventional vacuum thermal evaporation of initial glasses (3,6) and cyclic deposition of 4-20 nm thick sub-layers onto smooth oxide glass, NaCl crystal or Si wafer substrata. Periodical structures were created from a-Se,  $\text{As}_2\text{S}_3$ , AsSe,  $\text{Se}_x\text{Te}_{1-x}$  and similar materials with an equal initial thickness of combined layer pairs. Optimum period was 12 nm ( 6 nm thick sub-layers). Usually in such structures the largest recording efficiency and quantum-size effects were obtained.

Periodicity was controlled by Small Angle X-Ray Diffraction (SAXRD) method. Few cross-sections of multilayers were investigated by Transmission Electron Microscopy (TEM). The comparison of SAXRD and TEM results with a surface geometry analysis made with Atomic Force Microscope (AFM) showed rather smooth interfaces and surfaces in as-deposited samples with roughness not exceeding 1 nm.

Optical transmission and reflection changes were measured usually at  $0.63 \mu\text{m}$  (He-Ne laser with output capacity density  $P=0.8 \text{ W/cm}^2$ ). Holographic gratings with a period  $\Lambda \approx 1 \mu\text{m}$  were recorded with the same laser. The change of the transmission or reflection coefficients, as well as the diffraction efficiency  $\eta$  of the recorded hologram that depends on  $\Delta\tau$ ,  $\Delta n$ , were taken as a measure of the induced structural changes. As far as the "barrier" layer ( $\text{As}_2\text{S}_3$  for example) with larger optical bandgap is more transparent at  $\lambda=0.63 \mu\text{m}$  and less sensitive than "well" layer (a-Se, AsSe), the last are investigated first of all in the structures. Samples were heated and/or annealed *in situ* during the optical measurements or treated in a separate heated chamber with normal atmosphere.

## RESULTS AND DISCUSSION

The simplest and the most convenient sensitivity test - the light-induced change of  $\tau$  during the exposition in comparison with initial  $\tau_0$  value - shows (see Fig.1) that the amplitude recording characteristics are similar in a homogeneous and nanostructured AsSe-containing layers, but differ in the  $\text{As}_2\text{S}_3/\text{a-Se}$  structure. Some sensitivity decrease (curves 1,2 in Fig.1) may be caused by the absorption decrease at  $0.63 \mu\text{m}$ , in accordance with a "blue" optical absorption edge shift due to the quantum confinement effects in such structures (6). The homogeneous layer, made of  $\text{AsS}_{1.5}\text{Se}_{0.5}$  solid solution is known as less sensitive in comparison with AsSe (3), and its parameters do not change after annealing at 400 K (Fig.1, curves 4, 4').

Small change in  $\tau/\tau_0$  dependence on laser exposition  $E$  after the same annealing of  $\text{As}_2\text{S}_3/\text{AsSe}$  structure is the sign of the increased stability, which concerns not only the AsSe sub-layer, but the whole periodically modulated layer. SAXRD measurements showed even some improvement of its structure after annealing. Apparently interdiffusion processes are not favored in this system. So the main mechanism of local medium range order transformation (2) is realised in this amorphous structure during illumination or annealing, similar to the thick layers. It is influenced by the presence of certain built-in stresses and by the softening temperature shift towards lower temperatures, which were established from the analysis of the temperature dependent  $\eta$  relaxation measurements in the recorded hologram (Fig.2). So, as far as the hologram is a periodical relief of  $\tau$ ,  $n$ ,  $R$  change in the layers' plane, and these parameters are

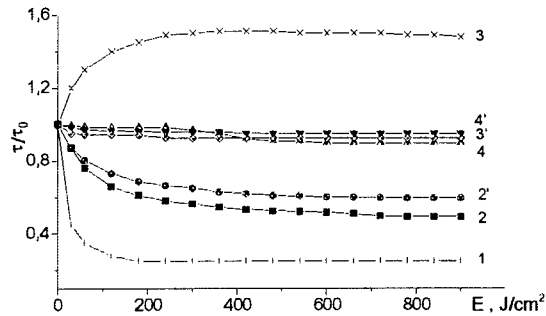


Fig.1. Optical transmission changes on laser exposition ( $\lambda=0.63 \mu\text{m}$ ) in as-deposited AsSe (1),  $\text{AsS}_{1.5}\text{Se}_{0.5}$  (4) homogeneous layers,  $\text{As}_2\text{S}_3/\text{AsSe}$  (2),  $\text{As}_2\text{S}_3/\text{a-Se}$  (3) multilayers at 293 K, and the same for the samples annealed at 400 K (2', 3', 4').

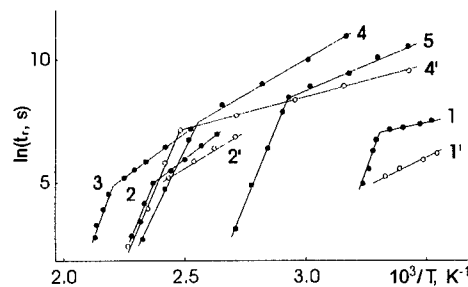


Fig.2. Temperature dependences of the hologram relief relaxation times  $t_r$  in as-deposited a-Se (1), AsSe (2),  $\text{As}_2\text{S}_3$  (3) and annealed a-Se (1'), AsSe (2') homogeneous layers or  $\text{AsS}_3/\text{AsSe}$  (4) and  $\text{As}_2\text{S}_3/\text{a-Se}$  (5) nanolayered structures. (4')- $\text{As}_2\text{S}_3/\text{AsSe}$  structure after annealing.

determined by the structure, density and stresses, thus we have a good experimental method for their investigations.

The break on the temperature dependence of the main relaxation time  $t_r$  (see Fig.2) corresponds to the glass softening temperature  $T_g$  (transition from  $\beta$  to  $\alpha$ -type relaxation in glasses (2)), which in turn is connected with the melting temperature of the same crystalline compound. So the shift of these breaks in  $\text{As}_2\text{S}_3/\text{a-Se}$  and  $\text{As}_2\text{S}_3/\text{AsSe}$  structures into different directions (up to + or - 20K, curves 1 and 4 in Fig.2) indicate different surface energy correlations (2,4) and tensions between adjacent layers. These influence the processes of optical recording by changing crystallization, diffusion conditions for the certain combined layers. Annealing of as-deposited layers causes larger structural relaxation in a-Se in comparison with AsSe (curves 1', 2', Fig.2), also indicating the different role of initial stress in the first recording process. This was proved also in the nanolayered structures, where the sensitivity decreases after annealing due to the structure relaxation or interdiffusion. In the case of  $\text{As}_2\text{S}_3/\text{a-Se}$  structure additional effects of interdiffusion influence the whole picture, including the hologram recording process.

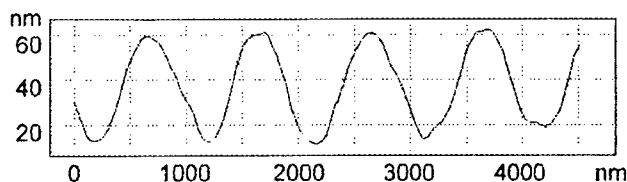


Fig. 3. Hologram surface relief profile in  $\text{As}_2\text{S}_3/\text{a-Se}$  multilayer obtained by AFM.

As-deposited structures possess photobleaching (curve 3 in Fig.1), but annealed ones behave similar to the homogeneous  $\text{AsS}_{1.5}\text{Se}_{0.5}$  solid solution layer (curves 3', 4, 4' in Fig.1). The recorded hologram diffraction efficiency increases essentially in comparison with single a-Se or even AsSe,  $\text{As}_2\text{S}_3/\text{AsSe}$  layers. This increase depends not only on the photobleaching, which causes better optical transmission of the hologram, but also on a well-pronounced surface relief formation (see Fig.3). This was almost not observable on homogeneous layers at our conditions. So the interdiffusion process is supposed to be a reason of this additional component in optical recording. This influences also the transmission changes observed after annealing (Fig.1, curves 3, 3'). Of course, the mechanism of such deep relief formation must take into account besides the known small (0.1-0.5 %) effects of volume expansion and light-stimulated viscosity changes (1), also the local volume and density change due to the intermixing. Similar effects of interdiffusion were observed in nanolayered structures, made of Te-containing glasses, under intensive laser irradiation.

### CONCLUSIONS

In conclusion, nanolayered structures made of light-sensitive chalcogenide glasses possess additional properties which are effective for tailoring this type of optical recording media. Besides basic light-sensitivity, diffusion parameters, thermodynamical and optical characteristics must be taken into account when selecting suitable components for such materials.

### ACKNOWLEDGMENTS

The authors would like to thank Prof. D.L. Beke and Dr. I. Szabo from University of Debrecen for providing AFM measurements and fruitful discussions.

### REFERENCES

1. Tanaka Ke., *Rev.Sol.St.Sci.*, 1990, 4, 641.
2. Kikineshi A., Mishak A., in *Phys. and Appl. of Non-Cryst. Semiconductors in Optoelectronics*, NATO ASI Ser., 3. High Tech., 1997, 36, 249.
3. Shvarts K.K., *Physics of optical recording in dielectrics and semiconductors*, Zinatne, Riga (in Russian), 1986, 230.
4. Komnik Yu. F., *Physics of metal films*, Atomizdat, Moscow (in Russian), 1979, 260.
5. Dohler G.H., *Optical Engineering*, 1986, 25, 211.
6. Mishak A., Kikineshi A., Fedor V., Barna P.B., Kovacs I., *Proc.SPIE*, 1997, 3055, 25.



## CHARACTERIZATION OF SELF-ASSEMBLED ALCOHOLS COATINGS ON AMORPHOUS IRON

G. Kataby<sup>a</sup>, R. Prozorov<sup>b</sup>, and A. Gedanken<sup>a</sup>.

a) Department of Chemistry, Bar-Ilan University, Ramat-Gan, 52900, Israel.

b) Department of Physics, Bar-Ilan University, Ramat-Gan, 52900, Israel.

**Abstract**---Self-assembled coatings of long chain alcohols on nanoparticles of amorphous iron were formed. FTIR, and XPS measurements demonstrated the formation of chemical bonds between the substrate and the alcohols. The thermal stability of these coatings was investigated by using thermogravimetric analysis (TGA) and differential scanning calorimetry (DSC). The superparamagnetic behavior of the coated nanoparticles was detected by magnetization measurements. ©1999 Acta Metallurgica Inc.

### INTRODUCTION

The thiol chromophore, as a surfactant for metals and metal oxides, has been studied in great detail in the past few years. It has been used in the coating of smooth surfaces and particles, using Langmuir-Blodgett and Self-Assembled methods (1). Alcohols have not been used so frequently for coating neither particles nor flat surfaces.

Amorphous iron and amorphous iron oxide (2) nanoparticles were used as substrates for coating, using self-assembled technique, with different surfactants, such as: sodium dodecyl sulfate (SDS), octadecyl-trichlorosilane (OTS) and long-chain thiols (3-6). In this work, the synthesis, and characterization of 1-octanol, 1-dodecanol, and 1-tridecanol coatings on amorphous iron nanoparticles are described. These coatings have been prepared by the self-assembled technique, at room temperature. FTIR, XPS, TGA, DSC, and magnetic measurements were carried out to characterize these coated particles.

### EXPERIMENTAL SECTION

Amorphous iron nanoparticles were prepared according to the procedure outlined by Suslick (7). The process of coating was similar to that described for the thiols (5).

The TGA analysis was done using a Mettler TG-50, and DSC measurements were done in a Mettler DSC-30. The room-temperature FTIR spectra were recorded on a Nicolet (Impact 410) spectrometer. The magnetization measurements were performed at room temperature using Oxford Instrument vibrating sample magnetometer (VSM). X-ray Photoelectron Spectroscopy measurements were carried out using a 5600 Multi-technique System (PHI, USA). The samples were irradiated with an Al K $\alpha$  monochromated source (1486.6 eV), and the outgoing electrons were analyzed by Spherical Capacitor Analyzer employing a pass energy of 11.75 eV.

## RESULTS AND DISCUSSION

The FTIR spectra of 1-tridecanol and the 1-tridecanol-coated amorphous iron particles in the  $2700\text{--}3600\text{ cm}^{-1}$  range are depicted in Fig. 1. The absorption peaks at  $2848.2$  and  $2918.6\text{ cm}^{-1}$  correspond to the  $\text{--CH}_2\text{--}$  symmetry and antisymmetric stretching bands of the coated iron particles. FTIR absorption frequencies and widths of  $\text{--CH}_2\text{--}$  band are used for evaluation of the degree of the different coatings (8). The frequencies of the  $\text{--CH}_2\text{--}$  stretching bands are  $2921.5$ ,  $2919.8$ ,  $2918.6\text{ cm}^{-1}$  for 1-octanol-, 1-dodecanol-, and 1-tridecanol-coated amorphous iron, respectively. This difference was interpreted as a result of a more liquidlike, disordered environment of the methylene units for the shorter chain length coated surfactants. In addition to the frequency shift, distinct bandwidths of  $25.6$ ,  $22$ ,  $21.4\text{ cm}^{-1}$  were obtained for the coatings prepared from 1-octanol, 1-dodecanol and 1-tridecanol, respectively. On the basis of these results, 1-octanol is the least organized coating, due to the more restricted interaction between the chains. The most important evidence for the formation of a chemical bond between the alcohol and the iron is found in the O–H stretching mode region,  $3000\text{--}3500\text{ cm}^{-1}$ . The O–H stretching vibration of the 1-tridecanol at  $3288\text{ cm}^{-1}$  disappears completely.

The XPS spectra in Fig. 2 (a) are of the Fe (2p) photoelectrons (9) of bare amorphous iron and the alcohol-coated iron particles. The spectrum of the bare iron is much broader than the analogous spectrum of the coated particles, due to partial oxidation of the iron in the uncoated particles. The XPS of the crystalline iron should exhibit a peak at  $707\text{ eV}$ , and  $\text{Fe}_2\text{O}_3$  - at  $710.9\text{ eV}$ . The observed shoulder at  $707\text{ eV}$  is due to zerovalent iron. It disappears for the 1-tridecanol-coated iron mostly due to bonding to the 1-tridecanol. The peak detected at  $719\text{ eV}$  in the bare particles, was assigned to  $\text{Fe}_2\text{O}_3$ , undergoes a red shift to  $716\text{ eV}$  upon a coating by the 1-tridecanol. We conclude that the oxidized surface layer and the zerovalent iron atoms that are found on the surface or close to the surface, are both bonding the 1-tridecanol molecules. In Fig. 2 (b) we present the O(1s) XPS spectra of amorphous iron and 1-tridecanol-coated iron nanoparticles (9). The spectra show that the most intense peak,

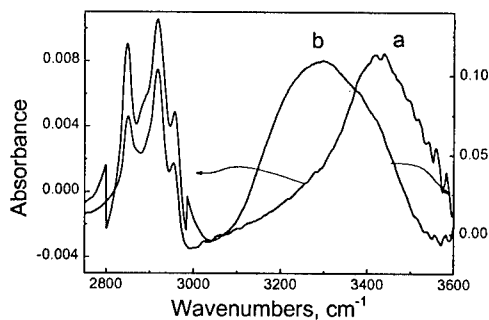


Figure 1. FT-IR spectra of (a) pure 1-tridecanol, (b) coated amorphous iron.

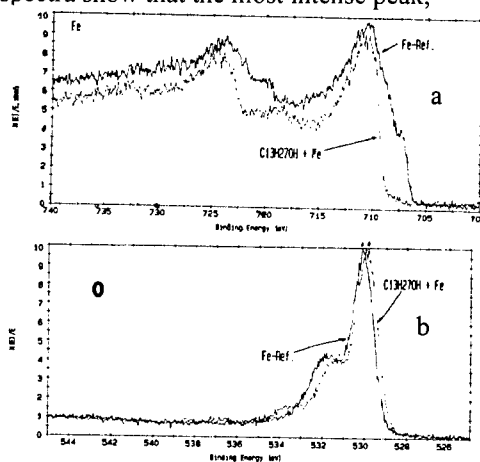


Figure 2. (a) Fe(2p) and (b) O(1s) XPS spectra of amorphous iron, noncoated and coated

appearing at 530.1 eV in the bare iron, undergoes a slight red shift to 529.95 eV upon a coating with tridecanol. This fits very well the reported binding energies for  $\text{Fe}_2\text{O}_3$  (530.2 eV) and for  $\text{Fe-O}^*(-\text{O-H})$  (530.1 eV). A red shift of 0.1 eV is explained by formation of the  $\text{Fe-O}(-\text{O})$  bonds. However, it is also consistent with a surfaces composed only of  $\text{Fe-O-C-C}\dots$  bonds, as the binding energies of the  $\text{Fe}_2\text{O}_3$  almost coincide with those of the  $\text{Fe-O}(-\text{O})$  moiety. This explanation would require the elimination of a water molecule when the alcohol forms a bond with the oxidized iron oxide ( $\text{Fe}_2\text{O}_3$ ) on the surface and the elimination of a hydrogen atom when it interacts with the bare iron atom. The IR spectrum of alcohol-coated iron particles shows two relatively strong bands at 1045 and 1093  $\text{cm}^{-1}$ . The IR spectrum of  $\text{Fe-O}(\text{O-H})$  reveals a broad adsorption feature peaked at 1120  $\text{cm}^{-1}$ . This is an unassigned band that we attribute to the O-O stretching mode. We conclude that the alcohols are bonded to the surface of the amorphous iron nanoparticles through two channels. The first bonding is through the  $\text{Fe-O-O}$  bonds, which are due to the oxidized iron layer on the surface, and the second (predominant bonding) is through direct  $\text{Fe-O-C}$  bonds resulting from the zero valence iron atoms on the surface.

Fig. 3(a) illustrates TGA behavior of 1-tridecanol-coated amorphous iron. The slope in the spectrum changes twice, the first one is in the temperature range of 300-400  $^{\circ}\text{C}$ , and the second is in the range of 400-550  $^{\circ}\text{C}$ . The overall weight-loss in 300-550  $^{\circ}\text{C}$  temperature range is 14%, 13.9% and 10.3% for 1-octanol-, 1-dodecanol-, and 1-tridecanol-coated amorphous iron, respectively. It can be noticed that the weight loss decreased as the chain length is longer. Fig. 3 (b) shows the DSC study of 1-tridecanol-coated amorphous iron. The strongest feature in the spectrum is the exothermic peak at 331.9  $^{\circ}\text{C}$ . This is related to the transition of the amorphous iron nanoparticles to the crystalline (2(a),7) phase. The second feature is an endothermic peak centered at 375  $^{\circ}\text{C}$ . This peak corresponds very well with the TGA weight-loss in the temperature range 300-400  $^{\circ}\text{C}$ , and it is related to the desorption of the coated molecules from the surface.

The results of magnetization loop of the 1-octanol-, 1-dodecanol-, -tridecanol-coated amorphous iron particles are presented in Fig. 4. Saturation is not detected for any of the samples even at 15 KG. Similarly, we do not observe hysteresis for any of the three samples.

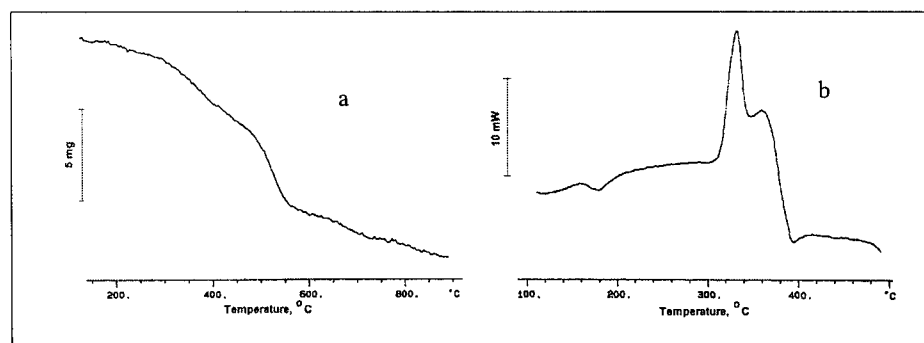


Figure 3 (a) TGA spectrum (b) DSC spectrum of 1-octanol-coated amorphous iron

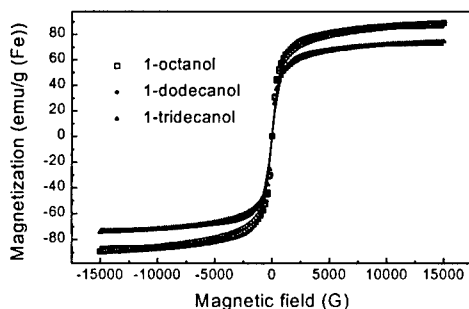


Figure 4. Magnetization loops for alcohol-coated amorphous iron

This behavior is typical for superparamagnetic (10) species. The loops in the figure demonstrate shapes characteristic for paramagnetic particles and indicate the size of the agglomerated particles to be 10-20 Å. The dependence of the magnetization values on the length of the alkyl chain reveals the tridecanol-coated iron particles to have the largest magnetization.

### SUMMARY

We have demonstrated that alcohols can form a coating on amorphous iron nanoparticles through the formation of chemical bonds.

### REFERENCES

1. For review, see: Ulman, A. *Chem. Rev.* 1996, 96, 1533.
2. a) Cao, X.; Koltypin, Y.; Kataby, G.; Prozorov, R. and Gedanken, A. *J. Mater. Res.*, 1995, 10, 2952; b) Cao, X.; Koltypin, Y.; Prozorov, R.; Kataby, G.; Felner, I. and Gedanken, A. *J. Mater. Res.*, 1997, 12, 402.
3. Rozenfeld, O.; Koltypin, Y.; Bamnolker, H.; Margel, S. and Gedanken, A. *Langmuir*, 1994, 10, 627.
4. Kataby, G.; Koltypin, Y.; Cao, X. and Gedanken, A. *J. Cryst. Growth*, 1996, 166, 760.
5. Kataby, G.; Prozorov, T.; Koltypin, Y.; Sucek, C. N.; Ulman, A. and Gedanken, A. *Langmuir*, 1997, 13, 6151.
6. Prozorov, T.; Kataby, G.; Prozorov, R. and Gedanken, A. *Thin Solid Films*, 1998, *submitted*.
7. Suslick, K. S.; Choe, S.-B.; Cicholas, A. A. and Grinstaff, M. W., *Nature*, 1991, 353, 414.
8. Brandriss, S. and Margel, S. *Langmuir*, 1993, 9, 1232.
9. Abdel-Samad, H. and Watson, P. R. *Appl. Surf. Sci.*, 1997, 108, 371.
10. Ishikawa, T.; Cai, W. Y. and Kador, K. *J. Chem. Soc., Faraday Trans.*, 1992, 88, 1173.





## SURFACE MORPHOLOGY AND COMPOSITIONAL VARIATIONS IN MOLECULAR BEAM EPITAXY GROWN $\text{GaN}_x\text{As}_{1-x}$ ALLOYS

O. Zsebök, J. V. Thordson, L. Ilver and T. G. Andersson

Applied Semiconductor Physics, Department of Physics and Engineering Physics,  
Chalmers University of Technology and Göteborg University, S-412 96 Göteborg, Sweden

**Abstract** --  $\text{GaN}_x\text{As}_{1-x}$ -layers were grown by molecular beam epitaxy with a nitrogen concentration ranging from low N-doping concentration in GaAs up to GaN. The average nitrogen concentration was assessed by secondary ion mass spectrometry and energy dispersive X-ray spectrometry. X-ray diffraction measurements provided two peaks from the grown layer, one arising from a lattice constant close to the GaAs(004) and one close to the GaN(004) diffraction, due to phase-separation. Scanning electron microscopy indicated a rough surface structure with improved smoothing for low and high nitrogen concentrations. Crystallite features were observed on the rough surfaces and characterised by Auger-electron spectroscopy. ©1999 Acta Metallurgica Inc.

### INTRODUCTION

The  $\text{GaN}_x\text{As}_{1-x}$  system exhibits a non-linear dependence of the band gap between GaAs and GaN, 1.42 - 3.45 eV, and is supposed to be a semi-metal for  $0.10 < x < 0.85$  (1). Scanning electron microscopy (SEM) studies (2,3) of  $\text{GaN}_x\text{As}_{1-x}$  revealed a rough surface, contrary to the smoother GaN, and transmission electron microscopy (TEM) exhibited presence of columnar grains (3). According to Qui *et al.* (4) the nitrogen-to-arsenic ratio is the crucial parameter to the layer quality. They constructed a phase diagram suggesting that as much as 10% nitrogen could be obtained without a phase-separation between GaAs and GaN.

In this work we report studies of growth and characterisation on a series of  $\text{GaN}_x\text{As}_{1-x}$  layers on GaAs(001) substrates, where the nitrogen content was increased from low N-doping of GaAs,  $10^{18}$  -  $10^{19}$  cm<sup>-2</sup>, up to GaN. The average composition,  $x_{\text{avg}}$ , of the structures was determined by secondary ion-mass spectrometry (SIMS). X-ray diffraction (XRD) provided two phases, GaAs(N) and GaN(As). High-resolution SEM studies revealed crystalline features with significant contrast differences.

### EXPERIMENTAL

The layers were grown with a solid source Varian GEN II Modular MBE system on indium-free mounted semi-insulating GaAs substrates. The active nitrogen was provided by a liquid-nitrogen cooled Oxford Applied Research CARS25 RF activated plasma source.

Three categories of  $\text{GaN}_x\text{As}_{1-x}$  structures were studied. First, GaAs:N-layers with low concentrations of nitrogen doping. Second, GaAs(N) layers with 1 - 30% nitrogen, and finally GaN(As)-layers, with arsenic concentrations below 5%. For growth of layers with  $x_{\text{avg}} \leq 0.3$ , a 1  $\mu\text{m/h}$  GaAs growth was established at a substrate temperature of 580°C. The details of the growth are presented elsewhere (5).

Average composition and structure were studied by SIMS and double crystal X-ray diffraction, respectively. High-resolution secondary electron (SE) images were taken by a JEOL JSM-6301F scanning microscope to reveal crystalline features and surface roughness. To characterise the micrometer sized features, energy-dispersive X-ray spectrometry (EDX) was performed, using a CamScan S4-80DV scanning electron microscope equipped with a LINK eXL EDX analysis system, applying 20 keV acceleration voltage with a beam current of 200  $\mu$ A. The provided analysis spot size was  $\sim 1$   $\mu$ m. For more accurate compositional characterisation of the features, Auger-electron spectroscopy (AES) was performed using a Perkin-Elmer Physical Electronics PHI 590 equipment. An electron accelerating voltage of 5 keV with 5 nA beam current was used to provide an analysis spot size of less than 500 nm. The composition was determined through the As/Ga and N/Ga ratios.

### RESULTS AND DISCUSSION

In Fig. 1 the XRD spectrum from a  $\text{GaN}_x\text{As}_{1-x}$  layer with an average nitrogen composition of  $\sim 20\%$  is shown. There are two evident features, one peak is very close to the GaAs peak and there is another rather broad peak at  $\sim 43^\circ$ , which is ascribed to the (004) zinc blende GaN. The two  $\text{GaN}_x\text{As}_{1-x}$ -related peaks are highlighted in the insets. The average nitrogen composition derived from the SIMS results is one order of magnitude higher than the value given by the XRD, indicating the formation of different phases. Therefore we believe that only  $\sim 10\%$  of the nitrogen is incorporated as real  $\text{GaN}_x\text{As}_{1-x}$ . In the left inset is shown that the GaAs(N) signal is quite intense at low nitrogen compositions (representing incorporated nitrogen) but with increasing  $x_{\text{avg}}$ -values it becomes fainter, and at compositions close or equal to 1 it is extinct. According to the other inset for the GaN-feature, from the samples with the lowest nitrogen content there is GaN-diffraction only from samples with nitrogen composition above the solubility level in GaAs.

In SEM studies of the surfaces we found that the surface of low N-doped GaAs was smooth. In the lower nitrogen composition range,  $0.05 < x_{\text{avg}} < 0.2$  (as determined by SIMS

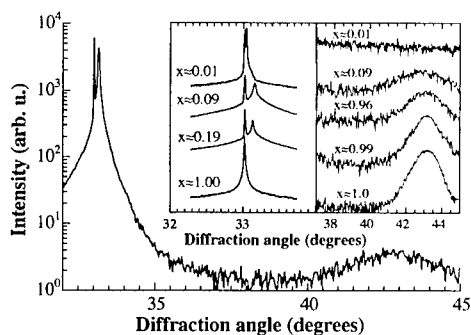


Figure 1. The XRD spectrum for a  $\text{GaN}_{0.2}\text{As}_{0.8}$  sample where both a GaAs(004) - ( $33^\circ$ ) and a GaN(004) peak ( $43^\circ$ ) from the layer can be seen. The insets show the corresponding peaks for different average nitrogen concentrations.

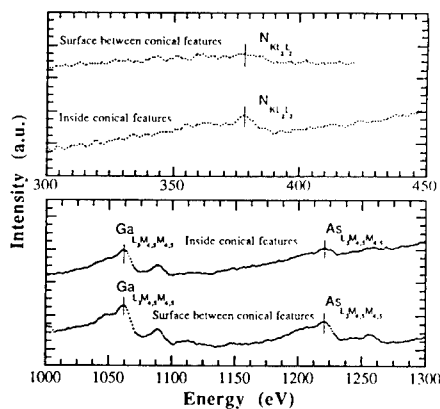


Figure 2. AES point analysis on a  $\text{GaN}_{0.1}\text{As}_{0.9}$  sample. The detected N (upper graph), Ga and As (lower graph) are shown for surface features and areas between them.

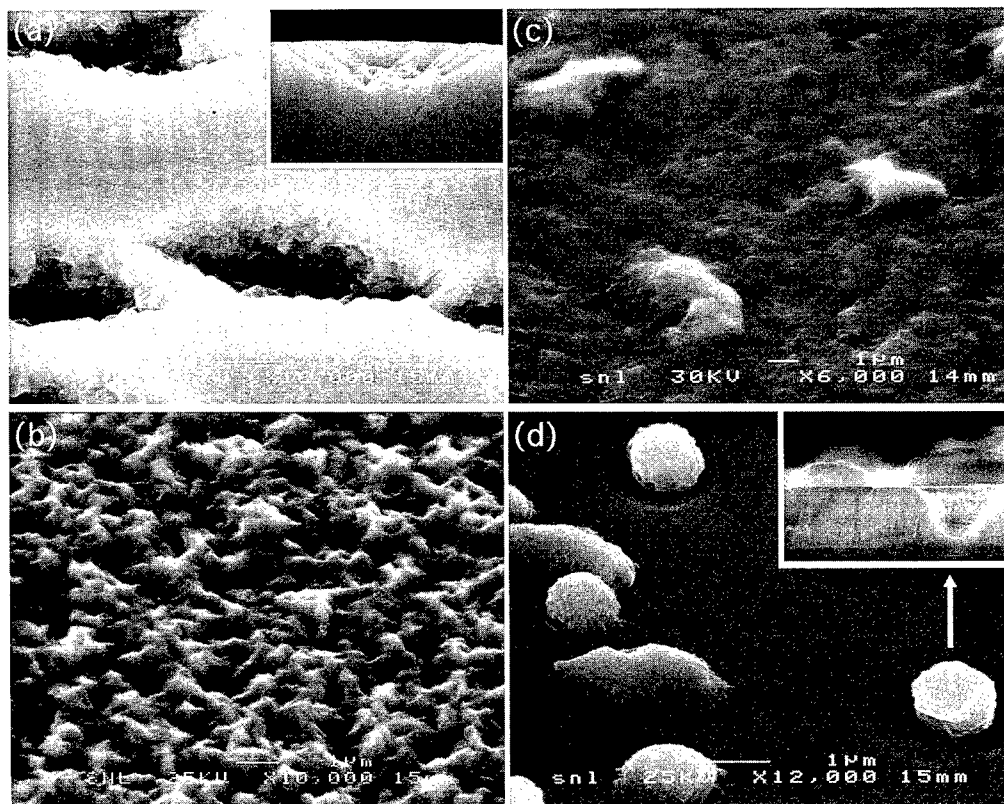


Figure 3. High-resolution SEM images. In (a) is shown a layer with low average nitrogen composition ( $x_{\text{avg}} \approx 0.1$ ) having a smooth surface with conical holes (inset) with crystallites on the walls. In (b) the very rough morphology of  $\text{GaN}_x\text{As}_{1-x}$  ( $x_{\text{avg}} \approx 0.3$ ) is shown. In (c) for high nitrogen content ( $x_{\text{avg}} \approx 0.95$ ) the surface smoothness is improved, but prolonged features with higher nitrogen content appear. Finally, in image (d) a  $\text{GaN}(\text{As})$  surface is shown with 0.5% As. The approximately  $1 \mu\text{m}$  sized round (arising from holes according to the layer cross-section inset) or prolonged features, respectively, are discussed in the text.

and EDX), a homogeneous distribution of elliptically shaped hollows with a diameter of 3-4  $\mu\text{m}$  were observed, Fig. 3a. The surface between the features was quite smooth. As shown in the inset of Fig 3a, the cross-section of those features had a conical shape, originating at the substrate interface. The EDX measurements were made at three different spots: at the flat surface, at the edge and in the middle of the defect, indicating that the arsenic content decreases by a factor of two from the flat surface to the bottom of the feature, where it was  $\sim 0.37$ . Based upon the micrometer size interaction volume of the characteristic X-ray generation and the narrowing shape of the hole, it is reasonable to assume that not all the characteristic X-rays originate from the conical volume of the hole. Consequently, the actual nitrogen content (assumed to be complementary to the arsenic) is higher than the detected one. The detected Auger intensities for As and the complementary N from the surface regions are seen in Fig. 2. It shows a definite arsenic-reduced content in the holes at  $\sim 50\%$ , compared

to the ~92% at surface parts. The intensity of the nitrogen peak on the surface was almost negligible compared to the the conical defect. However, the detected relative nitrogen concentration by AES was probably lower than the real value, due to a slight drift of the electron beam spot from the centre of the hole. Moreover, a significant arsenic cover-layer was present, which could only be partially removed due to shading effects within the conical features (by Ar<sup>+</sup> ion beam with 1 keV energy). Both EDX and AES have clearly indicated that the defects include large amount of accumulated nitrogen. Our interpretation is that GaN nano-crystallites are formed on the walls of the conical features by the excess nitrogen, which is not incorporated into the epitaxial layer, as shown in Fig. 3a.

Samples with nitrogen composition  $0.2 < x_{\text{avg}} < 0.4$ , representing the highest degree of mixing, gave the worst surface morphology with a typically 1  $\mu\text{m}$  surface roughness due to crystallite features, e.g. crystallites separated into two phases, in Fig. 3b.

With increasing N-content,  $x_{\text{avg}} > 0.95$ , the surface became smoother. Homogeneously distributed features with a random shape were observed, as seen in Fig. 3c. Both EDX and AES clearly indicated ~10% more nitrogen within these features as compared to the free surface.

In Fig. 3d, the surface roughness has decreased below 100 nm for  $x_{\text{avg}} \approx 0.995$ . Two types of features were seen, one having a prolonged shape, slightly similar to the features shown in Fig. 3c. The other type was rather spherical in shape, localised in a rounded ~1  $\mu\text{m}$  diameter crater originating at the layer-substrate interface, as shown on the cross-section image of the inset in Fig. 3d. The spherical features have higher brightness, meaning a larger secondary electron yield and consequently a different composition compared to the prolonged features. From the less accurate (due to its relatively large interaction volume) EDX data we conclude that there is an accumulation of arsenic in the prolonged features. The AES characterisation clearly indicated an arsenic accumulation in the prolonged features, up to ~6% from the initial average of 0.5%, determined by SIMS. The rounded features show the lowest amount of incorporated arsenic, indicating a probable formation of pure GaN.

### SUMMARY

Thin epitaxial layers of  $\text{GaN}_x\text{As}_{1-x}$  were grown on GaAs(001) substrates by solid source MBE and RF activated plasma source. The average nitrogen composition varied from low nitrogen doping concentration in GaAs up to GaN. Two diffraction peaks in XRD, one close to the GaAs(004) and one close to the GaN(004) position, gave evidence of phase separation. At low nitrogen composition, we found conical features in the samples by SEM. GaN nano-crystallites, accumulated on the walls of these features, were characterised by EDX and AES. At high nitrogen concentrations, spherical GaN particles were formed on the surface, while arsenic accumulation was detected in prolonged surface features. Samples with the highest degree of mixing gave the highest surface roughness.

### REFERENCES

1. Sakai, S., Ueta Y. and Terauchi, Y., *Jpn. Journal of Applied. Physics*, 4413, **32**, 1993.
2. Jenkins, L. C., Cheng, T. S., Foxon C. T., Hooper, S. E., Orton, J. W., Novikov, S. V. and Tret'yakov V. V., *J. of Vacuum Science and Technology B*, 1585, **13**, 1995.
3. Xin, Y., Brown, P. D, Dunin-Borkowski R. E., Humphreys, C. J., Cheng, T. S. and Foxon, C. T., *Journal of Crystal Growth*, 321, **171**, 1996.
4. Qiu, Y., Nikishin, A., Temkin, H., Faleev, N. N. and Kudriatsev, Yu. A., *Applied Physics Letters*, 3242, **70**, 1997.
5. Thordson, J. V., Zsebök, O., Södervall, U. and Andersson, T. G., *MRS Internet Journal of Nitride Semiconductor Research*, 8, **2**, 1997.



Pergamon

NanoStructured Materials, Vol. 12, pp. 429–432, 1999

Elsevier Science Ltd

© 1999 Acta Metallurgica Inc.

Printed in the USA. All rights reserved

0965-9773/99/\$—see front matter

PII S0965-9773(99)00151-8

## NANOSTRUCTURED MODEL BIOMATERIAL SURFACES PREPARED BY COLLOIDAL LITHOGRAPHY

P. Hanarp, D. Sutherland, J. Gold and B. Kasemo

Department of Applied Physics

Chalmers University of Technology, S-412 96 Göteborg, Sweden

**Abstract --** Adsorption of 110 nm negatively charged polystyrene particles on positively charged titanium surfaces was studied for the purpose of making surfaces with controlled nanotopography. Surfaces with 9–26 % saturation coverages of evenly spaced particles were produced by varying the salt concentration in the particle solution (0.01–1 mM NaCl). This is a quick and relatively simple method to make uniform nanostructures over large surface areas ( $\sim\text{cm}^2$ ). The produced surfaces are used for in vitro cell studies of how sub-micrometre topography influences cell adhesion and function. ©1999 Acta Metallurgica Inc.

### INTRODUCTION

Cells adhering to biomaterial surfaces are influenced by both surface structure and chemistry (1). Very little is known about cell behaviour on surfaces with nanometre sized features. To address this issue, we have used colloidal lithography (2) to produce surfaces with well-controlled nanotopography. With this method we can produce large nanostructured surface areas ( $\sim\text{cm}^2$ ) suitable for cell culture studies.

### MATERIALS AND METHODS

Surfaces of single crystal silicon wafers, pre-coated with 20 nm of thermally evaporated titanium, were treated with aluminium chloride hydroxide (1–5 % water solutions diluted by mass) for 30 s and then rinsed in milli-Q water (initial resistivity 18 M $\Omega$  cm). This gives a net positive charge at neutral pH. Then the surfaces were carefully immersed into dilute aqueous solutions of polystyrene particles (particle volume fraction  $\phi=10^{-3}$ , diameter 110 nm  $\pm$  5 nm, White-Sulphate Latex, IDC Portland, OR), and the negatively charged particles adsorbed onto the positively charged surfaces randomly by electrostatic interactions. The adsorption process was interrupted after controlled periods of time when the samples were withdrawn from the particle solution, rinsed under the tap with Milli-Q water, and blown dry with N<sub>2</sub>-gas. Particle adsorption is believed to be essentially irreversible (3), and particles remain attached during rinsing and drying. A submonolayer of particles was obtained with coverage controlled either by salt concentration (0.01–10 mM NaCl) in the colloidal solution for equilibrium adsorptions

(saturation), or particle concentration and adsorption time in interrupted (non-equilibrium) adsorptions. Scanning electron microscopy (SEM) and image analysis software (NIH image) were used to characterise the particle coverage and distribution. The kinetics of the adsorption system was investigated with a quartz crystal microbalance (QCM) (4). To produce chemically homogenous surfaces intended for cell culture studies, a thin film of titanium was evaporated on top of the particle films.

## RESULTS AND DISCUSSION

### *Adsorption Kinetics and Surface Saturation*

QCM measurements (not presented here) of the adsorption kinetics from particle solutions with no added salt showed that the initial adsorption rate was fast, with half of the saturation coverage being reached within 2 s. Subsequently the adsorption rate decreased as a result of exclusion of surface area by already adsorbed particles. Saturation coverage was reached in approximately 15 s after which time there was no significant change in the amount of adsorbed particles. When salt was added to the particle solution the time to saturation adsorption increased. This results from both a reduced particle diffusion rate at high salt concentration (3) and an increased number of adsorbed particles at saturation. For 1 mM NaCl the time to saturation was of the order of 30 min.

### *Saturation Coverage*

The coverage at saturation varies with salt concentration. This is clearly seen in figure 1a, which shows SEM images of particle films that were prepared with different NaCl concentrations with an adsorption time of 30 min (2 h for 10 mM NaCl). The coverage changes from 9 % for 0.01 mM NaCl to 38 % for 10 mM NaCl. The increase in coverage with salt concentration can be explained within the classical DLVO theory in terms of screening of the electrostatic repulsion between particles. An increased salt concentration gives a shorter Debye length (the characteristic decay length of the electrostatic repulsion,  $\kappa^{-1} \propto [\text{salt}]^{-1/2}$ ) so that particles can adsorb closer together, and the saturation coverage is increased.

The adsorbed layers at low salt concentrations (0.01-1 mM) are characterised by evenly spaced, isolated particles. This is clearly not the case for 10 mM NaCl with coverage 38 %, where the particles are 2D aggregated in small groups of 3-10 particles. We believe that this aggregation at high coverages takes place during drying of the samples, when strong capillary forces pull the closely spaced particles together (3). At lower coverages the particles are presumably too far apart for this to happen. As a rule of thumb, dried layers of particles are seen to aggregate for coverages higher than approximately 30 %.

The saturation coverage,  $\theta$ , dependence on the normalised Debye length  $1/\kappa a$  is shown in figure 1b ( $a$  is particle radius). The coverage increases nearly linearly with  $\kappa a$  (for low coverages, here  $\theta$  between 9 and 26 %), as predicted by simulations using the soft-sphere random sequential adsorption (RSA) model (5).

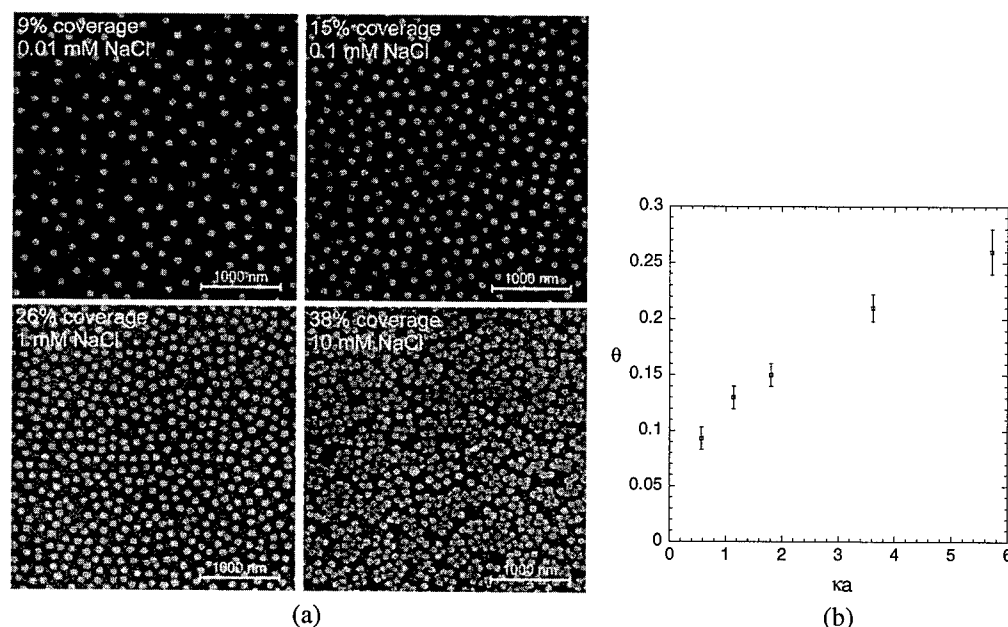


Figure 1. a) SEM images of saturation particle films prepared with different NaCl concentrations. b) Saturation coverage,  $\theta$ , vs. the screening parameter,  $\kappa a$ .

### Structure and Ordering of Particles

Figure 2a shows radial distribution functions ( $g(r)$ =concentration of particle centres at a distance  $r$  from one particle centre normalised to the average surface concentration) for the NaCl concentrations 0.01, 0.1 and 1 mM (coverages 9, 15 and 26 %). The average distance between neighbouring particles is given by the primary peak position. As the salt concentration is increased, the peak position is shifted so that the particles are closer together. The experimental radial distribution functions are in good qualitative agreement with theoretical soft-sphere RSA distributions (5).

The ordering of particles and maximum surface coverage are controlled primarily by electrostatic repulsion at low salt concentrations and by steric hard-sphere interactions at high salt concentrations (when the Debye length is small compared to the size of the particles). Figure 2b shows the average surface-to-surface interparticle distance,  $\bar{D}$ , compared to twice the Debye length. As the salt concentration is increased, hard-sphere interactions become more important, which is why  $2\kappa^{-1}$  falls off faster relative to  $\bar{D}$ .

### CONCLUSIONS

Adsorption of 110 nm polystyrene particles on titanium has been used to produce surfaces with controlled nanotopography. By varying the salt concentration in the particle solution (0.01-1 mM NaCl), we have made surfaces with 9-26 % saturation coverage of evenly

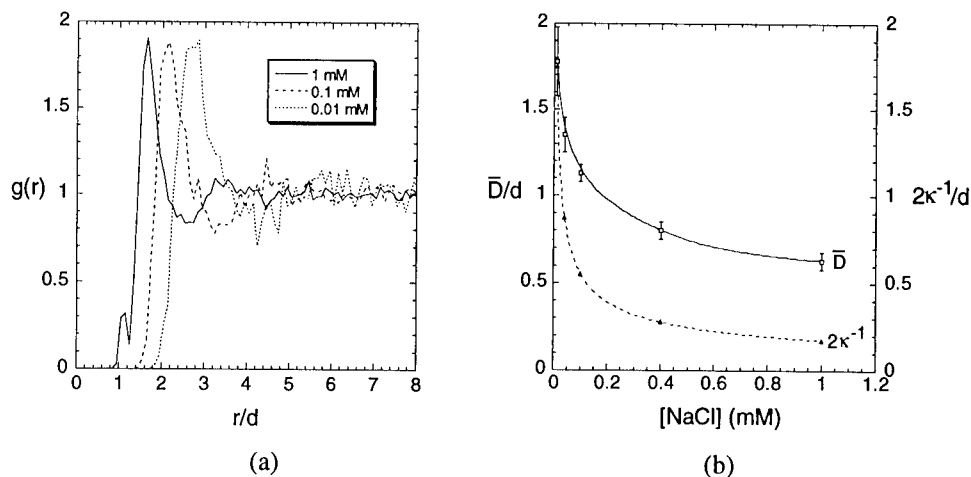


Figure 2. a) Radial distribution functions,  $g(r)$ , for different NaCl concentrations. b) Average surface-to-surface interparticle spacing between neighbouring particles,  $\bar{D}$ , compared to twice the Debye length,  $2\kappa^{-1}$ , for varying NaCl concentration. ( $d$  is the particle diameter)

spaced particles, with a high degree of short-range ordering. The coverage and structure of the particle films were in good qualitative agreement with the soft sphere random sequential adsorption model.

Colloidal lithography is a quick and relatively simple method to produce uniform nanostructures over large surface areas. Particle size and coverage may be varied to produce the required surface structure. Fabrication of controlled 3D nanoporous particle films may also be possible using this method, where repeated adsorption of particles and repeated charging of the substrate results in multilayer formation (6). *In vitro* cell studies of how nanotopography influences osteoblast (bone forming cell) adhesion and morphology are under way.

### ACKNOWLEDGEMENTS

This work was supported by the Swedish Foundation for Strategic Research (SSF).

### REFERENCES

1. Britland, S., et al., *Experimental Cell Research*, 1996, **228**, 313.
2. Sutherland, D. and Kasemo, B., *24th annual meeting of Society for Biomaterials*, San Diego, 1998.
3. Johnson, C. and A. Lenhoff, *Journal of Colloid and Interface Science*, 1996, **179**, 587.
4. Rodahl, M., *Thesis*, Chalmers University of Technology, Göteborg, 1995.
5. Adameczyk, Z., et al., *Journal of Colloid and Interface Science*, 1990, **140**, 123-137.
6. Krozer, A., Nordin, S.-A., and Kasemo, B., *Journal of Colloid and Interface Science*, 1995, **176**, 479.





Pergamon

NanoStructured Materials, Vol. 12, pp. 433–438, 1999

Elsevier Science Ltd

© 1999 Acta Metallurgica Inc.

Printed in the USA. All rights reserved

0965-9773/99/\$-see front matter

PII S0965-9773(99)00152-X

## SYNTHESIS AND PROPERTIES OF CERAMIC - POLYMER COMPOSITS

D. Vollath, D. V. Szabo, J. Fuchs

Forschungszentrum Karlsruhe, Institut für Materialforschung III

P.O. Box 3640, D-76021 Karlsruhe, Germany

dieter.vollath@imf.fzk.de

**Abstract** -- The microwave plasma process is capable to produce nanoparticulate powders with mean particle sizes in the range from 5 to 20 nm. The products may be oxides, nitrides, sulphides, selenides, or even metals. Additional, it is possible to coat these particles with a layer of a second ceramic or a polymer. The powder with the polymer coating can be densified by hot pressing at 100 °C. The resulting body may be used because of their special optical or magnetic properties. As an example of application the synthesis and the magnetic properties of a composite consisting of  $\gamma\text{-Fe}_2\text{O}_3$  as kernel and PMA as coating are given. The resulting material is superparamagnetic. This is demonstrated by the magnetisation curves and Mößbauer spectroscopy. ©1999 Acta Metallurgica Inc.

### INTRODUCTION

Nanoscaled particles often have interesting physical or chemical properties (1). In general, these are properties of isolated particles. For technical applications macroscopic bodies or other arrangements of many particles are a prerequisite. Therefore, nanoscaled powders must not be agglomerated. Additionally, in many cases the particles have to be kept on distance to avoid interaction. This is of special importance in the case of functional ceramics and magnetic, optical and opto-electronic devices. Depending on the application, this may be a dipole - dipole interaction requiring relatively large distances, or one has just to avoid tunneling interaction between the particles. In these cases, particles of nanoscaled powders have to be held within a certain distance or, in the latter case, they must not touch each other. Therefore, the particles need a second layer with well-defined thickness to adjust the necessary distance between the particles. This leads to nanocomposites. Synthesis of nanoscaled powders has to take these boundary conditions into account. To produce a macroscopic piece for technical applications the powder will be consolidated by pressing and sintering. During sintering, a high temperature thermal treatment, grain growth occurs. Coating the nanoparticles with a second phase, showing no miscibility with the kernel solves this problem.

Nanoparticles with sizes in the range from 5 to 20 nm and a coating of a second ceramic or polymer phase are the topic of this contribution. The thickness of this coating is also in the range of a few nanometers. The interaction of the nanoparticles in question determines the necessary thickness of the coating. Coating makes it possible to have particles with a cer-

tain set of physical properties in the kernel and a second tailored set of properties at the surface. Depending on the application, two strategies are possible to select the coating of nanoparticles:

Ceramic nanoparticles with ceramic coating.

A necessary prerequisite for successful coating is that kernel and coating have no mutual solubility in the temperature regime of synthesis, sintering, and application. For a few very special applications a stability for the time of synthesis is sufficient.

Nanoparticles with polymer coating.

This type of coating may be used for applications at ambient temperature. It is a necessary prerequisite that the polymer does not dissociate catalytically at the surface of the particle.

Using polymer coated ceramic particles it is possible to produce macroscopic parts simply by hot pressing at 100 °C. This is significantly cheaper than the standard fabrication process consisting of cold pressing and high temperature sintering. The strength obtained by hot pressing of these ceramic - polymer composites is sufficient for most applications.

Coated nanoparticles are synthesised by the microwave plasma process. (2,3) Ceramic coatings are obtained by cascading different microwave plasma reaction zones consecutively on one reaction tube. (4,5) Polymer coating is performed directly after the microwave plasma reaction zone outside the plasma region. (6)

## SYNTHESIS

Synthesising ceramic particles by gas phase reactions requires either relatively high temperatures or long reaction times. Both conditions lead to unfavourable large particles or broad particle size distributions. Therefore, processes based on high temperature or large residence time in the reaction zone may not be used for the synthesis of nanoparticles with strongly size dependent properties.

Chemical reactions, needing high temperature or long residence times for kinetic or thermodynamic reasons, can be performed in a microwave plasma. This is due to a partly dissociation and ionisation of the reactants in a plasma because existence of ionised and dissociated species in the plasma enhances the kinetics of the chemical reactions.

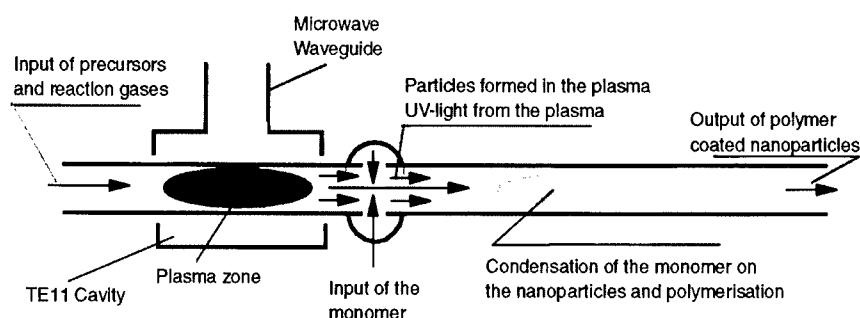
The energy transferred to a charged particle by an oscillating electric field is inversely proportional to the mass of the particle and the squared frequency. Additionally, collisions between energy rich charged particles and uncharged ones influence the energy transfer resulting in a significant influence of the gas pressure to the energy transfer. As the mass of the electrons is significantly smaller than the mass of the ions at microwave frequencies the transfer of energy is substantially higher to the electrons than to the ions. The neutral species obtain their energy from collisions with the charged ones. Therefore, the "overall temperature" of a gas passing a microwave plasma is not as high as in a dc or rf plasma. Depending on the gas pressure and the input of microwave energy the temperature determined directly after the plasma zone can be adjusted in a range from 120 to 800°C. It is very rare that it is necessary to exceed a temperature of about 600 °C. Adjusting the reaction temperature to such low values avoids the formation of hard agglomerates in the nanopowders.

The microwave plasma process to synthesised ceramic nanopowders is performed in a 50 mm diameter reaction vessel made of quartz, passing a single mode  $TE_{11}$  rotating mode cavity. (7) This cavity is connected to a 0.915 GHz microwave system using a IEC 153 R9 (equivalent to RETMA WR 975) waveguide. The total system is tuned using a tri-stub tuner. An equivalent design for 2.45 GHz uses reaction tubes with a diameter of 30 mm. For large scale applications the diameter of the reaction tube may be increased up to a diameter of about 180 mm. The  $TE_{11}$  rotating mode design uses no sliding short for tuning. The  $TE_{11}$  rotating mode cavity is not restricted by dimensions of the wave guide. Therefore, length and diameter of the cavity may be adjusted the to the needs of the process. An additional advantage of this design over the standard  $TE_{01}$  design is the increased efficiency in the use of the microwave power. For the  $TE_{11}$  cavity the region of efficient operation is relatively broad. Optimising tuning, e.g. for 40 mbar one has good operating conditions in the range from 10 to 70 mbar.

Depending on the mixtures of reaction gases it is possible to synthesise oxides, nitrides, sulphides, selenides, and in special cases metals and carbides. Precursors are chlorides, carbonyls, metallocenes, or organometallics. The precursors are evaporated and introduced into the reaction tube directly in front of the plasma zone where the particles are formed. The particles formed in the plasma zone carry electrical charges. This prevents the collision of the nanoparticles and reduces the probability of cluster formation. The reaction temperature, i.e. the temperature measured directly after the reaction zone, can be adjusted in the range from 150 to 800°C. The low temperatures are of special importance, because low temperatures reduce the probability of the formation of sintered clusters. The residence time of the particles in the reaction zone is less than 10 ms. Reaction rate and residence time are parameters to adjust the particle size within relatively narrow limits. The mean diameter of the smallest particles that can be produced with a reasonable production rate is about 3 nm. The largest mean particle diameter is in the range of about 20 nm. To produce larger particles it is necessary to change the reaction route. In the case of oxides the addition small quantities of water to the reaction gas leads to larger particles. (2)

Particles coated with a ceramic layer are produced in a system with two reaction zones. In this case the two different precursors are introduced into the system directly in front of each reaction zone. (4,5) To obtain a polymer coating an appropriate monomer is evaporated and introduced into the reaction tube directly after the reaction zone. This monomer condenses on the surface of the ceramic nanoparticles in the gas. Forced by temperature and UV radiation emitted by the microwave plasma properly selected monomers will polymerise. A schematic drawing of this set-up is given in figure 1.

The ceramic particles with the polymer coating are precipitated on cold surfaces. For oxides of the main group elements like  $Al_2O_3$ , this process works without major problems. It is more difficult with the oxides of the transition elements, such as  $TiO_2$  or  $Fe_2O_3$  because these oxides may act as catalysts. In these cases the monomers are catalytically dissociated before the polymerisation starts. Careful selection of the precursors and the conditions for coating may reduce this problem. The most versatile precursors are methacrylic (MA) acid and methyl methacrylate (MMA). In the case of alumina, isobutylmethacrylate (i-BMA) gave excellent results. (6) Finally, the product is collected on cooled surfaces and scrapped off. During this process, the particles lose their electrical charges. Therefore, a significant amount of the polymer



coated particles will agglomerate. At this step this is no longer a problem, because the active kernels remain separated.

### MORPHOLOGY OF THE PRODUCT

The particle size of the powder is, for crystallised material, in most cases in the range from 5 to 10 nm. High resolution electron microscopy is the main tool for characterisation. A micrograph of a typical product,  $\gamma\text{-Fe}_2\text{O}_3$  coated with PMA is depicted in figure 2. In this figure it is most striking that the size of the particles is nearly uniform. It is also important to realise that the magnetic kernels are not touching each other. These are perfect conditions to obtain good physical properties. Some of the polymer coated particles are glued together. This can be seen even better in figure 3, a high resolution micrograph of  $\text{Fe}_2\text{MnO}_4$  - PMA particles. In this micrograph the lattice fringes of the crystallised manganese spinell and the structure of the polymer can be seen.

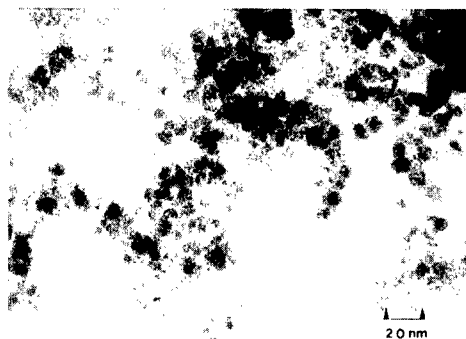


Figure 2: Maghemite ( $\gamma\text{-Fe}_2\text{O}_3$ ) poly-methacrylic acid (PMA) composite powder

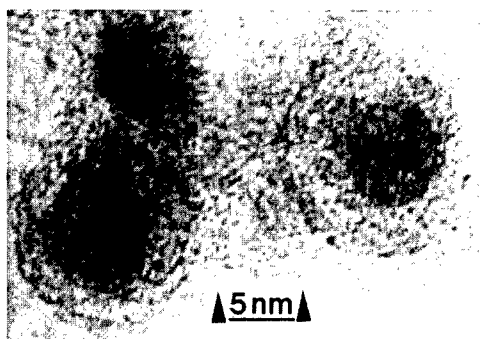


Figure 3: Manganese spinell ( $\text{Fe}_2\text{MnO}_4$ ) particles coated with poly-methacrylic acid (PMA).

A solid body is obtained after hot pressing at 100 °C and a pressure of 1.4 MPa. The densified body has a very regular structure. It is possible to use these bodies to measure hardness, index of refraction and magnetic properties.

## PROPERTIES OF CERAMIC - POLYMER NANOCOMPOSITES

A typical application of polymer coated ceramic nanoparticles are soft magnetic cores. Therefore, superparamagnetic composites are selected as an example for the application of nanocomposites. Due to the thermal fluctuation of the magnetisation, superparamagnetic particles are free of any magnetic hysteresis. (8,9) This is valid up to frequencies in the range of one Gigahertz. Superparamagnetism is a property of isolated small particles of ferrimagnetic materials. To produce a superparamagnetic core, the superparamagnetic particles have to be kept on distance to reduce their interaction. Figure 4 shows typical magnetisation curves of small cylinders made of such materials. These specimens were consolidated with hot pressing at 100 °C. In this figure one realises magnetisation curves that are obviously free of any hysteresis. Because of a significant polymer content the magnetisation of this material is smaller than the one obtained with pure ceramic ferrite.

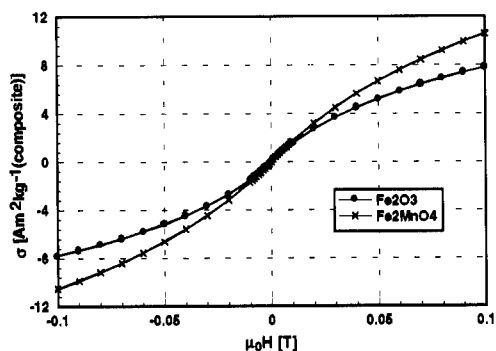


Figure 4: Magnetisation curves up to 0.1 T of superparamagnetic Fe<sub>2</sub>O<sub>3</sub> and Fe<sub>2</sub>MnO<sub>4</sub>-PMA composite cylinders (ca. 3 mm Ø, 4 mm high) at 300 K.

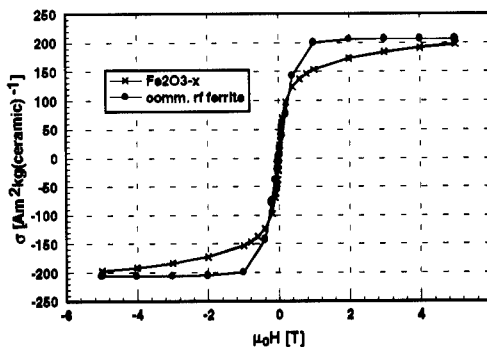


Figure 5: Magnetisation curves up to 5 T of superparamagnetic Fe<sub>2</sub>O<sub>3-x</sub> PMA composite cylinders (ca. 3 mm Ø, 4 mm high) and a commercial ferrite at 300 K.

Figure 5 depicts a comparison between superparamagnetic Fe<sub>2</sub>O<sub>3-x</sub> polymer composite and a commercial ferrite. For comparison the magnetisation of the composite is referred to the pure ceramic content. This comparison shows that the magnetisation at high fields (5 T) is quite similar whereas at low fields the susceptibility of the composite is higher.

To determine whether or not a specimen is fully superparamagnetic or not, Mößbauer spectroscopy is used. As in the superparamagnetic state the fluctuation frequency of the magnetisation is higher than the Lamor frequency of the iron nuclei, these nuclei "do not realise" that there is a high magnetic crystal field. Therefore, the Mößbauer spectra of superparamagnets show the quadrupol duplett of non-magnetic material instead of the sextett observed with magnetic materials. This phenomenon can be used to determine the amount of non-superparamagnetic material. This is shown in figure 6 for the Fe<sub>2</sub>O<sub>3</sub> - PMA composite specimen, whose magnetisation curve is plotted in figure 4.

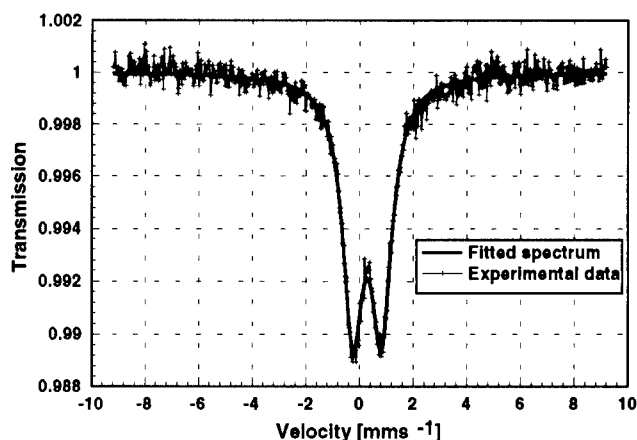


Figure 6: Mößbauer spectrum of a  $\text{Fe}_2\text{O}_3$  - PMA composite specimen. The magnetisation curve of this specimen is given in figure 4.

## CONCLUSIONS

Technical applications of nanomaterials, exploiting their special properties, make it necessary to use nanocomposites. The best starting material for nanocomposites are particles coated with a second phase. The best way to synthesise this type of material is the microwave plasma process. From the broad spectrum of possible products one application in the field of nanoscaled oxide particles has been demonstrated. Because of the dissociation and ionisation the reactants in the microwave plasma, this process excels in relatively low reaction temperatures. The low reaction temperature and the electrical charging of the particles in the plasma reduce the probability of agglomeration. Therefore, it is possible to pass the gas stream with the as-produced particles through a second reaction zone to coat the particles. The low reaction temperature allows to coat the ceramic particles with a polymer.

To prove the concept of coated particles the superparamagnetic behaviour of  $\gamma\text{-Fe}_2\text{O}_3$ -polymer composite cylinders was demonstrated. Besides its exiting magnetic properties it is remarkable that the fabrication processes to obtain macroscopic bodies is cheaper than the standard process consisting of cold pressing and high temperature sintering.

## References

1. H. Gleiter, Prog. in Materials Science 33(1989) 223
2. D. Vollath, K. E. Sickafus, J. Nanostr. Mater. 1, 427 (1992).
3. D. Vollath, K. E. Sickafus, J. Nanostr. Mater. 2, 451 (1993).
4. D. Vollath, German Patent G9403581.4 (1994).
5. D. Vollath, D. V. Szabó, J. Nanostr. Mater. 4, 927 (1994).
6. D. Vollath, D. V. Szabó, B. Seith, German Patent 196 38 601.2-43 (1997).
7. A. Moebius, M. Muehleisen, German Patent Application G29512436.9 (1995).
8. E. Kneller in Encyclopaedia of Physics, Springer Verlag, Berlin, 1966, pp. 478 ff.
9. D. Vollath, D. V. Szabó, R. D. Taylor, J. O. Willis, J. Mater. Res. 12(1997)2175.



Pergamon

NanoStructured Materials, Vol. 12, pp. 439–442, 1999

Elsevier Science Ltd

© 1999 Acta Metallurgica Inc.

Printed in the USA. All rights reserved

0965-9773/99/\$-see front matter

PII S0965-9773(99)00153-1

## NANOPHASE COMPOSITES IN EASY GLASS FORMING SYSTEMS

J. Eckert, M. Seidel, L.Q. Xing, I. Börner and B. Weiß

IFW Dresden, Institut für Metallische Werkstoffe, D-01171 Dresden, Germany

**Abstract** -- Nanophase composites based on Zr- and Mg-base easy glass forming alloys were prepared by partial crystallization of melt-quenched amorphous alloys or by mechanical alloying of elemental powder mixtures blended with oxide particles. The amorphous phases exhibit a wide supercooled liquid region before crystallization, even in the presence of second phase particles. This allows an easy consolidation of powders or shaping of bulk samples due to viscous flow. Room temperature mechanical properties will be presented and discussed with respect to the potential of the nanoscale microstructure for mechanical strengthening.

©1999 Acta Metallurgica Inc.

### INTRODUCTION

Devitrification of melt-quenched easy glass forming alloys is a promising way for obtaining new bulk nanophase materials (1,2). Glassy alloys are known to exhibit a beneficial combination of very high strength, relatively low Young's modulus and high wear resistance (3,4). Partial (nano)crystallization can lead to a further improvement of these properties (5,6). Alternatively, nanostructured composites can be prepared by mechanical alloying (7,8). This enables the synthesis of metallic glass/ceramic composites, which are difficult or impossible to obtain by melting techniques due to the different densities and melting points of the constituents and heterogeneous nucleation from the melt at high temperatures.

This work reports on the preparation of melt-quenched and mechanically alloyed Zr- and Mg-base composite materials containing nanoscale metallic precipitates or oxide particles in a glassy matrix, and presents room temperature mechanical properties for bulk samples.

### EXPERIMENTAL

Bulk glassy samples with 3 mm diameter and 50 mm length were prepared by alloying pure elements with electromagnetic levitation under He atmosphere and casting into a copper mold. Rapidly quenched ribbons were produced by single-roller melt spinning under argon atmosphere. Mechanical alloying of elemental powders was done in a planetary ball mill under argon atmosphere using hardened steel balls and vial and a ball-to-powder weight ratio of 15:1. The samples were characterized by x-ray diffraction (XRD), transmission electron microscopy (TEM) and differential scanning calorimetry (DSC) under argon atmosphere. Powder compaction was done by uni-axial hot pressing under vacuum. The Vickers microhardness ( $H_v$ ) was measured with a Neophot hardness tester and a load of 0.2 N. Constant compression rate tests at room temperature were conducted using an INSTRON 8562 testing machine.

## RESULTS AND DISCUSSION

Devitrification of melt-quenched amorphous  $\text{Zr}_{65}\text{Al}_{7.5}\text{Cu}_{17.5}\text{Ni}_{10}$  and  $\text{Zr}_{57}\text{Ti}_5\text{Al}_{10}\text{Cu}_{20}\text{Ni}_8$  samples was studied by time and temperature resolved XRD and TEM investigations. Figure 1 shows a schematic phase formation diagram for  $\text{Zr}_{65}\text{Al}_{7.5}\text{Cu}_{17.5}\text{Ni}_{10}$  ribbons. The details of phase formation strongly depend on the annealing conditions. Crystallization is governed by simultaneous precipitation of quasicrystalline, tetragonal  $\text{CuZr}_2$ , and hexagonal  $\text{Zr}_6\text{NiAl}_2$  phases which are embedded in the residual amorphous matrix. A metastable fcc  $\text{NiZr}_2$ -type phase forms as an intermediate crystallization product. At elevated temperatures the quasicrystals transform into  $\text{CuZr}_2$  and the fcc phase transforms into the stable  $\text{Zr}_6\text{NiAl}_2$  compound (for details see Ref. 9). The grain sizes of the different phases vary between about 10 and 70 nm as estimated from XRD line broadening according to the Scherrer formula and TEM images. Similar results were found for a variety of slowly cooled Zr-(Al/Ti)-Cu-Ni bulk samples with different compositions, revealing that nanoscale microstructures with different volume fractions of different phases can be obtained by proper choice of the annealing conditions.

Figure 2 shows compressive stress-strain curves for as-cast amorphous  $\text{Zr}_{57}\text{Cu}_{20}\text{Al}_{10}\text{Ni}_8\text{Ti}_5$  and for partially crystallized bulk samples containing different volume fractions of nanocrystals (for details see Ref. 10). The as-cast alloy [curve (a)] shows a Young's modulus of 65 GPa, an elastic strain of 2.6 % and microplasticity of about 1 % without work hardening. Hence, the yield strength and the flow stress are equal, reaching about 1600 MPa. These results agree well with data for other Zr-base amorphous alloys (3-6) and can be ascribed to inhomogeneous flow of the material (11), i.e., the strain is localized in very thin shear bands.

The elastic behavior of the partially crystallized samples is almost identical to that of the fully amorphous alloy regardless of the amount of nanocrystals (Fig. 2). However, the flow stress significantly increases and the plastic strain decreases with increasing volume fraction of

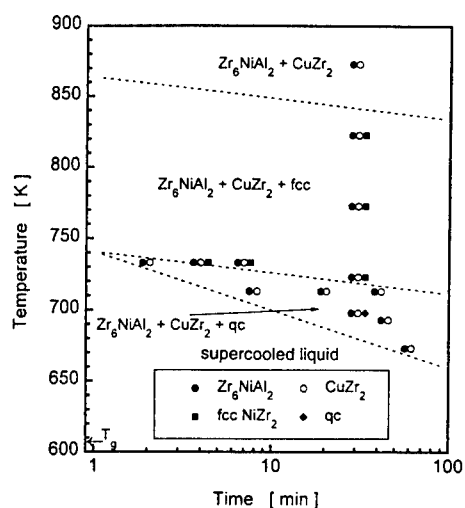


Figure 1. Schematic phase formation diagram for  $\text{Zr}_{65}\text{Al}_{7.5}\text{Cu}_{17.5}\text{Ni}_{10}$  ribbons. The lines are only guidelines for the eye.

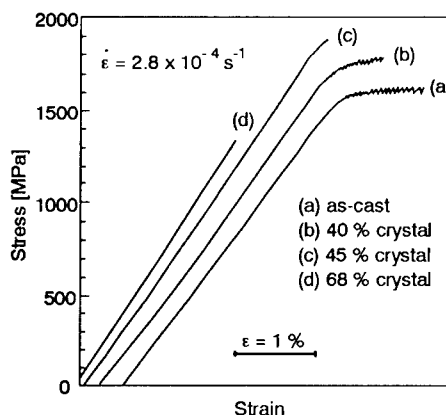


Figure 2. Compressive stress-strain curves for amorphous and partially crystallized  $\text{Zr}_{57}\text{Ti}_5\text{Al}_{10}\text{Cu}_{20}\text{Ni}_8$ : (a) as-cast, (b) 40 vol.% crystals, (c) 45 vol.% crystals and (d) 68 vol.% crystals.



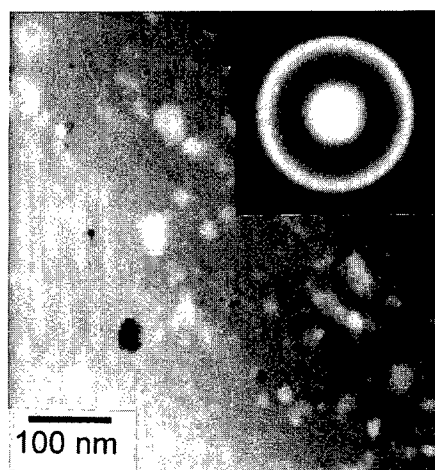


Figure 3. TEM bright-field image and corresponding diffraction pattern for 100 h mechanically alloyed  $\text{Zr}_{65}\text{Al}_{7.5}\text{Cu}_{17.5}\text{Ni}_{10}$ -5vol.% CaO powder.

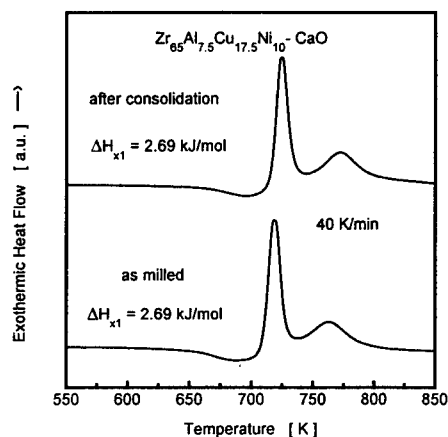


Figure 4. DSC scans for 100 h milled  $\text{Zr}_{65}\text{Al}_{7.5}\text{Cu}_{17.5}\text{Ni}_{10}$ -5vol.% CaO powder and for the consolidated bulk sample.

nanocrystals. Most likely, the nanoscale precipitates are too small to contain dislocations and are, therefore, free of internal defects which gives rise to a high mechanical strength (5,10). When the nanocrystal volume fraction exceeds about 50%, the brittle nature of the intermetallic phases dominates the mechanical behavior, leading to a decrease in fracture stress and ductility.

Besides crystallization of amorphous phases, nanostructured composites can also be prepared directly by mechanical alloying starting from elemental powders. Figure 3 shows TEM results for  $\text{Zr}_{65}\text{Al}_{7.5}\text{Cu}_{17.5}\text{Ni}_{10}$ -5 vol.% CaO as a typical example for oxide-containing composite powders. The bright-field image reveals a homogeneous distribution of dispersoids with 5–20 nm in size in the amorphous matrix and the diffraction pattern exhibits the diffraction spots of the dispersoids besides the typical diffuse halo of the amorphous phase. Similar results were found for other dispersoids as well as for  $\text{Y}_2\text{O}_3$  particles in amorphous

TABLE I

Mechanical data for 100 hours mechanically alloyed  $\text{Zr}_{65}\text{Al}_{7.5}\text{Cu}_{17.5}\text{Ni}_{10}$  and  $\text{Mg}_{55}\text{Y}_{15}\text{Cu}_{30}$  amorphous powders without dispersoids and for nanophase composites containing 5 or 30 vol.% of different oxides: microhardness  $H_v$  and yield strength  $\sigma_y$ .

	$\text{Zr}_{65}\text{Al}_{7.5}\text{Cu}_{17.5}\text{Ni}_{10}$			$\text{Mg}_{55}\text{Y}_{15}\text{Cu}_{30}$		
	without	5 vol.% MgO	5 vol.% CaO	without	5 vol.% $\text{Y}_2\text{O}_3$	30 vol.% $\text{Y}_2\text{O}_3$
$H_v$ (GPa)	4.39	5.07	4.77	3.49	3.98	4.85
$\sigma_y$ (GPa)	1.46	1.69	1.59	1.16	1.33	1.62

Mg<sub>55</sub>Y<sub>15</sub>Cu<sub>30</sub> composites. The amorphous phase exhibits a distinct glass transition before crystallization as shown in Fig. 4 for Zr<sub>65</sub>Al<sub>7.5</sub>Cu<sub>17.5</sub>Ni<sub>10</sub>-5 vol.% CaO as a typical example. This enables consolidation of bulk samples using the low viscosity of the supercooled liquid. XRD and TEM investigations proved that the consolidated samples retain an amorphous matrix without indications for crystallization. The features of the DSC scan of the bulk samples are the same as those for the as-milled powders (Fig. 4). The hot-pressed samples are more than 99.5% dense. The dispersoids significantly increase the Vickers hardness  $H_v$  and the yield strength  $\sigma_y$  of the nanophase composites compared to the values of dispersoid-free amorphous material (Table 1). Most likely this is due to suppression of shear slip, similar as for the strengthening effect of nanoscale metallic precipitates formed upon partial crystallization.

### SUMMARY

Nanophase composites based on Zr-(Al/Ti)Cu-Ni and Mg-Y-Cu easy glass forming alloys were prepared by melt-quenching and partial crystallization or by mechanical alloying and blending with second phase oxide particles. Slow cooling or consolidation of as-milled powders yields bulk samples. Second phase particles increase the mechanical strength of the material compared to the homogeneous amorphous alloy. These results promise to allow the development of new high-strength bulk nanostructured materials based on bulk metallic glasses.

### ACKNOWLEDGEMENTS

The authors thank U. Klement, N. Mattern and M. Zinkevitch for assistance with the XRD and TEM work. Stimulating discussions with M. Heilmaier, A. Kübler and A. Leonhard and financial support by the German Science Foundation (DFG Schwerpunktprogramm 'Unterkühlte Metallschmelzen'; Grant Ec 111/7-2) are gratefully acknowledged.

### REFERENCES

1. Greer, A.L., *Current Opinion in Solid State & Materials Science*, 1997, 2, 412.
2. Inoue, A., *Materials Science and Engineering*, 1994, A179/A180, 57.
3. Gilbert, C., Ritchie, R.O. and Johnson, W.L., *Applied Physics Letters*, 1997, 71, 476.
4. Johnson, W.L., *Materials Science Forum*, 1996, 225-227, 35.
5. Inoue, A. Zhang, T. and Masumoto, T., *Materials Transactions of JIM*, 1995, 36, 391.
6. Doglione, R., Spriano, S. and Battezzati, L., *Nanostructured Materials*, 1997, 8, 447.
7. Eckert, J., Seidel, M., Kübler, A., Klement, U. and Schultz, L., *Scripta Materialia*, 1998, 38, 595.
8. Moelle, C., Lu, I.-R., Sagel, A., Wunderlich, R.K., Perepezko, J.H. and Fecht, H.-J., *Materials Science Forum*, 1998, 269-272, 47.
9. Eckert, J., Mattern, N., Zinkevitch, M. and Seidel, M., *Materials Transactions of JIM*, 1998, 39, 623.
10. Xing, L.Q., Herlach, D.M., Cornet, M., Bertrand, C., Dallas, J.-P., Trichet, M.-F. and Chevalier, J.-P., *Materials Science and Engineering*, 1997, A226-228, 874.
11. Spaepen, F., *Acta Metallurgica*, 1977, 25, 407.



Pergamon

NanoStructured Materials, Vol. 12, pp. 443–446, 1999

Elsevier Science Ltd

© 1999 Acta Metallurgica Inc.

Printed in the USA. All rights reserved

0965-9773/99/\$-see front matter

PII S0965-9773(99)00154-3

## NANOPARTICLES IN AN AMORPHOUS $\text{Zr}_{55}\text{Al}_{10}\text{Cu}_{30}\text{Ni}_5$ -MATRIX - THE FORMATION OF COMPOSITES BY MECHANICAL ALLOYING

A. Kübler, J. Eckert and L. Schultz

IFW Dresden, Institut für Metallische Werkstoffe, Postfach 27 00 16,

D-01171 Dresden, Germany

**Abstract** -- Mechanical alloying of pure elemental powders blended with W,  $\text{Y}_2\text{O}_3$  and  $\text{SiO}_2$  particles was used to synthesize nanoscale composites consisting of an amorphous  $\text{Zr}_{55}\text{Al}_{10}\text{Cu}_{30}\text{Ni}_5$  matrix with a homogeneous dispersion of nanoparticles. The powders are characterized by x-ray diffraction, calorimetric measurements, thermal mechanical analysis and testing the microhardness. The amorphous matrix exhibits an extended supercooled liquid region before crystallization. The supercooled liquid region is not significantly reduced due to the addition of nanocrystalline particles whereas the viscosity of the composites increases with increasing volume fraction of nanoscaled particles within the amorphous matrix.

©1999 Acta Metallurgica Inc.

### INTRODUCTION

Bulk amorphous materials exhibit interesting properties such as high processability in the supercooled liquid state, high strength combined with perfect elastic behavior at room temperature and high corrosion resistance (1). Homogeneously dispersed particles in an amorphous matrix promise to further improve the strength, hardness and ductility of the material. This topic was investigated recently for example for Zr-Nb-Al-Cu-Ni alloys by adding WC particles (2), for Cu-Ti-Zr-Ni alloys containing SiC particles (3) and for Zr-Al-Cu-Ni alloys with ZrC particles (1). These samples were produced by casting. All these investigations do not point to a reduction of the extension of the supercooled liquid region by the addition of particles. In contrast, the supercooled liquid region is enlarged by adding SiC (3). The particles dispersed in the amorphous matrix have sizes of about 50  $\mu\text{m}$ . First mechanical property investigations indicate a linear increase in Young's modulus, compressive strength and the Vickers hardness of the composites with increasing volume fraction of ZrC particles (1). Alternatively, amorphous matrix composites can be prepared by mechanical alloying, yielding particle sizes in the nanometer range which are significantly smaller than the particles used in cast bulk specimens (4,5). The intention of this paper is to investigate the formation and properties of mechanically alloyed amorphous matrix composites with homogeneously dispersed W,  $\text{SiO}_2$  and  $\text{Y}_2\text{O}_3$  particles with a size of about 20 - 40 nm. The effect of these additions on the extension of supercooled liquid region, the viscous flow above  $T_g$  and the Vickers microhardness  $H_v$  will be reported.

## EXPERIMENTAL

The composites were produced in a planetary ball mill using hardened steel milling tools. The ball-to-powder weight ratio was 14:1. Pure elemental Zr, Al, Cu and Ni powders were filled in the vials in a glove box under purified argon atmosphere ( $< 1$  ppm  $O_2$  and  $H_2O$ ) to get a composition of  $Zr_{55}Al_{10}Cu_{30}Ni_5$ . This powder mixture was blended with  $Y_2O_3$ ,  $SiO_2$  and W particles, respectively. X-ray diffraction patterns were recorded with a Philips PW 1050 diffractometer using  $CoK\alpha$  radiation. Continuous heating experiments were done in a Perkin-Elmer DSC7 calorimeter under argon atmosphere. The heating rate was 40 K/min. Viscosity measurements using parallel plate rheometry were performed in a Perkin-Elmer TMA7 at 10 K/min heating rate. For this, the samples were relaxed to ensure measuring the viscosity of isoconfigurational states (5,6). The Vickers microhardness  $H_v$  was measured at room temperature with a Neophot hardness tester and a load of 0.2 N.

## RESULTS AND DISCUSSION

X-ray diffraction and transmission electron microscopy combined with energy-dispersive x-ray analysis (not shown here) revealed that the mechanically alloyed powders consist of an amorphous matrix with homogeneously distributed oxide or metallic particles with sizes  $\langle D \rangle$  of about 20 to 40 nm (Table 1). The amorphous matrix exhibits the desired composition of  $Zr_{55}Al_{10}Cu_{30}Ni_5$ . Evaluating the scattering vector  $Q_p = 2\pi \sin\theta/\lambda$  gives no evidence for a change

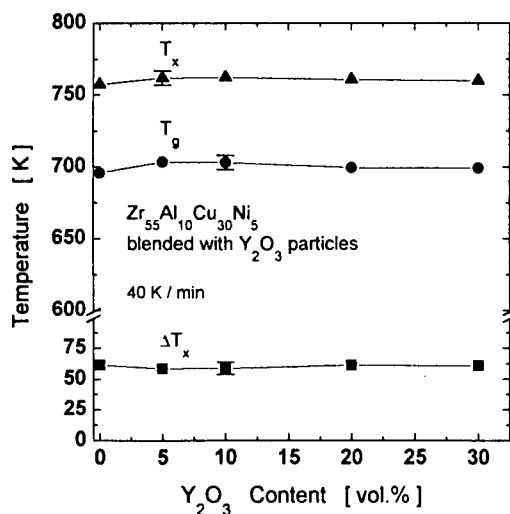


Figure 1: Thermal stability data for amorphous  $Zr_{55}Al_{10}Cu_{30}Ni_5$  and for composite powders with different volume fraction of  $Y_2O_3$  particles.

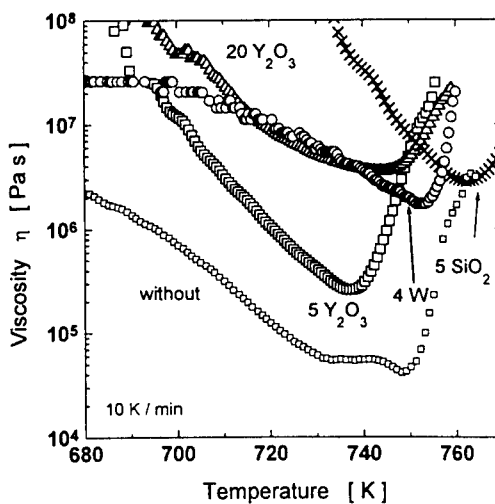


Figure 2: Viscosities of composite materials: 4 vol.% W (circles), 5 vol.%  $SiO_2$  (crosses), 5 vol.%  $Y_2O_3$  (squares), and 20 vol.%  $Y_2O_3$  (triangles).

TABLE 1

Crystallite size  $\langle D \rangle$  and Vickers microhardness  $H_v$  for  $Zr_{55}Al_{10}Cu_{30}Ni_5$  composite materials.

Dispersoid	$\langle D \rangle$ [nm]	$H_v$ [ GPa ]
without	---	$5.7 \pm 0.1$
5 vol.% $Y_2O_3$	29	$5.8 \pm 0.2$
10 vol.% $Y_2O_3$	26	$5.7 \pm 0.2$
20 vol.% $Y_2O_3$	31	$6.0 \pm 0.3$
30 vol.% $Y_2O_3$	22	$17.4 \pm 2.1$

in  $Q_p$  due to a variation in the composition of the amorphous matrix for the different particle additions ( $Q_p = 26.4 \text{ nm}^{-1}$  with a variation of  $\pm 0.2 \text{ nm}^{-1}$  for samples blended with particles). Figure 1 and Table 1 show thermal stability data for  $Zr_{55}Al_{10}Cu_{30}Ni_5$  blended with up to 30 vol.%  $Y_2O_3$  particles. The glass transition temperature  $T_g$  and the crystallization temperature  $T_x$  remain constant even for an addition of up to 30 vol.%  $Y_2O_3$ . Therefore, the extension of the supercooled liquid region  $\Delta T_x = T_x - T_g$  is also the same within the accuracy of experiment. This is consistent with the unchanged scattering vector  $Q_p$  and indicates that the dispersed oxide particles do not affect the composition or the thermal stability data of the amorphous matrix. Table 2 lists the thermal stability data for up to 17.5 vol.% W additions. There is also no significant change in  $T_g$ ,  $T_x$  and  $\Delta T_x$ . For an addition of up to 10 vol.%  $SiO_2$  we find the same extension of supercooled liquid region albeit there is a shift in  $T_g$  and  $T_x$  of nearly the same amount to higher temperatures. For more than 10 vol.%  $SiO_2$  we find a drastic change in the crystallization sequence and no supercooled liquid region can be detected although x-ray diffraction measurements show a broad diffuse halo due to an amorphous phase. Hence, a large  $SiO_2$  content seems to prevent the appearance of an extended supercooled liquid region.

Figure 2 shows the viscosity as a function of temperature for several composites as well as for a sample without blended particles. The viscosities are evaluated from parallel plate rheometry using the Stefan equation (7)  $\eta = -(2Fh^3)/[3\pi a^4(dh/dt)]$  where  $F$  is the applied load (2.6 N),  $h$  the height of the sample and  $a$  the radius of the plates (3.7 mm). Compared to the particle-free sample we find a significant increase in viscosity for the composite samples. For example, the viscosity for the sample blended with 5 vol.%  $Y_2O_3$  exhibits a lower viscosity than the sample blended with 20 vol.% due to the larger amount of  $Y_2O_3$  dispersoids in the amorphous matrix (Fig. 2). Most likely the particles hinder the viscous flow. This effect becomes more pronounced with increasing volume fraction of particles.

The Vickers microhardness  $H_v$  data for the different composites are summarized in Tables

TABLE 2

Thermal stability data as well as crystallite size  $\langle D \rangle$  and Vickers microhardness  $H_v$  for  $Zr_{55}Al_{10}Cu_{30}Ni_5$  amorphous powder blended with nanocrystalline W and  $SiO_2$  particles.

Dispersoid	$T_g$ [ K ]	$T_x$ [ K ]	$\Delta T_x$ [ K ]	$\langle D \rangle$ [nm]	$H_v$ [ GPa ]
0.9 vol.% W	715	754	39	43	$5.7 \pm 0.3$
4 vol.% W	722	759	37	39	$6.3 \pm 0.1$
8.5 vol.% W	717	752	35	26	$5.9 \pm 0.1$
17.5 vol.% W	718	757	39	29	$6.1 \pm 0.2$
5 vol.% $SiO_2$	742	780	38	---	$5.8 \pm 0.2$
10 vol.% $SiO_2$	740	780	40	---	---

1 and 2. For a small volume fraction of dispersoids in the amorphous matrix (up to 10 vol.%) we find only a small change in microhardness. Comparing the microhardness for the same volume fraction of 5 vol.% homogeneously dispersed W, SiO<sub>2</sub> and Y<sub>2</sub>O<sub>3</sub> we find that W ( $H_v = 6.3$  GPa) has the largest effect on the hardness of the samples whereas the values for Y<sub>2</sub>O<sub>3</sub> and SiO<sub>2</sub> are not significantly larger than the particle-free amorphous alloy ( $H_v = 5.7$  GPa). For Y<sub>2</sub>O<sub>3</sub> particles we find a significant increase in  $H_v$  for an addition of 30 vol.% of particles ( $H_v = 17.4$  GPa). To explain this sudden and significant increase in the Vickers microhardness further investigations are under way.

### SUMMARY

The addition of W, SiO<sub>2</sub> and Y<sub>2</sub>O<sub>3</sub> particles does not reduce the supercooled liquid region  $\Delta T_x$  compared to samples without additions. The scattering vector  $Q_p$  indicates that there is no significant change in the nearest-neighbour distances of the amorphous matrix indicating that there is no true alloying of the particles with the matrix. The W, SiO<sub>2</sub> and Y<sub>2</sub>O<sub>3</sub> additions lead to an increase in viscosity with increasing dispersoid content. This is believed to be the result of the nanocrystalline particles which are homogeneously embedded in the amorphous matrix and hinder the viscous flow. The higher the volume fraction of nanocrystalline particles the more the viscous flow is hindered. The Vickers microhardness reveals remarkable higher values than for the pure matrix alloy only for an addition of more than 20 vol.% of dispersoids. W has the largest effect on the microhardness  $H_v$  for a given volume fraction than SiO<sub>2</sub> and Y<sub>2</sub>O<sub>3</sub>. Further investigations are necessary to explain this behavior.

### ACKNOWLEDGEMENTS

The authors want to thank S. Schinnerling and H. Schulze for technical assistance, and M. Heilmaier, N. Schlorke, T. Fahr and M. Seidel for stimulating discussions. This work was supported by the German Science Foundation via the DFG Schwerpunktprogramm „Unterkühlte Metallschmelzen“ under contract Ec 111/7-2.

### REFERENCES

1. Kato, H. and Inoue, A., *Materials Transactions of JIM* 1997, 38, 793.
2. Choi-Yim, H. and Johnson, W.L., *Applied Physics Letters* 1997, 71, 3808.
3. Choi-Yim, H., Busch, R. and Johnson, W.L., submitted to: *Journal of Applied Physics*.
4. Moelle, C., Lu, I.-R., Sagel, A., Wunderlich, R.K., Perepezko, J.H. and Fecht, H.J. *Materials Science Forum* 1998, 269-272, 47.
5. Eckert, J., Seidel, M., Kübler, A., Klement, U. and Schultz, L., *Scripta Materialia* 1998, 38, 595.
6. Kübler, A., Eckert, J., Gebert, A. and Schultz, L., *Journal of Applied Physics* 1998, 83, 3438.
7. Stefan, M.J., *Akademie der Wissenschaften und der Literatur (Mainz), Mathematisch-Naturwissenschaftliche Klasse* 1874, 69, 713.



## ELECTRONIC AND OPTICAL PROPERTIES OF CETINEITES: NANOPOROUS SEMICONDUCTORS WITH ZEOLITE-LIKE CHANNEL STRUCTURE

U. Simon<sup>1)</sup>, J. Jockel<sup>1)</sup>, F. Starrost<sup>2)</sup>, E. E. Krasovskii<sup>2)</sup>, W. Schattke<sup>2)</sup>

<sup>1)</sup>Institut für Anorganische Chemie, Universität GH Essen, Schützenbahn 70, D-45127 Essen

<sup>2)</sup>Institut für Theoretische Physik, Universität Kiel, Leibnizstr. 15, D-24118 Kiel

**Abstract** -- *The electronic and optical properties of a promising new class of nanoporous semiconductors, crystals of the cetineite family, have been investigated experimentally and theoretically on an ab initio basis. Band structure, dielectric function and the trend in the gap's dependence on the chemical composition were found to be in remarkable agreement with the experimental results. ©1999 Acta Metallurgica Inc.*

The fabrication of nanostructured materials by chemical preparation techniques has evolved to an important interdisciplinary field of research. On the one hand various chemical routes have been developed to synthesize well defined metal or semiconductor nanoparticles of a few up to tens of nanometers, in which quantum size effects as well as charging effects occur, giving rise to various electro-optical or microelectronic applications (1-3). On the other hand attempts have been made to obtain semiconductor or metallic solids with defined void spaces, like in zeolites, which may be regarded as so called quantum-anti-dot lattices (4). Cetineites are oxoselenoantimonates with zeolite-like channel structure, the synthesis of which was described by Wang and Liebau (5). In contrast to zeolites and structurally related metal oxides, which are electrical insulators, cetineites have shown to be the first crystalline nanoporous material with a photo-semiconducting host lattice (6). This made the material attractive for further detailed experimental and theoretical investigations of the electronic structure of this novel class of nanomaterials.

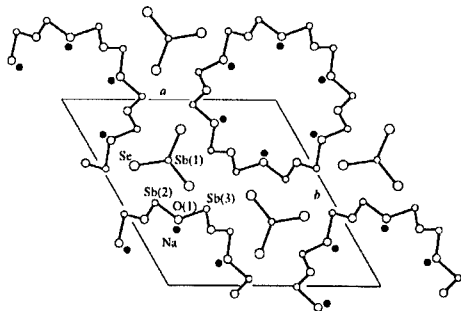
The general composition of cetineites is  $A_6(Sb_{12}O_{18})(SbX_3)_2 \cdot (6-mx-y)H_2O \cdot x(B^{m+}(OH)_m) \cdot y\Box$ , with  $A = Na^+, K^+, Rb^+, Sr^{2+}, Ba^{2+}$ ;  $X = S^{2-}, Se^{2-}$  and  $B = Na^+, Sb^{3+}, CO_3^{2-}$ , the phases with  $A = Na, K$  and  $X = S, Se$  being discussed in the present work. The crystal structures (Fig. 1) have space group symmetry  $P6_3$  or  $P6_{3/m}$  (5,6). Tubes of composition  $[Sb_{12}O_{18}]$  are formed by linking  $[SbO_3]$  pyramids. The lone electron pairs of their Sb(2) and Sb(3) atoms are perpendicular to the tube walls, which are arranged in a hexagonal rod packing. Single  $[Sb(1)X_3]^{3-}$  pyramids are located between the tubes with their lone pairs oriented parallel to the tube axes. The interior of the tubes, whose free diameter is approx. 0.7 nm, may be occupied by chains of face-sharing  $[H_2O]_6$  octahedra or by  $[(Na,Sb),(OH,H_2O)_6]$  octahedra, extended along the tubes of each channel. The arrangement of electroneutral  $[Sb_{12}O_{18}]$  tubes should be held together by ionic bonds between the  $[SbX_3]^{3-}$  pyramids and the  $A^+$  cations lining the tube walls, and by additional weaker secondary bonds between every second Sb atom of the tubes ( Sb(2) in

Fig. 1) and the X atoms of the  $[\text{SbX}_3]^{3-}$  pyramids.

The preparation of these phases results from hydrothermal reaction of elementary antimony and sulfur or selenium in aqueous NaOH or KOH, respectively, from which single crystals with a maximum length of 2 mm and a hexagonal cross section of  $3.1 \cdot 10^{-2} \text{ mm}^2$  have been obtained. UV/Vis transmission spectra between 250 nm and 750 nm have been measured at room temperature on single crystals and I(U)-characteristics were obtained along the c direction in the range of -10 V to +10 V in dark and under irradiation with monochromatic light (10 nm spectral resolution). To verify whether the optical excitation energy of the photoconductivity corresponds to the optical band gap, the conductivity has been probed at simultaneous variation of the wave length of the irradiated light in the range of 250 - 800 nm. To look for possible ionic conductivity and sample/electrode polarisation, impedance measurements were performed in a frequency range from  $10^{-2} \text{ Hz}$  to  $10^4 \text{ Hz}$ .

The numerical computation followed the linear augmented plane wave (LAPW) procedure (7,8) and yielded density of states (DOS), band structure and dielectric function. The channel filling ions  $\text{B}^{m+}$  and water molecules (or hydroxyl groups) are considered to be strongly disordered and have been discarded in the calculation because of their minor importance and the computational burden. Aspherical corrections to the muffin tin approximation are introduced, finally by adding an empty sphere within the tubes. We have calculated selfconsistently the potential for the four crystals with 44 atoms per unit cell and an empty sphere centered in the tube. In the unit cell there are eight different inequivalent types of atoms. The lattice constants used for (K;Se),(Na;Se),(K;S),(Na;S) are  $a = 1.4595, 1.4423, 1.4318, 1.4152 \text{ nm}$  and  $c = 0.5617, 0.5565, 0.5633, 0.5576 \text{ nm}$ , resp. The  $2 \times 2 \times 1$  superstructure of (K;Se) (6) has not been taken into account.

The optical excitation energy  $E_{\text{Ex,opt}}$  has been determined from the plot of  $(\text{Ex})^2$  vs. Energy (inset in Fig. 2), which identifies the transition to be direct. The dc measurements show that all four compounds are poor conductors in the dark with an almost linear characteristic. From irradiation an increase of conductivity results with a distinct nonlinearity at low voltages of approx.  $\pm 1 \text{ V}$ . This may hint at a Coulomb attraction between the photo generated charge carriers. Fig. 2 shows the energy resolved photoconductivity of Na;Se. The onset wave length for the four phases corresponds to the respective optical band gap. Above, the conductivity is almost constant to drop at shorter wave lengths due to the decrease of (i) the penetration depth and (ii) the light intensity of the Xe-lamp. The values obtained are summarized in Tab. 1.



**Fig.1:** Structure of cetineite (Na;Se) onto the ab plane; the channel filling ions are left out in the plot

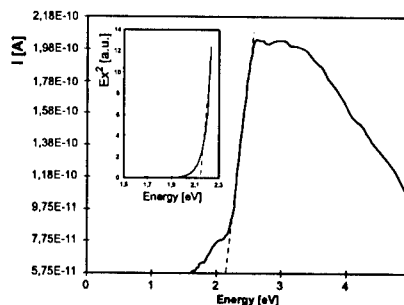


**Fig. 2:** Energy resolved photoconductivity and  $(\text{Ex})^2$  vs. Energy (inset) of (Na;Se) along c



Impedance measurements in dark and under irradiation with white light revealed a semicircle in the complex plane, indicating a Debye-like relaxation. The real part of the impedance obtained at the low frequency minimum of the semicircle corresponds to the dc resistance of the crystals. Thus the relaxation may be attributed to an electronic charge carrier relaxation in the volume of the crystals, which excludes significant ionic conductivity as could be suggested by the presence of water and/or by  $B^{m+}$  ions as well as interfacial polarization at the contacts.

As a prototype for these compounds the bandstructure of (Na;Se) has been calculated. It displays a stronger dispersion parallel to the c-axis, especially along the  $\Gamma$ A-direction, and a weaker one perpendicular to it. The binding is stronger along the tubes with main contributions occurring via Sb(2)- (Sb(3)- ) oxygen p bonds.

The fundamental gap is framed by states which to a significant degree are made up of orbitals belonging to the Sb and chalcogen atoms of the outer  $[SbX_3]^{3-}$  pyramids. The overall contribution of the antimony atoms becomes, mainly as p states, significant above the gap. The d states of the wall Sb atoms give an almost vanishing contribution within the first 4 eV ranges below and above the gap. The chalcogen X atoms are essentially of p-character and dominate together with the d states of Sb(1) the bound part of this energy range. The valence band maximum appears at the H-point and the conduction band minimum 0.2 eV above at the K-point. The direct gap of slightly more than 0.5 eV occurs at the K-point. The theoretical absorption, represented by the imaginary part of the dielectric function, shows a pronounced maximum if the field points parallel to the tube axes. Its dependence on the chemical composition (Fig. 3 (inset)) shows the same chemical trend as found in the onset of  $Im \epsilon$  above the fundamental gap. This maximum dominates also the extinction coefficient which together with the plot of the contributing transitions is displayed in Fig. 3 for Na;Se.

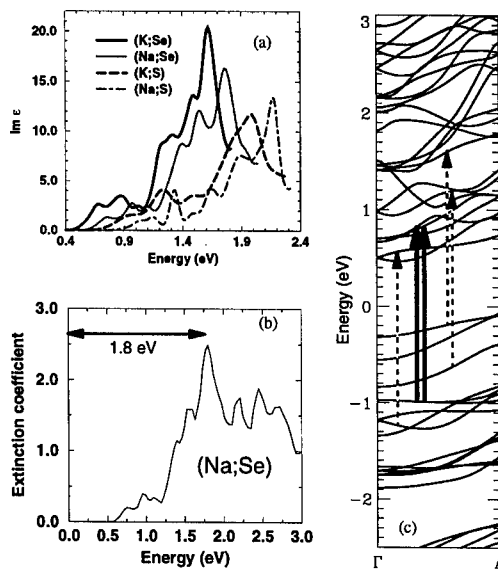


**Fig. 3:** In (a) the onset and the main maximum of the imaginary part of the dielectric functions for the four cetineites are shown for  $\vec{E} \parallel c$ . Associated with this, the extinction coefficient of (Na;Se) in (b) has a main peak at 1.8 eV. This peak results from a number of transitions the two most important (solid) of which and some minor ones (dashed) are shown in the band structure for  $\Gamma$ -A (c).

TABLE 1  
Experimental Band Gap  $E_{\text{Ex,opt}}$ , Energy of Maximum Absorption  $E_{\text{Ex,max}}$  and Fundamental Gap  $E_{\text{G,fund}}$  of Cetineites A;X

Compound (A;X)	$E_{\text{Ex,opt}}$ [eV]	$E_{\text{Ex,max}}$ [eV]	$E_{\text{G,fund}}$ [eV]
Na;S	2.38	2.18	0.82
K;S	2.29	1.98	0.68
Na;Se	2.12	1.77	0.54
K;Se	2.03	1.62	0.44

In the theoretical extinction coefficient two energy values can be derived characterizing each compound, i.e., (i) a fundamental band gap  $E_{\text{G,fund}}$ , which is the onset of the extinction coefficient, and (ii) the energy of maximum absorption  $E_{\text{Ex,max}}$ , which dominates the optical excitation of electrons. The respective values are summarized in Tab. 1. Whether the energetic coincidence of the maximum with the onset of the photoconductivity bears physical significance will be clarified by calculation of the conductivity which is in progress.

To conclude, we have selfconsistently calculated the electronic structure and optical properties of a most promising family of nanoporous compounds. A remarkable difference of more than 1 eV between the calculated fundamental band gap and the calculated pronounced maxima of absorption appears. The latter coincide in energy with the observed onsets of photoconductivity and absorption suggesting that at least the absorption measurements display the pronounced maxima in the frequency dependence of the dielectric function.

#### ACKNOWLEDGEMENTS

This work was supported by the "Deutsche Forschungsgemeinschaft" under contracts SI 609/2-1 and SCHA-360/14-1.

#### REFERENCES

1. G. Schmid (Ed.), *Clusters and Colloids* VCH, Weinheim, 1994
2. A.P. Alivisatos, J. Phys. Chem. **100**, 13226 (1996).
3. G. Schön and U. Simon, Colloid Polym. Sci. **273**, 101 (1995); idib. **273**, 202 (1995).
4. M. Reed, Sci. Am. **268**(1), 98 (1993).
5. F. Liebau and X. Wang, Beih. z. Eur. J. Mineral. **7**, **152** (1995); X. Wang, Z. Kristallog. **210**, 693 (1995).
6. U. Simon, F. Schüth, S. Schunk, X. Wang, and F. Liebau, Angew. Chem. Intern. Ed. Engl. **36**, 1121 (1997).
7. A. Trave, F. Buda, and A. Fasolino, Phys. Rev. Lett. **77**, 5405 (1996).
8. F. Starrost, E. E. Krasowskii, W. Schattke, J. Jockel, U. Simon, X. Wang, and F. Liebau, Phys. Rev. Lett. **89**, 3313 (1998)



Pergamon

NanoStructured Materials, Vol. 12, pp. 451–454, 1999

Elsevier Science Ltd

© 1999 Acta Metallurgica Inc.

Printed in the USA. All rights reserved

0965-9773/99/\$-see front matter

PII S0965-9773(99)00156-7

## LASER-INDUCED SYNTHESIS OF $\text{Al}_2\text{O}_3$ /CU-NANOPARTICLE MIXTURES

J. Naser and H. Ferkel

Institut für Werkstoffkunde und Werkstofftechnik, Technische Universität Clausthal,  
Agricolastrasse 6, D-38678 Clausthal-Zellerfeld

**Abstract** -- *Nanoscaled powder mixtures of the binary system  $\text{Al}_2\text{O}_3$  and Cu are produced by laser ablation from pressed  $\text{Al}_2\text{O}_3$  and CuO micro powder mixtures of various compositions with the pulsed radiation of a 1000W Nd:YAG-laser followed by condensation of the induced vapor in argon and hydrogen. The generated nanoparticles are analyzed regarding their grain size, crystalline structure and phase distribution in the powder by X-ray diffraction and transmission electron microscopy (TEM). The results reveal that any powder composition can be produced and that the different nanoparticle components are homogeneously distributed in the powder. ©1999 Acta Metallurgica Inc.*

### INTRODUCTION

The production of nanoscaled particles by ablation of solids with the radiation of a Nd:YAG laser is a useful technique for the production of single phased nanoparticles, nanoparticles mixtures as well as new phases (1-3). The particles have median diameters  $d_m$  less than 20 nm. The nanoparticles mixtures are generated during the particle synthesis in the laser-induced vapor. This technique is easy to handle, allows the generation of a large variety of nanopowder compositions and can be a key for the production of grainstabilized nanostructured materials. In this work we report on the generation and properties of various  $\gamma\text{-Al}_2\text{O}_3$ /Cu nanoparticle mixtures.

### EXPERIMENTAL

The nanoscaled particles were produced by ablation of pressed micro powder blends (pellets) of  $\alpha\text{-Al}_2\text{O}_3$  and CuO by the pulsed radiation of a Nd:YAG laser (wave length = 1064 nm) and subsequent condensation of the vapor in an Ar/H<sub>2</sub> atmosphere. H<sub>2</sub> was flushed directly into the nucleation zone of the particles and Ar was admitted by a bypass into the aggregation chamber. The Ar flow was kept constant at 6.5 l/min whereas the H<sub>2</sub> flow was varied between 0.25 l/min and 2 l/min. In order to modify the ratios of  $\text{Al}_2\text{O}_3$  to Cu in the nanopowders, pressed discs from micro powder mixtures with different amounts of alumina ( $\alpha\text{-Al}_2\text{O}_3$ , purity > 99.8 %,  $d_m = 2 \mu\text{m}$ ) and tenorite (CuO, purity >99.0 %,  $d_m = 10 \mu\text{m}$ ) were used as starting materials.

Samples containing 100, 80, 60, 40, and 20 wt.% of CuO were ablated. More details of the nanopowder fabrication plant are given elsewhere (3).

The nanopowders were inspected in a 200 kV TEM equipped with EDX detector and the structural measurements were also done by X-ray diffraction using  $\text{Cu}_{K\alpha}$  radiation.

### RESULTS AND DISCUSSION

Figure 1a displays XRD spectra of  $\text{Al}_2\text{O}_3/\text{Cu}$  nanoparticle mixtures produced from  $\text{Al}_2\text{O}_3/\text{CuO}$  micropowder pellets with 40 wt.% CuO at different  $\text{H}_2$  flows. As shown by the figure besides  $\gamma\text{-Al}_2\text{O}_3$  and metallic fcc-copper,  $\text{Cu}_2\text{O}$  can be found in the powder independent of experimental conditions. No CuO peaks appear in the spectra. The change in the modification of alumina (recall that the starting alumina has  $\alpha$ -structure) is generally observed in alumina nanopowder produced by Nd:YAG-laser radiation (2). The Cu portion in the nanopowder increases when the  $\text{H}_2$  flow is raised from 0.25 to 1 l/min. By further  $\text{H}_2$  increase a broadening of the Cu peaks in the spectrum is observed due to the decrease in  $d_m$  of the particles.  $d_m$  of the  $\text{Al}_2\text{O}_3$  and Cu nanoparticles were calculated from the full width of the half maximum of the peak intensities by the Scherrer formula and were found to be close to 10 nm. For the determination of the ratio  $\text{Al}_2\text{O}_3/\text{Cu}$  in the powder the surface under the  $\text{Al}_2\text{O}_3$  and Cu peaks has to be determined. The evaluation yields that from 1 to 2 l/min  $\text{H}_2$  flow no further increase of the Cu portion in the nanopowder was obtained. This behavior was proved by producing Cu nanopowder from pure CuO micropowder targets as shown in figure 1b. Here a significant decrease of the intensities of the  $\text{Cu}_2\text{O}$  portion was observed when the  $\text{H}_2$  flow was raised from 0.25 to 1.0 l/min. After a further increase of the  $\text{H}_2$  flow to 2.0 l/min only peak broadening occurs due to decreasing grain size. It was shown that the area under the  $\text{Cu}_2\text{O}$  and Cu peaks of the nanopowders produced with 1.0 and 2.0 l/min  $\text{H}_2$  are equal within the limits of error.

Figure 2 displays XRD spectra of  $\text{Al}_2\text{O}_3/\text{Cu}$  nanopowders produced from  $\text{Al}_2\text{O}_3/\text{CuO}$  micropowder discs with different contents of  $\text{Al}_2\text{O}_3$  at a  $\text{H}_2$  flow of 1 l/min. It is clearly shown that the ratio of Cu to  $\text{Al}_2\text{O}_3$  in the nanopowder can be easily varied by choosing different

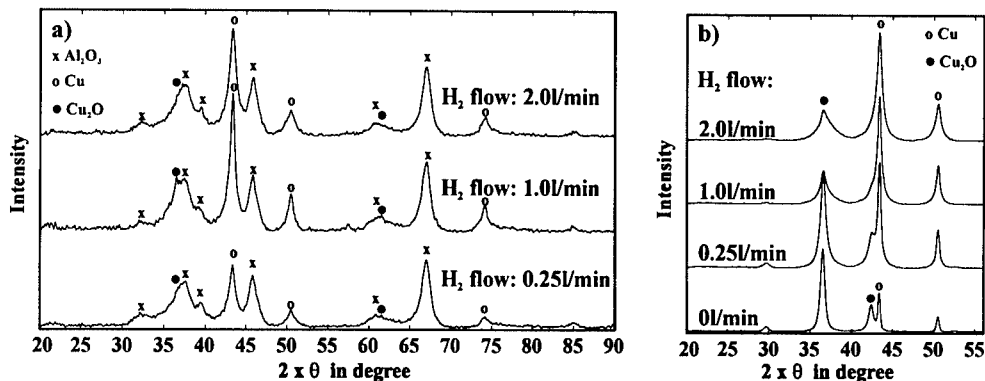


Figure 1. XRD spectra of nanopowders produced from  $\text{Al}_2\text{O}_3/\text{CuO}$  micropowder discs containing 40 wt.% CuO (a) and from CuO micropowder discs (b) at different  $\text{H}_2$  flows

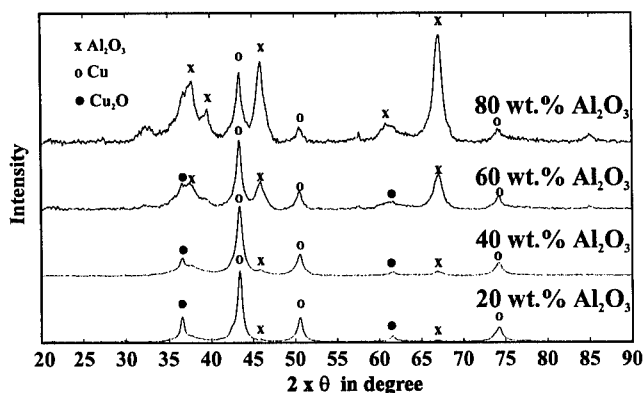


Figure 2. XRD spectra of  $\text{Al}_2\text{O}_3/\text{Cu}$  nanopowders produced with different contents of  $\text{Al}_2\text{O}_3$  in the micropowder pellets at a  $\text{H}_2$  flow of 1 l/min.

micropowder compositions in the pellets. Powder yields of more than 10 g/h at an average laser power of 1000 W can be reached.

It was also observed that at the beginning of powder fabrication the ratio of Cu to  $\text{Al}_2\text{O}_3$  in the produced nanopowder changes during the first few laser scans across the micropowder disc and approaches a constant ratio after the tenth scan and an equilibrium of the Cu to  $\text{Al}_2\text{O}_3$  ratio is reached. Compositions investigated in this work are all collected after the tenth laser scan.

In Figure 3 a bright and dark field TEM micrograph of the  $\text{Al}_2\text{O}_3/\text{Cu}$  nanopowder mixture containing 40 mol.% of alumina is shown. Some larger particles in the bright field image exhibit twinning (lower left corner of the micrograph) and can be identified by EDX as Cu nanoparticles. The bright particles in the dark field image (right part in Fig. 3) are Cu particles with their (111) zone axis parallel to the incident electron beam. The micrograph shows that the

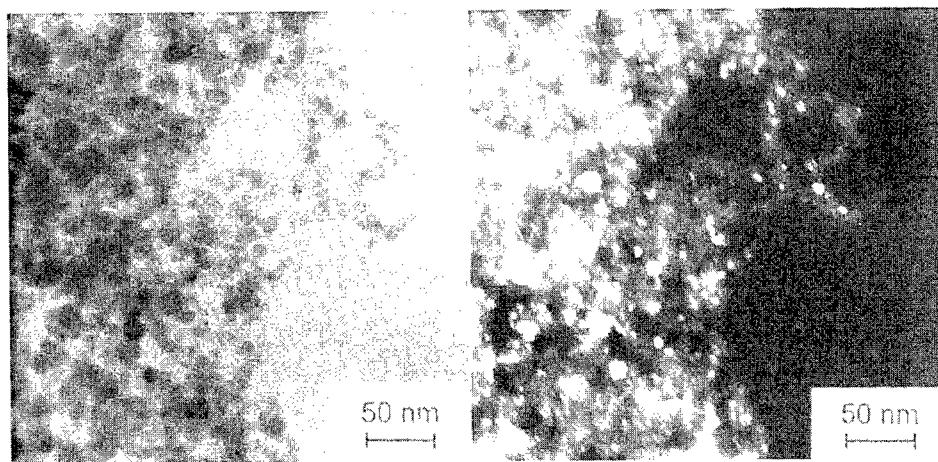


Figure 3. TEM micrograph of  $\text{Al}_2\text{O}_3/\text{Cu}$  nanopowder mixture containing 40 mol.%  $\text{Al}_2\text{O}_3$  (left) bright field image and (right) dark field image.

nanoparticles of different phase are homogeneously distributed in the powder. This is a requirement for the production of nanocomposites which resist grain growth at elevated temperatures.  $d_m$  of the  $\text{Al}_2\text{O}_3$  and Cu particles were determined from dark field images and were found to be less than 12 nm.

Finally nanoscaled  $\text{Al}_2\text{O}_3/\text{Cu}$  powder mixtures were synthesized from  $\text{Al}_2\text{O}_3/\text{CuO}$  micropowder with 60 wt.%  $\text{Al}_2\text{O}_3$  at a  $\text{H}_2$  flow of 1 l/min and from  $\text{Al}_2\text{O}_3/\text{Cu}$  micropowder with 70.7 wt.%  $\text{Al}_2\text{O}_3$  at a Ar flow of 1 l/min, respectively. This corresponds to a mol% ratio in both samples of  $\text{Al}_2\text{O}_3$  to Cu of 3 to 2. A comparison of XRD spectra taken from these powders (not shown here) reveals that both compositions are nearly identical and that both starting mixtures can be used for the production of the same nanopowder mixture whereby the first method yields about twice as much powder than the second one due to the high reflection of Cu in the pellets for the employed laser radiation. The result indicates that the  $\text{Cu}_2\text{O}$  found by XRD investigations in the powder is caused by oxidation of the copper nanoparticles during handling of the powder in air post production in  $\text{H}_2$ . When the powder was stored in air for several weeks an increase in the  $\text{Cu}_2\text{O}$  amount in the powders independent of the alumina content was observed as indicated by XRD analysis.

Experiments are underway to produce nanocrystalline  $\text{Al}_2\text{O}_3/\text{Cu}$  cermets by consolidation of laser generated nanopowder mixtures. It should be mentioned that  $\text{Al}_2\text{O}_3/\text{Cu}$  nanocomposites can also be produced by coablation of  $\text{Al}_2\text{O}_3/\text{CuO}$  targets in argon followed by consolidation of these oxide nanopowder mixtures at elevated temperature in hydrogen. These results will be given in a future publication.

## CONCLUSIONS

It has been shown that the  $\text{Al}_2\text{O}_3/\text{Cu}$  nanopowder mixtures of any compositions can be easily produced by laser ablation of different  $\text{Al}_2\text{O}_3/\text{CuO}$  micropowder blends in  $\text{H}_2$ . TEM, EDX and XRD investigations revealed that the constituents are homogeneously distributed in the powder and the particles have median particle diameters less than 12 nm. Powder yields of up to 20g/h at an average Nd:YAG-laser power of 1000W were achieved.

## ACKNOWLEDGEMENT

The authors would like to thank the German Research Council (Deutsche Forschungsgemeinschaft) for financial promotion and Prof. B.L. Mordike for his support.

## REFERENCES

1. G.F. Gaertner and H. Lydtin, *Nanostructured Materials* **4**, 559 (1994) and references cited therein.
2. H. Ferkel, and W. Riehemann, *Nanostructured Materials* **7**, 835 (1996).
3. H. Ferkel, J. Naser, and W. Riehemann, *Nanostructured Materials* **8**, 457 (1997).



Pergamon

NanoStructured Materials, Vol. 12, pp. 455–458, 1999  
Elsevier Science Ltd

© 1999 Acta Metallurgica Inc.  
Printed in the USA. All rights reserved  
0965-9773/99/\$-see front matter

PII S0965-9773(99)00157-9

## NANOCOMPOSITES PRODUCED BY MECHANICAL ALLOYING OF THE AL50FE25TI25 POWDERS MIXTURE

M. Krasnowski, V.I. Fadeeva\*, H. Matyja

Dept of Materials Science and Engineering, Warsaw University of Technology, Narbutta 85,  
02-524 Warsaw, Poland

\*Dept of Chemistry, Moscow State University, Vorobiovy Gory, 119899 Moscow, Russia

**Abstract** -- Nanocomposite powders were produced by high energy ball milling of the Al50-Fe25-Ti25 (at.%) powder mixture added with ethanol ( $C_2H_5OH$ ) and ammonium carbonate  $((NH_4)_2CO_3)$ . The phase transformations occurring in the material during the process were monitored by X-ray diffractometry and the structures of the milled samples were examined using transmission electron microscopy. The nanocrystalline composite powder, consisting of complex (Ti,Al)C carbide distributed in the Fe(Al) matrix was obtained as the final product of the milling with participation of ethanol whereas the process performed with an addition of ammonium carbonate led to the formation of (Ti,Al)N-Fe(Al) nanocomposite.

©1999 Acta Metallurgica Inc.

### INTRODUCTION

The formation of alloys by the solid state reaction that occurs during ball milling of elemental powders has been studied intensively over the last years. This process yields an amorphous, crystalline or nanocrystalline structure (1). Generally, a grain size reduction to the nanometer scale improves the physical and mechanical properties. Since this improvement is in this case substantial the mechanically alloyed nanocrystalline materials are attractive for many applications. The Al-Fe and Al-Ti alloys possess advantageous properties (2,3), in particular a high specific strength and a good corrosion resistance at elevated temperatures. The binary Al-Fe and Al-Ti alloys have been widely reported to be produced by mechanical alloying (MA) (4,5) whereas works concerning the ternary Al-Fe-Ti alloys obtained by MA are scarce. The addition of a third element to binary alloys mentioned above can improve their properties. It is known (6) that the phase composition of the MA final product depends on the environment in which the process takes place. In order to control the MA environment various agents neutral or active, are used. Active agents enter in a reaction with one of the milled elements.

The aim of this work was to study the structural and phase transformations that take place during the MA of the ternary Al50Fe25Ti25 alloy. One experiment was performed with an addition of ethanol and the other with addition of ammonium carbonate.

## EXPERIMENTAL

Elemental powder mixtures containing 50 at.% Al, 25 at.% Fe and 25 at.% Ti were mechanically alloyed using a Fritsch Pulverisette 5 planetary ball mill in an argon atmosphere at a ball-to-powder weight ratio of 15:1. In one process ethanol was added as the active agent in the amount of 5 % of the metal powder weight while the other process involved ammonium carbonate in about the same amount as the ethanol. The structural and phase changes in synthesised materials were examined by: X-ray diffraction (XRD) in a Philips 1830 diffractometer using  $\text{CuK}_\alpha$  and  $\text{CoK}_\alpha$  radiation, transmission electron microscopy (TEM) in a Philips EM300 and a JEOL 3010. Specimens for TEM investigations were prepared by embedding the milled powders into an aluminium matrix using the procedure described elsewhere (7) and also by suspending the powders in an epoxy resin. The samples were then dimpled and finally thinned by Ar ion beam milling using a precision ion polishing system.

## RESULTS AND DISCUSSION

Figure 1 (a) shows the XRD patterns of the powders after various times of milling with addition of ethanol. During MA, the Al peaks disappear gradually and all the Fe peaks become slightly shifted towards lower angles and broadened with increasing processing time.

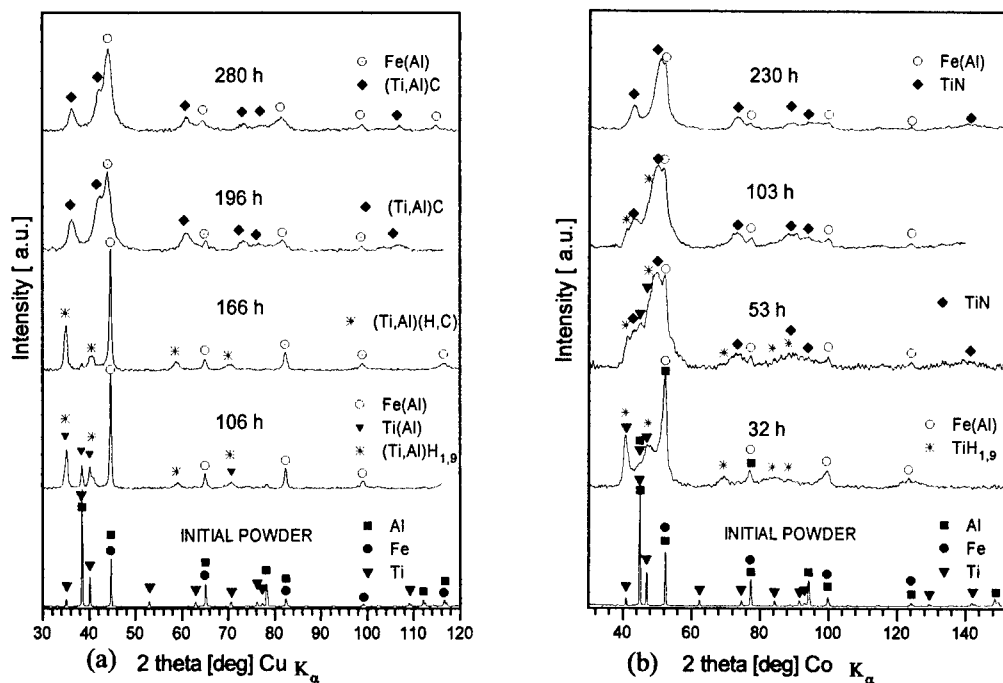


Figure 1. XRD patterns of powders after various times of milling (a) with ethanol, (b) with ammonium carbonate.



These changes suggest that a bcc Fe(Al) solid solution forms during the process. The Ti peaks are slightly shifted towards higher angles what can be due to Ti(Al) solid solution formation. Moreover the intensity of Ti(Al) peaks decreases with increasing milling time while new fcc phase peaks appear in the XRD patterns. This phase can be identified to be (Ti,Al)H<sub>1.9</sub> hydride at the early stage of milling, as (Ti,Al)(H,C)<sub>x</sub> hydrocarbide after milling up to 166 hours, and after the milling process is completed as (Ti,Al)C complex carbide with the fcc TiC lattice, but with the lattice parameter  $a_0 = 4.3 \text{ \AA}$ .

The TEM images and the corresponding selected area diffraction pattern (SADP) of the powders after 280 h of MA are shown in Figure 2. One can observe that, after the longest milling time, the structure of the powder particles becomes nanocrystalline with the crystallite size ranging from several to 20 nm. The final product obtained in this experiment is a nanocomposite built of (Ti,Al)C particles distributed in the Fe(Al) solid solution matrix.

The XRD patterns of the powder milled with ammonium carbonate are plotted in Figure 1 (b). In this case likewise in the process with ethanol during MA, the Al peaks disappear gradually and all the Fe peaks become slightly shifted towards lower angles and broadened. Also intensity of Ti peaks decreases and peaks of a new fcc phase are visible. The fcc phase can be identified as TiN nitride with the lattice parameter  $a_0 = 4.24 \text{ \AA}$ .

Figure 3 shows the TEM micrographs and the corresponding SADP of the powders milled with ammonium carbonate for 230 h. One can see that the structure of powder is nanocrystalline with crystallites sizes less than 10 nm.

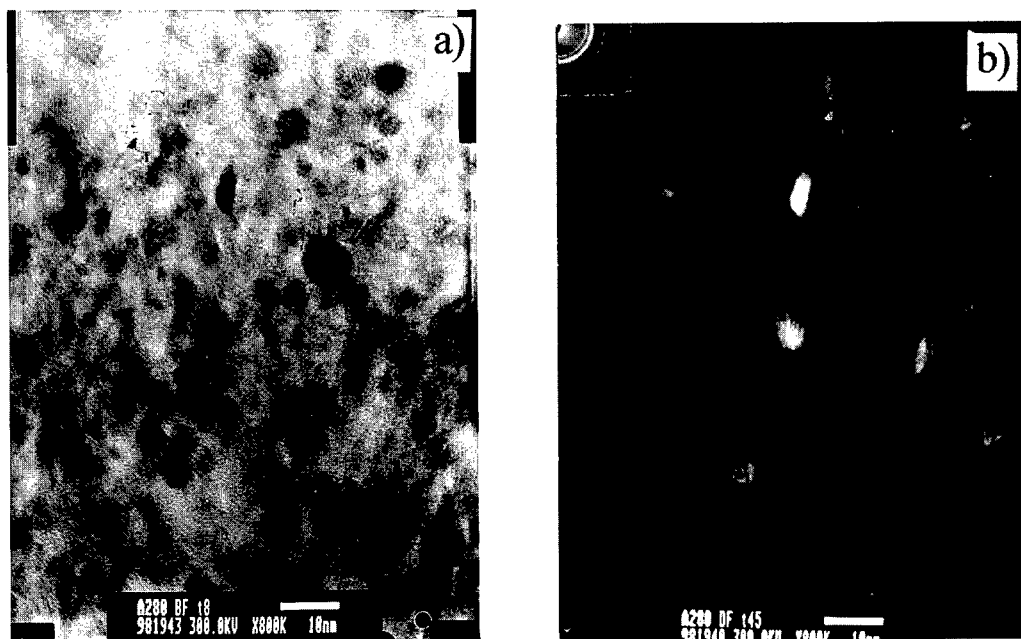


Figure 2. TEM micrographs of the powder milled with ethanol for 280 h: (a) bright field image, (b) dark field image taken using a part of the first and the second ring and the corresponding SADP.

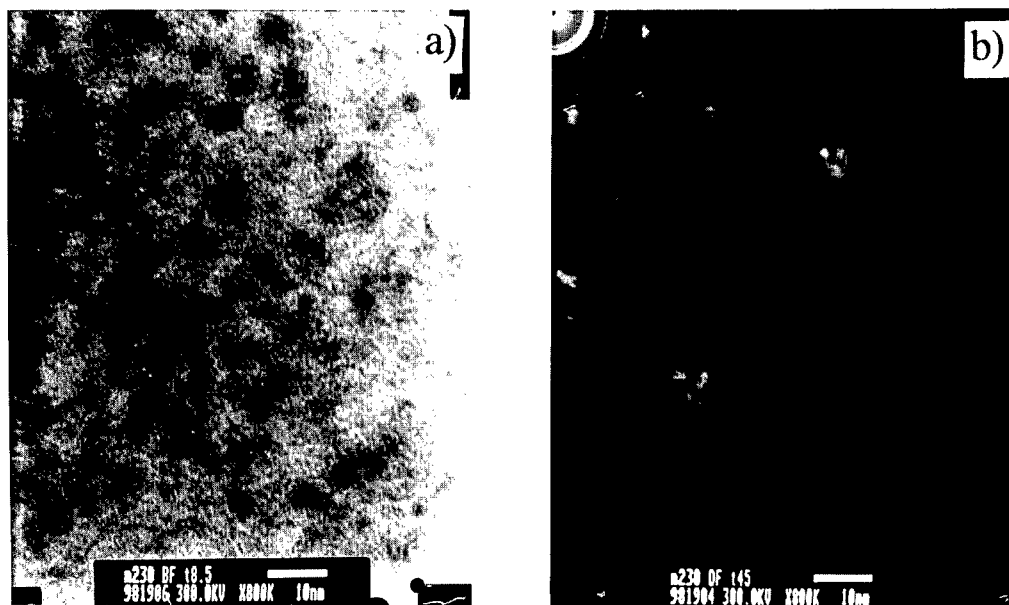


Figure 3. TEM micrographs of the powder milled with ammonium carbonate for 230 h: (a) bright field image, (b) dark field image taken using a part of the first and the second ring and corresponding SADP.

The concluding remark is: the nanocrystalline composite powder, consisting of (Ti,Al)C carbide distributed in the Fe(Al) matrix is the final product of MA of the Al50Fe25Ti25 powder mixture added with the ethanol whereas the same process performed with addition of the ammonium carbonate leads to the formation of TiN and Fe(Al) both nanocrystalline.

#### ACKNOWLEDGEMENTS

This work is supported by the Science Research Committee under the grant No. 7 T08D 007 14

#### REFERENCES

1. Koch C.C., *Mater. Trans. JIM*, 1995, **36**, 85.
2. Bonetti E., Scipione G., Enzo S., Frattini R. and Schiffini L., *Nanostr. Mater.*, 1995, **6**, 397.
3. Froes F. H., Suryanarayana C. and Eliezer D., *Journal of Mater. Sci.*, 1992, **27**, 5113.
4. Oleszak D. and Shingu P.H., *Mater. Sci. Eng. A*, 1994, **181/182**, 1217.
5. Itsukaichi T., Masuyama K., Umemoto M., Okane I. and Cabanas-Moreno J. G., *J. Mater. Res.*, 1993, **8**, 1817.
6. Cocco G., Mulas G. and Schiffini L., *Mater. Trans. JIM*, 1995, **36**, 150.
7. Angiolini M., Cardellini F., Krasnowski M., Mazzone G., Montone A. and Vittori-Antisari M., *Microsc, Microanal, Microstruct.*, 1995, **6**, 601.



## PREPARATION AND CHARACTERIZATION OF CdS AND ZnS NANOSIZED PARTICLES OBTAINED BY THE INERT GAS EVAPORATION METHOD

J.C. Sánchez-López, E.P. Reddy, T.C. Rojas, M.J. Sayagués, A. Justo, A. Fernández

Instituto de Ciencia de Materiales de Sevilla and Dpto. Química Inorgánica.

Centro de Investigaciones Científicas Isla de la Cartuja.

Avda. Américo Vespuccio s/n, 41092-Sevilla, Spain.

**Abstract**— *In the present paper we describe the preparation conditions to obtain CdS and ZnS nanocrystalline samples by the gas phase condensation method. The materials are constituted in both cases by very homogeneous spherical particles with a mean particle diameter of 8 and 15 nm respectively for the ZnS and CdS samples. Characterization has been carried out by X-ray diffraction (XRD) and transmission electron microscopy (TEM). High resolution images show that under certain conditions samples can be obtained with single crystallite grains of homogeneous size. Relative band-gap values have been determined from the UV-vis absorption spectra and correlated with quantum size effects for very small crystallite sizes in the nanostructured powders. ©1999 Acta Metallurgica Inc.*

### I. INTRODUCTION

Research focussed upon semiconductor nanostructured materials has become wide spread over the last year. In particular ZnS, CdS and also telluride compounds are some of the materials more widely investigated for the fabrication of optoelectronic devices (1,2). In addition, zinc and cadmium sulphide have been investigated as photocatalysts and for solar cell devices (3,4). Although the preparation of nanosized particles of ZnS and CdS have been widely studied by precipitation and stabilisation in micelles (5,6), to our knowledge there is no a previous study of the application of the inert gas evaporation method to the preparation of sulphide ultrafine powders. In the present paper we describe how this method leads, under adequated conditions, to the formation of ultrafine powders of ZnS and CdS formed by a very homogeneous distribution of spherical nanoparticles. Relative band gap values have been also determined from the UV-vis reflectance spectra.

### II. EXPERIMENTAL

The experimental “set-up” used for the synthesis of CdS and ZnS ultrafine powders consists of a small HV chamber pumped with a turbomolecular pump to a residual vacuum better than  $5 \times 10^{-7}$  Torr. Pressed pellets of commercial (from Aldrich) ZnS and CdS samples were evaporated on a tantalum boat at 1373 and 1173 K respectively. Helium was used at the gas phase at pressures of 1 and 0.5 Torr. The materials were collected on a cold copper substrate and passivated with oxygen before opening the chamber to air. The Cu substrate has two

regions: One in direct contact with a liquid nitrogen reservoir situated at a higher distance from the evaporation source and a second one situated at a shorter distance from the evaporation device. Two different portions of the sample have been collected according to the situation on the copper substrate.

TEM study of the samples was carried out in a Philips CM200 microscope working at 200 kV. The samples were dispersed in ethanol by sonication and dropped on a copper grid coated with a carbon film. XRD analysis was carried out using  $\text{CuK}\alpha$  radiation in a Siemens D5000 diffractometer. UV-vis absorption spectra were recorded for the powdered samples in the reflectance mode ( $R_\infty$ ) and transformed to a magnitude proportional to the extinction coefficient through the Kubelka-Munk function ( $F(R_\infty)$ ) (7). Measurements were carried out in a Shimadzu UV-2101 PC Spectrometer equipped with an integrating sphere accessory for diffuse reflectance.

### III. RESULTS AND DISCUSSION

Two representative micrographs of the CdS and ZnS nanocrystalline samples obtained at 1 Torr He pressure in the gas phase are included in Figure 1. The two samples have been collected on the substrate in direct contact with the liquid nitrogen reservoir. From several micrographs we have evaluated for the CdS sample a mean particle size of 15 nm and a particle size distribution ranging from 5 to 30 nm. In the case of ZnS a mean particle diameter of 8 nm has been measured with a particle size range from 6 to 12 nm.

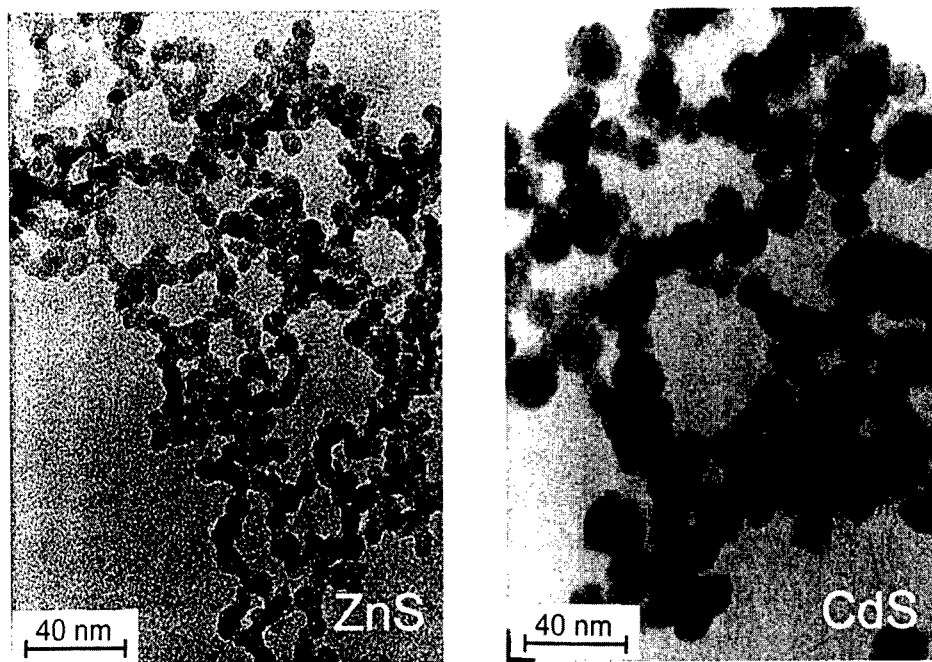


Figure 1. TEM micrographs for ZnS and CdS nanocrystalline powders prepared in 1 Torr He at the gas phase.

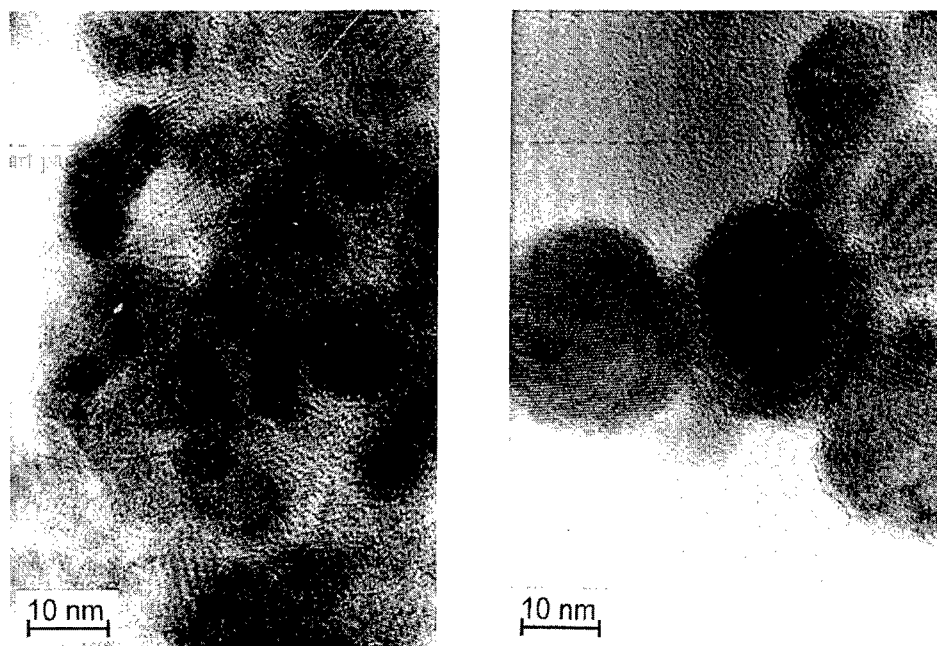


Figure 2. High Resolution TEM micrographs for CdS nanocrystalline samples prepared in 0.5 (left) and 1 (right) Torr He at the gas phase.

Several experiments have been carried out just by changing the He gas pressure and the collection point. It has been found that the preparation conditions are very critical to obtain the desired texture of homogeneous spherical grains. Figure 2 depicts two high resolution images corresponding to CdS samples obtained at 1 and 0.5 Torr Helium and collected on the colder part of the Cu substrate. It is clear in this figure the formation of almost single domain grains in the 1 Torr Helium preparation while the 0.5 Torr He condition leads to further aggregation of the particles. Different textures have been also achieved for the ZnS samples depending on the collection region of the Cu substrate. It should be also mentioned that samples collected near to the evaporation source can contain metallic Zn and Cd due to the decomposition of the sulfides.

The XRD patterns obtained for the original commercial ZnS and CdS materials show narrow peaks as corresponds to well crystallised CdS and ZnS mainly in the Greenockite and Sphalerite phases respectively. The nanocrystalline materials show very broad peaks as expected from the TEM images. In the case of ZnS a very small amount of wurtzite phase is formed in the nanocrystalline material.

Semiconductor crystallites in the diameter range of a few nanometers typically show a three-dimensional quantum size effect in their electronic structure and are referred as quantum dots. These quantum size effects on the band gap absorption energy can be measured by UV-vis absorption spectroscopy. In the present paper the nanostructured ZnS and CdS samples have been analyzed in respect to their optical properties by diffuse reflectance spectroscopy.

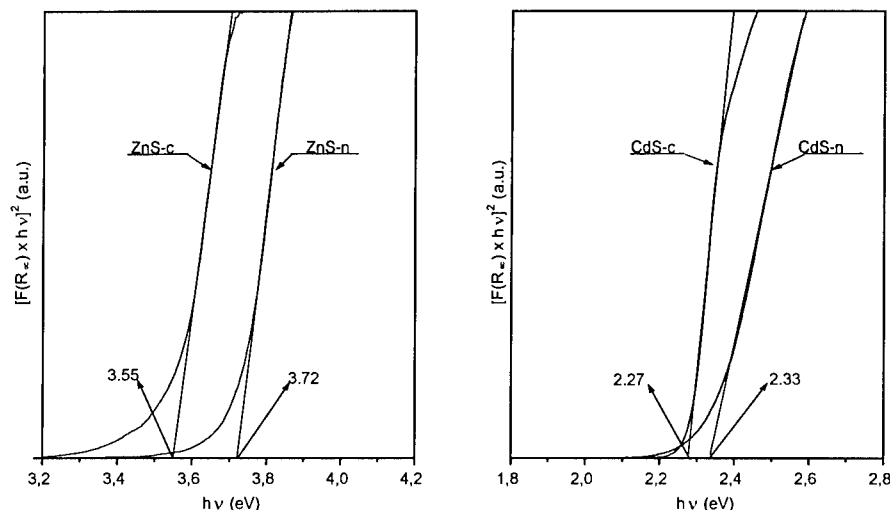


Figure 3. UV-vis absorption spectra in the band-gap region for ZnS (ZnS-n) and CdS (CdS-n) nanocrystalline powders prepared in 1 Torr He at the gas phase. Spectra for commercial ZnS (ZnS-c) and CdS (CdS-c) microcrystalline powders are also included as comparison.

We have plotted  $[F(R_{\infty}) \times hv]^2$  (where  $hv$  is the photon energy) against  $hv$ , as depicted in Figure 3. For direct interband transitions the linear portions of this curve can be extrapolated to absorption equal to zero (8) leading to relative band gap values. The nanocrystalline CdS and ZnS samples prepared at 1 Torr He and collected on the cold substrate, are compared in Figure 3 to the microcrystalline commercial samples. The observed blue shift of ca. 200 meV of the band-gap absorption edge of the nanocrystalline zinc sulfide sample in comparison to a commercial sample may be explained in terms of the quantum size effects previously observed for small semiconductor particles (9). This shift value is in good agreement with a mean particle diameter of 8 nm (9). In the case of the nanocrystalline CdS sample its higher mean particle size (15 nm) leads to a smaller band gap shift of 60 meV.

#### ACKNOWLEDGEMENTS

Authors thank the DGES (Project nr.: PB96-0863-C02-02) for financial support.

#### REFERENCES

1. Tsai, C.T., Chuu, D.S., Chen, G.L., Yang, S.L., *Journal Applied Physics*, 1996, 79, 9105.
2. Britt, J., Ferekides, C., *Applied Physic Letters*, 1993, 62, 2851.
3. Hetterich, W., Kisch, H., *Chemische Berichte*, 1989, 122, 621.
4. Chopra, K.L., Das, S.R., *Thin Film Solar Cells*, Plenum Press, New York, 1983.
5. Kamat, P.V., Patrick, B., *Journal of Physical Chemistry*, 1992, 96, 6829.
6. Korgel, B.A., Monbouquette, H.G., *Journal Physical Chemistry*, 1996, 100, 346.
7. Klier, K., *Catalysis Reviews*, 1967, 1, 207.
8. Zhang, D.H., Brodie, D.E., *Thin Solid Films*, 1992, 213, 109.
9. Brus, L., *Journal of Physical Chemistry*, 1986, 90, 2555.



Pergamon

NanoStructured Materials, Vol. 12, pp. 463–466, 1999

Elsevier Science Ltd

© 1999 Acta Metallurgica Inc.

Printed in the USA. All rights reserved

0965-9773/99/\$—see front matter

PII S0965-9773(99)00159-2

## NANOCRYSTALS AS STOICHIOMETRIC REAGENTS WITH UNIQUE SURFACE CHEMISTRY. NEW ADSORBENTS FOR AIR PURIFICATION

Abbas Khaleel, Weifeng Li, and Kenneth J. Klabunde

Department of Chemistry

Kansas State University

Manhattan, Kansas 66506, USA

**Abstract:** *Nanocrystals of MgO and CaO were prepared with high surface areas/gram, often as high as 500 m<sup>2</sup>/g [1]. These materials were investigated as adsorbents for typical volatile organic compounds that are representative of air pollutants. As a result of their high surface areas and their enhanced surface reactivity, nanocrystalline MgO and CaO have shown a remarkably high capacity to chemically adsorb such organic compounds. Compared to high surface area activated carbon, the most widely used material in this application, our nanocrystalline materials have shown much better adsorption in regards to the amount and the nature of adsorption. FT-IR investigation of acetaldehyde adsorption on AP-MgO indicates that a multilayer dissociative adsorption takes place as a result of surface interaction with the carbonyl bond followed by aldehydic hydrogen dissociation.*

©1999 Acta Metallurgica Inc.

### INTRODUCTION

Past work and current work has shown that nanocrystals of MgO, CaO and other oxides have a very high capacity for adsorption of toxic substances including SO<sub>2</sub>, chlorocarbons, military warfare agent mimics, and polar organic compounds[1]. The uniqueness of nanocrystalline MgO and CaO is due to two things: (1) huge surface areas, (2) enhanced surface reactivities which are due to their unusual crystal shape (polyhedral shapes with a high ratio of edge and corner surface sites that are inherently more reactive toward incoming adsorbates) [2].

Adsorption on solid surfaces has been one of the promising methods in removing volatile organic pollutants from air[3–5]. Although adsorption can occur on a variety of solid surfaces, only a few materials have adsorptive characteristics sufficiently favorable for air cleaning. These include activated carbon, zeolites, molecular sieves, silica gel and activated alumina. Herein we report the results of our investigation on the adsorption of several volatile organic molecules on nanocrystalline MgO as well as on nanoscale particles of activated carbon (for comparison). Due to the substantial concern about formaldehyde and other aldehydes as pollutants in air, we chose to study acetaldehyde in some detail.

## EXPERIMENTAL

Two systems were used in this study employing FT-IR spectroscopy to monitor the adsorption process. The first one involved a U-tube reactor equipped with a circulation pump that circulates the gas or vapor under study over the adsorbent in the system. FT-IR spectra were recorded for samples from the gas phase in the system over a period of time. The amount of reagent not adsorbed was obtained based on the integration of absorption bands in the IR spectra.

The second system involved an ultra high vacuum system equipped with FT-IR spectrometer. The adsorbent sample was pressed in a very thin film supported on a tungsten grid. The tungsten grid was mounted in an IR cell that can be heated to elevated temperatures or cooled down to low temperatures. The cell is also connected to a high vacuum system through which the adsorbates were admitted. Adsorbent samples were heated at 400 °C under vacuum for 12 hours and then cooled to room temperature under evacuation before exposure to the desired amount of adsorbate. After adsorption, the sample was evacuated at room temperature for two hours. FT-IR spectra were recorded for the solid before and after adsorption and evacuation. Temperatures were measured by a thermocouple positioned on the tungsten grid. All IR spectra were recorded on a Research Series 1 FT-IR Spectrometer from ATI Mattson.

The solid adsorbents discussed here included the following: autoclave prepared MgO (AP-MgO, surface area = 320-360 m<sup>2</sup>/g), Conventionally prepared MgO (CP-MgO, surface area = 100-140 m<sup>2</sup>/g), commercial MgO (CM-MgO, surface area = 30-40 m<sup>2</sup>/g) and activated carbon of surface area of 900 m<sup>2</sup>/g.

## RESULTS AND DISCUSSION

### *Adsorption of Acetaldehyde*

**a. Comparison of Different MgO Samples:** The capacity of AP-MgO, CP-MgO and CM-MgO samples to adsorb acetaldehyde was studied first, in the absence of air. Both the AP-MgO and CP-MgO were found to adsorb acetaldehyde in large quantities. One mole of AP-MgO adsorbed up to one mole acetaldehyde at room temperature over a short period of time. The adsorption was exothermic with considerable amount of heat evolved. The color of the solid sample changed dramatically from white-gray before adsorption to dark orange after adsorption. While the adsorption was very fast and vigorous on the AP- and CP-MgO samples, it was barely observed on the commercial MgO sample where no heat or color change were observed.

**b. MgO Compared to Activated Carbon and the Effect of Air Exposure:** We intended to compare the adsorptivity of our materials with that of activated carbon since activated carbon is the most widely used material in this application. We were also concerned about the effect of air on the performance of these materials. Figure 1 shows the results obtained from adsorption experiments, under atmospheric pressure of air, on samples exposed to open air and samples stored in an oven (60°C, under air) for different periods of time prior to



adsorption. Fresh samples of AP-MgO and commercial activated carbon, samples exposed to air for one day, samples exposed to air for ten days and samples stored in an oven for ten days were studied. From this study, we found that: first, exposure of AP-MgO to air has shown only a slight effect on the amount of adsorption. Second, under all conditions investigated nanocrystalline AP-MgO adsorbed much more acetaldehyde as compared to activated carbon.

c. **AP- MgO Powder Compared to Pelletized AP-MgO:** AP-MgO is obtained as a fine powder as prepared. For easier handling and volume minimization, it was pressed into pellets at 4000 psi prior to adsorption. The efficiency of adsorption on the pelletized sample was found to be very similar to that on powder samples (Figure 2). Adsorption on pellets has also produced a considerable amount of heat and changed the color of MgO to dark orange

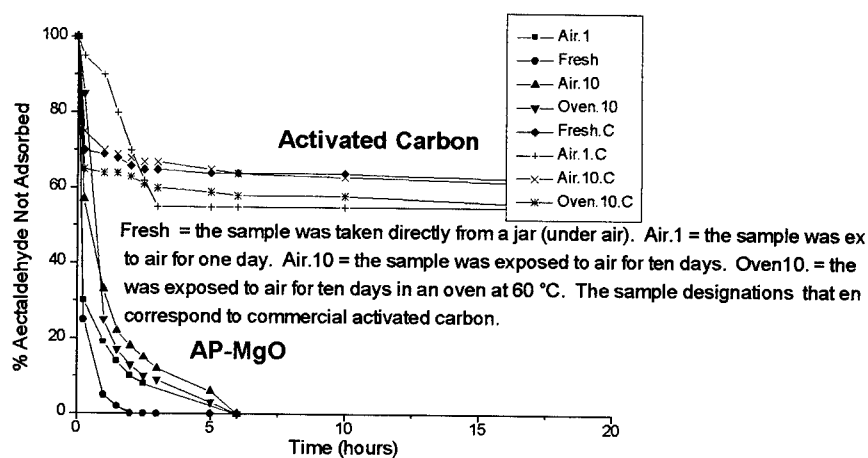


Figure 1. Adsorption of Acetaldehyde on AP-MgO and Activated Carbon. Air Effect.

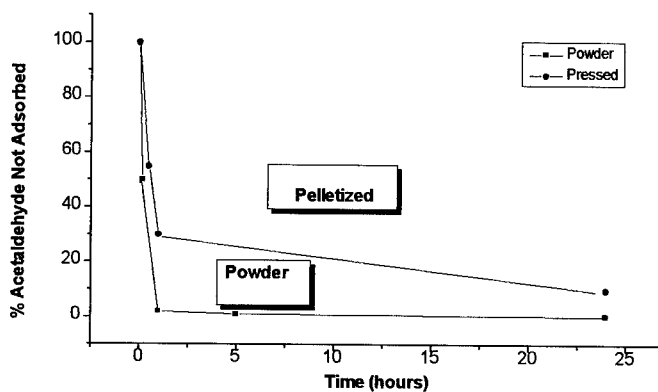


Figure 2. Adsorption of Acetaldehyde on Pelletized Vs. Powder AP-MgO

### *Adsorption of Other Organic Compounds*

Adsorption of other organic compounds including propionaldehyde, trimethylacetaldehyde, benzaldehyde, acetone, ammonia, dimethylamine, N-nitrosodimethylamine, and methanol was also investigated in a similar fashion. In our investigation of these compounds, we again found that nanoparticles of AP-MgO and CP-MgO possess a remarkably higher adsorptive capacity than activated carbon and commercial MgO. Using ten moles of MgO for every mole adsorbate, AP-MgO and CP-MgO dissociatively (as indicated by FT-IR spectra of the adsorbents after adsorption) adsorbed 60-80 % of these compounds over a period of ten hours while activated carbon physically adsorbed 10-40 % of them over the same period of time.

## CONCLUSIONS

- Nanocrystalline magnesium and calcium oxides were found to possess a remarkable potential to chemically adsorb a variety of volatile organic compounds.
- In the adsorption of acetaldehyde, the magnesium oxide surface has shown a special reactivity that has led to a multilayer dissociative adsorption of large amounts of the compound.
- MgO nanoparticles maintained their adsorptive potential to a good degree after their exposure to air or when the adsorption was performed under an atmospheric pressure of air.
- Compared to different activated carbon samples, nanocrystalline MgO adsorbed different organic compounds stronger and in much larger amounts.

## ACKNOWLEDGMENT

The financial support of the Indoor Air Research Center, Inc. is appreciated with gratitude.

## REFERENCES

1. Koper, O., *Ph.D thesis*, Department of Chemistry, Kansas State University, Manhattan, Kansas, USA, 1996, and references therein.
2. Stark, J., *M.S. thesis*, Department of Chemistry, Kansas State University, Manhattan, Kansas, USA, 1995.
3. Henrich, V. E. and Cox, P. A., *The Surface Science of Metal Oxides*, Cambridge University Press, Cambridge, 1994, P. 247.
4. Cordi, E. M. and Falconer, J. L., *J. of Catalysis*, **1996**, 162, 104.
5. Freun, H.-J., *Ber. Bunsenges. Phys. Chem.*, **1995**, 99, No. 11, 1261



## TRANSITION METAL DICHALCOGENIDE/POLYMER NANOCOMPOSITES

D. Yang, P. Westreich and R.F. Frindt

Department of Physics, Simon Fraser University  
Burnaby, British Columbia, Canada V5A 1S6

**Abstract**—Single molecular layers of transition metal dichalcogenides (TMDs) such as  $\text{MoS}_2$ ,  $\text{MoSe}_2$  and  $\text{WS}_2$ , have been formed in suspension in water by lithium intercalation of crystalline powders and then exfoliation in water. The two-dimensionality of such systems is readily identified using powder X-ray diffraction, where the strong asymmetric shape of the  $(hk0)$  peaks and the absence of  $(00\ell)$  peaks and mixed  $(hkl)$  peaks are observed. Water-soluble polymers, such as poly(ethylene oxide), poly(ethylene glycol) and poly(vinylpyrrolidone), can be encapsulated in TMD layers to form TMD/polymer lamellar nanocomposites. TMD/polymer nanocomposites are turbostratically restacked with the TMD layers parallel to each other with an expanded interlayer spacing due to the polymer insertion. The expansion of interlayer spacing varies from 8 to 22 Å and can be remarkably uniform. Highly oriented TMD/polymer films can be formed on glass substrates. ©1999 Acta Metallurgica Inc.

There has been considerable research activity in the synthesis of inorganic-polymer nanocomposites, especially for those where polymers are incorporated within layered compounds, resulting in a well-defined and expanded interlayer spacing. The host layered compounds include transition metal dichalcogenides<sup>1–4</sup>, clays<sup>4</sup>, layered metal oxides<sup>5–7</sup> ( $\text{MoO}_3$ ,  $\text{V}_2\text{O}_5$ ) and layered metal phosphorus chalcogenides<sup>4,8</sup> ( $\text{MPS}_3$ ).

An interesting property of layered transition metal dichalcogenides (TMDs), such as  $\text{WS}_2$ ,  $\text{MoS}_2$  and  $\text{MoSe}_2$ , is that they can be exfoliated to form single molecular layers in suspension in water<sup>9</sup>. An exfoliated molecular layer has a thickness of about 6 Å and a typical lateral size of up to a micron, and provides a convenient starting point for synthesis of TMD/polymer nanocomposites. By mixing a TMD single layer suspension with a polymer solution, polymer layers are adsorbed onto the basal planes of host TMD sheets and the sheets restack. This exfoliation-adsorption method is particularly useful for water soluble polymers.

The preparation technique for single molecular layers of TMDs has been described previously<sup>9</sup>. Briefly, it includes two steps: Li intercalation to form  $\text{LiMX}_2$  by soaking the TMD powder in a 2.5 M solution of butyl lithium in hexane for 24 hours (at room temperature for  $\text{MoS}_2$  and 100°C for  $\text{WS}_2$ ), and exfoliation of the Li-intercalated compound by immersion in distilled water. The two-dimensionality of the exfoliated single molecular layers of TMDs can be identified using powder X-ray diffraction. There are two unique features in the powder X-ray diffraction pattern of 2-D crystals<sup>10</sup>: (a) only  $(hk0)$  peaks result and all  $(00\ell)$  peaks are absent, due to the lack of periodicity in the third dimension; and (b) the line shape of Bragg peaks is

asymmetric, with a rapid increase on the low angle side and much slower decrease on the high angle side. Fig. 1 shows the X-ray diffraction patterns for  $\text{WS}_2$  single layers and  $\text{MoS}_2$  single layers. For comparison, Fig. 1 also shows the pattern for bulk 2H- $\text{WS}_2$  powders. The single layer samples used here are in a wet slurry form which contains 95% water by weight. The large amount of water in the samples is necessary to keep the single molecular layers apart and in random orientation. Fig. 1 clearly shows the 2-D features of the exfoliated  $\text{MoS}_2$  and  $\text{WS}_2$ , i.e., the presence of only (hk0) peaks in the pattern and the asymmetric shape of Bragg peaks. The asymmetric line shape for single layers is well demonstrated by the strongest (200) peak, which has a long tail on the high angle side. The line shape of the (200) peak for single layer  $\text{MoS}_2$  is quite different from that for single layer  $\text{WS}_2$ . This is due to the effect of structure factor modulation which occurs when the molecular layer contains more than one atomic sheet. The (200) peaks for exfoliated  $\text{MoS}_2$  and  $\text{WS}_2$  (Fig. b and c) correspond to the (100) peak in bulk  $\text{WS}_2$  due to the existence of a  $2a_0$  superlattice. The experimental diffraction patterns for single molecular layers of  $\text{MoS}_2$  and  $\text{WS}_2$  are in good agreement with calculated patterns<sup>10</sup>.

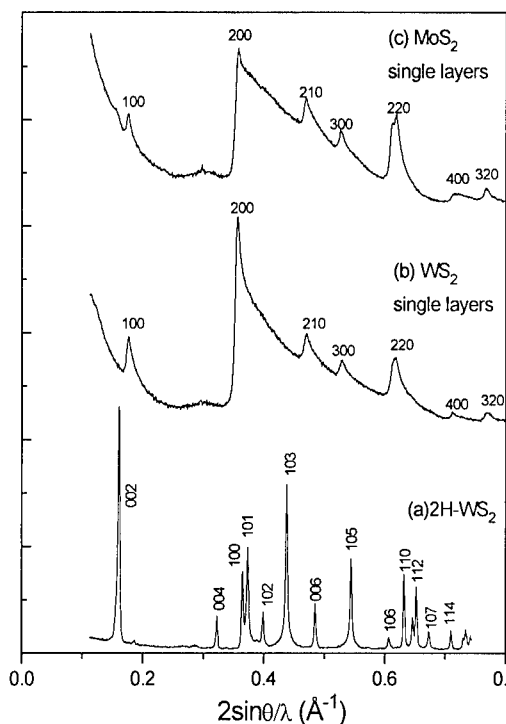


Fig.1 Powder x-ray diffraction patterns for (a) bulk 2H- $\text{WS}_2$ , (b) single layer  $\text{WS}_2$ , and (c) single layer  $\text{MoS}_2$ .

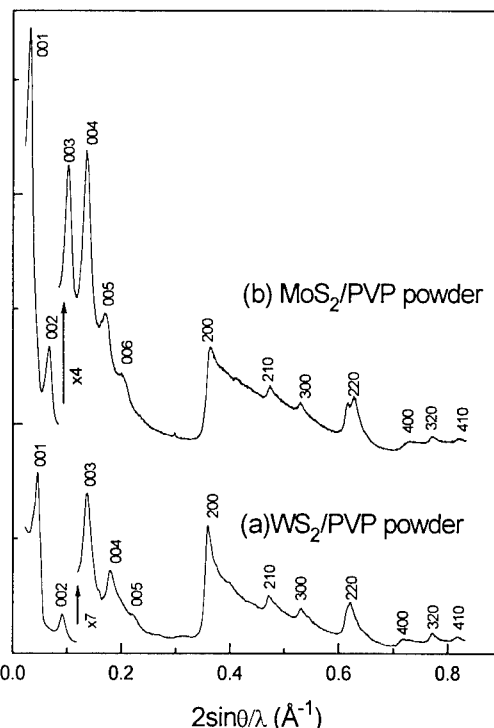


Fig.2 X-ray diffraction patterns for (a)  $\text{WS}_2(\text{PVP})_{0.74}$  nanocomposite (b)  $\text{MoS}_2(\text{PVP})_{0.94}$  nanocomposite, at a relative humidity of 38%.

The TMD/polymer nanocomposites were prepared as follows. A single layer suspension in water was mixed with a polymer solution (10-50 mg/ml). In the case of poly(ethylene oxide) (PEO) and poly(ethylene glycol) (PEG), the addition of the polymer solution causes immediate

flocculation of the  $\text{MoS}_2$  or  $\text{WS}_2$  suspension. For poly(vinylpyrrolidone) (PVP), no obvious flocculation was observed, but it is believed that the polymer is adsorbed on the basal planes of TMD layers. The mixture was centrifuged and decanted, and the remaining material was washed in distilled water and centrifuged twice to remove excess polymer. Finally the wet slurry was dried in vacuum for two hours and ground to form powder samples. The molecular ratio of polymer unit to  $\text{MoS}_2$  or  $\text{WS}_2$  was obtained by TGA experiments where the TMD/polymer nanocomposites were heated to  $500^\circ\text{C}$  and the weight loss due to the decomposition of the polymer was monitored.

Fig. 2 shows the powder diffraction patterns for  $\text{WS}_2(\text{PVP})_{0.74}$  and  $\text{MoS}_2(\text{PVP})_{0.94}$ . The patterns contain two sets of peaks: (00 $\ell$ ) peaks and (hk0) peaks. The (00 $\ell$ ) peaks are 3-D type with symmetric line shapes. The (hk0) peaks are 2-D type with strong asymmetric shapes, and are almost identical to the diffraction patterns for TMD single layers shown in Fig. 1. No mixed (hk $\ell$ ) peaks are observed in Fig. 2, demonstrating that the TMD/polymer nanocomposites are turbostratically-stacked<sup>11</sup>. Although there is a well-defined c-spacing ( $c=29.2$  Å for  $\text{MoS}_2(\text{PVP})_{0.94}$ ,  $c=25.0$  Å for  $\text{WS}_2(\text{PVP})_{0.74}$ ), these nanocomposites are not three-dimensional crystals. A turbostratically stacked system is like a pile of randomly stacked cards, where all layers are parallel to each other with the same interlayer spacing, but random in translation parallel to the layers and in rotation about the normal to the layers. The randomness in translation and rotation suppresses completely the mixed (hk $\ell$ ) peaks and makes the (hk0) peaks 2-dimensional.

There can be more than one interlayer spacing for a particular TMD/polymer nanocomposite. This is particularly true for TMD/PVP systems where by controlling the concentration of PVP solution during synthesis, we found three different phases, with c-spacings of 26.8 Å, 22.4 Å and 18.2 Å, respectively at a relative humidity (RH) of 0%. In some cases, mixed phases are observed. The inter-layer spacing for original unexfoliated powder is 6.15 Å for 2H- $\text{MoS}_2$ , and 6.18 Å for 2H- $\text{WS}_2$ . The inter-layer expansions over the original powder spacings for various nanocomposites are given in Table 1. It was observed that the inter-layer spacing increases by up to 5 Å as the relative humidity increases, due to the adsorption of water molecules. The data given in Table 1 were measured in dried air (RH=0%). There is no change in the interlayer expansion when  $\text{MoS}_2$  is replaced by  $\text{WS}_2$ .

Table 1. Nanocomposite Inter-layer Spacing, measured at RH=0%

nanocomposite	c-spacing(Å)	expansion(Å)	m.w. of polymer
$\text{MoS}_2(\text{PEO})_{1.4}$	14.3	8.1	1,000,000
$\text{MoS}_2(\text{PEG})_{1.4}$	14.2	8.0	1,000
$\text{MoS}_2(\text{PVP})_{0.94}$	26.8	20.6	10,000
$\text{MoS}_2(\text{PVP})_{0.74}$	22.5	16.3	10,000
$\text{MoS}_2(\text{PVP})_{0.53}$	18.2	12.0	10,000

Oriented TMD/polymer films can be formed by dropping or spreading a mixture of TMD single layer suspension and polymer solution onto a glass surface and then allowing the film to dry. Fig. 3 gives four X-ray diffraction patterns of such films for  $\text{MoS}_2(\text{PVP})_{0.74}$ ,  $\text{MoS}_2(\text{PVP})_{0.94}$ ,  $\text{MoS}_2(\text{PEG})_{1.4}$  and  $\text{MoS}_2(\text{PEO})_{1.4}$ , respectively. Only (00 $\ell$ ) peaks show up in these patterns,

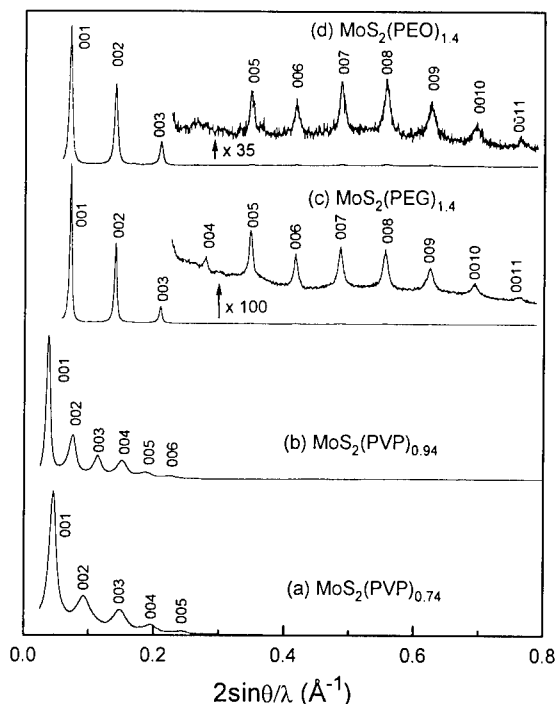


Fig. 3 X-ray diffraction patterns for oriented TMD/polymer films. The relative humidity is 0%.

indicating that these films are highly oriented with the layers parallel to the glass substrate. X-ray rocking curves typically give a layer misorientation halfwidth around  $\pm 4$  degrees. For the  $\text{MoS}_2(\text{PEG})_{1.4}$  and  $\text{MoS}_2(\text{PEO})_{1.4}$  films, more than 10 orders of (00 $l$ ) peaks are observed. We have observed up to 17 orders of (00 $l$ ) peaks for  $\text{WS}_2(\text{PEO})_{1.4}$  films. This implies that these films are remarkably well-ordered with a uniform interlayer spacing. On the other hand, only five or six (00 $l$ ) peaks are observed for  $\text{MoS}_2/\text{PVP}$  films. This can be attributed to a variation in the layer spacing which decreases the intensity of higher order reflections. The linewidths from Fig. 3 give coherence lengths normal to the layers of 200 Å for  $\text{MoS}_2(\text{PEO})_{1.4}$  and  $\text{MoS}_2(\text{PEG})_{1.4}$ , and 140 Å for  $\text{MoS}_2(\text{PVP})$ .

**Acknowledgment**-- We gratefully acknowledge the financial support of the Natural Sciences and Engineering Research Council of Canada.

#### References

1. H.L. Tsai, J.L. Schindler, C.R. Kannewurf and M.G. Kanatzidis, *Chem. Mater.* **9** 875(1997).
2. J.P. Lemmon, J. Wu, C. Oriakhi and M.M. Lerner, *Electrochimica Acta*, **40** 2245(1995).
3. C. Oriakhi, R.L. Nafshun and M.M. Lerner, *Mater. Res. Bull.*, **31** 1513(1996).
4. R.A. Vaia, S. Vasudevan, W. Krawiec, L.G. Scalton and E.P. Giannelis, *Adv. Mater.* **7** 154(1995).
5. Y.J. Liu, J.L. Schindler, D.C. DeGroot, C.R. Kannewurf, W. Hirpo and M.G. Kanatzidis, *Chem. Mater.* **8** 525(1996).
6. L. Wang, J.L. Schindler, C.R. Kannewurf and M.G. Kanatzidis, *J. Mater. Chem.* **7** 1277(1997).
7. H.P. Wang, B.C. Dave, F. Leroux, J. Harreld, B. Dunn and L.F. Nazar, *J. Mater. Chem.* **8** 1019(1998).
8. I. Lagadic, A. Leautic and R. Clement, *J. Chem. Soc., Chem. Commun.* 1396(1992).
9. P. Joensen, R.F. Frindt and S.R. Morrison, *Mater. Res. Bull.* **21**, 457 (1986).
10. D. Yang and R.F. Frindt, *J. Appl. Phys.* **79** 2376(1996)
11. D. Yang and R.F. Frindt, *J. Mater. Res.* **11**, 1733 (1996).



Pergamon

NanoStructured Materials, Vol. 12, pp. 471–474, 1999

Elsevier Science Ltd

© 1999 Acta Metallurgica Inc.

Printed in the USA. All rights reserved

0965-9773/99/\$—see front matter

PII S0965-9773(99)00161-0

## THE CHARACTERISTICS OF NANOSIZED $\text{TiO}_2$ POWDERS SYNTHESIZED BY CHEMICAL VAPOR CONDENSATION

S.Y. Kim, J.H. Yu and J.S. Lee

Department of Metallurgy and Materials Science,  
Hanyang University, Ansan, 425-791 KOREA

**Abstract** — *The effect of the ratio of  $\text{O}_2$ /He flow rate in the reactor on the characteristics of nanosized  $\text{TiO}_2$  powder synthesized by chemical vapor condensation process was investigated under fixed conditions of supersaturation ratio, collision rate and residence time. As the ratio of  $\text{O}_2$ /He flow rate increased, the particle size of  $\text{TiO}_2$  powder almost remained unchanged but the agglomeration of nanoparticles enlarged in which the degree of agglomeration was defined as the ratio of particle size to crystallite size. Based upon the reaction of  $\text{Ti}(\text{OR})_4 + 18\text{O}_2 \rightarrow \text{TiO}_2 + 14\text{H}_2\text{O} + 12\text{CO}_2$ , it is presumed that the water vapor released from the reaction of precursor with oxygen gas is responsible for the particle agglomeration.*

©1999 Acta Metallurgica Inc.

### INTRODUCTION

The chemical vapor condensation (CVC) process has been given enormous attention owing to the possibility of mass-production of monodispersed nanoscale ( $\sim 10$  nm) powders (1–3). However, the mechanism of powder synthesis kinetics is still not clear. This is mainly due to a lack of knowledge on the roles of thermodynamic and kinetic parameters which enable us to predict the process. In a chemical vapor process such as chemical vapor deposition, the oxygen reactant gas considerably affects the thermodynamics as well as kinetics of vapor reaction during the synthesis of oxide-film or particle. However, the influence of oxygen reactant gas in CVC process has not yet been fully understood. The present study has attempted to investigate the effect of oxygen content on the characteristics of nanosized  $\text{TiO}_2$  powder synthesized by the CVC process. For this purpose, the ratio of  $\text{O}_2$ /He flow rate in the reactor which is equivalent to oxygen content was chosen as an experimental parameter under fixed conditions of all the other thermodynamic and kinetic parameters such as reaction temperature, pressure, supersaturation ratio, collision rate and residence time (4).

### EXPERIMENTAL

Figure 1 shows a schematic diagram of the CVC system used in this experiment. Titanium-tetra-isopropoxide (TTIP, Sigma-Aldrich Co., 99.999%, boiling point  $232^\circ\text{C}$ ) used as

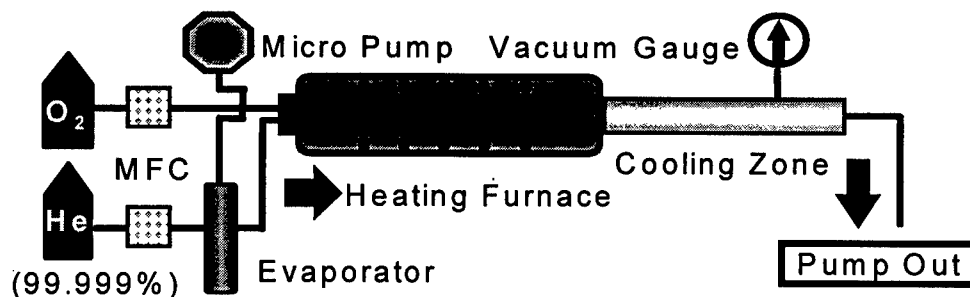


Figure 1. A schematic diagram of the CVC system.

a precursor was poured into the evaporator (held at 250°C) by micropump with a flow rate of 0.732 ml/min (5). The precursor vapor was delivered into the reaction furnace by He carrier gas in which it is decomposed and reacted with O<sub>2</sub> reactant gas. The total flow rate in the reactor was optimized at 3 slm on the basis of preliminary experiment. The flow rates of O<sub>2</sub> and He were varied to have various ratios of O<sub>2</sub>/He flow rate (0.5:1 to 3.0:1). The reaction temperature and pressure in the reactor were 1000°C and 10 mbar, respectively. The synthesized titania particles were deposited on the wall of the quartz cooling tube (held at room temperature) connected to the reactor. On the basis of the calculations of Knudsen number ( $Kn < 0.01$ ) and Reynolds constant ( $Re < 1$ ) (6), the laminar flow was assumed under this experimental condition. For the synthesized titania powders which were collected at the fixed position of the cooling tube, the phase identification and the measurement of crystallite size were conducted by X-ray diffractometry and BET analysis. The degree of agglomeration of the powder was determined by the size ratio of particle and crystallite,  $d_{BET}/d_{XRD}$  (7). The powder morphology and crystallinity were examined by TEM observation.

## RESULTS AND DISCUSSION

Figure 2 shows typical examples of TEM micrographs of titania powder synthesized with the ratio of O<sub>2</sub>/He = 2.0:1. It is seen that the powders consist of (a) loosely bond particles of about 20~30 nm and also (b) very fine particles less than 5 nm size. X-ray diffraction patterns for various ratios of O<sub>2</sub>/He are represented in Figure 3. Major part of the powders is composed of anatase phase and only a small amount of rutile phase is formed simultaneously. It appeared that the formation of rutile phase is not affected by the oxygen content.

Figure 4(a) and (b) show the variations of the crystallite size  $d_{XRD}$  and the particle size  $d_{BET}$  and their ratio  $d_{BET}/d_{XRD}$  as a function of O<sub>2</sub>/He ratio. The crystallite size and the particle size were evaluated from the XRD result by Scherrer formula and BET measurement. It seems from Figure 4(a) that the mean crystallite size of the powder does not change with varying O<sub>2</sub>/He ratio. To the contrary, the particle size measured by BET slightly increases with the oxygen ratio. Such discrepancy in the size of the powders is intuitively thought to result from the agglomeration of the powder. The result of the degree of agglomeration,  $d_{BET}/d_{XRD}$ , is shown in Figure 4(b), where the solid line of  $d_{BET}/d_{XRD}=1$  indicates non-agglomeration state of



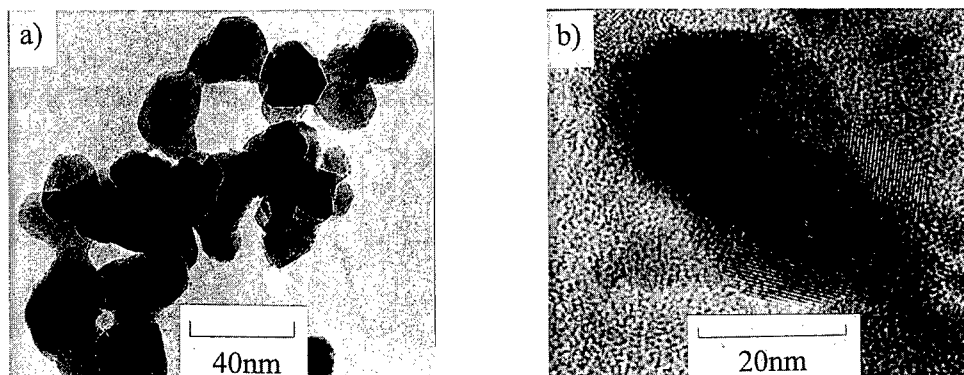
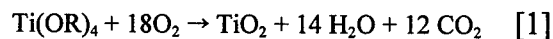


Figure 2. TEM micrographs of titania powder synthesized with the  $O_2/He$  ratio of 2.0:1.

the powder. However, as the ratio of  $O_2/He$  flow rate increases, the agglomeration becomes enlarged. Concerning this phenomena, presumably the influence of water vapor as by-product phase of the CVC reaction can be mentioned. The CVC reaction for titania powder is described as follows;



The reaction implies that the increasing oxygen content in the reactor may release a large amount of water vapor while the oxygen reacts with the decomposed alkoxide phase.

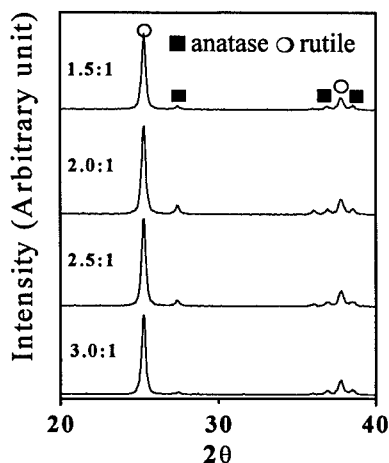


Figure 3. X-ray diffraction patterns of titania powders for various  $O_2/He$  ratios.

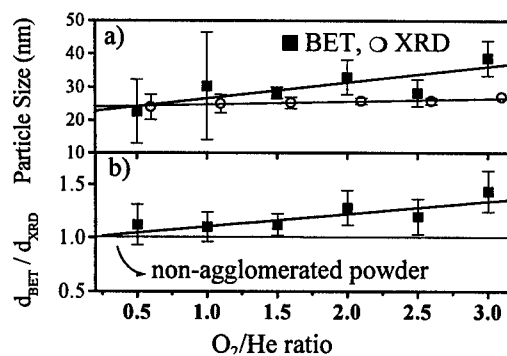


Figure 4. (a) Particles and crystallite size (b) degree of agglomeration calculated by  $d_{BET}/d_{XRD}$ ,  $O_2/He$  ratio.

As a result, the probability of capturing the particles by water vapor during the reaction becomes higher, resulting in the powder agglomeration. From these results, it can be concluded that the oxygen gas plays an important role for the powder agglomeration. Thus, in order to reduce the powder agglomeration, the control of surplus oxygen content in the process is very important.

### CONCLUSION

The effect of the ratio of  $O_2/He$  flow rate on the characteristics of nanosized titania powder synthesized by chemical vapor condensation process was investigated. It was found that the ratio of  $O_2/He$  flow rate almost does not affect particle size whereas it rather enlarges particle agglomeration. It is presumed on the basis of reaction [1] that the water vapor released from the reaction of precursor with oxygen gas is responsible for the agglomeration.

### ACKNOWLEDGEMENT

The authors gratefully acknowledge the financial support of the Korean Ministry of Science and Technology.

### REFERENCES

1. Chang, W., Skandan, G., Danforth, S.C., Kear, B.H., and Hahn, H., *NanoStructured Materials*, 1994, **4**, 5, 507.
2. Ennis, B.J., Green, J. and Davies, R., *Chemical Engineering Progress*, 1994, 32.
3. Kear, B.H. and Scandan, G., *NanoStructured Materials*, 1997, **8**, 6, 765.
4. Sivaram, S., *Chemical Vapor Deposition*, Van Nostrand Reinhold, 1990, p.10.
5. Schleich, D.M. and Walter, B., *NanoStructured Materials*, 1997, **8**, 5, 579.
6. Geiger, G.H. and Poirier, D.R., *Transport Phenomena in Metallurgy*, Addison-Wesley Publishing Co., Massachusetts, 1972, p.50.
7. Guillou, N., Nistor, L.C., Fuess, H., and Hahn, H., *NanoStructured Materials*, **8**, 5, 1997, 545.



Pergamon

NanoStructured Materials, Vol. 12, pp. 475-478, 1999

Elsevier Science Ltd

© 1999 Acta Metallurgica Inc.

Printed in the USA. All rights reserved

0965-9773/99/\$-see front matter

PII S0965-9773(99)00162-2

## MECHANO-CHEMICAL SYNTHESIS OF NANOSIZED STAINLESS STEEL POWDER

J.G. Nam and J.S. Lee

Department of Metallurgy and Materials Science,  
Hanyang University, Ansan, 425-791 KOREA

**Abstract** --- The present investigation has attempted to fabricate nanosized stainless steel powder of Fe-18Cr-8Ni(wt%) by mechano-chemical synthesis. The synthesis process was conducted by hydrogen reduction of a high energy ball milled mixture of  $\text{Fe}_2\text{O}_3$ -NiO- $\text{Cr}(\text{NO}_3)_3 \cdot 9\text{H}_2\text{O}$ . In-situ alloying of Ni-Fe-Cr nanophase simultaneously occurring during reduction process is presumably responsible for the formation of nanophase stainless steel powders. The powder characteristics were examined by X-ray diffractometry and SEM observation. The kinetic phenomena in association with the oxide reduction and the alloying process were investigated by thermogravimetry, hygrometry and X-ray diffractometry, and discussed in relation to powder characteristics. ©1999 Acta Metallurgica Inc.

### INTRODUCTION

Recently, nanosized  $\gamma$ -Ni-Fe alloy powder has been reported to be synthesized by mechano-chemical process by hydrogen reduction of ball milled metal oxide mixture (1). It seems that in-situ alloying of  $\gamma$ -Ni-Fe nanophase occurring during reduction effectively initiates the nanoparticle formation (2-4). From a technological viewpoint, the nanoalloy powder has great potential for applications to precision structural- and functional parts processed especially by near-net-shaping powder metallurgical (PM) route. As an example, stainless steel PM parts fabricated by powder injection molding process is mentioned. The present investigation has attempted to extend the in-situ alloying concept to fabrication of nanosized stainless steel powder. For this purpose, Fe-18Cr-8Ni corresponding to austenitic 304 stainless steel was chosen as a material system. The in-situ alloying process during hydrogen reduction of ball milled oxide mixture was investigated and discussed in terms of phase decomposition and powder characteristics.

### EXPERIMENTAL

Nanocrystalline Fe-18Cr-8Ni(in wt%) powder was attempted to be synthesized by hydrogen reduction of ball milled powder mixture of  $\text{Fe}_2\text{O}_3$  (99.9%, 1 $\mu\text{m}$ ), NiO (99.9%, 7 $\mu\text{m}$ ) and  $\text{Cr}(\text{NO}_3)_3 \cdot 9\text{H}_2\text{O}$  (99%). The use of hydrous chromium nitrate instead of chromium oxide is due to the faster decomposition of the latter at lower temperature. The ball milling was

conducted in an attritor with a speed of 300 rpm for 1 hour. The control of composition was aimed at having a final composition of Fe-18Cr-8Ni. The ball media and impeller were made of stainless steel and the milling agent was methyl alcohol. After ball milling, the powder mixture was dried at 60°C for 48 hours. The powders were heated by raising the temperature up to 800°C with 10°C/min or isothermally holding at 600°C in hydrogen gas atmosphere (dew point -76°C). The weight loss by decomposition during heat up was monitored by thermogravimetry (TG). The hygrometry system for measuring the content of water vapor in outlet gas was connected with the TG system in order to make both measurements simultaneously (5). The X-ray diffraction analysis was performed to identify the phase by the decomposition. The powder characteristics such as morphology and particle size were examined by FE-SEM.

## RESULTS AND DISCUSSION

Figure 1 shows the TG curve from a thermogravimetry experiment for the hydrogen reduction of a powder mixture of  $\text{Fe}_2\text{O}_3$ , NiO and  $\text{Cr}(\text{NO}_3)_3 \cdot x\text{H}_2\text{O}$  and it also represents the weight loss rate during heat up obtained from the derivative of the TG curve. It is seen from both curves that the powder mixture undergoes a weight loss at three different temperatures. The first part of the reaction is due to the removal of water from the compound  $\text{Cr}(\text{NO}_3)_3 \cdot x\text{H}_2\text{O}$  below 200°C, subsequently followed by reductions of NiO and  $\text{Fe}_2\text{O}_3$ , respectively.

The result of the hygrometry study shown in Figure 2 is in good agreement with the differential TG curve (Figure 1) for the whole temperature range. This indicates that the weight loss during heat up is basically due to the removal of water vapor generated by hydrogen reduction of the metal oxides. Moreover, in case of  $\text{Cr}(\text{NO}_3)_3 \cdot x\text{H}_2\text{O}$ , a large amount of water vapor gives rise to the first large peak in differential TG as well as hygrometry curves. It is thought that Cr is produced by decomposition of nitrate phase by hydrogen reduction even at lower temperature owing to large surface area of Cr nitrate salt. Preliminary experiment on the decomposition of only confirmed that  $\text{Cr}(\text{NO}_3)_3 \cdot x\text{H}_2\text{O}$  was completely decomposed into Cr

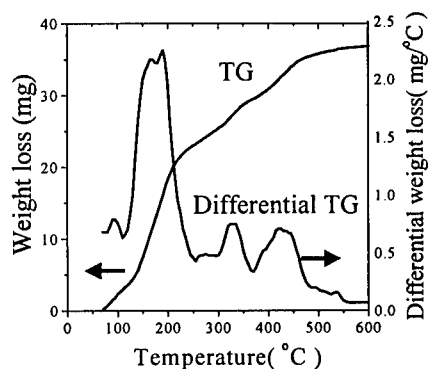


Figure 1. Thermogravimetric curve and differential thermogravimetric curve.

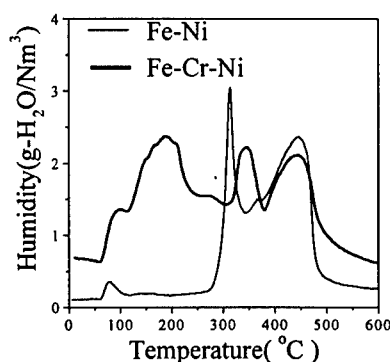


Figure 2. Hygrometric curves of  $\text{Fe}_2\text{O}_3$ -NiO and  $\text{Fe}_2\text{O}_3$ -NiO- $\text{Cr}(\text{NO}_3)_3 \cdot x\text{H}_2\text{O}$ .

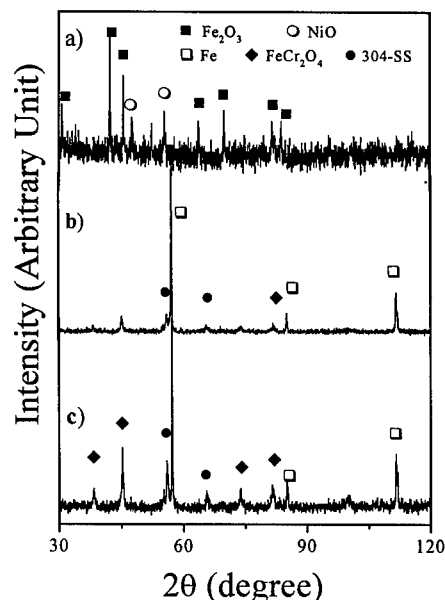


Figure 3. X-ray diffraction patterns of a) ball milled mixture powder and b) powders reduced by heating up to 800°C with 10°C/min and c) isothermal heating at 600°C.

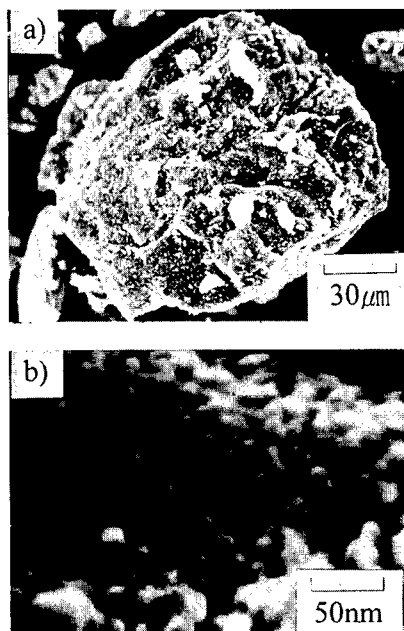


Figure 4. SEM micrographs of a) agglomerate and b) particles of powder obtained during heat up to 800°C with 10°C/min.

phase at 200°C. What is interesting in Figure 2 is that the early decomposition of Cr nitrate salt compound retards the subsequent reduction process of NiO. In comparison to the case of equally treated NiO-Fe<sub>2</sub>O<sub>3</sub> (1), the nickel oxide in the present experiment started to be reduced at a higher temperature of 310°C. As described above, it is thought that a large amount of water vapor generated from the decomposition of the compound may lead to unfavorable thermodynamic conditions for subsequent reduction reaction of NiO. However, the reaction for Fe<sub>2</sub>O<sub>3</sub> reduction appears not to be affected by this effect.

X-ray diffraction results of Figure 3 identify the phases formed by the reduction process during (b) heat up as well as (c) isothermal. The peak (a) of as dried sample shows a not decomposed mixture which consists of Fe<sub>2</sub>O<sub>3</sub> and NiO, where the absence of Cr(NO<sub>3</sub>)<sub>3</sub>·xH<sub>2</sub>O peak is ascribed by noncrystallinity of the compound phase. In the course of the reduction process, however, the oxide peaks have disappeared and as a consequence the metal phases are formed. In both cases X-ray diffraction peaks are composed of the same phases of Fe, FeCr<sub>2</sub>O<sub>4</sub> and the γ-phase which corresponds to the 304 stainless steel phase. The peak intensity of the γ-phase is higher in the isothermally treated sample than in the only heated-up one. It implies that the prolonged heating results in an increase of γ-phase formation and also FeCr<sub>2</sub>O<sub>4</sub>. Obviously, the occurrence of these two phases is very meaningful because they are produced from the reaction between Cr and the rest components in the powders. The retention of Cr phase in metallic state is difficult because of its strong affinity to oxygen. After decomposition of

$\text{Cr}(\text{NO}_3)_3 \cdot x\text{H}_2\text{O}$  at lower temperature a large volume of water vapor can be generated which might retard the subsequent reduction of  $\text{NiO}$ . It might be expected also that the decomposed Cr phase can be alloyed to form either  $\gamma$ -phase or a complex oxide as  $\text{FeCr}_2\text{O}_4$  depending on the thermodynamic conditions. This phenomenon can also be regarded as an in-situ alloying process as in the case of nanocrystalline  $\gamma$ -Ni-Fe powder (1). Particle size obtained from the Scherrer equation for X-ray peaks was 22nm for  $\text{FeCr}_2\text{O}_4$  and  $\gamma$ -phase respectively and 76 nm for Fe.

Figure 4 shows the morphology of the reduced powder attained by reducing the powder during heat up and quenching. It is seen that the coarse agglomerate (Figure 4a) consists of 20~30 nm particles (Figure 4b). It is intuitively concluded that these nanoparticle phase might be either  $\gamma$ -phase or  $\text{FeCr}_2\text{O}_4$  comparing with the crystallite size as described above.

### CONCLUSION

The most important finding of the present study is to discover a possibility of fabricating nanosized austenitic stainless steel powder of Fe-18Cr-8Ni(wt%) by mechano-chemical synthesis. In-situ alloying process might be responsible for the formation of nanophase stainless steel particle, which is mainly controlled by thermodynamic and kinetic conditions at reaction zone in the powder. Specially, a large amount of water vapor released by the decomposition of  $\text{Cr}(\text{NO}_3)_3 \cdot x\text{H}_2\text{O}$  presumably inhibits the alloying reaction through retarding subsequent oxide reduction process. However, this may not be the case for the reduction of  $\text{Fe}_2\text{O}_3$ . Based upon these results the aim of further investigation will be to understand the alloying mechanism relating to reduction process. A systematic study for finding optimized fabrication conditions of 304 stainless steel nanopowder is under way.

### ACKNOWLEDGEMENTS

The authors gratefully acknowledge the financial support of the Engineering Research Center for Interface Science and Technology of Materials.

### REFERENCES

1. Lee, J.S., Kim, T.H., Yu, J.H., and Chung, S.W., *Nanostructured Materials*, 1997, **2**, 153.
2. Yasuda, H. and Mori, H., *Annales de Physique Colloque C2*, Supplement au n°3, 1997, **22**, C2-27.
3. Yasuda, H. and Mori, H., *Physical Review Letters*, 1992, **69**, 26, 3747.
4. Mori, H. and Yasuda, H., *Journal of Microscopy*, 1995, **180**, 33.
5. Kim, T.H., Yu, J.H. and Lee, J.S., *Nanostructured Materials*, 1997, **2**, 213.



Pergamon

NanoStructured Materials, Vol. 12, pp. 479–482, 1999

Elsevier Science Ltd

© 1999 Acta Metallurgica Inc.

Printed in the USA. All rights reserved

0965-9773/99/\$—see front matter

PII S0965-9773(99)00163-4

## DENSIFICATION AND MICROSTRUCTURAL DEVELOPMENT OF NANOCRYSTALLINE $\gamma$ -Ni-Fe POWDERS DURING SINTERING

P. Knorr, J.G. Nam and J.S. Lee

Department of Metallurgy and Materials Science  
Hanyang University, Ansan, 425-791 Korea

**Abstract** -- The sintering behavior of nanocrystalline (nc)  $\gamma$ -Ni-Fe powders was investigated by laser-photo-dilatometry. The sinterability of nc powders was found to depend crucially on the state of agglomeration. The compacted  $\gamma$ -Ni-Fe powders exhibited a bimodal pore distribution comprised of nanoscale intra-agglomerate pores and large, microscale inter-agglomerate pores. The results are discussed on the basis of the microstructural evolution during densification which was followed by optical microscopy and BET specific surface area measurements. ©1999 Acta Metallurgica Inc.

### INTRODUCTION

The potential application of nanoscale materials as novel structural or functional engineering materials largely depends on the consolidation of powders into bulk nanoscale solids. The retention of the metastable microstructure in the course of this consolidation process is mandatory for preserving the often superior mechanical, magnetic or catalytic properties of the material (1). Pressure-assisted sintering proves adequate for both reaching full density and preventing grain coarsening (2). Both objectives can hardly be achieved by pressureless sintering. However, pressureless sintering is inevitable for the consolidation of near-net-shaped powders as in the case of powder injection molding. The present paper reports on investigations of the pressureless sintering of nc  $\gamma$ -Ni-Fe powders which were fabricated by mechano-chemical synthesis (3). Several communications have been dedicated to the synthesis of nc Ni-Fe solid solutions (4,5) mainly because of their improved magnetic properties compared to conventional permalloy. The densification process is discussed on the basis of the microstructural evolution which crucially depends on particle agglomeration.

### EXPERIMENTAL

Nc  $\gamma$ -Ni-Fe powders with a particle size of 30-50 nm were synthesized by a mechano-chemical process described in detail elsewhere (3). For the sintering studies powder compacts of 45 % theoretical density were compressed in a cylindrical hardened-steel die. The sintering

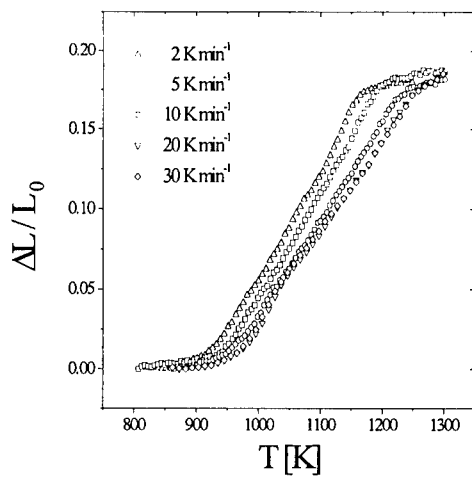


Figure 1. Diametral shrinkage of nc  $\gamma$ -Ni-Fe for different heating rates.

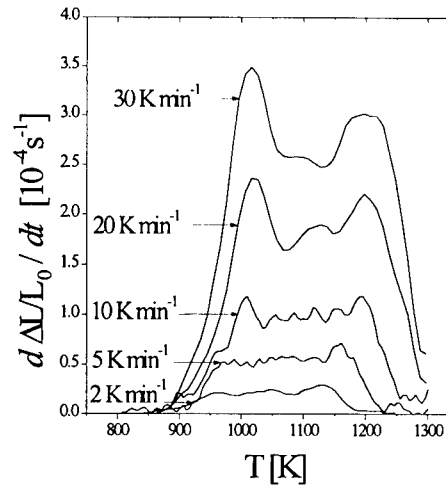


Figure 2. Diametral shrinkage rates as a function of temperature.

experiments were performed under hydrogen atmosphere in a tungsten lamp furnace allowing rapid heating rates. Diametral shrinkage was measured with a laser-photo dilatometer. For this purpose, the specimen was mounted on a mullite support with their front side facing the laser beam and the image of the specimen was magnified and recorded by a CCD camera. The displayed image was eventually evaluated with an image analyzer. To follow the evolution of the microstructure during sintering, a series of specimen was polished using standard metallographic techniques and photographed for examining the variation of *inter*-agglomerate porosity and *inter*-agglomerate pore size with temperature. Additionally, BET measurements were performed to follow the evolution of the *intra*-agglomerate pore size distribution.

## RESULTS AND DISCUSSION

The dilatometer results for different heating rates are depicted in Figure 1. The shrinkage curves show that active sintering occurs in the temperature range between 950 K and 1250 K. For all heating rates, the diametral shrinkage  $\Delta L/L_0$  reached a maximum linear dimensional change of 0.18. Densification proved to be fairly isotropic, as was revealed by a comparison of the linear shrinkage  $\Delta L/L_0$  with the volume shrinkage  $\Delta V/V_0$ . The final densities, achieved by the sintering experiments, are limited to about 80 % theoretical density. Previous experiments on pressureless sintering of nc (40 nm) iron powders led to a reduction of the onset of sintering from about 900 K for conventional powder to 500 K (6). Sintering of nc iron powder under a load of 10 MPa showed active sintering to begin at temperatures as low as 400 K to 500 K and yielded final densities well above 90 % (7). In comparison with the quoted references (6,7), the consolidation characteristics of nc  $\gamma$ -Ni-Fe powders appear to be



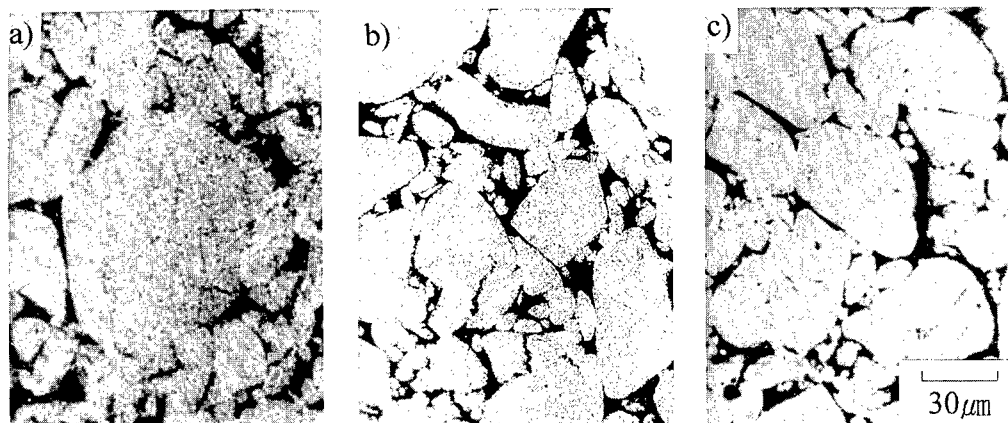


Figure 3. Polished cross section of nc  $\gamma$ -Ni-Fe (a) before sintering, (b) sintered to 1100 K, (c) sintered to 1300 K at a rate of 10 K min<sup>-1</sup>.

rather poor. The cause of this incomplete densification is accounted for by an examination of the microstructure which is shown in Figures 3a to 3c. It is seen from the micrographs that the compacts consist of large agglomerates of polygonal appearance, the size of which varies from 20  $\mu\text{m}$  to as large as 80  $\mu\text{m}$ . The arrangement of the agglomerates is such that small agglomerates reside in the interstices of the packing of the large ones. The high level of agglomeration clearly leads to a difficult-to-sinter bimodal pore size distribution: nanometer-scale, *intra*-agglomerate pores in the interstices of the bonded nanoparticles, and micrometer-sized, *inter*-agglomerate pores between the clusters of small particles. The first two micrographs (Figures 3a and b) reveal a fine network of *intra*-agglomerate pores which has disappeared after densification (Figure 3c) indicating that most of the *intra*-agglomerate porosity has been eliminated in the course of sintering. This finding is reflected by the BET results on the *intra*-agglomerate pore size distribution (Figure 4). It is seen that the *intra*-agglomerate porosity successively decreases until virtually no porosity remains. In contrast to the almost complete elimination of *intra*-agglomerate porosity, the micrographs show that *inter*-agglomerate porosity has remained to a large extent. As revealed by quantitative microscopy, out of a 33 % decrease of total porosity in the course of sintering, the contribution of *inter*-agglomerate densification is merely 8 %, whereas the decrease in *intra*-agglomerate porosity amounts to 25 %. Figure 5 shows the evolution of the *inter*-agglomerate pore size distribution during sintering. Obviously, significant reduction of the pore size takes place only at elevated temperatures.

Figure 2 shows a plot of the shrinkage rate versus temperature. Depending on heating rate, the shrinkage rates vary from  $3 \times 10^{-5}$  to  $3 \times 10^{-4} \text{ s}^{-1}$  which is in line with shrinkage rates observed previously for nc iron powders (6,7). A common feature of the sintering experiments on nc iron conducted by Bourell et al. (7) and Dominguez et al. (6) and the present study on the sintering behavior of  $\gamma$ -Ni-Fe is the occurrence of two distinct maxima in the temperature dependence of the shrinkage rate. The occurrence of maxima may cautiously be attributed to heating-rate dependent, relative variations of *intra*-agglomerate shrinkage and *inter*-agglomerate shrinkage which both superpose to the experimentally determined overall

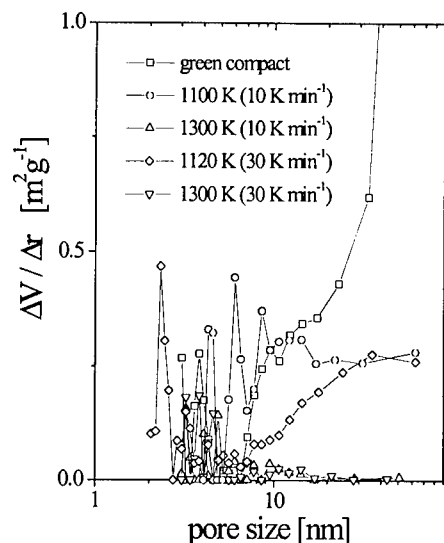


Figure 4. Intra-agglomerate pore distribution measured by BET for specimens sintered to different temperatures.

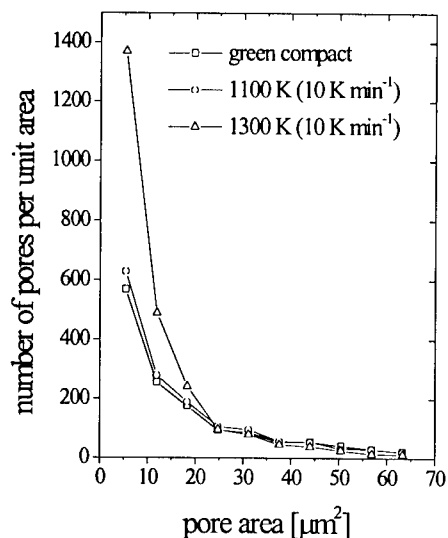


Figure 5. Inter-agglomerate pore distribution measured by quantitative microscopy for specimens sintered to different temperatures.

shrinkage rate. On the basis of these results the objective of further research will be to reduce particle agglomeration induced by the mechano-chemical production method. A systematic study for finding improved synthesis conditions is under way.

#### ACKNOWLEDGEMENTS

Financial support of the Korean Ministry of Education Research Fund for Advanced Materials in 1997 is gratefully acknowledged. One of the authors (P.K.) wishes to thank the Alexander-von-Humboldt Stiftung (Bonn) for supporting this work.

#### REFERENCES

1. Suryanarayana, *Int. Mat. Reviews*, 1995, **40**, 41.
2. Groza, J.R. and Dowding, R.J., *Nanostr. Mat.*, 1996, **7**, 749.
3. Lee, J.S., Kim, T.H., Yu, J.H. and Chung, S.W., *Nanostr. Mat.*, 1997, **9**, 153.
4. Cheung, C., Djuanda, F., Erb, U. and Palumbo, G., *Nanostr. Mat.*, 1995, **5**, 513.
5. Eroglu, S., Zhang, S.C. and Messing, G.L., *J. Mat. Res.*, 1996, **11**, 2131.
6. Dominguez, O. and Bigot, J., *Nanostr. Mat.*, 1995, **6**, 877.
7. Bourell, D.L. and Kaysser, W.A., *Metall. and Mat. Trans. A*, 1994, **25**, 677.



Pergamon

NanoStructured Materials, Vol. 12, pp. 483–486, 1999

Elsevier Science Ltd

© 1999 Acta Metallurgica Inc.

Printed in the USA. All rights reserved

0965-9773/99/\$—see front matter

PII S0965-9773(99)00164-6

## STRUCTURE, PHASE COMPOSITION AND MAGNETIC CHARACTERISTICS OF THE NANOCRYSTALLINE IRON OBTAINED BY MECHANICAL MILLING IN HEPTANE

E.P. Yelsukov, S.F. Lomayeva, G.N.Konygin, G.A. Dorofeev, V.I.Povstugar,  
S.S. Mikhailova, A.V.Zagainov, A.H. Kadikova

Physical-Technical Institute UrB RAS

132 Kirov str, 426001 Izhevsk, Russia, E-mail: yelsukov@fti.udmurtia.su

*The paper states that in the absence of carbon in the particle bulk the formation of the nanocrystalline state in  $\alpha$ -Fe by mechanical milling is not accompanied by the change in structural and magnetic parameters, with the exception of the increase of the coercivity. In case the source of carbon is present all the changes in magnetic characteristics of nanocrystalline  $\alpha$ -Fe, caused by milling time increase, may be explained by carbon segregation in boundary zones with the formation of supersaturated solid solutions and  $\text{Fe}_3\text{C}$ .*

©1999 Acta Metallurgica Inc.

### INTRODUCTION

The results obtained in the last decade concerning both the structure and magnetic characteristics of nanocrystalline (5–10 nm) iron demonstrate [1–3] the special role of grain boundaries. Yet a possibility remains that the obtained data may be influenced by the impurities segregated along the boundary or near-boundary regions. The purpose of this work was to study the influence of carbon on the structure and magnetic characteristics of nanocrystalline iron, prepared by milling in liquid hydrocarbon (heptane). Previously [4] it had been shown that carbide  $\text{Fe}_3\text{C}$  might form under these milling conditions.

### EXPERIMENTAL

The iron powder treatment was performed in a planetary ball mill of Pulverizette-7 type with a vial of 45 cm<sup>3</sup> and 16 milling balls of 12 mm diameter, made of hardened steel containing 1 wt.% C and 1.5 wt.% Cr. 10 g of initial powder (the size of the particles was  $\leq 300$   $\mu\text{m}$ ) together with heptane ( $\text{C}_7\text{H}_{16}$ ) was placed in the closed vial and milled for different times in the range from 1 to 99 h for each loading. The post-milling mass increase did not exceed 10% for maximum milling time. To estimate the chemical content of the particle surface layers and the particle size we used Auger-spectrometer JAMP-10S. X-ray investigation was carried out with a diffractometer using  $\text{FeK}_\alpha$  -radiation.  $^{57}\text{Fe}$  Mössbauer spectra were taken with a  $^{57}\text{Co}(\text{Cr})$  source. Specific saturation magnetization  $\sigma$  data were obtained with a vibrating

sample magnetometer. Thermomagnetic measurements were carried out in the temperature range 300-900 K with an a.c. magnetic susceptibility device.

## RESULTS

The following values characterized the initial iron powder with carbon content less than 0.03 wt. %:  $\sigma = 218 \text{ A}\cdot\text{m}^2/\text{kg}$ ,  $H_C = 5 \text{ Oe}$  and  $\langle L \rangle = 100 \text{ nm}$ . The size of the particles decreased with the time of mechanical treatment from 300 to 5-10  $\mu\text{m}$ . The powders were free of impurities, and only iron and carbon lines were present in Auger spectra.

$t_{\text{mil}} = 1 \text{ h}$ . X-ray structural investigations demonstrated (Fig.1, curves 1 and 2) no phase changes in the milled powder. The only BCC iron phase with the lattice parameter identical to that of the initial powder is present; the BCC phase lines are, however, broadened. The grain size was  $\langle L \rangle = 10 \text{ nm}$  (Fig.4a). No peculiarities in temperature plots of magnetic susceptibility  $\chi(T)$  (Fig.3, curve 1) or changes in the Mössbauer spectra of a milled sample (Fig.2, curves 1) were found compared to the initial powder.  $\sigma$  (Fig.4b) remained unchanged, and  $H_C$  (Fig.4c) drastically increased from 5 Oe for the initial state to 24 Oe for  $t_{\text{mil}} = 1 \text{ h}$ .

$t_{\text{mil}} = 3-47 \text{ h}$ . Phase content is still unchanged (Fig.1, curves 3 and 4),  $\langle L \rangle$  decreased to 4 nm (Fig.4a). A new sextet with broad lines appeared in the Mössbauer spectra. The appearance of a new component is clearly seen on Fig.2a (curves 2 and 3) by the spectra location relative to the background level, represented by solid horizontal lines. As it is seen from the  $P(H)$ -function for a sample milled for 47 h the new component has a wide distribution within the H-range 210-305 kOe. The shape of the temperature plots  $\chi(T)$  (Fig.3) is of special interest. When samples are heated a bend (indicated by vertical arrows) is found in the curves. This bend shifts from 660K for  $t_{\text{mil}} = 3\text{h}$  to 580K for  $t_{\text{mil}} = 47\text{h}$ . In contrast, with cooling, the bend location does not depend on the milling time and corresponds to the temperature 475K, which is in good correlation with Curie temperature of  $\text{Fe}_3\text{C}$  [5]. To get sure in the formation of  $\text{Fe}_3\text{C}$ , the samples after milling at  $t_{\text{mil}} = 3-47 \text{ h}$  were heated to 800K with the heating rate of 60 degrees/min with the following cooling to room temperature at the same rate. In all cases after such thermal treatment the second well-pronounced component appeared, with  $H = 208 \text{ kOe}$ , which was in good correlation with the known H-value in  $\text{Fe}_3\text{C}$  [6]. The milling time increase to 47 h leads to the decrease of  $\sigma$  to  $207 \text{ A}\cdot\text{m}^2/\text{kg}$  (Fig.4b) and to the monotonous decrease of  $H_C$  to 12 Oe (Fig.4c).

$t_{\text{mil}} = 99\text{h}$ . For the given milling time X-ray, Mössbauer and temperature magnetic measurements indicate the formation of  $\text{Fe}_3\text{C}$  in process of the treatment. (Figs.1-3).

## DISCUSSION

From the Mössbauer spectra of the milled samples with the following thermal treatment the content of  $\text{Fe}_3\text{C}$  was calculated and the time milling function of the total C content in the powder bulk obtained (Fig.4d).  $C(t_{\text{mil}})$  extrapolation to  $t_{\text{mil}} = 1\text{h}$  demonstrates a negligible value of C content in the powder bulk for this milling time. It thus follows that in the absence of carbon ( $C < 0.03 \text{ wt.}\%$ ) in the bulk, nanocrystalline iron ( $\langle L \rangle = 10\text{nm}$ ) possesses the structural and magnetic parameters identical to the initial  $\alpha\text{-Fe}$ . The exception is the coercivity  $H_C$ , the

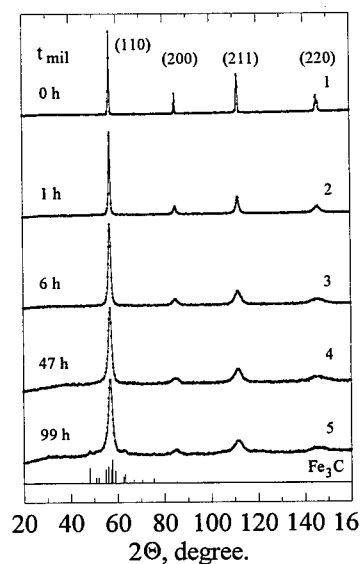


Fig.1. X-ray patterns of milled Fe powder.

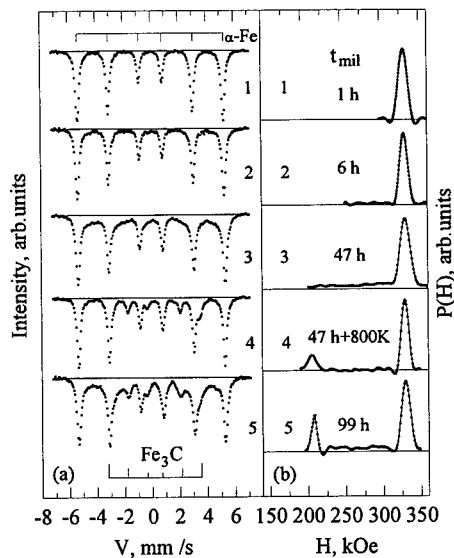
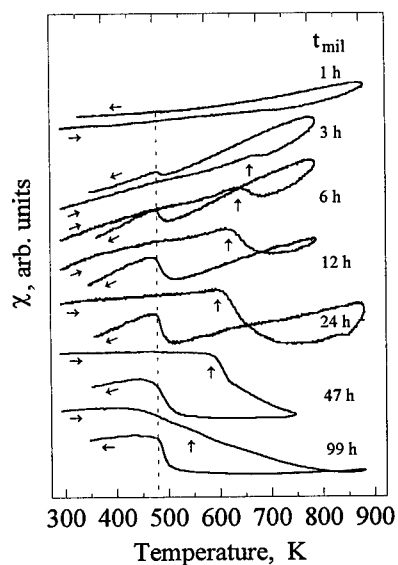
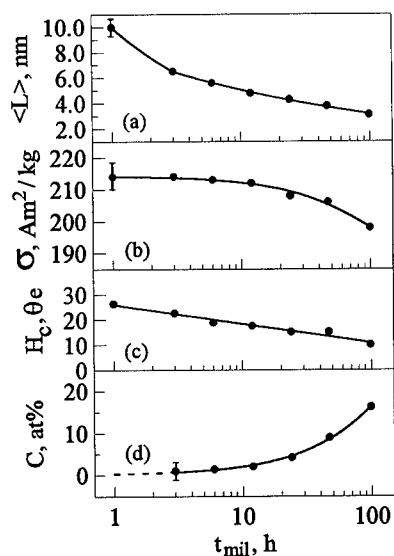
Fig.2. Mössbauer spectra - (a) and hyperfine magnetic field distribution functions  $P(H)$  - (b) of milled Fe powder.

Fig.3. Temperature dependences of a.c. magnetic susceptibility of milled Fe powder. Heating and cooling are shown by arrows along the curves.

Fig.4. Grain size  $\langle L \rangle$  - (a), specific saturation magnetization  $\sigma_s$  - (b), coercivity  $H_c$  - (c) and carbon total concentration  $C$  - (d) dependences on the milling time.

increase of which may be explained by the sample defectiveness after milling. On an example of the as-strained Al-Mn alloy (Fig.3 [7]) one can estimate the width of the grain boundaries corresponding to 1 interplanar distance. Near the boundary there is a distorted lattice zone embracing several layers. Suppose, that the changes in  $\alpha$ -Fe Mössbauer spectrum are only due to the atoms on grain boundaries, with the altered number of Fe-atoms in the nearest neighbourhood. The fraction of Fe atoms with the possible change of coordination number does not exceed 5% at  $\langle L \rangle = 10$  nm. Hence, these Fe atoms should not have influenced the shape of the Mössbauer spectrum of the nanocrystalline  $\alpha$ -Fe, which was just the case with the experiment for  $t_{\text{mil}} = 1$  h.

The diffusion of carbon from the surface particle layers along grain boundaries, and the dissolution of carbon in a near-boundary distorted zone was apparent from the next stage of mechanical milling in heptane ( $t_{\text{mil}} = 3-47$  h). This assumption is based on the results of [8], where a similar microscopic model of mechanical alloying was described. The Curie temperature values measured in the temperature range 580-660K (Fig.3), and not corresponding to those of the iron carbides known, and a wide P(H) distribution in the range of  $H = 210-305$  kOe (Fig.2b, curve 3) suggest the formation in the near-boundary regions of a supersaturated solid solution or amorphous phase.

Thus, the results obtained in the present work are in good agreement with the results on milling Fe in inert environment [3]. However they are explained not by a special magnetic state of grain boundaries, but by the carbon segregation in the near-boundary grain zones and by the formation of  $\text{Fe}_3\text{C}$  after the thermal treatment.

## CONCLUSION

1. In the absence of carbon in the particle bulk ( $C < 0.03$  wt.%) the formation of the nanocrystalline state in  $\alpha$ -Fe by mechanical milling is not accompanied by the change in structural and magnetic parameters, with the exception of the increase of the coercivity.

2. In case the source of impurities (carbon) is present, the time increase of the mechanical milling stimulates the diffusion of carbon along grain boundaries, its dissolution in a near-boundary grain zone and the formation of  $\text{Fe}_3\text{C}$ . If so, the magnetic characteristics of the nanocrystalline iron significantly depend on the total carbon content in the sample.

## REFERENCES

1. Herr, U., Jing, J., Birringer, R., Gonser, U. and Gleiter, H., *Appl. Phys. Lett.*, 1987, **50**, 472.
2. Beke, D.L., *Mater. Sci. Forum*, 1996, **225-227**, 701.
3. Del Bianco, L., Hernando, A., Bonetti, E. and Navarro, E., *Phys. Rev. B*, 1997, **56**.
4. Yelsukov, E.P., Barinov, V.A. and Ovetchkin, L.V., *J Mater. Sci. Lett.*, 1992, **11**, 662.
5. Huffman, G.P., Errington, P.R. and Fisher, P.M., *Phys. Stat. Sol.*, 1967, **22**, 473.
6. Ron, M., Shechter, H., Niedwieds, S., *J. Appl. Phys.*, 1968, **39**, 265.
7. Horita, Z., Smith, D.J., Furukawa, M., Nemoto, M., Valiev, R.Z. and Langdon, T.G., *Mater. Characterization*, 1996, **37**, 285.
8. Schwarz, R.B., *Mater. Sci. Forum*, 1998, **269-272**, 665.



Pergamon

NanoStructured Materials, Vol. 12, pp. 487–490, 1999

Elsevier Science Ltd

© 1999 Acta Metallurgica Inc.

Printed in the USA. All rights reserved

0965-9773/99/\$—see front matter

PII S0965-9773(99)00165-8

## NANOSTRUCTURED ZnO ELECTRODES FOR PHOTOVOLTAIC APPLICATIONS

Karin Keis, Lionel Vayssieres, Sten-Eric Lindquist and Anders Hagfeldt

Department of Physical Chemistry, Uppsala University, Box 532, S-75121 Uppsala, Sweden

**Abstract**--Photoelectrochemical properties of nanostructured ZnO (wurtzite) electrodes have been investigated. Studies were carried out on various types of electrodes with controlled morphology, particle size and doping. The monochromatic photon-to-current conversion efficiencies were recorded in the UV spectral region on bare ZnO and in the visible region on ruthenium dye-sensitized cells. The results show relatively high efficiencies for such systems and demonstrate the potential of ZnO nanostructured cells as materials for photovoltaic applications. ©1999 Acta Metallurgica Inc.

### INTRODUCTION

Recently, dye-sensitized nanostructured semiconductor electrodes have attracted interest due to their applicability in solar energy conversion (1). By using nanoporous TiO<sub>2</sub> films, resulting in a high internal surface area, overall solar-to-energy conversion efficiencies of about 10 % in simulated AM 1.5 sunlight have been reached (2). Investigations of other materials than TiO<sub>2</sub> are worthwhile doing and some studies have been presented in the literature, e.g. SnO<sub>2</sub> (3), Fe<sub>2</sub>O<sub>3</sub> (4), CdS (5) and ZnO (6). However, not only the material as such is of importance but parameters like morphology, porosity, film thickness and electrolyte composition may play an important role for the photoelectrochemical properties.

Previously, we have reported high conversion efficiencies of ZnO films based on 150 nm Al-doped crystallites (7). Lower efficiencies were obtained with ZnO films based on 15 nm undoped crystallites and it was suggested that the higher yield in Al-doped films was due to the fact that Al-doping increased the concentration of free electrons leading to better electronic conductivity of these films. However, arguments concerning the difference in particle size may also be of importance.

In this paper, the photoconversion properties of unsensitized and sensitized nanostructured ZnO films based on 150 nm undoped spherical crystallites will be compared with doped particles of similar size. Results show the possibility of using ZnO as a nanostructured material in a highly efficient regenerative solar cell. The particle size in these films is one order of magnitude larger than the ones used in most of the studies concerning nanostructured systems. The good photoconversion properties obtained with ZnO films show that the broad range of particle sizes can be efficiently used in nanostructured systems. In addition, the results indicate that the morphology of the ZnO nanostructured films plays an essential role in these systems.

## EXPERIMENTAL

The preparation of three different ZnO powders, referred below as ZnO (A) (7), (B) and (C) (8), has been described elsewhere. Briefly, the Al-doped ZnO (A) (0.2% Al) was prepared by precipitation of the powder and calcination at 350 °C. The synthesis of ZnO (B) and (C) powders were conducted at 80 °C. Film preparation was done in similar way as described earlier for TiO<sub>2</sub> powder (9). Colloidal solutions were spread out onto the fluorine doped SnO<sub>2</sub> conducting substrate using Scotch tape as a spacer and frame. The samples were sintered for 30 minutes at 400 °C in air flow. For dye-sensitization the electrodes were soaked into an ethanolic solution of cis-bis(4,4'-dicarboxy-2,2'-bipyridine)-bis(isothiocyanato)ruthenium(II).

The crystallographic structures were determined by X-ray powder diffractometer (Siemens D-5000). Film thicknesses were determined using a Tencor Alpha Step Profilometer. The morphologies and sizes were obtained by scanning electron microscopy (Zeiss DSM 900). The experimental setup for three-electrode measurements on unsensitized films is described elsewhere (10). 0.1M KI aqueous solution with pH=6.8 adjusted by a 0.02M potassium phosphate buffer, was used as a supporting electrolyte. The working electrode was biased to +0.3V (Ag/AgCl in sat. KCl). For two electrode measurements with dye-sensitized ZnO electrodes, a solution of 0.5M LiI/0.05M I<sub>2</sub> in 3-methoxypropionitrile was used as electrolyte and a platinum foil as counter electrode. The incident photon-to-current conversion efficiencies (IPCE) were recorded in the UV region (320-400 nm) for bare electrodes and in the visible region (400-800 nm) for the dye-sensitized ones. For unsensitized samples both back-side (illumination through the supporting glass, SE) and front-side illumination (illumination directly on the film, EE) were studied with an illumination area of about 0.5 cm<sup>2</sup>. For back-side illumination the photocurrents were corrected for the transmittance of the conducting substrate.

## DISCUSSION

The only crystallographic phase detected for powders (B) and (C) was ZnO wurtzite. The scanning electron micrographs of powders (A) and (B) are similar and show that the films consist of 150 nm spherical crystallites and that the films are highly porous. In case of ZnO (C) we observe agglomerated ZnO particles consisting of spherical crystallites with similar size. However, further comparison of the textures is difficult to do without further information about the effective surface area of these films. The SEM pictures of nanostructured ZnO (B) and (C) films are presented in Figure 1. In Figure 2, IPCE as a function of wavelength is shown for bare ZnO (A), (B) and (C) electrodes. The 80 % photon-to-current conversion efficiencies at 360 nm for back-side illumination of 7 µm thick ZnO (A) and 8 µm thick ZnO (B) indicates that even without doping similar efficiencies could be reached. Al-doping will mainly increase the bulk conductivity of the ZnO particles and therefore the results indicate that high efficiencies are not related directly to this effect. Thus, the particle size seems to be the determining factor for high conversion efficiencies. Surprisingly high efficiencies were also obtained for front-side illumination at short wavelengths, where higher photocurrent losses could be expected due to the charge separation in the outermost layer and therefore longer transport distance of the charge before reaching the back-contact (Figure 2 inset).



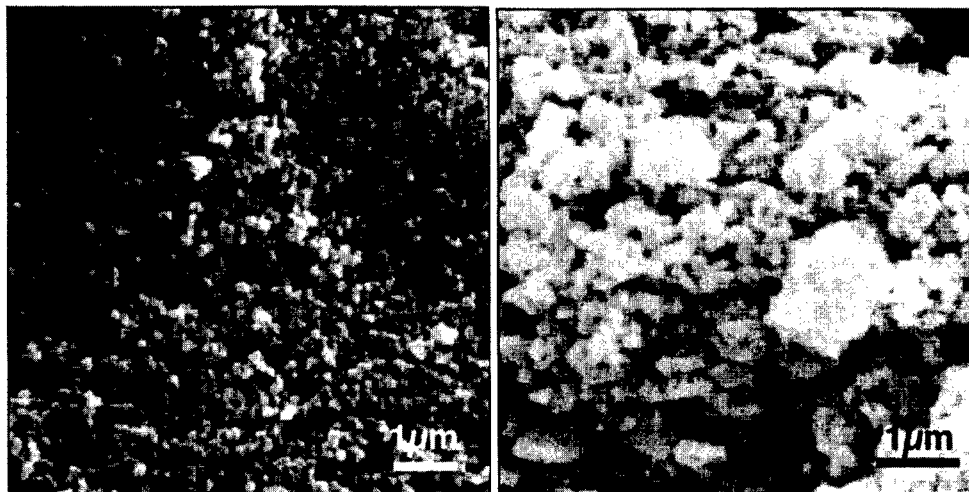


Figure 1. Scanning electron micrographs of ZnO (B) and (C).

We note, however, that direct comparison of the two ZnO films is not straightforward as the synthesis conditions (material history) are of importance. We do not have information about the surface composition and the amount of oxygen vacancies and interstitial zinc ions in these two materials which also may affect the conductivity.

For 8 μm thick ZnO (C) electrodes, low efficiencies were obtained both for back-side and front-side illumination. The electron losses during the transport to the back-contact may be directly related to a lower porosity because of agglomerated structure, which hinders the electrolyte penetration through the film giving rise to higher probabilities for electron-hole pair recombination.

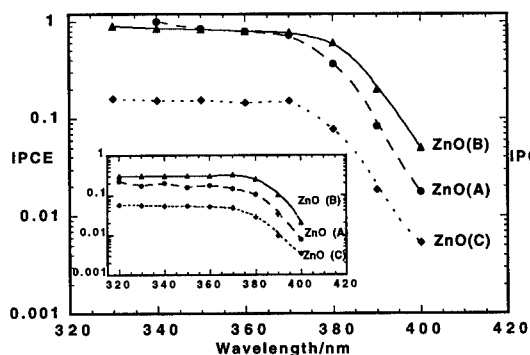


Figure 2. IPCE vs wavelength for an unsensitized ZnO (A), (B) and (C) for SE illumination. Inset shows results from EE illumination.

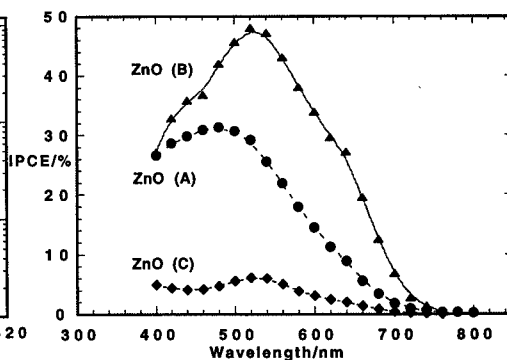


Figure 3. IPCE vs wavelength for a dye-sensitized (A), (B) and (C) electrodes.

It has been reported that the conditions for dye sensitization of nanostructured ZnO films (time, dye-concentration, solvent, etc.) are of importance (7). A maximum IPCE of 50 % is obtained at 540 nm for a 9  $\mu\text{m}$  thick electrode consisting of dye-sensitized 150 nm undoped ZnO (B) particles. The maximum IPCE for 9  $\mu\text{m}$  thick Al-doped films (A) and 6  $\mu\text{m}$  thick agglomerated ones (C) is 30 % and 8 %, respectively (Figure 3). The IPCE action spectra match closely the absorption spectrum of the dye in the solution, shown earlier (7, 11). The conversion efficiencies for sensitized ZnO (B) are higher than for sensitized ZnO (A), whereas the unsensitized films gave similar results. This may be due to the different charge separation processes in unsensitized and sensitized films. In the first case the charge separation takes place in the bulk, whereas in dye sensitized systems the electrons will be injected into the semiconductor. Due to the bulk Al-doping the local surface charge distribution may change and therefore dye adsorption may take place in a different manner and amount, compared to undoped ZnO. The observed blue shift of the IPCE maximum for ZnO (A) in Figure 3 may be an indication of such an effect. At present we are now trying to improve the photovoltaic efficiency for dye-sensitized nanostructured ZnO electrodes by optimizing the dye-adsorption process, the electrolyte composition and concentration.

## REFERENCES

1. O'Regan B., Grätzel M., *Nature*, 1991, 353, 737.
2. Nazeerudin M.K., Kay A., Rodicio I., Grätzel M., *J. Am. Chem. Soc.*, 1993, 115, 6382.
3. Bedja I., Hotchandani S., Kamat P.V., *J. Phys. Chemistry*, 1994, 98, 4133.
4. Björkstén U., Moser J., Grätzel M., *Chem. Mater.*, 1994, 6, 858.
5. Hodes G., Howell I.D., *J. Electrochem. Soc.*, 1992, 139, 3136.
6. Hoyer P., Weller H., *J. Phys. Chem.*, 1995, 99, 14096.
7. Rensmo H., Keis K., Lindström H., Södergren S., Solbrand A., Hagfeldt, A., Lindquist S.E., *J. Phys. Chem.*, 1997, 101, 2598.
8. Keis K., Vayssieres L., Rensmo H., Hagfeldt A., Lindquist S.E., to be published.
9. Lindström H., Rensmo H., Södergren S., Solbrand A., Lindquist S.E., *J. Phys. Chem.*, 1996, 100, 3084.
10. Rensmo, H., Lindström H., Södergren S., Willstedt A.K., Solbrand A., Hagfeldt A., Lindquist S.E., *J. Electrochem. Soc.*, 1996, 143, 3173.
11. Redmond G., Fitzmaurice D., *Chem. Mater.*, 1994, 6, 686.



## FORMATION OF NANO-SIZED LAYER COMPOSITE BY INTERCALATION TO ALUMINIUM TRI-HYDROGEN BIS (ORTHOPHOSPHATE) MONOHYDRATE

K.Sakamoto<sup>1</sup>, Y.Tsunawaki<sup>1</sup>, A.Nakahira<sup>2</sup>, K.Kitahama<sup>3</sup>,  
J.Ichihara<sup>3</sup>, and S.Yamaguchi<sup>3</sup>

<sup>1</sup>Osaka Sangyo University, 3-1-1 Nakagaito, Daito, Osaka 574-8530, JAPAN.

<sup>2</sup>Kyoto Institute of Technology, Goshokaidocho, Matsugasaki, Sakyo-ku, Kyoto 606-0962, JAPAN, <sup>3</sup>ISIR, Osaka University, Mihogaoka, Ibaraki, Osaka 567-0047, JAPAN.

**Abstract** Aluminium tri-hydrogen bis (orthophosphate) monohydrate  $[\text{AlH}_3(\text{PO}_4)_2 \cdot \text{H}_2\text{O}]$  is known as a material with a layered structure. We have synthesized the pure single phase of  $\text{AlH}_3(\text{PO}_4)_2 \cdot \text{H}_2\text{O}$  by solvothermal reaction, with high efficiency. It was formed by the reaction of  $\text{Al}(\text{OH})_3$  with  $\text{H}_3\text{PO}_4$  at 75 wt% : The optimum molar ratio of  $\text{H}_3\text{PO}_4$  to  $\text{Al}(\text{OH})_3$  is 7.5. The mixture of  $\text{H}_3\text{PO}_4$  and  $\text{Al}(\text{OH})_3$  in 1-propanol was refluxed at 94 °C for 24 hours under stirring. Furthermore, we intercalated phenylphosphonic acid into  $\text{AlH}_3(\text{PO}_4)_2 \cdot \text{H}_2\text{O}$  at room temperature and obtained a material with nano-sized layers ( $d = 1.52 \text{ nm}$ ). Measurements of XRD and DTA-TG, and observations of SEM and TEM were made on products.

©1999 Acta Metallurgica Inc.

### INTRODUCTION

The crystalline aluminium phosphates possess various kinds of structures ; *i.e.* pores, channels, layers, and so on. For example, molecular sieves such as AlPO-n and VPI-5 has nano-sized pores and channels, and can be used for adsorbent and catalyst etc. (1,2,3). Layered aluminium phosphates have a possibility to modify the chemical and physical properties by means of the intercalation of organic compound between the layers.

It is known that aluminium tri-hydrogen bis (orthophosphate) monohydrate  $[\text{AlH}_3(\text{PO}_4)_2 \cdot \text{H}_2\text{O}]$  possesses a layered structure (4). This material is a potent precursor for functional nano-composite because of layered structure and acidic protons in its structure. However, both efficient preparation method and its detailed properties are unclear so far.

In this work, a preparation method of pure  $\text{AlH}_3(\text{PO}_4)_2 \cdot \text{H}_2\text{O}$  has been investigated through the reaction of  $\text{Al}(\text{OH})_3$  with  $\text{H}_3\text{PO}_4$  in an organic solvent. We have studied the dependence on the reaction temperature, sort of organic solvent, and molar ratio of  $\text{H}_3\text{PO}_4$  to  $\text{Al}(\text{OH})_3$  for the preparation. Furthermore, the intercalation of organic compound into this substance was undertaken.

## EXPERIMENTAL PROCEDURE

Preparation of  $\text{AlH}_3(\text{PO}_4)_2 \cdot \text{H}_2\text{O}$  was carried out by the reaction of  $\text{Al}(\text{OH})_3$  with 75 wt%  $\text{H}_3\text{PO}_4$  in organic solvent (200 ml) under the condition of stir and reflux for 6~60 hours. The organic solvent used in this study is as follows ; isobutyl methyl ketone, methyl ethyl ketone, toluene, 1-propanol, 2-propanol, 1-butanol, 2-methyl-1-propanol, and ethanol. The molar ratio ( $R$ ) of  $\text{H}_3\text{PO}_4$  to  $\text{Al}(\text{OH})_3$  was changed in the range 3.0~7.5.

Preparation of materials with nano-sized layer structure was carried out by reaction of  $\text{AlH}_3(\text{PO}_4)_2 \cdot \text{H}_2\text{O}$  and organic compounds [phenylphosphonic acid, phenylphosphate disodium salt dihydrate, adenosine 5'-monophosphate, or glycerol 2-phosphate disodium salt hydrate]. The mixture of  $\text{AlH}_3(\text{PO}_4)_2 \cdot \text{H}_2\text{O}$  (2.0 mmol) and organic compound (0.1M-aqueous solution, 200 ml) was stirred at room temperature for 3 hours in an ultrasonic oscillator vessel and for 24 hours without it.

The reaction products were collected by filtration, washed with distilled water, and dried in air at 40°C for 5 hours. The obtained products were subjected to measurements of X-ray diffractometry (XRD ; Rigaku Geigerflex RAD I A) and differential thermal analysis, thermogravimetry (DTA-TG ; Shimadzu DTA-30, TG-30). Observation were made also on a scanning electron microscope (SEM ; Hitachi FESEM H1800) and a transmission electron microscope (TEM ; Hitachi H8000, 200 kV).

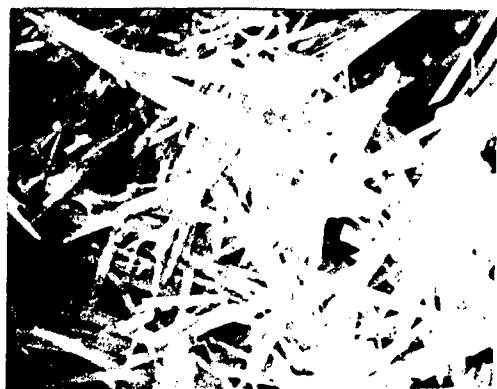
## RESULTS AND DISCUSSION

The reacted product of  $\text{Al}(\text{OH})_3$  and  $\text{H}_3\text{PO}_4$  was identified by XRD whose diagrams consisted of lines assignable to either  $\text{AlH}_3(\text{PO}_4)_2 \cdot \text{H}_2\text{O}$  or  $\text{Al}(\text{OH})_3$ . Comparison of the intensity of X-ray diffraction peaks between  $\text{AlH}_3(\text{PO}_4)_2 \cdot \text{H}_2\text{O}$  and  $\text{Al}(\text{OH})_3$  gave the relative amount of the yielded  $\text{AlH}_3(\text{PO}_4)_2 \cdot \text{H}_2\text{O}$ . It showed that the amount of  $\text{AlH}_3(\text{PO}_4)_2 \cdot \text{H}_2\text{O}$  increased with enhancing the hydrophilicity of organic solvent used in the preparation as following order except for ethanol ; 1-propanol > 2-propanol > 1-butanol > 2-methyl-1-propanol > isobutyl methyl ketone, methyl ethyl ketone, and toluene. In spite of high hydrophilicity of ethanol, the amount of formed  $\text{AlH}_3(\text{PO}_4)_2 \cdot \text{H}_2\text{O}$  was much smaller than expected. This phenomenon suggests that the temperature around 90°C contributes strongly to the reaction.

Increasing of the molar ratio ( $R$ ) of  $\text{H}_3\text{PO}_4$  to  $\text{Al}(\text{OH})_3$  also enhanced the formation of  $\text{AlH}_3(\text{PO}_4)_2 \cdot \text{H}_2\text{O}$ . It was found that the reaction was most effectively proceeded by the addition of unusual excess  $\text{H}_3\text{PO}_4$  of  $R = 6 \sim 7.5$ .

From these results, it is concluded that  $\text{AlH}_3(\text{PO}_4)_2 \cdot \text{H}_2\text{O}$  is most effectively prepared by the following method : The mixture of  $\text{H}_3\text{PO}_4$  (75 wt%) and  $\text{Al}(\text{OH})_3$  at  $R = 7.5$  is refluxed at 94°C for 24 hours under stirring in 1-propanol (200 ml). Figure 1 shows the SEM photograph of  $\text{AlH}_3(\text{PO}_4)_2 \cdot \text{H}_2\text{O}$  prepared in this work. The products of  $\text{AlH}_3(\text{PO}_4)_2 \cdot \text{H}_2\text{O}$  were long needle-like particles with length of 70~80  $\mu\text{m}$ .

Intercalation to  $\text{AlH}_3(\text{PO}_4)_2 \cdot \text{H}_2\text{O}$  were examined by using organic compounds such as phenylphosphonic acid, phenylphosphate disodium salt dihydrate, adenosine 5'-monophosphate, or glycerol 2-phosphate disodium salt hydrate. Only phenylphosphonic acid



100  $\mu\text{m}$

Figure 1. SEM photograph of  $\text{AlH}_3(\text{PO}_4)_2 \cdot \text{H}_2\text{O}$ .



50 nm

Figure 2. TEM photograph of the material prepared by the reaction of  $\text{AlH}_3(\text{PO}_4)_2 \cdot \text{H}_2\text{O}$  and phenylphosphonic acid.

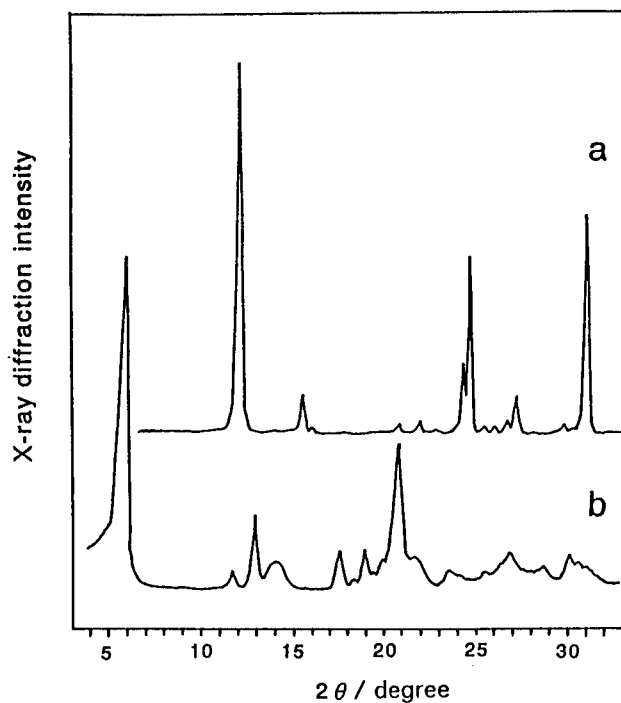


Figure 3. X-ray diffraction patterns for  $\text{AlH}_3(\text{PO}_4)_2 \cdot \text{H}_2\text{O}$  ( a ) and material prepared by the reaction of  $\text{AlH}_3(\text{PO}_4)_2 \cdot \text{H}_2\text{O}$  and phenylphosphonic acid ( b ).

contributed to the intercalation for  $\text{AlH}_3(\text{PO}_4)_2 \cdot \text{H}_2\text{O}$ , but the other organic compounds decomposed it. TEM photograph of intercalated product is shown in Figure 2. We can recognize the structure consisting of lamellae. X-ray diffraction patterns of reacted product and  $\text{AlH}_3(\text{PO}_4)_2 \cdot \text{H}_2\text{O}$  are shown in Figure 3. The comparison of their data showed that the intercalated product does not contain any starting materials and the peak at the lowest angle shifts toward lower angle of  $2\theta = 5.77^\circ$ . The latter phenomenon suggests that phenylphosphonic acid are intercalated into  $\text{AlH}_3(\text{PO}_4)_2 \cdot \text{H}_2\text{O}$ , and the distance between the layers is expanded to 1.52 nm.

In the DTA-TG measurement,  $\text{AlH}_3(\text{PO}_4)_2 \cdot \text{H}_2\text{O}$  showed the endothermic peaks with weight loss at 160 and 220°C due to dehydration from the water of crystallization and from the phosphate molecule, respectively. On the other hand, intercalated product had the strong endothermic peak at 565°C with 56.5 wt% loss through a small amount loss of 4 wt% at 140°C. It is considered that such a large weight loss would be due to the decomposition of the organic compound *i.e.* phenylphosphonic acid, between the layers. This phenomenon also seems to support the intercalation of phenylphosphonic acid into  $\text{AlH}_3(\text{PO}_4)_2 \cdot \text{H}_2\text{O}$ .

## CONCLUSION

Pure single phase  $\text{AlH}_3(\text{PO}_4)_2 \cdot \text{H}_2\text{O}$  was synthesized by solvothermal reaction with high efficiency. The optimum condition to prepare it was as follows ; the mixture of 75 wt%  $\text{H}_3\text{PO}_4$  and  $\text{Al}(\text{OH})_3$  (molar ratio of  $\text{H}_3\text{PO}_4$  to  $\text{Al}(\text{OH})_3 = 7.5$ ) was refluxed at 94°C for 24 hours under stirring in 1-propanol (200 ml). Phenylphosphonic acid was intercalated into  $\text{AlH}_3(\text{PO}_4)_2 \cdot \text{H}_2\text{O}$  at room temperature. It was observed that the product has nano-sized layers with  $d = 1.52$  nm.

In the further works, we will investigate the structure and chemical/physical properties of the intercalated product.

## REFERENCES

1. Wilson, S.T., Lok, B.M., Messina, C.A., Canan, T.R., Flanigen, E.M., *J. Am. Chem. Soc.*, 1982, **104**, 1146.
2. Davis, M.E., Saldarriaga, C., Montes, C., and Garces, J.M., *Nature*, 1988, **331**, 698.
3. Davis, M.E., Montes, C., Hathaway, P.E., Arhancet, J.P., Hasha, D.L., and Garces, J.M., *J. Am. Chem. Soc.*, 1989, **111**, 3919.
4. Kniep, R., Mootz, D., and Wilms, A., *Z.A. Naturforsch.*, 1978, **33b**, 1047.



Pergamon

NanoStructured Materials, Vol. 12, pp. 495–498, 1999

Elsevier Science Ltd

© 1999 Acta Metallurgica Inc.

Printed in the USA. All rights reserved

0965-9773/99/\$—see front matter

PII S0965-9773(99)00167-1

## STRUCTURAL AND MAGNETIC INVESTIGATION OF MECHANICALLY ALLOYED $\text{Fe}_{70}\text{Co}_{3.5}\text{Cu}_1\text{Nb}_3\text{B}_9\text{Si}_{13.5}$ POWDERS

H. Chiriac, A.E. Moga, M. Urse and F. Necula

National Institute of R & D for Technical Physics, 47 Mangeron Blvd. 6600 Iasi 3, Romania

**Abstract** Results concerning the preparation of nanocrystalline  $\text{Fe}_{70}\text{Co}_{3.5}\text{Cu}_1\text{Nb}_3\text{B}_9\text{Si}_{13.5}$  powders by high energy ball milling, in argon atmosphere, and their magnetic properties are presented. From X-ray diffraction patterns it follows that the powders with the above mentioned composition, obtained after 250 hours of milling, are nanocrystalline, with the crystallite size of about 8.6 nm. An improvement in the magnetic properties of the mechanically alloyed powders, by controlled heat treatment, can be noticed. A comparison between the magnetic properties of the  $\text{Fe}_{70}\text{Co}_{3.5}\text{Cu}_1\text{Nb}_3\text{B}_9\text{Si}_{13.5}$  and  $\text{Fe}_{73.5}\text{Cu}_1\text{Nb}_3\text{B}_9\text{Si}_{13.5}$  (FINEMET) mechanically alloyed powders is also reported. ©1999 Acta Metallurgica Inc.

### INTRODUCTION

Nanocrystalline magnetic materials based on FeBSi present excellent soft magnetic properties, the most widely studied alloy being the devitrified  $\text{Fe}_{73.5}\text{Cu}_1\text{Nb}_3\text{B}_9\text{Si}_{13.5}$  metallic glass (FINEMET). The substitution of small amounts of Fe with Co in Fe-based magnetic materials generally results in the increase of the saturation magnetization (1).

The aim of this paper is to study the structural transformations induced by mechanical alloying of  $\text{Fe}_{70}\text{Co}_{3.5}\text{Cu}_1\text{Nb}_3\text{B}_9\text{Si}_{13.5}$  powders mixture and their magnetic properties.

### EXPERIMENTAL DETAILS

Fe, Co, Cu, Nb, B and Si elemental powders having a purity over 99.5 % and particles size under 100  $\mu\text{m}$ , were mixed to give atomic nominal composition of  $\text{Fe}_{70}\text{Co}_{3.5}\text{Cu}_1\text{Nb}_3\text{B}_9\text{Si}_{13.5}$  alloy. The powders were sealed under Ar in a steel vial with steel balls and milled in a conventional planetary ball mill. The balls to powders weight ratio was 6:1.

X-ray diffraction (XRD) analyses were performed by a diffractometer using  $\text{MoK}\alpha$  radiation ( $\lambda=0.71069\text{\AA}$ ) in a Bragg-Brentano arrangement. Separation of the size and strain components of line broadening for the milled powders was accomplished by Warren and Averbach method (2). The thermal stability of the mechanically alloyed powders was characterized by means of differential thermal analysis (DTA) at a heating rate of  $10^\circ\text{C}/\text{min}$ . The magnetic properties of the samples were measured by a vibrating sample magnetometer (VSM), in an external field of 1270 kA/m, at room temperature.

## RESULTS AND DISCUSSION

Figure 1 shows the XRD patterns of  $\text{Fe}_{70}\text{Co}_{3.5}\text{Cu}_1\text{Nb}_3\text{B}_9\text{Si}_{13.5}$  powders for different milling times. After 250 hours of milling the peaks of elemental Co, Nb, Cu, B and Si disappear indicating the formation of alloy. The mean crystallite size of the mechanically alloyed powders is 8.6 nm, typical value for nanocrystalline materials.

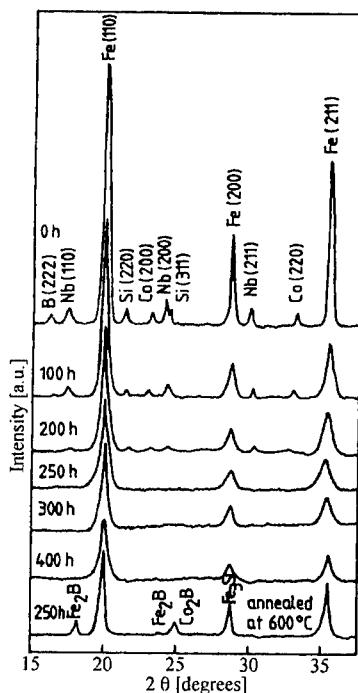


Figure 1: XRD patterns of  $\text{Fe}_{70}\text{Co}_{3.5}\text{Cu}_1\text{Nb}_3\text{B}_9\text{Si}_{13.5}$  powders for different times

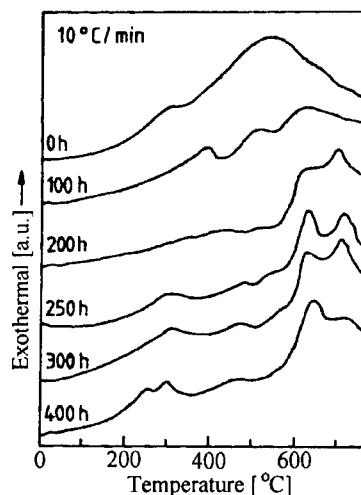


Figure 2: Typical DTA curves of  $\text{Fe}_{70}\text{Co}_{3.5}\text{Cu}_1\text{Nb}_3\text{B}_9\text{Si}_{13.5}$  powders for different times

After an increased milling time, up to 400 hours, the appearance of new phases can not be observed, the crystallite sizes remaining approximately constant. These phases could exist, but the crystallite size being very small, the maximum of newly formed phases could constitute a background which presents only a maximum for the (110) peak corresponding to the bcc structure of  $\alpha$ -Fe.

The results of DTA measurements for  $\text{Fe}_{70}\text{Co}_{3.5}\text{Cu}_1\text{Nb}_3\text{B}_9\text{Si}_{13.5}$  powders for different milling times are shown in Figure 2. During the heating of powders milled for 250 hours, many exothermic peaks appear: three broadened peaks at 300°C, 460°C and 540°C and two sharper ones at 620°C and 680°C. The first peak at 300°C may be due to the release of the strain energy during the heating process. The broadened peaks at 460°C and 540°C are related to the crystallization of  $\alpha$ -Fe and to the crystallization of an amorphous phase. Both peaks at 620°C



and 680°C are due to the precipitation of the various compounds:  $\text{Fe}_2\text{B}$ ,  $\text{Co}_2\text{B}$  and  $\text{Fe}_3\text{Si}$ . For increased milling times, the DTA curve has not revealed essential changes in the crystallization process.

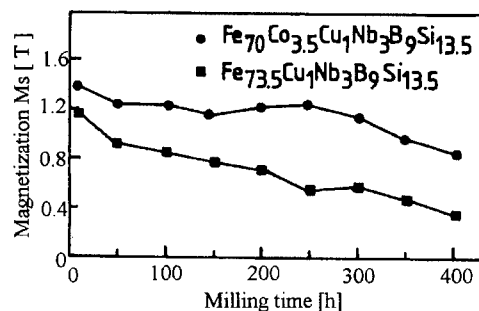


Figure 3: Variation of room temperature  $M_s$  of  $\text{Fe}_{73.5}\text{Cu}_1\text{Nb}_3\text{B}_9\text{Si}_{13.5}$  and  $\text{Fe}_{70}\text{Co}_{3.5}\text{Cu}_1\text{Nb}_3\text{B}_9\text{Si}_{13.5}$  powders vs. milling times.

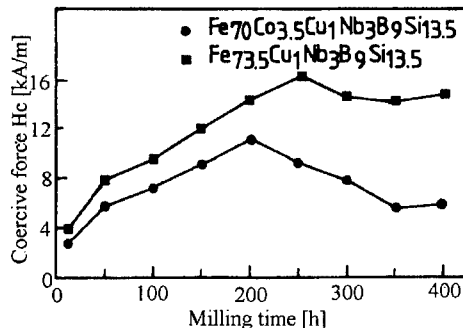


Figure 4: Coercive force  $H_c$  of  $\text{Fe}_{73.5}\text{Cu}_1\text{Nb}_3\text{B}_9\text{Si}_{13.5}$  and  $\text{Fe}_{70}\text{Co}_{3.5}\text{Cu}_1\text{Nb}_3\text{B}_9\text{Si}_{13.5}$  powders vs. milling times.

Figure 3 shows the variations of the room temperature saturation magnetization ( $M_s$ ) of mechanically alloyed  $\text{Fe}_{70}\text{Co}_{3.5}\text{Cu}_1\text{Nb}_3\text{B}_9\text{Si}_{13.5}$  and  $\text{Fe}_{73.5}\text{Cu}_1\text{Nb}_3\text{B}_9\text{Si}_{13.5}$  powders as a function of processing time. The decrease in magnetization is due to the refinement of crystallites during milling, and its small variations as a function of milling times may be related to changes of the powders microstructures. For the same processing time, the  $\text{Fe}_{70}\text{Co}_{3.5}\text{Cu}_1\text{Nb}_3\text{B}_9\text{Si}_{13.5}$  powders show higher saturation magnetization than  $\text{Fe}_{73.5}\text{Cu}_1\text{Nb}_3\text{B}_9\text{Si}_{13.5}$  ones, resulting from the substitution of Fe with Co in FINEMET. The values of saturation magnetization were 1.25 T and 0.6 T for the first alloy and for FINEMET respectively, after a milling time of 250 hours. For the same samples the coercive force ( $H_c$ ) as a function of milling time was also measured. The results are presented in Figure 4. The fragmentation of the magnetic particles during milling leads to an increase of the coercive force. After going through a maximum at 250 and 200 hours of milling for FINEMET and  $\text{Fe}_{70}\text{Co}_{3.5}\text{Cu}_1\text{Nb}_3\text{B}_9\text{Si}_{13.5}$  powders respectively, the coercivity decreases. This decrease of coercivity could be attributed to the strains relaxation and superparamagnetism of the smallest magnetic particles (3). The values of the coercivity for mechanically alloyed powders after 250 hours of milling were 17.2 kA/m and 8.8 kA/m for FINEMET and  $\text{Fe}_{70}\text{Co}_{3.5}\text{Cu}_1\text{Nb}_3\text{B}_9\text{Si}_{13.5}$  powders respectively.

Figure 5 shows the saturation magnetization and coercivity of  $\text{Fe}_{70}\text{Co}_{3.5}\text{Cu}_1\text{Nb}_3\text{B}_9\text{Si}_{13.5}$  powders milled for 250 hours after an additional treatment of 1 hour in vacuum, at temperatures between 100-600°C. An improvement in the soft magnetic properties of the  $\text{Fe}_{70}\text{Co}_{3.5}\text{Cu}_1\text{Nb}_3\text{B}_9\text{Si}_{13.5}$  nanocrystalline powders annealed for 1 hour at 200°C can be noticed, due to the microstructures rearrangement at the atomic level and to the strain relaxation. The values of the saturation magnetization and coercive force for  $\text{Fe}_{70}\text{Co}_{3.5}\text{Cu}_1\text{Nb}_3\text{B}_9\text{Si}_{13.5}$  powders annealed in vacuum at 200°C for 1 hour was  $M_s=1.32$  T, and  $H_c=6$  kA/m respectively. The

thermal treatments of nanocrystalline powders at temperatures over 300°C deteriorate the magnetic properties, probably due to the appearance of incipient crystallization phases of different compounds ( $\text{Fe}_2\text{B}$ ,  $\text{Co}_2\text{B}$  and  $\text{Fe}_3\text{Si}$ ), which appear clearly only on the XRD pattern of the powders annealed at 600°C (Figure 1).

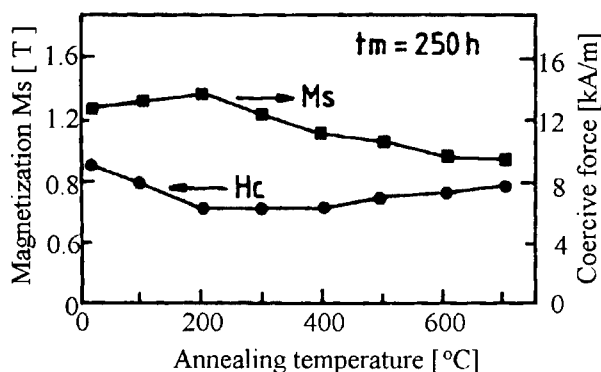


Figure 5: Saturation magnetization and coercive force of  $\text{Fe}_{70}\text{Co}_{3.5}\text{Cu}_1\text{Nb}_3\text{B}_9\text{Si}_{13.5}$  powders milled for 250 hours vs. annealing temperatures.

The crystallite sizes of  $\text{Fe}_{70}\text{Co}_{3.5}\text{Cu}_1\text{Nb}_3\text{B}_9\text{Si}_{13.5}$  powders after annealing at 600°C remain in nanocrystalline range (38 nm).

## CONCLUSIONS

The mechanical alloying was used for the preparation of  $\text{Fe}_{70}\text{Co}_{3.5}\text{Cu}_1\text{Nb}_3\text{B}_9\text{Si}_{13.5}$  nanocrystalline alloy from elemental powders. By this technique, soft magnetic nanocrystalline powders with the crystallite size of 8.6 nm were obtained after 250 hours of milling. The cyclic heavy cold deformation leads to an internally strained nanostructure so that additional heat treatment for stress relaxation is required. An improvement in the soft magnetic properties after annealing at 200°C for 1 hour, in vacuum, can be observed. The magnetic  $\text{Fe}_{70}\text{Co}_{3.5}\text{Cu}_1\text{Nb}_3\text{B}_9\text{Si}_{13.5}$  nanocrystalline powders present also an increased saturation magnetization compared to FINEMET because of the substitution of 3.5 at.% Fe with Co. This powder-shaped material has the advantage that can be compacted in any configuration.

## References

1. Wexler, D., Bennett, R., Emr, M. and Gilleard, K. P., *Proceedings of ISMANAM- 96*, Rome, Italy, 1996, *Materials Science Forum*, Vols. 235-238, 1997, p. 735
2. Klug, H. P. and Alexander, L. E., *X-Ray Diffraction Procedures for Polycrystalline and Amorphous Materials*, 2 nd edition (Wiley, N. Y.), 1974, p. 665.
3. Drbohlav, O., Secondi, J. and Yavary, A.R., *Proceedings of ISMANAM - 94*, Grenoble, France, 1994, *Materials Science Forum*, Vols. 179-189, 1995, p. 475.



Pergamon

NanoStructured Materials, Vol. 12, pp. 499–502, 1999  
Elsevier Science Ltd

© 1999 Acta Metallurgica Inc.  
Printed in the USA. All rights reserved  
0965-9773/99/\$-see front matter

PII S0965-9773(99)00168-3

## FORMATION OF NICKEL AND ZIRCONIA NANOCOMPOSITES BY THE COPRECIPITATION METHOD

Jadran Maček and Marjan Marinšek

University of Ljubljana, Faculty of Chemistry and Chemical Technology  
1000 Ljubljana, Aškerceva 5, Slovenia

**Abstract:** *The precursors for the Ni-YSZ cermets preparation were either a solution of nickel, zirconium and yttrium chlorides or separately prepared NiO and YSZ. When preparing Ni-YSZ cermets by utilising the gel-precipitation technique the average particle size of the Ni and YSZ grains after the thermal treatment up to 1000°C is no larger than 50–100 nm, but is in the micrometer range after the prolonged thermal treatment at 1300°C. The mechanical mixing of the cermet components results in a single phase region larger than several micrometer range. ©1999 Acta Metallurgica Inc.*

### INTRODUCTION

Nickel/yttria-stabilized zirconia (Ni-YSZ) cermets are the most commonly used anode materials in solid oxide fuel cells (SOFC) (1). The electrochemical performance of the Ni-YSZ cermet electrode is a very complex process, attributed to the anode microstructural and morphological properties (2). The morphology and microstructure of Ni-YSZ cermet anodes can be altered through the material preparation route. A general method currently used for manufacturing the anode material is the mechanical mixing of separately prepared NiO and YSZ powders prior sintering and reduction of the anode layer. However, a problem may occur during the mixing of NiO and YSZ due to the separation of NiO and YSZ particles resulting in non-uniform distribution of Ni in the cermet. As a result, recent studies have focused on manufacturing an anode with a uniform distribution of Ni particles by controlling the particle size distribution of YSZ particles or sintering temperature (3). The gel-precipitation method has been shown to be an attractive method for achieving these goals because it enables the mixing of precursors already in the starting solution, assuring the resulting products with a high degree of homogeneity, where different components of the cermet material are mixed in sub-micrometer range, meaning that one phase dominance is very small (4).

### EXPERIMENTAL

Samples were prepared in two different ways: either by the gel-precipitation method (Samples A) or by the mechanical mixing method (Sample B). The samples prepared by the gel-precipitation method were precipitated by introducing gaseous ammonia into the aqueous solutions of the corresponding Zr-Y-Ni chlorides producing the mixed gels (final pH was 8, Ni/10 mol.% YSZ). The products were filtered, washed until no reaction of chloride ions was observed (using the AgNO<sub>3</sub> test), dried for 6 hours at 120°C and calcined for two hours either at

500°C (Sample A1) or at 950°C (Sample A2). After calcination, samples were milled in a ball mill (the mean particle sizes were 0.46 and 0.52  $\mu\text{m}$ , and the standard deviations 0.35 and 0.31  $\mu\text{m}$  respectively), pressed into tablets (500 kg/cm<sup>2</sup>) and further thermally treated in two different ways. Sample A1 was sintered for two hours at 1000°C and then submitted to a temperature programmed reduction (TPR) at 1000°C for two hours in a dynamic reductive atmosphere (Ar, 4vol.% H<sub>2</sub>) to reduce NiO to metallic Ni. Sample A2, on the other hand, was sintered for ten hours at 1300°C prior to TPR at 1000°C for two hours. Sample B was prepared by milling the calcined oxides in a ball mill (separately prepared NiO and 10 mol.% YSZ). The mean particle size and the standard deviation of the milled sample were 0.63  $\mu\text{m}$  and 0.43  $\mu\text{m}$  respectively. The calcined and milled sample was pressed into tablet (500 kg/cm<sup>2</sup>), sintered at 1300°C for ten hours and finally subjected to a TPR at 1000°C for two hours.

## RESULTS AND DISCUSSION

The gel-precipitation method from solution has one major advantage over many other preparation techniques because it enables the mixing of suitable precursors in the starting solution theoretically on the molecular level. This fine phase dispersion is preserved in the gel and to a certain degree after thermal treatment as well (Figure 1). Micrograph of samples A2 exhibits a good distribution of Ni grains inside the YSZ matrix (Ni particles are represented by fine spheres captured inside the matrix). The fine Ni particles of the micro- or even submicrometer range are distributed uniformly inside the YSZ framework with fine pores surrounding them. Because the sintered non-reduced A2 sample is rather dense (91.90 % of the theoretical density), these pores seem to be formed by volume shrinkage caused by the reduction of the NiO to Ni particles. The volume reduction during TPR results in the formation of very fine pores just next to the Ni particles increasing the triple phase boundary area between fuel gas, iono-conductor (YSZ) and electrocatalyst Ni. The grain size distribution of the YSZ and the Ni grains is the most apparent difference in the microstructure between samples A2 and B. Ni grains in sample B are much larger ( $\approx 5 \mu\text{m}$ ) because mechanical mixing cannot provide homogenization of the phases on the same level as the wet-chemical gel-precipitation process. Although the mean particle sizes after grinding are very similar in both cases, the mechanical mixing process results in NiO and post-reduction Ni particles not being trapped inside a rigid ceramic network and thus submitted to the excess coarsening (sample B). The YSZ phase is in both cases continuous, although there is an essential difference in the size of the area of the dominant YSZ phase among these two samples. The average particle size of Ni and YSZ particles, which is the area where one or the other phase is dominant, is much greater in sample B (however, the uniformity of the phase and pore distribution is poorer).

According to the EDS analysis of sample A2 (Figure 2), the pale grey phase in the BEI image represents Ni grains distribution, while the dark grey phase corresponds to the YSZ matrix. The black parts in the image show pore distribution through the composite.

Although the area of the dominance of one or the other phase during further thermal treatment rises, the gel-precipitation technique enables very fine Ni dispersions in a YSZ matrix. If the composite is not meant to be used in extremely high temperature processes (e.g. Ni promoted catalysis) and thus does not require very high thermal treatment temperatures, a homogeneous phase distribution can be prepared even on a finer scale. As sample A1 was thermally treated up to 1000°C the enlargement of Ni and YSZ grains did not occur to such a great extend as in the case of sample A2. The one phase dominance (average particle sizes of Ni

and YSZ grains) after calcination at 950°C, sintering at 1000°C and reduction of NiO to Ni at 1000°C is no larger than 50-100 nm (Figure 3). This very fine distribution of Ni particles in the YSZ phase after the thermal treatment is a consequence of the preparation technique, where all the precursors are mixed already in the starting solution, enabling mixing theoretically on the molecular level. Ni grains in the composite form spheres randomly distributed. Because the one phase dominance is very small we tried to determine the distribution of the Ni and YSZ phase through the A1 composite by etching it with hydrochloric acid. In such a way Ni particles dissolve leaving a more porous matrix structure.

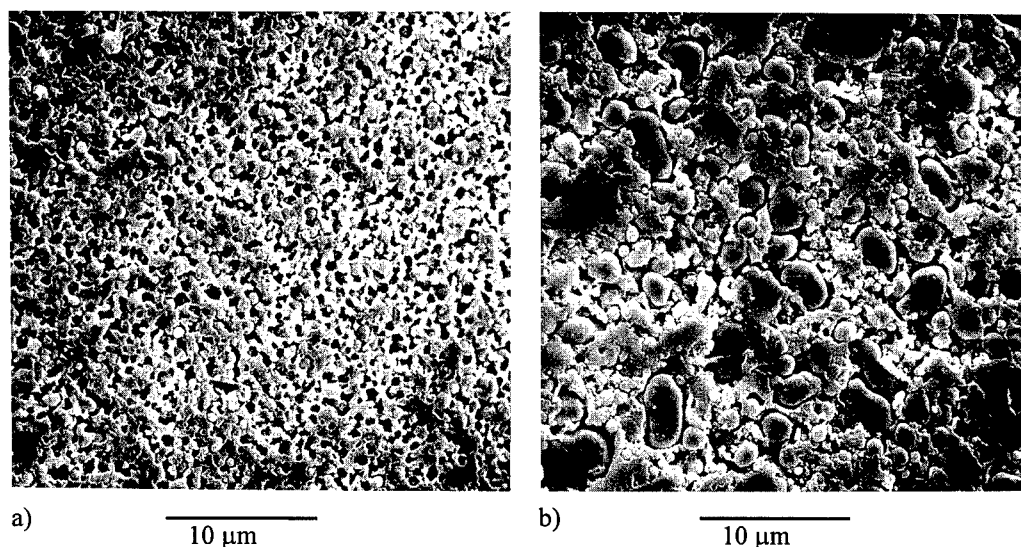


Figure 1: Microstructures of the cross sections of the samples (a) A2 and (b) B after the TPR

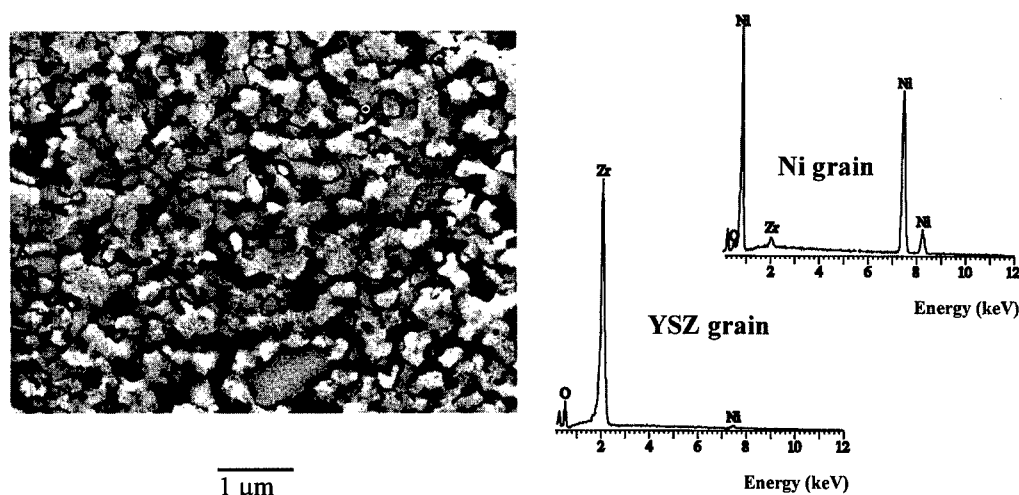


Figure 2: BEI image of the cross section of the A2 sample and EDS analysis of the phases

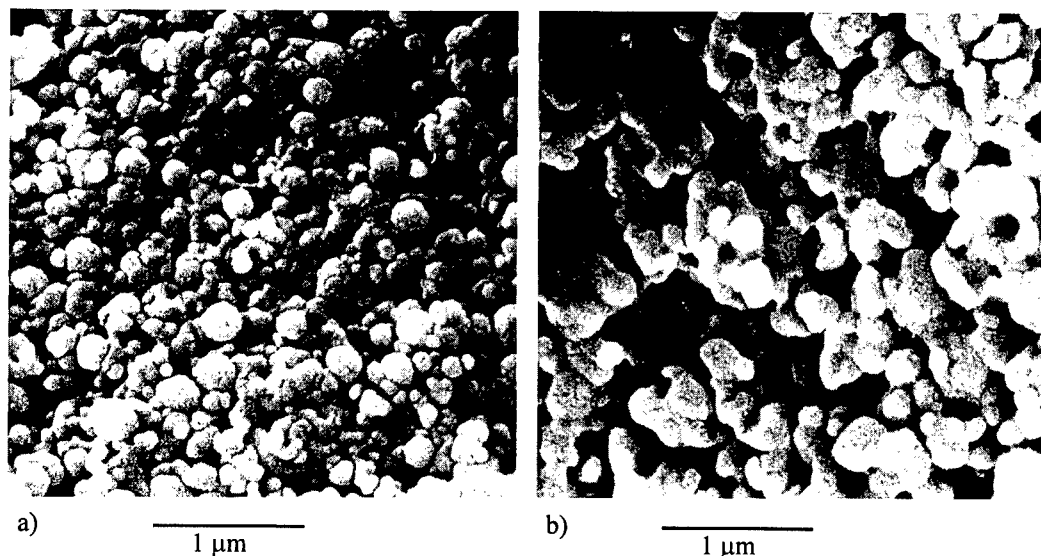


Figure 3: Microstructures of the cross section of the sample A1(a) after the TPR and (b) after etching the sample with HCl

### CONCLUSION

The gel-precipitation method is a promising method for preparing sub-micro Ni-YSZ dispersions with an extended three phase boundary. The region of one phase dominance (average particle size of Ni and YSZ) in the composite material reaches 50-100 nm after thermal treatment up to 1000°C. After prolonged sintering at 1300°C this single phase area grows to approximately micrometer range and still exhibits a very homogenous Ni dispersion. Although composites prepared by the gel-precipitation technique require more preparation steps than the mechanical mixing of the separately prepared metal oxides, final cermet show a much higher degree of homogeneity.

### ACKNOWLEDGEMENTS

The research was financed by the Ministry of Science and Technology of the Republic Slovenia.

### LITERATURE

1. Minh, N.Q., *J. Am. Ceram. Soc.*, **76** (3), 1993, 563.
2. Kawada, T., Sakai, N., Yokokawa, H., Dokiya, M., Mori, M. and Iwata, T., *J. Electrochem. Soc.*, **137** (10), 1990, 3042.
3. Shirakawa, T., Matsuda, S. and Fukushima, A., *Proc. of 3<sup>rd</sup> Int'l Symp. on Solid Oxide Fuel Cells*, (Ed. Singhal, S.C. and Iwahara, H.), Electroch. Soc., Pennington, NJ., 1993, 464.
4. Johnson, W. Jr., *Ceramic Bulletin*, **64** (12), 1985, 1597.



Pergamon

NanoStructured Materials, Vol. 12, pp. 503–506, 1999  
Elsevier Science Ltd

© 1999 Acta Metallurgica Inc.  
Printed in the USA. All rights reserved  
0965-9773/99/\$—see front matter

PII S0965-9773(99)00169-5

## DEFORMATION MECHANISM OF AMORPHOUS AND PARTIALLY CRYSTALLIZED ALLOYS

L.Q. Xing, J. Eckert and L. Schultz

IFW Dresden, Institut für Metallische Werkstoffe, Postfach 270016, D-01171 Dresden,  
Germany

**Abstract**—The deformation behaviour of  $Zr_5Ti_5Cu_{20}Ni_8Al_{10}$  amorphous and partially crystallized alloys was studied by compressive test. Precipitates of micrometer size ( $\mu m$ ) have serious effect on initiating cracks leading to early fracture. Precipitates of 2–10 nm exhibit effect of increasing yield stress and fracture stress but do not exhibit significant effect to initiate cracks when the crystalline volume fraction is below about 40%. Vein pattern is the characteristic fracture morphology of alloys with amorphous matrix. It is formed during the quick final fracture from a viscous layer along the fracture plane which is formed due to local adiabatic heating by the work of plastic shear. The plastic deformation of amorphous alloys is in fact composed of sections of elastic deformation. Each section of the elastic deformation is followed by local quick plastic shear deformation in the specimen to release stress.

©1999 Acta Metallurgica Inc.

### INTRODUCTION

Recent development of alloys of high glass forming makes it possible to cast bulk amorphous samples at a cooling rate of 1–100K/s [1–4]. These findings light up the application of bulk amorphous alloys as structural materials. In practical casting of bulk amorphous sample, a microstructure of amorphous matrix containing crystalline precipitates of micrometer size ( $\mu m$ ) can usually be obtained when the melt contains heterogeneous catalysts. Annealing or hot working above glass transition temperature may lead to an amorphous matrix with crystalline precipitates of nanometer size (nm). Therefore, partial crystallization and its effect on the mechanical property of the alloy should be considered. The deformation mechanism of amorphous or partially amorphous alloys is not so understood as that of crystalline alloys. For example, what is the reason for a slight work hardening? what is the mechanism for the plastic deformation of amorphous alloy? There are different hypothesis for the formation of vein patterns of the fracture morphology [5–7].

### EXPERIMENTAL PROCEDURES

Bulk  $Zr_{57}Ti_5Al_{10}Cu_{20}Ni_8$  amorphous alloys were prepared by copper mould casting. The mechanical test was performed by compression with specimens of 3 mm diameter and 6 mm length at a strain rate of  $2.8 \times 10^{-4} s^{-1}$ .

## RESULTS AND DISCUSSION

The compressive strain-stress curve of fully amorphous alloy is shown in Fig. 1 (a). It is characteristic of a large elastic deformation, followed by a yielding point, a slight working hardening and a typical serrated plastic deformation. Precipitation of  $\mu\text{m}$  crystals reduce the plastic deformation significantly. When the volume fraction of  $\mu\text{m}$  precipitates is above 5%, the alloy exhibits no plastic strain, as shown in Fig. 1 (c). Further increase of the  $\mu\text{m}$  crystalline volume fraction leads to decrease of the fracture strength. In contrast, the precipitates of 2-10 nm increase the yield stress and fracture stress without reducing the plastic deformation significantly when the crystalline volume fraction is less than about 40% [Fig. 1 (b)]. When the nm crystalline volume fraction is around 50%, the strain of plastic deformation decreases significantly, and more crystalline fraction leads to the decrease of fracture strength. The yield stress and fracture stress reaches the highest values for a nm crystalline fraction of about 50 %, i.e. a yield stress of 1800 MPa and a fracture stress of 1950 MPa. In contrast, the as-cast amorphous alloy exhibit a yield stress of 1560 MPa and a fracture stress of 1650 MPa.

Figure 2 shows the fracture morphologies of amorphous and partially crystallized alloys. When the alloys have an amorphous matrix as dominant phase, the fracture morphologies are characteristic of vein patterns [Fig. 2(a)], e.g. fully amorphous alloy, the as-cast alloy with approximately 5% volume fraction of  $\mu\text{m}$  precipitates and the annealed alloy with about 40% volume fraction of nm precipitates. However, the diameter of the vein pattern decreases with

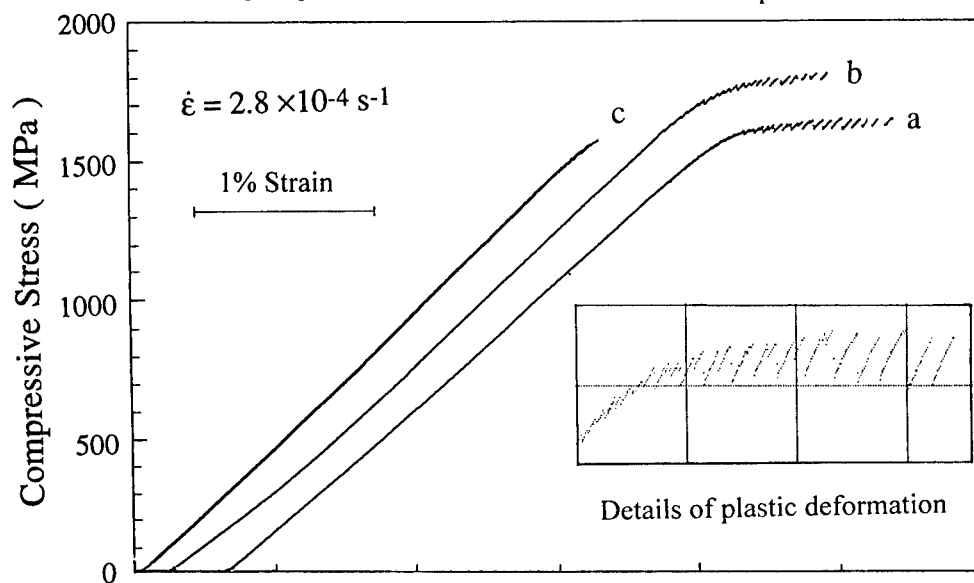


Figure 1. Compressive stress-strain curves of  $\text{Zr}_{57}\text{Ti}_5\text{Al}_{10}\text{Cu}_{20}\text{Ni}_8$  alloys: (a) as-cast amorphous alloy, (b) annealed with about 40% volume fraction of 2-10 nm crystalline precipitates, (c) as-cast with about 5% volume fraction of 1-3  $\mu\text{m}$  crystalline precipitates. The inserted figure is the enlarged illustration of the plastic deformation part.



increasing the crystalline volume fraction. The amorphous alloy has plastic strain [Fig.1(a)] but the alloy containing about 5% volume fraction of  $\mu\text{m}$  precipitates has not [Fig. 1 (c)]. This means that the vein pattern of the fracture surface is not related to the serrated plastic deformation but is created in the quick final fracture. When the fracture propagates along the fracture plane, local large deformation under a high shear stress creates an adiabatic heating. This is proofed by the flash of light when the compressed specimens crash. Since the viscosity of amorphous alloy decreases significantly with increasing temperature, a viscous layer is formed along the fracture plane. As a results, the fracture morphology looks like a viscous layer deformed between two parallel plates.

Figures 2 (b) and (c) shows the fracture morphologies of the annealed alloys containing nm crystalline precipitates between about 50% to 70% and above 70%, respectively. When the amorphous phase hold the matrix phase, a viscous layer may form along the fracture plane, leading to vein patterns. When the crystalline phase hold the dominant phase, a viscous layer can not be formed along the fracture plane since the viscosity of the crystalline phase does not decrease so significantly as amorphous phase when the temperature is increased. The fracture surface looks like a crash morphology of brittle solid with locally very flat planes [Fig 2(c)]. When the crystalline fraction is between 50% and 70%, a layer of viscous phase mixed with nanosized solid particles may be formed. The fracture morphology looks like a thin concrete layer deformed between two plates. These results indicate that the fracture morphology of partially crystallised alloys depends on the crystalline volume fraction.

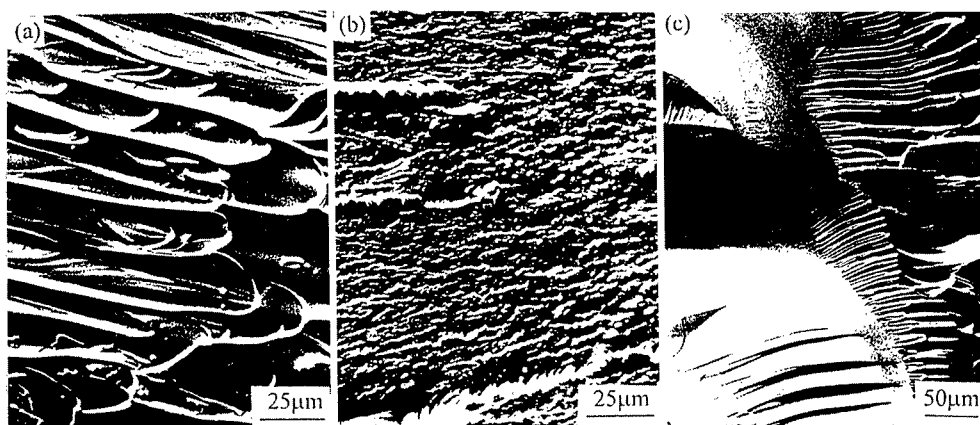


Figure 2. Characteristic fracture morphology of  $\text{Zr}_{57}\text{Ti}_5\text{Al}_{10}\text{Cu}_{20}\text{Ni}_8$  alloys: (a) matrix is dominantly amorphous phase, (b) with nanosize crystalline precipitates between about 50%-70% volume fraction, (c) with nanosize crystalline precipitates above 70 % volume fraction.

The details of the serrated plastic deformation are shown in the insert of Fig. 1. The serrated plastic strain-stress curve consists of many sections which are nearly parallel to the elastic deformation part. Each section indicates a stress increase with a strain until a maximum

value followed by a sudden drop with little strain. The maximum value is nearly the same, indicating that there is slightly working hardening. This deformation behaviour is different from that of crystalline alloys. The plastic deformation of crystalline alloys is carried out by local dislocation movement, leading to a continuous strain-stress curve and working hardening. There is no dislocation movement in amorphous alloy. The plastic deformation is in fact composed of sections of elastic deformation. For each section, strain increases with stress. When the stress reaches the maximum value, local deformation is initiated in the specimen, which should also take the form of viscous layers. The rapid local deformation exhibit no strain in the strain-stress curve because the set deformation speed of the compression facility is relatively very low. The local deformation is compensated by the elastic deformation of the whole specimen, leading to a sudden decrease of the stress. As a result, the observed plastic strain-stress curve exhibits sections parallel to the elastic part, and each section ends by a sudden drop of stress with little strain. The local deformations do not change the microstructure of the specimens homogeneously and massively, therefore, they do not have significant effect on the critical stress initiating further local deformation, leading to slight working hardening. In contrast, plastic deformation in crystalline alloys creates massive dislocations or defects in the specimen, which reduces further movement of dislocations, leading to working hardening.

### CONCLUSION

The fracture morphology of partially crystallized amorphous alloys depends on the crystalline volume fraction. Vein pattern is the characteristic fracture morphology of alloys with amorphous matrix. It is formed during the quick final fracture from a viscous layer along the fracture plane due to local adiabatic heating by the work of plastic shear. The plastic deformation of amorphous alloys is in fact composed of sections of elastic deformation. Each section of the elastic deformation is followed by a local quick plastic shear deformation in the specimen to release stress. Precipitates of  $\mu\text{m}$  size have serious influence on initiating nucleation of cracks leading to fracture. A proper amount of precipitates of 2-10 nm size increase the strength but do not exhibit much effect on initiating cracks.

### REFERENCES

1. Inoue, A., Zhang, T., Nishiyama, N., Ohba, K and Masumoto, T., *Materials Transactions JIM*, 1993, 34, 1234.
2. Peker, A. and Johnson, W.L., *Applied Physics Letters*, 1993, 63, 2342.
3. Xing, L.Q., Ochin, P., Harmelin, M., Faudot, F. and Bigot, J., *Journal of Non-Crystalline Solids*, 1996, 205-207, 597.
4. Lin, X.H. and Johnson, W.L., *Materials Transactions JIM*, 1997, 38, 473.
5. Tabachnikova, E.D., Bengus, V.Z., Molokanov, V.V., *Materials Science Forum*, 1996, 225-227, 107.
6. Xing, L.Q., Bertrand, C., Dallas, J.P. and Cornet, M., *Materials Science & Engineering A*, 1998, 241, 216.
7. Spaepen, F. and Turnbull, D., *Scripta Metallurgica*, 1974, 8, 563.



Pergamon

NanoStructured Materials, Vol. 12, pp. 507–510, 1999

Elsevier Science Ltd

© 1999 Acta Metallurgica Inc.

Printed in the USA. All rights reserved

0965-9773/99/\$—see front matter

PII S0965-9773(99)00170-1

## SYNTHESIS AND MECHANICAL PROPERTIES OF TiO<sub>2</sub>-EPOXY NANOCOMPOSITES

C.B. Ng, L.S. Schadler, and R.W. Siegel

Materials Science and Engineering Department

Rensselaer Polytechnic Institute, Troy, NY 12180, USA

**Abstract**—New developments in the synthesis of nanometer scale TiO<sub>2</sub> particles have enabled the processing of exciting new nanoparticle/epoxy composites. An ultrasonic method was used to disperse the nanoparticles in epoxy, thus eliminating the need for solvent without sacrificing the ease of processing. Composites were processed at the 5, 10, 15 and 20 weight percent level and were characterized by SEM, tensile tests and scratch tests. These results at 10 percent loading were also compared with an equal loading of micron-size TiO<sub>2</sub> fillers in epoxy to evaluate the strain-to-failure and scratch resistance.

©1999 Acta Metallurgica Inc.

### INTRODUCTION

It has long been known that the presence of fillers in a polymer increases the mechanical properties of the polymer. Moloney *et al.* (1) reported that increasing the volume fraction and the filler modulus increases the modulus of particulate-filled epoxy resins. However, their studies were done on micron-size silica, alumina and silicon carbide particles.

Materials consolidated from nanometer-size particles have been found to yield superior mechanical properties compared to their micron-size counterparts. Strain-rate sensitivity values, for example, obtained by Mayo *et al.* (2) indicated ductile behavior of nanophase ceramics at room temperature. Elsewhere, Guermazi *et al.* (3) demonstrated the ability of dense nanophase TiO<sub>2</sub> to deform extensively at elevated temperature without cracking or fracture. A similar effect has been reported by Jain and Christman (4) in a mechanically attrited nanophase intermetallic compound. These and numerous other reports prompted us to consider the exciting possibility of incorporating the nanometer-size particles in a polymer system to study their effects on the mechanical properties of the composites. The following study describes the synthesis and results of our research, with highlights on the exceptional strain-to-failure and scratch resistance of the TiO<sub>2</sub>-epoxy nanocomposites.

### EXPERIMENTAL

The polymer used in this experiment was epichlorohydrin-based epoxy resin (Shell

Oil Company). The nanometer size  $\text{TiO}_2$  particles (avg. diameter 32 nm), with compositions of 90% anatase and 10% rutile (Nanophase Technologies Corporation) were added to the epoxy resin in at  $60^\circ\text{C}$  to lower the viscosity of the resin. The particles were mixed in the polymer with a glass rod. The  $\text{TiO}_2$  fillers were then dispersed in epoxy by placing a beaker in the mixture in an ultrasonic bath (Branson Model B220) for about 1 hour. The temperature of the bath was kept constant at about  $60^\circ\text{C}$  throughout the whole sonication. 1,3-phenylenediamine (Sigma-Aldrich Inc.) was added at the end of the sonication as a hardener. The mixture was quickly poured into a preheated silicone mold to form the tensile and scratch specimens.

The micron-size  $\text{TiO}_2$  particles with average diameter of  $0.24\text{ }\mu\text{m}$  (Tioxide Inc.) were chosen to match the surface chemistries and the crystallographic composition of the nanometer-size  $\text{TiO}_2$  as closely as possible. The micron-filled  $\text{TiO}_2$  epoxy composites were made the same way as the nano-filled  $\text{TiO}_2$  epoxy composites.

The gauge length of our tensile specimen was about 5 cm with a cross sectional area of about  $11\text{ mm}^2$ . For the scratch specimens, the composites were molded into a bar which was then cut to dimensions of  $2\text{ cm(l)} \times 1\text{ cm(w)} \times 0.5\text{ cm(h)}$ . All samples were polished using a 400 grid paper prior to testing. Tensile tests were performed on a Electro-Mechanical Testing Machine Model 4204 at a stroke rate of  $2.54\text{ mm/min}$  at room temperature. Scratch test was performed with a BYK Gardener SG-8101 balance beam scrape adhesion with a 4 kg load. Fracture and scratch morphology were observed in a JOEL-JSM 840 SEM.

## RESULTS AND DISCUSSION

Dispersion studies were carried out by SEM. The micrographs obtained from the surface of the nanocomposites showed the presence of individual  $\text{TiO}_2$  particles embedded in an epoxy matrix. There were some agglomerates, but overall the dispersion was good.

Figure 1 shows the effect of different weight percents of nanometer-size  $\text{TiO}_2$  fillers on the 1% secant modulus and the strain-to-failure of the nanocomposites. Each data point is an average of 4 measured values. As observed, the 1% secant modulus increased with increased  $\text{TiO}_2$  loading. However, the strain-to-failure showed a sudden increase at 10 w%  $\text{TiO}_2$ . The lower strain-to-failure for the 5 w% nanometer- $\text{TiO}_2$ -filled epoxy was found to be caused by particle agglomerates, which act as defects.

Figure 2 shows the effect of different size  $\text{TiO}_2$  fillers on the strain-to-failure of 10 weight percent epoxy composites. The bar chart plotted in Figure 2 is taken from an average of 4 measured values. As can be seen, an advantage of the nanometer- $\text{TiO}_2$ -filled epoxy is the higher strain-to-failure over the pure epoxy and the micron- $\text{TiO}_2$ -filled epoxy. The nanometer- $\text{TiO}_2$ -filled epoxy has a failure strain of about 15% higher than that of the pure epoxy, while the micron-  $\text{TiO}_2$ -filled epoxy has the lowest strain-to-failure.

Changing the filler particle size at a constant weight fraction has a significant influence on the scratch resistance of the composites. This is clearly shown in Figure 3 for pure epoxy resin and an epoxy resin filled with 10 weight percent micron-size and nanometer-size  $\text{TiO}_2$ . The nanometer-size  $\text{TiO}_2$  filled epoxy showed a dramatic increase in the scratch resistance when compared to pure epoxy and micron- $\text{TiO}_2$ -filled epoxy. The

scratch morphology obtained by SEM revealed that the nanometer-TiO<sub>2</sub> scratch exhibited the least damage.

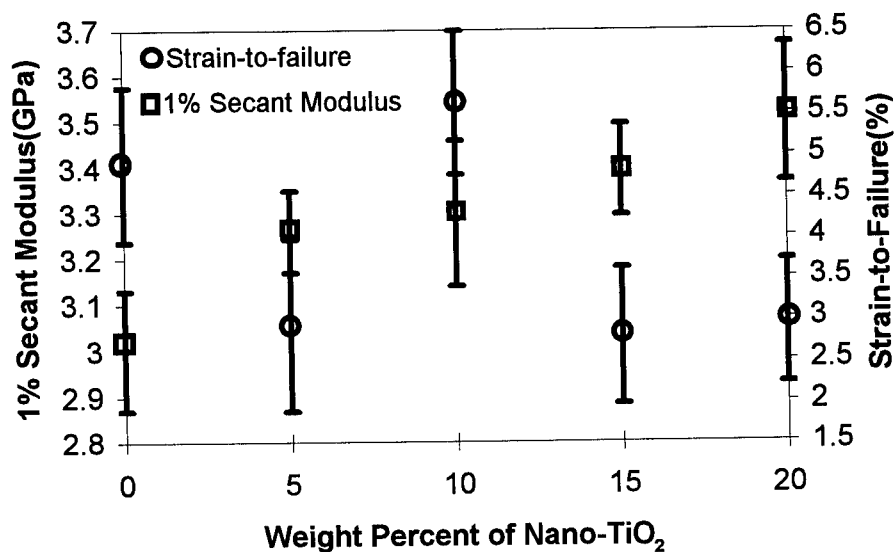


Figure 1. Graph of 1% Secant Modulus (GPa) and Strain-to-Failure (%) vs. Weight Percent of Nanometer-Size TiO<sub>2</sub> in Epoxy.

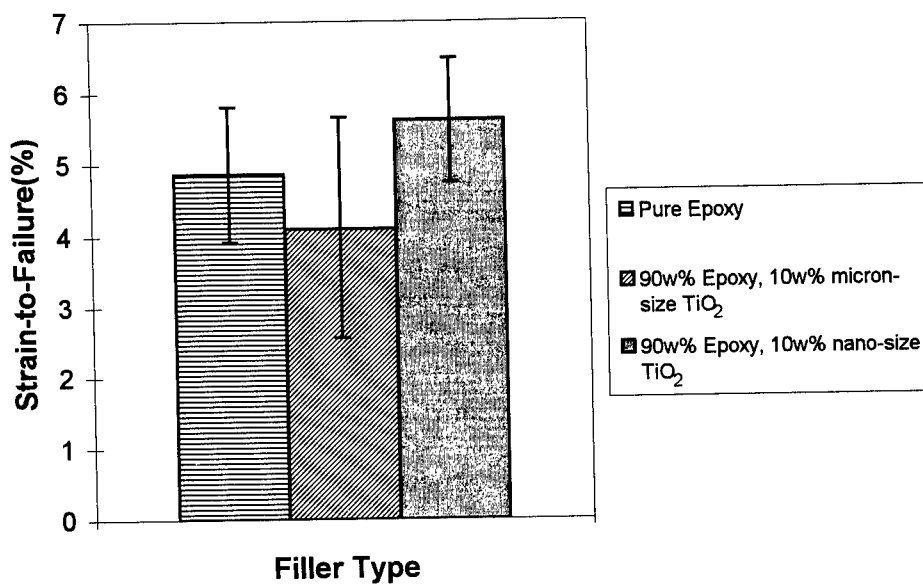


Figure 2. Effects of Different Size TiO<sub>2</sub> Fillers on the Strain-to-Failure of Epoxy Composite.

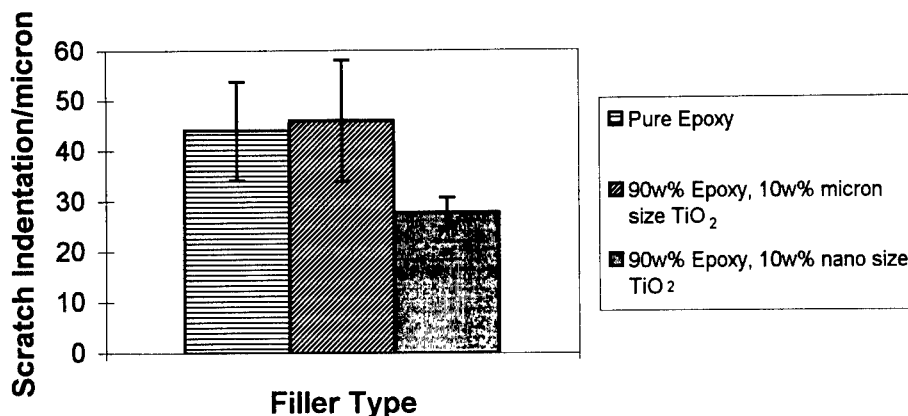


Figure 3. Effects of Different Size  $\text{TiO}_2$  Fillers on the Scratch Indentation of Epoxy Composites

### SUMMARY

At the 10 weight percent level, nanophase  $\text{TiO}_2$  particle fillers increase both the modulus and the strain-to-failure of epoxy. Micron-size  $\text{TiO}_2$  filler increases the epoxy modulus, but decreases the strain-to-failure. Thus, nanometer- $\text{TiO}_2$ -filled epoxy at some levels of loading results in a tougher composite than the traditional filled epoxy composites. Nanometer- $\text{TiO}_2$ -filled epoxy composites have a higher scratch resistance than both pure epoxy and micron- $\text{TiO}_2$ -filled epoxy composites. Further results and discussion will be published in an upcoming paper.

### ACKNOWLEDGEMENT

This work was funded in part by the NSF National Young Investigator Program. Thanks to Rensselaer Polytechnic Institute, Elena Petrovicova and Donald Van Steele. Thanks also to Nanophase Technologies Corporation and Tioxide Inc. for supplying the  $\text{TiO}_2$  fillers.

### REFERENCES

1. Moloney, A.C., Kausch, H.H., Kaiser, T. and Beer, H.R., *Journal of Materials Science*, 1987, 22, 381.
2. Mayo, M.J., Siegel, R.W., Narayanasamy, A. and Nix, W.D., *Journal of Materials Research*, 1990, 5, 1073.
3. Guermazi, M., Hofler, H.J., Hahn, H. and Averbach, R.S., *Journal of American Ceramics Society*, 1991, 74, 2672.
4. Jain, M. and Christman, T., *Acta Metall. Mater.*, 1994, 42, 1901.



## PREPARATION OF M/TiO<sub>2</sub> (M = Au, Pt) NANOCOMPOSITE FILMS USING CO-SPUTTERING METHOD

Takeshi Sasaki<sup>1</sup>, Naoto Koshizaki<sup>1</sup>, Michio Koinuma<sup>2</sup>, Yasumichi Matsumoto<sup>2</sup>

<sup>1</sup> National Institute of Materials and Chemical Research (NIMC), Agency of Industrial Science and Technology, MITI, 1-1 Higashi, Tsukuba, Ibaraki 305-8565, Japan.

<sup>2</sup> Department of Applied Chemistry and Biochemistry, Faculty of Engineering, Kumamoto University, 2-39-1 Kurokami, Kumamoto 860-8555, Japan.

**Abstract** — Au/TiO<sub>2</sub> and Pt/TiO<sub>2</sub> nanocomposite films were deposited on quartz glass substrates by the co-sputtering method. As-deposited Pt/TiO<sub>2</sub> and Au/TiO<sub>2</sub> nanocomposite films consist of amorphous nanoparticles of Pt, Pt-Ti-O or PtO<sub>2</sub> in amorphous TiO<sub>2-x</sub> and crystallized Au nanoparticles in amorphous TiO<sub>2-30</sub>, respectively. The chemical states of Pt in as-deposited Pt/TiO<sub>2</sub> nanocomposite films were strongly dependent upon the content of Pt in the nanocomposites. The heated Au/TiO<sub>2</sub> and Pt/TiO<sub>2</sub> nanocomposite films were composed of Pt metal and Au metal nanoparticles in the matrix of rutile-type TiO<sub>2</sub>, respectively. Both Pt and Au nanoparticles in the nanocomposite films inhibit the formation of anatase-type TiO<sub>2</sub> during heat treatment.

©1999 Acta Metallurgica Inc.

### INTRODUCTION

Nanocomposites doped with semiconductors or metal have been extensively studied because of their unique optical properties such as high third-order nonlinear susceptibility  $\chi^{(3)}$  (1) and photoluminescence (2). These unique optical and/or chemical properties result from quantum size effects of the embedded nanoparticles in the matrix, and interface and/or surface effects between nanoparticles and the matrix.

Typically, silicon dioxide (SiO<sub>2</sub>) is used as the main matrix material for these optical functional nanocomposites because it is an inert material which is transparent in the visible light range. Titanium dioxide (TiO<sub>2</sub>) has photoactivities which have been previously used for photocatalyst and photoelectrode applications. TiO<sub>2</sub> is a typical material which can be used as a functionally active matrix. The use of the functionally active materials as the matrix in nanocomposites can create a new type of functional nanocomposite, an *active matrix nanocomposite*, where the interaction between the nanoparticles and matrix can be utilized.

Particles of noble metals such as Pt, Pd and Au have been deposited on TiO<sub>2</sub> to improve the catalytic and photocatalytic activity (3, 4). These composites have been prepared by the chemical methods such as the sol-gel method. In this paper we report on the preparation and characterization of Pt/TiO<sub>2</sub> and Au/TiO<sub>2</sub> nanocomposite films using the rf magnetron co-sputtering method and demonstrate the chemical state of Pt and Au in these nanocomposite films.

## EXPERIMENTAL

Pt/TiO<sub>2</sub> and Au/TiO<sub>2</sub> nanocomposite films were deposited on quartz glass substrates by the co-sputtering method using an rf sputtering apparatus (Shimadzu, HSR-521). Platinum and/or gold wires were placed symmetrically on a hot-pressed TiO<sub>2</sub> target. The sputtering conditions were the same as in the previous study for Pt/TiO<sub>2</sub> deposition (5). The length of the metal wires on the TiO<sub>2</sub> target was changed to obtain nanocomposite films with various levels of metal content. The thickness of as-deposited nanocomposite films measured from the edge profile by a surface roughness meter ranged from 200 to 1000 nm. All the samples were heated in air at 600 °C for 5 h. The structures of the films were examined by XRD analysis using CuK $\alpha$  radiation (Rigaku, RAD-C). The nanostructures, compositions, and chemical states of constituents for the nanocomposite films were characterized by TEM (JEOL, JEM2000-FXII) and XPS (PHI, 5600ci).

## RESULTS AND DISCUSSION

Figure 1 shows the atomic ratio of M/Ti (M = Pt, Au) in the as-deposited nanocomposite films as a function of metal wire length placed on the TiO<sub>2</sub> target. The Pt/Ti and the Au/Ti atomic ratios were calculated from Ti 2p, Pt 4f and Au 4f peak areas in the X-ray photoelectron spectra of nanocomposite films. Both atomic ratios in the deposited nanocomposite films increased with an increase in the metal wire length, suggesting that the content of metals in the deposited nanocomposites can easily be controlled by the length of the wire placed on the TiO<sub>2</sub> target. The Au/Ti atomic ratios tended to be larger than the Pt/Ti atomic ratios, resulting from a higher sputtering rate for Au than for Pt in Ar atmosphere (6).

TEM observation indicated that the Pt and Au nanoparticles were embedded in the TiO<sub>2</sub> matrix. The size of Au nanoparticles exceeded that of Pt nanoparticles which ranged from 1 to 2 nm in the as-deposited Pt/TiO<sub>2</sub> nanocomposite film (5). Both as-deposited nanocomposite films have inhomogeneous nanostructures. The nanoparticle size in the nanocomposite films was increased by the heat treatment.

Figures 2 shows the M 4f<sub>7/2</sub> and Ti 2p binding energies as a function of the atomic ratio of M/Ti (M = Au, Pt) in the as-deposited nanocomposite films. The Ti 2p<sub>3/2</sub> binding energy in as-

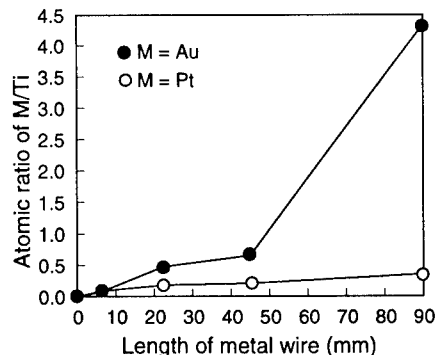


Figure 1. M/Ti atomic ratio in the as-deposited M/TiO<sub>2</sub> (M = Pt, Au) nanocomposite films as a function of metal wire length placed on the TiO<sub>2</sub> target.



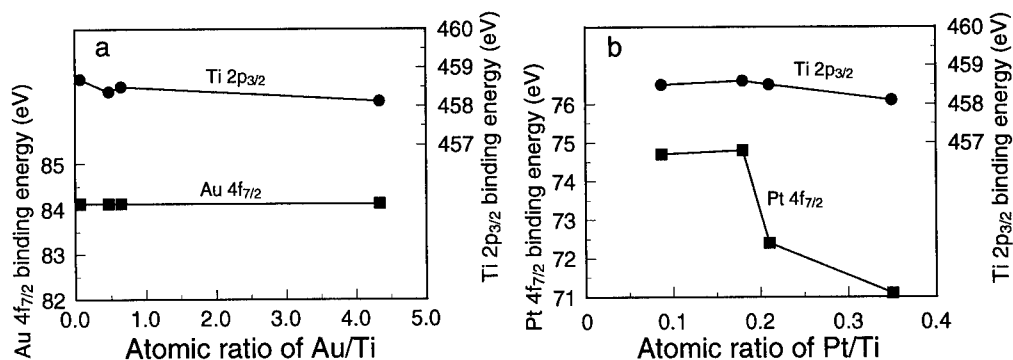


Figure 2. M 4f<sub>7/2</sub> and Ti 2p binding energies as a function of the atomic ratio of M/Ti (a: M=Au; b: M=Pt) in the as-deposited nanocomposite films

deposited nanocomposite films was observed in an energy range from 458.1 to 458.6 eV, which is smaller than the Ti 2p<sub>3/2</sub> binding energy of TiO<sub>2</sub> (458.7 eV) (7). These results indicate that the matrix in both as-deposited Pt/TiO<sub>2</sub> and Au/TiO<sub>2</sub> nanocomposites can be TiO<sub>2-x</sub>, where the oxygen vacancies may be formed by a slight reduction during the sputter deposition process in an argon atmosphere.

As shown in Fig. 2a, the Au 4f<sub>7/2</sub> binding energies were independent of the atomic ratio of Au/Ti in the Au/TiO<sub>2</sub> nanocomposites. The Au 4f<sub>7/2</sub> binding energies in Au/TiO<sub>2</sub> nanocomposites were constant at 84.1 eV, which is very close to the Au 4f<sub>7/2</sub> binding energy of Au metal (84.0 eV) (8). These results indicate that the chemical state of Au nanoparticles in the as-deposited Au/TiO<sub>2</sub> nanocomposites were Au metal. In contrast, the Pt 4f<sub>7/2</sub> binding energies were strongly dependent on the atomic ratio of Pt/Ti in the Pt/TiO<sub>2</sub> nanocomposites, as shown in Fig. 2b. The Pt 4f<sub>7/2</sub> binding energies at smaller Pt/Ti atomic ratios than 0.2 were very close to the energy of PtO<sub>2</sub> (74.9 eV) (9), indicating that the chemical states of Pt nanoparticles in the as-deposited Pt/TiO<sub>2</sub> nanocomposites with the Pt/Ti atomic ratio of 0.08 and 0.18 were PtO<sub>2</sub>. Pt 4f<sub>7/2</sub> binding energies of the nanocomposite films with Pt/Ti atomic ratios of 0.21 and 0.35 were 72.4 eV and

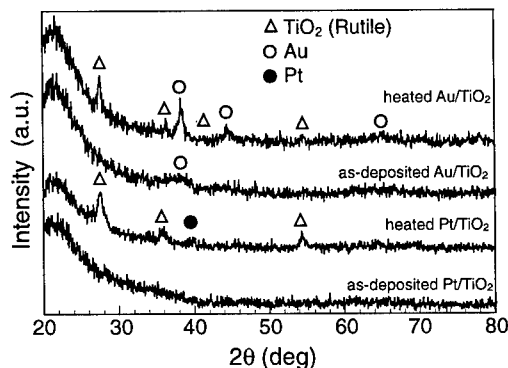


Figure 3. X-ray diffraction patterns of as-deposited and heated Pt/TiO<sub>2</sub> film (Pt/Ti = 0.21) and Au/TiO<sub>2</sub> film (Au/Ti = 0.07) at 600°C.

71.1 eV, respectively. These data indicate that the chemical states of Pt nanoparticles in the nanocomposite films with Pt/Ti atomic ratio of 0.21 and 0.35 were almost Pt-O-Ti (72.0 eV) (9) and Pt metal crystallite (71.3 eV) (9), respectively. The chemical state of Pt in Pt/TiO<sub>2</sub> nanocomposite films were Pt metal after the heat treatment at 600 °C.

Figure 3 shows X-ray diffraction patterns of Pt/TiO<sub>2</sub> film with Pt/Ti atomic ratio of 0.21 and Au/TiO<sub>2</sub> film with Au/Ti atomic ratio of 0.07 before and after heat treatment at 600 °C. No diffraction peak was observed in as-deposited Pt/TiO<sub>2</sub> film, indicating that the as-deposited Pt/TiO<sub>2</sub> nanocomposite films were amorphous. In contrast, broad Au diffraction peaks were observed in as-deposited Au/TiO<sub>2</sub> nanocomposites, indicating that the nanoparticles of Au in as-deposited Au/TiO<sub>2</sub> nanocomposites were crystalline even when there is a very low content of Au, and matrix of TiO<sub>2</sub> in the as-deposited nanocomposites is amorphous. After heat treatment at 600 °C, diffraction peaks of TiO<sub>2</sub> rutile phase were observed as shown in Fig. 3. The anatase-type TiO<sub>2</sub> is in a stable phase at temperatures below 800 °C, and is transformed into the rutile-type TiO<sub>2</sub> at 800 to 900 °C (10). These results indicate that the both Pt and Au nanoparticles in the nanocomposite films can inhibit the formation of anatase-type TiO<sub>2</sub> during the heat treatment.

### CONCLUSIONS

Au/TiO<sub>2</sub> and Pt/TiO<sub>2</sub> nanocomposite films were deposited on quartz glass substrates by the co-sputtering method. As-deposited Pt/TiO<sub>2</sub> and Au/TiO<sub>2</sub> nanocomposite films consist of amorphous nanoparticles of Pt, Pt-Ti-O or PtO<sub>2</sub> in amorphous TiO<sub>2-x</sub>, and crystallized Au nanoparticles in amorphous TiO<sub>2-x</sub>, respectively. The heated Au/TiO<sub>2</sub> and Pt/TiO<sub>2</sub> nanocomposite films were composed of Pt metal and Au metal nanoparticles in the matrix of rutile-type TiO<sub>2</sub>. Both Pt and Au nanoparticles in the nanocomposite films inhibit the formation of anatase-type TiO<sub>2</sub> during the heat treatment.

### REFERENCES

1. Hache, F., Ricard, D., Flytzanis, C. and Kreigig, U., *Applied Physics*, 1998, **A47**, 347.
2. Hayashi, S., Kataoka, M. and Yamamoto, K., *Japanese Journal of Applied Physics*, 1993, **32**, L274.
3. Zhao, G., Kozuka, H. and Yoko, T., *Thin Solids Films*, 1996, **277**, 147.
4. Boccuzzii, F., Chiorino, A., Tsubota, S. and Haruta, M., *Journal of Physical Chemistry*, 1996, **100**, 3625.
5. Sasaki, T., Koshizaki, N., Terauchi, S., Matsumoto, Y. and Koinuma, M., *Nanostructured Materials*, 1998, **8**, 1077.
6. Vossen, J.L. and Cuomo, J.J., *Thin Film Process*, Academic Press, 1978, p. 15.
7. Nefedov, V.I., Salyn, Y.V., Chertkov, A.A. and Padurets, L.Z., *Zhurnal Neorganicheskoi Khimii*, 1974, **19**, 1443.
8. Aita, C.R. and Tran N.C., *Journal of Vacuum Science Technology A*, 1991, **9**, 1498.
9. Decker, F., Neuenschwander, R.T., Cesar, C.L. and Penna, A.F.S., *Journal of Electroanalytical Chemistry*, 1987, **228**, 481.
10. DeVries, R.C. and R., Roy, *American Ceramic Society Bulletin*, 1954, **33**, 370.



Pergamon

NanoStructured Materials, Vol. 12, pp. 515–518, 1999

Elsevier Science Ltd

© 1999 Acta Metallurgica Inc.

Printed in the USA. All rights reserved

0965-9773/99/\$—see front matter

PII S0965-9773(99)00172-5

## SOLIDIFICATION AND MELTING OF GALLIUM AND MERCURY IN POROUS GLASSES AS STUDIED BY NMR AND ACOUSTIC TECHNIQUES

**D. Michel<sup>1</sup>, B.F. Borisov<sup>2</sup>, E.V. Charnaya<sup>2</sup>, W.-D. Hoffmann<sup>1</sup>, P.G. Plotnikov<sup>2</sup>, Yu.A. Kumzerov<sup>3</sup>**

<sup>1</sup> Faculty of Physics and Geosciences, University of Leipzig, D-04103 Leipzig, Germany

<sup>2</sup> Institute of Physics, St.Petersburg State University, St.Petersburg, 198904 Russia

<sup>3</sup> A.F.Ioffe Physico-Technical Institute RAN, St.Petersburg, 194021, Russia

**Abstract** - *The melting and freezing phase transitions of mercury and gallium in porous glasses were studied. A depression of the phase transition temperatures, a pronounced hysteresis between melting and freezing, and the melting and freezing broadening were found. The measurements on confined mercury showed that melting could be treated within the frameworks of the model of a liquid layer on solid cores, while freezing is probably driven by nucleation. The Knight shift and line shape studies revealed peculiarities in the structure of liquid confined gallium. No correlation was obtained between the melting reduction and pore sizes for the glasses filled with gallium that was treated as a result of various confined solid modifications formed within pores. ©1999 Acta Metallurgica Inc.*

### INTRODUCTION

Phase transitions in materials confined within porous glasses are the object of continuing interest. They differ significantly from those in the corresponding bulk samples and depend on many factors, such as pore size and geometry, wetting, and interactions with the inner surface. Among the different phase transitions, the melting and freezing phase transitions are of particular interest because they are purely first order and are well studied for bulk samples [see (1-3) and references therein]. Here we present results of studies of the melting and freezing phase transitions for gallium and mercury in porous glasses using NMR and acoustic techniques. The NMR measurements provided direct information on the total amount of liquid metals versus temperature. Furthermore they allow us also to get some information about the peculiarities in the structure of liquid confined metals through the Knight shift and the line shape. Acoustic measurements supplied information about changes in elastic moduli and relaxation phenomena.

## EXPERIMENTAL

The samples under study were prepared from phase-separated soda borosilicate glasses whose pore structure was produced by acid leaching. After acid leaching, an interconnected network of pores was formed with the average pore diameter determined by mercury intrusion porosimetry. The pore size in the sample filled with mercury was 7 nm. The pore size distribution was fairly narrow with 80 % of the pore diameters lying within 0.5 nm of the average size. The liquid mercury was introduced into the porous glass under high pressure up to 10 kbar using the same procedure as for mercury intrusion porosimetry. The mercury volume was about 9% of the total sample volume. The filling factor was about 90% of the total pore volume.

The average pore size for the samples filled with gallium was 3.5, 8, and 200 nm. The latter exhibited a well defined bimodal pore size distribution, with diameters about 200 nm and near 7 nm for the coarse and fine pores, respectively. The coarse pores showed a broad variation in diameter, while the fine pore size distribution was fairly narrow. The fine pore size distributions for the samples with 3.5 and 8 nm pores were also rather narrow. The liquid metal was introduced into the porous glasses under high pressure up to 9 kbar. The volume fraction for the samples under study was about 12, 18, and 26%, respectively. The filling factor of the pore volume was 85 to 90%. After filling, i.e. when the pressure had been removed, all the samples under study were stable and did not exhibit any substantial weight loss.

The NMR measurements were run using a pulse Bruker MSL500 NMR spectrometer. The temperature dependence of the  $^{199}\text{Hg}$  and  $^{71}\text{Ga}$  NMR line has been studied in the temperature ranges covering the bulk mercury and gallium melting points (234.3 K and 303 K). First the samples under study were cooled down from temperatures well above the bulk melting point and then warmed up again to high temperatures. The rate of warming and cooling was very slow to prevent temperature overshoots, which were in our measurements no more than 0.5 K. Prior to each measurement, the samples were kept at a fixed temperature for about 5 minutes. The accuracy of temperature control was better than 0.5 K. Furthermore, the samples were held at several fixed temperatures for two hours to study whether this would result in any changes in NMR signals. To detect the intensity of the mercury and gallium NMR signals, free induction decays acquired after a single pulse and a solid-echo pulse sequence were observed.

Acoustic measurements were performed using the conventional pulse acoustic technique, which gave the relative sound velocity value  $\Delta v/v$  with an accuracy better than  $10^{-5}$  and the relative attenuation coefficient  $\Delta\alpha$  with an accuracy within 5%. Temperature dependencies of velocity and attenuation for longitudinal and transverse waves were studied. The frequency of the longitudinal and transverse waves were near 6 - 8.5 MHz and near 5.5 MHz, respectively. Repeated cycles of slow cooling and warming similar to that used in the NMR studies were carried out for the samples cut from the same bulk specimens as for NMR. The same procedure of holding the samples at a constant temperature for many hours was applied. In addition, we measured acoustic velocity and attenuation during partial cycling to reveal the temperature regions of reversible and irreversible behaviour at cooling and warming.

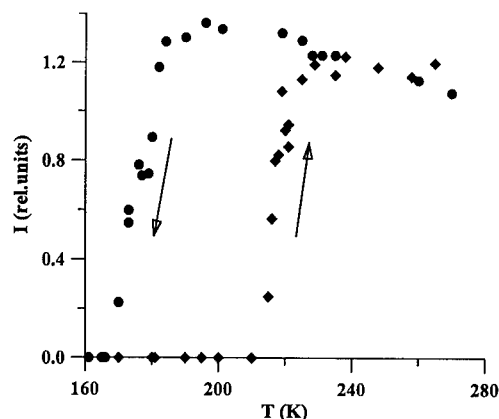


Figure 1. Intensity  $I$  of the  $^{199}\text{Hg}$  NMR signal versus temperature on cooling (solid circles) and on warming (solid diamonds) in the porous glass filled with mercury.

## RESULTS AND DISCUSSION

A depression of the melting and freezing phase transition temperatures and a pronounced hysteresis between melting and freezing were found for all the samples under study. As an example, the temperature dependence of the integral intensity of the NMR signal attributed to liquid mercury is shown in Fig.1. Holding the samples at any fixed temperature for more than 2 h did not lead to noticeable changes in the NMR intensity. We could not find any signal from confined solid mercury and the signal from confined solid gallium was seen only in the sample with 200 nm pores (1,2). Results of acoustic measurements for longitudinal and transverse ultrasound waves in the sample filled with mercury are shown in Fig.2 for one of the complete temperature cycle. One can see clearly that temperatures of merging the curves obtained during cooling and warming differ for different polarisations. The detailed studies of acoustic properties for partial thermal cycles revealed a clear asymmetry in the freezing and melting processes. In particular, the irreversible behaviour for both transverse and longitudinal waves was observed upon freezing, while the alterations in transverse waves were reversible within the whole range of melting mercury and the alterations in longitudinal waves became irreversible only at the final stage of melting, i.e. above the temperature for which the two curves associated with cooling and warming for the transverse waves merge. Comparing the results obtained by NMR and acoustic techniques allowed us to assume that a liquid layer was formed on the confined mercury surface upon the reversible melting as for small metallic particles, the irreversibility range corresponded to melting of the solid mercury cores (2). In such a case, the longitudinal acoustic waves show the real temperature of offset of melting. The freezing was suggested to be driven by heterogeneous or homogeneous nucleation, the reproducible hysteresis between freezing and melting arose because of an extremely steep temperature dependence of the nucleation rates as for bulk materials.

For porous glasses filled with gallium there was no direct correlation between pore sizes

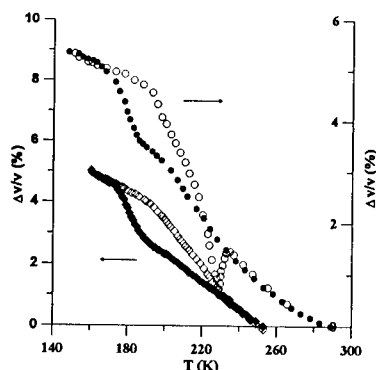


Figure 2. Longitudinal (circles) and transverse (diamonds) ultrasound velocity versus temperature upon cooling (solid symbols) and warming (open symbols) for the porous glass filled with mercury.

and lowering of the transition temperatures. Such a behaviour was explained by various modifications of solid gallium formed within pores in agreement with some x-ray data (4). The studies performed showed also that indirect methods such as acoustic one could be sensitive to melting and freezing within some particular modifications of confined materials (1).

The Knight shift was studied in details for confined liquid gallium. The values of the Knight shift and its temperature variations were found to depend on the pore sizes and to be different from the corresponding shift for the bulk liquid supercooled gallium. The line shapes together with the values of the Knight shift showed that the structure of confined liquid gallium has some peculiarities. Two models of interpretation of the NMR line shape and of the Knight shift were suggested. The first one assumed the dependence of the Knight shift on the distance from the confined liquid particle surface. The second one took into account clusters within confined liquids.

#### ACKNOWLEDGMENTS

The present work was supported by the Russian Foundation of Fundamental Investigations under grant 96-02-19523 and by the Deutsche Forschungsgemeinschaft within the Innovationskolleg INK 24.

#### REFERENCES

1. Borisov B.F. et al, *J.Phys.:Condens.Matter*, 1997, 9, 3377.
2. Borisov B.F. et al, *Phys.Rev.B*, 1998, 58, 5329.
3. Unruh K.M., Huber T.E., and Huber C.A., *Phys.Rev.B*, 1993, 48, 9021.
4. Tien C. et al, *Phys.Rev.B*, 1996, 54, 11880.



## ON THE INFLUENCE OF NANO-SCALING ON THE GLASS TRANSITION OF MOLECULAR LIQUIDS

J.K. Krüger, R. Holtwick, A. le Coutre and J. Baller

Fachbereich 10.2, Experimentalphysik, Universität des Saarlandes, Bau 38, Postfach 151150,  
66041 Saarbrücken, Germany

**Abstract** -- *The nature of the glass transition is still a matter of debate. We used temperature modulated DSC (TMDSC) and Brillouin spectroscopy (BS) to investigate the freezing behaviour of canonical glasses (salol and di-n-butyl-phtalate (DBP)) confined to controlled pore glasses (CPG) with pore diameters between 2.5 and 20 nm. The temperature behaviour of the heat capacity of the composite system deviates from the bulk fluid properties and we interpret the remaining kink-like anomaly at  $T_g$  as a static glass transition. In smaller pores  $T_g$  is only slightly shifted to lower temperatures. This operative  $T_g$  is in good agreement with sound velocity data showing a sharp kink at  $T_g$ . The working hypothesis of the existence of a static glass transition is supported by the fact that the  $\alpha$ -relaxation process disappears with decreasing pore diameter. ©1999 Acta Metallurgica Inc.*

### INTRODUCTION

The glass transition in classical glass formers is intimately connected to a structural relaxation process ( $\alpha$ -relaxation). Usually the time constant of the  $\alpha$ -process is believed to diverge below  $T_g$  following a Vogel-Vulcher-Tammann law (VFT) (1,2). The VFT-behaviour is related to growing cooperatively rearranging units with decreasing temperature (3). Up to now there is no consensus whether the thermal glass transition is a pure kinetic effect or whether accompanying kinetic effects mask a well defined intrinsic glass transition (4). Recently dielectric investigations have shown that the  $\alpha$ -process of classical glass formers is seriously modified in reduced dimensions (5). However, the expected shift of  $T_g$  to higher temperatures with decreasing pore diameter was not confirmed. The aim of this paper is to show that the  $\alpha$ -relaxation tends to disappear for small pore diameters although the static elastic and  $c_p$ -anomalies are conserved indicating the existence of a static glass transition. The static and dynamic behaviour of the elastic as well as the specific heat properties are analyzed by BS and TMDSC respectively.

### EXPERIMENTAL

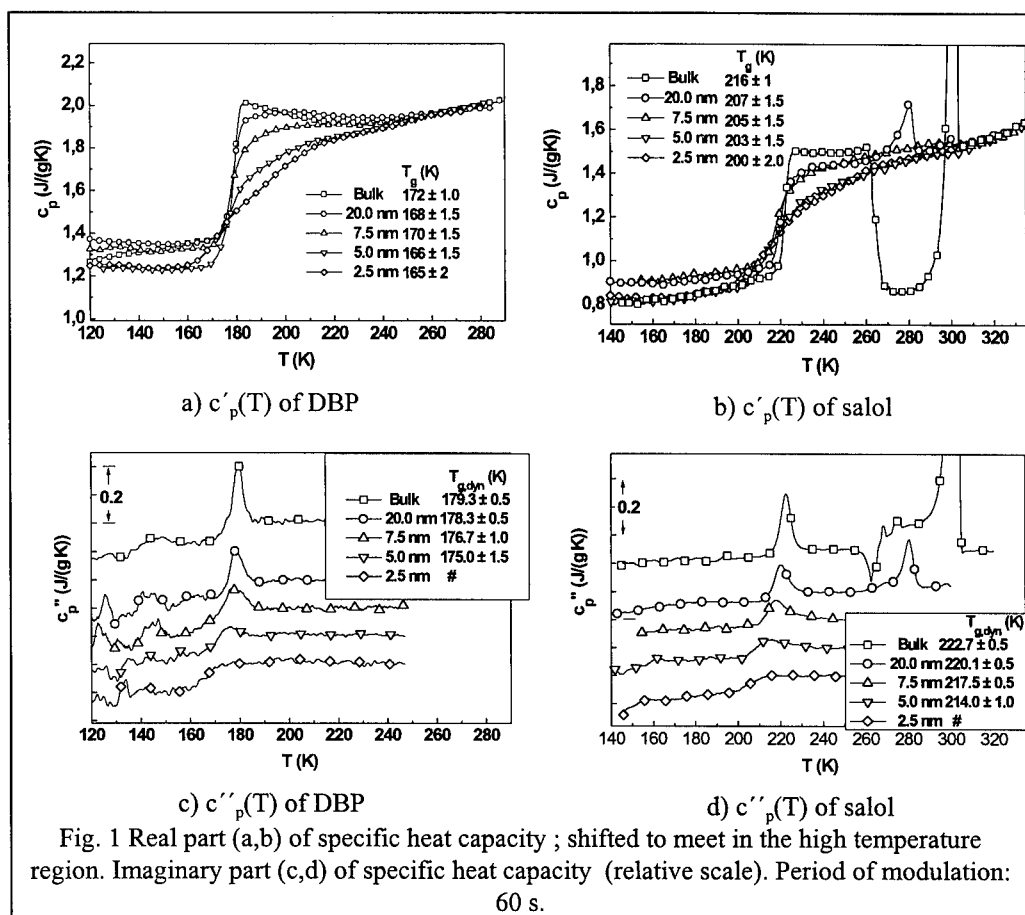
We used CPG from Geltech Inc. with pore diameters of nominal 2.5 nm to 20 nm consisting of an open pore glass matrix of >99 % pure  $\text{SiO}_2$ . The samples were dried 10 hours in vacuum (about 1-3 mbar) at 345 K and subsequently filled with the fluid glass former. For

the calorimetric studies we used a modified DSC 2920 MDSC™ (TA-Instruments). In order to apply small temperature scanning rates while covering a large temperature range we modified the measuring cell and the cooling unit. Constructional details of the hermetically closed, vacuum insulated, top-loading cell are described elsewhere (6). The TMDSC technique (7,8) applies a sinusoidal temperature modulation to the sample and records the resulting heat flow. From these signals a complex specific heat capacity  $c_p^* = c_p' - i c_p''$  can be deduced yielding information about the temperature behaviour of the  $\alpha$ -relaxation process close to  $T_g$  (9). In all TMDSC measurements the amplitude and the period of the temperature modulation were 0.2 K and 60 s respectively. Additional to this modulation an underlying heating rate of 0.2 K/min was applied. In order to determine the specific heat capacity of the pure glass forming material within the glass matrix (pore content) the raw  $c_p$ -data have to be corrected for the heat capacity of the glass matrix. For this purpose we assumed the additivity of the heat capacity of the matrix and the pore content. In consequence, the derived  $c_p'$  is comparable for different pore sizes. The optical investigations were performed with a six pass tandem Fabry Perot interferometer using the 90A-scattering geometry (10). It is worth noting that in the vicinity of the thermal glass transition BS measures acoustic properties in the slow motion regime ( $f \tau_\alpha \gg 1$ ,  $f$ : hypersonic frequency of Brillouin experiment,  $\tau_\alpha$ : relaxation time of the  $\alpha$ -relaxation process) e.g. (11).

## RESULTS AND DISCUSSION

Fig. 1 shows the specific heat capacity of CPG with different pore diameters filled with DBP and salol, respectively. The real part of  $c_p$  is plotted in a) and b) showing systematic deviations from the bulk behaviour depending of the pore size only in the middle temperature range around and above  $T_g$ . In the case of salol the bulk shows recrystallisation with  $c_p'$  falling abruptly to the crystal  $c_p$ -value at about 260 K. At about 300 K the melting peak is obvious. Salol in 20 nm pores also shows a melt peak but shifted to lower temperatures. Since in this case the melt peak is much smaller, it is only a small fraction of the material that shows the melt transition. Therefore most of the material is still in the supercooled and not in the crystalline state. These recrystallization and melting effects are as well seen in  $c_p''(T)$  (fig. 1d)). The plots in fig. 1 c) and d) are stacked and are on a relative scale. Since the absolute  $c_p'$ -precision for different samples is not as good as the precision within one measuring run, the  $c_p'$ -curves were slightly vertically shifted (within the error margins of the absolute precision of the instrument) in order to emphasis their common asymptotic behaviour in the high temperature region. The differences of the  $c_p$ -values in the glassy region are not correlated with the pore size and probably due to calibration errors rather than carrying a physical impact. As a difference to the typical bulk glass-step the curves  $c_p'(T)$  in the pores are asymmetric with respect to the inflection point. Bohn et. al. investigated the glass transition in the atactic polymer poly-vinyl-acetate (PVAC) with BS and TMDSC (12). He found a static anomaly (a kink-like changing of the temperature behaviour of the hypersound frequency) at the same temperature where  $c_p(T)$  deviates from the linear course in the glassy state. In the pores the same behaviour even becomes more evident (fig. 2): BS measurements on salol in 2.5 nm pores show a sharp kink indicating an anomaly of the static elastic properties at the temperature of the onset of the excess specific heat.





It is worth noting that in small pores even quenching of the sample prior a measurement did not influence the thermal properties (no overshoot of  $c_p'$  or heat flow DSC-signal in following heating run could be found). The glass transition temperatures yielded from the onset of the excess  $c_p'$  are noted in fig. 1a) and b). As can be seen in fig. 1 c) and d) the peak of  $c_p''(T)$  which reflects the  $\alpha$ -relaxation process loses intensity in smaller pores without significant broadening. In the 2.5 nm pores no  $c_p''$  peak can be seen. This probably is due to the confined space not allowing relaxations in this low frequency range. The temperature of the  $c_p''(T)$ -maximum is usually called dynamic glass transition temperature and therefore is frequency dependent (9). The dynamic glass transition temperatures (noted in fig. 1 c) and d)) are at higher temperatures than the static anomalies in  $c_p'(T)$  and BS results and agree with temperatures determined by Arndt et. al. (5) by the measurement of dynamic dielectric constants in the same frequency range. Furthermore they also found the  $\alpha$ -relaxation process disappearing in small pores. Since the  $\alpha$ -relaxation process at low frequencies is believed to incorporate rearranging units of several nm diameter (3), we assume that these cooperative relaxations are hindered by the restriction to the pore size. Since the  $\alpha$ -relaxation process

disappears in small pores it no longer masks the static anomaly at  $T_g$ . Now  $c'_p(T)$  reflects static properties as well as BS does (see fig. 2). This indicates that usual glass transitions are a superposition of dynamic and static processes. Even without the dynamic process the static glass transition still takes place. This adds another argument to the hypothesis of the existence of an intrinsic glass transition.

### ACKNOWLEDGEMENTS

This work was kindly supported by the Deutsche Forschungsgemeinschaft and the Sonderforschungsbereich 277.

### REFERENCES

1. Debenedetti, P.G., *Metastable Liquids : Concepts and Principles* Princeton Univ. Press, 1996
2. Donth, E., *Relaxation and thermodynamics in polymers, glass transition*, Akademie-Verlag, Berlin, 1992
3. Fischer, E.W., Donth, E., Steffen, W., *Phys. Rev. Letters*, 1992, **68**, 2344.
4. Krüger, J.K., Bohn, K.-P., Schreiber, J., *Phys. Rev. B*, 1996, **54**, 15767.
5. Arndt, M., Stannarius, R., Gorbatschow, W., Kremer, F., *Phys. Rev. E*, 1996, **54**, 5377.
6. Krüger, J.K., Bohn, K.-P., le Coutre, A., Mesquida, P., *Meas. Sci. Technol.*, 1998, **9**, 1866.
7. Boller, A., Jin, Y., Wunderlich, B., *Journal of Thermal Analysis*, 1994, **42**, 307.
8. Reading, M., Elliot, D., Hill, V.L., *Journal of Thermal Analysis*, 1993, **40**, 931.
9. Hensel, A., Dobbertin, J., Schawe, J.E.K., Boller, A., Schick, C., *Journal of Thermal Analysis*, 1996, **46**, 935.
10. Krüger, J.K., Marx, A., Peetz, L., Roberts, R., Unruh, H.-G., *Colloid & Polymer Science*, 1986, **264**, 403.
11. Krüger, J. K., in *Optical Techniques to Characterize Polymer Systems*, ed. H Bässler, Elsevier, 1989.
12. Krüger, J. K., Bohn, K.-P., Jimenez, R., *Condensed Matter News*, 1996, **5**, 10.

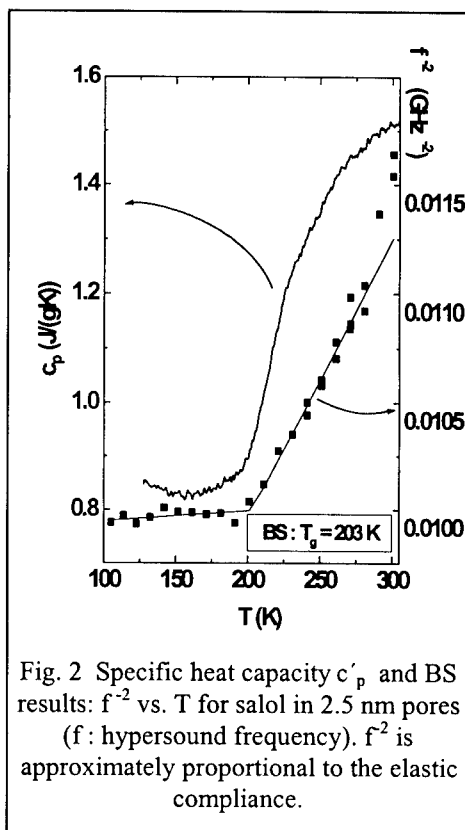


Fig. 2 Specific heat capacity  $c'_p$  and BS results:  $f^{-2}$  vs.  $T$  for salol in 2.5 nm pores ( $f$ : hypersound frequency).  $f^{-2}$  is approximately proportional to the elastic compliance.



Pergamon

NanoStructured Materials, Vol. 12, pp. 523–526, 1999

Elsevier Science Ltd

© 1999 Acta Metallurgica Inc.

Printed in the USA. All rights reserved

0965-9773/99/\$—see front matter

PII S0965-9773(99)00174-9

## MAGNETIC COMPOSITES COMPOSED OF IRON-NITRIDE NANOGRAINS DISPERSED IN A SILVER MATRIX

T. A. Yamamoto, K. Nishimaki, T. Harabe, K. Shiomi, T. Nakagawa  
and M. Katsura

Department of Nuclear Engineering, Osaka University  
2-1 Yamadaoka, Suita, Osaka 565-0781, Japan.

**Abstract** -- Magnetic nanocomposites in which iron nitride nanograins are dispersed in a silver matrix were synthesized by nitriding iron-oxide nanograins buried in the matrix. The iron nitride nanocomposite is regarded as a promising material from viewpoint of magnetic applications, since iron nitride family involves various magnetisms with large magnetic moments comparable to that of metallic iron and chemical stabilities better than those of metallic nanophase. Ferromagnetic iron nitride of  $\gamma$ -Fe<sub>4</sub>N or  $\epsilon$ -Fe<sub>2.4</sub>N was selectively obtained in the silver matrix by controlling the nitriding potential during the reaction with ammonia gas streams with various flow conditions. The composites were characterized with XRD, TEM and the magnetic properties were studied by a SQUID magnetometer.

©1999 Acta Metallurgica Inc.

### INTRODUCTION

Magnetic nanocomposites, in which nanosized magnetic species are dispersed in a non-magnetic matrix, have been attracting much attention among materials scientists (1). Numerous interesting and important science and technology issues, such as giant magneto-resistance and magnetic refrigeration, have been suggested as occurring in those new materials. Yamamoto *et al.* have synthesized superparamagnetic nanocomposites composed of 10–30 nm grains of magnetic iron oxide in a silver matrix by the inert gas condensation method and found their magnetic properties sensitive to conditions of the synthesis and heat treatments (2). This sensitivity is caused by coexistence of magnetically different phases intimately in contact with each other (Fe, Fe<sub>3</sub>O<sub>4</sub>,  $\gamma$ -Fe<sub>2</sub>O<sub>3</sub>,  $\alpha$ -Fe<sub>2</sub>O<sub>3</sub> and Ag) (3,4), which implies versatility in material processing and properties of the nanocomposites. Ferromagnetic iron nitrides,  $\gamma$ -Fe<sub>4</sub>N and  $\epsilon$ -Fe<sub>2.4</sub>N, are also regarded as an attracting magnetic components of such the nanocomposite because they have some advantages over the iron oxides and metal: their magnetic moments are larger than those of the oxides and comparable to that of metallic iron, and these nitrides are chemically stabler than metallic iron especially in the nanophase. The  $\gamma$ -phase is practically stoichiometric and in fcc structure, while the  $\epsilon$ -phase has a wide nonstoichiometric region designated by the formula of Fe<sub>2.4</sub>N and in hcp structure. In this paper, we report experimental results on synthesis of magnetic nanocomposites containing nitride nanograins in a silver matrix.

### EXPERIMENTAL

The present nitride nanocomposites were prepared by nitriding nanocomposites composed of about 10-nm iron-oxide grains buried in a silver matrix which have been

synthesized by the inert gas condensation method (2). In the starting composite, iron exists mainly as ferrimagnetic  $\text{Fe}_3\text{O}_4$  and/or  $\gamma\text{-Fe}_2\text{O}_3$  grains and partially as metallic Fe and metastable clusters embraced in silver grains. The nitridation was performed by heating the starting composite in a gas stream containing  $\text{NH}_3$  after a reduction heat treatment in hydrogen gas at  $350^\circ\text{C}$  for 4 h. In this nitridation reaction, the nitrogen potential was carefully controlled by adjusting the flow rate and/or addition of hydrogen gas into the stream in order to form selectively  $\gamma\text{-Fe}_4\text{N}$  or  $\epsilon\text{-Fe}_{2-4}\text{N}$ . The detail of the nitriding procedure is reported elsewhere (5). The matrix of metallic silver did not react with the  $\text{NH}_3$ . The magnetization was measured with a SQUID magnetometer at temperatures from room temperature down to the lowest temperature (5 or  $7.5\text{K}$ ) by sweeping the applied field between  $\pm 5$  Tesla. A full hysteresis loops at room and the lowest temperatures, and quarter loops at temperatures between them at intervals about of  $50^\circ$  were measured by cooling down the sample in the maximum field. Grain sizes in the composites obtained were determined by a transmission electron microscope (TEM). Their iron contents were evaluated by the energy dispersive x-ray fluorescence spectroscopy. Phase identification of nitrides formed in the composites were performed by x-ray diffraction.

## RESULTS AND DISCUSSION

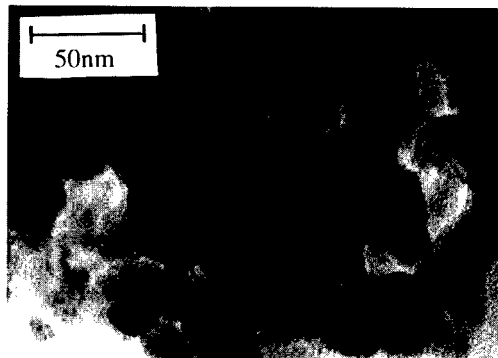
The nitridation reactions were carried out at  $350$  and  $450^\circ\text{C}$  for 4 h with the starting composites containing iron of 40 and 6% in metallic atom fraction, respectively. A grain growth, 2- 3 fold in diameter, was found to occur in the nitridation at  $350^\circ\text{C}$ , while at  $450^\circ\text{C}$  some grains have grown up as larger than  $100\text{ nm}$ . A typical TEM micrograph is shown in Fig.1 for the sample nitrided at  $350^\circ\text{C}$ . Any distinction between grains made of silver and iron-nitride was not performed in this work.

Figure 2(a) and (b) show the magnetization hysteresis loops measured at room temperature and  $7.5\text{K}$  of the samples nitrided at  $350^\circ\text{C}$  both with (a) a higher and (b) a lower nitrogen potentials aiming at the  $\epsilon$ - and  $\gamma$ -nitrides, respectively. These loops show sharp slopes around the origins, saturations at large fields, which are characteristics of the ferromagnetism. It is noticed that the saturation magnetizations in (b) seem far larger than those in (a), and that gaps between the values at room temperature and  $7.5\text{K}$  are more remarkable in (a) than (b). Almost the same magnetization behavior has been observed in those nitrided at  $450^\circ\text{C}$ . In Fig.3, the magnetization at 5 Tesla is plotted against temperature together with those measured in the composites nitrided at  $450^\circ\text{C}$  and the reference iron nitrides well characterized by XRD. All the

**Table 1**  
Remanences  $M_r$  and coercivities  $H_c$   
in  $\gamma$ -nitride nanocomposites

Fe contents	40-at% Fe		6-at% Fe	
	RT	7.5 K	RT	5 K
Temperature				
$M_r/M_s$	0.24	0.43	0.15	0.31
$H_c$ (Tesla)	0.036	0.080	0.036	0.064

Remark)  $M_s$  is  $M$  at 5 Tesla and at 5 or  $7.5\text{ K}$ .



**Fig.1** TEM micrograph of nanocomposites composed of  $\gamma\text{-Fe}_4\text{N}$  and silver matrix nitrided at  $350^\circ\text{C}$ .  $\text{Fe}/\text{Ag}=2/3$  in metal atomic ratio.

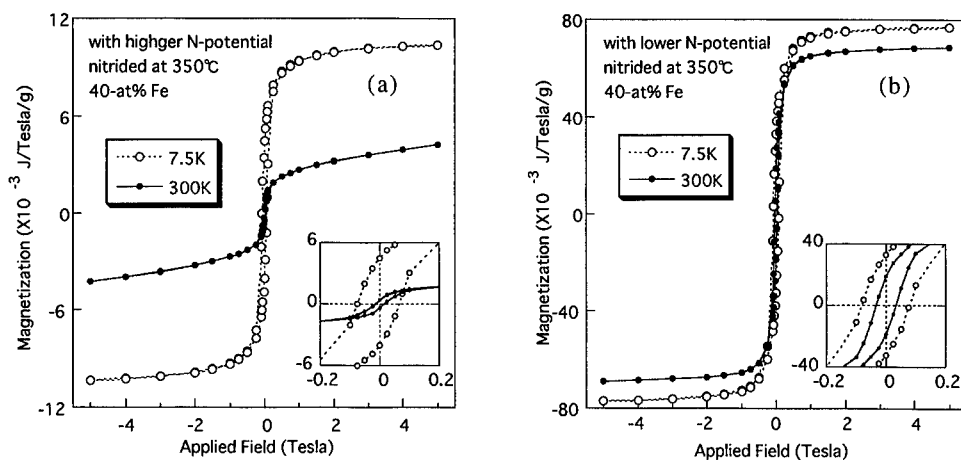


**Fig.2** Magnetization hysteresis loops of the iron nitride nanocomposites, (a)  $\epsilon$ -phase and (b)  $\gamma$ -phase, measured at room temperature and 7.5K. Insets are details around the origins. Note that the vertical scales are different from each other.

plots, as shown there, fall onto two curves drawn with shaded lines, which indicates that the composites nitrided with a lower nitrogen potential contains the  $\gamma$ -phase and that with a higher does the  $\epsilon$ -phase. Since the magnetization at 5 Tesla would be regarded as the saturation magnetization as the first approximation, the temperatures at which the curves in Fig.3 would intersect should reflect the Curie point  $T_c$  of the ferromagnets. Reported values,  $T_c(\gamma\text{-Fe}_4\text{N})=761\text{ K}$  (6) and  $T_c(\epsilon\text{-Fe}_{2.4}\text{N})=398\text{ K}$  (7), are consistent with the present results. In fact, the samples at 350°C corresponding to Fig.2(a) and (b) gave XRD peaks due to the  $\epsilon$ - and  $\gamma$ -phases, respectively, while that at 450°C no peak because of the far smaller iron content, 6%, and an x-ray shielding effect of the silver matrix. The iron-oxide nanograins buried in the silver matrix were thus successfully nitrided selectively to form  $\gamma$ - or  $\epsilon$ -phase by controlling the nitriding potential.

In order to examine the magnetic interaction amongst the nitride grains in these composites, the measured magnetization  $M$  was plotted against  $H/T$  in Fig.4, where  $H$  and  $T$  are the applied field and temperature, respectively. If all the plots fall onto a single curve regardless of the temperatures all the magnetic moments can be regarded as monodomain and magnetically independent, that is evidence of the Langevin superparamagnetism (8). Such curves, though not perfect ones, were indeed observed from room temperature down to 200 K in the  $\gamma$ -composites nitrided at 350 and 450°C. At lower temperatures the plots exhibited considerable deviations from the curves, indicating that the thermal energy can no longer kick off the magnetic interactions amongst them. Note that  $M$  was normalized to the values at 5 Tesla and at the lowest temperatures (5 or 7.5K). It is remarked that both sets of the plots exhibit a unique saturation curve denoted by a shaded line in spite of the differences in the nitriding temperatures and the iron contents. It means that there is no significant difference in the effective size of the elemental magnetic moment between these two composites and then no significant growth of the grains giving rise to the superparamagnetism. Therefore, the grain growth observed in the composites nitrided at 450°C could be attributed to the growth of silver grains not of the iron-containing species. The  $\epsilon$ -composite can not exhibit such universal curve even with the independent monodomain nanograins, since their magnetic moment size depends on temperature as pointed out in Fig.3.

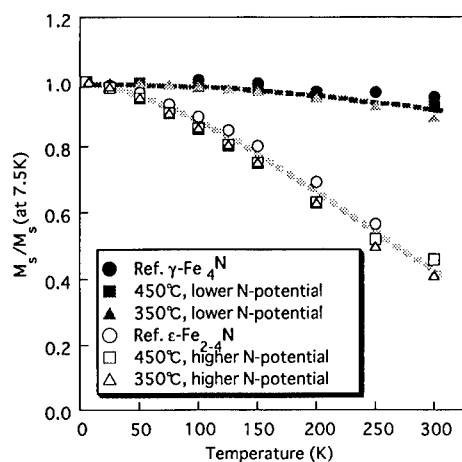


**Fig.3** Temperature dependences of magnetization at 5 Tesla normalized to that at 5 K or 7.5K measured in the nitride composites and reference iron nitrides.

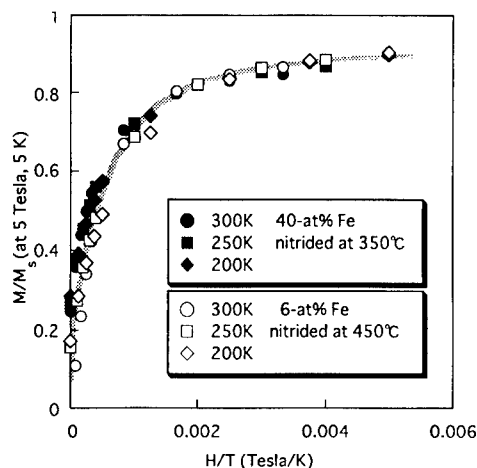


**Fig.4** Magnetizations of the  $\gamma$ -nanocomposites measured at various temperatures plotted against  $H/T$ , which are normalized to those at 5 Tesla and at 5 K or 7.5K.

Coercivities  $H_C$  and remanences  $M_r$  observed in the present composites are tabulated in Table 1 for the  $\gamma$ -composites. It is noticed that  $M_r/M_s$  of the composite of 40%-Fe is significantly higher than that of 6%-Fe, while  $H_C$  seems not so dependent on the iron contents. These  $H_C$  and  $M_r$ , observed in the samples composed substantially of monodomain grains, are given by assemblies of magnetic moments which clumped each other through the dipole-dipole interactions, in addition to those by frozen magnetic moments (9). Since the  $H_C$  is considered to be related to the strongest interaction of the clumping, the constancy in  $H_C$  would support the substantial equality in the effective moment size claimed from Fig. 4. The  $M_r$  could be related to the total amount of the moments thus clumped, so that it should increase with the iron contents as indeed shown in the table. Similar interpretation on  $H_C$  and  $M_r$  of the  $\epsilon$ -composites was unsuccessful. Crystal anisotropy of the hexagonal  $\epsilon$ -nitride much higher than that of the  $\gamma$ -nitride could have been involved these values.

#### ACKNOWLEDGEMENT

The authors thank: Prof. K. Niihara and T. Nakayama (ISIR, Osaka Univ.) for their support in materials preparation and TEM, and Dr. I. Matsubara and R. Hunahashi (Osaka National Res. Inst.) for their support in the SQUID measurements.

#### REFERENCES

1. Krishnan, K.M., *MRS Bulletin* 20(10) (1995)24 and other articles in the issue.
2. Yamamoto, T., Shull, R.D., Bandaru, P.R., Cosandey, F. and Hahn, H., *Jpn. J. Appl. Phys.* 33, L1301 (1994).
3. Yamamoto, T., Croft, M.C., Shull, R.D. and Hahn, H.W., *NanoStructured Materials* 6, 965 (1995)
4. Yamamoto, T., Shull, R.D. and Hahn, H.W., *NanoStructured Materials* 9 (1997) 539-542.
5. Nishimaki, K., Ohmae, S., Yamamoto, T.A. and Katsura, M., *NanoStructured Materials (in this issue)*.
6. Mekata, M., Yoshimura, H. and Takaki, H., *J. Phys. Soc. Jpn.*, 33, 62 (1972).
7. Frazer, B.C., *Phys. Rev.* 112, 751 (1958).
8. Bean, C.P. and Livingston, J.D., *J. Appl. Phys.*, Suppl. 30, 120S (1959).
9. Majetich, S.A., Scott, J.H., Kirkpatrick, E.M., Chowdary, K., Gallagher, K. and McHenry, M.E., *NanoStructured Materials*, 9, 291 (1997).



Pergamon

NanoStructured Materials, Vol. 12, pp. 527-530, 1999

Elsevier Science Ltd

© 1999 Acta Metallurgica Inc.

Printed in the USA. All rights reserved

0965-9773/99/\$-see front matter

PII S0965-9773(99)00175-0

## FORMATION OF IRON-NITRIDES BY THE REACTION OF IRON NANOPARTICLES WITH A STREAM OF AMMONIA

K. Nishimaki, S. Ohmae, T.A. Yamamoto and M. Katsura

Department of Nuclear Engineering, Osaka University,

2-1 Yamadaoka, Suita, Osaka 565-0871, Japan

**Abstract** -- Iron-nitride formation by reaction of iron particles of various grain sizes (20 nm to 1  $\mu\text{m}$ ) with an ammonia stream was studied to examine correlation between the nitrogen content in the product and dissociation extent of the ammonia. Dependence of the nitridation reaction on the grain size was investigated in the same conditions by fixing mass of reactant, flow rate and temperature (723 K). It was found that nanoparticles enhance ammonia dissociation and that the product was therefore of lower nitrogen content than that of coarse particles. This result is understood as follows: The larger specific surface of nanoparticles has enhanced ammonia dissociation occurring on the surface in parallel with nitridation and then reduced the chemical potential of nitrogen in the gas phase surrounding the nanoparticles in equilibrium. ©1999 Acta Metallurgica Inc.

### INTRODUCTION

Nano-sized particles usually have high chemical reactivity as exemplified by the fact that nano-sized iron particles are easily and rapidly oxidized even in the ambient atmosphere while coarse iron particles hardly are. It has been suggested that iron particles with fine grain sizes enhance the nitridation reaction in mechano-chemical processing (1). Such high reactivity possessed by nano-sized particles could be attributed to their high specific surface to some extent. One of the common methods for preparation of iron-nitrides with high nitrogen contents, such as  $\gamma$ -Fe<sub>4</sub>N and  $\epsilon$ -Fe<sub>2.4</sub>N, is the ammonia (NH<sub>3</sub>) flowing method, by which metallic iron reacts with flowing NH<sub>3</sub>.  $\gamma$ -Fe<sub>4</sub>N is an almost stoichiometric nitride with fcc structure, and  $\epsilon$ -Fe<sub>2.4</sub>N is in hcp with a wide non-stoichiometric range from Fe<sub>4</sub>N to Fe<sub>2</sub>N. At the contact of metallic iron with NH<sub>3</sub> caused by this method, not only direct nitridation with NH<sub>3</sub> but also dissociation of NH<sub>3</sub> into nitrogen and hydrogen gas molecules should occur on the surface, as suggested by Darken and Gurry (2). The present authors have pointed out that this dissociation occurring in parallel with nitridation should be carefully taken into account in studying the nitridation reaction (3). Therefore, it is reasonably expected that the specific surface of iron particles would affect the nitridation occurring on the surface. In this work, reactions of iron particles of various grain sizes (20 nm to 1  $\mu\text{m}$ ) with flowing NH<sub>3</sub> were studied to examine the grain size effect on the equilibrium between the NH<sub>3</sub> stream and iron-nitride formed.

## EXPERIMENTAL

The following five kinds of iron source materials were used for nitride formation reactions with flowing  $\text{NH}_3$ ; (C-I) coarse metallic iron particles with 99.99% purity, (C-II) coarse iron oxide particles with 99.99% purity, (C-III) coarse oxide obtained by milling C-II, (N-I) nano-sized oxide with 99.95% purity provided by NanoTek and (N-II) nano-sized oxide specially produced in an inert gas condensation chamber (3). Their grain sizes were determined by transmission electron microscopy (TEM) observation as follows: C-I, about 1  $\mu\text{m}$ ; C-II, 150 nm; C-III, 100 nm; N-I, 25 nm; and N-II, 10 nm.

Each powder of 0.10 g was put in a quartz boat in a length as short as possible to minimize the change in the extent of  $\text{NH}_3$  dissociation, as reported in the previous work (3). The oxide materials were reduced by flowing  $\text{H}_2$  at 623 K for 4 h in advance of nitridation. X-ray diffraction (XRD) analysis showed that all the materials after reduction have been converted into metallic iron. TEM observation showed that the grain size of N-II after reduction was twice as large as that of original oxide grains, but such grain growth was not observed for other kinds of particle. The grain sizes of all the samples after reduction are given in the second column of TABLE 1. These are the sizes of primary grains observed by TEM, and are not those of aggregates of particles. They were neither needle- nor rod-shaped, but of almost spherical shape. The BET specific surface of N-I measured by the provider was 45  $\text{m}^2/\text{g}$ , in agreement with that observed by TEM. Assuming spherical particles, the specific surfaces of the other materials were calculated on the basis of this value of N-I and their grain sizes determined by TEM, and are shown in the third column of TABLE 1.

All the nitridation reactions were made to proceed at 723 K by supplying  $\text{NH}_3$  at a constant linear flow rate of 55 mm/min (22 ml/min). The total pressure of the system,  $P_{\text{total}}$ , was determined by a capacitance manometer. Partial pressures,  $P_{\text{NH}_3}$  and  $P_{\text{N}_2}$ , in the gas phase exhausted from the reaction tube were measured by a gas chromatograph, and  $P_{\text{H}_2}$  was calculated by the relation  $P_{\text{total}} = P_{\text{NH}_3} + P_{\text{N}_2} + P_{\text{H}_2}$ . Nitridation was made to proceed until the composition of the exhausted gas showed no more change. Reaction products were then submitted to XRD analysis for phase identification. This procedure has been reported in detail in Ref. (3).

## RESULTS AND DISCUSSION

Results are given in TABLE 1 together with the nitride phase identified by XRD.  $\epsilon\text{-Fe}_{2.4}\text{N}$  phase was found, when the coarse particles (C-I, C-II and C-III) were used. The lattice parameters of the hcp  $\epsilon$ -phase,  $a$  and  $c$ , were observed to decrease with decreasing grain size of iron particles. According to the relations between  $a$ ,  $c$  and nitrogen contents (4), the nitrogen content in the  $\epsilon$ -phase is lower for smaller lattice parameters. Thus, the nitrogen content in the  $\epsilon$ -phase obtained decreases as the grain size of the iron particles decreases. For N-II, *i.e.*, the sample of the smallest grain size, the synthesized phase was  $\gamma'\text{-Fe}_4\text{N}$  with lower nitrogen content. For N-I, *i.e.*, the sample of the intermediate grain size,  $\gamma'$ - and  $\epsilon$ -phases were found to coexist, which indicated the product lay on the two-phase region of  $\gamma'$ - and  $\epsilon$ -phases. It has been found that the nitrogen contents in the synthesized nitride phases decrease with decreasing grain size of iron particles. That is, the ability of nitridation decreases with decreasing grain size. This contrasts with the fact that the nano-sized grains enhance the reaction rate of iron oxidation by



TABLE 1  
Results of Reaction of Iron Particles with NH<sub>3</sub> at 723 K.

Sample	Grain size (nm)	Specific surface* (m <sup>2</sup> /g)	Extent of NH <sub>3</sub> dissociation, $\alpha$	Obtained Phase	Lattice constant (nm)
C-I	1.0x10 <sup>3</sup>	1.1	0.01	$\epsilon$	$a = 0.2710$ $c = 0.4414$
C-II	1.5x10 <sup>2</sup>	7.5	0.02	$\epsilon$	$a = 0.2700$ $c = 0.4375$
C-III	1.0x10 <sup>2</sup>	11	0.05	$\epsilon$	$a = 0.2695$ $c = 0.4372$
N-I	25	45	0.27	$\left( \begin{array}{l} \epsilon \\ \gamma' \end{array} \right.$	$\left( \begin{array}{l} a = 0.2692 \\ c = 0.4370 \end{array} \right.$
N-II	20	56	0.30	$\gamma'$	$a = 0.3796$ $a = 0.3794$

\*The values in this column are calculated on the basis of the observed value for N-I.

O<sub>2</sub> gas as described in the first section.

Figure 1 shows the extent of NH<sub>3</sub> dissociation,  $\alpha$ , plotted against the specific surface of iron particles. Here  $\alpha$  is defined as the ratio of the number of dissociated NH<sub>3</sub> molecules to that of the supplied. As shown in this figure,  $\alpha$  increases with increasing specific surface almost linearly. The line in this figure was drawn by the method of least squares. This linearity is explained by the fact that the probability of any surface reaction is proportional to the surface area of a solid phase. When sizes of aggregates (providers' data on C-I and C-II are mesh 100 and 200, respectively) were adopted as the size for estimating the specific surface, such a linearity was not seen. In a sense, the linearity in Fig. 1 verifies that grain sizes obtained from primary grains are more reasonable than those from aggregates of particles. The larger specific surface of the present nano-sized grains should have the higher reactivity with respect to the NH<sub>3</sub> dissociation reaction occurring on solid surfaces. In fact, the specific surface of the nano N-II was about 50 times as large as that of the coarse C-I, so that the higher  $\alpha$  found in the nanoparticles is understood as caused by this higher reactivity. It should be pointed that the higher specific surface of the smaller grain size enhances NH<sub>3</sub> dissociation and decreases the nitrogen contents of nitrides obtained.

The above fact can be explained by the thermodynamic nitrogen activity,  $\tau_N$ , *i.e.*, the ability of nitridation, given by Katsura (5). It is given by

$$\tau_N = \frac{1}{K_p} \frac{P_{\text{NH}_3}}{P_{\text{H}_2}^{3/2}} \quad [1]$$

where  $K_p$  is the equilibrium constant for NH<sub>3</sub> formation reaction, and  $P_{\text{NH}_3}$  and  $P_{\text{H}_2}$  are partial pressures of NH<sub>3</sub> and H<sub>2</sub> surrounding the nitride, respectively. The enhanced NH<sub>3</sub> dissociation caused by higher specific surface of a smaller grain size leads to a lower nitrogen activity,  $\tau_N$ , through Eq. [1]. As shown in Fig. 2,  $\tau_N$  evaluated by Eq. [1] using the measured values of  $P_{\text{NH}_3}$  and  $P_{\text{H}_2}$  decreases with increasing specific surface. Namely, the ability of nitridation in the gas phase decreases with increasing specific surface. The chemical potential of nitrogen in the gas

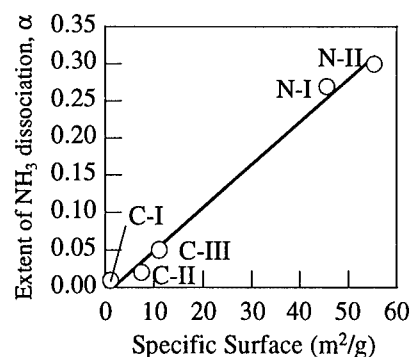


Figure 1: Dependence of extent of NH<sub>3</sub> dissociation,  $\alpha$ , on specific surface.

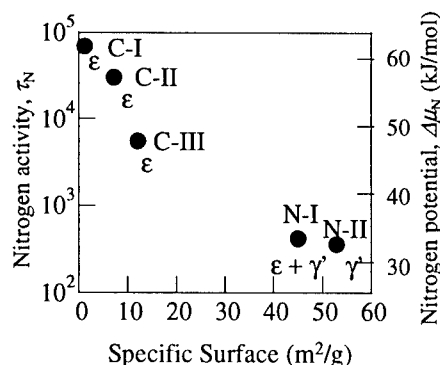


Figure 2: Dependence of nitrogen activity,  $\tau_N$ , and nitrogen potential,  $\Delta\mu_N$ , in gas phase on specific surface.

phase just surrounding the nitride,  $\mu_N$ , is given by the relation (5),

$$\Delta\mu_N = \mu_N - \frac{1}{2} \mu_{N_2}^{\circ} = RT \ln \tau_N = RT \left( \ln P_{NH_3} - \frac{3}{2} \ln P_{H_2} - \ln K_p \right) \quad [2]$$

where  $\mu_{N_2}^{\circ}$  denotes chemical potential of nitrogen gas at the standard state (10<sup>5</sup> Pa). When a steady state is attained by the NH<sub>3</sub> flowing method, the chemical potential of nitrogen in the gas phase should be in equilibrium with that in the solid phase. Figure 2 indicates that higher  $\Delta\mu_N$  in the gas phase results in higher nitrogen content in the solid phase that corresponds to the chemical potential in it. This is consistent with the above-mentioned assumption that the equilibrium between the gas phase and the solid phase is established. It would be possible to derive various thermodynamic properties of iron nitride phases with high nitrogen contents from the chemical potential thus estimated.

The present experimental results clearly show that  $P_{NH_3}$  and  $P_{H_2}$  in the gas phase just surrounding the nitride synthesized govern its nitrogen content in the nitride. A highly reactive surface of the nanoparticles does not increase the nitrogen content of iron-nitrides, but enhances NH<sub>3</sub> dissociation. This enhancement creates a state of low  $P_{NH_3}$  and high  $P_{H_2}$ , and low  $\Delta\mu_N$ , and eventually produces a nitride with low nitrogen content. The ability of nitridation of the gas phase in the neighborhood of the sample thus decrease due to higher surface reactivity of NH<sub>3</sub> dissociation of the nanoparticles. Consequently, the resultant nitride phase depends strongly on its own state, such as its amount, grain size and form.

## REFERENCES

1. Kaczmarek, W.A., *Scripta Metall. Mater.*, **33**, 1687, 1995.
2. Darken, L. and Gurry, R., *Physical Chemistry of Metals*, McGraw-Hill, New York, 1953, p. 374.
3. Nishimaki, K., Nakagawa, T., Yamamoto, T.A. and Katsura, M., *Tecnol. Repts., Osaka Univ.*, **48**, 153, 1998.
4. Yamamoto, T., Shull, R.D., Bandaru, P.R., Cosandey, F. and Hahn, H., *Jpn. J. Appl. Phys.*, **33**, L1301, 1994.
5. Wriedt, H.A., Gokcen, N.A. and Nafziger, R.H., *Bull. Alloy Phase Diag.*, **8**, 355, 1987.
6. Katsura, M., *J. Alloys & Comp.*, **182**, 91, 1992.



Pergamon

NanoStructured Materials, Vol. 12, pp. 531–534, 1999

Elsevier Science Ltd

© 1999 Acta Metallurgica Inc.

Printed in the USA. All rights reserved

0965-9773/99/\$-see front matter

PII S0965-9773(99)00176-2

## **POLYMER MATRIX COMPOSITES FILLED WITH NANOPOROUS METAL POWDERS: PREPARATION AND ELECTRICAL PROPERTIES**

**Hans-Gerd Busmann, Bernd Günther, Udo Meyer**

Fraunhofer-IFAM, Lesumer Heerstrasse 36, D-28717 Bremen, GERMANY

**Abstract** -- *The production of a new kind of silver powder for the preparation of electrically conducting polymers is described. This comprises the method of inert-gas-condensation with forced gas flow in a closed-loop system and a quasi continuous collection of the nanoporous metal deposits via filter separation. After sieving, powders of various morphologies are obtained. The electrical resistance of polymers filled with two kinds of such powders as a function of filler content is presented, showing percolation at filler contents below 5 vol%. In a two component epoxy resin system, the metal-like resistance observed for samples cured at room temperature changes into a semiconductor-like resistance upon thermal annealing. However, a thermal pretreatment of the powder retains the metal-like conductivity.* ©1999 Acta Metallurgica Inc.

### **INTRODUCTION**

The electrical properties of composite materials of metallic filler particles embedded in polymer matrices strongly depend on the concentration and morphology of the particles (1). The electrical resistance shifts from dielectric to metallic behavior with increasing metal content (2), whereas solid filler materials in general tend to deteriorate mechanical properties of such composites. Therefore, filler systems with a low percolation threshold are preferred in applications like isotropically conductive adhesives and injection molding feedstocks. Commercially available adhesives for uses in electronics are generally filled with more than 25 vol% of Ag-flakes. Recently, a novel nanoscale metal / polymer matrix composite made by the dispersion of a porous silver powder into a polymer matrix has been developed and led to a reduction of the percolation threshold to less than 7 vol% (3,4). This powder is made from porous silver obtained by the technique of inert gas condensation. This paper reports on the development of a continuously operating apparatus for the production of porous metals of aggregated nanoparticles and on the influence of the morphology and thermal treatments of the hereof produced powders on the electrical resistance of the final composite.

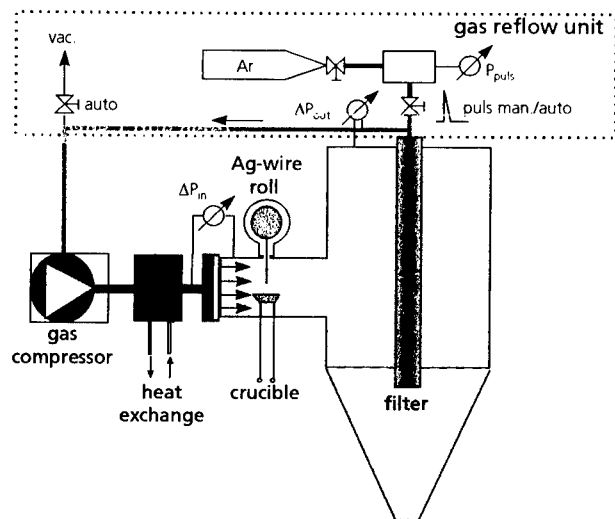


Fig.1: Schematic drawing of an apparatus for continuous production of highly porous metals by aggregation of metallic nanoparticles.

## PRODUCTION OF POROUS SILVER

The porous silver has been produced by inert gas condensation in two different devices. In both cases, a Ag-wire is continuously fed onto a tungsten crucible and evaporated into an inert gas atmosphere ( $10^3$  Pa to  $10^4$  Pa, argon or helium). The Ag-nanoparticles formed hereby coagulate and form highly porous aggregates. In the first device, these aggregates are deposited on liquid nitrogen cooled substrates. During warm-up to room temperature, sintering leads to highly conductive Ag-networks (5).

With respect to increase the efficiency of production, a new device with forced gas flow in a closed-loop cycle and continuous powder collection was set-up – Fig.1. The main components are the Ag-crucible, a filter with a gas-reflow unit, a gas compressor (oil-free vacuum pump) and a heat exchange box. The latter counterbalances the heating of the gas at the crucible. The silver is evaporated into the gas and collected on the outer surface of the filter. The porous Ag-deposit is periodically removed from the filter by pulsed gas reflow and collected at the bottom of the chamber.

## POWDER MORPHOLOGY

With the goal of producing polymer matrix composites with well-defined and reproducible mechanical and electrical properties, the porous powder deposits were further processed. Several methods like vibrational sieving, air jet milling and air jet sieving have been applied, whereupon the resulting powders were dispersed into epoxy resins. Fig. 2 shows micrographs taken with a transmission electron microscope of two powders of principally different morphologies. Powder 1 – Fig. 2a – was obtained by vibrational sieving using a mesh size of  $50\text{ }\mu\text{m}$ . Powder 2 – Fig. 2b – was obtained by air-jet sieving and exhibits a size distribution of the powder particles with a much smaller mean size ( $< 10\text{ }\mu\text{m}$ ). Obviously different powder morphologies result from the two types of processing methods: The surfaces of the particles of powder 1 are well defined and compressed and those of powder 2 are frayed.

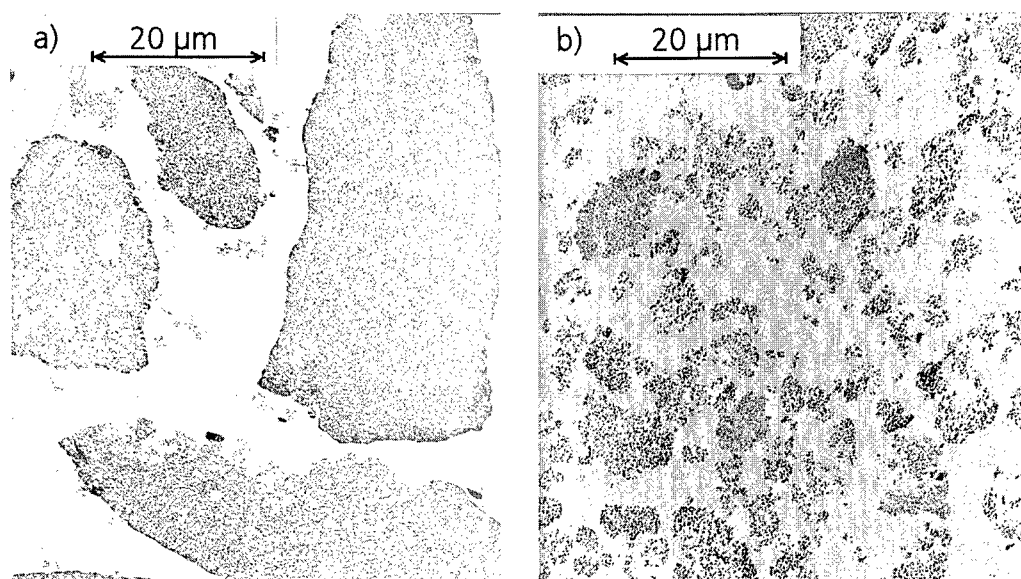


Fig.2: Transmission electron micrographs (bright field, 200 kV) of polymer matrix composites filled with nanoporous silver powders. The powder was prepared by a) mechanical sieving and b) by air-jet sieving of aggregated silver nanoparticles.

### ELECTRICAL RESISTANCE

Fig. 3 shows the DC-resistance of composites of powder 1 and 2 in Vitralit and Araldit 2020, respectively, as a function of filler content. They exhibit a specific resistance of  $\sim 15 \Omega\text{cm}$  and  $3300 \Omega\text{cm}$  at 2 vol% and drop down to  $0,005 \Omega\text{cm}$  and  $0,5 \Omega\text{cm}$  at 10 vol%, respectively. Since the unfilled polymer matrix has a resistance of  $\sim 10^{15} \Omega\text{cm}$ , a steep decrease of the resistance has to be assumed for an increase of the Ag-content from 0 vol % up to 2 vol%. Thus, the transition regime from high to low resistance is much broader for powder 2 than for powder 1. This is to be expected owing to the dependence of percolation behavior on the morphology of the powder (1).

Important for all applications is the thermal stability of the composites. Fig. 4 shows the resistance of powder 1 in Araldit 2020 (10 vol%) as a function of temperature in the range from  $-20^\circ\text{C}$  to  $40^\circ\text{C}$  before and after a thermal treatment of the composite at  $85^\circ\text{C}$  for 2 h. The as-prepared sample cured at RT for 24 h shows a positive temperature-coefficient of  $0,017 \Omega/\text{K}$  (pure Ag:  $0,004 \Omega/\text{K}$ ) indicating a conductivity determined by a continuous Ag-network with metal-like contacts within and between the agglomerates. After the heat-treatment at  $85^\circ\text{C} / 2 \text{ h}$ , the resistance increases drastically to  $2600 \Omega\text{cm}$  and the temperature-coefficient becomes semiconductor-like ( $-7,4 \Omega/\text{K}$ ). This indicates a loss of metal-like contacts between and/or within the agglomerates. The large difference in the coefficients of thermal expansion of the polymer matrix ( $\sim 200 \times 10^{-6}/\text{K}$ ) and the Ag-filler ( $20 \times 10^{-6}/\text{K}$ ) might lead to an interruption of the metal-like agglomerate-agglomerate interfaces

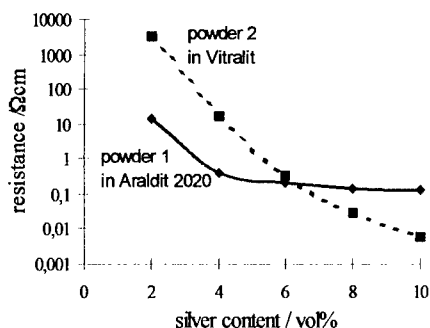


Fig.3: DC-resistance as a function of filler content for different powders – cf. Fig.2. Standard four probe I-U-measurements, sample size 1 mm x 1mm x 18 mm.

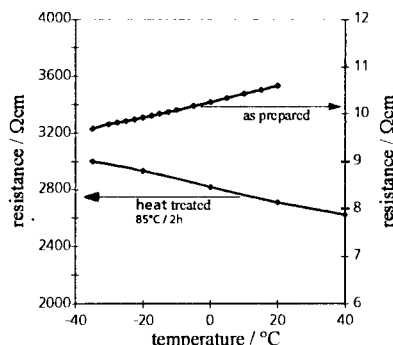


Fig.4: Resistance of powder 1 in Araldit (10 vol%) as a function of temperature of an as-cured and a post-annealed sample. Measured with a HP Impedance Analyzer at 1 MHz.

and to a tearing of the agglomerates. Subsequent covering of hereby newly formed metallic surfaces with the polymer would prevent the recovery of metal-like contacts after the treatment. In an attempt to stabilize powder 1 against this thermal instability, the powder was heat treated at 100 °C for 2 h prior to its dispersion into the Araldit matrix. The resistance of this composite after a heat treatment at 85 °C for 2 h was found to be 100  $\Omega\text{cm}$ . This value is only slightly higher than that of the untreated powder and shows that the thermal pretreatment of the powder retains the metal-like resistance of the composite.

## CONCLUSIONS

The technology of inert gas condensation can be used for the production of a nanoporous Ag-filler in a quantity that is sufficient for its commercial use specifically in electrically conducting polymers. By means of different processing technologies, the morphology and size distribution of the nanoporous aggregates can be varied, thermally stabilized, and tailored to specific demands. E.g., a percolation behavior as in the system powder1 in Araldit 2020 may be preferred if the filler content must be kept as low as possible, whereas a behavior as in the system powder2 in Vitralit may be preferred if the absolute conductivity should be adjustable over a large range of resistivity.

## REFERENCES

1. For an overview, see e.g.: Gul, V.E., *Structure and Properties of Conducting Polymer Composites*, Utrecht VSP, 1996, ISBN 90-6764-204-5.
2. R.Pelster, P.Marquardt, G.Nimtz, A.Enders, H.Eifert, K.Friedrich, and F.Petzoldt, *Phys.Rev.B* **45**(16),8929,1992.
3. H.Eifert, B.Günther, pat. DE 42 28 608 C 2, 1994.
4. S.Kothaus, B.Günther, R.Haug, H.Schäfer, *IEEE Trans. A* **20**,15,1997.
5. H.Eifert, B.Günther, J.Neubrand, *Int.J.Electronics* **73**(5),945,1992.



Pergamon

NanoStructured Materials, Vol. 12, pp. 535-538, 1999

Elsevier Science Ltd

© 1999 Acta Metallurgica Inc.

Printed in the USA. All rights reserved

0965-9773/99/\$-see front matter

PII S0965-9773(99)00177-4

## ELLIPSOMETRIC STUDIES OF NANOCOMPOSITE CERMETS

G.B. Smith and S. Dligatch

Department of Applied Physics, University of Technology, Sydney  
PO Box 123, Broadway, NSW 2007 Australia

*Abstract - The three pairs of complex refractive indices and the direction of the optical axis for metal insulator thin film composites in which the very small metal particles form narrow tilted columns which are arranged asymmetrically have been found using a combination of ellipsometry and spectrophotometry. Results have been used to theoretically model transmittance which depends on the two angles defining incident direction in these films. Insights into the unusual optical response of the nano-size silver particles are also given.*

©1999 Acta Metallurgica Inc.

### INTRODUCTION

Cermets containing small metal particles in an insulating matrix can absorb optical radiation anisotropically in terms of direction of incidence if either the metal particle has a non-spherical shape or the particles are arranged into an asymmetric array. Such structures can be manufactured by oblique vacuum deposition of both constituents and the resultant thin films are of interest for advanced solar thermal and lighting control in window applications. They are known as angular selective coatings [1,2].

A complete optical characterisation of such materials requires measurement of three complex optical constants involving six independent numbers. These constants are defined within a frame which is internal to the material and linked to the laboratory or measurement frame by rotational transformations [3]. The orientation of the optical axis must be known in addition to the three complex optical constants. This can be measured by electron microscopy [1,4] or can be fitted in the modelling procedures. There are a number of motivations for solving this complex problem. Data for energy and lighting analysis by direct measurement is a copious task so an optical model can save a lot of work. The generalised modelling tools are now available for thin films with six optical constants and arbitrary optical axis[3]. Optical constants for such structures provide insights into fundamental issues in effective medium theory and such models can allow the metal particles constants to be modelled say with a general array of Lorentz oscillators and compared with bulk values. In this way changes in optical properties and energy level structures in nano-size particle might be examined. Since the metal may be thinner in some directions than others the optical properties of these nanoscale particles can be quite anisotropic and qualitatively different for different field directions. This is an issue of fundamental importance to the physics of material properties at the nanoscale.

## EXPERIMENTAL AND MODELLING PROCEDURES

Good starting “guesses” and as much pre-determined geometric and composition information as possible is important. Approximate film thickness, component volume fractions and optical axis orientation should be known. Volume fractions help indirectly by giving useful starting “guesses” for some optical constants and enable checks on final answers using effective medium theory. Spectroscopic rather than monochromatic data is used since the geometric parameters are constant at each wavelength and some solutions may be disallowed on grounds of unphysical dispersion.

Several independent, carefully chosen data sets are needed to solve all 6 unknowns. Sets of s and p polarised transmission and reflection spectra, and ellipsometry, each for several angles of incidence are used. We have found with our available modelling tools that it is preferable to work with a fixed sample orientation and then to check predictions for other orientations. Generalised ellipsometry, is better at discriminating between complex optical models than spectrophotometric data, but requires one to establish three pairs of ellipsometric parameters. Limited ellipsometry is possible when the sample is orientated so that the optical axis lies within the plane of incidence as then only “normal”  $\Delta$  and  $\Psi$  vary with wavelength, and the others are  $0^\circ$ ,  $90^\circ$  or  $180^\circ$ . Many angles of incidence [5] are needed and simple ellipsometry did not work well in practice. Thus we present results obtained using a combination of ellipsometry and spectrophotometry with the sample oriented with the optical axis in the plane of incidence. One benefit of having such optical constant results is also demonstrated.

### *Sample preparation and optical measurement details*

Smooth cathodic arc alumina was deposited at an angle of incidence of  $70^\circ$  to the silica substrate with the included metal silver deposited simultaneously by thermal evaporation at  $70^\circ$  but from the opposite side of the normal to the oxide. The refractory oxide defines the overall columnar structure and the silver columns have finer cross sections than the oxide columns which are 10 to 50 nm across. A single set of ellipsometric parameters ( $\Delta$ ,  $\Psi$ ) were found at each wavelength from 300 to 800 nm, using a UVISSEL spectroscopic phase modulated ellipsometer. Transmittance and reflectance for p and s polarised light was found from 300 to 2500 nm. Angles of incidence in ellipsometry were varied from  $50^\circ$  to  $70^\circ$ , and in spectrophotometry from  $0^\circ$  to  $60^\circ$  using both sides of the normal for p polarised transmittance.

### *Optical constant modelling*

Multi-angle of incidence ellipsometry by itself did not work well so expressions for T and R for s and p polarised light, and ( $\Delta$ ,  $\Psi$ ), at  $\pm 60^\circ$  angles of incidence, were simultaneously solved independently at each wavelength for the three desired (n,k) pairs using exact expressions for each quantity [3]. This worked well provided suitable starting guesses were made. A total mean square solution error was generated over all data points. Optical axis tilt angle ( $\sim 50^\circ$ ) and film thickness ( $\sim 800\text{\AA}$ ) for these expressions are fixed at the experimental values from electron microscopy and profilometry. The final solution was refined across all  $\lambda$  by allowing these to



vary slightly to 825 Å thickness and 62° tilt, then a smoothing function was applied to all solution points and it was plotted against actual data points as shown in Fig. 1. As a check data at all other angles of incidence was compared with the predictions of these final (n,k) solutions. Excellent fits strongly indicated we had the actual physical solution. An *isotropic* Maxwell-Garnett (MG) model for the refractive indices with the silver fill factor  $f=0.1$ , was found to be a useful starting guess in the solution process used, even though the final result shows a quite different anisotropic system with deposition conditions indicating  $f$  around 0.3.

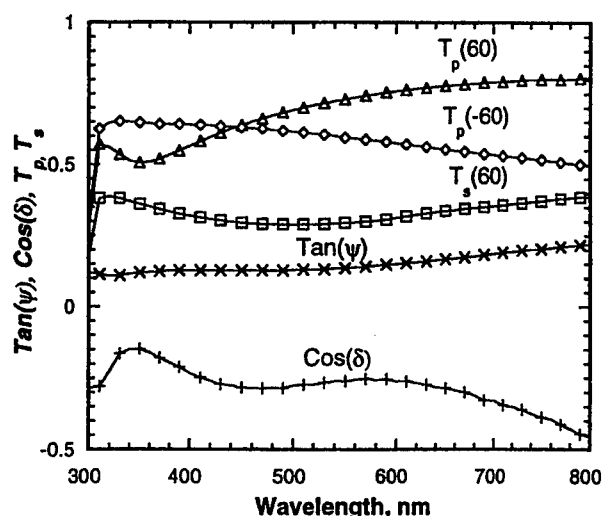


Figure 1. Model fits of biaxial complex refractive index (solid lines) to ellipsometry and spectrophotometry data (markers), at  $\pm 60^\circ$  angles of incidence.

## FINAL RESULTS AND APPLICATIONS

The three n,k pairs (the real and imaginary parts of refractive index) for each direction, which gave the solution of Fig. 1 are plotted in Fig. 2. Data in Fig. 2 is in the internal frame of reference with z parallel to the columns, x in the column plane and y normal to the column plane. Uniaxial models could not give good fits, so the film is clearly biaxial. This correlates with the large observed difference in column spacing, in the column tilt plane and in the plane normal to it. Models of the dispersion relations including a number of effective medium models with Lorentz oscillators for the silver, will be presented later. Summarising them, the z direction can be modelled with a Maxwell-Garnett model for anisotropic composites [6] with very fine needle like ellipsoids (principle axes ratios 1/50) but the x and y behaviours require advanced effective medium models plus a silver treatment very different to the bulk. These models also indicate that the unusual wavelength dependence of some constants is due to resonances in the limited  $\lambda$  range for ellipsometry, and that over a broader  $\lambda$  range results are physically acceptable. The y direction is interesting and bulk metal like in its dispersion curve. The usual observation that Drude relaxation times shorten in nano-size particles is found.

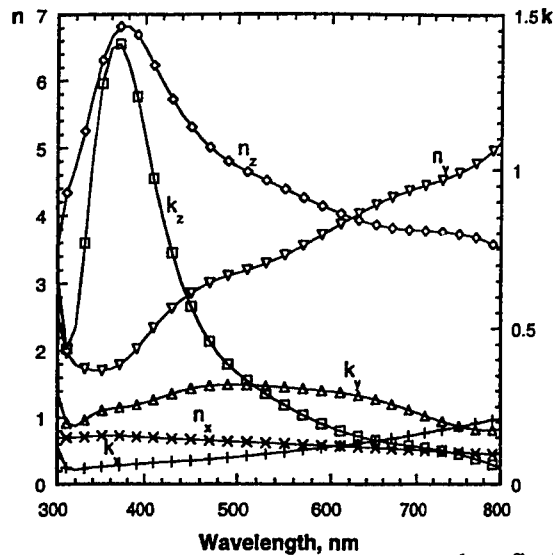


Figure 2. Anisotropic complex optical constants used to produce fits in Fig.1 and to other data

This optical constant data is used to predict transmittance for arbitrary azimuth angles of the incident ray using thin film models from reference 3. Predicted spectral transmittance curves at  $60^\circ$  angle of incidence for s and p-polarised light versus azimuth angles are quite distinct at all azimuth values except  $\pm 90^\circ$  for the s polarisation case. The s-wave transmittance spans a range of 0.15 to 0.45 and for p, 0.2 to 0.75. *In isotropic films, in each polarization, these curves are all co-incident*. Measurement verifies this behaviour, but having the model saves much tedious measurement and data handling. We note significant s-wave angular selectivity (ie a change in  $T$  at azimuths differing by  $180^\circ$ ) of order 60% relative shift with one azimuth angle within  $\pm 45^\circ$  of azimuth zero. Azimuth zero plane in the laboratory frame includes the y axis from our "crystal" or internal frame and is normal to the deposition plane.

#### Acknowledgments

Dr Roger Netterfield of CSIRO for help with modelling absorbing biaxial films and with ellipsometry. Some of the work was supported by the an Australian Research Council grant.

#### References

1. Smith, G.B., Dligatch, S., Sullivan, R. and Hutchins, M.G., J Solar Energy (Advanced Glazing, special issue) in press 1998.
2. Mbise, G.W., Le Bellac, D., Niklasson, G.A. and Granqvist, C.G., J.Phys.D:Appl.Phys. 1997, 30, 2103.
3. Schubert, M., Phys Rev B, 1996, 53, 4265.
4. Mbise, G.W., Smith, G.B. and Granqvist, C.G., Thin Solid Films, 1989, 174, L73.
5. Schubert, M., Rheinlander, B., Woollam, J.A., Johs, B. and Herzinger, C.M., J.Opt.Soc.Am., 1996, 13, 875.
6. Skryabin, I., Radchik, A.V., Moses P. and Smith, G.B., Appl.Phys Lett., 1997, 70, 2221.



Pergamon

NanoStructured Materials, Vol. 12, pp. 539–542, 1999

Elsevier Science Ltd

© 1999 Acta Metallurgica Inc.

Printed in the USA. All rights reserved

0965-9773/99/\$—see front matter

PII S0965-9773(99)00178-6

## PREPARATION OF Dy AND Mn NANOPARTICLES

J. A. Christodoulides, N. B. Shevchenko, and G. C. Hadjipanayis

Department of Physics and Astronomy, University of Delaware, Newark, DE 19716, USA

**Abstract** -- We have recently extended our studies on nanoparticles to rare earth and Mn particles. The nanometer scale Dy and Mn particles have been prepared using a new method in which particles are first formed from high purity constituent materials in an inert gas atmosphere and then embedded into a matrix by planar magnetron sputtering. The Dy-containing samples consisted of particles with diameters on the order of 10 nm, which were separated by the matrix material. A strong relationship was observed between the particle size and the magnetic ordering temperature with the absence of antiferromagnetic transition observed at 176 K in the bulk. This method allows for the synthesis of a wider variety of materials by reducing the problems of miscibility and reactivity between the particles and the matrix material. ©1999 Acta Metallurgica Inc.

### INTRODUCTION

Most of the studies in magnetic nanoparticles so far have been focused on transition metals (Fe, Co, Ni) and their alloys and showed properties much different from those in bulk. These studies include free standing passivated particles and those embedded in ceramic and metallic matrices which are immiscible and do not alloy with the particles [1,2,3]. The unusual properties include changes in Curie temperature, reductions in magnetic moment and the presence of an enhanced anomalous magnetic hysteresis especially at cryogenic temperatures attributed to a core/shell particle morphology [4].

Limited studies have been done on rare-earth based nanoparticles mainly because of difficulties involved in preparation. Rare earths are known to be very reactive and this becomes more of a problem with the large surface area of nanoparticles. Because the RKKY coupling in rare earths are very sensitive to interatomic spacing which varies drastically at the particle surface, profound effects are also expected in the magnetic properties of rare earth nanoparticles and this is shown clearly by the very few scattered studies. The most common way used successfully to prepare the rare earth nanoparticles is by co-sputtering the rare earths with an immiscible material (such as Mo, Ta, Ti, W) and then annealing the film to precipitate out the rare earth particles [5,6]. Tb nanoparticles prepared this way showed a maximum coercivity of 22 kOe, 2.4 times larger than in a film. Interestingly, gadolinium nanoparticles also showed a relatively high coercivity (2.2 kOe) even though the anisotropy of bulk gadolinium is low. In both of these nanoparticles, the Curie temperature was found to decrease with decreasing particle size. Studies on Gd/W [7] and Er/Ta granular films revealed a similar behavior in which the high temperature magnetic transitions were absent. The co-sputtering technique discussed

above has some limitations. It is limited to only a few immiscible systems; it can not control the size and uniformity of particles and sometimes leads to alloying effects.

The new process presented here allows the preparation of isolated particles for a wider variety of systems, without worrying about alloying effects and formation of undesired phases upon annealing. We have used this technique to prepare dysprosium nanoparticles with unique properties including the absence of the antiferromagnetic transition, which in the bulk material occurs at 176 K. The technique was also used to prepare and embed in a Mg matrix pure manganese particles which are also highly reactive and oxidizing.

### EXPERIMENTAL

Granular thin film samples were prepared by the simultaneous use of both sputtering and particle guns. Dysprosium and manganese particles were prepared from high purity targets (99.99%) using the particle gun and the aluminum and magnesium matrices in which the particles were respectively fixed, were deposited by sputtering. Deposition of the two constituents was done in tandem using a rotating platform. The base pressure of the chamber was in the order of  $10^{-8}$  Torr whereas during deposition, an argon pressure of 5 mTorr in the chamber area and 1 Torr inside the particle gun was maintained. Pressures in both cases were measured using convectron gauges. The carrier gas supply was adjusted by a way of a needle valve and the sputtering gas by a mass flow controller. The gases were removed from the differential system by a cryogenic high vacuum pump. The throttle valve at the pump throat was used in conjunction with the needle valve to set the chamber and gun pressures. Magnetic hysteresis loops and thermomagnetic data were collected by a Quantum Design MPMSR2 SQUID magnetometer. The structure and microstructure of the films were examined using a Jeol JEM 2000 FX transmission electron microscope (TEM).

### RESULTS AND DISCUSSION

Figure 1a shows the bright field images of Dy nanoparticles embedded in an Al matrix. The selected area diffraction pattern for this sample (Figure 1b) shows rings that correspond to the hcp Dy phase. The histogram of particle diameters for this sample shows a most probable diameter of 4 nm (Figure 1c). By changing the preparation conditions it was possible to produce

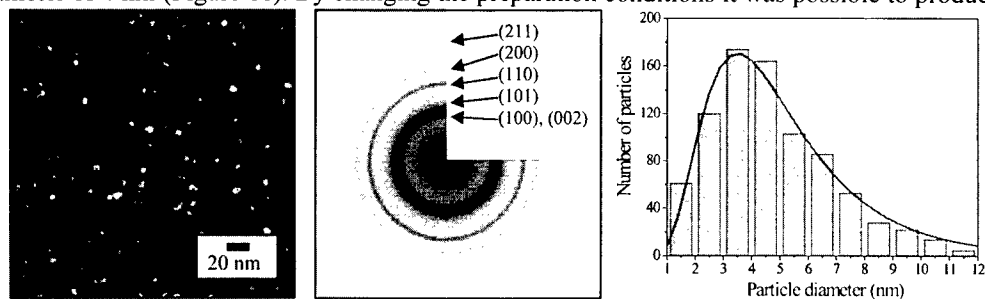


Figure 1. (a) Dark field image of Dy particles in an Al matrix, (b) SAD pattern showing the hcp phase, and (c) histogram for the Dy particles with 4 nm average size.

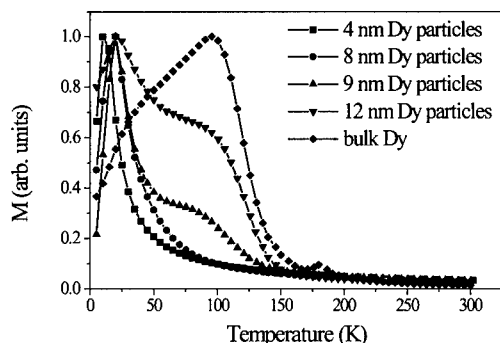


Figure 2. Thermomagnetic data taken for various sizes of Dy particles and bulk

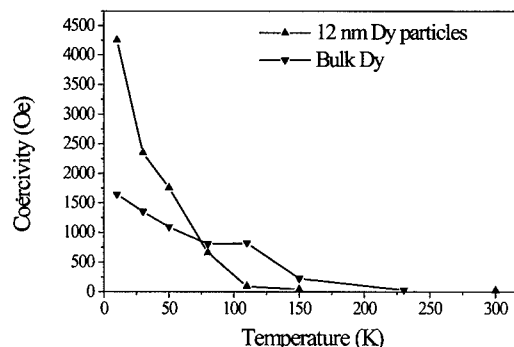


Figure 3. Temperature dependence of coercivity in 12 nm Dy particles compared with bulk

samples with different mean particles size ranging from 4 to 12 nm, with similar microstructure. Thermomagnetic data on the 4 nm particles sample showed a blocking temperature at 13 K. The blocking temperature was estimated as the point at which the magnetization on the zero field cooled curve begins to decrease (the peak value). This transition shifts to 20 K for the 8 nm particles and a second magnetic transition is observed at around 88 K for the 9 and 12 nm particles samples. The thermomagnetic curves obtained for the particle samples were compared to data obtained for bulk dysprosium (Figure 2). Two magnetic transitions are observed in bulk dysprosium. The basal plane ferromagnetic ordering transforms to helical antiferromagnetic above 92 K (87 K upon cooling), which persists up to 176 K. At higher temperature paramagnetism is observed. The second magnetic transition observed in the bulk material also occurs in the 9 and 12 nm samples [8]. The antiferromagnetic to paramagnetic ordering transition observed in the bulk (at 176 K) is not observed in the particle systems. At cryogenic temperatures bulk dysprosium is a basal plane ferromagnet with a preferred magnetic direction along the *a* axis. Its axial anisotropy is huge ( $2.5 \times 10^8$  erg/cm<sup>3</sup>) but the in plane anisotropy  $K_6$  is two orders of magnitude lower,  $2.9 \times 10^6$  erg/cm<sup>3</sup>. Using the measured value of  $T_B$  and the particle size in the expression  $KV = 25kT_B$  the calculated anisotropy of the 4 nm dysprosium particles was  $4 \times 10^6$  erg/cm<sup>3</sup>, which is close to the plane (basal) anisotropy  $K_6$ . This causes the easy direction of magnetization to fluctuate within the basal plane and the particle to behave like a superparamagnet.

Coercivities measured show a drastic increase for the low temperature values as the particle diameter increases. At 30 K the 4 nm particles have zero coercivity as expected for superparamagnetic particles. The coercivity of the 8 nm particles is small (15 Oe) at 30 K. The value is nearly 430 Oe for the 9 nm particles and greater than 2300 Oe for the 12 nm particles. Figure 3 compares the coercivity values of the 12 nm particles and the bulk material. The drop in coercivity with temperature is more rapid for the particles because of the larger thermal effects in nanoparticles.

In a similar fashion, manganese particles were embedded into a magnesium matrix. The bright field image of such sample (Figure 4a), indicates a shell/core morphology. Further structural studies through SAD patterns (Figure 4b) reveal that pure Mn composes the core whereas the shell is MgO. The average size was calculated from a distribution histogram (Figure 4c) and found to be about 6.5 nm. Preliminary *M* vs. *T* data show a transition around 100 K which is close to the bulk antiferromagnetic transition. Studies of *M<sub>s</sub>* and hysteresis loops are underway to fully characterize the behavior of the small Mn particles.

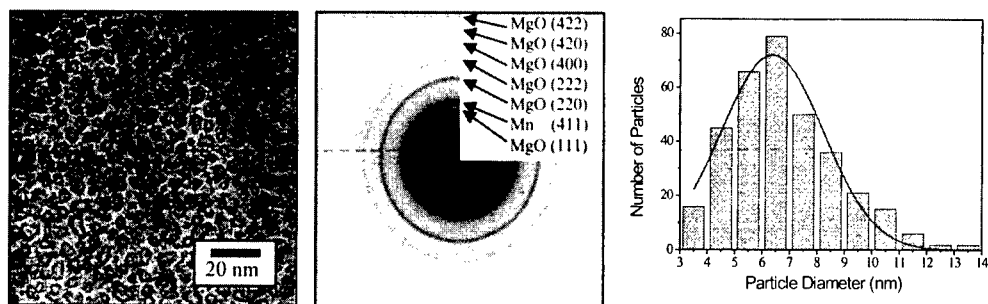


Figure 4. (a) Bright field image of Mn particles in a Mg matrix, (b) SAD pattern indicating the presence of MgO and (c) histogram for the Mn particles with 6.5 nm average size.

### CONCLUSIONS

In this work a method for preparing particles by evaporation and tandem sputter deposition was developed and successfully used to prepare nanoparticles of Dy and Mn. Size effects on the magnetic ordering and hysteresis were observed in Dy nanoparticles. The absence of the antiferromagnetic transition was shown even in particles with size 12 nm. The hysteresis effects were found to be in agreement with what was expected for single domain particles with anisotropy close to the bulk in plane value. The highly reactive manganese was prepared in a similar way with particles in the size range of 6 nm showing no MnO and a magnetic transition at around 100 K. These particles were coated by MgO and embedded in a Mg matrix. This method overcame the limitations of reactivity and miscibility between the constituents of the granular film.

### ACKNOWLEDGEMENTS

Work was supported by NSF DMR 9307676.

### REFERENCES

- 1 C. L. Chien in "Science and Technology of Nanostructured Magnetic Materials," ed. G. C. Hadjipanayis and Gary Prinz, NATO Series **259** 477 (1991).
- 2 J. R. Childress and C. L. Chien, Phys. Rev. B, **43** 8089 (1991).
- 3 A. Tsoukatos, H. Wan, and G. C. Hadjipanayis, Nanostructured Materials **3** 399 (1993).
- 4 S. Gangopadhyay, G. C. Hadjipanayis, B. Dale, C. M. Sorensen, K. J. Klabunde, V. Papaefthymiou, and A. Kostikas, Phys. Rev. B, **45**, 9778 (1992)
- 5 M. J. O'Shea, J. Appl. Phys. **81**, 6174 (1994).
- 6 D. Johnson, R. Perera and M. J. O'Shea, J. Appl. Phys. **79**, 5299 (1996).
- 7 N. B. Shevchenko, A. S. Murthy and G. C. Hadjipanayis, Materials Science and Engineering A **204**, 39 (1995).
- 8 N. B. Shevchenko in "A Novel Process for the Preparation of Granular Films and Application to Dy and Gd," Ph.D. Thesis, University of Delaware (1998).



Pergamon

NanoStructured Materials, Vol. 12, pp. 543–546, 1999

Elsevier Science Ltd

© 1999 Acta Metallurgica Inc.

Printed in the USA. All rights reserved

0965-9773/99/\$—see front matter

PII S0965-9773(99)00179-8

## A METHOD TO PRODUCE TWO-PHASE NANOCOMPOSITES IN SOLID STATE

L. He<sup>1</sup>, L.F. Allard<sup>2</sup>, and E. Ma<sup>1,3</sup>

1. Mechanical Engineering Department, Louisiana State University, Baton Rouge, LA 70803
2. High Temperature Materials Laboratory, Oak Ridge National Laboratory, Oak Ridge, TN 37831
3. Current address: Department of Materials Science and Engineering, The Johns Hopkins University, Baltimore, MD 21218

**Abstract**--We demonstrate that full-density, bulk, two-phase nanocomposites can be produced starting from a powder mixture of two coarse-grained individual phases in equilibrium. Instead of going through liquid or vapor phase precursors, mixing is achieved through mechanical milling, a highly nonequilibrium driven process imposing external forcing. The precursor created is a supersaturated solid solution with nanocrystalline grain sizes. Upon subsequent hot consolidation to bulk samples, phase separation occurs on the scale of the nanograins, forming two-phase nanocomposites in situ. Transmission electron microscopy of the Cu<sub>60</sub>Fe<sub>40</sub> sample presented in this paper confirm that, after full density processing using the sinter forging consolidation scheme, nanophase grains are maintained and a homogeneous two-phase microstructure is obtained. ©1999 Acta Metallurgica Inc.

### THE APPROACH

Nanocomposites can be formed through codeposition or coprecipitation from vapor or liquid solutions [1,2]. To create a nanocomposite in solid state, however, one needs a suitable precursor such that the two desired solid phases can be uniformly mixed on nanoscale. In addition, the nanoscale microstructure and uniformity needs to be maintained after hot consolidation to full density.

We use the following strategy in this work. Suppose the two constituent phases to be formed into a nanocomposite are thermodynamically stable and in equilibrium at processing temperatures. In other words, they have tie-line compositions and will not react to form a single phase thermally. A highly nonequilibrium process, high-energy ball milling, will be used to mix the two powders. In many metallic systems, such a mechanical alloying process can lead not only to a simple mechanical mixture of the two phases, but more often to a nonequilibrium single phase that is nanocrystalline and alloys the elements on atomic scale [3]. Using this

nanocrystalline solution (or metastable compound) as the precursor, a two-phase composite with both grain sizes and uniformity on nanoscale can be formed *in situ* during the hot consolidation step when the precursor decomposes in nanograins into the two equilibrium phases.

In the following, the feasibility of this approach is demonstrated using a simple system, Cu-Fe, where the two elements have negligible solid solubility at room temperature (RT). However, this approach is not restricted to such spinodal systems and can be extended to many combinations in two-phase regions in a large number of phase diagrams. The two phases can be selected to combine strength and ductility (a metal and an intermetallic), strength and conductivity, a magnetic phase embedded in a nonmagnetic matrix, etc. Also, the starting powder mixture can be composed simply of elemental powders in proper proportions even when the eventual composite involves intermediate phases, because the latter form through decomposition of a nonequilibrium precursor and are not necessarily the same as the starting materials. To help attain full density while maintaining the desired nanostructure, a sinter-forging procedure recently developed in our laboratory will be employed [4,5].

### EXPERIMENTAL

Mechanical alloying (ball milling) was conducted using a SPEX 8000 shaker mill/mixer. Powder mixture of commercial Cu (99% purity, -325 mesh) and Fe (99.9% purity, 10 micron) and the hardened stainless steel milling balls were sealed in a hardened stainless steel vial under purified Ar, with a ball to powder weight ratio of 4:1. Due to the high Cu content, the powders were milled at the liquid nitrogen temperature (LN<sub>2</sub>T) to reduce agglomeration and welding to milling tools [6]. This temperature was obtained by spraying LN<sub>2</sub> continuously onto the outside of the vial. After 10 hrs of milling to reach steady state, the vial was warmed up to RT before opening to avoid contamination from condensation.

For consolidation, a preform was first compacted at RT using a 6.35 mm ID tungsten carbide die at a pressure of 1 GPa for 10-24 hours. The resultant green density was typically around 70-80% of theoretical density. The green compact was then transferred into a second tungsten carbide die (7.1 mm ID) and pressed at the desired temperature for 30 min. in a HP20-4560-20 Laboratory Hot Press system. The chamber was evacuated using a mechanical pump and then back-filled with argon. The consolidation temperature used was in the range of 380-410°C and the pressure applied in the range of 320 to 870 MPa. Such a procedure may be termed 'constrained sinter-forging', or 'upset hot forging'. Density of the consolidated compacts was determined using the buoyancy method applying the Archimedes Principle. The final density of the consolidated sample was typically above 99.5% of theoretical density. Scanning electron microscopy was also used to detect the residual pores for full density verification.

Grain size and phase distribution in the consolidated samples were examined at 200 keV in a Hitachi HF-2000 field emission transmission electron microscope (FE-TEM). Specimens were prepared using a standard process of grinding, dimpling, followed by ion milling with LN<sub>2</sub> cooling. Energy dispersive X-ray (EDX) spectra were acquired with the electron beam in the microanalysis mode, which permits a beam diameter of 1 nm to a few microns to be used for composition analysis.

### RESULTS AND DISCUSSION

Samples of various phase volume fractions have been processed using the milling and consolidation procedures described above. This report, however, will concentrate on one



representative composition,  $\text{Cu}_{40}\text{Fe}_{60}$ , which is a case of fcc solid solution precursors. Formation of single-phase solid solution with nanophase grain sizes (10 to 20 nm) using milling conditions similar to those in this work has been reported and analyzed in detail before by this and several other groups [e.g., 7,8].

Figure 1 is a bright-field TEM micrograph of a  $\text{Cu}_{40}\text{Fe}_{60}$  sample after consolidation to full density, showing fairly uniform nanoscale grain sizes. Both Fe and Cu rings are clearly seen in the corresponding selected area diffraction pattern (not shown), which demonstrates that the product is indeed a two-phase mixture. In fact, it was possible to identify individual Cu and Fe grains using EDX with a focused electron beam spot, as labeled in Figure 1. When the beam spot is relatively large, the area analyzed contains both Fe and Cu grains in large numbers, giving an averaged composition very close to the nominal composition of the sample. From the grain size distribution for this sample determined from dark-field and bright-field micrographs taken at different locations, the average grain size for Cu and Fe grains is approximately 35 nm. These results indicate that the processing protocol used in this work indeed yielded a true two-phase nanocomposite with a uniform microstructure. The final grain size of the sample can be controlled by adjusting the consolidation temperature, duration, and pressure applied. Figure 2 is a bright-field TEM micrograph of another consolidated sample showing grain sizes somewhat larger than those in Fig. 1. The average grain size is nevertheless still well within that of typical nanophase materials (<100 nm).

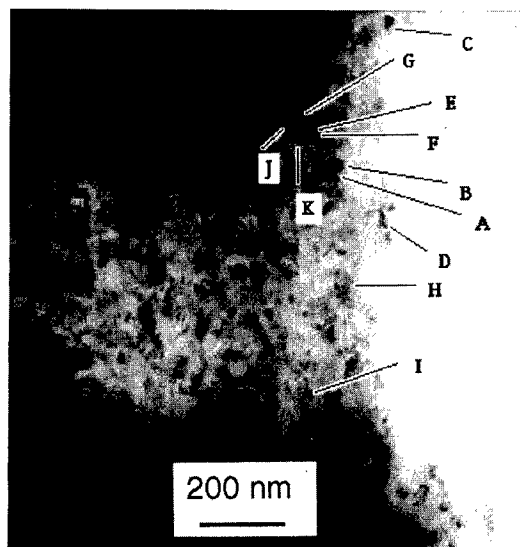


Figure 1 Bright-field TEM (in analytical mode) micrograph showing Cu and Fe grains as identified by EDX (A-D, F, and H-J: Fe; E, G, and K: Cu).

### SUMMARY

In summary, we have outlined a new approach to produce bulk two-phase nanocomposites from powders. The idea is to create in solid state a nanocrystalline solution precursor which ensures the uniform mixing of the constituent elements. Phase separation from the alloyed nonequilibrium precursor during consolidation provides the natural mechanism for the *in situ* formation of a nanocomposite with a homogeneous two-phase microstructure. Constrained sinter-forging has been used to achieve full density at fairly low temperatures while maintaining nanophase grain sizes.

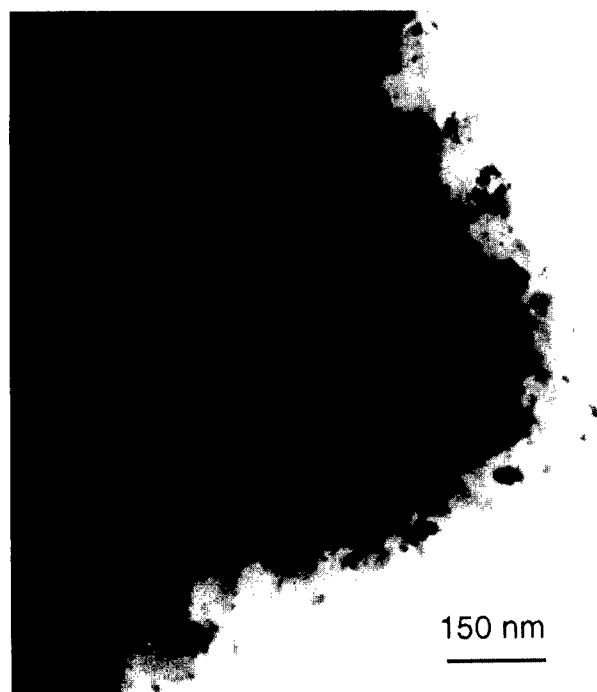


Figure 2 Bright-field TEM micrograph of another consolidated  $\text{Cu}_{40}\text{Fe}_{60}$  sample.

#### ACKNOWLEDGMENT

This work has been supported by the National Science Foundation, Grant No. CMS-9409750 and CMS-9424324. Research performed at ORNL was sponsored by the SURA-ORNL-University Graduate Summer Research Program in Materials Science, and by the High Temperature Materials Laboratory User Program, ORNL, managed by Lockheed Martin Energy Research Corp. for the U.S. DoE under contract number DE-AC05-96OR22464.

#### REFERENCES

1. A. Möller and H. Hahn; J. Macek and M. Marinsek, these Proceedings of NANO'98, *Nanostruct. Mater.* (in press).
2. R.L. Holtz and V. Provenzano, *Nanostruct. Mater.* **4**, 241 (1994).
3. C.C. Koch, in *Materials Science and Technology*, eds. R.W. Cahn, P. Hassen, and E.J. Kramer, VCH, Weinheim, Vol. 15, p. 193 (1991).
4. L. He and E. Ma, *J. Mater. Res.* **11**, 72 (1996).
5. L. He and E. Ma, *Nanostr. Mater.* **7**, 327 (1996).
6. J. Xu, J.H. He and E. Ma, *Metall. Trans.* **28A**, 1569 (1997).
7. J. Eckert, J.C. Holzer, C.E. Krill III, and W.L. Johnson, *J. Mater. Res.* **7**, 1751 (1992); E. Ma, M. Atzmon, and F. Pinkerton, *J. Appl. Phys.* **74**, 955 (1993).
8. O. Drbohlav and A.R. Yavari, *Acta metall. mater.* **43**, 1799 (1995); D. G. Morris and M. A. Morris, *ibid.* **39**, 1763 (1991); C. Biselli and D. G. Morris, *ibid.* **44**, 493 (1996).



Pergamon

NanoStructured Materials, Vol. 12, pp. 547–550, 1999

Elsevier Science Ltd

© 1999 Acta Metallurgica Inc.

Printed in the USA. All rights reserved

0965-9773/99/\$—see front matter

PII S0965-9773(99)00180-4

## A STUDY OF Al-Mo ALLOYS SYNTHETIZED BY MECHANICAL TREATMENT AND ANNEALED IN-SITU.

S. Enzo\*, R. Frattini<sup>+</sup>, P. Canton<sup>@</sup>, G. Mulas\* and P. Radaelli<sup>#</sup>

\*Istituto Nazionale di Fisica della Materia (INFM) e Dipartimento di Chimica dell'Università di Sassari, via Vienna 2, 07100 Sassari (Italy),

enzo@micromat.dipchim.uniss.it

+INFM e Dipartimento di Chimica Fisica dell'Università di Venezia, Dorsoduro 2137,

30123 Venezia (Italy), e.m. frattini@unive.it

@ Dipartimento di Chimica Fisica dell'Università di Venezia.

# ILL B.P. 156, f-38042 Grenoble Cedex 9 (France) Present Address: ISIS Facility Rutherford Appleton Laboratory, Bldg. R3 Chilton, Didcot Oxon. OX11 0QX United Kingdom

**Abstract**— $Al_{75}Mo_{25}$  alloys were synthesised by ball milling of pure elements. The decrease of fcc aluminium peaks from the neutron diffraction patterns as a function of mechanical treatment time suggests the formation of an extended Mo(Al) solid solution, even though no significant change of the bcc lattice parameter is observed. Further evidence of the existence of a metastable phase is supplied a posteriori by in situ annealing of the processed metal powders at temperatures below 750 °C. The main product is the intermetallic  $Al_8Mo_3$  compound.

©1999 Acta Metallurgica Inc.

### INTRODUCTION

There is an interest in material science for the structural characterisation of aluminium-based nanocrystalline alloys, owing to their enhanced physical, electrocatalytic and mechanical properties (1). We have previously studied extensively the structural behaviour and thermal stability of Al-Fe alloys as a function of mechanical alloying (MA) treatment time and of annealing temperature (2). Analysis of diffraction data for line broadening and lattice parameter changes were biased to a large extent by the fact that FCC Al peaks with indices even strongly overlapped with all peaks of BCC iron (3). Thus, to get more insight into the structural transformation of initial phases and the formation of nanostructured solid solution and/or intermetallic phases we have extended the study of Al-based alloys replacing Fe with Mo. In fact, the lattice parameter of Mo is different from that of Fe and such to avoid significant peak overlapping. In addition to this, the peak broadening due to mechanical damage is expected isotropic for the Mo phase (4). These facts permit a better analysis of size and strain effects from the diffraction data. Therefore the structural behaviour of  $Al_{75}Mo_{25}$  alloys, produced by MA of pure elemental powders was studied as a function of treatment time and temperature annealing by means of the constant wavelength neutron diffraction instrument D20 of Grenoble (France), equipped with a furnace facility for in-situ heating.

### EXPERIMENTAL PROCEDURE

Samples in the atomic composition  $\text{Al}_{75}\text{Mo}_{25}$  were produced after mixing aluminium and molybdenum powders of 99.99 wt. % purity. The milling was performed for 4, 8, 32, 57 and 78 hours in a hardened steel vial using a Spex mixer/mill model 8000, under an inert atmosphere of argon.

Neutron Diffraction measurements were performed at the instrument D20 of ILL laboratory in Grenoble (France). The wavelength employed was 12.946 nm. The heating ramp velocity varied from 50 to 100 °C/h and an entire pattern was collected each 5 min. approximately. Diffraction data were analysed with the Rietveld method (5), using the Fullprof code (6), according to the methodology reported in our previous publications (7).

### RESULTS AND DISCUSSION

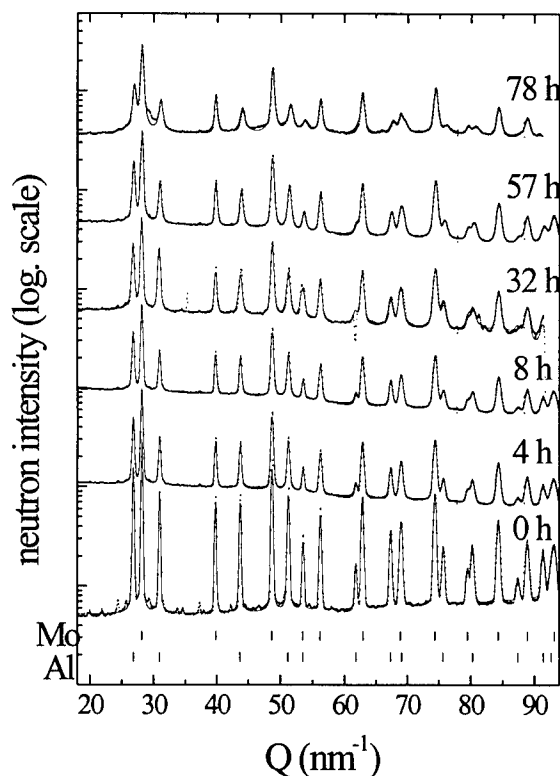


Figure 1. Neutron diffraction patterns of Al-Mo specimens mechanically treated for the quoted times. Notice the peak broadening and the partial disappearance of FCC peaks of aluminium.

Figure 1 shows the neutron diffraction patterns of MA specimens (data points) together with the Rietveld fit (full lines). Initially, the parental powders of Al and Mo shows well distinct and sharp diffraction peaks. In the background there are additional weak and unidentified peaks, not seen in the correspondent X-ray pattern taken with a conventional laboratory goniometer. It is possible that these peaks belong to metal oxide and nitride phases. In spite of the absence of terminal solid solutions in Al-Mo phase diagram (8), a progressive reduction of Al integral intensity can be observed during the milling. This suggests that this element dissolves in the remaining BCC Mo-based phase, in analogy to what observed for the Al-Fe case. However, during the mechanical treatment, the Mo phase does not seem to change the lattice parameter value of 0.31472 nm, while this is not completely true for the remaining FCC Al. As a matter of fact, after 78 h of MA, peaks of FCC Al still persist in the pattern

dominated by the BCC Mo-based phase. Thus, we observe that no single phase solid solution nor an amorphous phase can be achieved within the experimental parameters of the mill.

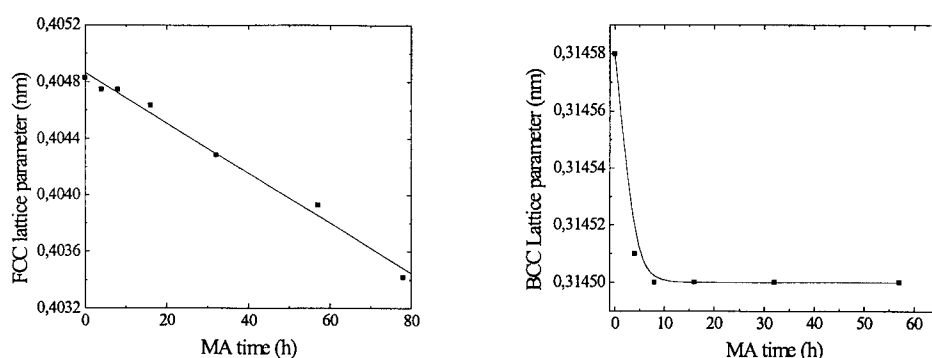


Figure 2. Lattice parameters as a function of milling time Plot (a) refers to FCC aluminium phase, (b) to BCC molybdenum phase respectively.

The lattice parameter change of the BCC phase is within the experimental error bar, whilst that of FCC Al changes linearly as a function of MA time (figure 2) and after prolonged times of milling amounts to  $\Delta a/a = 3.5 \cdot 10^{-3}$ . It should also be noted that the relative uncertainty of lattice parameters is correlated to peak broadening and, then, increases as a function of MA time.

Simultaneous crystallite size and lattice strain analysis in the hypothesis of isotropic behavior, incorporated directly in the Rietveld method for the data of figure 1, has given, for the specimens mechanically treated for long times, volume weighted means between 13.0 and 16.0 nm and microstrain values about  $5 \cdot 10^{-3}$ . Quantitative phase evaluation according to the fit of figure 1 showed a sudden decrease of the initial FCC/BCC molar ratio 3:1 to saturation of ca 0.7, immediately after 4 h. Similar weaken of intensity of phases, accompanied by unchanged lattice parameters of the remaining phases have been ascribed to a different X-ray absorption of the MA powders. In any case, even in the simple hypothesis of optical effects, it should be interesting to answer why the powders are changing their properties.

To verify the degree of atomic interaction induced by the mechanical treatment, the specimens were placed in a furnace and subjected to an increasing temperature until 750 °C. For space reason we can not discuss in much detail the results, so only the most important transformations induced by the thermal treatments will be pointed out here.

As it can be seen in Figure 3, the specimen mechanically treated for 57 h and heated at 750 °C shows essentially the  $\text{Al}_8\text{Mo}_3$  phase, whose structure is monoclinic, space group C2/m, with  $a=0.92133$  nm;  $b=0.36389$  nm;  $c=1.0062$  nm;  $\beta=100^\circ 92'$ , in satisfactory agreement with ref. 9. According to the Al-Mo phase diagram,  $\text{Al}_8\text{Mo}_3$  is supposed to melt congruently around 1575 °C, so this unconventional synthesis route may be taken as a further evidence of the metastable BCC Al(Mo) solid solutions created by the MA technique.

Finally, the results of thermal treatment can be summarised as it follows: a transformation was observed in the specimen MA 4 h, at about 600 °C, while the data referring to specimen 32 h MA show the presence of two different transformations, the first at about 400 °C, the second at about 500 °C. Furthermore, the specimen 78 h MA shows just one transformation at a temperature near to 390 °C. Concerning the nature of products after annealing, in the specimen milled 4 h mainly the  $\text{Al}_8\text{Mo}_3$  phase is present, with a minor quantity of unknown phase,

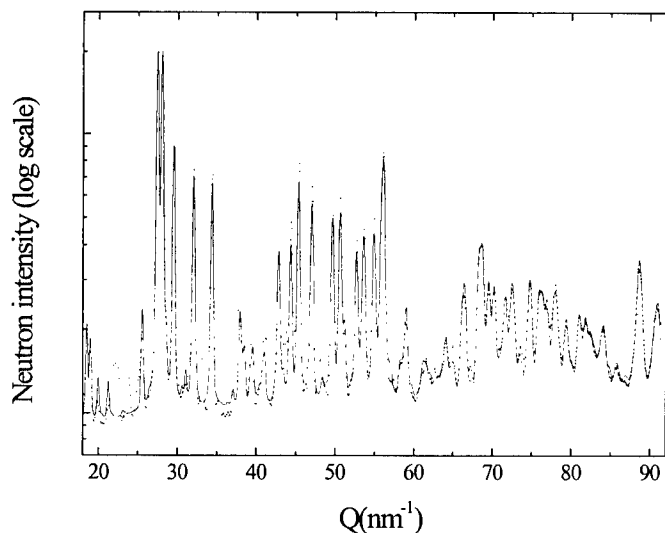


Figure 3. Neutron diffraction pattern of  $Al_{75}Mo_{25}$  specimen MA treated for 57 h and annealed at 750 °C. Dots are experimental data points and the full line is the Rietveld fit using the  $Al_8Mo_3$  structure factor. Unindexed minor peaks probably belong to the  $Al_3Mo$  phase.

attributable to tetragonal  $Al_3Mo$ . The same products seem to precipitate after annealing at 700 °C of the specimens 32 h and 78 h MA, though the relative content seems to vary as a function of the treatment time. This confirms that the nature of the transformed phases is related to the quantity of mechanical energy (dose) transferred to the system during the treatment.

Further data analysis is in progress with the Rietveld method to give a full account of structural and nano-structural properties of annealed specimens.

### ACKNOWLEDGMENTS

Thanks are due to prof. G. Cocco and dr. G. Budroni for useful discussions. This research is part of a project supported by MURST (ex 40%) and INFN of Italy. We acknowledge also the staff of the D20 diffractometer at ILL, Grenoble (France).

### REFERENCES

1. C.P. Chang and M.H. Loretto, *Acta Metall.*, 1998, **36**, 805.  
M. Zdujic, K.F. Kobayashi and P.H. Shingu, *Z Metallkde*, 1990, **81**, 380
2. E. Bonetti, G. Scipione, R. Frattini, S. Enzo and L. Schiffini, *J. Appl. Phys.* 1996, **79**, 753.
3. S. Enzo, R. Frattini, R. Gupta, P. P. Macri, G. Principi, L. Schiffini and G. Scipione, *Acta Mater.* 1996, **44**, 3105.
4. C.N.J. Wagner, in J.B. Cohen and J.E., *Local Atomic Arrangements Studied by X-ray Diffraction*, Hilliard (eds), New York, 1966, p. 219.
5. R. A. Young, *The Rietveld Method*, Oxford University Press, 1993;
6. J. Rodriguez Carvajal, *Physica B*, 1993, **192**, 55.
7. S. Enzo, *Mater. Sci. Forum*, 1998, **363**, 269.
8. T.B. Massalski, *Binary Alloy Phase Diagrams*, vol I, J.L. Murray, L.H. Bennett and H. Baker eds, AMS Metals park, Ohio, p 133.
9. J.B. Forsyth and G. Gran, *Acta Cryst.* 1962, **15**, 100.



## THE MORPHOLOGY OF NANOSCALE DEPOSITS OF RUTHENIUM OXIDE IN SILICA AEROGELS

C. I. Merzbacher<sup>a</sup>, J. G. Barker<sup>b</sup>, J. W. Long<sup>c</sup> and D. R. Rolison<sup>c</sup>

<sup>a</sup> Optical Sciences Division, Naval Research Laboratory, Washington, DC 20375.

<sup>b</sup> Center for Neutron Research, NIST, Gaithersburg, MD 20899.

<sup>c</sup> Chemistry Division, Naval Research Laboratory, Washington, DC 20375.

**Abstract**— Ruthenium oxide was deposited on the internal surfaces of silica aerogel by solution impregnation of a Ru(III)tris-acetylacetonate solution followed by reduction and oxidation. The structure of the Ru phase was determined by contrast-matching SANS, which allows independent collection of scattered intensity from SiO<sub>2</sub> and Ru oxide components of composite samples. The structure of the Ru oxide deposit depends strongly on the oxidation temperature and very little on the reduction temperature. The Ru oxide forms particles, rather than a conformal layer, which coarsen from a few nanometers after oxidation at room temperature to several tens of nm after oxidation at 250 °C. ©1999 Acta Metallurgica Inc.

### INTRODUCTION

Aerogels are a class of nanostructured materials with extremely high porosity, low density and high surface area, which are typically prepared by synthesizing a highly porous sol-gel and removing the solvent from the pores under supercritical conditions. The resulting material generally consists of nanoscale (~10 nm) microporous particles connected in an open, mesoporous network (1). Some applications require not only the high porosity and surface area innate to aerogels, but also electrical conductivity. One of our approaches is to deposit Ru dioxide, which is a metallic conductor (10<sup>4</sup> S/ohm-cm in single crystal at 25 °C (2)), on the internal surfaces of a silica aerogel. RuO<sub>2</sub> can be formed by solution impregnation with a Ru organometallic precursor, followed by thermal decomposition.

The morphology of the deposited material as a function of post-deposition heat treatments has been characterized by small angle neutron scattering (SANS), which probes structures on the scale of 1 to 100 nm. In order to measure the scattering from the silica aerogel and the Ru oxide phase independently, the technique of 'contrast matching' was used. This technique takes advantage of the fact that it is possible to match the neutron scattering length density,  $\rho_l$ , of SiO<sub>2</sub> or RuO<sub>2</sub> by an appropriate mixture of H<sub>2</sub>O and D<sub>2</sub>O. When the pores of a composite are filled with an H<sub>2</sub>O:D<sub>2</sub>O mixture that matches the  $\rho_l$  of SiO<sub>2</sub> or RuO<sub>2</sub>, the observed scattered intensity arises solely from the unmatched phase.

We have demonstrated the ability to refill the mesopores of a silica aerogel monolith (~88% porous) with water (3). In addition, there is no effect on the structure of the aerogel, on the level detected by SANS, once the rewetting process is complete.

This paper reports the critical effect of the post-deposition treatment on the final morphology of Ru oxide formed via solution impregnation of silica aerogel. A similar study of iron oxide deposited on silica aerogel (4) indicated that when the Fe precursor is first reduced to metal and then oxidized at low temperature, the metal oxide structure is conformal with that of the silica substrate. In this study, the effect of both the reduction and the oxidation temperature have been investigated.

## EXPERIMENTAL PROCEDURE

### *Sample preparation*

Silica aerogels were prepared by a method described in detail elsewhere (3). Gels were formed by hydrolysis and condensation of tetramethoxysilane (TMOS) in the presence of an acid catalyst. After aging, washing in acetone, and drying under supercritical CO<sub>2</sub>, the samples were heated to 500 °C in air to remove residual water and organic compounds. The resulting aerogels have a bulk density of ~0.25 g/cm<sup>3</sup> and a multipoint BET surface area of ~675 m<sup>2</sup>/g.

Aerogel disks (8-mm diam. × 1-2 mm thick) were immersed in an acetonitrile solution saturated in Ru(III)tris-acetylacetonate (~90 mg/ml) overnight and dried in air at room temperature. The impregnated samples gain ~20 wt%, and were uniformly dark red in color, due to impregnation. The disks were first heated to either 250 °C or 400 °C in flowing Ar/H<sub>2</sub> (13 vol% H<sub>2</sub>) for 1 h and then oxidized by heating to 250 °C in air for 1 h or simply by exposure to air at room temperature for at least 7 days prior to analysis. The final weight gain after reduction and oxidation was only a few percent, and difficult to quantify due to the presence of up to 4 wt% surface adsorbed water on the substrates prior to deposition. All samples are amorphous, with the exception of those oxidized at 250 °C, which have a few vol% RuO<sub>2</sub>, based on powder X-ray diffraction.

### *Sample characterization*

Scattering measurements were performed on a 30-m SANS spectrometer at the National Institute of Standards and Technology (NIST, Gaithersburg, MD). A neutron wavelength of 0.6 nm and three sample-to-detector distances were used to cover a momentum transfer ( $q$ ) range of 0.04 nm<sup>-1</sup> to 4.5 nm<sup>-1</sup>. The raw data were corrected as described previously (4).

Samples were held in quartz cells filled with air or a mixture of H<sub>2</sub>O and D<sub>2</sub>O that matched either  $\rho_f(\text{SiO}_2)$  or  $\rho_f(\text{RuO}_2)$ . The scattering length density is a function of composition and mass density. Silica of mass density 2.2 g/cm<sup>3</sup> is matched by a 42:58 volume ratio of H<sub>2</sub>O:D<sub>2</sub>O and ruthenia of mass density 6.97 g/cm<sup>3</sup> is matched by a 5:95 volume ratio of H<sub>2</sub>O:D<sub>2</sub>O. In order to minimize stress on the aerogel structure during refilling, samples were exposed to an atmosphere saturated in the appropriate H<sub>2</sub>O/D<sub>2</sub>O mixture at 85 °C for at least 9 h before immersion in the contrast-matching liquid.



## RESULTS AND DISCUSSION

Scattering data for various contrast-matched samples are shown in Fig. 1 on a log-log plot of  $q$  vs. intensity. Scattering from the Ru oxide portion of the composites is measured on the samples filled with  $\text{SiO}_2$ -matching liquid. The SANS is unaffected by the temperature at which the samples are reduced, therefore only data for  $\text{SiO}_2$ -matched samples prepared at one reduction temperature (250 °C) are shown. Also shown, are data from a representative composite sample filled with  $\text{RuO}_2$ -matching liquid, which is due solely to the scattering from the silica component, and an uncoated silica aerogel filled with silica-matching liquid, representing the effective background. The similarity between the  $\text{RuO}_2$ -matched composite and the bare silica aerogel indicate that the coating does have the scattering properties of  $\text{RuO}_2$ . The steep slope at low  $q$  is observed for all re-wetted samples and is attributed to a few large air bubbles. Large scatter at high  $q$  in the curves for the  $\text{SiO}_2$ -matched samples is the result of subtracting the large incoherent background scattering from hydrogen in the pore-filling liquid.

The scattering from the sample oxidized at room temperature resembles the background curve at low  $q$  and shows an increase in intensity at  $\log q > -1 \text{ nm}^{-1}$ . Because  $q$  is inversely related to length, intensity observed at larger  $q$  is due to scattering from smaller features. The lineshape of the room-temperature oxidized sample is attributed to scattering from Ru oxide particles a few nanometers in diameter.

By comparison, scattering from the sample oxidized at 250 °C is greater than background across the entire range in  $q$ . This lineshape is consistent with a coarsening of the Ru oxide

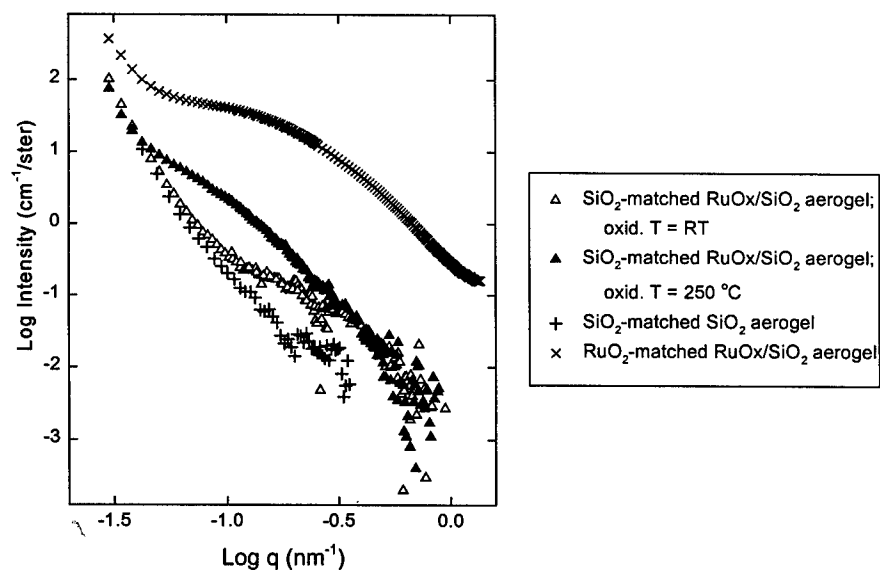


Fig. 1. SANS of various contrast-matched silica aerogels. Errors are less than the size of the symbols.

particles during oxidation at elevated temperatures. If the difference in scattering as a function of oxidation is strictly due to increasing particle size, without a change in the volume fraction of Ru oxide, then the intensity at large  $q$  should theoretically be higher for the sample with smaller particles. The lack of an observed crossover between the two curves is due to (a) the relatively small increase in intensity at high  $q$  from the small scatterers, and (b) the high noise level at high  $q$  due to the large background correction for the silica-matched samples.

If the Ru oxide were forming a conformal layer on the internal surfaces of the silica aerogel, mimicking the morphology of the silica aerogel substrate, then the shape of the Ru oxide scattering curve should be similar to that of the silica aerogel component. Such similarity has been observed for iron oxide deposited on silica aerogel by vapor infiltration followed by reduction and room-temperature oxidation (4). The Ru oxide curves in this study, however, do not parallel the silica aerogel curve nearly as well as the Fe oxide data in the earlier study. They resemble more closely the curves for Ru oxide deposits which were not reduced at all, and oxidized at 400 °C.

### CONCLUSIONS

Ruthenium oxide has been deposited on the internal surfaces of silica aerogel by solution impregnation of an acetone solution of Ru(III)trisacetylacetonate, followed by reduction and oxidation at various temperatures. The structure of the deposited phase, as determined by contrast-matching SANS, is independent of the reduction temperature, but is strongly affected by the temperature of oxidation. The scattering data are consistent with the presence of particles a few nanometers in diameter in the samples that oxidized in ambient conditions and a coarser particle size after oxidation at 250 °C.

### ACKNOWLEDGMENTS

This work was supported by the ONR and DARPA, and is based upon activities supported by the National Science Foundation under Agreement No. DMR-943101.

### REFERENCES

1. Brinker, C. J. and Scherer, G.W., *Sol-Gel Science: The Physics and Chemistry of Sol-Gel Processing*, Academic Press, San Diego, 1990, p. 520.
2. Schafer, H., Schneidereit, G. and Gerhardt, W., *Z. Anorg. Allg. Chem.*, 1963, 319, 372.
3. Merzbacher, C.I., Barker, J.G., Swider, K.E. and Rolison, D.R., *J. Non-Cryst. Solids*, 1998, 224, 92.
4. Merzbacher, C.I., Barker, J.G., Swider, K.E., Ryan, J.V., Bernstein, R.A. and Rolison, D.R., *J. Non-Cryst. Solids*, 1998, 225, 234.
5. Schaefer, D.W. and Keefer, K.D., *Phys. Rev. Lett.*, 1986, 56, 2199.



## Fe DIFFUSION IN NANOCRYSTALLINE ALLOYS AND THE INFLUENCE OF AMORPHOUS INTERGRANULAR LAYERS

R. Würschum<sup>a)</sup>, T. Michel<sup>a)</sup>, P. Scharwaechter<sup>a)</sup>,  
W. Frank<sup>a,b)</sup>, and H.-E. Schaefer<sup>a)</sup>

<sup>a)</sup>Univ. Stuttgart, Inst. f. Theoret. u. Angew. Phys., 70550 Stuttgart, Germany,

<sup>b)</sup>Max-Planck-Institut für Metallforschung, 70506 Stuttgart, Germany

**Abstract**— <sup>59</sup>Fe tracer diffusion is used as a highly structure-sensitive tool for probing the interface structure and residual amorphous intergranular phases in nanocrystalline (n-) Fe<sub>90</sub>Zr<sub>10</sub> produced by crystallization of melt-spun amorphous ribbons. Analyses of <sup>59</sup>Fe-diffusion profiles show the existence of two types of interfaces. In the one type the diffusivities are low; the other type acts as fast diffusion paths like conventional grain boundaries in  $\alpha$ -Fe. In accordance with positron-annihilation and hydrogen-site spectroscopy of the interfacial structure on n-Fe<sub>90</sub>Zr<sub>10</sub>, the slow diffusion process may indicate the presence of amorphous intergranular layers similar as recently found for n-Fe<sub>73.5</sub>Si<sub>13.5</sub>B<sub>9</sub>Nb<sub>3</sub>Cu<sub>1</sub>. ©1999 Acta Metallurgica Inc.

### INTRODUCTION

Atomic transport in nanocrystalline (n-) solids represents a key issue since it controls both the physical properties, e.g., plasticity, and the structural stability of these materials. In addition to these application-oriented aspects, atomic transport, as studied by radiotracer techniques, may serve as a highly structure-sensitive probe of interfaces.

According to recent studies, the diffusion in relaxed interfaces of nanocrystalline pure metals is similarly fast as in conventional grain boundaries (n-Pd [1, 2], n-Fe [3]). On the other hand, much lower Fe self-diffusivities were found for interfaces in nanocrystalline Fe<sub>73.5</sub>Si<sub>13.5</sub>B<sub>9</sub>Nb<sub>3</sub>Cu<sub>1</sub> (Finemet) prepared by crystallization after melt-spinning [4]. This low diffusivity arises from intergranular amorphous layers which persist after the formation of D0<sub>3</sub>-Fe<sub>80</sub>Si<sub>20</sub> nanocrystallites in the Finemet alloy [4]. These results raise the question whether low interface diffusivities represent an intrinsic property of crystallization-produced nanocrystalline alloys or whether interfaces with high and low diffusivities may coexist or even can be tailored by appropriate annealing conditions. Information on this subject would be of interest, for instance, with respect to metallic amorphous layers used in microelectronic devices as diffusion barriers [5].

In an initial attempt to answer the aforementioned questions concerning interface diffusion, the present work has aimed at <sup>59</sup>Fe-tracer diffusion studies on nanocrystalline Fe<sub>90</sub>Zr<sub>10</sub> after complete crystallization [6, 7]. In contrast to what is true for the Finemet alloy, a potential residual amorphous phase in n-Fe<sub>90</sub>Zr<sub>10</sub> is expected to be strongly reduced due to the formation of  $\alpha$ -Fe and Fe<sub>2</sub>Zr nanocrystallites during nanocrystallization

[8, 9]. Moreover, an assessment of interface diffusion is easier for n-Fe<sub>90</sub>Zr<sub>10</sub> since, in contrast to Finemet, in this material volume diffusion in the nanocrystallites may be ruled out [10]. The <sup>59</sup>Fe-tracer diffusion experiments were performed as described elsewhere [1, 4].

## RESULTS AND DISCUSSION

Nanocrystalline Fe<sub>90</sub>Zr<sub>10</sub> crystallized under ultra-high vacuum conditions from melt-spun amorphous ribbons consists of  $\alpha$ -Fe and Fe<sub>2</sub>Zr nanocrystallites with a mean size of 29 nm (Fig. 1). Hot-extraction analysis yielded an oxygen content of 0.8 at. %.

After a 2h-pre-relaxation at 668 K an <sup>59</sup>Fe-tracer-diffusion coefficient for the amorphous state of  $D_{\text{amorph}} = 4.3 \times 10^{-9} \exp(-1.25 \text{ eV}/kT) \text{ m}^2/\text{s}$  has been determined (Fig. 3), which reasonably agrees with previous data (see [11] and refs. therein). From this, the diffusion behaviour in nanocrystalline Fe<sub>90</sub>Zr<sub>10</sub> differs as follows: (I) The dominant Gaussian parts of the diffusion profiles measured on n-Fe<sub>90</sub>Zr<sub>10</sub> are characterized by <sup>59</sup>Fe-tracer diffusivities  $D_{\text{nano}}^{\text{slow}}$  (slow diffusion process) which lie below  $D_{\text{amorph}}$  by about one to two orders of magnitude (Figs. 2, 3). (II) The diffusion profiles show tails reaching to great penetration depths, which are non-Gaussian and which indicate a second, fast diffusion process ( $D_{\text{nano}}^{\text{fast}}$ , Fig. 2).

**Slow diffusion process:** Since volume diffusion in the nanocrystallites of n-Fe<sub>90</sub>Zr<sub>10</sub> is negligible in the temperature regime studied here [10], the slow diffusion process I ( $D_{\text{nano}}^{\text{slow}}$ ) is attributed to interface diffusion. Note that this interface diffusion must differ fundamentally from the grain-boundary self-diffusion in polycrystalline  $\alpha$ -Fe since it is slower by more than 3 orders of magnitude (Fig. 3, [12]). For an assessment of this behaviour both chemical and structural effects have to be taken into consideration.

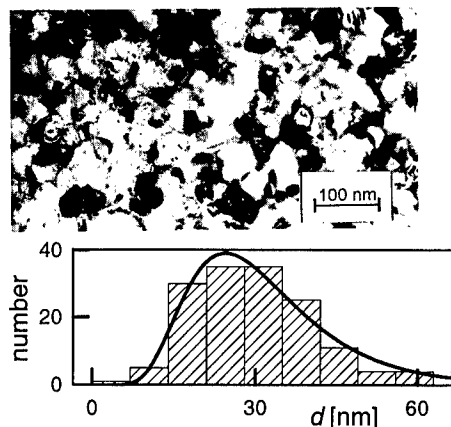


**Fig. 1:** Transmission electron micrograph (top) of nanocrystalline Fe<sub>90</sub>Zr<sub>10</sub> crystallized at 883 K for 48 h and histogramme (bottom) of crystallite sizes  $d$  (150 crystallites) fitted by a log-normal function.

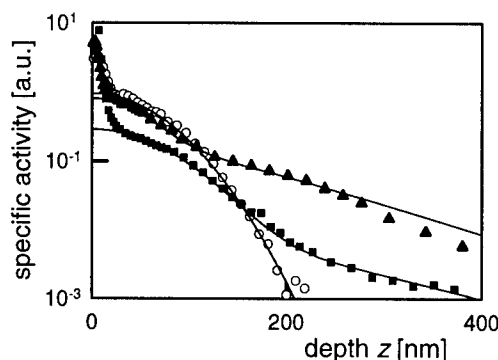


**Fig. 2:** <sup>59</sup>Fe-diffusion profiles in relaxed amorphous (○) and n-Fe<sub>90</sub>Zr<sub>10</sub> crystallized for 48 h at 878 K (■) or 895 K (▲). Temperature and durations  $t$  of diffusion: 671 K, 0.5 h (○), 729 K, 1 h (■), 767 K, 0.5 h (▲). The fitting takes into account two interface diffusivities (see text).

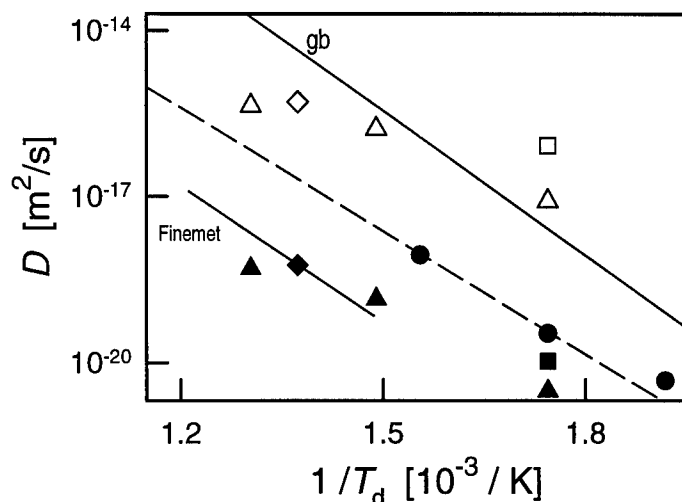


**Fig. 3:** Arrhenius plots of  $^{59}\text{Fe}$ -tracer diffusivities  $D$ : Nanocrystalline  $\text{Fe}_{90}\text{Zr}_{10}$  after crystallization at 878 K ( $\blacklozenge, \lozenge$ ), 881 K ( $\blacksquare, \square$ ), or 895 K ( $\blacktriangle, \triangle$ ); filled and open symbols denote  $D_{\text{slow}}^{\text{slow}}$  and  $D_{\text{fast}}^{\text{fast}}$ , respectively (see text). Relaxed amorphous  $\text{Fe}_{90}\text{Zr}_{10}$  ( $\bullet$ , present work; dashed line, see [11]). Nanocrystalline  $\text{Fe}_{73.5}\text{Si}_{13.5}\text{B}_9\text{Nb}_3\text{Cu}_1$  (Finemet) crystallized at 813 K [4]. Extrapolated values for grain boundaries in  $\alpha\text{-Fe}$  [12] are shown for comparison (gb).

For  $\alpha\text{-Fe}$  it is well documented that segregation of impurities may reduce the grain boundary diffusivity [13]. In the case of  $\text{n-Fe}_{90}\text{Zr}_{10}$  the interaction of the Fe tracer atoms with Zr, which forms intermetallic compounds with Fe, may further reduce the interface diffusivity. It appears unlikely, however, that these chemical effects alone may account for the substantial difference in the interface diffusivities of  $\text{n-Fe}_{90}\text{Zr}_{10}$  and  $\alpha\text{-Fe}$ .

The low diffusivities  $D_{\text{slow}}^{\text{slow}}$  in  $\text{n-Fe}_{90}\text{Zr}_{10}$  are considered to arise, in addition to chemical effects, from residual amorphous phases between the nanocrystallites, similarly as found recently for  $\text{n-Fe}_{73.5}\text{Si}_{13.5}\text{B}_9\text{Nb}_3\text{Cu}_1$  [4]. Although, in contrast to the Finemet alloy [4], for  $\text{n-Fe}_{90}\text{Zr}_{10}$  amorphous phases have not been detected unambiguously by X-ray diffraction within the present detection limit of 5 at.%, indirect evidence for intergranular amorphous phases was obtained earlier from positron annihilation [8] and hydrogen-site spectroscopy by means of magnetic after-effect measurements. [14]. These studies showed identical spectra of free volumes in amorphous  $\text{Fe}_{90}\text{Zr}_{10}$  and in the interfaces of  $\text{n-Fe}_{90}\text{Zr}_{10}$  [8, 14].

**Fast diffusion process:** The second, fast diffusion process ( $D_{\text{fast}}^{\text{fast}}$ , Fig. 2) is also attributed to interface diffusion since rapid diffusion, e.g., due to open pores, can be excluded in the crystallization-produced highly dense nanocrystalline alloy. In the analysis of the tails of the diffusion profiles we therefore assume the existence of two types of interconnected interfaces, namely interfaces of type II, in which fast diffusion ( $D_{\text{fast}}^{\text{fast}}$ ) occurs, and interfaces of type I, in which tracer atoms entering from type-II interfaces diffuse slowly. Slow diffusion ( $D_{\text{slow}}^{\text{slow}}$ ) from the specimen surface directly into type-I interfaces

gives rise to the above-mentioned Gaussian-shaped parts of the diffusion profiles next to the surface. In analogy to type-B kinetics of interface diffusion [15] the fast interface diffusivity  $D_{\text{nano}}^{\text{fast}}$  can be determined from the tails of the tracer concentration profiles  $c(z)$  according to  $\delta D_{\text{nano}}^{\text{fast}} \simeq 1.322 \sqrt{D_{\text{nano}}^{\text{slow}}/t} (-\partial \ln c(z) / \partial z^{6/5})^{-5/3}$ , where  $\delta (= 1 \text{ nm})$  denotes the interface thickness (fitted curves in Fig. 2). Within the framework of this model [16] the fast interface diffusivities are of the same order of magnitude as the grain-boundary self-diffusivities in conventional polycrystalline  $\alpha$ -Fe (Fig. 3) or in cluster-synthesized n-Fe [3].

The present studies yield first evidence for the existence of interfaces with different diffusion characteristics in crystallization-produced n-alloys, i.e. interfaces in which diffusion is slow, presumably due to intergranular amorphous layers, and interfaces in which diffusion occurs similarly fast as in conventional grain boundaries.

**Acknowledgements:** The authors are grateful to Miss M. Kelsch for the TEM analyses. Financial support by Deutsche Forschungsgemeinschaft (SFB 277, project B9, and grant Scha428/25-1) is appreciated.

- [1] R. Würschum, K. Reimann, S. Größ, A. Kübler, P. Scharwaechter, W. Frank, O. Kruse, H.-D. Carstanjen, and H.-E. Schaefer, *Phil. Mag. B*, 1997, **76**, 407.
- [2] R. Würschum, U. Broßmann, and H.-E. Schaefer, in *Nanostructured Materials: Processing, Properties, and Potential Applications*, ed. C.C. Koch, to be published.
- [3] H. Tanimoto, P. Farber, R. Würschum, R.Z. Valiev and H.-E. Schaefer, these proceedings.
- [4] R. Würschum, P. Farber, R. Dittmar, P. Scharwaechter, W. Frank, and H.-E. Schaefer, *Phys. Rev. Letters*, 1997, **79**, 4918.
- [5] M.-A. Nicolet, *Defect Diff. Forum*, 1997, **143–147**, 1271; S. Raud, J.S. Chen, and M.-A. Nicolet, *Appl. Phys. A*, 1991, **52**, 151.
- [6] T. Michel, diploma thesis, Universität Stuttgart, 1998.
- [7] For the influence of small degrees of crystallization on the diffusion behaviour, see T. Schuler, J. Pavlovský, P. Scharwaechter, W. Ulfert, and W. Frank, *Nanostruct. Mater.*, 1995, **6**, 863.
- [8] R. Würschum, W. Greiner, R.Z. Valiev, M. Rapp, W. Sigle, O. Schneeweiss, and H.-E. Schaefer, *Scripta metall. mater.*, 1991, **25**, 2451.
- [9] C.U. Maier and H. Kronmüller, *Z. Metallkd.*, 1993, **84**, 6.
- [10] In the temperature regime studied here the self-diffusion coefficient in coarse-grained  $\alpha$ -Fe is smaller than  $2 \times 10^{-23} \text{ m}^2/\text{s}$  (M. Lübbhusen and H. Mehrer, *Acta Metall. Mater.* 1990, **38**, 283). The same should be true for the intermetallic compound FeZr<sub>2</sub> with a melting temperature higher than that of Fe.
- [11] W. Frank, A. Hörner, P. Scharwaechter, and H. Kronmüller, *Mater. Sci. Eng. A*, 1994, **179/180**, 36.
- [12] J. Bernardini, P. Gas, E.D. Hondros, and M.P. Seah, *Proc. Roy. Soc. London A*, 1982, **379**, 159.
- [13] I. Kaur, W. Gust, and L. Kozma, *Handbook of grain and interface boundary diffusion data, Vol. 1*, Ziegler Press, Stuttgart, 1989, p. 536.
- [14] M. Hirscher, S. Zimmer, and H. Kronmüller, *Z. Phys. Chem.*, 1994, **183**, 51.
- [15] I. Kaur, Y. Mishin, and W. Gust, *Fundamentals of Grain and Interphase Boundary Diffusion*, John Wiley, Chichester, 1995.
- [16] The conditions of type-B kinetics (i)  $\sqrt{D_{\text{nano}}^{\text{slow}} t} > \delta$  and (ii)  $\sqrt{D_{\text{nano}}^{\text{slow}} t} < d$  [15] are reasonably well fulfilled for low diffusion temperatures ( $\sqrt{D_{\text{nano}}^{\text{slow}} t} \simeq 10 \text{ nm}$ ). At high temperatures the  $D_{\text{nano}}^{\text{fast}}$  values represent lower limits due to deviations from (ii) ( $\sqrt{D_{\text{nano}}^{\text{slow}} t} \simeq 30 - 50 \text{ nm}$ ).



Pergamon

NanoStructured Materials, Vol. 12, pp. 559–562, 1999  
Elsevier Science Ltd

© 1999 Acta Metallurgica Inc.

Printed in the USA. All rights reserved  
0965-9773/99/\$—see front matter

PII S0965-9773(99)00183-X

## EXPERIMENTAL EVIDENCES OF LATTICE DISTORTION IN NANOCRYSTALLINE MATERIALS

K. Lu and Y.H. Zhao

State Key Laboratory for Rapidly Solidified Non-equilibrium Alloys (RSA)  
Institute of Metal Research, Chinese Academy of Sciences, Shenyang 110015, P.R. China

**Abstract** – *Lattice parameters for nanocrystalline (nc) materials were found to be alerted with respect to the corresponding coarse-grained polycrystalline counterparts in several systems. In this work, experimental evidences of the lattice structure distortion in various nc materials processed by means of different approaches will be summarized and discussed. Strong evidences showed the lattice structure distortion in nc samples which is manifested by an evident change in the lattice parameters, Debye-Waller parameter, and the thermal properties of the nanocrystalline lattice. These results imply that the property changes of nc materials should be attributed not only to the numerous non-equilibrium grain boundaries, but to the distorted nanocrystallites as well. ©1999 Acta Metallurgica Inc.*

### INTRODUCTION

Owing to the ultrafine-grained structure, nanocrystalline (nc) materials exhibit many properties that are found to be fundamentally different from, and often superior to, those of the conventional polycrystalline counterparts [1,2]. The property enhancements in nc materials are frequently attributed to either the numerous amount of grain boundaries and/or the specific grain boundary structure that was claimed to differ fundamentally from that of the conventional grain boundary [1]. While many structure investigations on the nc grain boundary structure yield rather controversy results [3,4], the structure characteristics of the nm-sized crystallites, which still constitute a major part of nc materials, has received seldom attention.

In recent years, a series of experimental investigations have been carried out on the microstructure and properties of the nm-sized crystallites in nc materials. It shows that the lattice structure parameters in nc materials differ evidently from those in their conventional coarse-grained counterparts [2,5,6]. In this paper, we will summarize the experimental evidences on the lattice structure parameter measurements in different nc materials processed by means of different synthesis techniques.

### EXPERIMENTAL RESULTS AND DISCUSSION

#### *Lattice parameters*

Lattice parameters in a number of nc samples have been measured by means of the quantitative x-ray diffraction (XRD) technique. Table 1 summarizes the experimental data on lattice parameter of nc materials reported in the literature. For bcc metals (Cr and Fe) and fcc metal (Cu) synthesized by means of different approaches (e.g., consolidation of ultrafine powders, ball-milling, electrodeposition, and severe plastic deformation etc.), lattice parameters of nanocrystallites were found to be slightly increased (0~0.09%) with respect to the equilibrium lattice constant for bulk materials. An evident grain size dependence of lattice parameter was observed in fully-dense nc Cu samples [10] (made by means of electrodeposition, ball-milling, and severe plastic deformation, respectively) and ball-milled nc Fe samples [8] that  $a$  value increases with a reduction of grain size following an approximate  $1/d$  rule. The only negative  $\Delta a$  value found in the nc Pd sample, as listed in Table 1, might be attributed to the porosity effect in the sample of which the density is only 80% of the bulk value [4]. It is reported that the lattice parameters for ultrafine metal particles are decreased (lattice contraction) owing to the large surface tension [15].

For nc semiconductors (Si, Ge and Se), significant lattice parameter changes were observed. Evident lattice distortion (up to about 0.2% in the lattice parameter) was seen in ball-milled nc Si and Ge prior to their solid state amorphization process [11,12]. In a nc Se sample with a mean grain size of about 13 nm,  $a$  value is about 0.30% higher than the tabulated bulk value, while  $c$  is about 0.12% smaller. The overall unit cell volume is increased by as high as 0.7% relative to that of the conventional polycrystalline Se. The grain size dependence of the lattice parameters in the crystallized nc Se samples (from amorphous Se) agrees well with that in the ball-milled nc Se. For nc bct intermetallic compounds ( $\text{Ni}_3\text{P}$  and  $\text{Fe}_2\text{B}$ ), a similar variation tendency of lattice parameters with grain size was detected, *i.e.*, when grain size reduces,  $a$  increases but  $c$  decreases, resulting in an evident increase in the unit cell volume (as much as 0.3%) [6,14].

#### ***Debye-Waller Parameters***

The Debye-Waller parameter (DWP) is a measure of the displacement of atoms from their ideal positions. In the nc element samples, DWPs determined from quantitative XRD measurements by using the Warren method or other methods, show an evident enhancement relative to the tabulated values for bulk polycrystals. The static DWP in various nc samples, which reflects the static atomic displacement, increases by 100~900% compared to the equilibrium values, as listed in Table 1. This behavior verifies the existence of the lattice distortion in the nanocrystallite lattice. Measurement results in the nc Se crystallized from amorphous Se [16] and in the nc Cr sample [7] indicated that the static DWP increases with a reduction of grain size following an approximate  $1/d$  rule.

The Debye characteristic temperature for nc materials decreases significantly with a reduction of grain size. The Debye temperature in a nc Se (with an average grain size of 13 nm) is only 119 K compared to the tabulated value of 136 K for bulk Se [16]. The depressed Debye temperature in nc samples implies a decrease in the cohesion of atoms in the nanocrystallites, which agrees well with the measured grain size dependence of static DWP and lattice parameters (unit cell volume expansion).

#### ***Lattice thermal expansion behavior***



Thermal expansion behavior of nanocrystallites, that is closely related to the lattice structure, has been measured in several nc materials by using XRD at different temperatures. With decreasing grain size, thermal expansion coefficient in nc Se samples increases, but that exhibits evident anisotropy, i.e., upon heating,  $a$  value increases but  $c$  decreases. The overall unit cell volume expands at elevated temperatures [16]. For the ball-milled nc Fe, enhanced thermal expansion coefficient by about 100% was detected when grain size is down to 8 nm [8]. The Debye temperature deduced from the grain size dependence of the thermal expansion coefficient in nc Se coincides with that of the direct measurements. It means the lattice distortion is obviously reflected from the thermal property of the nanocrystallites.

From the results presented above, one may see that the lattice distortion exists in various nc materials synthesized by means of different techniques. Similar grain size dependence of lattice parameter change was observed for nc samples (Cu and Se) with different synthesis methods. It is also noticed that lattice distortion is sensitive to various influencing factors such as sample porosity, contamination, segregation, etc. Therefore, more systematic experimental investigation with ideal (clean and dense) nc samples is highly needed prior to a clear understanding of the intrinsic nature of the lattice distortion in nc materials.

The observed lattice distortion in nc materials, which is characterized by lattice expansion and increased atomic displacement (or depressed cohesion of atoms), will definitely result in property variation with respect to that of the perfect lattice. For instance, elastic modulus is expected to be depressed when the crystal lattice is dilated, that may lead to more or less softening of the material. The observed abnormal hardening/softening behaviors in nc materials may be intrinsically related with the lattice structure distortion. It is noticed that grain refinement in the nanometer regime yields hardening for most bcc and fcc metals but softening for alloys and intermetallic compounds [17]. This result may be correlated to our observation that lattice distortion is rather small for bcc and fcc metals, while a relative large lattice distortion is seen for nc intermetallics ( $\text{Ni}_3\text{P}$  and  $\text{Fe}_2\text{B}$ ). The nc lattice distortion is also found to be correlated with the apparent thermal expansion behavior of nc samples [18]. Further intensive studies are necessary to reveal the lattice distortion effect on the property variation in nc materials.

### CONCLUDING REMARKS

Solid experimental evidences of lattice distortion have been obtained in various nc materials made by means of different synthesis methods. The nanocrystallite is found to exhibit dilated lattice with an increased unit cell volume and atomic displacement (or depressed cohesion of atoms) with respect to the corresponding perfect crystal lattice. The lattice distortion is weak for most nc fcc and bcc metals, while much significant for nc intermetallic compounds and semiconductors. Such a lattice structure distortion may intrinsically related to the observed property variation in nc materials, that deserves further intensive investigations in the future.

#### *Acknowledgements:*

This work is financially supported by National Science Foundation of China (under grants of 59431021, 59625101, and 59771019) and the Chinese Academy of Sciences.

## References

1. Gleiter, H., *Prog. Mater. Sci.*, 1989, **33**, 223.
2. Lu, K., *Mater. Sci. Eng. R*, 1996, **16**, 161.
3. Thomas, G.J., Siegel, R.W. and Eastman, J.A., *Scripta Metall. Mater.*, 1990, **24**, 201.
4. Eastman, J.A., Fitzsimmons, M.R. and Thompson, L.J., *Philos. Mag. B*, 1992, **66**, 667.
5. Lu, K. and Sui, M.L., *J. Mater. Sci. Tech.*, 1993, **9**, 419.
6. Sui, M.L. and Lu, K., *Mater. Sci. Eng. A*, 1994, **197-180**, 541.
7. Eastman, J.A. and Fitzsimmons, M.R., *J. Appl. Phys.*, 1995, **77**, 522.
8. Zhao, Y.H. and Lu, K., to be published work.
9. Zhang, K., Alexandrov, I.V., Valiev, R.Z. and Lu, K., *J. Appl. Phys.*, 1996, **80**, 5617.
10. Lu, L., to be published work.
11. Gaffet, E. and Harmelin, M., *J. Less-Comm. Metals*, 1990, **157**, 201.
12. Gaffet, E., *Mater. Sci. Eng. A*, 1991, **136**, 161.
13. Zhao, Y.H., Zhang, K. and Lu, K., *Phys. Rev. B*, 1997, **56**, 14322.
14. Liu, X.D., Lu, K., Hu, Z.Q. and Ding, B.Z., *Nanostructured Mater.*, 1993, **2**, 581.
15. Gamarnik, M.Ya., *Phys. Stat. Sol. B*, 1991, **168**, 389.
16. Zhao, Y.H. and Lu, K., *Phys. Rev. B*, 1997, **56**, 14330.
17. Siegel, R.W. and Fougere, G.E., *Nanostructured Mater.*, 1995, **6**, 205.
18. Lu, K. and Sui, M.L., *Acta Metall. Mater.*, 1995, **43**, 3325.

TABLE 1

A list of the lattice parameter changes ( $\Delta a = (a - a_0) / a_0$  and  $\Delta c = (c - c_0) / c_0$ ) and the static DWP change ( $\Delta B_s = (B_s - B_{s0}) / B_{s0}$ , where  $a_0$ ,  $c_0$  and  $B_{s0}$  are the equilibrium tabulated values) in various nc samples processed by means of different techniques (UFP = ultrafine powder consolidation,

BM = ball-milling, SPD = severe plastic deformation, ED = electrodeposition, XL = crystallization from amorphous solids).

Sample	$d$ (nm)	Synthesis	Lattice Distortion		Reference
			$\Delta a, \Delta c$	$\Delta B$	
Cr (bcc)	11	UFP	$\Delta a = +0.04\%$	$\Delta B_s = +230\%$	7
Fe (bcc)	8	BM	$\Delta a = +0.09\%$	$\Delta B_s = +110\%$	8
Cu (fcc)	85	SPD	$\Delta a \approx 0$	$\Delta B_s = +100\%$	9
Cu (fcc)	11	BM	$\Delta a = +0.06\%$	---	8
Cu (fcc)	27	ED	$\Delta a = +0.06\%$	---	10
Pd (fcc)	8	UFP	$\Delta a = -0.04\%$	$\Delta B_s = +220\%$	4
Si (diamond)	8	BM	$\Delta a = +0.20\%$	---	11
Ge(diamond)	4	BM	$\Delta a = +0.20\%$	---	12
Se (trigonal)	13	XL	$\Delta a = +0.30\%$ $\Delta c = -0.12\%$	$\Delta B_s = +900\%$	13
Se (trigonal)	14	BM	$\Delta a = +0.15\%$ $\Delta c = -0.01\%$	---	8
Ni <sub>3</sub> P (bct)	7	XL	$\Delta a = +0.21\%$ $\Delta c = -0.13\%$	---	6
Fe <sub>2</sub> B (bct)	23	XL	$\Delta a = +0.20\%$ $\Delta c = -0.23\%$	---	14



Pergamon

NanoStructured Materials, Vol. 12, pp. 563–566, 1999

Elsevier Science Ltd

© 1999 Acta Metallurgica Inc.

Printed in the USA. All rights reserved

0965-9773/99/\$—see front matter

PII S0965-9773(99)00184-1

## NANOSTRUCTURAL CHARACTERIZATION OF SOLID CLUSTERS AND OXIDE BY HREM WITH RESIDUAL INDICES

Takeo Oku\*, Jan-Olov Bovin<sup>1</sup>, Satoru Nakajima<sup>2</sup>, Hiroshi Kubota<sup>3</sup>, Takeshi Ohgami<sup>3</sup>  
and Katsuaki Suganuma

Institute of Scientific and Industrial Research, Osaka University, Mihogaoka 8-1, Ibaraki,  
Osaka 567-0047, Japan

<sup>1</sup>National Center for HREM, Inorganic Chemistry 2, Chemical Center, Lund University,  
P. O. Box 124, S-221 00 Lund, Sweden

<sup>2</sup>Department of Chemistry, Tohoku University, Aramaki, Aoba-ku, Sendai 980-8578, Japan

<sup>3</sup>Department of Electrical Engineering and Computer Science, Kumamoto University,  
Kumamoto 860, Japan

\*e-mail: Oku@sanken.osaka-u.ac.jp

**Abstract** — Although it is difficult to determine the atomic arrangement of boron, carbon, and oxygen in the solid clusters and oxides because of their low atomic number, it is believed that the high-resolution images should have “some” information for disordering, ordering, and doping atomic positions in these materials. In the present work, we obtained and predicted the information for disordering, ordering, and doping atomic positions in  $\text{YB}_{56}$ ,  $\text{HgTlBa}_2\text{CuO}_x$ , and  $\text{N@C}_{60}$  from digital HREM images. Residual indices ( $R_{\text{HREM}} = \sum |I_{\text{obs}} - I_{\text{cal}}| / \sum I_{\text{obs}}$ ) were used for image analysis. Difference images between observed and simulated images were also calculated for structure analysis. The present work indicates that this kind of atomic detection would be very useful for evaluation of local atomic positions in the crystal with light elements such as boron, carbon, nitrogen and oxygen atoms.

©1999 Acta Metallurgica Inc.

## INTRODUCTION

$\text{B}_{12}$ ,  $\text{C}_{60}$ -based solid clusters and Hg-based superconducting oxides are expected to show various structures and properties. The purpose of the present work is to obtain and predict the nanostructural information in  $\text{YB}_{56}$  (1-3),  $\text{HgTlBa}_2\text{CuO}_x$  (4,5), and  $\text{N@C}_{60}$  (6) from digital HREM images. Residual indices ( $R_{\text{HREM}} = \sum |I_{\text{obs}} - I_{\text{cal}}| / \sum I_{\text{obs}}$ ,  $0 \leq R_{\text{HREM}} \leq 1$ ) were used for image analysis (5,7,8). Based on the crystal thickness and defocus value which show the minimum  $R_{\text{HREM}}$  value, absolute difference images between observed and simulated images were calculated. The present work will indicate the effectiveness of the  $R_{\text{HREM}}$  values and difference images for nanostructural characterization of solid clusters and oxides with light elements.

## EXPERIMENTAL PROCEDURES

YB<sub>56</sub> single crystals and HgTlBa<sub>2</sub>CuO<sub>x</sub> samples were prepared by an indirect heating floating-zone method and a solid-state reaction using a sealed quartz tube technique (1,4). Structure analysis of YB<sub>56</sub> was carried out by x-ray diffraction (2). It was assumed that the N@C<sub>60</sub> has the same basic structure of fcc C<sub>60</sub> (9), and that atomic coordinates of carbon are the same as that of RbC<sub>60</sub> (10). It was also assumed that nitrogen atoms exist at the center of C<sub>60</sub> cluster, which was detected by electron paramagnetic resonance (6).

Samples for HREM observations were prepared by dispersing crushed materials on holey carbon grids. HREM observations were performed with a 400 kV electron microscope (JEM-4000EX) having a point-to-point resolution of 0.17 nm. The electron microscope is equipped with a slow-scan CCD camera (Gatan SSC model 694). The area of detection of the CCD camera is 1024 × 1024 pixels with a pixel size of 24 × 24 μm. Negative films were also digitized by a CCD camera. For image processing (Fourier transformation, averaging, and symmetrization) of the observed HREM images, Digital Micrograph, Adobe Photoshop, and Semper software were used. HREM images were calculated by the multi-slice method using the MacTempas software. The cumulative distribution functions were used to get the minimum R<sub>HREM</sub> values (5,7), which have simple form and are very useful for determining crystal thickness and defocus values.

## RESULTS AND DISCUSSION

HREM images and a projected model of one unit cell of YB<sub>56</sub> along the [111] direction are shown in Fig. 1. A processed HREM image of one unit cell is shown in Fig. 1 (a), which was taken by a 400kV TEM and symmetrized by Semper. Figure 1 (b) is a calculated image ( $t = 4.06$  nm,  $\Delta f = -45$  nm) based on the x-ray data, which showed the minimum R<sub>HREM</sub> values of 0.251. Figure 1 (c) is an absolute difference image of Fig. 1 (a) and (b). Yttrium atom positions and non-icosahedral B<sub>80</sub> clusters around the Y-holes show white contrast, which indicates large difference between the observed and calculated image. The super-icosahedral (B<sub>12</sub>)<sub>13</sub> clusters also show dark contrast. This result indicates the atomic arrangements of the Y-holes and non-icosahedral B<sub>80</sub> clusters are disordered.

Figure 2 is (a) HREM and (b) enlarged HREM images of HgTlBa<sub>2</sub>CuO<sub>x</sub>. Darkness or size of black spots corresponding to (Hg, Tl), Ba and Cu positions can be identified to be nearly proportional to their atomic numbers. Although oxygen atoms are not represented as dark spots, information on the oxygen positions should be included in the image. In the (Hg,Tl) layers in Fig. 2 (b), oxygen positions indicated by arrows A show brighter contrast compared to those indicated by arrows B. This HREM image of the HgTlBa<sub>2</sub>CuO<sub>x</sub> shows the existence of separated Hg layers and oxygen vacancies in the double (Hg,Tl) layers, and the structure model for HgTlBa<sub>2</sub>CuO<sub>x</sub> was proposed from the HREM image using residual indices. Image calculations (indicated by an asterisk in Fig. 2 (b),  $t = 1.54$  nm,  $\Delta f = -26$  nm) based on the proposed structure model of HgTlBa<sub>2</sub>CuO<sub>5</sub> agreed well with the observation. The proposed HgTlBa<sub>2</sub>CuO<sub>5</sub> model showed lower R<sub>HREM</sub> values of 0.153 compared to a (Tl<sub>0.5</sub>Hg<sub>0.5</sub>)<sub>2</sub>Ba<sub>2</sub>CuO<sub>6</sub> model (0.177), which indicates the ordering of Hg layers and oxygen vacancies.

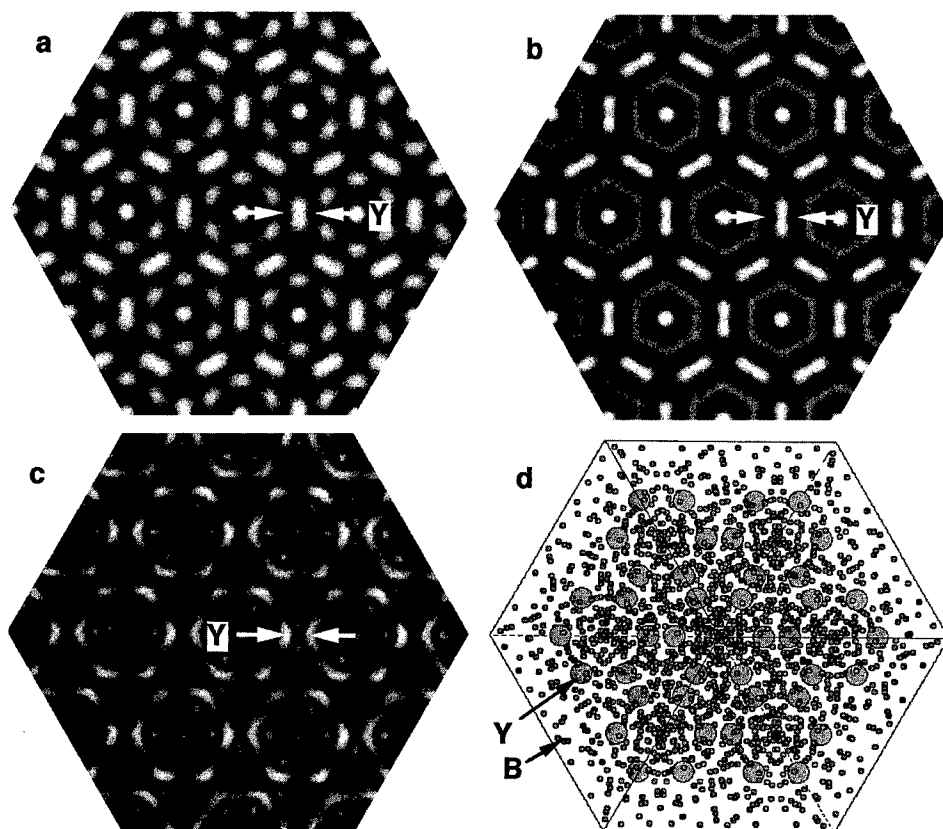


Fig. 1. (a) Experimental processed HREM image, (b) calculated image, (c) difference image of (a) and (b), and (d) structure model of  $\text{YB}_{56}$  projected along the  $[111]$  directions.

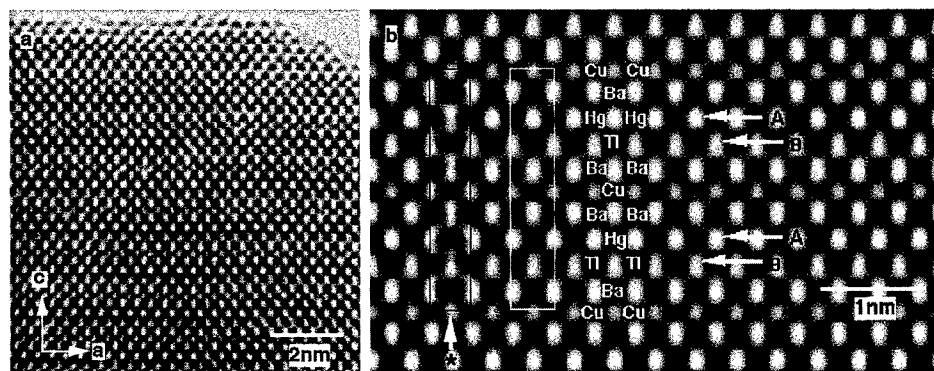


Fig. 2. (a) HREM and (b) enlarged image of  $\text{HgTlBa}_2\text{CuO}_x$  taken along the  $[100]$  direction.

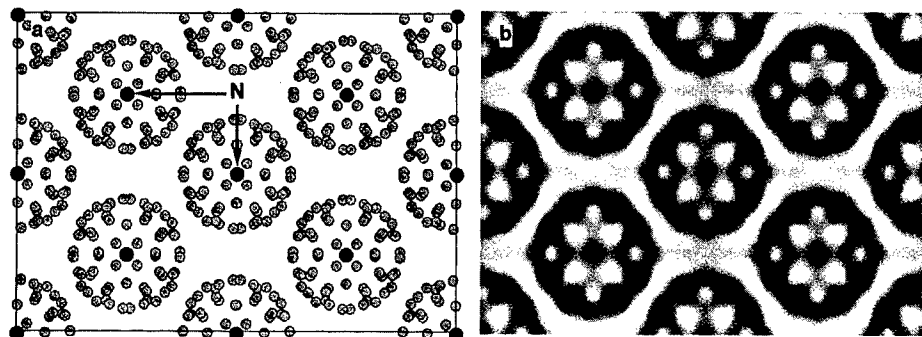


Fig. 3. (a) Projected model and (b) calculated image of  $N@C_{60}$  ( $t = 2.00$  nm,  $\Delta f = -41$  nm).

Possibility of direct detection of doping atoms in  $C_{60}$  solid clusters by HREM was investigated by using  $R_{HREM}$  values and difference images. HREM images of  $C_{60}$  doped with nitrogen atoms were calculated as functions of accelerating voltage of microscope and crystal thickness. A structural model of  $N@C_{60}$  and the simulated HREM image calculated at 1250kV-TEM are shown in Fig. 3 (a) and (b), respectively. The calculated difference image between  $C_{60}$  and  $N@C_{60}$  showed the  $R_{HREM}$  value of  $\sim 0.03$ , which could be detected by digital HREM imaging. The present work indicates that the doping atoms at the inside of  $C_{60}$  solid clusters could be detected by HREM with difference images and  $R_{HREM}$  values.

#### ACKNOWLEDGEMENTS

This work was supported by the Swedish Natural Science Research Council, The Mitsubishi Foundation and the COE project in ISIR, Osaka University.

#### REFERENCES

1. T. Tanaka, Y. Ishizawa, J. Wong, Z. U. Rek, M. Rowen, F. Schäfers and B. R. Muller., *Jpn. J. Appl. Phys. Series*, 1994, **10**, 110.
2. I. Higashi, K. Kobayashi, T. Tanaka, and Y. Ishizawa, *J. Solid State Chem.*, 1997, **133**, 16.
3. T. Oku, A. Carlsson, L. R. Wallenberg, J. -O. Malm, J. -O. Bovin, I. Higashi, T. Tanaka, and Y. Ishizawa, *J. Solid State Chem.*, 1998, **135**, 182.
4. S. Nakajima, T. Oku, K. Nagase, and Y. Syono, *Physica C*, 1996, **262**, 1.
5. T. Oku and S. Nakajima, *J. Mater. Res.*, 1998, **13**, 1136.
6. T. A. Murphy, Th. Pawlik, A. Weidinger, M. Höhne, R. Alcalá, and J. M. Speath, *Phys. Rev. Lett.*, 1996, **77**, 1075.
7. A. R. Smith and L. Eyring, *Ultramicroscopy*, 1982, **8**, 65.
8. D. Shindo, T. Oku, J. Kudoh, and T. Oikawa, *Ultramicroscopy*, 1994, **54**, 221.
9. W. I. F. David, R. M. Ibberson, T. Matsuo, *Proc. Royal Soc. Lond. A*, 1993, **442**, 129.
10. A. R. Kortan, N. Kopylov, S. Glarum, E. M. Gyorgy, A. P. Ramirez, R. M. Fleming, F. A. Thiel and R. C. Haddon, *Nature*, 1992, **355**, 529.



## STRUCTURAL MEASUREMENTS FOR SINGLE-WALL CARBON NANOTUBES BY RAMAN SCATTERING TECHNIQUE

E.D. Obraztsova<sup>1</sup>, J.-M. Bonard<sup>2</sup>, V.L. Kuznetsov<sup>3</sup>, V.I. Zaikovskii<sup>3</sup>, S.M. Pimenov<sup>1</sup>,  
A.S. Pozarov<sup>1</sup>, S.V. Terekhov<sup>1</sup>, V.I. Konov<sup>1</sup>, A.N. Obraztsov<sup>4</sup>, A.P. Volkov<sup>4</sup>

<sup>1</sup> General Physics Institute, RAS, 38 Vavilov street, 117942, Moscow, elobr@kapella.gpi.ru

<sup>2</sup> Institute de Physique Experimentale, EPFL, CH-1015, Lausanne, Switzerland

<sup>3</sup> Boreskov Institute of Catalysis, Lavrentieva 5, 630090, Novosibirsk, Russia

<sup>4</sup> Physics Department of M.V. Lomonosov MSU, 119899, Moscow, Russia

**Abstract** --The single-wall carbon nanotubes grown by different techniques have been investigated by Raman scattering and high resolution transmission electron microscopy (HRTEM). The tube diameter values and the tube distribution over diameter have been estimated from the position and shape of the low-frequency band in the Raman spectrum containing the "breathing" modes. The diameter-dependent enhancement of the Raman signals from the different nanotube fractions occurred not only due to optical resonance with the laser excitation energy, but also due to thermo-induced resonances. The low-field electron emission from the single-wall carbon nanotube material has been measured. The threshold fields were 0.75–2 V/μm, the emission current reached the value 15 mA/cm<sup>2</sup> at fields of 10 V/μm. ©1999 Acta Metallurgica Inc.

### INTRODUCTION

A pure carbon exists in nature in many modifications differing from each other at the "macro"-level. Last few years have shown that this chemical element also gave a birth to a big family of materials having a different geometry at the "nano"-level: *carbon nanotubes*, *nanospheres*, *nanococones*. The Raman scattering appeared to be among the most informative techniques being able to measure the structural parameters of such new materials. Though the Raman scattering doesn't possess a direct high spatial resolution (as HRTEM or STM), a spectrum shape is strongly influenced by the atomic-scale variation of a nano-geometry which dictates the selection rules for the Raman scattering process. This property is the basis of a quick and correct estimation of the average sizes of nanostructures [1].

An additional advantage in case of single-wall carbon nanotubes (SWNT) is a possibility of a diameter-selective resonance enhancement of the Raman signal [2,3]. This phenomenon is a consequence of a discrete character of a diameter-dependent density of electronic states (DOS) for a single-wall carbon nanotube. A successive excitation of resonances for nanotubes with different diameters constituting a real SWNT material allows to estimate correctly the tubes diameters by measuring the frequency of a dominating "breathing" mode in the Raman spectrum.

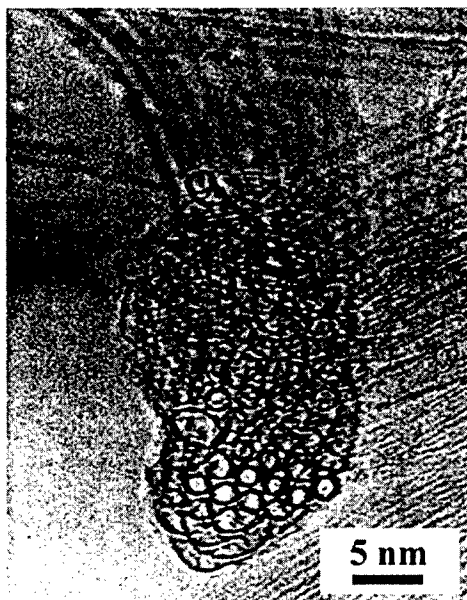


Fig.1. HRTEM image of the rope of single-wall carbon nanotubes.

In this work SWNT produced by laser ablation and arc-discharge techniques (with a variety of conditions) have been analyzed by HRTEM and Raman scattering techniques to characterize quantitatively the structure of the material.

### EXPERIMENTAL

One type of SWNT material was produced by a double-pulse laser ablation technique [4] followed by an efficient purification procedure [5] combining a nitric acid reflux, a centrifugation, a surfactant action and a tangential filtration.

The second type of SWNT was produced by arc discharge under static pressure of helium (600 mBar) between two graphitic electrodes: 20 mm (cathode) and 10 mm (anode) in diameter. A 7 mm diameter hole was drilled in the anode and filled with a graphite-Ni-Y mixture in different proportions. The voltage and current used were 20 V and 90 A correspondingly. The nanotubes were found in the webs rather than in the cathodic deposit.

The HRTEM measurements were performed with JEM 100CX and JEM 4000 Instruments (with lattice resolution 1 nm). The tube diameter values were measured with the calibration on the lattice parameter of Ni catalytic particles being found in the samples.

The Raman measurements were performed with the spectrometer «Jobin-Yvon S-3000». A survive intact of the material surface was controlled by a microscope. The working wavelengths of Ar<sup>+</sup>-laser (in the range 2.41-2.71 eV) were used for spectra excitation.

### RESULTS AND DISCUSSION

HRTEM shows (Fig.1) that the real SWNT material contains mono-shell tubes



with different diameters in the range 1.0-1.5 nm. The tubes are combined into the ropes with cross sections of 10-30 nm (Fig.1).

The Raman scattering (RS) characterizes a surface region of a few microns, integrating the signals from all possible nanotube fractions comprised in the material. The Raman spectrum of a single-wall carbon nanotube has two main peculiarities differing it from the spectrum of a planar graphite: (i) a splitting of TO mode at  $1582\text{ cm}^{-1}$  (being single in a planar graphite); (ii) an appearance of a "breathing" radial  $A_g$  mode in the low-frequency region  $150\text{-}220\text{ cm}^{-1}$ . Its position shows no chirality dependence. Its frequency  $\omega(r)$  is almost inversely proportional to the nanotube radius  $r$  in the range  $3\text{Å} < r < 7\text{Å}$ :

$$\omega(r) = \omega_{(10,10)} \cdot (r_{(10,10)} / r)^{1.0017 \pm 0.0007}, \quad (1)$$

where  $\omega_{(10,10)} = 165\text{ cm}^{-1}$ ,  $r_{(10,10)} = 6.785\text{ Å}$  [6].

In case of an ensemble of different tubes a Raman band containing all corresponding "breathing" modes gives information about the width of the tube distribution over diameter. The diameters of SWNT produced by laser method are ranged from 1.1 nm to 1.5 nm (Fig.2). The distribution of SWNT produced by arc-discharge technique appears to be narrower (1.25-1.50 nm).

In Raman spectra of single-wall carbon nanotubes the signals from fractions with different diameters could be selectively enhanced due to corresponding resonances of the laser excitation energy with the optically allowed transitions in a discrete electronic DOS of a nanotube. In this work we have observed the resonances for nanotubes with different diameters while the laser excitation energy was scanned in the range 2.4-2.7 eV. The energy increasing leads to the enhancement of signals from the smaller tubes showing the higher Raman frequency (Fig.3).

A new interesting phenomenon has been observed in the Raman spectra of SWNT grown by both techniques: a heating of the material in the probing laser spot (without any tuning the laser excitation wavelength) leads to the selective resonant excitation of the additional "breathing" Raman modes corresponding to the tubes of a smaller diameter than those observed at room temperature.

We have studied this phenomenon systematically using the excitation wavelength 514.5 nm (2.41 eV). Initially only the mode at  $184\text{ cm}^{-1}$  dominated in the spectrum. It was ascribed to the tubes with diameter 1.22 nm. The laser power density was varied step-by-step, and the corresponding temperature on the sample surface was estimated from the ratio of Stokes and anti-Stokes components in the SWNT Raman spectrum. While the temperature increased in the range 300-700 K, the new modes at  $193\text{ cm}^{-1}$  (the tube diameter of 1.16 nm) and  $201\text{ cm}^{-1}$  (the tube diameter of 1.11 nm) appeared in the spectrum. Their contributions increased with the temperature. The "breathing" modes contour gradually approached the shape being observed for the higher laser excitation energy - 2.54 eV. Unfortunately we haven't reached a complete coincidence because the material has been ablated at 700 K.

The electronic density of states (DOS) for SWNT may be represented as a set of spikes being mirror symmetrical relative to the Fermi level. The energy separation between symmetrical spikes is inversely proportional to the tube diameter. The calculated difference in the diameters of nanotubes contributed to the Raman signal at the room temperature and at the elevated temperatures is less than 0.1 nm. In this case the corresponding spikes in the

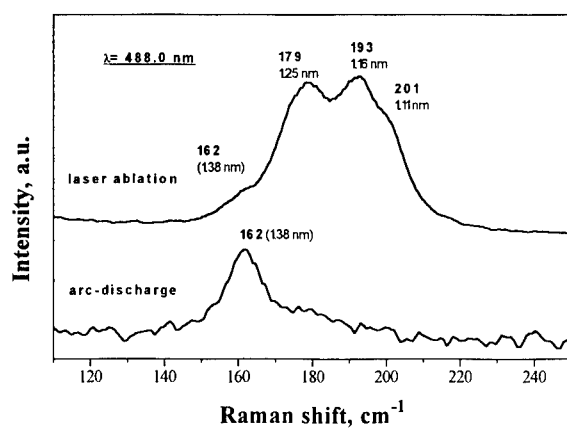


Fig.2. The summary “breathing modes” contour including the contributions from the tubes of different diameter for SWNT materials grown by different techniques

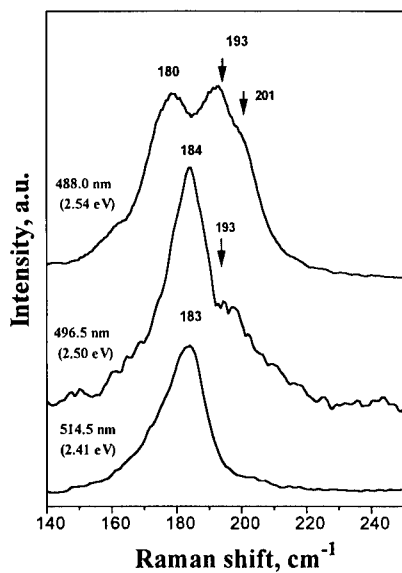


Fig.3. Transformation of the “breathing modes” contour in the Raman spectrum of SWNT induced by changing the laser excitation wavelength.

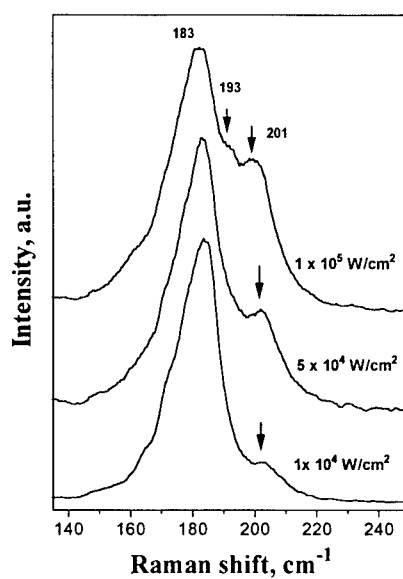


Fig.4. Transformation of the “breathing modes” contour in the Raman spectrum of SWNT due to the sample heating by probing laser beam.

electron DOS are separated by less than 0.1 eV. The thermal excitation energy ( $E=kT$ , where  $k$  is a Boltzman constant,  $T$ - temperature) is enough to cover this difference and to provide (in sum with the energy of an optical excitation) new resonances corresponding to the tubes of a smaller diameter.

The observed phenomenon of *thermo-induced resonances* in Raman spectra of SWNT opens a new possibility for the revealing of all nanotube fractions existing in the material: the selective enhancement of the characteristic modes may be reached either by a variation of the laser excitation energy or by a temperature variation. Moreover this phenomenon allows to estimate indirectly the energy of the spike separation in the electronic DOS of a nanotube of a fixed diameter.

The *field electron emission (FEE)* was studied for SWNT deposited on Cu foil placed near the reaction zone during the arc synthesis process. FEE current ( $I$ ) was measured in the vacuum chamber ( $10^{-6}$  Torr) by using a tungsten plate anode (20 mm in diameter) positioned by a screw translator with an accuracy about 5  $\mu\text{m}$ . The  $I$ - $V$  measurements were performed with the *anode-to-cathode voltage* ( $V$ ) varied in the range 0-1500 V. The protective circuit limited the maximum current by 3.5 mA. The correspondent current density was about 1 mA/cm<sup>2</sup>.

Fig.5 (insert) shows the typical  $I$ - $E$  dependence (where  $E=V/d$  is an average value of electric field between the anode and the SWNT film cathode separated by a distance  $d$ ). The FEE turn-on field is determined as 0.8 V/ $\mu\text{m}$ . The emission current is found to obey the classical FEE Fowler-Nordheim equation [7] for the quantum tunneling over a barrier:

$$I=A(\beta E)^2 \exp(-B\phi^{3/2}/\beta E), \quad (2)$$

where  $I$  is the current density (A/m<sup>2</sup>),  $\phi$  is the barrier height (eV),  $E$  is the electric field (V/m),  $\beta$  is the field enhancement factor,  $A=1.4 \cdot 10^{-2}$ ,  $B=6.8 \cdot 10^9$ . The data give a reasonable fit to Eq.2 for the current densities of  $10^{-9}$  to  $10^{-3}$  A/cm<sup>2</sup> (Fig.5). The slope of the plots gives the effective emission barriers  $\phi=0.012$  eV (in frames of a formal assumption of an ideal plane emitter with a field enhancement factor  $\beta$  of 1). This value for  $\phi$  is too small even in comparison with the graphite work function (5 eV). For  $\phi=5$  eV Eq.2 gives  $\beta$  value of  $10^4$ . It means that for the curvature radii of nanotubes of 1 nm the length of the emitting tips oriented along the electric field should be more than 10  $\mu\text{m}$ . This is in conflict with our HREM data (Fig. 1). They allow to propose the maximal value of  $\beta$  being much smaller than  $10^3$ . This value is confirmed by our experiments [8] and by published data [9]. The calculated  $\phi$  value for  $\beta=1000$  (Eq.2) is much smaller than 1 eV. This is in agreement with the mechanism of FEE in carbonaceous materials supposing an essential decrease of the work function at the emitter surface [8]. The measured FEE for SWNT is promising for the applications of this material in a vacuum electronics.

### CONCLUSION

The Raman and HRTEM measurements have been performed for SWNT produced by *laser ablation* and *arc discharge* techniques. A few nanotube fractions with the diameters in the range 1.1-1.5 nm have been revealed in the material via the excitation of the diameter-selective optical and thermo-induced resonances. The effective field electron emission from SWNT film has been registered.

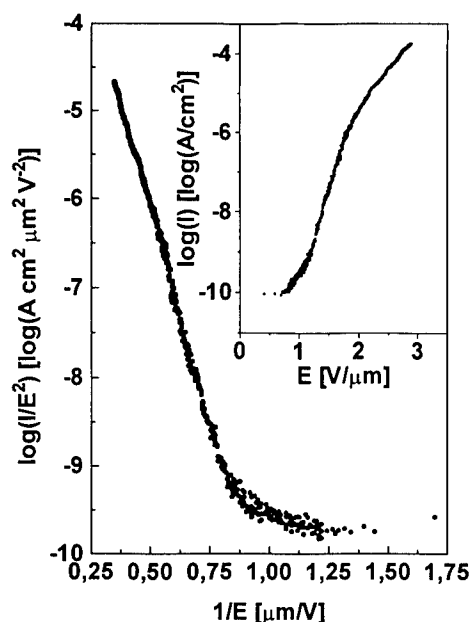


Fig.5. A typical  $I$ - $E$  dependence  
(in  $F$ - $N$  and  $\log(I)$ - $E$  (insert) coordinates)  
measured at 150  $\mu\text{m}$  -distance between cathode and anode  
for the electron emission from SWNT thin film deposited  
onto Cu foil.

## REFERENCES

1. E.D. Obratsova, V.L. Kuznetsov, E.N. Loubnin et al., *NATO ARW series "Nanoparticles in solids and solutions"*, ed. by J. Fendler and I. Dekany, Kluwer, 1996, v.18, p.485.
2. M.S. Dresselhaus, G. Dresselhaus, P.S. Eklund, *"Science of Fullerenes and Carbon Nanotubes"*, Academic Press Inc., San Diego, 1996.
3. A.M. Rao, E. Richter, S. Bandow et al., *Science* **275** (1997) 187.
4. A. Thess, R. Lee, P. Nikolaev et al., *Science*, **273** (1996) 483.
5. A.G. Rinzier, J. Lin, H. Dai et al., *Science* **269** (1995) 1550.
6. R. Saito, T. Takeya, T. Kimura et al., *Phys. Rev. Lett.*, **57** (1998) 4145.
7. R.H. Fowler and L. Nordheim, *Proc. R. Soc. London, Ser.A* **119** (1928) 173.
8. A.N. Obratsov, A.P. Volkov, I.Yu. Pavlovsky, *JETP Lett.* **68** (1998) 55.
9. W. A. de Heer, A. Châtelain, D. Ugarte, *Science* **270** (1995) 1179.

## ACKNOWLEDGMENT

The work is supported in part by the grant N97-02-17282 of the Russian Foundation for Fundamental Research, by the grant NK1129 of the Russian Federal Program "Integration" and by IP Project (No. 7IPO51215) of Swiss National Science Foundation. The authors are grateful to R.E. Smalley and A.G. Rinzier for SWNT material produced by laser ablation method.



## MICROSTRUCTURE CHANGE IN $\text{Co}_{46}\text{Al}_{19}\text{O}_{35}$ GRANULAR THIN FILMS BY ANNEALING

M. Ohnuma<sup>1</sup>, K. Hono<sup>1</sup>, H. Onodera<sup>1</sup>, S. Mitani<sup>2</sup>, J.G. Ha<sup>2</sup> and H. Fujimori<sup>2</sup>

<sup>1</sup>National Research Institute for Metals, 1-2-1 Sengen, Tsukuba 305-0047, Japan

<sup>2</sup>Institute for Materials Research, Tohoku University, Sendai 980-8577, Japan

**Abstract** - We have studied changes in microstructures of  $\text{Co}_{46}\text{Al}_{19}\text{O}_{35}$  granular thin films on annealing by transmission electron microscopy (TEM) and small angle x-ray scattering (SAXS). The as-deposited film exhibits a large magnetoresistance (MR) ratio of approximately 9% at room temperature. The films consist of nearly spherical cobalt particles of a few nanometer in diameter embedded in an amorphous aluminum oxide matrix. Although the MR ratio decreases during annealing at 300°C, no visible changes in the microstructure are evident. However, the interparticle distance of the particles estimated from the peak position in the SAXS data shows apparent increase after 10 min annealing. Upon further annealing, the interparticle distance does not change noticeably, but the MR ratio continues to decrease. Electron diffraction results show that a considerable amount of cobalt oxide appears during long term annealing. Thus the degradation of the MR ratio after long term annealing is attributed to oxidation of the Co particles. ©1999 Acta Metallurgica Inc.

### INTRODUCTION

Co-Al-O granular thin films are composed of nanoscale Co particles embedded in an insulating amorphous oxide. Super-paramagnetic Co-Al-O granular films were reported to exhibit giant magnetoresistance (GMR) in spite of their high electrical resistivity [1]. This unique character is attributed to the fact that conduction occurs by electron tunneling and its probability depends on the orientation of the spins in the neighboring metallic particles. The tunneling probability in an applied magnetic field is higher than that in a zero magnetic field because electrons can tunnel only from a given spin state to the same spin state [2]. Thus the existence of super-paramagnetic state is essential to exhibit GMR behavior. In order to achieve the super-paramagnetic state, the size of the metallic grains must be of nanoscale dimension, and each particle has to be separated so that they are not coupled by the exchange interaction. On the other hand, smaller interparticle distance is favorable for tunneling because the tunneling probability decreases with an increasing tunneling path length. Thus the magnitude of the tunneling type GMR depends strongly on the microstructure. In fact we have observed a close correlation between the MR ratio and the interparticle distance in  $(\text{Co}_{72}\text{Al}_{28})_{1-x}\text{O}_x$  films, where the maximum MR ratio is obtained in the film with the minimum interparticle distance as determined by SAXS measurement [3]. Recently, Ha et al. [4] reported that MR ratio of the  $\text{Co}_{46}\text{Al}_{19}\text{O}_{35}$  film decreases by annealing at 300°C and they attributed this decrease to the

formation of larger magnetic particles. However, it has not been studied whether or not the formation of the larger magnetic particles is accompanied by the change in the film microstructure. Thus, this study aimed to investigate changes in the microstructure of the  $\text{Co}_{46}\text{Al}_{19}\text{O}_{35}$  granular films accompanying annealing, and to correlate them with the magnetic property changes. For evaluating the microstructure changes, we have employed transmission electron microscopy (TEM) and small angle x-ray scattering (SAXS).

### EXPERIMENTAL

$\text{Co}_{46}\text{Al}_{19}\text{O}_{35}$  granular thin films were prepared on glass substrates by Ar+O<sub>2</sub> reactive rf sputtering using a  $\text{Co}_{72}\text{Al}_{28}$  alloy target. The detailed specimen preparation procedure was described elsewhere [1,5]. Small-angle x-ray scattering (SAXS) was measured from as-prepared and annealed  $\text{Co}_{46}\text{Al}_{19}\text{O}_{35}$  granular thin films by using a conventional x-ray generator with a Mo target and a pinhole collimation. Samples for TEM observations were thinned from the substrate side by argon ion milling initially, and subsequently thinned from both sides for removing surface contaminates. HREM observations were performed using a JEOL-4000EX electron microscope. To obtain the diffraction profiles qualitatively selected area diffraction (SAED) patterns were recorded on imaging plates (IP) and digitized radially [6].

### RESULTS AND DISCUSSION

The magnetoresistance (MR) ratio is defined by  $(\rho_0 - \rho)/\rho_0$ , where  $\rho_0$  and  $\rho$  are resistivities measured in a zero magnetic field and in a magnetic field of 12 kOe, respectively.

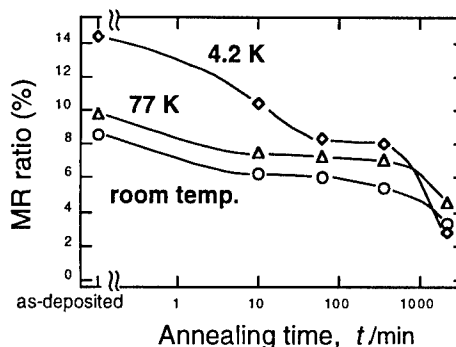


Fig.1 MR ratio ( $\Delta\rho/\rho_0$ ) at different temperatures as functions of the annealing time at 300°C.

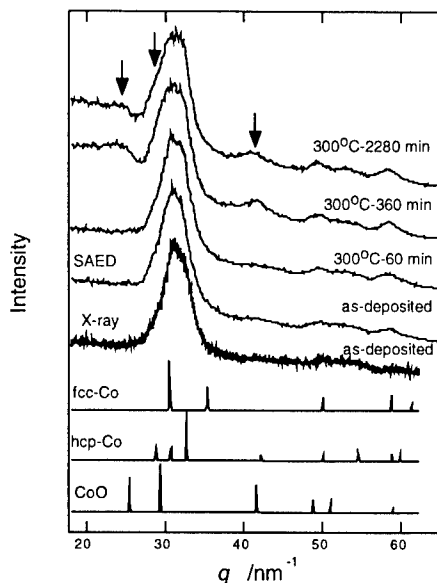


Fig.2 SAED profiles for as-sputtered and annealed samples at 300°C for various times in the upper part of the figure. An x-ray diffraction profile for the as-deposited sample is shown in the middle. The lower three profiles are simulated profiles for fcc-Co, hcp-Co and CoO phases. Arrows correspond to the planes of {111}, {200} and {220} of the CoO phase (NaCl type).

The values of the MR ratio measured at three different temperatures are plotted in Fig.1 as functions of the annealing time at 300°C. The MR ratio measured at all temperatures decreases after annealing. A large decrease in the MR ratio occurs during the initial 10 min of annealing. The value measured at 4.2K continues to decrease up to 60 min. After these initial rapid decreases in the MR ratio, the MR ratio as a function of annealing time shows a plateau, then decreases again after 360 min. Thus the degradation of the MR ratio occurs in two steps by

annealing. First, an initial rapid decrease and a later gradual degradation.

Figure 2 shows SAED profiles for as-deposited and annealed samples at 300°C for various times. For comparison, x-ray diffraction profile of the as-deposited specimen is shown as well. The profiles obtained by electron diffraction using imaging plates show good matching with the x-ray profile. The diffraction profiles of the as-sputtered and the specimen annealed for 60 min are almost identical. They exhibit one prominent diffuse peak corresponding to {111} and {200} for the fcc-Co and {110}, {002}, {101} for the hcp-Co. Additional diffuse peaks due to the appearance of the CoO phase (NaCl type) can be observed for the films annealed for 360 and 2280 min as indicated by the arrowheads. The appearance of the CoO phase would likely contribute to the decrease in the MR ratio after long term annealing.

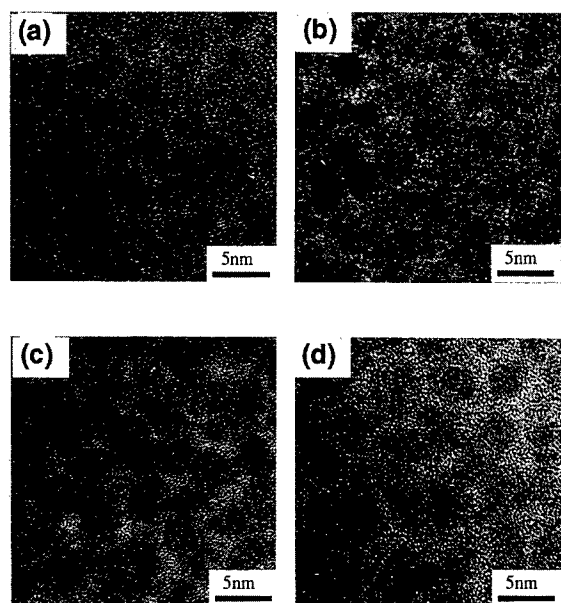


Fig.3 shows HRTEM micrographs of  $\text{Co}_{46}\text{Al}_{19}\text{O}_{35}$  thin films annealed at 300°C for (a) 0 min (as-deposited), (b) 60 min, (c) 360 min and (d) 2280 min.

Figure 3 shows HRTEM micrographs of  $\text{Co}_{46}\text{Al}_{19}\text{O}_{35}$  thin films annealed for various periods of time at 300°C. They have typical granular microstructures, where darkly imaging metallic particles are completely surrounded by brightly imaging amorphous oxide. As the particles include many stacking faults, they exhibit both fcc and hcp features in the HREM image [3] and the diffraction profiles shown in Fig.2. We previously reported that the Co particles do not contain any aluminum in spite of their large solubility [3]. Thus most of the aluminum is thought to be included in the intergranular amorphous oxide phase. Although annealing does not cause any obvious difference in the microstructure, the lattice fringes of the Co particles become unclear with the appearance of the CoO phase as shown in Fig.3(c) and (d). This may be caused by distortions induced by oxidation of the Co particles. However most of the particles are still surrounded by amorphous aluminum oxide and the features of the global distribution of the particles is almost the same for all samples. Except for the difference inside the particles annealed for longer than 60 min, the microstructural difference is very small. In

particular, the microstructural features and the constituent phases do not show any difference between the as-deposited specimen and the one annealed for 60 min. Nevertheless a large decrease in MR ratio occurs during the initial 10 min of annealing as shown in Fig.1.

SAXS profiles of the samples annealed for various annealing times are shown in Fig.4. The peaks due to the interparticle interference can be observed clearly. The interparticle distance is estimated from these peaks by Bragg equation and plotted in Fig.5. It becomes larger with increasing annealing time up to 60 min, then it nearly saturates after 60 min. Hence we can conclude that smaller interparticle distance is favorable for larger MR value. This result agrees with our previous result that the maximum MR value can be obtained in the sample with the minimum interparticle distance in  $(\text{Co}_{72}\text{Al}_{28})_{1-x}\text{O}_x$  films ( $x=20\sim50$  at%) [3].

## CONCLUSIONS

Microstructures of as-deposited and annealed  $\text{Co}_{46}\text{Al}_{19}\text{O}_{35}$  granular thin films have been investigated by high resolution transmission electron microscopy, electron diffraction and small angle x-ray scattering. The MR ratio decreases in two steps during annealing. An initial rapid decrease in the MR ratio is attributed to an increase in the interparticle distance during annealing. The gradual decrease in the MR ratio after 360 min annealing is due to the formation of CoO phase.

## REFERENCE

- [1] H.Fujimori, S.Mitani, and S.Ohnuma, Mater. Sci. Eng. B **31**, 219(1995)
- [2] H.Itoh, J.Inoue and S.Maekawa, Phys. Rev.B **17**, 5809(1993)
- [3] M.Ohnuma, K.Hono, E.Abe, H.Onodera, S.Mitani and H.Fujimori, J.Appl.Phys. **82**, 5646(1997)
- [4] J.G.Ha, S.Mitani, K.Tkanashi and H.Fujimori, J. Magn. Magn. Mater , to be published
- [5] S.Mitani, H.Fujimori, and S.Ohnuma, J. Magn. Magn. Mater. **165**, 141(1997)
- [6] M.Mori, T.Oikawa, J.Miyahara, and Y. Harada, J. Electron Microscopy, **39**, 433 (1990).

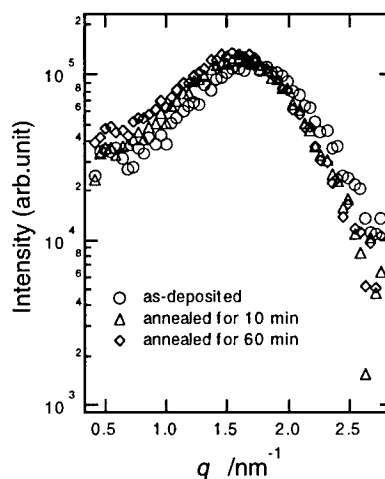


Fig.4 SAXS profiles of the samples annealed for 0 (as-deposited), 10 and 60 min . The peaks are attributed to interparticle interference.

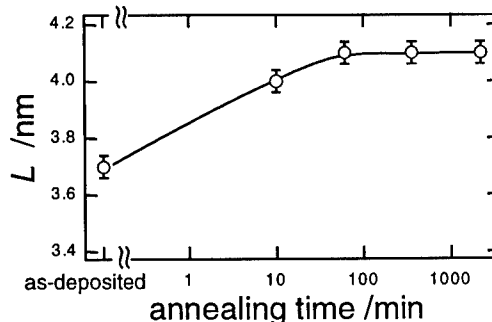


Fig.5 Interparticle distance  $L$  as a function of annealing time.  $L$  is estimated from the equation,  $L = 2\pi/q_{\text{max}}$  where  $q_{\text{max}}$  is the peak position.





## X-RAY ABSORPTION STUDY IN NANOCRYSTALLINE Fe, Co, Ni AND Cu METALLIC POWDERS

L. Y. Jang<sup>1</sup>, Y. D. Yao<sup>2</sup> and Y. Y. Chen<sup>2</sup>

<sup>1</sup> Synchrotron Radiation Research Center, Hsinchu 300, Taiwan

<sup>2</sup> Institute of Physics, Academia Sinica, Taipei 115, Taiwan

**Abstract** - The X-ray absorption was investigated for nanocrystalline, bulk, and oxides of Fe, Co, Ni, and Cu. From the k edge spectrum measurements, we have found that the band lengths in both nanocrystalline and bulk metallic powders we studied are roughly the same. However, the coordination number in nanocrystalline samples for Fe and Co is 8.6 and 7.4 respectively, which is a little bit larger than that of bulk samples; and it is 11.7 and 11.2 for Ni and Cu, which is a little bit smaller than that of bulk samples. Difference between their crystal structure is used to explain our experimental results. The mean-square disorder factor of nanocrystalline samples is always larger than that of the bulk samples. This indicates that both ordered and disordered crystalline phases may exist in nanocrystalline metallic powders. ©1999 Acta Metallurgica Inc.

### INTRODUCTION

Nanocrystalline (NC) materials are single- or poly- crystalline materials with grain sizes roughly below 100 nm. This means NC materials contain a higher volume percentage of the grain or interphase boundaries. It is expected that the structure of grain boundaries plays an important role in determining and controlling the physical properties of NC materials. X-ray absorption fine structure (XAFS) measurements can provide useful information on the short-range-order structure, thus is well suited for investigating the local environment around the constituent atoms in NC materials. In recent years, the study of XAFS spectra of nanocrystalline metallic materials have been gradually increased [1-7]. In the present study, the k-edge spectra is employed to investigate the local environment surrounding of the NC metallic atoms in Fe, Co, Ni and Cu.

### EXPERIMENTAL

The nanocrystalline Fe, Co, Ni, and Cu samples were prepared from commercially available high purity fine particles with particle sizes of about 20 nm for Fe, Co, and Ni, and about 50 nm for Cu, which were prepared by the evaporation technique and bought from Vacuum Metallurgical Co., Japan. The X-ray absorption fine structure (XAFS), which includes extended X-ray absorption fine structure (EXAFS) and near-edge absorption fine structure (XANES), measurements were performed at Synchrotron Radiation Research Center

(SRRC), Hsinchu, Taiwan. Data were obtained by measuring the transmission k-edge absorption spectra through layers of powders spread on Scotch tapes. A high-order multiple-scattering approach method [8-10] was used for the calculation of XAFS spectra.

## RESULTS AND DISCUSSION

The k-edge XANES spectra for NC Fe, Cu, Ni and Co with their oxides and bulk materials are shown in Figs. 1(a) to 1(d), respectively. All the materials were prepared in powder forms. There are three oxides for Fe (i.e. FeO, Fe<sub>3</sub>O<sub>4</sub> and Fe<sub>2</sub>O<sub>3</sub>), two oxides for Cu (i.e. Cu<sub>2</sub>O and CuO), one oxide for Ni (NiO), and two oxides for Co (i.e. CoO and Co<sub>3</sub>O<sub>4</sub>). The energy range studied is from 7100 to 7180 eV for Fe system, from 8970 to 9010 eV for Cu system, from 8320 to 8360 eV for Ni system, and from 7700 to 7760 eV for Co system.

In general, the curves for nanocrystalline powders are located between the curves of bulk material and oxides. The Fourier transform of the k-edge EXAFS spectra ( $k^3$  - weighted) for all the samples were used for calculation of the XAFS spectra. The calculated coordination number of nanocrystalline Fe and Co is 8.6 and 7.4, respectively, which is a little bit larger than that of bulk samples; and it is 11.7 and 11.2 for Ni and Cu, which is a little bit smaller than that of bulk samples. This is explained due to their different crystal structure. We know that both Ni and Cu are F.C.C. structure with a theoretical packing fraction of 0.740, and Fe is B.C.C. structure, and Co is H.C.P. structure both with a smaller theoretical packing fraction than that of F.C.C. structure. The order factor is variable which is dependent on the historical conditions and the annealing condition etc. of the samples. As an example, for annealed NC Ni samples, a quite large peak near 2.6 Å (Ni-O bond) for nanocrystalline Ni was observed [11], this tells us that the surface oxidation is manifest. This was confirmed by the magnetic exchange anisotropy effect studies between the Ni core and the surface NiO layers of the nanocrystalline Ni. For electronic configuration, also for example, considering the nanocrystalline Ni samples after annealing between 300 and 900 °C, their ordering factors and coordination numbers slowly approach the bulk value; however, according to their absorption curves, the electronic configuration remains the same.

The mean-square disorder factor of nanocrystalline samples is always larger than that of the bulk samples. This means that the ordering factor is significantly reduced in nanocrystalline materials. For example, the mean square disorder factor for nanocrystalline Fe, Cu, and Co samples is  $0.0064 \pm 0.0008$ ,  $0.0083 \pm 0.0005$ , and  $0.0117 \pm 0.0025$ , respectively; they are slightly larger than the values of  $0.0044 \pm 0.0003$ ,  $0.0078 \pm 0.0004$ , and  $0.0068 \pm 0.0005$  for bulk Fe, Cu, and Co, respectively.

EXAFS spectra contain important information on their near neighbor configurations. Changes in the radial distribution functions around the atoms studied are reflected in the Fourier transform. As an example, the Fourier transform of the k-edge EXAFS spectra ( $k^3$  - weighted) of nanocrystalline and bulk Co and Cu samples is plotted in Figs. 2(a) and 2(b), respectively. It shows that the bond lengths in both nanocrystalline and bulk samples are roughly the same. The mean-square disorder factor about the average distance can be calculated from these curves, and it shows that the mean-square disorder factor of nanocrystalline samples is always larger than that of the bulk samples.

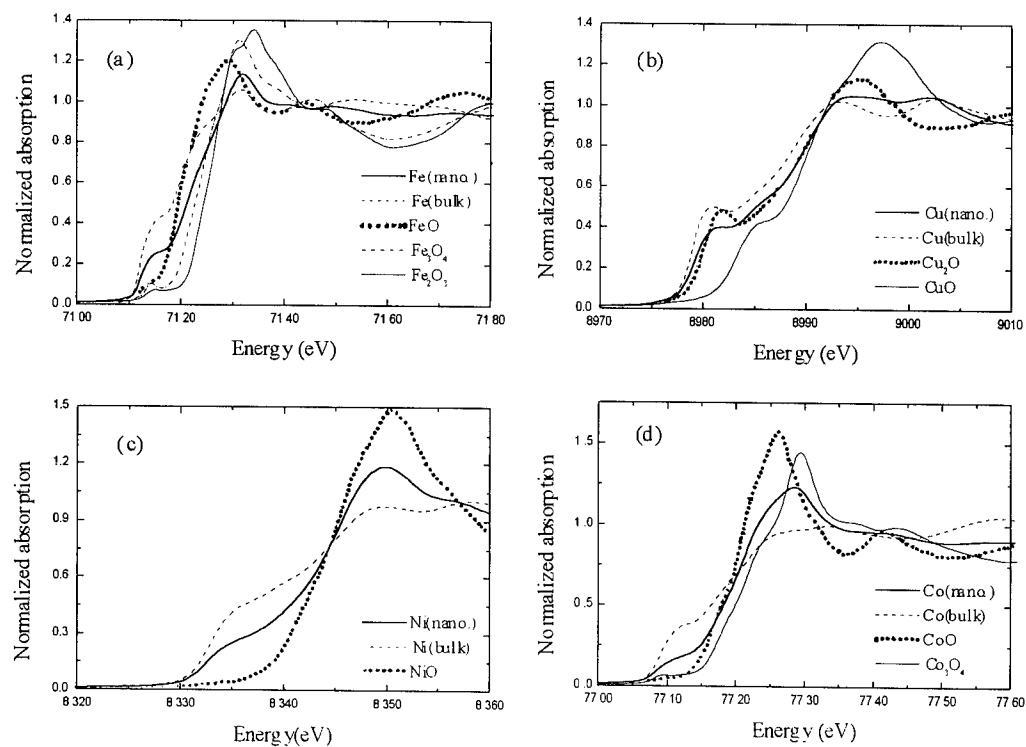


Figure 1 Normalized absorption spectra of NC Fe (Fig. 1a), Cu (Fig. 1b), Ni (Fig. 1c), and Co (Fig. 1d) compared with their oxides and bulk materials.

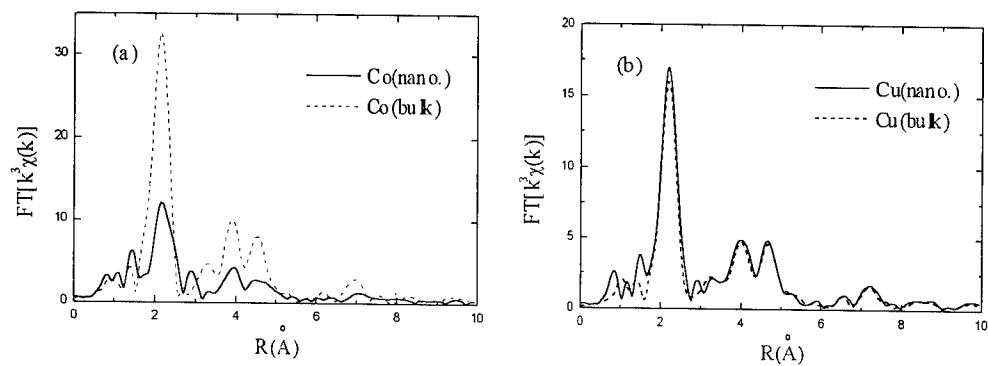


Figure 2 The Fourier transform of the k-edge EXAFS spectra of nanocrystalline and bulk (a) Co and (b) Cu samples.

### CONCLUSION

In conclusion, our measurements of the k-edge spectrum of nanocrystalline, bulk, and oxides for Fe, Cu, Ni, and Co show that the bond lengths in both nanocrystalline and bulk metallic powders we studied are roughly the same. However, the coordination number in nanocrystalline samples for Fe and Co is 8.6 and 7.4, respectively, which is a little bit larger than that of bulk samples; and it is 11.7 and 11.2 for Ni and Cu, which is a little bit smaller than that of bulk samples. Difference between their crystal structure is used to explain our experimental results. The mean-square disorder factor of nanocrystalline samples is always larger than that of the bulk samples. This indicates that both ordered and disordered crystalline phases may exist in nanocrystalline metallic powders.

### ACKNOWLEDGMENTS

We would like to thank the National Science Council, ROC for financial support through Contract Number NSC88-2112-M-001-038.

### REFERENCES

1. Haubold, T., Krauss W. and Gleiter H., *Philos. Magn. Lett.*, 1991, **63**, 245.
2. Cicco A. D., Berrettoni M., Stizza S., Bonetti E. and Cocco G., *Phys. Rev. B*, 1994, **50**, 12386.
3. Zubavichus Y. V., Slovokhotov Y. L., Kvacheva L. D., Novikov Y. N., *physica B*, 1995, **208**, 549.
4. Babanov Y. A., Golovshchikova I. V., Boscherini F., Haubold T. and Mobilio S., *physica B*, 1995, **208**, 140.
5. Schilling P. J., He J. H., Cheng J. and Ma E., *Appl. Phys. Lett.*, 1996, **68**, 767.
6. Hwu Y., Yao Y. D., Cheng N. F., Tung C. Y. and Lin H. M., *NanoStruc. Mater.*, 1997, **9**, 355.
7. Panfilis S. D., d'Acapito F., Haas V., Konrad H., Weissmüller J. and Boscherini F., *J. Phys. IV France*, 1997, **7**, C2-979.
8. Rehr J. J., Mustre de Leon J., Zabinsky S. I. And Albers R. C., *J. Am. Chem. Soc.*, 1991, **113**, 5135.
9. Zabinsky S. I., Rehr J. J., Ankudinov A., Albers R. C. and Eller M. N., *Phys. Rev. B*, 1995, **52**, 2995.
10. Rehr J. J., Albers R. C. and Zabinsky S. I., *Phys. Rev. Lett.*, 1992, **69**, 3397.
11. Jang L. Y., Yao Y. D., Chen Y. Y. and Hwu Y., *NanoStruc. Mater.*, 1997, **9**, 531.



Pergamon

NanoStructured Materials, Vol. 12, pp. 581-584, 1999

Elsevier Science Ltd

© 1999 Acta Metallurgica Inc.

Printed in the USA. All rights reserved

0965-9773/99/\$-see front matter

PII S0965-9773(99)00188-9

# STRUCTURAL AND MAGNETIC INFORMATION ABOUT A NANOSTRUCTURED FERROMAGNETIC FeCuNbB ALLOY BY NOVEL MODEL INDEPENDENT EVALUATION OF MÖSSBAUER SPECTRA

O. Hupe, H. Bremers, J. Hesse, A. M. Afanas'ev<sup>2</sup> and M. A. Chuev<sup>2</sup>

Institut für Metallphysik und Nukleare Festkörperphysik

Technische Universität, Mendelssohnstr.3, 38106 Braunschweig

<sup>2</sup>Institute of Physics and Technology, Academy of Sciences of Russia

Krasikov Street 25a, 117218 Moscow

**Abstract** -- *A novel method for analysing complex  $^{57}\text{Fe}$  Mössbauer spectra was successfully applied to nanostructured  $\text{Fe}_{79}\text{Cu}_1\text{Nb}_7\text{B}_{13}$ . This method allows to find a model with the largest meaningful number of lines, which is given by the criteria that all parameters should be well defined. The model results in information about the iron nanograins, the amorphous residual phase and the so-called interface zone.*

©1999 Acta Metallurgica Inc.

Recently, a new method for analysis of complex Mössbauer spectra has been developed, which provides spectral models with the maximum possible number of lines and quantitative representation of the spectra with well-defined average values and dispersions of the parameters derived (1). In this method the spectral model is not prescribed in advance, but is derived directly in the course of fitting the spectrum. The number of lines appears to be an adjustable parameter. One of the basic concepts of the method is the "densest possible" solution (DPS) which -at given source parameters- contains the maximum possible number of lines with parameters being well-defined, while the  $\chi^2$ -parameter of mean-square fitting is very close to unity. In some special cases, the DPS can be regarded as the final result of analysis (1) but, in general, the discrete forms found for the spectra can only approximate the real spectra, in which continuous line distributions may exist along with the discrete lines. As a rule, the shape of these distributions is unknown and must be analysed separately, but the most popular used shape is a Gaussian distribution. The simplest way to test the presence of continuous distributions is to combine two closely spaced lines into a single line of a particular shape (e.g., Voigt profile) whose width are additional parameters. If  $\chi^2$  decreases as a result of this adjustment, the assumption that there is a continuous distribution is confirmed. The ideas mentioned above are realized within the computer program DISCOVER. At the

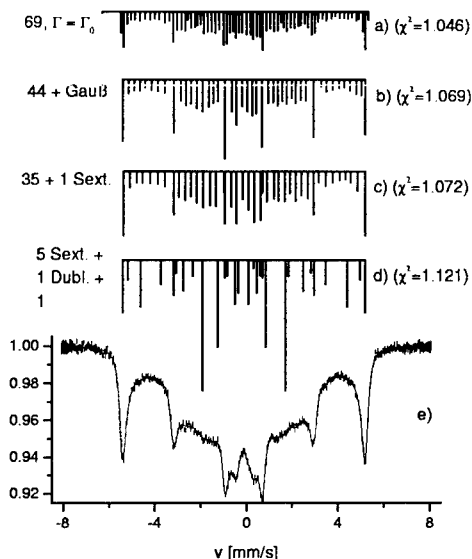


Figure 1: Intermediate stages (a-d) in the developing of the model. The fit of the models is shown in e).

first stage of analysis the DPS for a given spectrum is automatically found by DISCOVER. An example of such a solution for the Mössbauer spectrum of  $\text{Fe}_{79}\text{Cu}_1\text{Nb}_7\text{B}_{13}$  taken at  $T=297$  K is presented in Fig.1,a (DPS with 69 single lines with natural line width). It is clear that in this case -in spite of very good description of the spectrum ( $\chi^2 = 1.069$ )- all the lines in this model are hardly possible to be interpreted which is quite natural for the sample where a distribution of parameters only can be expected. Therefore at the next stage of analysis we assume a variable Gaussian width-broadening of some lines (as a rule, the more intensive ones). Broadening of these lines during the fitting usually reduces the total number of lines (see Fig.1,b: 44 lines with Gaussian broadening of the six most intensive lines). Such a description is considered to be adequate when  $\chi^2$  decreases or at least increases not too much. It is natural to suppose that the distributions observed at the previous stage of fitting describe first of all distributions of the hyperfine fields in the ferromagnetic sample. That is why, as a next step of analysis, an extraction of magnetic sextets of lines is to be performed in order to get real physical information. Such a step-by-step procedure results in describing the spectrum within a model with a number of sextets (with different line width) and some single lines which can not be bound into a sextet (Fig.1,c: 35 single lines and a sextet of Gaussian broadened lines). These not bounded single lines may represent either any real sites of Mössbauer atoms in the sample or an imperfectness of the model in the description of real distributions by

the set of Gaussian lines. Generally speaking, such lines should be kept in the model if their removal highly increases  $\chi^2$ . The credibility of the finally derived model has to be checked by collecting and fitting further spectra i.e. by variation of the temperature.

The melt-spun amorphous ribbons (about 19  $\mu\text{m}$  thick and 15 mm) were produced by the Vacuumschmelze GmbH Hanau, Germany. Annealing took place at 475° for 1 h in a home made furnace under He-atmosphere. Investigations with electron microscopy showed that the sample consists of  $\alpha$ -Fe-nanograins (about 4 nm in diameter), embedded in an amorphous remainder. The temperature for the Mössbauer measurements varied in the range of 300 to 740 K. Room-temperature Mössbauer spectra have been recorded again after those at elevated temperatures to check the intactness of the initial state. Figure 2 shows (left) some measured spectra of  $\text{Fe}_{79}\text{Cu}_1\text{Nb}_7\text{B}_{13}$ , together with their corresponding hyperfine field distributions (right). While the dotted lines represent the mean-square deviations from the mean value, the fraction of the magnetically split components in the total spectral areas is given by the numbers below the temperatures of measurement. The final model which was achieved as a result by using DISCOVER is shown in Fig.1,d. It consists of 4 sextets at temperatures below the Curie temperature of the amorphous phase (AM I:  $T_c \approx 410$  K in Fig.3, abbreviations in accordance to (2,3)). Above these temperatures, the AM I will be described by a single line and a quadrupole.

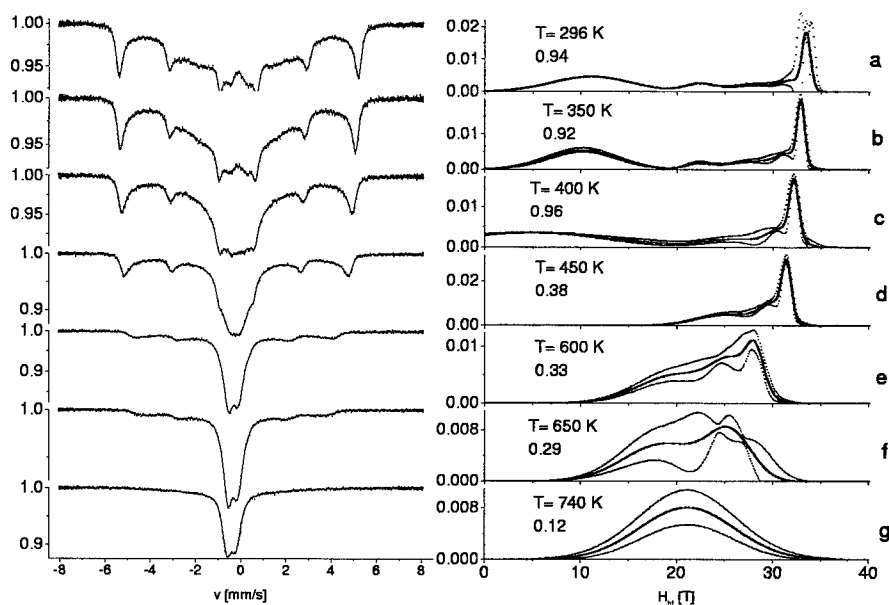


Figure 2: Spectra and corresponding hyperfine field distributions of  $\text{Fe}_{79}\text{Cu}_1\text{Nb}_7\text{B}_{13}$ .

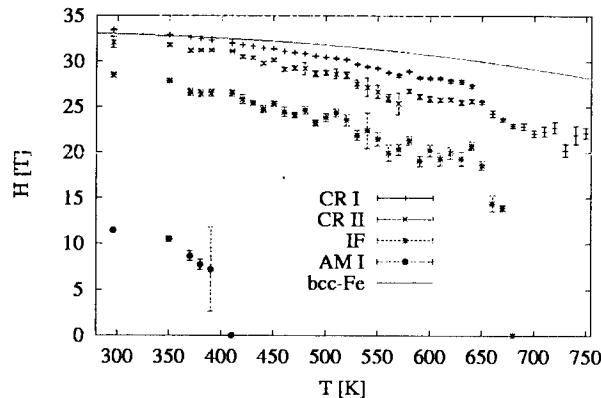


Figure 3: Mean values of the derived hyperfine fields for  $\text{Fe}_{79}\text{Cu}_1\text{Nb}_7\text{B}_{13}$ .

These parameters can not be presented here because of the limited space. The sharp lines of the spectra can be associated with the crystalline (CR) iron nanograins (CR I, values about 33 T at RT). The broadening of these sharp lines with increasing temperature (also to be seen in the increasing width of the hyperfine field distribution) can be explained by a thermal fluctuation of the particles' magnetization. In Fig.3 the mean values for the hyperfine fields are plotted vs. temperature. The curve for bcc-Fe indicates the values measured for a foil of pure iron. It is obvious that the decrease of the hyperfine field for CR I is much stronger than for the foil-iron. The interface (IF) is magnetically coupled on the nanocrystalline iron (CR I) and not on the amorphous phase (AM I), otherwise there had to be a kink in the curve at the Curie temperature of AM I.  $T_c$  of AM I is about 410 K. CR II can be interpreted as nano iron grains with impurities or perhaps as iron atoms on the surface of nanograins which would belong to the interface (2,3), too. The separation into CR I and CR II is no more possible after crossing 650 K (reversible process). The hyperfinefield of IF disappears at about 680 K.

In conclusion, the sample consists of nano- $\alpha$ -Fe-grains with about 4 nm in diameter, which are embedded in an amorphous remainder. The fractions of the phases manifested in the spectra can be determined from their relative areas ( $\text{CR} \approx 25\%$ ,  $\text{IF} \approx 16\%$ ,  $\text{AM} \approx 59\%$ ). The evidence for an interface phase, proposed in (2,3) is confirmed through our novel evaluation procedure.

**Acknowledgements** We are grateful to the "Internationales Büro des BMBF", Bonn and the Russian Ministry of Science, Moscow, for supporting our collaboration.

#### References

1. A.M. Afanasev and M. A. Chuev JETP **80** (3) 560 1995
2. M.Miglierini and J-M. Greneche J.Phys.Condens.Matter **9** 2321 1997
3. J-M. Greneche, A. Slawska-Waniewska Mat.Sci.a. Eng. **A226-228** 526 1997





## NANOCRYSTALLISATION OF FeCuNbB ALLOYS

T. Girchartd<sup>1</sup>, B. Friedrichs<sup>2</sup>, E. Woldt<sup>2</sup>, J. Hesse<sup>1</sup>,  
K. G. Efthimiadis<sup>3</sup>, S. C. Chadivasiliou<sup>3</sup>

1) Institut für Metallphysik und Nukleare Festkörperphysik, TU Braunschweig,  
Mendelssohnstr. 3, 38106 Braunschweig, Germany

2) Institut für Werkstoffkunde, TU Braunschweig, Langer Kamp 8,  
38106 Braunschweig, Germany

3) Aristotle University of Thessaloniki, GR-54006 Thessaloniki, Greece

**Abstract** -- We investigated the alloy system of  $Fe_{86-x}Cu_1Nb_xB_{13}$  ( $x=4, 5, 7$ ) in order to obtain information on the crystallisation behaviour of the amorphous precursor alloy and the resulting structural composition. Onset temperatures of different crystallisation steps were studied with DSC measurements. Dilatometric and thermomagnetic measurements as well as those of the electrical resistivity were applied in order to detect changes not being correlated with a change of the heat capacity. For a structural investigation, Mössbauer effect and electron diffraction experiments were carried out.

Our results show that - up to a certain annealing temperature depending on the Nb content - there is only a nanocrystalline  $\alpha$ -Fe phase, embedded in an amorphous matrix. At higher annealing temperatures crystalline FeB phases appear. ©1999 Acta Metallurgica Inc.

## INTRODUCTION

In 1988 Yoshizawa et al. reported on a new kind of Fe-based amorphous alloys which form - after an annealing process - a nanocrystalline structure (1). Those alloys have become well known as Finemet or Vitroperm. Their structure is the cause for many interesting physical properties (2,3). The grains in those alloys consist of FeSi, whereas the alloys discussed here do not contain any Si. When the amorphous ribbons of FeCuNbB alloys are annealed they develop in a first crystallisation step a nanocrystalline structure, containing  $\alpha$ -Fe grains embedded in an amorphous matrix. At higher annealing temperatures they form additional FeB phases. In order to learn more about the crystallisation behaviour of these alloys, we investigated them with different experimental techniques.

## EXPERIMENTAL

The amorphous ribbons of the three alloys were heated up with a rate of 3 K/min, starting at room temperature and going up to 1000 °C (or less, due to technical reasons). During that process the measurements were done. In the following we will discuss measurements

of the following properties: thermal expansion, heat flow, electrical resistivity and magnetisation. Due to the limited space we will focus on only one alloy, i. e. Fe<sub>82</sub>Cu<sub>1</sub>Nb<sub>4</sub>B<sub>13</sub>. The qualitative behaviour of the other two alloys is very similar.

## RESULTS AND DISCUSSION

Fig. 1 shows the development of four of the measured properties of Fe<sub>82</sub>Cu<sub>1</sub>Nb<sub>4</sub>B<sub>13</sub> versus temperature. In the upper part temperature ranges marked with letters A to E indicate interesting properties or developments.

### *A: invar behaviour*

In the temperature range A the sample shows an invar like behaviour, concerning length and resistivity. The Curie point of the amorphous sample ( $T_C=225$  °C) is reached. The other alloys have a lower Curie temperature (Nb<sub>5</sub>: 200 °C, Nb<sub>7</sub>: 165 °C).

### *B: structural relaxation*

Temperature range B reveals some structural relaxation. A reduced thermal expansion, indicating an increase of the density due to the reduction of free volume, and a weak heat emission over a wide temperature range can be observed.

### *C: 1<sup>st</sup> crystallisation step*

The first crystallisation takes place in the temperature range C, beginning already in range B. This can be seen by the narrow exothermal peak in the heat flow curve. Even more significant is the decreasing electrical resistivity and the increasing magnetisation, which cannot be caused by the amorphous phase. However there is no significant change observable with the dilatometer. A phase analysis, done via Mössbauer spectrometry and electron diffraction clearly shows the formation of crystalline  $\alpha$ -Fe grains in a remaining amorphous matrix. The grain size depends on the Nb content. Nb is enriched in the grain boundaries and finally stops the growth of the grains. The transmission electron microscope shows an average grain size of 30 nm; the alloy containing 5 at% Nb has grains of 10 nm diameter and the one with 7 at% has the smallest grains with only 3.5 nm in diameter.

Further nucleation processes take place in the range C-D, indicated by small exothermal DSC peaks. The step in the magnetisation curve hints to a second ferromagnetic phase besides Fe.

### *D: 2<sup>nd</sup> crystallisation step*

In the temperature range D a second crystallisation takes place, indicated by a narrow exothermal peak in the heat flow curve. This coincides with a notable contraction of the sample as seen in the dilatometer curve. A phase analysis points to the eutectic crystallisation of the remaining amorphous phase into  $\alpha$ -Fe and Fe<sub>3</sub>B. As we are already above the Curie point

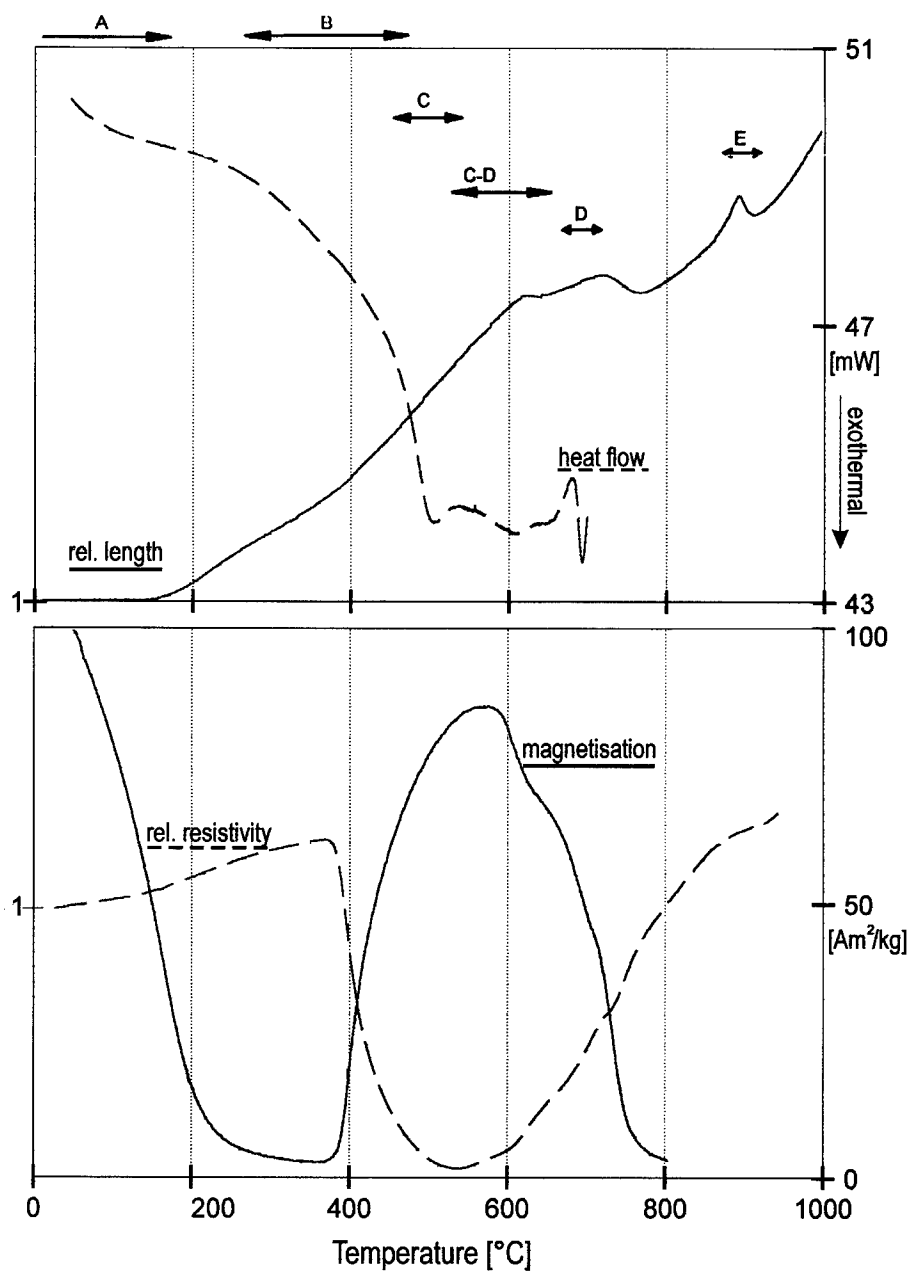


Figure 1. Relative length, relative resistivity (both normalised to room temperature), heat flow and magnetisation of  $\text{Fe}_{82}\text{Cu}_1\text{Nb}_4\text{B}_{13}$  vs. temperature

of Fe<sub>3</sub>B (500-550 °C, depending on the lattice type), the slight step in the magnetisation curve at about 700 °C might hint to Fe<sub>2</sub>B with T<sub>c</sub>=742 °C. Attempts to analyse the structure by electron diffraction however produced no clear results in favour of either borides. At the same time already existing grains grow strongly.

*E: 3<sup>rd</sup> transformation step*

In the temperature range E the coefficients of the electrical resistivity change. A strong contraction can be observed, which is caused by the  $\alpha$ - $\gamma$  phase transformation of the iron components. This transformation (and the contraction) is reversible when subsequently lowering the temperature, but with a hysteresis of about 100 K.

### SUMMARY

Phase and structural investigations - done by Mössbauer spectrometry and electron diffraction - show, that in the first crystallisation process only  $\alpha$ -Fe nanocrystals appear. There remains an amorphous phase still containing more than 50 % of the iron atoms in the sample. We have shown, that the crystallisation process of FeCuNbB alloys is very similar to that of the well known FeCuNbSiB. The main difference is - as there is no Si in these alloys - that no FeSi nanocrystals are formed, but  $\alpha$ -Fe grains. The nanostructure is very similar and so is the crystallisation in two steps. In both cases FeB phases develop during the second crystallisation step.

### ACKNOWLEDGEMENTS

The authors wish to thank Dr. G. Herzer, Vacuumschmelze GmbH, Hanau, Germany, for the amorphous samples. The work was financially supported by the Deutsche Forschungsgemeinschaft (DFG) and the "Internationales Büro des BMBF".

### REFERENCES

1. Y. Yoshizawa, S. Oguma and K. Yamauchi, *Journal of Appl. Physics* **64** (10), 6044, 1988
2. G. Herzer, *Physica Scripta* **T49**, 307, 1993
3. T. Graf, M. Kopcewicz and J. Hesse, *J. Phys: Condens. Matter* **8**, 3897, 1996



## HYDROXIDES AS PRECURSORS OF NANOCRYSTALLINE OXIDES

X. Bokhimi<sup>1</sup>, A. Morales<sup>1</sup>, M. Portilla<sup>2</sup>, and A. García-Ruiz<sup>3</sup>

1. Institute of Physics, UNAM, A. P. 20-364, 01000 México D. F., Mexico.

2. Faculty of Chemistry, UNAM, A. P. 70-197, 01000 México D. F., Mexico.

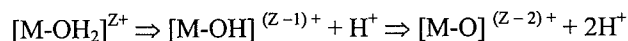
3. UPIICSA-COFAA, IPN, Té No. 950 Esq. Resina, 08400 México D. F., Mexico.

**Abstract.** The formation of nanocrystalline oxides by hydrolysis is analyzed. X-ray powder diffraction was used to measure atom distribution; when it was crystalline the structure was refined by the Rietveld method. Three systems were studied: zirconia, titania and magnesia; they were prepared by using the sol-gel technique. During hydrolysis, the proportions of aquo, hydroxo and oxo bindings determined the initial atom distribution and its evolution with temperature. In zirconia, the amorphous structure was fixed by aquo bondings; this structure was obtained in titania samples only at high water to alkoxide molar ratios. In magnesia system, synthesis ions also affected the concentration of these bindings. ©1999 Acta Metallurgica Inc.

### INTRODUCTION

Nanostructured oxides prepared chemically have hydroxides as intermediate precursor phases; for example, in the sol-gel technique where it is a consequence of hydrolysis.

When a transition metal ion  $M^{Z+}$  is dissolved in water, it becomes solvated by the surrounding water molecules and gives rise to the  $[M-OH_2]^{Z+}$  ion, which has a partial covalent bond between metal and oxygen atoms. Some charge transfers from the filled  $3a_1$  bonding orbital of the water molecule to the empty  $d$  orbitals of the transition metal ion [1]. This increases the positive partial charge on hydrogen and causes water molecules to become more acidic. Depending on the electron transfer, the following reactions occur:



If  $N$  (coordination) is the number of water molecules covalently bound to one cation  $M^{Z+}$ , the formula for any hydrolyzed ion can be written as  $[MO_NH_{2N-A}]^{(Z-A)+}$ , where  $A$  is defined as the molar ratio of hydrolysis. When  $A = 0$ , the result is an aquo-ion  $[M(OH_2)_N]^{Z+}$  with only aquo ligands ( $-OH_2$ ), while for  $A=2N$  it is an oxo-ion  $[TiO_N]^{(2N-Z)-}$  with only oxo ligands ( $=O$ ). If  $0 < A < 2N$ , the ion can be either an hydroxo complex  $[M(OH)_N]^{(Z-N)+}$  ( $A=N$ ) with only hydroxo ligands ( $-OH$ ), an oxo-hydroxo complex  $[MO_x(OH)_{N-x}]^{(N+x-Z)-}$  ( $A > N$ ), or an hydroxo-aquo complex  $[M(OH)_A(OH_2)_{N-A}]^{(Z-A)+}$  ( $A < N$ ). Therefore, oxo, hydroxo, and aquo ligands coexist in hydrolysis. When hydrolyzed samples are annealed, they dehydroxylize, changing the proportion of the different ligands.

In the present paper we report the temperature evolution of hydrolyzed zirconium, titanium, and magnesium until they form the corresponding nanocrystalline oxide.

## EXPERIMENTAL

Samples were prepared by using the sol-gel technique; details about synthesis are published elsewhere [2-5]. Atom distributions were measured by x-ray powder diffraction with  $\text{CuK}\alpha$  radiation; crystalline structures were refined with the Rietveld technique [6].

## RESULTS AND DISCUSSION

**Zirconia.** Samples annealed below 300°C were amorphous (Fig. 1A). The basic element building this structure is the zirconyl group  $[\text{Zr}_4(\text{OH})_8(\text{OH}_2)_{16}]^{8+}$ , which has 8 hydroxo-bridges and 16 aquo bindings [7]. Since the group has sixteen sites at which condensation takes place, polymeric growth can proceed in many different paths. Polymerization occurs byolation (hydroxo binding) between tetramers to produce oligomers, composed of a few zirconyl groups, distributed at random.

When samples were annealed, aquo bindings were transformed into hydroxo bonds, oligomers ordered partially and the samples crystallized. After heating samples at 400°C, they were composed of nanocrystalline tetragonal and monoclinic phases (Fig. 1B); for the refinement, these phases were modeled with the corresponding tetragonal and monoclinic structures of zirconia [5]; the tetragonal structure was significantly zirconium deficient (4.8 %). When samples were annealed at higher temperatures, the tetragonal phase was transformed into the monoclinic one (Fig. 1C).

The large zirconium deficiency can be explained by assuming that the system was not only composed of zirconium and oxygen, but of zirconium, oxygen, and hydrogen atoms. Oxygen atoms occupied the same sites that they do in tetragonal zirconia, but hydrogen was associated to some of them, forming the hydroxyl groups that were stabilizing the tetragonal symmetry [5]. A simple analysis of electrical charge equilibrium implies that empty zirconium sites must be in hydroxyls neighborhood.

**Titania.** At low temperatures, the atom distribution depended on hydrolysis conditions. The strongly hydrolyzed titanium, which was achieved at large water to alkoxide molar ratios, was amorphous (Fig. 2A). Since a high water to alkoxide molar ratio produces insoluble giant molecules [8], the observed amorphous structure can be explained as a non-correlated mixture of these molecules. Their structure is unknown; but it must contain many aquo bindings.

At low and medium water to alkoxide molar ratios, samples contained only nanocrystalline anatase and brookite (Fig.2B). FTIR studies shows that they have many hydroxyls in their crystalline structures [4]; the number of hydroxyls decreases with temperature, while the phases transform into rutile. After refining crystalline structures, we observed that anatase and brookite were titanium deficient; this was produced by the presence of hydroxyls in the crystalline structures.

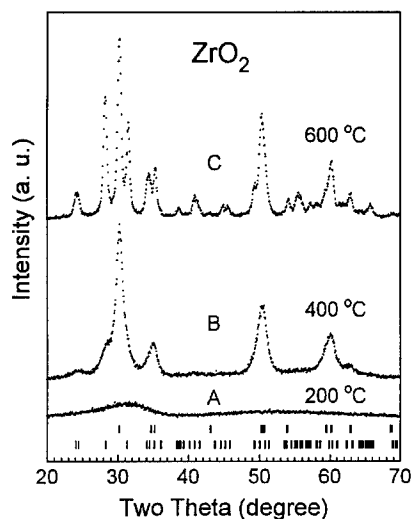


Fig. 1 Sol-gel zirconia annealed at different temperatures. Upper tick marks correspond to tetragonal zirconia; lower, to monoclinic zirconia.

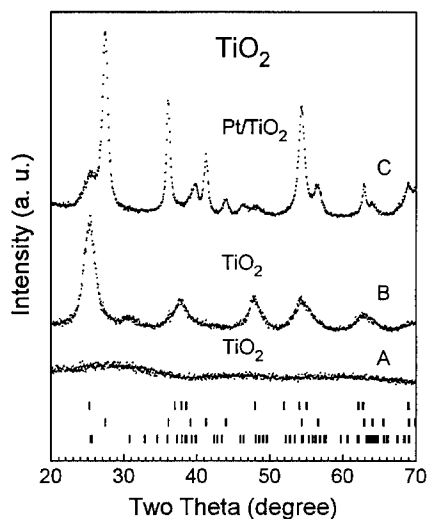


Fig. 2 Sol-gel titania prepared with a large (A) and a small (B) water to alkoxide molar ratio, and doped with platinum (C). Upper tick marks correspond to anatase; middle, to rutile; and lower, to brookite.

Rutile can also be produced at low temperatures (Fig. 2C), this occurred by doping the sample with platinum [9], which catalyzes the generation of oxo bindings.

**Magnesia.** During synthesis, not only water to alkoxide molar ratio determined the atom distribution, but also all involved ions (Figs. 3 and 4) [3]. When only hydroxyls were present, the starting phase was nanocrystalline MgO (Fig. 3A); this group favors the formation of oxo bindings. When carboxyl was the group, the initial phase was glushinskite ( $C_2MgO_4 \cdot 2H_2O$ ) (Fig. 3B); this phase was partially transformed into nanocrystalline brucite and periclase when the sample was annealed at 300 °C in air (Fig. 3C). Ammonium ions gave rise to an amorphous structure (Fig. 4A); this behavior changed when platinum was added to the solution [4]; it promoted the formation of hydroxo bindings, producing nanocrystalline brucite (Fig. 4B).

## CONCLUSIONS

The aquo, hydroxo, and oxo bindings, generated during hydrolysis, determined the initial atom distribution and its crystallization in nanostructured phases. The proportion of each binding depended on the system and the ions present in the sample preparation. A large proportion of aquo bindings favored the formation of amorphous structures. These bindings are easily transformed at low temperatures, generating nanocrystalline phases.

When samples were annealed, the produced crystalline oxides were rich in hydroxyls that stabilized their structure and gave rise to cation vacancies.

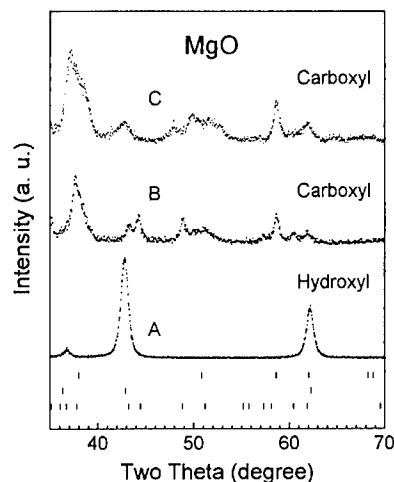


Fig. 3 MgO prepared with different hydrolysis catalysts: (A) HCl, (B) and (C) acetic acid. Upper tick marks correspond to brucite; middle, to MgO and lower to glushinskite.

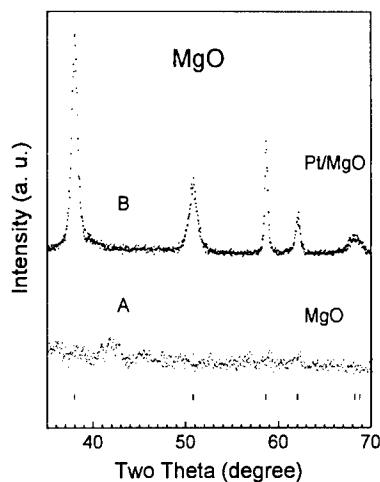


Fig. 4 Sol-gel MgO: (A) non-doped, (B) doped with platinum. Tick marks correspond to brucite.

## REFERENCES

1. Livage, J., Henry, M. and Sánchez, C., *Prog. Solid State Chem.*, 1988, 18, 259.
2. Bokhimi, Morales, A., López, T. and Gómez, R., *J. Solid State Chem.*, 1995, 115, 411.
3. Bokhimi, Aceves A., Novaro, O., López, T. and Gómez, R., *J. Phys. Chem.*, 1995, 99, 14403.
4. Sánchez, E., López, T., Gómez, R., Bokhimi, Morales, A. and Novaro, O., *J. Solid State Chem.*, 1996, 122, 309.
5. Bokhimi, X., Morales, A., Novaro, O., Portilla, M., López, T., Tzompanzi, F. and Gómez, R., *J. Solid State Chem.*, 1998, 135, 28.
6. "The Rietveld Method", Edited by R. A. Young, Oxford University Press, N. Y, USA, 1993.
7. Turrillas, X., Barnes, P., Tarling, S. E., Jones, S. L., Norman, C. J. and Ritter, C., *J. Mater. Sci. Lett.*, 1993, 12, 223.
8. Bradley, D. C., Gaze, R. and Wardlaw W., *J. Chem. Soc.*, 1955, 3977.
9. Sanchez, E., López, T., Gómez, R., Bokhimi, Morales, A. and Novaro, O., *J. Solid State Chem.*, 1996, 122, 309.





## NANOCRYSTALLINE TETRAGONAL ZIRCONIA STABILIZED WITH YTTRIUM AND HYDROXYLS

X. Bokhimi<sup>1</sup>, A. Morales<sup>1</sup>, O. Novaro<sup>1</sup>, T. López<sup>2</sup>, R. Gómez<sup>2</sup>, T. D. Xiao<sup>3</sup>, and P. R. Strutt<sup>3</sup>

1. Institute of Physics, UNAM, A. P. 20-364, 01000 México D. F., Mexico.

2. Department of Chemistry, UAM-I, A. P. 54-534, 09340 México D. F., Mexico.

3. Imframmat Co., 20 Washington Av., Suite 106, North Haven, CT 06473-2342, USA.

**Abstract.** *Nanocrystalline tetragonal zirconia was prepared by soft chemistry: via the hydrolysis of an aqueous solution of zirconyl and yttrium chlorides, and by using the sol-gel technique with zirconium n-butoxide as precursor and HCl, CH<sub>3</sub>COOH, and NH<sub>4</sub>OH as hydrolysis catalysts. In the samples with yttrium, the tetragonal phase appeared yet at crystallization beginning. Since the x-ray diffractograms of the amorphous samples were equal and independent of yttrium concentration, it is suggested that yttrium substituted for zirconium atoms already in the formation of the amorphous structure. In the sol-gel samples, hydroxyls stabilized the tetragonal phase. After sample dehydroxylation at 600 °C, the main phase was monoclinic zirconia, except in the samples prepared with acetic acid; here, the main phase was tetragonal zirconia, which was stabilized by carboxyls. ©1999 Acta Metallurgica Inc.*

### INTRODUCTION

Zirconia can exist in three polymorphic phases: one monoclinic, one tetragonal and one cubic. In polycrystalline samples, the monoclinic is the stable phase at room temperature; the other two are only stable at high temperatures. The tetragonal and cubic phases also exist at room temperature after doping zirconia with atoms like Ca, Mg, Y, Ce, ... [1]. When zirconia is produced by soft chemistry, the tetragonal phase can also be stabilized by the hydroxyls involved in the synthesis [2].

Nowadays, zirconia is one of the most important ceramics; it has unique physical and chemical properties that allow it to be used as oxygen sensor [3], catalyst support [4], corrosive coating [5], and as inclusion in composites for increasing toughness [6]. These properties change with crystallite size; in special, when it is of the order of nanometers. With these dimensions, zirconia can also be used as a ceramic binder for high temperatures, or as a self-lubricating material in sliding.

Since the tetragonal is the most used zirconia phase in applications, its production and characterization is very important. To contribute to the characterization of this phase, we prepared nanocrystalline tetragonal zirconia by using soft chemistry, and characterized, by x-ray diffraction, its stabilization with temperature.

## EXPERIMENTAL

Nanocrystalline tetragonal zirconia stabilized with yttrium was prepared via the hydrolysis of an aqueous solution of zirconyl and yttrium chlorides; yttrium concentration varied from 0.0 to 5.0 mol %. The sol-gel nanostructured tetragonal zirconia was prepared with zirconium *n*-butoxide as precursor and HCl, CH<sub>3</sub>COOH, and NH<sub>4</sub>OH as hydrolysis catalysts.

Crystalline structures were measured with x-ray powder diffraction (CuK $\alpha$  radiation), and refined by using the Rietveld technique [7].

## RESULTS AND DISCUSSION

The samples prepared with zirconyl chloride had an amorphous atom distribution when they were annealed below 300°C (Fig. 1); their x-ray diffraction patterns were independent of yttrium concentration. This implies that yttrium atoms substituted for zirconium in the zirconyl group (Fig. 2), which is the basis of the amorphous atom distribution [8].

When samples were annealed at 400°C, they crystallized (Fig. 3). The sample without yttrium (Fig. 3A) was a mixture of nanocrystalline monoclinic zirconia (82 wt. %) and tetragonal zirconia (18 wt. %). Yttrium-doped samples only had nanocrystalline tetragonal zirconia with a bimodal distribution (Figs. 3B and 3C): average crystallite sizes were 7.2(6) and 19.9(5) nm for 2.5 mol % yttrium, and 6(1) and 12.2(2) nm for 5.0 mol %. When samples were annealed at higher temperatures, the bimodal distribution disappeared, but the average crystallite size did not grow significantly.

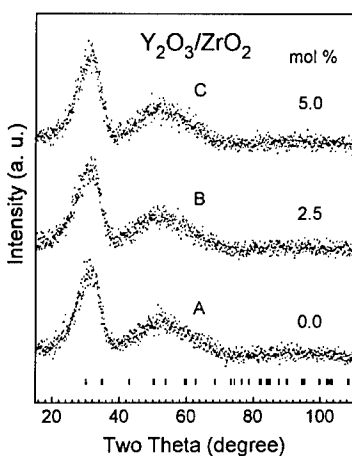


Fig. 1 Zirconia calcined at 200°C and doped with different yttrium concentrations. Tick marks correspond to the tetragonal phase

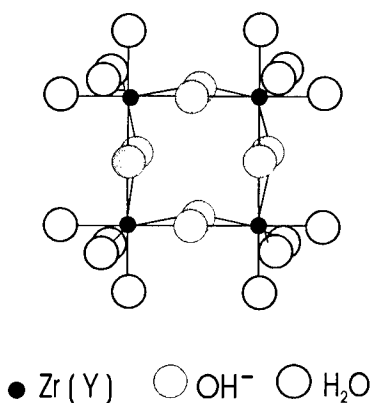


Fig. 2 Zirconyl group.

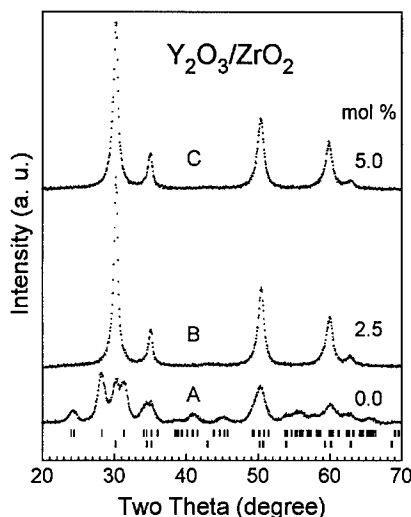


Fig. 3 Doped zirconia, calcined at  $400^\circ\text{C}$ , for different yttria concentrations. Upper tick marks correspond to monoclinic zirconia; the lower, to the tetragonal phase.

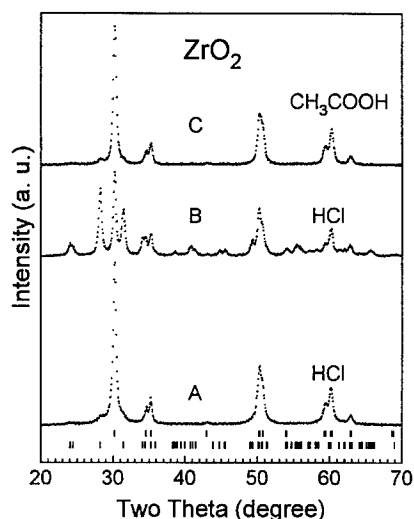


Fig. 4 sol-gel Zirconia: prepared with  $\text{HCl}$  and calcined at  $400^\circ\text{C}$  (A) and  $600^\circ\text{C}$  (B); prepared with  $\text{CH}_3\text{COOH}$  and annealed at  $600^\circ\text{C}$  (C). Upper tick marks correspond to tetragonal zirconia; the lower, to the monoclinic phase.

The zirconia samples prepared by the sol-gel technique were amorphous when they were heated below  $300^\circ\text{C}$ ; this occurred, because zirconyl group (Fig. 2) has 16 aquo bindings at which condensation randomly occurs, preventing crystallization.

When samples were annealed at higher temperatures, the hydroxo bridges (Fig. 2) between zirconium atoms were transformed, causing the system to crystallize into the tetragonal zirconia nanophase (Fig. 4A). In microcrystalline zirconia, this phase is only stable at high temperatures [9], or when it is doped with large ions [1].

During sample preparation, the ions present in the synthesis were hydroxyls, *n*-butoxyls, and (through the hydrolysis catalysts)  $\text{Cl}^-$ , methyls, carboxyls, and ammonium. Since methyl and *n*-butoxyl groups have only carbon and hydrogen, to incorporate them into the crystalline structure of zirconia, carbon must substitute for oxygen, which, however, requires a lot of energy; therefore, they were discarded to stabilize the tetragonal structure. If  $\text{Cl}^-$  ions formed part of the tetragonal structure, they would substitute for oxygen atoms too, or form chlorate ions, which also requires too much energy; therefore, they were also discarded as structure stabilizers. If ammonium ions participated in tetragonal structure, nitrogen atom would substitute for oxygen, which can not occur at the used synthesis temperatures.

In sample preparation, the only groups having oxygen atoms that could occupy sites in the crystalline structure of zirconia, were hydroxyls and carboxyls. Since hydroxyls were present in all samples, it can be assumed they stabilized the tetragonal structure. When samples were annealed at 600°C, at which they were strongly dehydroxylated, the tetragonal phase was only stable in the sample prepared with acetic acid as hydrolysis catalyst (Figs. 4B and 4C). This implies that carboxyls also stabilized this structure.

### CONCLUSIONS

Yttrium stabilized the tetragonal phase of zirconia yet at crystallization beginning. This and the fact that the x-ray diffractogram of the amorphous phases were the same for doped and non-doped zirconia, imply that yttrium substituted for zirconium atoms already in the amorphous structure.

In sol-gel synthesis, hydroxyls and carboxyls were incorporated into zirconia crystalline structure, stabilizing the tetragonal phase. In all samples heated at 400°C, the main phase was nanocrystalline tetragonal zirconia; but at 600°C, it was the main phase only in the samples prepared with acetic acid: carboxyls participated in the stabilization.

This result opens the possibility of finding new tetragonal zirconia stabilizers based on C-O bindings.

### REFERENCES

1. Boutz, M. M. R., Winnubst, A. J. A., Van Langerak, B., Oldescholtenhuis, R. J. M., Kreuwel, K. and Burggraaf, A. J., *J. Mater. Sci.*, 1995, 30, 1854.
2. Bokhimi, X., Morales, A., Novaro, O., Portilla, M., López, T., Tzompanzi, F. and Gómez, R., *J. Solid State Chem.*, 1998, 135, 28.
3. Fouletier, J., *Ceramurgia*, 1995, 25, 209.
4. Gómez, R., López, T., Ferrat, G., Domínguez, J. M. and Schifter, I., *Chem. Lett.*, 1992, 1941.
5. Yuan, Q.-M., Tan, J.-Q. and Jin, Z.-G., *J. Am. Ceram. Soc.*, 1986, 69, 265.
6. Garvie, R. C., Hannink, R. H. and Pascoe, R. T., *Nature*, 1975, 258, 703.
7. Bokhimi, Morales, A., Lucatero, M. A. and Ramírez, R., *Nanostructured Materials*, 1997, 9, 315.
8. Turrillas, X., Barnes, P., Tarling, S. E., Jones, S. L., Norman, C. J. and Ritter, C., *J. Mater. Sci. Lett.*, 1993, 12, 223.
9. Ruff, O. and Ebert, F., *Z. Anorg. Allg. Chem.*, 1929, 180, 19.



Pergamon

NanoStructured Materials, Vol. 12, pp. 597-600, 1999

Elsevier Science Ltd

© 1999 Acta Metallurgica Inc.

Printed in the USA. All rights reserved

0965-9773/99/\$-see front matter

PII S0965-9773(99)00192-0

## MORPHOLOGICAL CHARACTERISATION OF NANOCRYSTALS WITH LAYERED STRUCTURES

D. V. Szabó, D. Vollath

Forschungszentrum Karlsruhe, Institut für Materialforschung III  
P.O. Box 3640, D- 76021 Karlsruhe, Germany

**Abstract** -- Nanocrystalline compounds with layered structures such as  $\text{MoS}_2$ ,  $\text{WS}_2$ ,  $\text{MoSe}_2$ ,  $\text{WSe}_2$ ,  $\text{SnS}_2$ , or  $\text{ZrSe}_2$  show interesting structural features. These particles are synthesised in a microwave plasma. The morphology of the particles is characterised by high resolution transmission electron microscopy. Depending on the parameters of the synthesis different morphologies are observed. The size of the particles is in a range from 5 to 10 nm. Many odd shaped particles with bent lattice planes and varying distances between the planes are observed. Additionally, the lattice parameters differ from sizes found in crystals in the micrometer range. ©1999 Acta Metallurgica Inc.

### INTRODUCTION

Some sulphides and selenides of the transition metals crystallise in layered structures of the type C7 ( $\text{MoS}_2$ -structure) or C6 ( $\text{PbJ}_2$ -structure). These structures consist of covalently bond groups of three planes. In these groups one hexagonal plane of metal ions  $Me$  is placed between two layers of the non-metal  $S$ . Therefore, these structures exhibit a sequence of layers like  $S\text{-}Me\text{-}S$   $S\text{-}Me\text{-}S$   $S\text{-}Me\text{-}S$ . The binding between these layers is of the van der Waals type. In the C7 structure the stacking sequence is  $B\text{-}A\text{-}B$   $A\text{-}B\text{-}A$   $B\text{-}A\text{-}B$ , whereas in the C6 structure the hexagonal layers have a stacking sequence of  $B\text{-}C\text{-}A$   $B\text{-}C\text{-}A$   $B\text{-}C\text{-}A$ . Tenne et al. (1) found nested fullerene like onion crystals in  $\text{WS}_2$  or  $\text{MoS}_2$  thin films on quartz substrates. Within this study nanoscaled sulphide or selenide particles are synthesised in a microwave plasma under various experimental conditions and characterised by high resolution electron microscopy.

### EXPERIMENTAL

Nanoscaled sulphide or selenide particles were synthesised using the microwave plasma process (2,3). The plasma is powered either from a magnetron with a frequency of 2.45 or 0.915 GHz. The reactions are performed in quartz tubes passing the microwave cavities. For the formation of sulphides the precursors, carbonyls of the metals, are vaporised outside the reaction vessel and introduced with preheated argon carrier gas. To obtain sulphides, a mixture of Ar/1 vol%  $\text{H}_2\text{S}$  is used as reaction gas. For the formation of selenides the chlorides of the metals and  $\text{SeCl}_4$  are mixed mechanically in the proper stoichiometric

ratio and reacted under Ar/4 vol% H<sub>2</sub>. The pressure in the system was set to 10 mbar for the 2.45 GHz and to 30 mbar for the 0.915 GHz equipment. The nanoparticles are formed in the plasma zone which is located at the intersection between the reaction tube and the microwave wave guide. The reaction time in the plasma zone is in the range of 4 ms in the case of 2.45 GHz and 8 ms in the case of 0.915 GHz. The energy transfer to charged particles in an oscillating electrical field is proportional to  $1/(mf^2)$ , with  $m$  = mass of the charged particles and  $f$  = frequency. Therefore, performing the synthesis at 2.45 GHz means in general lower reaction temperatures (150 - 250°C) and shorter residence time in the plasma as compared to a synthesis performed at 0.915 GHz (500° - 600°C). The morphology of the nanoparticles is characterised by high resolution electron microscopy. Lattice fringes were evaluated quantitatively in the Fourier space to obtain precise values of the lattice spacing.

## RESULTS AND DISCUSSION

Depending on the synthesis parameters, different morphologies are observed. Besides more or less platelet-like particles, many particles exhibiting odd shapes, bent lattice planes, varying distances between the planes or step dislocations are found.

In the case of MoS<sub>2</sub> irregularly shaped particles with sizes from 5 to 8 nm are formed at 250°C. The spacing between the lattice fringes were determined to be  $0.65 \pm 0.07$  nm, which is larger than the standard value of 0.615 nm for the {0002} planes. At longer residence times and higher reaction temperatures (0.915 GHz) bent lattice planes with varying distances and polyhedral crystals are formed. This is shown in figure 1. The power spectrum of the image shows a relatively broad distribution of the lattice spacing for the {0002} planes.

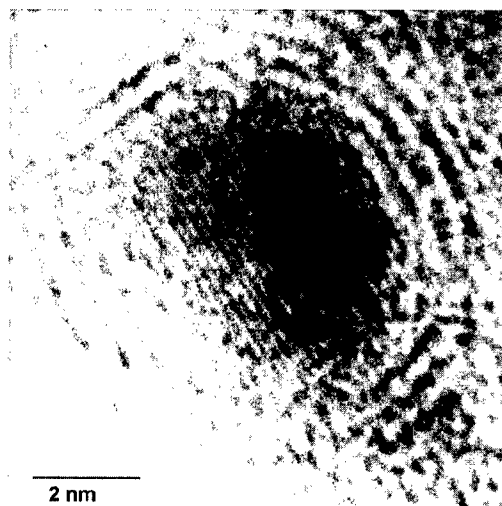


Figure 1: High resolution micrograph and power spectrum of a polyhedron shaped MoS<sub>2</sub> particle. The side walls, consisting of three S-Mo-S triple planes have a spacing of 0.64 nm, whereas the distance of the inner lattice fringes is 0.23 nm. The power spectrum reveals a broad radial distribution of the spots representing the {0002} planes.

In the case of WS<sub>2</sub> synthesised at 160°C, small and uniform particles with bent lattice planes are formed (Figure 2). The distance between these fringes is 0.65 nm, which again is larger than the distance of the {0002} planes in macroscopic crystals. Additionally, dislocations are found in the {0002} planes of particles smaller than 5 nm (Figure 3). As shown in Figure 4 particles with heavily bent planes are found.

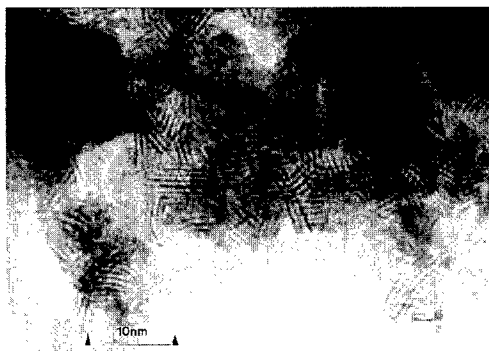


Figure 2: Typical appearance of  $\text{WS}_2$  particles produced at  $160^\circ\text{C}$  and 2.45 GHz. Polyhedral shaped particles, bent lattice planes, and dislocation like structures can be seen clearly.

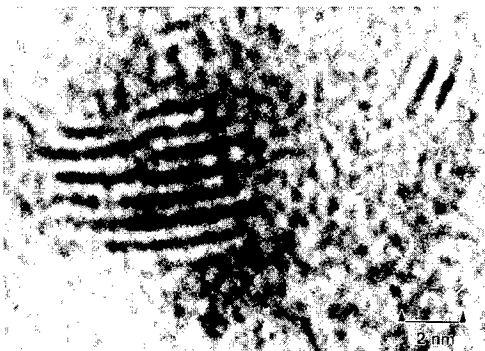


Figure 3:  $\text{WS}_2$  particle showing a step dislocation in the  $\{0002\}$  plane. The size of the particle is about 4-5 nm.

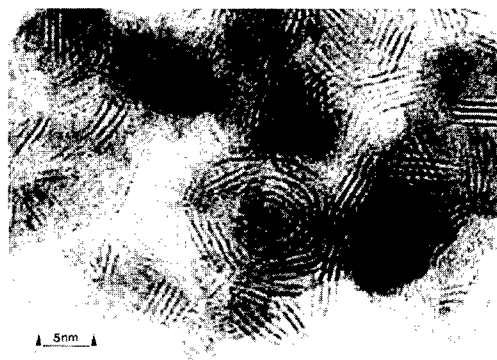


Figure 4: A collection of  $\text{WS}_2$  particles produced at  $580^\circ\text{C}$  and 0.915 GHz.

The structural features of  $\text{MoSe}_2$  are similar to those of  $\text{MoS}_2$  and  $\text{WS}_2$  (Figure 5). In this case the distance between the layers is 0.59 nm, which is about 8.7 % smaller than  $\{0002\}$  distances in macroscopic crystals. In contrast to  $\text{MoS}_2$ ,  $\text{WS}_2$  or  $\text{MoSe}_2$ , belonging to the same structural type C7, glassy particles are found in  $\text{WSe}_2$  synthesised at a temperature of  $200^\circ\text{C}$ . At a synthesis temperature of  $500^\circ\text{C}$  these glassy particles contain crystalline inclusions with sizes in the range from 3 to 5 nm. These inclusions are crystallised in a different not layered structure. The configuration of glassy particles with crystallised inclusions is obviously not a stable one. During observation in the electron microscope these particles change their structure into the expected layered one.

Nanoparticles belonging to the structural type C6 exhibit completely different features.  $\text{SnS}_2$  synthesised at 2.45 GHz exhibit a rope-like morphology. These ropes have a length of up to 50 nm and consist of about 8 to 10 layers. The layers within these ropes contain dislocations (Figure 6). The distance between these layers is 0.59 nm and can be attributed to the  $\{0002\}$  planes of  $\text{SnS}_2$ .  $\text{SnS}_2$  is identified by electron diffraction (JCPDS 21-1231). Layered, rope like structures are found in  $\text{ZrSe}_2$ , too (Figure 7). These ropes contain highly distorted lattice planes and varying distances between the layers. During extended observation in the electron microscope fullerene like onions (Figure 8) are formed.

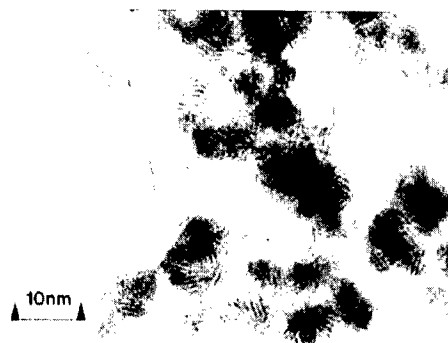


Figure 5: Typical morphology of  $\text{MoSe}_2$ . Odd shaped particles and dislocation like structures can be seen.



Figure 6: Rope-like structure of  $\text{SnSe}_2$ . The distance of the lattice fringes is 0.59 nm.

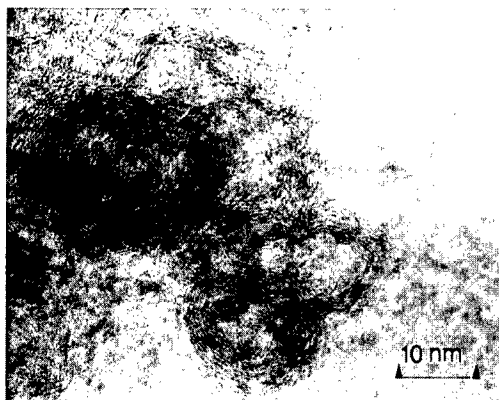


Figure 7: Typical rope-like morphology found in  $\text{ZrSe}_2$ . The structures seem to be closed. The lattice spacing is 0.36 nm.

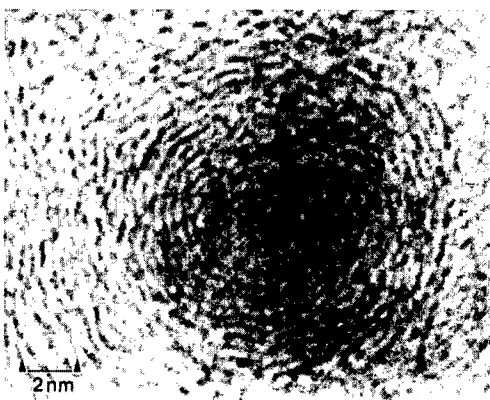


Figure 8: Onion-like particle of  $\text{ZrSe}_2$ . The distances between the fringes is in the range of 0.34 nm

### Conclusions

It is possible to synthesise nanoscaled sulphides and selenides by the microwave plasma process. The size of the particles is in a range from 5 to 10 nm. Due to the short residence time in the plasma and the small particle size many particles with odd shapes, bent lattice planes, varying distances between the planes, or step dislocations are formed. The investigated C7 type compounds  $\text{MoS}_2$ ,  $\text{WS}_2$ ,  $\text{MoSe}_2$ , and  $\text{WSe}_2$  show similar as well as different structural features whereas the C6 type compounds  $\text{SnS}_2$  and  $\text{ZrSe}_2$  exhibit a rope-like morphology. In some cases the particles are not stable under the electron beam.

### References

1. Tenne, R., Margulis, L., Genut, M. and Hodes, G., *Nature*, 1992, 360, 444
2. Vollath, D., Szabó, D. V. and Seith, B., German patent application, 1996, 19628357.4
3. Vollath, D. and Szabó, D. V., *Materials Letters*, accepted for publication, 1997



---

## Notes for the Guidance of Authors

### NanoStructured Materials

Manuscripts will be considered for publication which are short papers of new work or discussions of work already published. Papers should address the aspects of nanostructured materials defined in the Aims and Scope statement. Manuscripts must be submitted in English *only* and it is the responsibility of *authors* to see that proper use of English and style is maintained. Poorly written papers will be returned to authors, thus delaying publication.

*Submission of Papers:* An original and one copy, **both containing original micrographs**, plus one diskette copy of manuscripts should be submitted. Manuscripts should be submitted directly to: Editorial Office, Professor Thomas Tsakalakos, Nanostructured Materials, College of Engineering, Rutgers University, 98 Brett Road, Piscataway, NJ 08854-8058, USA. Tel: +1 732-445-2888; Fax: +1 732-445-3229; Email: [nanostru@rci.rutgers.edu](mailto:nanostru@rci.rutgers.edu) or [tsakalak@rci.rutgers.edu](mailto:tsakalak@rci.rutgers.edu)

Please note that email submissions are not accepted. Authors of multiple-authored papers must sign a statement to the Principal Editor that all authors have agreed to the submission of the paper.

*Acceptance of Papers:* The Editors and competent referees will decide whether a paper is to be accepted or not. This procedure is designed to ensure that decisions are reached in the minimum possible time.

*Format and Layout:* Manuscripts should be typed single spaced on sheets of 8.5" × 11" (21.6 × 27.94 cm) (A4) paper, leaving a space of 8.5" × 4.5" (21.6 × 11.43 cm) on top of the first page for printing the title, authors' affiliations and received/accepted dates. Articles should include an abstract of approximately 100–150 words. Appropriate blank space should be left within the text for the positioning of figures and tables.

Authors should send figures that need little or no reduction for printing. The figures should be no more than 5.67" (14.4 cm) wide. Depths may vary, but one third of the text page, i.e. 2.5" (6.35 cm), would be ideal. Halftone micrographs are reduced on average by 25% and line art may be reduced by 25% to 50% to fit the page. Because of the reduction of the micrographs, magnifications should be indicated by nm,  $\mu$ m, and mm markers. Markers and other lettering should be placed 3 mm from the edge of the micrograph.

References should be indicated in the text by consecutive numbers in parentheses, e.g. (1,2), as part of the text, not raised above it, the full reference being cited in a numbered list at the end of the text. References should contain the names of the authors together with their initials, the title of the journal, volume number, first page number, and year, as illustrated below. References to books should contain the publisher's name and location. Use single spacing between references.

[1] Sack HS, Moriarity MC. Solid State Comm. 1955;3:93.

[2] Rosenberg HS, Low Temperature Solid State Physics. Oxford: Clarendon Press, 1963:210.

SI units must be used exclusively. Use only standard SI symbols and abbreviations in text and illustrations.

**Computer Disks:** In order to speed publication and ensure accuracy, authors are required to submit a computer disk (5.25" or 3.5" HD/DD disk) containing their paper along with the manuscript to the Editorial Office. Please observe the following criteria: (1) Send a hard copy and computer disk when first submitting your paper. (2) When your paper has been refereed, revised if necessary and accepted, send a disk containing the *final* version with the *final* hard copy. **Make sure that the disk and hard copy match exactly.** (3) Specify what software was used, including which release (e.g., WordPerfect 6.0). (4) Specify what computer was used (either IBM compatible PC or Apple Macintosh). (5) Include both the text file and ASCII file, and separate table and illustration files, if available. (6) The file should follow the general instructions on style/arrangement and, in particular, the reference style of this journal as given in the Notes for the Guidance of Authors. (7) The file should be single-spaced and the wrap-around end-of-line feature should be used (i.e., no returns at the end of each line). All textual elements should begin flush left, with no paragraph indents. Place two returns after every element such as title, headings, paragraphs, figure and table callouts, etc. (8) Keep a backup disk for reference and safety.

**Color:** Figures can be reproduced in full color, however, the author or institution will be expected to contribute towards the costs involved. For 1999, the cost of printing in color will be US\$650.00 per printed color page.

**Copyright Agreements:** Since the enactment of U.S. Copyright laws on January 1, 1978, a Transfer of Copyright Agreement is required by the publisher to accompany every article accepted for publication. Upon acceptance for publication, the corresponding author of each manuscript will be sent an agreement to be completed prior to preparation for publication.

Reprints and copies of the issue (at a specially reduced rate) can be ordered on the form which accompanies the letter of acceptance. This along with the Transfer of Copyright Form should be returned to: Elsevier Science, Inc., 655 Avenue of the Americas, New York, NY 10010 at your earliest convenience.